FUSION ENERGY 1996

SIXTEENTH CONFERENCE PROCEEDINGS
MONTREAL, CANADA
7-11 OCTOBER 1996

IAEA

Vol.3

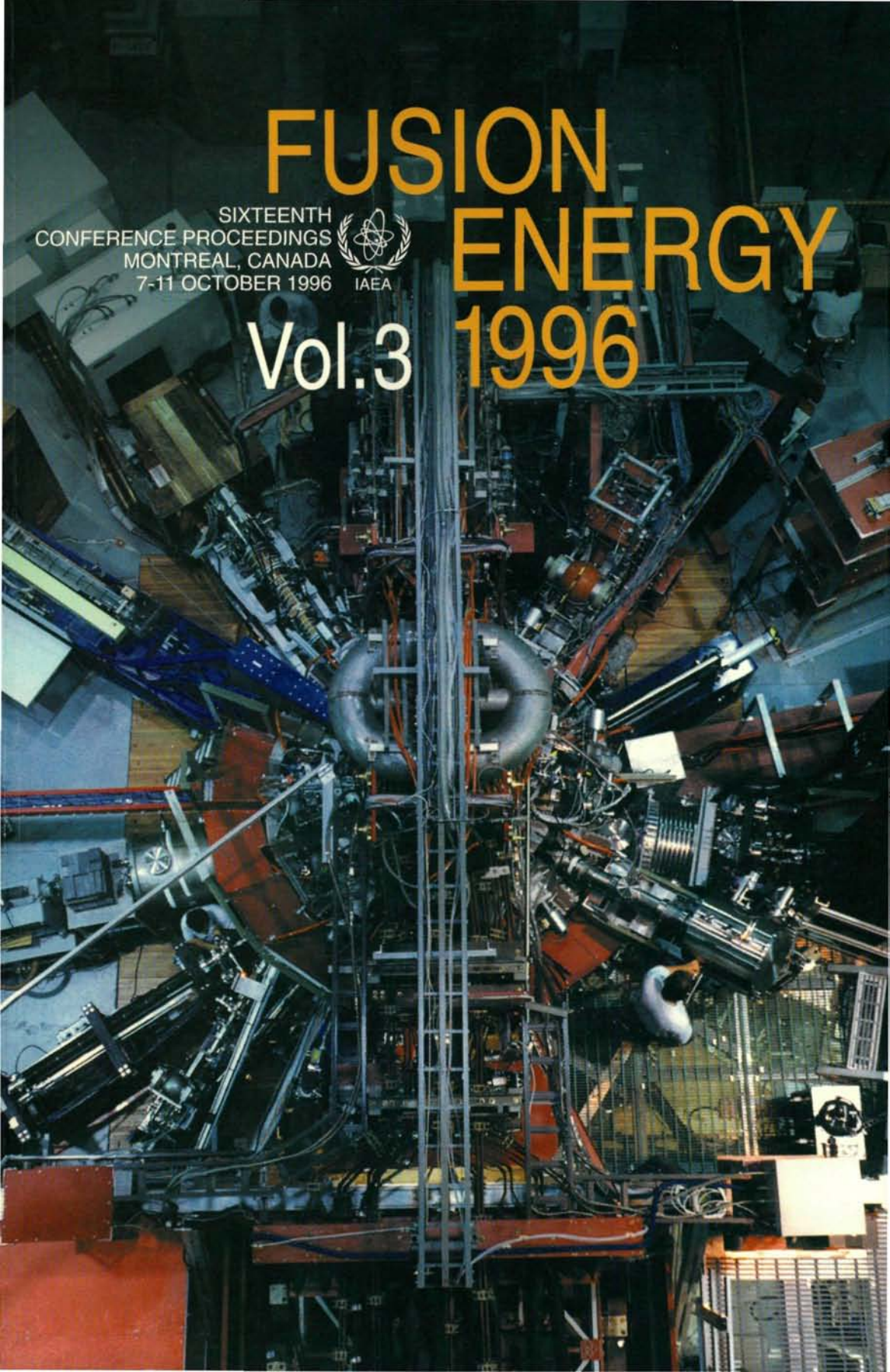

The cover picture shows the top view of the Tokamak de Varennes (TdeV) and its diagnostics. By courtesy of the Centre canadien de fusion magnétique (CCFM), Varennes, Quebec, Canada.

FUSION ENERGY 1996

VOLUME 3

The following States are Members of the International Atomic Energy Agency:

AFGHANISTAN
ALBANIA
ALGERIA
ARGENTINA
AUSTRALIA
ARMENIA
AUSTRIA
BANGLADESH
BELARUS
BELGIUM
BOLIVIA
BOSNIA AND HERZEGOVINA
BRAZIL
BULGARIA
CAMBODIA
CAMEROON
CANADA
CHILE
CHINA
COLOMBIA
COSTA RICA
COTE D'IVOIRE
CROATIA
CUBA
CYPRUS
CZECH REPUBLIC
DEMOCRATIC REPUBLIC OF THE CONGO
DENMARK
DOMINICAN REPUBLIC
ECUADOR
EGYPT
EL SALVADOR
ESTONIA
ETHIOPIA
FINLAND
FRANCE
GABON
GEORGIA
GERMANY
GHANA
GREECE
GUATEMALA
HAITI
HOLY SEE
HUNGARY
ICELAND
INDIA
INDONESIA
IRAN, ISLAMIC REPUBLIC OF
IRAQ
IRELAND
ISRAEL
ITALY
JAMAICA
JAPAN
JORDAN
KAZAKHSTAN
KENYA
KOREA, REPUBLIC OF
KUWAIT
LATVIA
LEBANON
LIBERIA
LIBYAN ARAB JAMAHIRIYA
LIECHTENSTEIN
LITHUANIA
LUXEMBOURG
MADAGASCAR
MALAYSIA
MALI
MALTA
MARSHALL ISLANDS
MAURITIUS
MEXICO
MONACO
MONGOLIA
MOROCCO
MYANMAR
NAMIBIA
NETHERLANDS
NEW ZEALAND
NICARAGUA
NIGER
NIGERIA
NORWAY
PAKISTAN
PANAMA
PARAGUAY
PERU
PHILIPPINES
POLAND
PORTUGAL
QATAR
REPUBLIC OF MOLDOVA
ROMANIA
RUSSIAN FEDERATION
SAUDI ARABIA
SENEGAL
SIERRA LEONE
SINGAPORE
SLOVAKIA
SLOVENIA
SOUTH AFRICA
SPAIN
SRI LANKA
SUDAN
SWEDEN
SWITZERLAND
SYRIAN ARAB REPUBLIC
THAILAND
THE FORMER YUGOSLAV REPUBLIC OF MACEDONIA
TUNISIA
TURKEY
UGANDA
UKRAINE
UNITED ARAB EMIRATES
UNITED KINGDOM OF GREAT BRITAIN AND NORTHERN IRELAND
UNITED REPUBLIC OF TANZANIA
UNITED STATES OF AMERICA
URUGUAY
UZBEKISTAN
VENEZUELA
VIET NAM
YEMEN
YUGOSLAVIA
ZAMBIA
ZIMBABWE

The Agency's Statute was approved on 23 October 1956 by the Conference on the Statute of the IAEA held at United Nations Headquarters, New York; it entered into force on 29 July 1957. The Headquarters of the Agency are situated in Vienna. Its principal objective is "to accelerate and enlarge the contribution of atomic energy to peace, health and prosperity throughout the world".

Printed by the IAEA in Austria
December 1997
STI/PUB/1004

PROCEEDINGS SERIES

FUSION ENERGY 1996

PROCEEDINGS OF THE
SIXTEENTH INTERNATIONAL CONFERENCE
ON FUSION ENERGY
ORGANIZED BY THE
INTERNATIONAL ATOMIC ENERGY AGENCY
AND HELD IN MONTREAL, 7–11 OCTOBER 1996

In three volumes

VOLUME 3

INTERNATIONAL ATOMIC ENERGY AGENCY
VIENNA, 1997

VIC Library Cataloguing in Publication Data

International Conference on Fusion Energy (16th : 1996 : Montreal, Canada)
Fusion energy 1996 : proceedings of the sixteenth International Conference on Fusion Energy / organized by the International Atomic Energy Agency and held in Montreal, 7–11 October 1996. — Vienna : The Agency, 1997.
3 v. ; 24 cm. — (Proceedings series, ISSN 0074–1884)
Contents: v.3.
STI/PUB/1004
ISBN 92–0–103997–2
"Formerly called the International Conference on Plasma Physics and Controlled Nuclear Fusion Research."
Includes bibliographical references.

1. Nuclear fusion—Congresses. 2. Controlled fusion—Congresses. 3. Plasma (Ionized gases)—Congresses. I. International Atomic Energy Agency. II. Title. III. Title: International Conference on Plasma Physics and Controlled Nuclear Fusion Research. IV. Series: Proceedings series (International Atomic Energy Agency).

VICL 97-00178

FOREWORD

The 16th International Atomic Energy Agency Fusion Energy Conference (formerly called the International Conference on Plasma Physics and Controlled Nuclear Fusion Research) was held in Montreal, Canada, from 7 to 11 October 1996. This series of meetings, which began in 1961, has been held biennially since 1974.

In addition to these biennial conferences, the IAEA organizes co-ordinated research projects, technical committee meetings, advisory group meetings and consultants meetings on fusion research topics. The objectives of the IAEA activities related to fusion research are to:

—Promote fusion energy development and worldwide collaboration;
—Support developing Member State activities in fusion research;
—Emphasize the safety and environmental advantages of fusion energy;
—Encourage the utilization of plasmas and fusion technology in industry;
—Provide auspices for the International Thermonuclear Experimental Reactor (ITER).

This conference, which was attended by some 500 participants from over thirty countries and two international organizations, was organized by the IAEA in co-operation with the Centre canadien de fusion magnétique and the Canadian National Fusion Program, to which the IAEA wishes to express its gratitude. Some 270 papers were presented in 19 oral and 8 poster sessions on magnetic and inertial confinement systems, plasma theory, computer modelling, alternative confinement approaches, fusion technology and future experiments. The opening session was designated the Artsimovich Memorial Session, in honour of Academician Lev Andreevich Artsimovich.

Fusion research is continuing to make excellent progress. Since the previous conference (Seville, 1994) over 10 MW of fusion power has been produced in the Tokamak Fusion Test Reactor, plasma conditions equivalent to breakeven have been demonstrated in the JT-60U experiment, the reversed shear mode has been demonstrated, low aspect ratio tokamaks have produced promising results and plans have been drawn up for powerful new inertial confinement fusion experiments. We can look forward to further encouraging results at the next conference (Yokohama, 1998), when the Joint European Torus will have employed a 50:50 mix of deuterium–tritium fuel, the Large Helical Device will be operating and the ITER Engineering Design Activities will be complete.

EDITORIAL NOTE

The Proceedings have been edited by the editorial staff of the IAEA to the extent considered necessary for the reader's assistance. The views expressed remain, however, the responsibility of the named authors or participants. In addition, the views are not necessarily those of the governments of the nominating Member States or of the nominating organizations.

Although great care has been taken to maintain the accuracy of information contained in this publication, neither the IAEA nor its Member States assume any responsibility for consequences which may arise from its use.

The use of particular designations of countries or territories does not imply any judgement by the publisher, the IAEA, as to the legal status of such countries or territories, of their authorities and institutions or of the delimitation of their boundaries.

The mention of names of specific companies or products (whether or not indicated as registered) does not imply any intention to infringe proprietary rights, nor should it be construed as an endorsement or recommendation on the part of the IAEA.

The authors are responsible for having obtained the necessary permission for the IAEA to reproduce, translate or use material from sources already protected by copyrights.

Material prepared by authors who are in contractual relation with governments is copyrighted by the IAEA, as publisher, only to the extent permitted by the appropriate national regulations.

CONTENTS OF VOLUME 3

INERTIAL CONFINEMENT 1 (Session B1)

INERTIAL CONFINEMENT 2 (Session B2)

INERTIAL CONFINEMENT (Poster Session BP)

HEATING AND CURRENT DRIVE (Session E)

HEATING AND CURRENT DRIVE (Poster Session EP)

REACTOR STUDIES (Session G1)

TECHNOLOGY AND NEW DEVICES (Session G2)

TECHNOLOGY, NEW DEVICES AND REACTOR STUDIES (Poster Session GP)

INERTIAL CONFINEMENT 1

(Session B1)

Chairperson

C. YAMANAKA
Japan

HIGH ENERGY DENSITY PHYSICS RESEARCH USING LASER AND PULSED POWER ICF FACILITIES

C.J. KEANE, D.H. CRANDALL,
K.W. BIEG, T.T. SAITO
US Department of Energy,
Germantown, Maryland,
United States of America

Abstract

HIGH ENERGY DENSITY PHYSICS RESEARCH USING LASER AND PULSED POWER ICF FACILITIES.

The study of high energy density plasmas involves a number of basic physics issues and is relevant to applied problems in a variety of areas such as inertial fusion and astrophysics. Motivated by its goal of demonstrating laboratory ignition and eventual high gain, the US ICF Program has played a major role in developing the experimental, theoretical and modeling capabilities necessary to pursue laboratory studies of high energy density phenomena. Facilities built by the Program for this purpose include the Nova, Omega, Nike and Trident lasers (located at the Lawrence Livermore National Laboratory, the Laboratory for Laser Energetics at the University of Rochester, the Naval Research Laboratory and the Los Alamos National Laboratory, respectively), as well as the Particle Beam Fusion Acceleration (PBFA) and SATURN pulsed power facilities at Sandia National Laboratories. Target fabrication work is ongoing at the facilities above as well as at General Atomics. An active related program in theory and computer simulation is also under way at these laboratories. The paper reviews the high energy density physics program of research carried out on ICF facilities.

1. INTRODUCTION

The mission of the ICF Program is twofold: 1) to develop a laboratory microfusion capability for defense and energy applications, and 2) to address high energy density physics issues for the science based stockpile stewardship program. The ICF Program seeks to fulfill this mission by providing a state-of-the-art capability to investigate high energy density physics in the laboratory. The near term goals are to a) demonstrate ignition in the laboratory, and b) use the capabilities developed for the ignition program to address important defense and other questions. The program currently carries out high energy density physics experiments using laser and pulsed power drivers.

The ICF FY97 budget of $175M is apportioned to major program activities as shown in Table 1. These funds are primarily expended by the organizations mentioned above. In addition to the ICF budget, $191M has been appropriated for Title I design of the National Ignition Facility.

Table 1
ICF FY97 Budget

Category	*$ (Mil)*
Target Physics, Theory & Modeling	88.1
Glass Laser & Related Technology	42.6
Target Development, Fabrication & Handling	32.0
Advanced Driver Development	10.5
Other	2.2
ICF Sub-Total	175.4
National Ignition Facility	191.1
ICF & NIF Total	366.5

Target physics activities in the program are divided into ignition related physics and other high energy density science activities. Current plans in each of these areas are described below.

2. THE IGNITION PROGRAM

The U.S. ICF Program is currently in the engineering design phase of the National Ignition Facility (NIF), a 192 beam Nd glass laser which will produce 1.8 MJ of 0.35-μm light and will be designed to allow ignition experiments to be carried out in both indirect and direct drive geometry. In order to reduce space requirements and cost, the NIF is designed with a new laser architecture that utilizes multi-pass amplification. This architecture required several innovations (such as large area Pockels cells) and involved some technical risk. Therefore, a scientific prototype called Beamlet was constructed and tested. This prototype was designed with similar architecture to that proposed for the NIF and was designed to operate at near NIF-scale beam sizes and fluences. The Beamlet has met or exceeded all of its design goals for energy (at 351 nm), power, pulse shaping and fluence.[1] It has therefore validated the scientific soundness of the concept. The current NIF schedule calls for facility completion in 2002.

The ignition physics portion of the U.S. ICF Program is focused on enhancing confidence in demonstrating ignition on NIF. For both indirect and direct drive, ignition physics studies can be broken into four major areas: hydrodynamics, drive symmetry and energetics, plasma physics and ignition target design. Work planned in these areas is summarized below for direct and indirect drive.[2]

2.1 Indirect Drive

Hydrodynamics. Planned studies include the effects of convergence on instability growth studies of capsule fabrication defects, the effects of "beam phasing" (see below) on implosions and the assessment of novel techniques for instability mitigation. Shock timing measurements will also be carried out on PBFA-Z and other laser facilities.

Drive Symmetry and Energetics. Further studies of gas-filled hohlraums (the baseline design used for NIF) will continue in order to confirm our understanding of relevant important physics issues. Control of time dependent drive symmetry in NIF hohlraums relies on spatially separating the laser input energy into two pieces or "cones" of independent temporally shaped pulses. This technique for controlling drive symmetry is known as "beam phasing." This concept will be studied in experiments on Nova and Omega. The effects of beam smoothing using smoothing by spectral dispersion (SSD) will also be assessed.

Plasma Physics. Further experiments will be carried out to assess the laser energy and intensity regimes that are achievable before plasma instabilities result in excessive loss or scattering of laser energy input to the hohlraum.

Ignition Target Design. Continuing work on NIF target design will focus on targets that are increasingly robust and thus more likely to ignite. The effects of symmetry, hydrodynamics and plasma physics constraints will be incorporated into ignition target designs as new results appear.

The bulk of laser-driven indirect drive experiments have been conducted on Nova,[2] but comparable performance has recently been achieved on Omega, as well.[3] Figure 1 shows results from Nova and OMEGA. The OMEGA data was taken with three different illumination geometries (using a 58° cone, the 58° and 42° cones, and the 58°, 42° and 21° cones). Future experiments will further investigate symmetry and drive in cylindrical and tetrahedral hohlraums.

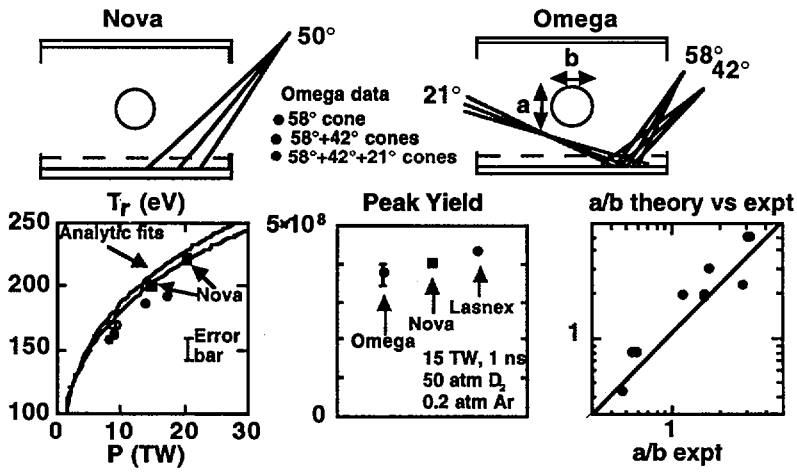

FIG. 1. Similar geometries of illumination cones for indirect drive on both Nova and Omega (top). Analytic and experimental results for radiation temperature, peak yield and implosion symmetry (a/b) of the compressed target shown to agree (bottom).

2.2 Direct Drive

Hydrodynamics. Planar Rayleigh-Taylor instability experiments similar to those done previously for indirect drive will be carried out on OMEGA, Nike and Nova. These experiments will determine the hydrodynamic stability constraints and associated laser uniformity requirements for direct drive ignition. In particular, these experiments will determine the feasibility of direct drive ignition on NIF. An important feature of the OMEGA program is that cryogenic implosion experiments are planned for 2000. These implosions will test direct drive physics issues and are also important to test engineering concepts for the NIF cryogenic system.

Symmetry. Experiments planned on OMEGA will determine the levels of low to moderate mode number drive nonuniformities that may be tolerated and verify that the degree of drive symmetry expected on NIF is adequate for direct drive ignition.

Plasma physics. The interaction of incident laser light with ablated material from the capsule can also lead to excessive scattered laser light. Experiments on OMEGA will assess this issue.

Ignition target design. A design for a direct drive NIF ignition target has been proposed by the University of Rochester. Assessment of this target will continue. Continuing design work will incorporate results from ongoing experiments.

Advanced ignition concepts will also be examined in the next few years. Two particular noteworthy examples of this are the fast ignitor program and z-pinch driven hohlraums. The former involves the use of a high power short pulse laser to ignite a precompressed mass of fusion fuel; the recent demonstration of a petawatt short pulse laser[4] is an important step in this project.

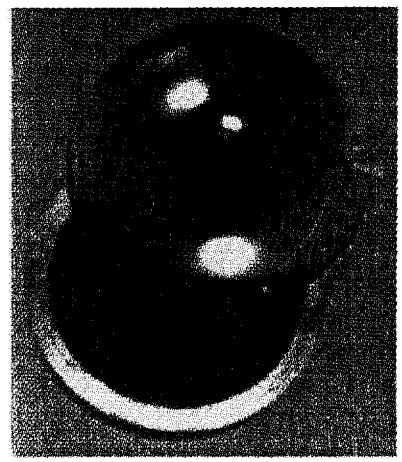

FIG. 2. NIF scale (2 mm diameter) Be hemishells machined from wrought material using the quick flip locator.

Though target physics is the primary area of interest for this article, it should be noted that a vigorous effort in ignition-related technology development is underway. Ongoing laser and optics technology development is critical to completing NIF construction on schedule and budget. Significant resources are being devoted to cryogenic target development and engineering and target fabrication, generally. A cryogenic target handling system is scheduled for deployment on Omega near 2000, and this will provide guidance in designing the NIF system. Target chamber area and diagnostic development activities are also in progress.

An example of target fabrication progress is the beryllium hemishells[5] shown in Figure 2. Beryllium capsules offer potential improvements in implosion performance over polymer shells because of their reduced susceptibility to Rayleigh-Taylor instabilities. In addition, they have sufficient material strength to contain the required high pressure DT fill at room temperature and offer improved ice layer concentricity due to the higher thermal conductivity of Be. Research with beryllium shells includes developing the optimum method of joining and filling these hemishells to produce an ignition target.

3. OTHER HIGH ENERGY DENSITY SCIENCE ACTIVITIES

Other aspects of high energy density science studied by the ICF Program include:

Basic Hydrodynamics. Planar experiments on Nova, Omega and Nike will investigate, as feasible, the nonlinear phase of instability growth and the transition to turbulence. Jet formation will be studied using hemispherical and other targets.

Atomic Physics and Radiative Properties. Measurements of mid-Z material opacity will continue using both laser and pulsed power facilities. Preparatory work for NIF opacity experiments such as x-ray backlighter development will be done.

Material Properties and Equation of State. Methods for measuring on- and off-Hugoniot equations of state will continue to be developed. The use of flyer plate techniques to achieve high pressures (pressures near ~ 1 Gbar have been observed to date) will be explored.[6,7] As shown in Figure 3, the equation of state of deuterium was measured in a series of experiments on the Nova laser using cryogenic (liquid) deuterium foil targets.[8] These were the first such cryogenic experiments carried out on Nova and also the first experimental demonstration of the importance of molecular dissociation in determining equations of state. Use of the new "dissociation model" in NIF ignition target calculations results in improved target performance (~ 15% higher calculated yield).

Plasma Physics. Basic laser-matter interaction studies will continue, as will experiments related to developing fundamental understanding of dense plasma phenomena. Plasma physics issues that limit certain goals, such as the achievement of high temperature hohlraums, will also be investigated.

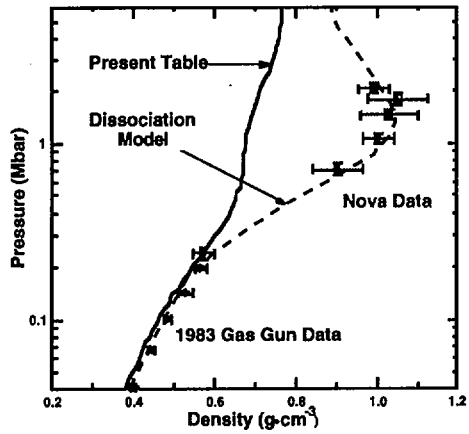

FIG. 3. D_2 equation of state measurements obtained on Nova, showing enhanced compressibility consistent with the dissociation model.

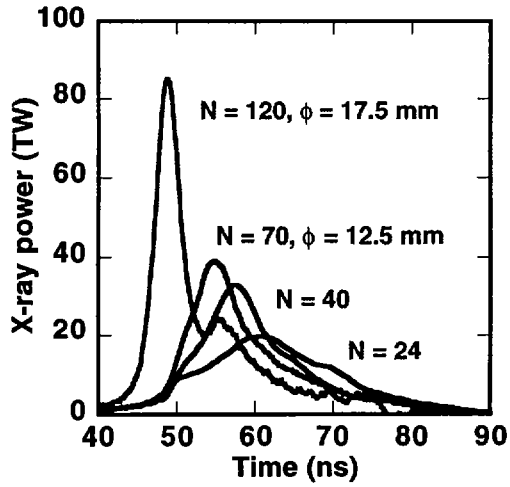

FIG. 4. Record x-ray production achieved on SATURN. Results show x-ray power as a function of time for differing numbers of wires (N) placed at different diameters (ϕ).

Applied hydrodynamic studies. Hydrodynamic experiments will be carried out on Nova, Omega and Nike to assess the effects of gaps, cracks and other complex features capable of affecting capsule performance. Such experiments also serve as a severe test for new three-dimensional hydrodynamic codes under development.

Astrophysics. Laboratory astrophysics experiments are in progress to examine phenomena such as hydrodynamic instabilities in regimes relevant to supernovas.

Recent advances with the pulsed power driven z-pinch will significantly enhance the ICF program's capability in high energy density science.[9] Radiation driven response of materials is being studied on the pulsed power facility SATURN located at Sandia National Laboratories. Record x-ray power has been achieved from SATURN as shown in figure 4 which presents the peak x-ray power as a function of time for varying number of wires (24-120) at diameters up to 17.5 mm in the SATURN device configured for Z-pinch. The experiment can be arranged to yield a pulse-shape comparable to Nova. The potential for these sources to drive hohlraum environments is under investigation.

SUMMARY

The laser and pulsed power facilities developed by the U.S. ICF Program, along with their associated theoretical, modeling and target fabrication facilities, represent some of the most sophisticated capabilities for high energy density physics research in the world. Over the next few years the Program will be focused on two major goals: demonstrating ignition on NIF and addressing important high energy density science issues. The Program also plans to increase access to its facilities by outside users and involve universities and others currently outside the Program in its activities. The use of a variety of facilities and the involvement of a broad spectrum of researchers should allow the Program to make faster progress towards its ignition and other goals.

REFERENCES

[1] VAN WONTERGHEM, B.M., System Description and Initial Performance Results for Beamlet, ICF Annual Report, Rep. UCRL-LR-105820-95, Lawrence Livermore National Laboratory, CA (1995).
[2] LINDL, J.D., Phys. Plasmas 2 (1995) 3933.
[3] MURPHY, T.J., LANDEN, O.L., personal communication (1996).
[4] PERRY, M.D., et al., Petawatt Laser Final Report, Rep. UCRL-ID-124933, Lawrence Livermore National Laboratory, CA (1996).
[5] GOBBY, P.L., et al., Current progress in NIF target concepts, Fusion Technol. (in press).
[6] CAUBLE, R., et al., Phys. Rev. Lett. **69** (1993) 265.
[7] KILKENNY, J.D., LEE, R.W., Phys. Rev. Lett. **70** (1993) 2102.
[8] DaSILVA, L.B., et al., Absolute equation of state measurements of shocked liquid deuterium up to 200 GPa (2 Mbar), Phys. Rev. Lett. (in press).
[9] DEENEY, C., et al., Power enhancement by increasing initial array radius and wire number of tungsten z pinches, Phys. Plasmas (in press).

DISCUSSION

D.E. POST: In ITER, we are making a strong effort to use reactor relevant technology whenever possible. The ICF community, since the early 1970s, has stated that the reactor driver is likely to be a heavy ion accelerator. The problem is that such

an accelerator would cost US $1 billion, and so intermediate research is being carried out with lasers, which are cheaper. However, the NIF will also cost US $1 billion. Why not use this sum to build a reactor relevant heavy ion accelerator for ignition physics studies, rather than spending it on a non-reactor-relevant laser facility such as the NIF? This would potentially reduce the time required to achieve inertial fusion energy by ten to twenty years.

C.J. KEANE: The purpose of the NIF is to carry out high energy density science experiments (such as the demonstration of laboratory ignition) relevant to US defence needs. Heavy ion drivers are not appropriate for a facility designed for this purpose, as they have yet to demonstrate the output characteristics and overall driver/facility flexibility necessary to carry out the high energy density science programme scheduled for the NIF.

T. DESAI: You mentioned that beryllium ablators are attractive for ICF capsules. Can you indicate the advantages of Be over any other pure materials as ablators?

C.J. KEANE: Beryllium ablator targets are attractive for several reasons. First, these capsules are somewhat more hydrodynamically stable than plastic ablator capsules. In particular, Be capsules are more resistant to the Rayleigh–Taylor instability growth seeded by surface non-uniformities in the DT ice layer at the DT gas/DT ice interface. (Details of this can be found in M. Cray's paper, IAEA-CN-64/B2-5, this volume.) Secondly, Be capsules have some advantages in terms of target fabrication. It appears that NIF Be targets may be strong enough to be filled with DT at room temperature. Plastic ablator capsules need to be maintained in a cryogenic condition once they are filled in order to prevent the high gas pressure of DT at room temperature from rupturing the ablator. Offsetting these advantages of Be, however, is the fact that Be capsules cannot be permeation filled with DT as plastic capsules can. Investigation of these trade-offs is continuing to identify capsule designs which are both reasonably easy to make and expected to ignite.

H.L. BERK: I am very impressed to see the statement that ignition will be achieved by 2002. But what is the instability picture for this? Do you expect that the compressions will be instability free, or do you think that with the instabilities you will be able to obtain the compressions you need in plasmas, fluids or whatever is associated with the compression? I assume that the Rayleigh–Taylor instability is the great obstacle.

C.J. KEANE: Hydrodynamic and plasma instabilities are well known to be important issues in inertial confinement fusion. A major effort over the past five to ten years has resulted in very significant quantitative progress in defining the physics requirements for ignition. For indirect drive, these requirements are quite well defined and have been incorporated into the design of the NIF. Experiments in progress on Omega, Nike, Nova and other ICF facilities will address these requirements for direct drive. The NIF has also been designed to allow direct drive. Further detail is available in other papers, e.g. in that by J.D. Lindl (IAEA-CN-64/B1-4, this volume).

R.J. GOLDSTON: Could you explain the scientific logic for the selection of 'backup' drivers being studied in ICF? Why is the heavy ion driver not included if you are studying heavy ion target physics?

C.J. KEANE: A long term goal of the ICF Program is a facility capable of producing high yield (greater than approximately 100 MJ) for defence purposes. The higher efficiency and repetition rate associated with heavy ion drivers make them interesting candidates for inertial fusion energy applications but may not necessarily be of great value for defence applications. Given recent progress in the ICF Program, it is now appropriate to review our plans for advanced driver development, and this will be done in the near future. Finally, it should be noted that the ICF Program is not funding a large effort in heavy ion target physics. Certain calculations requiring the use of classified codes are funded as needed.

RECENT PROGRESS OF LASER FUSION RESEARCH WITH THE GEKKO LASERS AT ILE, OSAKA

K. MIMA, M. NAKATSUKA, H. AZECHI, H. FUJITA,
H. HONDA, M. HONDA, R. ISHIZAKI, Y. IZAWA,
N. IZUMI, T. JITSUNO, T. KANABE, Y. KATO,
Y. KITAGAWA, R. KODAMA, S. MATSUOKA,
N. MIYANAGA, M. MURAKAMI, M. NAKAI,
S. NAKAI, K. NISHIHARA, H. NISHIMURA,
T. NORIMATSU, S. SAKABE, K. SHIGEMORI,
H. SHIRAGA, H. TAKABE, M. TAKAGI,
K.A. TANAKA, M. YAMANAKA,
T. YAMANAKA, G.Y. YOON
Institute of Laser Engineering,
Osaka University,
Suita, Osaka

A. NISHIGUCHI
Faculty of Engineering,
Osaka Institute of Technology,
Osaka

S. MIYAMOTO
Himeji Institute of Technology,
Himeji, Hyogo

K. TSUBAKIMOTO, C. YAMANAKA
Institute for Laser Technology,
Nishiku, Osaka

Japan

Abstract

RECENT PROGRESS OF LASER FUSION RESEARCH WITH THE GEKKO LASERS AT ILE, OSAKA.

The irradiation symmetry of GEKKO XII has recently been improved. It is crucial for laser implosion to form a hot spark in a highly compressed cold fuel. Uniform laser irradiation was achieved by introducing partially coherent light with angular spectral dispersion and by improving the power balance among the 12 beams. Implosion experiments with the improved GEKKO XII have been carried out to increase the neutron yield normalized by the 1-D simulation result. The normalized neutron yield is of order unity for a convergence ratio of less than 8. The improved uniformity also makes it possible

to obtain experimental data which are necessary for the ignition target design. Namely, the Rayleigh-Taylor instability growth rate, the bandwidth dependence of the initial imprint, the effects of an X ray prepulse in reducing the initial imprint and so on have been investigated. As a new project directed towards ignition and burn, an ultra-intense short pulse laser beam is to be added to the GEKKO XII system. This short pulse laser is capable of delivering 100 J/1 ps into the compressed core plasma for investigating the feasibility of the fast ignition concept. In future, it will be upgraded to 1 kJ/1 ps to heat plasmas imploded by GEKKO XII.

1. INTRODUCTION

In implosion experiments, high density compression up to 600 g/cm^3 has been achieved by using random phase plates (RPPs) [1]. However, the neutron yield is strongly degraded in comparison with that of 1-D implosion simulation because of the turbulent mixing caused by the Rayleigh–Taylor (R–T) instability which is triggered by laser irradiation non-uniformity. In order to improve irradiation uniformity, the beam intensity profile uniformity and the power balance between the beams of GEKKO XII have been improved in the past two years [2].

In the first phase of the improvement, the laser beam intensity profile on the target has been made extremely uniform through the introduction of partially coherent light (PCL) with angular spectral dispersion. In the second phase, the power balance between the beams has been improved by developing a fine beam monitoring system. At present, the power imbalance has been reduced to 3–5% RMS.

By using the PCL laser beams of GEKKO XII, rippled shock propagation, laser imprint and its reduction by X ray preirradiation, and the subsequent R–T instability were investigated. In these experiments, the laser pulse consisted of a 1.8 ns low intensity foot pulse ($\sim 10^{13}$ W/cm^2) and a 2 ns main pulse ($\sim 10^{14}$ W/cm^2). A sinusoidal intensity modulation was imposed on the foot pulse for imprinting. The amplitudes of the modulation of the areal mass density were diagnosed by streaked face-on X ray backlighting. The imprinted areal mass perturbations were amplified by the R–T instability in the following acceleration driven by the uniform main pulse. It has been found that the imprint amplitude of the PCL, σ_{RMS}, is less than 50 nm for long wavelength fluctuations.

With the improved GEKKO XII, the implosion experiments were performed under well controlled conditions. In these experiments, the target non-uniformity was characterized in detail and the laser pulse shape was designed to reduce the R–T instability growth rate. The e-foldings (γt) of the linear R–T instability growth were evaluated for various irradiation conditions. γt versus mode number was evaluated for different pulse shapes: a 1.3 ns Gaussian pulse and a 1.6 ns square pulse, and a 1.6 ns square pulse with a 0.2 ns prepulse which preceded it by 0.2–0.4 ns. The γt must be less than 6–8 in typical ignition designs. With a single Gaussian pulse irradiation, γt is 12, which is too large for stable implosion. According to the recent Fokker–Planck simulation, γt for the square pulse is not higher than 8. Therefore,

the implosion experiments have been done with a square pulse with various prepulses.

The neutron yields have been compared with the corresponding 1-D simulations ILESTA (Spitzer–Harm) and HIMICO (Fokker–Planck). The neutron yield ratios (experimental yield/1-D simulation yield) for various fuel gas pressures and laser pulse shapes have been obtained. The neutron yield ratios in the good power balance experiments are found to be of order unity when the convergence ratio is lower than 8.

We also investigated how the neutron yield ratio depends on the maximum e-folding, which is varied by changing the pulse shape. It is found that when the maximum e-folding is less than 4, the normalized neutron yield ratio is of order unity.

In order to reduce initial imprints further, we recently carried out a hybrid implosion experiment in which we used high Z coated foam on a plastic pellet. The preliminary experiments show that the initial imprint at a wavelength of around 100 μm is reduced by a factor of 2 in the hybrid scheme [3].

As a new project directed towards ignition and burn, an ultra-intense short pulse laser beam is to be added to the GEKKO XII system [4]. This short pulse laser is capable of delivering 100 J/1 ps in the first phase and will be upgraded to 1 kJ/1 ps in 2–3 years. Using this petawatt laser, the 600 g/cm^3 compressed core plasma will be heated to demonstrate the feasibility of the fast ignition concept. In order to clarify the fundamental physics related to fast ignition, we studied the ultra-intense laser interactions with a solid target in experiments with the short pulsed GEKKO MII laser. The ignition and burn of a partially heated high density plasma are demonstrated by simulations with ILESTA-2D. It is found that ignition can be achieved by 1 kJ energy input into high density plasmas.

Section 2 of this paper is devoted to laser technology developments related to the improvement of the irradiation symmetry of GEKKO XII. Section 3 summarizes the results of implosion experiments. In Section 4 precise experiments on elementary hydrodynamics related to direct implosion are described. The laser construction, theory and experiment related to the fast ignition concept are reviewed in Section 5. Finally, a brief summary is given in Section 6.

2. IMPROVEMENT OF LASER IRRADIATION UNIFORMITY

The uniformity of laser irradiation is one of the key issues in direct drive inertial confinement fusion (ICF). The overall irradiation non-uniformity ($\sigma_{RMS} = (\Sigma\sigma_\ell^2)^{1/2}$, ℓ is the spherical mode number) required for ignition is estimated to be below 1%. In this section recent technology developments related to uniformity improvement for the GEKKO XII laser system are reported. These developments include beam focusing control to optimize the intensity envelope on the target, development of beam smoothing techniques, pulse shape control and power balance control among the beams. A proposed laser pulse consists of a foot pulse of PCL [5–8] followed by a main pulse of smoothing by spectral dispersion (SSD) [9].

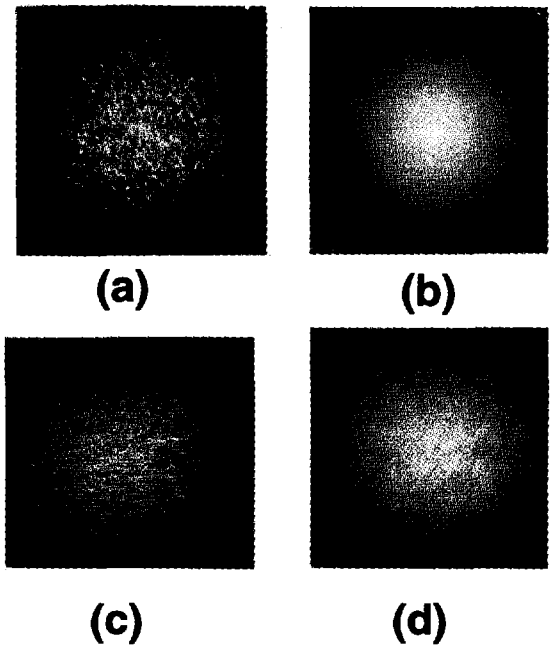

FIG. 1. Beam patterns on the target plane measured with a cooled CCD camera for (a) coherent laser, (b) PCL with angular spectral dispersion, (c) 1-D SSD and (d) 2-D SSD. RPPs were used in all cases.

2.1. Improvement of RPPs

The RPP [10] is a device that divides a laser beam into a large number of small beamlets. These beamlets randomly interfere with each other on the target plane, creating a fully developed speckle pattern with a relatively uniform intensity envelope. RPPs with 1.85 mm (diameter of a circumscribed circle) hexagonal elements are being used for illuminating targets of about 500 μm diameter. The error of coating thickness was measured to be less than 1% by means of the Zernike interference technique with a resolution of $\pi/250$ for a 0.527 μm laser. The focusing condition, d/R, is usually -3, so that the central coherent spike becomes insignificant, where R is the target radius and d is the distance between the centre of the target and the focal position. (The negative sign means a focal position beyond the target centre.) The time integrated laser pattern measured on the target plane is shown in Fig. 1(a).

2.2. PCL

We have developed a front end system which consists of fibre optics for generating a PCL beam [11]. It has been demonstrated that the optical fibres are quite

useful for the coherence control [12]. To control the spectral width, we used self-phase-modulation in a single mode fibre, while a step index multimode fibre was used to introduce the spatial incoherence [13]. This front end system also has the capability for flexible pulse shaping [11]. The PCL pulse used here was the square pulse with variable duration from 50 ps to 2.2 ns.

The beam pattern of the focused PCL on the target plane has medium mode ($20 \leq \ell \leq 40$) non-uniformity due to the residual coherence [7]. This non-uniformity can be substantially reduced by angular spectral dispersion [9]. The dispersion rate along the extraordinary axis of the type II KDP crystal for frequency doubling was adjusted to be 239 μrad/nm for the 1.05 μm beam. The doubling efficiency was approximately 50% for the 2 cm thick KDP crystal at an intensity of 0.65 GW/cm^2. To avoid non-linear effects in the amplifier chain, such as self-phase-modulation, which causes deformation of the pulse shape, spectral change and the increase of beam divergence, the maximum intensity of the PCL was limited to about 2 GW/cm^2 at the final amplifier output. Figure 1(b) shows the measured PCL pattern. A significant smoothing effect is evident compared with Fig. 1(a). The time resolved irradiation non-uniformity was calculated from the measured beam patterns on the target plane with varying pulse widths from 50 ps to 1.6 ns.

2.3. SSD

Another important beam smoothing technique is SSD with either 1-D or 2-D dispersion. The measured SSD patterns are shown in Fig. 1(c, d) for 1-D and 2-D dispersion.

In the 1-D scheme, a phase modulated laser is temporally skewed across the beam using a diffraction grating. Then 1-D colour cycles across the beam are created with 1-D angular spectral dispersion in the same direction. In order to easily change the modulation frequency (i.e. the number of colour cycles across the beam), cross-phase-modulation in a polarization preserving single mode fibre is used. The modulation frequency can be changed in the range 5–20 GHz with a time averaged bandwidth of 0.6 nm. Figure 1(c) shows a beam pattern taken with 1-D SSD at 10 GHz modulation frequency.

Two dimensional SSD is achieved by adding another phase modulator and a second diffraction grating. The second temporal skew (i.e. the second angular spectral dispersion) is perpendicular to that of the first dispersion, while the direction and the rate of composite angular spectral dispersion are kept to meet the phase matching condition of the KDP crystal. The second phase modulation is done using an optoelectronic modulator. Domain inverted $LiTaO_3$ is driven by a 9.4 GHz microwave under quasi-velocity-matching. In Fig. 1(d), the modulation frequency of the first phase modulation was temporally varied from 10 to 18 GHz in 500 ps. The modulation depth was set to obtain a 0.35 nm bandwidth for each modulator.

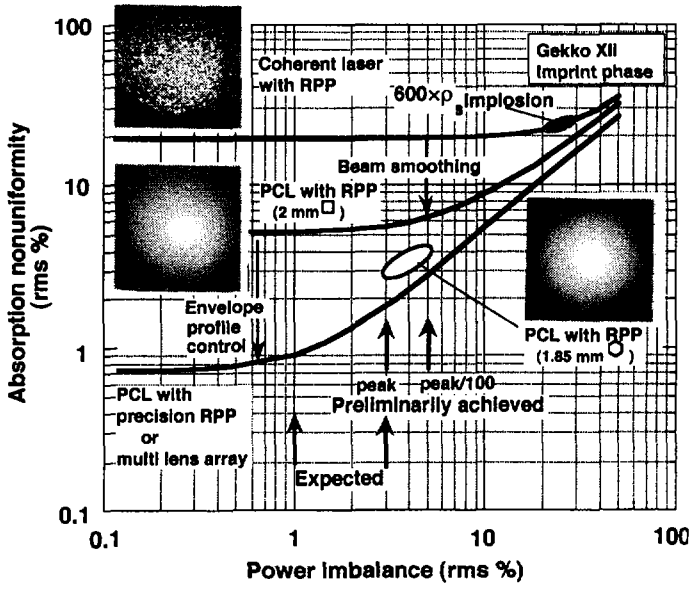

FIG. 2. Laser absorption non-uniformity as a function of the power imbalance among the 12 beams for three different beam patterns: coherent laser with RPP, PCL with RPP and PCL with the improved RPP.

2.4. Overall absorption uniformity

As the beam smoothing techniques reduce the high mode ($\ell \geq 10$) non-uniformity, the power imbalance among the beams that causes the low mode non-uniformity becomes significant. The low mode non-uniformity due to the beam imbalance is larger than that which originates from the asymmetry of the focused beam pattern.

The absorption non-uniformity for different laser conditions was calculated by means of ray tracing [14]. The simulated target was a plastic shell of 600 μm diameter and 6 μm wall thickness irradiated with a 6 kJ trapezoidal pulse having a full width at half-maximum (FWHM) of 2 ns and a rise time of 1 ns. Figure 2 shows the absorption non-uniformity as a function of time constant power imbalance calculated for the imprint phase (before the first shock break-out). Three different beam patterns were considered: coherent laser with RPP, PCL with RPP, and PCL with the improved RPP. The measured beam patterns are shown in the figure. The calculated absorption non-uniformity of 3–4% has been achieved with PCL combined with the improved RPP with a 1.85 mm hexagonal element and a power imbalance of 3–5% RMS. We expect that with further improvement of the envelope profile control and power balance control we may realize the 1% non-uniformity required for ignition.

3. IMPLOSION EXPERIMENTS WITH THE UNIFORMITY IMPROVED GEKKO XII

3.1. Experimental conditions

The important parameter in the target design is the growth of the R–T instability. We have made a linear analysis of the e-folding of the R–T instability, $\Gamma \equiv \int \gamma \, dt$, for various implosion conditions on the basis of the 1-D Lagrangian hydrodynamic simulation code ILESTA-1D [15], where γ is the growth rate and t is time. Spitzer–Harm heat transport with a flux limit factor of 0.1 is assumed in the code. Figure 3 shows Γ versus the mode number calculated for different pulse shapes: a 1.3 ns width Gaussian pulse, a 1.6 ns width square pulse and a 1.6 ns width square pulse preceded by a 0.2 ns width prepulse with a varying time gap. The Γ value allowed in typical ignition targets is 6–8, the shaded region in Fig. 3. With a single Gaussian pulse irradiation, Γ is 12, which is too large for stable implosion over the whole implosion process. Shortening the pulse rise time increases the adiabat, thereby reducing Γ to around 7. Adding a prepulse further reduces the R–T growth, making the implosion more stable, although it is accompanied by a decrease in the compression density. In the present experiment, we have varied Γ by changing the time gap between the prepulse and the main pulse.

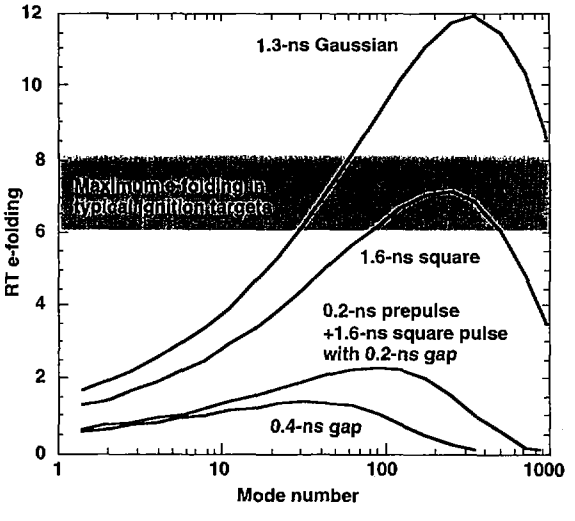

FIG. 3. The e-folding, $\Gamma \equiv \int \gamma \, dt$, of the R–T instability versus the mode number for different laser pulse shapes: 1.3 ns Gaussian pulse, 1.6 ns square pulse and prepulse plus square pulse. The Γ value in typical ignition targets is shown by the shaded region.

A polystyrene shell of 520 μm diameter and 8 μm thickness was filled with deuterium gas. The polystyrene shell was used because of its state of the art uniformity [16] (thickness non-uniformity of better than 1% and surface roughness of 2 nm RMS for $\ell \geq 50$). The shell thickness was measured over 4π rad using a reflection microscopic spectrometer with 5 nm measurement accuracy. The surface roughness measured with a high precision interferometer, WYKO, was expanded into spatial frequencies to determine the mode number distribution of the initial perturbation, which was used for evaluation of the instability growth.

The square laser pulse with a prepulse was produced from a fast rise 0.2 ns single pulse at the front end using a fibre coupling pulse adder. After amplification, the prepulse and the main pulse had a rise time of less than 50 ps. The square pulse had power constant to within 5% over the 1.6 ns pulse duration and the prepulse had the same peak power. The separation between the prepulse and the main pulse was varied from 0 (no prepulse) to 0.8 ns.

3.2. Experimental results

The irradiation uniformity on the target was evaluated by two independent measurements: the X ray emission distribution measured with an advanced Kirkpatrick–Baez (AKB) microscope [17] coupled to an X ray charge coupled device (CCD) camera, and the spatial intensity distribution of the second harmonics (0.263 μm wavelength) of the irradiation laser [18]. The measurements indicate that the major non-uniformity arises from lower laser energy deposition in the oblique incidence region of the target. The mode 6 non-uniformity due to this factor may amount to 3.5% in the present configuration.

The stability in the acceleration phase was studied using a tracer layer target [19], where a chlorinated polystyrene (CHCl) shell was coated with a 5 μm thick layer of parylene. The X ray image of the Cl line emission was observed with monochromatic X ray imaging with 10 μm and 10 eV resolution. The emission region of the Cl He β line was only slightly smaller than the initial target size in the case with no prepulse, although the 1-D simulation predicts no ablation of the CHCl layer in the acceleration phase. This indicates that the perturbation at the layer interface grew, so that the CHCl material penetrated into the ablation region in early time. The addition of the prepulse in front of the main pulse reduced the emission region of the Cl He β line, indicating the stabilization of the acceleration phase.

Figure 4 shows the neutron yield versus the time gap between the prepulse and the main pulse. The closed and open squares represent the experimental and the calculated neutron yield, respectively. The open circles represent the calculated yield at the time when the reflected shock wave in the fuel first hits the shell.

The difference between the experimental yields and the calculation decreases as the time gap increases from 0 to 0.4 ns. This indicates that, with large prepulse time gaps, the implosion is more stable owing to the decrease of the R–T e-folding. With

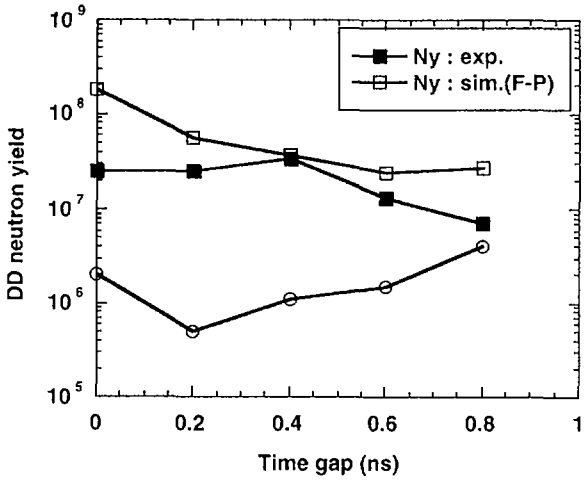

FIG. 4. Neutron yield versus time gap between the prepulse and the main pulse. Closed squares show the experimental results, open squares the 1-D simulation yields time integrated over the whole implosion with the Fokker–Planck treatment for the electron transport.

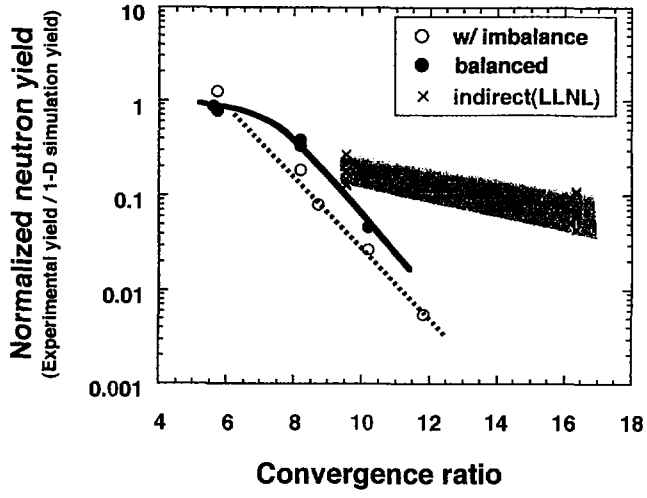

FIG. 5. Neutron yield ratio (experimental yield/1-D simulation yield) versus gas convergence ratio. Closed and open circles show the present experimental results with and without good power balance, respectively. Crosses show the results reported in Ref. [20].

a 0.4 ns time gap, the experimental yield is comparable to the 1-D simulation value and 20 times higher than the value at the start of stagnation.

The dependence of the neutron yield on the convergence ratio (initial fuel radius/compressed fuel radius) was studied in the case of prepulse plus square pulse irradiation with a time gap of 0.4 ns by varying the deuterium pressure from 30 to 5 atm. The closed circles in Fig. 5 show the neutron yield ratio (observed yield/ 1-D simulation yield) versus the convergence ratio. The yield ratio decreased to 0.05 as the convergence ratio was increased to 10. Although the yield ratio is less than unity, the value of 0.05 for the 10× convergence is significantly higher than our previous results obtained with a single Gaussian pulse PCL irradiation (0.008 for the 7.4× convergence). For comparison, the results of the indirect drive experiments [20] at Lawrence Livermore National Laboratory (LLNL) with the precision Nova laser facility are shown by the crosses in Fig. 5, where the radial convergence ratio reported in Ref. [18] (initial target outer radius/compressed fuel radius) has been renormalized to the gas convergence in the present definition.

However, the implosion still does not exhibit spherical symmetry, as shown in Fig. 6. The X ray emission distribution of the compressed core observed with the AKB microscope with a 3 μm resolution shows that the core image consists of localized X ray emission regions that correspond to the 12 beam configuration of GEKKO XII.

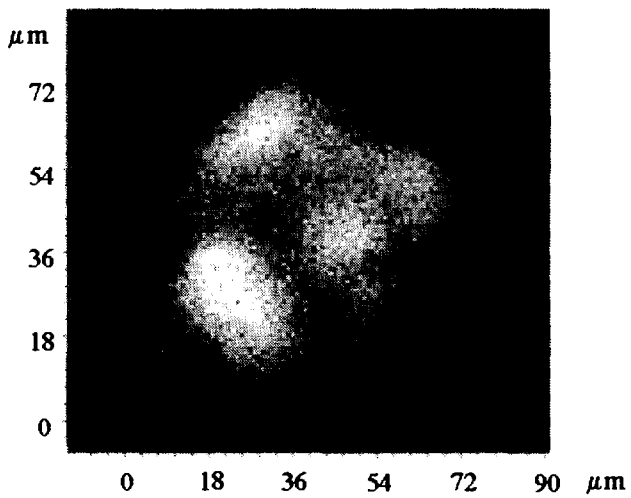

FIG. 6. X ray image of the compressed core. An AKB microscope with a magnification of 25 was utilized to take a picture in the range 1–3 keV with a spatial resolution better than 3 mm. A 489 μm diameter polystyrene shell with 30 atm deuterium gas was irradiated by the prepulse and the main pulse with a time gap of 0.4 ns.

4. DATABASE FOR IGNITION DESIGN

A database on the hydrodynamic properties of ICF plasmas is being accumulated through planar experiments with the new GEKKO XII. Especially hydrodynamic instabilities, which play a crucial role in the implosion, have been investigated intensively.

In the initial phase of pellet implosion, target roughness and laser irradiation non-uniformity give rise to shock wave rippling and to areal density and momentum perturbations to the shell. The fluctuation printed on the shell will grow owing to the hydrodynamic instabilities, resulting in fuel–pusher mixing that degrades the implosion performance. Therefore, comprehensive understanding of the instabilities and their initiation is necessary for ICF target design. In the series of experiments reported here, plastic foil targets were irradiated by the PCL beams with a flat-topped pulse shape of 1.8 or 2.2 ns FWHM to investigate the rippled shock propagation, laser imprint and its reduction by X ray preirradiation, and the subsequent R–T instability.

Polystyrene targets with sinusoidal corrugation were uniformly irradiated by PCL beams at an intensity of 4.0×10^{13} W/cm^2. The perturbation wavelengths of the irradiated targets were either 60 or 100 μm. The thicknesses and amplitudes of the targets were 25–160 μm and 2–10 μm, respectively. Ripples of the shock front were observed by the optical emission that occurs when the shock breaks out on the rear surface of the target. The growth of areal density perturbation and displacement of the target surface were observed by face-on and side-on X ray backlighting. The experiments have shown that the areal density perturbation grows as a result of the damped oscillation of the rippled shock front, whereas the displacement of the ablation front does not grow [21].

The high illumination uniformity achieved by using PCL enabled us to carry out a controlled experiment on the initial imprint for the first time. Flat plastic targets were irradiated with three PCL beams. One beam was turned on to make a foot pulse with an intensity of about 5×10^{12} W/cm^2 and then the others were turned on simultaneously to accelerate the target at an intensity of about 10^{14} W/cm^2. The foot beam was modulated in two ways. In the first case, a grid mask was used to give a quasi-sinusoidal profile to the focusing pattern on the target. In this way, a single spatial mode with a wavelength of 100 μm was successfully induced with a modulation amplitude of 0.1 and 0.4. In the other case, we just changed the divergence of the foot beam.

The low level of areal density perturbation on the target imprinted by the foot pulse was amplified to a detectable level by subsequent instability growth. The temporal evolution of the perturbation on the target was observed by the face-on backlighting method. The observed X ray streak images are shown in Fig. 7 with time integrated irradiation patterns. It is shown that reduction of the beam divergence degrades the irradiation uniformity and increases the imprint level.

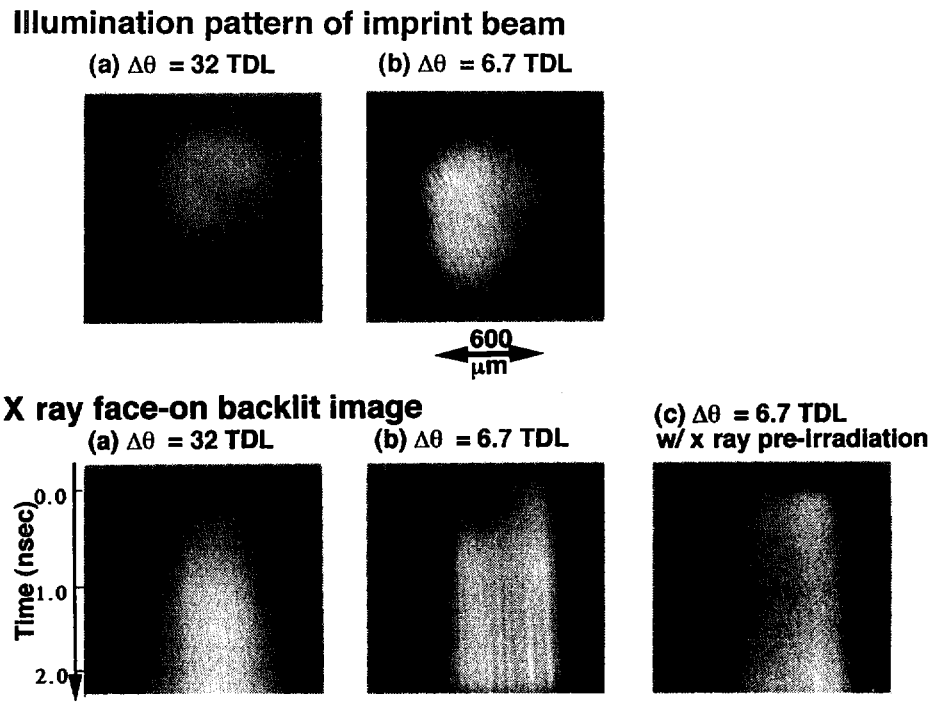

FIG. 7. Typical results of imprint experiments. Perturbation growth on the planar plastic targets imprinted by the foot pulse and accelerated by uniform main beams is measured by use of the X ray face-on backlighting method. The irradiation pattern of the imprinting foot pulse is modified by changing the divergence of the beam: (a) $\Delta\theta$ = 32TDL; (b, c) $\Delta\theta$ = 6.7TDL. In case (c) the target was irradiated by an external soft X ray prepulse to show the smoothing effect of the preforming plasma.

In this figure the effect of the X ray preirradiation is demonstrated. The target was illuminated for 400 ps by the external soft X ray prepulse, the intensity of which was estimated as 7×10^{10} W/cm^2. The imprint is shown to be reduced significantly by soft X ray preirradiation. This smoothing effect is explained as follows. The target surface is irradiated with a low intensity soft X ray prepulse to produce a uniform preformed plasma with a certain scale length. When the direct laser beam comes later, the target already has a substantial stand-off distance between the ablation front and the absorption region. Thus the thermal smoothing effect in the transport layer works more effectively than in the case without X ray preirradiation. As a result, the initial imprint due to the beam non-uniformity is reduced.

Experimental study of R–T instability in the linear growth regime was carried out. Because of the noise before the installation of the PCL system it was not possible for us to observe the linear R–T growth rate on the target directly irradiated by the

laser. The experimental conditions were very similar to those for the imprint experiment except for the uniform foot pulse and the corrugated target. The initial perturbation wavelength was 60 μm and the initial amplitude was varied from 0.1 to 1 μm. We measured areal density perturbation $\Delta(\rho l)$ growth by face-on backlighting. The observed growth factor was about 50. The growth rate was approximately 50% of the classical growth.

The growth factors for the small initial amplitude case, 0.1 and 0.3 μm, are well fitted to an exponential curve with $\gamma_{exp} = 1.0 \times 10^9$ s^{-1}. We also measured the trajectory of an irradiated foil to acquire the acceleration by edge-on backlighting. Using the acceleration, we can calculate the classical growth rate for R–T instability $\gamma_{classical} = (kg)^{1/2} = 2.4 \times 10^9$ s^{-1}, where k is the wavenumber of the initial perturbation and g is the acceleration. The solid line in Fig. 8 shows the growth factor for the classical growth. The growth rate is reduced to about 50% of the classical growth rate.

The theoretical R–T growth rate with the ablative stabilization may be given by the Takabe formula [20],

$$\gamma = 0.9\sqrt{kg} - \beta k v_a$$

where v_a is the ablation velocity in the frame of the accelerated target and β is a constant. For the values of g and v_a calculated with the ILESTA-1D simulation, the mean growth rate is calculated from the Takabe formula to be 2×10^9 s^{-1} for $\beta = 3$–4, which is still larger than the experimental growth rate. The reason for this discrepancy is under investigation. We tentatively presume that non-local heat transport preheats the target to reduce the density, thereby increasing the ablative velocity.

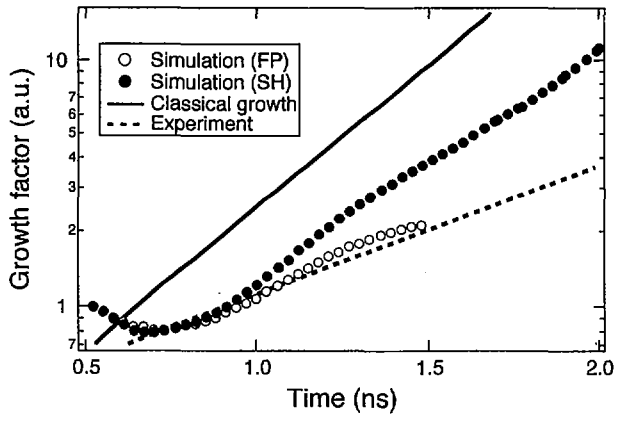

FIG. 8. Growth factors calculated by the 2-D simulation code KEICO-2d with the Fokker–Planck treatment and the Spitzer–Harm treatment for electron transport are plotted with the experimental result and the corresponding classical values.

In Fig. 8 the experimental results are compared with the prediction using the 2-D Eulerian simulation code KEICO-2d [22]. The code can solve either the Fokker–Planck equation or the Spitzer–Harm equation with the flux limiter f = 0.1 for electron transport. Figure 8 shows the growth factors from the simulation for these two cases. In the simulation, initial perturbation was introduced as a density perturbation at t = 0.5 ns. The experimental results are in better agreement with the simulation results of the Fokker–Planck case than of the Spitzer–Harm case. This implies that the non-local electron transport plays an important role also in the hydrodynamic instability of the direct drive implosion.

5. LASER DEVELOPMENT AND FUSION RESEARCH FOR FAST IGNITION [23]

Recently we started a new project in which a few petawatt short pulse laser beam will be injected into a 600 g/cm^3 compressed plasma to demonstrate the significant increase of neutron yield. Two high power short pulse laser modules, one for GEKKO XII and the other for GEKKO MII, have been constructed. The short pulse laser added to GEKKO XII is shown in Fig. 9. The oscillator and amplifiers of this system consist of a Ti:sapphire oscillator, a Ti:sapphire regenerative amplifier, a 4 pass glass rod amplifier and a 35 cm disc amplifier with Cassegrain type 3 pass geometry. A few hundred femtosecond pulse from the Ti:sapphire oscillator is stretched to 0.6 ns and amplified to the millijoule level by the 4 pass glass rod amplifier and the 5 cm rod amplifier. Finally the Cassegrain type amplifier increases

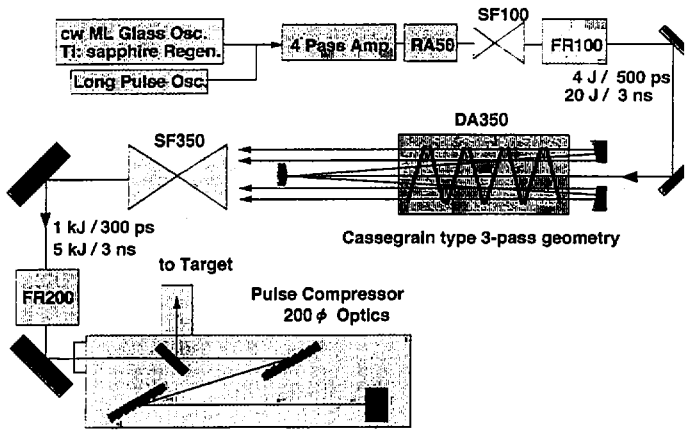

FIG. 9. The 13th chain of the GEKKO XII. The additional one beam chain is under construction.

the total pulse energy to the kilojoule level. At present the beam diameter is reduced to 20 cm because the available grating for a compressor is of 40 cm diameter, which allows us to compress an 18 cm diameter beam. Therefore, the output energy is limited to 100 J in 1 ps because of the limited diameter and the low damage threshold of the gratings. After the compression the laser beam is injected into the chamber for the direct drive implosion to be focused by an on-axis parabolic mirror of 65 cm focal length onto high density implosion plasmas. In the second phase of this project, the beam diameter to the compressor will be increased to 35 cm and we will deliver a 1 kJ/1 ns pulse onto the target plasmas.

As another module for the petawatt laser, a 30 J/0.5 ps laser beam has been completed by modifying GEKKO MII. In the first test experiment, we are going to irradiate a CD plastic foil target to observe the energy coupling between the laser and the solid density plasma. As has been reported by the group at Rutherford Appleton Laboratory [24], we expect that 10^8–10^9 DD neutrons will be generated in the

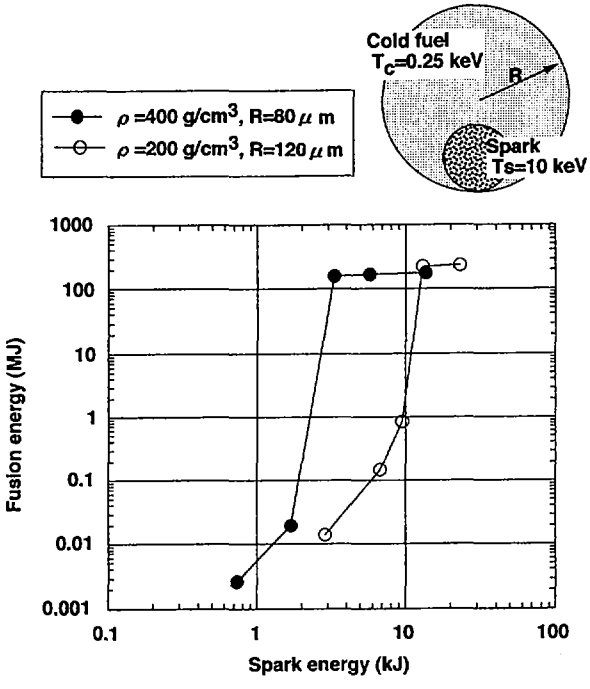

FIG. 10. Gain calculation for off-central ignition. The expected fusion energy in the case of off-central fast ignition has been calculated using the 2-D hydrodynamic code ILESTA-2D as a function of the spark energy. The spark energy was changed by changing the volume of the spark region. The temperatures of the cold fuel and the spark were fixed to be 0.25 and 10 keV, respectively.

experiment. We are also investigating the transfer efficiency of a 10^{19}–10^{20} W/cm^2 picosecond pulse through a solid density plasma whose thickness is a few micrometres. According to the simulation results, a 10^{20} W/cm^2 laser pulse makes a channel in an overdense ($n/n_c = 7$) plasma slab with 2 μm thickness, and 90% of the pulse energy passes through the foil.

Off-central ignition has been investigated by using the ILESTA-2D hydrodynamic simulation. The ignition condition for the off-central spark is found to be the same as for the central spark. Namely, the condition on the required spark energy (GJ) is

$$E_s = 10.6 \times \left(\frac{\rho_s}{\rho}\right)^2 (\rho R)^3 T \tag{1}$$

where T is the spark temperature in keV, ρR is the areal mass density in g/cm^2 and ρ_s and ρ are the solid DT density and the spark plasma density, respectively. The ignition condition for T = 5–20 keV is given by

$$(\rho R)^3 T = 1 \tag{2}$$

Equations (1) and (2) indicate that the spark energy can be less than 1 kJ when $\rho/\rho_s \geq 3000$. The ignition and gain curves are shown in Fig. 10. From the above analysis, we concluded that a pulse of several kJ·ps can ignite cold superdense DT fuel (≥ 600 g/cm^3) which could be generated by a multikilojoule blue laser system, such as the upgraded GEKKO XII laser.

6. SUMMARY

The GEKKO XII laser system has been improved to carry out uniform implosion experiments. The implosion experiments show that the normalized neutron yield reaches order unity when the convergence ratio is less than 8 and the e-folding of the R–T instability is less than 4. The limitations of the new GEKKO XII performance are due to the finite beam number effects. In order to increase the normalized neutron yield for higher convergence ratio implosion, it is necessary to control the laser beam intensity profile by introducing an appropriate kinoform plate.

In the fundamental planar experiments, we investigated initial imprint, rippled shock propagation and precise R–T instability growth rate, and we carried out fundamental experiments for hybrid schemes. The database obtained through these experiments will be further improved and used for ignition and high gain target design in the future.

REFERENCES

[1] AZECHI, H., et al., Laser Part. Beams **9** (1991) 193.
[2] NAKAI, S., et al., in Plasma Physics and Controlled Nuclear Fusion Research 1994 (Proc. 15th Int. Conf. Seville, 1994), Vol. 3, IAEA, Vienna (1996) 3.
[3] SHIRAGA, H., et al., IAEA-CN-64/B2-4, this volume.
[4] KATO, Y., et al., IAEA-CN-64/B2-6, ibid.
[5] KATO, Y., et al., "Implosion experiments with uniformity-improved GEKKO XII: Overview", Proc. 12th Int. Conf. on Laser Interaction and Related Plasma Phenomena, Osaka, 1995, AIP Conf. Proc. **369** (1996) 101.
[6] NAKANO, H., et al., Opt. Commun. **73** (1990) 123.
[7] MIYANAGA, N., et al., in Laser Interaction and Related Plasma Phenomena, Vol. 10 (MILEY, G.H., HORA, H., Eds), Plenum Press, New York (1992) 251.
[8] NAKANO, H., et al., J. Appl. Phys. **73** (1993) 2122.
[9] SKUPSKY, S., et al., J. Appl. Phys. **66** (1989) 3456.
[10] KATO, K., et al., Phys. Rev. Lett. **53** (1984) 1057.
[11] MATSUOKA, S., et al., Proc. SPIE **2633** (1995) 627.
[12] NAKANO, H., et al., Appl. Phys. Lett. **63** (1993) 580.
[13] VERON, D., et al., Opt. Commun. **65** (1988) 42.
[14] NISHIHARA, K., et al., Phys. Plasmas **1** (1994) 1653.
[15] TAKABE, H., Hydrodynamic simulation code for laser driven implosion physics and algorithm of ILESTA code (in preparation).
[16] TAKAGI, M., NORIMATSU, T., YAMANAKA, T., NAKAI, S., J. Vac. Sci. Technol. A **9** (1991) 2145.
[17] KODAMA, R., et al., Proc. SPIE **2523** (1995) 165.
[18] TANAKA, K.A., et al., "Measurement of absorption distribution by second harmonic and x-ray images", Proc. 12th Int. Conf. on Laser Interaction and Related Plasma Phenomena, Osaka, 1995, AIP Conf. Proc. **369** (1996) 131.
[19] NISHIMURA, H., et al., "Experimental study on direct-drive implosion dynamics and stability with power-balanced, partially coherent GEKKO XII green light", Proc. 12th Int. Conf. on Laser Interaction and Related Plasma Phenomena, Osaka, 1995.
[20] CABLE, M.D., et al., Phys. Rev. Lett. **73** (1994) 2316.
[21] ENDO, T., et al., Phys. Rev. Lett. **74** (1995) 3608.
[22] HONDA, M., et al., in preparation.
[23] TABAK, M., et al., Phys. Plasmas **1** (1994) 1626.
[24] NORREYS, P., et al., in Proc. 12th Int. Conf. on Laser Interaction and Related Plasma Phenomena, Osaka, 1995.

DISCUSSION

D.D. RYUTOV: In your Fokker–Planck calculations of the non-local heat transport, did you take into account the radial electric field? If so, what was its effect?

K. MIMA: Yes. The electric field is determined by the current neutrality condition. It reduces high energy electron transport.

D.D. RYUTOV: In your experiment with the foam coating, what was the size of the non-uniformities of the foam itself? Could these non-uniformities serve as seeds for the R–T instability?

K. MIMA: The size of the foam cell is approximately 0.3 μm. If there is a large variation in cell size, it triggers the R–T instability.

D.D. RYUTOV: A related comment: An interesting option is to use shells with an emulsion-like structure, with suitably chosen non-uniformities impregnated into the matrix material. By using grains of properly chosen size, one can considerably reduce the growth rate. This idea will be published shortly in a paper of mine (Phys. Plasmas **3** (1996) 4336).

K. MIMA: I am not sure about the effects of the grain size on the R–T growth rate. However, your idea sounds interesting.

B. COPPI: The Fast Ignitor approach to ignition from the low temperature side is similar in certain ways to that of the Ignitor experiment with magnetic confinement. You seem to imply that there would not be great difficulty in making the Fast Ignitor idea work. Could you comment on the major objections that have been raised and the difficulties that have been predicted for this.

K. MIMA: The most critical physical issue is the propagation of an intense laser pulse in a large scale corona plasma and the energy deposition process in the over-dense region. Specifically, the coupling efficiency has to be higher than 20%, otherwise the Fast Ignitor concept is not very interesting.

THE FIRST YEAR OF ICF EXPERIMENTS AT THE OMEGA LASER FACILITY

T.R. BOEHLY, R.L. McCRORY, C.P. VERDON, J.M. SOURES, A. BABUSHKIN, R.E. BAHR, R. BONI, D.K. BRADLEY, R.S. CRAXTON, J.A. DELETTREZ, W.R. DONALDSON, R. EPSTEIN, D.R. HARDING, P.A. JAANIMAGI, S.D. JACOBS, K. KEARNEY, R.L. KECK, J.H. KELLY, T.J. KESSLER, R.L. KREMENS, J.P. KNAUER, S.A. LETZRING, D.J. LONOBILE, S.J. LOUCKS, L.D. LUND, F.J. MARSHALL, P.W. McKENTY, D.D. MEYERHOFER, S.F.B. MORSE, A. OKISHEV, S. PAPERNOV, G. PIEN, T. SAFFORD, W. SEKA, R.W. SHORT, M.J. SHOUP III, M.D. SKELDON, S. SKUPSKY, A.W. SCHMID, D.J. SMITH, S. SWALES, M.D. WITTMAN, B. YAAKOBI
Laboratory for Laser Energetics,
University of Rochester,
Rochester, New York,
United States of America

Abstract

THE FIRST YEAR OF ICF EXPERIMENTS AT THE OMEGA LASER FACILITY.

OMEGA, a 60-beam, 351-nm, Nd:glass laser with an on-target energy capability of more than 40 kJ, is a flexible laser and experimental facility that can be used for both direct- and indirect-drive targets and is designed to ultimately achieve irradiation nonuniformities of $<2\%$ on direct-drive capsules with shaped laser pulses (dynamic range $>400:1$). The OMEGA program includes plasma physics experiments to investigate laser–matter interaction physics at temperatures and densities approaching those of direct-drive capsules designed for the 1.8-MJ National Ignition Facility (NIF); experiments to characterize and mitigate the deleterious effects of hydrodynamic instabilities; and implosion experiments with capsules that are hydrodynamically equivalent to high-gain, direct-drive capsules. Results are presented of recent enhancements to the OMEGA system performance, including a new design for distributed phase plates (DPPs), 2-D smoothing by spectral dispersion (SSD), polarization rotators, pulse shaping and a backlighter driver. Results from several direct-drive experiments are presented along with an overview of an indirect-drive experiment. A key result is that OMEGA has achieved the highest thermonuclear yield (1.4×10^{14} DT neutrons) and the highest yield efficiency (1% of scientific breakeven) ever attained in laser-fusion experiments. Other experiments demonstrated OMEGA's versatility at performing experiments that are not spherically symmetric, i.e., planar-target and indirect-drive experiments.

I. INTRODUCTION

The primary objective of the OMEGA experimental program [1] is to test the predictions of future, high-gain, direct-drive capsule performance by investigating capsules that are "hydrodynamically equivalent" to those envisioned for use on the National

Ignition Facility (NIF) [2]. Based on hydrodynamic behavior alone, the laser parameters can be scaled to the capsule by the following relations: energy $E \propto R^3$, power $P \propto R^2$, and time $\propto R$, where R is the capsule radius. Comparing the performance of NIF capsules with that of energy-scaled implosions using 30 kJ of 351-nm laser light, one-dimensional simulations of OMEGA capsules show a similar number of Rayleigh-Taylor (RT) e-foldings during both the acceleration and deceleration phases of the implosion, similar hot-spot convergence ratios (C_R) in the range of 20–25, and similar implosion velocities [1].

Based on these considerations, the LLE experimental program culminates in experiments that demonstrate "near-ignition" conditions in the hydrodynamically equivalent cryogenic DT capsules. A key step in this program was the design and construction of the OMEGA laser [3], a 40-kJ, 60-beam laser that ultimately will produce on-target irradiation with less than 2% nonuniformity.

Since the completion of the laser system in May 1995, OMEGA experiments have been conducted to characterize the system performance, activate experimental diagnostics, and begin the experimental program. The latter consists of several key campaigns, each of which begins by assessing various aspects of target performance irradiated with nominal unsmoothed laser beams. Results from these experiments will provide a benchmark to which future experiments that employ various uniformity enhancements can be compared. Each time the irradiation uniformity is increased, a subset of these experiments will be repeated to gauge the efficacy of that change. As the program progresses, each of these measurements will become fine-tuned for the ultimate experiments at 1%–2% nonuniformity.

II. OMEGA PERFORMANCE

During system-activation experiments [4] performed in April–May 1995, OMEGA met or exceeded the required baseline performance: on-target energy exceeded 37 kJ on 60-beam shots; beam-to-beam energy balance was held to less than ±8% rms; one beam was tested with an on-target energy equivalent to full-system operation of 45 kJ UV; 15 60-beam, high-energy shots were taken in less than 15 h; and the UV on-target energy was stable to better than 1% in a four-shot series taken in less than 4 h. During the first year of operation, OMEGA continued to perform at this level. Typically, experimental campaigns were allotted four days per week of laser time during which 20 or more target shots were routinely obtained.

Several enhancements to the laser have been implemented during the first year of operation: Distributed phase plates (DPP's) [5] have been developed to permit greater control over the shape of the beam's intensity envelope without sacrificing energy on target. (With the previous DPP's, 15%–20% of the laser light was lost around the target.) The technique of beam smoothing by spectral dispersion [6] (SSD) has been extended to include spectral dispersion in a second direction (2-D SSD). This reduces the rms nonuniformity by factors of 2 to 5 over time intervals of interest for hydrodynamic implosions. Prototype polarization shifters [7] (wedges) are being implemented (initially on a subset of beams) to reduce the nonuniformity by an additional factor of $\sqrt{2}$. Also, pulse shaping has been implemented and demonstrated on experiments where different pulse shapes were propagated down different beamlines.

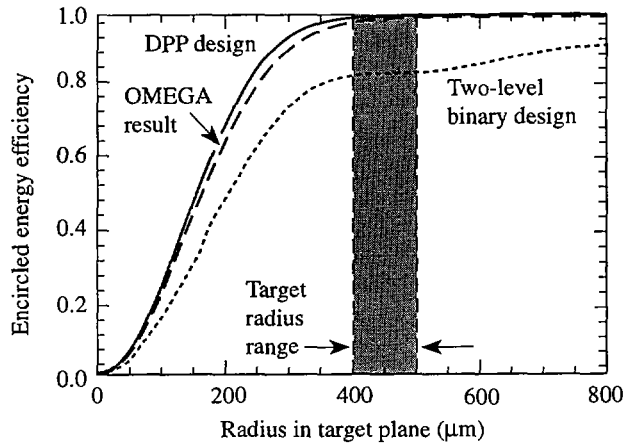

FIG. 1. On-target energy fraction as a function of radius. An increase in energy efficiency from 78 to 96% is obtained by replacing the binary phase plate with a continuous phase plate (dotted line). The calculated (solid line) and experimental (dashed line) results for the continuous phase plates agree closely.

The new continuous DPP's perform nearly lossless phase conversion of high-power laser beams, providing a transmission to the target of ~95%. The residual loss of a few percent is due to imperfections in the manufacturing process such as surface scatter and reflections. The new DPP's also operate over the full range of target diameters planned for the LLE experimental fusion program. This is in contrast to the binary-element DPP that could operate over only a narrow range in the focal direction. Figure 1 shows that the energy coupled to a target using a new continuous DPP is substantially greater than that using a two-level binary phase plate — a 20%–25% increase in the total energy delivered to the target. Direct-drive implosions normally require DPP's that produce center-peaked (i.e., ~Gaussian) focal spots. A set of 12 super-Gaussian $[\exp(r/r_0)^8]$ have been developed for planar-target experiments.

2-D SSD was implemented on OMEGA in January 1996, a year ahead of schedule. It was important to adopt a conservative strategy in regard to bandwidth during the time that the operating characteristics of the new laser and SSD were being studied because spectrally dispersed bandwidth can introduce intensity fluctuations that can damage laser optical components. The initial implementation of 2-D SSD used bandwidths of 1.5 Å and 0.75 Å. Figure 2 depicts five time-integrated, equivalent-target-plane (ETP) images of the single-beam UV intensity profile for various levels of smoothing, ranging from none to full 2-D SSD.

The increased uniformity achieved is characteristic of an SSD smoothing time roughly equal to the pulse width, which was ~1 ns for this experiment. Figure 3 depicts spatial frequency "power spectra" for the images shown in Fig. 2. The accompanying table shows the agreement between predicted and measured rms intensity fluctuations around smooth envelopes. A large part of the improved uniformity for

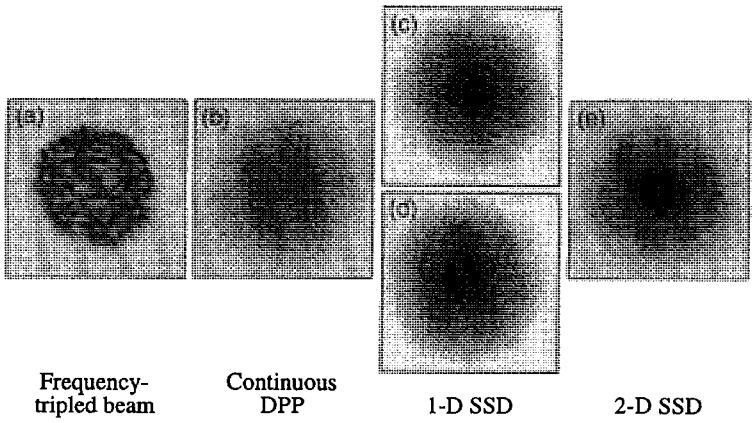

FIG. 2. Equivalent-target-plane (ETP) images of the single-beam UV intensity distribution: (a) UV beam without phase plate or SSD; (b) UV beam with phase plate (note the well-defined intensity envelope with highly modulated speckle); (c) and (d) smoothing with 1-D SSD (the 'stripes' represent deflection of speckle along the direction of spectral dispersion); (e) improved smoothing due to 2-D SSD.

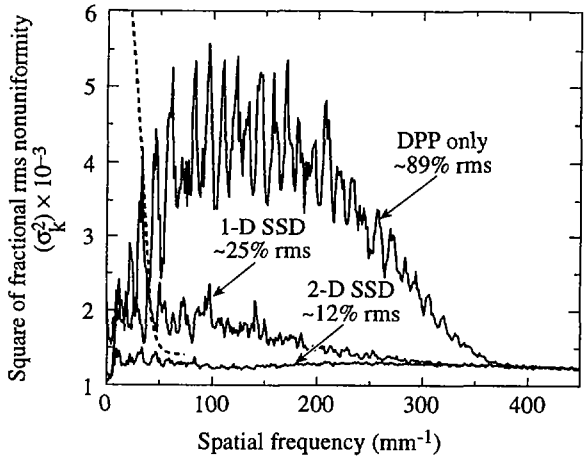

Single-beam predictions

Smoothing time (ns)	σ_{rms} % 1-D SSD	2-D SSD
0.0	95	95
0.1	32	26
0.2	26	19
0.3	23	17
0.5	23	14
1.0	21	11

$$\sigma_{rms} = \sqrt{\Sigma \sigma_k^2}$$

FIG. 3. Square of amplitudes in Fourier space σ_k^2 of deviations from smooth envelopes in the single-beam far-field patterns as a function of the wavelength of the nonuniformity. Solid lines are three cases with a DPP: no SSD, 1-D SSD and 2-D SSD. The case with no DPP and no SSD is indicated by the dotted line.

2-D SSD compared with 1-D SSD (a factor of ~2) is related to the smoothing time: 1-D SSD reaches an asymptotic level of uniformity after ~300 ps; 2-D SSD continues to smooth throughout the entire time of the pulse (1 ns). There is an increased bandwidth for 2-D SSD (due to contributions from both modulators); for this example, however, it has a much smaller effect on the improved uniformity than the increased smoothing time. Recently, prototype polarization wedges were tested on OMEGA. The results are very encouraging in that the predicted $1/\sqrt{2}$ reduction in nonuniformity was obtained. Since these devices instantaneously reduce nonuniformities in the beam, they are expected to reduce the irradiation imprinting that occurs before appreciable SSD smoothing takes effect.

In July 1996, OMEGA was equipped with a pulse-shaping system that provides to the power amplifiers an IR pulse shape that produces the desired UV pulse shape on-target. These temporally shaped IR pulses are generated by applying specifically shaped electrical waveforms to a waveguide integrated-optic amplitude modulator that is fiber coupled to the OMEGA driver. Three such systems are needed, one for each of the OMEGA drivers. The shaped electrical waveforms are generated using optically activated Si photoconductive switches and variable-impedance microstrip lines [8].

Since its implementation, pulse shaping has been used on several experiments and four different pulses have been created: a 3-ns square, a 1-ns ramp to 2-ns flattop, a 200-ps Gaussian, and 1-ns square. To accommodate x-ray backlighting for several experiments, a different pulse shape was propagated through the different legs of the laser. The result was a group of 40 beams that had a ramped pulse, and 20 beams that had the 3-ns flattop. Fiber-optic coupling and multiple drivers (currently OMEGA has three) allow variations in pulse shape and beam configuration to occur with minimal impact on the system or its shot rate.

III. ICF EXPERIMENTS

The initial experiments evaluated and refined the precision with which beams are pointed and focused onto spherical targets. These tests demonstrated a pointing precision of ±16 μm rms—the precision required for the near-ignition-conditions experiments ultimately planned for OMEGA. Similarly, the location of the focal cone for each beam can be determined to a precision of ±85 μm along the laser propagation direction. This enables precise control of the laser-spot size on target, a requirement for control of on-target energy and power balance. Planar-target experiments demonstrated similar pointing and focusing precision for targets deliberately displaced 4.5 mm from target-chamber center. The success of pointing experiments performed on hohlraum targets (see below) further demonstrated OMEGA's versatility.

The first series of target experiments was carried out primarily to activate and calibrate diagnostics as well as to establish a baseline target performance with unsmoothed laser beams. During the first year, nearly all of the ICF experiments were conducted without DPP's. To assess the irradiation uniformity for these experiments, the variations in x-ray emission from gold-coated targets were measured with various x-ray cameras. The observed variations of ±12.5% rms are consistent with estimates of the laser-irradiation nonuniformity that take into account the intensity distribution of unsmoothed laser beams and a beam-to-beam energy balance of ±6.6% rms.

One series studied implosions of mainly glass microballoons (GMB's) having high initial aspect ratios ($R/\Delta R$, where R is the target radius and ΔR is the shell thickness) of ~150 to 300, filled with either pure deuterium or an equimolar mixture of deuterium and tritium at pressures ranging from 5 to 20 atm. These low-mass shells were accelerated to high implosion velocities. The compressed fuel was predicted to have a high electron temperature (up to 6 keV) and a density in the range of 0.2 to 2 g/cm^3.

Neutron yields up to 1.4×10^{14} (1% of scientific breakeven)—the highest recorded to date from any laser system—were obtained from DT targets, yields up to 1.1×10^{12} were obtained from DD targets, and fuel ion temperatures up to 13 keV were measured. Spectroscopic diagnostics based on the continuum slope and krypton line ratios demonstrated electron temperatures from 3 to 4 keV [9].

Preliminary experiments were performed to investigate the stability of spherical implosions and study fuel-pusher mixing. These experiments are designed to study both the development of unstable growth at the ablation surface during capsule acceleration and the pusher-fuel mix that occurs during target deceleration. Acceleration-phase instability growth is studied using the so-called "burnthrough" technique in which time-resolved spectroscopy is used to detect the onset of characteristic line emission from a signature layer buried under several microns of plastic. It has been shown that the emission onset time is highly sensitive to instability growth and is a strong indicator of incident drive nonuniformity [10–12].

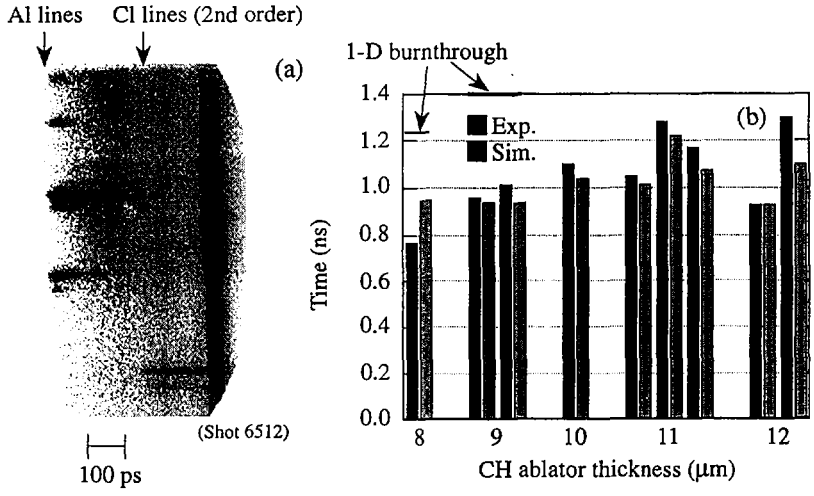

FIG. 4. (a) Time-resolved x-ray spectrum from an imploding target containing a Cl-doped signature layer. The x-ray emission from the Cl signals the time at which the heat front penetrates the ablator layer outside the signature layer; (b) comparison of the experimental burnthrough times with those predicted using the mix model discussed in Refs [10–12].

Figure 4(a) depicts a time-resolved x-ray spectrum from an imploding target containing a Cl-doped signature layer. X-ray emission from the Cl signals the time at which the heat front penetrates the ablator layer outside the signature layer. In an attempt to quantify the level of mixing, a model was developed [10–12] that uses a postprocessor to the 1-D hydrocode to predict the mix using experimentally measured laser nonuniformity spectra as seeds to the instability. Figure 4(b) graphically compares the experimental burnthrough times with those predicted using such a model. Good agreement is observed over a range of outer ablator thicknesses. For comparison, we also show the emission onset times predicted for the case of no instability growth: emission would be expected for only the two thinnest ablators, and in each case much later than observed. These measurements, recorded using unsmoothed laser beams, are the comparison baseline for subsequent laser-uniformity and pulse-shape changes.

In a related experiment, mixing at the fuel-pusher interface was studied using targets with an inner layer of deuterated plastic (CD) and filled with hydrogen gas. The neutron yields produced by imploding these targets indicate the amount of mixing of the CD layer with the hydrogen gas and surrounding ablator material. As different-thickness layers of pure plastic (CH) are inserted between the hydrogen gas and the CD, the extent to which mix occurs can be gauged from the relationship of yield to CH-layer thickness. The yield from these preliminary experiments was sufficiently high to provide adequate signals for the neutron diagnostics. These yields along with the trends in data obtained for a limited number of CH thicknesses indicate that this experimental technique will be a powerful diagnostic for fuel-pusher mixing.

In addition to spherical-target shots, several multifoil, planar-target experiments were performed to study the Rayleigh-Taylor (R-T) instability. These experiments, which are a continuation and extension of an existing collaboration between LLNL and LLE, study two aspects of direct-drive target stability: growth rates and irradiation imprinting. To begin this work at LLE, an investigation of energy coupling to the target was first performed. Later experiments studied measurement of R-T growth rates for various target types and investigated a novel technique to study imprinting.

Typical planar-target stability experiments use six to ten beams to drive a CH foil with intensities around 2 to 4 $\times 10^{14}$ W/cm^2. Various other beams (10 to 20) are used to produce x rays that backlight the driven target for time-resolved radiography. Figure 5(a) is the streaked side-on radiographic image of a 20-μm CH foil irradiated by 10^{14} W/cm^2 in an ~3-ns pulse. Note that *LILAC* simulates the target trajectory (black line) quite well. In another experiment, face-on radiography of an accelerated target was used to measure the growth target-mass perturbations intentionally molded into the target. Data from a target with a 50-μm mass perturbation and an initial amplitude of 0.5 μm show very good agreement with the simulations [Fig. 5(b)]. The growth rates obtained from similar OMEGA experiments are also consistent with experimental results on Nova. Figure 6 shows three framing-camera images (at 1.6, 2, and 2.4 ns) of an experiment similar to that shown in Fig. 5 (except with a 1-ns drive pulse). Note that the central portion (~500-μm diameter) of the target remains planar (i.e., little bowing or 2-D effects) over nearly 200 μm of displacement and 2 ns [image (b)]. These target trajectories are also simulated by *LILAC*. These data provide confidence in the code's ability to model the energy coupling to target and demonstrate that pla-

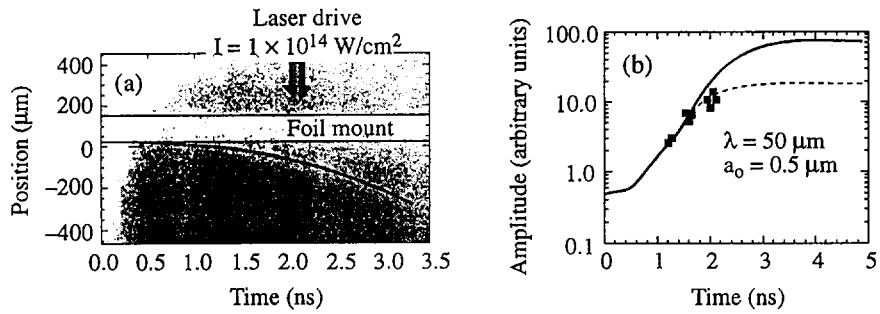

FIG. 5. (a) Streak image of a 20-μm CH foil accelerated by a 3-ns UV pulse with an intensity of 1.5 × 10^{14} W/cm^2. The target was backlit by x-rays from a gold backlighter target. The target displacement simulated by LILAC *is superposed (solid curve) over the shadow of the target. (b) Measured growth (points) of a 50-μm-wavelength, 0.5-μm-amplitude perturbation compared to simulations with (dotted) and without (solid) a saturation model.*

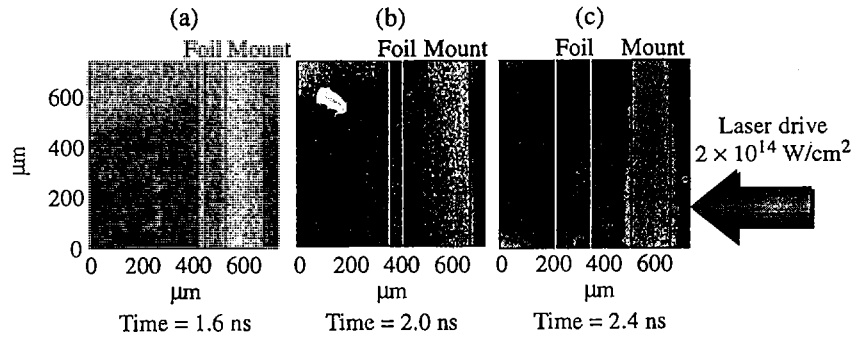

FIG. 6. Three framing camera images of a 20-μm CH foil irradiated at 2 × 10^{14} W/cm^2 by a 1-ns UV pulse. The central 500 μm diameter of the accelerated foil remains planar after 200 μm displacements.

nar-target conditions (i.e., little 2-D effects) are maintained over target displacement to sufficiently conduct R-T stability experiments.

To demonstrate the effect of initial laser nonuniformities on planar-target stability, a "perturbing" beam was added to the beams that drive the CH foil. The objective was to accelerate a foil with as uniform irradiation pattern as available and add this perturbing beam at different times or energies. By relating changes in the conditions of the perturbing beam to changes in the observed growth, one can study the times and contrasts over which imprinting is important.

Mass variations in the driven target were measured using time-resolved face-on radiography. Modulations in transmitted backlighter intensity are related to spatial modes of the perturbations in the target. For the perturbing-beam experiments, the nominal drive beams were 1000 μm in diameter and the perturbing beam was 400 μm.

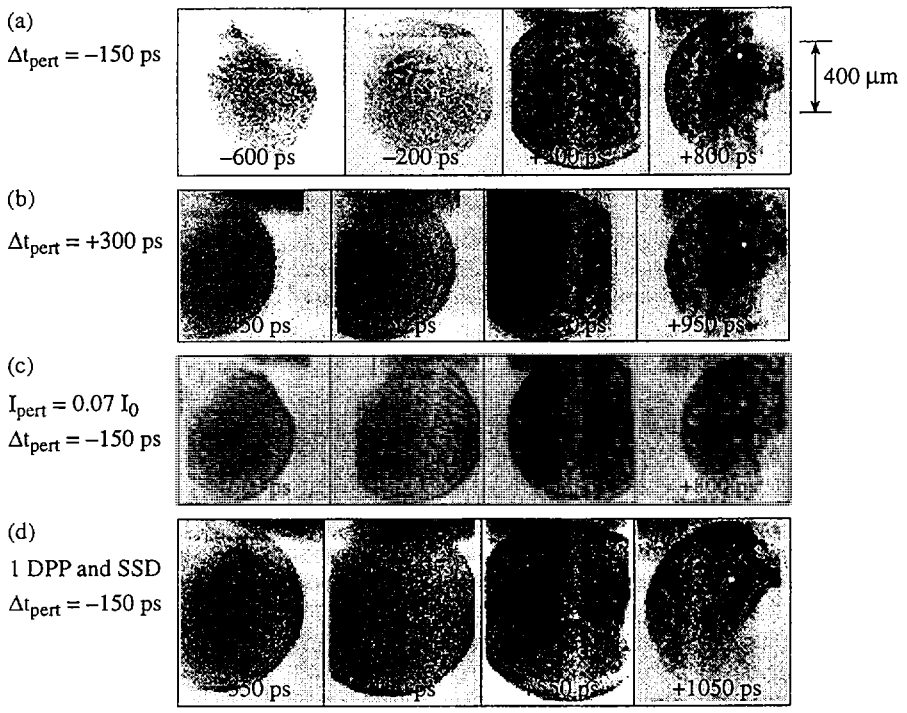

FIG. 7. Four sets of face-on radiographic images from imprinting beam experiments. In each case the imprinting beam is 400 μm in diameter, but its conditions change: (a) timed 150 ps ahead of drive, same intensity; (b) timed 300 ps after drive, same intensity; (c) timed 150 ps ahead of drive, 0.1 intensity; (d) timed 150 ps ahead of drive, same intensity with SSD.

Qualitatively, significant differences can be seen in the radiographic images as the irradiation conditions were changed. Figures 7(a)–7(d) depict images from four shots with various conditions on the perturbing beam. The upper row of images [Fig. 7(a)] shows that, when timed 150 ps before the drive pulses, the perturbing beam imprints its features onto the target, seeding unstable growth (seen as modulations) that occurs later in time. This effect of the perturbing beam is obviously diminished when it is delayed by 300 ps with respect to the drive beams [Fig. 7(b)]. This is likely the result of sufficient plasma formation to allow smoothing of the irradiation nonuniformities. In both cases, the perturbing beam had an intensity equal to the total drive-beam intensity, i.e., $\sim 2 \times 10^{14}$ W/cm^2. When the intensity of the perturbing beam was reduced to 7% of the drive beams, its effect was no longer observed in the radiographic images, as depicted in Fig. 7(c).

The most notable change in target behavior occurred when SSD (with no DPP's) was applied to all incident beams. Figure 7(d) shows radiographic images for an experiment using identical irradiation configuration [as in Fig. 2(a)], except that all beams

have SSD. Although it is not a standard implementation on OMEGA, SSD without DPP's was utilized because increases in uniformity can be achieved over a moderate range of spatial frequencies (i.e., wavelengths between 40 and 200 μm). Once these perturbing-beam experiments are refined, they will be used to study the following: effects of deliberately created modulations in the irradiation, imprinting mitigation schemes such as foam overcoatings, and the effectiveness of uniformity enhancements to the laser.

Finally, we discuss a significant departure from the type of experiments normally conducted at LLE. The usefulness of OMEGA for conducting indirect-drive experiments was recently demonstrated in a two-week series of experiments. This campaign involved a collaboration of approximately 28 scientists from LANL, LLNL, and LLE. A total of 42 shots were taken, and the target performance was diagnosed using six x-ray pinhole cameras, two x-ray microscopes, three x-ray framing cameras, DANTE (time-resolved, absolutely calibrated, soft x-ray emission), neutron yield and neutron time-of-flight detectors, a single-hit detector array, and a number of other laser and plasma diagnostics. This represents one of the largest arrays of diagnostics ever fielded on a hohlraum target campaign to date.

The most important goal for these experiments was verification of OMEGA's ability to provide accurate alignment of the hohlraum targets and accurate pointing of the laser beams. This was unequivocally demonstrated. Figure 8, an x-ray image of a thin-walled hohlraum irradiated by 30 OMEGA beams, shows the beam positions as well as the imploded core. A beam-pointing error of 30 μm was measured for these experiments. Additionally, data were obtained on implosion core symmetry, neutron yield, and radiation temperature to compare with the existing Nova data base, and new capabilities arising from OMEGA's unique 60-beam geometry were demonstrated [13]. Discussions with LLNL and LANL have begun on future hohlraum experiments to be conducted on OMEGA.

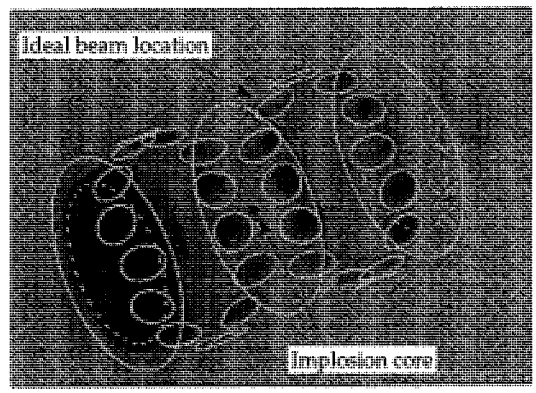

FIG. 8. An x-ray image of a thin-walled hohlraum irradiated by 30 OMEGA beams. The desired beam locations (white ellipses) have been superposed onto the figure. The imploded core is clearly visible in the image as is the on-axis stagnation of the hohlraum plasma.

The near-term experimental plan is to achieve <4% rms beam-to-beam energy balance and to implement 60 of the new, continuous DPP's on OMEGA. It is expected that these improvements will greatly reduce the on-target irradiation nonuniformities. This along with the ability to control the on-target pulse shape will produce considerably improved target performance. In addition, this will enable quantitative studies of spherical implosion stability and fuel-pusher mixing experiments, both of which are very sensitive to irradiation nonuniformities.

IV. SUMMARY

In the first year of experiments, OMEGA has demonstrated laser performance in excess of its specifications and exceeded previously obtained laser-fusion neutron yields. The initial phases of several direct-drive, spherical-implosion experiments show very promising results. High-quality, indirect-drive experiments have also been performed on OMEGA. The planar-target-stability experiments have demonstrated consistency (and continuity) with experiments performed elsewhere and have demonstrated the utility of multibeam experiments that can be performed only on OMEGA. These results have demonstrated the facility's utility and versatility.

ACKNOWLEDGMENT

This work was supported by the U.S. Department of Energy Office of Inertial Confinement Fusion under Cooperative Agreement No. DE-FC03-92SF19460, the University of Rochester, and the New York State Energy Research and Development Authority. The support of DOE does not constitute an endorsement by DOE of the views expressed in this article.

REFERENCES

[1] McCRORY, R.L., et al., in Plasma Physics and Controlled Nuclear Fusion Research 1994 (Proc. 15th Int. Conf. Seville, 1994), Vol. 3, IAEA, Vienna (1995) 33.
[2] STORM, E., et al., in Plasma Physics and Controlled Nuclear Fusion Research 1990 (Proc. 13th Int. Conf. Washington, D.C., 1990), Vol. 3, IAEA, Vienna (1991) 99.
[3] BOEHLY, T.R., et al., Rev. Sci. Instrum. **66** (1995) 508.
[4] BOEHLY, T.R., et al., Opt. Commun. (in press).
[5] LIN, Y., et al., Opt. Lett. **20** (1995) 764; High-Efficiency Distributed Phase Plate Generation and Characterization, LLE Rev. **65**, NTIS document DOE/SF/19 460-117 (1995) 1.
[6] SKUPSKY, S., et al., J. Appl. Phys. **66** (1989) 3456.
[7] LABORATORY FOR LASER ENERGETICS, Phase Conversion Using Distributed Polarization Rotation, LLE Rev. **45**, NTIS document DOE/DP40 200-149 (1990) 1.
[8] WILCOX, R.B., et al., in Laser Coherence Control: Technology and Applications (Proc. Conf. SPIE, Bellingham, WA, 1993), **1870** (1993) 53;
OKISHEV, A., et al., in Superintense Laser Fields (Proc. SPIE, Bellingham, WA, 1996) **2770** (1996) 10.
[9] SOURES, J.M., et al., Phys. Plasmas **3** (1996) 2108.
[10] DELETTREZ, J., et al., Phys. Rev A **41** (1990) 5583.
[11] BRADLEY, D.K., et al., Phys. Rev. Lett. **68** (1992) 2774.
[12] DELETTREZ, J., et al., Phys. Plasmas **1** (1994) 2342.
[13] MURPHY, T.J., et al., in Anomalous Absorption (Proc. 26th Conf. Fairbanks, AK, 1996) (in press).

DISCUSSION

K. MIMA: Is a foam overcoated target going to be used for the full scale implosion experiment?

T.R. BOEHLY: Yes.

K. MIMA: When will the experiment be carried out? Please give us the future experiment schedule.

T.R. BOEHLY: A proposal is being considered for experiments in 1997.

K. MIMA: Is foam coating necessary even with the precise power balance and beam smoothing?

T.R. BOEHLY: The LLE programme plan does not require foam overcoatings to reach its objectives. However, we will investigate any technology that may enhance our probability of success. Experiments have demonstrated that foams can mitigate irradiation imprinting. We intend to study that phenomenon to determine whether it will be useful to our programme.

T. DESAI: You have reported a world record neutron yield. Have you measured the corresponding dense plasma temperature? What is the technique?

T.R. BOEHLY: On the basis of neutron time of flight measurements, the ion temperature in the core was inferred to be 10–12 keV.

PROGRESS ON THE PHYSICS OF IGNITION FOR RADIATION DRIVEN INERTIAL CONFINEMENT FUSION (ICF) TARGETS

J.D. LINDL, M.M. MARINAK
Lawrence Livermore National Laboratory,
Livermore, California,
United States of America

Abstract

PROGRESS ON THE PHYSICS OF IGNITION FOR RADIATION DRIVEN INERTIAL CONFINEMENT FUSION (ICF) TARGETS.

Extensive modelling of proposed National Ignition Facility (NIF) ignition targets has resulted in a variety of targets using different materials in the fuel shell, using driving temperatures which range from 250 to 300 eV, and requiring energies which range from less than 1 MJ up to the full 1.8 MJ design capability of the NIF. Recent experiments on Nova have shown that hohlraum walls composed of a mixture of high Z materials could result in targets which require about 20% less energy. Nova experiments are being used to quantify the benefits of beam smoothing in reducing stimulated scattering processes and laser beam filamentation for proposed gas filled hohlraum targets on the NIF. Use of smoothing by spectral dispersion (SSD) with 2-3 Å of bandwidth results in <4-5% of stimulated Raman scattering (SRS) and less than about 1% stimulated Brillouin scattering (SBS) for intensities less than about 2×10^{15} W/cm^2 for this type of hohlraum. The symmetry in Nova gas filled hohlraums is affected by the gas fill. A large body of evidence now exists which indicates that this effect is due to laser beam filamentation which can be largely controlled by beam smoothing. Here the first 3-D simulations of hydrodynamic instability for the NIF point design capsule are presented. These simulations, with the HYDRA radiation hydrodynamics code, indicate that spikes can penetrate up to 10 μm into the 30 μm radius hot spot before ignition is quenched. With capsules whose surface is modified by laser ablation, Nova experiments have been used to quantify the degradation of implosions subject to near NIF levels of hydrodynamic instability.

The ignition threshold for radiation driven ICF targets, as indicated in Fig. 1, is governed by the limitations imposed by laser–plasma interactions, which affect the peak driving flux and symmetry of X rays in hohlraums, and by the growth of hydrodynamic instabilities in the imploding shell containing the fusion fuel, which sets a minimum on the required driving pressure (or radiation flux) [1]. Laser–plasma parametric instabilities limit the radiation temperature, in long pulse hohlraums suitable for ignition, to about 300 eV. Hydrodynamic instabilities, which enforce a minimum drive pressure, place a minimum temperature requirement of about 250 eV for the NIF. Hence, the NIF has about a factor of two margin in both power and energy above the ignition threshold.

Increasingly detailed LASNEX [2] computer calculations [3, 4] carried out over the past several years have identified a wide variety of potential target designs which can achieve ignition. Targets have been evaluated which achieve ignition over a range

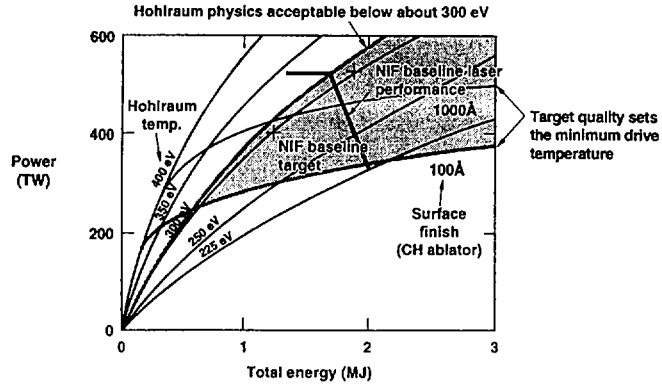

FIG. 1. Plasma physics issues constrain the achievable hohlraum temperatures, and hydrodynamic instabilities establish the minimum required temperatures for ignition. Above ~0.6–1.0 MJ, depending on the target surface finish, there is a region in laser power/energy space consistent with ignition.

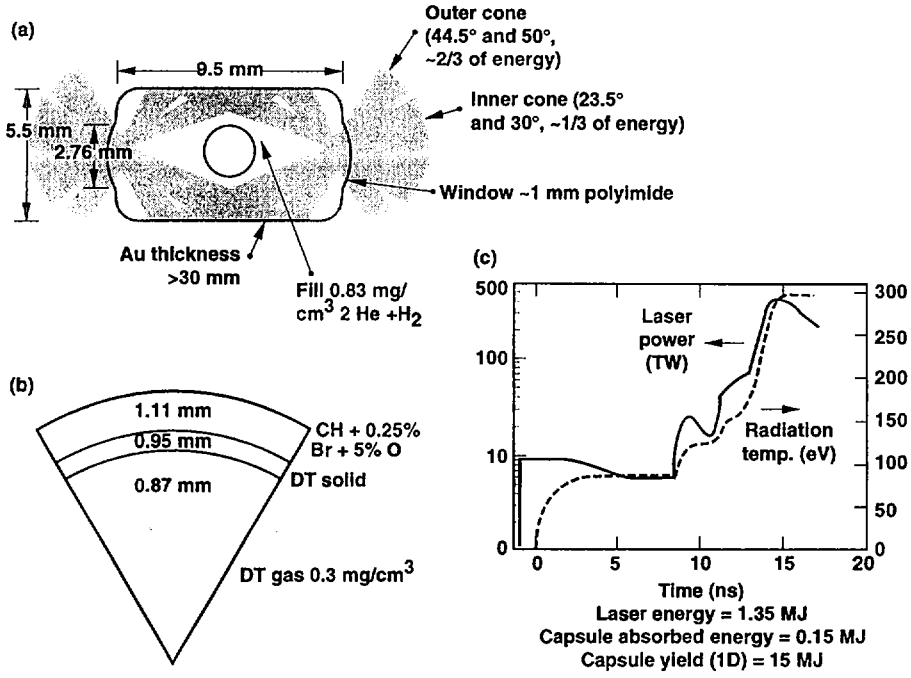

FIG. 2. Most of the LASNEX integrated modelling and detailed analysis of Rayleigh–Taylor instability has concentrated on a target, called the PT, which absorbs about 1.3 MJ of 0.35 μm laser light.

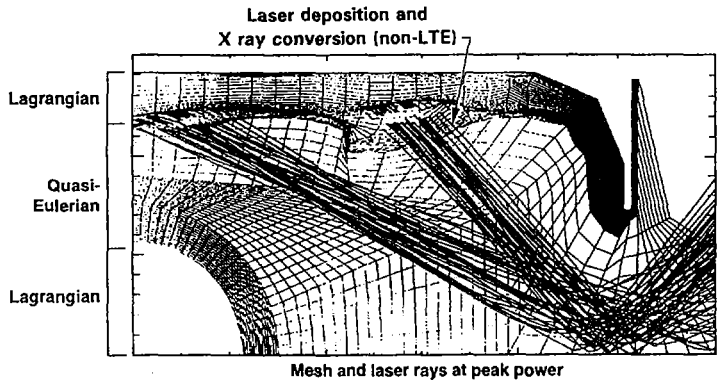

FIG. 3. Integrated LASNEX simulations include, in one simulation, all the physics except small scale hydrodynamic instability and laser-plasma instability growth. Shown is a numerical grid at the peak of the laser pulse. The calculation has a plane of mirror symmetry about the left vertical axis and an axis of rotation about the lower horizontal axis.

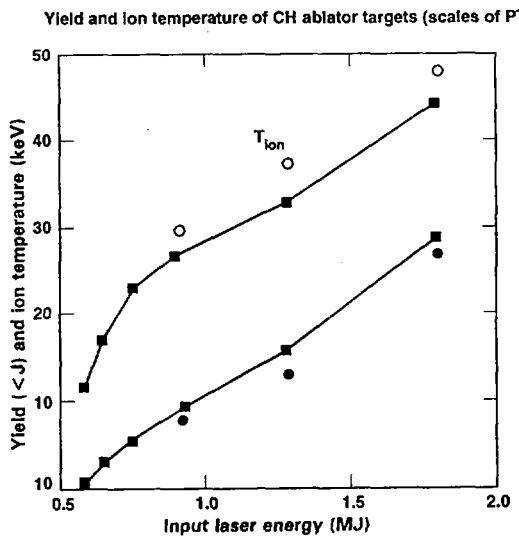

FIG. 4. In integrated calculations, the ignition threshold is less than 1 MJ for scales of the PT. Circles are from 2-D LASNEX integrated calculations. The lines are from 1-D calculations.

of energies from 0.9 MJ to the full 1.8 MJ of the NIF and from 250 eV to 300 eV. In addition, a variety of materials including various plastics, beryllium, and B_4C can be used as ablators on the fuel capsule.

Figure 2 shows a schematic of the target design: the PT design, which has had the most detailed analysis. It uses a plastic ablator doped with Ge for the fuel capsule, which also contains a cryogenic layer of DT. The hohlraum has Au walls and is filled with a mixture of He/H gas. Two rings of beams, with independent pulse shape, from each side are located to provide symmetry. Typical LASNEX calculations include the laser propagation and deposition, X ray production and transport, material evolution in the hohlraum and the capsule implosion in a single integrated calculation. The numerical grid and the laser rays from a calculation of the PT design at peak power are shown in Fig. 3. The performance of the PT design at various sizes, corresponding to the laser energies indicated, is shown in Fig. 4. Asymmetry modelling from the integrated LASNEX calculations is used to determine how good the symmetry must be, and provides specifications on the NIF. The principal sources of capsule non-uniformity are capsule perturbations from the ablator and cryogenic fuel and non-uniformities in the radiation flux produced in the hohlraum. From the simulations we find that these various sources add approximately in quadrature so we require:

$$\left(\frac{\text{Cryolayer non-uniformity}}{\text{Max. tolerable}}\right)^2 + \left(\frac{\text{Ablator non-uniformity}}{\text{Max. tolerable}}\right)^2$$

$$+ \left(\frac{\text{Symmetry non-uniformity}}{\text{Max. tolerable}}\right)^2 < 1$$

For the effects of long wavelength flux non-uniformity from the hohlraum to be about comparable to the shorter spatial scale perturbations from the ablator and cryogenic fuel layer in the above equation, the imploded configuration must be spherical to $<25\%$. This degree of sphericity requires a time average X ray flux uniformity of about 1%. Depending on the time duration, the target can tolerate symmetry variations which are 5–10%. The ignition capsules can also tolerate several hundred picoseconds of variation in the pulse shape timing. The NIF laser specifications have been chosen so that pointing, power balance and pulse shape specifications are consistent with this degree of precision. For example, pointing errors of 50 μm rms produce a capsule asymmetry of $<0.3\%$, and power balance errors of 8% rms produce an asymmetry of $<0.5\%$. The expected level of uncertainty from the laser specifications and the tolerable variations are indicated in Table I.

Because of computer size constraints, we are not able to include the microphysics of laser–plasma interaction or the short spatial scale hydrodynamic instabilities in these integrated calculations. The laser–plasma coupling is treated as a constraint which limits the achievable hohlraum temperature. The short spatial scale

TABLE I. INTEGRATED CALCULATIONS SHOWING THAT PT TARGET DESIGN SENSITIVITIES ARE CONSISTENT WITH NIF SPECIFICATIONS
Tolerable variations correspond to FWHM in yield, based on integrated calculations, expected variations are preliminary estimates of system uncertainty, based on NIF laser specifications and experimental uncertainties

Laser parameter	Tolerable	Expected
Power during foot (%)	30	<5
Peak power (%)	35	<5
Second rise timing (ps)	500	<100
Third rise timing (ps)	500	<100
Duration of peak power (ps)	800	<100
Inner beam power during foot (total power fixed) (%)	25	<5
Inner beam power during peak (total power fixed) (%)	35	<5
Inner beam power during peak (outer cone power fixed) (%)	25	<5
Pointing of inner beams (μm)	200	<200
Pointing of outer beams (μm)	350	<20

hydrodynamic instabilities are treated in separate calculations which include the effects of asymmetry on the capsule from the integrated calculations.

Hohlraums which achieve 300 eV radiation temperatures in NIF size, geometry, and time scales produce large volumes of plasma at a density of $\sim 10^{21}/cm^3$ with temperatures of 4–5 keV. The single beam laser intensity at a laser wavelength of 0.35 μm is (1–2) $\times$ 10^{15} W/cm^2 during the peak of the laser pulse. As shown in Fig. 5, extensive experiments on the Nova laser have demonstrated that under these conditions it will be possible to limit the combined level of SBS and SRS to less than 10% [5]. To achieve these levels, SSD beam smoothing with 2–3 Å of bandwidth will probably be required. Current topics of research include non-linear saturation mechanisms and coupling between SBS and SRS [6, 7].

As indicated in Fig. 2, the NIF hohlraum design utilizes a low Z gas fill. This fill ensures that the laser absorption occurs primarily near the hohlraum wall, as required for efficient symmetry control. Early Nova experiments, which showed excellent control of symmetry and good agreement between LASNEX calculations and experiment, did not have this gas fill [1]. Experiments on Nova over the past two years have shown that symmetry can also be controlled in gas filled hohlraums. As shown in Fig. 6, the implosion symmetry in gas filled hohlraums can be tuned by varying the length of the hohlraum. The sensitivity to changes in hohlraum length is essentially the same as for hohlraums without gas. However, the gas filled hohlraums show a shift in the hohlraum length for optimum symmetry which is not predicted by LASNEX. This shift is about 150 $\pm$ 25 μm, or about 20% of the diameter of the

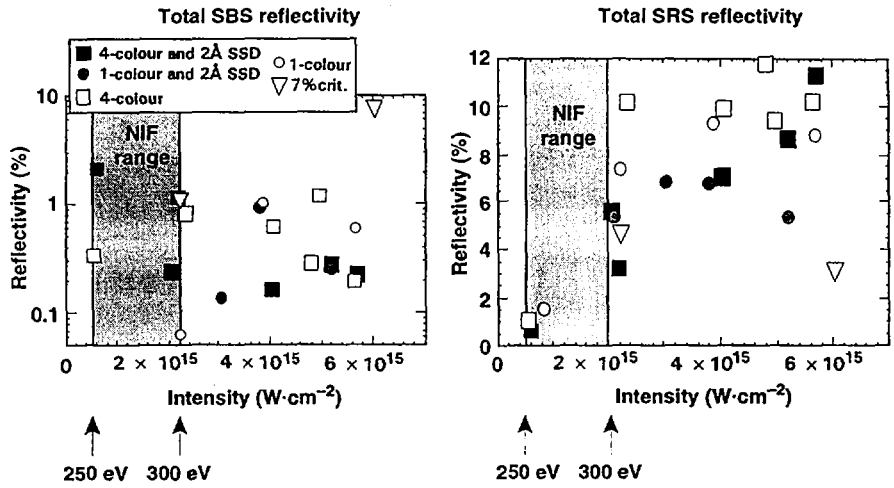

FIG. 5. A variety of targets has been used on Nova to simulate NIF-like plasma conditions. The data shown were obtained from submicrometre thick plastic balloons filled with neopentane at a density of $n/n_c \sim 0.1$, where $n_c = 9 \times 10^{21}$ cm^{-3} is the critical density for 0.35 μm laser light.

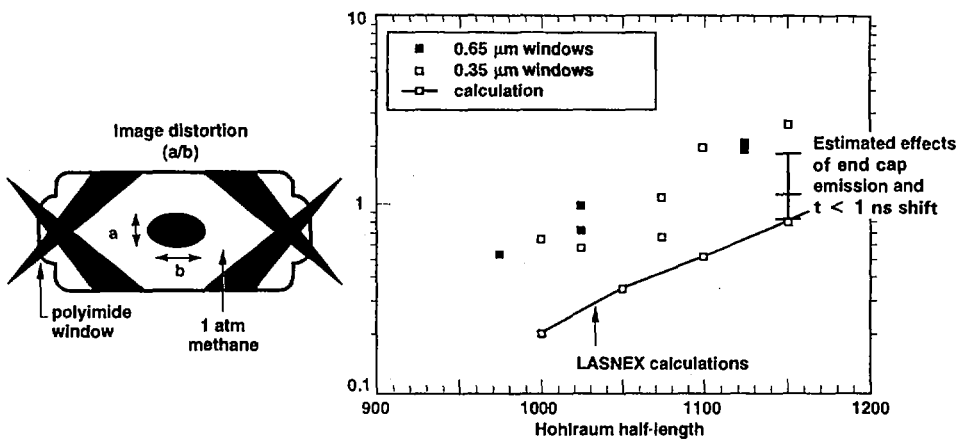

FIG. 6. Symmetry experiments with gas filled hohlraums showing the same sensitivity to beam pointing as earlier vacuum hohlraums. However, there is an offset between the measured and calculated image distortions equivalent to a 150 ± 25 μm shift in beam pointing. Emission profiles taken with RPP smoothed beams indicate that beam smoothing will bring symmetry into agreement with LASNEX modelling.

laser spot on the hohlraum wall [8, 9]. These results are for hohlraums having 1 atm of methane gas fill which have a plasma density similar to NIF hohlraums. There is an increasing body of evidence that this shift is due to the effects of plasma flow across the laser beam on laser beam filamentation. The Nova laser beams have significant modulation; this modulation leads to filamentation as the beam propagates towards the hohlraum wall. Ponderomotive and thermal effects in high intensity portions of the beam act to expel plasma from those regions. Refraction of the beam in the reduced density plasma leads to an enhanced intensity and an increased expulsion of plasma. Without flow across the beam, this process is spatially symmetric and the average propagation direction of the beam is unaffected. However, with flow across the beam, the plasma profiles which result from filamentation are asymmetric, resulting in a deflection in the beam propagation direction [10, 11]. This process, which is not included in LASNEX, is expected to produce an angular deflection in NIF targets which is comparable to that in Nova targets [11]. Compared to targets without gas fill, Nova experiments show a shift in the X ray emission pattern that is sufficient to account for the symmetry shift [9]. In experiments using a slot in the hohlraum wall, this shift is composed of an early time shift in the laser spot location, and a late time redistribution of energy towards the laser entrance hole which is consistent with filamentation in flow. Use of SSD beam smoothing is calculated to greatly reduce the effects of filamentation on Nova and NIF beams. Experiments on Nova have shown that even a random phase plate (RPP) alone, without bandwidth, can largely eliminate the shift in the X ray emission pattern seen in gas filled hohlraums. To date, these experiments have been carried out with only a single beam on Nova. Symmetry experiments with SSD on all ten Nova beams are being planned.

All ignition target designs require that the bulk of the fuel be in a cryogenic layer on the inside surface of the ablator. Bulk heating of the DT by β decay of the tritium provides an effective technique for producing uniform layers of DT in ICF targets. If the capsule outer surface is at a uniform temperature, β decay will cause thick regions of DT to be at a higher temperature than thinner regions. These hotter regions will sublime more rapidly and become thinner. This process continues until the layer has a nominally uniform thickness. However, the DT tends to deposit as a large number of small crystallites. The β heating process does not completely eliminate discontinuities which arise at the boundaries of these crystallites, resulting in about a 1 μm microscale roughness [12]. The β decay in 50/50 DT produces about 0.16 W/g. If external heating is applied to augment the β decay, smoother layers can be produced. Both optical techniques, which couple to rotational/vibrational transitions in DT, and radiofrequency heating, which couples to the free electrons produced by β decay, have been shown to produce smoother DT layers [13]. The optical absorption technique applies equally well to DD or DT fuel. This will be important in non-ignition experiments which may utilize DD fuel.

The effects of Rayleigh–Taylor (RT) instabilities are modelled in a variety of ways. The NIF ignition targets are designed to remain in the linear or weakly nonlinear regime. Hence, it is possible to develop a model of the effects of hydrodynamic

instability which is based on linear analysis, with an extension into the weakly non-linear regime [14, 1]. The most thoroughly tested approach utilizes a series of 2-D single mode LASNEX calculations which are run in the small amplitude linear regime to develop a dispersion relation. It is easy to check linearity, mode preservation, zoning convergence and other numerical issues in these calculations. Such single mode calculations are also close to a large Nova database which is modelled in the same way. These growth factors are combined with an assumed initial surface spectrum to determine the ignition time perturbation layer thickness. In this approach, the effects of this perturbed layer on the ignition hot spot are evaluated by using a one dimensional model in which thermal mixing is represented as an enhanced thermal conductivity in the perturbed region.

To test the weakly non-linear analysis, full simulations of multimode perturbations with realistic initial amplitudes are also run although the number of modes that can be included is limited. A variety of two dimensional multimode simulations have been run on several capsules, at solid angles ranging from relatively small conic sections to half-spheres. Results are consistent with the weakly non-linear analysis above but this is an area of current work [3, 4].

The growth of perturbations in the linear regime, for perturbations with the same wavenumber, is the same in 2-D and 3-D. However, simulations of the RT instability on classical interfaces [15–19], as well as on foils driven by laser light [20, 21] and X rays [22], predict that symmetric three dimensional perturbations should grow largest in the non-linear regime. These predictions, along with those of third order perturbation theory [23], are consistent with results of single mode RT experiments done on an air–water interface [24] and on foils driven by X rays [22]. Because of the dependence of the non-linear saturation amplitude upon perturbation shape, direct 3-D simulations represent the most accurate method of modelling the non-linear evolution of hydrodynamic instabilities which evolve from realistic surface perturbations.

Development of the three dimensional HYDRA code has allowed us to perform the first 3-D multimode simulations of the PT ignition capsule design. HYDRA [25] is a 3-D radiation hydrodynamics code with arbitrary Lagrange–Eulerian (ALE) capability. For simulations of ignition capsules, HYDRA uses a thermonuclear burn package to treat depletion and production of isotopes. An efficient multigroup routine transports energetic charged particles produced during the burn phase. Since the capsules are thin to neutrons, an accurate treatment of neutron energy deposition is obtained with a neutron transport model derived in the free streaming limit. As energetic particles slow down, they deposit energy in separate electron and ion channels. Electron and ion conductions are treated, as well as electron–ion energy exchange.

Hydrodynamic instabilities were simulated over a portion of the capsule solid angle which extends equal amounts in the polar and azimuthal angles ($\Delta\theta$, $\Delta\phi$), with one boundary coincident with the capsule equator. Multimode surface perturbations imposed were of the form $G(\theta, \phi) = \sum_m \sum_n a_{mn} \cos(m\pi\theta/\Delta\theta) \cos(n\pi\phi/\Delta\phi)$, with symmetry boundary conditions at transverse boundaries. These are analogous to

modes used in previous 2-D axisymmetric simulations over a portion of a quadrant [3]. Perturbations on the outer ablator surface are based upon traces from a Nova capsule, while those on the inner DT surface are based upon measurements of cryogenic ice. This information is converted to an estimated 3-D power spectrum [26], and power is distributed isotropically among the 3-D modes with equivalent wavenumber.

As an example, we consider a capsule having perturbation amplitudes, in the range of modes $1 \geq 10$, equal to 24 nm rms on the outer surface and 1 μm on the inner cryogenic DT surface. Modes in the range $\ell = 10$–40 are simulated over a domain extending 18° in each angle. These are the modes most capable of generating spikes of cold fuel during the compression of the hot spot. During the implosion phase, the simulated shell areal density strongly resembles the initial outer surface perturbation. This demonstrates that the modes growing in the ablator are seeded predominantly by initial ablator surface perturbations, not from the perturbed rarefaction wave which returns from the ice surface after the first shock has broken out. Depressions that are initially on the surface develop into bubbles in the ablator surrounded by interconnecting spike sheets and larger individual spikes.

Figure 7 shows bubble and spike ridge structures which are growing on the pusher–hot spot interface after the rebounding shock has reached it. These correspond to the locations of the equivalent lower mode structures in the ablator which have fed through the shell. The resemblance to the initial surface perturbation is characteristic of weakly non-linear behaviour. Only very late in the simulation, as the capsule approaches ignition, does the perturbation structure on the inner surface evolve towards lower mode numbers. This behaviour appears to be strongly influenced by conductive ablation and the effect of convergence in this case, rather than by mode coupling, as was seen in planar geometry [21, 27–29].

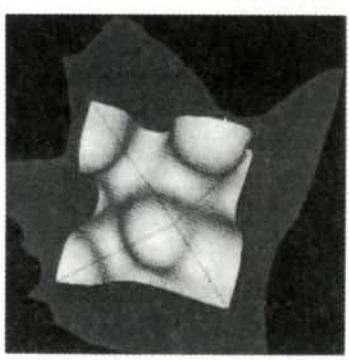

FIG. 7. Isodensity contour surfaces of 60 g/cm^3 near ignition time from a PT capsule simulation having 24 nm and 1 μm rms perturbations initially on the outer ablator and inner ice surfaces, respectively. The perspective shows the pusher–hot spot interface viewed from the inside.

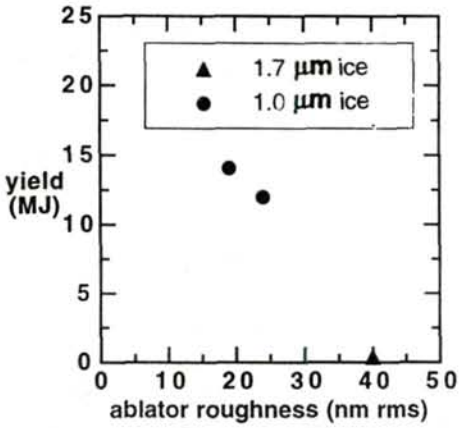

FIG. 8. Yields from HYDRA PT capsule simulations performed with various roughnesses on the ablator and cryogenic ice. Initialized perturbations contained modes with ℓ = 10–40.

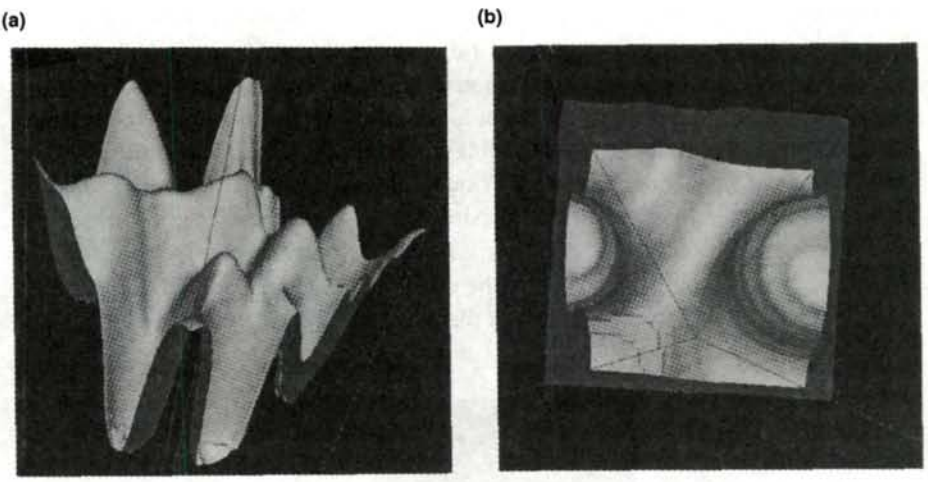

FIG. 9. Isodensity contour surfaces near ignition time for a PT capsule simulation containing modes with ℓ = 15–120: (a) 130 g/cm^3 surface just inside the DT-ablator interface; (b) 650 g/cm^3 surface at pusher–hot spot interface as seen from the inside.

Figure 8 shows yields from simulations of several PT capsules having different multimode surface perturbations containing modes in the range of ℓ = 10–40. The capsule with the largest perturbation amplitudes failed to ignite because, at the time of stagnation, spikes had penetrated 10 μm into the 30 μm radius hot spot. The location of the yield cliff corresponds to a roughness on the outer surface which is ~40% smaller than that obtained with previous 2-D multimode simulations over this range of modes. Results from a 3-D multimode simulation have been compared with an

axisymmetric 2-D HYDRA simulation with an equivalent initial rms surface roughness. The comparison confirms that the non-linear growth rates which are obtained for the round 3-D bubble spike features, and which are higher than those for the 2-D bubble spike ridges, are responsible for the smaller permissible surface roughness found in these calculations.

RT unstable modes in the range of $40 < l < 120$ are much less capable of feeding through the shell and producing spikes upon deceleration than the modes considered above. They can, however, threaten the shell integrity during the implosion

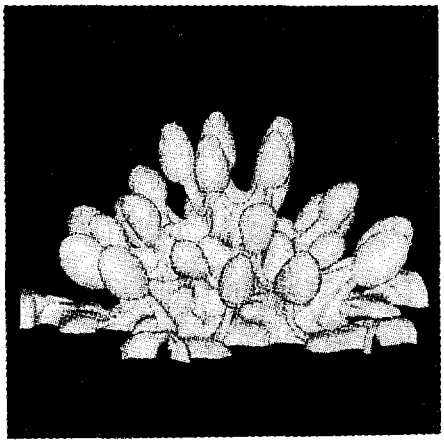

FIG. 10. Hemispherical portion of the fuel–pusher interface seen from the outside near bang time for a Nova capsule having an initial 0.15 μm multimode perturbation.

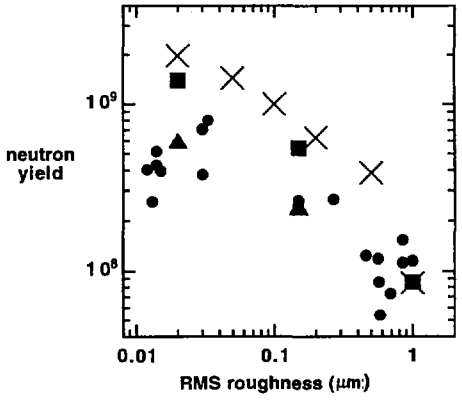

FIG. 11. Solid circles show experimental yields of Nova capsules having multimode perturbations of various amplitudes. The crosses indicate yields from the 1-D mix model. The solid squares are from 3-D HYDRA simulations, including drive asymmetry. The triangles represent simulations which also include low mode thickness variations.

phase, when the shell is thinnest. We have simulated surface perturbations which include modes spanning both of these ranges (ℓ = 15–120) on a 12° wedge. The outer surface corresponded to the best surface finish measured on a Nova capsule. The surfaces simulated have amplitudes of 21 nm and 1.3 μm peak to valley on the outer ablator and the inner DT ice, respectively. The simulation shows that the shell integrity is well preserved throughout the implosion. Figure 9(a) and (b) shows the isodensity contours corresponding to locations just inside the DT–ablator interface and at the pusher–hot spot interface close to ignition time. The high modes apparent in Fig. 9(a), typically in the range of ℓ = 90, have not fed through appreciably to the inner interface, which has features typically in the range of ℓ = 15–20. The yield, 15.5 MJ, approaches the value obtained for an unperturbed capsule. Thus, a PT capsule with a surface finish equal to the best measured on a Nova capsule easily ignites in the simulation. The margin of ignition in this simulation implies that substantially larger perturbation amplitudes can be tolerated on the outer surface than were used in this case, even with high ℓ modes present. Future work will quantify the sensitivity of the capsule to surface roughness contained in different ranges of modes.

Single mode radiation driven planar experiments mentioned earlier [22] demonstrated the effect of mode shape on perturbation growth and provided a test of the ability of HYDRA to simulate these efforts accurately.

Also, capsules with multimode surface perturbations, created by ablating pits with a laser at 200 randomly selected locations, have been used in Nova experiments to quantify the degradation of implosions subject to near NIF levels of hydrodynamic instability. HYDRA simulated multimode growth on these capsules over a 1/20 sphere domain, extending from the pole to the equator and 36° in azimuthal angle, with symmetry conditions at transverse boundaries. The perturbation simulated was based upon a portion of the actual surface, projected onto spherical harmonics compatible with the boundary conditions. Figure 10 shows a portion of the classical fuel–pusher interface at 2.05 ns, near bang time, for a Nova capsule having an initial 0.15 μm rms multimode surface perturbation. The bubbles are rising at the same locations initially occupied by pits ablated on the outer surface. Modal analysis of the shell perturbation structure indicates that most of the spectrum is due to growth of modes initially present, an indication of weakly non-linear behaviour.

Other sources of asymmetry, besides those imposed on the capsule surface, are found to be important in the simulations of Nova capsules. The relatively small number of beams on Nova leads to substantial 3-D azimuthal variation in the hohlraum X ray drive. The variation in radiation drive is large enough in the Nova hohlraum for 3-D coupling with imposed surface perturbations to have a dramatic effect on simulated capsule performance. Low mode drive asymmetry combined with surface roughness can cause a few spikes to approach the capsule centre ahead of the rest. These can continue into the capsule centre nearly in free fall. Figure 11 compares experimental yields for Nova capsules having multimode surface perturbations with yields from HYDRA simulations and from our 1-D mix mode [30]. For the

rough 1 μm rms capsules, there is good agreement between the 1-D model and experimental yields. But the experimental yields for smoother capsules are substantially less than the 1-D model predicts. The 3-D HYDRA simulations which include imposed surface roughness and radiation drive asymmetry, shown as squares in Fig. 11, give lower yields for the smoother capsules which are closer to the data. Low mode wall thickness variations are also present in these Nova capsules. HYDRA simulations which also include low mode thickness variations with peak to valley amplitudes typical of measured values, oriented to enhance the effect of coupling, are shown as triangles in Fig. 11. Coupling between the various asymmetries results in spikes quenching the hot spot before bang time. When the combined effects of known asymmetries are included, the 3-D simulations produce neutron yields that are close to the experimental values. The effect of pointing errors and power imbalance will be examined in future simulations.

The advances in NIF target design, together with the advances on Nova on laser-plasma coupling, symmetry in gas filled hohlraums, hydrodynamic instability and cryogenic layer uniformity have resulted in a recommendation by the ICFAC, the US Department of Energy (DOE) advisory board on ICF, that the DOE should move ahead with detailed engineering design of the NIF.

ACKNOWLEDGEMENT

This work was performed under the auspices of the US Department of Energy by the Lawrence Livermore National Laboratory under Contract No. W-7405-Eng-48.

REFERENCES

[1] LINDL, J.D., Phys. Plasmas **2** (1995) 3933.
[2] ZIMMERMAN, G.B., KRUER, W.L., Comments Plasma Phys. Control. Fusion **2** (1975) 51.
[3] HAAN, S.W., et al., Phys. Plasmas **2** (1995) 2480.
[4] KRAUSER, W.J., et al., Phys. Plasmas **3** (1996) 2084.
[5] McGOWAN, B.J., et al., Phys. Plasmas **3** (1996) 2029.
[6] KIRKWOOD, R.K., et al., Phys. Rev. Lett. **78** (1996) 104.
[7] FERNANDEZ, J.C., et al., Phys. Rev. Lett. **78** (1996) 257.
[8] DELAMETER, N.D., et al., Phys. Plasmas **3** (1996) 2022.
[9] POWERS, L.V., et al., in Interaction of Lasers with Matter (Proc. 24th Eur. Conf. London, 1996), Institute of Physics Publishing, London (1997).
[10] ROSE, H.A., Phys. Plasmas **3** (1996) 1709.
[11] HINKEL, D.E., WILLIAMS, E.A., STILL, C.H., Phys. Rev. Lett. **77** (1996) 1298.
[12] SANCHEZ, J., Lawrence Livermore National Laboratory, and HOFFER, J., Los Alamos National Laboratory, personal communication (1995).
[13] COLLINS, G., et al., Heat-Flux Induced Changes to Multicrystalline d2 Surfaces, Rep. LLNL-UCRL-JC-124261, Lawrence Livermore National Laboratory (1996).
[14] HAAN, S., Phys. Rev. A **39** (1989) 5812.

[15] TRYGGVASON, G., UNVERDI, S.O., Phys. Fluids A **2** (1991) 656.
[16] YABE, T., HOSHINO, H., TSUCHIVA, T., Phys. Rev. A **44** (1991) 2756.
[17] HECHT, J., OFER, D., ALON, U., SHVARTS, D., ORSZAG, S.A., McCRORY, R.L., Laser Part. Beams **13** (1995) 423.
OFER, D., HECHT, J., SHVARTS, D., ZINAMON, Z., ORSZAG, S.A., McCRORY, R.L., in Physics of Compressible Turbulent Mixing (Proc. 4th Int. Workshop, 1993), Cambridge University Press, Cambridge (1993) 199.
[18] SAKAGAMI, H., NISHIHARA, K., Phys. Rev. Lett. **65** (1990) 432.
[19] TOWN, R.P.J., BELL, A.R., Phys. Rev. Lett. **67** (1991) 1863.
[20] DAHLBURG, J.P., GARDNER, J.H., DOOLEN, G.D., HAAN, S.W., Phys. Fluids B **5** (1993) 571.
[21] DAHLBURG, J.P., FYFE, D.E., GARDNER, J.H., HAAN, S.W., BODNER, S.E., DOOLEN, G.D., Phys. Plasmas **2** (1995) 2453.
[22] MARINAK, M.M., et al., Phys. Rev. Lett. **75** (1995) 3677.
[23] JACOBS, J.W., CATTON, I., J. Fluid Mech. **187** (1988) 329.
[24] JACOBS, J.W., CATTON, I., J. Fluid Mech. **187** (1988) 353.
[25] MARINAK, M.M., et al., Phys. Plasmas **3** (1996) 2070.
[26] See National Technical Information Service Document No. DE 95-011970 (POLLAINE, S.M., HATCHETT, S.P., LANGER, S.H., Spectral Analysis of ICF Capsule Surfaces, Rep. UCRL LR-105821-94-3, ICF Quarterly Rep. **4** (3) 87). Copies may be ordered from the National Technical Information Service, Springfield, VA 22161.
[27] SHARP, D.H., Physica D **12** (1984) 3.
[28] ALON, U., SHVARTS, D., MUKAMEL, D., Phys. Rev. E **48** (1993) 1008; Phys. Rev. Lett. **72** (1994) 2867.
[29] SHVARTS, D., ALON, U., OFER, D., McCRORY, R.L., VERDON, C.P., Phys. Plasmas **2** (1995) 2465.
[30] KEANE, C.J., et al., J. Quant. Spectrosc. Radiat. Transfer **54** (1995) 207.

PROGRESS ON LASER MEGAJOULE TARGETS PHYSICS STUDIES AT CEA LIMEIL-VALENTON PHEBUS AND NOVA EXPERIMENTS*

CEA LIMEIL-VALENTON ICF TEAM
(Presented by C. Drevet)

Commissariat à l'énergie atomique,
Etablissement de Limeil-Valenton (CEA-LV),
Villeneuve Saint Georges,
France

Abstract

PROGRESS ON LASER MEGAJOULE TARGETS PHYSICS STUDIES AT CEA LIMEIL-VALENTON PHEBUS AND NOVA EXPERIMENTS.

An outline of the present CEA-Limeil Laser Megajoule (LMJ) target is given. The main potential physical effects that may degrade the 1-D gain of the capsule are underlined. Phebus and Nova experiments, which allow better knowledge of these effects, are presented. The experimental results are compared with FC11 and FC12 simulations. The discrepancies are discussed, and the areas where particular experimental and theoretical effort will be made in the future are pointed out.

1. INTRODUCTION

The main objective of the CEA-Limeil inertial confinement fusion (ICF) laser programme is to predict, as accurately as possible, the specifications of Laser MegaJoule (LMJ), through experiments with present lasers and the corresponding numerical modellings.

In the LMJ project, we intend to achieve in laboratory, by the first decade of the 21st century, ignition and gain of small spherical capsules filled with a few 100 μg of DT.

The nominal scheme is indirect drive in which laser beams, at 0.35 μm, enter a low density gas filled gold hohlraum where the laser energy is converted into soft X rays which drive the implosion of the capsule.

With a hot spot structure (areal density > 0.3 g/cm^2, temperature > 60 M K), igniting and propagating to the surrounding cold isentropically compressed fuel through slowing-down α particles, 1-D and 2-D simulations have shown that 1.5 to 2 MJ laser energies are sufficient to obtain a significant gain of ten. To achieve this value, the capsule must be ablatively driven, the initiating laser pulse has to be tailored (pulse shape PS) and the initial DT density is required to be as high as possible (initial cryogenic DT). The prediction of performances relies upon numerical simulations with the FCI1 and FCI2 hydrodynamic codes developed at Limeil to describe the behaviour of the target.

---

* Nova experiments were performed in the framework of a CEA/DOE collaboration. The CEA Limeil-Valenton ICF Team thanks the LLNL and LANL ICF teams for helping to prepare the common Nova experiments and sharing fruitful discussions on pertinent simulations.

After a quick recall of the LMJ target and the key physics issues, we present the most representative experiments performed with PHEBUS (Limeil) and NOVA (LLNL) laser facilities in similar physics situations. These experiments have been interpreted by Limeil codes mentioned above.

2. LMJ PROJECT

We present, in Fig.1, the hohlraum target and its irradiation by the laser beams at the main pulse and, in Fig.2, the initial capsule configuration.

The total laser power is tailored (Fig. 3) and leads to a shaped radiative temperature (T_R) , which culminates at 350 eV on the capsule (Fig. 4).

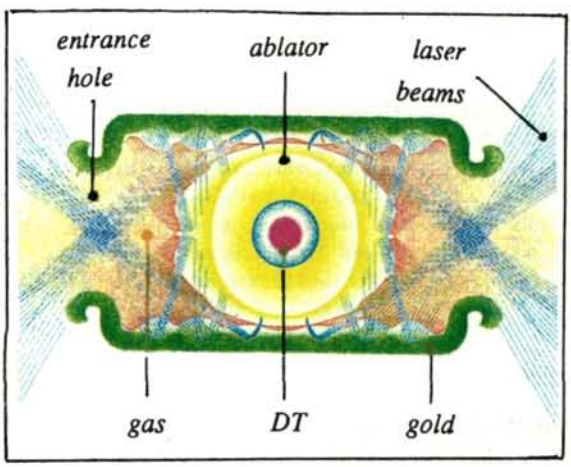

FIG. 1. LMJ target.

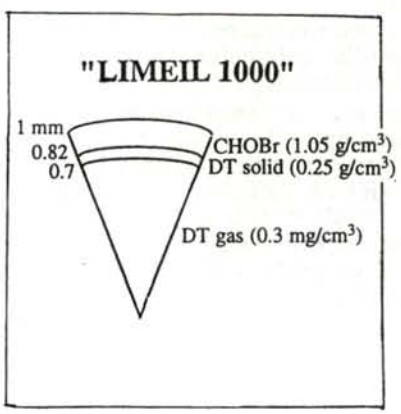

FIG. 2. LMJ capsule.

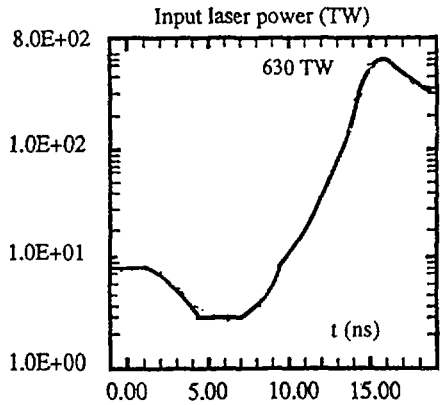

FIG. 3. Total laser power.

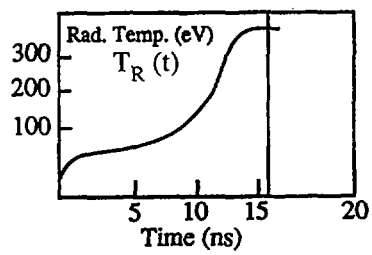

FIG. 4. Radiative temperature.

In the indirect drive scheme, since the laser beams enter a cylindrical hohlraum and energy losses through the holes play an important role, there is an intrinsic asymmetric X ray drive of the capsule. To remedy this situation, it is necessary to irradiate the internal wall of the cavity on several rings by laser beams located on a few cones.

Moreover, the plasma expansion of the internal gold wall induces the displacement of the X rays sources, leading to an extra time varying asymmetry. In order to prevent these displacements, the hohlraum is filled with He/H gas which implies closing the entrance holes with two thin polyimide films. Furthermore, to achieve a degree of symmetry of ±2% rms, a phasing of beams is necessary (balance between cones). The irradiation of the capsule is optimized through FCI2 simulations.

Unfortunately, the use of a gas and windows enhances the development of parametric instabilities, i.e. beam deflection close to the windows due to filamentation and stimulated Brillouin and Raman scattering along the beams (reflectivities SBS and SRS). This can modify the beams' phasings, hence affect the symmetry and also decrease the laser energy reaching the wall, reducing the radiative temperature around the capsule. Smoothing techniques of the laser beams have been developed to minimize the effects of parametric instabilities and were tested on specific experiments.

Another important effect are the hydrodynamic instabilities which develop in the capsule and are due to the surface roughnesses of all interfaces. This mechanism can lead to a mixing of cold and hot DT, preventing ignition. This implies precise specifications of the permissible roughnesses of the shell surfaces deduced from numerical calculations.

3. LASER-PLASMA INTERACTION

Experiments on beam smoothing have been performed for many years:

At PHEBUS (0.35 μm, one 1.3 ns square pulse), with planar targets, we have studied the effect of random phase plates (RPPs) on SRS reflectivity for various materials and for several laser intensities. This effect is the smaller the higher is the atomic number (Fig. 5). For intensities close to that of LMJ and a planar gold target (without gas), we have only a few per cent of time integrated SRS reflectivity.

At NOVA (0.35 μm, nine unsmoothed PS, one smoothed or unsmoothed PS), the effect of smoothing on reflectivity has been tested on one of the ten beams. To begin with, in hohlraums with dimensions about 0.3 times the dimension of the LMJ target, LLNL has measured the SBS and SRS reflectivities on the unsmoothed tenth beam, as a function of time, for an empty cavity (Fig. 6) and a gas filled cavity (C_3H_8) (Fig. 7). The results confirm the unfavourable effect of gas (increased reflectivity).

In Fig. 8, we show the effects in gas hohlraums of both RPP and smoothing by spectral dispersion (SSD) on the SBS peak reflectivity for the tenth beam, which can drop from more than 30% (Fig. 7) to a few per cent. With gas and an RPP/SSD smoothed beam, the reflectivity is even weaker than that we had before without gas and without beam smoothing (Fig. 6). For SRS reflectivity, the effect is of the same order.

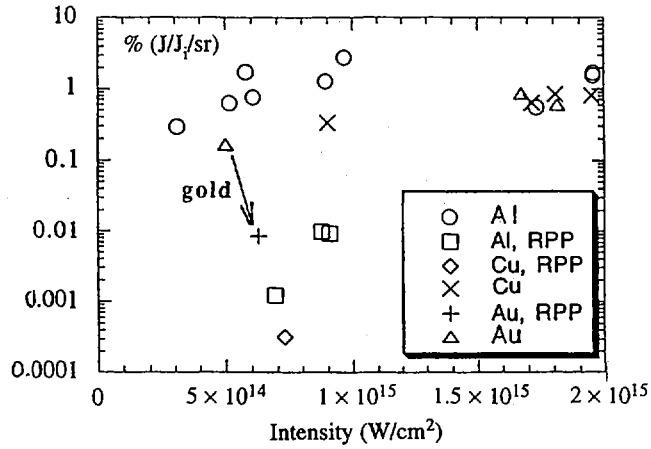

FIG. 5. Raman backscattering (SRS reflectivity).

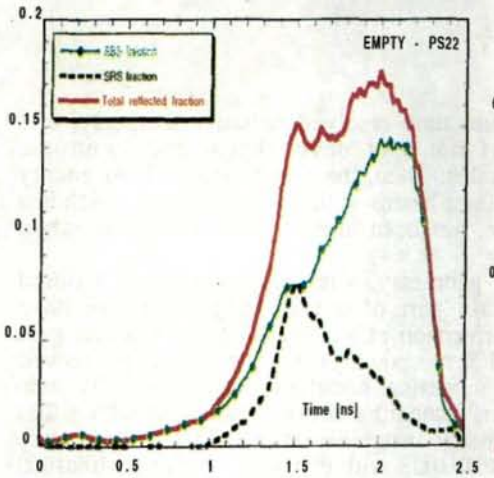

FIG. 6. Reflectivities for empty cavity.

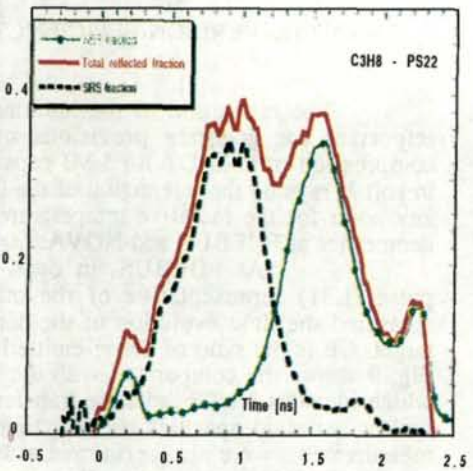

FIG. 7. Reflectivities for C_3H_8 cavity.

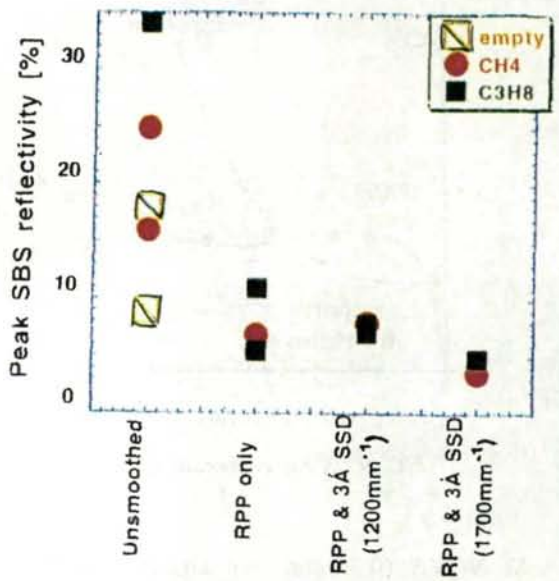

FIG. 8. Peak SBS reflectivity for different smoothings and gases.

At the same time, we have developed two codes: a post-processor, Piranah, which in a simplified way models the SRS and SBS gains along the laser beam path and a more sophisticated 2-D and 3-D filamentation code, Colibri (in collaboration with S. Huller at "Ecole Polytechnique") .

4. X-RAY CONVERSION EFFICIENCY

The restitution of the hohlraum time resolved radiative temperature is important for accurate previsions of hot spot development and isentropic compression of cold DT for LMJ capsules. Then, the conversion of laser energy in soft X rays by the interaction of the laser beams with the cavity wall, which is a key point for the radiative temperature, has been investigated in different target geometries at PHEBUS and NOVA:

At PHEBUS, in open geometry, with an unsmoothed tailored pulse (L31) representative of the main part of a LMJ ring pulse, we have measured the time evolution of the conversion efficiency (CE) for a planar gold target. CE is the ratio of the re-emitted X ray power to the incoming laser power. Fig. 9 shows the comparison with the numerical simulation using the FCI1 code which includes NLTE radiative transfer, standard electron conduction with a flux limitor, standard opacities but no parametric instability effects. Many temperature measurements were also performed at PHEBUS with different cavities (cylindrical or spherical) and various pulses square or PS, and were compared to FCI2 simulations (with the same physics as FCI1). The agreement was quite acceptable, too.

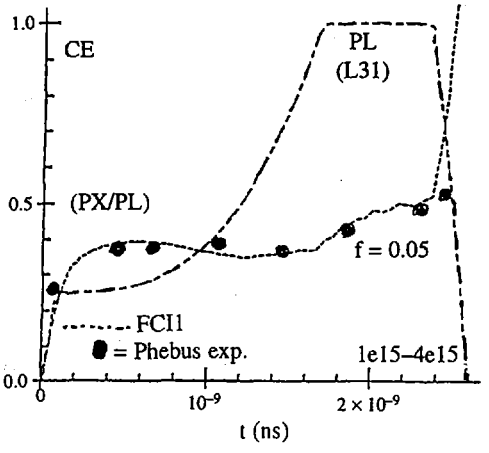

FIG. 9. X ray conversion efficiency.

At NOVA (0.35 μm, ten unsmoothed PS), we have jointly measured the X ray spectrum emitted by the internal wall of empty gold hohlraums, or filled with C_3H_8, and have deduced the wall temperature (T_{wall}). The T_R in the cavity is related to T_{wall} through gold opacities.

Numerical simulations with our standard FCI2 and diagnostic code are in good agreement with the experimental results (Fig. 10), provided the actual power losses due to SRS and SBS are taken into account. With regard to the ideal case where the laser energy is fully absorbed, a reflectivity of 40% for the C_3H_8 gas filled hohlraum and unsmoothed beams leads to a drop of 10% on the radiative temperature which would be utterly inappropriate for our present specifications for LMJ.

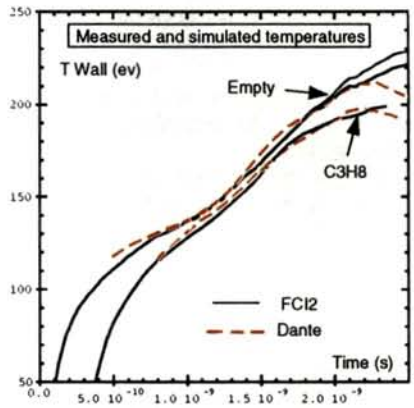

FIG. 10. T_{wall} versus time.

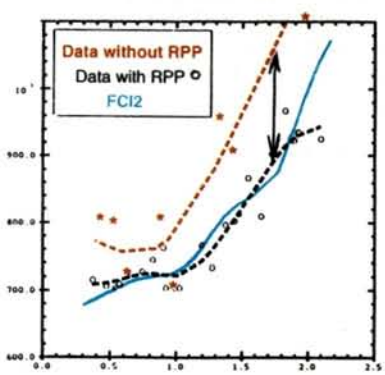

FIG. 11. Spot motion in CH_4 hohlraum. Ordinate: μm, abscissa: ns.

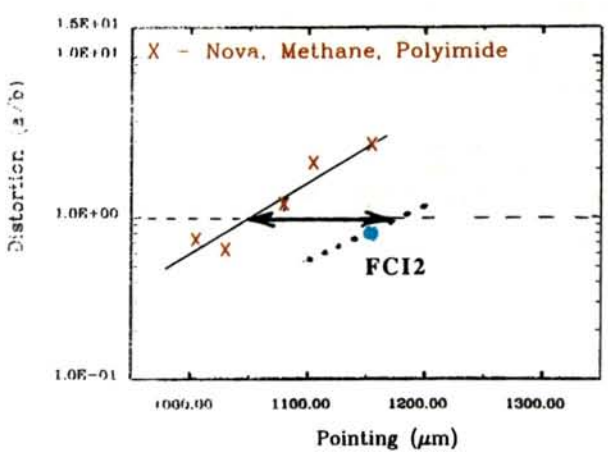

FIG. 12. Distortion versus pointing.

5. EFFECT OF SYMMMETRY ON IMPLOSION

Defects of symmetry in implosion dynamics have been experimentally tested at PHEBUS and NOVA. As examples, we show symmetry studies performed at NOVA in two ways:

- First, through the position of the X ray source created by the focalization of one of the ten laser beams on the cavity wall which moves away as the time grows (spot motion experiments). Fig. 11 shows the displacement of this source for the case of ten unsmoothed beams and also for one case of RPP smoothed (over ten) beams, with shaped pulses and a cavity filled with CH_4. The agreement is quite good with FCI2 simulations when the beam is smoothed. For gas filled hohlraums, there is a no good agreement with the unsmoothed beam, because filamentation occurs at the cavity entrance hole, deflecting the beam of 150 μm towards the entrance hole. Furthermore, we note a large scattering of the experimental data when using an unsmoothed beam.

- Second, through implosion of (D_2 + Ar) filled capsules with ten unsmoothed beams by varying the beam pointings. 2-D imaging of Ar emission gives a measure of the asymmetry of the implosion. Fig. 12 shows the ratio of equator to pole lengths (a/b) as a function of the beam pointing. FCI2 plus diagnostic code simulation does not agree with these results. In particular, the experimental optimum pointing (a/b = 1) is shifted by more than 150 μm. This is again the shift observed between smoothed beam (equivalent to FCI2) and unsmoothed beam on spot motion experiments (see Fig. 11).

Figs 13(a) and (b) show the 2-D images at the pointing 1150 μm. The experimental data exhibit a ratio of 2.3 different from the calulated value of 0.8.

6. THE PHYSICS OF THE CAPSULE

To increase the hydrodynamic efficiency of the CH ablator, a few per cent of high Z dopant is mixed to it (which corresponds to a higher opacity). In a first step, it was important to test the effect of the Br dopant on the motion of the ablator. This has been done at PHEBUS with a 1.3 ns unsmoothed square pulse, at 0.35 μm [1]. The CH-Br ablator is driven by soft X rays coming from the rear side of a thin gold planar target, and the ablator motion is measured by a side backlighting technique. Figs 14(a) and 14(b) show good agreement between the experimental data and the simulation with FCI2 and the diagnostic code.

On the other hand, doping the ablator increases the hydrodynamic instabilities inside the capsule. It was important to test this effect in a converging geometry. This has been performed at NOVA with the implosion of a cylindrical CH-Br ablator perpendicular to the hohlraum axis. Its external surface was initially perturbed by a polygonal 1 μm defect, mode 10, parallel to the cylinder axis. When imploded, the defect grows and is transmitted to an opaque inner marker layer. Backlighting along the cylinder axis gives the image of the perturbed marker layer, i. e. a measure of feedthrough and convergence effects which are inaccessible in planar experiments. Figs 15(a) and 15(b) show the experimental and simulated images. FCI2 simulation assumes uniform drive on the cylinder whereas 3D-asymmetry cavity effects occur on the ablator and

[1] W. Hsing (LANL), to be published.

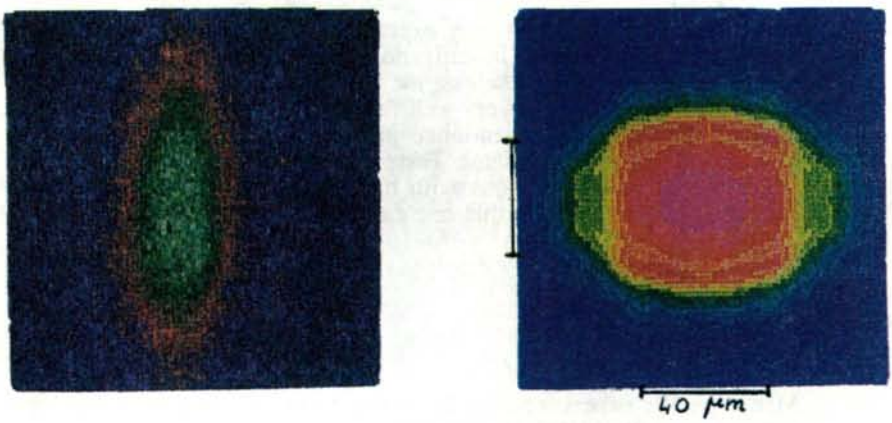

FIG. 13. (a) Experimental data; (b) FC12 simulation.

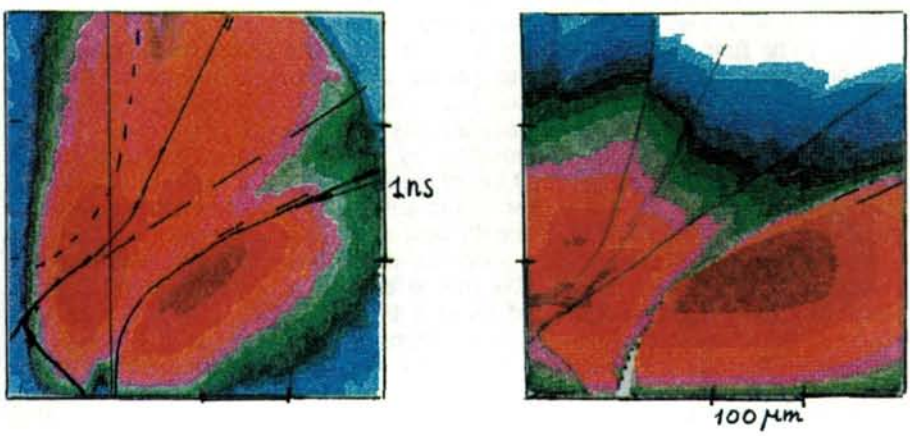

FIG. 14. (a) Experimental data; (b) FC12 simulation.

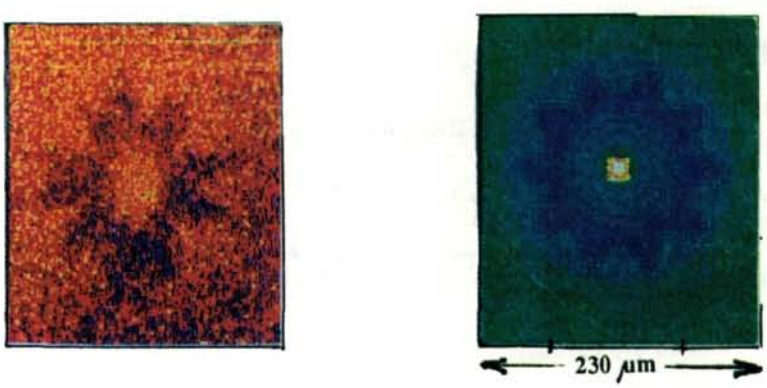

FIG. 15. (a) Experimental data; (b) FC12 simulation.

couple with roughness effects. This may explain the slight discrepancy between the two 2-D images. More precise investigations of this geometry would need a 3-D evaluation of growths. Nevertheless, the experimental mean motion of the internal face of the marker layer is very well fitted by FCI2, which confirms, in a converging geometry, the result mentioned just above at PHEBUS concerning the rear face of a planar CH-Br ablator. Tests of growth in the capsule can also be performed in spherical implosions with measurement of neutron emission. But this implies 1-D implosions so that one can be sure to test only the effect of roughness.

7. CONCLUSIONS

Many specific experiments useful to the design of the LMJ target have been performed at both PHEBUS and NOVA facilities. Our 1-D and 2-D hydrodynamic codes (FCI1, FCI2) have given good description of the mean radiative temperature around the capsule and of the evolution of a doped ablator when all energy losses are taken into account. So, in these situations, ignition and gain of DT would work. Unfortunately, uncertainties remain.

The first major uncertainty today is about the best way to smooth the 240 beams of the LMJ in order to get rid of parametric instabilities. In the NOVA configuration, a solution has been proposed to minimize the effect on SBS, SRS and filamentation and has already been successfully tested for one beam. Shots with ten beams smoothed by KPP (kinoform phase plate, an improvement of the RPP) and SSD are planned at NOVA to confirm the benefit on drive and implosion. Better description and understanding of the parametric instabilities is our objective to define the best smoothing technique for LMJ.

The second uncertainty concerns the irradiation asymmetry of the capsule which may not exceed ±2% rms to ensure hot spot ignition and gain. Symmetry on capsule is optimized through FCI2 simulations, which take into account the beams' positions in the cavity (cones, rings, beam phasing, etc.). The principles of rings and phasings should be checked experimentally with an appropriate laser (two cones or more with balance).

At last, the study with 2-D and 3-D evaluations of the perturbation growths of the different capsule interfaces and their coupling in converging geometry (cylindrical and spherical) will permit us to define the roughness specifications for the LMJ capsule.

Efforts will also be made on target fabrication, diagnostics and their precision.

REFERENCES

[1] CHOCS, Revue scientifique et technique de la Direction des Applications Militaires, No. 13 (April 1995).

[2] LINDL, J., Development of the indirect-drive approach to inertial confinement fusion and the target physics basis for ignition and gain, Phys. Plasmas **2** 11 (1995) 3933.

INERTIAL CONFINEMENT 2

(Session B2)

Chairperson

J.D. LINDL
United States of America

INERTIAL CONFINEMENT FUSION RESEARCH AT IMPERIAL COLLEGE

O. WILLI, T. AFSHAR-RAD, L. BARRINGER, A. BELL,
M. BORGHESI, J. FINDLAY, R. GAILLARD, M.G. HAINES,
A. IWASE, A. MACKINNON, C. MEYER, S. NURUZZAMAN,
R. TAYLOR, R. TOWN
Blackett Laboratory,
Imperial College of Science, Technology and Medicine,
London, United Kingdom

D. HOARTY
AWE Aldermarston,
Reading, United Kingdom

R. WATT
Los Alamos National Laboratory,
Los Alamos, New Mexico,
United States of America

J.P. DAHLBURG
Naval Research Laboratory,
Washington, D.C.,
United States of America

A. PUKHOV, J. MEYER-TER-VEHN
Max-Planck Institut für Quantenoptik,
Garching, Germany

Abstract

INERTIAL CONFINEMENT FUSION RESEARCH AT IMPERIAL COLLEGE.

The paper summarizes experimental and theoretical work relevant to inertial confinement fusion. A quantitative study of laser imprinting and subsequent Rayleigh-Taylor (R-T) growth of directly driven planar, solid, thin foil targets has been carried out. The experimental results are well reproduced by two and three dimensional radiation transport hydrodynamics simulations. The reduction of the hydrodynamic target breakup due to imprinting was investigated for several laser and target conditions on targets which were overcoated with a low density foam jacket facing the incident laser radiation. The shock in the foam produced by laser ablation, and the density and temperature profiles of the shocked material generated in the foam, were measured. The preheating in solid targets caused by the shock and the radiation wave was measured on targets with and without foam overcoats. Measurements were carried out of the R-T instability in planar modulated foil targets driven by soft X ray radiation emitted from a laser heated hohlraum. This allowed the Takabe-Morse rollover due to ablative stabilization to be investigated. Mode coupling was studied by using modulated targets with several short wavelength

modes. A new multimode coupling model of the R–T instability was developed. An analytical model was developed which describes the saturation of self generated magnetic fields in laser produced plasmas. Finally, short pulse, high intensity experiments were carried out to study some aspects of the fast ignitor concept. In particular, the propagation of a short laser pulse at relativistic intensities through an underdense plasma was studied.

1. INTRODUCTION

It is essential for laser fusion that a high degree of symmetry is maintained during the implosion phase. Asymmetries in the ablation pressure must be smaller than a few per cent, otherwise an unacceptable level of instability growth occurs, reducing the fusion gain. Recent studies at Imperial College and elsewhere have demonstrated that the most sophisticated optical smoothing schemes available to date do not provide a sufficiently smooth laser beam to eradicate the initial imprinting of the laser drive on the cold target surface during the 'startup' phase. Once a plasma has been formed, thermal conduction from the absorption region to the solid target provides some smoothing of further absorbed irradiation, but the initially imprinted non-uniformities rapidly grow through the Rayleigh–Taylor (R–T) instability and other hydrodynamic instabilities. The imprint problem imposes severe constraints on capsule design, forcing designers to operate on a less efficient, higher isentrope, in order to provide sufficient stabilization of the instability growth such that the imprint seed can be tolerated and does not grow sufficiently to buckle the capsule shell and render the implosion ineffective.

An extensive programme has been carried out to investigate the initial imprint phase on the cold solid target surface. Face on, high resolution, soft X ray images clearly show that the target breakup is caused by the initial imprint which induces the R–T instability [1].

Recent advances have demonstrated the promise of a novel direct drive smoothing scheme, foam buffered direct drive (FDD). The FDD scheme addresses the imprinting problem by utilizing a thin overcoat of a high Z material on a low density foam layer formed on the capsule's outer surface [2]. The initial laser drive is converted to a brief soft X ray flash, which supersonically preforms a plasma from the foam directly ahead of the advancing laser driven shock front, providing rapid smoothing and demonstrably suppressing the imprinting. Recent experimental observations [3] obtained on the VULCAN laser in Britain, the TRIDENT laser at Los Alamos and the PHEBUS laser at Limeil have shown a substantial reduction in the initial laser non-uniformity imprinting of directly irradiated targets when the foam buffer is used.

The R–T instability was studied in the short wavelength regime by using single and multimode targets which were driven by hohlraum radiation. This allows the Takabe–Morse rollover due to ablative stabilization to be determined. A cylindrical hohlraum was heated with a number of laser beams, and the driven modulated targets were imaged at 250 eV with a high resolution system.

The R–T instability was studied in convergent geometry using thin plastic cylindrical targets. The targets were irradiated with six green laser beams focused symmetrically around the cylinder waist. Both bare and foam overcoated targets, unfilled or filled with low density foam, were irradiated at intensities of 5×10^{13} W·cm^{-2}. In addition, targets with modulations on the inside were used. The implosion was diagnosed with an X ray probe with an energy between 1.3 and 1.5 keV along the target axis. Sixteen frames were obtained with a GXI pinhole system during the implosion phase.

A new multimode coupling model of the RT instability was developed. Two dimensional hydrocode simulations were compared with Haan's mode coupling model. A saturation criterion was developed which is used in a new, extended mode coupling model. The extended model accurately follows the mode development to amplitudes two to three times larger than Haan's model. An analytical model was developed which describes the saturation of self generated magnetic fields in laser produced plasmas.

Experimental studies investigating the propagation of an intense laser pulse through preformed plasmas have been performed at relativistic intensities. These experiments have great relevance for the fast ignitor concept. The experimental observations were modelled with a 3-D PIC code. Excellent agreement was obtained.

2. LASER BEAM IMPRINTING

Laser imprinting was studied on planar thin foil plastic targets using soft X ray face on radiography. Several different laser beam profiles were used including random phase plate smoothing (RPP), which generates a multimode spatial spectrum, induced spatial incoherence (ISI) and a single mode, sinusoidal pattern produced by laser beam interference. Typically, 10 μm thick CH foil targets were irradiated with one $\lambda = 0.53$ μm beam of the VULCAN or TRIDENT Nd:glass lasers or with a $\lambda = 0.35$ μm beam of the PHEBUS laser at irradiances from 5×10^{12} to 1×10^{14} W·cm^{-2}. Face-on radiography was performed by imaging transmitted soft X ray radiation from a gold backlighter target with a spherical section, multilayered mirror which reflects a narrow band ($\Delta E \sim 5$ eV) around 250 eV. Multiple, temporally separated images were recorded on each shot by a gated framing camera with ~ 120 ps temporal resolution. The spatial resolution of the system was measured to be a few micrometres. Side-on radiographs were also recorded with a similar system allowing target acceleration to be obtained. Computational simulations were performed in 1-D, 2-D and 3-D, using both the NRL FAST laser matter interaction model and the 1-D and 2-D codes MEDUSA and POLLUX. Figure 1 shows a comparison of the root mean squares (rms) variation in optical depth as measured from the experimental data and from the code for two different experiments [1]. In Fig. 1(a), a 7.3 μm C_8H_8 foil was irradiated at an intensity of 4.2×10^{12} W·cm^{-2} and in Fig. 1(b) an 8 μm CH_2 foil at 1.8×10^{13} W·cm^{-2}. Foils driven with

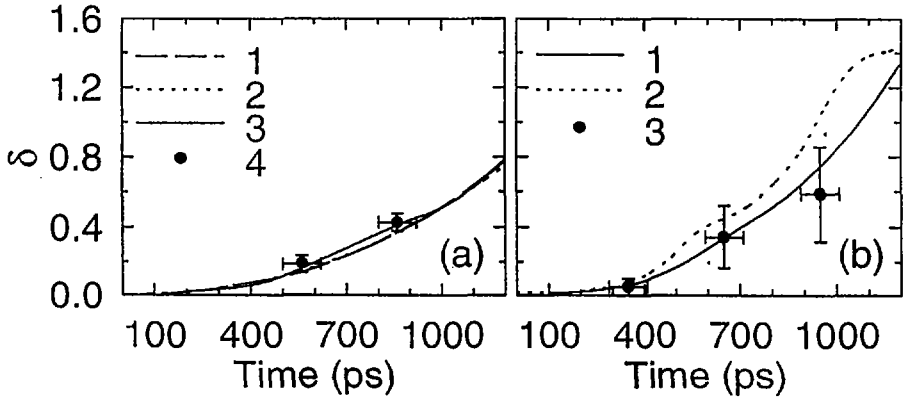

FIG. 1. Comparison of δ for experimental data and for 2-D and 3-D simulations for (a) C_8H_8 and (b) CH_2 targets, irradiated at $I \sim 4.2 \times 10^{12}$ W·cm^{-2} and $I \sim 1.8 \times 10^{13}$ W·cm^{-2}, respectively. (a)4 and (b)3 are the experimental data points; (a)1 2-D rms equivalent case without radiation transport; (a)2 2-D rms equivalent case with radiation transport; (a)3 3-D case. (b)1, (b)2 2-D case with radiation transport for intensities of 1.3×10^{13} and 2.3×10^{13} W·cm^{-2}.

temporally incoherent irradiation (RPP + 5 × 5 etalon ISI smoothing with bandwidth $\delta\omega/\omega = 0.1$) exhibited slower growth, e.g. rms $\delta = 0.36$ at 2.4 ns for a 3 μm C_8H_8 foil irradiated at 8.3×10^{12} W·cm^{-2}.

Single mode imprinting was studied by irradiating similar CH targets with a modulated laser profile which was generated by interference in a transmissive etalon type arrangement. The technique provided variable wavelength spacing of the fringes, with a modulation depth of about 15 to 20%. The beam modulation technique used produced an intensity ($\sim 5 \times 10^{12} - 5 \times 10^{13}$ W·cm^{-2}) drive on a large spot (>400 μm in diameter). A new target imaging technique was developed at a higher X ray energy (1540 eV) by using a crystal reflector in place of the normal XUV mirror in the Hi-Mag imaging system.

3. REDUCTION OF IMPRINTING USING LOW DENSITY FOAM TARGETS

Recently, we have proposed a novel foam buffered direct drive scheme to reduce imprinting in directly driven targets [2]. The solid shell is overcoated with a low density foam jacket. The foam is preheated to preform a plasma ahead of the shock front. Depending on the target and laser conditions, several different possibilities exist for preforming the plasma. Firstly, a supersonic ionization wave can be produced with a low intensity flash of soft X rays emitted from a thin gold layer which is overcoated on the foam. Secondly, if the shock in the foam is large, the

emission from shock heated material propagates ahead of the shock front. In addition, a supersonic thermal front or non-local heat flow can break down the foam to produce a plasma. This is particularly the case for low density foams.

Targets consisting of a 10 μm CH foil that was overcoated with a low density foam with a density between 10 and 50 mg·cm^{-3} and a length between 25 and 100 μm were irradiated with a green laser beam at an intensity between 5×10^{12} and 1×10^{14} W·cm^{-2} [3]. Uncoated foams and foams with a thin layer of gold ($\sim$160 Å) were used. Face-on radiography at an energy of 250 eV was used to diagnose the target breakup. A clear reduction in imprinting has been observed for wavelengths shorter than the foam length. The preheat level in the solid target caused by the shock and the radiation wave was measured by observing K shell absorption lines. It was seen that significant target preheating occurs if the gold layer used to preform the foam plasma was >200 Å.

4. CHARACTERIZATION OF LASER DRIVEN SHOCKS

Laser driven shock waves propagating through foam targets have been diagnosed by side-on time resolved K shell absorption spectroscopy obtaining ionization and density distributions in the shocked material [4]. The experiments used triacrylate cylindrical foam targets at a density of 50 mg·cm^{-3}, which were doped with 25% by weight of chlorine. The foams were typically between 170 and 200 μm long and about 250 μm in diameter. The foam targets were either uncoated or overcoated on one end of the cylinder with 1000 Å aluminium. Three frequency doubled beams (wavelength $\sim$0.53 μm) in a cluster arrangement of the VULCAN laser system were focused onto one end of the bare or aluminium coated cylindrical target. The targets were irradiated at 1×10^{14} W·cm^{-2}.

The shock induced in the foam was studied in a direction perpendicular to the incident laser beams, i.e. normal to the axis of the cylindrical target. The ionization and density were measured by using point projection spectroscopy. The spectrometer was set to record the absorption spectrum of chlorine due to transitions from the K shell to the 2p and 3p orbitals. A detailed atomic physics model was matched to the absorption spectra to infer the temperature distribution. The inferred temperatures, shock positions and widths from the absorption measurements and the shock velocity from the streak data were compared with simulations performed with NYM, a 2-D hydrocode. The simulations agree within the experimental errors. Preheating of material ahead of the shock front by radiation from the shocked region was shown to make an important contribution to the measured temperature profile.

5. RAYLEIGH–TAYLOR INSTABILITY IN CONVERGENT GEOMETRY

The R–T instability was studied in convergent geometry by using thin plastic cylindrical targets. The targets were irradiated with six green laser beams with a pulse duration of 1.5 ns focused symmetrically around the cylinder waist. Both bare

and foam overcoated targets, unfilled or filled with low density foam, were irradiated at intensities of 5×10^{13} W·cm^{-2}. In addition, targets with 2 μm amplitude modulations on the inside were used. The implosion was diagnosed with an X ray probe with an energy between 1.3 and 1.5 keV along the target axis. Sixteen frames were obtained with a gated pinhole system during the implosion phase. Initial analysis clearly shows cylinder breakup for large aspect ratio targets. R–T growth was also observed for the modulated targets. Simulations with the 1-D hydrocode MEDUSA have been carried out and show agreement with the implosion history.

6. SHORT WAVELENGTH RAYLEIGH-TAYLOR INSTABILITY DRIVEN BY SOFT X RAY RADIATION

The R–T instability was studied in the short wavelength regime by using single mode targets which were driven by hohlraum radiation allowing the Takabe–Morse rollover due to ablative stabilization to be investigated. The soft X ray drive was generated by focusing six beams of the VULCAN laser onto the inner surface of a cylindrical gold hohlraum of 1 mm in diameter and 1.3 mm in length. The beams delivered ~600 J at a wavelength of 0.53 μm in a 1 ns pulse, which yielded a radiation drive temperature of about 130 eV. Targets with sinusoidal modulations with wavelengths between 6 and 36 μm, and perturbations of either 5 or 10% of the wavelength, were used. The targets were probed at an X ray energy of 250 eV with a spatial resolution of <2 μm. The magnification from the target to the film plane was about 90 times. The backlighter was either the hohlraum radiation itself or a laser irradiated gold target. No R–T growth was observed for a wavelength of 12 μm or shorter when CH targets were used. When, however, the target opacity was increased by using a plastic doped with 50% of oxygen, clear R–T growth was seen at a wavelength of 15 μm, even in the hohlraum geometry. Further, large growth was seen for targets with 18 and 24 μm perturbations. However, virtually no growth was observed for 24 μm modulated targets which were overcoated with a low density foam layer facing the soft X ray drive. In addition, multimode coupling was investigated for similar drive conditions. Targets with initial 10 and 15 μm wavelength perturbations clearly showed substantial growth at 30 μm. Preliminary 2-D POLLUX hydrodynamic code simulations indicate that mode coupling occurred.

7. MODEL FOR MULTIMODE COUPLING

For accurate calculation of the fusion yield, fluid codes must take account of the R–T instability. In particular, an accurate description of mode coupling is essential. To resolve the high k modes and their coupling to lower k modes during the implosion phase, an extremely high resolution is required. Such a high resolution makes the regular use of multidimensional simulations impractical. For this reason

a multimode mix model was developed [5], which can be incorporated into a one dimensional hydrocode.

We compared Haan's mode coupling model with two dimensional hydrocode simulations in the classical R–T geometry (heavy fluid supported by a light fluid in a gravity field). It was found that when mode coupling was included, the low k mode growth was much larger than predicted by Haan's model. This implies that the low k modes, which dominate at late times, are largely determined by the high k modes and thus place a more stringent condition on the initial capsule perturbation. We found that Haan's model gave good agreement up to the point at which the dominant high k modes driving the stimulated modes saturated and became non-linear. In our extended mode coupling model, the dominant modes are allowed to make a smooth transition from classical, exponential growth through saturation to constant acceleration growth. By calculating the third order contribution to the dominant modes' amplitude and comparing this to multimode hydrocode simulations we were able to derive a new saturation criterion to employ in our model. Comparisons between the new extended model, Haan's model and two dimensional simulations in a classical configuration have been performed. These comparisons show that the new model can accurately follow the growth of the modes for times which are two to three times longer than Haan's model.

8. MODEL DESCRIBING THE SATURATION OF SELF GENERATED MAGNETIC FIELDS

An analytical model was developed which describes the saturation of self generated magnetic fields in laser produced plasmas [6]. Magnetic fields can be generated by laser–plasma interactions through several mechanisms, in particular the $\nabla T \times \nabla n/n_e$ effect, most of which require some transverse non-uniformity. The scaling laws for the non-linear growth and saturation mechanisms in various regimes have been examined. A universal diagram is found in which the magnetic field can be saturated by microturbulent processes such as the lower hybrid drift instability at small transverse scale-lengths, and by ablative convection at large scale-lengths. At the intersection of these regimes, and provided the mean free path exceeds the collisionless skin depth, the magnetic pressure can equal the plasma pressure. At this point the transverse scale-length is an ion collisionless skin depth. At lower temperatures, classical resistive diffusion limits the magnetic field in the intersecting region, causing the electron Hall parameter, $\omega_e\tau_e$, to be below one. At the triple point, we have $\omega_e\tau_e = 1$, and the mean free path equals the electron collisionless skin depth.

9. FAST IGNITOR STUDIES

Experimental studies investigating the propagation of an intense laser pulse through preformed plasmas have been performed [7]. These experiments have great relevance for the fast ignitor concept [8]. The pulse (1 ps in duration, 10 TW,

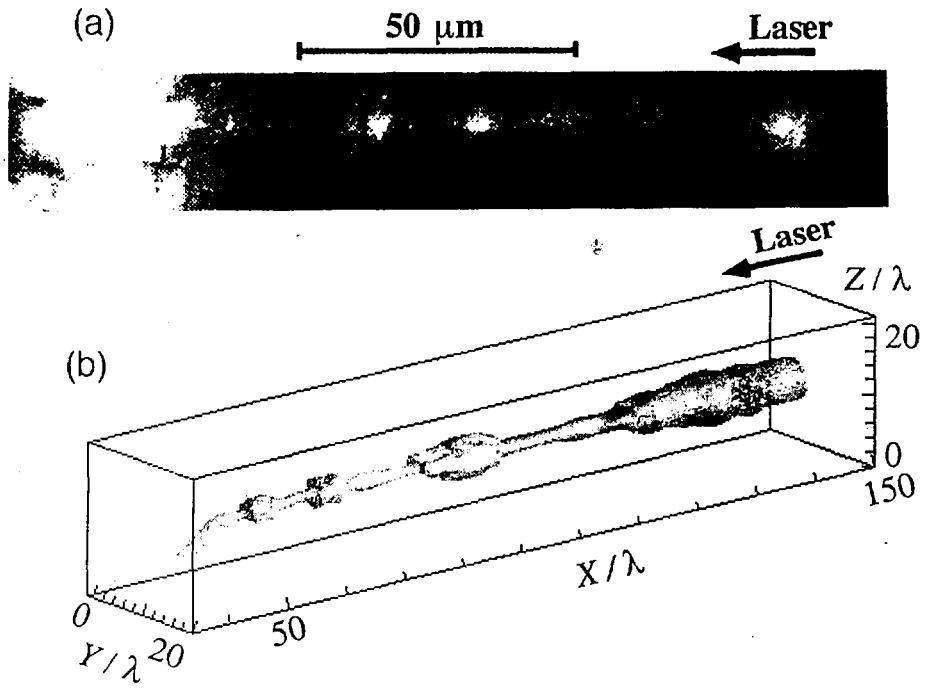

FIG. 2. (a) Self emission channel showing pulsation along the channel after interaction of a 1 ps, 1.054 μm laser pulse at an irradiance of (6–8) × 10^{18} W·cm^{-2} with a preformed plasma of peak density $n_c/2$. (b) Snapshot of a 3-D PIC simulation after 150 laser cycles performed with parameters as used in the experiment; the plotted surface corresponds to 67% of the cycle averaged maximum intensity, $\langle I_{max} \rangle$.

λ = 1.054 μm) was focused at an irradiance exceeding 5 × 10^{18} W·cm^{-2} onto a near critical, underdense plasma preformed by laser irradiation of a thin (0.1–0.5 μm) plastic foil. The interaction in the investigated regime, i.e. significantly above the threshold for relativistic filamentation, appeared to be characterized by relativistic self channelling of the pulse. The channelling was detected through spatially resolved second harmonic emission. A single emission filament (typically, 5 μm in diameter and extending over several Rayleigh lengths) was observed and interpreted as a signature of the spatial extent of the beam during the propagation. In addition, the transverse size of the channel appears to oscillate with a characteristic period of about 20 μm. These oscillations have also been observed in 3-D PIC code simulations at the MPQ, Garching [9], for conditions used in the experiment. The experimental observation and a 3-D PIC simulation are shown in Fig. 2. The code has also predicted the generation of large magnetic fields during the interaction, due

to the current of relativistic electrons co-moving with the laser pulse. These magnetic fields contribute to the confinement of the laser energy into the narrow channel [9]. Faraday rotation measurements were carried out to study the self generated magnetic fields produced during the interaction. The measurements show that two different types of toroidal magnetic field are generated. On the outer edge of the plasma, a field with an amplitude of a fraction of an MG was detected, with the direction consistent with the conventional thermoelectric generation mechanism. In the region closely surrounding the laser propagation axis, a significantly higher magnetic field was observed. Its direction was opposite to the thermoelectric magnetic field, consistent with the 3-D PIC predictions. Spectral measurements of second harmonic emission were also performed that indicate a large broadening towards the red, as expected from self phase modulation effects in the presence of pulse channelling.

ACKNOWLEDGEMENTS

The authors would like to acknowledge the staff of the Central Laser Facility for their assistance and technical support. In addition, they would like to thank the staff at the TRIDENT Laser Facility (Los Alamos) and PHEBUS Laser Facility (Limeil). This work was supported by EPSRC and some joint EPSRC/MoD grants.

REFERENCES

[1] TAYLOR, R., DAHLBURG, J., IWASE, A., FYFE, D.E., GARDNER, J.H., WILLI, O., Phys. Rev. Lett. **76** (1996) 1643.
[2] DESSELBERGER, M., JONES, M., EDWARDS, J., DUNNE, M., WILLI, O., Phys. Rev. Lett. **74** (1995) 2961.
[3] DUNNE, M., BORGHESI, M., IWASE, A., JONES, M., TAYLOR, R., WILLI, O., GIBSON, R., GOLDMAN, S.R., MACK, J., WATT, R.G., Phys. Rev. Lett. **75** (1995) 3858.
[4] HOARTY, D., IWASE, A., MEYER, C., EDWARDS, J., WILLI, O., Phys. Rev. Lett. (in press).
[5] TOWN, R.P.J., FINDLAY, J.D., BELL, A.R., Laser Part. Beams **14** (1996) 237.
[6] HAINES, M., submitted to Phys. Rev. Lett.
[7] BORGHESI, M., MACKINNON, A.J., BARRINGER, L., GAILLARD, R., GIZZI, L., MEYER, C., WILLI, O., PUKHOV, A., MEYER-TER VEHN, J., submitted to Phys. Rev. Lett.
[8] TABAK, M., HAMMER, J., GLINSKY, M.E., KRUER, W.L., WILKS, S.C., WOODWORTH, J., CAMPBELL, M.E., PERRY, M.D., Phys. Plasmas **1** (1994) 1626.
[9] PUKHOV, A., MEYER-TER VEHN, J., Phys. Rev. Lett. **76** (1996) 3975.

DISCUSSION

K. MIMA: Please comment on the comparison of various foam coated targets from the standpoint of hybrid drive symmetry improvement; for example: (1) thin gold layer on a thick foam layer; (2) high Z doped foam layer; (3) single low Z foam

on a target; (4) gold layer plus vacuum layer plus target. Which are better for implosion?

O. WILLI: At present, it is difficult to give a definite answer as to which is the best scheme owing to the limited number of experimental measurements and limited computational understanding.

EXPERIMENTS ON INDIRECT/DIRECT HYBRID DRIVE SCHEME

H. SHIRAGA, H. AZECHI, Y. KATO, K. MIMA, N. MIYANAGA,
M. MURAKAMI, M. NAKAI, S. NAKAI, K. NISHIHARA,
H. NISHIMURA, T. NORIMATSU, K. SHIGEMORI,
H. TAKABE, M. TAKAGI, T. YAMANAKA
Institute of Laser Engineering,
Osaka University,
Osaka

T. ENDO[1], C. YAMANAKA
Institute for Laser Technology,
Osaka

Japan

Abstract

EXPERIMENTS ON INDIRECT/DIRECT HYBRID DRIVE SCHEME.

An indirect/direct hybrid irradiation scheme of laser fusion targets to reduce the initial imprint of the laser irradiation non-uniformities has been proposed and examined experimentally. The initial imprint of non-uniformities in laser irradiation (direct drive) was successfully reduced by X ray pre-irradiation emitted by an external source (indirect drive). The indirect/direct hybrid irradiation scheme has been applied to spherical implosion experiments.

1. INTRODUCTION

In direct drive inertial confinement fusion, the initial imprint of spatial non-uniformities in driving the laser beam is considered to cause perturbation seeding on the target surface at the very beginning of the irradiation; this imprint may be amplified by a Rayleigh–Taylor (RT) instability during the later acceleration phase of the implosion and may be deleterious to spherical implosion and efficient heating of the hot spark in the imploded core plasma. Recently, the uniformity of the drive beam has been drastically improved by introducing the partially coherent light (PCL) technique [1] coupled with the random phase plate (RPP) [2]. However, the initial imprint still remains a critical issue because the PCL takes several tens of picoseconds to manifest its excellent effect. The plasma scale length, which grows from zero, remains too small during this period to produce a sufficient thermal smoothing effect.

[1] Present address: Division of Global Environment Science, Center for Integrated Research in Science and Engineering, Nagoya University, Nagoya, Japan.

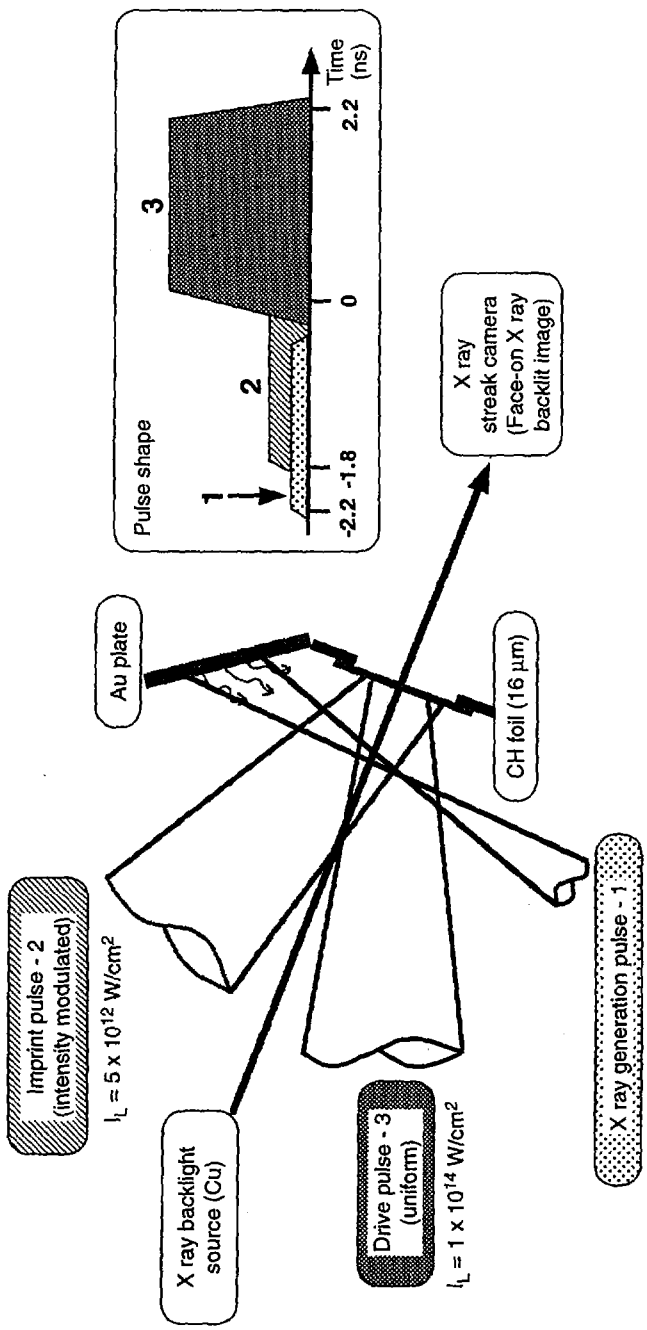

FIG. 1. Experimental arrangement for planar target experiments on the indirect/direct hybrid scheme.

To solve the problem, we here propose a new scheme called indirect/direct hybrid drive scheme [3]. It is a combination of uniform indirect drive in the early stage and efficient direct drive afterwards. The idea is that the target surface should first be irradiated very uniformly by a low intensity soft X ray prepulse to cause uniform expansion of the preformed plasma, with a certain scale length. When, later on, the main direct drive beam arrives, in the target there already exists a substantial stand-off distance between the ablation front and the beam absorption region. Thus the thermal smoothing effect can take place in this transport layer, reducing the initial imprint of the beam non-uniformity.

2. PLANAR TARGET EXPERIMENTS

We have performed a series of planar target experiments in order to demonstrate the effect of this scheme in reducing the imprint. Figure 1 shows the experimental arrangement and the pulse shapes of the drive beams. The surface perturbation of a planar target seeded by the initial imprint due to an intensity modulation of 10% with a wavelength λ of 100 μm in a foot pulse partially coherent light (PCL) beam (5×10^{12} W/cm^2, 1.8 ns flat-top pulse) was amplified with linear Rayleigh–Taylor (RT) instability growth, in the subsequent acceleration phase driven by the uniform main drive pulse from another PCL beam (1×10^{14} W/cm^2, 1.8 ns flat-top pulse). Another gold plate was set beside the sample foil as an external X ray source.

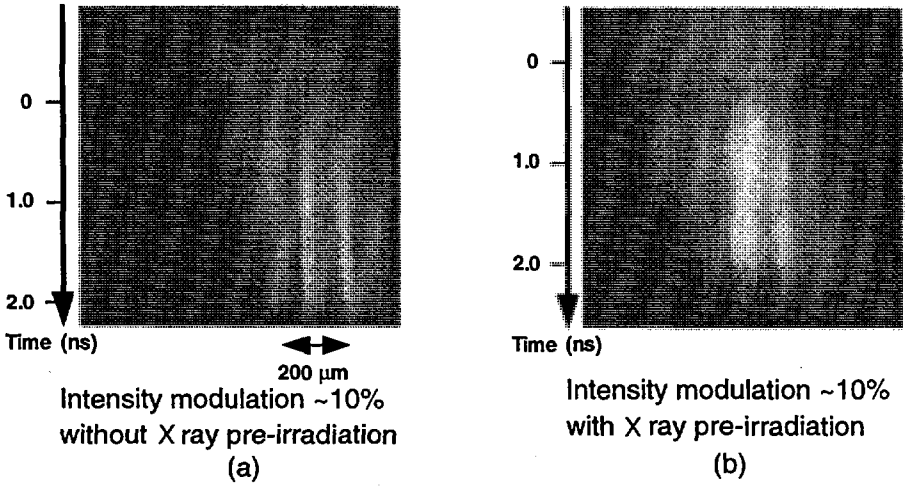

FIG. 2. Streaked face-on X ray backlighting observing the RT growth of resulting areal mass density perturbation caused by the initial imprint.

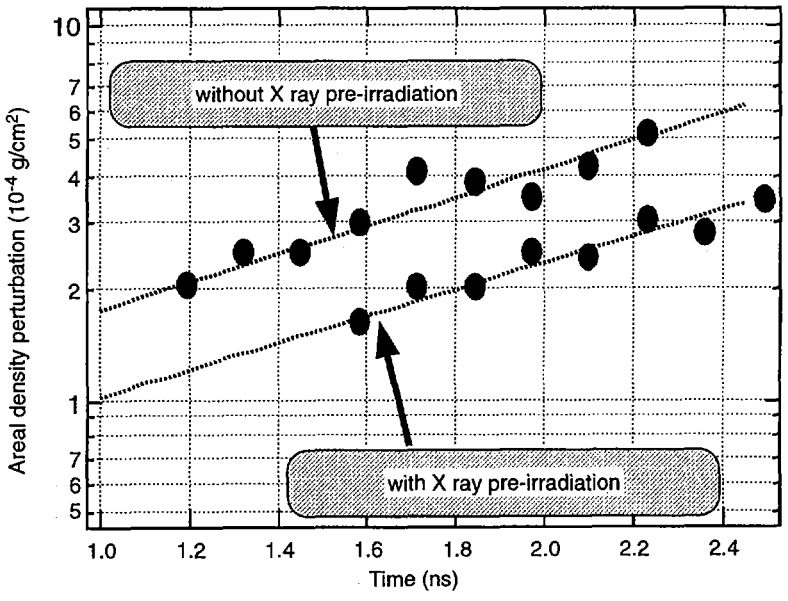

FIG. 3. Growth of areal density perturbation amplitudes for cases with and without X ray pre-irradiation. The perturbation growth was reduced to 60% with X ray pre-irradiation. $t = 0$ corresponds to the start of the main drive beam.

This gold plate was located 1.8 mm from the sample foil. It was irradiated with a separate PCL beam at an intensity of 5×10^{13} W/cm^2 in a flat-top pulse, which started 0.4 ns before the foot pulse. The growth of the resulting areal mass density perturbation was observed with streaked face-on X ray backlighting, as shown in Fig. 2. Bright portions correspond to a smaller product of density times thickness, and darker ones to a larger product. Figure 2(a) shows that the bright-to-dark contrast grew in time. When the target was pre-irradiated by X rays, the perturbation growth was significantly reduced, as shown in Fig. 2(b). In Fig. 3 we see the perturbation growth derived from the data of Fig. 2 for cases with and without X ray pre-irradiation. It is shown that the growth is in a linear RT phase for each case, and we see clearly that the amplitude in the X ray pre-irradiated case is reduced to 60% of that in the normal case.

The observed smoothing effect can be explained by the cloudy day model. Assuming the X ray conversion efficiency on the gold foil to be 50% and the X ray emission to be isotropic in 2π, the X ray irradiation intensity on the sample foil is estimated to be 7×10^{10} W/cm^2. The stand-off distance D may be given by $D = c_S\tau$, where c_S is the sonic speed of the X ray irradiated plasma and τ is the duration. For $c_S = 3.5 \times 10^6$ cm/s estimated from the X ray intensity and

τ = 400 ps, we obtain D = 14 μm. According to the cloudy day model, the thermal smoothing effect is described as $f = \exp(-kD)$, where f is the reduction factor and $k = 2\pi/\lambda$ is the wavenumber of the perturbation. For k = 630 cm^{-1} (λ = 100 μm) and D = 14 μm, f becomes 0.4, which is close to the experimentally observed reduction factor of 0.6.

3. APPLICATION TO SPHERICAL TARGET IMPLOSIONS

Several types of target using the hybrid drive concept have been proposed: (A) targets with external X ray emitters separated from the fuel pellet; (B) targets with a thin gold layer surrounding the fuel pellet with a void separation layer; (C) targets coated with a low density foam layer having a thin gold layer on the outer surface; (D) targets coated with high Z doped low density foam, etc. Among these targets, the external X ray emitter (A), the thin gold layer (B, C) or the high Z material doped in the foam (D) act as X ray pre-irradiation sources when irradiated by laser prepulses. Plasmas are preformed by X ray pre-irradiation of the fuel pellet surface (A, B) or of the foam layer (C, D).

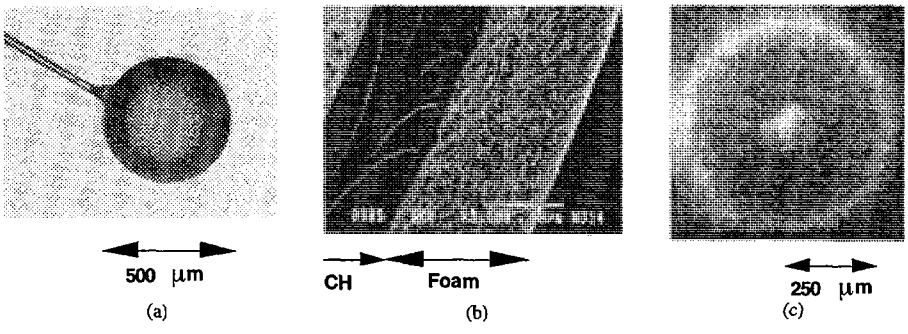

FIG. 4. Example of CH shell target coated with Pb doped foam layer. (a) target view; (b) cross-sectional view of Pb doped foam layer coated on a CH shell; (c) X ray framing picture of imploded target.

Figure 4 shows a Pb doped foam coated target and an X ray framing picture of its implosion. The initial diameter of the target was 500 μm. Thickness and mass density of the foam layer were 15 μm and 250 mg/cm^3, respectively. The Pb content was 30 wt%. The target was irradiated with 12 beams of 5 kJ/1.4 ns GEKKO XII 0.53 μm laser light. The mass density of the foam layer was too high and the thickness uniformity was poor in this case. We are improving these target characteristics.

4. SUMMARY

From these results, we conclude that the initial imprint of the non-uniformity in the direct drive beam was reduced by using X ray preformed plasma in the indirect/direct hybrid drive scheme. This implies that the uniformity requirement for the main direct drive beam can be greatly relaxed. Several types of target configuration are proposed and are being examined so that indirect/direct hybrid drive spherical implosion can be realized.

REFERENCES

[1] MIYANAGA, N., et al., in Solid State Lasers for Application to Inertial Confinement Fusion (Proc. 1st Ann. Int. Conf. 1995), SPIE Proc. **2633** (1995) 183.
NAKANO, H., et al., J. Appl. Phys. **73** (1993) 2122.
[2] KATO, Y., et al., Phys. Rev. Lett. **53** (1984) 1057.
[3] KATO, Y., et al., in Plasma Physics and Controlled Nuclear Fusion Research 1994 (Proc. 15th Int. Conf. Seville, 1994), Vol. 3, IAEA, Vienna (1995) 45.
DESSELBERGER, M., et al., Phys. Rev. Lett. **74** (1995) 2961.

DISCUSSION

T. DESAI: Have you measured the ablation pressure and mass ablation rate when the ICF target is irradiated with the X ray prepulse and then the main pulse?

H. SHIRAGA: We have measured them for the main drive pulse in separate shots, but not yet for the X ray prepulse.

T. DESAI: A thin layer of gold on the target surface will generate a lot of X rays, of which almost 50% are emitted to the vacuum. This is a loss to the system. How do you take account of this loss to the laser–plasma coupling efficiency?

H. SHIRAGA: Yes, it is a loss. However, this X ray irradiation is used only as a prepulse, with a very small energy compared with the later main laser drive. Therefore we do not have to worry about this loss.

O. WILLI: How much of the reduction in the R–T growth in the direct/indirect scheme is due to thermal smoothing in the preformed plasma and decompression in the target caused by the X ray pulse?

H. SHIRAGA: The R–T growth rate was essentially the same for both cases, with and without the X ray pulse. The X ray pulse was effective in reducing the initial amplitude of the perturbation. We are going to measure the density profile to check this result.

J.D. LINDL: What are your plans for optimizing the imprint reduction that can be achieved with an X ray prepulse?

H. SHIRAGA: It depends on the imprint features of the direct drive beam, its amplitude and smoothing rate. Hence, it depends on the capsule design, taking those factors into account. The physics of the imprint reduction is the cloudy day effect. We can control the intensity and the duration of the X ray pulse to create the required pre-expansion of the plasma.

APPROACHES TO FAST IGNITION IN INERTIAL CONFINEMENT FUSION AT ILE, OSAKA

Y. KATO, Y. KITAGAWA, R. KODAMA, H. TAKABE,
H. FUJITA, T. JITSUNO, T. KANABE, M. NAKATSUKA,
K.A. TANAKA, H. SHIRAGA, K. SAWAI, S. MIYAMOTO,
M. HONDA, S. NAKAI, K. MIMA
Institute of Laser Engineering,
Osaka University,
Suita, Osaka

H. SAKAGAMI
Computer Engineering,
Himeji Institute of Technology,
Himeji

C. YAMANAKA
Institute of Laser Technology,
Osaka

Japan

Abstract

APPROACHES TO FAST IGNITION IN INERTIAL CONFINEMENT FUSION AT ILE, OSAKA.

Using ILESTA-2D, a two dimensional hydrodynamic code that includes α particle transport, as well as a one dimensional Fokker–Planck code, the authors show that not only a central but also an off-central spark can ignite the main fuel even with an implosion velocity perturbation of 15%. An anomalous penetration mechanism into an overdense plasma is studied with a 1½ dimensional electromagnetic particle code (EMPAC). A preliminary experiment shows that a laser bores a hole into the overdense region. A 1 ps, 30 TW pulse from the GEKKO MII glass laser system is used to irradiate a solid target to investigate laser boring of overdense plasmas and high energy particle generation. A 100 TW laser module is being constructed as the 13th arm of the GEKKO XII glass laser system (a 12 beam system) to experimentally verify fast ignition.

1. INTRODUCTION

Progress with high power short pulse lasers using a chirped pulse amplification technique [1] is opening the possibility of a concept for additional heating, fast ignition [2], in inertial confinement fusion (ICF). In this concept, compressed fuel, with a high fuel density created by a conventional laser implosion, is heated by an ultra-intense short pulse (a few picoseconds) laser before core disassembly (in less than

a few tens of picoseconds). The concept will achieve reduction of the required laser energy and implosion uniformity for ignition in ICF.

We have already demonstrated laser compression [3] with core densities and areal densities greater than those needed for fast ignition. One of the critical issues for realizing fast ignition is the mechanism of the additional heating of core plasmas. The effect of additional heating on the neutron yield has been studied by using a one dimensional Fokker–Planck hydrodynamic simulation code [4]. Details of the core heating were simulated in an isochoric model with ILESTA-2D, a two dimensional hydrodynamic code including α particle transport. Both central and off-central ignition can occur. We have also studied the possibility of off-central ignition of the core, where some fuels are mixed with shell materials owing to implosion non-uniformity.

Another critical issue for realizing fast ignition is efficient laser energy deposition into an overdense region around the core. The laser propagates through the overdense plasma with a long scale length and then deposits the energy in the core plasma. Using the GEKKO XII glass laser at the Institute of Laser Engineering (ILE), Osaka, we have carried out a preliminary experiment related to laser hole boring into the overdense region [5].

Another idea is to use a prepulse-free ultra-intense laser. By increasing the laser intensity, a relativistic mass effect reduces the plasma frequency and changes the reflective index, with the result that the critical point apparently recesses into the overdense region. The effect has been studied by using a 1½ dimensional electromagnetic particle code (EMPAC).

Another approach is to use a circularly polarized high intensity laser. The self-induced transparency of a circularly polarized beam is also being examined.

To experimentally study the phenomena related to fast ignition, we are constructing high power short pulse lasers in both the GEKKO MII and GEKKO XII glass laser systems: a 1 ps, 30 TW pulse from GEKKO MII (a two beam system) [6] and a 100 TW pulse from GEKKO XII (a 12 beam system) with an energy of 100 J and a beam diameter of 200 mm. The 13th beam of GEKKO XII is to irradiate the spherical target, preimploded by the remaining 12 beams.

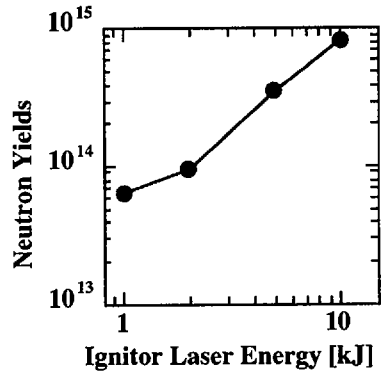

FIG. 1. Neutron yield as a function of the ignitor laser energy. The ignitor is a 1 ps laser.

2. NUMERICAL STUDIES OF FAST IGNITION

The effect of the additional heating on the neutron yield has been studied by using a one dimensional Fokker–Planck hydrodynamic simulation code, as shown in Fig. 1 [4], where the compression laser energy is 10 kJ. The compressed core plasma can be heated to more than 5 keV by injecting 100 keV hot electrons, resulting in the enhancement of the neutron yield.

Details of the core heating were simulated in an isochoric model with ILESTA-2D. Not only a central but also an off-central spark can ignite the core plasma. The ignition condition for the off-central spark is found to be the same as for the central spark, namely, the required spark energy E_s (GJ) is

$$E_s = 10.6 \times \left(\frac{\rho_s}{\rho}\right)^2 (\rho R)^3 T \qquad (1)$$

where T is the spark temperature in keV, ρR is the areal mass density in g/cm^2 and ρ_s and ρ are the solid DT density and the spark plasma density, respectively. The ignition condition for T = 5–20 keV is given by

$$(\rho R)^3 T = 1 \qquad (2)$$

Equations (1) and (2) indicate that the spark energy can be less than 1 kJ when $\rho/\rho_s \geq 3000$. The ignition and gain curves are shown in Figs 2 and 3. From the above analysis we conclude that a pulse of several kJ·ps could ignite a cold super-dense DT fuel (≥ 600 g/cm^3), which could be generated by a multikilojoule blue laser system, namely the New GEKKO XII laser. We expect ignition and burning in the range $0.45 < \rho R < 0.5$ g/cm^2 for $T_s = 10$ keV and $0.3 < \rho R < 0.6$ g/cm^2 for $T_s = 20$ keV.

For given ρR and T, the energy of the spark is proportional to ρ^{-2}, as shown in Fig. 2. For two cases, namely $\rho = 200$ g/cm^3, main fuel R = 120 μm ($\rho R = 2.4$ g/cm^2), and $\rho = 400$ g/cm^3, R = 80 μm ($\rho R = 3.2$ g/cm^2), the resultant fusion energy is plotted in Fig. 2 as a function of the spark energy. The numbers represent the spark ρR value in g/cm^2. In both cases the spark temperature is assumed to be 10 keV. A spark ρR of 0.4–0.5 g/cm^2 is critical for fuel burning. The minimum energy for spark ignition is 2–3 kJ for $\rho = 400$ g/cm^3 and 10–15 kJ for $\rho = 200$ g/cm^3.

In Fig. 3 the core gain is more than 2000 near $E_M = 100$ kJ. This indicates that a 1 MJ driver provides a pellet gain of 200, if the coupling efficiency is 10% from the laser to the compressed core. The heating efficiency of the short pulse is still unknown. If it is, say, 30%, a short pulse energy of 40 kJ will be required to ignite the compressed core. Note that an abrupt increase of the gain is seen near the fuel ρR = 1–1.5 g/cm^2. Across that region a front of the self-heating area propagates as a detonation wave in the fuel.

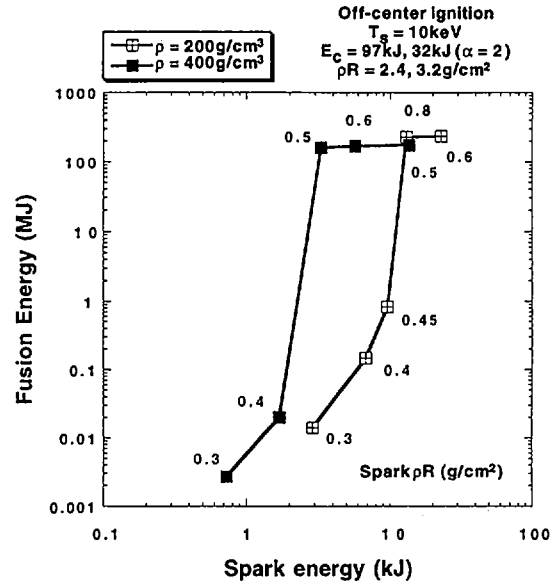

FIG. 2. Fusion energy for off-central ignition as a function of spark energy.

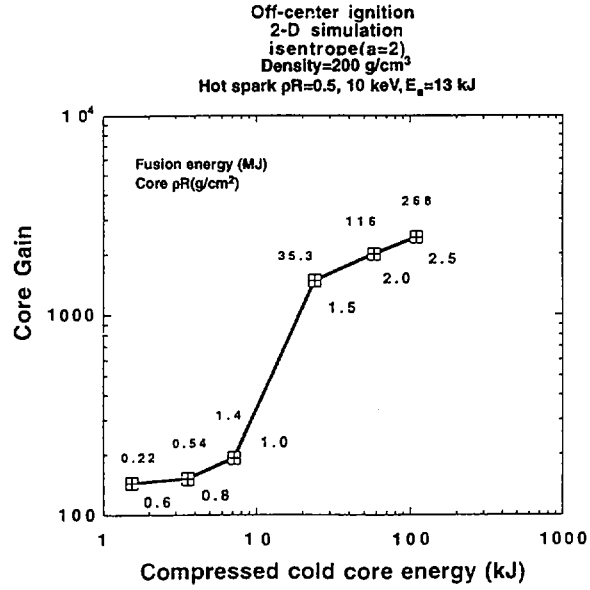

FIG. 3. Core gain versus compressed core energy for off-central ignition.

Another important issue is efficient laser energy deposition into an overdense region around the compressed core. The laser propagates through a peripheral overdense plasma with a long scale length and then deposits the energy in the core plasma. One of the conventional ideas for depositing the laser energy into the high density plasma is to use a laser with a shorter wavelength, e.g. 0.25 μm, because of its higher critical density. High photon pressure will be useful for laser hole boring into the overdense region. After a hole has been bored into the overdense region with a prepulse, the main short pulse is injected through the hole and deposits the energy into the core.

Another idea is to use prepulse-free ultra-intense lasers. By increasing the laser intensity, a relativistic mass effect reduces the plasma frequency and changes the reflective index, with the result that the critical point apparently recesses into the overdense region. The effect has been studied by using a 1½ dimensional electromagnetic particle code (EMPAC). Laser light with an intensity above 10^{20} W/cm^2 can penetrate into a plasma with ten times the critical density, owing to the relativistic mass effect. The penetration dynamics have been studied by taking account of the ion dynamics.

3. EXPERIMENT ON HOLE BORING

The experiment was carried out using the GEKKO XII laser system at ILE [5]. A CH plastic plane target with a thickness of 100 μm was irradiated obliquely by two 351 nm laser beams (each of 5 J) of GEKKO XII to produce a preplasma with a 300 μm focal spot at 50° incidence angle to the normal. A 1053 nm laser light as the main interaction pulse was focused normally onto the preplasma with an f/3 aspheric lens after 0.9 ns of the prepulse. The intensity of the main pulse was 2×10^{17} W/cm^2 at the best focus with a 30 μm spot diameter and 120 J beam energy. The spot diameter of the best focus was estimated from X ray images. All the pulse shapes were a Gaussian profile with a 100 ps full width at half-maximum (FWHM). The main laser focal positions were varied from 100 to 400 μm from the plastic target surface. The focus lens had a 30 μm spot size with approximately 160 μm depth of focus ($\pm$80 μm). The intensity at the critical density n_c was 2×10^{17} W/cm^2 for the 100–250 μm focus conditions and 3×10^{16} W/cm^2 for the 400 μm focus, on the basis of a density profile obtained by one dimensional hydrodynamic simulation. Time resolved spectra of the backscattered lights were measured with a 1/4 m spectrometer coupled to an S-1 streak camera. The covered spectra were from 1050 to 1070 nm with a flat spectral response at a spectral resolution of 0.4 nm. The temporal resolution of the system was 13 ps, limited by the width of the streak camera slit and spectral resolution.

Figure 4 shows typical streak camera images of the backscattered spectra at focal positions of 100 μm and 250 μm from the target surface. As a common feature in all the focus conditions, a 2–3 nm blueshift from the fundamental

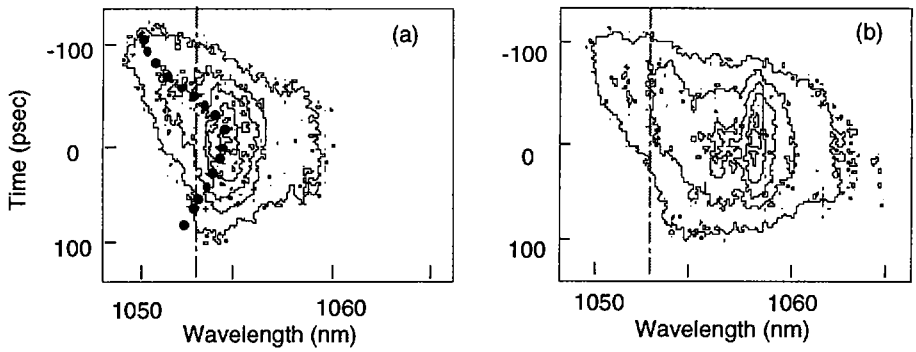

FIG. 4. Linear intensity contours of time resolved spectra of backscattered light at focal positions of (a) 100 μm and (b) 250 μm. The broken lines correspond to the fundamental wavelength. The closed circles in (a) are estimations of Doppler shifts due to the critical surface moving inward under the photon pressure.

(1053 nm) was observed at 100 ps prior to the pulse peak. The blueshift was observed only early in the time of the pulse and rapidly moved to the red side in time. However, no such blueshift was observed without a preplasma. This initial blueshift is due to the Doppler shift caused by the expansion of the preplasma, since this shift depends on the prepulse laser intensity as $\Delta\lambda_b \propto I_L^{0.18-0.29}$ at intensities of (0.4–5) $\times 10^{14}$ W/cm^2. The spectral peak was shifted to the red side and the shape changed in time. The overall shapes depend on the focal position. The peaks of the redshifts from the fundamental wavelength were 1–2 nm for the 100 μm focus, 5–6 nm for the 250 μm focus and 6–7 nm for the 400 μm focus.

Assuming the redshift of the intensity peak of the backscattered light as shown in Fig. 4 is a Doppler shift due to the critical surface moving inward under the photon pressure, e.g. 60 Mbar at 10^{17} W/cm^2, the propagation distance of the critical surface is of the order of 20 μm for the 100 μm focus. The propagation distance was 120 μm from the redshift for the 250 μm focus, close to the distance between the initial critical surface and the target surface. The Doppler shift due to the critical surface moving inward was evaluated from a simple snowplough model calculation, which estimated the momentum balance between the photon pressure and mass flow at the critical surface by using a performed plasma density profile from one dimensional simulation and a 100 ps (FWHM) Gaussian profile of the laser pulse. This estimated value is close to the redshift measured at the focal position of 100 μm shown as a broken line in Fig. 4(a). However, a laser intensity of 2×10^{18} W/cm^2, where relativistic self-focusing becomes an important factor, may be necessary to yield a Doppler shift as large as 5 nm to move the critical point. The X ray image showing the tight spot on the target surface, obtained only for the 250 μm focus, is consistent with the strong redshift (5 nm) of the backscattered light if a whole beam channel is self-focused into the overdense region close to the target surface.

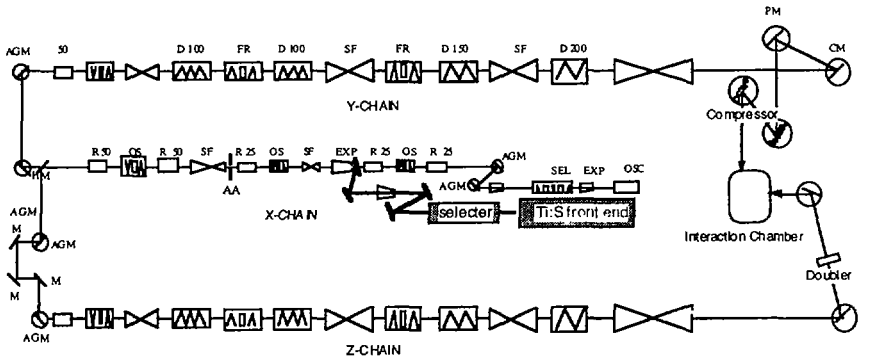

OSC:YLF Oscillator EXP:Expanders
SEL:Pulse selector
R:Rod amplifiers D:Disk amplifiers
OS:Optical shutters FR:Faraday rotators
AA:hard aperture SF:Spatial filter

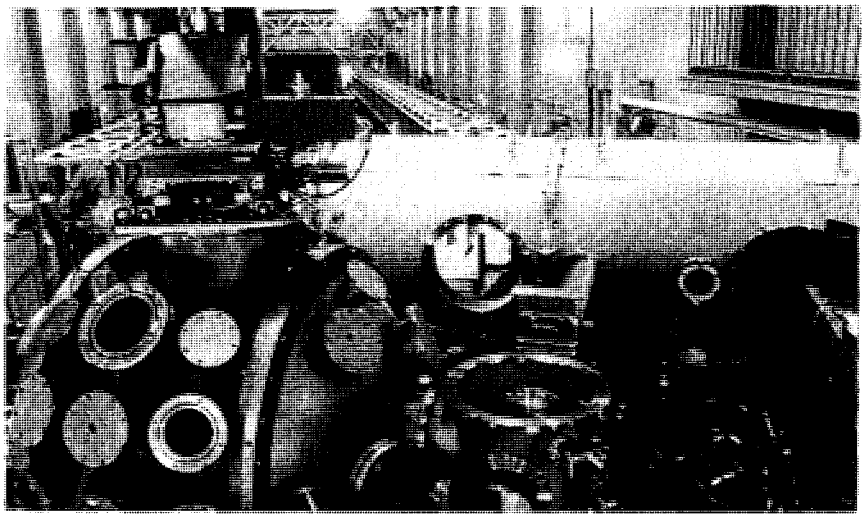

FIG. 5. Layout of the GEKKO MII short pulse laser system. The Y chain is a short pulse beam and the Z chain a long pulse beam. The photograph shows the grating pair compression chamber and the interaction chamber of GEKKO MII.

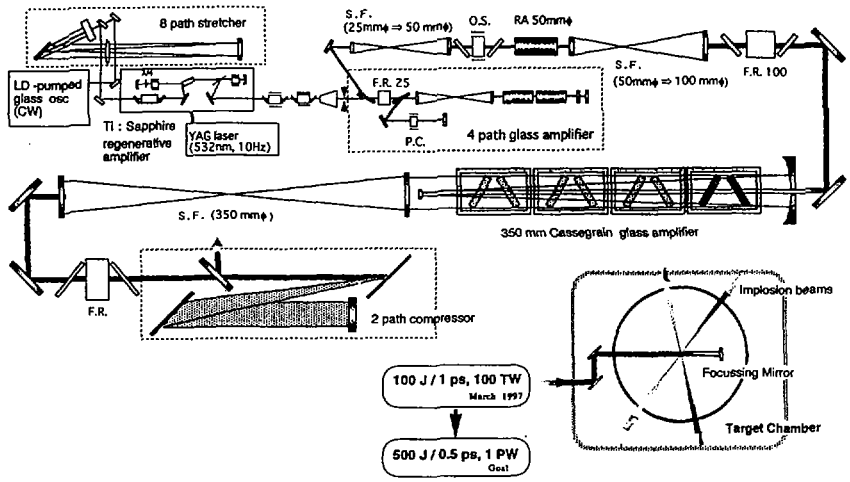

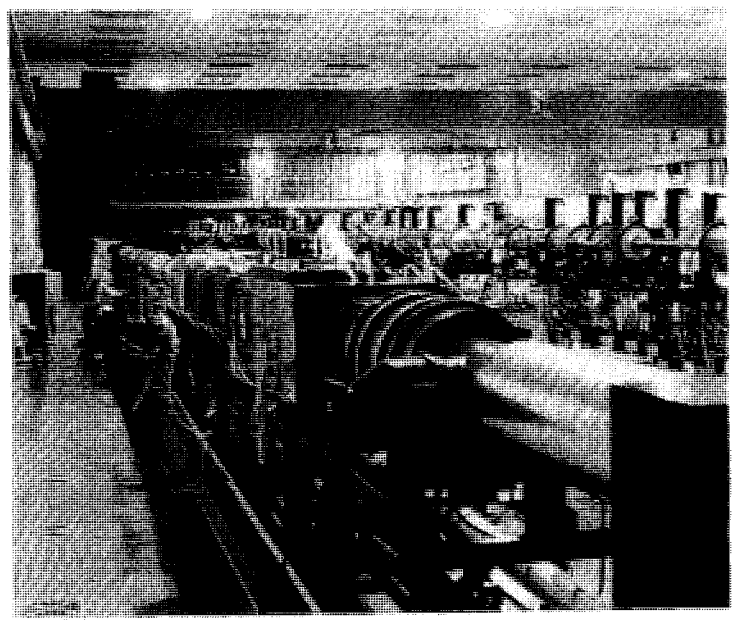

FIG. 6. Petawatt laser module as the 13th beam of the GEKKO XII laser system. This laser is to heat the high density core precompressed with 12 beams of GEKKO XII. The photograph shows the petawatt laser amplifier chain.

4. HIGH POWER SHORT PULSE LASER CONSTRUCTIONS

To experimentally study the phenomena related to fast ignition, we are constructing high power short pulse lasers in both the GEKKO XII and GEKKO MII glass laser systems. Using a single mode optical fibre front end system, we have previously generated a 1 ps, 30 TW pulse from GEKKO MII [6]. Now the front end is to be replaced by the combination of a mode locked Ti:sapphire oscillator and a Ti:sapphire regenerative amplifier to obtain a 50 TW output. The beam, with a diameter of 140 mm, limited by the pulse compressor grating, will be focused with an off-axis parabolic mirror onto a target at intensities above 10^{18} W/cm^2. The system layout and a photograph of the compression chamber are shown in Fig. 5. The laser will irradiate both solid and gas targets to investigate laser boring of overdense plasmas and high energy particle generation from underdense plasmas, respectively.

In the first test experiment, we shall irradiate a CD plastic foil target to observe the energy coupling between the laser and a solid density plasma. As is reported by researchers at Rutherford Appleton Laboratory, we expect that 10^8–10^9 DD neutrons will be generated in the experiment. We are also investigating the transfer efficiency of a 10^{19}–10^{20} W/cm^2·ps pulse through solid density plasmas whose thickness is a few millimetres. According to the simulation results, a 10^{20} W/cm^2 laser pulse makes a channel in an overdense ($n/n_c = 7$) plasma slab with 2 μm thickness, and 90% of the pulse energy comes out the rear side.

We are constructing another ultra-intense short pulse laser module as the 13th arm of GEKKO XII, as shown in Fig. 6. The purpose is to experimentally verify fast ignition. A mode locked glass oscillator and a Ti:sapphire regenerative amplifier are used as the front end system. Preamplification is performed with a 4 pass glass rod amplifier. The final 35 cm disc amplifier of a Cassegrain type 3 pass geometry provides the output of 1 kJ/300 ps to 7 kJ/3 ns with a beam diameter of 200–350 mm. After the grating pair compression, the system will provide 100 TW with an energy of 100 J and a beam diameter of 200 mm. The system can provide 1000 TW if the beam diameter is increased to 350 mm. The new 13th beam is to irradiate the spherical target, preimploded with 12 beams. The additional heating effects such as neutron yield enhancement will then be investigated.

REFERENCES

[1] STUART, B.C., et al., Chirped-pulse amplification in Ti:sapphire beyond 1 mm, IEEE J. Quantum Electron. **31** (1995) 528.

[2] TABAK, M., et al., Ignition and high gain with ultrapowerful lasers, Phys. Plasmas **1** (1994) 1626.

[3] AZECHI, H., et al., High-density compression experiments at ILE, Osaka, Laser Part. Beams **9** (1991) 193.

[4] NISHIGUCHI, A., et al., Kinetic effects of electron thermal conduction on implosion hydrodynamics, Phys. Fluids B **4** (1992) 417.

[5] TAKAHASHI, K., et al., "Scattered light measurements of high-intensity laser plasma interaction above 10^{17} W/cm^2", Proc. 5th Int. Symp., Inst. for Solid State Physics, Tokyo Univ., 1996.

[6] YAMAKAWA, K., et al., Prepulse-free 30 TW, 1 ps Nd:glass laser, Opt. Lett. **16** (1991) 1593.

PROGRESS IN THE PULSED POWER INERTIAL CONFINEMENT FUSION PROGRAM*

J.P. QUINTENZ, M.K. MATZEN, T.A. MEHLHORN
Sandia National Laboratories,
Albuquerque, New Mexico,
United States of America

Abstract

PROGRESS IN THE PULSED POWER INERTIAL CONFINEMENT FUSION PROGRAM.

Pulsed power accelerators are being used in Inertial Confinement Fusion (ICF) research. In order to achieve the goal of a fusion yield in the range of 200–1000 MJ from radiation driven fusion capsules, it is generally believed that ~ 10 MJ of the driver energy must be deposited within the ICF target in order to deposit ~ 1 MJ of radiation energy in the fusion capsule. Pulsed power represents an efficient technology for producing both these energies and these radiation environments in the required short pulses (few tens of a nanosecond). Two possible approaches are being developed to utilize pulsed power accelerators in this effort: intense beams of light ions and z-pinches. The paper describes recent progress in both approaches. Over the past several years, experiments have successfully answered many questions critical to ion target design. Increasing the ion beam power and intensity is the next objective. Last year, the Particle Beam Fusion Accelerator II (PBFA II) was modified to generate ion beams in a geometry that will be required for high yield applications. This modification has resulted in the production of the highest power ion beam to be accelerated from an extraction ion diode. Fast magnetically driven implosions (z-pinches) as platforms for ICF ablator physics and EOS experiments are also evaluated. The z-pinch implosions driven by the 20 TW Saturn accelerator have efficiently produced high x-ray power (> 75 TW) and energy (> 400 kJ). Containing these x-ray sources within a hohlraum produces a unique large volume (> 6000 mm^3), long lived (> 20 ns) radiation environment. In addition to studying fundamental ICF capsule physics, there are several concepts for driving ICF capsules with these x-ray sources. Progress in increasing the x-ray power on the Saturn accelerator and promise of further increases on the higher power PBFA II accelerator will be described.

* This work was supported by the US Department of Energy under Contract No. DE-AC04-94AL85000. The work was done in collaboration with R.G. Adams, G.O. Allshouse, J.E. Bailey, D.D. Bloomquist, J. Boyes, G.A. Chandler, R.S. Coats, D.L. Cook, M.E. Cuneo, C. Deeney, M.S. Derzon, M.P. Desjarlais, M.R. Douglas, R.J. Dukart, D.L. Fehl, A.B. Filuk, T.A. Haill, D.L. Hanson, D.J. Johnson, M.L. Kiefer, R.J. Leeper, R.W. Lemke, T.R. Lockner, J.E. Maenchen, M.G. Mazarakis, D.H. McDaniel, E.J. McGuire, C.W. Mendel, P. Menge, L.P. Mix, A.R. Moats, T. Nash, C.L. Olson, R.E. Olson, T.D. Pointon, J.L. Porter, J.W. Poukey, T.J. Renk, S.E. Rosenthal, C.L. Ruiz, T.W. Sanford, J.F. Seaman, D.B. Seidel, I.R. Shokair, S.A. Slutz, R.B. Spielman, W.A. Stygar and M.A. Sweeney.

1. INTRODUCTION

Sandia National Laboratories is investigating the feasibility of using a pulsed power accelerator as a driver for Inertial Confinement Fusion (ICF). High power accelerators have been used in ICF research for over 20 years to produce intense beams of light ions and energetic x-ray sources from fast magnetic implosions (z-pinches). In order to achieve the US National ICF program goal of a fusion yield in the range of 200 - 1000 MJ from radiation-driven fusion capsules, it is generally believed that ~10 MJ of driver energy must be deposited within the ICF target in order to deposit ~1 MJ of radiation energy in the fusion capsule. Pulsed power represents an efficient technology for producing both these energies and these radiation environments in the required short pulses (few tens of ns).

2. IONS FOR HIGH YIELD AND ION BEAM TARGET PHYSICS

Sandia National Laboratories is investigating the feasibility of obtaining high fusion yield for defense and energy applications using intense beams of light ions as a driver. This long term goal would be realized in a High Yield Facility (HYF). The fusion capsules in our ion-driven [1] ICF targets are indirectly driven by the radiation that is produced when the ion beam travels through a high-Z radiation case and deposits the bulk of its energy in a low density foam that surrounds the fusion capsule. Capsule symmetry and ion diode requirements have led us to a spherically symmetric ion beam configuration, where the two steps of the ion beam drive consist of twenty and twelve beams that are spatially arranged on the vertices and faces, respectively, of a dodecahedron. During the first step (or "foot") of the HYF ion beam drive pulse, 24 MeV lithium ions at a flux of 5 TW/cm^2 produce temperatures approaching 100 eV. In 1993 a lithium ion beam from a radial ion diode was focused to ~1.4±0.4 TW/cm^2 and was used to heat a hohlraum to 58±4 eV on the PBFA-II accelerator. The key physics principles of an ion beam ICF target were demonstrated in these radial diode experiments including ion beam deposition, radiation conversion, tamping of the radiation case by an optically thin foam, and radiation smoothing [2].

The second step, or main HYF drive pulse, consists of 35 MeV lithium ions at a flux of just over 50 TW/cm^2, producing drive temperatures of approximately 250 eV. Generation, transport and focusing of lithium to HYF target intensities presents a formidable challenge to the ion beam project. A major limitation in achieving higher lithium beam intensities with the radial ion diode on PBFA II was the parasitic load that limited the lithium beam power to about 6 TW [3]. Research on PBFA II and the SABRE accelerators in 1994 and 1995 identified the parasitic load as contaminant ions that are desorbed from the anode and ionized during the accelerator pulse. In 1995, the lithium beam generation efficiency was increased by a factor-of-three on the SABRE extraction diode by anode cleaning that included RF discharges and inductive anode heating [5] as shown in Fig. 1.

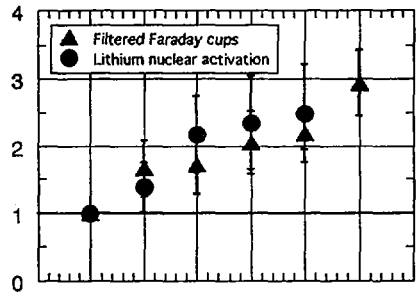

FIG. 1. SABRE relative lithium production versus increasing heating and cleaning level results.

2.1. PBFA-X

In 1996 Sandia's target physics research program moved to laser and z-pinch drivers and the world's most powerful accelerator (PBFA II) was modified to generate ion beams in a geometry and at a power level that will allow the remaining key physics issues of light ion driven ICF to be resolved. This modification has resulted in the production of the highest power ion beam (4 TW lithium) to be accelerated from an extraction ion diode. A new modeling capability for generating uniform ion current density was developed and successfully tested on PBFA-X. We evaluated the application of SABRE cleaning techniques to ion diodes at PBFA power levels and demonstrated a dramatic increase in ion diode impedance using a LiF passive ion source. We achieved 15 MV and 0.3 MA lithium ion diode operation. Finally, we performed preliminary experiments using an active laser-produced ion source and achieved a 10 ns earlier production of ion current at a 25% higher ion power compared to a LiF ion source, yielding the 4 TW of lithium beam power. FY97 and FY98 ion beam experiments to explore the key research issues in ion beam generation, focusing, and transport physics will be primarily performed on the SABRE accelerator as well as the COBRA accelerator at Cornell University and the GAMBLE-II accelerator at the Naval Research Laboratory (NRL). Related experiments will be conducted in Germany, Japan, and Russia.

2.2. Key issues

The key ion beam issues to be resolved fall into two main areas: beam intensity and standoff. The ion beam intensity is determined by the total ion beam power and the ion beam divergence (FWHM of focus). Our 3-D electromagnetic particle-in-cell simulations of ion diodes suggest that the electromagnetic contribution to the ion beam divergence can be controlled by controlling the electron sheath through high magnetic fields or by physical limiters that keep electrons away from the anode[4]. Electron control is also important because cross field diffusion allows electrons to reach the anode which reduces power efficiency. The electron loss also heats the anode leading to thermal and stimulated desorption of monolayer surface

contaminants that become ionized and generate a parasitic loss current of ions. RF discharge cleaning of the electrode surfaces can help suppress this parasitic current; the efficiency of lithium production has increased three-fold on the SABRE accelerator using these techniques[5] as shown previously in Fig. 1. Recent experiments on PBFA-X have shown a large increase in diode impedance using RF cleaning. Limiting the electron flux to the anode also reduces the parasitic current problem by limiting the anode temperature rise. However, limiting the electron flux to the anode means that a passive ion source, such as the thin film LiF lithium ion source, cannot be used. Spectroscopic measurements of the electric field in the diode indicate that LiF requires an 8 MV/cm field to emit lithium and that the source divergence is ~17 mrad [6]. An active ion source where an independent energy source is used to prepare an anode plasma is required to allow both control of the electron distribution and reduce the source divergence to an acceptable level. Two-stage acceleration is attractive because acceleration at roughly constant emittance in the second stage reduces the total beam divergence and also increases the total efficiency of the diode-to-beam power coupling. In our conceptual designs, the power, voltage, impedance and divergence requirements placed on the HYF ion diode require the use of a two-stage ion diode.

Standoff is required for high yield applications to protect the ion diode from the target blast. The baseline transport mode of our previous HYF study was an achromatic lens system that required an ion beam divergence of 6-8 mrad. Self-pinched ion beam transport is an attractive mode for all high yield and fusion energy applications and could relax the ion beam divergence requirements on the ion diode. The primary physics issue is whether gas breakdown will produce sufficient net currents to allow self-pinched experiments. A more complete description is found in a companion paper [7].

Success in establishing scaling laws and controlling solutions for these key issues on the SABRE, COBRA, and GAMBLE accelerators could lead to future high- power ion diode experiments on HERMES-III and eventually to an HYF module initiative.

2.3. Additional applications of ion beam technology

Near term applications of light ion beam technology are being developed in addition to the long term use of high intensity ion beams for high yield ICF. Low-power, large-area, repetitive ion beams are being generated by magnetically insulated ion diodes for use in advanced materials modifications including increased surface hardness, decreased surface roughness, and increased corrosion resistance [8]. Light ion beams are also being used at the Research Center in Karlsruhe, Germany, to perform shock-wave physics experiments that can provide information on equation of state, the dynamics of beam interaction with condensed targets, and the properties of solids and plasmas at high-energy densities [9].

3. FAST MAGNETIC IMPLOSIONS

We are also evaluating fast magnetically-driven implosions (z-pinches) as platforms for ICF capsule ablator physics, EOS, opacity, and capsule implosion experiments.

3.1. X-ray production with z-pinches

Z-pinch implosions are efficient sources of x-rays. On the 20 TW Saturn accelerator, for example, greater than 10% (> 400 kJ) of the electrical energy stored within the capacitor banks can be converted into x-rays [10]. Maintaining cylindrical symmetry, i.e. perfect axial and azimuthal uniformity, in the initial load design is an important element in controlling the power generated by these sources . The additional requirement of low mass, typically less than 500 μg/cm for fast drivers such as Saturn, makes fabricating the ideal cylinder challenging. The high symmetry, low-mass tradeoff has led historically to the choice of gas puffs, low-density foams, or thin foils over cylindrical arrays of thin wires. Recent data [11] from aluminum wire array implosions on Saturn, where the gap between adjacent wires within the array was varied from 6 mm down to 0.4 mm, show a dramatic increase in x-ray power output below a circumferential gap spacing of 1.4 mm (Fig. 2). From 2D calculations of these implosions, this sharp increase in power corresponds to the transition where the imploding plasma behaves as a plasma sheath instead of an ensemble of individual imploding wires. We have applied this same concept to

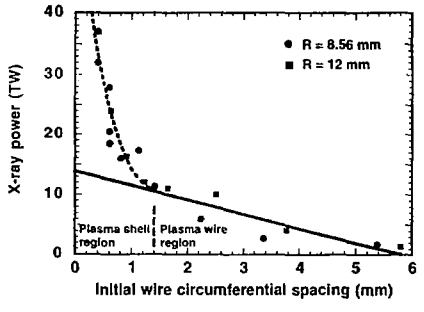

FIG. 2. X-ray power versus wire spacing.

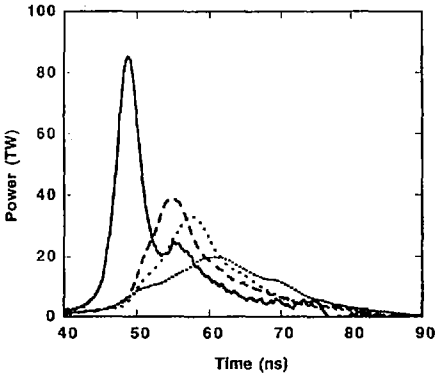

FIG. 3. X-ray power versus wire number.

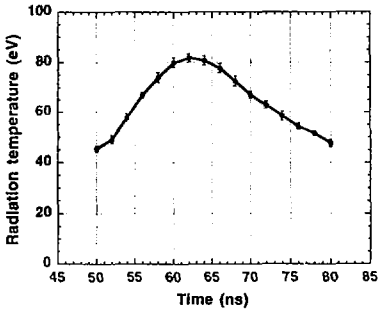

FIG. 4. Hohlraum temperature.

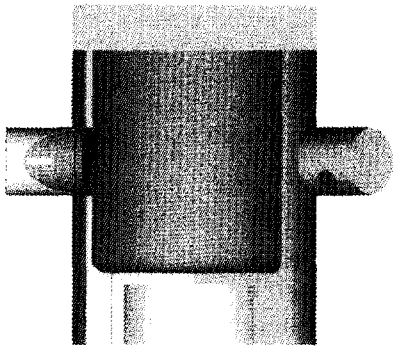

FIG. 5. Main and side hohlraums.

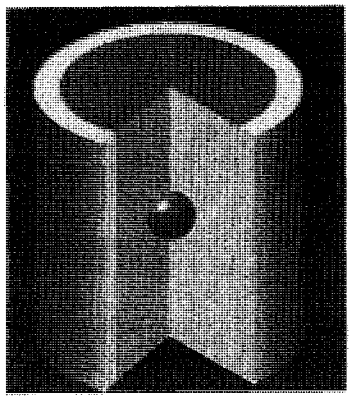

FIG. 6. Imploding hohlraum concept.

increase the power output from the z-pinch implosion of wire arrays containing high-Z elements. In Fig. 3 we show representative time-dependent x-ray power output from arrays of tungsten wires[12]. The 24, 40, and 70-wire arrays at an initial diameter of 12.5 mm result in peak x-ray powers of 20, 27, and 40 TW, respectively. Increasing the wire number to 120 at an initial diameter of 17.5 mm resulted in a peak x-ray power of ~80 TW, which represents a power gain of approximately four over Saturn's electrical power.

3.2. Z-pinch heated hohlraums

To both increase the x-ray intensity and improve the x-ray spatial uniformity, we have enclosed these wire array z-pinch x-ray sources within a large, 2-cm diameter, 2-cm long cylindrical hohlraum. If we assume that 80% of the x-rays that are incident on the high-Z inner walls of this hohlraum are re-radiated back into the hohlraum volume, then a simple power balance predicts that the x-ray intensity inside this container will be a factor of five larger than the power generated by the z-pinch source itself. Measurements of the time-dependent hohlraum temperature produced by containing the x-rays produced by imploding a 40-wire tungsten array within this hohlraum are shown in Fig. 4. Although the re-radiation of the z-pinch x-rays from the high-Z walls of the hohlraum effectively produces a Planckian radiation source, any ICF capsule-relevant physics package that is attached to the side of this hohlraum will also directly view the non-Planckian z-pinch source. To eliminate this direct line of sight to the z-pinch source, we have added two smaller cylindrical hohlraums (~ 6 mm in diameter by 10 mm in length) to the side of the z-pinch hohlraum. This geometry, as illustrated in Fig. 5, provides a spatially uniform, nearly-Planckian radiation source for capsule ablator physics and EOS experiments and allows for simultaneous measurements in multiple hohlraums. In 3-mm-diameter samples attached to these smaller hohlraums, we have generated 1 Mbar shocks in aluminum that show spatial uniformity of ~ 1 eV/mm over the extent of the sample.

3.3. Z-pinch driven capsule implosions

A concept for efficiently using the energy of a z-pinch implosion to indirectly drive an ICF capsule is shown in Fig. 6, which illustrates this imploding hohlraum concept at the time when an imploding plasma shell is beginning to stagnate upon a cylinder of low density foam that contains an ICF capsule. The shock waves produced when this stagnation occurs heat the plasma and create radiation fronts that propagate both into the foam and outward through the imploding plasma shell. In a high-Z material, the radiation front is subsonic and the imploding plasma shell can contain the radiation produced by the stagnation. In a low-Z, low density foam, however, the radiation front is supersonic and quickly bathes the ICF capsule in a uniform radiation environment. In one-dimensional calculations, the time differential between the arrival of the radiation front and the shock front at the cylindrical axis of symmetry can exceed 10 ns. In addition, our two-dimensional calculations show that the ablation of the capsule itself isolates the imploding capsule ablation front from the imploding z-pinch plasma. This isolation allows the spherical ICF capsule to reach its peak compression with minimal asymmetric effects from the cylindrical symmetry

of the imploding plasma shell. Key physics issues in this imploding hohlraum concept include the Rayleigh-Taylor instabilities in the imploding plasma, capsule preheat mechanisms, and the time-dependent radiation drive symmetry at the capsule ablation surface. In initial experiments on Saturn, we have tested this concept by imploding arrays of tungsten wires onto low density (3-6 mg/cm^3) aerogel foams. Comparisons of the end-on to side-on x-ray output are consistent with our calculations and indicate the potential to both contain the radiation within the high-Z imploding plasma and produce a time-dependent radiation drive within the foam.

3.4. PBFA-Z

The modifications that will enable PBFA II to drive imploding plasma loads [13] will be completed and tested in 1996. In this configuration, PBFA II can deliver up to 18 MA of current to a wire array load with a rise time of ~100 ns. With tungsten wire arrays, our calculations predict that PBFA will produce up to four times the energy (>1.5 MJ) and twice the power (>150 TW) of similar wire array configurations on Saturn. At these energy and power levels, the temperatures within the vacuum hohlraums should exceed 125 eV. Experiments to verify these predictions will begin this fall.

4. CONCLUSIONS AND FUTURE PLANS

Experiments on pulsed power accelerators have demonstrated that x-rays can be generated with high efficiency using fast z-pinches and intense light ion beams can be focused and interact with matter to produce x-rays in a favorable way. Over the next few years, the scaling of these z-pinch results to higher x-ray energy and power will be attempted on PBFA-Z. If favorable results are obtained, the way will be clear to even higher energies and powers on follow-on accelerators. The key issues limiting the intensities of focused light ion beams will also be addressed. Favorable results in this area will allow consideration of a high yield facility based upon light ion beam driver technology.

REFERENCES

[1] J.P. QUINTENZ, et al., Light Ion Driven Inertial Confinement Fusion, Progress in Nuclear Energy, **30** 2 (1996) 183-242.

[2] M.S. DERZON, et al., Li beam-heated hohlraum experiments at Particle Beam Fusion Accelerator II, Phys. Rev. Lett., **76** 3 (1996) 435-438.

[3] T.A. MEHLHORN, et al., Progress in lithium beam power, divergence, and intensity at Sandia National Laboratories, Proc. 10th Inter. Conf. on High Power Particle Beams, NTISPB95-144317 (1994) 53-56.

[4] J.P. QUINTENZ, et al., Theory of instability-generated divergence of intense ion beams from applied-B ion diodes, Proc. IEEE, **80** 6 (1992) 971-984.

[5] M.E. CUNEO, et al., Cleaning techniques for applied-B ion diodes, to be published, Proc. 10th Inter. IEEE Pulsed Power Conf., July 10-13, 1995, Albuquerque, NM.

[6] J.E. BAILEY, et al., Measurements of acceleration gap dynamics in a 20 TW applied-magnetic-field ion diode, Phys Rev Lett. **74** 10 (1995) 1771-1774.

[7] C.L. OLSON, et al., IAEA-F1-CN-64/BP-14, this meeting.
[8] R.W. STINNETT, et al., Thermal surface treatment using intense, pulsed ion beams, Mat Res. Soc. Symp Proc **316** (1994) 521-531.
[9] K. BAUMUNG, et al., Shock-wave physics experiments with high-power proton beams, Laser and Particle Beams **14** 2 (1996) 181-209.
[10] R. B. SPIELMAN, et al., AIP Conference Proceedings 195, Second International Conference on Dense Z-Pinches, Laguna Beach, CA, (1989) 3-16.
[11] T. W. L. SANFORD, et al., "Improved Azimuthal Symmetry Greatly Increases X-ray Power form Wire-Array Z-pinches", submitted to Phys. Rev. Lett.
[12] C. DEENEY, et al.,"The Roles of Wire Number, Implosion Velocity, Non-kinetic Heating and Implosion Time on the Production of Planckian X-rays from Tungsten Wire Arrays", Proc. 23rd IEEE International Conference on Plasma Science, June 3-5, 1996; Boston, Massachusetts; C. DEENEY, et al., "Power Enhancement by Increasing Initial Array Radius and Wire Number of Tungsten Z pinches", submitted to Phys. Rev. E.
[13] R. B. SPIELMAN, et al., "PBFA-Z: A 20-MA Z-pinch Driver for Plasma Radiation Sources", 11th International Conference on High-Power Particle Beams, ed. P. Sunda, K. Jugwrith & J. Ullschmied, Prague, June (1996), Paper O-43.

DISCUSSION

J.D. LINDL: What limits the maximum number of wires in the z pinch wire arrays?

J.P. QUINTENZ: On Saturn we have fielded over 150 wire arrays. The limitation is on the strength of the wires themselves and on how precisely they can be positioned while maintaining the 500 μg total array mass. This becomes less of a problem on PBFA, where the optimum assay mass is higher.

INERTIAL CONFINEMENT

(Poster Session BP)

EFFECTS OF PREHEAT AND IRRADIATION NON-UNIFORMITIES ON RADIATIVELY DRIVEN SHOCK WAVES

T. LÖWER, M. BASKO[1], K. EIDMANN,
J. MEYER-TER-VEHN, R. SIGEL[2],
G. TSAKIRIS, K. WITTE
Max-Planck-Institut für Quantenoptik,
Garching, Germany

Abstract

EFFECTS OF PREHEAT AND IRRADIATION NON-UNIFORMITIES ON RADIATIVELY DRIVEN SHOCK WAVES.

Three different hohlraums, two for single beam and one for multiple beam irradiation, are investigated as to their suitability for shock wave and equation of state experiments. Important in this respect is how strongly the sample material is preheated before the shock arrival and how uniformly the sample is irradiated. Spherical hohlraums turned out to be unsatisfactory. A good performance is achieved with a D-shaped hohlraum for multiple beam irradiation and even a better one with a recently developed cavity for single beam irradiation using an internal converter.

1. Introduction

During the last few years it was demonstrated that powerful laser pulses can generate strong shock waves in condensed matter either by direct [1, 2] or indirect [3-6] drive with pressures not accessible by conventional means. In the first case the sample is directly irradiated with laser light whereas in the second case soft X ray radiation created in a millimetre sized gold cavity heated by the laser pulse is used as the driver. This paper deals with the indirect drive scheme. The cavity temperature and the equation of state of matter are subjects to be studied by the use of shock waves; both applications are highly relevant to ICF.

2. Spherical Cavity

A natural choice for the hohlraum is a sphere (see upper half of Fig.1) because of its unique property that a wall element irradiated by a laser pulse or some other source and acting like a Lambertian radiator heats the whole wall of the sphere homogeneously. In the case of a laser pulse with an intensity of a few times 10^{14} W/cm^2, the radiation emitted from the hot spot contains a considerable fraction of

---

[1] On leave from the Institute for Theoretical and Experimental Physics, Moscow, Russian Federation.

[2] Present address: Technische Hochschule Darmstadt, Institut für Angewandte Physik, Darmstadt, Germany.

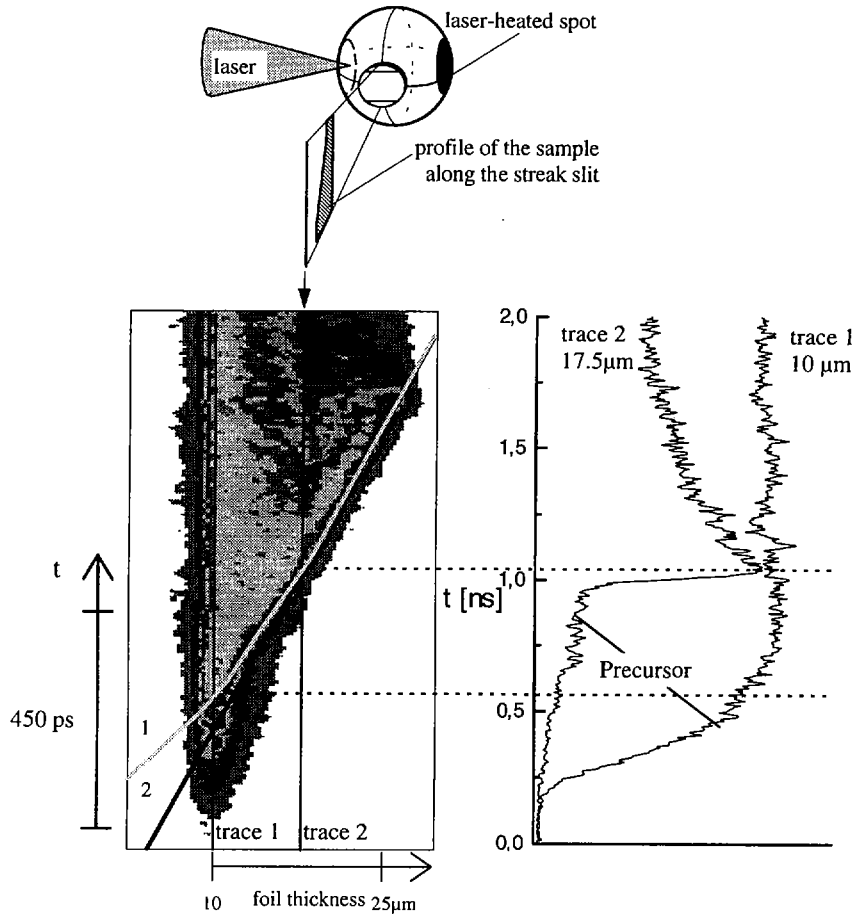

FIG. 1. Upper half: Spherical cavity for single-beam heating used with the iodine laser ASTERIX delivering 0.45 ns pulses with energies of up to 300 J at the third harmonic with a wavelenngth of 438 nm.
Lower half: Shock trajectory of a wedged aluminium sample, i. e. luminosity signal emitted from the rear side of the sample and recorded with a streak camera in the wavelength range from 400 to 700 nm. Line 1 shows the trajectory in the preheated material. The straight line 2 refers to cold material and is extrapolated into the thin sample region. Because of material expansion, the shock arrives later in the pre-heated material. The signals shown on the right are cuts through the trajectory at the indicated positions.

hard keV X rays. The portion hitting the sample foil under a relatively steep angle of incidence of 45°, or less, can penetrate and thus preheat it, causing its pre-expansion before the arrival of the shock front. That this indeed happens can be inferred from the shock trajectory of a wedged low Z aluminium sample foil shown in the left hand lower half of Fig.1. Where the sample is thin the trajectory (line 1) is curved. This curvature can only result from a pre-expansion of the sample material due to preheat. This interpretation is further supported by the time behaviour of the breakout signal shown in the right lower half of Fig.1. In the thin sample region the signal does not increase sharply, but rather slowly, indicating a softening of the unshocked material due to temperature elevation. This latter effect and the expansion have the disadvantageous consequence that the state of the matter behind the shock wave, i. e. pressure, density, and temperature, cannot be determined accurately.

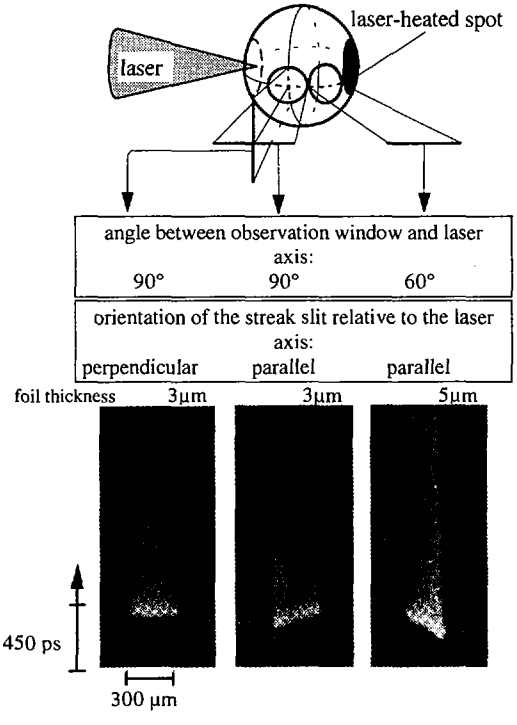

FIG. 2. Streak camera records of the shock breakout in gold samples taken with the spherical cavity heated by third harmonic ASTERIX pulses. The emission of the shock sample has been observed at different positions relative to the laser axis and under different orientations of the streak camera slit. The variation of the shock arrival time along the slit indicates gradients of the heating X ray radiation across the sample.

In principle, this problem can be alleviated by making the foil thicker. However, when stationary shocks are aimed at, the foil thickness, d, is limited by the duration of the laser pulse, t_p, according to the approximate relation $d \leq 2Dt_p$ where D is the velocity of the shock front [7]. The physical background of this formula is the occurrence of a rarefaction wave originating at the front side of the sample when the driving laser pulse has just passed its maximum intensity. Since this wave travels through compressed hot matter at sonic speed it is faster than the shock front. When the sample is too thick both waves can interact with each other whereby the shock front is weakened and becomes unsteady. For our ASTERIX laser pulses with t_p = 450 ps, the foil thickness should not exceed a value of 25 μm in aluminium. Hence, because of the limited foil thickness, there is always some level of unavoidable preheat. In metal foils we could detect its strength down to temperatures of 0.3 eV in the unshocked material by measuring the intensity level of the precursor.
There is an additional effect that is due to the expansion of the hot plasma cloud created by the laser pulse. When this cloud moves through the cavity towards the laser its radiation is no longer homogeneously deposited on the cavity wall and on the sample as is the case when the radiation comes from a spherical surface element. Thus, the assumption of an Ulbricht sphere has to be abandoned. Consequently, the sample is irradiated by a non-uniform radiation field. Hence gradients in the heat flux into the sample and also in the ablation rate are introduced, resulting in different shock arrival times at the rear side of the sample. This conclusion is proven by the streak camera records of Fig.2, which reveal a variation of the shock breakout time across a gold sample located at two different angles, 60° and 90°, with respect to the laser axis. At 60° the shock arrives earlier on that side of the sample which is closest to the laser spot. At 90° the situation is reversed: the shock arrives earlier on the side closest to the laser entrance hole. For reasons of symmetry, the X ray intensity should be constant on parallels of latitude with respect to the laser axis. If the streak slit is then oriented perpendicularly to the laser axis the shock front should be found to arrive simultaneously across the sample. This is indeed observed as proven by the left hand streak in Fig.2. However, for reasons of clean experimental conditions which are indispensable for EOS measurements a situation is preferable where gradient effects and also the preheat phenomena as described above are absent. This has stimulated us to develop hohlraum configurations other than the sphere.

3. D-Shaped Cavity and Labyrinth Cavity

A major improvement was achieved with the cavities shown in the upper half of Fig.3. The D-shaped, rotationally symmetric hohlraum is suited for multiple beam exposure whereas the other one which we termed 'Labyrinth' cavity [4] is again for single-beam irradiation. In both cases preheat due to primary X rays is practically avoided and the sample is uniformly irradiated as will be detailed below.
In the D-shaped cavity the primary hard X rays hit the sample under grazing incidence so that the absorbed rays encounter a path long enough to get completely absorbed in the front sample region. This argument is evidenced by two experimental findings. First, the precursor of the shock signal stays at a noise level indicating a preheat temperature of at most 0.3 eV. Second, the shape of the needle-like shock si-

gnals does not change with the foil thickness (see traces in the lower right half of Fig.3). This proves that the density jump across the free surface at the rear side of the sample is steplike and not ramplike, because of preheating. In order to obtain some quantitative information on how the sample temperature scales with the preheat level (primary and secondary X rays) we calculated the temperature distribution inside the sample. For the primary X rays we took an experimentally recorded spectrum [4] and for the secondary X rays a Planck spectrum. The opacities used are those of the cold material. For a 10 μm thick aluminium sample we find a temperature of 0.1 eV at the rear side. Samples which are thicker than 10 μm and hence meet the requirement for the occurrence of a stationary shock wave should therefore practically be free of any

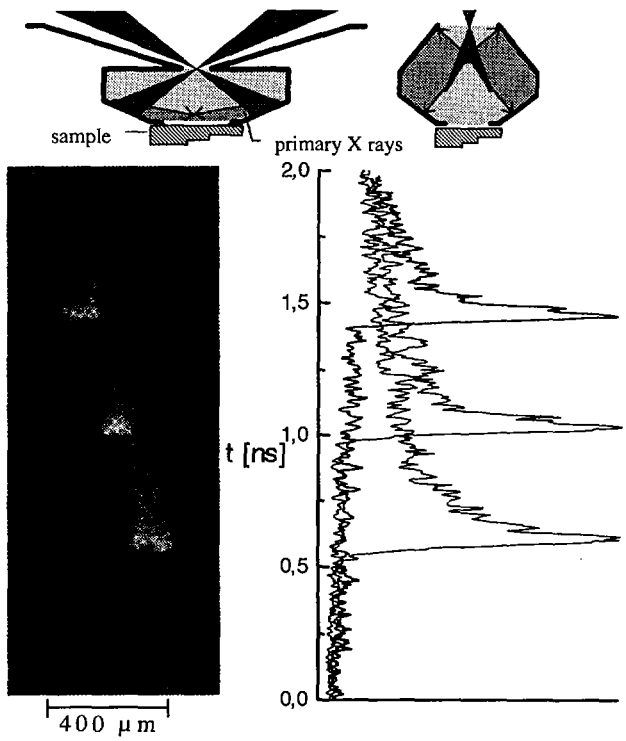

FIG. 3. Upper half: Two different laser heated gold cavities. On the left hand side there is a D-shaped, rotationally symmetric cavity for multiple-beam heating used with the GEKKO XII laser located at OSAKA university (4 beams/2.2 kJ in total/0.8 ns/0.35 μm). Right is the new Labyrinth cavity for single-beam heating used with ASTERIX under the same operating conditions as those given in Fig. 1.
Lower left half: Shock breakout signal from the rear side of a double-step aluminium sample recorded with a streak camera in the wavelength range from 400 to 700 nm. The streak shown holds for the D-shaped cavity. For the Labyrinth hohlraum a streak with the same characteristics was obtained.
Lower right half: Traces through the three breakout signals.

preheat which is in agreement with the experimental observations. Uniform sample irradiation is obtained with four laser beams as employed in the GEKKO XII experiments with 550 J/0.8 ns/0.35 μm pulses per beam and is verified by the fact that for a planar sample the shock arrival time along the camera slit stays constant as shown in Fig.3 for aluminium and in Ref. [5] for gold.

The prominent feature of the Labyrinth hohlraum is its converter shielding the sample located on the common symmetry axis of the laser beam and the cavity from the primary X rays emitted from the 'converter plasma'. Its expansion is so slow that within the shock transit time it cannot directly irradiate the sample. From these considerations, the sample should be free of any preheat. This conclusion is confirmed by the same experimental findings as those noted above for the D shaped cavity.

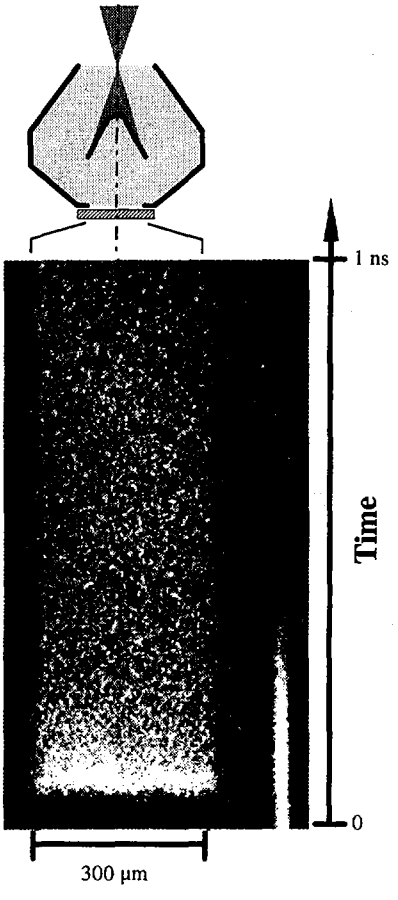

FIG. 4. Streak camera record of the shock induced light emission from a planar gold sample of 3 μm thickness. The signal at the right is the time fiducial generated by the laser pulse.

Moreover, by analysing the shock signals from silicon foils whose absorption coefficient for hard X rays is about the same as that for aluminium, we could prove that the preheat level is below 0.01 eV. The higher sensitivity of silicon foils results from the transparency properties of silicon in the visible. The corresponding absorption coefficient already responds to temperature changes as small as 0.01 eV. Uniform sample irradiation is again evident from the straightness of the arriving shock front along the camera slit for a planar sample (Fig.4). We further investigated the uniformity issue by a theoretical analysis based on a two-dimensional hydro-code [8] and an analytical 'view factor' model [9, 10]. We find that the temperature of the soft X rays across the sample surface is uniform within 1% during the entire laser pulse duration. This is an additional confirmation of the conclusion drawn from the experimental observations that the labyrinth hohlraum is an ideal tool for shock wave and EOS experiments with a single laser beam.

REFERENCES

[1] TRAINOR, R., et al., Phys. Rev. Lett. **42** (1979) 1154.
[2] KOENIG, M., et al., Phys. Rev. Lett. **74** (1995) 2260.
[3] CAUBLE, R., et al., Phys. Rev. Lett. **70** (1993) 2102.
[4] KAUFMANN, R., et al., Phys. Rev. Lett. **73** (1994) 2320.
[5] LÖWER, Th., et al., Phys. Rev. Lett. **72** (1994) 3186.
[6] LÖWER, Th., SIGEL, R., "Uniform shock waves driven by thermal radiation from laser-heated cavities", Shock Compression of Condensed Matter (Proc. APS Conf. Seattle, 1995), American Inst. Phys. Conf. **370** (1995) 1261.
[7] ANISIMOV, S., et al., Sov. Phys. - Usp. **27** (1984) 181.
[8] MEYER-TER-VEHN, J., RAMIREZ, J., RAMIS, R., in Heavy Ion Fusion (Proc. Int. Symp. Princeton, New Jersey, USA, 1995), to appear as a special issue of Fusion Eng. Des.
[9] TSAKIRIS, G., Phys. Fluids B **4** (1992) 992.
[10] BASKO, M., Phys. Plasmas **3** (1996) 520.

INERTIAL FUSION TARGET STUDIES: HEAVY-ION TARGET DESIGN AND FAST IGNITOR PHYSICS

S. ATZENI, M.L. CIAMPI[1], A.R. PIRIZ, M. TEMPORAL[2]
Associazione Euratom-ENEA sulla Fusione,
Centro Ricerche Frascati,
Frascati, Rome,
Italy

J. MEYER-TER-VEHN, M. BASKO[3], A. PUKHOV, A. RICKERT
Max-Planck-Institut für Quantenoptik,
Garching, Germany

J. MARUHN, K.H. KANG, K.-J. LUTZ
Institut für Theoretische Physik,
Universität Frankfurt,
Frankfurt, Germany

R. RAMIS, J. RAMIREZ, J. SANZ, L.F. IBAÑEZ
E.T.S.I. Aeronáuticos,
Universidad Politécnica,
Madrid, Spain

Abstract

INERTIAL FUSION TARGET STUDIES: HEAVY-ION TARGET DESIGN AND FAST IGNITOR PHYSICS.

Theoretical and computational studies on ICF targets, conducted co-operatively by researchers from different European institutions (ENEA-Frascati, MPQ-Garching, University of Frankfurt and UPM-Madrid) are reviewed: (1) Targets for heavy-ion fusion are studied by 1-D and 2-D radiation-hydrodynamics simulations and by view factor codes; a new configuration is proposed aiming at achieving ignition with 2-3 MJ of heavy ion energy. (2) Some aspects of the physics of fast ignitor targets are addressed, including beam requirements for D-T ignition, deuterium burning and ultra-intense laser beam channeling in plasma. (3) Results on ablative Rayleigh-Taylor instability are reported.

---

[1] ENEA-SIF fellow.

[2] ENEA-SIF fellow; INFN, Laboratori Nazionali di Legnaro.

[3] On leave from ITEP, Moscow, Russian Federation.

1. INTRODUCTION

Motivated by a recent initiative for heavy-ion fusion [1] and by the recommendations of the European Science and Technology Assembly Working Party on ICF [2], researchers from different European laboratories are conducting cooperative research in the areas of ICF target design and basic ICF physics.

A central goal is to develop numerical tools and to study new target configurations for inertial fusion [3]. Two-dimensional (2-D) hydrodynamics codes are developed for simulating radiation hydrodynamics of hohlraum targets (MULTI-2D, UPM-Madrid and MPQ-Garching [4]) and for the study of Rayleigh-Taylor Instability (RTI) with high resolution [3] as well as non-spherical burn configurations (DUED, ENEA-Frascati). A 3-D particle-in-cell (PIC) code is developed at MPQ to investigate fast ignition with laser pulses at relativistic intensities. Here we present, in Sec. 2, studies on hohlraum targets, including MULTI-2D simulations of a new target design for heavy-ion beam fusion, and results from 1-D capsule simulations, in Sec. 3, (a) conditions obtained with DUED for igniting precompressed fuel by external beams, and (b) results on self-channeling of laser pulses in near-critical plasma at 10^{19} W/cm^2. Analytic results on ablative RTI are also reported in Sec. 4.

2. HEAVY-ION HOHLRAUM TARGETS

Heavy-ion beam drivers are attractive for ICF because of high driver efficiency and the potential for high repetition rate. They require indirect-drive (hohlraum targets) to implode the fusion capsule with sufficient spherical symmetry and limited RTI growth. Ignition of a capsule with 1 mm radius and 0.2 mg of DT fuel requires about 150 kJ of radiation energy, absorbed with the appropriate time shape [5].

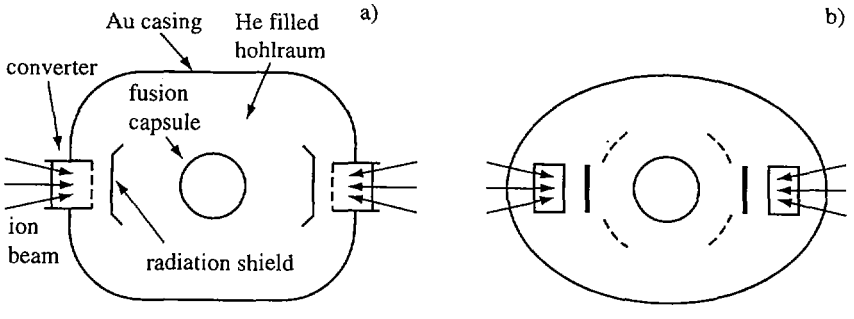

FIG. 1. Cylindrically symmetric, two-side illuminated hohlraum targets for heavy-ion fusion: (a) target proposed by the LLNL group [6], whose symmetry issues have also been studied by the ENEA group [7]; (b) target proposed by the Frankfurt group [8].

Two target designs for two-sided illumination are shown in Fig. 1; radiation shields are placed in the hohlraum between converters and capsule to reduce the $l = 2$ and $l = 4$ asymmetry of capsule illumination. Though targets of this type may satisfy the symmetry requirements [6–8], our recent viewfactor and MULTI-2D studies indicate that their beam to capsule coupling efficiency is inherently low. Ignition with pulse energy below 3 MJ, as postulated for the European Study Group "Heavy Ion Ignition Facility" [1], seems therefore not feasible within this design.

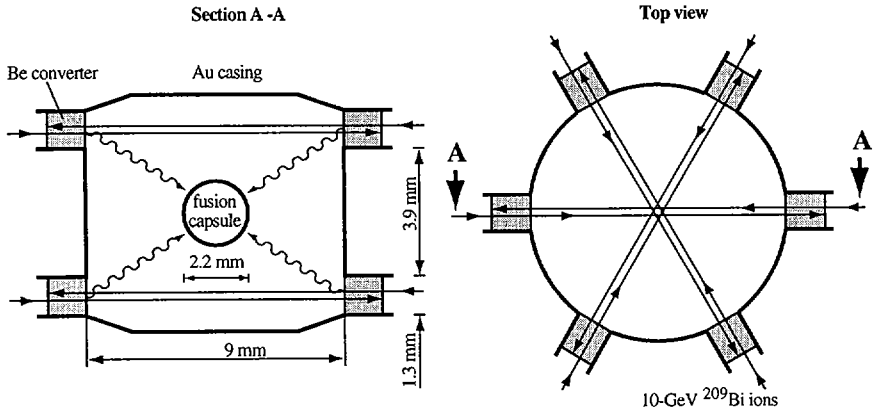

FIG. 2. Hohlraum target, proposed by the ITEP group [9], with 12 converters, irradiated by six pairs of anti-parallel beams of 10 GeV Bi ions. The dimensions refer to a target driven by 2.5 MJ beam energy and enclosing a fusion capsule absorbing 140 kJ of radiation energy (with appropriate pulse shape).

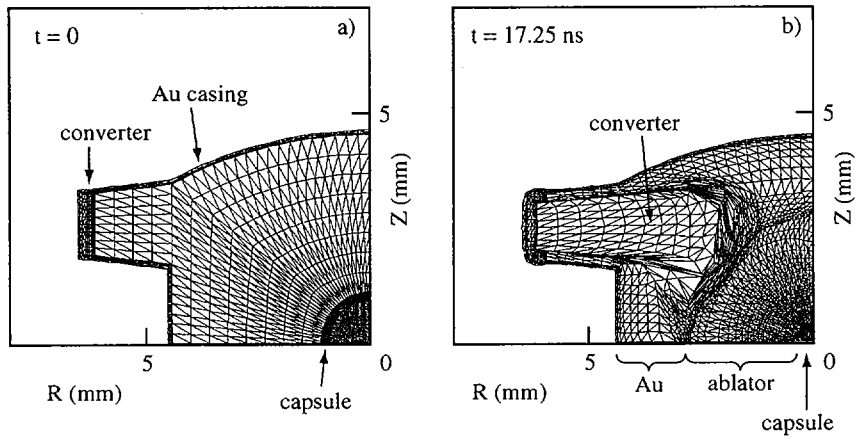

FIG. 3. MULTI-2D simulation of ITEP target. A cylindrical equivalent (vertical symmetry axis) of the configuration in Fig. 2 is simulated: (a) initial Lagrangian mesh; (b) distorted mesh at the end of the heavy-ion beam pulse with imploded capsule at the centre.

Here, we report a new design which may achieve ignition with 2–3 MJ pulses, and is shown in Fig. 2. It was first developed at ITEP-Moscow [9] and consists of 12 thin converters heated by six pairs of of anti-parallel beams and has no radiation shields. 2-D equivalents of this target, replacing the 12 converters by two horizontal converter rings, have now been analyzed. Static viewfactor calculations by Basko give 13% radiation/capsule coupling, negligible $l = 2$ non-uniformity and $l = 4$ time-integrated non-uniformity $P_4 = 0.009$. First MULTI-2D simulations are displayed in Fig. 3. It is found that 140 kJ of radiation energy are transferred to the capsule when the target is irradiated by about 2.5 MJ of 10 GeV Bismuth ions. No major problem concerning the interaction between the converter material, the cavity walls and the capsule ablator is observed; the viewfactor results concerning $l = 2$ asymmetry are confirmed. Presently, due to numerical difficulties, the computation can follow the capsule implosion down to radial convergence ratios of only 2–3. This does not allow to assess in full measure the effects of the supposedly most dangerous $l = 4$ asymmetry. Nevertheless, an implosion velocity of 3.5×10^7 cm/s is obtained, close to the value needed for fuel ignition in corresponding 1-D simulations.

1-D capsule studies. Capsule implosion, ignition and burn has been studied at ENEA [7] and ITEP [9] by one-dimensional capsule simulations. In agreement with Ref. 5, we find that ignition is achieved when the capsule absorbed energy exceeds $E_{cap}(\mathrm{MJ}) \approx 0.25\hat{m}^{0.7}\alpha^{0.5}$, where $\hat{m}$ is the fuel mass in mg, and $\alpha \geq 1$ is the isentrope parameter, measuring the deviation from ideal, cold compression. The corresponding implosion velocity is $v \approx 2.7 \times 10^7 \hat{m}^{-0.14}\alpha^{0.3}$ cm/s. Taking usual constraints on the shell in-flight-aspect-ratio [5], the typical duration of the highest power portion of the pulse is $t_p(ns) \approx 5\hat{m}^{0.6}$.

The minimum capsule size for ignition thus depends on the achievable implosion velocity (limited by drive temperature and stability constraints) and isentrope α (depending on the drive pulse shape). In the above hohlraum study we have taken a NIF-class capsule [5] (with $m = 0.21$ mg, radius = 1.1 mm, $E_{cap} = 140$ kJ), but it is worth stressing that this implies a low entropy compression, with $\alpha = 1.5$–2, and hence an accurate pulse shaping.

3. FAST-IGNITOR PHYSICS

In standard ICF target design, the requirement of central ignition sets the most stringent conditions on beam parameters (symmetry, pulse shape, etc.). Ignition by external beam interaction applied after implosion, as proposed in the fast ignitor scheme [10,11], would considerably relax these conditions. It may also offer an option to burn almost pure deuterium fuel.

Pulse requirements for DT ignition. A wide range of fuel densities can be of interest for fast ignition, ranging from $\rho = 100$–300 g/cm^3 for high-gain D-T burning [10,11], to much higher values for deuterium burning.

The pulse parameters (energy E_p, power P, and flux Φ) for fast ignition can be roughly estimated by using the ignition conditions for an isochoric spherical

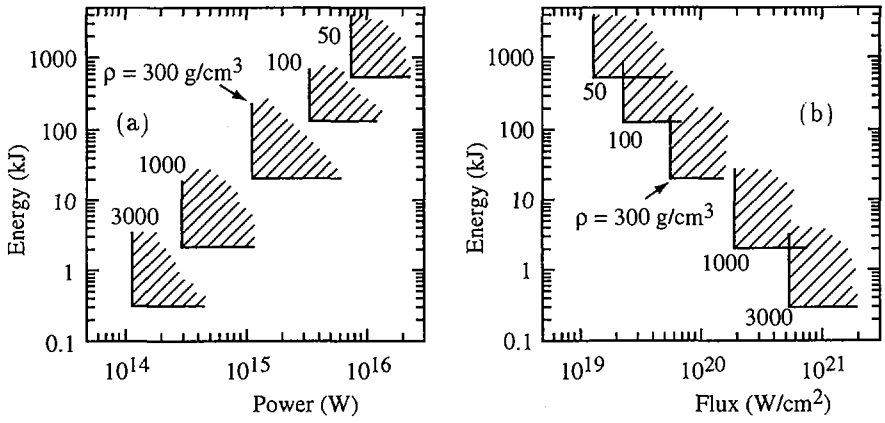

FIG. 4. Pulse requirements for fast ignition. Ignition regions for different values of the compressed fuel density ρ in (a) the power-energy plane and (b) in the flux-energy plane. Fits to the minimum values as a function of the density are given by Eqs (1)-(3).

D-T assembly [12] ($\rho_0 r_0 = 0.5$ g/cm^2; $T_0 = 12$ keV, where r_0, ρ_0 and T_0 are, respectively the radius, density and temperature of the hot region) and taking the spark mass as $m_0 \approx (4\pi/3)\rho_0 r_0^3$, the pulse duration $t \approx E_p/P$, as $t \approx r_0/c_s$, (c_s: sound speed) and the beam radius equal to the spark radius. One thus gets $t \approx 40/\hat{\rho}$ ps, and energy $E_p \geq 72/\hat{\rho}^2$ kJ, where $\hat{\rho} = \rho/(100\ \mathrm{g/cm^3})$. For a better evaluation, two of us (S.A. and M.L.C.) have performed 2-D DUED numerical simulations, in which a hot spot is created close to the surface of a DT sphere precompressed at high density ρ. The ignition regions in the relevant beam parameter space are shown in Fig. 4.

For $50 \leq \rho \leq 3000$ g/cm^3 the minimum beam parameters for ignition turn out to be fitted, to within 12%, by

$$E_p = 140\ \hat{\rho}^{-1.85}\ \mathrm{kJ}\,, \tag{1}$$

$$P = 2.9 \times 10^{15}\ \hat{\rho}^{-1}\ \mathrm{W}\,, \tag{2}$$

$$\Phi = 2.4 \times 10^{19}\ \hat{\rho}^{0.90}\ \mathrm{W/cm^2} \tag{3}$$

Equation (1) is similar to the scaling published by Caruso and Pais [11], and extends it to a much wider density range. Notice that E_p is a factor six larger at $\rho = 300$ g/cm^3 than estimated in earlier publications [10], a factor of three being due to the isochoric rather than isobaric initial conditions, and a factor about two to 2-D effects.

Tritium-lean fast-ignitors. While direct ignition of pure-deuterium seems unfeasible, we are studying the burn of precompressed deuterium targets, with a DT seed, ignited by a pulse satisfying Eqs. (1)-(3). Preliminary 2-D DUED calculations have been performed, taking diffusion of all relevant charged fusion

products and knock-on deuterons into account, but with rough neutron treatment. They show that high temperature ($\approx$ 100 keV) deuterium burning is achieved in 10–20 mg targets with total tritium fraction about 5% and density $\rho \approx 1000$ g/cm^3. Better neutron modeling is required to study ignition and burn of targets with 1–2% tritium content, and to assess the feasibility of a fuel cycle without external tritium breeding. Work is now in progress to introduce a neutron transport scheme in DUED.

Ultra-intense laser beam channeling. Chirped-Pulse-Amplification (CPA) lasers now under development, may provide an option to achieve the intensities, given by Eq. (3), required for fast ignition [10]. This option relies on (1) hole-boring into strongly overdense (up to 10^5 times) plasma surrounding the imploded core and (2) efficient production of a collimated beam of relativistic (1–10 MeV) electrons to heat the ignition spot. Both points involve relativistic laser-plasma interaction and are not well understood so far. First three-dimensional particle-in-cell (PIC) simulations have been performed at MPQ [13,14], which demonstrate the drive of relativistic electron current at incident laser intensities $I \geq 10^{19}$ W/cm^2, current filamentation by Weibel instability, generation of magnetic fields of 100 MegaGauss and higher, pinching of current and light filament, and formation of a single propagation channel. So far, results are limited to plasma densities close to critical. Channel formation into 10 times overcritical plasma was demonstrated [14].

4. RAYLEIGH-TAYLOR INSTABILITIES

A new analytical model has been developed [15] for the linear stage of the ablative Rayleigh-Taylor instability, which is valid in a wide range of the parameter $\Gamma = \chi_2 g/\rho_2 v_2^3$ (here χ is the conductivity, ρ is the density and v the fluid velocity, with the subscript 2 referring to the cold phase, and g is the acceleration). For $\Gamma < 1$ a sharp boundary model is considered, whose novel feature is the inclusion of the thermal conduction behind and across the front. This allows for obtaining a self-consistent dispersion relation in terms of a density jump r_D associated to the instability ($r_D = \rho_1/\rho_2$, where ρ_1 is the density behind the front, i.e. in the hot phase). This is an external parameter and relates to the well known problem of the missing information when a weak expansion is treated as a discontinuity [16]. We calculate r_D from a model for a diffusive corona and by assuming that only a region within a distance $1/2k$, where k is the wavenumber, from the front is affected by the instability [16]. Furthermore, the model is extended to $\Gamma \gg 1$ by assuming that (diffusive) lateral transport is the most relevant effect arising in this regime, and a simple formula is obtained for the instability growth rate γ, valid for $10^{-3} \leq \Gamma \leq 10^2$:

$$\gamma = \sqrt{gk\left(A - \frac{2\phi_0 - 1 + r_D}{1 + r_D}\frac{kv_2^2}{gr_D}\right) + \left(\frac{1+\phi_0}{1+r_D}kv_2\right)^2} - \frac{1+\phi_0}{1+r_D}kv_2 \qquad (4)$$

where $A = (1 - r_D)/(1 + r_D)$, $\phi_0 = 1 + kL_2$, and $L_2 = (3/5)(\chi_2/\rho_2 v_2)$. Equation (4) shows that although also convection and fire polishing contribute to the reduction of γ, full stabilization at high k is due to the dynamic pressure.

References

[1] HOFMANN, I., et al., in Plasma Physics and Controlled Nuclear Fusion Research (Proc. 15th Int. Conf. Seville, 1994), Vol. 2, IAEA, Vienna (1995) 709–714.

[2] Report on Inertial Confinement Options to Controlled Nuclear Fusion, rep. ESTA/96-202/final, Brussels (April 1996).

[3] ATZENI, S., et al., Target design activities for the European Study Group 'Heavy Ion Ignition Facility', Fusion Eng. Design, in press.

[4] MEYER-TER-VEHN, RAMIREZ, R., RAMIS, R., Integrated two-dimensional simulations of hohlraum targets, Fusion Eng. Design, in press, and refs therein.

[5] LINDL, J.D., Phys. Plasmas **2** (1995) 3933–4024.

[6] HO, D.D.-M., HARTE, J.A., TABAK, M., Nucl. Fusion **35** (1995) 1125–1132.

[7] ATZENI, S., TEMPORAL, M., Energetics and symmetry of hohlraum targets driven by ion beam pulses with simple time shape, Fusion Eng. Design, in press.

[8] KANG, K.A., MARUHN, J., Dynamic effect on the symmetrization in indirectly driven ICF hohlraum targets, preprint of the Inst. Theor. Physik, Univ. Frankfurt (1995), summarized in Ref. 3.

[9] BASKO, M.M., et al., ITEP conception of a heavy ion fusion facility, Fusion Eng. Design, in press.

[10] TABAK, M., et al., Phys. Plasmas **1** (1994) 1626–1634.

[11] CARUSO, A., PAIS, V.A., Nucl. Fusion **36** (1996) 745–757.

[12] ATZENI, S., Jpn. J. Appl. Phys. **34** (1995) 1980–1992.

[13] PUKHOV, A., MEYER-TER-VEHN, J., Phys. Rev. Lett. **76** (1996) 3975–3978.

[14] PUKHOV, A., MEYER-TER-VEHN, J., in High Energy Density in Matter Produced by Heavy Ion Beams, Annual Report 1994, report GSI-95-06, Darmstadt (1995), p. 42–43.

[15] PIRIZ, A.R., SANZ, J., IBAÑEZ, L.F., Rayleigh-Taylor instability of steady ablation fronts: the discontinuity model revisited, submitted to Phys. Plasmas (October 1996).

[16] SANZ, J., Phys. Rev. Lett. **73** (1994) 2700–2703; GONCHAROV, V. N., et al., Phys. Plasmas **3** (1996) 1402–1414.

DEVELOPMENT OF HIGH POWER KrF LASER FOR FUNDAMENTAL RESEARCH OF IFE DRIVER AND LASER-PLASMA INTERACTION

Naiyan WANG, Yusheng SHAN, Weiyi MA, Changzhi ZHOU,
Kun GUNG, Xiaojun WANG, Jiandong JIANG,
Dawei YANG, Xiuzhang TANG
China Institute of Atomic Energy

Ganchang WANG
China National Corporation of Nuclear Industry

Beijing, China
China

Abstract

DEVELOPMENT OF HIGH POWER KrF LASER FOR FUNDAMENTAL RESEARCH OF IFE DRIVER AND LASER-PLASMA INTERACTION.

A high power KrF laser system is under development at the China Institute of Atomic Energy. This system consists of a front end, two-stage KrF laser amplifiers and two-stage Raman amplifiers providing two KrF laser beams with a total energy of 100 J. In the first step, the laser pulse duration is 8 ns. A power density of 10^{14} W/cm^2 on target is expected for the fundamental research on laser-plasma interaction. Some important technologies such as e-beam two-side pumped KrF laser, KrF laser angular multiplexer and a method of measuring the main parameters of KrF laser amplifiers are discussed.

1. INTRODUCTION

KrF lasers have many advantages as fusion drivers: a short wavelength which couples well to the target, the capability of producing a 1–10 Hz repetition rate, the possibility to scale up to high powers and energies (1 MJ in 5 ns), high intrinsic efficiency ($\sim 10\%$) and a relatively low cost.

At the China Institute of Atomic Energy, we are at present constructing a KrF laser system with an output energy of 100 J, a pulse width of 8 ns and a power density of $> 10^{14}$ W/cm^2 on target, with a view to addressing laser-plasma interaction research and some of the related technologies of KrF laser fusion such as pulsed power technology, laser pulse compression, angular multiplexing of 8 ns beamlets and a Raman cleanup system. This system consists of two parts: the KrF laser amplification chain, which includes a front end, two e-beam pumped KrF laser amplifiers and the Raman amplification chain which includes one Raman oscillator and two Raman amplifiers [1].

The KrF laser pre-amplifier is driven by a 100 mJ, 8 ns KrF laser provided by an electro-optic switch fitted to a Lambda Physik LPX-150 laser. This beam is split into eight beams; one of them triggers the laser switches for timing synchronization between two KrF laser amplifiers, and the remaining seven beams are first amplified by a KrF laser pre-amplifier. The total output energy of the pre-amplifier is about 30 J. One of these output beams pumps Raman amplifier 1, and the remaining six beams are again amplified by the main KrF laser amplifier. After amplification these six beams, with a total energy of 300 J, are used to pump Raman amplifier 2 simultaneously.

Raman oscillator and Raman amplifier are being developed at the Shanghai Institute of Fine Mechanics and Optics. By using Raman beam cleanup, a diffraction limited laser ($\beta \approx 2$, $\theta \approx 0.2$ mrad, E $\approx$ 10 mJ) has been obtained. A further effort to improve this Raman cleanup system is being made in order to provide an output laser with a smaller divergence of 0.04 mrad as a diffraction limited Stokes source of Raman amplifier 1. One laser of about 4 J from the KrF laser pre-amplifier and six laser beams of about 300 J from the main KrF laser amplifier are used to pump Raman amplifiers 1 and 2, respectively. 1.3 J and 100 J will be expected from the outputs of Raman amplifiers 1 and 2, respectively.

The main parameters of the KrF laser amplifiers are measured, which is very useful for the design of these KrF laser amplifiers.

2. THE KrF LASER AMPLIFIERS

The main parameters of the KrF laser pre-amplifier and the main amplifier are given in Table I. For the main amplifier, when the voltage of the Marx generator reaches 1300 kV, 600 kV of diode voltage, 19 kJ of total electron beam energy and 276 J of output KrF laser energy have been obtained. The basic parameters of these KrF laser amplifiers such as the net small signal gain, $g_0 - \alpha_0$; the non-saturated absorption coefficient, α_n; the saturation intensity, I_s; the zero gain intensity, I(0); and the ratio of net small signal gain to non-saturated absorption coefficient, γ, have been measured by using a simpler method as shown in Fig. 1. A part of the laser cell is used as an oscillator and the other part as an amplifier; both are pumped by an electron beam. The output laser radiation from the oscillator is injected into the amplifier, and the diode is operated at a maximum voltage of 600 kV and a current density of 80 A/cm^2. The input and output laser energies are measured by two LE-3A volume absorbing calorimeters.

The relationship between input and output laser intensities can be written as:

$$\ln\left(\frac{I_0}{I_i}\right) = (g_0 - \alpha_0 - \alpha_n)\,\ell + \gamma \ln\left[\frac{I_0 - I_s(\gamma - 1)}{I_i - I_s(\gamma - 1)}\right] \tag{1}$$

TABLE I. MAIN PARAMETERS OF KrF LASER PRE-AMPLIFIER AND MAIN AMPLIFIER

Device	Quantity	Pre-amplifier	Main amplifier
Marx generator	Capacitance (nF)	14.3	35
	Voltage (kV)	980	1400
	Stored energy (kJ)	6.87	34
Pulse forming line	Number of lines	2	1
	Capacitance (nF)	14.3	34
	Voltage (kV)	910	1300
	Stored energy (kJ)	5.69	31
	Impedance (Ω)	7	2.5
	Pulse duration (ns)	100	170
Diode	Number of diodes	2	4
	Voltage (kV)	400	600
	Impedance (Ω)	7	10
	Anode current (kA)	57.1	60
	Cathode area (mm^2)	400 × 100	450 × 170
	Current density (A/cm^2)	143	78
	Total diode energy (kJ)	4.6	24
Laser cell	Pumping way	two sides	two sides
	Diameter of laser cell (mm)	120	270
	Gas pressure (MPa)	0.2	0.25
	Gas content	Ar:Kr:F_2	Ar:Kr:F_2
		89.6%:10%:0.4%	89.6%:10%:0.4%
	Power pumping rate (MW/cm^3)	0.99	1.04
	Energy deposited in gas (kJ)	0.45	8

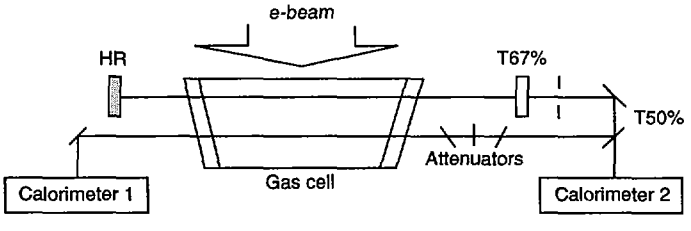

FIG. 1. Experimental set-up for parameter measurement.

where I_0 is the output intensity, I_i the input intensity and ℓ the pumping length. If I_i and I_0 are much smaller than $I_s(\gamma - 1)$, expression (1) can be simplified:

$$I_0 - I_s \cong \frac{\gamma - 1}{\gamma} I_s (g_0 - \alpha_0 - \alpha_n) \ell - \ln \left(\frac{I_0}{I_i}\right) \tag{2}$$

$$\ln \left(\frac{I_0}{I_i}\right) \cong (g_0 - \alpha_0 - \alpha_n) \ell \tag{3}$$

$g_0 - \alpha_0 - \alpha_n$ is determined by $\ln (I_0/I_i) \ell$ when I_i approaches zero. $[(\gamma - 1)/\gamma] I_s$ is determined by the slope of the curve of $\ln (I_0/I_i)$ as a function of $I_0 - I_i$.

For a steady state, the relation between zero gain intensity I(0) and saturation intensity I_s is given by:

$$I(0) = I_s(\gamma - 1) = I_s \left(\frac{g_0 - \alpha_0}{\alpha_n} - 1\right) \tag{4}$$

The net gain is measured by an attenuated probe beam using neutral, attenuated coefficient filters. The variation of the net gain as a function of the input intensity from 0.02 to 15 MW/cm^2 is shown in Fig. 2. As the input intensity increases, the amplifier net gain decreases monotonically until the saturated net gain is smaller than the non-saturable absorption. Zero gain for an input intensity of 15.3 MW/cm^2 is clearly obtained in the gain curve so $(\gamma - 1) I_s$ equals 15.3 MW/cm^2.

A set of parameters as shown in Table II has been obtained.

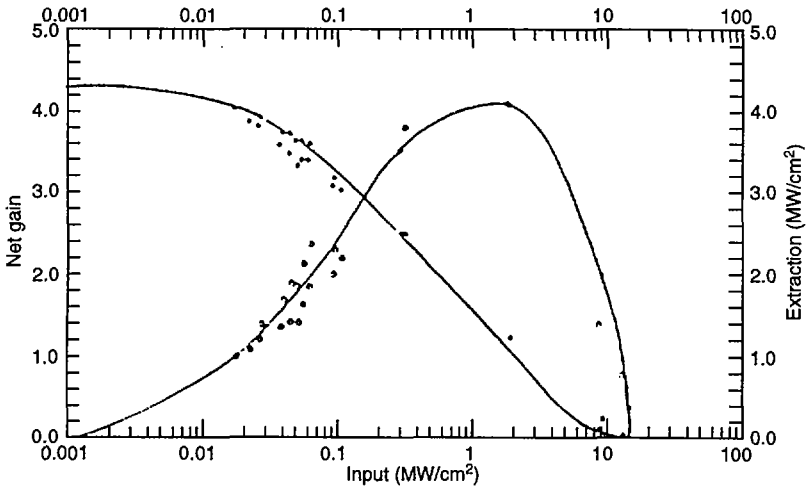

FIG. 2. Gain and extraction as functions of input intensity.

TABLE II. MAIN PARAMETERS OF KrF LASER AMPLIFIER

γ	7.1
I_s	2.5 MW/cm^2
$g_0 - \alpha_0$	0.057/cm
α	0.008/cm

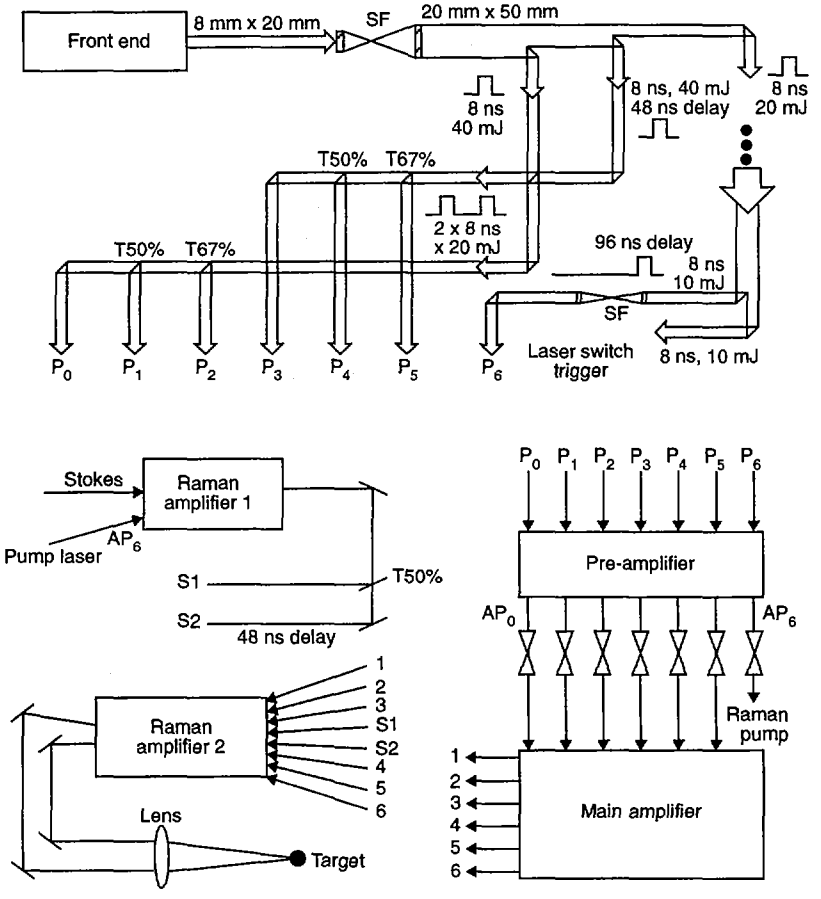

FIG. 3. Conceptual design of six beam multiplexer.

3. THE KrF LASER MULTIPLEXER

A scheme of the six beam multiplexers is shown in Fig. 3. The dimensions of the Lambda Physik LPX-150 laser output is 8 mm × 20 mm, and a spatial filter with a magnification factor of 2.5 is used to extend the beam dimensions to 20 mm × 50 mm. Then the beam is cut into three beams; their dimensions and energies are 20 mm × 20 mm, 40 mJ; 20 mm × 20 mm, 40 mJ; and 20 mm × 10 mm, 20 mJ, respectively. One 20 mm × 20 mm beam is delayed by 48 ns and mixes with another beam of 20 mm × 20 mm; then they are split into six beams by using dielectric coated beam splitters. The beam of 10 mm × 20 mm is also cut into two beams; one beam with 8 ns, 10 mJ is delayed by 96 ns. A spatial filter with a magnification factor of 2 is used to enlarge these beam dimensions to 20 mm × 20 mm, another one, an 8 ns, 10 mJ, 10 mm × 10 mm beam is used as laser switch trigger. The output from this system consists of seven 8 ns pulses with a delay of 8 ns between two pulses. These pulses are then amplified sequentially in the e-beam pumped KrF pre-amplifier over a time period of 104 ns. After amplification, the energy of each beam is about 4 J, and the beam dimensions are 20 mm × 20 mm. The last beam from the pre-amplifier is separated out to pump Raman amplifier 1, the remaining six beams are then amplified sequentially in the main amplifier. Each of the six output beams from the main amplifier has an energy of about 50 J. The time delay between these beams can be eliminated by using different light paths. These six beams are put into Raman amplifier 2 simultaneously and two Stokes sources, s_1 and s_2, are amplified and then s_1 and s_2 are demultiplexed again by different paths. Finally, two laser beams of a total energy of approximately 100 J can be obtained for the target experiments.

All optical components of these two amplifiers have already been manufactured; the adjustment will start soon.

4. SUMMARY

As a first step, we are constructing a 100 J, 8 ns KrF laser to meet the requirements of laser–plasma interaction research. The 8 ns pulse width is, however, too long for target experiments so that the second step, pulse compression, will become very important. An 8 ns pulse duration must be compressed to 1 ns. The experiment on the main KrF laser amplifier has shown that this amplifier can deliver 276 J output laser energy when the charging voltage of the Marx generator is 1300 kV only. With the charging voltage increasing to 1400 kV, the output laser energy will exceed 300 J. The main KrF laser amplifier works very stably.

REFERENCE

[1] WANG, Naiyan, et al., "Hundred joule level KrF laser pumped by intense electron beam", paper presented at KrF Laser Technology Workshop, Banff, Alberta, Canada (1990).

ANGARA-5 PROGRAMME: DEVELOPMENT OF BRIGHT X RAY SOURCES FOR INERTIAL CONFINEMENT FUSION BASED ON SUPERFAST IMPLODING PLASMA — 'COLD START' AND PLASMA COMPACT IMPLOSION PROBLEM

E.V. GRABOVSKIJ, S.L. NEDOSEEV, G.M. OLEJNIK,
V.P. SMIRNOV, V.I. ZAJTSEV, V.V. ZAJIVIKCHIN,
S.V. ZAKHAROV
Troitsk Institute of Innovative and
Thermonuclear Investigations,
Troitsk,
Russian Federation

Abstract

ANGARA-5 PROGRAMME: DEVELOPMENT OF BRIGHT X RAY SOURCES FOR INERTIAL CONFINEMENT FUSION BASED ON SUPERFAST IMPLODING PLASMA — 'COLD START' AND PLASMA COMPACT IMPLOSION PROBLEM.

Experiments are carried out with cylindrical liners in a wide range of initial parameters. The results are compared with those based on theoretical considerations. The studies are motivated by the fact that imploding liner plasma instabilities driven by an axial current are the most dangerous obstacle to compact liner implosion. Comparison with Saturn results confirms the validity of the authors' approach.

1. INTRODUCTION

Instabilities of an imploding liner plasma driven by an axial multi-MA current are apparently the most dangerous obstacle to compact liner implosion. Azimuthal and axial inhomogeneities are recorded in experiments with liners having an azimuthally homogeneous plasma producing substance — gas puffs or foam [1–3]. An understanding of the origin of these instabilities is a necessary condition for overcoming them.

Some models are used to analyse the instabilities. Essentially, it is assumed in these models that the initial liner plasma conductivity is sufficient to produce an external current skin layer thinner than the liner plasma thickness. Then the pressure of the current magnetic field is applied to the external surface of the liner plasma and accelerates it in radial direction. The Rayleigh–Taylor (R–T) instability accelerating the liner, sausage MHD instabilities of the plasma current shell [1] and a collisionless magnetized plasma instability [2, 3] are treated as the most significant instabilities in liner implosion. The R–T or MHD instabilities as the original cause of subsequent

small scale Hall effect or ion acoustic instabilities of collisionless plasma are proposed in Refs [2, 4]. The conditions of instability of a magnetized plasma with a large Hall parameter, $\omega_{He}\tau_{ei} \gg 1$, are analysed in Ref. [3]. This instability is dangerous for low mass, low density gas liners driven by a relatively small (1–3 MA) current. There is no danger that this kind of instability may accelerate massive liners by very high multi-MA current I, as well as liners with a high density plasma. Really, in these cases the current driving plasma is collisional, and $\omega_{He}\tau_{ei} < 1$. Then it is necessary to accelerate thin liners in order to prevent an instability of the collisionless magnetized plasma. To avoid this instability in our experiments, we have replaced our thick ($\sim$2 mm) gas liners by thin ($\sim$50–100 μm) foam liners, and we have realized very fast current switching onto the foam liner in order to prevent foam expansion, using an opening switch process in an auxiliary, external, low mass, annular liner corona [2]. Nevertheless, we had non-compact liner implosion again, in spite of the above mentioned proposal. Then we have analysed our previous experimental data, referring to gas puff liners, and concluded that, in the same way as foam, gas liners driven by current could also be fractured before implosion, because of effects of 'cold start'. If so, efforts different from those mentioned above have to be made, first of all in order to realize compact liner implosion.

2. EXPERIMENTAL RESULTS

In our experiments, we have investigated current drive of cylindrical liners in a wide range of initial parameters. The composition was: gas (Xe, Ar, Ne, propane or agar foam) plus 10–50% of CsI, Mo, KCl dopants; linear mass, M_{lin} = 10–400 μg/cm; liner thickness = 1–0.005 cm, radius = 0.1–2.5 cm; current = 2–5 MA; current rise time ($\sim$100 ns or $\sim$10 ns, using the opening switch process in an external, low mass plasma liner corona).

We find that the current density is azimuthally inhomogeneous and the current filaments are the usual ones (for foam and gas liners). For example, foam–plasma transfer with fast current switching is shown in Fig. 1. The upper picture is a laser shadow photo of the cold foam liner, M_{lin} = 130 μg/cm, diameter = 22 mm. The three lower shadow pictures were taken with 15 ns intervals and 2 ns exposure. Filaments of foam plasma density and axial inhomogeneities of the disrupted external plasma corona fast opening switch of 50 mm diameter are shown. The total current was $\sim$2 MA during this period.

During approximately the first half of the current rise time (20–50 ns) the liner (foam or gas) stays motionless, and the visible brightness of the filaments rises gradually. Then the radiation intensity of the filaments and their visible thickness increase abruptly. As a rule, this intensification of visible radiation moves like a wave from cathode to anode at a velocity of $\sim$0.1 cm/ns, which is rather homogeneous azimuthally. An example of this effect is shown in Fig. 2.

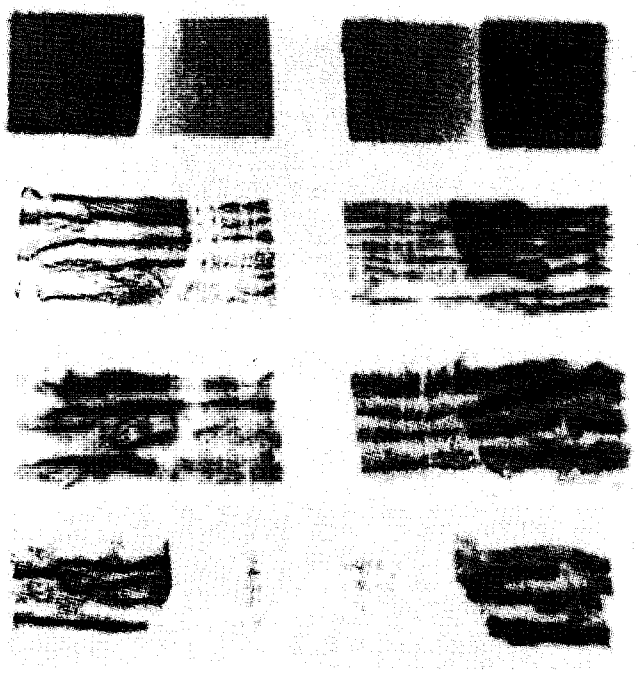

FIG. 1. Foam–plasma transfer with fast current switching.

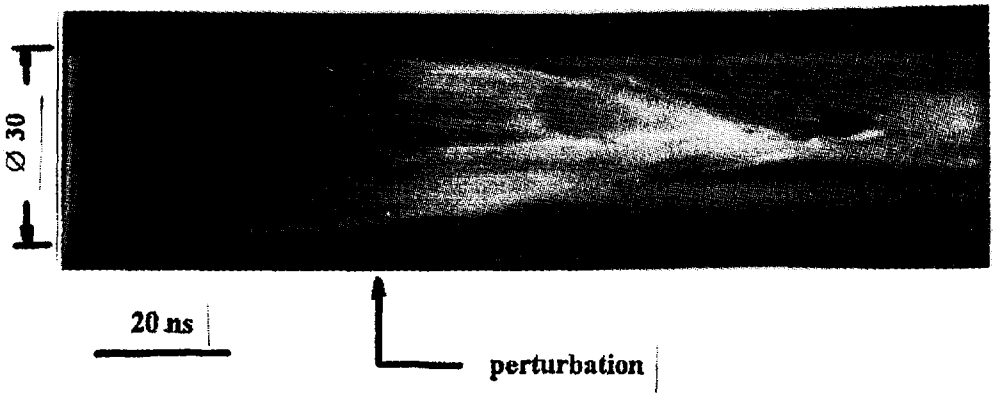

FIG. 2. Current filament perturbation.

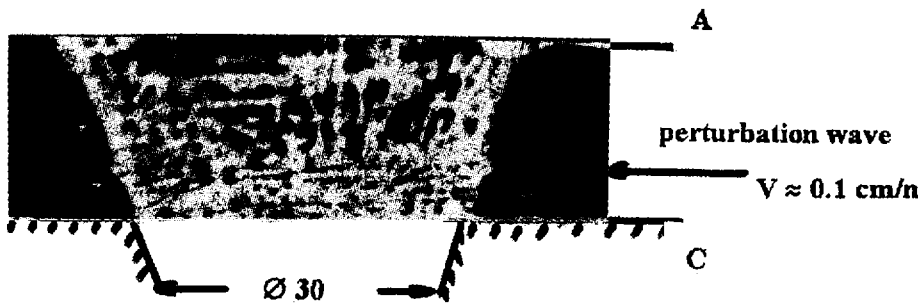

FIG. 3. Laser shadow picture of Ar solid gas puff.

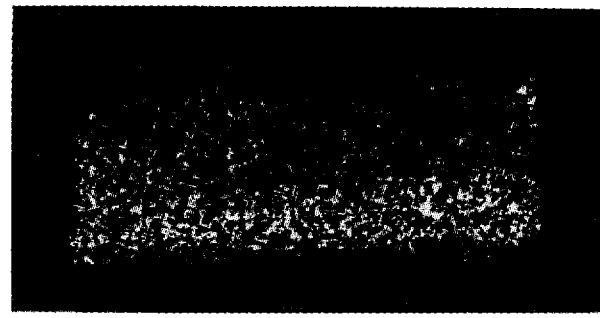

FIG. 4. Visible light perturbation wave in the foam liner.

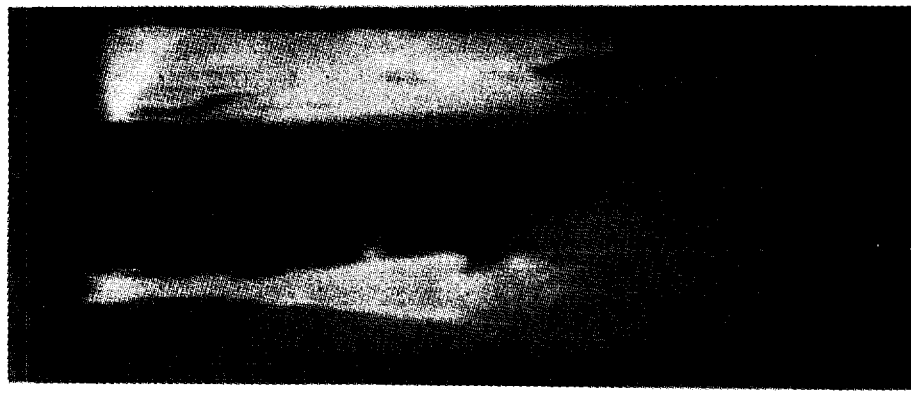

FIG. 5. Perturbation wave along inner foam radiator.

Figure 2 is a visible light streak camera photo of a radial slit, situated in the middle of the Xe gas liner ($M_{lin} \sim 200$ μg/cm, diameter = 30 mm). The instant when the wave arrives at the liner centre is designated the 'perturbation'. After the perturbation, part of the liner matter begins to accelerate in radial direction, while another part stays motionless; consequently, the liner is fractured by the perturbation. At this moment, the current is ~ 2 MA.

Figure 3 is an instant (~ 2 ns) laser shadow picture of an Ar solid gas puff taken at the moment when the wave perturbation fronts shifted from the cathode to $\sim 1/3$ of the anode–cathode gap. A change of the azimuthal to the axial character of the plasma electron density inhomogeneity is seen well behind the perturbation wave. Figure 4 illustrates the same effect for the visible light perturbation wave in the foam liner ($M_{lin} = 200$ μg/cm, diameter = 22 mm), taken by an image camera with an exposure of ~ 3 ns. The wave front is positioned at $\sim 1/2$ of the anode–cathode gap.

In this experiment, effective liner current rise sharpening was achieved by using an external Xe gas corona, low mass, unstable liner (~ 10 μg/cm, diameter = 50 mm) as the very fast opening switch [2], the switched current being ~ 2 MA, and the switching time < 10 ns. Figure 5 shows the perturbation wave along the inner foam radiator of 2 mm diameter (agar + 50% Mo), inserted onto the axis of low mass Xe disrupting liner, fast opening switch [2]. This picture is taken in visible light using both axial (upper picture) and radial slit streaks. It is seen on the axial slit streak that the perturbation wave moves from cathode to anode, crossing 1 cm of the foam plasma in ~ 12 ns, the plasma bulk remaining uncompressed during this period (see the radial slit streak).

3. DISCUSSION

The experimental basis forces us to assume that the 'perturbation' is an indicator of early liner fracturing, which is the first cause of a subsequent non-compact liner implosion. The above-mentioned instabilities of the magnetically accelerated plasma could be a secondary factor. What is the physical mechanism of the 'perturbation'?

As a matter of fact, all Z pinch or fast liner implosion experiments, using (multi)terawatt pulsed power generators, start the plasma implosion after a 'cold start' — an electric breakdown of the plasma producing substance, gas, solid or foam, positioned in the anode–cathode gap. Current filamentation due to thermal instabilities of the plasma conductivity is a specific feature of this breakdown, independent of the initial homogeneity of the plasma producing matter. No kind of pre-ionization applied in these experiments could prevent filamentation. In fact, currentless pre-ionization (flashboard radiation, etc.) has a very small power in comparison with the power of the liner plasma Joule heating just before the start of the implosion. The fast current switching method used in our experiments with foam liners does not change the situation fundamentally. So, the 'cold start' and the current filamentation in Z pinch or liner initial plasma always take place. Because of the random nature

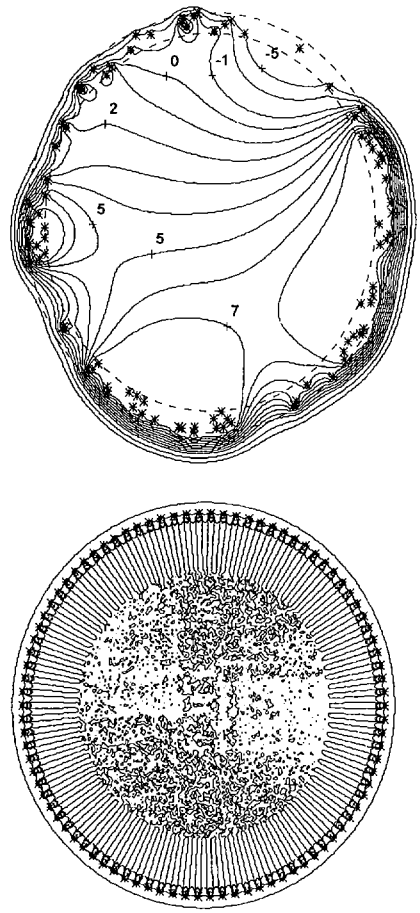

FIG. 6. Magnetic field lines for randomly and uniformly distributed (N = 90) current channels. Stars designate current locations.

of the breakdown, filaments are introduced into the liner bulk and the azimuthal magnetic field structure is non-regular; it can produce azimuthal inhomogeneities of the initial liner plasma in spite of homogeneous plasma producing matter. An example of 90 randomized current channels of the magnetic field is shown in Fig. 6. It is an important feature that the summary magnetic flux crosses the liner matter in some places and penetrates into the region enveloped by the liner. Consequently, the real initial conditions of the liner implosion are quite different from the theory model mentioned.

From the energetic standpoint, the magnetic energy of the filamentary current is high in comparison with the homogeneous case. Thus, a perturbation of the

filamentary current magnetic structure towards an azimuthally more homogeneous structure could happen. We assume that it is just the effect we have recorded as the wave of light perturbation. It is highly significant that the axial fine structure of the perturbed liner plasma is inhomogeneous as well (Figs 3 and 5). We have no theory of this effect, as yet. It is only possible to propose that axial inhomogeneities of the separate filaments and the azimuthal direction of the magnetic field could generate the axial stratification.

Anyway, the 'cold start' current filamentation can fracture the liner matter before the instabilities of the magnetically accelerated plasma appear. Consequently, arrangements different from the proposals made in Ref. [3] have to be provided in order to decrease this effect. It seems that the most effective method of overcoming the 'cold start' effects is to apply a powerful currentless pre-ionization of ~ 0.1 TW. For example, the ion beam could be used for this purpose, involving a rather complex technology.

Another possibility to overcome this 'cold start' effect is to use liners with azimuthally structured plasma producing matter, such as a multiwire array. A magnetic field structure of 90 equal currents uniformly positioned on a circle is shown in Fig. 6. There is no plasma producing matter between the wires; hence, there are no random filaments, no perturbations and no early liner fracturing during the initial period of the current rise for an ideal wire array. Of course, it is assumed that wire evaporation finishes before their acceleration and the wire plasma does not fill the interval between the wires. Being surrounded by its own magnetic field, each wire plasma of this array is accelerated by itself, and its own instability does not spread to the other sections. Perhaps, the present excellent results of wire array implosion on Saturn confirm the validity of this proposal [5].

REFERENCES

[1] BAKSHT, R.B., et al., Fiz. Plazmy **21** (1995) 959.

[2] BATUNIN, A.N., et al., "Inhomogeneous Z-pinch investigation on Angara-5-1", in Proc. 3rd Int. AIP Conf. London (1993) 580.

[3] RUDAKOV, L.I., SEVASTYANOV, A.A., Fiz. Plazmy **23** (1997) 403.

[4] BRANITSKIJ, A.V., et al., Fiz. Plazmy **22** (1996) 511.

[5] SANFORD, T.W.L., et al., "X-ray power increase from symmetrized wire-array Z-pinch implosions", paper presented at BEAMS 96, Prague (1996), paper O-4-2.

SUPPRESSION OF HYDRODYNAMIC INSTABILITIES IN LASER ABLATED THIN SOLID TARGET — AN EXPERIMENTAL STUDY

T. DESAI, M. ASTHANA, M. SHUKLA, V.N. RAI
Laser Programme,
Centre for Advanced Technology,
Indore, India

Abstract

SUPPRESSION OF HYDRODYNAMIC INSTABILITIES IN LASER ABLATED THIN SOLID TARGET — AN EXPERIMENTAL STUDY.

One of the major impediments to achieving stable ablative acceleration in laser induced inertial confinement fusion is the Rayleigh–Taylor (R–T) instability. Owing to laser induced high pressure, the R–T instability grows at the interface of the accelerated low density coronal plasma and high density DT filled shell fluid. The aim of the experimental work presented in the paper is to study the growth of the hydrodynamic instability in laser irradiated targets at moderate intensities. Laser (1.06 μm) radiation was focused on the plastic (base) target seeded with microinclusions of aluminium and gold at various concentrations. The targets had a planar geometry and were of few micrometres in thickness. The target stability was studied using an optical backlighting technique. The results are analysed by considering the coherent structure effects of the plasma such as vortices, the self-generated magnetic field in the accelerated target and non-linear conversion of long wavelength perturbation into short wavelength perturbation.

1. INTRODUCTION

The Rayleigh–Taylor (R–T) instability is an important detrimental mechanism in reducing the fusion efficiency in laser induced thermonuclear fusion. This can be briefly described as follows:

A spherical microballoon filled with DT is symmetrically irradiated by multiple high power laser beams. The laser radiation interacts with the surface of the microballoon and generates a few tens of megabars of pressure which isentropically compresses the DT material to a few eV and a density of the order of 1000 times the liquid DT density. This forms an envelope around the central low density, but high temperature plasma ($\tau_e \sim 5$ keV, due to shock heating). Actually, the core plasma serves as an ignitor. In the directly driven ICF scheme, the ignitor size is $\sim 2\%$ of the initial target radius. Therefore, for efficient fusion reactions, the ignitor surrounded by isentropically compressed fuel places a stringent requirement on the stability of implosion.

The implosion symmetry of an ablatively accelerated target is affected by the following reasons:

(1) Non-uniformity in the incident laser beam (optical smoothing techniques such as induced spatial incoherence (ISI), random phase plate arrays and smoothing by spectral dispersion can reduce the laser beam spatial non-uniformities).
(2) R–T instability arising during the implosion phase appears in two stages:
   (a) Acceleration of high dense fluid by low density hot ablating plasma,
   (b) Deceleration of high dense fluid by the ignitor.

In either of these two phases, if the instability grows it can destroy the symmetry of implosion: in the acceleration phase by causing shell breakup, and in the deceleration phase by degrading the fuel compression with pusher–fuel mixing.

The growth of these instabilities will reduce the fusion yield because of incomplete transformation of the kinetic energy into the internal energy of the compressed fuel. Classically, the eigenmodes of the surface waves have the form:

$$A \sim \cos kx\, e^{-kz}$$

where $k = 2\pi/\lambda$, x is the direction of propagation and z is the direction of the amplitude growth perpendicular to the x axis.

The growth rate of such a perturbation is given by

$$\gamma = (\alpha\, kg)^{1/2}$$

where α is the Atwood number, $\alpha = (\rho_{max} - \rho_{min})/(\rho_{max} + \rho_{min})$, $k = 2\pi/\lambda$ is the wavelength of the perturbation, and g is the acceleration (or deceleration) of the fluid.

It is hence necessary to understand the growth of these instabilities and the means to suppress them. It is, however, shown by theory and simulation that in ICF the growth rate of the R–T instability depends on the following implosion parameters: Atwood number, wavelength of perturbation, flow velocity, thermal conduction, mass ablation, viscosity and surface tension. A good estimate of the linear growth rate of the instabilities has been reported by Takabe [1]: $\gamma = 0.9\ (kg)^{1/2} - \beta\ kV$, where $\beta = 3$–4, $k = 2\pi/\lambda$ and V is the velocity of the heavy fluid.

When high power laser radiation interacts with the target surface, a hot plasma layer is formed. This is due to the absorption of laser radiation in the vicinity of the critical density layer ($n_c \sim \lambda_L^{-2}$). The plasma state is formed up to the ablation layer as a result of thermal conduction from the critical density layer. Owing to momentum conservation of the plasma blow-off, high pressure is generated and acts on the cold (initial), unevaporated target. The pressure generation in the self-regulating [2] and the deflagration [3] models has the following dependence:

$$P = 3.3 \times 10^{-10}\, \lambda^{-2/9}\, R_{\mu m}^{-1/9}\, A^{7/18}\, [Z^Z(1 + Z)]^{-1/6}\, I^{7/9}\ Mb$$

$$P = 12\, (I/10^{14})^{2/3}\, \lambda_{\mu m}^{-2/3}\, (A/2Z)^{1/2}\ Mb$$

where the wavelength of the laser radiation, λ, and the focal spot radius, R, are in micrometres, A is the target mass number and Z is the effective ionization of the plasma. I is absorbed laser intensity in W/cm^2. Owing to this high pressure, a plasma slab of thickness $d = P/a\rho_a$ is accelerated, where ρ_a is the ablation front density, a is the fluid acceleration, and the R–T instability arises at the ablation surface. The speed of sound in the unevaporated part of the target is low ($\sim$(2–3) $\times$ 10^5 cm/s) compared to the characteristic velocities ((3–5) $\times$ 10^6 cm/s) of the plasma [4].

Therefore, the perturbations are transported from the outer boundary to the inner layer mainly by the first shock. The fluid interchange decreases the potential energy content of the system, which is the cause of the instabilities [5]. These instabilities distort the uniform compression of the DT fuel, which results in poor ignition and, hence, poor fusion energy yield. The schematic of the ablation layer during laser–plasma interaction is shown in Fig. 1.

In this paper, we discuss coherent structure effects such as vortices, self-generated magnetic field and non-linear conversion of long into short wavelength perturbations as a possible mechanism for the stabilization of the R–T instabilities.

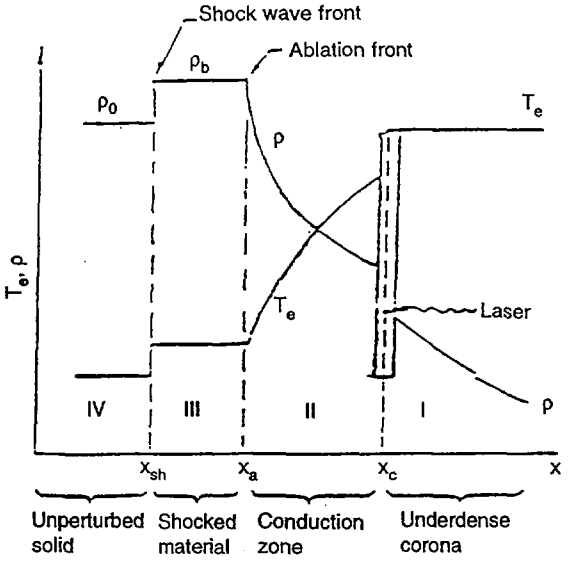

FIG. 1. Schematic of the ablation layer during laser–plasma interaction.

2. EXPERIMENT

The basic interest in the experiments was to study the hydrodynamic stability of low Z plastic material seeded with microinclusions. Two types of planar target were chosen for laser irradiation: low density, pure plastic targets (ρ = 0.9 g/cm^3), 20 μm thick, and plastic targets containing microinclusions of aluminium and gold particles. Al dust contained particles of diameters ranging from 0.3 to 0.5 μm, whereas the gold dust particles had diameters of 1.5–2 μm. It was not, however, possible to use particles of similar diameter as seeds in the target.

Targets with microinclusions will form a superlattice structure. Gold particles were used because they emit copious soft X rays ($h\nu \leq 1.5$ keV). Hence, the effect of X rays on the R–T instability can be studied by a comparison with Al seeded targets since Al is a relatively poor X ray emitter. The concentration of the microinclusions was varied from 5 to 100 mg/cm^3 of the plastic solution. Seeded targets have certain advantages over pure material targets, such as:

(1) High Z microinclusions can be treated as X ray sources and, hence, some advantage can be drawn from short wavelength ablation.
(2) X ray emission from such targets is low compared to that from pure high Z materials. Therefore, the absorbed laser energy and, as a consequence, the ablation efficiency are higher.
(3) Such seeded targets have been used as a shield against the preheating of the plasma due to hot electrons and hard X rays.

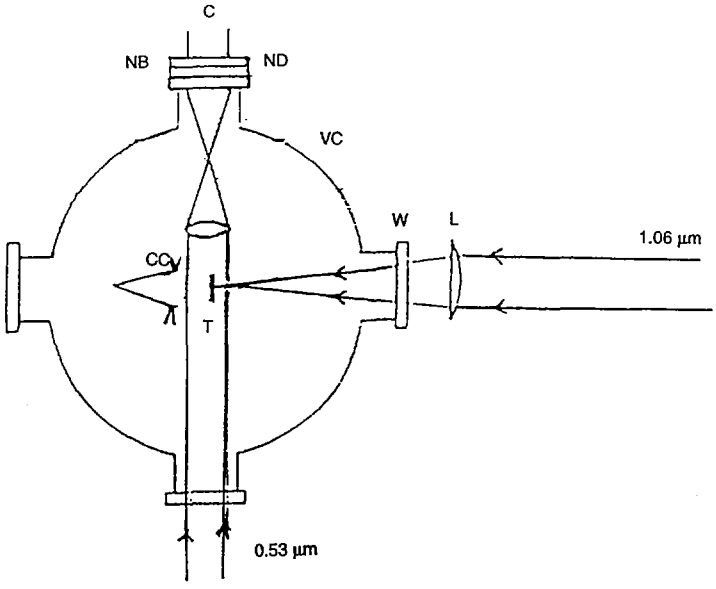

FIG. 2. Experimental set-up. VC — plasma chamber, W — window, T — target, C — camera, L — lens, CC — cone calorimeter, NB — narrow band filter, ND — neutral density filter.

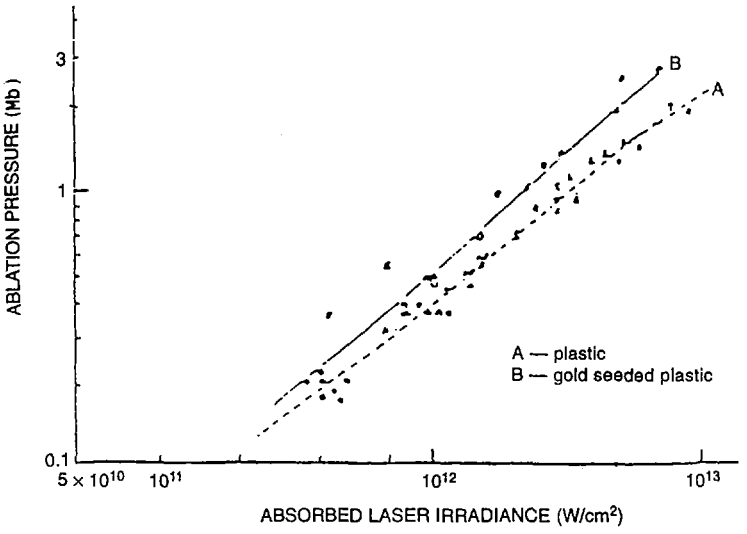

FIG. 3. Ablation pressure as a function of absorbed laser intensity.

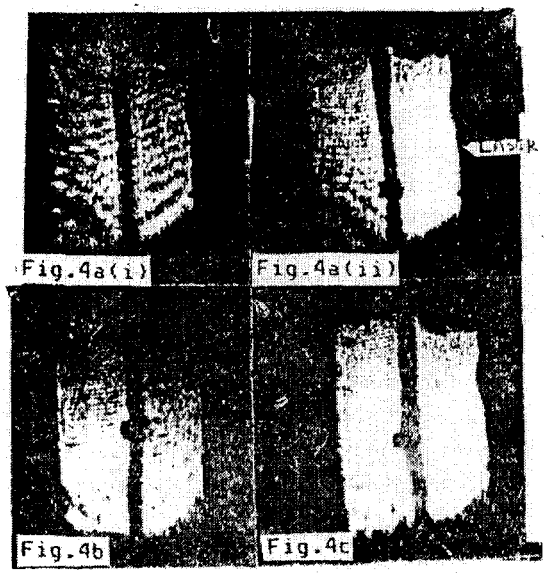

FIG. 4. Accelerated target motion for pure and seeded targets.

The present experiments were performed by using a 1.06 μm laser of 5 ns and 40 ps duration on planar targets. The laser radiation was focused to ~ 110 μm in diameter on the target surface. The intensity on the target surface was $I \leq 5 \times 10^{12}$ W/cm^2. Thin planar foil targets were held on a specially designed holder and placed at the centre of the plasma chamber, which was evacuated to 10^{-5} mm of mercury. The experimental set-up is shown in Fig. 2.

The laser induced ablation pressure was measured by using a rear side cone calorimeter (for 5 ns laser pulse irradiation), and the pressure was calculated to be $P = \rho t V_t/\tau$ where ρ, t, V_t are the density, the thickness and the terminal velocity of the accelerated target; τ is the acceleration time ($\approx$ laser pulse duration). Details of this technique are discussed in Ref. [2].

The motion of the ablatively accelerated target was studied by a shadowgraphy technique using a second harmonic probe beam (0.53 μm) with polaroid film and CCD camera. The shadowgrams were recorded on polaroid films 25 and 35 ns after the peak of the laser pulse.

3. RESULTS

The ablation pressure as a function of the absorbed laser intensity is shown in Fig. 3 for gold seeded plastic and pure plastic targets. The ablatively accelerated target motion for pure and seeded targets is shown in Fig. 4. The laser intensity for all these shadowgrams was constant: $I = 5 \times 10^{12}$ W/cm^2. Figure 4a(i) represents the unirradiated $t \approx 20$ μm thick pure plastic with $\rho t \approx 18.1 \times 10^{-4}$ g/cm^2, whereas Fig. 4a(ii) shows the accelerated target motion due to laser irradiation of the plastic shown in Fig. 4a(i). This is compared with an Al seeded plastic target of $\rho t \approx 18.4 \times 10^{-4}$ g/cm^2 (Fig. 4(b)).

Figure 4(c) shows gold seeded plastic targets (50 mg/cm^3 of plastic solution) of $\rho t \approx 38 \times 10^{-4}$ g/cm^2. Figures 4(a), (b) and (c) were recorded 25 and 35 ns, respectively, after the peak of the laser pulse.

4. DISCUSSION

In this paper our discussion is limited to the accelerated target region. We observe that the seeded targets show a better stability than the pure plastic target. These results are analysed according to the following factors: vortex formation and self-generated magnetic field during the ablatively accelerated phase of the target.

4.1. Vorticity and R–T instability

When a laser irradiated target is accelerated, the instabilities grow at the interface. The heavy fluid 'troughs', and the light fluid extends into 'crests'. Because of

the slope at the midpoint, there is a component of acceleration at the interface. The resulting differential acceleration drives a velocity shear or vorticity such that $\xi = \nabla \times \mathbf{u} \neq 0$, where **u** is the fluid velocity [6]. In physical terms, this is nothing but a self-organized structure in the turbulent medium. Therefore, in a seeded target, it is possible to have more vortices with particles or seeds.

By deliberately introducing microinclusions, the wavelength of the perturbation can be controlled. The average spacing between these particles depends on the concentration of the microinclusions. With an average spacing of $a = 0.4$ μm in the case of an Al seeded target and of $a = 1.00$ μm for a gold doped plastic target, we can estimate the harmonic mode number as follows: when a plasma slab (disc) of ~ 100 μm radius, R, is accelerated, the perturbations grow on the surface such that $n\lambda = 2R$; the harmonic mode number n is approximately 500 and 200, respectively, when λ is almost of the order of the interatomic spacing.

These instabilities become non-linear if $KA \sim 1$, where $K = 2\pi/\lambda$ and A is the amplitude; there is an energy transfer from long to short wave perturbation [4]. As short wavelength perturbations are not dangerous, the higher harmonic mode number becomes advantageous with target materials having microinclusions.

4.2. Self-generated magnetic field and vorticity

Electrons quickly respond to the plasma gradient. Hence, we can describe the evolution of the magnetic field on the basis of the electron density and temperature gradient. The connection between vorticity and magnetic field evolution is obtained by using Ampère's and the generalized Ohm's laws:

$$\mathbf{J} = [\mathbf{E} + (\mathbf{V} \times \mathbf{B})/c] + \nabla p_e/en_e$$

Taking the curl of Faraday's equation, we obtain:

$$\partial B/\partial t = c\nabla^2 B/4\pi\sigma + \text{curl}\,(\mathbf{V} \times \mathbf{B}) + (c/e)\,\text{curl}\,(\nabla p_e/n_e)$$

The magnitude of the field B is given by $B = \xi\, c\, M_i/e\,(Z + 1)$, where M_i is the ion mass, $\xi = K \times u$, u is the plasma vortex velocity, K is the wavenumber of the R–T mode, corresponding to the perturbation wavelength [7], and c is the velocity of light.

The $\mathbf{J} \times \mathbf{B}$ force acts on these instabilities. The influence of this force can be obtained by comparing the energy in the magnetic field B with the energy density in the fluid vorticity $\rho u^2/2$, where u is the vortex velocity:

$$U_B/U_\xi = (B^2/8\pi)/(\rho u^2/2) = c^2\, M_i\, k^2 Z/W_p^2 m_e\,(Z + 1)^2$$

where W_p is the plasma frequency.

If $U_B/U_\xi \geq 1$, the magnetic fields are stronger. For $n = 10^{23}$ cm^{-3} and assuming $(Z + 1)/Z \approx 1$, this condition can be satisfied if $\lambda = 5.5Z^{-1/2}$. The

existence of a megagauss magnetic field has been reported in Ref. [7]. The role of a higher field implies that it acts like a surface tension and stabilizes the growth rate.

In the case of a laser accelerated target, the plasma behind the ablation surface is dense ($n_i \approx 10^{23}$ cm^{-3}) and relatively cold with a temperature of 1–30 eV. In these conditions the interionic spacing is around a $\sim$ 1 Å. The thermodynamic behaviour of such a system can be described by the non-ideality parameter $\Gamma = Z^2e^2/akT$, where Z and kT are the plasma's charge state and temperature, respectively. In our experimental conditions, for a laser intensity of $I = 10^{13}$ W/cm^2, we have $n_i = 10^{23}$ cm^{-3}, $Z = 5$, $T_e = T_i = 5$ eV and $\Gamma = 70$. This increases the viscosity of the fluid [8]. However, there is no concrete evidence for the stabilization of the R–T instability due to the non-ideality of the plasma, so far.

Previously, the stability of a tungsten (particles of 3 μm diameter) doped plastic target was reported, where the X radiation generated by the high Z microinclusions was believed to be the cause of target stabilization [9]. Tungsten and gold particles being high Z elements, the X ray yield is higher than that of aluminium reported in this work, but the experimental results indicate that the X radiation effect on the stability of the accelerated target motion seems to be weaker, although it cannot be completely ruled out.

5. CONCLUSIONS

The growth of R–T instabilities in laser ablated thin plastic targets is observed. These instabilities can be reasonably controlled when the plastic foil targets are seeded with metallic particles (diameter $\leq$ 1–2 μm) of aluminium and gold. We have found that even Al microinclusions produce stability. This indicates that the effects discussed in this paper are, perhaps, the controlling factors of the R–T instability. The contribution of each of these mechanisms, along with a further analysis of our experimental results, will soon be published.

REFERENCES

[1] TAKABE, H., et al., Phys. Fluids **28** (1985) 3676.
[2] SHIRSAT-DESAI, T., PARAB, H.D., PANT, H.C., Laser Part. Beams **7** (1989) 795.
[3] FABBRO, R., et al., Phys. Fluids **28** (1985) 1463.
[4] GAMALII, E.G., et al., Sov. Phys. - JETP **52** (1980) 230.
[5] KULL, H.J., Phys. Rep. (review section of Phys. Lett.) **206** (1991) 200.
[6] STAMPER, J.A., Laser Part. Beams **9** (1991) 841.
[7] BORISENKO, N.G., MARKULEG, Yu.A., Preprint 47, P.N. Lebedev Physical Institute, Academy of Sciences, Moscow (1990).
[8] ITOH, N., KOHYAMA, Y., TAKEUCHI, H., Astrophys. J. **317** (1987) 733.
[9] DHARESHWAR, L.J., PANT, H.C., in Plasma Physics and Controlled Nuclear Fusion Research 1992 (Proc. 14th Int. Conf. Würzburg, 1992), Vol. 3, IAEA, Vienna (1993) 165.

HEAVY ION FUSION DRIVER RESEARCH AT BERKELEY AND LIVERMORE

P. SEIDL, B. BANGERTER, C.M. CELATA, W. CHUPP,
F. delaRAMA, S. EYLON, A. FALTENS, W.M. FAWLEY,
T.J. FESSENDEN, W. GHIORSO, K.D. HAHN, E. HENESTROZA,
R. HIPPLE, D. JUDD, S. MacLAREN, C. PETERS, L. REGINATO,
D. VANECEK, J.D. STOKER, S. YU
Lawrence Berkeley National Laboratory,
Berkeley, California

J.J. BARNARD, M.D. CABLE, D.A. CALLAHAN, T.V. CIANCIOLO,
F.J. DEADRICK, A. DEBELING[1], A. FRIEDMAN, D.P. GROTE,
K.A. HOLM, H.A. HOPKINS, V.P. KARPENKO, H.C. KIRBIE,
D.B. LONGINOTTI, S.M. LUND, L.A. NATTRASS, M.B. NELSON,
M.A. NEWTON, T.C. SANGSTER, W.M. SHARP
Lawrence Livermore National Laboratory,
Livermore, California

United States of America

Abstract

HEAVY ION FUSION DRIVER RESEARCH AT BERKELEY AND LIVERMORE.

The Department of Energy is restructuring the US fusion programme to place a greater emphasis on science. As a result, the ILSE or Elise heavy ion fusion (HIF) facilities described in the 1992 and 1994 Plasma Physics Conferences will not be built. Instead smaller experiments to address important scientific questions are being performed. The accelerator technology for HIF is similar to that for other applications such as high energy physics and nuclear physics. The beam physics, however, differs from the physics encountered in most accelerators, where the pressure arising from the beam temperature (emittance) is the dominant factor determining beam size and focusing system design. In HIF, space charge is the dominant feature, leading into a parameter regime where the beam plasma frequency becomes comparable to the betatron frequency. The present experiments address the physics of non-neutral plasmas in this novel regime. Since the beam plasma frequency is low, particle in cell (PIC) simulations provide a good description of most of the experiments. Accelerators for HIF consist of several subsystems: ion sources, injectors, matching sections, combiners, acceleration sections with electric and magnetic focusing, beam compression and bending sections, and a system to focus the beams onto the target. Currently experiments to address the physics of all these subsystems are being assembled or performed. The paper discusses experiments in injection, combining and bending.

[1] Bechtel Nevada Corporation, Las Vegas, Nevada, USA.

1. EXPERIMENTS WITH THE 2 MV K^+ INJECTOR

A driver scale, one beam heavy ion injector has been constructed and operated at LBNL. The new injector has, as its design goals, a particle energy of 2 MV, a line charge density of 0.25 μC/m (800 mA of K^+) and a normalized edge emittance of < 1 π-mm-mr. These design parameters are the same as in a full scale driver. The low emittance is essential for near ballistic final focusing onto a small target. The line charge corresponds to the optimal transportable charge in a full scale electrostatic quadrupole channel, and the high injector energy has significant cost advantages in a fusion driver. The ultimate injector for a fusion accelerator is conceptually a replicate of this one beam injector to many beams, with an extended pulse length of many microseconds, instead of the one to two microseconds (budget determined) in this 2 MV injector. While the particle energy and particle current have been achieved separately in previously built injectors, the unique combination of energy, current and emittance requirements pose a new technical challenge. Furthermore, the required beam parameters must stay constant over the entire pulse, and the injector must run reliably.

The new injector is based on an electrostatic quadrupole (ESQ) configuration [1, 2]. The ion beam, after extraction from an axisymmetric diode, is injected into a lattice of electrostatic quadrupoles arranged to provide simultaneous acceleration and strong focusing. The ESQ configuration was chosen over the more conventional electrostatic aperture column primarily because of high voltage breakdown considerations. The accelerating gradient of an ESQ can be made quite low, and the strong transverse fields sweep out secondary electrons which may initiate breakdown processes. However, the ESQ configuration has an inherent beam aberration, which must be carefully controlled to minimize emittance degradation. The key design

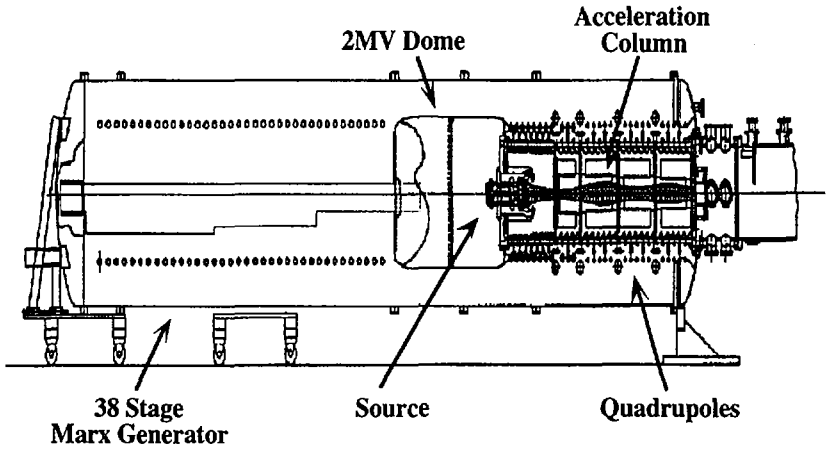

FIG. 1. 2 MV injector schematic.

issues centre around the control of high voltage breakdown and phase space distortions.

The injector column consists of a diode followed by four electrostatic quadrupole sections (Fig. 1). The source is a curved hot aluminosilicate source emitting K^+ ions. These sources have been shown to produce beams with temperature limited emittances and have long lifetime and high reliability. The injector is powered by a 2 MV Marx with parallel LC and RC circuits that produce a 4 μs flat-top.

One key design issue is the dynamics of the space charge dominated ion beam. A low energy ion beam in a strong electrostatic focusing channel experiences an aberration which can lead to an increase in beam emittance. The cause of this effect is that ions at a given axial location within the quadrupole channel do have variable energies, depending on their relative proximity to the electrodes. Variations in beam energy lead to a spread in betatron motion, which results in a kinematic aberration of the beam. This effect is most serious for low beam energy and strong quadrupole fields. The beam dynamics are further complicated by the facts that the interdigital geometry of the electrode package is fundamentally three dimensional and that the beam is space charge dominated. Detailed theoretical predictions required extensive 3-D PIC simulations and code developments with WARP-3D [3].

The engineering design and construction of the ESQ injector took about one year and was completed in October 1993. On the first day of operation, a K^+ beam in excess of the design parameters of 2 MV and 800 mA was produced. The current was measured for a range of Marx and pulser voltages, and the agreement with code predictions was excellent. The highest energy and current achieved thus far is 2.3 MV and 950 mA of K^+, or 15% above the design goals. We have not yet attempted to push the injector to its limit of performance.

The transverse emittance was measured with a double-slit scanner. Over a broad range of parameters, the measured normalized edge emittance was less than 1 π-mm-mr. As the current is increased, phase space distortions are enhanced, as predicted by theory and simulations.

We have successfully fine tuned the extraction pulser and Marx voltage to the point where the exiting beam is flat to less than $\pm 0.2\%$ over 1 μs. Variations in emittance and the beam envelope over the pulse duration are minimal.

2. BEAM COMBINING

Transverse beam combining is an important cost saving feature of standard driver designs for HIF. At the low energy end of a driver, electrostatic quadrupoles are used to focus each beam of the multiple beam array. Voltage breakdown and economic considerations dictate a small aperture for these quadrupoles and, thus, a large number of beams. At higher energies it is more economical to accelerate fewer, larger diameter beams through large aperture magnetic quadrupoles. Analysis indicates that transverse beam combining is best implemented at about 100 MeV.

Since space charge dominates beam dynamics for these intense beams, the interactions between particles during merging serve as a source of emittance growth, along with the usual 'phase space filling' seen, for example, in beam stacking in storage rings. As shown in previous work [4], transverse emittance growth is minimized by packing the beams as tightly as possible. Near the merge point the small space between beams makes it difficult to insert focusing structures with good field quality. The experimental challenge is to position the beams with sufficient accuracy to allow tight packing and to keep them focused as their centroids converge.

2.1. Description of the experiment

At LBNL, an experiment to demonstrate 4 to 1 transverse beam combining is under way [5]. The combiner consists of Cs^+ source, 200 keV diode and focusing transport channel for each of the four beams. The beamlines converge with an angle of 6° relative to the combiner centreline (Fig. 2). Four electrostatic quadrupoles, followed by an electrostatic combined function (quadrupole and dipole) element, are used to focus each beam and straighten its trajectory so that the beams emerge from the combiner almost parallel. The design configuration for the beam cross-sections as they emerge from the combiner is x–y asymmetric to allow good packing of the elliptical beams. After the combiner the merged beam will be transported and diagnosed through 30 lattice periods.

Because of length restrictions, matching of the beam from the cylindrically symmetric diode to the alternating gradient transport channel is done in the combiner rather than in a separate matching system. For the same reason, the need for initial

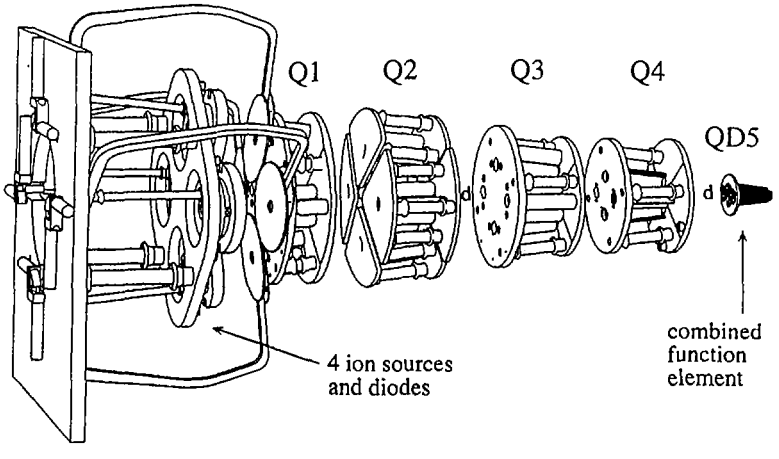

FIG. 2. Schematic of the combiner experiment (d: diagnostic location).

dipoles (that would bend the trajectories of the beams towards a common axis in a driver) has been removed by aiming the sources towards a common point of convergence. The first three combiner quadrupoles consist of circular electrodes, with the ratio of electrode radius to aperture set to minimize the lowest order 2-D non-linear field component — the dodecapole. At the fourth quadrupole, the space between beams is too small for cylindrical electrodes; so hyperbolic electrodes have been designed which both shield the beams from each other and produce minimal field non-linearity.

The small spacing between the beams at the downstream end of the fifth lattice element does not allow adequate space for large electrodes. Quadrupole and dipole fields are instead produced by surrounding the beams with an elliptical 'squirrel cage' of tungsten rods,. The rods have a spacing of ~ 1 mm and are nearly parallel to the beam path. The voltage on each rod is set so that the rods approximate the correct Dirichlet boundary condition. Since the beams emerge from the combiner separated by about 4 mm, their clearance from the rods within the squirrel cage is only about 1.5 mm near the exit of the cage. Thus, beam alignment must be correct to the submillimeter level.

2.2. Simulation results and status of the experiment

Experiments and simulations of the current carrying capacity of MBE-4 have indicated that the MBE-4 channel can transport a low emittance (unmerged), 20 mA beam with only a few per cent beam loss. This implies that beam merging experiments of four, ~ 4 mA beams could be possible with relatively little beam loss. Following this result, transport through the entire combiner, with both merging and subsequent transport of the merged beam, has been simulated using the 2-D electrostatic PIC code HIBEAM. The results further substantiated the practical nature of the design.

Image effects of the electrodes of the first four quadrupoles, field aberrations in the squirrel cage, phase space filling and the conversion of electrostatic potential energy of the beams to transverse thermal energy during the merging process all increase the emittance. Beam loss is negligible. The simulations demonstrate that this experiment is, like a driver, in the regime where both space charge and phase space filling determine the final emittance growth. Because of the relatively large spaces between the small beams in this experiment, the emittance growth is proportionately larger than it would be in a driver, where the much larger beams are expected to have approximately the same separation. Simulations have shown adequately low emittance growth for the driver.

At present, all components of the combiner have been fabricated, aligned and installed. At the time of this writing, experiments are under way to measure the distribution function of the beams at the entrance to the squirrel cage for detailed comparison to the simulations above. Later, the effect of the combiner on one beam will measured, followed by four-beam merging experiments.

3. EXPERIMENTS IN BENDING AND RECIRCULATION

A recirculating induction accelerator (recirculator) potentially offers reduced cost relative to a 'conventional' linac because the accelerating and focusing elements are reused many times in a single target shot. The overall accelerator length is reduced (to about 3.6 km in the 'C-design' recirculator of Ref. [6], and possibly less), and the accelerating cores are smaller and are not driven so close to saturation because it is not necessary to accelerate the beam at the maximum possible rate. The recirculator designs considered to date employ greater axial pulse compression than is typically assumed for linac designs, with a smaller number of longer beams used initially, and do not employ beam combining. Current research on recirculator drivers has centred on multiring designs, with each ring augmenting the beam's energy by an order of magnitude over ~ 100 laps. Relative to a 'conventional' linac, the length is reduced by a factor of order two to three, but the beam path length increases to perhaps ~200 km. Hybrid designs (with a recirculator at the low energy end) are also possible.

The beam dynamics issues which must be resolved before a recirculating driver can be built include centroid control, longitudinal beam confinement, acceleration schedule, avoidance of phase space dilution in bends and insertion/extraction of the beam into/out of the rings. As will be described below, these can be addressed at reduced scale in a small prototype recirculator. The waveform generators in a driver must supply variable accelerating pulses at ~ 100 kHz repetition frequencies, and accurate time varying dipole fields with good energy recovery. These requirements are challenging, but advances in solid state power electronics should make it possible to meet them through a technology development programme. Collisional interactions can drive beam or gas ions into the walls of the beam pipe and so cause the desorption of wall material. This material will interact with the beam on its next pass. Thus, and because of the long path length, a high vacuum of 10^{-10} to 10^{-11} torr is especially important. There remain uncertainties in some of the relevant cross-sections; many of these can be resolved through experiments on existing accelerator facilities.

3.1. Experimental programme

LLNL, in collaboration with LBNL, is currently developing a small prototype heavy ion, recirculating induction accelerator. This 'small recirculator' is intended to explore, in a scaled manner, the physics and technology issues involved in constructing a full scale recirculating driver. The small recirculator will be assembled and operated as a series of experiments over several years' time. Over the past year a linear transport experiment using permanent magnet quadrupoles was carried out. The next major experiment will be a study of beam transport around a bend (initially without acceleration). In the later experiments, the machine will be operated in a full recirculating mode with a variety of beam manipulations, requiring sophisticated pulsed power waveform synthesis.

The small recirculator will have a circumference of 14.4 m, a 3.5 cm aperture radius for the beam focusing and bending elements, and a half-lattice period (HLP) of 36 cm. The beam will be transversely focused by permanent magnet quadrupoles with a field of ~0.3 T at the pipe wall and will be bent with electric dipole deflector plates. The quadrupoles and dipoles will each occupy about 30% of the axial lattice length, and the full ring will consist of 40 HLPs, including two large aperture quadrupole magnets through which the beam will be inserted and extracted. The K^+ beam will be accelerated from an initial particle kinetic energy of 80 keV to 320 keV over 15 laps by 34 induction cores. The current will increase from 2 to 8 mA, with half of the current amplification from halving the length of the bunch, the other half from doubling the velocity. The phase advance of the betatron motion of the ions in the ring will range from $\sigma_0 = 78°$ to 45° per lattice period in the absence of beam space charge, and from $\sigma = 16°$ to 12° in its presence. The average beam radius will be ~1.2 cm.

Since the heavy ion beam in the small recirculator is non-relativistic and accelerating, the waveforms required to accelerate (via pulses supplied to the induction cores) and bend the beam (via voltages applied to the electric dipole plates) will be technologically challenging. The induction waveforms will require the accurate synthesis of detailed voltage pulses with a repetition rate increasing from 40 to 90 kHz at the initial and final beam energies, because of the increasing beam velocity. Furthermore, detailed 'ear' pulse structures and lap to lap variation of the pulse duration must control the beam length. A prototype induction modulator has been developed which meets these demands on repetition rate and pulse variability. The voltage waveform for the electric dipoles must also be correctly timed with respect to the pulses that power the induction cores for beam acceleration. A modulator which produces the precise, high voltage, temporally ramped dipole voltage pulse is under development at LBNL.

Until the rest of the ring is complete it will be possible to employ intercepting diagnostics and to use these to calibrate the non-intercepting diagnostics that will be critical to operation of the full ring. The ring will incorporate two extraction sections, so the extracted beam can be diagnosed with detailed intercepting diagnostics twice each lap. As with earlier linac experiments at LBNL, excellent shot to shot repeatability is anticipated.

As of this writing, the source and the injector diode are in operation, and a beam has been transported through a linear focusing channel consisting of an electrostatic quadrupole matching section, which is a modified segment of LBNL's SBTE apparatus, and a magnetic transport section consisting of seven quadrupole magnets. The design of the HLP for the recirculator ring has been completed, aided substantially by simulations using the 3-D PIC code WARP-3D. The simulations allowed the dipole plates to be shaped, minimizing the sextupole component and providing equal focusing in the two transverse directions. Two HLPs are undergoing final alignment; the beam through them is expected in September 1996. Capacitive, non-intercepting diagnostics for beam centroid monitoring have been developed, tested and calibrated.

Additionally, the beam has been well characterized by using a number of intercepting diagnostics. For additional details on results of the linear transport experiments, see Ref. [7].

ACKNOWLEDGMENTS

This work was supported by the Director, Office of Energy Research, Office of Fusion Energy, US Department of Energy, under Contract Nos DE-AC03-76SF00098 and W-7405-ENG-48.

REFERENCES

[1] ABRAMYAN, E.A., GAPANOV, V.A., At. Ehnerg. **20** (1966) 385.
[2] ANDERSON, O.A., et al., in Particle Accelerators (Proc. Conf. Chicago, 1989).
[3] FRIEDMAN, A., et al., Phys. Fluids B **4** (1992) 2203.
[4] CELATA, C.M., FALTENS, A., JUDD, D.L., SMITH, L., TIEFENBACK, M.G., in Particle Accelerators (Proc. Conf. Washington, DC, 1987) 1167.
[5] CELATA, C., et al., Fusion Eng. Des. **34** (1997) 223.
[6] BARNARD, J.J., et al., Phys. Fluids B: Plasma Physics **5** (1993) 2698.
[7] FESSENDEN, T.J., et al., Intense heavy-ion beam transport with electric and magnetic quadrupoles, Fusion Eng. Des. (in press).

DIAGNOSTICS FOR HIGH DENSITY IMPLOSIONS AT THE NATIONAL IGNITION FACILITY*

M.D. CABLE[1], T.W. BARBEE, R.A. LERCHE, M.B. NELSON,
M.J. MORAN, D.B. RESS, T.C. SANGSTER, J.E. TREBES,
R.E. TURNER, T.W. PHILLIPS
Lawrence Livermore National Laboratory,
University of California,
Livermore, California

D. HICKS, C.K. LI, R.D. PETRASSO, F. SEGUIN
Plasma Fusion Center,
Massachusetts Institute of Technology,
Cambridge, Massachusetts,

United States of America

Abstract

DIAGNOSTICS FOR HIGH DENSITY IMPLOSIONS AT THE NATIONAL IGNITION FACILITY.

The proposed National Ignition Facility (NIF) is a large (1.8 MJ on target at 0.35 μm) multibeam laser facility that will be used for Inertial Confinement Fusion (ICF). ICF implosions at this facility will produce core plasma temperatures over 10 keV and densities over 100 g/cm^3. The properties of these plasmas can be measured by a variety of optical, X ray and nuclear diagnostic techniques such as those used at existing facilities like the Nova laser at the Lawrence Livermore National Laboratory (LLNL). Some of these currently used techniques will be directly applicable to NIF; others require significant development. Damage of components close to the target will be a much greater issue at NIF, necessitating the development of distant detector techniques. X ray based core diagnostics will need to utilize substantially higher energies than are in routine use today. Penetrating, nuclear particle based diagnostics will be particularly well suited to these implosions, and the higher nuclear yields will allow new techniques to be developed. A summary of diagnostics used for high density implosion experiments at Nova and development of new techniques for NIF are discussed.

* This work was performed under the auspices of the US Department of Energy by Lawrence Livermore National Laboratory under Contract No. W-7405-ENG-48.

[1] Current address: University of Rochester, Laboratory for Laser Energetics, Rochester, NY, USA.

2. Introduction

The National Ignition Facility (NIF) will deliver ~1.8 MJ of 0.35 μm light onto mm scale hohlraum targets with the expectation of controlled thermonuclear ignition and gain (20 MJ yield). Ignition targets will achieve core plasma temperatures in excess of 10 keV and densities of order 100 g/cm^3. Under these conditions, the expected fusion yields of up to 10^{19} neutrons will far surpass the record neutron yields achieved at Nova (4×10^{13}) and, more recently, at the Omega Laser Facility at the University of Rochester (10^{14}). Before the first ignition experiments can occur, however, a comprehensive set of diagnostic measurements will be required to characterize the performance of both the laser and the hohlraum targets. Many of these diagnostics have counterparts at laser facilities such as Nova; however, some will require the development of new techniques and instrumentation.

The diagnostics required to validate NIF hohlraum targets fall into two distinct categories: (1) those used to measure the hohlraum temperature and radiation drive spatial symmetry, and (2) those used to characterize the performance of the imploding capsule. The first category of diagnostics will utilize x ray imaging systems and shock break-out measurements; the second category will rely heavily on nuclear reaction products and very high energy x ray based techniques. The implosion diagnostics are discussed below.

3. Fuel Areal Density

The compressed fuel areal density (<ρR>) at burn time is a critical parameter for an ICF implosion. In order for a capsule to ignite and burn, a <ρR> of 1–2 g/cm^2 is required. At Nova, <ρR> is determined by measurements of secondary neutrons[1,2,3] produced in the following two-step reaction sequence in initially pure deuterium fuel:

1) $d + d \longrightarrow p + t$ (1.01 MeV t)
2) $t + d \longrightarrow \alpha + n$ (11.8–17.1 MeV n)

Since the probability that the energetic triton produced in reaction 1 produces a "secondary" neutron in reaction 2 is a function of the fuel <ρR> through which the triton passes, a measurement of the number of secondary neutrons and a determination of their energy spectrum can be used to determine areal density. However, the 1.01 MeV triton range must be greater than the fuel <ρR> to be determined, limiting this technique to values less than about 0.1 g/cm^2.

For larger targets with higher yields, a similar measurement can be made of "tertiary" neutrons produced in the following three-step reaction sequence in a mixed deuterium and tritium fuel:

3) $d + t \longrightarrow \alpha + n$ (14.05 MeV n)
4) $n + d \longrightarrow n' + d'$ (0–12.5 MeV d)
5) $d' + t \longrightarrow \alpha + n$ (12–30 MeV n)

Note that high-energy tertiary neutrons are also produced if reaction 4 (elastic scattering) occurs between a neutron and a fuel triton or even between the alpha particle produced in reaction 3 and a fuel deuteron or triton. However, the sequence shown results in the highest reaction product energies. Figure 1 shows the neutron energy spectrum produced from all reactions for a Nova scale implosion.

The probabilities of both reactions 4 and 5 occurring are dependent upon the fuel <ρR> through which the energetic particle initiating the reaction passes. Thus, as for the secondary neutron case, a measurement of tertiary neutrons can provide a determination of fuel areal density. In this case, however, the energies of the charged particles (and, correspondingly, their ranges) are much higher. Tertiary neutron measurements can be used to determine fuel areal densities up to several g/cm^2. At Nova, secondary neutron measurements are made with an array of neutron time of flight detectors[4]; the yields and areal densities are too low to allow detection of tertiary neutrons. However, at NIF, even pre-ignition experiments will result in high enough yields and areal densities that a similar instrument will allow measurements of tertiary neutrons.

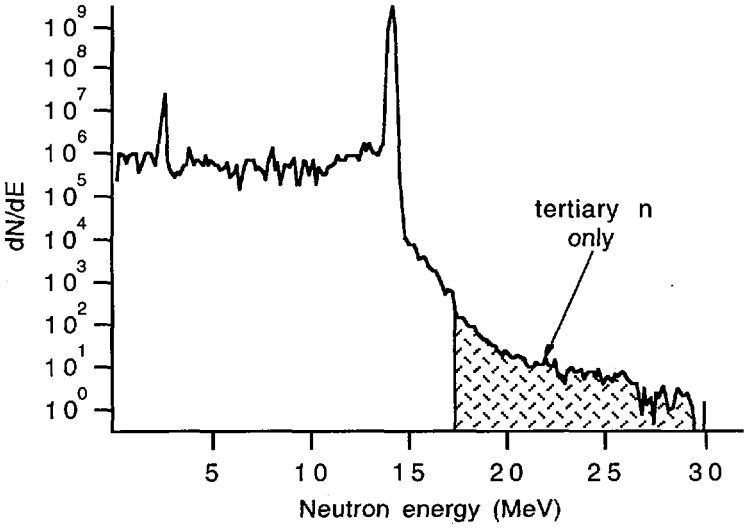

FIG. 1. Neutron energy spectrum for a deuterium and tritium filled Nova target. The region containing only neutrons from the tertiary sequence of reactions is shaded.

4. Nuclear Reaction History

Nuclear reaction rate measured as a function of time (nuclear reaction history) is an important quantity to determine the dynamics of the implosion process. At Nova, nuclear reactions proceed at a measurable rate for the 100–200 ps of the implosion. Neutron yield is measured as a function of time with <30 ps-resolution, using a neutron sensitive, plastic scintillator located a few centimeters from the target[5]. Light from this scintillator is imaged to a streak camera located outside the target chamber. The fast rise time of the scintillator (<20 ps) allows a deconvolution of the observed signal that results in a measurement of the reaction history. Figure 2 shows data obtained from a typical Nova target[6].

The scintillator is located close to the target in order to avoid the time dispersion associated with the spread in neutron velocities due to the broadening of the energy spectrum for neutrons produced in a high temperature plasma (see below). For NIF, the high energy of the laser and the even higher energies of

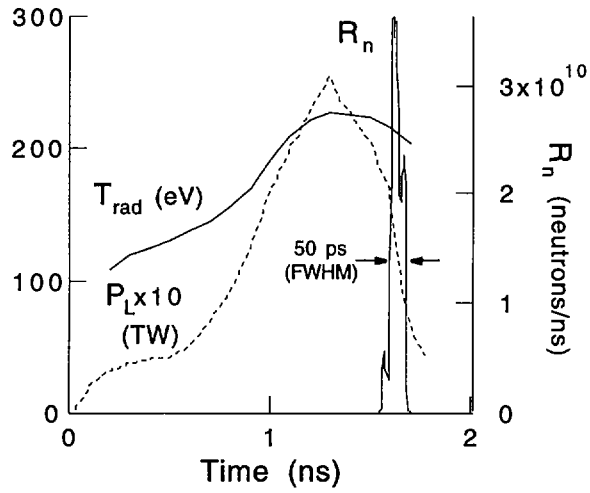

FIG. 2. Nuclear reaction history measured at Nova with the neutron based technique shown relative to the laser power (P_L) and the hohlraum radiation temperature (T_{rad}).

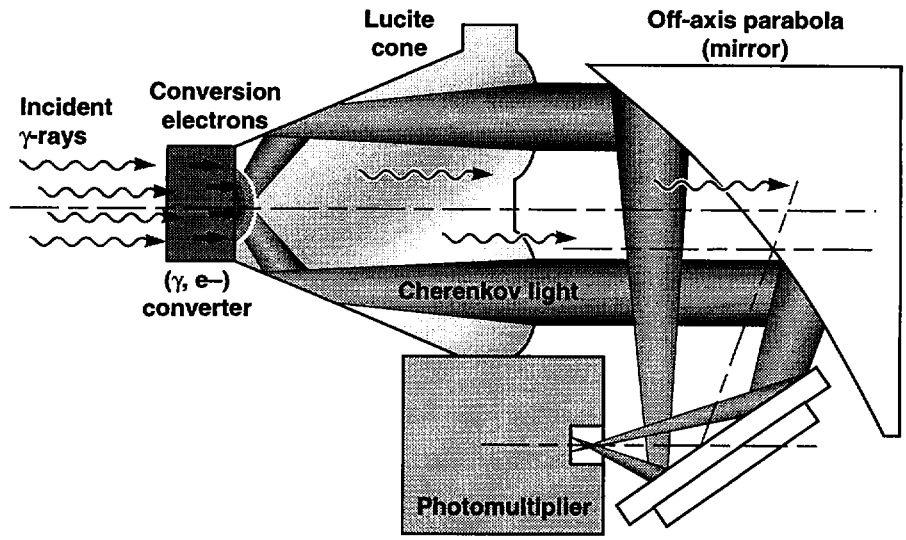

FIG. 3. High efficiency Cherenkov radiator. High energy γ rays scatter high energy electrons into the Lucite Cherenkov cone, which is designed to reflect and focus light onto a detector at the focal plane.

high gain targets will preclude locating diagnostic components this close to the target. Therefore, a system based on measurement of the 16.7 MeV γ rays produced in the $^3H(d,\gamma)^5He$ reaction is being developed. These γ rays are produced in much smaller numbers (branching ratio approximately 5×10^{-5}) than the primary neutrons from the $^3H(d,n)^4He$ reaction, so a sensitive, background resistant technique is required.

One such approach currently under development at LLNL is to replace the scintillator with an aerogel foam that serves as a low density Cherenkov radiator. Incident high energy γ rays react in a surrounding Hevimet shield to produce high energy positrons and electrons, which travel into the foam and produce Cherenkov light if they are above the several MeV threshold determined by the index of refraction of the aerogel used. This system can be made very insensitive to lower energy photons and has been used successfully to observe high energy γ rays at Nova. In order to increase system sensitivity and thus allow operation with the detector several meters from a NIF target, high efficiency Cherenkov radiator designs are also being developed. Figure 3 shows a diagram of a specially shaped Lucite radiator designed so that the cone angle matches the conical angle of emission of the Cherenkov light, thus allowing efficient collection and focusing from a large solid angle[7].

5. Fuel Ion Temperature

Another important parameter of an ICF implosion is the fuel ion temperature. Nuclear reactions between the fuel ions produce products with energy spectra that are dependent upon the ion temperature (Doppler broadening)[8]. In particular, neutron time-of-flight spectroscopy has been used to measure the energy spectra of the 2.45 MeV neutrons from the $D(d,n)^3He$ reaction, and of the 14.05 MeV neutrons from the $^3H(d,n)^4He$ reaction[9]. For the relatively low yields and temperatures of present facilities, such as Nova, it has been necessary to use sensitive, high resolution spectrometers based on arrays of time of flight detectors similar to those used for the secondary neutron measurements described above[10]. For the higher yields and temperatures of NIF, simpler current mode detectors will suffice to measure the burn averaged fuel ion temperature. For this measurement, maintaining clear, well collimated flight paths around the crowded target area is likely to be the major consideration for obtaining good measurements.

However, higher yields and temperatures not only simplify measurements of burn averaged temperature, but additionally open the possibility of time resolved ion temperature measurements. Nuclear reactions at NIF will occur over a period of several hundred picoseconds in the final stages of the implosion (see the discussion of reaction history above), thus making it possible to observe the evolution of the fuel temperature during this time. There are two possibilities under consideration. The first is a neutron time of flight based measurement. However, as in the measurements of nuclear reaction histories, the broadened energy spectrum of neutrons produced from a high temperature target results in time dispersion at the end of the flight path. This necessitates a simultaneous determination of both the arrival time and the energy of each neutron. Such a measurement can possibly be achieved via, for example, an array of proton recoil detectors, however the high resolution required for both the time (<50 ps) and energy (<20 keV) measurements makes it challenging. A second approach, which may turn out to be simpler, is to use a γ ray based system to circumvent the time dispersion problem, as is being done for reaction history measurements. Here,

the ion temperature measurement would be made using a direct energy measurement of the Doppler broadened γ ray spectrum from an appropriate nuclear reaction. Time resolution could be achieved by a gating technique. Technology development appropriate for both approaches is currently underway.

6. Imaging

Implosion symmetry for ICF has been typically measured with various x ray imaging schemes. For NIF, the larger target sizes and thicker shells will necessitate the use of more penetrating radiations than currently used. Higher energy x rays, neutrons and γ rays are all potentially useful.

X ray imaging at Nova is done predominantly with systems requiring components close to the target (e.g., pinholes). In order to allow a larger stand-off distance at NIF and to work at x ray energies that will penetrate from the core, a high energy (8 keV) x ray imaging system based on a multi-layer coated Wolter optic is being developed. Using conventional fabrication techniques will result in an unaffordable cost for multiple imagers, so the use of replica fabrication techniques is being pursued. In this approach, a Wolter shaped mandrel is manufactured and coated with the material to be used for the mirror surface. The mandrel surface figure and roughness are critical, but costs are reduced because its exterior surface is accessible compared to the interior surface of a conventionally manufactured Wolter. The mandrel is then coated with a backing material, and the whole assembly is cooled. Differential contraction is used to break the Wolter mirror surface free from the mandrel. The mandrel can be re-used multiple times.

Neutron images of the implosion cores at Nova have been obtained by use of a thick neutron aperture and a penumbral imaging technique[11]. A new system based on this method is currently under development at Nova and should produce images with 20 micron spatial resolution. A similar system is being designed for use at NIF. The main difficulty anticipated with the NIF system is the necessity to move the aperture far from the target. The high magnification system currently used (200) would then result in an unreasonably long system; thus high resolution neutron detectors that can be used in a lower magnification instrument are being developed. γ ray based systems are also under consideration, since gated instruments could be developed that give time-resolved images similar to those obtained with x ray based instruments. Such images are difficult to obtain with neutrons, due to the Doppler broadening discussed above.

7. Charged Particles

A variety of nuclear reactions produce multi-MeV charged particles that can escape from the implosion core and be used to make measurements complementary to those discussed above. A general use magnetic spectrometer based on an innovative scheme using CCDs as single particle charged particle detectors is being developed at Massachusetts Institute of Technology for use at Nova and Omega and eventually at NIF[12]. Such a detector will allow measurements of fuel areal density similar to those discussed above, utilizing neutron-based techniques. In particular, tertiary protons are produced in the following three-step reaction sequence in a mixed deuterium, tritium, and ^{3}He fuel:

6) $d + t \longrightarrow \alpha + n$ (14.05 MeV n)
7) $n + d \longrightarrow n' + d'$ (0–12.5 MeV d)
8) $d' + {}^3He \longrightarrow \alpha + p$ (13–31 MeV p)

Most NIF target designs utilize a cryogenic fuel shell surrounding a central gas-filled region where the ^{3}He will be localized. This central region then converges to become the "hot spot" where burn originates in the capsule. Proper formation of this hot spot is essential to high gain ICF target designs. With the ^{3}He localized to this region, an areal density measurement based on tertiary protons gives the areal density of the hot spot, which nicely complements the areal density measurement of the total fuel obtained in the tertiary neutron technique discussed above.

The highest energy protons in the above sequence of reactions are only produced if the momenta vectors of the neutron, deuteron, and proton in reactions 7 and 8 are close to collinear. Thus, if measurements focus on high energy (>28 MeV) tertiary protons, then the areal density is determined specifically along a line from the center of the target to the detector. Multiple detectors placed at different angles could therefore be used to determine implosion symmetry. (This is also true for tertiary neutrons, but the larger, array-style detectors used for that measurement make multiple detectors less practical.) Also, energy loss as the proton leaves the target will be sensitive to the amount of material along the path of the proton, allowing another determination of asymmetries.

8. Conclusion

Many new target-measurement techniques will become possible at NIF due to the higher yields and larger targets. Damage issues and higher backgrounds also necessitate the development of new methods. However, many of the proposed schemes require technology development prior to implementation as a NIF diagnostic. A vigorous program to develop such technologies and to subsequently design and field appropriate NIF diagnostics is underway.

REFERENCES

[1] BLUE, T.E., HARRIS, D.B., Nucl. Sci. and Eng. **77** (1981) 463.
[2] AZECHI, H., et al., Appl. Phys. Lett. **49** (1986) 555.
[3] CABLE, M.D., et al., Bull. Am. Phys. Soc. **31** (1986) 1461.
[4] NELSON, M.B., CABLE, M.D., Rev. Sci. Instr. **63** (1992) 4874.
[5] LERCHE, R.A., et al., Rev. Sci. Instr. **66** (1995) 933.
[6] CABLE, M.D., et al., Phys. Rev. Lett. **73** (1994) 2316.
[7] LEWIS, K.P., et al., Rev. Sci. Instr. **63** (1992) 1988.
[8] BRYSK, H., Plas. Phys. **15** (1973) 611.
[9] LERCHE, R.A., et al., Appl. Phys. Lett. **31** (1977) 645.
[10] CHRIEN, R.E., et al., Rev. Sci. Instr. **63** (1992) 4886.
[11] LERCHE, R.A., et al., Laser Part. Beams **9** (1992) 99.
[12] PETRASSO, R.D., et al., to be published in Phys. Rev. Lett.

THEORETICAL STUDIES ON UNIFORMITY AND STABILITY IN DIRECT DRIVE LASER FUSION

K. NISHIHARA, H. TAKABE, M. MURAKAMI, R. ISHIZAKI,
J.G. WOUCHUK, M. HONDA, A. SUNAHARA, S. HASEGAWA,
Y. SHIMUTA, Y. UESHIMA, H. AZECHI, H. SHIRAGA,
H. NISHIMURA, N. MIYANAGA, M. NAKAI,
K. SHIGEMORI, Y. FUKUDA, K. MIMA
Institute of Laser Engineering,
Osaka University,
Suita, Osaka

A. NISHIGUCHI
Electrical Engineering,
Osaka Institute of Technology,
Osaka

H. SAKAGAMI
Computer Engineering,
Himeji Institute of Technology,
Himeji City

Japan

Abstract

THEORETICAL STUDIES ON UNIFORMITY AND STABILITY IN DIRECT DRIVE LASER FUSION.

Uniformity and stability issues are investigated for three phases of a laser implosion process: startup, acceleration and stagnation. Hydrodynamic perturbation growth in the startup phase seeds the Rayleigh–Taylor (RT) instability in the subsequent phases. An analytical model is developed to study the propagation of a rippled shock and the deformation of an ablation surface driven by non-uniform laser ablation. Agreement between theory and experiment is found in the propagation of the shock front ripple and also in areal mass density perturbation. A new instability of the uniform contact surface is found to be driven by the rippled shock. For both linear and non-linear cases, the growth rate depends on the phase of the oscillating shock wave at the time when the shock hits the contact surface. Exact analytical solutions of the linear growth rates for the Richtmyer–Meshkov instability are found for both reflected shock and reflected rare action cases. They agree well with recent experiments. Two dimensional (2-D) Fokker–Planck heat transport is introduced in a 2-D hydrodynamic code to study the RT instability at the ablation surface. Non-local heat transport is shown to play an important role in reducing the growth rate. 2-D simulations are also carried out to study the neutron yield reduction observed in the GEKKO XII laser implosion experiments. It is found that odd number non-uniformity is dominant in repelling the fuel from the centre and in reducing the neutron yield. A new type of self-similar solution, which determines the stagnation dynamics, is obtained, and the density gradient generated by the conduction is shown to reduce the RT growth.

1. INTRODUCTION

To achieve ignition and high gain in inertial confinement fusion, a spherical pellet must implode efficiently and symmetrically. The laser implosion process can be divided into three phases: startup, acceleration and stagnation. A shock wave driven by the laser ablation propagates through a shell in the startup phase, and shell acceleration follows. The ablation surface and the interface between the hot core and the surrounding cold main fuel are Rayleigh–Taylor (RT) unstable in the acceleration and stagnation phases, respectively. Hydrodynamic perturbation growth in the startup phase seeds the RT instability in the subsequent acceleration and stagnation phases. Uniformity and stability issues corresponding to the three phases are investigated systematically.

As startup problems, we consider smoothing of laser absorption non-uniformity in the ablation layer, propagation of a rippled shock driven by non-uniform laser ablation and the Richtmyer–Meshkov (RM) instability at the shocked interface. Initial target surface roughness and non-uniform laser irradiation cause ripple on the shock front and deformation of the ablation surface. In addition, a shocked interface becomes unstable both when a uniform shock passes through a corrugated interface (RM instability) and when a rippled shock passes through a uniform interface. A unified analytical model is developed to describe all these hydrodynamic perturbation growths. Analytical results are compared with recent experiments [1, 2]; good agreement is shown. We have also analysed the uniformity requirement for target surface, DT full surface and laser irradiation.

The RT instability at the ablation surface is investigated by a newly developed, two dimensional Fokker–Planck simulation code. The 2-D Fokker–Planck simulation shows that the growth rate of the RT instability becomes much lower than that obtained by Spitzer–Harm simulation. Beam smoothing and power balance of the GEKKO XII laser system have been achieved, and a proof of improvement has been given by the increase of neutron yield by two orders of magnitude [3]. However, a factor of ten yield reduction remains in the experiment, compared with 1-D simulations. 2-D simulation shows that odd mode non-uniformity is dominant in repelling the fuel from the target centre and in reducing the neutron yield.

On the basis of a new type of self-similar solution which determines the dynamics of the stagnation, the density gradient generated by the conduction is found to reduce the RT growth substantially. The turbulent interface of a fully developed RT instability in the stagnation phase is also investigated by a 2-D simulation code and by applying multifractal theory.

2. HYDRODYNAMIC PERTURBATION GROWTH IN THE STARTUP PHASE

2.1. Smoothing of non-uniformity in the ablation layer

Smoothing of perturbations in a steady state ablative flow is studied with an analytical model [4], in which the obviously invalid boundary conditions that were commonly used in previous analytical models are corrected. As a result, it turns out that the momentum flux perturbation is smoothed down even more significantly than the perturbations in the previous models. On the other hand, the mass flux perturbation, which is supposed to affect the subsequent RT instability as the seed, decays much less effectively than the momentum flux perturbation and is roughly reproduced by the cloudy day model. The smoothing effect is essentially attributed to lateral fluid flow and heat transport. However, one should keep in mind that such smoothing performance may be subject to preceding initial imprints at the very beginning of laser illumination.

2.2. Rippled shock wave and ablation surface deformation by non-uniform laser ablation

A simple analytical model is developed to study the propagation of a rippled shock driven by non-uniform laser ablation induced by initial surface roughness of

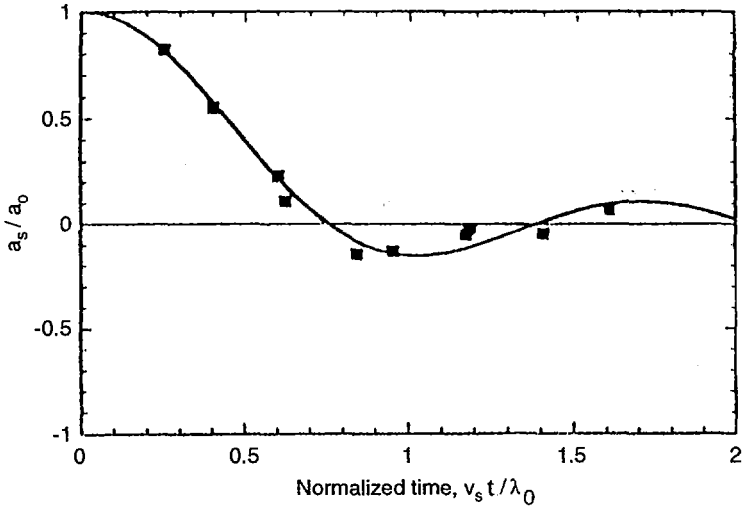

FIG. 1. Shock front ripple a_s/a_0 as a function of normalized time $v_s t/\lambda_0$. Solid line: theory; squares: experiment. a_0 is the initial target surface roughness and u_s the a shock speed. The parameters used are $I = 4 \times 10^{13}$ W/cm^2, $\lambda_r = 0.53$ μm; a CH target and a perturbation wavelength of 100 μm.

a target and non-uniform laser irradiation. We can demonstrate the behaviour of the rippled shock and ablation fronts by solving a wave equation of the pressure perturbation in the shock compression region with suitable boundary conditions, for example, the Rankine–Hugoniot jump condition at the shock front [5–7], and the Chapman–Jouguet deflagration jump condition at the laser ablation surface [8].

When uniform ablation pressure is applied to a target with rippled surface, a rippled shock wave is launched, corresponding to the target surface. Once a shock front is rippled, a pressure perturbation is induced by the lateral fluid motion behind the shock front. This pressure perturbation causes the ripple of the shock front to be reversed and subsequently to oscillate and the perturbation amplitude of the ablation front to grow. In the weak shock limit, we obtain approximate formulas for the shock front ripple and the asymptotic value of the ablation front deformation. In Fig. 1, we compare the theoretical value with the experimental results [1] on the shock front ripple. Both oscillation period and decay rate of the shock front perturbation agree quite well with experiments. Agreement between theory and experiment is also found in the areal mass density perturbation induced by the rippled shock propagation.

We also investigate a rippled shock induced by non-uniform laser irradiation. In this problem, since non-uniform ablation pressure is continuously supplied by laser irradiation, a finite growth rate of the ablation deformation exists. We obtain approximate formulas for the perturbation amplitude of the shock front and the asymptotic velocity perturbation of the ablation front.

2.3. Instability of a contact surface driven by the rippled shock wave

A new instability of the contact surface is found; it is driven by a rippled shock wave [7]: a uniform contact surface becomes unstable when a rippled shock wave passes the surface. We obtain a theoretical equation for the growth rate in linear evolution by regarding this instability as a gravitational instability where the acceleration is induced by the velocity perturbation of the shock front and by the oscillatory, damped pressure perturbation behind the shock. The equation shows clearly that growth rate and direction strongly depend on the phase of the oscillating shock at the time when the shock hits the contact surface. The non-linear evolution of the instability is also investigated for a large amplitude of the rippled piston. The contrast in Fig. 2 shows the isodensity contour for an Atwood number of $A = -0.5$, in a reference frame that moves with the piston. As shown in Fig. 2, a mushroom shape of the unstable contact surface appears when the shock hits the uniform contact surface at the phase when the shock front distortion is maximum, while the square shape appears when the shock front velocity perturbation is maximum. For both linear and non-linear cases, the growth rate depends essentially on the phase of the oscillating shock.

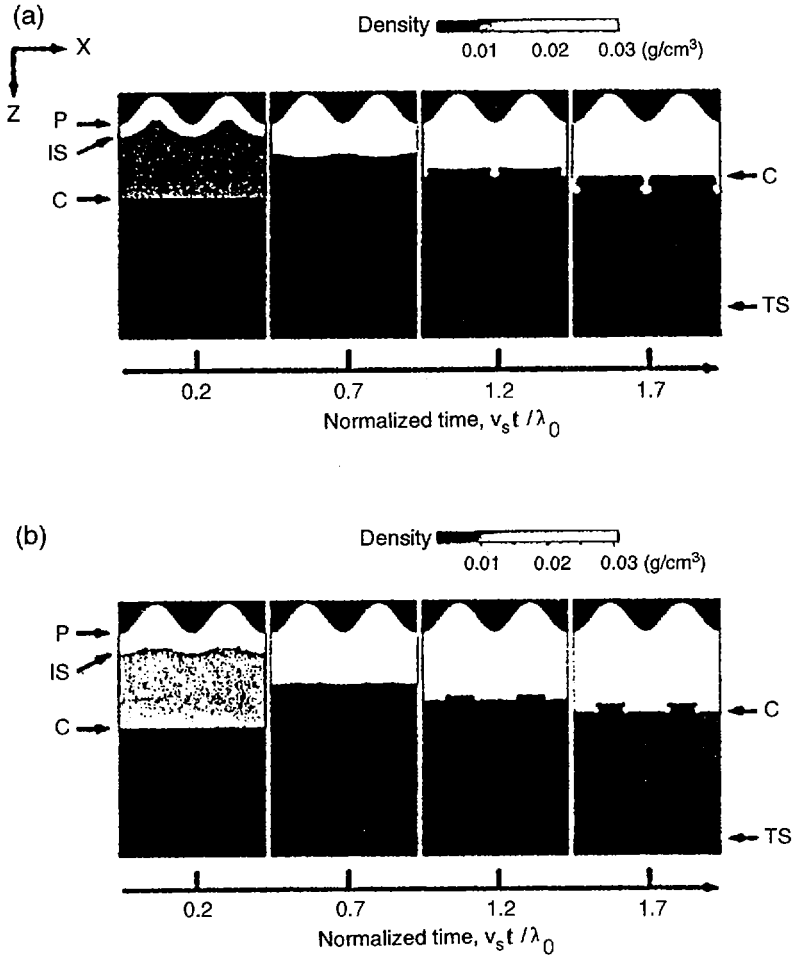

FIG. 2. Non-linear evolution of uniform contact surface instability shown by isodensity contours with contrast for an Atwood number of −0.5. P, IS, TS and C stand for ripple piston, incident rippled shock, transmitted shock and contact surface, respectively. Pictures are taken at (a) 0.2, 0.7, 1.2 and 1.7; (b) 0.4, 0.9, 1.4 and 1.9 of normalized time.

2.4. Richtmyer–Meshkov instability

Any time a shock wave crosses an interface that separates two fluids with different thermodynamic properties, vorticity is deposited at the interface. This vorticity is responsible for later interface growth, a phenomenon known under the name of Richtmyer–Meshkov instability [6]. As the shocks separate away, the pressure perturbations that bounce between the fronts and the interface interact with the zero

order density gradient at the interface, generating additional velocity deposited at $t = 0+$. This later vorticity generation can increase or reduce its original value. It is possible to obtain the analytic form of the perturbed pressure in the homogeneous zones between the shock fronts and the interface. This allows us to obtain a formula for the interface asymptotic velocity in the limit of weak incident shock:

$$\delta v_i \approx k v_i \frac{R\psi_{i0} - \left(1 - \frac{v_1}{v_i}\right)\psi_{r0}}{R + 1} \tag{1}$$

where k is the interface perturbation wavenumber, R the ratio of final densities, the velocity v_1 is the fluid velocity behind the incident shock and the velocity v_i is that acquired by the interface after shock refraction at $t = 0+$. ψ_0 is the initial interface perturbation amplitude. The amplitudes ψ_{i0} and ψ_{r0} are the amplitudes of the transmitted and reflected shocks at $t = 0+$, respectively. When a rarefaction is reflected, the same formula is obtained for the asymptotic interface velocity, but ψ_{r0} must be replaced by ψ_{r0}, the amplitude of the rarefaction tail at $t = 0+$. In Fig. 3, we show a comparison between the last formula and experiments performed at LLNL [2]. The horizontal axis corresponds to the experimental values and the vertical axis to the values predicted by the model formula. Fair agreement is seen, except for the shortest wavelength perturbations.

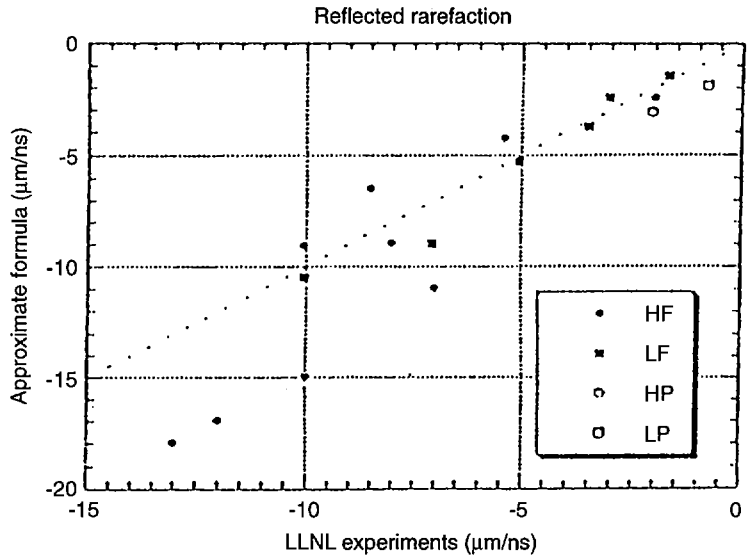

FIG. 3. Comparison of RM growth rates between theory and experiment for the rarefaction reflected case. HF, LF: high and low frequency, HP, LP: high and low power.

Another quantity that is of interest — because it is accessible to experiments — refers to the mass areal density perturbations that are left by the shocks. As the shocks move away, they leave residual entropy perturbations that are frozen to the fluid elements. These perturbations in entropy give rise to perturbations in density that do not decay in time [9].

If the rarefaction surface of the shell, i.e. the DT fuel surface, is corrugated, a large distortion of the rarefaction surface of ψ_{r0} is found to be generated when the shock passes through the interface. This large distortion affects the ablation surface stability because the rarefaction wave propagates towards the ablation surface. The requirement for the DT fuel surface smoothness becomes much less stringent than that predicted before.

3. RAYLEIGH–TAYLOR INSTABILITY IN ACCELERATION AND STAGNATION PHASES

3.1. Non-local heat transport effects on Rayleigh–Taylor instability

On the laser ablation front, non-local properties of the electron heat transport play an important role, even for moderate intensity laser irradiation, because the electron mean free path is comparable to the scale-length of the temperature gradient.

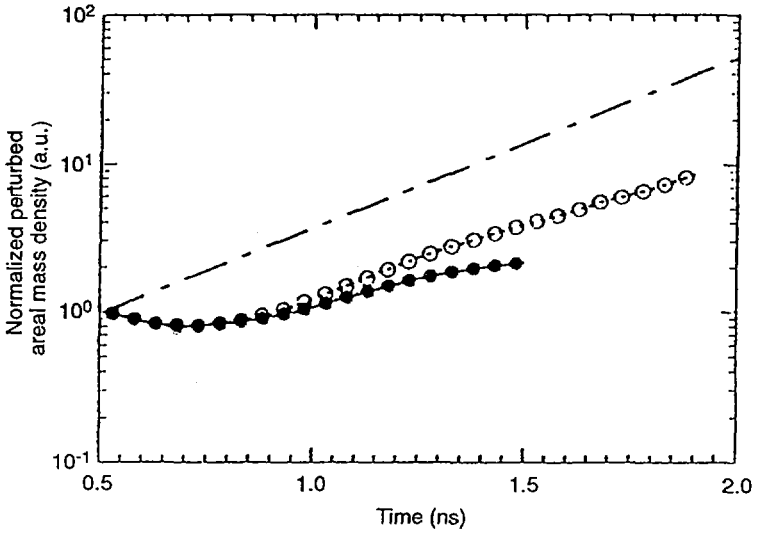

FIG. 4. Linear growth of RT instability. The solid line with closed circles and the dashed line with open circles correspond to the Fokker–Planck and Spitzer–Harm cases, respectively. The dash-dotted line shows the classical growth.

The energy spectrum of the electrons in the coronal plasmas typically becomes bi-Maxwellian, and the high energy tail electrons cause significant preheating of the cold dense region. Hence, it is expected that the target expansion due to preheating enhances the ablative stabilization of the RT instability. We have developed a two dimensional, spatial co-ordinate and one dimensional velocity space multi-diffusion Fokker–Planck (FP) simulation code which is coupled with an ideal fluid equation [10].

Let us present the results of RT instability analysis in Fig. 4 [11]. We have found that the linear growth rate of the RT instability in the Spitzer–Harm (SH) simulation is 1.5 times higher than that in the FP simulation. This reduction may be explained by preheating of the ablation front by the non-local electron thermal transport. At 1.0 ns, the corona plasmas are heated up to ~ 1 keV, and the maximum mass densities are 1.47 g/cm^3 (FP) and 1.94 g/cm^3 (SH), respectively. Thus, it is found that significant target swelling occurs in the FP simulation, even though the absorbed laser intensity is moderate. The linear growth rates of the RT instability in Fig. 4 are found to be 1.4 ns^{-1} (FP) and 2.1 ns^{-1} (SH), respectively; the classical growth rate is 2.6 ns^{-1}, where $k = 1.0 \times 10^3$ cm^{-1}, $g = 6.7 \times 10^{15}$ cm/s^2. At 1.5 ns, the ablation velocities in both cases are $v_a = 2.7 \times 10^5$ cm/s (FP) and 2.4×10^5 cm/s (SH), respectively, so that the ablative flow is enhanced in the FP case because of the density lowering of the ablation front; the mass ablation rates are almost the same in both cases. We can then roughly calculate the numerical factor of the ablative stabilization term in Takabe's formula [12]. It has been found that the results show the values of $\beta = 4.4$ (FP), and 2.4 (SH), respectively.

3.2. Simulations of GEKKO XII implosion experiments

Beam smoothing and power balance of the GEKKO XII laser system have been achieved, and improvement has been demonstrated in the implosion experiments [3], which were analysed by both 1-D and 2-D codes. The full 2-D simulation was used to study the neutron yield reduction in the weakly non-linear regime, and also a second order Godunov code in the Eulerian scheme has been developed to study details of two dimensional hydrodynamics in the stagnation phase. With this code, we mainly focus on the effect of relatively long wavelength perturbation modes with odd ℓ numbers. With such a non-uniformity, the target centre is no longer singular and the kinetic energy of implosion cannot be converted to thermal fuel energy and, hence, degrades the fusion performance.

In the implosion experiment, a prepulse of 0.2 ns width is separated from the 1.6 ns width main pulse by a gap; this time interval is used as a parameter. By increasing the pulse gap, we can reduce the ablation front density in order to enhance ablative stabilization. We have compared this with 1-D simulations for real shots. For example, shot No. 16 623, in which a CH shell of 488 mm diameter and 0.2 mm thickness, filled with 30 atm DD fuel, is irradiated by 1.63 kJ on target with a 0.4 ns gap, has a yield that is one order of magnitude below the 1-D result. For shot

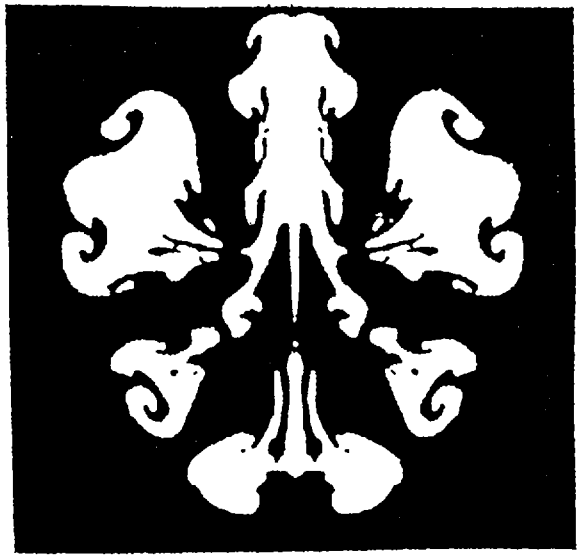

FIG. 5. DD fuel concentration distribution in the stagnation phase with $\ell = 1$ and $\ell = 6$ modes having the same amplitudes.

No. 16 623, the perturbations generated by laser non-uniformity have been calculated for modes of $\ell = 2$–50 with the 2-D code. In the acceleration phase, small ℓ modes are dominant, while in the stagnation phase large ℓ modes start to grow, owing to the RT instability.

Normalized neutron yield, which is defined by the neutron yield in the 2-D code divided by that in the 1-D code, has been obtained. The velocity non-uniformity of the pusher when the shock wave collides at the target centre ($t = 2$ ns) is used as a parameter. In order to explain the factor of ten yield reduction in the experiment, we conclude that 20–30% velocity perturbations are generated in the acceleration phase. We note that the modes of $\ell = 1$ and $\ell = 6$ are imposed with the same amplitude. In Fig. 5, a typical simulation result of the DD fuel concentration near the peak emission rate of the neutrons is shown for the case that odd mode non-uniformity is dominant in repelling the fuel from the target centre.

3.3. Dynamics and stability of a stagnating hot spot

To assess the feasibility of ignition and high gain, using down sized targets, two aspects of implosion should be addressed, i.e. the growth factor of the fluid instabilities (hydrodynamically equivalent) and hot spot formation. Concerning the latter aspect, a simple model [13] is developed, where the key parameters are the maximum

areal density, the peak central temperature and the implosion velocity. The dynamics is dominated by mechanical compression work and thermal conduction loss. A new type of self-similar solution is then found, describing the fluid motion. The RT instability in the stagnation phase is evaluated by using the self-consistent spatial profile with density gradients, which is attributed to the thermal conduction. Substantial reduction of the RT growth is then found, compared with previous work without density gradients.

The turbulent interface of a fully developed RT instability in the stagnation phase is also investigated with the 2-D code. Generalized fractal dimension and singularity spectrum are obtained as functions of time.

4. SUMMARY

We have investigated uniformity and stability for three phases of laser implosion: startup, acceleration and stagnation. A unified model is developed to analyse different types of hydrodynamic perturbation growth in the startup phase, such as ablation surface deformation or shocked interface instabilities. The analytical results agree quite well with the experiments. Different 2-D simulations are carried out to further our understanding of the ablative stabilization of the RT instability and the neutron yield reduction observed in the GEKKO XII experiments. The 2-D FP simulation leads to a reduction in the RT growth rate. Odd number non-uniformity is also found to be important for an explanation of the neutron yield reduction. The stabilizing effect of the density gradient in the stagnation phase is also studied.

REFERENCES

[1] ENDO, T., et al., Phys. Rev. Lett. **74** (1995) 3608.
[2] DIMONTE, G., FRERKING, C.E., SCHNEIDER, M., REMINGTON, B., Phys. Plasmas **3** (1996) 614.
[3] MIMA, K., et al., Phys. Plasmas **3** (1995) 2077.
[4] MURAKAMI, M., Phys. Plasmas **3** (1996) 2710.
[5] ZAIDAL, P.M., J. Appl. Math. Mech. **24** (1960) 316.
[6] RICHTMYER, R.D., Commun. Pure Appl. Math. **13** (1960) 297.
[7] ISHIZAKI, R., et al., Phys. Rev. E **53** (1996) 5592.
[8] TAKABE, H., et al., J. Phys. Soc. Jpn **45** (1978) 2001.
[9] WOUCHUK, J.G., NISHIHARA, K., Phys. Plasmas (in preparation).
[10] EPPERLEIN, E.M., Phys. Rev. Lett. **61** (1988) 2453.
[11] SHIGEMORI, K., et al., to be published.
[12] TAKABE, H., MIMA, K., MONTIERTH, L., MORSE, R.L., Phys. Fluids **28** (1985) 3676.
[13] MURAKAMI, M., SHIMOIDE, M., NISHIHARA, K., Phys. Plasmas **2** (1995) 3466.

DEVELOPMENT OF PLASMA LAYERING TECHNIQUE FOR CRYOGENIC LASER FUSION TARGET

T. NORIMATSU, M. TAKAGI, Y. IZAWA,
T. YAMANAKA, K. MIMA
Institute of Laser Engineering,
Osaka University,
Suita, Osaka,
Japan

Abstract

DEVELOPMENT OF PLASMA LAYERING TECHNIQUE FOR CRYOGENIC LASER FUSION TARGET.

Fabrication of a cryogenic target with a uniform solid fuel layer is one of the key technologies for the success of laser fusion. The authors have proposed a plasma layering technique in which a non-uniform solid fuel layer is redistributed into a uniform one, with a glow discharge initiated in the void by an external intense microwave field. This technique produces a uniform, crack free solid fuel layer in a much shorter time than beta layering does. The plasma layering was demonstrated by using solid deuterium frozen in a reactor size quartz shell at the centre of a microwave cavity. Optically opaque and localized, the solid hydrogen turned into a more uniform, transparent shape after initiation of the discharge; the time constant of the redistribution was 80 s.

1. INTRODUCTION

Cryogenic targets with a uniform, crack free solid fuel layer are required to demonstrate thermonuclear ignition and burn. Candidates for the production of a cryogenic target are beta layering [1], IR layering [2], plasma layering [3] and the foam method [4]. Beta layering can redistribute a non-uniform, solid deuterium–tritium (D–T) layer into a uniform one by simply keeping the target in an isothermal environment. If there is a negative radial temperature gradient in the solid hydrogen, voids and cracks in the solid layer move inward through a sublimation and deposition cycle. It is well known that the time constant for the redistribution is 28 min for fresh D–T fuel without ^{3}He. In other words, it takes one hour to obtain a solid D–T layer with a thickness uniformity of $>99\%$, and the long time needed for the redistribution results in a large tritium inventory in the pellet factory of a future laser fusion reactor.

In the IR layering, the principle itself is similar to beta layering but the heat source is provided by an IR laser. In both techniques, the heating processes are volumetric. As a result, the radial temperature gradient is zero at the inner surface of a solid layer of average thickness. Voids and cracks in this area cannot be removed by this technique.

The plasma layering technique can reduce the time required to produce the uniform solid fuel layer. When a cryogenic pellet located in an isothermal environment has a uniform heat source at the centre of the pellet that can uniformly heat the inner surface of the solid fuel layer, the inner surface temperature of thicker areas becomes higher than that of thinner areas. This temperature difference induces sublimation of the solid hydrogen in thicker areas and condensation of the vapour in thinner areas. As a result, the non-uniform solid fuel layer becomes uniform, in analogy to that seen in the beta layering method. Plasma layering can be used to smooth both solid deuterium and deuterium–tritium fuel layers inside a plastic capsule. Since the heating process in this technique is surface heating, a radial temperature gradient exists in the solid hydrogen layer, even after the solid layer has become uniform. This technique has the capability to eliminate voids and cracks more efficiently than does a volumetric process.

2. ISSUES TO BE SOLVED

The principle of plasma layering was already demonstrated by using Kr gas cooled by liquid nitrogen instead of deuterium with liquid helium as a coolant. However, the following issues remain to be solved:

(1) Ultimate uniformity achievable in a one dimensional external electric field

In the current plasma layering technique, the pellet is located in a microwave resonator in order to initiate a glow discharge in the void of the pellet. The heating uniformity depends strongly on the gas density in the void since the discharge is one dimensional. Some technique is required to keep the discharge as an abnormal glow discharge.

(2) Time constant for the redistribution

The time constant is theoretically estimated to be primarily determined by the cooling rate of the pellet. The actual time constant in the system has to be studied.

(3) Peeling-off of the solid deuterium due to the large temperature gradient at the inner surface induced by plasma heating

The discharge in a microwave field of constant intensity is expected to be intermittent, which may cause a heat shock in the solid hydrogen.

(4) Cracks and deformation in the solid deuterium during heating of the pellet from 11 K for plasma layering to 17 K for implosion

The plasma layering will be carried out at 11 K, and laser irradiation of the cryogenic pellet will be done at 17 K. Since the solid hydrogen has a large volume expansion rate, cracks may happen during the heating process.

(5) Isotope separation

In the future reactor class pellet, the maximum neutron yield will be obtained from a fuel with 60% deuterium and 40% tritium since some of the tritium will be produced through D–D reactions. During the redistribution process, light D–D molecules move faster than D–T molecules leaving tritium at the site. As a result, the deposited area may be rich in deuterium and the etched area rich in tritium. This non-uniform distribution of isotopes results in a non-uniform density which may degrade the implosion performance.

3. EXPERIMENTAL SET-UP

We have measured the time constant for the redistribution by using a 6 mm diameter quartz shell with a gas feeder. The shell used in this experiment is of non-uniform thickness, ranging from 30 μm at the bottom to 300 μm at the top. The shell is located at the centre of a microwave cavity at 10 K that is housed in a liquid He cooling jacket as shown in Fig. 1.

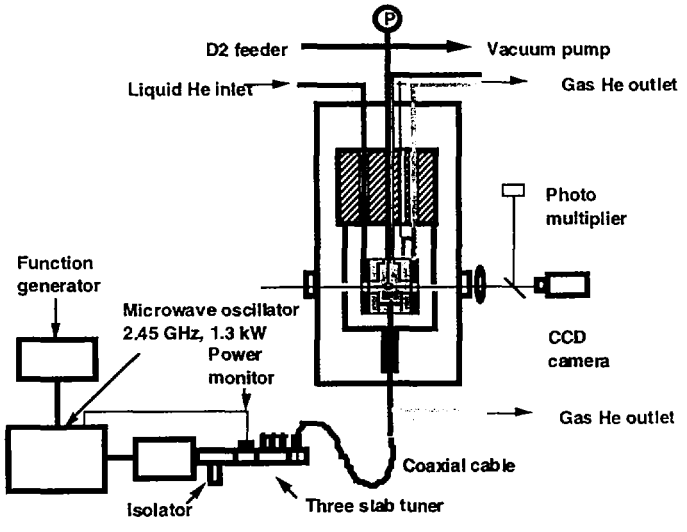

FIG. 1. Schematic diagram of apparatus to demonstrate plasma layering.

The jacket is filled with 1 atm helium gas to cool the shell efficiently and also to prevent a discharge outside the shell. The major cooling process is free convection cooling.

After an appropriate amount of deuterium has been frozen in the shell, 2.45 GHz microwave pulses are fed into the cavity through a coaxial cable. Since the inner diameter of the gas feeder is 30 μm, the feeder is automatically plugged with solid hydrogen after initiation of the discharge. The power of the microwave in duty is 50 W. The pulse width and the repetition rate are varied from 0.1 to 100 ms and 500 to 10 pulses per second, respectively. Visible emission from the glow discharge is detected by a photomultiplier so that the characteristics of the discharge become known.

4. RESULTS

The visible emission from the discharge is shown in Fig. 2. When the pulse width of the microwave is longer than 0.2 ms, the discharge time is almost independent of the width of the microwave pulse. The longest discharge time is 0.5 ms, with a full width at half maximum that can be explained by a simple model in which the dissipated power is used to heat the sublimated gas and a very thin surface layer of solid deuterium. The discharge is automatically quenched by a rapid increase in the

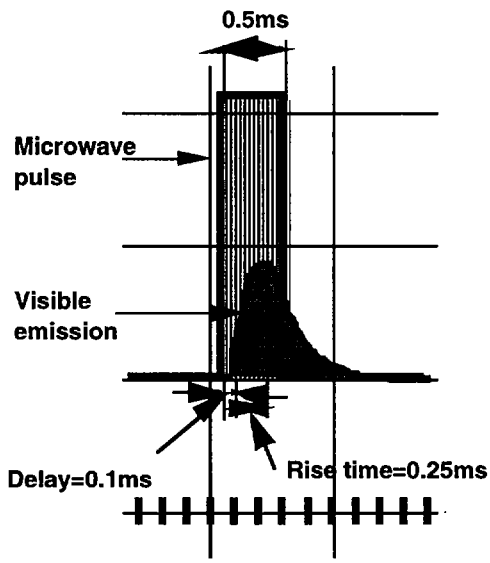

FIG. 2. Oscilloscope traces of visible emission from glow discharge in the void of solid hydrogen and microwave pulse.

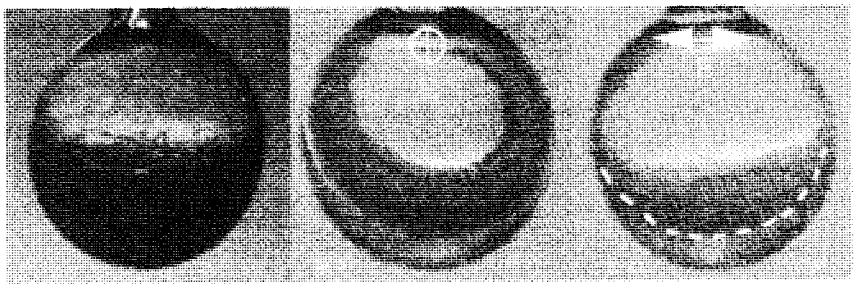

FIG. 3. Redistribution of solid deuterium by 0.1 ms microwave pulses: (a) before discharge; (b) view from discharge axis; (c) view perpendicular to the electric field.

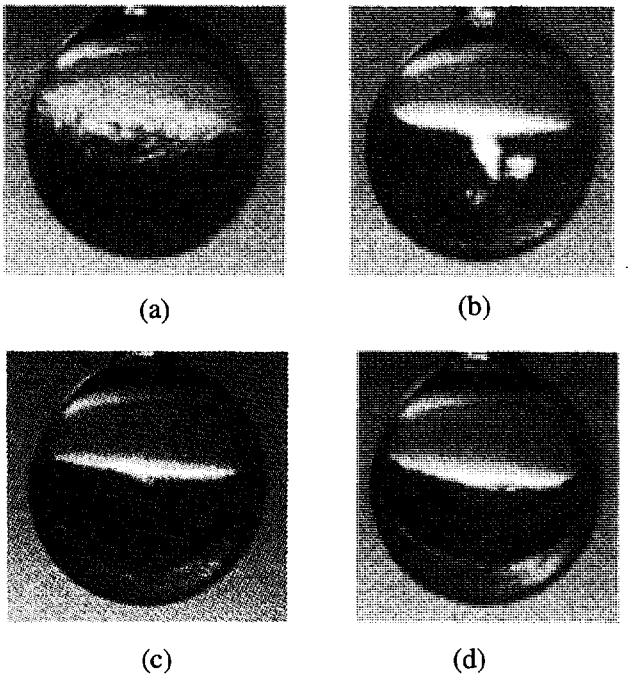

FIG. 4. Temporal change of solid deuterium seen from the discharge axis: (a) before discharge; (b) 30 s; (c) 90 s; (d) 180 s after start of discharge.

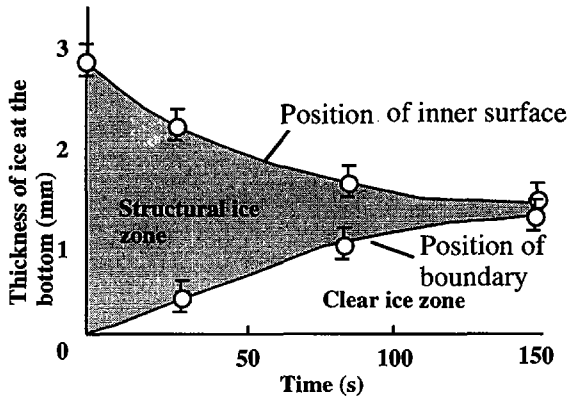

FIG. 5. Temporal change of solid deuterium layer thickness. Time constant of redistribution: 80 s (estimate).

vapour pressure in the void. In this case, the uniformity of heating is insufficient because the discharge moves into a normal glow discharge region and no redistribution of solid hydrogen takes place in the direction of the electric field.

When the microwave pulse width is less than half the longest discharge time, the solid deuterium at the bottom of the shell is successfully redistributed to the upper region of the shell, as is shown in Fig. 3.

The temporal change of the solid deuterium after the discharges is shown in Fig. 4. Note that with the lapse of time the initially opaque solid deuterium becomes transparent from outside to inside. This means that cracks grown during the freezing process are swept away. In parts (b) and (c) of the figure, the inner surface of the opaque solid deuterium is not shown clearly. However, it could be observed with backlighting of the discharges. The temporal change in the thickness of the solid deuterium layer at the bottom of the shell is shown in Fig. 5. The thickness approaches its ultimate thickness exponentially and from the bottom a clear ice zone appears that is initially opaque because of cracks; the clear solid deuterium zone expands to the inner surface. From this exponential change, we can estimate that the time constant for the redistribution by plasma layering is 80 s, i.e. one tenth of that of the beta layering method.

During the discharges, no cracks larger than 10 μm (optical resolution limit) were observed in the solid deuterium layer. After the redistribution is over, the shell is heated up to the designated temperature. When the heating rate is less than 0.5 K/min, no crack is optically observed.

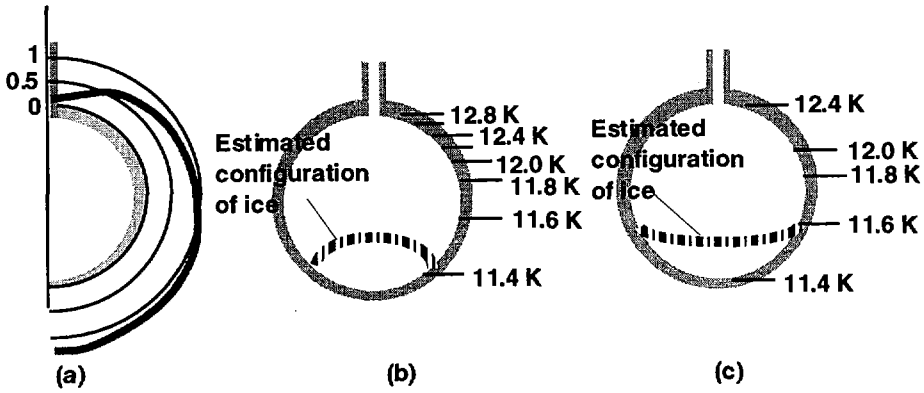

FIG. 6. Estimated temperature and configuration of solid deuterium: (a) using a steady state local heat transfer coefficient [5]; (b) with tangential heat conduction in the glass wall; (c) with high heat conduction material such as solid hydrogen.

5. DISCUSSION

5.1. Effect of convection cooling

Although uniform heating and cooling are essential in this technique, the influence of free convection of He gas around the shell is unavoidable for a stationary shell in a 1 atm He gas.

We have estimated the influence of the convection on the configuration of the ice layer. For simplicity, the inner surface of the shell is assumed to be heated uniformly. The tangential heat flow in the glass wall is numerically calculated by using steady state, local heat transfer coefficients as reported in Ref. [5] (Fig. 6(a)). The results are summarized in Figs 6(b) and (c), where the total heat dissipation in the shell is 10 mW and the temperature of the cooling He gas is 10 K. Actually, 98.5% of the resistance to heat transfer occurs between the shell and the microwave cavity. The influence of the glass wall non-uniformity is less than 1.5%. If we ignore the heat conduction in the ice layer, a temperature difference of 1.7 K exists between the top and the bottom of the shell, and the configuration of the ice is almost spherical. If we assume that the shell is made of high heat conduction material such as solid hydrogen, the temperature difference is 1.0 K and the solid deuterium is smeared on the inner surface as is shown in Fig. 6(c).

Our experimental results were better than both cases. This discrepancy is attributed to the transient cooling in our experimental conditions. The heating process is intermittent, and solid deuterium and wall play the role of heat capacities. The transient cooling uniformity is much better than the steady state cooling uniformity.

5.2. Black zone in optical images

During the discharges, a black zone is seen in optical images, as is shown in Figs 4(c) and (d). What we know of this black zone is that this zone:

(a) always appears during discharges;
(b) cannot be explained by refraction of light at the inner surface of solid deuterium;
(c) expands to an upper glass area when the power dissipation per pulse is large; and
(d) disappears when the shell is slowly heated up to 17 K after the discharges.

On the basis of these observations, we think of two candidates:

One possibility is that this black zone is due to the frost of solid deuterium. Since the thermal conductivity of solid hydrogen is 50 times as large as that of glass, the solid hydrogen more quickly cools the vapour than the glass wall, resulting in frost on the inner surface of the ice layer only. The second possibility are microcracks on the inner surface caused by intermittent heating.

Since this black zone disappears with the lapse of time after the discharges, this problem is not serious from the viewpoint of target quality.

6. SUMMARY

Smoothing of a solid deuterium layer by plasma layering is demonstrated for the first time; the time constant for the redistribution was 80 s. Experimental results indicate that plasma layering can redistribute a non-uniform solid layer into a uniform one much faster than the beta layering does and can also eliminate cracks inside the solid layer. The shorter redistribution time is beneficial to reducing the tritium inventory in a future laser fusion reactor. No cracks due to intermittent heating by a glow discharge plasma were observed in the solid layer.

The ultimate uniformity achievable with this technique and the inner surface quality of the solid layer are under discussion.

In a future pellet factory, cryogenic targets with a uniform solid fuel layer will first be produced by plasma layering in order to generate a roughly uniform solid layer with no cracks or bubbles. During the discharges, the pellets will be slowly rotated to avoid non-uniform cooling by free convection. Then the pellet will be heated up to 18 K to enhance beta layering. By these processes, a solid fuel layer of 99% thickness uniformity will be produced at an acceptable production rate.

REFERENCES

[1] MARTIN, A.J., SIMMS, R.J., JACOBS, R.B., J. Vac. Sci. Technol. **A6** (1988) 1885.

[2] BITTNER, D., et al., "Formation of uniform solid D2 layers by IR-radiation", paper presented at 42nd Nat. Symp. American Vacuum Society, Minneapolis, October 1995.

[3] CHEN, C.M., NORIMATSU, T., IZAWA, Y., YAMANAKA, T., NAKAI, S., J. Vac. Sci. Technol. **A13** (1995) 2908.

[4] NORIMATSU, T., ITO, H., YASUMOTO, Y., TAKAGI, M., TANAKA, K.A., YAMANAKA, T., NAKAI, S., Rev. Sci. Instrum. **63** (1992) 3378.

[5] OMAR AWANG, M.A., RILEY, N., J. Eng. Math. **17** (1983) 355.

LASER SCATTERING IN LARGE SCALE LENGTH PLASMAS RELEVANT TO NATIONAL IGNITION FACILITY HOHLRAUMS*

B.J. MacGOWAN, R.L. BERGER, B.B. AFEYAN, C.A. BACK, M.A. BLAIN[1], B. CANAUD[1], B.I. COHEN, D.E. DESENNE[1], K.G. ESTABROOK, S.H. GLENZER, D.E. HINKEL, R.K. KIRKWOOD, W.L. KRUER, A.B. LANGDON, B.F. LASINSKI, D.S. MONTGOMERY, J.D. MOODY, C. ROUSSEAUX[1], C.H. STILL, E.A. WILLIAMS
Lawrence Livermore National Laboratory,
University of California,
Livermore, California,
United States of America

Abstract

LASER SCATTERING IN LARGE SCALE LENGTH PLASMAS RELEVANT TO NATIONAL IGNITION FACILITY HOHLRAUMS.

Homogeneous plasmas of high density (up to 1.3×10^{21} electrons per cm^3) and high temperature (~3 keV) with large density scale lengths (~2 mm) were used to approximate conditions within National Ignition Facility (NIF) hohlraums. Within these plasmas, the dependence of stimulated Raman (SRS) and Brillouin (SBS) scattering on beam smoothing and plasma conditions at the relevant laser intensity (3ω, 2×10^{15} $W \cdot cm^{-2}$) was studied. Both SBS and SRS are reduced by the use of smoothing by spectral dispersion (SSD).

Current target designs for the NIF consist of gas-filled, gold hohlraums, 9 mm in length, heated with a 1.3 MJ laser (430 TW peak power) at 3ω (λ_0 = 0.351 μm wavelength)[1]. The laser energy is delivered to the hohlraum by 192 beams in shaped pulses about 15 ns long. The beams are focused with f/20 lenses arranged in clusters of 4 to produce effectively an f/8 beam. Beam smoothing, accomplished by the use of smoothing by spectral dispersion SSD[2], with kinoform random phase plates(RPP)[3,4], produces a flat top focal spot with an intensity that varies by a factor of two over the 3 to 5 mm laser path length within the hohlraum. At the time of maximum power the laser intensity peaks at $2\ 10^{15} W cm^{-2}$ at the best focus of the f/8 cluster, with other regions, along the beam path, at intensities between 10^{15} and $2\ 10^{15} W cm^{-2}$. Symmetric capsule implosions are accomplished by using two rings of beams, inner and outer, that reach the hohlraum wall at different distances from the laser entrance hole (LEH)

* This work was performed under the auspices of the US Department of Energy by Lawrence Livermore National Laboratory under Contract No. W-7405-ENG-48.

[1] Centre d'études de Limeil-Valenton, France.

and have different path lengths within the hohlraum plasma. Over most of their path length, the laser beams interact with a low-Z, fully-ionized gas (a mix of He and H_2), but for the last 400 μm, with high-Z, high-T_e gold plasma blown off from the hohlraum wall. The low-Z plasma between the hohlraum wall and the LEH has electron temperature (T_e) from 3 to 6 keV and electron density (n_e) from 7%n_{crit} to 12%n_{crit} , where n_e is expressed as a percentage of critical density (n_{crit} = 9 10^{21} cm^{-3} for 3ω). There is concern that the conditions within the plasma, together with the intensity of the laser beam, will lead to significant (>20%) scattering of laser light by stimulated Brillouin (SBS) and Raman backscattering (SRS)[6,7]. Calculations of the gain exponents, from linear theory, for SBS and SRS with plasma parameters taken from LASNEX[8] designs show both to be greater than 20[5,9]. For growth from thermal noise, gain exponents of 20 or larger result in significant reflectivities (>10%), in the absence of nonlinear effects other than pump depletion. In the gold plasma near the hohlraum wall, SBS is of particular concern because the acoustic wave is weakly damped.

The linear gain calculations do not include the small scale structure in the laser beam, hotspots with a typical intensity of twice the average local intensity whose length, $\lambda_s = 8f^2\lambda_0$, and width, $\lambda_{perp} = f\lambda_0$, vary with f, the f-number of the lens. Simulations and calculations have shown that inclusion of hotspots lowers by about a factor of 2 the average intensity at which significant reflectivity occurs[10]. Filamentation, i. e., self-focusing of the hotspots, is expected to increase the danger of SRS and SBS because it increases the amount of laser energy at high intensity. Without filamentation, the hotspot intensities have a distribution that decreases as $\exp(-I/I_0)$ with ~4% of the laser energy in hotspots with intensity greater than 5 times the average. The power in a typical hotspot, $4.10^{-8}I_0f^2\lambda_0^2$, is above the self-focusing threshold power [11] equal to $17(n_{crit}/n_e)10^6T_e(keV)$ (W), if $G = 5(I_0/2\ 10^{15}\ W{\cdot}cm^{-2})(f^2\lambda_0^2/T_e(keV))(n_e/n_{crit}) > 1$, where λ_0 is measured in microns. For the portion of the NIF beam path at $2\ 10^{15} W{\cdot}cm^{-2}$, filamentation is above threshold according to this simple criterion. However, the e-folding growth times for filamentation are slow enough (~10 ps) that temporal beam smoothing (e.g. SSD) with 0.8Å bandwidth (5 ps intensity autocorrelation time) is expected to restore stability by moving the hotspots faster than the plasma can respond. These estimates have been tested with F3D, a three dimensional laser propagation code that employs the paraxial approximation for the light wave, nonlinear hydrodynamics for the plasma response, and includes nonlocal heat transport[10]. The F3D results displayed in Fig. 1 show the reduction of filamentation with increase in SSD bandwidth in a low-Z plasma. The value plotted is the fraction of the laser light energy at intensity above 5 times the average. In an experiment we would expect to see a reduction in SBS and SRS backscatter as SSD reduces the fraction of the beam at high intensity. The modification of the intensity distribution function does not persist over a great length. Further into the plasma, the filamentation process diffracts the light to larger angles and the distribution of intensities returns to the initial one, namely, $\exp(-I/I_0)$, but with a decrease in the typical hotspot size and an increase in beam size characteristic of a smaller f-number (with a consequent decrease in I_0). Above the filamentation threshold and at sufficient depths into the plasma, the hotspot locations are not stationary but move about in a random manner. Intensity correlation times as short as 4 ps (equivalent to 1Å of SSD bandwidth) have been measured in simulations (for $I_0 = 2x10^{15}\ W{\cdot}cm^{-2}$). Thus, if

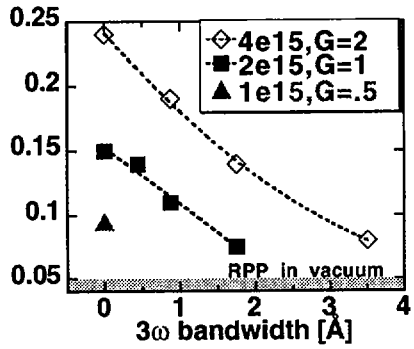

FIG. 1. Fraction of f/8 beam with intensity five times the spatial average (no time averaging). Filamentation in the plasma has increased this fraction above the 4–5% expected for an RPP beam in vacuum. (F3D simulation [10], CH_2 plasma, 10% n_{crit}, T_e = 3 keV, $I_0 = 10^{15}$, 2×10^{15} and 4×10^{15} $W \cdot cm^{-2}$.)

filamentation is required for the generation of large amounts of SBS and SRS, the process could limit SBS and SRS gain to regions where filaments first form.

The NIF laser 3ω bandwidth can be as large as 1.7Å but lower bandwidths are more desirable because the frequency conversion process is noticeably less efficient for bandwidths in excess of 0.8Å. SSD is not the only temporal smoothing scheme proposed for the NIF. A four colour scheme was also proposed in which each of the four f/20 beams in a cluster differed in wavelength by 3Å at 3ω. This scheme smooths the laser hotspots faster in fact than SSD but, unlike SSD, it cannot smooth at all spatial scales. That is, the hotspots that are formed as a result of the interference of beamlets from each phase plate within a given f/20 quadrant are never smoothed. Over the time scale that filaments form, the rapid motion of the small scale structure produces no hydrodynamic response but the f/20 hotspots can still self-focus. F3D simulations of 4 colours confirmed their ineffectiveness, provided the simulation allowed the laser to propagate the longer distance a lower intensity hotspot takes to self-focus.

Experiments were performed using the Nova laser at LLNL with targets developed to reproduce the plasma conditions and length scales of the NIF. The two plasma conditions that are important for the NIF are the inner beam plasma, which is a large scale length low-Z plasma with a high gain exponent for SRS and SBS, and the outer beam plasma which has shorter scale lengths and a higher gain exponent for SBS in the plasma near the gold wall[5]. The low-Z inner beam case was modeled with gasbag targets consisting of two membranes on either side of a thin washer which are inflated with an atmosphere of a heavy gas (typically C_5H_{12}) to produce an almost spherical volume of gas. Symmetric irradiation by nine "heater beams" leads to the production of a 6 -15%n_{crit} plasma with 1 - 2 mm scale lengths and T_e of 3 keV[12]. The NIF outer beam plasma was modeled with a cylindrical, "Scale-1" hohlraum, 1.6mm diameter by 2.7mm long, filled with methane gas. The gas retards the expansion of the gold wall and forms a shelf of gold similar in density and temperature to that seen by the NIF outer

beam[5], with a similar calculated gain exponent for SBS. The experiments used the tenth Nova beam as an interaction beam configured at f/8 and with the capability of either; 4-colour operation[13] with 1.4Å separation (at 3ω) between its 4 separate quadrants; or 1-colour, with all the quadrants the same wavelength.

Between April 1994 and March 1996 three experimental campaigns measured backscatter from the f/8 beam focused on these new targets, at irradiances near 2 10^{15}Wcm^{-2}, the peak intensity along the NIF beam path. The results from the first two campaigns indicated that 4-colour beam smoothing had little advantage over 1-colour in reducing SBS and SRS in gasbag plasmas. The experiments showed that adding ~0.5Å of SSD beam smoothing did reduce SBS and SRS at 10%n_{crit} [5]. The last f/8 interaction campaign, in March 1996, focused on a 1-colour laser configuration and investigated how much SSD bandwidth was required to reduce backscatter. This experiment also enlarged the parameter space in the gasbag measurements by studying plasmas whose density varied from 7% to 14% n_{crit}. The measurements also used the Scale-1 hohlraums to study the effect of beam smoothing on SBS on the outer NIF beam. During all of the measurements the f/8 interaction beam was smoothed with a random phase plate[3]. For the gasbags, the interaction beam was a 1 ns long constant power pulse with an intensity in the target plane of 2 10^{15}Wcm^{-2}. The Scale-1 hohlraums used a shaped pulse that increased its power in time, to a peak of 2.5 10^{15}Wcm^{-2}. SSD was added with a bandwidth of 0 to 1Å at 3ω.

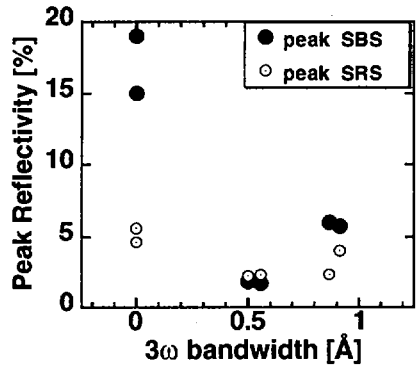

FIG. 2. SBS and SRS backscatter data from Scale-1 methane filled hohlraums with gold shelf plasmas similar to those encountered by the NIF outer beams. The reflectivity shown is the peak in time (averaged over the 50 ps diagnostic resolution), corresponding to the time of peak incident intensity (2.5 × 10^{15} W·cm^{-2}).

Fig. 2 shows SBS and SRS reflectivity as a function of SSD bandwidth for the scale-1 methane filled hohlraums. Both SBS and SRS are the peak value observed during the shaped pulse experiment, at the peak of the incident pulse. The quoted reflectivities include all backscatter from 0° out to 20° from the center of the beam. The SBS backscatter with no bandwidth is quite high (15-20%); addition of 0.5Å bandwidth reduces the SBS considerably (~2%). Two experiments were done at each bandwidth condition and the data seem reproducible. The experimental uncertainty is ±25% of the quoted value of reflectivity.

Similar results were obtained from the gasbag plasmas at densities of 7 - 7.5% n_{crit} and 9.5 -10%n_{crit}. The gasbag is heated by a 1 ns pulse of ~22kJ of 3ω light. The f/8 interaction pulse turns on at 0.5 ns and is 1 ns in duration. The f/8 interaction beam irradiance was kept fixed at 2 10^{15}W·cm^{-2} while the SSD bandwidth was varied from zero to 1Å at 3ω. The backscatter data are shown in Fig. 3 where the peak SBS is plotted together with the SRS at peak T_e (averaged over the 50 ps diagnostic resolution). The SBS peaks at 0.8 - 0.9 ns while the SRS is plotted at 1 ns, when T_e is a maximum, just before the heaters turn off and the plasma cools[5]. The effect of SSD bandwidth is shown in Fig. 3(a) for the 10% n_{crit} targets. SSD reduces SRS slightly from 7% to 4% , the effect on SBS is similar, 6% to 3%. For the lower density, 7.5%n_{crit}, data in Fig. 3(b), SBS reduces from 10% to 6% while SRS drops from 4% to 1%. At 10% n_{crit} there is a slight benefit to increasing the bandwidth from 0.5 to 1Å, while for the lower density plasmas and Scale-1 hohlraums, backscatter is minimized with 0.5Å bandwidth.

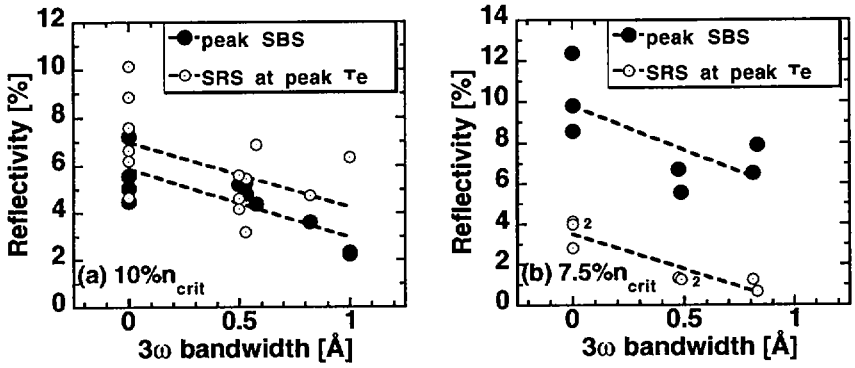

FIG. 3. (a) Peak SBS reflectivity, together with SRS reflectivity at peak T_e (t = 1 ns), from gasbag plasmas used to simulate the plasma encountered by the NIF inner beam at 10% n_{crit} at 2 × 10^{15} W·cm^{-2}; (b) similar data for 7.5% n_{crit} gasbags. Dashed lines are linear fits to the data, '2' indicates overlapping data points.

Apart from the reduction in SBS and SRS as SSD is applied, there is some additional evidence that the SSD is suppressing filamentation. Reference 5 describes SRS backscatter spectra from gasbags at 10%n_{crit} with and without SSD. SSD reduces the short wavelength SRS associated with lower density plasma. It is possible that this lower density SRS is coming from filaments where plasma has been moved out of the hotspot, reducing the density, while the higher intensity compensates for the lower SRS growth rate at low density. SSD, in reducing the fraction of energy at high intensity (Fig. 1), reduces the short wavelength SRS. In reference 5, and the newer experiments described here, the lower density SRS is reduced by either adding SSD or decreasing the laser intensity, both actions likely to reduce filamentation. The decrease in the total SRS at 10%n_{crit} is not large, as SSD is added, even though the SRS spectra indicate that filamentation has been

reduced. It is possible that the gain exponent for SRS at the average intensity is high enough that filamentation is not necessary to drive large levels of SRS. The best that SSD (at these limited bandwidths) can do is reduce the intensity seen by SBS and SRS to that of the vacuum propagated RPP (i.e. the SSD will prevent the plasma response increasing hot spot intensities further). Since the SSD bandwidth cannot alter the intensity distribution on time scales comparable to the growth time for SBS and SRS (0.1 - 1 ps) we reach the point where once filamentation has been stabilized, the bandwidth cannot do any more to reduce SBS and SRS.

A fuller discussion of this data and modeling will be published in a longer paper. However it is worth mentioning a trend in the data, shown in Fig 3, that is currently being studied. While the SRS is seen to increase with density, consistent with linear theory, the SBS decreases with increasing density, contrary to linear theory[14]. SBS decreases from 6% at 7.5%n_{crit} to 3% at 10%n_{crit} (Fig.3) to 0.3 - 0.4% between 11% and 14%n_{crit} (not shown). These trends are the subject of ongoing experiments that focus on the mechanisms that saturate SBS and SRS in large scale length, "NIF-like" plasmas[14,15]. However, the results of the studies shown here are that SBS and SRS in NIF-scale hohlraums should be at tolerable levels with moderate amounts of beam smoothing.

REFERENCES

[1] HAAN, S.W., et al., Phys. Plasmas **2** (1995) 2480.
[2] SKUPSKY, S., et al., J. Appl. Phys. **66** (1989) 3456.
[3] KATO, Y., et al., Phys. Rev. Lett. **53** (1984) 1057.
[4] DIXIT, S.N., et al., Opt. Lett. **19** (1994) 417.
[5] MacGOWAN, B.J., et al., Phys. Plasmas **3** (1996) 2029.
[6] KRUER, W.L., Phys. Fluids B **3** (1991) 2356.
[7] See, for example, ROSENBLUTH, M.N., SAGDEEV, R.Z., Handbook of Plasma Physics, Vol. 3: Physics of Laser Plasma, Elsevier, Ch. 9 and references therein.
[8] ZIMMERMAN, G.B., KRUER, W.L., Comments Plasma Phys. Control. Fusion **2** (1975) 85.
[9] BERGER, R.L., WILLIAMS, E.A., SIMON, A., Phys. Fluids B **1** (1989) 414.
[10] BERGER, R.L., et al., Phys. Rev. Lett. **75** (1995) 2078.
[11] MAX, C., Phys. Fluids **19** (1976) 74.
[12] KALANTAR, D.H., et al., Phys. Plasmas **2** (1995) 3161; GLENZER, S.H., et al., Phys. Rev. E (in press).
[13] PENNINGTON, D.M., et al., SPIE Proc. **2633** (1995) 214.
[14] MONTGOMERY, D.S., et al., Phys. Rev. Lett. (in press).
[15] KIRKWOOD, R.K., et al., Phys. Rev. Lett. **77** (1996) 2706; FERNANDEZ, J.C., et al., Phys. Rev. Lett. **77** (1996) 2702.

THE CRYOGENIC TARGET HANDLING SYSTEM FOR THE OMEGA LASER*

N.B. ALEXANDER, G.E. BESENBRUCH, W.A. BAUGH,
C.T. BEAL, K.K. BOLINE, L.C. BROWN, W. EGLI,
J.F. FOLLIN, C.R. GIBSON, D.T. GOODIN, R.Q. GRAM[1],
M.J. HANSINK, E.H. HOFFMANN, W. LEE, S.A. LETZRING[2],
R.A. MANGANO, J.D. McDANIELS[3], A. NOBILE[2], J. NASISE[2],
K.R. SCHULTZ, R.W. STEMKE, T.A. TORRES
General Atomics,
San Diego, California,
United States of America

Abstract

THE CRYOGENIC TARGET HANDLING SYSTEM FOR THE OMEGA LASER.

The next series of inertial fusion experiments will approach ignition conditions. To achieve sufficient power density to approach ignition conditions with reasonable laser power, these experiments call for cryogenic targets with a uniform condensed fuel layer and a smooth inner surface inside a thin spherical shell. To field such targets, General Atomics is designing and building the OMEGA Cryogenic Target System (OCTS) for the upgraded OMEGA laser at the University of Rochester's Laboratory for Laser Energetics (LLE). The OCTS contains subsystems that operate on targets to fill, freeze, transport, layer, characterize, position to laser confluence and expose them for laser illumination milliseconds before shot time. The OCTS will fill targets with deuterium-tritium (DT) to densities of up to 0.031 mol/cm^3. The pressure cell and rack that contains the filled targets is cooled to cryogenic temperatures in the fill system cryostat. The rack of targets is transferred cold by the cold transfer cryostat to the transfer station cryostat. The transfer station separates individual targets from the rack and inserts them into the moving cryostat. The moving cryostat transports a target out of the LLE tritium laboratory, layers the target and inserts the target into the center of the OMEGA target tank. Targets are characterized optically during a pause in the insertion. At shot time, the end of the cryostat is rapidly removed by high acceleration motors mounted in a port on the target tank directly opposite that used to insert the target. Prototypes of the target filling and cold transfer equipment have been built and operated with deuterium. Mounted targets were successfully filled to densities of 0.026 mol/cm^3. Cold transfer of high density targets into and out of the fill system with the cold transfer cryostat was also successfully carried out.

* Work supported by the US Department of Energy under Contract No. DE-AC03-95SF20732.

[1] Laboratory for Laser Energetics, Rochester, New York, USA.

[2] Los Alamos National Laboratory, Los Alamos, New Mexico, USA.

[3] NU-TEC, Solana Beach, California, USA.

1. INTRODUCTION

The next series of inertial fusion experiments will approach ignition conditions. These experiments are planned for the upgraded OMEGA laser at the University of Rochester's Laboratory for Laser Energetics (LLE) [1] and will lead towards ignition experiments in the National Ignition Facility [2] proposed to be built at Lawrence Livermore National Laboratory. To achieve sufficient power density to approach ignition conditions with reasonable laser power, these experiments call for cryogenic targets with a uniform condensed fuel layer and a smooth inner surface, distributed inside a thin spherical shell. To field direct drive high density cryogenic targets, General Atomics is designing and building the OMEGA Cryogenic Target System (OCTS) for the OMEGA laser.

1.1. Functions and Requirements

The OCTS accepts mounted but unfilled polymer shell targets and processes them up to the instant of the laser shot. The main processing steps are the permeation filling of the shells, layering the fuel uniformly and smoothly on the inside of the shell, characterizing the fuel layer, insertion of the target into the target chamber, and a rapid and timed exposure of the target to the laser beams at the instant of the laser shot. The OCTS must process targets at the rate of the experimental schedule for cryogenic shots; four targets per day, four days per week.

The targets consist of spherical shells, ranging in diameter between 700 μm and 1100 μm, with wall thicknesses between 5 μm and 10 μm. They are made of polymers comprised mostly of carbon and hydrogen; polystyrene and GDP (glow discharge polymer). Targets are individually mounted in-between three parallel spider webs stretched between the ends of a C-shaped beryllium wire. The target is held in place half-way in-between the arms by a 0.3 μm thick conformal coating of paralyene. A post runs down from the spine of the C-wire. The base of this post is used by the OCTS to manipulate the mounted target.

Targets will be fueled with an equi-molar deuterium-tritium (DT) mixture. The solid fuel layer in the targets will be up to 100 μm thick. The fuel must be layered on the inner wall of the shell with a uniformity of at least 2%. The smoothness of the fuel inner surface should be better than 1000 Å. The "beta-layering" technique [3,4] will be used to produce the uniform fuel layer.

The current tritium license at LLE puts stringent requirements on the OCTS design. The quantity of tritium allowable is 1 gram. The location of LLE adjacent to a residential neighborhood restricts the release of tritium to very low concentrations. Based on the tritium lab's stack flow rate, no more than 200 mCi may be released yearly. A single target may hold as much as 600 mCi. This extremely low release limit makes tritium containment a severe design driver.

2. OMEGA CRYOGENIC TARGET SYSTEM OVERVIEW

The layout of the OCTS is shown in Fig. 1. Also shown is the target tank where the laser beams will implode the target. The target tank (the sphere inside the 60 hexagonal support structures) is 3.3 m in diameter. The OCTS processes targets as follows:

(a) Empty mounted targets are placed into a rack. The rack is placed into a room temperature cold transfer cryostat (CTC).

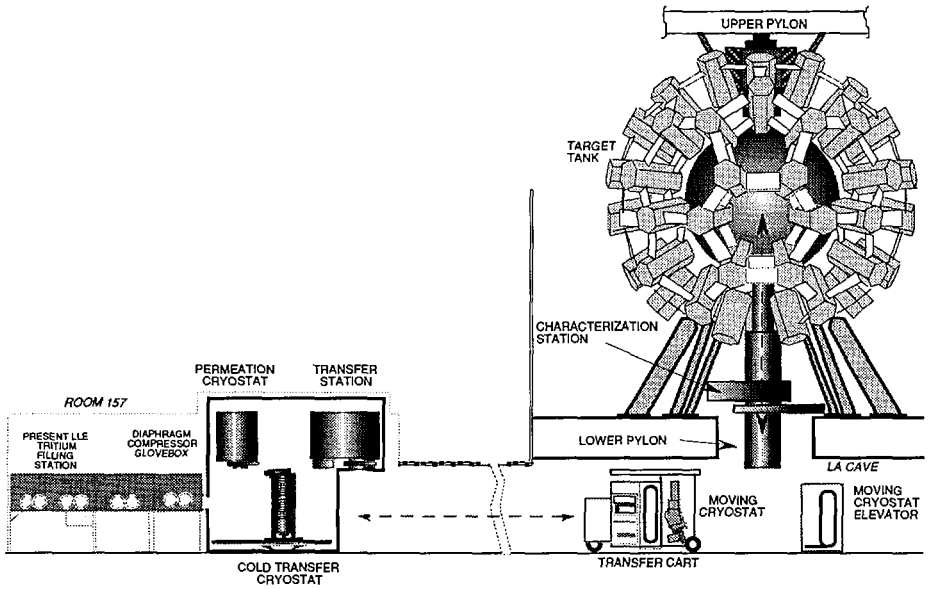

FIG. 1. Major components of the OMEGA Cryogenic Target System and the OMEGA Target Tank.

(b) The CTC inserts the target rack into the permeation cell in the fill station's permeation cryostat through a vacuum lock. The CTC detaches from the cell and begins cooling. Once the targets are cold, all subsequent operations on them by the OCTS will maintain them at cryogenic temperatures.

(c) The targets are permeation filled at room temperature to pressures as high as 150 MPa. The targets are then cooled until the gas inside reaches the saturated liquid phase and the pressure inside the target is low enough to prevent shell rupture when the DT external to the targets is removed from the cell. At these high densities, thin wall targets will rupture at 35 K with no external applied pressure.

(d) Once the excess DT in the cell is removed, the cell is further cooled. The CTC, now cold, removes the target rack from the cell and cocoons it in a gas tight cryogenic shroud. The shroud is maintained with a low pressure of helium gas to thermally link the self heating targets to the shroud. The targets' spider web supports have insufficient thermal conductivity for this task.

(e) The CTC retracts the shrouded targets from the fill station. After disengaging from the fill station, the CTC travels to the vacuum lock of the transfer station on a motorized rail system inside the glove box and then inserts the shrouded target rack into the transfer station.

(f) The transfer station disassembles the targets rack. A manipulator in the transfer station places an individual target onto the positioning stalk of the moving cryostat. The moving cryostat enters the transfer station through a vacuum lock that penetrates the glove box and the transfer station.

(g) After the transfer station has replaced the moving cryostat's shroud around the target, the moving cryostat is retracted from the transfer station and wheeled down a hallway into the room below the target tank.

(h) The target is layered in an isothermal environment created in the shroud of the moving cryostat.

(i) The moving cryostat is attached to the lower pylon through a vacuum lock. A rigid chain[1] is inserted from the moving cryostat elevator into the vacuum can of the moving cryostat through a vacuum lock. The rigid chain pushes the moving cryostat up to the characterization station. The characterization will be by an optical interferometric technique provided by LLE.

(j) After the fuel layer of the target is characterized, the moving cryostat is pushed up into the target tank, where it is mechanically locked in place.

(k) A fast shroud retractor descends from the upper pylon and attaches to the moving cryostat shroud.

(l) Fine positioners in the moving cryostat adjust the target position to the point where the laser beams will converge in the target tank.

(m) The shroud retractor rapidly removes the shroud to expose the target. The lasers fire at the target shortly after the shroud has cleared the target, ~100 ms.

2.1. Fill Station and Transfer Station

A layer thickness of 100 μm requires densities of up to 0.031 mol/cm^3 in smaller targets. This corresponds to 150 MPa at 300 K. The polymer targets can be easily crushed during permeation filling. The pressure difference on the weakest targets must be kept well below 280 kPa.

The existing LLE tritium fill system will supply moderate pressures (~200 bar) to the high pressure system from a cryogenic condensation tube. This gas will be metered into the cell and diaphragm compressor through a small volume trapped between two valves. Once sealed off, the diaphragm compressor will slowly reduce its volume by 30:1; boosting an initial 124 bar to 1500 bar. Pressure is increased at a rate slow enough to allow DT to permeate into the targets and prevent target crushing.

The permeation cell is sealed with a replaceable, cone and taper seal in a breech lock. Force is applied to the seal by high pressure (130 bar) helium acting on a diaphragm.

The fill station's permeation cryostat contains the permeation cell and the shroud manipulator. The shroud manipulator removes and replaces the CTC's shroud. The permeation cell is thermally isolated from the inner wall of the permeation cryostat. Two independent secondary cooling loops operate using helium to remove heat to two Gifford-McMahon cryocoolers. One loop is used to continually keep the inner wall of the cryostat and the shroud manipulator cold. The other rapidly cycles the cell between room and cryogenic temperatures. In order to facilitate maintenance in the glove box, the permeation cryostat features a wide mouthed Dewar design for access to items in its inner vessel. Only removal of one room temperature elastomer seal is required to gain access to the cell and shroud manipulator. Both the cryostat body and lid are vacuum and super-insulated and have liquid nitrogen shields.

---

[1] Serapid France, Z.I. BP 15 - Route DE Dieppe, 76660 Londiniers, France.

The transfer station contains a shroud manipulator, manipulators for disassembling the target rack and placing individual targets onto the moving cryostat positioning stalk, and a fast cooler for the moving cryostat's shroud. As with the permeation cryostat, the transfer station is designed with the wide-mouthed configuration and the dual cooling loops to cryocoolers. One loop is dedicated to maintaining cryostat temperature, the other to supply cooling to the fast shroud cooler.

2.2. Cold Transfer System

A motorized rail system shuttles two cold transfer cryostats between the fill and transfer stations. The rail line has a spur line to allow the cryostats to pass each other. The CTC attaches to the stations through a vacuum lock formed with gate valves. The CTC inserts a cryogenic shroud into the stations by collapsing the long welded metal bellows that forms its outer vacuum boundary. A cryocooler removes heat from the shroud through conduction. Shroud manipulators in the stations remove (replace) the CTC's shroud to expose (enclose) the target rack. A manipulator at the tip of the CTC is used to actively grasp the target rack and cell plug assembly. The manipulator floats on a spring loaded plate to provide compliance during mating with the cell. Removing the cell plug with the target rack after each fill cycle allows the cell seal to be replaced each time. The breech-locked shroud is sealed vacuum tight at cryogenic temperatures with an indium coated copper gasket [5]. This seal is actuated by a mechanical linkage to an air cylinder located in the room temperature base of the CTC.

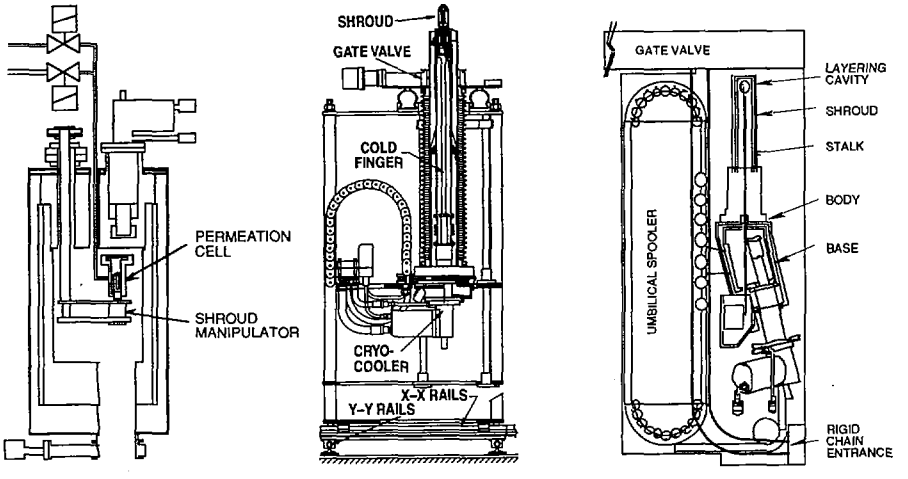

FIG. 2. Permeation, cold transfer and moving cryostats.

2.3. Moving Cryostat

The moving cryostat resides in a vacuum can located on the transfer cart. Once a target is picked up from the transfer station, the moving cryostat layers it in a spherical cavity in a copper block located in the tip of the moving cryostat's shroud. Smooth, uniform layers are formed using beta-layering [6] by maintaining a uniform temperature

(42 μK/mm or better across shell) around the target; just below the fuel triple point. The low thermal conductivity of DT and its internal heat generation cause thick portions of the layer to be hotter. The vapor pressure above the hotter portions condenses on the cooler thinner portions until the inner boundary of the fuel is isothermal and of equal thickness. Once the layer is formed, until the target is shot, the temperature must remain within ±0.3 K, otherwise thermal strain is expected to deform the layer.

The moving cryostat is divided into three main parts: the base, the body and the shroud. The wheeled base holds the cryocooler. The captured wheels roll in the same channel as the rigid chain that is used to push the cryostat up the lower pylon to the target tank center. There are gaps in the channel that are crossed at vacuum lock gate valves. The cryostat body holds the target positioning stalk piezo-motor drives. The cryostat's cryogenic shroud rides on top of the body and is connected to a special thermal joint. The joint can be opened to a low friction state just before the shroud's fast retraction by the upper pylon at shot time. The mating part of the joint in the body connects to the cryocooler with copper wire cable. When positioning the target, the body is clamped to the target tank and the base is slightly lowered by the chain. This imposes the building floor between the cryocooler and the target stalk, leaving only flexible cable as a path for cryocooler vibrations to the target stalk. The shroud contains windows to the target for characterization and positioning.

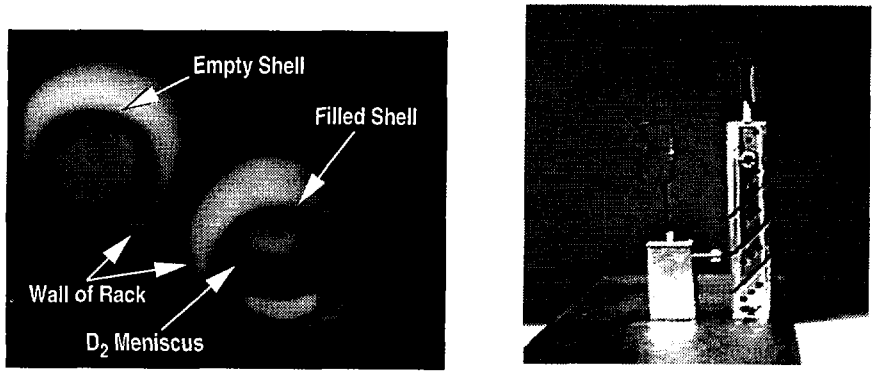

FIG. 3. Left: unmounted polymer shell shown before and after 110 MPa fill and cryocondensation. Right: C-mount target and rack for filling unmounted shells.

3. TECHNOLOGY DEVELOPMENT

Prototypes of a deuterium fill station and cold transfer cryostat were built and operated. C-mounted polymer targets were filled to a density of 0.026 mol/cm^3 (110 MPa at 300 K), cooled to 20 K, and removed from and returned to the fill station with the cold transfer cryostat without damage. A prototype diaphragm-actuated permeation cell was successfully built and operated.

4. SCHEDULE

Design of the OCTS is underway. We are in the detailed design phase for the fill station and cold transport system. A number of equipment sub-units are currently

undergoing DT testing at Los Alamos National Laboratory (LANL). The transfer station and moving cryostat are in the late preliminary design stage.

After fabrication, the OCTS will be tested in a component-wise and then integrated fashion at General Atomics using deuterium. It will then be shipped to LANL for component and integrated testing with DT. After successful completion of integrated system testing, the OCTS will be shipped to LLE and put into operation after acceptance testing. The system is expected to be delivered to LLE and operational by August 1999.

REFERENCES

[1] BOEHLY, T.R., et al., "The upgrade to the OMEGA laser system", Technology of Fusion Energy (Proc. 11th Top. Mtg New Orleans, LA) (1994).

[2] PAISNER, J.A., CAMPBELL, E.M., HOGAN, W.J., "National ignition facility design, schedule and cost", ibid.

[3] MARTIN, A.J., SIMMS, R.J., JACOBS, R.B., J. Vac. Soc. Technol. A **6** (1988) 1885.

[4] HOFFER, J.K., FOREMAN, L.R., Phys. Rev. Lett. **60** (1988) 1310.

[5] ALEXANDER, N.B., in Target Fabrication Specialists Meeting (Proc. 10th Conf., 1995), Rep. LA-UR-95-2938, Los Alamos Scientific Lab., Los Alamos, NM (1995) 223.

[6] HOFFER, J.K., et al., in Plasma Physics and Controlled Nuclear Fusion Research 1992 (Proc. 14th Int. Conf. Würzburg, 1992), Vol. 3, IAEA, Vienna (1993) 443.

SELF-PINCHED TRANSPORT FOR ION BEAM DRIVEN INERTIAL CONFINEMENT FUSION*

C.L. OLSON, D.L. HANSON, M.E. CUNEO,
T.R. LOCKNER, P.R. MENGE, J.E. BAILEY,
A.B. FILUK, J.W. POUKEY, I.R. SHOKAIR,
B.M. MARDER, S.A. SLUTZ, J.P. QUINTENZ
Sandia National Laboratories,
Albuquerque, New Mexico

P.F. OTTINGER, F.C. YOUNG, D.D. HINSHELWOOD,
T.G. JONES, D. MOSHER, J.M. NERI,
B.V. OLIVER, D.V. ROSE, S.J. STEPHANAKIS
Naval Research Laboratory,
Washington, D.C.

E.P. LEE, K.D. HAHN, S.S. YU, R.O. BANGERTER
Lawrence Berkeley National Laboratory,
Berkeley, California

D.R. WELCH
Mission Research Corporation,
Albuquerque, New Mexico

A. FRIEDMAN, A.B. LANGDON, B.G. LOGAN
Lawrence Livermore National Laboratory,
Livermore, California

R.R. PETERSON, J.J. MacFARLANE,
P. WANG, G.L. KULCINSKI
University of Wisconsin,
Madison, Wisconsin

United States of America

P. HOPPÉ, H. BLUHM, A. NAKAGAWA
Forschungszentrum Karlsruhe,
Karlsruhe, Germany

* Work supported by US Department of Energy.

Abstract

SELF-PINCHED TRANSPORT FOR ION BEAM DRIVEN INERTIAL CONFINEMENT FUSION.

Self-pinched transport is an attractive ion beam final transport mode for all high yield and fusion energy applications using ion drivers. Recent code and analytic theory results are presented that predict that net currents will be sufficient for all ion driver scenarios. The status of experiments on GAMBLE II and SABRE is discussed.

1. INTRODUCTION

The primary driver option following the National Ignition Facility (NIF) is an ion driver [1]. Ignition and modest gain will be demonstrated on NIF by about the year 2005, using a laser input beam energy of 1.8 MJ with yields of 1-20 MJ. Following NIF, high yield and energy applications will be pursued using ion beam input energies of 5-10 MJ with yields of 200-1000 MJ. Standoff is required for these applications, meaning that the ion beams must be transported from the containment vessel wall to the ICF target over distances of several meters. Although there are many transport options [2-4], recent interest has centered on the self-pinched mode [1-3].

2. SELF-PINCHED TRANSPORT CONCEPT

Self-pinched propagation should be ideal for LIF (light ion fusion), HIF (heavy ion fusion), or middle-weight ions. For this mode, the ion beam is focused down to a small radius, stripped (if it isn't already), and then injected into a low pressure gas. The azimuthal magnetic field produced by the resultant net current confines the beam and allows it to propagate with a small radius over several meters to the target. The parameters are chosen so that the radius of the beam during transport is slightly less than the desired target spot radius, to allow for slight beam expansion in the multi-beam overlap region near the target. The minimum net current I_c required to contain an ion beam of initial radius R and microdivergence θ_μ in a self-pinched equilibrium of radius r_c is $I_c = 2 (R\theta_\mu / r_c)^2 I_m$ where r_s is the spot radius at the entrance to the self-pinched channel, $r_s = (2^{-1/2}) r_c$ and the ion Alfvén current is $I_m = \beta\gamma (A/Q) M_p c^3/e$ [2,4]. Here $\beta = v_i/c$, v_i = ion velocity, c = speed of light, $\gamma = (1 - \beta^2)^{-1/2}$, A is the ion mass number, Z is the atomic number, Q is the actual charge state of the ion, M_p is the proton rest mass, and e is the charge of an electron. For HIF and LIF fusion energy applications, net currents in the range of 4 - 100 kA are typically needed.

For LIF, an annular ion beam from an extraction ion diode is ballistically focused to a small spot, transported in the self-pinched mode in a guide tube (for up to a few meters), and then propagated in the self-pinched mode inside the target chamber. Advantages of this mode are that there are only small holes in the chamber wall, there is no transport apparatus in the chamber (only gas), and the diode is shielded. For HIF, the ion beam from an induction linac is focused to a small spot, transported in the self-pinched mode in a guide tube (for up to a few meters), and then propagated in the self-pinched mode inside the target chamber. Alternatively, the HIF beam could be focused to a small spot about 400 m upstream of the target, and then transported in the self-pinched mode in a small tube for 400 m as it undergoes drift compression. Advantages

TABLE I. SELF-PINCHED TRANSPORT PARAMETERS FOR ION BEAM DRIVERS FOR ICF

Status	Experiments Initiated		Future High-Power Experiments		Long-Term Goals			
Facility	GAMBLE II (NRL)	SABRE (SNL)	PBFA-X	HERMES III	LIF LMF module	LIBRA-SP module	HIF LMF beam	PROMETHEUS -H beam
ion	p	Li	Li	Li	Li	Li	Kr	Pb
A	1	7	7	7	7	7	84	207
Z	1	3	3	3	3	3	36	82
Q_a(accel)	1	1	1	1	1	1	1	2
Q_s (stripped)	1	3	3	3	3	3	35	82
Q_seV(MeV)	1.5	5	14	14	35	30	2,500	4,000
β	0.056	0.039	0.065	0.065	0.10	0.095	0.25	0.20
I_p (kA) article	150	50	1,000	300	1,000	463	10.7	12.1
P (TW)	0.23	0.25	14	4.2	35	14	27	48
t_b (ns) at diode	60	30	40	30	30	40	**8	**18
t_r (ns) current	50	15	15	10	10	10	2	2
ϵ (kJ)	14	7.5	560	126	1,050	560	210	860
I_e (kA) electric	150	150	3,000	900	3,000	1,400	375	990
I_e (kA)/t_r (ns)	3	10	200	90	300	140	190	500
R_{out} (cm)	10.5	6.5	22.5	15	12	14.1	***24	***15
R_{in} (cm)	8	4.5	13.5	8	8	10	0	0
A (cm^2) at anode	150	70	1,000	500	250	309	***1,800	***700
θ_μ (mrad)	20	40	40	40	6 - 12	4	***0.08	***<0.3
J_p (A/cm^2)	1,000	700	1,000	600	4,000	1,500	6	17
J_p (A/cm^2)/θ_μ^2(mrad)	2.5	0.44	0.63	0.38	111 - 28	94	940	>190
J_pQ_aV/θ_μ^2	3.75	2.2	8.8	5.3	3,900 - 980	2,800	2,350,000	>760,000
$[Q_s^2(A\beta)][J_p/\theta_\mu^2]$	45	14.5	12.5	7.5	1,400 - 360	1,300	54,800	>30,900
r_c (cm)	10.1 - 1.85	16.0 - 2.9	4.4	3.6	0.85	0.7	0.2	0.25
I_c (kA)	1.5 - 45	1.5 - 45	*400	270	105 - 420	90	3.6	10.4
net current fraction (%)	1 - 30	1 - 30	13	30	3.5 - 14	6.4	1	1
n (# prepulse beams)					12	12	6	6
N (# main beams)					12	12	18	12
ϵ (MJ) total at target					14	7.2	5	7

*practical max, including hydro expansion **at target ***at final focus

of this mode are that there are only small holes in the chamber wall, the focusing magnets are simplified, and the acceptance of sizable longitudinal velocity spreads makes a lower-cost accelerator possible and suppresses any longitudinal instability.

In Table I, self-pinched transport parameters are summarized for both LIF and HIF. Parameters are listed for light ion experiments initiated on GAMBLE II at NRL and on SABRE at SNL, for future high-power experiments on PBFA-X or HERMES III at SNL, and for the long-term goals of high yield and energy. The latter include the LIF Laboratory Microfusion Facility [5], the light ion power plant LIBRA-SP that uses self-pinched transport [6], the HIF Laboratory Microfusion Facility [7], and the heavy ion power plant PROMETHEUS-H that uses self-pinched transport [8]. Most of the symbols used in Table I are self-explanatory; however, a few comments are appropriate. The charge state during acceleration (Q_a) and the charge state of the final stripped ion beam (Q_s) are usually different. The beam electrical current $I_e = Q_s I_p$ where I_p is the particle current. All LIF cases employ annular beams from extraction diodes with outer radius R_{out} and inner radius R_{in}, whereas all HIF beams are solid. Three quantities relating to beam brightness are given: the usual brightness J_p/θ_μ^2, the power brightness $J_p Q_a V/\theta_\mu^2$ [4], and the quantity $[Q_s^2/(A\beta)]\,[J_p/\theta_\mu^2]$ which is of importance for the filamentation instability [2,9]. Values of the self-pinched radius r_c are given together with the net current fraction for a range of cases. Note that for all high yield and energy cases (the last four cases), net current fractions of only 1 - 14% are needed.

3. PHYSICS OF GAS BREAKDOWN AND SELF-PINCHED TRANSPORT

The primary issue is whether gas breakdown will produce sufficient net currents to allow self-pinched propagation. Past computer simulation studies showed net currents too small to confine the beam [4]. However, non-local breakdown effects caused by fast electrons were not included. Fast electrons ($\gtrsim$ 100 eV) result from ion impact ionization (beam ion, bound electron), knock-on collisions (beam ion, free electron), and runaway electrons during avalanching. The IPROP computer code has been developed to follow the fast electrons [10]. IPROP is a 3-D EM hybrid code with ion PIC, and electron PIC for electrons above some energy (typically 100 eV), and electron fluid below that energy. Detailed gas breakdown experiments have been performed on GAMBLE II at NRL (1 MeV protons, 10 kA, 1-2 kA/cm^2) for several gases and pressures [11]. IPROP agrees with the NRL experiments, and also with results on PBFA II at SNL (8 MeV Li, 800 kA).

The IPROP code has been used extensively to study self-pinched transport, and it is in agreement with an analytic theory of self-pinched transport [3]. From a wide variety of code runs, it has been concluded that (1) net current fractions up to 30% can be achieved independent of the peak current for short or long current risetimes (1-20 ns) by optimizing the gas pressure, and (2) the optimum gas pressure is typically in the range of 1-100 mTorr. Some code results are shown in Figs. 1-3. In Fig. 1, trajectory results using the simpler code TRAJ (which does not have gas breakdown physics, but assumes a fixed net current fraction in the self-pinched region) shows ballistic focusing for a beam with SABRE parameters, and capture in a self-pinched channel with a net current fraction of 30%. In Fig. 2, the full IPROP code with gas breakdown shows ballistic transport in 1 Torr He with good transport efficiency for SABRE parameters. In Fig. 3,

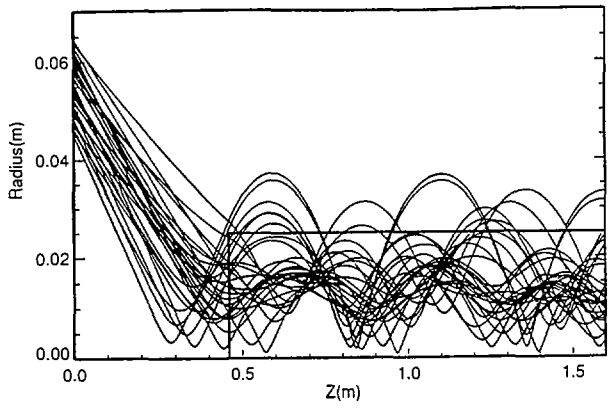

FIG. 1. TRAJ simulation of the ballistic focus region (f_e = 1, f_m = 1) and the self-pinched region (f_e = 1, f_m = 0.7) for SABRE parameters (5 MeV Li^{+3}, I_e = 150 kA, θ_μ = 40 mrad) in both r and θ. At output, r_b (rms) = 1.7 cm. The charge (current) neutralization fraction is f_e (f_m).

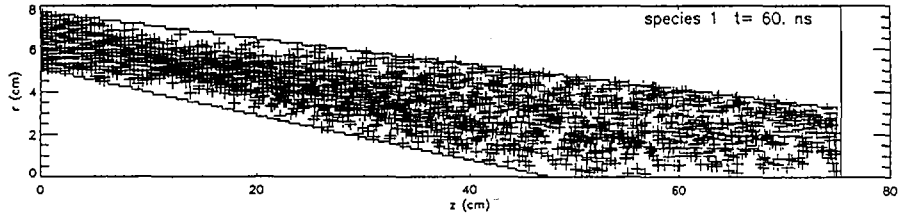

FIG. 2. IPROP simulation of the ballistic focus region for 1 torr He for SABRE parameters (6 MeV Li^{+3}, I_e = 100 kA, θ_μ = 40 mrad, t_r = 12 ns).

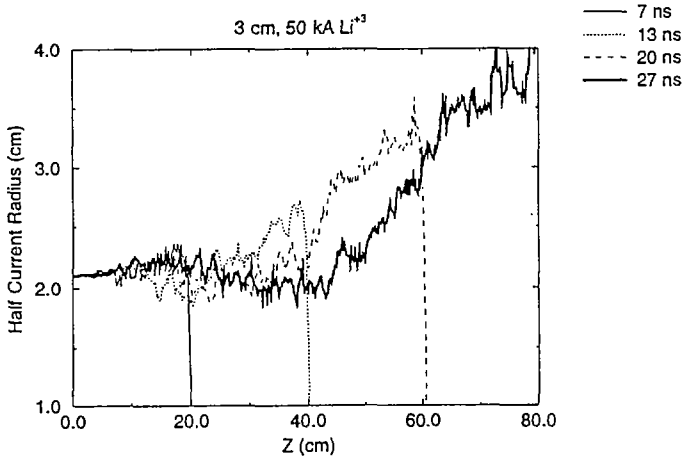

FIG. 3. IPROP simulation of the self-pinched transport region for 10 mtorr Ar for 35 MeV Li^{+3}, I_e = 50 kA, θ_μ = 40 mrad, t_r = 10 ns.

the full IPROP code simulates the self-pinched region for a pressure of 10 mTorr Ar, and shows good self-pinched transport. All of these results are encouraging since they show that the net currents needed for fusion (as shown in Table I) should be attainable.

Further IPROP runs and analytic studies will examine inductive erosion, emittance-driven erosion, effects of passive conditioning cells (such as a metal cone on axis), and effects of potential instabilities (hose, two-stream, and filamentation).

4. SELF-PINCHED TRANSPORT EXPERIMENTS INITIATED

Experiments to demonstrate self-pinched transport are being initiated with proton beams on GAMBLE II at NRL, and with Li beams on SABRE at SNL. The GAMBLE II experiments will use a 1.5 MeV, 150 kA proton beam from a new shallow-focusing, applied-B extraction ion diode designed specifically for self-pinched transport experiments. The 2-D magnetic field code DATHETA was used to determine the anode shape. The diode has been tested at 1.2 MV, and the beam has been injected through a foil into 1 Torr air; at half the predicted focal length of the diode (36 cm from the anode), the beam was recorded on a witness plate and imaged through multiple pinholes onto radiachromic film. Preliminary analysis suggests that the beam focusing is similar to DATHETA predictions. IPROP simulations have been done that will guide self-pinched transport experiments at 1.5 MV after optimization of beam focusing is completed.

The SABRE experiments will use a 5 MeV, 50 kA Li^+ beam from another new, shallow-focusing, applied - B, extraction ion diode. The extraction diode with an appropriate magnetic field profile for uniform Li production and focusing is being designed using the codes DATHETA and TWOQUICK. This diode is very similar to the existing SABRE diode, with the inclusion of a shallow-focusing angle of about 100 mrad. IPROP simulations are in progress (as shown in Figs. 2,3) to optimize the design of the ballistic and self-pinched transport sections.

5. CONCLUSIONS

Self-pinched transport is a very attractive transport mode for all ion driver scenarios. Code results and analytic theory predict net currents large enough for all high yield and energy applications. Experiments with self-pinched transport have been initiated at the 0.25 TW level on GAMBLE II and SABRE.

REFERENCES

[1] OLSON, C. L., QUINTENZ, J. P., BANGERTER, R. O., LOGAN, B. G., LINDL, J. D., "ICF Driver Strategies for IFE," Proc. IAEA Technical Committee Meeting on Drivers for Inertial Confinement Fusion, Paris, France, November 14-18, 1994 (Edited by J. Coutant, CEA), May, 1995, p. 259.

[2] "Workshop on Transport for a Common Ion Driver," Chairmen: C. Olson, E. Lee, and B. Langdon, Sandia National Laboratories, Albuquerque, NM, September 20-21, 1994, SAND95-0116, UC-712 (1995).

[3] WELCH, D. R., OLSON, C. L., "Self-Pinched Transport for Ion-Driven ICF", Proc. Int. Symp. on Heavy Ion Fusion, Princeton Plasma Physics Laboratory, Princeton, NJ, September 6-9, 1995 (to be published in J. Fusion Engineering Design).

[4] OLSON, C. L., "Ion Beam Propagation and Focusing," J.Fusion Energy 1, 309 (1982).

[5] "Laboratory Microfusion Capability Study, Phase II Report," U.S. Dept. of Energy DOE/DP-0017, p. IV-1 (May, 1993). Available from NTIS, U.S. Dept. of Commerce, 5285 Port Royal Rd., Springfield, VA 22161.

[6] BADGER, B., BRUGGINK, D., COUSSEAU, P., ENGELSTAD, R. L., LEE, Y-M., KHATER, H. Y., KULCINSKI, G. L., MACFARLANE, J. J., MOGAHED, E. A., MOSES, G. A., PETERSON, R. R., RUTLEDGE, S., SAWAN, M. E., SVIATOSLAVSKY, I.N., WANG, P., WITTENBERG, L. J., OLSON, C. L., OLSON, R. E., "LIBRA-SP, A Self Consistent Design of a Commercial Fusion Power Plant Based on Self-Pinched Propagation of Ions," Fusion Power Associates Report FPA-94-6 (December 1994).

[7] "Laboratory Microfusion Capability Study, Phase II Report," U.S. Dept. of Energy DOE/DP - 0017, p. VI-1 (May, 1993). Available from NTIS, U. S. Dept. of Commerce, 5285 Port Royal Rd., Springfield, VA 22161.

[8] "Inertial Fusion Energy, Reactor Design Studies, Prometheus - L, Prometheus - H," McDonnell Douglas Aerospace Team, Final Report, Volumes I - III, DOE/ER - 54101, MDC 92E0008 (March, 1992).

[9] LEE, E. P., YU, S., BUCHANAN, H. L., CHAMBERS, F. W., and ROSENBLUTH, M. N., "Filamentation of a Heavy Ion Beam in a Reactor Vessel," Phys. Fluids 23, 2095 (1980).

[10] WELCH, D. R., OLSON, C. L., SANFORD, T. W. L., "Simulation of Charged-Particle Beam Transport in a Gas Using a Hybrid Particle-Fluid Plasma Model," Phys. Plasmas 1, 764 (1994).

[11] YOUNG, F. C., HINSHELWOOD, D. D., HUBBARD, R. F., LAMPE, M., NERI, J. M., OLSON, C. L., OTTINGER, P. F., ROSE, R. V., SLINKER, S. P., STEPHANAKIS, S. J., WELCH, D. R., "Current Neutralization of Intense MeV Proton Beams Transported in Low-Pressure Gas," Phys. Rev. Lett. 70, 2573 (1993).

A SOLUTION TO THE PROBLEMS OF PROTON-BORON FUSION

S. ELIEZER, Z. HENIS
Soreq Nuclear Research Centre,
Yavne, Israel

J.M. MARTINEZ-VAL, M. PIERRA, G. VELARDE
Instituto de Fusión Nuclear,
Universidad Politécnica de Madrid,
Madrid, Spain

Abstract

A SOLUTION TO THE PROBLEMS OF PROTON-BORON FUSION.

The proton + $^{11}B \rightarrow 3\ \alpha$ fusion reaction is considered to be the cleanest (i.e. neutronless) method of exploiting nuclear energy. However, the very high ignition temperature (~ 200 keV), the bremsstrahlung losses and the relatively moderate fusion yield per reaction (8.7 MeV) make it very difficult to achieve a high energy gain. The idea proposed in the paper is based on the creation of a heat detonation wave (energy supplied by α particles) and a non-linear heat wave (by electron transport), where both waves move with some delay, but at the same speed, into a precompressed target. These heat waves are induced by a proton beam, by proton plasmas, by a laser beam fast ignitor or by jets, directed into a region called the 'ignitor', and they propagate into the 'cold' ($\lesssim 1$ keV) and compressed ($< 10^3$ g/cm^3) ^{11}B–proton fuel. It is crucial that the boron to proton number ratio is smaller than one third. The heat waves propagate supersonically, and thus a large fraction ($> 30\%$) of the boron is burnt. If the conditions for propagation are satisfied, the internal energy gain can be as high as 1000, so that an overall (real) gain can be achieved. The most difficult requirement of this approach is the need for a very intense ignitor beam, acting for a very short time (~ 10 ps). New accelerators or new lasers would be needed for this purpose.

1. INTRODUCTION

The proton + $^{11}B \rightarrow 3\ \alpha$ fusion reaction is considered to be the cleanest (i.e. neutronless) method of exploiting nuclear energy. For a magnetic confinement fusion reactor using p–^{11}B, Dawson [1] concluded that the internal gain (defined as the fusion energy divided by the internal energy) can be slightly above one if the produced α particles can be taken away while the system is being refuelled.

For an inertial confinement fusion [2–4] reactor using p–^{11}B, densities of the order of 10^5 g/cm^3 and spark ($< 10\%$ in mass) temperatures of about 200 keV have to be achieved while the bulk of the matter must reach temperatures lower than 10 keV. These conditions might impose prohibitive laser (or ion) uniformities necessary in order to avoid hydrodynamic instabilities. An analysis for the volume ignition scheme with negative conclusions has been made [5–8]. For this approach, the

extremely high areal density targets would require [7, 8] driver energies in the range of gigajoules (GJ) and a potential burst of several GJ.

The idea proposed in this paper is based on the creation of a heat detonation wave (energy supplied by α particles) and a non-linear heat wave (by electron transport), where both waves move with some delay, but at the same speed, into a precompressed target.

2. ENERGY BALANCE

The fusion energy W_f is given by:

$$W_f\left(\frac{\text{eV}}{\text{cm}^3\cdot\text{s}}\right) = 3.38 \times 10^{-9}\,\frac{\epsilon n^2}{(1+\epsilon)^2}; \qquad \epsilon = \frac{n_B}{n_p}; \qquad n = n_B + n_p \tag{1}$$

where the fusion rate was calculated for an ion Maxwellian distribution with an ion temperature of $T_i = 200$ keV and was taken to be 4×10^{-16} cm$^3\cdot$s^{-1}. n_B and n_p are the boron and proton densities, respectively. The fraction of the proton beam or α fusion energy deposited in the electrons can be fitted as a function of the electron temperature, T_e:

$$\eta = \frac{150}{150 + (T_e\,(\text{keV}))^{1.5}} \tag{2}$$

Since in our scheme the ion temperature is higher than the electron temperature, the energy flows from ions to electrons by collisions:

$$P_{ie}\left(\frac{\text{eV}}{\text{cm}^3\cdot\text{s}}\right) = 0.5 \times 10^{-8} \ln\Lambda\,\frac{(1+5\epsilon)(1+2.27\epsilon)}{(1+\epsilon)^2}\,n^2\,\frac{T_i - T_e}{T_e^{1.5}} \tag{3}$$

For very low densities ($n_e \approx 10^{14}$ cm^{-3}), the Coulomb logarithm is about 20 for $T_e \approx 100$ keV. For a high density plasma ($n_e \approx 10^{26}$ cm^{-3}), this term is about 5. In Eq. (3), the temperatures are given in eV. The main energy sink is the bremsstrahlung radiation emitted by the electrons. If relativistic corrections are included, this term is given by

$$P_B\left(\frac{\text{eV}}{\text{cm}^3\cdot\text{s}}\right) = 9.3 \times 10^{-14}\,n_e\left(\sum_i n_i Z_i^2\right) T_e^{0.5}\left(1 + \frac{2T_e}{m_e c^2}\right) \tag{4}$$

where T_e is in eV, m_e is the electron mass and n_i and Z_i are the ion densities and their charges, respectively.

The other important sink terms are the mechanical disassembly of the nuclear fuel and the heat conduction by the electrons. The latter is not entirely a loss mechanism because it heats the cold (precompressed) target and thus imposes the condition that a large fraction of α particles is deposited in the ion fuel (borons and protons). A fraction ($\sim 25\%$) of the α particles created in the hot part will go into the cold part and 'feed' the heat detonation wave, while the non-linear heat transport of the electrons will induce a heat wave.

3. THE ELECTRON HEAT WAVE

The heat wave equation is given by:

$$\rho_0 c_v \frac{\partial T}{\partial t} = \frac{\partial}{\partial x}\left(\chi T^{2.5} \frac{\partial T}{\partial x}\right) + \frac{\partial q}{\partial x} \tag{5}$$

where T is the electron temperature, ρ_0 and c_v are the density and the specific heat of the unburnt material (cold fuel), χ is the conductivity and q stands for the source of the energy flow (in $\mathrm{erg \cdot cm^{-2} \cdot s^{-1}}$).

It is important to specify the boundary conditions for our problem. The source of the energy flow will be placed at $x = 0$, and there will be a small hot region in front of it, given by

$$x_1 (t = 0) = X^* \sim R_\alpha; \qquad T_0 (t = 0, x < X^*) = T_e \sim 100 \text{ keV} \tag{6}$$

where R_α is the range of the α particles, i.e. the thickness of the heat wave, $x_1(t)$ and $T_0(t)$ are calculated by using energy conservation.

At any instant in time, there are three regions of space to be considered: the precompressed cold region ($T_e < 1$ keV) — (I), the domain heated by the electron heat wave ($T_e \sim 100$ keV) — (II) and the fusion area where $T_i \sim 200$ keV and $T_e \sim 100$ keV — (III). In region I, the electrons will be heated must faster than the ions, both by electron conduction and by a fraction of the α particle energy deposition. In this region, the electrons are heating the ions via collisions (Eq. (3)). In region II, the α particles are heating mainly the ions (see Eq. (2)), implying that the fusion process starts and changes this region into region I, thus inducing the propagation of the heat wave into the cold fuel.

The electron heat conduction wave will be travelling in front of the fusion front. Nevertheless, as the electron hot front departs from the burning front, the speed decreases. Hence, the electron heat front will run before the burning front in such a way that both speeds become equal, i.e. the heat electron front will reach a given position a few seconds before the burning front such that $U_h(t_l) = U_{BW}$, where t_l is the advance time of the electron heat wave and U_{BW} is the fusion front speed.

4. FUSION DETONATION HEAT WAVE ('BURNING WAVE')

The heating time by the α particles of the cold zone is obtained from

$$t_b = \frac{(n_p + n_B)\Delta T_i + n_e \Delta T_e}{f \langle \sigma v \rangle n_p n_B E_f} \tag{7}$$

where f is the escape fraction and E_f is the fusion yield per reaction (8.7 MeV). For $\Delta T_i = 200$ keV, $\Delta T_e = 100$ keV, $f = 0.25$ and $\epsilon = 0.2$, the heating time is (in cgs units) $t_b = 2.5 \times 10^{-9}/\rho$. This time gives an estimate of the burning wave speed, $U_{BW} = R_\alpha/t_b \sim (1.1/\rho)/(2.5 \times 10^{-9}/\rho) = 4 \times 10^8$ cm/s. There are two mechanisms that modify the value of this speed: the space profile of the density and the burnup effect; they affect t_B in opposite senses. Although t_B and U_{BW} should be calculated from a hydrodynamic simulation with a good equation of state, it is conceivable, in a first approach, that the effects of burnup and overcompression, owing to the creation of a shock wave, cancel each other so that Eq. (7) is a reasonable estimate. The equality of the burning wave with the heating wave is satisfied to a good approximation for $t < t_l$ if $x_l\rho$ equals the range of the α particles. For example, for $\rho = 444$ g/cm^3 and $T_e = 100$ keV, we have $x_l = 25$ μm, $x_l\rho = 1.1$ g/cm$^2 \approx R_\alpha\rho$, $t_l \sim 6.2$ ps and $t_b \sim 5.7$ ps. Therefore, it can be concluded that if the ignitor succeeds in launching a burning wave, a heat wave with two temperature profiles (for ions and electrons) will expand into the precompressed plasma and heat it to ignition temperature. This phenomenon will take place during the confinement time of the plasma.

5. THE IGNITOR AND THE PROTON BEAM

The ignitor performance is analysed and simulated by an average energy balance involving the ion and electron temperatures that are governed by the following equations:

$$\frac{3}{2} n_e \frac{dT_e}{dt} = P_{ie} - P_B + f\eta W + \eta_P W_P - P_{he} - P_{me} \tag{8}$$

$$\frac{3}{2} n_i \frac{dT_i}{dt} = -P_{ie} + f(1 - \eta) W + (1 - \eta_P) W_P - P_{mi} \tag{9}$$

where P_{ie} is the ion–electron energy exchange term, given by Eq. (3), and P_B is the bremsstrahlung power given by Eq. (4). W and W_P are the fusion and the proton power densities, respectively, η and η_P are the fractions of the fusion α particles and the proton beam deposited in the electrons, and f is the fraction of fusion

born α particles remaining in the ignitor. Our simulations show that it is possible to start a burning wave, but a very high density proton beam is needed, $W_P \sim 5 \times 10^{28}$ erg·cm^{-2}·s^{-1} with 5 MeV per proton during a pulse duration of about 10 ps. For a 5 mg fusion target with a precompressed density of 1000 g/cm^3 and a beam focus with a radius of the α range, one needs a 100 kJ proton beam.

6. GAIN AND CONFINEMENT CONDITIONS

The gain, defined by the ratio of fusion energy and internal heating energy, is given by

$$G = \frac{8.7 \times 10^3 \, \xi n_B R^3}{\frac{3}{2}(n_i T_i + n_e T_e) R_\alpha^3} \tag{10}$$

where R is the fusion target size, R_α is the dimension of ignition, approximately equal to the α range, and ξ is the boron burnup fraction, which in our calculations amounts to about 45%. For $T_i = 2T_e = 200$ keV and $\epsilon = 0.2$, we obtain $G \approx (R/R_\alpha)^3 \equiv y^3$. The confinement conditions require that (a) the disassembly time be longer than the fusion heating time and (b) the burning wave speed be higher than the shock induced particle flow. The first condition is satisfied for $y > 2.2$, while the second constraint, together with a realistic equation of state, implies $y < 20$. Thus for $y \sim 10$ a gain of 10^3 can be achieved.

7. CONCLUSIONS

The main conclusion drawn from this study is that a fusion burning wave can be triggered in a proton–boron plasma of optimized isotopic concentration, provided a fraction of this plasma reaches burning conditions by supersonic heating. The greatest difficulty in meeting this requirement is the need for a very intense beam of charged particles (either protons or boron ions). The values obtained in the numerical simulation show that ultrahigh currents are needed to reach the levels of power deposition that heat the plasma up to fusion temperatures. A second important issue is the need to compress the plasma before igniting it.

In summary, it seems conceivable that the proton–boron reaction can be exploited by igniting a fusion burning wave in a compressed fuel [9]. Unfortunately, particle beams needed for ignition are not available at present, and new accelerators are required for this purpose. In order to overcome this drawback, some new ideas can be tested: for example, particle beam compression inside an imploding cylinder containing the proton boron plasma.

We conclude this paper with a comment regarding DT fusion in the suggested scheme. In particular, the proton energy and the irradiance needed to trigger a fusion burning wave in the deuterium–tritium plasma is calculated. The surrounding plasma is precompressed to a density ρ. For a 1 MeV proton beam, the following scaling laws are derived: (a) ignitor mass: M_{ig} (mg) = 5.7 ρ^{-2} (ρ in g/cm^3); (b) igniting (proton) beam energy: E_p (MJ) = 24 ρ^{-2}; (c) proton pulse duration (before mechanical disassembly): t_p (ns) = 3.1 ρ^{-1}; (d) proton beam power: P_p (10^{15} W) = 8 ρ^{-1}; (e) intensity: I (W/cm^2) = 1.3 × 10^{17} ρ. The positive power in ρ is due to the fact that the spot dimension of the ignitor is of the order of the α range, R_α, which scales as ρ^{-1}. The heat detonation burning of a DT plasma in comparison with a p–^{11}B plasma requires less restrictive constraints on the proton beam and on the precompression of the fusion fuel, by two to three orders of magnitude.

REFERENCES

[1] DAWSON, J.M., CTR Using the p–^{11}B Reaction, Plasma Physics Group Rep. PPG-273, University of California, CA, USA (1976).
[2] BRUECKNER, K.A., JORNA, S., Rev. Mod. Phys. **46** (1974) 325.
[3] KIDDER, R.E., Nucl. Fusion **14** (1974) 953.
[4] BODNER, S., Phys. Rev. Lett. **33** (1974) 761.
[5] HORA, H., RAY, P.S., Z. Naturforsch. **33A** (1978) 890.
[6] MARTINEZ-VAL, J.M., ELIEZER, S., PIERRA, M., Laser Part. Beams **12** (1994) 681.
[7] MILEY, G.H., et al., Fusion Technol. **19** (1991) 43.
[8] PIERUSCHKA, P., et al., Laser Part. Beams **10** (1992) 145.
[9] MARTINEZ-VAL, J.M., ELIEZER, S., PIERRA, M., VELARDE, G., Phys. Lett. A **216** (1996) 142.

DIRECT DRIVE EXPERIMENTS USING THE NIKE LASER

S.E. BODNER, D.G. COLOMBANT, J.P. DAHLBURG,
R.H. LEHMBERG, E.A. McLEAN, S.P. OBENSCHAIN,
C.J. PAWLEY, A.J. SCHMITT, V. SERLIN,
J.D. SETHIAN, J.A. STAMPER
Plasma Physics Division,
Naval Research Laboratory,
Washington, D.C.

C.M. BROWN, J.F. SEELY
Space Science Division,
Naval Research Laboratory,
Washington, D.C.

J.H. GARDNER
Laboratory for Computational Physics
and Fluid Dynamics,
Naval Research Laboratory,
Washington, D.C.

Y. AGLITSKIY, A. DENIZ, T. LEHECKA, N. METZLER
Science Applications International Corporation,
McLean, Virginia

M. KLAPISCH
Artep Corporation,
Columbia, Maryland

United States of America

Abstract

DIRECT DRIVE EXPERIMENTS USING THE NIKE LASER.

The Nike laser has been operating routinely for laser-target experiments since mid-1995 and has routinely operated at its designed energy level. The laser has 56 beams, with a total energy at the target of ~3 kJ. Each of the beams has a root mean squares non-uniformity of ~1–1.5% in a 4 ns pulse. With 40 of the beams overlapped, the net laser non-uniformity is estimated to be ~0.2%. Measurement of the Rayleigh–Taylor growth of a sinusoidally modulated foil target is in excellent agreement with computer simulations, but the smooth foil targets have less mass modulation than predicted; this modulation is below the diagnostic resolution and sensitivity.

1. INTRODUCTION

The development, in the 1980s, of various beam smoothing techniques has revitalized the direct drive approach to laser fusion. Since this type of fusion target has a high overall coupling efficiency from the laser energy to the imploding fuel (70–90%), there is the potential of achieving energy gains in the range of 100–200, sufficient for a power reactor. However, the fusion community has not yet fully solved the problems associated with the residual non-uniform laser imprinting (Richtmyer–Meshkov instability) and the subsequent Rayleigh–Taylor (RT) growth. Although the current laser facilities have much improved the laser beam quality, the residual laser non-uniformities are predicted still to be the limiting factor in target performance. The fluid instabilities can probably be controlled with sufficient pre-heating of the target, but then the predicted energy gain drops well below 100.

The NRL fusion programme is addressing this problem first by maximizing the laser uniformity, using induced spatial incoherence (ISI) optical smoothing with a KrF laser called Nike. Each of the Nike beams has a measured root means squared (rms) fluctuation of 1–1.5%, averaged over a 4 ns pulse. This laser beam non-uniformity is a factor of 5–10 better than any existing glass laser when used in the UV. With Nike, we overlap multiple beams (37–44) on the target, reducing the effective non-uniformity to a few tenths of a per cent (ignoring the very short wavelength interference between beams). Nike is now being used to evaluate whether this outstanding beam uniformity is sufficient for laser fusion applications.

Our laser–target experiments have used smooth foils, roughened foils and foils with initial sinusoidal mass modulations. When we accelerate targets with the sinusoidal modulations, the growth of the RT instability is in excellent agreement with our 2-D computer simulations. However, when we use the smoothest targets and the smoothest laser beams, the net mass modulation is less than what we can measure with our diagnostics and less than predicted by our computer simulations. We are now investigating the various possible reasons for these surprisingly favourable results.

2. LASER PERFORMANCE

Routine laser–target experiments began in May 1995, and the laser facility now operates routinely with approximately 30 shots per month, many with ~ 3 kJ energy in the 56 laser beams. The limiting factor on laser maintenance has been the hibachi foil lifetime in the large 60 cm amplifier. Currently, these foils last about 50 shots. We then have to shut down for one or two days for foil replacement.

We currently use 40 of the laser beams to accelerate the foil target, with four additional beams to produce an X ray sidelighter, and four additional beams for an X ray backlighter. The full width at half-maximum (FWHM) portion of the main laser pulse is 4 ns, with an FWHM spot size of 750 μm, the same as each individual

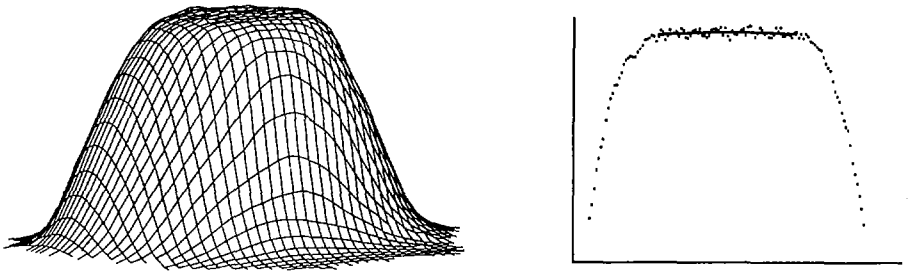

FIG. 1. Measured non-uniformity of a single Nike laser beam, integrated over a 4 ns pulse. The rms non-uniformity is 1% over the central 50% of the profile. With 40 overlapped beams, the effective non-uniformity would be ~0.2%, neglecting the small beam tilt and curvature.

laser beam. The peak laser intensity is, typically, 1×10^{14} W/cm^2. There is also a low level prepulse, with an intensity of $< 10^{-6}$ of the main pulse. This prepulse heats the front of the foil target, but with a measured temperature less than 0.4 eV.

In front of the main laser pulse we typically introduce a 4 ns foot with ~3% of the peak intensity. This pulse shaping reduces the isentrope of the target, in order to better match the behaviour of a fusion pellet. The foot can be introduced in two ways: either by diverting one of the laser beams so that it arrives 3–4 ns early, or by adding a foot onto all 40 of the accelerating beams. The laser intensity at the target is the same in both cases, but the non-uniformity in the foot differs by $\sim\sqrt{40}$. We use both types of pulse shape to evaluate the effects of laser beam uniformity. Of course, the most important parameter of the Nike laser is its superb beam uniformity as shown in Fig. 1.

A single beam has a measured rms non-uniformity of only 1–1.5% in a 4 ns pulse (neglecting the few per cent tilt and curvature). With 40 overlapped beams, the rms laser non-uniformity is currently below our diagnostic resolution, but is estimated to be reduced by almost $\sqrt{40}$, to ~0.2%. (Computer simulations of laser imprinting on targets indicate that the imprinting of mass perturbations typically lasts several nanoseconds; this imprinting time is similar to the averaging time used to measure the Nike laser quality.)

3. TARGET ACCELERATION EXPERIMENTS

The Nike targets have been CH foils, typically 30–40 μm thick. We have used three types: smooth, rippled and roughened. The smooth targets, typically, have a surface roughness of 10–40 Å. The rippled targets have had sinusoidal modulations with a wavelength of 30 and 60 μm and an amplitude of 0.1–1.0 μm. The roughened targets have a broad spectrum of surface roughness, with amplitudes in the range of 0.2–2.0 μm.

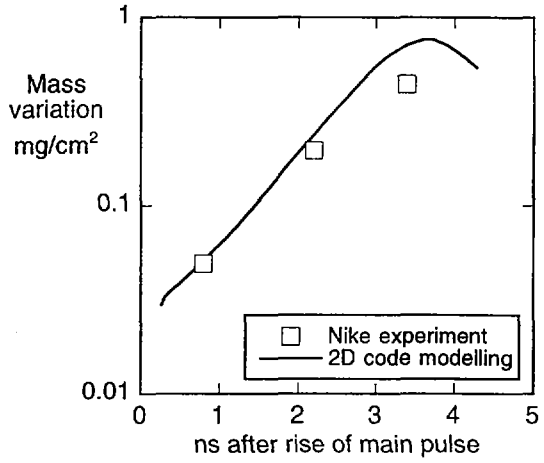

FIG. 2. Growth of mass modulations in a 47 μm thick CH foil. The target had an imposed 60 μm sinusoidal modulation with 0.5 μm peak-to-valley amplitude. Times are measured relative to the 50% rise of the main pulse. The foot on the pulse is therefore at negative time.

The targets have been studied with a wide variety of diagnostics, including optical pyrometry of the rear surface, optical streak camera emission from the rear surface, side-on X ray streak camera measurements of the foil acceleration, side-on optical shadowgrams of the plasma structure, front surface X ray emissions with a 250 eV narrow band X ray cassegrainian telescope, and X ray backlighting with a four frame camera to measure the mass modulations.

For the X ray backlighting, we have used two types of X ray imaging techniques: a standard pinhole arrangement and a new type of spherically curved quartz crystal that has excellent spatial resolution (~ 10 μm with a framing camera and 3 μm on film) and excellent spectral resolution (~ 0.02 Å).

Using the sinusoidally rippled targets, we have verified that the backlighting diagnostics work correctly and that the computer modelling accurately calculates both the linear and the non-linear growth of a perturbation. Figure 2 shows the measured mass modulation of a 60 μm perturbation at three times, using the spherically curved crystal imaging, along with the predictions of our 2-D computer model. At the first two measurement times, the agreement between experiment and modelling is excellent. (There are no free parameters in the modelling.) At the latest time, the target behaviour is very non-linear, and the experiment shows evidence of structures developing along the target grooves that could not be modelled with a 2-D code. This is probably the reason for the small late-time deviation between prediction and experiment.

With the smooth target and a single beam in the foot of the pulse, we observe a small measurable mass modulation late in the acceleration. With a smooth target and 40 overlapped beams in the foot of the pulse, the mass non-uniformity is below the diagnostic resolution, in disagreement with our computer modelling. These experimental results are promising for fusion, but not yet understood. We are now investigating the reasons for our surprisingly successful acceleration of the foil targets.

4. CONCLUSIONS

The Nike programme had three initial objectives: (1) to demonstrate that KrF lasers produce an ultra-uniform laser illumination; (2) to develop KrF laser technology so that it can be used routinely for target experiments; (3) to evaluate the laser uniformity requirements and the target design requirements to provide sufficient control of the fluid instabilities for high gain laser fusion. The first two objectives have been successfully accomplished; the third is ongoing. The initial results have been very positive, with surprisingly low mass perturbations when we accelerate a smooth target. We hope to have an initial overall evaluation of this approach to fusion in the next two years, before the next IAEA Conference in 1998.

ACKNOWLEDGEMENTS

This research work is supported by the US Department of Energy.

DISCUSSION

B. COPPI: You referred to fusion experiments to be done with the next generation of KrF lasers. Do you have a plan for these experiments?

S.E. BODNER: The role of NRL is to pioneer new ideas. Any next generation KrF laser should be developed at other laboratories. We would of course be happy to work with other laboratories that want to develop KrF for fusion.

J. SHEFFIELD: Since the gain in energy absorption for direct drive versus indirect drive is seven to nine times, the 3 kJ of your laser is equivalent to 21 to 27 kJ for indirect drive. Do you plan any direct drive experiments with spherical targets?

S.E. BODNER: At the present level of energy the target would have to be small and the pulse length would have to be about 1 ns. The existing laser has a 4 ns pulse. Therefore information would be better obtained from a combination of planar target experiments with NIKE and spherical targets using the Omega glass laser.

C. YAMANAKA: Direct drive is suitable for energy applications, whereas the indirect scheme is for weapons simulation. Direct drive is thus of central importance for energy production. What is your opinion?

S.E. BODNER: I agree completely.

T. DESAI: Have you measured the space resolved growth of mass modulation, and whether the growth of mass modulation coincides with the peaks of 60 μm perturbations (rough surface of the target)?

S.E. BODNER: We can only measure the space resolved growth in the large amplitude non-linear regime. In that regime, the code is in excellent agreement with the measured amplitudes of the 60 μm perturbation. With regard to randomly rough perturbations, or smooth targets, we have not yet been able to compare the measurements with the code predictions.

SUPER-ASHURA KrF LASER PROGRAMME AT ETL

Y. OWADANO, I. OKUDA, Y. MATSUMOTO,
I. MATSUSHIMA, E. TAKAHASHI, E. MIURA,
H. YASHIRO, T. TOMIE, K. KUWAHARA[1], M. SHINBO[1]
Electrotechnical Laboratories, AIST, MITI,
Umezono, Tsukuba, Ibaraki,
Japan

Abstract

SUPER-ASHURA KrF LASER PROGRAMME AT ETL.

In the Super-ASHURA KrF laser at the Electrotechnical Laboratories, the main amplifier with full pumping duration (270 ns) and 12 optical beam lines has been completed. At present, the main amplifier can generate 3.7 kJ output energy with full aperture, and a total output energy of 2.7 kJ has been demonstrated with 12 beams (20 ns × 12) double pass amplification. For irradiation smoothing, a two dimensional smoothing effect has been demonstrated by combining one dimensional broadband random phase irradiation and angular dispersion. In the Raman amplification, which is to be used for pulse shaping, short Stokes pulses (67 ps, 2 ns) have been stably generated in mixed gas, and a power conversion efficiency of 73% has been demonstrated in the double pass amplifier. The two dimensional target acceleration profile has been measured by using short (< 100 ps) 268 nm probe pulses.

1. INTRODUCTION

Krypton fluoride (KrF) laser is an efficient ultraviolet gas laser that is considered to be one of the most promising drivers for inertial confinement fusion (ICF). The efficiency of the KrF laser medium exceeds 10%, and the gas medium allows rapid cooling for high repetition rate operation. Its short wavelength (248 nm) yields good target coupling (high classical absorption, high ablation pressure, etc.), and its broad bandwidth (1 nm) enables smooth irradiation by means of wavelength dispersion and/or induced incoherence. At the ETL, a KrF laser system, Super-ASHURA, is being developed to establish KrF laser driver technology and to perform target shooting experiments with laser energies up to 5 kJ [1]. A main amplifier with 60 cm window aperture and an optical system for 12 pulse multiplexing with irradiation smoothing and pulse shaping functions are added to ASHURA (660 J, six beams).

[1] Science University of Tokyo, Noda, Chiba, Japan.

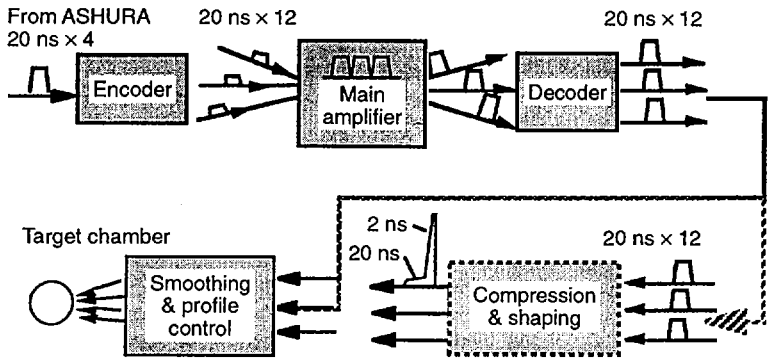

FIG. 1. Optical system of Super-ASHURA.

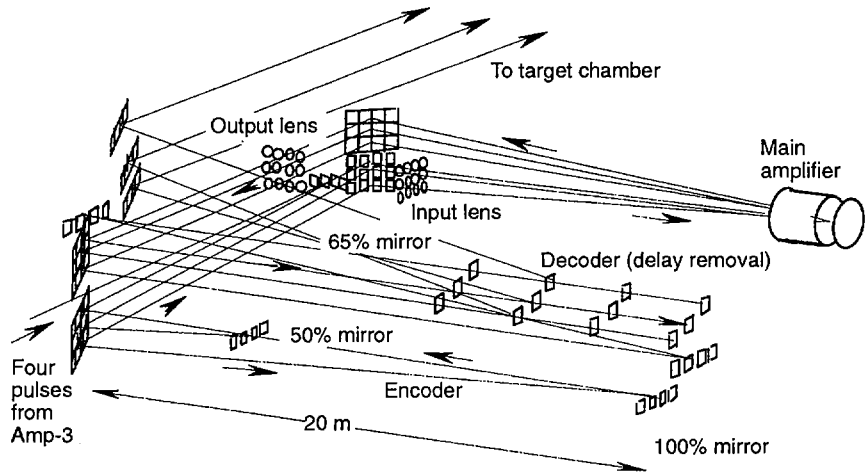

FIG. 2. Twelve beam encoder and decoder of Super-ASHURA.

2. THE SUPER-ASHURA SYSTEM

The optical system of Super-ASHURA is shown in Fig. 1. Four pulses from ASHURA are angularly multiplexed to form a 20 ns × 12 pulse train by the encoder; then, the pulse train is double pass amplified by the main amplifier. Details of the twelve beam encoder and decoder are shown in Fig. 2. Because of the short distance between amplifier and input/output mirror arrays, the angle for angular multiplexing is rather large (2.1°), and the average filling factor of the output beams at the amplifier output window is limited to 74%.

Delays between output pulses are removed in the decoder; then the pulses are directed towards the target chamber by final turning mirrors.

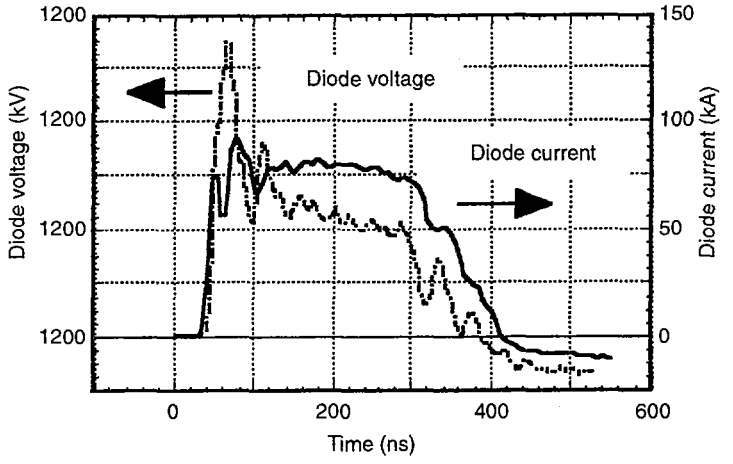

FIG. 3. Electron beam voltage and current waveforms.

3. MAIN AMPLIFIER

The main amplifier of Super-ASHURA, Amp-4 (gas volume = 60 cm diameter × 2 m length), is pumped by eight electron beam diodes (750 kV, 100 kA × 16) arranged cylindrically around the laser gas cell.

The e-beam diodes are fed by four pulse forming lines (PFLs, 68 cm diameter, 3.7 Ω, 270 ns) charged by two Marx banks. The electron beam current and voltage waveforms are shown in Fig. 3. Because of the temporal change of the anode–cathode spacing of the e-beam diode (diode closure by cathode plasma expansion), the e-beam voltage drops gradually and becomes rather low at the end of the pulse. The time averaged impedance (5.5 Ω) is lower than the design value (7.5 Ω). So far, starting from 128 kJ stored in the PFLs, 38 kJ has been deposited in 850 torr laser gas.

The pumping power density is estimated to be 250 kW/cm^3. The efficiency of the e-beam deposition can still be improved by matching the diode impedance and controlling the e-beam shape. Also, the initial PFL stored energy can be increased up to 180 kJ at full power operation of the Marx banks. By combining these improvements, we expect to deposit >60 kJ into the laser gas.

In the main amplifier, a fluorine partial pressure of 1 torr was found to be optimum because self-absorption increases at higher concentration and fluorine consumption during pumping becomes apparent at lower concentration. The laser gas mixture being used consists of 1 torr F_2, 150 torr Kr and 700 torr Ar.

In double pass amplification of one beam, a maximum output energy of 240 kJ (20 ns) has been obtained with an putput window filling factor of 80%. In the case of 12 beam (20 ns × 12 beams) amplification, a total output energy of 2.7 kJ has

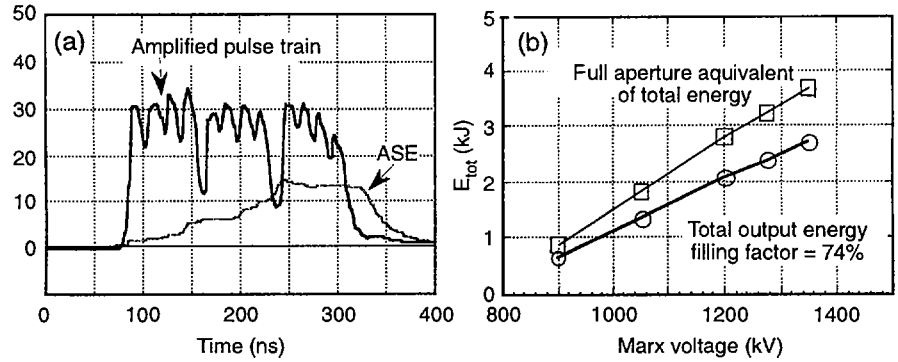

FIG. 4. (a) Waveform of pulse train from main amplifier; (b) total output energy from main amplifier.

been obtained. The waveform of the output pulse train is shown in Fig. 4(a), and the dependence of the total output energy on the Marx voltage is shown in Fig. 4(b). Taking the average filling factor of 74% into account, this result corresponds to a full aperture output energy of 3.7 kJ; the local intrinsic efficiency (output optical energy/deposited e-beam energy) has reached 9.5%. The output power density (5.2 MW/cm^2) is 3.8 times as high as the saturation intensity and lies already in the highly saturated region.

4. TWO DIMENSIONAL IRRADIATION SMOOTHING

For smoothing the focal intensity profile the one dimensional broadband random phase (BRP) irradiation scheme has been extended to the two dimensions [2]. In this technique, the original broadband output from the master oscillator is angularly dispersed in vertical direction by multiple reflection in a slightly wedged etalon; then,

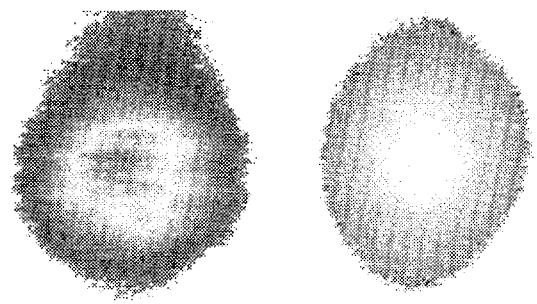

FIG. 5. Left: 1-D horizontal smoothing; right: 2-D smoothing.

after amplification, the beam is spectrally dispersed in horizontal direction by refraction in a thin wedge and focused through a random phase plate. The effect of 2-D smoothing is shown in Fig. 5. Although this technique uses a combination of angular and spectral dispersion, a similar effect can be obtained by angular dispersion in both horizontal and vertical directions. This purely angular, two dimensional smoothing can be applied to narrow band pulses which are shaped by the Raman process to be discussed below.

5. RAMAN AMPLIFICATION

Raman amplification is being investigated for pulse shaping and power multiplication of the 20 ns high energy pulse. For this purpose, a short Stokes pulse generator and a multipass Raman preamplifier have been developed.

In the short Stokes pulse generator, in which a hydrogen and methane (or hydrogen and SF_6) gas mixture is used as Raman medium, 2 to 5 ns forward Stokes pulses (268 nm) can be generated stably from the 20 ns master oscillator output. This Stokes pulse duration is determined by the difference in vibrational level transient time (30 ps for methane, 1 ns for hydrogen) and saturated Raman gain which can be adjusted by the partial pressures of the two gases. The output pulse from the generator has been double pass amplified by a preamplifier filled with methane (Fig. 6). In this case, the timing between the Stokes and pump pulses was varied in the first and second pass so that the Stokes pulse could extract energy from different parts of the

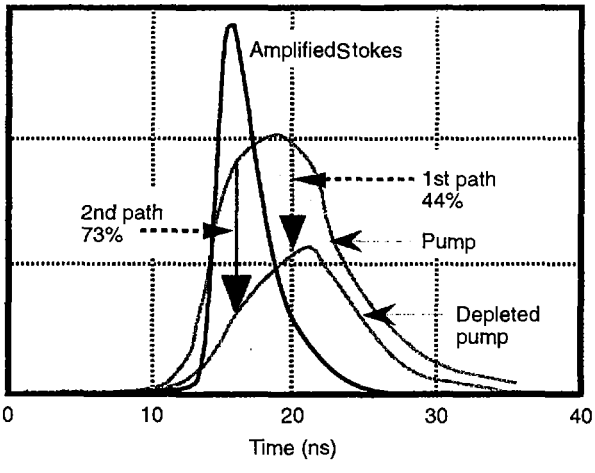

FIG. 6. Double pass amplified Stokes pulse shape.

pump pulse. In this preliminary experiment, the Stokes pulse extracted 73% of the pump energy in the second pass, and the peak power reached 1.4 times pump power. In this scheme, a power multiplication of five to six can be expected, with a negligible second Stokes generation.

In parallel to the Raman amplification, a Ti sapphire, laser based front end is being installed to obtain the extremely high power that is required for the fast ignition related experiment. Several terawatts per pulse can be expected by direct amplification of 2 ps pulses.

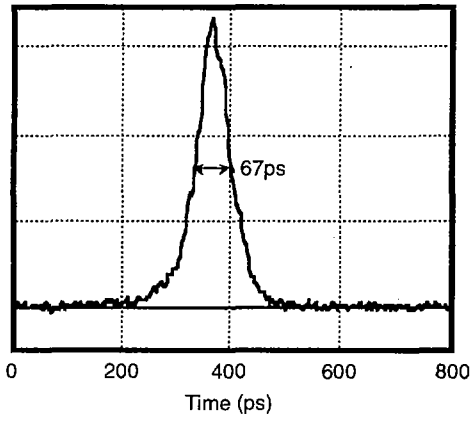

FIG. 7. Waveform of probe pulse produced by backward Stokes generation in mixed gas.

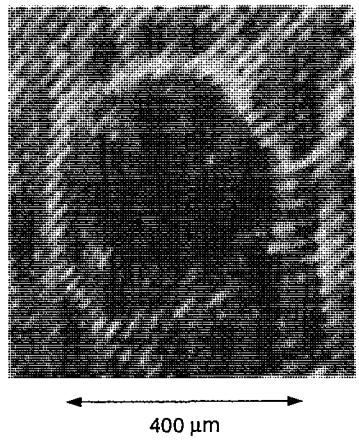

FIG. 8. Reflective interferogram of the aluminium foil target rear surface.

7. TARGET SHOOTING

Planar foil target shooting experiments are being performed with ASHURA in order to investigate the effect of irradiation smoothing on the hydrodynamic motion of the target. To measure the target acceleration profile two dimensionally, a short Stokes (268 nm) probe pulse which is perfectly synchronized with the main pulse was used [3]. The probe pulse is produced from a part of the 20 ns master oscillator pulse by backward Stokes generation in the mixed gas; the pulse width becomes as short as 67 ps. The waveform of the probe pulse is shown in Fig. 7. Figure 8 shows the reflective interferogram of the rear surface of the 50 μm aluminium target taken with the short probe pulse. In this case, only a random phase plate was used with a 10 ns flat-top laser pulse, and the probe was injected at the rising edge of the main pulse. Detailed experiments are being performed with various smoothing techniques.

REFERENCES

[1] OWADANO, Y., et al., in Plasma Physics and Controlled Nuclear Fusion Research 1994 (Proc. 15th Int. Conf. Seville, 1994), Vol. 3, IAEA, Vienna (1995) 121.

[2] MATSUSHIMA, I., et al., Opt. Commun. **120** (1995) 299.

[3] TAKAHASHI, E., et al., Jap. J. Appl. Phys. **34** (1995) 856.

HYDRODYNAMIC INSTABILITY EXPERIMENTS AT GEKKO XII

H. AZECHI, M. NAKAI, K. SHIGEMORI,
A. NISHIGUCHI[1], N. MIYANAGA, M. HONDA,
H. SHIRAGA, R. KODAMA, O. MAEKAWA,
R. ISHIZAKI, H. TAKABE, K. NISHIHARA,
Y. KATO, T. YAMANAKA, S. NAKAI, K. MIMA
Institute of Laser Engineering,
Osaka University,
Suita, Osaka

T. ENDO[2], C. YAMANAKA
Institute for Laser Technology,
Osaka

Japan

Abstract

HYDRODYNAMIC INSTABILITY EXPERIMENTS AT GEKKO XII.

Hydrodynamic instabilities play an important role in inertial confinement fusion implosions. Target surface perturbations will grow, primarily owing to the Rayleigh–Taylor (R–T) instability and finally resulting in fuel–pusher mixing that degrades the implosion performance. Good understanding of the instabilities is necessary to limit the mixing to a tolerable level. At the GEKKO XII laser facility, an extensive series of direct drive experiments has been conducted on the effect of rippled shock propagation, initial imprinting and its suppression by X ray pre-irradiation, and the R–T instability in the linear regime. As to the drive laser, partially coherent light achieves the state-of-the-art uniformity by which spurious imprints are minimized. For the initial imprinting experiments, a single mode perturbation was introduced on the foot pulse for imprint, followed by a uniform main pulse for R–T amplification. The experimental R–T growth rate was significantly reduced in comparison to the classical growth rate.

1. INTRODUCTION

As is well known, hydrodynamic instabilities such as the Rayleigh–Taylor (R–T) instability play an important role, not only in inertial confinement fusion (ICF) implosions [1] but also in supernova explosions [2]. The R–T instability in supernova explosions results in hydrodynamic mixing between layers of different materials.

---

[1] Present address: Osaka Institute of Technology, Omiya, Osaka, Japan.

[2] Present address: Center for Integrated Research in Science and Engineering, Nagoya University, Nagoya, Japan.

This is a more probable explanation for the earlier X ray and γ ray emissions from the SN1987A supernova than that predicted by spherically symmetric models. In ICF implosions, target perturbations are seeded, in addition to original perturbations, by initial imprinting of laser irradiation non-uniformity. These perturbations may be amplified by rippled shock propagation before the shock breakout and will grow as a result of the R–T instability after the shock breakout. Subsequent feedthrough seeds the perturbations at the fuel–pusher interface. These, together with the initial inner surface perturbations, will grow again because of the R–T instability during the deceleration phase, resulting in fuel–pusher mixing, which may degrade the implosion performance significantly. Good understanding of the instabilities is, therefore, necessary to limit the mixing to a tolerable level. The perturbations on an ablation surface of the ICF targets are seeded and/or amplified in the following processes:

(1) When the ablation pressure is first applied to an ICF target, a rippled shock wave [3, 4] is launched, in accordance with a target surface perturbation. A concave shock launched from a region where the target is initially thicker than the neighbours tends to focus and strengthen the shock wave, and a convex shock launched from a region where the target is initially thinner behaves in the opposite way. Accordingly, the wave front is first flattened and, since at this instance the pressure perturbation behind the shock becomes maximum, afterwards the wave front perturbation overshoots. This causes an oscillation of the shock front. The amplitude of the perturbation decreases with the propagation distance, because of the increase in the volume of the perturbed region [5]. Therefore, any rippled shocks are flattened after sufficient propagation (typically, more than one perturbation wavelength). The propagation of rippled shocks is accompanied by lateral mass flow. The shock with the concave (convex) wave front causes concentration (deconcentration) of the fluid mass. Thus, the lateral fluid motion associated with the rippled shock propagation amplifies the areal density perturbation, even without any growth of the perturbation on the ablation front. The areal density perturbation itself does not reverse its phase, but grows and saturates as a result of the decrease in the perturbation amplitude of the rippled shock wave.

(2) When perturbed drive is applied, an initially flat shock is forced to be rippled, in accordance with the pressure perturbation. The wave front of the rippled shock behaves as a decreasing oscillation, in the same way as in case (1). The ablation front is now deformed, according to the pressure perturbation. The areal density perturbation is introduced and amplified both by the propagation of the rippled shock and by the deformation of the ablation front. Experimental studies of these hydrodynamic responses, referred to as imprint, have recently been started for various laser smoothing techniques [6] and for imposed single mode non-uniformities [7, 8]. The imprint may be relaxed in a preformed corona generated by X ray preirradiation [9] or in a foam buffer layer [10].

(3) These amplifications of the perturbations before the shock breakout will determine the initial perturbation of the subsequent R–T instability after the shock has

broken out and the rarefaction has reached the ablation front. Since the initial perturbations in most ICF targets are much smaller than the wavelength, the perturbation first grows exponentially with time, up to a point when the amplitude becomes about 0.1 of the perturbation wavelength. The R–T growth rate is expected to be reduced from the classical growth rate because material ablation on the unstable surface may remove the perturbation away from the surface [11]. Thus, in most cases, the R–T instability in the linear regime leads to the largest growth of perturbation. The growth rate γ that includes the ablation effect is given by the Takabe formula [12]: $\gamma = 0.9\sqrt{kg} - \beta k\dot{m}/\rho_a$, where k is the wavenumber of the perturbation, g the acceleration, $\dot{m}$ the mass ablation rate per unit area and ρ_a the peak density at the ablation front. The factor β depends on the structure of the ablation surface; $\beta \approx 3$–4 is expected [12] in direct drive ablation. The R–T instability in the linear regime has been extensively studied in the X ray driven ablation [13]. Extensive studies [14] have also been made for direct drive ablation. However, very few experiments [15] refer to the linear regime because small initial perturbations as are necessary for linear growth measurements may easily be influenced by the initial imprint of the laser irradiation non-uniformity.

In this report, we will present an accumulated database on the rippled shock propagation with varying initial perturbation. We will also describe the first experiment [7] on the single mode initial imprint as well as the imprint suppression by soft X ray pre-irradiation [16]. We will present the observation of the linear R–T growth rate in imprint free conditions.

2. EXPERIMENTAL SET-UP

We employed two different experimental set-ups: one for the experiments on rippled shock waves and another for the experiments on imprint and its suppression by soft X ray pre-irradiation, as well as on R–T growth rates. The common parameters are as follows: The drive laser beam is frequency doubled ($\lambda_L = 0.53$ μm), partially coherent light (PCL) [17, 18] with a bandwidth of 0.2 nm, a beam divergence of 64 times the diffraction limit and a one dimensional angular spectral dispersion, generating a time integrated non-uniformity of 2%. The PCL pulse has a flat-top shape with a 50 ps rise time and a 100 ps fall time. The targets were polystyrene foils of 1.06 g/cm^3 density.

In the rippled shock experiments, the targets, with sinusoidal perturbation on the laser irradiation side, were irradiated at 4×10^{13} W/cm^2 intensity and at an incidence angle of 31.7°. The targets were diagnosed in three ways: first, ripples of the shock front were observed by optical emission due to shock breakout at the rear surface of the targets. Second, perturbations of the areal density were observed by face-on X ray backlighting using a Ge X ray source producing 1.6–1.8 keV X rays. Third, ripples of laser irradiated surfaces were observed by side-on X ray backlighting using Mo targets generating 2.5–2.9 keV X rays.

In the experiments on imprint, its suppression and the R–T instabilities, targets with 16 μm thickness were irradiated with a stepwise pulse consisting of a foot pulse of (1 or 0.5) $\times$ 10^{13} W/cm^2 intensity and 1.8 ns long followed by a main pulse of 1 $\times$ 10^{14} W/cm^2 intensity and 1.8 or 2.2 ns long. The angle of incidence was 37.4°. In the imprint experiments, the foot pulse intensity was sinusoidally modulated by varying amplitudes of 10–40% at a perturbation wavelength of 100 μm, while the main pulse intensity was kept uniform to amplify the imprint perturbation by the R–T instability. In the imprint suppression experiments, the targets were pre-irradiated by soft X rays before the onset of the foot pulse at 400 ps. The soft X rays were generated in a separate Au foil that was irradiated by a separate beam. As to the R–T experiments, sinusoidal perturbations of 60 μm wavelength were imposed on the laser irradiation side of the target. The targets were then irradiated by unmodulated PCL beams. The areal density perturbations were measured with face-on X ray backlighting using Cu targets producing 1.1–1.3 keV X rays.

3. EXPERIMENTAL RESULTS

3.1. Rippled shock wave

Figure 1(a) shows the rippled shock amplitude normalized by the initial amplitude at the ablation front, a_s/a_0, as a function of the shock travelling distance normalized by the perturbation wavelength, d/λ. The ripple amplitude was determined by multiplying the shock velocity by the difference in the shock breakout times. The shock travelling distance corresponds to the target thickness, which was varied from 25 to 160 μm. The perturbation wavelengths were either 60 or 100 μm. The initial perturbation amplitudes were 2.5–5 μm for the 60 μm perturbation wavelength and 3.5–10 μm for the 100 μm wavelength. The data show oscillations with decreasing amplitude. The phase inversion of the shock front perturbation occurs at $d/\lambda \approx 0.7$–0.8, in agreement with previous measurements [4], and again at $d/\lambda \approx 1.5$. There is no noticeable dependence on the initial amplitudes for $a_0/\lambda \approx 1/30$–$1/10$. The open plotting symbols show the results of the two dimensional simulation code IZANAMI [19] and agree fairly well with the experimental results.

Figure 1(b) shows the data of the areal density perturbation. The areal density perturbation first grows up to about a factor of four for the normalized propagation distance $d/\lambda < 1$ and nearly saturates thereafter. This is consistent with the perturbation growth due solely to the rippled shock propagation, as will be described below. Since the sound velocity behind the shocks is high compared to the shock velocity, density perturbations behind the shock are expected to be fairly smoothed. Accordingly, if one makes the approximation that the shock compressed density is spatially uniform, and using the previous finding [4] that perturbations on ablation fronts are stable before shock breakout, the areal density perturbation is given by

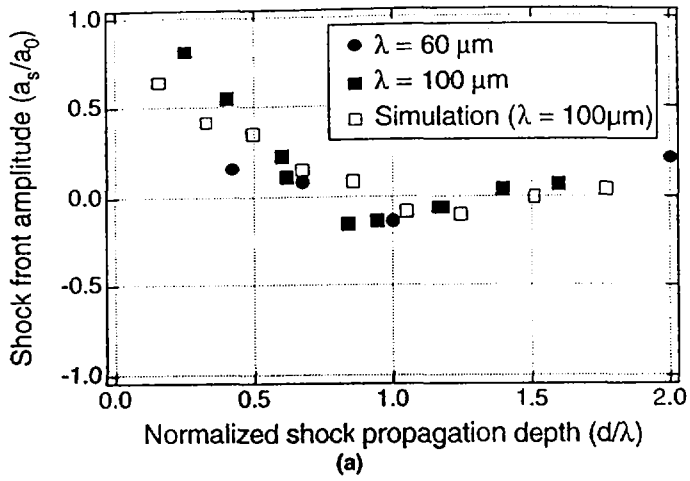

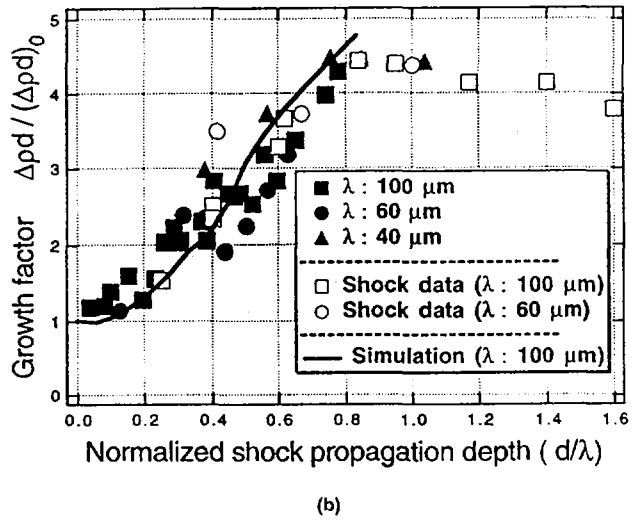

FIG. 1. (a) Shock front ripple amplitudes normalized by initial amplitudes versus shock propagation distances normalized by perturbation wavelengths; (b) growth factor of areal density perturbations versus normalized propagation distance.

$\rho_s(a_0 - a_s) + \rho_0 a_s$, where ρ_s is the density behind the shock, ρ_0 the initial density, a_s the ripple amplitude of the shock front and a_0 the initial ripple amplitude at the ablation surface. Using a density ratio for strong shock compression of $\rho_s/\rho_0 = 4$, we obtain the ratio of the areal density perturbation to the initial one as $\Delta\rho d/(\Delta\rho d)_0 = \Delta\rho d/\rho_0 a_0 = 4 - 3\, a_s/a_0$. Thus, the growth factor of the areal density perturbation can be deduced from the measured rippled shock amplitude. This is shown in

Fig. 1(b) by open symbols. The areal density perturbation evaluated from the rippled shock data agrees well with that directly measured by face-on X ray backlighting. These data extend the parameter region of the previous measurements [4].

3.2. Imprint

In the imprint experiments, small imprint amplitudes were amplified by the R–T instability so as to become observable. This procedure is, indeed, indirect as imprint measurement, but may provide an equivalent initial perturbation which gives the same amplitude after the R–T growth as that from the initially imposed perturbation. Figure 2 shows X ray streak images for the case of (a) 40%, (b) 10% and (c) no modulation. In cases (a) and (b), the X ray contrast increases with increasing modulation depth. No observable perturbation growth is seen in the no-modulation case. Since the perturbation growth due solely to the PCL is lower than the detection limit ($\approx 5 \times 10^{-5}$ g/cm^2 or 0.5 μm) even at the end of the drive (maximum R–T growth), the imprint amplitude is deduced to be < 0.05 μm, which is much less than the imprints for the perturbed drive. A comparison with modelling is under way.

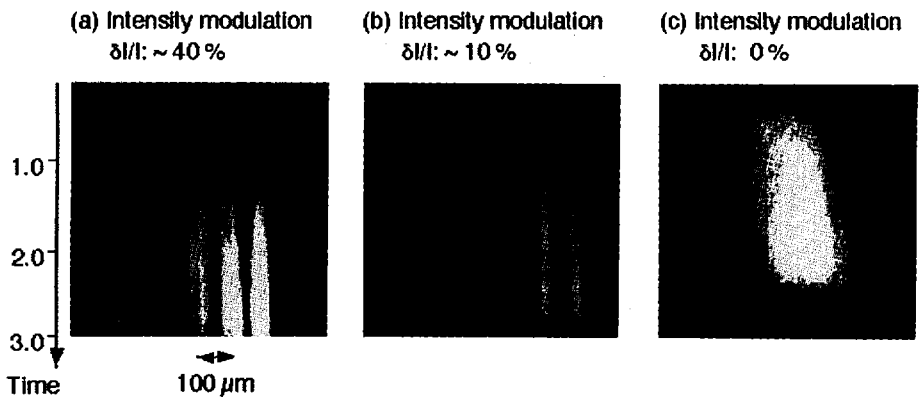

FIG. 2. Streaked X ray backlighting images of the accelerated plastic planar targets irradiated with a sinusoidally modulated laser beam of (a) 40% and (b) 10% modulation depth. The imprinted areal density perturbations are amplified by the subsequent R–T instability driven by uniform laser irradiation. No significant perturbation is observed for the case of no modulation (c). The timing of the vertical axis is arbitrarily offset.

3.3. Imprint suppression by soft X ray pre-irradiation

In the imprint suppression experiments by soft X ray pre-irradiation, the imprint amplitude with X ray pre-irradiation was reduced to be 60% of that without X ray pre-irradiation. The details of the experiments are described in Ref. [16]. We

estimate the smoothing effect by using the cloudy day model. Assuming that the X ray emission is isotropic in 2π, the X ray irradiation intensity on the sample target is calculated to be 7×10^{10} W/cm^2; hence, the corona temperature is 30 eV. The expansion distance, D, is estimated to be $D = c_s\tau$, where c_s is the sound speed of the corona plasma and τ is the duration. For $c_s = 3.5 \times 10^6$ cm/s, from the corona temperature, and $\tau = 400$ ps (time difference between the onset of the X ray pulse and that of the foot pulse), we obtain $D = 14$ μm. According to the cloudy day model, the thermal smoothing factor becomes $\exp(-kD) = 0.4$ for $k = 2\pi/100$ μm. This is in close agreement with an experimental reduction factor of 0.6.

3.4. Rayleigh–Taylor instability

Figure 3 shows results of the growth factor (areal density perturbation divided by the initial perturbation) for three initial amplitudes with the same perturbation wavelength (60 μm). The time origin corresponds to the onset of the main drive. For the large amplitude case (1 μm), the growth saturates and switches to the non-linear growth regime at an early time of around 0.5 ns. For the small initial amplitude case, 0.1 and 0.3 μm, the growth factors are well fitted by an exponential curve (dashed line) with $\gamma_{exp} = 1.2 \pm 0.1$ ns^{-1}. In contrast, the classical growth rate of the

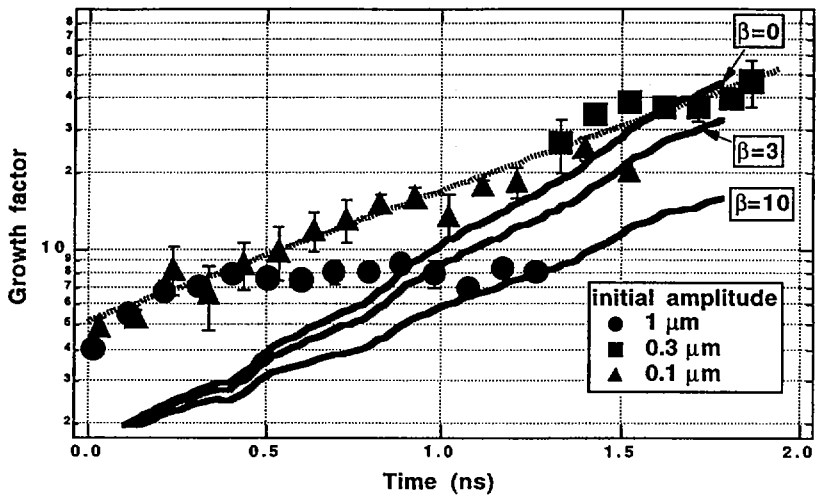

FIG. 3. Growth factor of areal mass density perturbation versus time for three different initial amplitudes. Dotted line: best fit to the experiments. Solid lines: calculated perturbation growth using gravity, mass ablation rate and ablation density from the one dimensional simulation, with laser flux adjusted to reproduce experimental acceleration.

R-T instability is calculated to be $\gamma_{classical} = (kg)^{1/2} = 2.1 \pm 0.1$ ns^{-1}, where the acceleration g was measured by side-on backlighting to be g = 41 μm/ns^2. The observed growth rate is reduced to about 60% of the classical growth rate.

Among various mechanisms able to reduce the growth rate, the density gradient is ruled out because the simulated density scale length of < 1 μm is much smaller than the perturbation wavelength. The finite thickness effect [20] may contribute only a few per cent of the reduction. The ablation effect is commonly considered to be the dominant stabilizing mechanism. For a quantitative comparison, we have numerically solved a simple differential equation, $d^2\xi/dt^2 = \gamma^2\xi$, for the perturbation amplitude ξ, where the growth rate γ is given by the Takabe formula quoted above, and $\dot{m}(t)$, $\rho_a(t)$ and g(t) are given by the one dimensional hydrocode ILESTA-1D [21]. The incident laser flux was adjusted to fit the calculated target trajectory with the experimental one. The calculated surface perturbation ξ is then multiplied by the target density ρ_a to yield a comparison with the experimentally measured areal density perturbation. This is shown in Fig. 3 for $\beta = 0$, 3 and 10. The slope of the calculated growth curve is excessively higher than that given by the experiments. (The initial growth at $t < 0$ is described by a tentative model, which is not discussed here. Only the slope for $t > 0.5$ ns is meaningful in the present discussion.) This comparison indicates that the β value is much larger than expected or the ablation density is lower than the simulation value.

One probable mechanism reducing the ablation density is preheating due to non-local heat transport. High energy electrons in the tail of a Maxwellian distribution may penetrate into, and preheat, the target, thereby reducing the density at the ablation front. The two dimensional hydrocode KEICO-2d [22], with a Fokker-Planck (F-P) equation, shows that the growth rate is significantly reduced when non-local heat transport is included. The experimental results are in closer agreement with the simulation results of the F-P case than those of the classical transport. The non-local transport effect is expected to be more pronounced for higher laser irradiance. Our recent experiments on the intensity scaling of the growth rate support this conclusion.

REFERENCES

[1] NUCKOLLS, J.H., WOOD, L., THIESSEN, A., ZIMMERMAN, G.B., Nature (London) **239** (1972) 129.

[2] ARNETT, W., et al., Astrophys. J. **341** (1989) L63; SHIGEYAMA, T., NOMOTO, K., Astrophys. J. **360** (1990) 242.

[3] MUNRO, D.H., Phys. Fluids B **1** (1989) 134.

[4] ENDO, T., et al., Phys. Rev. Lett. **74** (1995) 3608.

[5] ISHIZAKI, R., NISHIHARA, K., "Propagation of a rippled shock wave driven by nonuniform laser ablation" (submitted to Phys. Rev. Lett.).

[6] TAYLOR, R.J., et al., Phys. Rev. Lett. **76** (1996) 1643; KALANTAR, D.H., et al., Phys. Rev. Lett. **76** (1996) 3574.

[7] AZECHI, H., et al., "Dynamics of rippled shock wave in laser-irradiated targets", Physics of Compressible Turbulent Mixing (Proc. 5th Int. Workshop Stony Brook, 1995); "Single-mode initial imprinting of laser-irradiated targets" (Proc. 37th APS/DPP, Louisville, 1995; post deadline).
[8] WOLFRUM, E., et al., "Measurement of single mode imprint by XUV laser radiography" 24th ECLIM, Madrid, 1996.
[9] DESSELBERGER, M., et al., Phys. Rev. Lett. **68** (1992) 1539.
[10] KATO, Y., et al., in Plasma Physics and Controlled Nuclear Fusion Research 1994 (Proc. 15th Int. Conf. Seville, 1994), Vol. 3, IAEA, Vienna (1995) 45.
[11] BODNER, S.E., Phys. Rev. Lett. **33** (1983) 761.
[12] TAKABE, H., et al., Phys. Fluids **28** (1985) 3676.
[13] REMINGTON, B., et al., Phys. Rev. Lett. **67** (1991) 3259.
[14] RAVEN, A., et al., Phys. Rev. Lett. **47** (1981) 1049; COLE, J., et al., Nature (London) **299** (1982) 328; GRUN, J., et al., Phys. Rev. Lett. **58** (1987) 2672; GLENDINNING, S.G., et al., Phys. Rev. Lett. **69** (1992) 1201.
[15] KNAUER, J., et al., Bull. Am. Phys. Soc. **39** (1994) 1640.
[16] SHIRAGA, H., et al., IAEA-CN-64/B2-4, this volume.
[17] NAKANO, H., et al., J. Appl. Phys. **73** (1993) 2122.
[18] MIYANAGA, H., et al., in Plasma Physics and Controlled Nuclear Fusion Research 1994 (Proc. 15th Int. Conf. Seville, 1994), Vol. 3, IAEA, Vienna (1995) 153.
[19] NISHIGUCHI, N., YABE, T., J. Comput. Phys. **52** (1983) 390.
[20] REMINGTON, B.E., Phys. Fluids B **4** (1992) 967; LANDAU, L.D., LIFTSHITZ, E.M., in Fluid Mechanics, 2nd ed., Section 12, Pergamon Press, New York (1987) 36.
[21] TAKABE, H., et al., Phys. Fluids **10** (1988) 2884.
[22] HONDA, M., et al., "2d Fokker–Planck Simulation for Ablative Rayleigh–Taylor Instability", paper presented at 24th ECLIM, Madrid, 1996.

HYDRODYNAMIC INSTABILITY EXPERIMENTS ON THE NOVA LASER*

B.A. REMINGTON, S.G. GLENDINNING, D.H. KALANTAR, K.S. BUDIL, O.L. LANDEN, B.A. HAMMEL, J.D. KILKENNY, M.M. MARINAK, S.V. WEBER, S.W. HAAN, A. RUBENCHIK, R.J. WALLACE, P. MILLER, T. PEYSER, K. MIKAELIAN, M.H. KEY[1], J.P. KNAUER[2], W.W. HSING[3], D. GALMICHE[4], M.A. BLAIN[4], J. KANE[5], W.M. WOOD-VASEY[6], M. BERNING[7], D. OFER[8], D. SHVARTS[8]
Lawrence Livermore National Laboratory,
Livermore, California,
United States of America

Abstract

HYDRODYNAMIC INSTABILITY EXPERIMENTS ON THE NOVA LASER.

Hydrodynamic instabilities are studied at the Nova laser in experiments in planar and spherical geometries. In indirect drive, the evolution of the Rayleigh-Taylor (RT) instability is examined. The effects of 2D versus 3D single-mode perturbation shape, the location of the perturbation at the ablation front versus at an embedded interface, the drive pulse shape, the multimode perturbation growth, and spherical convergence effects are investigated. In direct drive, the linear regime RT dispersion curve and the effect of laser imprinting on planar foils irradiated with blue versus green laser light are studied.

1. INTRODUCTION

Hydrodynamic instabilities play a critical role in efforts to achieve thermonuclear ignition through laser driven inertial confinement fusion (ICF).[1] The parameter regime for ignition is typically mapped out as laser power versus energy.[2] The upper (high-power) bound is set by the need to stay below the threshold for initiating laser-plasma instabilities. The low-power boundary is set by the limits imposed by hydrodynamic instabilities. For example, for a fixed total laser energy, a capsule imploded at relatively low power needs a higher aspect ratio (initial capsule radius/wall thickness, R/ΔR) to achieve sufficient implosion velocity to trigger ignition. However, since perturbation e-foldings due

* Work performed under the auspices of the US Department of Energy by Lawrence Livermore National Laboratory under Contract No. W-7405-ENG-48.

[1] Rutherford-Appleton Laboratory, UK.

[2] Laboratory for Laser Energetics, University of Rochester, New York, USA.

[3] Los Alamos National Laboratory, Los Alamos, New Mexico, USA.

[4] Centre d'études de Limeil-Valenton, France.

[5] University of Arizona, Tucson, Arizona, USA.

[6] Harvey Mudd College, Claremont, California, USA.

[7] Düsseldorf University, Düsseldorf, Germany.

[8] Nuclear Research Center, Negev, Israel.

to the Rayleigh-Taylor (RT) instability are roughly proportional to $(R/\Delta R)^{1/2}$, high aspect ratio designs are more prone to performance degradation due to hydrodynamic instabilities.[3] In optimizing an ignition design at a fixed total laser energy, one has to balance concerns about hydrodynamic instabilities at low power against the risk of triggering laser-plasma instabilities at high power. We discuss in this paper our experimental program at the Nova laser[4] to investigate hydrodynamic instabilities relevant to ICF.[5]

2. HYDRODYNAMIC INSTABILITIES IN INDIRECT DRIVE

We have experimentally investigated the 3D effect of perturbation shape on RT-induced perturbation growth,[6] as shown in Fig. 1a. The experiment was conducted by pre-imposing a precisely formed perturbation on one side of a ~60 μm thick planar plastic foil doped with bromine, $C_{50}H_{47}Br_3$ or CH(Br). The foil is placed across an opening on a 3 mm x 1.6 mm gold cylindrical hohlraum. Eight of the ten Nova laser beams are focused into the hohlraum with a shaped, 3.3 ns laser pulse with a peak-to-foot intensity contrast ratio of 8:1. This generates a nominally thermal x-ray drive with a peak radiation temperature of 200 eV, which ablatively accelerates the foil at a peak acceleration of 75 μm/ns^2. The imposed perturbations at the ablation front grow due to the RT instability, and are diagnosed in-flight using time resolved face-on radiography. The three perturbations studied all had the same magnitude wave vector, $k=(k_x^2+k_y^2)^{1/2}$ and the same initial amplitude,~2.5 μm, differing only in their shape: 3D square

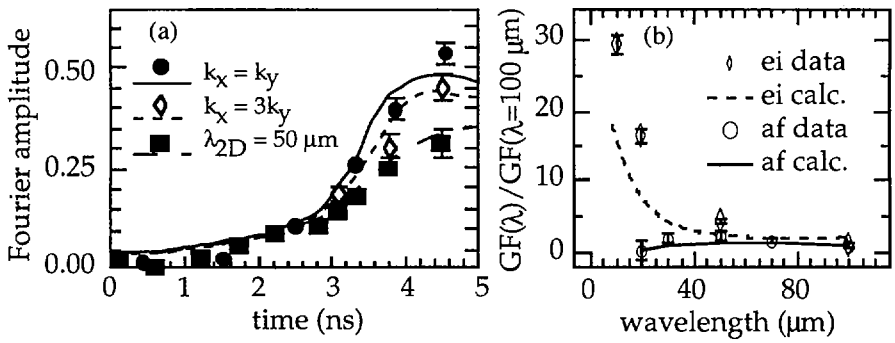

FIG. 1. (a) Results from indirect-drive experiments examining single-mode, Rayleigh-Taylor growth at an ablation front in 2D versus 3D. The plotting symbols represent the data, and the curves correspond to results from 3D numerical simulations. (b) Results from indirect-drive experiments examining 2D single-mode Rayleigh-Taylor growth at an embedded interface (ei) versus at an ablation front (af). Symbols are the data; the curves are calculations assuming classical growth (dashed curve) and ablatively stabilized growth (solid curve).

$k_x=k_y$ ($\lambda_x=\lambda_y=71$ μm), 3D stretched $k_x=3k_y$ ($\lambda_x=53$ μm, $\lambda_y=158$ μm), and a 2D ripple $k=k_x=k_{2D}$ ($\lambda_{2D}=50$ μm). The growth versus time of the fundamental mode Fourier amplitudes of optical depth of the perturbations is shown in Fig. 1a. In the linear regime, all three modes grow at the same rate, as expected from linear theory, since they all have the same magnitude wave vector. In the

nonlinear regime, the square $k_x=k_y$ mode grows the largest, the 2D $k=k_x$ ripple grows the least, and the 3D stretched $k_x=3k_y$ perturbation falls in between. This nonlinear shape effect has been predicted theoretically by several groups,[7,8] but has not been observed experimentally before, and can be understood qualitatively both from perturbation theory[7] and from a simple buoyancy versus drag argument.[8] The latter argument is based on the asymptotic limit of terminal bubble velocity, where buoyancy is exactly balanced by kinematic drag at the bubble tip. But drag/buoyancy $\propto$ surface-area/volume is smallest for the square mode here, allowing it to grow the fastest.

Radiation flow leads to mass ablation and density gradients, both of which can significantly affect the degree of RT instability growth. This is clearly illustrated in recent experiments[9]comparing RT growth at an ablation front with that at an RT-unstable embedded interface, as shown in Fig. 1b. The embedded interface target was a 35 μm doped plastic ablator, backed by a 15 μm Ti payload, with a 2D sinusoidal ripple at the plastic-metal interface. These experiments used the same x-ray drive as those described in Fig. 1a. The largest growth factors at the embedded interface were observed for the shortest perturbation wavelengths, λ=10-20 μm. For comparison, nearly identical experiments were also done for ablation-front RT growth, using ~60 μm thick CH(Br) foils. The combined effects of a density gradient and ablation velocity strongly stabilize growth of short wavelength perturbations at the ablation front, with perturbations of $\lambda \leq 20$ μm essentially not growing at all.

We have done embedded interface experiments with two superposed wavelengths, using (λ_i, λ_j) = (10, 15 μm), as shown in Fig. 2a, and (4, 5 μm), as shown in Fig. 2b. The laser pulse shape, here 4.5 ns long with a contrast ratio of 5:1, was designed to give higher growth factors to drive the RT evolution into the nonlinear regime. Once the perturbation development enters the nonlinear regime, second order perturbation theory predicts mode coupling to occur,[10]

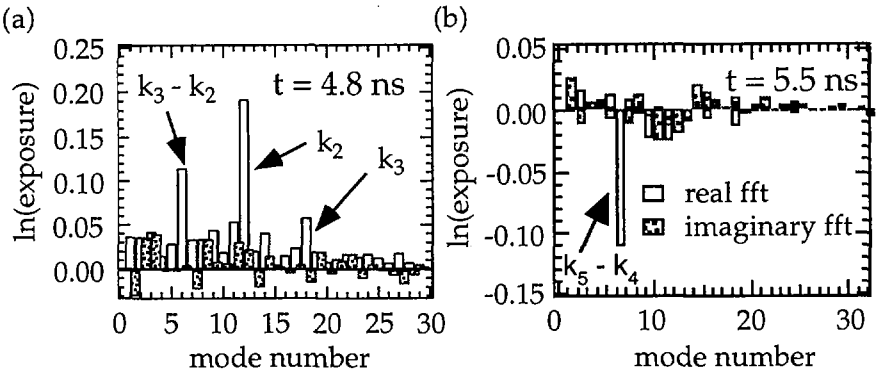

FIG. 2. Results from indirect-drive experiments examining 2D Rayleigh-Taylor growth at an embedded interface for two superposed modes: (a) k_2 and k_3 are perturbation wavenumbers corresponding to wavelengths of λ_2=15 μm and λ_3=10 μm. The k_3-k_2 term represents the coupled mode of wavelength λ_1=30 μm. (b) Same as (a), but only the down-coupled λ_1=20 μm mode is observed; the pre-existing λ_4=5 μm and λ_5=4 μm modes are below the experimental resolution.

spawning new modes with amplitudes given by $\eta_{i\pm j} = \mp 1/2(k_i \pm k_j)\eta_i\eta_j$ and wavelengths $\lambda_{i\pm j}=2\pi/(k_i\pm k_j)$. Figure 2a shows this clearly in Fourier space, with the two pre-imposed modes of λ_2=15 μm and λ_3=10 μm (initial amplitudes of 1 μm) growing into the nonlinear regime at 4.8 ns, generating the k_3-k_2 coupled mode at λ_1=30 μm. (The k_2+k_3 mode corresponding to λ_5=6 μm is below the resolution limit.) To make a simple numerical estimate, we first remove the effect of the instrument spatial resolution (i.e., divide by the modulation transfer function, MTF) from the data, by writing η_k(actual)≈η_k(measured)/MTF. We then convert from perturbation amplitude in optical depth (OD) to perturbation spatial amplitude in μm, ie, $\eta_k(\mu m) \approx \eta_k(OD)\cdot mfp/compression$, where *mfp* is the mean free path length of the backlighter x-rays (here, 7 μm), and *compression* = $\rho/\rho_o \approx 2$ at 4.8 ns. Having done these conversions, the amplitudes for the k_2, k_3, and k_3-k_2 modes from Fig. 2a are 3.3 μm, 4.2 μm, and 1.3 μm, respectively. Applying the 2nd-order mode coupling equation gives a prediction of 1.45 μm for the k_3-k_2 down-coupled term, which is in reasonable agreement with our data.

The (4, 5 μm) pattern (initial amplitudes of 0.3 μm) is particularly interesting because both the pre-imposed wavelengths are below the experimental resolution of ~10 μm. However, these wavelengths correspond to the fifth and fourth harmonics of the λ_1 = 20 μm, which will be spawned in the nonlinear regime as the down coupled k_5-k_4 mode. As shown in Fig. 2b at t=5.5 ns, the 20 μm coupled term stands out well above the experimental noise. Applying the second

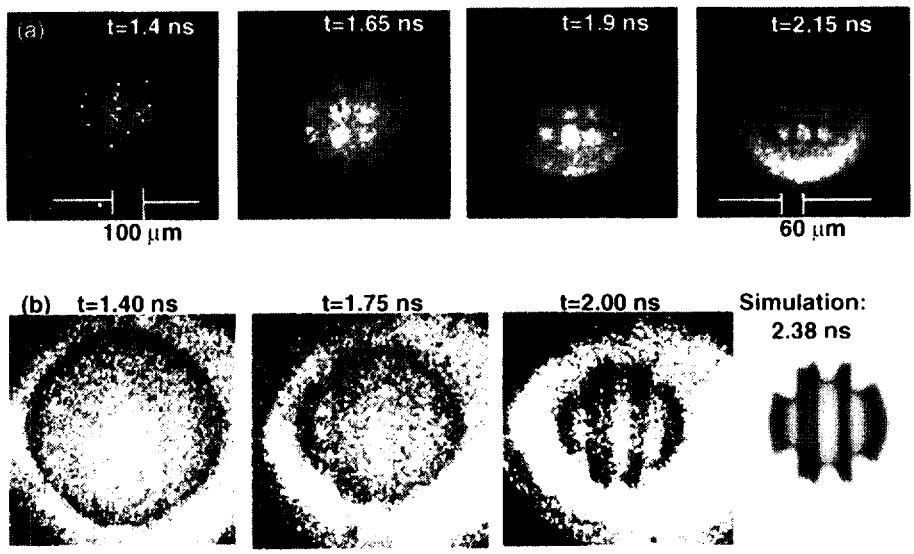

FIG. 3. Results from indirect-drive experiments examining Rayleigh-Taylor perturbation growth at an ablation front in converging geometry: (a) on imploding hemispheres mounted on the wall of the hohlraum, and (b) on a full capsule implosion, where the capsule was mounted at the center of the hohlraum.

order coupling equation, and assuming that $\eta_4 \approx \eta_5$, we write $\eta_{5\text{-}4} \approx 1/2(k_5 - k_4)\eta_4^2$. This leads to an estimated growth factor of ~20 for the two unobserved modes, corresponding to spatial amplitudes of 3-4 μm. So $\eta_{4,5} \approx \lambda_{4,5}$, implying that the RT evolution is far into the nonlinear regime. Hence, by judicious choice of two superposed patterns, along with second order perturbation theory, we have extended the resolution of our gated x-ray pinhole camera down to a few μm.

Perturbation growth experiments can also be carried out in convergent geometries. We show in Fig. 3a the growth of a 3D $k_x=k_y$ square mode perturbation ($\lambda_x=\lambda_y=100$ μm) in spherically converging geometry.[11] The perturbation was imposed on the outer surface of a ~500 μm diameter hemisphere of germanium-doped plastic ($C_{50}H_{48.8}Ge_{1.2}$), which was mounted on the wall of a hohlraum, facing inwards. The laser pulse shape here was 2.3 ns with 6:1 contrast ratio. As the hemisphere is ablatively accelerated, the perturbations grow due to the ablation front RT instability at the same time that the hemisphere converges (implodes). This is illustrated in Fig. 3a with a sequence of face-on radiographs (using Rh L-band x-rays at 3-4 keV), showing perturbation growth over an observed convergence (R_o/R) of just under 2. Analysis of the growth of the first (fundamental) and second harmonics of the perturbation shows that the evolution enters the nonlinear regime at ~2 ns, as is evidenced by the appearance of the second harmonic (not shown). At this point, the growth factor is only 2.0-2.5. On a planar foil, this amount of growth for an $\eta_o=2.5$ μm, $\lambda_x=\lambda_y=100$ μm perturbation would still be in the linear regime, since $\eta/\lambda < 10\%$. The early entry into the nonlinear regime observed here is due to convergence. For the same overall growth, the ratio η/λ increases more rapidly because λ is decreasing. Also, in convergent geometry, the overall growth is larger, since the pusher does not decompress immediately upon shock breakout. We have also done radiography (using Ti He-α x-rays at 4.7 keV) of perturbed capsules imploding at the center of the hohlraum,[12] as shown in Fig. 3b. The perturbation pattern imposed was a set of three grooved rings, each ~100 μm wide and ~3 μm deep, separated by 210 μm and 160 μm. The drive was the same as that used for the hemisphere experiments (Fig. 3a), and the convergence, $R/R_o \approx 2$, was similar. The perturbation growth is clearly visible as dark bands corresponding to spikes and light bands to bubbles, and compares very well with the simulation, given by the image at the far right in Fig. 3b. The simulated perturbation peak-to-valley growth factor is about 10.

3. HYDRODYNAMIC INSTABILITIES IN DIRECT DRIVE

In Fig. 4 we show the results from a new series of direct-drive, linear regime RT experiments[13] where green laser light ($\lambda_L=0.528$ μm) directly illuminated a 20 μm thick CH_2 foil ($\rho=0.95$ g/cm^3), giving 2 ns of nearly constant acceleration at ~60 μm/ns^2. A range of initial wavelengths was investigated, λ=20-70 μm, each with small initial amplitude such that the RT growth remained in the linear regime. We show the results in Fig. 4a as the linear regime RT dispersion curve. There is some scatter in the data, due to the difficulty of measuring a slope. The results of the LASNEX simulations are also shown, and slightly overpredict the observed growth rates. This slight overprediction may be due to the treatment of electron heat transport in the simulations.[14] Single-group, flux-limited Spitzer-Harm diffusion was used in our simulations, which does not correctly treat the transport of fast electrons. To illustrate this, we have done a 1D simulation with Fokker-Planck (FP) heat transport, from which we calculate the RT growth rate,

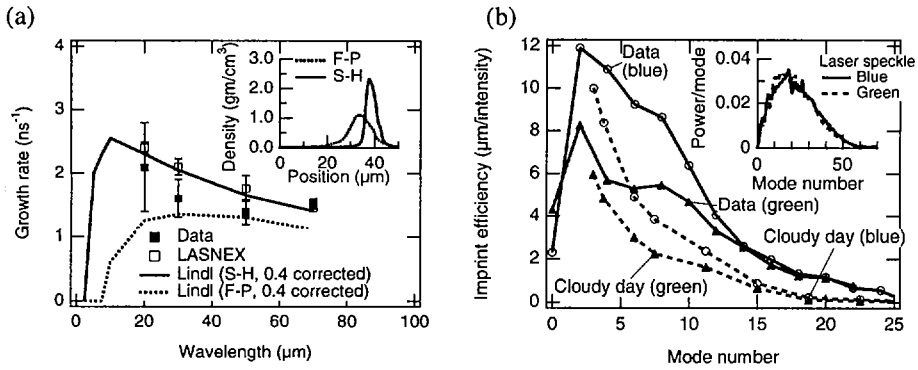

FIG. 4. (a) Results from direct-drive experiments of linear regime 2D single-mode, RT growth at an ablation front. Closed symbols are the data; open symbols are the result of numerical simulations. The solid curve corresponds to a calculated, ablatively stabilized RT dispersion curve using Spitzer-Harm diffusion heat conduction (S-H), and the dotted curve is the same, only where the electron heat transport was treated with a 1D Fokker-Planck model (F-P). The inset shows the density profiles for diffusion and for Fokker-Planck heat transport. (b) Results from direct-drive experiments examining imprinting due to laser nonuniformities, comparing green with blue light. The upper solid curve is for blue light, and the lower solid curve for green. The laser nonuniformities in both cases were the same, as shown in the inset. The two dashed curves correspond to the results from a simple "cloudy-day" calculation for blue (upper) and green (lower) laser light.

γ_{RT}, using the dispersion curve, $\gamma_{RT}=[kg/(1+kL)]^{1/2}-\beta k v_a$. Here, $k=2\pi/\lambda$ is the perturbation wave vector, g is acceleration, $L=\rho/\nabla\rho$ is the density gradient scale length, $\beta=3$ is a constant, and $v_a=/\rho$ is the ablation velocity. This leads to the dotted curve in Fig. 4a. The effect of the FP heat transport is to preheat the foil, due to the long mean free path of the higher energy electrons in the tail of the electron distribution. This causes the foil to decompress, as shown by the density profiles in the inset in Fig. 4a, which increases both L and v_a, hence lowering γ_{RT}. The data appear to lie in between our two calculated results, suggesting that a more careful treatment of heat transport in LASNEX could potentially resolve the observed discrepancy between measured and simulated growth rates.

We have also done laser imprinting studies on Nova.[15-17] We show in Fig. 4b the imprint levels in CH_2 foils from blue (λ_L=0.351 μm) versus green (λ_L=0.528 μm) laser illumination for otherwise identical conditions.[17] We used a random phase plate (RPP) with no bandwidth to generate a static laser speckle pattern at the target, and adjusted the F# such that both the green and blue light had the same nonuniformity power spectrum (see the inset). The imprint efficiency is calculated from η_k(μm imprinted)/η_k(incident), as shown in Fig. 4b . Here, η_k(μm imprinted) corresponds to the imprinted mode converted to the equivalent pre-imposed surface modulation that would have led to the same observed η_k(OD),[15] and η_k(incident) represents the fractional time-integrated laser intensity nonuniformity at the same mode k. It is evident from the two solid

curves in Fig. 4b that the blue light imprints considerably more that the green light, about 50% more for modes $n \leq 10$, (where λ_n=300 μm/n). This is consistent with the green laser more rapidly developing a standoff layer between the critical surface and the ablation front, as suggested by $\delta P_a/P_a \approx 2/3\ \delta I_c/I_c\ e^{-k\Delta z_{ac}}$, where P_a is pressure at the ablation front, I_c is laser intensity at the critical surface, and Δz_{ac} is the separation between these two locations.[17] A more careful analysis, keeping track of where the incident laser deposits its energy, leads to our "cloudy-day" calculations, shown in Fig. 4b by the two dashed curves, which qualitatively reproduce the observed lower imprint with green laser light due to the larger standoff layer.

REFERENCES

[1] LINDL, J.D., Phys. Plasmas **2** (1995) 3933.

[2] HAAN, S.W., et al., Phys. Plasmas **2** (1995) 2480; KRAUSER, W.J., et al., Phys. Plasmas **3** (1996) 2084.

[3] MARINAK, M.M., et al., Phys. Plasmas **3** (1996) 2070.

[4] CAMPBELL, E.M., Laser Part. Beams **9** (1991) 209.

[5] KILKENNY, J.D., et al., Phys. Plasmas **1** (1994) 1379.

[6] MARINAK, M.M., et al., Phys. Rev. Lett. **75** (1995) 3677.

[7] HECHT, J., et al., Laser Part. Beams **13** (1995) 423; DAHLBURG, J.P., et al., Phys. Fluids B **5** (1993) 571; TOWN, R.P.J., et al., Laser Part. Beams **12** (1994) 163; SAKAGAMI, H., NISHIHARA, K., Phys. Rev. Lett. **65** (1990) 432; TRYGGVASON, G., UNVERDI, S.O., Phys. Fluids A **2** (1990) 656; JACOBS, J.W., CATTON, J., Fluid Mech. **187** (1988) 329.

[8] SHVARTS, D., et al., Phys. Plasmas **2** (1995) 2465; OFER, D., et al., Phys. Plasmas **3** (1996) 3090.

[9] BUDIL, K.S., et al., Phys. Rev. Lett. **76** (1996) 4536.

[10] HAAN, S.W., Phys. Fluids B **3** (1991) 2349; REMINGTON, B.A., et al., Phys. Rev. Lett. **73** (1994) 545; Phys. Plasmas **2** (1995) 241.

[11] CAMPBELL, E.M., HOLMES, N.C., LIBBY, S.B., REMINGTON, B.A., TELLER, E., submitted to Laser Part. Beams; Rep. UCRL-JC-124258 (1996).

[12] KALANTAR, D.H., et al., Rev. Sci. Instrum.; Rep. UCRL-JC-123285 (in press).

[13] GLENDINNING, S.G., et al., submitted to Phys. Rev. Lett.; Rep. UCRL-JC-124653.

[14] GLENDINNING, S.G., et al., Phys. Rev. Lett. **69** (1992) 1201.

[15] SHIGEMORI, K., et al., submitted to Phys. Rev. Lett.

[16] GLENDINNING, S.G., et al., Phys. Rev. E **54** (1996) 157.

[17] KALANTAR, D.H., et al., Phys. Rev. Lett. **76** (1996) 3574.

[18] GLENDINNING, S.G. (in preparation).

HEATING AND CURRENT DRIVE

(Session E)

Chairperson

R. BOLTON
Canada

FAST WAVE HEATING AND CURRENT DRIVE IN DIII-D IN DISCHARGES WITH NEGATIVE CENTRAL SHEAR*

R. PRATER, M.E. AUSTIN[1], F.W. BAITY[2], S.C. CHIU, R.W. CALLIS, W.P. CARY, J.S. DeGRASSIE, R.L. FREEMAN, C.B. FOREST, S.W. FERGUSON[3], H. IKEZI, E.F. JAEGER[2], E. JOFFRIN[4], J.H. LEE[5], Y.R. LIN-LIU, T.C. LUCE, M. MURAKAMI[2], C.C. PETTY, R.I. PINSKER, D.A. PHELPS, M. PORKOLAB[6], D.W. SWAIN[2], DIII-D TEAM
General Atomics,
San Diego, California,
United States of America

Abstract

FAST WAVE HEATING AND CURRENT DRIVE IN DIII-D IN DISCHARGES WITH NEGATIVE CENTRAL SHEAR.

The noninductive current driven by fast Alfvén waves (FWCD) has been applied to discharges in DIII-D with negative central shear. Driven currents as high as 275 kA have been achieved with up to 3 MW of fast wave power with the efficiency and profile as predicted by theory based modeling. When counter-current FWCD was applied to discharges with negative central shear, the negative shear was strengthened and prolonged, showing that FWCD can help to control the current profile in advanced tokamak discharges. Under some conditions in negative central shear, the plasma spontaneously makes a transition into a regime of improved performance, with a reduction in both the ion and the electron heat diffusivities. Up to 3 MW of fast wave power has been successfully coupled into H-mode discharges with large edge localized modes through the use of an innovative decoupler/hybrid power splitter combination.

* Work supported by the US Department of Energy under Contract Nos DE-AC03-89ER51114, DE-AC05-96OR22464, W-7405-ENG-48 and Grant Nos NDE-FG05-86ER5 and DE-FG03-86ER53266.

[1] University of Maryland, College Park, Maryland, USA.
[2] Oak Ridge National Laboratory, Oak Ridge, Tennessee, USA.
[3] Lawrence Livermore National Laboratory, Livermore, California, USA.
[4] Association Euratom-CEA, Cadarache, France.
[5] University of California, Los Angeles, California, USA.
[6] Massachusetts Institute of Technology, Cambridge, Massachusetts, USA.

1. INTRODUCTION

Discharges with weak or negative central magnetic shear (NCS) in DIII–D are characterized by access to improved performance: normalized beta has reached 4.0 while the confinement remains very high, $H \approx 4.5$, with high power neutral heating above a threshold value [1]. These current profiles with negative shear have been generated using heating by neutral beams during the current ramp phase of the discharge in order to raise the conductivity of the plasma [2,3]. Current profiles generated in this way decay into normal (positive) shear discharges on a resistive time scale; to sustain the high performance phase, it is necessary to maintain negative shear by noninductive current drive in combination with bootstrap current. The present work describes the application of fast wave current drive (FWCD) for this purpose.

Discharges with NCS with an L–mode edge are well suited for FWCD experiments. Mild neutral beam heating of 3 to 5 MW during the current ramp keeps the electron temperature high enough, typically above 2.5 keV, that the fast waves are effectively damped by the thermal electrons. At the same time, the density is low enough, typically below 3×10^{19} m^{-3}, that the noninductively driven currents can be moderately high. Equally important, sawteeth are absent since the safety factor q is everywhere greater than unity; this allows application of the technique developed by Forest for determining the profile of the noninductive currents in the plasma [4]. Maintaining beam heating during the FWCD phase also provides information on the ion temperature and the poloidal fields through the charge exchange recombination and motional Stark effect diagnostics.

The FWCD system has been extended by adding two 2 MW transmitters which have a frequency range of 30–120 MHz to the 2 MW 30–60 MHz system. The experiments described have typically 2–3 MW of power coupled to the plasma, with a third of the power at 60 MHz and the remainder at 83 MHz. The antennae are three phased arrays of four current-carrying straps each, with phasing between adjacent straps of $\pi/2$. The parallel index of refraction of the coupled power is ~5 for both systems.

2. FAST WAVE CURRENT DRIVE IS CONSISTENT WITH THEORY

Driven currents have become larger as we have increased the fast wave power. Fast wave driven currents (not counting the bootstrap current) up to 275 kA have been generated in non-sawtoothing discharges with weak negative shear. The driven current is analyzed using a time sequence of magnetic reconstructions to determine the profiles of total current density and toroidal electric field, and the noninductive current density is found by subtracting the inductive current density from the total current density assuming neoclassical resistivity [4]. Noninductive current densities from similar discharges with co-current drive and counter-current drive are compared to eliminate the bootstrap current and neutral beam driven current, and the remainder is attributed to fast wave current drive. The profile of fast wave current so determined is shown in Fig. 1 for a discharge with 275 kA of fast wave current. Operation at 2.14 T was used to minimize absorption of waves by energetic beam ions, as discussed below. The driven current is highly localized on axis, as expected due to the strong temperature dependence of wave absorption and the higher current drive efficiency near the center, and it is in good agreement with the modeling calculations with the PICES full wave

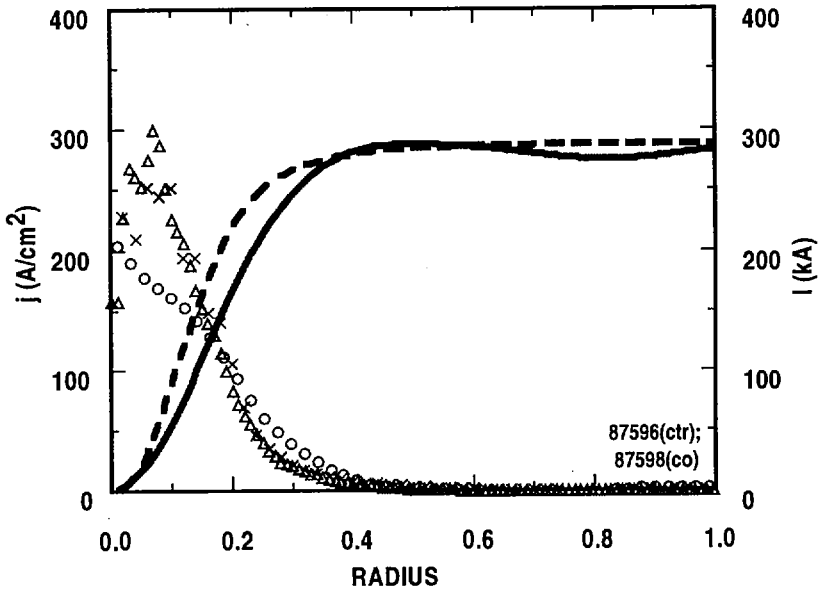

FIG. 1. Experimental profile of current density for FWCD and modeling calculations for the same case. Circles: experimental values; triangles: results of a calculation using PICES; crosses: results from CURRAY code. The curves are the radial integral of experiment (solid curve) and PICES (dashed curve). Magnetic field: 2.1 T; plasma line-averaged density: 2 × 10^{19} m^{-3}; peak electron temperature: 7 keV; plasma current: 1.6 MA.

code and CURRAY ray tracing code. The peak in the driven current density is more than double the net current density in the plasma, but the driven current is partially canceled by the reverse ohmic current driven by the back-emf which appears in order to conserve flux on a resistive time scale.

In previous work [5,6] the current drive figure of merit $\eta_{fw} = n(10^{20}\ m^{-3})$ I(MA) R(m)/P(MW) was measured for a set of discharges with toroidal field 1 T. These are shown as the data points below 4 keV in Fig. 2. These data have been extended now to higher temperature through operation in discharges with negative central shear and VH–mode with toroidal field of 1.9 to 2.1 T and with higher fast wave power, and these data points appear in Fig. 2 above 4 keV. The higher temperature data extend the same scaling derived previously: $\eta_{fw} \propto T_e$. The data are consistent with full modeling same scaling derived previously: $\eta_{fw} \propto T_e$. The data are consistent with full modeling using the CURRAY ray tracing code, which uses the measured profiles of density, temperature, and Z_{eff} to calculate the expected driven currents. The range of the CURRAY calculations is indicated by the shaded band in Fig. 2. This scaling of the figure of merit with T_e is also consistent with the simple scaling derived for ITER [7]. The calculated first pass damping for the points in Fig. 2 ranges typically from about 9% to 13%, averaging over a large number of rays representing the coupled spectrum of poloidal and toroidal wavenumbers.

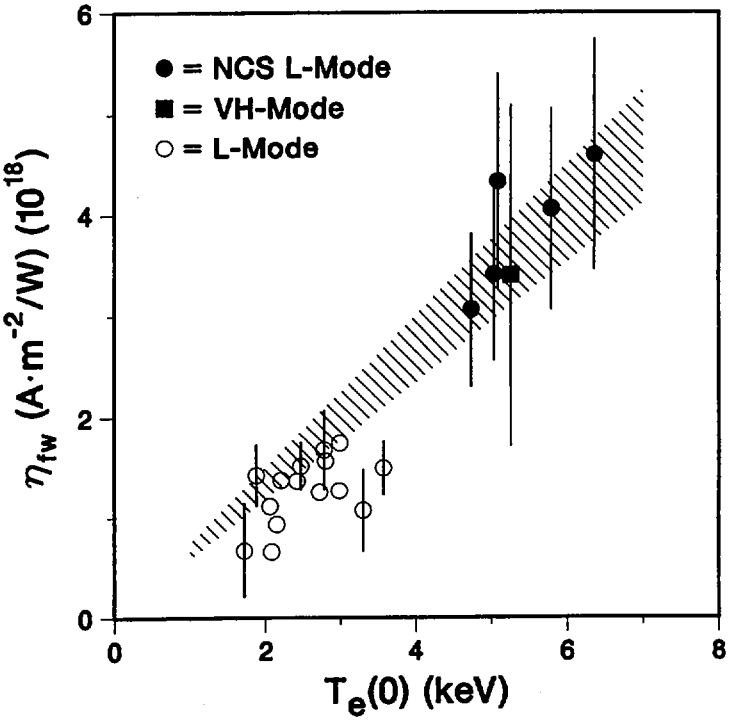

FIG. 2. Experimentally determined figure of merit, η_{fw}, for FWCD in DIII-D, as a function of central electron temperature. The filled circles are taken at a toroidal field of B_t = 1.9–2.1 T in L-mode NCS or VH-mode discharges. The shaded band represents the range of modeling results using the CURRAY code on some of the discharges represented by the data points.

Measurements made with an array of rf probes in DIII–D show that k_tR is downshifted and the spectrum of the toroidal wavenumber k_t is broadened as the path length of the rays increases [8], for a broad range of conditions. However, CURRAY (and all other fast wave analysis codes) is constructed under the assumption that the toroidal mode number of fast waves is conserved due to axisymmetry; i.e., k_tR is constant. This makes the good agreement of η_{fw} with theory in Fig. 2 appear somewhat surprising. However, this can be resolved by consideration of the range over which $n_{||}$ changes as a ray progresses, as shown in Fig. 3(a) for a typical ray in the center of the coupled forward spectrum of $n_{||}$, as a function of the normalized minor radius. The ray shown in Fig. 3(a) starts with $n_{||}$ of 4.8 and decays to 28% of its initial energy along the path shown. Due to the effects of the poloidal field, the $n_{||}$ gets as large as +11 and as small as –3. The wave absorption in the plasma as a function of $n_{||}$ for a large number of rays which simulate the full spectrum is plotted in Fig. 3(b). This shows that most of the power is absorbed with $n_{||}$ near 8.4, compared to an expected value of 7 from geometric upshift of the launched spectrum peaked at 5. But if the initial wave spectrum is downshifted by 25% in the ray tracing calculation, the peak in

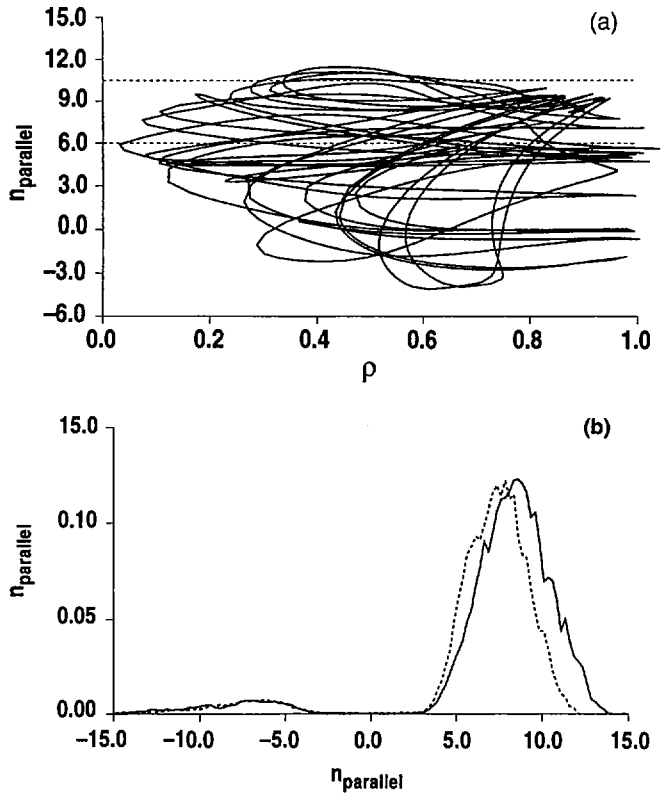

FIG. 3. (a) Parallel index of refraction as a function of normalized minor radius, as a single ray propagates on multiple passes through the plasma. The ray is launched with $n_{\|} = 4.8$ and a frequency of 60 MHz into an L-mode plasma. (b) Power damping (arbitrary units) as a function of $n_{\|}$ for an ensemble of 90 rays with poloidal and toroidal spectrum corresponding to the antenna (solid line), and for a toroidal spectrum arbitrarily downshifted by 25% (dashed line). The dashed lines in (a) correspond to the $n_{\|}$ at half the peak power damping of (b).

the absorption spectrum downshifts by less than 10%. This shows that the absorbed spectrum is not closely coupled to the launched spectrum due to the large variations in $n_{\|}$ as the wave propagates. It also suggests that as the absorption increases at high temperature and density, as for ITER, some improvement in the current drive figure of merit may be obtained by having the power absorbed at lower $n_{\|}$ corresponding better to the launched spectrum.

A mechanism for loss of effective FWCD which can represent up to a third of the fast wave power is partial absorption of waves by energetic beam ions. This ion absorption has important implications for FWCD on ITER where an unthermalized population of fusion alphas is present. The evidence for beam ion absorption of the fast

waves in DIII–D comes from the equilibrium reconstruction of these discharges using the EFIT code. For discharges with NBI only (no fast wave injection), the location of the magnetic axis determined in this manner is in excellent agreement with the calculated Shafranov shift using the measured thermal plasma pressure profile and the theoretical fast beam ion pressure profile. However, when 2 MW or more of FWCD is added to these NBI heated plasmas, the magnetic axis shifts outward several centimeters more than can be explained by the thermal and fast beam ion pressure profiles. In order to reconcile this discrepancy, an additional fast particle population must exist near the plasma center which can have up to 60% of the stored energy of the beam ion population. The source of this excess fast particle pressure is almost certainly energetic deuterium ions since experimentally this excess fast particle stored energy correlates with an anomalous increase in the neutron rate. A scan of the magnetic field strength from 1.6 to 2.1 T at fixed NBI power determined that the excess fast ion stored energy was largest at 1.9 T; at this field, the sixth harmonic cyclotron resonance of deuterium passes through the magnetic axis for the main FWCD frequency of 83 MHz. The excess fast ion stored energy was also found to increase as the NBI power was increased. The most plausible mechanism for this excess energetic deuterium population is high harmonic ion cyclotron absorption of the fast waves by the fast beam ions. Modeling of this process using the CQL3D Fokker-Planck code is underway. It appears that careful adjustment of the discharge parameters is necessary to avoid excessive losses to fast ions and that some loss may be unavoidable.

3. COUNTER-FWCD EXTENDS NEGATIVE CENTRAL SHEAR

FWCD has a strong heating effect in NCS discharges. Figure 4 shows data from a discharge with NCS with 3.7 MW of neutral beam heating starting at 0.35 s and 2.2 MW of coupled fast wave power with the antennas phased for counter-current drive. The electron density is low for this discharge, rising gradually from 1.0×10^{19} m^{-3} at the start of the fast wave pulse to 1.6 at the end, and the electron temperature rises from 3.5 keV to 6 keV. The stored energy also rises gradually, nearly doubling over the duration of the fast wave power, as shown in Fig. 4(b). The radiated power remains fixed at 1 MW throughout this period. The current driven by fast waves is 200 kA in this discharge. This is about 80% of the theoretically expected value, with the deficit presumably due to absorption of fast waves by beam ions.

The central counter-current driven by FWCD has a strong effect on the current profile in the discharge illustrated in Fig. 4. Figure 4(i) shows the central safety factor q for this discharge and for one with co-current drive. With co-FWCD, q drops to unity at 1.6 s, as verified by the start of sawtoothing activity visible in the central temperature in Fig. 4(e). With counter-FWCD, the safety factor is held above unity for 0.75 s longer, until 2.35 s. No sawteeth are present until that time. Concurrently, the negative shear is strengthened by the counter-FWCD. The quantity $q(0)-q_{min}$ is plotted in Fig. 4(h) as a measure of the magnitude of the shear reversal. The NCS configuration is maintained for much longer with counter-FWCD than with co-FWCD. For steady-state maintenance of the NCS configuration, it is preferable to use an off-axis co-current drive technique like electron cyclotron current drive, rather than counter-FWCD which is always central, as modeling shows that with central counter-current drive it is difficult to maintain the central safety factor above unity on a long time scale.

Some discharges show a spontaneous transition to enhanced confinement when the current profile relaxes to weak negative shear with FWCD used to provide counter-current drive and central electron heating [9]. This can be seen in the discharge of

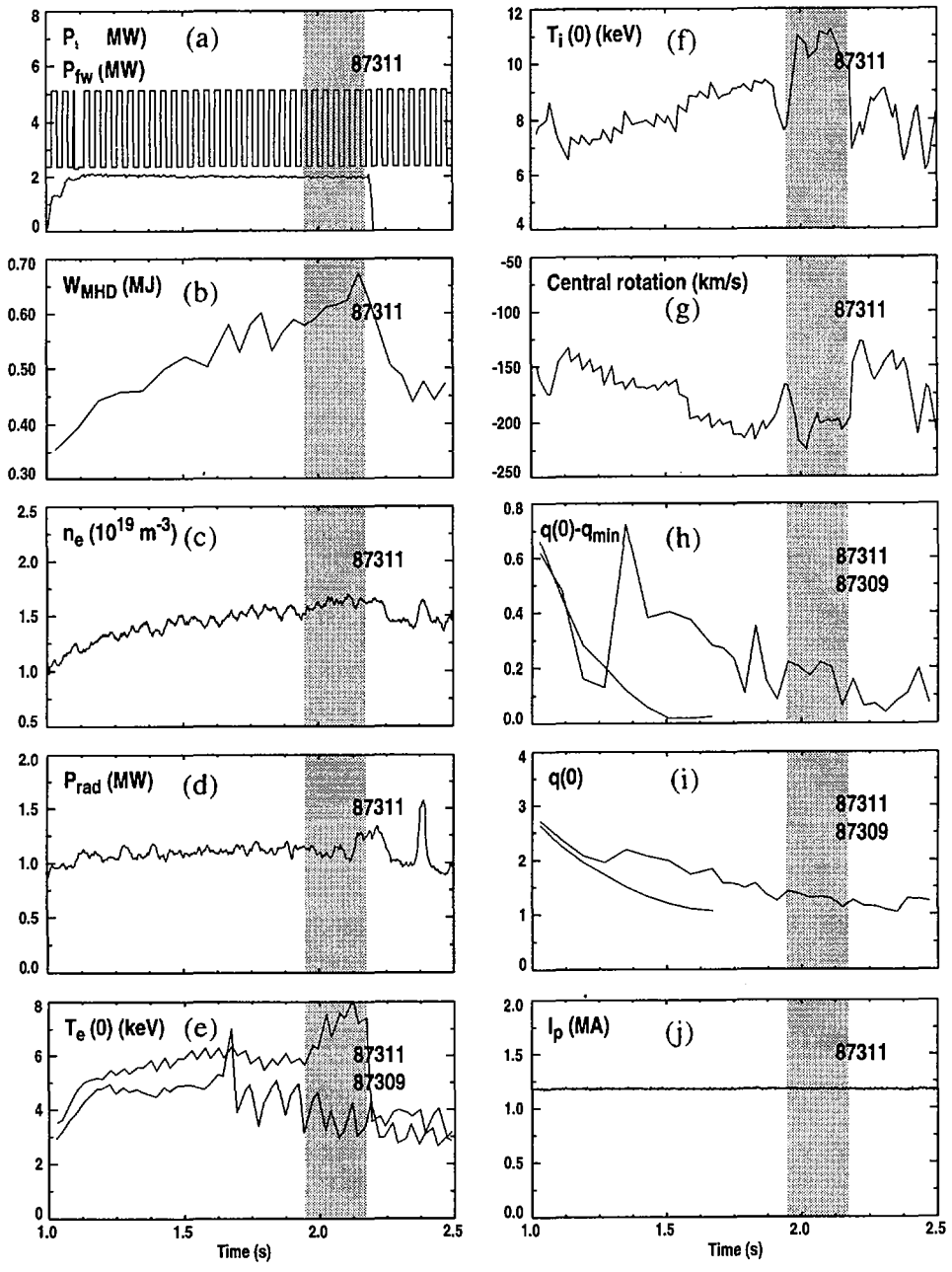

FIG. 4. Time history for a discharge with NCS and counter-FWCD: (a) neutral beam and fast wave power; (b) plasma stored energy; (c) line averaged density; (d) total radiated power; (e) peak electron temperature from ECE; (f) ion temperature from CER; (g) core rotation from CER; (h) $q(0) - q_{min}$; (i) $q(0)$; (j) plasma current. Data from a similar discharge but with co-FWCD are shown as the lower curves in (e), (h) and (i). The toroidal field is 1.9 T.

Fig. 4 at 1.95 s, nearly one second after the start of the fast wave power. At the transition, the electron temperature increases from 6 to 8 keV, the ion temperature also increases by 2 keV, and the density profile peaks slightly. The q-profile exhibits negative shear before and during the phase of enhanced performance, which ends when the minimum of q becomes unity and the sawteeth start. Transport analysis shows that the central electron thermal diffusivity decreases by a factor 2 after the transition, while ion thermal transport decreases by a factor 3 to 5. The cause of the transition is believed to be stabilization of MHD modes by the negative shear, which permits the plasma pressure and rotation to gradually build up sufficient flow shear to stabilize microturbulence [9].

4. HIGH FAST WAVE POWER WAS COUPLED TO ELMING DISCHARGES

An important requirement for a fast wave system is that power be coupled efficiently to H–mode discharges with edge localized modes (ELMs), as some of the advanced tokamak scenarios are such cases. The ELMs transiently increase the electron density at the edge which results in a significant increase in the antenna loading, which in turn causes a substantial increase in the reflection coefficient of the antennas. Were this reflected power all to return to the transmitter, the transmitter would fault.

The transmission system [10] of the FWCD system on DIII–D incorporates a decoupler [11] in conjunction with a hybrid power splitter, a combination which greatly ameliorates the effect of large reflections caused by ELMs [12]. The hybrid splitter acts to divert reflections which are uniform across the four strap antenna (as apparently are those due to ELMs) to the dummy load when the system is phased for directed current drive operation. Power is effectively coupled to the plasma between ELMs and passively diverted from being reflected to the transmitter during ELMs.

High average power can be coupled to ELMing plasmas using this system. An ELMing H–mode discharge in which 3 MW of peak fast wave power is coupled is illustrated in Fig. 5. The H–mode is triggered at 1500 ms by an elongation ramp in this high-ℓ_i experiment. Fast wave power is injected into the H–mode phase. The ELMs are indicated by the peaks in the D_α trace. The time averaged fast wave power coupled to the plasma throughout the pulse is 2.6 MW, or 85% of the peak coupled power. Figure 5(b) displays with expanded time scale the reflection coefficient at the 60 MHz generator. The coupled power from this generator remains high on average throughout significant ELM activity.

5. CONCLUSIONS

The current driven by fast waves has been extended to 275 kA in discharges with negative central shear and neutral beam heating. The current drive efficiency is consistent with theory, using a full wave code or a ray tracing code. While probe measurements show that the assumption built into the codes that the toroidal mode number of the waves is conserved is not fully valid, the calculations show that the wave power is absorbed at the largest $n_{||}$ experienced by the wave, so the absorbed spectrum is not very sensitive to the launched spectrum. Loss of wave power to energetic beam ions has been shown to affect the current drive efficiency, and studies are underway to model this process quantitatively. When counter-FWCD was applied to discharges with negative central shear, the negative shear was strengthened and the relaxation to sawteeth which occurs when q_{min} reaches unity was delayed, showing that FWCD can help to control the current profile in advanced tokamak discharges.

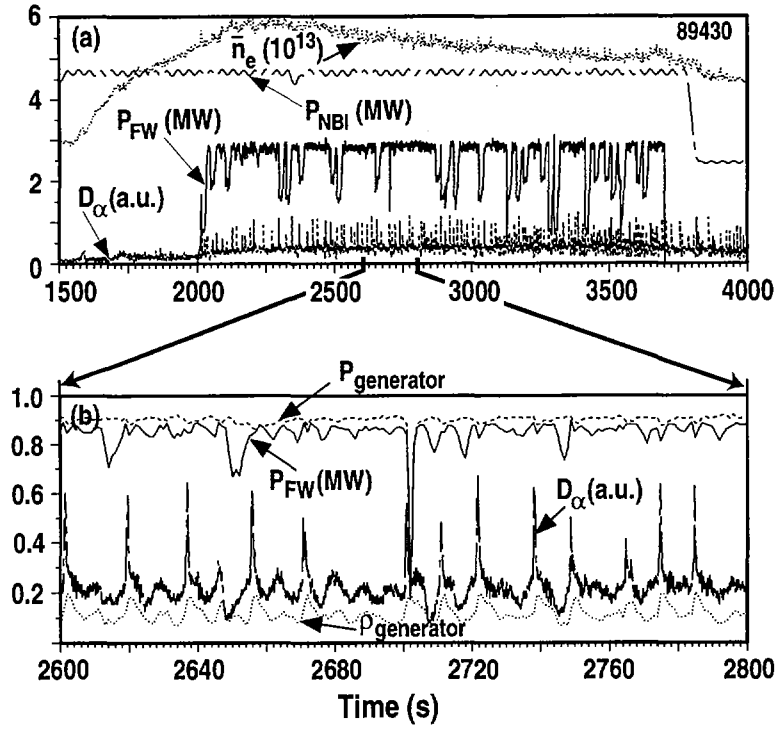

FIG. 5. 3 MW of peak fast wave power coupled to an ELMing H-mode discharge in DIII-D: (a) injected fast wave power, P_{FW} (MW), injected neutral beam power, P_{NB} (MW), line averaged density, $\bar{n}_e$ (10^{19} m^{-3}), and divertor D_α light emission; (b) expanded time trace showing coupled fast wave power from the 60 MHz generator, P_{FW} (MW), D_α, and the reflection coefficient at the generator, $P_{generator}$.

Under some conditions in NCS the plasma can spontaneously make a transition into a regime of improved performance, with a reduction in both the ion and the electron heat diffusivities. Recent results show that high power FWCD can be applied even in ELMing H-mode plasmas through use of a transmission system which passively directs power reflected from the antenna to a dummy load rather than the generator.

REFERENCES

[1] LAZARUS, E.A., et al., Higher fusion power gain with pressure profile control in strongly shaped DIII-D tokamak plasmas, Phys. Rev. Lett. (in press).

[2] LAZARUS, E.A., et al., Phys. Fluids B 3 (1991) 2220.

[3] STRAIT, E.J., et al., Phys. Rev. Lett. 75 (1995) 4421; LEVINTON, F.M., et al., Phys. Rev. Lett. 75 (1995) 4417.

[4] FOREST, C.B., et al., Phys. Rev. Lett. 73 (1994) 2444.

[5] PINSKER, R.I., et al., in Plasma Physics and Controlled Nuclear Fusion Research 1992 (Proc. 14th Int. Conf. Würzburg, 1992), Vol. 1, IAEA, Vienna (1993) 109.
[6] PETTY, C.C., et al., Nucl. Fusion **35** (1995) 773.
[7] UCKAN, N.A., et al., ITER Physics Design Guidelines: 1989, IAEA, Vienna (1990).
[8] IKEZI, H., et al., Phys. Plasmas **3** (1996) 2306.
[9] FOREST, C.B., et al., Phys. Rev. Lett. **77** (1996) 3141.
[10] DeGRASSIE, J.G., et al., in Fusion Engineering (Proc. 15th SOFE Symp. Hyannis, 1993), Institute of Electrical and Electronics Engineers, Piscataway (1993) 1073.
[11] PINSKER, R.I., et al., ibid., p. 1077.
[12] GOULDING, R.H., et al., RF Power in Plasmas (Proc. 11th Top. Conf. Palm Springs, 1995), American Institute of Physics, Woodbury, New York (1995) 397.

DISCUSSION

C.K. PHILLIPS: In the fast wave electron heating experiments in negative central shear discharges, does the ICRF affect the NBI induced plasma rotation?

R.P. PRATER: In most but not all cases, the addition of ICRF decreases the NBI induced rotation.

J.-M. NOTERDAEME: Have you seen any differences in efficiency between co- and counter-current drive?

R.P. PRATER: Yes. Counter-FWCD is typically 15% more efficient than co-FWCD. Calculations with the full wave code PICES by Jaeger et al. show that this asymmetry may be attributed to the effects of the poloidal magnetic field on the generation of the $k_{\parallel}$ spectrum.

D. MOREAU: Your experiment in which you observe a transition in the electron and ion temperatures exhibits a phenomenon which is somewhat similar to what we called LHEP transitions in Tore Supra. I would like to know what the q profile was before the application of the counter-current drive and whether there is a correlation between the time of the transition and the time when the q profile becomes flat in the central region. Would you conclude that weak magnetic shear is better than strongly negative shear?

R.P. PRATER: Before the application of the FWCD power, which starts immediately at the end of the ramp of the plasma current, the q profile exhibits strong negative shear. From the time delay to the transition, we conclude that weak shear is preferable to stronger negative shear in the development of the transition.

APPLICATION OF LHCD TO SUSTAINMENT AND CONTROL OF A REVERSED MAGNETIC SHEAR PLASMA IN JT-60U

S. IDE, O. NAITO, T. FUJITA, T. OIKAWA,
M. SEKI, JT-60 TEAM
Naka Fusion Research Establishment,
Japan Atomic Energy Research Institute,
Naka-machi, Naka-gun, Ibaraki-ken,
Japan

Abstract

APPLICATION OF LHCD TO SUSTAINMENT AND CONTROL OF A REVERSED MAGNETIC SHEAR PLASMA IN JT-60U.

In JT-60U, it has been demonstrated experimentally that, by using lower hybrid current drive (LHCD), reversed magnetic shear can be maintained for a long period (7.5 s) and can be controlled non-inductively. The formation of a reversed magnetic shear configuration by a lower hybrid wave (LHW) injection alone was attempted and successfully achieved. Strongly reversed magnetic shear, even stronger than that formed by a normal scenario (NBI heating at current ramp-up), with a large area of shear reversal, was formed by the LHW alone. Moreover, the attainable β_N, the normalized plasma beta, in this discharge was found to be comparable to that of a normal reversed shear discharge. Furthermore, the experimental results show that the area of good confinement can be changed, in coincidence with the reversed magnetic shear control by LHCD. In view of the recent success in improving plasma performance in reversed magnetic shear discharges with high power heating in TFTR, D-IIID and JT-60U, these results should not only affect the enhancement of performance but also the study of the physics involved. Recent results of JT-60U LHCD experiments with reversed magnetic shear plasmas are described in the paper.

1. INTRODUCTION

In recent tokamak experiments, an improvement of plasma performance in reversed magnetic shear discharges has been found [1–3]. Here the magnetic shear, s, is defined as $s = (\rho/q)(dq/d\rho)$, where q is the safety factor and ρ is the normalized flux radius. A reversed magnetic shear configuration is characterized by negative s in the inner plasma region (for example, in JT-60U, typically, $\rho \leq 0.6$ [1]), and by positive s in the outer region. These results have emphasized the importance of current profile control in a tokamak plasma. In order to achieve stable steady state operation of a fusion plasma of good confinement and a high bootstrap current fraction, a reversed shear configuration is advantageous from the viewpoints of better confinement and MHD stability. However, since in these experiments [1–3] the reversed magnetic shear is initially formed by using a current penetration delay, it

is a transient phenomenon. To investigate not only the characteristics of MHD activities but also the physics mechanism in a plasma with reversed magnetic shear, it is very important to sustain and modify the reversed magnetic shear by means of an active and independent scheme. By using a lower hybrid wave (LHW) not only the highest current drive efficiency [4, 5], but also flexible controllability of the current profile [4–7] in JT-60U were achieved. Thus, it is expected to maintain and control reversed shear by lower hybrid current drive (LHCD) and the current drive by an LHW. The Tore Supra team has succeeded in producing and maintaining a reversed shear configuration, as well as in controlling it by varying the toroidal magnetic field, in other words, by LHW accessibility [8]. However, from the viewpoint of utilizing the advantages of a reversed shear configuration, it is very important to maintain a region of reversed shear, as wide as possible, and to control it independently of the pressure profile [9]. In this sense, it is very attractive to maintain a preformed reversed shear configuration generated by retarding current penetration with neutral beam injection heating at current buildup, since we have succeeded in generating a wide extent of the reversed shear region by this technique (about 65% of the minor radius). Furthermore, it would also be attractive if other methods than NBI heating could be successfully used to produce initial reversed shear. In JET, weak reversed shear was reported to have been formed by injections of LHW and ion cyclotron resonance frequency (ICRF) [10]. However, the results were not very successful, in the sense that the shear was not largely reversed and the region of the negative shear was not wide. Moreover, from the viewpoint of systematic reversed shear plasma studies, it is necessary to control the shear keeping plasma parameters such as the toroidal field, the plasma current, etc. Furthermore, on the JT-60U tokamak, a motional Stark effect (MSE) diagnostic is installed [11] and yields local and more accurate information on the current profile. In this paper, the results of sustainment of a reversed shear configuration for 7.5 s [12], control of magnetic shear and formation of a strong reversed shear with a wide area of negative shear by LHCD in the JT-60U tokamak are reported.

2. SET-UP OF EXPERIMENTS

The experiments were carried out with a single null divertor configuration; the major radius, R_0, and the minor radius, a, were about 3.5 and 1 m, respectively. On the tokamak, two multijunction LHW launchers are installed. One of them is placed in a port at a poloidal angle of $\theta \approx 45°$; it consists of four rows of eight multijunction modules (MJ) with three subwaveguides and is referred to as the 'C launcher' [13]. The spectrum of the ray refractive index parallel to the magnetic field lines, $N_\parallel$, has a full width at half maximum, $\Delta N_\parallel$, of about 0.5. The other launcher is installed in a horizontal port and consists of four rows of four MJ modules with 12 subwaveguides [14, 15]. The lower two rows and the upper two rows of this launcher can be operated separately as if they were individual launchers; hence, they are referred to as 'A launcher' and 'B launcher', respectively, in this paper.

The current density spatial profile was measured by the MSE diagnostics. Since no dedicated probe beam is installed, one of the four tangential beam lines was used for the MSE measurement. In the fitting procedure, the MSE polarization angles and the magnetics data were used, and the best fit for the toroidal current profile was found by minimizing the sum of the squares of the differences between measured and calculated polarization angles [11]. From the fitted toroidal current profile, the profiles of q, s, etc. were calculated. In experiments described in this paper, the number of the MSE measuring points was five for hydrogen discharges and fourteen for deuterium discharges since the diagnostics system was modified between the hydrogen and the deuterium campaigns. However, the actual number of data used in the analysis might vary, depending on data quality, due to, for example, the beam attenuation. Details of the diagnostics system are found in Ref. [11].

3. EXPERIMENTAL RESULTS

3.1. Sustainment of reversed magnetic shear by LHCD

Here, the experimental results of reversed magnetic shear sustainment by LHCD are presented.

One basic idea is to substitute a hollow current profile driven by LHW for a hollow current profile formed by retarding current penetration by NBI heating in the I_P ramp-up phase. Therefore, it would be a key point to know how to form a hollow driven current profile effectively by LHCD. For this purpose, A and C launchers were used simultaneously since it was shown in JT-60U that a hollow current profile can be formed effectively by injecting higher and lower $N_\parallel$ spectra at the same time [6]. The resultant spectrum (summation of both spectra) is shown in Fig. 1, by the solid curve. The higher $N_\parallel$ component is expected to enhance the absorption of the lower $N_\parallel$ component, which drives the current more efficiently, in the outer region of the plasma. Thus, a hollow driven current is expected.

In Fig. 2(a), the temporal evolution of I_P is plotted. As is shown in Fig. 2(b) by the dashed line, the NBI power was applied in the current ramp-up phase in order to retard the penetration of the ohmic current by raising the electron temperature. This is a common way of forming a reversed shear configuration [1–3]. However, at variance with the usual reversed shear discharges, the NBI power was turned off except for the beam for the MSE measurement when I_P reached flat-top. The injection of the LHW power started, as shown in Fig. 2(b), by the solid line. The line averaged electron density at the plasma centre, $\bar{n}_e$, was kept constant at about 1×10^{19} m^{-3}. The toroidal magnetic field at the geometric plasma centre, B_{T0}, was 2.95 T. It should be noted that in this discharge the main working gas and the beam particles were hydrogen.

As was mentioned before, the q profile is obtained by the MSE measurement, taken at five spatial points in this hydrogen discharge; the best fitting was found.

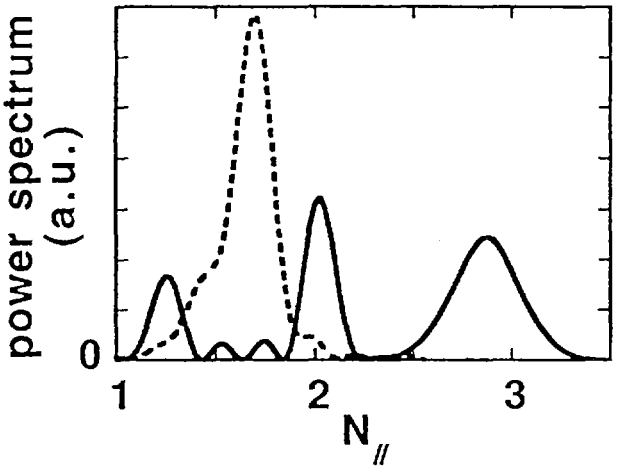

FIG. 1. LHW $N_{\parallel}$ spectra. Broadening spectrum: solid curve; peaking spectrum: dashed curve.

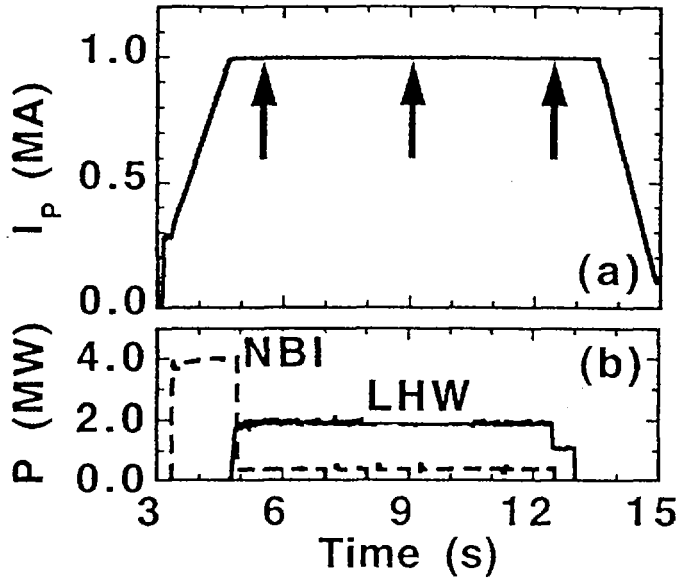

FIG. 2. Discharge scenario: (a) plasma current; (b) injected powers of LHW (solid line) and NBI (dashed line). Arrows indicate the instants where the q profiles shown in Fig. 3 were evaluated.

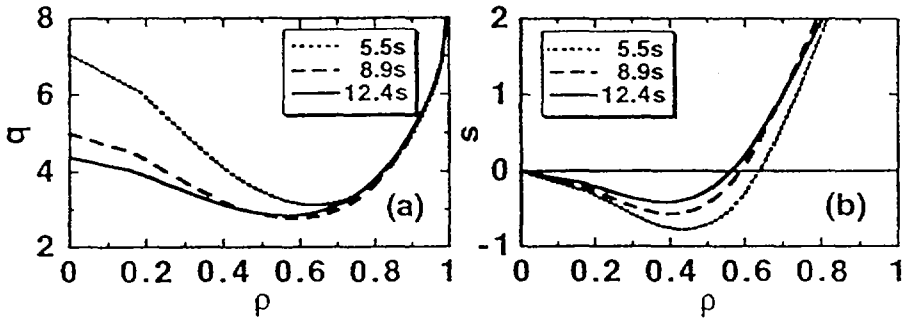

FIG. 3. Evaluated profiles of (a) q and (b) s at 5.5 s (dotted), 8.9 s (dashed) and 12.4 s (solid) for the shot shown in Fig. 2.

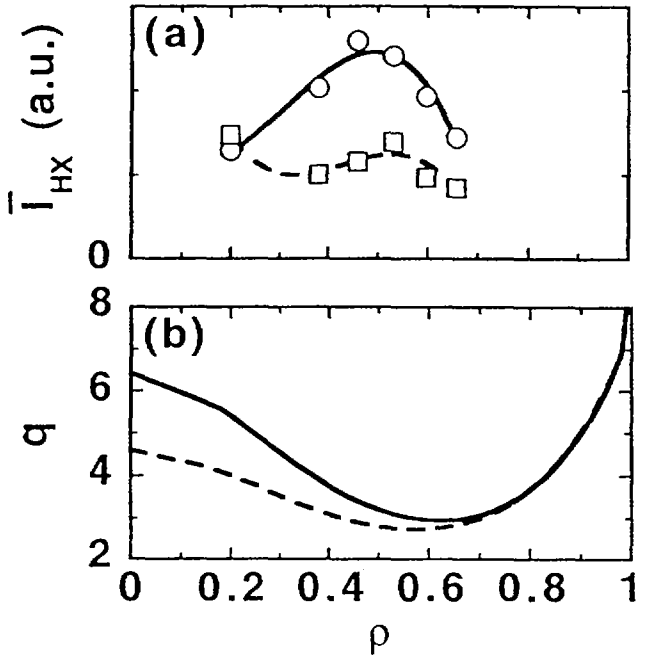

FIG. 4. (a) Profiles of $\bar{I}_{HX}$ for broadening (solid curve with circles) and peaking (dashed curve with squares) spectrum injections; (b) corresponding q profiles.

Fitted q profiles at 5.5, 8.9 and 12.4 s (these times are indicated by arrows in Fig. 2(a)) are shown in Fig. 3(a) by dotted, dashed and solid curves, respectively. It is clearly shown in the figure that the q profile with reversed shear is maintained even at the very end of the LHW pulse. Magnetic shear profiles are also plotted in Fig. 3(a) for the corresponding times. In the figure, the region of negative shear is found to extend up to about $\rho = 0.55$, even at 12.4 s.

The decay of the reversed shear can be attributed to the fact that I_p was not fully driven by LHCD. The fraction of the LH driven current was estimated to be 60–75% of I_p. In such a case, it is difficult to obtain the LH driven current profile separately. However, since the hard X ray (HX) emission intensity profile, measured by an NaI scintillation tube array (in the energy range of 100 keV to 1 MeV), was kept unchanged during the LHW pulse, the LH driven current profile was expected to be unchanged. (The line averaged HX intensity, $\bar{I}_{HX}$, profile is the same as that shown in Fig. 4(a) by the circles.) In the experimental conditions, both the beam driven and the bootstrap currents were found, by numerical calculations, to be negligibly small. Therefore, the decay should be attributed to the change in the ohmic current, 25–40% of I_p. By nature, an ohmic current keeps penetrating into a plasma until it reaches an equilibrium. Thus, the ohmic current raises the current density in the central plasma region and weakens the reversed shear. However, once the ohmic current profile is saturated the total current profile should be fixed since the LH driven current profile is unchanged. This is the situation after around 9 s when the q profile becomes fixed.

We should also mention here the MHD stability of a reversed shear configuration sustained by LHCD, since this is important from the viewpoint of steady state operation of the reversed shear. By magnetic probe measurements, no noticeable mode is found during the period where the reversed shear configuration is sustained.

3.2. Modification of reversed magnetic shear by LHCD

Now the results of modification of reversed shear by LHCD and its application to confinement studies are presented.

As is well known, an LH driven current profile can be controlled by changing the $N_{\parallel}$ input spectrum of the LHW. Therefore, we expect that magnetic shear can be controlled by using LHWs of different $N_{\parallel}$ spectra. For this purpose, we use another spectrum (referred to as peaking spectrum), which is expected to drive a stronger current in the central plasma region than that (referred to as broadening spectrum) used in the previous experiments. This spectrum is plotted in Fig. 1, by a dashed curve. The target plasma is the same as that shown in Fig. 2, except that $\bar{n}_e$ was a little higher, 1.2×10^{19} m^{-3}. The difference in the driven current profiles between broadening and peaking spectrum injections can be derived from the line averaged HX intensity, $\bar{I}_{HX}$, profiles averaged during 5 to 6.5 s, as shown in Fig. 4(a). In this figure, the case of broadening spectrum injection is shown by circles and the case of peaking spectrum injection by squares. The corresponding profiles

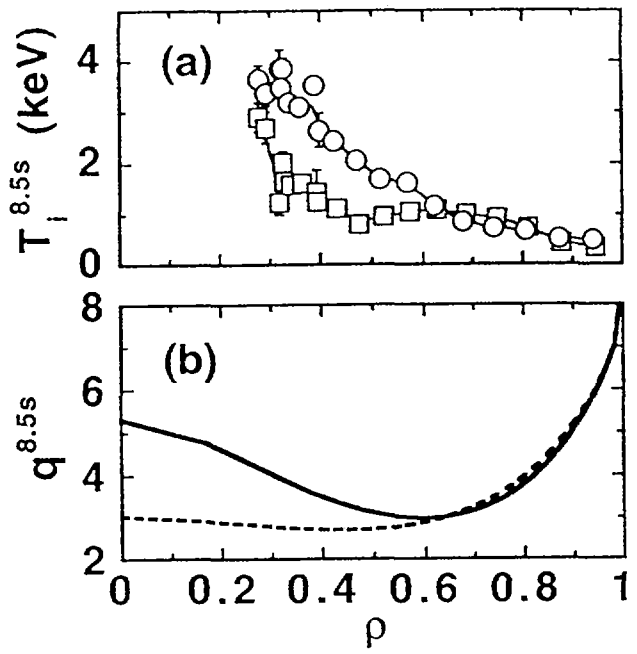

FIG. 5. (a) Profiles of T_i for broadening (circles) and peaking (squares) spectrum injection cases, at 8.5 s; (b) evaluated q profiles for broadening (solid) and peaking (broken) spectrum injection cases at 8.5 s.

of q at 6.5 s are shown in Fig. 4(b), the broadening spectrum injection case by a solid and the other one by a dashed curve. Since the peaking spectrum drives a stronger current in the central region, q becomes lower in the central region, in this case. Also, the position of the minimum q, q_{min}, is shifted a little inward.

In order to be able to observe an effect of magnetic shear control on the plasma performance, a higher NBI power (about 13 MW, including the MSE probe beam) was applied to these plasmas. The onset of the NBI pulse was at 6.5 s, just after the q profiles shown in Fig. 4(b) had been measured. During the higher NBI pulse, the plasma stored energy kept increasing, and a steep gradient was formed in the electron density, temperature and ion temperature profiles, in the same way as in the ordinary reversed shear discharges. Profiles of the ion temperature, T_i, measured by charge exchange recombination spectroscopy (CXRS) at 8.5 s, 2 s after the onset of the higher NBI power, are plotted in Fig. 5(a). Here, the profile of the broadening spectrum injection case is designated by circles and the other case by squares. As is shown in the figure, T_i starts increasing steeply towards the plasma centre at a certain position in both cases. However, that position is clearly different in these two cases, i.e. at $\rho \simeq 0.7$ in the case of broadening spectrum injection and at $\rho \simeq 0.4$

in the other case. One notable feature of the reversed shear discharges in JT-60U is that a steep gradient is found also in the electron temperature profile [1]. This was also observed in the LHCD experiment. Furthermore, the position where the steep T_e gradient occurred was also clearly different in the two cases and almost the same as that found in the T_i profiles shown in Fig. 5(a). In Fig. 5(b), q profiles at 8.5 s are plotted, and it is found that quite strong negative shear remained in the case of the broadening spectrum injection. It seems that a point where a steep T_i gradient exists corresponds to the position of minimum q, but further systematic and careful investigation is necessary for definite conclusions to be reached.

3.3. Formation of reversed magnetic shear by LHCD

Finally, we show that a strong reversed magnetic shear can be formed by an LHW alone.

So far, the scenario of producing a reversed shear configuration by applying NBI heating during the I_P ramp-up phase has been very successful [1–3]. However, searching for other possible schemes is still attractive from the viewpoints of extending the plasma operation regime, investigation of detailed physics, etc. For example, although a wider region of negative shear can be formed by applying a higher NBI power at I_P ramp-up, it might cause disruption due to the beta limit before the plasma reaches I_P flat-top. It is also possible that a higher NBI power tends to induce a toroidal rotation in the plasma, which might confuse our physics understanding. In JT-60U, the formation of a reversed shear configuration by means of LHW injection was attempted and also achieved as will be shown below.

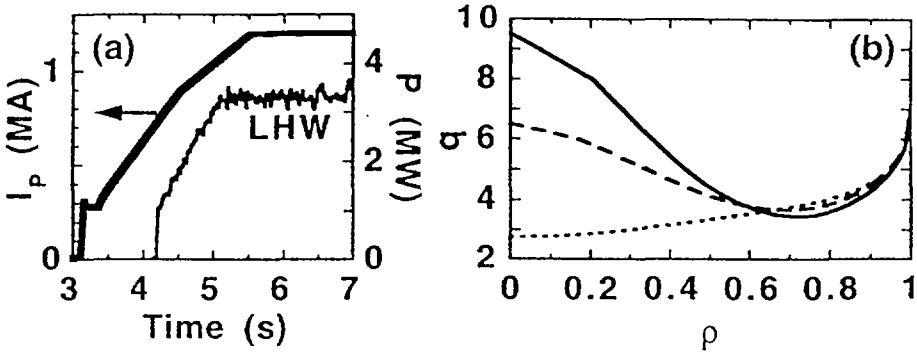

FIG. 6. (a) Temporal evolution of I_P (bold solid), LHW (solid) and NBI (broken) powers. (b) Evaluated q profile, at 5.5 s, of discharge shown in (a) plotted by solid curve; of discharge with normal reversed shear formation by dashed curve and of discharge without LHW injection by dotted curve.

In Fig. 6(a), the temporal evolutions of I_P (bold solid line) and LHW (solid line) power are plotted. No NBI, except the one (1 MW) used for MSE measurements, was applied. The line averaged electron density increased to about 1×10^{19} m^{-3} almost linearly with time up to 5 s and then stayed nearly constant. The toroidal field strength was the same as in the previous experiments. It should be noted that the main working gas and the beam particles were deuterium in these experiments. Furthermore, all three launchers were used in order to inject higher power, and the injected spectra were chosen so as to drive a hollow current profile. Since D–D neutrons produce secondary HX, no HX measurement was available. However, a hollow HX intensity profile like that shown in Fig. 4(a) was observed in a similar discharge in which no NB was injected. An evaluated q profile at 5.5 s is shown in Fig. 6(b) by the solid curve. As is shown in the figure, strongly reversed magnetic shear is found to be formed in a wide area up to $\rho \simeq 0.7$. For comparison, q profiles in a normal scenario (NBI heating at current ramp-up, dashed curve) and in a case without LHW (with 1 MW of the MSE probe beam only, dotted curve) are shown. In the normal scenario, the NBI power was about 3.3 MW. The reversed shear formed by LHW is even stronger than that formed in a normal scenario. During LHW injection in the ramp-up phase, T_e was found to rise strongly. A profile of T_e at 5 s, measured by Thomson scattering diagnostics in a similar discharge, is shown in Fig. 7 by circles. For comparison, a T_e profile in a normal scenario, whose q profile is shown by the dashed curve in Fig. 6(b), is plotted by squares in Fig. 7.

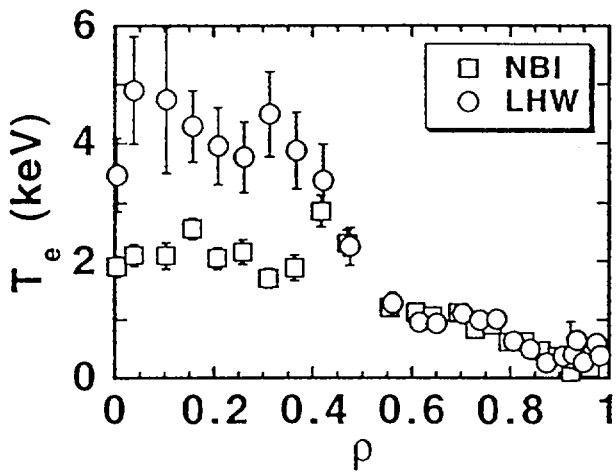

FIG. 7. Electron temperature profile at 5 s of a shot similar to that shown in Fig. 6(a), plotted by circles. Normal scenario: squares.

As was mentioned before, the NBI power was about 3.3 MW, in this case. Evidently, T_e is much lower than in the case with LHW. Although a current drive effect is expected by LHCD, this high temperature might help to form strongly reversed magnetic shear as is shown in Fig. 6(b). The large increase in the electron temperature might be attributed to an improvement of confinement due to reversed shear, such as that found in Tore Supra [8].

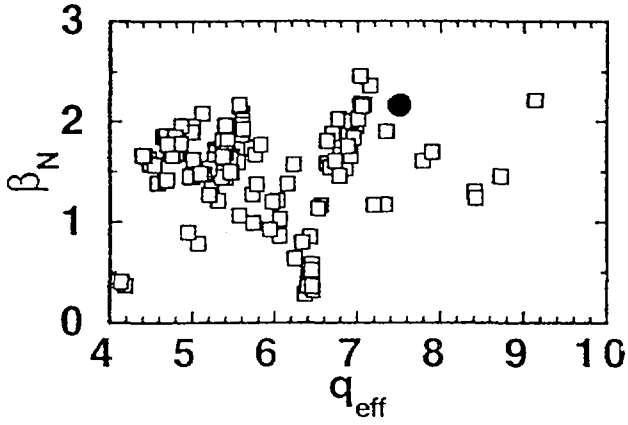

FIG. 8. β_N just before β collapse in reversed shear discharges versus q_{eff}. Discharge with reversed shear formed by LHW alone: solid circle; normal reversed shear formation: open squares.

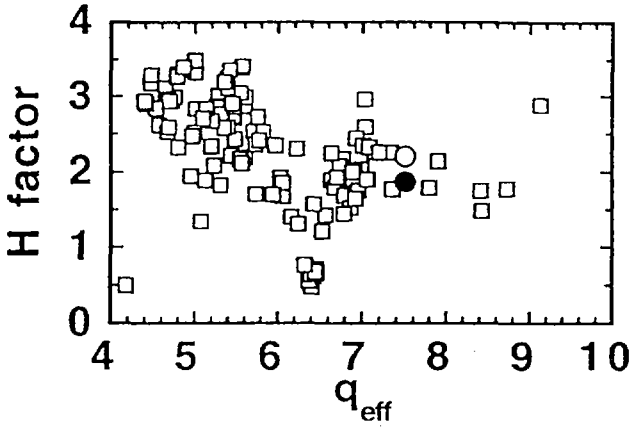

FIG. 9. H factor just before β collapse in reversed shear discharges versus q_{eff}. Discharge with reversed shear formed by LHW alone: solid circle; normal reversed shear formation: open squares. Open circle: same shot as that of the solid circle, but 40% ripple loss for perpendicular beam power taken into account.

Into this plasma, high power NBI was injected so that the effect on plasma performance could be seen. About 22 MW of NBI (including a beam used for MSE measurement from I_P ramp-up) power was turned on at 7 s, after 1.5 s of I_P flat-top. In the same way as in normal reversed shear discharges, the stored energy kept increasing and, finally, the plasma disrupted owing to the β limit. The value of normalized plasma beta, β_N, just before the disruption of this shot is shown in Fig. 8 by a solid circle, together with the values of normal reversed shear discharges shown by open squares versus q_{eff}. We find from the figure that the β limit of this shot is one of the highest values. The H factor, the ratio of experimental energy confinement time to energy confinement time as estimated by using the ITER-89 power law, is also shown by a solid circle versus q_{eff} in Fig. 9. Although this value seems modest, even among higher q_{eff} discharges, this might be attributed to the ripple loss of high energy ions. To maintain effective wave-plasma coupling, plasmas for LHCD experiments are larger in volume than in normal reversed shear discharges. This leads to larger ripple loss. The open circle in Fig. 9 was obtained by assuming 40% of ripple loss for the perpendicular beam power. The open circle is found to be comparable to the data of normal reversed shear discharges in the higher q_{eff} regime. It is very important to achieve high performance with a reversed shear configuration formed by a different scheme.

4. CONCLUSIONS

In the JT-60U tokamak, LHWs were applied to reversed shear plasmas in order to investigate the applicability of LHCD to sustainment, control and formation of reversed magnetic shear. Owing to MSE measurements, local current profiles have been obtained in the experiments.

(1) Sustainment of reversed magnetic shear by means of LHCD was successfully achieved in a plasma with $I_P = 1$ MA, $B_{T0} = 2.95$ T and $\bar{n}_e \simeq 1 \times 10^{19}$ m^{-3}. The duration of the sustainment was about 7.5 s, and a wide region of negative shear up to $\rho \simeq 0.55$ was maintained up to the end of the LHW pulse. A q profile with $q_{min} \simeq 3$ was found to be stable during this period.

(2) It was demonstrated that magnetic shear can be changed by controlling the injection $N_\parallel$ spectrum of the LHWs. Furthermore, by applying NBI heating to these plasmas, it was found that the existence of a region of better confinement depends on the injected wave spectrum, in other words, the target magnetic shear.

(3) It was successfully demonstrated that well reversed magnetic shear with a wide area of negative shear could be formed by means of LHW application alone in a plasma with $I_P = 1.2$ MA. Moreover, a reversed shear plasma produced by this scheme proved to have the same potential of good confinement as normally produced — i.e. by NBI heating in the I_P ramp-up phase — reversed shear dis-

charges have. These results are important, not only for improving plasma performance but also for the investigation of the physics of improved confinement in reverse shear plasmas.

ACKNOWLEDGEMENTS

The authors would like to acknowledge all members of the Japan Atomic Energy Research Institute who have contributed to the JT-60U project. They also express their gratitude to Drs C.B. Forest, M. Kikuchi and T. Ozeki for valuable discussions.

REFERENCES

[1] FUJITA, T., et al., these Proceedings, Vol. 1, p. 227.
[2] LEVINTON, F.M., et al., Phys. Rev. Lett. 75 (1996) 4417.
[3] STRAIT, E.J., et al., Phys. Rev. Lett. 75 (1996) 4421.
[4] NAITO, O., JT-60 TEAM, Plasma Phys. Control. Fusion 35 (1993) B215.
[5] KONDOH, T., JT-60U TEAM, Phys. Plasmas 1 (1994) 1489.
[6] IDE, S., et al., Phys. Rev. Lett. 73 (1994) 2312.
[7] IDE, S., et al., in Plasma Physics and Controlled Nuclear Fusion Research 1994 (Proc. 15th Int. Conf. Seville, 1994), Vol. 1, IAEA, Vienna (1995) 641.
[8] HOANG, G.T., et al., Nucl. Fusion 34 (1994) 75.
[9] OZEKI, T., et al., in Plasma Physics and Controlled Nuclear Fusion Research 1992 (Proc. 14th Int. Conf. Würzburg, 1992), Vol. 2, IAEA, Vienna (1993) 187.
[10] SÖLDNER, F.X., in Controlled Fusion and Plasma Physics (Proc. 22nd Eur. Conf. Bournemouth, 1995), Vol. 19C, Part IV, European Physical Society, Geneva (1995) 113.
[11] FUJITA, T., et al., Fusion Eng. Des. (in press).
[12] IDE, S., FUJITA, T., NAITO, O., Plasma Phys. Control. Fusion (in press).
[13] SEKI, M., et al., in Fusion Technology (Proc. 16th Symp. SOFT London, 1990), Vol. 2, Elsevier, Amsterdam (1991) 1060.
[14] IKEDA, Y., et al., in Fusion Engineering (Proc. 15th Symp. San Diego, 1991), Vol. V, IEEE, Piscataway (1992) 122.
[15] IKEDA, Y., et al., Fusion Eng. Des. 24 (1994) 287.

DISCUSSION

R.J. HAWRYLUK: The data presented on the sustainment of the reversed shear regime by LHCD are very encouraging. A key issue in the research is to demonstrate control of the current profile at high values of j_{BS}/j_{tot} and in the presence of a strong internal transport barrier. What value of j_{BS}/j_{tot} was achieved in the discharge in which the current profile was sustained?

S. IDE: Since we only used an LHW of 2 MW and NBI of 0.4 MW in the experiment, the value of β_p was not high. Therefore, although we have not yet estimated it, j_{BS}/j_{tot} should be quite low.

LONG PULSE RF EXPERIMENTS ON TORE SUPRA: RESULTS AND SIMULATIONS

Y. PEYSSON, G. REY, R. ARSLANBEKOV, V. BASIUK,
B. BEAUMONT, G. BERGER-BY, P. BIBET, J.J. CAPITAIN,
J. CARRASCO, J.P. CRENN, P. FROISSARD, P. GARIN,
M. GONICHE, L. LADURELLE, X. LITAUDON,
D. MOREAU, M. PAIN, M. TAREB, G. TONON
Département de recherches sur la fusion contrôlée,
Association Euratom-CEA,
Centre d'études de Cadarache,
Saint-Paul-lez-Durance, France

J.P. BIZARRO, J.S. FERREIRA, P. RODRIGUES
Centro de Fusão Nuclear,
Associação Euratom-IST,
Instituto Superior Técnico,
Lisbon, Portugal

Abstract

LONG PULSE RF EXPERIMENTS ON TORE SUPRA: RESULTS AND SIMULATIONS.

Long pulse RF experiments at high power level have been carried out on Tore Supra by coupling lower hybrid (LH) waves to the plasma. Plasma pulses lasting two minutes have been obtained successfully, leading to a new injected energy record of 280 MJ. Full current drive discharges have been also sustained beyond 60 s using active feedback control of the LH power on the plasma current; power densities of up to 24 MW/m^2 have been achieved. Experiments on power coupling at distances of up to 15 cm from the plasma have provided new potentialities concerning far distance coupling in a reactor environment. Steady state conditions were also achieved in combined scenarios with 2 MW of LH power and 2 MW launched by the ion cyclotron resonance heating (ICRH) system, corresponding to a power density of 8 MW/m^2. With a view to improving long pulse performance, several ongoing projects relevant to ITER are being carried out for the LH system: mode converter, passive-active multijunction and new lateral protections. Progress in the understanding and modelling of LH power deposition profiles is reported, taking into account the toroidal magnetic field ripple in the wave dynamics, which reaches 7% at the Tore Supra plasma edge. Despite the rather modest amplitude of the local ray perturbation, its global effect may be strong, as a consequence of the combined effects of toroidal and poloidal inhomogeneities. Simulations of LH experiments have been performed by coupling ray tracing calculations with a one dimensional relativistic Fokker-Planck code. In the 'few passes' regimes where the wave makes some, but not many, passes inside the plasma before it is absorbed, the effect of magnetic ripple usually leads to a broadening of the power deposition profile and a shift towards the plasma centre, a behaviour which may be explained by an increase of the overall ray stochasticity. A comparison between simulations and experimental observations is reported.

1. INTRODUCTION

The achievement and control of steady state fusion plasmas with economically relevant performance is one of the major challenges of tokamak physics during the next few decades. With its superconducting toroidal coils, active heat and particle control systems and an available large choice of RF heating methods, the Tore Supra tokamak is especially well designed for this type of studies, the 'advanced tokamak scenarios'. High density steady state tokamak operation with active control of heat, particles, impurity influxes and current density profiles raises several questions on the route towards achieving such plasmas, their stability, performance, and ability to be driven by external feedback control systems.

The lower hybrid (LH) wave has for a long time been recognized as the most efficient means of generating non-inductive currents in moderate temperature plasmas. It is, therefore, a potential candidate for controlling the current profile in an advanced steady state reactor, especially in the low β early phase of the discharge, when most of the current shaping would have to be done in order to ensure high Q fusion gain and stability during the burn. For this purpose, the LH heating system has to demonstrate the capability for very long pulses, so that steady state operation may be achieved for tokamaks with high plasma performance [1]. In addition, it must be ascertained that combined scenarios using other RF heating systems such as ICRH or ECRH may be achieved. In this paper, recent RF system performance obtained on Tore Supra is presented, with special emphasis on steady state discharges and far distance coupling capability of the LH wave at high power, a critical issue in a reactor environment. Ongoing development relevant to ITER aiming at an improvement of long pulse performance with RF systems is also reported.

A possible application of the LH heating system to a fusion reactor is closely related to the ability to control the power deposition profile for an efficient shaping of the current density profile in the plasma. In this paper, progress in the understanding and modelling of the LH wave dynamics is reported, by taking into account the toroidal magnetic field ripple in all simulations of Tore Supra LH experiments.

TABLE I. CHARACTERISTICS OF THREE RF HEATING SYSTEMS

System	Frequency	Source	Power (MW)[a]	Power density (MW/m^2)[b]
ICRH	40–80 MHz	6 tetrodes	14/9.5	16 (Faraday screen)
LHCD	3.7 GHz	16 klystrons	8/6.2	37 (grill)
ECRH	118 GHz	6 gyrotrons	3/—	—

[a] Installed/injected.

[b] Achieved on plasma.

Indeed, with N = 18 toroidal field coils, the Tore Supra tokamak shows a large magnetic ripple at the plasma edge, reaching 7% and possibly affecting the numerical predictions obtained by ray tracing and Fokker–Planck codes. First, the ray dynamics in a toroidal equilibrium that is periodically modulated along the toroidal direction is depicted in detail. A global analysis is carried out in order to identify in which regimes magnetic ripple plays an important role. Then, realistic simulations are considered for standard plasma conditions on Tore Supra, and a comparison between experimental observations and numerical predictions is presented.

2. RF SYSTEM PERFORMANCE

The Tore Supra tokamak is especially designed for long pulse discharges at a high power level. With three different RF heating systems, whose characteristics are summarized in Table I, a wide range of operating conditions may be foreseen.

Although shown in Table I, the ECRH heating system of Tore Supra has not yet been fully installed. From the power source (500 kW per gyrotron) to the antenna (quasi-optical launcher with actively cooled mirrors for beam focusing and localization), all components have been designed for quasi-continuous operation. In particular, the transmission line is a circular, corrugated waveguide especially designed for the HE_{11} propagation mode, which enables low level losses without a need for active cooling. The prototype of the tube is at present tested up to 5 s at its nominal power, and it is foreseen to increase its duration up to 210 s.

Stationary enhanced plasma performance has been achieved in weak or reversed shear LH driven discharges for up to 2 mn, as shown in Fig. 1, and a new injected energy record of up to 280 MJ has been obtained [2]. During this type of discharge, the temperatures of the grill protections (300°C) remain constant as does the pressure inside the launcher tank, which indicates stable outgassing. In some cases, a slight increase in density is observed after 60 s, which may be ascribed to an oxygen and silver impurity influx [3]. However, this effect is not routinely observed, as is shown in Fig. 2 for the case of a nearly full current drive pulse sustained during 75 s. For this shot, a power density of 24 MW/m^2 is obtained in steady state conditions, a level which validates the design of the new Tore Supra launchers for quasi-continuous operation [4] and may be used as a reference for application to the ITER tokamak. This has been obtained by an unbalanced power level between the two launchers (0.5–2.0 MW).

The coupled LH power as a function of the pulse duration is shown in Fig. 3. For very short pulses ($\Delta t \leq 8$ s) and a reflection coefficient level below 3–4%, the LH power which may be coupled to the plasma is only limited by the available power at the generator. When the pulse duration is increased up to 25 s, the LH power limit scales well with a maximum plasma energy content of 100 MJ. Such a dependence may be ascribed to a rise in the temperatures of the poorly cooled components in the vacuum vessel, leading to outgassing and plasma collapse. However, the deviation

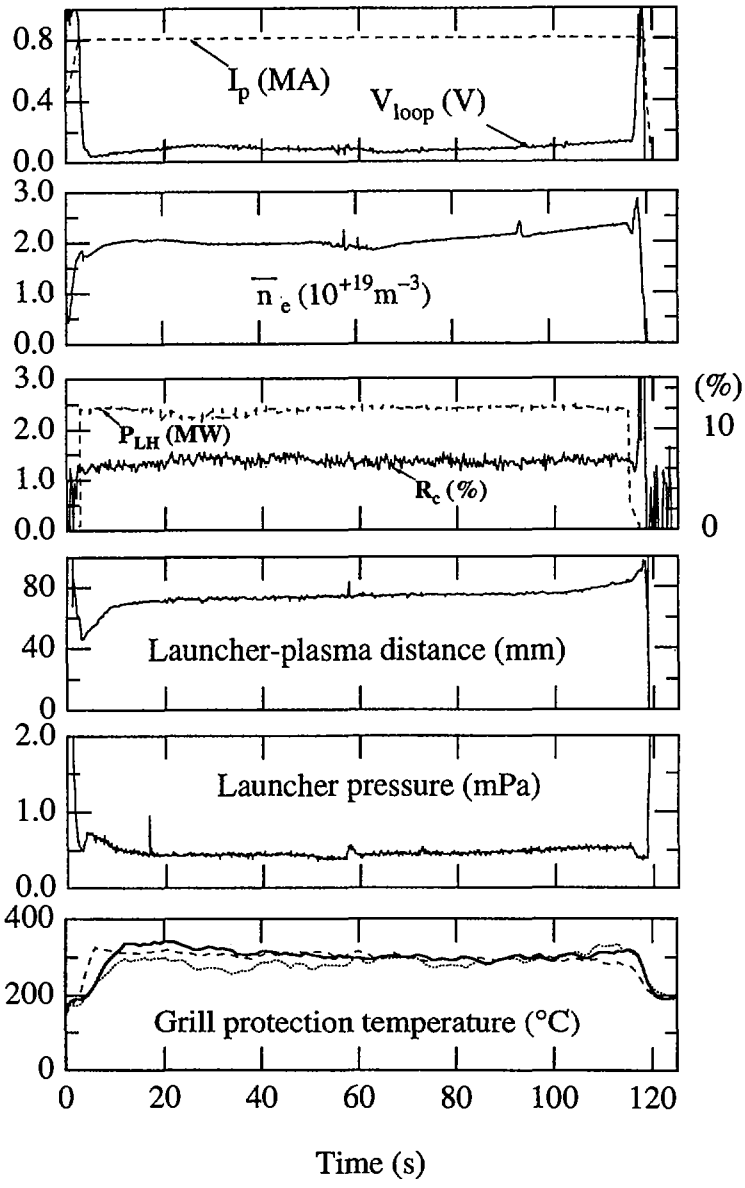

FIG. 1. 2 mn long shot experiment No. 19 980.

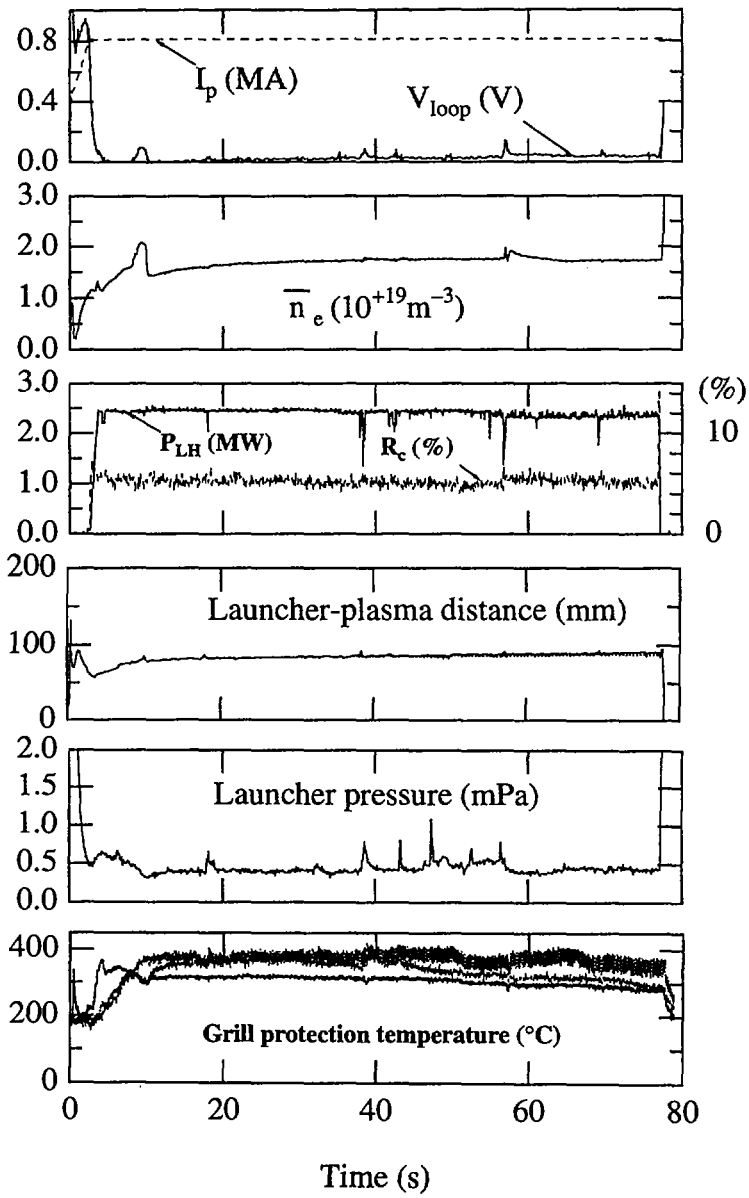

FIG. 2. 75 s long shot experiment No. 19 984.

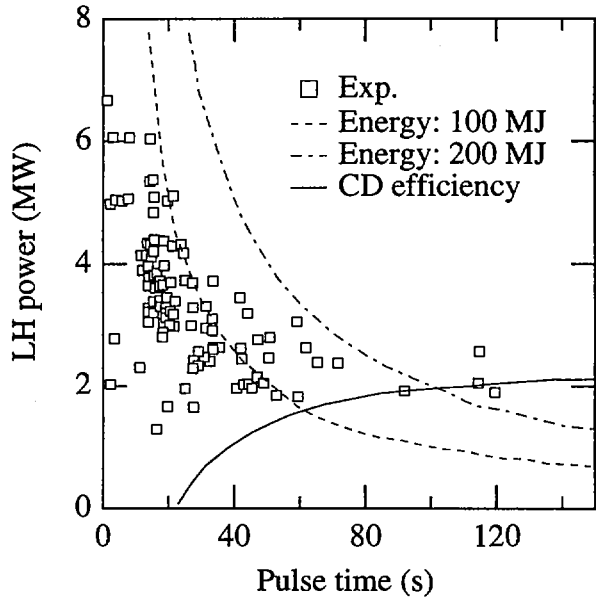

FIG. 3. LH power and shot duration limit on Tore Supra.

which is observed when the LH power launched into the discharge is lower than 3.5 MW probably indicates that thermal equilibrium has almost been reached and that the temperatures of most of the components in the vacuum vessel are nearly constant. In this regime, the LH power launched into the discharge must exceed the lower limit given by the current drive efficiency for long pulse duration, in order to sustain all the plasma current. For the usual plasma parameters of long shots on Tore Supra (line averaged density: 2×10^{19} m^{-3}, plasma current $I_p = 0.8$ MA, CD efficiency: 0.8×10^{19} $A \cdot W^{-1} \cdot m^{-2}$), the LH power to be coupled to the plasma is of the order of 2.5 MW, as is shown in Fig. 3. It should be noted that in this case true quasi-continuous operation could be achieved.

Combined operations in stationary conditions with both LH and ICRH power have been carried out successfully on Tore Supra. During 30 s, 2 MW of ICRH power were launched together with the same level of LH power, as is shown in Fig. 4. In this case, the ICRH power is coupled to the plasma by only one antenna, though demonstrating the capability to operate at an antenna power density of up to 8 MW/m^2 in a steady state manner. Indeed, despite the high power density level, the temperatures on the septum and the lateral protections of the antenna remain constant [5].

Far distance coupling of the LH power to the plasma is a critical issue for convenient operation in a reactor grade tokamak. This question was addressed on Tore Supra in various plasma conditions, by coupling up to 4 MW of LH power.

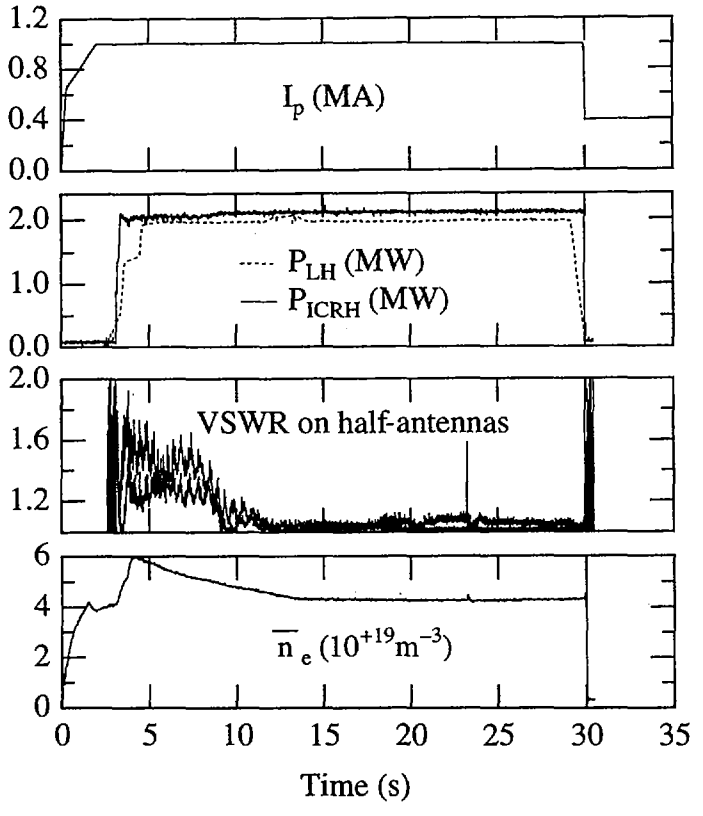

FIG. 4. 30 s pulse with combined ICRH and LH powers.

Irrespective of the plasma parameters and configurations studied, the reflection coefficients remain lower than 8% for distances up to 150 mm between the launcher and the last flux surface, as is shown in Fig. 5. The fact that an efficient power coupling may be obtained, even if the density decay length ranges between 4 and 8 cm at the plasma edge, suggests that the density at the grill mouth is self-sustained by the LH power. On the basis of Langmuir probe measurements, the density growth rate in the vicinity of the antenna is estimated to be $1.5 \pm 0.7\ 10^{17}$ m^{-3}/MW, a value which appears to be independent of the edge density level before the onset of the RF power, even if it is below the LH cut-off density. The constant loop voltage observed during the pulse when the launcher (or the plasma) is moved proves that the global current drive efficiency is not affected by the position of the antenna. Furthermore, as the power handling and coupling may be affected by the appearance of hot spots on the plasma facing components of the antennas, robust operating conditions for LH driven current drive may be obtained when the power is coupled at a

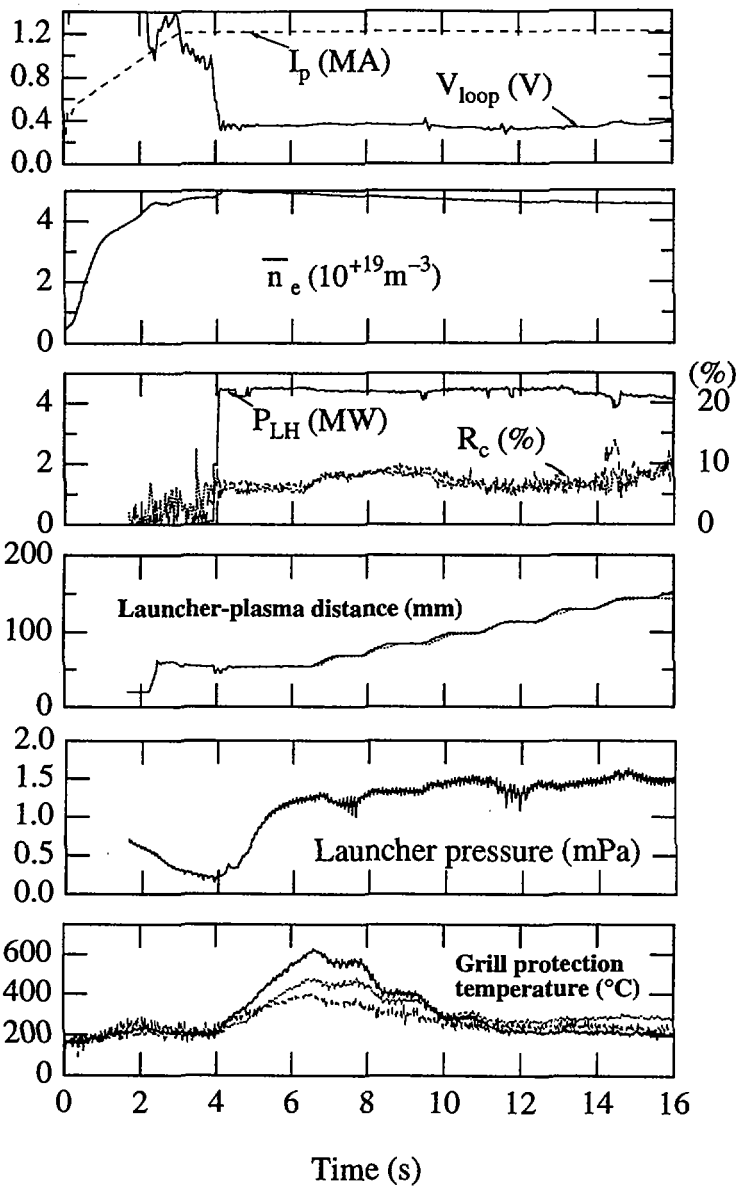

FIG. 5. LH power coupling at far distance from plasma (No. 18 642).

far distance from the plasma. Indeed, in this case, a strong reduction of the thermal heat load on the grill protections is observed, which corresponds to a temperature drop from 500 to 200°C (Fig. 5).

A good deal of technical development is under way in order to improve long pulse performance at high power on Tore Supra. Long test pulses have been performed successfully with ICRH antennas on the RF test bed. No visible degradation of the antennas was observed after an operation of 2–3 mn. Moreover, it was possible to increase the pulse up to 12 mn, at RF voltages comparable to those obtained during standard plasma operation (30 to 35 kV). Furthermore, new lateral protections have been designed to increase the operating reliability during long plasma discharges and to avoid thermal limitations and, as a consequence, degradation of the graphite tiles. These components, which are based on the same technology as is used to upgrade the first inner wall power exhaust capabilities, are designed for a continuous thermal heat flux of 8–10 MW/m^2. They will also be used for the next LH launcher of Tore Supra. Much in the same way, an improved design concept for the LH launchers, which may be useful for an antenna installed on ITER, is considered. The new concept, based on passive–active multijunctions supplied by TE_{10-30} mode converters, enables good coupling of the slow wave to the plasma, and an efficient cooling of the grill mouth [6]. The power handling capabilities of such a design are directly deduced from the long pulse performance achieved in steady state conditions on Tore Supra, and special components feeding the passive–active multijunctions have been tested successfully up to 300 kW during 1000 s on the LH test bed facility.

3. LOWER HYBRID CURRENT DRIVE AND THE MAGNETIC RIPPLE

Since the first studies of LH current drive, an accurate prediction of radial and spectral power deposition profiles had remained a very difficult task, owing to the uncertainties inherent to the propagation of the wave along trajectories which are spiralling a long way around the torus before the wave energy is absorbed, and as a result of the absence of any wave resonance. Generally, one relies on ray tracing plus Fokker–Planck models, and careful comparisons of the simulations with non-thermal bremsstrahlung emission measurements and other experimental data have to be made in order to assess the validity of the modelling effectively. Although toroidal couplings seem to be dominant in modifying the wave spectrum such that a strong quasi-linear interaction with the electron population can take place, other effects can significantly alter the numerical predictions. In the case of Tore Supra, the toroidal magnetic ripple, which reaches 7% at the outboard edge of the plasma, is large enough to modify strongly the predictions obtained with an axisymmetric equilibrium, whatever the plasma conditions, because of the perturbation of the ray paths. Indeed, it has been shown that the discreteness of the toroidal field system may alter the picture of the LH wave propagation obtained from a straight cylindrical

geometry [7–9]. For parameters of practical interest, magnetic ripple may induce stochastic behaviour in the ray dynamics so that the well known cylindrical accessibility condition for the LH wave to penetrate to the plasma centre is no longer valid, as a result of the non-integrability of the ray equations. Therefore, the predicted power deposition profile is expected to be greatly modified.

In the toroidal case [10, 11], results have been obtained by integrating numerically the usual ray equations

$$\frac{d\mathbf{r}}{dt} = -\frac{\partial D(\omega, \mathbf{r}, \mathbf{k})}{\partial \mathbf{k}} \Big/ \frac{\partial D(\omega, \mathbf{r}, \mathbf{k})}{d\omega}$$

and

$$\frac{d\mathbf{k}}{dt} = \frac{\partial D(\omega, \mathbf{r}, \mathbf{k})}{\partial \mathbf{r}} \Big/ \frac{\partial D(\omega, \mathbf{r}, \mathbf{k})}{\partial \omega}$$

where $D(\omega, \mathbf{r}, \mathbf{k}) = 0$ is the local electromagnetic dispersion relation for the LH wave including warm plasma effects, and $\mathbf{k} = (k_r, m, n)$ is the wave momentum canonically conjugate to the toroidal co-ordinate vector $\mathbf{r} = (r, \theta, \varphi)$. Because of the breaking of axisymmetry, the toroidal mode number n is no longer a constant of the ray motion, and its evolution must be followed along the ray trajectories, much in the same way as that of the poloidal mode number m, which varies as a consequence of the poloidal inhomogeneity. To complete the description of the wave propagation, a consistent treatment of the toroidal equilibrium in the presence of ripple has to be made, following the usual perturbative approach. Neglecting plasma diamagnetism, we can show that, up to the first harmonic in the toroidal angle φ, the isoripple surfaces are circles shifted towards the torus axis. In the calculations, the electron and ion temperatures and densities are considered to be constant on a flux surface ρ, which is defined up to the same order in the ripple perturbation by the condition $\Delta\rho \cdot \mathbf{B} = 0$, where $\mathbf{B}$ is the total magnetic field.

In Fig. 6, a typical ray evolution is presented as a function of the toroidal angle φ, with and without account of the ripple correction for Tore Supra. In the two cases, the ray conditions at launch are similar ($\varphi_0 = \pi/N$ in the equatorial midplane, which corresponds to the centre of an antenna between two consecutive toroidal coils), and the parallel refractive index at the antenna is set to $n_{\parallel 0} = 2.0$. High frequency modulation of the toroidal mode number n is observed; its periodicity matches the magnetic ripple one ($2\pi N$, $N = 18$). This modulation takes place only where the magnetic ripple corrections are high, close to the outboard edge of the plasma. Even if the relative variations of n may reach $\pm 100\%$, variations of $n_\parallel$ exhibit only very weak oscillations in φ, which may numerically be estimated to be of the order of the local ripple amplitude, δ. Qualitative features of the evolution of n and $n_\parallel$ may be well recovered by using the electrostatic limit of the cold plasma

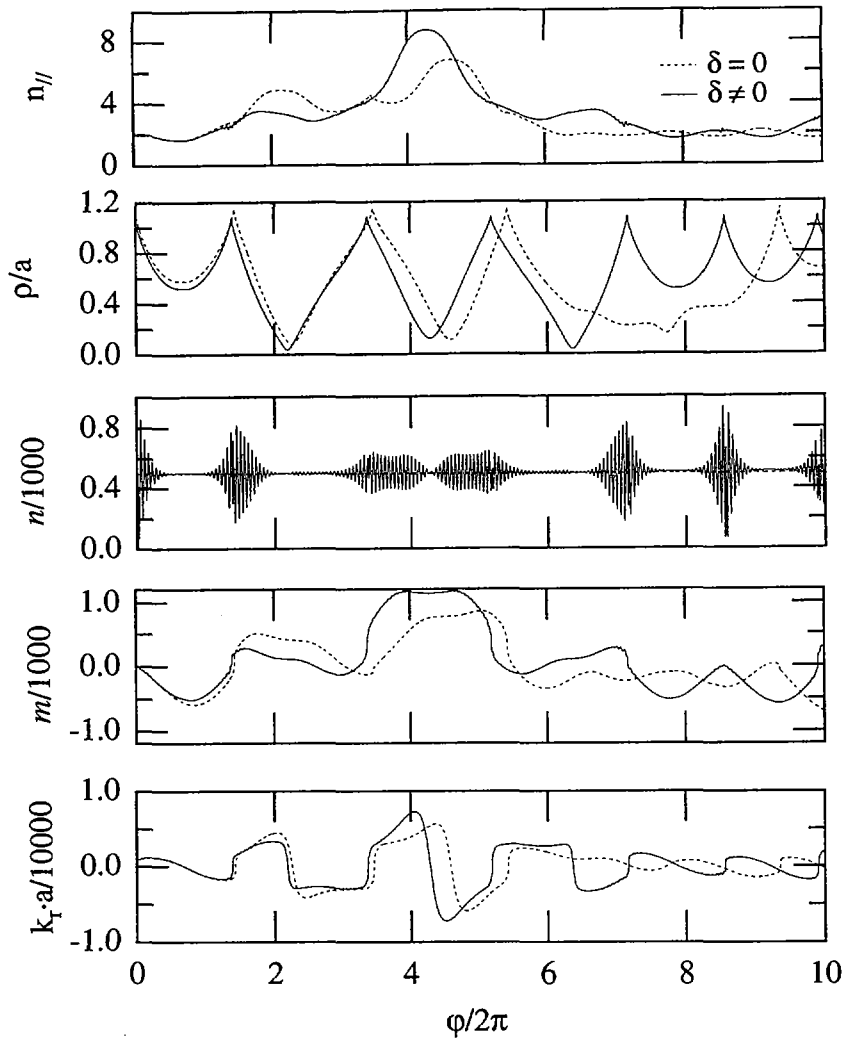

FIG. 6. Code predicted ray behaviour for axisymmetric (dashed line) and rippled toroidal equilibrium (solid line) as a function of toroidal angle.

dispersion relation if one observes that the ray motion is characterized by a slow evolution in the radial and poloidal directions, and a fast evolution in the toroidal direction [11]. As is shown in Fig. 7, the position of the toroidal launch point of the ray path strongly affects the ray evolution in the plasma. In real toroidal simulations, this issue becomes of great importance because the LH antenna usually lies in the highest ripple region, in the equatorial midplane. Hence, in a detailed description of the LH power deposition, not only the poloidal extent of the antenna but also its toroidal

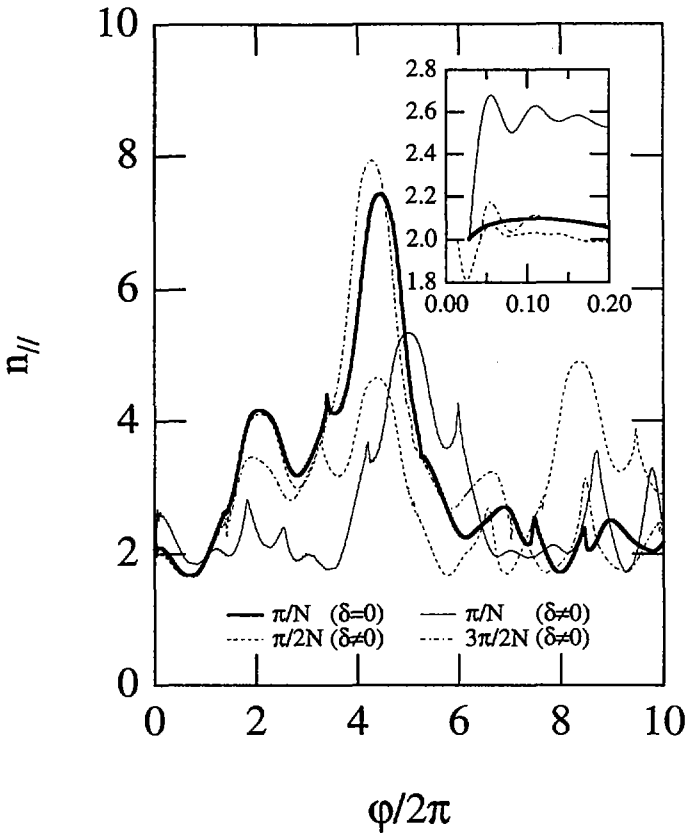

FIG. 7. Ray path for different toroidal angles at launch: thick line (no ripple), solid, dashed and dot-dashed lines (ripple case, centre and edges of the antennna). In the insert, details of ray behaviour in the vicinity of the launching point are shown.

width must be taken into account. Interestingly, for neighbouring initial conditions, the ray trajectories may diverge rapidly, a well known behaviour that is explained by the onset of ray stochasticity in toroidal geometry.

The effect of magnetic ripple has been investigated in various plasma conditions. A significant modification of the power deposition profiles is in general observed in the 'few passes' regime, where no single pass absorption occurs and the wave makes some, but not many, passes inside the plasma before it is totally absorbed. In fully stochastic regimes, the very large number of passes ends up cancelling all effects due to ripple perturbation. For typical low plasma current operation on Tore Supra (I_p = 0.8 MA, $T_{e0} \approx 3.3$ keV, $n_{e0} \approx 4.5 \times 10^{19}$ m^{-3}, B_0 = 3.9 T, with a launched spectrum peaked at 1.8), a sharp off-axis power deposition profile at $\rho/a \approx 0.38$ is predicted without taking into account the magnetic rip-

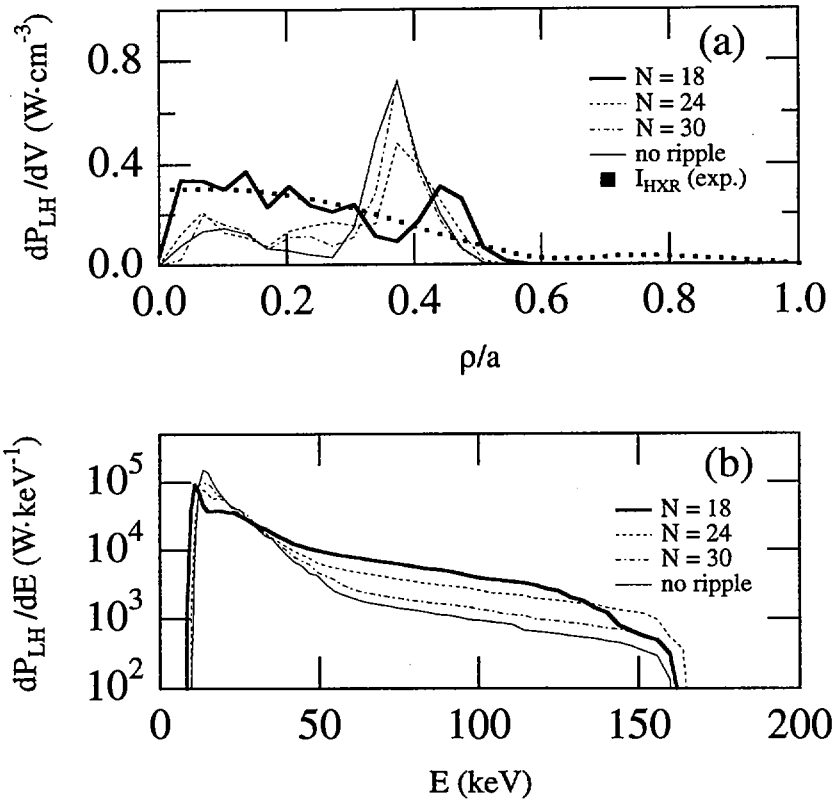

FIG. 8. Tore Supra shot No. 13 550. Simulations of (a) power deposition profiles and (b) absorbed power energy spectra for various ripple levels. Full square: Abel inverted profile of non-thermal bremsstrahlung emission at 75 ± 25 keV.

ple in the ray dynamics. When ripple perturbation is considered, a broad and more pronouncedly centred power density profile averaged over all electron energies is predicted. This is in good agreement with the Abel inverted profile determined from the experimental non-thermal bremsstrahlung emission, as is shown in Fig. 8. Such a modification in the power deposition profile may be explained by a reduction in the absorption process when magnetic ripple is included in the ray calculations, so that the stochastic nature of the ray motion may comes into play in predicting the power deposition pattern. A detailed analysis of a test ray with an initial value chosen close to the peak of the launched spectrum confirms this interpretation, i.e. that the LH wave absorption becomes weaker and also much more regular along the ray path [11]. As a consequence, a significant fraction of the power is deposited in the central region of the plasma, and the fraction of LH power absorbed by fast electrons is strongly increasing (Fig. 8). By increasing the number of coils in the simulations, it

is possible to investigate how effects scale with the ripple amplitude. When the ripple amplitude is reduced by a factor of three (N = 18 → N = 24), the power deposition profile corresponding to no ripple is nearly recovered, while the energy spectrum of the absorbed power remains significantly modified as compared to the axisymmetric case. When the ripple level is less than 1% (N = 30), most of the ripple effects fade away. Therefore, for the ITER tokamak, it is likely that magnetic ripple may be neglected in the simulations of LH power absorption, all the more as single pass absorption will take place because of the expected high electron temperature of the burning plasma.

Comparisons between numerical predictions and experimental observations have been carried out for Tore Supra. For full, stationary current drive discharges, plasma current and non-thermal bremsstrahlung emission of the plasma are expected to arise from the same quasi-linear modification of the electron distribution function, a unique opportunity for a robust benchmark of the code predictions in the presence of ripple, in the 'few passes' regime. The main plasma parameters used for the simulation correspond to Tore Supra shot No. 10 558: $B_0 = 3.7$ T, $I_p = 0.78$ MA, $T_{e0} = 6.0$ keV, $n_{e0} = 3.0 \times 10^{19}$ m^{-3}. The power launched is $P_{LH} = 3.4$ MW at $n_{\parallel peak} = 1.8$. The absorbed power density profile, which is hollow and localized at $\rho/a \approx 0.35$ for an axisymmetric equilibrium, is replaced by a more pronouncedly centred profile with a satellite peak at $\rho/a \approx 0.5$. The profile shape looks as if the absorbed LH power spectrum had been split into two well defined parts because of magnetic ripple, one at lower $n_\parallel$ values with a reduced absorption rate, and the other one at much higher $n_\parallel$ values so that the absorption can take place in colder regions of the plasma. Even if this rough picture may be misleading because of the non-linear coupling of the propagation and absorption processes, it nevertheless indicates that magnetic ripple corrections have led to a significant broadening of the absorbed power spectrum with respect to the axisymmetric case. Such an analysis is confirmed by the fact that the fraction of absorbed power deposited in the plasma core region lies at the very place predicted by a wave diffusion code based on a statistical treatment of the wave propagation [12]. This latter approach is valid when ray stochasticity comes fully into play in the numerical predictions, because of a weak damping rate of the power carried by the LH wave. The predicted power deposition profile, which is more distinctly centred when magnetic ripple is considered, is in good agreement with the Abel inverted profile of the non-thermal plasma bremsstrahlung emission determined between 50 and 100 keV and the current density profile deduced from polarimetry and magnetic measurements, as is shown in Fig. 9. It must be noted that both Abel inverted hard X ray and current density profiles deduced from experiments have a similar radial dependence, a consistent behaviour in a full current drive regime. An interesting consequence of the spatial modification of the power deposition is that there is no more need to introduce a large radial diffusion rate of fast electrons in order to link the radial dependence of the experimentally determined current density profile to the numerically computed absorbed power density profile. Whereas the radial diffusion coefficient must be as

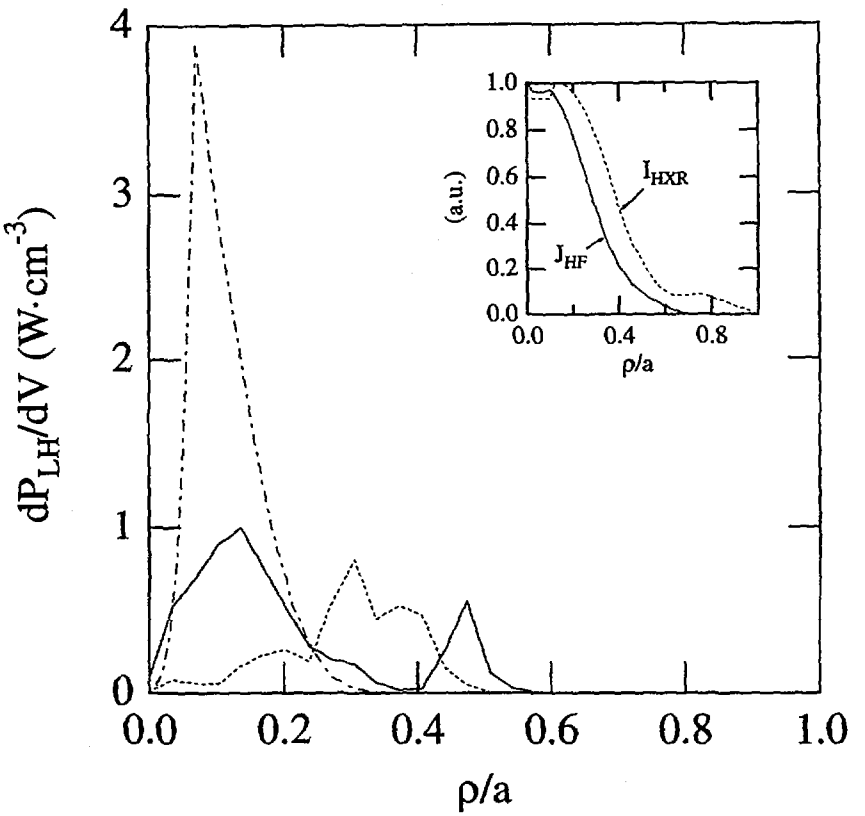

FIG. 9. Power deposition profile for the full current drive Tore Supra shot No. 10 558. Solid line: ripple case, dashed line: no ripple, dot-dashed line: wave diffusion model. Insert: experimental current density and non-thermal bremsstrahlung emission (at 75 ± 25 keV) profiles.

large as 2.0 $m^2 \cdot s^{-1}$ for simulations carried out with axisymmetric equilibrium, only weak radial transport is necessary when the full magnetic topology including ripple is considered to account for the small differences in shape between the two profiles. Though specific to Tore Supra, this result is in agreement with the fact that collisional slowing-down seems to prevail over radial diffusion of fast electrons in LH experiments [13]. This also illustrates the difficulty in using modelling codes to extract reliable information on fast electron transport.

4. CONCLUSIONS

Significant progress has been made in trying to achieve stable steady state discharges on Tore Supra, from the technology involved in high power density RF

transmission and coupling to the plasma, to the physics of LH wave propagation and absorption for an efficient shaping of the current profile.

Stationary enhanced plasma performance, which has been achieved in discharges for up to two minutes, provides convenient databases for the ITER design. Far distance coupling of the LH wave has been obtained successfully at high power density, which is an encouraging perspective for an application of LH current drive to reactor grade plasmas. Stationary discharges were sustained by using LH and ICRH heating systems simultaneously over 30 s, which demonstrates that antennas may operate in conditions where other coupling parameters are compatible for both systems. A good deal of development in RF systems relevant to ITER has been successfully under way on Tore Supra, aiming at an improvement of long pulse performance. In particular, new components such as the TE_{10-30} mode converter for the LH heating system, which have been tested up to 300 kW during 1000 s, may lead to an attractive simplification in the launcher design [14]. With the ECRH heating system, which is now in the construction phase and has reached its nominal performance during a few seconds, interesting experiments may be foreseen, with the possibility of very fine tuning of the power deposition localization.

As far as modelling of the LH wave power deposition profiles is concerned, recent progress has been made in intermediate regimes, between strong single pass damping and full multipass damping. It is shown that in this case the large magnetic ripple on Tore Supra may lead to strong modifications of the numerical predictions obtained with ray tracing plus Fokker–Planck codes, as compared to simulations with axisymmetric equilibrium. Indeed, despite the rather modest amplitude of the local ray perturbation when the ray crosses a high ripple region, its global influence may be large, as a consequence of the combined effects of toroidal and poloidal inhomogeneities. In the 'few passes' regime, the magnetic ripple usually leads to a broadening of the power deposition profile and a shift towards the plasma centre, a behaviour that may be explained by an increase in the overall ray stochasticity. A large modification of the LH absorbed power spectrum averaged over the plasma volume is also observed in this regime, which corresponds to a better coupling with high energy electrons. In very low absorption regimes, where full ray stochasticity prevails, the very large number of passes ends up cancelling all effects due to ripple perturbation. By taking into account magnetic ripple in LH simulations, a better agreement is found between numerical predictions and experimental observations, such as non-thermal bremsstrahlung emission or current profile, when plasma conditions correspond to the 'few passes' regime.

REFERENCES

[1] WIJNANDS, T., et al., Nucl. Fusion 36 (1996) 1201.

[2] LITAUDON, X., et al., in Controlled Fusion and Plasma Physics (Proc. 23rd Eur. Conf. Kiev, 1996), Vol. 20C, European Physical Society, Geneva (1996).

[3] EQUIPE TORE SUPRA (presented by B. SAOUTIC), IAEA-CN-64/O2-2, these Proceedings, Vol. 1, p. 141.
[4] FROISSARD, P., et al., in Fusion Technology (Proc. 19th SOFT Symp. Lisbon, 1996), Elsevier, Amsterdam.
[5] GONICHE, M., et al., in Controlled Fusion and Plasma Physics (Proc. 23th Eur. Conf. Kiev, 1996), Vol. 20C, European Physical Society, Geneva (1996).
[6] BIBET, P., et al., Nucl. Fusion 35 (1995) 1213.
[7] BIZARRO, J.P., et al., in Plasma Physics (Proc. Int. Conf. Foz do Iguaçu, 1994), Vol. 1, São José dos Campos, Brasil (1994) 329.
[8] BIZARRO, J.P., FERREIRA, J.S., "Lower-hybrid ray stochasticity due to magnetic ripple", Transport, Chaos and Plasma Physics (Proc. 2nd Workshop Marseille, 1995).
[9] BIZARRO, J.P., et al., Phys. Rev. Lett. 7 (1995) 1308.
[10] ARSLANBEKOV, R., et al., in Controlled Fusion and Plasma Physics (Proc. 21st Eur. Conf. Montpellier, 1994), Vol. 18B, Part III, European Physical Society, Geneva (1994) 1046.
[11] PEYSSON, Y., et al., Magnetic ripple and the modeling of lower-hybrid current drive in tokamaks (in preparation).
[12] KUPFER, K., et al., Phys. Fluids B 5 (1993) 4391.
[13] PEYSSON, Y., Plasma Phys. Control. Fusion 35 (1993) B253.
[14] Report on ITER Energy Task Agreement, Reports ETA-EC-IVA-LH (1993), JET-R (94) 07, EUR-CEA-FC 1529 (1994).

DISCUSSION

T. CHO: Regarding absorbed power energy spectra with ripples, the high energy part increases as compared to the case without ripples. From the viewpoint of resonant particles with lower hybrid waves, this seems to correspond to a reduction in $n_{\parallel}$. Have these effects been verified, for example by the data on soft X ray energy spectra along with the X ray radial profile data you have presented?

Y. PEYSSON: From a careful analysis of the ray motion, it appears that the toroidal magnetic ripple induces both upshifts and downshifts of the $n_{\parallel}$ value, as compared with the case corresponding to an axisymmetric equilibrium. However, in the 'few passes' regime, it turns out that the $n_{\parallel}$ downshift dominates on average, leading to a weaker power absorption of the LH wave and a better coupling to the fast electron population. The quantitative assessment of this effect against experiment has been carried out successfully in connection with simulations of the non-thermal bremsstrahlung energy spectra. It must be pointed out that an important additional ingredient for such simulations is to consider the full 2-D description of the fast electron dynamics in momentum space.

ADDITIONAL HEATING AND REVERSED MAGNETIC SHEAR IN THE FTU TOKAMAK

F. ALLADIO, L. ACITELLI[1], P. AMADEO[1], B. ANGELINI, M.L. APICELLA, G. APRUZZESE, E. BARBATO, R. BARTIROMO[2], A. BERTOCCHI, M. BORRA[1], G. BRACCO, A. BRUSCHI[3], G. BUCETI, P. BURATTI, A. CARDINALI, C. CENTIOLI, R. CESARIO, S. CIATTAGLIA, M. CIOTTI, S. CIRANT[3], V. COCILOVO, F. CRISANTI, R. DE ANGELIS, F. DE MARCO, B. ESPOSITO, D. FRIGIONE, L. GABELLIERI, G. GATTI, E. GIOVANNOZZI, G. GIRUZZI[4], C. GOURLAN, G. GRANUCCI[3], M. GROLLI, A. IMPARATO, H. KROEGLER, M. LEIGHEB, L. LOVISETTO, G. MADDALUNO, G. MAFFIA, A. MANCUSO, M. MARINUCCI, G. MAZZITELLI, P. MICOZZI, F. MIRIZZI, S. NOWAK[3], A. OREFICE[3], P. ORSITTO, D. PACELLA, L. PANACCIONE, M. PANELLA, V. PERICOLI, L. PIERONI, S. PODDA, G.B. RIGHETTI, F. ROMANELLI, F. SANTINI, M. SASSI, S.E. SEGRE[5], A. SIMONETTO[3], G. SOLARI[3], C. SOZZI[3], S. STERNINI, A.A. TUCCILLO, O. TUDISCO, F. VALENTE, V. VITALE, G. VLAD, V. ZANZA, M. ZERBINI
Associazione Euratom–ENEA sulla Fusione,
Centro Ricerche Energia Frascati,
Frascati, Rome,
Italy

Abstract

ADDITIONAL HEATING AND REVERSED MAGNETIC SHEAR IN THE FTU TOKAMAK.

After one year of shutdown devoted to the installation of the toroidal molybdenum limiter, the Frascati Tokamak Upgrade (FTU) has recently resumed operation. The experimental programme is focused on the three radiofrequency (RF) heating and non-inductive current drive systems: electron cyclotron resonant heating (ECRH), lower hybrid current drive (LHCD) and ion Bernstein wave heating (IBWH). The main aim of the experiments reported here is to demonstrate LHCD at high density and to sustain and heat reversed magnetic shear configurations, with a large reversal radius ($r_s/a \approx 0.5$). A transient heating of the shear reversed discharges achieved in ohmic conditions has been performed through ECRH. The results show that good confinement properties are maintained within the shear reversal surface. The FTU 8 GHz LH system was upgraded so that up to 1.4 MW of LH could be injected into the plasma. A value of 0.14×10^{20} A·W^{-1}·m^{-2} was obtained for the figure of merit of

---

[1] ENEA guest.

[2] Istituto Gas Ionizzati del CNR, Padua, Italy.

[3] Istituto di Fisica del Plasma CNR, Milano, Italy.

[4] CEA Cadarache, Saint-Paul-lez-Durance, France.

[5] Dipartimento di Fisica, II Università degli Studi di Roma, Rome, Italy.

the CD efficiency. Furthermore, in ohmic and LH heated discharges a confinement time of up to 1.6 times the ITER89-P value was observed. The first shear reversed discharge driven by 0.8 MW of LHCD was produced at I_p = 350 kA, $\bar{n}_e = 7 \times 10^{19}$ m^{-3}; it shows a regime where regular m = 2, n = 1 relaxations with extremely large amplitude ($\tilde{B}_\theta/B_\theta$ = 2.5% at the plasma edge) coexist with a high temperature plasma (T_{e0} = 1.6 keV).

1. INTRODUCTION

Plasma configurations with reversed magnetic shear have shown reduced transport in the core [1] and are a leading candidate for advanced tokamak operation, also in ITER. MHD stability calculations show that these configurations should allow a high normalized Troyon factor β_N, at a high bootstrap current fraction [2]. A critical issue concerning the reversed shear profiles is the stability of double tearing modes (DTMs), which might affect central confinement.

2. REVERSED MAGNETIC SHEAR IN FTU OHMIC DISCHARGES

Ohmic shear reversed configurations have been obtained in FTU mostly during the early phase of the discharges (Fig. 1), with a metallic (Inconel, tungsten or molybdenum) poloidal limiter [3] or with the molybdenum toroidal limiter [4]. They are characterized by bursts of magnetic relaxations in the presence of peaked radiation loss profiles and hollow electron temperature profiles. These bursts are more easily obtained when the plasma internal self-inductance $\ell_i/2$ is still rising after the current has reached its plateau value. An MHD equilibrium reconstruction code [5], which uses the measured density and temperature profiles to determine the shape of the pressure profile in the Grad–Shafranov equation, has been widely applied to the FTU database for deriving the current density profile j_ϕ and the safety factor q. For sawtoothing discharges with $q_a < 4$, the position of the $q_s = 1$ surface as determined by the code is in good agreement with the observed sawtooth inversion radius. During the bursts of magnetic reconnections, the j_ϕ profile is found to remain hollow in the plasma core, in agreement with numerical simulations of resistive diffusion based on the assumption of Spitzer resistivity associated with the measured T_e profile. Since the q profile in such discharges is non-monotonic, double resonant perturbations may be ocalized at radii $r_{s1} < r_{s2}$ with low poloidal (m) and toroidal (n) mode numbers ($q(r_{s1}) = q(r_{s2}) = q_s = m/n$). Bursts of double resonance reconnections have indeed been observed systematically in FTU by the ECE polychromator, with sawtooth-like character and a remarkably constant relaxation period [6]. Up to 40 DTM sawteeth can be found in each burst; their period ranges from 3 to 12 ms. The temperature variation resembles that of the usual sawtooth activity, in the sense that it exhibits a sudden crash, a well defined inversion radius and diffusive behaviour outside a 'mixing radius', with the remarkable difference that it vanishes near the

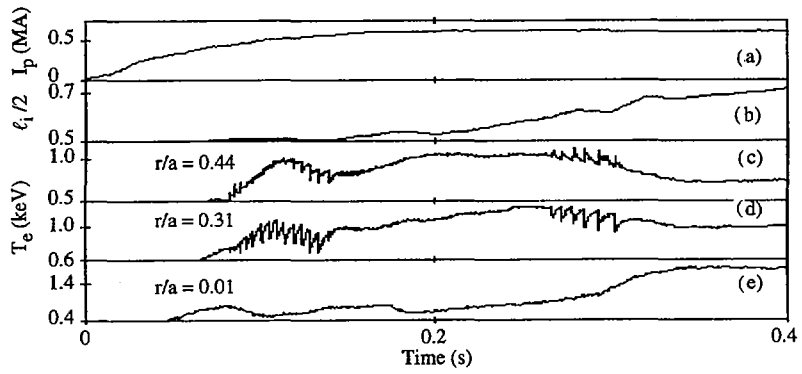

FIG. 1. FTU shot No. 5959 ($\bar{n}_e$ = 6.5 × 10^{19} m^{-3}, B_T = 6 T, Z_{eff} = 3.5) during DTM relaxations: (a) total plasma current, I_p; (b) internal self-inductance, $\ell_i/2$; (c), (d), (e) electron temperature, from ECE polychromator, at r/a = 0.44, 0.31 and 0.01.

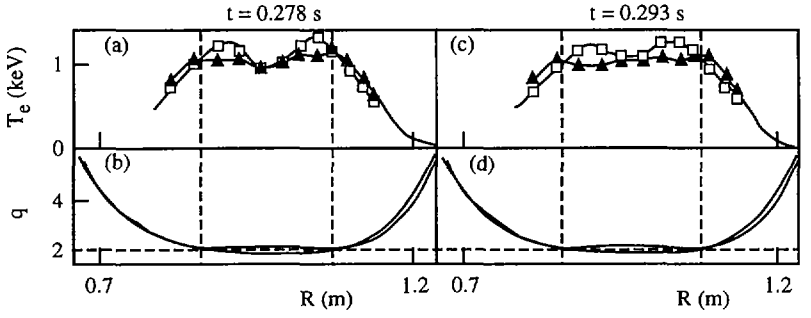

FIG. 2. FTU shot No. 5959 during DTM relaxations: (a) electron temperature profile, T_e, as measured by ECE, just before (squares) and after (triangles) a DTM relaxation at t = 0.278 s; (b) range of safety factor q profiles, as inferred from the equilibrium reconstruction code for times 0.26 < t < 0.30; (c) and (d) the same for the last relaxation of the cycle at t = 0.293 s.

plasma magnetic axis (Fig. 2). A single discharge may exhibit several cycles of these DTM sawteeth separated by quiescent phases. The possibility of instabilities leading to full reconnection in the presence of two resonances close enough to each other has been predicted both by the Kadomtsev heuristic arguments [7] and by numerical calculations [8]. During each cycle of DTM sawteeth, the T_e profiles become less and less hollow; accordingly, the radiation loss profile becomes less and less peaked, the period of the DTM sawteeth lengthens, and the reconnection encompasses increasingly larger radii until, during the last one or two crashes, it reaches the

magnetic axis. This evolution within a cycle can be explained by the evolution of the current profile: the T_e and j_ϕ profiles become less and less hollow, owing to the diffusion of the heat pulses towards the magnetic axis, which is rather slow and indicates a small central thermal diffusivity, $\chi_0 \leq 0.4$ m^2/s. Within the accuracy of the measurements, an incompressible reconnection conserving helical flux, particles and energy describes these MHD events very well. This statement of agreement with the kinematics of the Ladomtsev reconnection model only applies to the discontinuities in the profiles of n_e and T_e caused by the relaxations and is not a statement on the dynamics (time-scales, precursors and postcursors, resistive or ideal MHD processes) which play a role in the relaxation itself. As a matter of fact, in the last reconnections of each cycle, the presence of pre/inter/postcursor oscillations becomes more and more marked: this does not fit with the simple Kadomtsev model of two resonance full reconnection, where after the crash no resonant surface should be present in the plasma. At the end of each cycle of DTM reconnections the central q_0 value starts dropping, and the q profile becomes flat or slightly monotonic. The successive cycles of sawtooth-like DTM reconnections are characterized by decreasing values of q_s (there is full evidence of resonant $q_s = 4$, 3, 2 and 3/2, whereas larger values of q_s are not so clearly identified). After this transient phase the discharge usually evolves into a $q_s = 1$ sawtoothing plasma, but sometimes sawtooth free discharges with episodic $q_s = 3/2$, or, in a few cases, $q_s = 2$, crashes are observed. Similar reconnections with $q_s = 3/2$ or 2 are also induced by pellet injection [9].

3. ECRH IN FTU REVERSED MAGNETIC SHEAR DISCHARGES

The results of the first campaign of ECRH experiments [10], at 140 GHz, fundamental resonance, O mode outside launch [11, 12], have been analysed in detail. The ECRH pulse duration was limited to 15 ms by the available power supply, while the energy confinement of the ohmic plasma ranged from 28 to 50 ms. Owing to the strong localization of the wave damping, and in spite of the short pulse duration and of the relatively low power (35–60% of the ohmic input), large temperature increases (up to 2.5 keV at $n_{e0} \approx 10^{20}$ m^{-3}) and large temperature gradients (up to 40 keV/m) were obtained. In the case of central heating with 365 kW for 15 ms of shot No. 8282 (Fig. 3), which occurs in between the cycle of $q_s = 2$ sawteeth and the first episodic $q_s = 3/2$ DTM relaxation and in the presence of an $m = 2$, $n = 1$ island left over by the last DTM crash, an increase of T_{e0} from 1.0 to more than 3.5 keV has been obtained at $n_{e0} = 0.9$ s $\times 10^{20}$ m^{-3}. The diffusion of the T_e perturbation, inside the $q_s = 2$ central region ($r < r_{s2} = a/2$), can be fitted by a thermal diffusivity, $n_e(r)\chi(r) = \text{const}$, such that $\chi_0 \leq 0.4$ m^2/s. No significant deterioration of the thermal conductivity is observed inside the $q_s = 2$ surface, in spite of the large temperature variation.

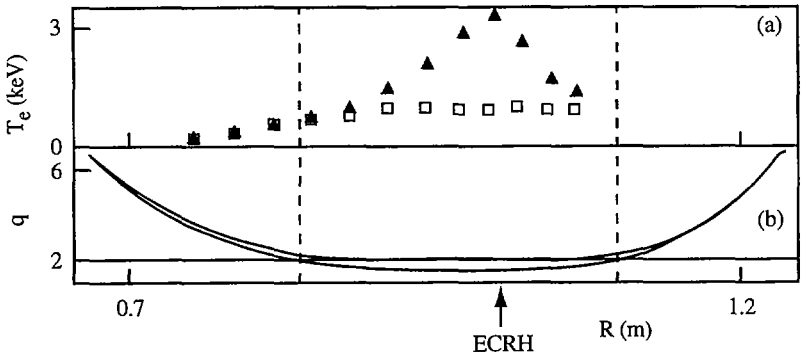

FIG. 3. FTU shot No. 8282 (central ECRH heating, I_p = 400 kA, $\bar{n}_e = 6 \times 10^{19}$ m^{-3}, B_T = 5 T, Z_{eff} = 2.0, tungsten poloidal limiter) in between cycles of q_s = 2 and q_s = 3/2 DTM relaxations: (a) electron temperature profile, T_e, before (squares) and 15 ms after ECRH (triangles); (b) range of q profiles, from the equilibrium reconstruction code.

The scenario of central ECRH of an ohmic shear reversed discharge, while quite useful for assessing the confinement properties in a transient experiment, is bound to produce a peaked current density profile within a short time. As a matter of fact, a small amplitude transient q_s = 1 sawtooth appears between 30 and 70 ms after the ECRH heat pulse during the temperature decay phase. Thus, the presence of a non-ohmic current drive system that can sustain the reversed shear configuration is mandatory. The FTU 8 GHz lower hybrid system is a convenient tool for sustaining such current density profiles, even near the critical densities for the ECRH waves.

4. LOWER HYBRID EXPERIMENTS IN FTU

During the FTU shutdown, an extensive characterization campaign of the 8 GHz LH system gyrotrons [13] was carried out, together with the installation of a second launcher to connect three more gyrotrons to the machine. As a result of these activities, four gyrotrons are now in operation on FTU (three with 1 MW and one with 0.5 MW); the last two gyrotrons of the second launcher will soon be in operation. These gyrotrons are oscillator tubes. The tests allowed an increase of the range of power output and a larger operational flexibility [14]. The LH experimental activity in this phase has mainly concerned the optimization of the coupling and the preliminary investigation of the experimental scenarios envisaged for FTU. Up to 1.4 MW of LH power have been coupled to the plasma with reflection coefficients lower than 10% and specific power at grill as high as 10 kW/cm^2. A figure of merit

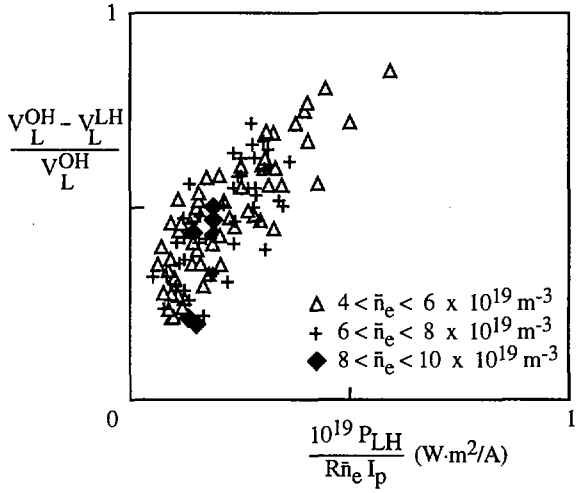

FIG. 4. Relative loop voltage drop $(V_L^{OH} - V_L^{LH})/V_L^{OH}$ versus LH power P_{LH}, normalized to the product $R\bar{n}_e I_p$ (I_p = 350-500 kA, B_T = 6 T, $N_\parallel$ = 1.55). The current drive efficiency can be estimated by the reciprocal of the intercept at unity loop voltage drop.

of the current drive (CD) efficiency is reported in Fig. 4, where the relative loop voltage drop is plotted versus the LH power P_{LH}, normalized to the product $R\bar{n}_e I_p$. All data in Fig. 4 were obtained with a parallel refractive index $N_\parallel$ = 1.55, but refer to different linear averaged plasma densities in the range $5 \times 10^{19} < \bar{n}_e < 10^{20}$ m^{-3} and to plasma currents in the range $350 < I_p < 500$ kA. At lower currents and densities, a reduction of the loop voltage of 85% has been obtained, while from the fit to these data a CD efficiency of 1.4×10^{19} $A \cdot W^{-1} \cdot m^{-2}$ can be extrapolated. No difference in the extrapolated CD efficiency characterizes the points at higher density, but at $\bar{n}_e = 10^{20}$ m^{-3} only ~30% of the injected power is accessible to the centre of the discharge. Moreover, at I_p = 350 kA the q_s = 1 sawtooth is stabilized when the loop voltage drops by 65% at $\bar{n}_e = 6 \times 10^{19}$ m^{-3} and P_{LH} = 700 kW. During this stabilization only an m = 1 activity is present, indicating that the q_s = 1 resonance is still within the plasma. The time evolution of a few plasma parameters in a discharge with $\bar{n}_e = 9 \times 10^{19}$ m^{-3}, I_p = 500 kA, B_T = 6 T is shown in Fig. 5, where 50% reduction in the loop voltage is obtained with 800 kW of LH power at $N_\parallel$ = 1.55. The central temperature increases by 500 eV with $n_{e0} = 1.2 \times 10^{20}$ m^{-3}, as measured by the 19 spatial point Thomson scattering system. The signature of electron interaction is evident from the large increase of the sawtooth period as seen from central chord soft X ray emission and from the high level of electron cyclotron and hard X ray emission. Furthermore, from the equilibrium reconstruction [5], no change in $\ell_i/2$ is recorded, and so the increase of

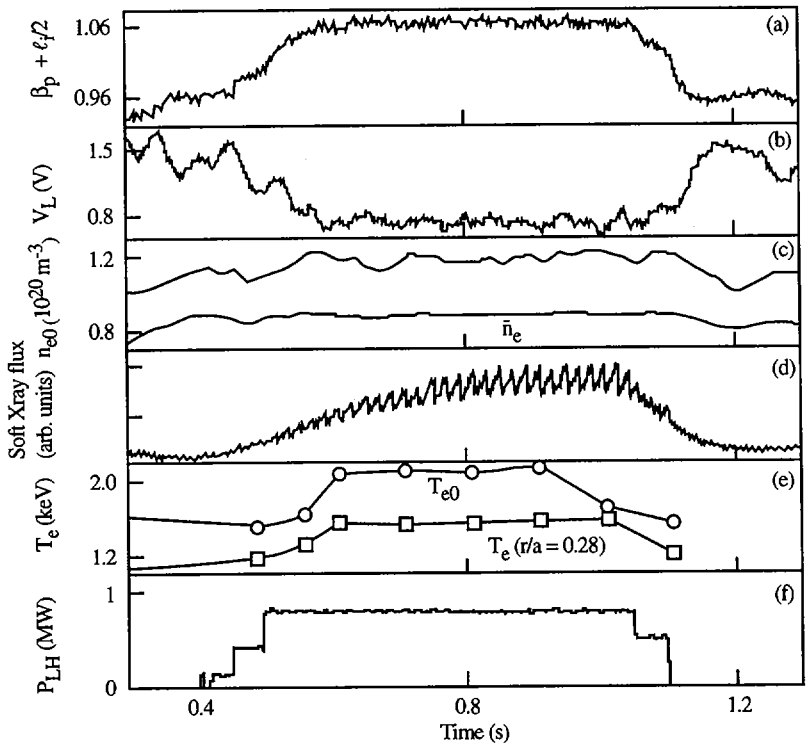

FIG. 5. FTU shot No. 10 624 (LHCD with $N_{\parallel} = 1.55$, $I_p = 500$ kA, $\bar{n}_e = 9 \times 10^{19}$ m^{-3}, $B_T = 6$ T, $Z_{eff} = 1.4$); (a) $\beta_p + \ell_i/2$, from magnetics; (b) loop voltage; (c) central n_{e0} and line averaged electron density, $\bar{n}_e$; (d) central soft X ray flux; (e) electron temperature, T_e, at r/a = 0 and r/a = 0.28, from Thomson scattering (at 1 s, the laser fired at the sawtooth crash); (f) coupled LH power P_{LH}.

$\beta_p^{EQ} + \ell_i/2$ has to be attributed both to the perpendicular (mostly thermal) beta poloidal $\beta_{p\perp}$ and to the parallel fast electron $\beta_{p\parallel}$, as $\beta_p^{EQ} = (\beta_{p\perp} + \beta_{p\parallel})/2$. The kinetic energy confinement time has been evaluated by using the electron density, from the DCN interferometer, the electron temperature, measured by the Thomson scattering system, and the ion temperature, obtained by solving the ion power balance equation with the Chang–Hinton neoclassical ion thermal conductivity. During the LH heating the total input power increases up to a factor of two, compared to the ohmic plasma target. In the LH phase the ohmic power fraction is reduced down to 20% in the low current, low density cases. The ratio between the experimental energy confinement time and the ITER89-P scaling [15] is shown in Fig. 6, as a function of $\bar{n}_e$, for LH heated discharges at three different values of the plasma current. At low plasma current the energy confinement time is up to 1.6 longer than the ITER89-P scaling.

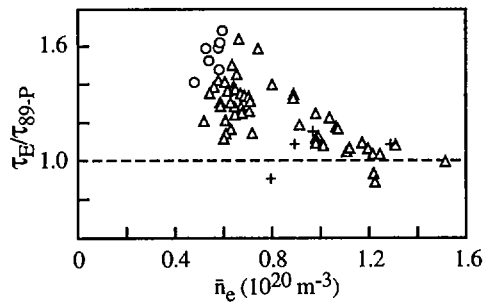

FIG. 6. Ratio between global energy confinement time, τ_E, and ITER89-P scaling, $\tau_{89\text{-}P}$, versus line averaged density, $\bar{n}_e$, at (o) 0.35 MA, (Δ) 0.5 MA and (+) 0.7 MA.

It has previously been reported [16] that FTU data in the saturated ohmic confinement regime are in agreement with ITER89-P scaling, while data in the linear regime do not agree with the L mode current and power dependences. It is remarkable that this behaviour is also retained for the additionally heated discharges, at least in the present range of applied power.

5. LOWER HYBRID REVERSED SHEAR DISCHARGES

The production of a shear reversed profile through LHCD has been addressed in the experimental scenario of forcing a $q_s = 1$ sawtoothing discharge to reach the shear reversal by LHCD in the external part of the plasma column, as suggested by numerical simulation of LH wave deposition. It has mainly been tried on sawtoothing discharges with $B_T = 4$ T, $I_p = 300$–350 kA, $\bar{n}_e = (6\text{–}8) \times 10^{19}$ m^{-3}, $N_\parallel = 1.55$ and $P_{LH} \approx 0.8$ MW. In this latter case, the time evolution is quite low, as it takes 0.3–0.4 s to suppress the sawtooth and to switch on a large MHD rearrangement of the discharge. This rearrangement quite often leads to strong MHD activity and soft disruptions looking very similar to the DTM activity observed in the ohmic regime, but accompanied by a strong Mirnov signal, which makes the coupling of the LH to the plasma very critical. However, the discharge can survive the MHD rearrangement (Fig. 7), maintaining good plasma–antenna coupling, and can achieve a stable relaxation regime, which is sustained until the LH power is switched off, without any soft or hard disruption. These relaxations bear a remarkable magnetic signature: they are detected as a slowly rotating (100–150 Hz) $m = 2$, $n = 1$ MHD mode with extremely large amplitude: $\tilde{B}_\theta/B_\theta = 2.5\%$. In this regime the equilibrium reconstruction shows a flat or hollow q profile, with the $q_s = 2$ resonance lying roughly at half plasma minor radius, $r_{s2} = a/2$. The corresponding normalized island width is estimated to be in the range of $w/a = 0.2$–0.3. These relaxations seem quite similar

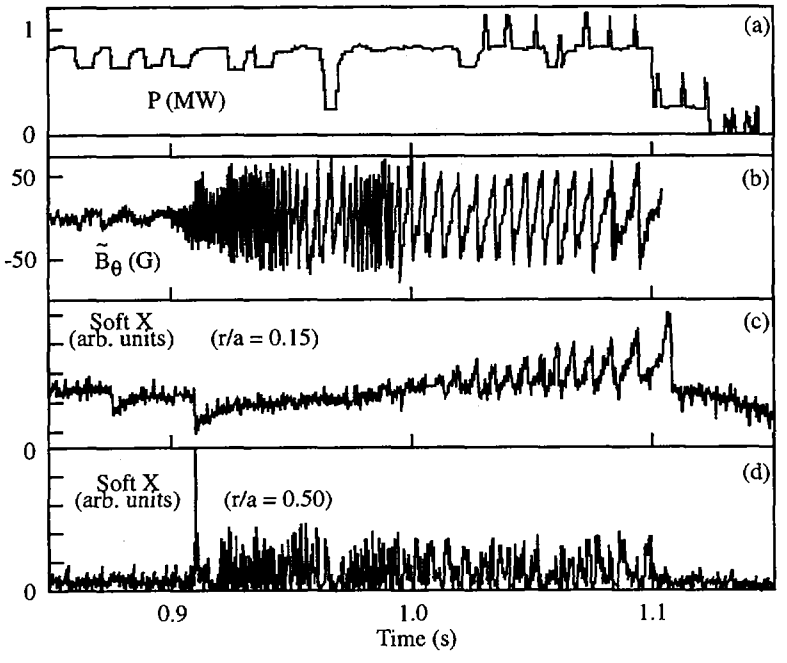

FIG. 7. FTU shot No. 10 888 (peripheral LHCD, I_p = 350 kA, $\bar{n}_e$ = 7 × 10^{19} m^{-3}, B_T = 4 T, Z_{eff} = 1.3). Wave forms of: (a) coupled LH power; (b) fluctuating field B_θ at the plasma edge, on the outboard of the torus; (c) soft X ray flux from the plasma centre and (d) from r = a/2.

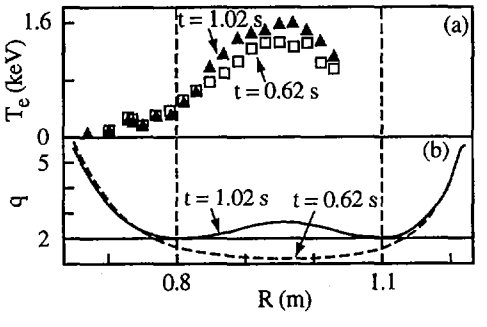

FIG. 8. FTU shot No. 10 888 (peripheral LHCD); (a) electron temperature profile (squares) at t = 0.62 s (P_{LH} = 0.8, P_{OH} = 0.4 MW, $\bar{n}_e$ = 7.2 × 10^{19} m^{-3}) and t = 10.2 s (triangles) in the shear reversal regime (same P_{LH} and P_{OH}, $\bar{n}_e$ = 6.6 × 10^{19} m^{-3}); (b) q profile at t = 0.62 and t = 1.02 s.

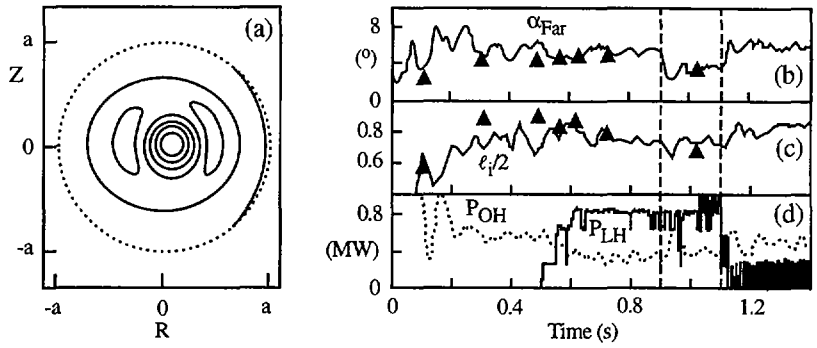

FIG. 9. FTU shot No. 10 888 (peripheral LHCD): (a) FTU soft X ray tomographic reconstruction during low/reversed shear driven by LHCD; (b) Faraday rotation angle through chord at r/a = 0.5, compared with prediction from equilibrium reconstruction (triangles); (c) internal plasma self-inductance from unconditioned equilibrium reconstruction and from Thomson scattering conditioned equilibrium reconstruction (triangles); (d) ohmic power and coupled LH power.

to those observed in Tore Supra [17] during LHCD at low plasma density. The electron temperature profile (measured from Thomson scattering roughly half-way in between two crashes) is quite peaked, even more peaked than before the reversed shear regime is achieved (Fig. 8). The relaxations that are observed in the soft X ray flux show, through tomographic reconstruction, the presence of a large m = 2 magnetic island (w/a = 0.2–0.3), sitting at half plasma minor radius (Fig. 9(a)), which is able to produce an elliptical helical plasma core. The first results of Faraday rotation polarimetry confirm that, within the reversal radius r_{s2} = a/2, the plasma current decreases at the MHD rearrangement and stays low during the reversed shear phase. A more reproducible access to this regime through more powerful LH power (up to 2.5 MW launched into the plasma in 1997), at higher plasma current and density, is one of the main tasks of FTU, which will also attempt to deposit localized ECRH power (up to 1.5 MW within 1997) or accessible LH power, either in the central elliptical helical core or in the large magnetic island of these shear reversed discharges driven by LH current drive.

REFERENCES

[1] MAUEL, M.E., et al., in Controlled Fusion and Plasma Physics (Proc. 22nd Eur. Conf. Bournemouth, 1995), Vol. 19C, Part IV, European Physical Society, Geneva (1995) 137.
[2] OZEKI, T., AZUMI, M., TOKUDA, S., Nucl. Fusion 33 (1993) 1025.
[3] ALLADIO, F., et al., Plasma Phys. Control. Fusion 36 (1994) B253.
[4] CIOTTI, M., FERRO, C., MADDALUNO, G., J. Nucl. Mater. 196–198 (1992) 725.

[5] ALLADIO, F., MICOZZI, P., Nucl. Fusion **35** (1995) 305.
[6] ALLADIO, F., BURATTI, P., MICOZZI, P., TUDISCO, O., in Controlled Fusion and Plasma Physics (Proc. 20th Eur. Conf. Lisbon, 1993), Vol. 17C, Part I, European Physical Society, Geneva (1993) 203.
[7] KADOMTSEV, B.B., in Plasma Physics and Controlled Nuclear Fusion Research 1976 (Proc. 6th Int. Conf. Berchtesgaden, 1976), Vol. 1, IAEA, Vienna (1977) 555.
[8] CARRERAS, B., HICKS, H.R., WADDELL, B.V., Nucl. Fusion **19** (1979) 583.
[9] ALLADIO, F., et al., Plasma Phys. Control. Fusion **35** (1993) B241.
[10] CIRANT, S., et al., in Plasma Physics and Controlled Nuclear Fusion Research 1994 (Proc. 15th Int. Conf. Seville, 1994), Vol. 2, IAEA, Vienna (1995) 159.
[11] BURATTI, P., et al., in Controlled Fusion and Plasma Physics (Proc. 22nd Eur. Conf. Bournemouth, 1995), Vol. 19C, Part III, European Physical Society, Geneva (1995) 21.
[12] CIRANT, S., in Controlled Fusion and Plasma Physics (Proc. 23rd Eur. Conf. Kiev, 1996), Vol. 20C, European Physical Society, Geneva (1996).
[13] DI GIOVENALE, S., et al., in Fusion Technology (Proc. 17th SOFT Symp. Rome, 1992), Vol. 1, North-Holland, Amsterdam (1992) 462.
[14] MIRIZZI, F., et al., in Strong Microwaves in Plasmas (Proc. 3rd Int. Workshop Moscow, 1996).
[15] YUSHMANOV, P.N., et al., Nucl. Fusion **30** (1990) 1999.
[16] BRACCO, G., BURATTI, P., TUDISCO, O., FTU TEAM, in Controlled Fusion and Plasma Physics (Proc. 21st Eur. Conf. Montpellier, 1994), Vol. 18B, Part I, European Physical Society, Geneva (1994) 1192.
[17] TURLUR, S., et al., in Controlled Fusion and Plasma Physics (Proc. 22nd Eur. Conf. Bournemouth, 1995), Vol. 19C, Part IV, European Physical Society, Geneva (1995) 73.

DISCUSSION

F. ENGELMANN: Has it been possible to identify the dependence of the lower hybrid current drive efficiency on the electron temperature in the experiments in which the plasma density was varied over a wide range?

F. ALLADIO: The available data are not yet sufficient to allow a precise statement on this subject. We hope that, by increasing the lower hybrid power to 2.5 MW and by adding ECRH, we can obtain data that will give some indication of this.

ICRF HEATING AND TAE MODES IN REACTOR RELEVANT JT-60U DISCHARGES

H. KIMURA, S. MORIYAMA, M. SAIGUSA, Y. KUSAMA,
T. OZEKI, G.J. KRAMER[1], T. FUJITA, T. OIKAWA, T. FUJII,
M. NEMOTO, K. HAMAMATSU, O. DaCOSTA[2], S. ISHIDA,
Y. KAMADA, T. KONDOH, A. MORIOKA, Y. NEYATANI,
K. KOBITA, V.I. AFANASSIEV[3], JT-60 TEAM
Naka Fusion Research Establishment,
Japan Atomic Energy Research Institute,
Naka-machi, Naka-gun, Ibaraki-ken,
Japan

G.Y. FU, C.Z. CHENG, R. NAZIKIAN
Plasma Physics Laboratory,
Princeton University,
Princeton, New Jersey,
United States of America

Abstract

ICRF HEATING AND TAE MODES IN REACTOR RELEVANT JT-60U DISCHARGES.

Second harmonic ICRF minority heating in deuterium negative shear discharges was found to efficiently heat bulk plasmas inside the transport barrier. The tail ion stored energy due to ICRF heating was comparable to that of a positive shear discharge. Toroidicity induced Alfvén eigenmodes (TAE) were stable when a strong internal transport barrier was formed in the negative shear discharges. TAE modes (90–110 kHz, n = 5–8) were observed only after the density profile had broadened, because of sequential partial collapses. The behaviour of TAE modes in negative shear plasmas was analysed with the NOVA-K code. It was found that the stability of TAE modes is sensitive to the gap alignment just inside q_{min} and the calculations agree qualitatively with the experimental results. An n = 0/m = 1 mode (~40 kHz), driven by ICRF heating, was observed over a much wider parameter range than TAE modes in negative shear discharges. High power ICRF heating of a 4 MA hot ion H mode discharge with a 15 cm gap between the antenna and the plasma was demonstrated. The antenna operating voltage and the power density satisfied the design base of the ITER antenna. Control of TAE modes through the toroidal rotation profile control was validated.

[1] STA fellow from FOM, Netherlands.
[2] STA fellow from Ecole polytechnique, France.
[3] A.F. Ioffe Physico-Technical Institute, St. Petersburg, Russian Federation.

1. INTRODUCTION

The objectives of ICRF heating experiments in JT-60U are: (1) demonstration of second harmonic heating in reactor relevant conditions and (2) contributions to fast ion studies. Both objectives are important issues in the development of an experimental fusion reactor such as ITER. Previously, efficient sawtooth stabilization at high electron density [1] and excellent coupling performance of the antennas with large antenna–plasma gaps [2] were demonstrated. The behaviour of high n (toroidal mode number) toroidicity induced Alfvén eigenmodes (TAE), which were driven by fast ions produced by high power ICRF heating, was investigated systematically in ITER relevant high I_P and low q_{eff} discharges [3–6]. Recently, second harmonic ICRF heating was first applied to negative shear plasmas [7].

This paper presents new experimental results on ICRF heating in the negative shear configuration as well as on the behaviour of TAE modes in negative shear plasmas. In addition, ICRF heating in high I_P hot ion H mode discharges with a 15 cm antenna–plasma gap and the control of TAE modes through toroidal rotation profile modification are presented.

The maximum coupled ICRF power to the plasma is 7 MW in an L mode discharge whereas the maximum generator output power is 8 MW. In this year, the operating frequency was changed from 116 to 102 MHz, which yields a proton second harmonic cyclotron resonance at 3.3 T.

2. HIGH POWER ICRF HEATING IN REACTOR RELEVANT CONDITIONS

2.1. ICRF heating in negative shear plasmas

The applicability of ICRF minority heating in negative shear (N/S) discharges is an important issue in the development of a steady state tokamak reactor, where the high bootstrap current fraction makes the current profile hollow with efficient α particle heating. Fast ions should be well confined inside the transport barrier to heat the bulk plasma efficiently with a relatively weak poloidal field. In 1995, second harmonic ICRF heating was successfully applied in the negative shear configuration using hydrogen and ^{4}He mixture plasma and hydrogen beams [7]. These plasmas had high concentrations of hydrogen. Recently, minority second harmonic heating has been applied in negative shear deuterium plasmas with deuterium beams. Hydrogen was contained only as a minority component. Then, the more severe conditions for ICRF heating in negative shear configurations were examined.

A target negative shear configuration was produced with current ramp-up (dI_P/dt = 0.6 MA/s) and early beam injection. A typical example is shown in Fig. 1. After the start of ICRF heating, the diamagnetic stored energy and the electron and ion temperatures in the core as well as the electron density increased remarkably although the ICRF heating power was relatively small (3 MW). They

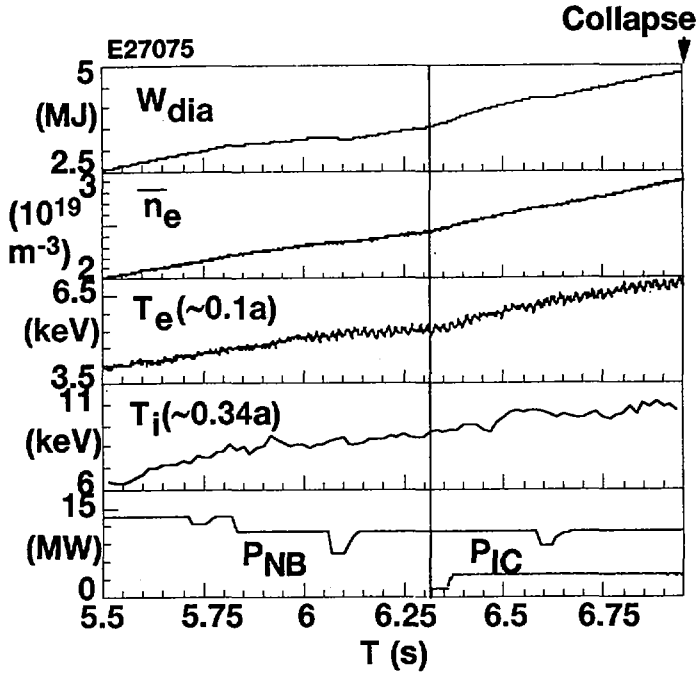

FIG. 1. Typical time evolution of a negative shear experiment with combined ICRF (3 MW) and NBI (8.9 MW) heating at I_P = 2 MA and B_T = 3.3 T. The plasma current reaches flat-top at 5.8 s. The NBI power was reduced from 10.8 MW for preheating to 8.9 MW for main heating at 5.8 s.

reached, respectively, 4.7 MJ, 7 keV, 10.5 keV and 4.5 × 10^{19} m^{-3} on-axis just before a collapse at 6.957 s. The H factor ($\tau_E/\tau_E^{ITER89\text{-}P}$) without correction of the ripple induced fast ion losses increased from 1.6 (just before ICRF injection) to 1.9 (just before the collapse).

The pressure profiles and the safety factor (q) profiles just before ICRF injection and just before the collapse are shown in Fig. 2. A steep gradient layer appeared in the pressure profile, indicating the formation of an internal transport barrier (ITB) associated with negative shear operation [7]. The normalized radius of the position of the steep gradient layer (r_{ITB}/a) was ~0.65, which almost coincides with the position of the minimum value of q (q_{min}). The value of r_{ITB}/a is much larger than that of the hydrogen discharge (r_{ITB}/a ~ 0.45), resulting in improved performance relative to hydrogen discharges. The pressure gradient at the transport barrier increased further during ICRF heating from 0.27 MJ/m^4 (just before ICRF injection) to 0.38 MJ/m^4, leading to a collapse (major disruption) at 6.957 s. A fast growing MHD mode (growth time < 10 μs, frequency ~20 kHz) was detected just

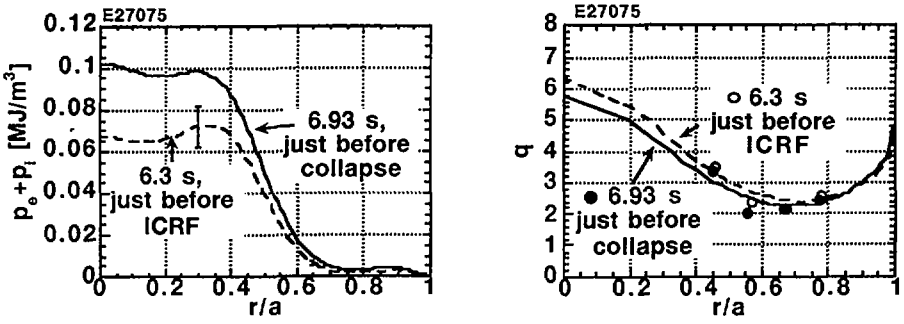

FIG. 2. Pressure profile from kinetic measurements (left) and q profile from motional Stark effect (MSE) spectroscopy measurements (right) at 6.3 s and 6.93 s of shot E27075 in Fig. 1.

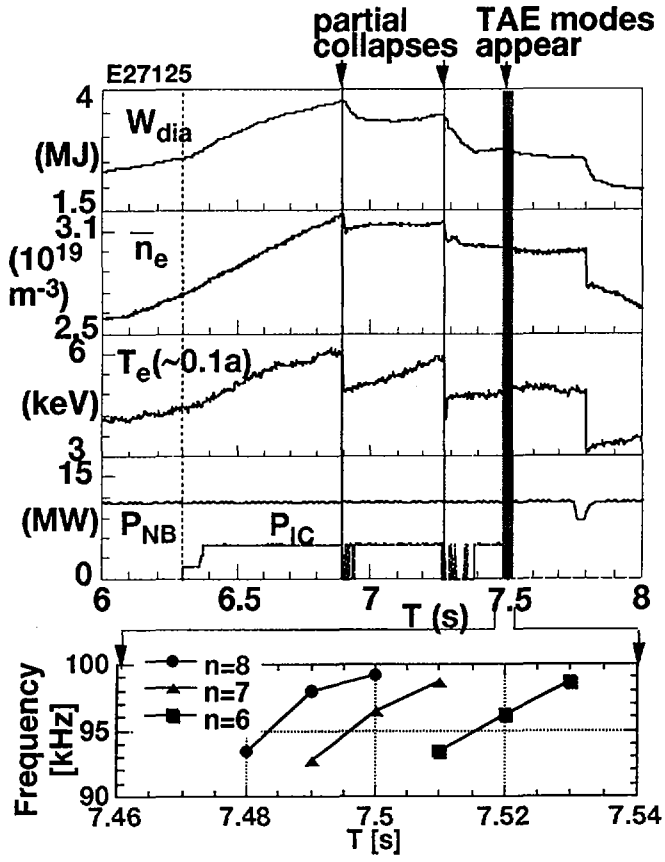

FIG. 3. Time evolution of negative shear experiment with combined ICRF (3.9 MW) and NBI (8.9 MW) heating at I_P = 2 MA and B_T = 3.3 T. TAE mode frequencies are also indicated by expanded horizontal axis.

before the collapse. The mode was localized at the internal transport barrier as found from ECE polychromator measurements. Its toroidal mode numbers consisted of both n = 1 and n = 2 components. The poloidal distribution of the mode has a strong in-out asymmetry as is peculiar to a pressure driven mode. Here, the target electron density, $\bar{n}_e^{target}$ (defined at 5.8 s), was 2.2 × 10^{19} m^{-3} in the shot of Fig. 1. If $\bar{n}_e^{target}$ is slightly higher, repetitive partial collapses (sawtooth-like behaviour) are observed with a pressure gradient less than 0.34 MJ/m^4. A typical example is shown in Fig. 3. A mode growing somewhat more slowly (growth time ~20 μs, frequency ~10 kHz) was observed just before each partial collapse with a toroidal mode number of n = 1. The radial location and the poloidal distribution of the mode were similar to those in the major collapse. The partial collapses occurred even with a pressure gradient as low as 0.22 MJ/m^4. In the course of repetitive partial collapses, the transport barrier was still maintained, but its radial size was shrinking with the partial collapses, resulting in degradation of energy confinement. Therefore, the plasma performance was limited by a major collapse or by partial collapses.

The tail ion stored energy due to ICRF heating (W_{tail}^{IC})was evaluated by using the diamagnetic stored energy and the kinetic plasma stored energy. Figure 4 shows W_{tail}^{IC} as a function of the ICRF heating power. Closed and open circles indicate data of negative shear discharges with deuterium and hydrogen, respectively. The open square indicates data of a positive shear (P/S) discharge with the same combined NBI heating power. Crosses are data of sawtooth stabilized ^{4}He discharges with ICRF heating alone, with a central electron density similar to that of negative shear discharges. We see that the W_{tail}^{IC} of the deuterium negative shear case is about the same

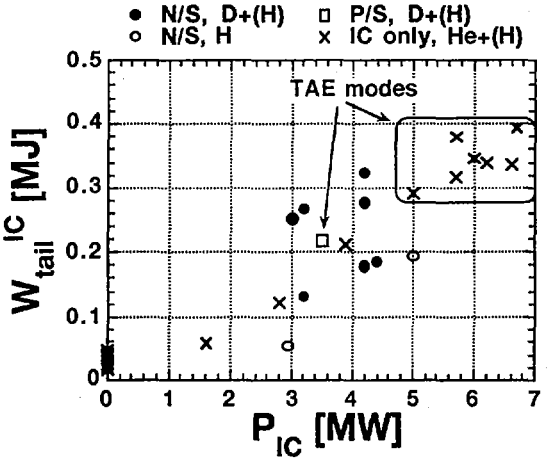

FIG. 4. Tail ion stored energy due to ICRF heating in various heating regimes as a function of ICRF heating power. I_P = 2 MA.

as that of the positive shear discharges, although the data scatter is significant because of differences in the quality of the negative shear discharges. The hydrogen tail ion temperature (T_{tail}) was measured by an MeV range neutral particle analyser [8, 9]. T_{tail} was in the range of 200 keV in the deuterium N/S discharge, which is similar to that of the ICRF-only case, but much higher than that of the hydrogen N/S case ($T_{tail} \sim 120$ keV). This may be due to the lower concentration of protons.

2.2. ICRF heating in high I_P hot ion H mode discharges

Antenna–plasma coupling is a critical issue to be solved in the application of ICRF heating to ITER. For ITER, the coupling to H mode plasma, with a distance between the separatrix and the antenna, δ_{SF}, of at least 15 cm, is demanded. In JT-60U, 5 MW of ICRF power was successfully coupled with a 4 MA hot ion H mode plasma with δ_{SF} of 15 cm in combination with 26 MW of NBI (Fig. 5). The ICRF heating used the second harmonic ion cyclotron resonance, which is the same as that considered for ITER. The sawtooth activity was successfully stabilized during the ELM free period, although the edge safety factor (q_{eff}) was as low as 2.8,

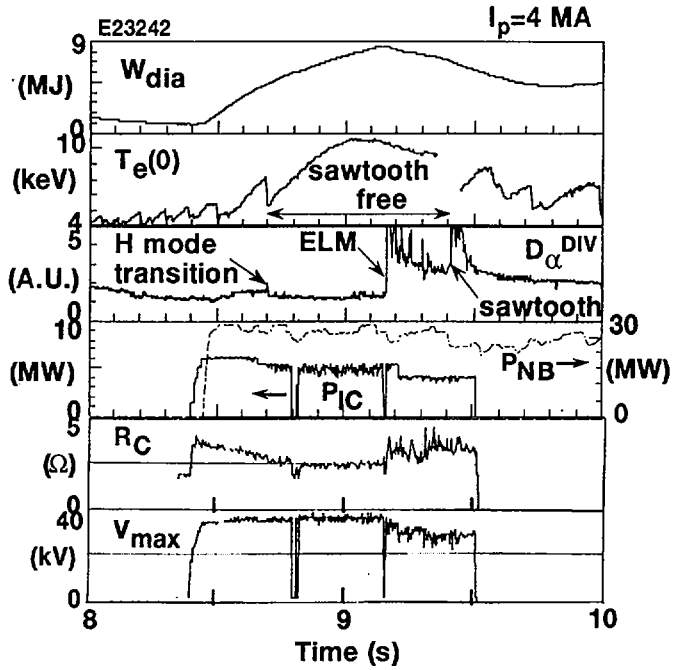

FIG. 5. Time evolution of 4 MA hot ion H mode discharge with combined ICRF and NBI heating. Antenna coupling resistance and antenna maximum voltage are also displayed.

leading to the achievement of the highest level of stored energy (~ 8 MJ (~ 1 MJ by ICRF)) among the H mode discharges in JT-60U. The maximum voltage generated in the antenna system and the injection power per unit area of antennas were, respectively, 38 kV and 4.0 MW/m^2, satisfying the design base of the ITER ICRF antenna.

3. TAE MODE STUDY WITH HIGH POWER ICRF HEATING

3.1. TAE modes in negative shear plasmas

As was described in Section 2.1, the values of W_{tail}^{IC} in the negative shear discharges are comparable to those of positive shear discharges. TAE modes were observed in the positive shear discharge as indicated in Fig. 4. In the negative shear discharge, however, TAE modes were not observed during the formation of a strong ITB, i.e. just before the major collapse or before the second partial collapse. Weak TAE modes (frequency range 90–110 kHz, toroidal mode number n = 5–8) were detected only after the second partial collapse occurred. A typical example is shown in Fig. 3. The mode frequency range is consistent with the theoretical TAE mode frequency, assuming q ~ 2, which is close to the value of q_{min}. The toroidal mode numbers are relatively high, in contrast to the n = 1, 2 modes in otherwise similar discharges with positive shear and q_0 = 1.6. This result may indicate that, in the negative shear case, only higher modes can be unstable, because of the limited gap alignment in the Alfvén continuum spectrum. The ratio of the TAE mode amplitude in the negative to that in the positive shear discharge was about one fourth. It should be noted that an n = 0/m = 1 mode, with a frequency of about 40 kHz, was observed in periods different from that of TAE modes (e.g. from 6.57 to 6.75 s in the shot in Fig. 3). The mode was also driven by ICRF heating. This mode has not yet been identified. Furthermore, after each partial collapse, an n = 1/m = 2 mode with a frequency of 5–7 kHz appeared. This mode persists for 0.2–0.5 s and disappears before the next partial collapse. This mode was observed during NBI heating, irrespective of ICRF injection. The poloidal mode structure has a rather strong in/out asymmetry (ratio of about 1/3).

In Fig. 6, experimental data are plotted in a plane defined by the pressure gradient ($dp/d\rho$, where ρ is an averaged radius) at ITB and the magnetic shear ($S = (\rho/q)(dq/d\rho)$) at $\rho = 0.5a_p$ (a_p is an averaged minor radius), which shows whether a TAE mode appeared or not. It appeared that, in the negative shear case, the TAE modes become unstable with slightly weaker negative shear and a much lower pressure gradient. In other words, the TAE modes are stable with strong ITB in negative shear discharges, even if W_{tail}^{IC} is large. Figure 6 also shows data points of the n = 0 mode, which appeared over a much wider range of $dp/d\rho$ than the TAE modes.

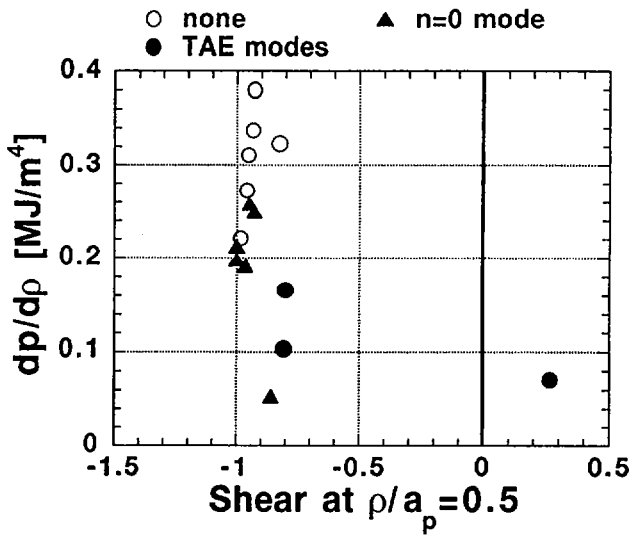

FIG. 6. Parameter domain where TAE modes and n = 0 mode appear. P_{IC} = 3–4.4 MW, P_{NB} = 8.9 MW, I_P = 2 MA and B_T = 3.3 T.

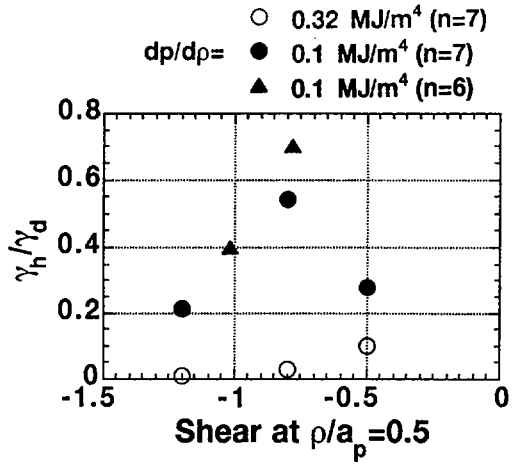

FIG. 7. Ratio of growth rate to damping rate of TAE modes, calculated by NOVA-K code, versus shear.

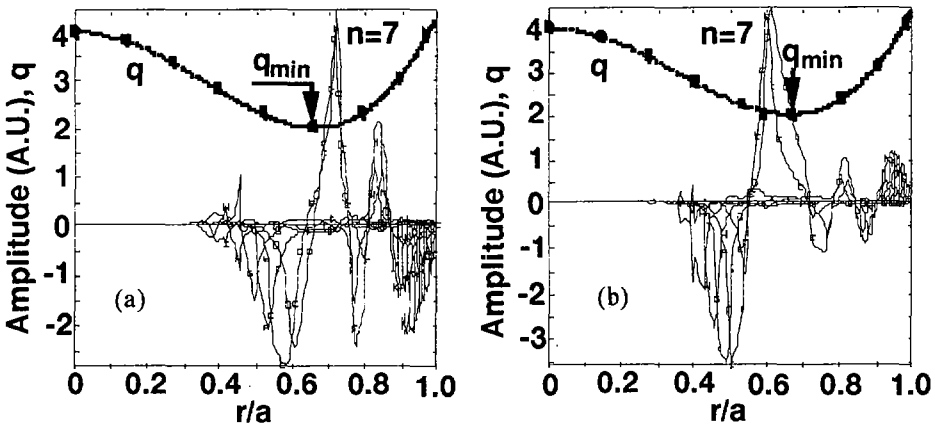

FIG. 8. Eigenfunctions of TAE modes and safety factor versus normalized radius for the (a) strong and (b) weak ITB cases. The q profile is the same in (a) and (b).

Stability analyses of TAE modes using the present experimental parameters were performed with the NOVA-K code [10]. Two representative temperature and density profiles, corresponding to strong ITB ($dp/d\rho$ = 0.32 MJ/m^4) and weak ITB ($dp/d\rho$ = 0.1 MJ/m^4), were employed for the calculation and q_0 was scanned while q_{min} = 2.01 was kept at $\rho = 0.7a_p$. The values of W^{IC}_{tail}, T_{tail} and a scale-length (L_h) of the fast ion pressure profile ($\beta_h \propto \exp(-(r/L_h)^2)$) were taken to be 0.15 MJ, 200 keV and 0.4 m, respectively. Figure 7 shows the ratio of the growth rate to the damping rate as a function of the shear at half-radius. Solid symbols indicate weak ITB, while open symbols refer to strong ITB. Circles and triangles indicate n = 7 and n = 6 modes, respectively. It is shown that TAE modes can be unstable with negative shear for the weak ITB case. Thus the calculation results agree qualitatively with the experimental results.

In the negative shear configuration, the Alfvén continuum gap is not aligned in the central region. Therefore, TAE modes do not exist near the central region, because of continuum damping. However, it was found that in the NOVA-K calculation that TAE modes of relatively high toroidal mode number (n = 5–7) can exist just inside the position (r_{min}) of q_{min} if the density gradient at the ITB is not too steep (i.e., for weak ITB). The reason is that the continuum gaps are better aligned inside r_{min}, if the density gradient is not too steep. Figure 8 compares TAE mode eigenfunctions in the strong and weak ITB cases. We see that for weak ITB the mode peaks inside r_{min}, while for strong ITB the mode peaks outside. If the mode peaks inside, the fast ion drive is large. On the other hand, if the mode is peaked outside, the fast ion drive is small and the radiative damping is large because of its narrow mode width. These are the reasons why the TAE modes become more unstable for weak ITB.

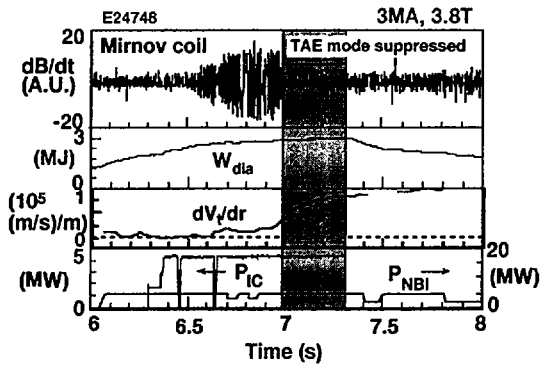

FIG. 9. Time evolution of TAE mode experiment, showing that the TAE mode amplitude decreases and disappears by increasing the toroidal rotation velocity shear. The fractions of the co-tangential NBI power to the counter-tangential NBI power, normalized by the total NBI power, were, respectively, 0.4/0.15 before 6.8 s and 0/0.55 after 6.8 s.

3.2. Control of TAE modes by toroidal rotation shear

Previously, the control of TAE modes by current profile control (mainly in the peripheral region) using lower hybrid current drive or a current ramp method had been investigated [5]. Recently, it was validated in JT-60U that TAE modes can be controlled through toroidal rotation velocity control. A typical example is shown in Fig. 9. ICRF power was injected to drive TAE modes, while the toroidal rotation velocity was scanned during ICRF heating by changing the tangential NBI units from co- to counter-direction. A TAE mode, which appeared during co-beam injection, disappeared after switching to counter-beam injection at 6.8 s. For counter-injection, a large rotation velocity gradient appeared, suppressing the TAE mode. Conversely, for co-injection, the gradient of the rotation velocity profile diminished, resulting in sustainment of the TAE mode. The new control method is based on momentum control so that the response time is much shorter than that of the current profile control.

4. CONCLUSIONS

Efficient bulk plasma heating was achieved by ICRF minority heating in negative shear plasmas. High power ICRF injection in the ELM free period with a 15 cm antenna–plasma gap was demonstrated. TAE modes are stable in negative shear plasmas with a strong transport barrier, because of the lack of gap alignment. Toroidal counter-rotation shear can suppress TAE modes.

ACKNOWLEDGEMENTS

The authors would like to express their appreciation to the members of JAERI who have contributed to the JT-60 project.

REFERENCES

[1] KIMURA, H., et al., Fusion Eng. Des. **26** (1995) 95.
[2] SAIGUSA, M., et al., Nucl. Fusion **34** (1994) 276.
[3] SAIGUSA, M., et al., Plasma Phys. Control. Fusion **37** (1995) 295.
[4] KIMURA, H., et al., Phys. Lett. A **199** (1995) 86.
[5] KIMURA, H., et al., J. Plasmas Fusion Res. **71** (1995) 1147.
[6] FU, G.Y., et al., Nucl. Fusion **36** (1996) 1759.
[7] KIMURA, H., et al., Phys. Plasmas **3** (1996) 1943.
[8] KUSAMA, Y., et al., Rev. Sci. Instrum. **66** (1995) 339.
[9] AFANASIEV, V.I., et al., in Controlled Fusion and Plasma Physics (Proc. 22nd Eur. Conf. Bournemouth, 1995), Vol. 19C, Part II, European Physical Society, Geneva (1995) 57.
[10] CHENG, C.Z., et al., Phys. Rep. **211** (1992) 1.

DISCUSSION

Y. ONO: Have you observed any expulsion of energetic particles during the TAE mode activity in your ICRF experiments?

H. KIMURA: In the case of negative shear discharges, we did not observe any appreciable effect on energetic particle loss because of weak TAE mode activities. In high I_p/low q discharges with normal shear, we observed a significant amount of fast ion losses due to TAE modes driven by ICRF heating.

HEATING AND CURRENT DRIVE

(Poster Session EP)

ICRF HEATING SCENARIOS IN ALCATOR C-MOD*

P.T. BONOLI, S.N. GOLOVATO[1], P. O'SHEA, M. PORKOLAB,
Y. TAKASE, R.L. BOIVIN, F. BOMBARDA[2], C. CHRISTENSEN,
C.L. FIORE, D.T. GARNIER, J.A. GOETZ, R.S. GRANETZ,
M.J. GREENWALD, S.F. HORNE, A.E. HUBBARD, I.H. HUTCHINSON,
J.H. IRBY, B. LaBOMBARD, B. LIPSCHULTZ, E.S. MARMAR,
M. MAY[3], A. MAZURENKO, G.M. McCRACKEN[4], J. REARDON,
J.E. RICE, C. ROST, J. SCHACHTER, J.A. SNIPES, P. STEK,
J.L. TERRY, R.L. WATTERSON[5], B. WELCH[6], S.M. WOLFE
Plasma Fusion Center,
Massachusetts Institute of Technology,
Cambridge, Massachusetts,
United States of America

Abstract

ICRF HEATING SCENARIOS IN ALCATOR C-MOD.

Successful high power ICRF heating of L-mode and H-mode plasmas has been performed in the Alcator C-Mod tokamak with up to 3.5 MW of RF power at 80 MHz. Efficient absorption (90–100%) of the RF power was observed for D(H) heating at 5.3 T (here the minority ion species is indicated in parentheses). Lower single-pass absorption experiments were also performed in D(^{3}He) at 7.9 T, D($2\Omega_{^3He}$) at 4.0 T, and D($2\Omega_H$) at 2.6 T. Boronization has been found to improve the heating efficiency of these lower single-pass absorption schemes through a reduction in the radiated power. Direct on-axis electron heating via mode converted ion Bernstein waves (IBWs) has been observed in H(^{3}He) plasmas at 6.5 T, and off-axis electron heating has been observed in D(^{3}He) at 7.9 T. The electron heating power density profiles were inferred in these experiments by using an RF power modulation technique. The implications of these heating results for steady state advanced tokamak operation in C-Mod are discussed.

* Work supported by the US Department of Energy Contract No. DE-AC02-78ET51013.

[1] Present address: Tokyo Electron America, Beverly, Massachusetts, USA.

[2] Associazione Euratom-ENEA sulla Fusione, Frascati, Italy.

[3] The Johns Hopkins University, Baltimore, Maryland, USA.

[4] Present address: JET Joint Undertaking, Abingdon, Oxfordshire, UK.

[5] Present address: CP Clare Corporation, Lexington, Maryland, USA.

[6] University of Maryland, College Park, Maryland, USA.

1. INTRODUCTION

Alcator C-Mod is a compact high field tokamak [1] (a = 0.21 m, R_0 = 0.67 m, $\kappa \lesssim 1.8$) with present operating range of $0.5 \lesssim I_p(MA) \lesssim 1.5$, $2.5 \lesssim B_T$ (T) $\lesssim 8.0$, and $0.5 \times 10^{20} \lesssim \bar{n}_e(m^{-3}) \lesssim 1 \times 10^{21}$. Up to 3.5 MW of RF power at 80 MHz has been coupled into the tokamak through two dipole antennas. Each antenna consists of two straps (0.1 m in width) driven out of phase and separated toroidally by 0.17 m (on-center) [2]. Extremely high power densities are obtained during ICRF injection (5 MW/m^3 volume averaged and 0.6 MW/m^2 surface averaged). The large range in magnetic field makes possible a variety of minority ion heating scenarios, including D(H) at 5.3 T, D(^{3}He) at 7.9 T, D($2\Omega_{^3He}$) at 4.0 T, and D($2\Omega_H$) at 2.6 T. The highest RF absorption rates were observed in the D(H) minority heating scheme as expected theoretically. The RF absorption rates were found to be lower in D(^{3}He) plasmas. This result is expected since the left circularly polarized component of the fast wave electric field is significantly reduced in D(^{3}He) minority heating relative to D(H). Even so, H-mode plasmas were achieved in all of the minority heating schemes.

Efficient on-axis electron heating via mode converted IBW has been observed in H(^{3}He) plasmas at 6.5 T and $n_{^3He}/n_e \simeq 0.2 - 0.3$. In this scenario, the ion-ion hybrid layer is located near the plasma center, the hydrogen cyclotron resonance layer is located on the low field side at about $r/a \simeq 0.75$, and the ^{3}He cyclotron layer is on the high field side at $r/a \simeq 0.56$. The location of the electron heating could be controlled by varying the magnetic field or changing the ^{3}He concentration. The location and shape of the electron heating profiles were found to be in agreement with the predictions of a 1-D full-wave ICRF model (FELICE) [3] which solves explicitly for the IBW electric fields. Off-axis ($r/a \simeq 0.6$) electron heating via mode converted IBW has also been demonstrated in D(^{3}He) discharges at 7.9 T and $n_{^3He}/n_e \simeq 0.2 - 0.3$. Again the experimentally inferred power deposition profiles agree with the predictions of 1-D full-wave ICRF calculations.

It is noteworthy that C-Mod can operate for pulse lengths of $t_{pulse} \simeq (5-7)$ s at intermediate fields of (4–5) T. For $T_e(0) \gtrsim 5$ keV the current skin time is $t_{skin} \simeq 1$ s , $\tau_{L/R} \simeq 3$ s, and hence $t_{pulse}/\tau_{L/R} \lesssim 2$. Furthermore, the direct electron heating via mode converted IBW could be used for off-axis current profile control by employing directional wave excitation. Thus C-Mod offers the unique opportunity to study both noninductive current drive and fully relaxed reversed shear current profiles in advanced tokamak configurations near the β-limit. The possibility of achieving such operating modes in C-Mod is discussed in the final section.

2. MINORITY ION HEATING RESULTS IN C-MOD

During the Dec. 1995 to March 1996 experimental campaign, high quality H-mode plasmas were obtained routinely after boronization of the tokamak [4]. The D(H) minority heating scheme was used at $B_T = 5.3$ T and $I_p \simeq 1.0$ MA. An RF power absorption rate of 90–100% was inferred for this type of heating based

on a break in slope analysis of the stored energy at the time of RF turn-off. A confinement time enhancement factor defined as $H_{ITER89-P} = \tau_E/\tau_{ITER89-P}$ of up to 2.5 was observed in ELM-free H-modes, where $\tau_{ITER89-P}$ is the empirical L-mode confinement time [5]. The corresponding normalized $\beta \equiv \beta_N$ was about 1.5, where $\beta_N = \beta_t/(I_p/aB_T)$ (%−m−T/MA), $\beta_t = < p > /(B_T^2/2\mu_0)$, and <> denotes a volume average. At $\overline{n}_e \simeq 3.0 \times 10^{20}$ m^{-3} and $P_{RF} = 2.4$ MW, the maximum electron and ion temperatures achieved were $T_e(0) \simeq 5.7$ keV (sawtooth peak) and $T_i(0) \simeq 3.9$ keV (sawtooth averaged). The relative concentration of hydrogen was estimated to be $n_H/n_e \lesssim 6 - 8\%$, from charge exchange analyzer measurements. The FPPRF Fokker Planck / ICRF package [6] has been used to determine the minority tail power balance. At these concentrations and electron density, $\frac{1}{2} - \frac{2}{3}$ of the power absorbed by the minority ions should dissipate collisionally via electron drag and the remainder of the tail power should be dissipated collisionally into background deuterons.

ELM-free H-mode plasmas have also been obtained in D(^{3}He) minority heating at 7.9 T. An example of this is shown in Fig. 1, where $P_{RF} = 2.4$ MW, $I_p = 1.2$ MA, and $\overline{n}_e \simeq 3.4 \times 10^{20}$ m^{-3}. After a period of dithering (from 0.73–0.86 s), a transition into ELM-free H-mode is observed, as is evident on the edge T_e and D_α signals. The stored energy increases from an ohmic value of 0.056 MJ to a near–maximum value of 0.200 MJ. Assuming 100% of the RF power is absorbed, the confinement time at this point is 0.061 s, which yields a confinement enhancement factor $H_{ITER89-p}$ of 1.5. Again, using a break in slope analysis of the stored energy at the RF turn-off point, an RF absorption rate of about 75% is inferred. Assuming this absorption rate for the RF, the confinement time is 0.073 s and $H_{ITER89-P} \simeq 1.7$. The maximum electron and ion temperatures were $T_e(0) \simeq 3.3$ keV and $T_d(0) \simeq 2.9$ keV. Thus H-modes have been achieved in C-Mod with $T_e \simeq T_i$. The relative concentration of ^{3}He in this discharge is estimated to be $\simeq 5$ %. At this density and concentration, FPPRF calculations indicate more than $\frac{2}{3}$ of the power absorbed by the ^{3}He ions is dissipated collisionally into background deuterons. The increased tail power flow to the deuterons relative to D(H) is largely a consequence of the double charge state of the (^{3}He) minority component.

Second harmonic minority heating experiments have also been performed at $\simeq 4$ T in D($2\Omega_{^3He}$). This heating scheme was unsuccessful [7] prior to boronization. The reason was thought to be the presence of an H fundamental resonance layer on the high field side edge of the tokamak at r/a $\simeq 0.75$, which resulted in parasitic absorption at that location. After boronization, the H resonance appears to result in edge heating which helps to attain H-mode. The best heating results were found at $B_T \simeq 4.2$ T where the H resonance had moved in on the high field side to r/a $\simeq 0.63$. The field was also reduced to 3.4 T to remove the fundamental H layer from the plasma. However, the overall heating was reduced and the impurity production increased, presumably because the $2\Omega_H$ resonance then appeared on the low field side edge of the tokamak at r/a $\simeq 0.91$. Typical discharge parameters for this heating scheme were $I_p \simeq 0.6$ MA, $\overline{n}_e \simeq 0.8–1.0 \times 10^{20}$ m^{-3} (before H-mode), $T_e(0)$, $T_d(0) \simeq 1.5$ keV

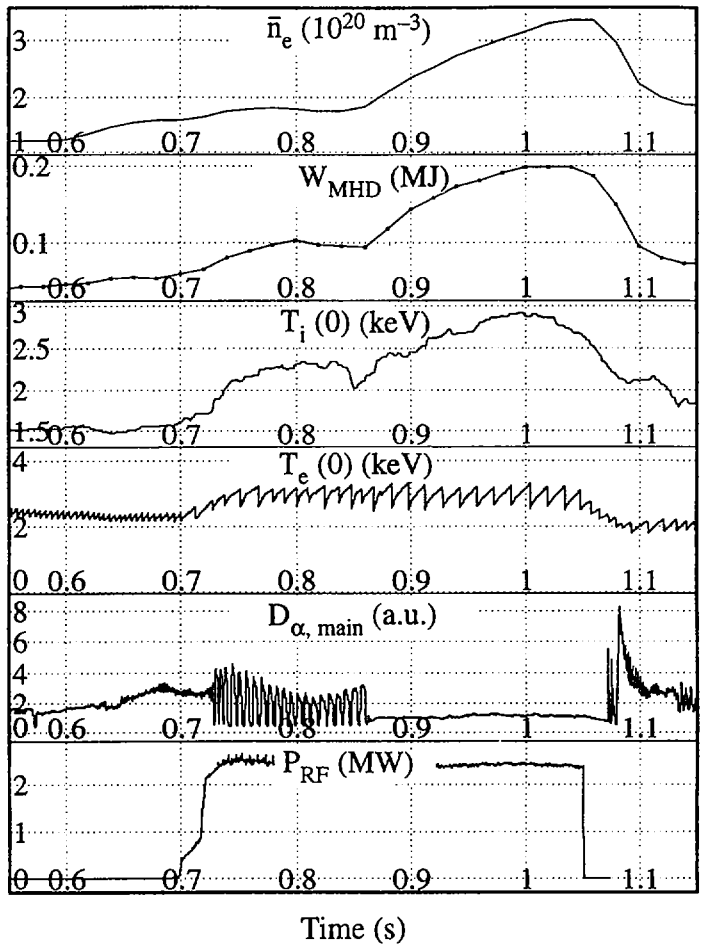

FIG. 1. D(^{3}He) ICRF heated H-mode (B_T = 7.9 T, I_p = 1.2 MA).

during ICRF injection, and $P_{RF} \simeq 2.2$ MW, with stored energy increases from 0.025 MJ to about 0.045 MJ. The confinement enhancement factors for these H-modes were $H_{ITER89-P} \simeq 1.0$, assuming an RF absorption rate of 100%. However, break in slope analysis of the diamagnetic stored energy indicates an RF absorption rate of only 30% in which case $H_{ITER89-P} \simeq 1.3$. The relative concentration of ^{3}He was typically low in these shots (2–3%). We expect better heating with $D(2\Omega_{^3He})$ at 80 MHz when combined with fundamental D(^{3}He) heating at 40 MHz.

Second harmonic heating at 2.6 T in $D(2\Omega_H)$ plasmas also resulted in achievement of H-mode. These experiments were performed at $I_p \simeq 0.55$ MA,

$\overline{n}_e \simeq (0.5-1.2) \times 10^{20}$ m^{-3}, and $P_{RF} \simeq 1.3-1.4$ MW. The stored energy typically doubled in these H-mode plasmas (increasing from about 0.02 MJ to 0.035-0.043 MJ), and the confinement enhancement factors were $H_{ITER89-P} \simeq 1.4$, assuming 100% of the ICRF power was absorbed. Again, taking into account the RF absorption rate estimated from diamagnetic stored energy rate change at the RF turn-off, an absorption rate of about 80% with $H_{ITER89-P} \simeq 1.6$ is inferred. Both ohmic and ICRF heated H-modes were obtained at low density, only ICRF heated H-modes were observed at intermediate density, and no H-modes were observed at high densities ($\overline{n}_e \gtrsim 1.1-1.2 \times 10^{20}\ m^{-3}$). The relative concentration of H injected into the plasma was varied from 0-100% and similar heating results were obtained at all concentrations. However, H_α/D_α measurements indicated the concentration of H only varied from $\simeq 5-40\%$.

3. MODE CONVERSION ELECTRON HEATING EXPERIMENTS IN C-MOD

Direct on-axis electron heating via mode converted ion Bernstein waves (IBW) has been observed [7] in H(^{3}He) plasmas at $B_T \simeq 6.0-6.5$ T, $\overline{n}_e \simeq 1.4 \times 10^{20}$ m^{-3}, $I_p = 0.8$ MA, $P_{RF} \simeq 1.2$ MW, and $n_{^3He}/n_e \simeq 0.2-0.3$. These experiments were carried out in 1995 prior to boronization and the plasmas remained in L-mode during ICRF injection. The central T_e was observed to increase from 2.1 keV to 4.7 keV (sawtooth peak) and the stored energy increased from 0.043 MJ to 0.050 MJ. In these experiments the ICRF power was modulated to obtain the electron RF power density from a break in slope analysis of the electron temperature versus time (as given by grating polychromator measurements). The result of such an analysis is shown in Fig. 2.

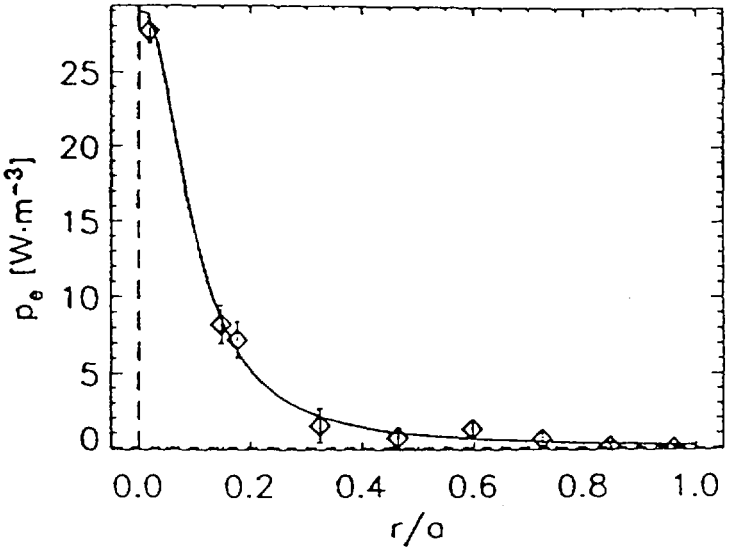

FIG. 2. On-axis H-^{3}He mode conversion heating at 6.5 T.

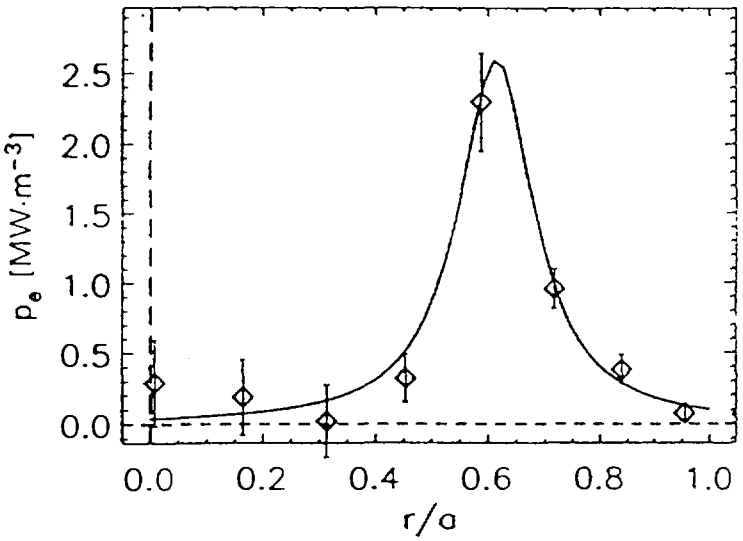

FIG. 3. Off-axis D–^{3}He mode conversion heating at 7.9 T.

The on-axis value of the RF power density ($\simeq$ 25 MW/m^3) is about a factor of 10 higher than the local ohmic power density. The RF power density profile in Fig. 2 corresponds to an electron absorption rate of about 66%. The location and shape of the electron heating power density profile in Fig. 2 is in qualitative agreement with the predictions of the 1-D slab geometry code FELICE. However, the electron power densities predicted by FELICE are about a factor of 2-3 less than what is observed experimentally, presumably due to the absence of wave focussing effects in the 1-D slab model.

Direct off-axis heating of electrons was also measured in D(^{3}He) L-mode plasmas after boronization, at B_T = 7.9 T, I_p = 1.0 MA, $\bar{n}_e \simeq 1.5 - 2.0 \times 10^{20}$ m^{-3}, and $n_{^3He}/n_e \gtrsim 0.15 - 0.20$. In this heating scheme the ^{3}He minority resonance is at the plasma center and the IBW mode conversion layer is located on the tokamak high field side at r/a $\gtrsim$ 0.5. In these experiments the RF power was stepped from about 1 to 2.5 MW and the electron heating rate at the RF power transition was inferred using a break in slope analysis of the electron temperature channels. An example of off-axis electron heating determined from this method is shown in Fig. 3. The absorbed RF power fraction to electrons in Fig. 3 is $\simeq 0.4 - 0.45$. The electron power density profile shown in Fig. 3 is also in qualitative agreement with 1-D full-wave results from FELICE.

4. DISCUSSION

Significant heating has been achieved during minority heating experiments in C-Mod and direct electron heating via mode converted ion Bernstein waves

has been clearly demonstrated. This plasma heating and direct electron interaction are two key elements necessary for the access of steady state advanced tokamak modes of operation in C-Mod. A current drive simulation code (ACCOME) and MHD equilibrium and stability package (JSOLVER/PEST II) have been used to study the stability properties of non-inductively driven, reversed shear type current profiles that may be achieved for C-Mod parameters [$I_p \simeq 0.8$ MA, $R_0/a = 3$, $T_e(0) \simeq T_D(0) \simeq 5$ keV, and $< n_e > \gtrsim 1.2\times10^{20}$ m^{-3}] [8]. It is found that highly shaped C-Mod equilibria ($\kappa_x \simeq 1.8$, $\delta_x \simeq 0.7$) are stable up to $\beta_N \simeq 3.7$, without a conducting shell, to the n = ∞ ideal ballooning mode and the n=1,2,3 external kink modes. These equilibria have relatively broad pressure profiles ($p_0/p_{avg} \simeq 3$), $q_{min} \gtrsim 2.2$, $q_0 \gtrsim 3$, and high bootstrap current fractions ($f_{BS} \simeq 0.75$). The off-axis current profile control used in these studies could be provided by mode converted ion Bernstein waves in D(^{3}He) plasmas at $B_T \simeq 4$ T, 40 MHz, and $n_{^3He}/n_e \simeq 0.2 - 0.3$.

REFERENCES

[1] HUTCHINSON, I.H., et al., Phys. Plasmas **1** (1994) 1511.

[2] TAKASE, Y., et al., in Fusion Engineering (Proc. 14th SOFE Symp. San Diego, 1992), IEEE, Piscataway (1992) 118.

[3] BRAMBILLA, M., Nucl. Fusion **28** (1988) 549.

[4] TAKASE, Y., et al., IAEA-CN-64/A5-4, these Proceedings, Vol. 1, p. 475.

[5] YUSHMANOV, P.G., et al., Nucl. Fusion **30** (1990) 1999.

[6] HAMMETT, G.W., Fast Ion Studies of Ion Cyclotron Heating in the PLT Tokamak, PhD Diss., University Microfilms Int. No. GAX86-12694. Princeton University (1986).

[7] TAKASE, Y., et al., in Controlled Fusion and Plasma Physics (Proc. 22nd Eur. Conf. Bournemouth, 1995), Vol. 19C, Part II, European Physical Society, Geneva (1995) 341.

[8] BONOLI, P.T., et al., Negative Central Shear Modes of Operation in the Alcator C-Mod Tokamak Near the β-Limit, Rep. PFC/JA-96-24, MIT Plasma Fusion Center (1996); to be published in Plasma Phys. Control. Fusion.

ICRF HEATING AND CURRENT DRIVE EXPERIMENTS ON TFTR

J.H. ROGERS, J.C. HOSEA, B. LeBLANC, R. MAJESKI,
C.K. PHILLIPS, G. SCHILLING, J.R. WILSON,
S.H. BATHA[1], M.G. BELL, D.S. DARROW, H.H. DUONG[2],
K.W. HILL, F.M. LEVINTON[1], S.S. MEDLEY,
M.P. PETROV[3], E.J. SYNAKOWSKI, G. TAYLOR,
M.C. ZARNSTORFF, S.J. ZWEBEN, TFTR GROUP
Plasma Physics Laboratory,
Princeton University,
Princeton, New Jersey,
United States of America

Abstract

ICRF HEATING AND CURRENT DRIVE EXPERIMENTS ON TFTR.

Recent experiments in the Ion Cyclotron Range of Frequencies (ICRF) at TFTR have focused on the RF physics relevant to advanced tokamak D-T reactors. Experiments performed either tested confinement in reactor relevant plasmas or tested specific ICRF heating scenarios under consideration for reactors. H-minority heating was used to supply identical heating sources for matched D-T and D only L-mode plasmas to determine the species scaling for energy confinement. Second harmonic tritium heating was performed with only thermal tritium ions in an L-mode target plasma, verifying a possible start-up scenario for the International Thermonuclear Experimental Reactor (ITER). Direct electron heating in Enhanced Reverse Shear (ERS) plasmas has been found to delay the back transition out of the ERS state. D-T mode conversion of the fast magnetosonic wave to an Ion Bernstein Wave (IBW) for off-axis heating and current drive has been successfully demonstrated for the first time. Parasitic Li^7 cyclotron damping limited the fraction of the power going to the electrons to less than 30%. Similar parasitic damping by Be^9 could be problematic in ITER. Doppler shifted fundamental resonance heating of beam ions and alpha particles has also been observed.

1. INTRODUCTION

ICRF has been used extensively on TFTR to explore a variety of important topics relevant to the D-T reactor regime. The focus of this paper is confinement, heating, current drive, and wave interactions with alpha particles for extrapolation to ITER. Second harmonic tritium heating of the low density start-up plasma in ITER is expected to bring the plasma to an H-mode transition. On TFTR, a favorable isotope scaling of the confinement time has been demonstrated going from D to D-T, and the second harmonic tritium heating scenario has been verified. Advanced tokamak scenarios with improved confinement and stability will require current profile control. Direct heating of

---

[1] Fusion Physics and Technology, Torrance, California, USA.

[2] General Atomics, San Diego, California, USA.

[3] A.F. Ioffe Physico-Technical Institute, St. Petersburg, Russian Federation.

electrons with RF power is therefore another important application of ICRF. On TFTR, efficient core heating of ERS plasmas has been demonstrated with direct electron heating from the fast wave which, in addition, was observed to sustain the ERS mode. Strongly localized electron heating and current drive have also been achieved in multi-ion species plasmas via mode conversion of the fast wave to an Ion Bernstein Wave (IBW). The efficiency of a tokamak reactor may be greatly enhanced if the IBW properties are properly controlled so that the wave interaction with the alpha particles channels energy from the alpha particles to the thermal ions [1]. During mode conversion experiments, coupling of the RF power to energetic beam ions and alpha particles has been observed.

2. SPECIES SCALING OF TRANSPORT IN L-MODE

H-minority heating in deuterium (D) plasmas and deuterium-tritium (D-T) plasmas has been used to provide a heating mechanism which is independent of the majority ion species, giving a good test of confinement time scaling with species. Such identical heating profiles for different species are not possible with neutral beam heating, because of the velocity dependence of the energy deposition profile. Similarly, it is not possible to utilize the same RF heating scheme in hydrogen and deuterium plasmas, making TFTR uniquely qualified for this experiment.

Density feedback gas puffing was used to maintain closely matched densities ($n_e(0) \sim 5.5$ - 6.0×10^{19} m^{-3}). The H-minority absorption profile was the same for all the plasmas, and the energy distribution in the hydrogen minority ion tail was measured to be the same for a given RF power in D and D-T plasmas. Figure 1 shows that the total stored energy increased when going from a deuterium plasma (8% H, 2-3% C, 1% T) to a plasma with 35-40% tritium and 40% deuterium (5% H, 2-3% C). The increase in stored energy is consistent with the energy confinement time improving proportional to the average atomic number of the ions to the power of 0.35-0.50 (Fig. 2). These measurements are

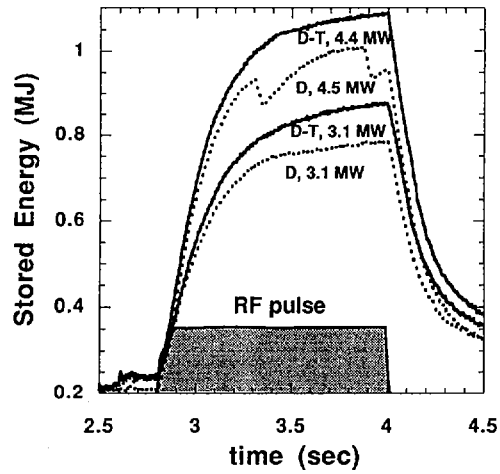

FIG. 1. Stored energy in D (dashed lines) and D–T (solid lines) plasmas with two levels of ICRF H-minority heating.

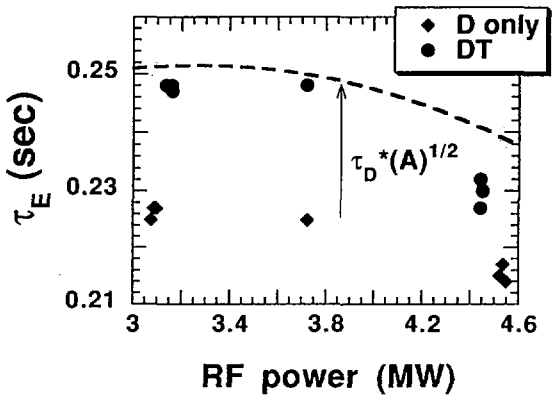

FIG. 2. Measured energy confinement time versus RF power for D only plasmas (diamonds) and D–T plasmas (circles). The dashed line is the D only value times the square root of the effective mass ratio.

consistent with other isotope experiments on TFTR [2,3], but they contradict gyro-Bohm diffusion scaling which predicts a decrease in the confinement time as the effective ion mass increases. The positive isotope effect observed in this experiment supports the enhancement of the performance of ITER in D-T.

3. ITER STARTUP SCENARIO: SECOND HARMONIC TRITIUM HEATING IN L-MODE

One possible ITER startup scenario would feature second harmonic tritium heating of the L-mode plasma to heat it to the H-mode transition threshold and on to ignition. Because of the low single pass absorption by low temperature tritium, this scenario might prove to be too inefficient. On TFTR, second

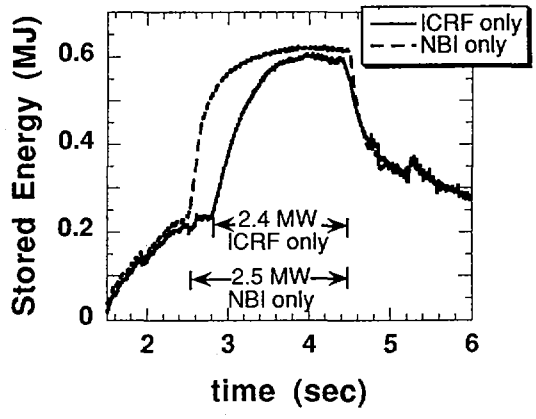

FIG. 3. Stored energy for 2.5 MW neutral beam injection and 2.4 MW of second harmonic tritium heating in 50/50 D/T L-mode plasma.

harmonic tritium heating of an L-mode plasma with only thermal low temperature tritium (no tritium neutral beams) has been demonstrated to be an effective means of heating the plasma. An energetic tritium tail distribution was formed quickly (T_{tail}~ 0.5 MeV in ~100 ms), thereby significantly enhancing the RF damping. The increase in total stored energy per MW was the same as that for neutral beams with identical target plasmas (Fig. 3). These experiments used 43 MHz RF to heat an approximately 50:50 mix of D:T with 1.8 MA plasma current, 4.7 T toroidal magnetic field and peak density of $5x10^{19}$ m^{-3}.

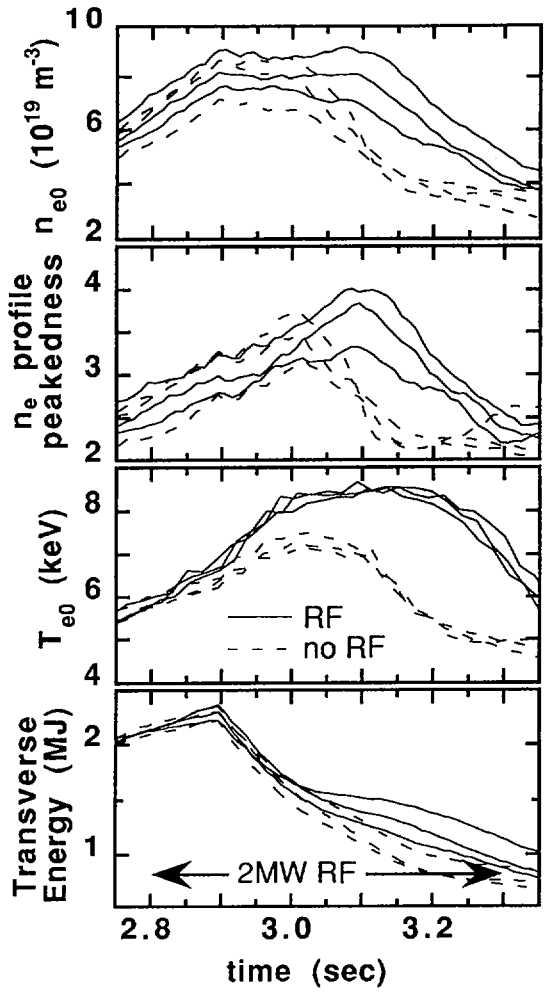

FIG. 4. ERS plasmas: three shots with no RF (two with three co-beam postlude, one with four co-beam postlude) and three RF heated shots (two with three co-beam postlude, one with four co-beam postlude).

4. DIRECT ELECTRON HEATING IN ERS PLASMAS

Much attention has been focused recently on the Enhanced Reverse Shear (ERS) mode in TFTR [4]. The distinguishing characteristic of this mode is that the particle and energy diffusivity are dramatically reduced in the core of the plasma. The resulting discharges have a very high central density (~ $1x10^{20}$ m^{-3}) but more modest ion and electron temperatures than the typical TFTR supershot. Direct fast wave electron heating with ICRF was used to provide additional heating of the ERS plasma in order to investigate the effect of the higher electron temperature on the evolution of the ERS mode. The RF electron heating is found to delay the transition out of the ERS state.

The target plasma is based on a reproducible ERS shot in which low power neutral beam heating (~ 7.5 MW) starts at 0.7 sec during the current ramp up. The plasma current reaches 1.6 MA by 2.0 sec, at which time (usually) a lithium pellet is injected. The ERS transition is triggered during a high power neutral beam heating phase which occurs from 2.5 to 2.9 seconds. The central density remains high during the low power "postlude" (2.9-3.5 sec, 7.5 - 10 MW neutral beam heating) until the plasma has a back-transition out of the ERS mode [5].

Direct electron heating was performed with 43 MHz RF and a toroidal magnetic field of 4.57 T at the machine major radius (2.62 m). The only ion heating competition for the fast wave was second harmonic tritium heating of the recycled tritium. From the D-T neutron rate, the tritium density could be estimated as ~ .3 % of the deuterium density and should not have absorbed much of the RF power.

When the RF power changes abruptly during square wave modulation, there is a discontinuity in the time derivative of the electron stored energy density which is equal to the local power density going to the electrons (assuming a time scale short compared to the transport times). The power deposition profile to the electrons can then be estimated by using the measured quantities n_e and T_e. Figure 4 shows profiles of RF power deposition, T_e, and n_e during the postlude with and without 2 MW of RF.

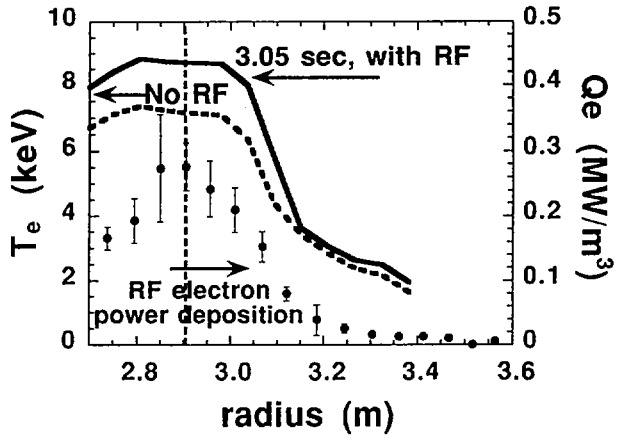

FIG. 5. Electron temperature profile at 3.05 sec in ERS plasma with RF (solid line) and without RF (dashed line). Symbols show RF electron heat deposition (right vertical axis).

With co-only injection of the neutral beams, the back transition occurs ~100 ms into the postlude without RF heating, and ~200 ms into the postlude with the addition of ~ 2 MW of electron heating (see Fig. 5). The addition of another co-directed neutral beam (2.5 MW) did not change the time of the back-transition (with or without the RF power). At the end of the high power phase, 2.9 sec, the density and ion temperature with and without RF are the same. The cause of the delay of the back transition is still under investigation but may be due to the additional electron pressure gradient or a slower q-profile evolution caused by the increase in electron temperature or an RF induced change in the toroidal plasma rotation.

5. MODE CONVERSION HEATING AND CURRENT DRIVE

Recent experiments on TFTR have measured current profile modifications resulting from mode conversion current drive (MCCD) with 43 MHz RF in D-He^4-He^3 plasmas [6]. When co- and counter-current drive antenna phasing (± 90°) are compared, the difference in loop voltage after ~1 s is consistent with the current drive expected from theory. The current density profile measured by the Motional Stark Effect (MSE) diagnostic for co- and counter-current drive phasing with the mode conversion surface at r/a = .17 is shown in Fig. 6. During off axis current drive, the inductive current opposing the driven current appears to be predominately on axis, which allows a change in the current profile in a time less than the usual current diffusion time, L/R. A dramatic example of the capability for localized off axis mode conversion power deposition is shown in Fig. 7, where a hollow electron temperature profile persists for approximately two energy confinement times (τ_E ~ 160 ms).

The frequency of a pair of transmitters driving two antennas was lowered to 30 MHz for TFTR operation in 1996 to allow mode conversion at the D-T ion-ion hybrid resonance at full toroidal field on TFTR. The fraction of RF heating power going to the electrons was found to be less than 30%. This low efficiency is believed to be due to competition with Li^7 minority heating. The mass to charge ratio for Li^7 is 2.33, placing the Li^7 cyclotron resonance between D and T, generally on the low field side of the D-T mode conversion layer in TFTR.

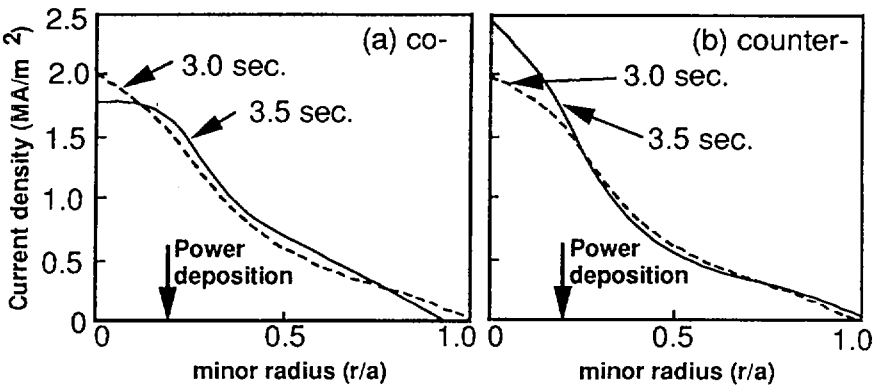

FIG. 6. Current density profile at the start of the RF pulse (3.0 sec) and 0.5 sec later for co-current antenna phasing (a), and counter-current antenna phasing (b) with mode conversion layer at r/a ~ 0.17.

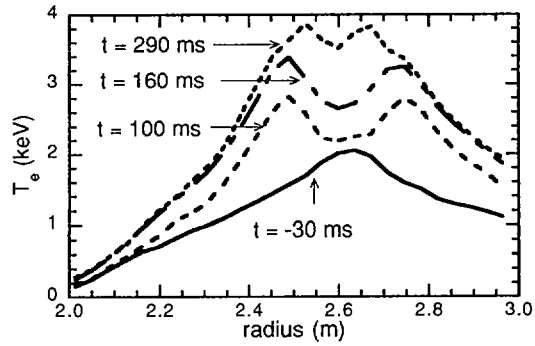

FIG. 7. Hollow T_e profile from off-axis mode conversion heating in a D-He^3 plasma. Times are relative to the start of the RF pulse.

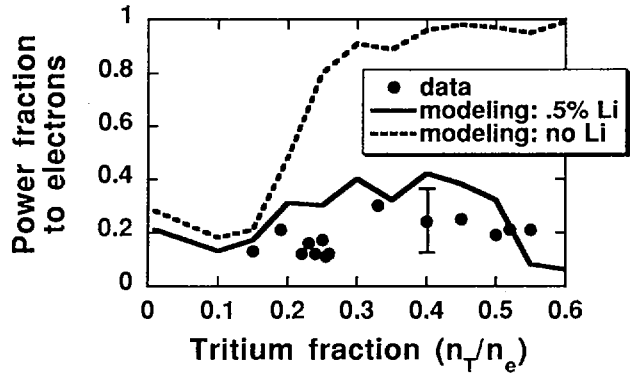

FIG. 8. Calculated power split of the RF power with 0.5% Li^7 (solid line) and no Li^7 (dashed line), and measured fraction of heating to electrons (circles).

Though fundamental resonance heating of the tritium beam ions is also expected, it has been minimized by arranging the tritium beam and directed ICRF to be counter propagating with respect to each other.

Because use of lithium pellets has become common on TFTR to reduce the recycling rate, lithium has now become an unavoidable impurity. Even after several hours of high power (> 10 MJ/shot, H-minority heated) helium conditioning discharges, the ratio of lithium ions to carbon ions is estimated spectroscopically to be approximately 0.1, corresponding to a lithium density of typically 0.5% of the electron density in the plasma core. This small amount of Li^7 can be an efficient absorber with sufficient tritium in the plasma such that the Li^7 ion becomes a "light" minority ion. Figure 8 shows the expected and measured fraction of RF power going to the electrons as a function of tritium fraction with 0.5% Li^7 and no Li^7. With low tritium fractions, most of the wave energy goes to the tritium ions; at high tritium fractions significant energy goes to the lithium ions, if Li^7 is present in sufficient quantity.

In 1997, Li^6 will be used for wall conditioning to avoid the complication of lithium absorption (Li^6 constitutes 7.5% of naturally occurring Li). Since the charge to mass ratio for Li^6 is 1/2 (as it is for D and C^{12}), it is equivalent to deuterium in the wave dispersion relation. For tokamaks in which beryllium (Be^9) is used for wall conditioning, as proposed for ITER, comparable minority Be^9 ion heating will arise in D-T plasmas because the charge to mass ratio is between that of tritium and deuterium. However, unlike lithium, there is no stable isotope of beryllium which has a charge to mass ratio of 1/2. Therefore, electron heating in the frequency range $\omega_{cT} < \omega < \omega_{cD}$ will not be consistent with using Be on plasma facing components in ITER unless the level of Be entering the plasma can be held to very low values.

6. FUNDAMENTAL CYCLOTRON RESONANCE HEATING

Ions with sufficient energy can be heated because of Doppler broadening. The resonance condition for fundamental cyclotron resonance heating is $\omega = \vec{k} \cdot \vec{v} + \omega_{ci}$. In general, during 30 MHz operation in TFTR, both the deuterium and tritium resonances are in the plasma. The fast wave field is predominately right circularly polarized near the deuterium resonance because of the high fraction of deuterium in the plasma. However, energetic particles such as deuterium or tritium beam ions or alpha particles can have large enough values of $\vec{k} \cdot \vec{v}$ to be resonant far from the cyclotron layers. In reactor plasmas where there is a significant fraction of alpha particles and ion temperatures are high, fundamental resonance absorption can become important.

Alpha particle heating due to fundamental ICRF auxiliary heating has been observed with the pellet charge exchange (PCX) diagnostic [7] during D-T mode conversion experiments. It has not been determined whether the fast wave or the mode converted IBW wave is responsible for the wave-alpha interaction.

Deuterium and tritium neutral beam ion wave absorption has also been detected. Heating of deuterium beam ions was measured with the lost fast ion probe [8] during D-He^3 mode conversion heating experiments. Only a small fraction of the RF power was absorbed by the energetic ions in this case (T_e measurements indicate ~ 80% of the power going to the electrons). Because the lost fast ion probe signal is sensitive to the location of the mode conversion layer, it is most likely that the mode converted IBW is heating the deuterium beam ions (because the IBW is very spatially localized, whereas the fast wave is not).

7. SUMMARY

ICRF experiments on TFTR have verified a number of reactor relevant physics issues and auxiliary heating scenarios. In L-mode plasmas with $T_i \sim T_e$, a favorable isotope scaling was demonstrated going from D plasmas to D-T plasmas. Second harmonic tritium heating was verified as an efficient means of heating the ITER start-up plasma. Electron heating in ERS plasmas was found to sustain the ERS mode. Current profile control has been demonstrated using strongly localized electron heating with MCCD. D-T mode conversion heating and heating of fusion alpha particles has been performed for the first time.

8. FUTURE PLANS

For the 1997 operation of TFTR, three two strap fast wave ICRF antennas will be replaced with new antennas. A four strap direct launch IBW antenna will be used to explore development of a transport barrier and access to high confinement modes using the poloidal sheared flow generated by the IBW (4 MW source power) [9]. Two four strap fast wave antennas in adjacent bays will

be used to test D-T mode conversion current drive at higher RF driven current to levels that may assist ERS optimization and wave coupling to the alpha particles (8 MW source power, 30 MHz).

ACKNOWLEDGMENTS

The authors express their appreciation to the technical, engineering, and scientific staff of TFTR, and to R. J. Hawryluk for his support. This work is supported by US Department of Energy contract No. DE-AC02-76CH03073.

REFERENCES

[1] FISCH, N.J., et al., these Proceedings, Vol. 1, p. 271.
[2] SCOTT, S.D., et al., Phys. Plasmas **2** (1995) 2299.
[3] SCOTT, S.D., et al., these Proceedings, Vol. 1, p. 573.
[4] LEVINTON, F.M., et al., Phys. Rev. Lett. **75** (1995) 4417.
[5] LEVINTON, F.M., et al., these Proceedings, Vol. 1, p. 211.
[6] MAJESKI, R., et al., Phys. Rev. Lett. **76** (1996) 764.
[7] MEDLEY, S.S., et al., Rev. Sci. Instrum. **67** (1996) 1.
[8] ZWEBEN, S.J., et al., Nucl. Fusion **30** (1990) 1551.
[9] ONO, M., et al., in Plasma Physics and Controlled Nuclear Fusion Research 1994 (Proc. 15th Int. Conf. Seville, 1994), Vol. 1, IAEA, Vienna (1995) 469.

DISCUSSION

J. JACQUINOT: Have you observed TAEs generated by ICRH driven fast ions in the DT experiments at $2\omega_{cT}$?

J.H. ROGERS: No. The coupling of energy from the energetic tritium tail to the bulk plasma is sufficiently strong for the energy in the tail to be too low to drive the TAE unstable (at the power levels used).

K. IDA: ERS discharges are sustained longer with ICRF heating, because of deceleration of plasma co-rotation. What is the mechanism for slowing down the co-rotation by ICRF heating in the ERS discharge?

J.H. ROGERS: The mechanism is still not understood and warrants further investigation.

R. PRATER: On TFTR you have co- and counter- neutral beam injection, and several heating methods in the ICRF (mode conversion, fast wave electron heating, minority heating). What is the effect of the ICRF power on beam induced rotation for these different modes?

J.H. ROGERS: We have only observed evidence of the RF slowing down the plasma rotation. We have noticed the effect most frequently in the past during H minority heating. Unfortunately, we have never performed a systematic study to identify the important physics.

K. LACKNER: You reported on scenarios on C-Mod with 40–50% power absorption. Do you have an idea where the rest of the power has gone and whether any deleterious effects have been observed?

J.H. ROGERS: We measured 40–50% of the injected RF power going into direct on-axis electron heating via mode converted ion Bernstein waves in H(^{3}He) plasmas. The remaining power may be dissipated at the fundamental (H) cyclotron resonance on the low field side of C-Mod at r/a $\approx$ 0.7. However, no deleterious effects on the plasma were found to accompany this off-axis absorption.

EXPERIMENTAL OBSERVATION OF RF DRIVEN PLASMA FLOW IN THE PHAEDRUS-T TOKAMAK

S. WUKITCH[1], N. HERSHKOWITZ, C. LITWIN,
M. HARPER, R. PARKER
Department of Nuclear Engineering
and Engineering Physics,
University of Wisconsin,
Madison, Wisconsin,
United States of America

Abstract

EXPERIMENTAL OBSERVATION OF RF DRIVEN PLASMA FLOW IN THE PHAEDRUS-T TOKAMAK.

The authors have observed frequency shifts of the 2/1 resistive tearing mode in the Phaedrus-T tokamak that are consistent with injecting momentum with low frequency (below the majority ion cyclotron frequency) rf waves. The 2/1 frequency can be increased or decreased by varying the directionality of the rf wave and frequency shift, $\Delta f_{2/1}$, scaled with rf power. The $\Delta f_{2/1}$ is interpreted to result from a change in the toroidal plasma velocity. The change in toroidal plasma velocity calculated from the observed $\Delta f_{2/1}$ and the rf momentum frictionally coupled to ions by the driven rf current are comparable. In addition, the $\Delta f_{2/1}$ increased with increasing toroidal magnetic field, B_ϕ, and this scaling was independent of the rf wave directionality. The location of the rf power absorption also scales with the B_ϕ field, suggesting that $\Delta f_{2/1}$ is affected by the position of the rf absorption. This experiment is the first demonstration of rf modification of the 2/1 frequency through rf momentum input and is a new application for rf in plasmas.

Introduction

Tailoring the flow velocity profile in tokamak plasmas is suggested by both theory and experiment to significantly modify the stability and transport characteristics. Improved plasma transport and stability characteristics, when achieved simultaneously, result in significant improvement of the tokamak concept.[1] Increased plasma stability to tearing modes associated with plasma rotation has long been recognized.[2] However, recent theoretical work and experiments suggest external kink modes can be stabilized with plasma rotation velocities a fraction of the Alfven speed.[3,4] In addition, the impact of sheared plasma rotation on plasma stability has been suggested.[5,6] Sheared plasma rotation is predicted to result in linear coupling of ballooning modes which increases damping. This may enable these plasmas to reach the second stability regime. In addition, models describing the experimentally observed enhanced confinement modes have identified the importance of plasma rotation and sheared rotation in the formation of transport barriers.[7]

---

[1] Current affiliation: Max-Planck-Institut für Plasmaphysik, D-85748 Garching, Germany.

External control of the momentum input has been demonstrated with neutral beam injection. While the net momentum transfer is efficient, the deposition profile is broad. Furthermore, several experiments have reported modifications of the plasma toroidal rotation velocity with the application of ion cyclotron heating.[8-10] The rotation is generated by the spatial diffusion of resonant ions which leads to a modification of the radial electric field (E_r).[11]

In contrast, we present here experimental evidence of plasma rotation, as measured by the frequency of the 2/1 tearing mode, due to rf wave momentum. The data indicate that the plasma rotation speed can be increased or decreased by varying the directionality of the rf wave. The increase in rotation speed for current drive antenna phasing was linear with rf power and driven current. The change in toroidal plasma velocity calculated from the observed frequency shifts and the calculated rf momentum are comparable. In addition the shift in the 2/1 frequency increased with increasing B_ζ independent of the rf wave directionality.

Experimental parameters

The experiments were carried out on the Phaedrus-T tokamak which is an ISX-B class tokamak (major radius, R, = 0.93 m, minor radius, a, = 0.255 m, toroidal field,B_ζ, = 0.6-0.9 T, peak electron density, n_{e0},=0.2-3.0 x 10^{19} m^{-3}, and plasma current, I_p, <100 kA). No neutral beam injection was present and the rf is characterized by a vacuum $N_{||}$ = 80. RF waves below the majority ion cyclotron frequency were excited by a two-strap, fast-wave antenna (toroidal separation 0.155 m, strap width 0.05 m, and poloidal extent 60°) located on the low field side of the tokamak. The antenna excites a carrier mode which mode converts at the Alfvén resonance to a heavily damped electrostatic mode, the kinetic Alfvén wave (KAW), that is absorbed at approximately the Alfvén resonance.[12] Previous experiments have shown that the Alfvén resonance position can be controlled by varying the B_ζ field for a given antenna phase and plasma density. For relative antenna strap phasing, ϕ_{ant},= $\pi/2$ and plasma density of 7x10^{18} m^{-3}, analysis of the loop voltage indicates that the Alfven resonance moves from r ≈ 0.10 m at B_ζ ≈ 0.75 T to r ≈ 0.18 m at B_ζ ≈ 0.65 T. Furthermore, the observed loop voltage temporal behavior indicates that the rf current source is localized.[13] This implies that momentum can be injected local to the Alfven resonance allowing for tailoring of the toroidal plasma flow profile.

The plasma parameters are: n_{e0} = 7.0 x 10^{18} m^{-3}, central electron temperature, T_{e0}, = 500 eV, and effective plasma charge, Z_{eff}, = 1.7-2.0 with carbon as the dominant impurity and the working gas is hydrogen. The ratio of the electron-ion collision frequency to the trapped electron bounce frequency is less than one, ≤ 0.1 for r = 0.05 - 0.2 m, where the electron-ion collision frequency, υ_{ei}, is approximately 6 x 10^4 s^{-1}. The rf power coupled to the plasma is approximately 300 kW with ϕ_{ant} = $\pm\pi/2$ and π, where ϕ_{ant} is the phase

between the currents in the two antenna straps. For reference, π phase heats the plasma,[14] $\pi/2$ phase drives current parallel to the ohmic current,[15] and $-\pi/2$ should drive current opposite to the ohmic current. The ratio of the rf frequency to the hydrogen cyclotron frequency is approximately 0.7. In addition, the hydrogen cyclotron resonance is outside the plasma and the carbon cyclotron resonance (and species with similar charge to mass ratios) is on the high field side plasma edge. This suggests coupling to ions directly through cyclotron damping is negligible.

The plasma rotation frequency was monitored by measuring the frequency of the 2/1 resistive mode which is located at $r \approx 0.18$ m. The mode was identified using an array of poloidal and toroidal magnetic fluctuation pickup coils and the 2/1 mode was observed to be rotating in the electron drift direction. The wave momentum is injected in the same (opposite) direction as the ohmic plasma rotation for $\phi_{ant} = \pi/2$ $(-\pi/2)$, and no net momentum is injected for $\phi_{ant} = \pi$. Since the antenna is poloidally symmetric, no poloidal momentum should be injected.

Experimental Results

The 2/1 frequency shift ($\Delta f_{2/1}$) with the application of rf for $\phi_{ant} = \pm\pi/2$, π and $B_\zeta = 0.6 - 0.8$ T is shown in Fig 1. The most prominent feature of the data is the $\Delta f_{2/1}$ dependence on ϕ_{ant}. This agrees with the expectation that the $\Delta f_{2/1} > 0$ with the application of $\phi_{ant} = \pi/2$ and $\Delta f_{2/1} < 0$ for $\phi_{ant} = -\pi/2$. However,

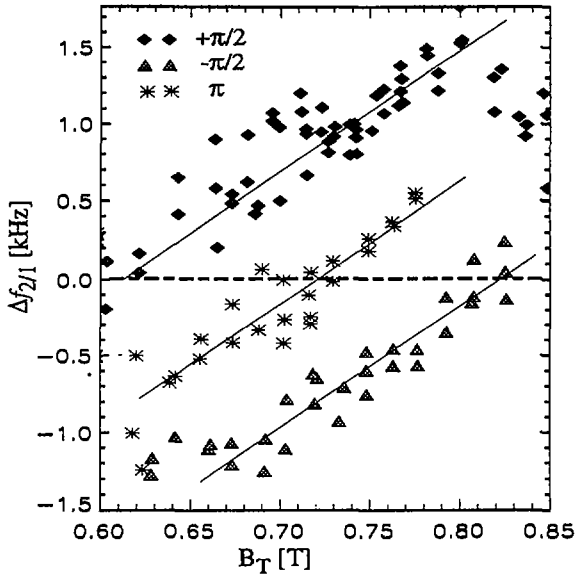

FIG. 1. $\Delta f_{2/1}$ scales linearly with magnetic field for all the antenna phases examined. The lines drawn have the same slope.

the $\Delta f_{2/1}$ with $\phi_{ant} = \pi$ was unexpected based on the momentum injection argument. Two other features are the $\pm \pi/2$ data are approximately symmetric about the π data and $\Delta f_{2/1}$ scales with B_ζ independent of ϕ_{ant}. Since the scaling on B_ζ is independent of ϕ_{ant}, this component is removed by fitting a line to the π data and subtracting the contribution from the $\pm \pi/2$ $\Delta f_{2/1}$ data. Thus, the $\Delta f_{2/1}$ is flat for $0.65 \leq B_\zeta \leq 0.8$ T, and the average $\Delta f_{2/1} = 0.92 \pm 0.19$ kHz and $= -0.79 \pm 0.16$ kHz for $\pm\pi/2$, respectively. The mechanism responsible for this B_ζ scaling will be discussed later.

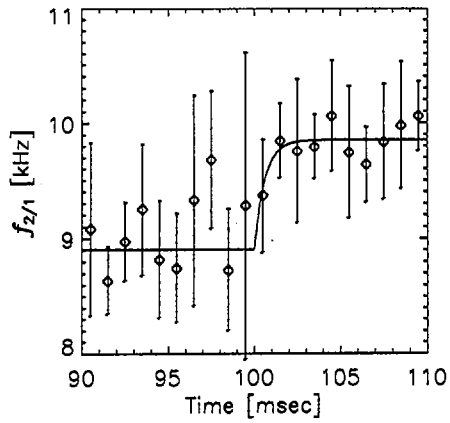

FIG. 2. Average temporal behavior of the 2/1 frequency with the application of rf, where the error bars represent one standard deviation. The 2/1 frequency was found by maximum entropy analysis of the magnetic fluctuation pickup coil signal for 1 msec time intervals.

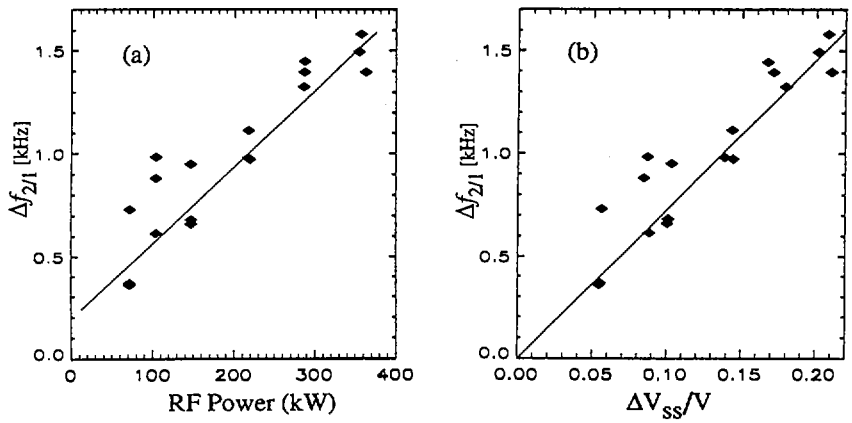

FIG. 3. $\Delta f_{2/1}$ is proportional to (a) the rf power and (b) the steady-state fractional loop voltage change, which is proportional to the driven current.

Examining the frequency evolution, an asymptotic frequency was reached in < 5 msec and an averaged frequency evolution is shown in Fig 2. The data shown in Fig. 2 are an average of 12 similar discharges, where the time history was divided into 1 msec intervals and the power spectra were found using a maximum entropy method. The error bars represent one standard deviation and the data were fit with $f(t) = f_{OH} + \Delta f_{2/1}(1 - e^{-t/\tau_m})$, where f_{OH} is the 2/1 frequency prior to the rf and τ_m represents the characteristic momentum diffusion time. The τ_m was found to be 0.6 ± 0.6 msec. The $\Delta f_{2/1}$ associated with $\pi/2$ was found to scale linearly with applied rf power and fractional change in loop voltage (which is proportional to the driven current). This is shown in Fig 3.

The ϕ_{ant} dependent $\Delta f_{2/1}$ is interpreted as a change in the toroidal plasma flow velocity. The frequency shift is related to the change in the plasma flow velocity, $\Delta \underline{v}$, by

$$\Delta f_{2/1} = \frac{1}{2\pi}[\underline{k} \cdot \Delta \underline{v}] = \frac{1}{2\pi}\left[k_\theta \cdot \Delta v_\theta + k_\varsigma \cdot \Delta v_\varsigma\right], \quad (1)$$

where $\underline{k} = \underline{k}_\theta + \underline{k}_\varsigma = \frac{m}{r}\hat{\theta} + \frac{n}{R}\hat{\varsigma}$ is the wavenumber of the 2/1 tearing mode. The vacuum poloidal antenna spectrum is symmetric so $\Delta v_\theta = 0$, which gives,

$$\Delta v \cong 2\pi \Delta f_{2/1} \frac{R}{n} \quad (2)$$

where R is the major radius. From $\Delta f_{2/1}$, the estimated Δv is approximately 6 x 10^3 m/s for $+\pi/2$.

The Δv due to the addition of rf momentum is estimated by considering the ion toroidal momentum balance which can be written as

$$m_i \frac{dv_i}{dt} = m_e v_e \upsilon_{ei} + m_i \frac{E_r}{B_\theta}\frac{1}{\tau_m} - \frac{m_i v_i}{\tau_m}, \quad (3)$$

where v_e is the electron velocity driven by the rf, v_i is the ion flow velocity, m_e and m_i are the electron and ion masses, and τ_m is the ion momentum diffusion time. We assume that the plasma flow velocity is equal to the ion flow velocity, the change in E_r/B_θ component is negligible compared with the rf term and we analyze the steady state condition. For $\phi_{ant} = \pi/2$,

$$\Delta v \cong \pm \frac{m_e}{m_i}\frac{I_\varsigma}{en_e}\frac{\tau_m}{\tau_e}\hat{\varsigma} \qquad \phi = \pm\pi/2 \quad (4)$$

where I_ς is the rf driven current, n_e is the local plasma density, $\tau_e = 1/\upsilon_{ei}$, and τ_m is the momentum diffusion time. Using I_ς=10-15 kA (which is estimated

from the loop voltage), Δv is 3.5-7.0x10^3 m/s, which is consistent with the Δv from $\Delta f_{2/1}$.

The $\Delta f_{2/1}$ scaling with B_ζ is equivalent to stating that $\Delta f_{2/1}$ increases as the Alfvén resonance moves closer to the B-axis. Since the B_ζ scaling is ϕ_{ant} independent, the scaling could be a result of a modification to E_r or the diamagnetic contribution. However, the $\phi_{ant} = \pi$ data indicate that the mechanism changes sign as a function of the power deposition location. From magnetohydrodynamic theory, one can show that the 2/1 flow velocity is the sum of the bulk plasma flow, electron drift velocity, and the electron diamagnetic flow. In the absence of rf, this can be expressed as

$$v_{2/1} = \left|\frac{E_r}{B_\theta}\right| + v_d + \frac{|\nabla p_e \times \underline{B}|}{n_e e B^2}, \tag{5}$$

where p_e is the electron pressure, v_d is the electron drift velocity, and $v_{2/1}$ is in the positive toroidal direction. The first term of Eq 5 is from the bulk plasma flow and is determined from the ion momentum balance. The other terms are due to electron dynamics: v_d and electron diamagnetic drift, v_*. Concentrating $\phi_{ant} = \pi$ data (rf momentum is zero and v_d is constant), the simplest mechanism is modification of v_* resulting from broadening and peaking of the pressure profile due to rf heating. For rf deposition near the plasma center (high B_T), the v_* would increase because of the increase in T_{e0}. For off axis, the pressure profile would broaden and result in a decrease in the v_*. However, direct and accurate measurements of the pressure profile are unavailable.

Acknowledgement

The authors would like to acknowledge P. Probert, M. Vukovic, C. Hegna, and the Phaedrus-T staff for their cooperation and assistance. This work was supported by the office of Fusion Energy of the United States Department of Energy, grant DE-FG02-88ER53264.

REFERENCES

[1] GALAMBOS, J.D., et al., Nucl. Fusion **35** (1995) 551.
[2] JENSEN, T.H., CHU, M.S., J. Plasma Phys. **30** (1983) 57.
[3] BONDESON, A., WARD, D.J., Phys. Rev. Lett. **72** (1994) 2709.
[4] STRAIT, E.J., et al., Phys. Rev. Lett. **72** (1994) 2709.
[5] MILLER, R.L., WALTZ, R.E., Phys. Plasmas **1** (1994) 2835.
[6] MILLER, R.L., et al., Phys. Plasmas **2** (1995) 3676.
[7] DIAMOND, P.H., et al., Phys. Rev. Lett. **72** (1994) 2565.
[8] ERIKSSON, L.-G., et al., Plasma Phys. Control. Fusion **34** (1992) 863.
[9] IDA, K., et al., Nucl. Fusion **31** (1991) 943.
[10] HSUAN, H., et al., in Proc. 11th Topical Conf. on Radio Frequency in Plasmas, Palm Springs, CA, 1995, AIP Conf. Proc. **355** (1996) 39.

[11] HELLSTEN, T., Plasma Phys. Control. Fusion **31** (1989) 1391.
[12] VUKOVIC, M., Toroidal Effects on the Alfvén Resonance in the Phaedrus-T Tokamak, PhD Thesis, Univ. of Wisconsin, Madison (1995).
[13] LITWIN, C., Phys. Plasmas **2** (1995) 4542.
[14] MAJESKI, R., et al., Phys. Fluids B **5** (1993) 2506.
[15] WUKITCH, S., et al., Phys. Rev. Lett. **74** (1995) 2260.

ICRF HEATING RESULTS IN ASDEX UPGRADE AND W7-AS

J.-M. NOTERDAEME, S. WUKITCH, D.A. HARTMANN,
M. BRAMBILLA, F. BRAUN, G. CATTANEI, J. GAFERT,
J.F. LYON[1], R. NEU, V. PLYUSNIN[2], W. SUTTROP,
J. SCHWEINZER, W. SCHNEIDER, P. VERPLANCKE[3],
F. WESNER, ICRF TEAM, NI TEAM,
ASDEX UPGRADE TEAM, W7-AS TEAM
Max-Planck-Institut für Plasmaphysik,
Euratom-IPP Association,
Garching, Germany

Abstract

ICRF HEATING RESULTS IN ASDEX UPGRADE AND W7-AS.

On the divertor tokamak ASDEX Upgrade, it was shown that H-modes with ion cyclotron resonance frequency (ICRF) heating can also be achieved when the Faraday screen of the antenna is removed. Plasma energy and electron temperature increase are, for operation of the antennas (with screen) in 0 phasing, a factor of two lower than in π phasing, but little difference is seen in impurity effects. With mode conversion heating (He_3 in H), strong heating of the electrons can be achieved on or off-axis. On the stellarator W7-AS, ICRF heating has been successfully demonstrated. A novel antenna, designed to excite a narrow $k_{\parallel}$ spectrum, was used. Second harmonic hydrogen heating and hydrogen in deuterium minority heating both showed an increase in diamagnetic energy of about 10–15% and no enhanced impurity radiation loss. In the H minority in D scenario, it was even possible to sustain the plasma with ICRH alone.

1. ICRF on ASDEX Upgrade

Up to 4 MW of ICRF heating was achieved in ASDEX Upgrade (AUG) using 4 antennas fed by 4 generators with a capability of 2 MW each. We operated in the frequency range 30 - 38 MHz with H minority in D, He_3 minority in H, and He_3 mode conversion heating in H. The experiments concentrated on the comparison of antennas with and without Faraday screen, edge plasma-antenna interaction, heating of plasmas at high density, operation at π and 0 phasing and direct e-heating off-axis using mode conversion. Recently, by using a 3 dB coupler [1] on two of the systems, we could increase the power to the plasma, with only those two systems, to 3.2 MW.

---

[1] Oak Ridge National Laboratory, Oak Ridge, Tennessee, USA.
[2] Kharkov Institute of Physics and Technology, Kharkov, Ukraine.
[3] National Fund for Scientific Research (NFWO), Belgium.

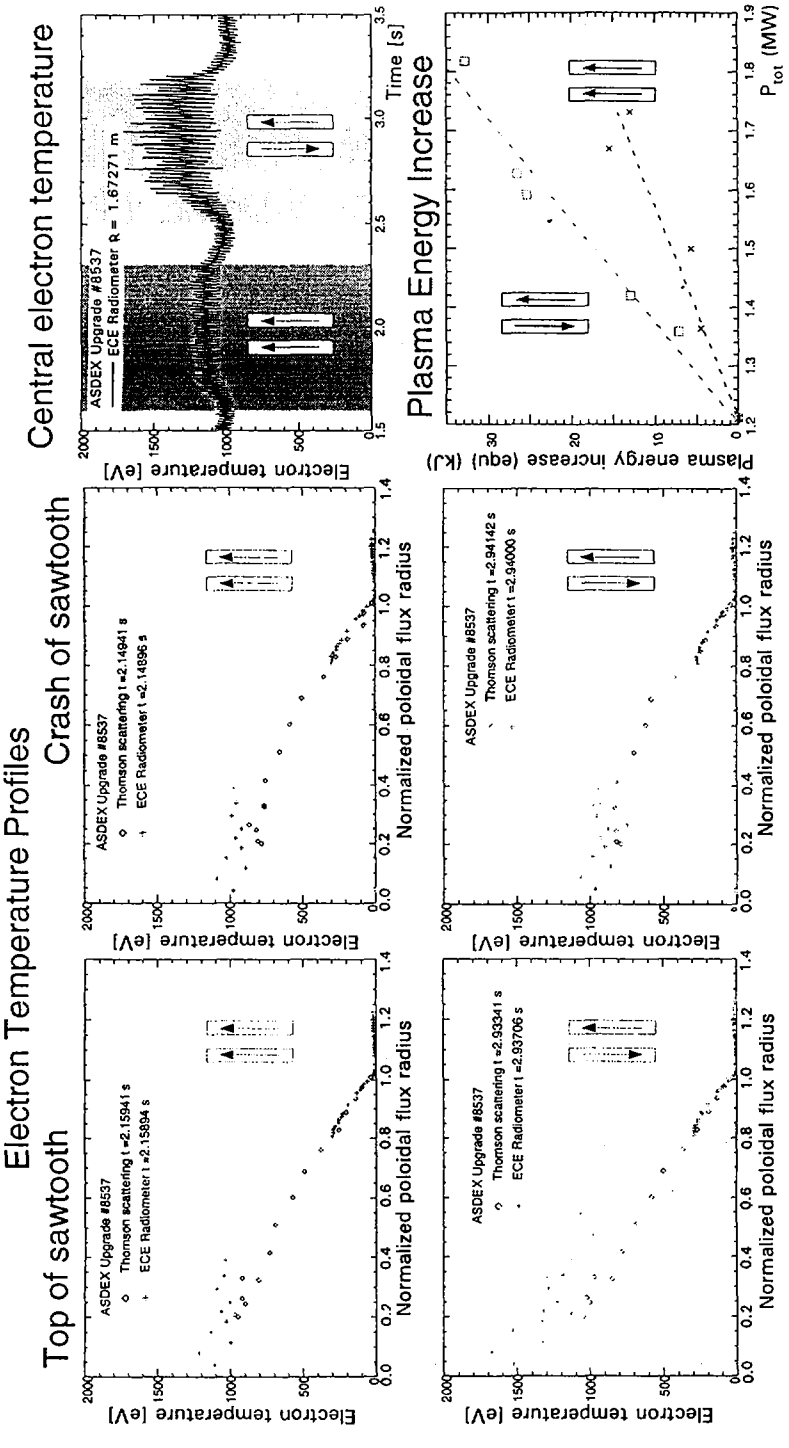

FIG. 1. Operation of the antennas in-phase and out-of-phase. Shown are the electron temperature time trace for a generator power of 0.7 MW, as well as the electron temperature profiles at the top and the crash of the sawtooth. The increase in plasma energy (equ) as a function of total power shows the different heating efficiency.

1. Operation without Faraday Screen

Experiments on screenless ICRF antenna operation, carried out in TEXTOR [2] and DIII-D [3], have provided somewhat contradictory results on the merits of a antenna without Faraday screen. It remained unclear whether or not H-modes were compatible with screenless operation of the antenna. Direct comparison of two identical antennas, except for the presence/absence of a Faraday screen, were performed on AUG in the H minority heating regime in D plasmas (I_p = 1 - 1.2 MA, B_T = 2 - 2.5 T, $\overline{n}_e$ = 3 - 10 $\times 10^{19}$ m^{-3} , f = 30 MHz, π phasing between the loops of one antenna). The experiments covered operation in L-mode, H-mode (ELMy type III, ELM free, ELMy type I) with those antennas alone (P_{RF} up to 1.2 MW), in combination with strong NI injection (up to 7.5 MW), in combination with additional ICRF power (up to 3 MW total), under conditions of CDH mode (completely detached H-mode, NI injection, strong Ne and D gas puffing, type III ELMs), and with reversed magnetic field (angle of the Faraday screen off by 30° for the antenna with screen). Under all those operating conditions, the antenna without screen behaved (with only small differences) like the antenna with screen. H-modes could for the first time be achieved with a screenless antenna. The small differences are a 10 % higher threshold power for the antenna without screen, and, when comparing both antennas at the same power level slightly above the threshold, a somewhat better quality of the H-mode for the antenna with screen [4].

Two antennas were also successfully operated without a Faraday screen in several other heating scenarios ($P_{RF} \approx$ 2 MW) : direct fast wave, He_3 minority in H and fast wave mode conversion heating. The slight difference in H-mode threshold in the H minority in D scenario was confirmed using two antennas.

2. Variation of the edge density

The edge/SOL density, measured in AUG using a fast Li beam diagnostic, is influenced by the RF, particularly in the region behind the antenna. By varying the q value, the relative location (mapped along field lines) of the Li beam density measurement can be placed in the shadow of an antenna. The changes in the edge/SOL density are sudden at turn-on and turn-off of the antenna, indicating that this is a direct effect due to the RF. The relative changes are small between separatrix and antenna limiters but marked in the region beyond the antenna limiters on field lines connected to an active antenna [5]. For experiments where densities in the shadow of the antenna limiter were in the 0.2 $\times 10^{19}$ m^{-3} range, the density decreases. At lower density values, the effect is less pronounced. Under completely detached H-mode (CDH) conditions, where the density in the shadow of the antenna was above 1 $\times 10^{19}$ m^{-3}, the density increased slightly. The influence of RF on the plasma density outside the antenna, on field lines connected to it, can partly be seen as a model of the changes due to the RF to a possible plasma density inside the antenna (for an antenna without Faraday screen). The thus inferred reduction of the plasma density in the antenna, for medium to low density, is consistent with a decrease of the parasitic loading observed on other machines, when RF power ($\geq$ 100 kW) is applied.

3. Comparing operation of the antenna loops in-phase and out-of-phase

Two antennas with Faraday screen were compared with 0 and π phasings at powers up to 1 MW. The conditions were B_T = -2.1 T, I_p = 1 MA, $\overline{n}_e$ = 6

$\times 10^{19}$ m^{-3}, f= 31.6 MHz (H minority in D). In the discharges (see Fig. 1), an antenna with 0 phasing and an antenna with π phasing (n_ϕ peaking at 14, $k_{||} \approx 6.5$ m^{-1}) was energized in sequence. The electron temperature, the sawtooth amplitude and the plasma energy increase was typically twice as high as for the in-phase case (Fig. 1) at the same generator power. The heating efficiency (increase of plasma energy vs total power increase taking into account the reduced OH power because of the higher electron temperature increase in the out-of-phase case and a factor of 0.8 between generator power and power in the plasma) is a factor 2 higher than for operation in phase (incremental confinement time 58 ms compared to 28 ms). Tungsten, the material of the divertor, stayed below the detection level in both phasings. There was no significant difference between the increase of carbon concentration as a function of generator power between both phasings. The increase of O concentration vs generator power was somewhat higher (40%) in 0 phasing than in π phasing. The absence of impurity problems even in 0 phasing indicates that current drive phasings will be possible.

4. Mode conversion heating

The He_3 in H mode conversion scenario [6] is a candidate for off-axis current drive. We first investigated the RF power deposition profiles in the heating mode to test that direct coupling to the electrons off-axis was feasible with the AUG's RF system. The experiment was performed in single null L-mode plasmas (B_T = 2.5 T, $\overline{n}_e$ = 5 $\times 10^{19}$ m^{-3}, I_p = 0.8 MA, and T_e = 1 keV, f = 30 MHz). The ICRF power was square wave modulated between 0 and 1.6

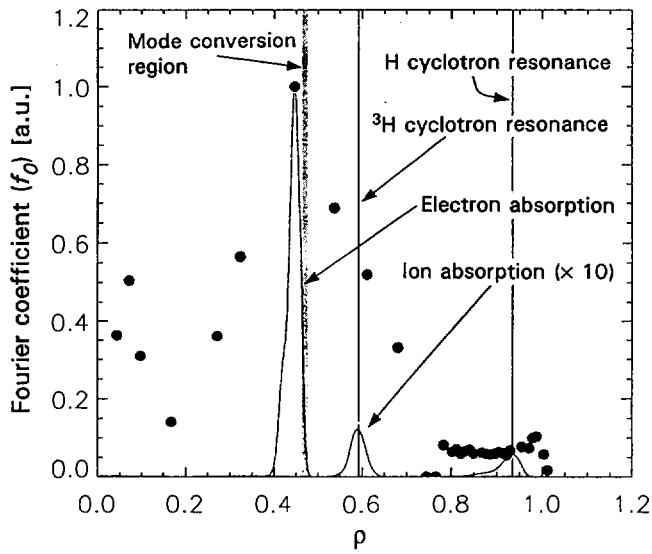

FIG. 2. Comparison of the measured power deposition profile with the one calculated by FELICE, mapped to flux surfaces.

MW at 55 Hz. The sawtooth frequency was 63 Hz. The electron temperature was measured with a 45 channel ECE system with 30 μsec time resolution. The data is Fourier analyzed and the fundamental Fourier coefficient is taken as being proportional to the power deposition profile. Higher harmonics of the RF modulation were investigated in the ECE data but their addition did not modify the profile. One drawback of this technique is that the deposition will appear broader for slow modulation frequencies due to energy diffusion. For good frequency resolution, relatively long modulated signals are also required to minimize influence of sawtooth phenomena on the results. This profile was then compared with the 1-D FELICE code [7]. The measurement and the FELICE results are shown in Fig.2 as a function of the poloidal flux coordinate ρ. The results of the FELICE calculation with 6.5% He_3 minority is mapped from the high field side where direct ECE measurements are unavailable. The width of the profile is different for several reasons. First the resonance layer is approximately a vertical line and cuts across several flux surfaces. This will lead to power absorption on the intersected flux surfaces thereby broadening the absorption profile while the FELICE code is a slab model. A comparison with a toroidal code is planned. Second, the measurement includes the direct absorption, heat wave propagation and energy diffusion. An another method of calculating the absorption is by the so called change-of-slope technique [8]. However, the presence of sawteeth at a frequency not well separated from the RF modulation frequency makes this analysis difficult.

2. ICRF on W7-AS

Ion cyclotron resonance heating (ICRH) has, for the first time, successfully been demonstrated on the stellarator W7-AS. A novel broad antenna [9, 10] designed to excite a narrow spectrum of fast waves was used. Two different heating scenarios were investigated: second harmonic heating of neutral beam heated hydrogen plasmas and hydrogen-minority heating of ECRH deuterium plasmas. Both scenarios showed plasma heating without a significant concurrent increase in plasma density or impurity radiation loss. In addition, it was possible to sustain the plasma with ICRH alone.

The ICRH antenna, shown in Fig. 3, is located on the high field side in the elliptical cross-section of the non-axisymmetric plasma. It has four feeders that allow operation in 0 and π phasing. Typically it is operated in π phasing. Then the poloidal current has an almost sinusoidal distribution along the toroidal direction as shown and excites a narrow $k_{||} \approx 6m^{-1}$ spectrum of fast waves.

Closing the poloidal antenna feeders off against plasma penetration eliminated the anomalously high loading of the antenna during plasma operation observed previously [11]. Extensive condititoning increased the maximum rf-voltage at which electrical breakdown (arcing) occurred to about 50 kV for 400 msec. Real time visual observation of the antenna during plasma operation and inspection after the vacuum break confirmed that arcs did not occur in the antenna, but only in the feeders and in the transmission lines. Most plasma targets had $\iota \approx 0.33$ and were shaped by inside limiters. In those plasmas the distance from the antenna to the fast-wave cutoff is about 6 cm and the observed antenna plasma loading is about 0.5 Ω.

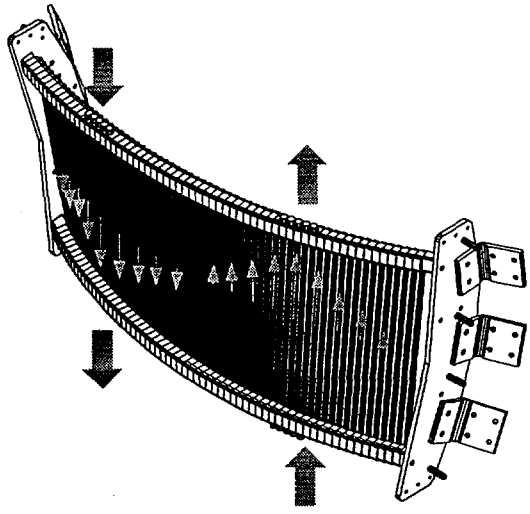

FIG. 3. W7-AS ICRH antenna shown without Faraday screen. The current distribution for π phasing is indicated.

In the second harmonic hydrogen heating scenario (B_T = 1.25 T, f = 38 MHz) with a neutral beam heated target plasma an increase in the diamagnetic energy of about 10 % (0.6 kJ) was obtained. The central hydrogen temperature was about 800 eV and central electron density was $6 \times 10^{19} m^{-3}$. One estimates that about 60% of the power (P = 150 kW) radiated from the antenna is found in the plasma, if P is the generator power reduced by the ohmic losses in the antenna (about 60 %) and $P^{-0.6}$ scaling of the energy confinement time is invoked. Under good wall conditions, the plasma density could be kept constant during the rf-pulse, even though the H_α observation indicated enhanced outgassing at the antenna. The impurity radiation inferred from the bolometer did not increase. An increase in the flux of hydrogen atoms with energies between 10 keV and 33 keV was observed; however, this was not accompanied by an increase in the bulk hydrogen temperature. Maximum heating occurred if the location of the second harmonic resonance coincided with the center of the plasma; almost no heating occurred if the resonance was outside of the plasma. The antenna loading was independent of the location of the resonance even though a rf-probe (located half-way around the torus) detected a wave signal only if the resonance was outside of the plasma. Heating at 0 phasing showed similar increases in the diamagnetic energy as in π phasing and no enhanced impurity radiation. No significant heating was observed in ECRH plasmas of the same density, presumably because the hydrogen temperature of the target plasma was too low (about 350 eV).

In the H-minority heating scenario (B_T = 2.5 T, f = 38 MHz) with an ECRH target deuterium plasma an increase in the diamagnetic energy of about 15 %

(1 kJ) was obtained. This corresponds to absorption of about all of the radiated power $P \approx 200$ kW. The spectroscopically estimated H/D ratio was about 10%. The line-of-sight averaged deuterium temperature rose from 300 eV to 400 eV; the central electron temperature rose slightly. Energetic hydrogen atoms with energies up to 33 keV were observed. The impurity radiation did not increase. In this heating scenario it was possible to sustain an ECRH-created plasma with ICRH alone for as long as 500 msec. The duration of the ICRH-only phase of the plasma was solely limited by arcing in the transmission lines. An almost steady state condition could be obtained about 200 msec into the ICRH-only phase of the discharge. Typical parameters were diamagnetic energy of 2 kJ, average electron density of $4 \times 10^{19} m^{-3}$, central electron temperature of 300 eV, and central deuterium temperature of 350 eV.

An example of an ICRH sustained plasma is shown in Fig. 4 starting at 400 msec. The generator frequency and the approximate H/D-ratio were such that both, the H-resonance and the ion-ion-resonance, were located inside of the plasma volume. The average electron density first rose by increased outgassing

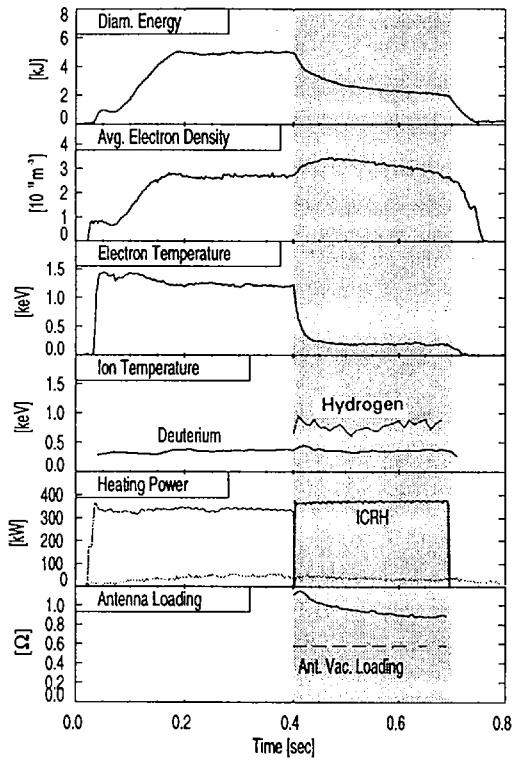

FIG. 4. Time trace of shot 33 634. Ion temperatures inferred from unweighted line-of-sight average of CX fluxes. $B_T = 2.5$ T, $\iota = 0.34$.

of the antenna but returned towards the initial value near the end of the ICRH plasma. The central electron temperature dropped rapidly within an energy confinement time and then stayed constant throughout the ICRH phase. The total radiation measured with bolometers stayed constant, even though an accumulation of iron and chromium could be inferred from VUV observation; yet soft X-ray measurements indicated that Z_{eff} did not increase. We therefore conclude that, at least in the range of parameters investigated, the ICRH sustained plasma is not hampered either by uncontrolled density increase or by enhanced impurity production.

The plasma density profile, measured with lithium beam diagnostic, Langmuir probes, microwave reflectometry and Thomson scattering, was narrower and had steeper edges during the ICRH sustained plasma than during comparable ECRH heated plasmas. The transition between these two profiles occurredwithin approximately one energy confinement time. Further narrowing of the plasma was observed on a longer time-scale. The resulting increase of the distance from the antenna to the fast wave cutoff could explain the decrease of the antenna plasma loading and therefore the decrease in diamagnetic energy. A radial electric field of about -1.5 kV/m built up at the beginning of the ICRH phase of the discharge presumably due to increased high-energy hydrogen losses as indicated by CX measurements.

REFERENCES

[1] GOULDING, R., et al., in Radiofrequency Power in Plasmas (Proc. 11th Top. Conf. Woodbury, 1995), American Institute of Physics (1995) 397.

[2] VAN NIEUWENHOVE, R., et al., Nucl. Fusion **32** (1992) 1913.

[3] PINSKER, R., et al., in Radiofrequency Power in Plasmas (Proc. 11th Top. Conf. Woodbury, 1995), American Institute of Physics (1995) 43.

[4] NOTERDAEME, J.-M., et al., ibid., p. 47.

[5] NOTERDAEME, J.-M., et al., in Controlled Fusion and Plasma Physics (Proc. 23th Eur. Conf. Kiev, 1996), Vol. 20C, European Physical Society, Geneva (1996).

[6] MAJESKI, R., et al., Phys. Rev. Lett. **73** (1994) 2204.

[7] BRAMBILLA, M., et al., Nucl. Fusion **28** (1988) 549.

[8] GAMBIER, D., et al., Nucl. Fusion **30** (1990) 23.

[9] CATTANEI, G., et al., Nucl. Fusion **29** (1989) 15.

[10] CATTANEI, G., et al., in Radiofrequency Heating an Current Drive of Fusion Devices (Abstracts Conf. Brussels, 1992), European Physical Society, Geneva (1992) 121.

[11] BALLICO, M., Minority heating experiments on the W7-AS stellarator, IAEA Technical Committee Meeting on Stellarators and Other Helical Confinement Systems, Garching (1993) 413.

LOWER HYBRID CURRENT DRIVE AND ANTENNA COUPLING EXPERIMENTS ON TdeV*

A. CÔTÉ, Y. DEMERS, P. BROOKER, C. CÔTÉ, P. JACQUET, J. MAILLOUX, G. ABEL, C. BOUCHER, D. BOYD[1], R. DÉCOSTE, V. FUCHS, M. GONICHE[2], J.-L. LACHAMBRE, X. LITAUDON[2], D. MICHAUD, G.W. PACHER, Y. PEYSSON[2], I.P. SHKAROFSKY, M.M. SHOUCRI, F. SKIFF[1], M. St.-ONGE, B. TERREAULT
Centre canadien de fusion magnétique,
Varennes, Quebec, Canada

Abstract

LOWER HYBRID CURRENT DRIVE AND ANTENNA COUPLING EXPERIMENTS ON TdeV.

At a coupled RF power density of 50 MW/m^2, the LHCD system installed on TdeV has achieved record performance at 3.7 GHz. With TdeV's unique set of RF diagnostics, lower hybrid wave coupling was found to be in agreement with the antenna modelling code SWAN. Discrepancies exist at high RF power but the launched spectra do not seem to be affected. Strong toroidal asymmetries in power deposition on divertor and first wall components during LHCD were observed and characterized. A possible mechanism for the power dissipation is described. Current drive experiments have been performed and comparison with codes is presented. Results from a set of diagnostics suggest that the radial profile of suprathermal electrons is broader than code predictions. Furthermore, the velocity distribution extends well beyond the $N_{\parallel}$ resonance energies permitted by the LH wave accessibility. Large current profile modifications ($-0.4 \leq \Delta l_i \leq 0.2$) in steady state have been obtained by tailoring the power deposition of the LH wave in TdeV. These profile modifications have an impact on energy confinement, as W_e^{KIN}/W_e^{RL} increases with Δl_i.

1. INTRODUCTION

Lower hybrid current drive (LHCD) is one of the most promising methods of driving current and controlling the plasma current profile in a steady state tokamak reactor. The LHCD system installed on TdeV (R = 0.86 m; a = 0.25 m; $B_T < 1.8$T; $I_p < 250$ kA) was used to achieve stationary current profile modification in divertor geometry and has allowed a better understanding of lower hybrid wave coupling. The TdeV system operates at 3.7 GHz and has routinely delivered the full 1.3 MW of RF power at the generator [1]. Its antenna consists of 2 rows of 8 four-way multijunction modules. The main peak of the launched $N_{//}$ spectrum can be adjusted within the limits $2.0 \leq N_{//} \leq 3.3$. Fully LH-driven discharges of 190 kA were sustained at moderate densities ($\bar{n}_e = 1.9 \times 10^{19}$ m^{-3}) [2]. The duration of the LH current driven plasma is limited only by the power handling capabilities of the divertor plates (maximum 4 s).

* The Centre canadien de fusion magnétique is funded by the Government of Canada, Hydro-Québec and the Institut national de la recherche scientifique.

[1] University of Maryland, College Park, Maryland, USA.

[2] Association Euratom-CEA, Cadarache, France.

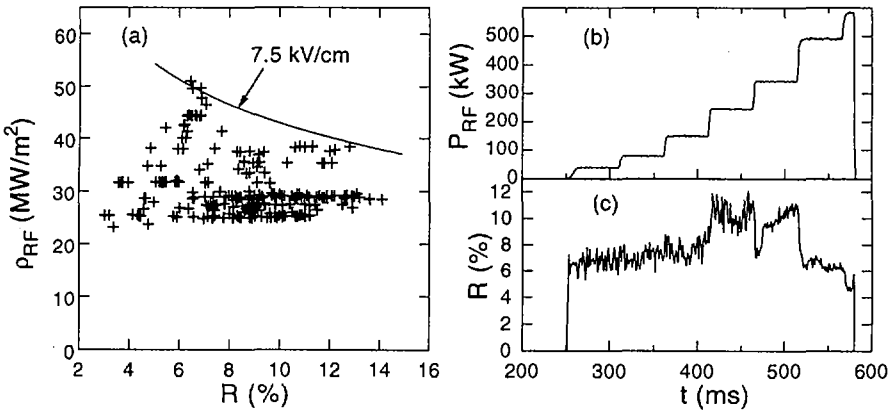

FIG. 1. (a) RF power density (p_{RF}) versus the reflection coefficient. Time traces showing the evolution of the reflection coefficient (c) with RF power (b).

2. ANTENNA COUPLING EXPERIMENTS

Figure 1(a) summarizes all the LH shots of TdeV for which the power injected by the lower row exceeded 300 kW. No significant arcing has been observed even at the maximum power density reached at the grill mouth (50 MW/m^2). Because of the power ratings of the RF windows, the operating region of the antenna was limited to a maximum electric field of 7.5 kV/cm in the reduced waveguides. The low outgassing rate of the module [1] combined with good pumping speed are probably responsible for the high power handling capabilities of the antenna and its short conditioning time. These results confirm that the grill material, Glidcop, is appropriate for the next generation of LHCD couplers.

Studies of LH wave coupling were carried out in order to characterize the operation of the TdeV antenna and to validate the predictions of the antenna modelling code SWAN [3]. The code is an important tool as it is routinely used to evaluate the launched spectra using measurements performed with bi-directional couplers at the input of the antenna multijunction modules. Two regimes of RF power are analysed in view of the nonlinear dependence of the reflection coefficient on injected power, as illustrated in Fig. 1(b) and 1(c). At low RF power ($\leq$ 5 MW/m^2) the reflection coefficients of the modules can be well reproduced by the SWAN code. The edge plasma parameters used in these calculations (vacuum gap = 0.5 mm, n_e = 0.45 x 10^{18} m^{-3}, ∇n_e = 1.5 x 10^{20} m^{-4}) suggest that a low density layer is present in front of the grill [4]. This density reduction in front of the grill could be due to cross-field transport followed by plasma neutralization on the grill surface. A more detailed comparison with the experiment is made possible on TdeV by a microwave probe diagnostic which measures the RF fields in some of the reduced waveguides [5]. Figure 2(a) shows a comparison between the measured fields at the antenna mouth and the code results for low RF power densities. The good agreement validates the launched spectra obtained from the SWAN code using only the couplers measurements.

In the high RF power regime of interest for LHCD system operation (~40 MW/m^2), the reflection coefficients of the individual modules cannot be reproduced for any density profile considered in the SWAN code. The reason for this could be that the high RF power modifies locally the edge plasma parameters in front of the grill. On Fig. 2(b) we compare

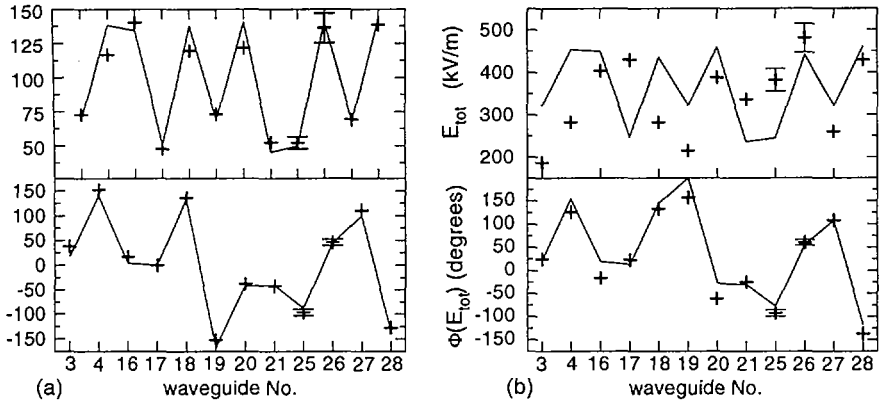

FIG. 2. Amplitude and phase of the electric fields in the instrumented waveguides at the antenna mouth. Comparison between measurements (+) and SWAN calculations (solid lines) for two power densities: (a) 3 MW/m^2 and (b) 40 MW/m^2.

the microwave probe measurements with SWAN calculations for conditions such that the code reproduces the averaged reflection coefficient measured with the couplers. The amplitude of the measured fields is not accurately reproduced, however fairly good agreement is found for the phase progression. This result implies that in these high power conditions, the spectrum of the RF field at the antenna mouth is not significantly degraded despite the strong modifications of the edge plasma by the RF power. A more quantitative evaluation of the launched spectra would require an accurate model for the plasma surface impedance at high power.

Strong toroidal asymmetries in power deposition on the divertor plates and first wall components are observed during LHCD [6]. The toroidal location of the hot spots corresponds to components magnetically connected to the grill mouth (both drift sides). Measurements indicate that the hot spots are caused by fast electrons ($0.2 \lesssim E \lesssim 5$ keV) created by the RF fields in a thin layer of plasma in front of the antenna. Under normal operating conditions, the fraction of RF power lost through this channel can be greater than 5% and lead to localised heat loads in excess of 5 MW/m^2. This RF power dissipation in the SOL increases with the density at the grill mouth (see Fig. 3(a)) and P_{RF}, but does not vary significantly with $N_{//}$.

A possible mechanism for the power dissipation is the acceleration of SOL electrons by RF waves through Landau damping. The electric field at the grill mouth can be represented by a superposition of travelling waves with different $N_{//}$ values. In addition to the lowest $N_{//}$ component, which interacts with the electrons near the plasma centre, there are lobes at much higher values of $N_{//}$ with non negligible intensity. They correspond to small parallel wavelengths and are due to small scale length features of the grill. For $|N_{//}| \geq 50$, the waves have a phase velocity low enough to interact through Landau damping with thermal electrons in front of the grill. Acceleration up to a few keV is possible because the field intensity in front of the grill is large enough for the high $N_{//}$ modes to form an overlapping system of resonances [7]. This can be shown using a simple model which calculates the trajectories of electrons in the RF electric field near the antenna mouth,

neglecting the effects of plasma and wave propagation. Figure 3(b) shows the energy distribution of the electrons after their interaction with the antenna RF field, compared with the 20 eV initial Maxwellian distribution. The final distribution is non-Maxwellian, with a mean energy of 320 eV and a maximum energy of 2.2 keV. Several approaches to reduce the fraction of the RF power lost in the SOL are currently under study, one of which is to reduce from the outset the available power in the high $N_{//}$ part of the spectrum by modifying the small scale length features of the antenna.

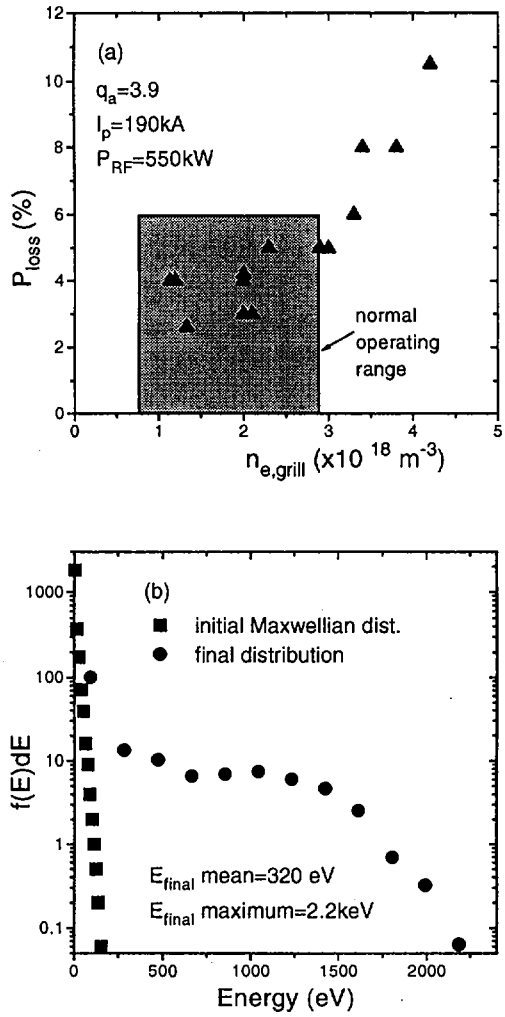

FIG. 3. (a) Fraction of RF power lost on components connected to the antenna (ion-drift direction only) as a function of the density at the grill mouth. (b) Electron energy distribution before and after acceleration by the SWAN calculated RF field.

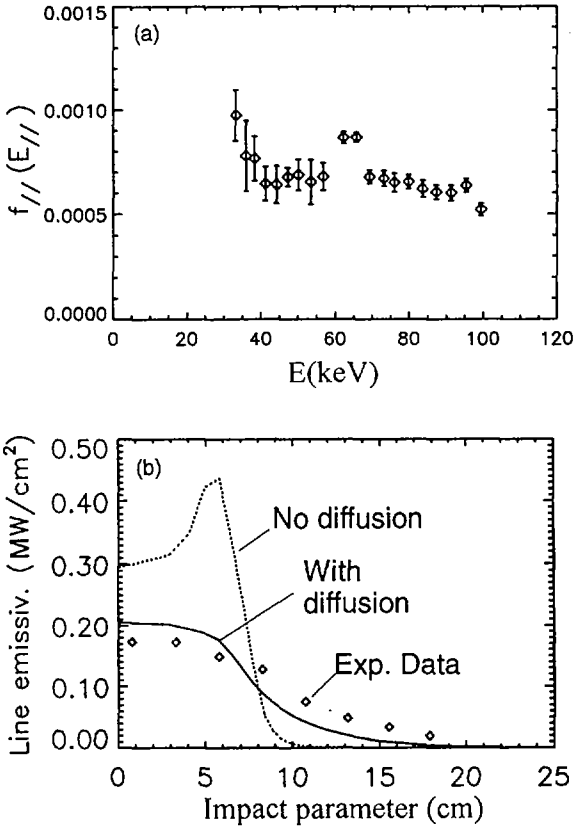

FIG. 4. (a) EC absorption signal for shot 27654 showing extended RF quasi-linear plateau. (b) Experimental and simulated X-ray line integrated emissivity (27821).

3. LOWER HYBRID CURRENT DRIVE EXPERIMENTS

The LHCD physics studies undertaken at TdeV are current drive efficiency scaling, suprathermal electron characterization and current profile modification. Current drive experiments have been performed over a wide range of parameters [2]. The $N_{//}$ dependence of the current drive efficiency is not as strong as expected from simple theory. Nevertheless, current drive efficiencies obtained on TdeV ($\eta_{CD} \leq 0.8 \times 10^{19}$ A/Wm^2) are generally in good agreement with predictions of two simulation codes, TSC-LSC and ACCOME. ACCOME simulations suggest that the reduced efficiency at low $N_{//}$ values is mostly due to the large upshift in the LH wave spectrum needed to fill the spectral gap.

Results from a set of diagnostics (Electron Cyclotron Absorption, hard X-ray, filtered soft X-ray) have been combined with detailed numerical simulations (ACCOME and FP-2D) to study the suprathermal electron physics in LHCD plasmas [8]. The EC-absorption diagnostic [9] measures the asymmetric part of $f_{//}(|p_{//}|)$ along two chords,

at r/a = 0 and r/a ~ ½. Figure 4(a) shows the results of the off-axis channel for shot 27654, [I_p = 142 kA, n_{e0}=2.0×10^{19} m^{-3}, T_{e0} = 2.2 keV, P_{rf} = 680 kW]. The flat distribution is representative of a RF "quasi linear plateau" that extends to at least 95 keV and is consistent with the energy spectrum of the plasma X-ray emission measured by the hard X-ray camera. However, the plateau extends to energies well beyond $E_{//}$ = 30 keV corresponding to the injected $N_{//}$ = 3. Pitch angle scattering, wave propagation boundaries for down-shifted $N_{//}$ and a residual electric field (V_{loop} = 0.05 V) have been considered and were found insufficient to explain the observed extended tail.

The filtered X-ray tomographic array consists of a linear array of silicon photodiodes sensitive to suprathermal radiation between 9 and 15 keV. Figure 4(b) shows data for shot

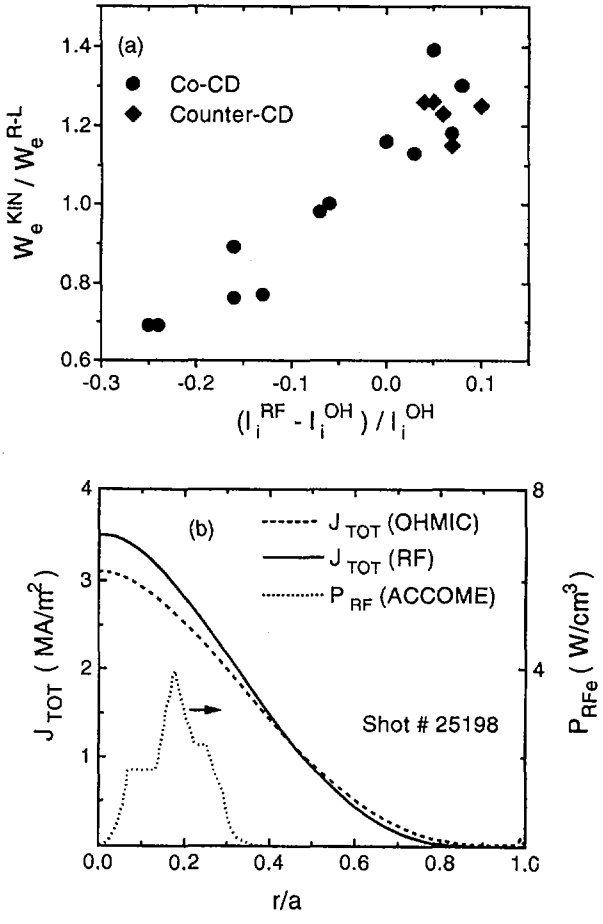

FIG. 5. (a) Variation of electron energy enhancement factor (H^{RL} = W_e^{KIN}/W_e^{RL}) with changes in (l_i^{RF} − l_i^{OH})/l_i^{OH}. (b) Current density profile before and during RF for LHEP shot and predicted power deposition profile.

27821, which is a typical shot [I_p = 180kA, P_{rf} = 700kW, $N_{//}$ = 2.5, $\bar{n}_e = 1.6\times10^{19}m^{-3}$]. The diamonds are the experimental line integrated X-ray intensities. Note that there is significant emission all the way up to 18 cm, as confirmed also by the hard X-ray camera. Simulations have been made which use the power deposition profile outputs of the 1½D ACCOME code [10] as inputs to a fast 2D FP solver [11] that includes radial diffusion. The results are plotted in Fig. 4(b) for no radial diffusion and for a magnetic turbulent diffusion coefficient of $0.1q\, v_{//} / v_{th}$ m^2/sec. In general, the calculated distributions predict the signal measured by the filtered array fairly well near the centre of the plasma but underestimate the emission for impact parameters greater than mid radius. This suggests that the deposition profile is broader than that calculated by the ray tracing code or that other diffusion mechanisms, like the collisionless diffusion of [12], should be considered.

The aim of LH current profile experiments is to explore the confinement and stability of various current density shapes under stationary conditions. Figure 5(a) illustrates the large changes in internal inductance that can be induced with LHCD for discharges with q_{95} between 4 and 6.5. Peaking of the current profile at large q_{95} is obtained by launching LH waves with large $N_{//}$, for which the plasma centre is accessible ($N_{//} > N_{//}^{acc}$) or by counter-propagating LH waves. Inversely, broadening of the current profile is obtained with small $N_{//}$ and/or LH waves for which the plasma centre is inaccessible. Increases in internal inductance (l_i) are accompanied by peaking of temperature, current density, soft X-ray (2-20 keV) and hard X-ray (30-80 keV) emission profiles. In contrast, a decrease of l_i is associated with broadening of all the previous profiles.

In TdeV, the global electron confinement time follows Rebut-Lallia scaling [13]. Improvements in the electron kinetic energy versus the Rebut-Lallia predictions are correlated with changes in internal inductance induced by LH as shown in Fig. 5(a). These improvements are attributed to an increase of the magnetic shear in the confinement zone. For example, Fig. 5(b) illustrates the steepening of the current density profile where the LH power is deposited. This shot [25198: I_p = 140kA, P_{rf} = 540kW, $N_{//}$ = 3.3, $\bar{n}_e = 1.9\times10^{19}m^{-3}$] with an H^{RL} = 1.4 has the characteristics of a LHEP mode as observed on Tore-Supra [14]. ACCOME simulations of the RF current coupled with CRONOS simulations of current diffusion agree fairly well with experimental polarimetry data.

4. FUTURE PLANS

For the next experimental campaign, improvements in the power handling of the divertor plates [15] and the LH antenna limiter will extend the plasma duration up to 10 sec. Smoothing of the small scale length features of the antenna and addition of a moveable antenna guard limiter are expected to reduce the localised power dissipation in front of the grill. Finally, the installation of a 110 GHz ECRH system (1.4 MW) combined with the LH system will allow the study of synergistic effects on current drive efficiency and will add more flexibility for current profile modification and heating scenarios.

REFERENCES

[1] DEMERS, Y., et al., in Radiofrequency Heating and Current Drive of Fusion Devices (Proc. Eur. Topical Conf. Brussels, 1992), Vol. 16E, European Physical Society, Geneva (1992) 73.

[2] DEMERS, Y., et al., in Proc. 11th Topical Conf. on Radio Frequency in Plasmas, Palm Springs, CA, 1995, AIP Conf. Proc. 355 (1996) 118.

[3] LITAUDON, X., et al., Nucl. Fusion **32** (1992) 1883.
[4] JACQUET, P., et al., in Proc. 11th Topical Conf. on Radio Frequency in Plasmas, Palm Springs, CA, 1995, AIP Conf. Proc. **355** (1996) 122.
[5] JACQUET, P., et al., Rev. Sci. Instrum. **68** (1997) 1176.
[6] MAILLOUX, J., et al., J. Nucl. Mater. **241–243** (1997) 745.
[7] FUCHS, V., et al., Phys. Plasmas **3** (1996) 4023.
[8] BROOKER, P., et al., in Controlled Fusion and Plasma Physics (Proc. 23rd Eur. Conf. Kiev, 1996), Vol. 20C, European Physical Society, Geneva (1996).
[9] BOYD, D., SKIFF, F., GULLICK, S., Rev. Sci. Instrum. **68** (1997) 496.
[10] FUCHS, V., et al., Nucl. Fusion **35** (1995) 1.
[11] SHKAROFSKY, I.P., SHOUCRI, M., Internal Rep. 462, CCFM, Varennes (1996).
[12] MANFREDI, G., et al., Fusion Technol. **29** (1996) 244.
[13] CÔTÉ, A., et al., in Controlled Fusion and Plasma Physics (Proc. 22nd Eur. Conf. Bournemouth, 1995), Vol. 19C, Part II, European Physical Society, Geneva (1995) 361.
[14] HOANG, G.T., et al., Nucl. Fusion **34** (1994) 75.
[15] DÉCOSTE, R., et al., these Proceedings, Vol. 1, p. 129.

ULTRA-LONG TOKAMAK DISCHARGE BY LOWER HYBRID CURRENT DRIVE ON TRIAM-1M

S. ITOH, K. NAKAMURA, M. SAKAMOTO,
K. MAKINO, E. JOTAKI, S. KAWASAKI,
H. NAKASHIMA, T. YAMAGAJO
Advanced Fusion Research Center,
Research Institute for Applied Mechanics,
Kyushu University,
Kasuga, Japan

Abstract

ULTRA-LONG TOKAMAK DISCHARGE BY LOWER HYBRID CURRENT DRIVE ON TRIAM-1M.

A new position control system with an image processing circuit and a gas supply system with feedback control using the H_α line intensity as monitor of the plasma density for steady state operation has been developed in TRIAM-1M. This progress has resulted in the achievement of an ultra-long discharge with a duration of 2 h 13 s in 2.45 GHz LHCD experiments and a ~ 1 min high density discharge in 8.2 GHz LHCD experiments. Thus, automatic position and gas supply control for the steady state tokamak discharge could be demonstrated, and steady state tokamak operation with reactor grade plasma density by non-inductive current drive would be possible.

1. INTRODUCTION

The experimental programme of the superconducting high field tokamak TRIAM-1M ($R = 0.8$ m, $a \times b = 0.12$ m $\times$ 0.18 m, $B_t = 8$ T, SUS wall and Mo limiters) has been mainly devoted to the investigation of physics and technology of steady state current drive plasma; two kinds of lower hybrid current drive (LHCD) systems were used. So far, a long tokamak discharge lasting more than one hour has been achieved in 2.45 GHz LHCD experiments [1–5], and a high density ($\bar{n}_e \sim 2 \times 10^{19}$ m^{-3}) and long duration ($\tau_j > 20$ s) discharge was obtained in 8.2 GHz LHCD experiments [6].

In the long duration discharge, a hot spot appears on the Mo limiter, as a result of the heat flux from the plasma. In order to prevent concentration of the heat flux at one spot of the limiter surface, the plasma position was slowly moved by manually changing a 'reference position' of the feedback control system in the previous experiments. The hot spot was observed through a tangential port by a TV camera. In such manual position control, the achievement of the long duration discharge depends on the operator's know-how. In order to automate the manual position control, we have developed a new position control system with an image processing circuit. Furthermore, a gas supply system with feedback control using the H_α line intensity as

plasma density monitor for steady state operation has been developed. This progress has resulted in the achievement of an ultra-long discharge with a duration of 2 h 13 s in 2.45 GHz LHCD experiments and of a ~1 min discharge with similar plasma density of D–T burning plasma in JET [7] and TFTR [8] in 8.2 GHz LHCD experiments.

In this paper, the operation and the experimental results achieved with the ultra-long and the high density discharges are reported.

2. CONTROL OF ULTRA-LONG DISCHARGE

2.1. Position control with image processing circuit

During the initial phase ($t < 5$ s) of the discharge, the plasma position is controlled by magnetic coils as sensors for the detection of the poloidal magnetic field to obtain a fast response of the feedback loop; afterwards, the Hal generators are used as plasma position control which is done every millisecond. In such a feedback control, the heat flux from the plasma concentrates in a certain area of the poloidal limiter since the plasma position is fixed. So far, the plasma position was moved slowly by manually changing a 'reference position' of the feedback control system. In order to automate the manual position control, an image processing circuit has been developed and applied to the feedback position control system.

The image processing circuit can detect position and brightness of the interacting area (i.e. the hot spot) between the plasma and the limiter by a TV image. The position of the hot spot is defined by weighted average:

$$\sum_i \mathbf{r}_i I_i \Big/ \sum_i I_i$$

where I and **r** are the brightness and the position of the point whose brightness exceeds a certain threshold. This threshold is set to eliminate the dark noise of the TV camera and the light of the plasma. The image processing circuit sends the signal to change the 'reference position' of the feedback control system to prevent the heat flux from concentrating in a certain area of the Mo limiter according to the position and the brightness of the hot spot. The time needed to send the signal from the TV image is about 0.3 s, which is short compared with the characteristic time of increase in the limiter temperature.

2.2. Hydrogen recycling and density control of long duration discharge

Figure 1 shows the time evolution of the recycling ratio R of the 2.45 GHz LHCD discharge; the RF power is about 20 kW, the plasma current is about 22 kA and the line averaged electron density is about 2×10^{18} m^{-3}. It is found that R increases gradually and approaches one. The variation in R, however, is different

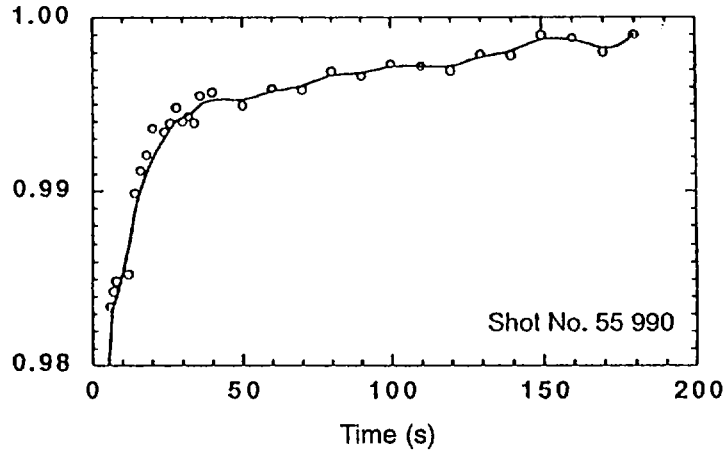

FIG. 1. Time evolution of recycling ratio of 2.45 GHz LHCD discharge.

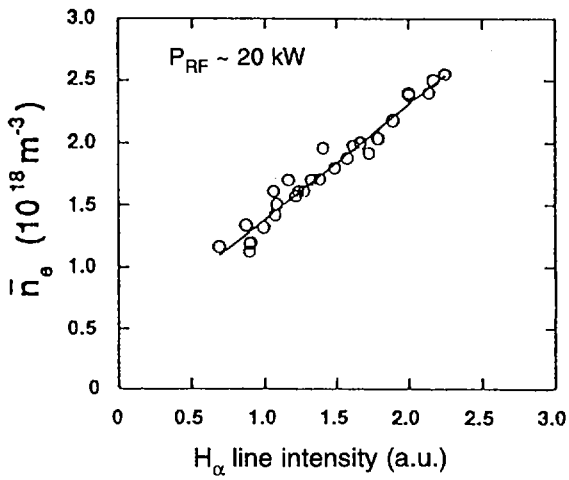

FIG. 2. Line averaged electron density versus H_α line intensity at the plasma central chord.

from shot to shot since it depends on both plasma (e.g. plasma density) and wall conditions. So, the gas supply should be controlled according to the variation in R during the discharge in order to control the plasma density.

We have improved the gas supply system by adopting feedback control using the H_α line intensity plasma density monitor to control the plasma density because there is a possibility of failure in counting the interferometer fringes for density measurement at plasma breakdown. Figure 2 shows the dependence of the line

averaged electron density on the H_α line intensity at the plasma central chord steady state conditions. In the typical operational regime of the long discharge, the line averaged electron density increases linearly with the H_α line intensity. This means that the plasma density can be controlled by using the H_α line intensity.

3. ULTRA-LONG DISCHARGE

Through the progress of the new position and gas supply control systems, we have succeeded in sustaining an ultra-long discharge with a duration of 2 h 13 s in 2.45 GHz LHCD experiments. During this discharge, the RF power is about 18 kW, and a plasma current of about 20 kA is maintained nearly constant as is shown in Fig. 3. The line averaged electron density is about 1.5×10^{18} m^{-3}, and the ion

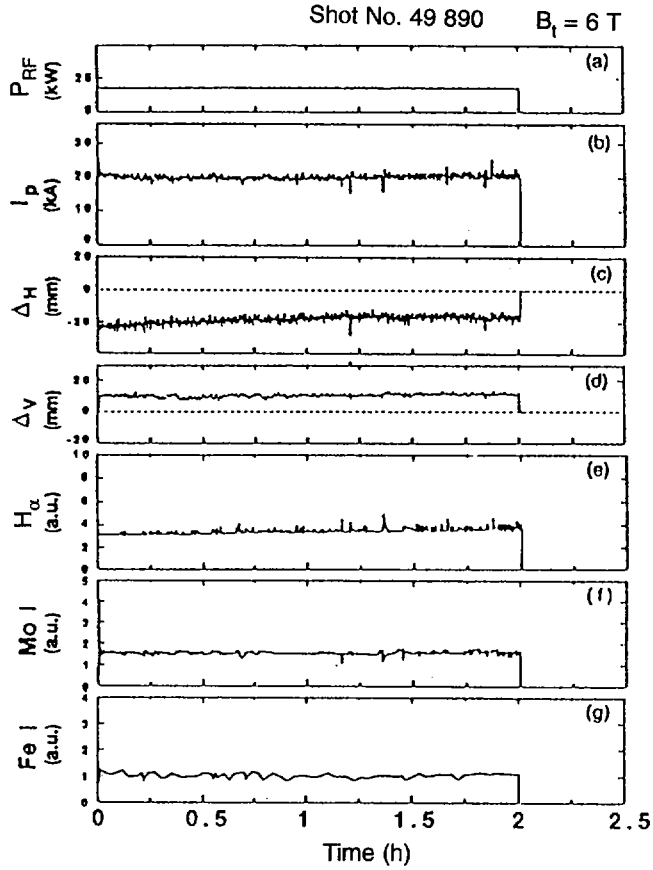

FIG. 3. Time evolution of ultra-long discharge: (a) RF power; (b) plasma current; (c) horizontal displacement; (d) vertical displacement; (e) H_α line intensity; (f) Mo I line intensity; (g) Fe I line intensity.

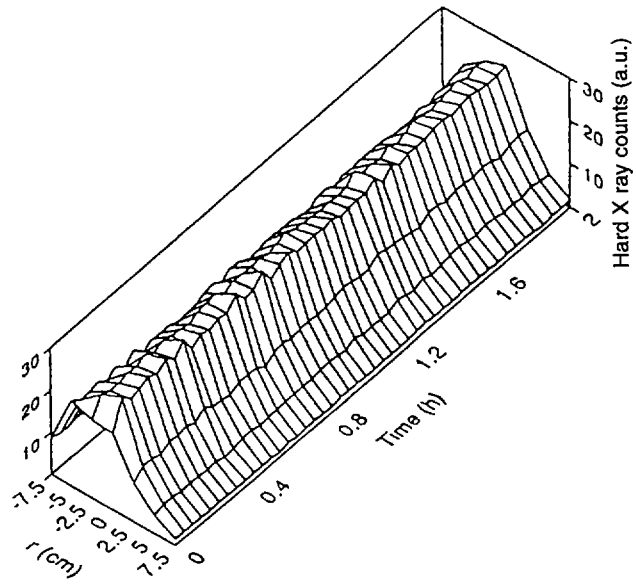

FIG. 4. Time evolution of hard X ray emission profile of ultra-long discharge.

temperature at the plasma centre is about 0.6 keV. The H_α line intensity at the plasma centre (Fig. 3(e)) increases slightly with time in accordance with the feedback control of the gas supply system. The impurity line intensity does not change significantly with time. The hard X ray emission profile is relatively peaked and remains stationary throughout the discharge as is shown in Fig. 4. It is assumed that the plasma current has a relatively peaked and stationary distribution.

4. HIGH DENSITY DISCHARGE

In the 8.2 GHz LHCD experiments, we have achieved a duration of about 1 min by applying the new position and gas supply control systems. A plasma with a line averaged electron density of about 1.5×10^{19} m^{-3} is sustained for about 58 s by RF power (105 kW) alone, as shown in Fig. 5. A plasma current of $I_p \sim 30$ kA is maintained almost constant until 43 s. Thereafter, I_p decreases gradually and drops abruptly to a level of 20 kA at $t \sim 47$ s. The H_α, Fe I and O II line intensities increase simultaneously with the drop in I_p. Furthermore, the hard X ray (80 keV) emission profile becomes broader as is shown in Fig. 5(h). Other, similar discharges show that the electron density of the scrape-off layer increases with decreasing I_p. From these results, we conclude that the plasma density in the peripheral region increases as a result of plasma–wall interaction. The abrupt decrease in I_p may be related to wave accessibility as was observed in previous experiments [4].

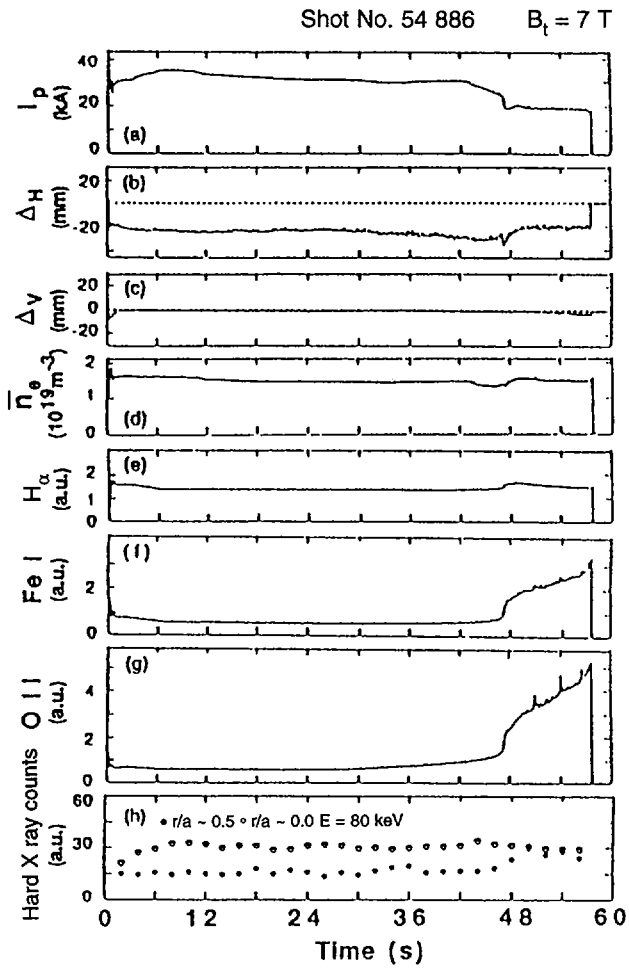

FIG. 5. Typical time evolution of high density LHCD discharge: (a) plasma current; (b) horizontal displacement; (c) vertical displacement; (d) line averaged density; (e) H_α line intensity; (f) Fe I line intensity; (g) O II line intensity; (h) hard X ray counts.

5. SUMMARY

A new position control system with an image processing circuit which can automatically control the plasma position in order to prevent the heat flux from concentrating in a certain area of the Mo limiter has been developed. Furthermore, we have developed a gas supply system with feedback control using the H_α line intensity as plasma density monitor since there is a linear relationship between the plasma density and the H_α line intensity in the typical operational regime of the long discharge.

This progress has resulted in the achievement of an ultra-long discharge with a duration of 2 h 13 s in 2.45 GHz LHCD experiments and of a ~1 min high density discharge in 8.2 GHz LHCD experiments. Thus, the automatic position and gas supply control for the steady state tokamak discharge could be demonstrated, and it was shown that steady state tokamak operation with reactor grade plasma density by non-inductive current drive may be possible.

REFERENCES

[1] ITOH, S., et al., in Plasma Physics and Controlled Nuclear Fusion Research 1988 (Proc. 12th Int. Conf. Nice, 1988), Vol. 1, IAEA, Vienna (1989) 629.
[2] ITOH, S., et al., in Plasma Physics and Controlled Nuclear Fusion Research 1990 (Proc. 13th Int. Conf. Washington, 1990), Vol. 1, IAEA, Vienna (1991) 733.
[3] MORIYAMA, S., et al., Nucl. Fusion **30** (1990) 47.
[4] NAKAMURA, Y., et al., Nucl. Fusion **30** (1990) 689.
[5] JOTAKI, E., ITOH, S., Fusion Technol. **27** (1995) 171.
[6] ITOH, S., et al., in Plasma Physics and Controlled Nuclear Fusion Research 1992 (Proc. 14th Int. Conf. Würzburg, 1992), Vol. 1, IAEA, Vienna (1993) 743.
[7] JET TEAM, ibid., p. 99.
[8] HAWRYLUK, R.J., et al., in Plasma Physics and Controlled Nuclear Fusion Research 1994 (Proc. 15th Int. Conf. Seville, 1994), Vol. 1, IAEA, Vienna (1995) 11.

A SUCCESSFUL METHOD TO PROMOTE CURRENT DRIVE EFFICIENCY ON THE HT-6M TOKAMAK

F.X. YIN, J. LI, B.N. WAN, Y.X. LIU, X. GAO,
J.R. LUO, Y.X. WAN, Y.G. SHAO, S.Y. ZHANG,
W. XU, F. YIN, X.Z. GONG, Y.X. JIE, Z.W. WU,
Y.F. LIANG, J.G. JIANG, S. LIU, N.C. LUO, M.J. WU,
Y.Q. HAN, D.Y. XUE, Y.P. ZHAO, J.Y. DING, X.K. YANG
Institute of Plasma Physics,
Academia Sinica,
Hefei, Anhui, China

Abstract

A SUCCESSFUL METHOD TO PROMOTE CURRENT DRIVE EFFICIENCY ON THE HT-6M TOKAMAK.

High current drive efficiency has been achieved on the HT-6M tokamak. A successful method has been found to promote the efficiency of lower hybrid current drive (LHCD). The key points are to control plasma impurities effectively and to utilize the synergy between LHCD and various heating approaches. Titanium gettering and boronization were used to reduce the impurities. The LHCD plasma was successfully heated by electron cyclotron resonance heating, edge ohmic heating and ion cyclotron resonance heating, and the current drive efficiency was increased considerably. The full current drive efficiency reached 1.8×10^{15} $cm^{-2} \cdot A \cdot W^{-1}$, which is 1.8 times higher than the JT-60 1989 scaling. The energy range of fast electrons measured by the hard X ray spectrometer is well beyond the tail achieved with LHCD only. The reason for the fast electron behaviour and the high drive efficiency is mainly the mode conversion at the ion–ion hybrid resonance layer to an ion Bernstein wave. The fraction of the fast wave converted to the ion Bernstein wave is more than 90% under the configuration of the HT-6M high field side launching structure, according to the modelling results. Direct off-axis electron heating was achieved by Landau damping. The same fraction of power was coupled to the electrons that contributes to the high current drive efficiency.

1. INTRODUCTION

Plasma current drive through use of a transformer, as performed in tokamaks, is not available for fusion reactors. Finding other methods to drive current is necessary. On the other hand, non-inductive techniques have already made it possible not only to drive the plasma current but also to make long pulse experiments. The techniques used in various tokamaks are tangential neutral beam current drive, fast wave current drive, lower hybrid wave current drive and so on.

Of these techniques, lower hybrid current drive (LHCD) has the highest current drive efficiency (3.4×10^{15} $m^{-2} \cdot A \cdot W^{-1}$, JT-60) in plasmas with the largest non-inductive current (3.6 MA, JT-60U), the longest current sustainment (70 min, TRIAM-1M) and the highest density ($\sim 10^{14}$ cm^{-3}, Alcator-C) achieved so far [1].

The current drive efficiency η_{CD} is defined as:

$$\eta_{CD} = \langle n_e \rangle R_p I_{CD}/P_{LH} \quad (1)$$

where $\langle n_e \rangle$ is the line average density, R_p is the major radius, I_{CD} is the plasma current driven by P_{LH}, and P_{LH} is the injected lower hybrid power. The product $\langle n_e \rangle R_p I_{CD}$ may be of the order of 10^{18} MA·cm^{-2} in a fusion reactor. To maintain this product by non-inductive current drive with the maximum efficiency presently observed ($\eta_{CD} \leq 4 \times 10^{15}$ cm^{-2}·MA·MW^{-1}), a current drive power of several hundred megawatts would have to be injected. This power is too large to satisfy the economic requirements of a reactor.

Finding a way to improve the current drive efficiency is very important. Synergies between various waves may be a good way. In JET experiments, synergistic effects between LHCD and ion cyclotron resonance heating (ICRH) have led to substantially improved current drive efficiencies, as high as 4.0×10^{15} cm^{-2}·A·W^{-1} [2].

HT-6M is a medium air core tokamak with a circular cross-section in which the plasma parameters are $R_p = 65$ cm, $a = 20$ cm, $B_T \approx 1.1$ T, $I_p \approx 70$ kA, $T_e = 500$–750 eV, $T_i = 200$–300 eV and $n_e = (0.5\text{–}4.0) \times 10^{13}$ cm^{-3}. In recent years we have carried out many plasma experiments on HT-6M, such as edge ohmic heating [3], Ti gettering and boronization [4], pump limiter operation and electron cyclotron resonance heating. Now lower hybrid wave and ICRH systems have been installed on HT-6M. It is found that the LHCD efficiency can be promoted by the synergy between LHCD and ICRH, with effective control of plasma impurities. The full current drive efficiency reaches 1.8×10^{15} cm^{-2}·A·W^{-1}.

2. HT-6M LHCD AND ICRH SYSTEMS

The lower hybrid wave system consists of a 120 kW magnetron and a multi-junction waveguide antenna that has an eight subwaveguide grill with $N_\parallel = 3.0 \pm 0.5$. The frequency has been fixed at 2.45 GHz. The wave electric field is nearly parallel to the magnetic field and the waveguide array generates the waves at the plasma boundary. The wave is damped by electron Landau damping, giving parallel energy to plasma electrons moving at the wave phase velocity ($\omega = k_\parallel v_\parallel$ or $v_\parallel = c/N_\parallel$). $N_\parallel = 3.0$, which means that the wave is resonant with 50 keV electrons in HT-6M. The accessibility condition is

$$N_\parallel^{acc} \approx 1.015B^{-1}n_e^{0.5} + [1 + n_e(1.03B^{-2} - 0.44f^2)]^{0.5} \quad (2)$$

$N_\parallel^{acc} \approx 2.4$ for HT-6M parameters.

The high power density ICRH system was successfully installed in HT-6M. A half-turn loop antenna was installed on the high field side of the torus. The

RF frequency is 15.5 MHz, which corresponds to a toroidal field of 1 T. The minority heating mechanism was chosen and D_2 working gas was used. More than 300 kW of RF power was injected into the plasma with less than 10% reflection in ICRH experiments. The ion temperature increased from 250 to 750 eV and the electron temperature from 600 to 780 eV.

3. CURRENT DRIVE RESULTS

Current drive experiments with lower hybrid waves have been carried out at line average densities between 0.7×10^{13} and 1.1×10^{13} cm^{-3}. The loop voltage decreases and the plasma current increases when the lower hybrid wave (40 kW of power) is launched into the plasma. Figure 1 shows a typical discharge. In this discharge the loop voltage decreases from 2.6 to 0.7 V and the plasma current increases from 20 to 40 kA. It is clear that the lower hybrid wave drives the current higher. The drive efficiency estimated according to Eq. (1) is $\sim 0.89 \times 10^{15}$ $cm^{-2} \cdot A \cdot W^{-1}$. Non-inductive current driven by higher injected power is over 70 kA in these experiments.

LHCD can be used to achieve long pulses. The plasma duration was extended from 80 ms in normal ohmic heating to 120 ms. This is a volt-second-saving discharge. LHCD is well adapted to this electron density phase, where the current drive efficiency is improved by the synergistic acceleration of the LHCD fast electrons by the loop voltage necessary to raise the current. These experiments show that lower hybrid waves generate fast electrons in the plasma.

Synergy with ICRH has been observed to accelerate fast electrons near the several hundred kiloelectronvolt range, and the current drive efficiency has been increased. Figure 2 shows a typical discharge. The current drive efficiency reaches 1.8×10^{15} $cm^{-2} \cdot A \cdot W^{-1}$. This is 1.8 times higher than the JT-60 $12\langle T_e \rangle (5 + Z_{eff})^{-1}$ scaling and about 1.5 times higher than the JET $\langle n_e \rangle \langle T_e \rangle (5 + Z_{eff})^{-1}$ scaling. This is because, when the power is launched using

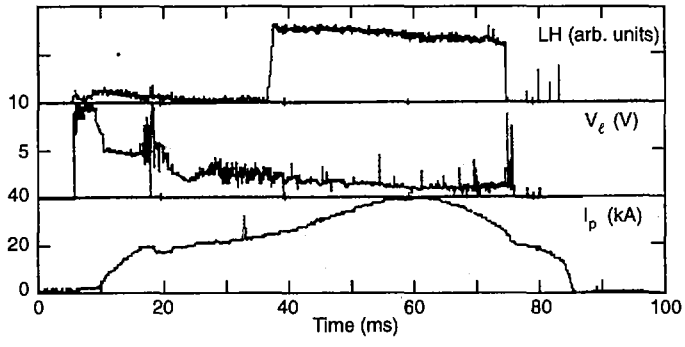

FIG. 1. Typical shot with LHCD only.

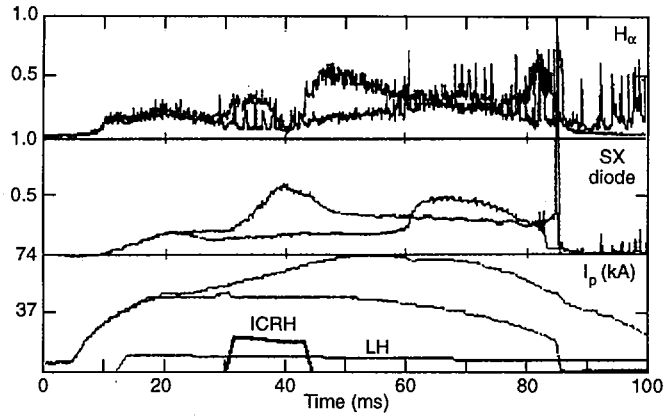

FIG. 2. Typical shot with high LHCD efficiency through synergy with ICRH.

antennas located on the high field side of the plasma, 100% of the power is mode converted to the ion Bernstein wave (IBW) when the wave reaches the mode conversion region.

To reach higher current drive efficiency, a key point is to control plasma impurities effectively. Titanium gettering and boronization are effective methods to achieve this on HT-6M. Z_{eff} decreased from 4.0 to 2.8 after Ti gettering and was further decreased to 1.7 by boronization. The density limit increased from 1.7×10^{13} to 5.0×10^{13} cm^{-3}. The H/(H + D) ratio was controlled in the range 10–15%. By using Ti gettering shot by shot, current drive efficiency improvement could clearly be observed.

4. ANALYSIS OF RESULTS

The present analysis shows that the observed efficiency of current drive with synergy between LHCD and ICRH is in good agreement with the relativistic theory of Karney and Fisch for Landau damped waves.

In a DH plasma, by lowering the relative concentration n_H/n_D, the relative distance between the ion–ion hybrid resonance layer ω_{ii} and ω_{cH} decreases. Thus including a small concentration of H in a D plasma locates the field resonance ω_{ii} in the neighbourhood of ω_{cH}, which provides a non-zero electric field on ω_{cH} and gives rise to a net fundamental cyclotron damping [5]. On the ion–ion hybrid layer, the fast wave, as it reaches ω_{ii}, converts to an IBW, with a dominant electrostatic behaviour. Since the half-turn loop antenna was installed on the high field side of the torus, 100% of the power is mode converted to the IBW when the fast wave reaches the mode conversion region. The appropriate choice of parameters (magnetic field, wave frequency, ion mixture composition) allows the power deposition to be located on or off the axis.

As we know, the lower hybrid wave drives a fast electron tail, parallel to B_T, from the thermal velocity to approximately its injection phase velocity v_φ^{LH}. If power from the IBW is superimposed, with a chosen phase velocity $v_\varphi^{IBW} > v_\varphi^{LH}$, the fast electron tail will extend up to v_φ^{IBW}. This synergistic effect considerably increases the LHCD efficiency, as it consists of a real deformation of the electron distribution towards higher parallel velocities. Evidence of strong electron acceleration has been observed from hard X ray measurements.

5. DISCUSSION AND SUMMARY

In HT-6M experiments we have obtained a current drive efficiency of 0.89×10^{15} cm$^{-2}\cdot$A$\cdot$W^{-1} with LHCD only and 1.8×10^{15} cm$^{-2}\cdot$A$\cdot$W^{-1} with synergy between LHCD and ICRH.

The current drive efficiency is one of the most important parameters in non-inductive current drive. In LHCD experiments in small machines, as the lower hybrid pulse length is limited, the effect of the inductive voltage due to the change in the internal inductance cannot be neglected. On the other hand, the confinement time of fast electrons produced by the lower hybrid wave is shorter than their slowing down time. Therefore some of the launched power must be lost through the fast electrons before they are thermalized. In these cases, a correct estimation of current drive efficiency according to Eq. (1) is very difficult.

ACKNOWLEDGEMENTS

This work is supported by Academia Sinica and the World Laboratory. The authors are grateful to the HT-6M group for their excellent work.

REFERENCES

[1] USHIGUSA, K., in Proc. Int. Summer School on Nuclear Fusion and Plasma Physics, World Scientific Publishing, Singapore (1995) 154.

[2] JACQUINOT, J., et al., Phys. Fluids B **4** (1992) 2111.

[3] LI, J., et al., in Plasma Physics and Controlled Nuclear Fusion Research 1994 (Proc. 15th Int. Conf. Seville, 1994), Vol. 1, IAEA, Vienna (1995) 249.

[4] LI, J., et al., paper presented at Tech. Comm. Mtg on Research Using Small Tokamaks, 1994.

[5] BECOULET, A., in Controlled Fusion and Plasma Physics (Proc. 23rd Eur. Conf. Kiev, 1996), Vol. 20C, European Physical Society, Geneva (1996).

RECENT RESULTS ON ELECTRON CYCLOTRON CURRENT DRIVE AND MHD ACTIVITY IN RTP

A.J.H. DONNÉ, F.C. SCHÜLLER, A.A.M. OOMENS,
M. DE BAAR, C.J. BARTH, M.N.A. BEURSKENS, F.M.A. BOX,
J.F.M. VAN GELDER, B.J.J. GROBBEN, B. DE GROOT,
J.M. HERRANZ, G.M.D. HOGEWEIJ, S.A. HOKIN[1],
J. HOWARD[2], C.A.J. HUGENHOLTZ, F.A. KARELSE,
J. DE KLOE, O.G. KRUIJT, S. KUYVENHOVEN, J. LOK,
N.J. LOPES CARDOZO, H.J. VAN DER MEIDEN, F.G. MEIJER,
A. MONTVAI, T. OYEVAAR, F.J. PIJPER, R.W. POLMAN,
J.H. ROMMERS, F. SALZEDAS, B.C. SCHOKKER, P.H.M. SMEETS,
C.P. TANZI, C.J. TITO, G.C.H.M. VERHAAG, E. WESTERHOF
FOM Instituut voor Plasmafysica 'Rijnhuizen',
Association Euratom–FOM,
Nieuwegein, Netherlands

Abstract

RECENT RESULTS ON ELECTRON CYCLOTRON CURRENT DRIVE AND MHD ACTIVITY IN RTP.

The RTP tokamak (R = 0.72 m, a = 0.164 m, $B_\phi < 2.5$ T, $I_p = < 150$ kA) is equipped with three gyrotrons (2 × 60 GHz, 180 kW, 100 ms each; 1 × 110 GHz, 500 kW, 200 ms) for electron cyclotron heating (ECH) and current drive (ECCD). The power from one of the 60 GHz gyrotrons is launched via an adjustable mirror from the high field side (HFS) in the 1X-mode. The power of both other gyrotrons is sent in perpendicularly to the toroidal magnetic field from the low field side (LFS). A comprehensive set of high-resolution multichannel plasma diagnostics is available to study the detailed behaviour of various plasma phenomena. First, recent diagnostic innovations are briefly discussed. Then, new physics results are presented for ohmic and EC heated plasmas. ECCD, slide-away discharges, discharges with a hollow temperature profile and MHD phenomena, including sawteeth and disruptions, are treated.

1. DIAGNOSTIC INNOVATIONS

The 20-channel heterodyne radiometer for studying electron cyclotron emission (ECE) in the 2nd harmonic X-mode has been extended with an antenna at the HFS, that is connected to a sweep-tuneable microwave source [1]. In this way the electron pressure profile, $p_e(r)$, can be deduced from the optical thickness profile, $\tau(r)$, measured by means of electron cyclotron absorption (ECA). By sweeping the source, ECE and ECA measurements are performed alternatingly during the discharge. After accounting for non-resonant effects (e.g. refraction,

[1] Royal Institute of Technology, Stockholm, Sweden.
[2] Australian National University, Canberra, Australia.

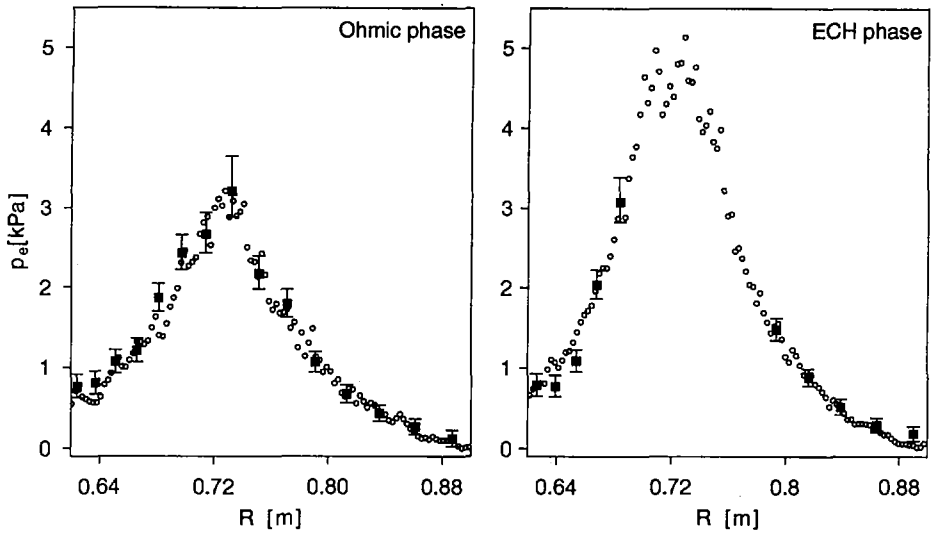

Fig. 1. Pressure profiles measured by ECA (full squares) and Thomson scattering (open circles) during the ohmic and the ECH phase of a discharge. During the ECH phase no information can be obtained with the central five channels since the plasma is optically thick for the corresponding frequencies.

scattering, mode conversion) a very good agreement is found between the p_e profiles measured with ECA and those obtained from Thomson scattering (see Fig. 1). Since the RTP plasmas are semi-opaque under most experimental conditions, the measured values for τ can be used to correct the $T_e(r)$ for finite optical thickness effects. Finally, by combining $p_e(r)$ determined from ECA with $n_e(r)$ from the 19-channel interferometer an electron temperature profile can be derived that is insensitive to non-thermal electron populations.

The HFS horn allowed comparison between ECE received at the HFS and the LFS. The difference between the two spectra is directly related to the existence of a suprathermal electron population. Simulation with Fokker-Planck codes including particle diffusivity and EC emissivity showed excellent agreement with the experimental LFS/HFS spectra.

The far-infrared interferometer was recently extended with a polarimeter option [2]: the Faraday rotation is measured along 19 vertical chords. Three CO_2-pumped far-infrared lasers are employed to simultaneously measure the refractive indices for the two polarisation eigenstates in the plasma. The time resolution of the device is determined by the signal-to-noise ratio only and can be as high as 100 kHz. A resolution of 10 kHz and an accuracy of better than 0.2° have already been obtained. The interferometer/polarimeter has been successfully used to study the dynamic behaviour of the electron density and current density profiles at higher densities, as a response to externally induced perturbations like ECH and pellet injection. Unfortunately, at the low density needed for significant ECCD the error bars became too large to extract reliable information on the distribution of the driven current.

2. ELECTRON CYCLOTRON CURRENT DRIVE (ECCD)

ECCD is accomplished by preferentially heating electrons moving in one toroidal direction. Their reduced collisionality results in a toroidal current. In RTP ECCD has been achieved in the down-shifted resonance scheme. The dependence of I_{ECCD} on the location of the resonance layer and on the toroidal launch angle has been measured. The results are compared with Fokker-Planck simulations which take into account radial transport of non-thermal electrons, and which have been carried out for the parameters covered by the experiments.

The linearly polarised waves are obliquely launched from the HFS via a flat adjustable mirror, located halfway the equatorial plane and the top. The launch angles range from -30° to +30° off-perpendicular (standard settings) in the toroidal direction. In the poloidal plane the power is directed downwards towards the magnetic axis. Most experiments have been done with a power of about 130 kW and pulse lengths of up to 100 ms, I_p = 60 kA, $T_e(0) \approx 1.5$ keV, and $\langle n_e \rangle \approx (1.0 - 1.3) \times 10^{19}$ m^{-3}; B_ϕ was varied between 2.1 and 2.5 T. In some discharges a second gyrotron was used to achieve higher temperatures of the target plasma ($T_e(0) \approx 3$ keV). The density was feedback controlled.

In RTP — apart from a few experiments with constant inductively coupled power [3]— the total plasma current, I_p, is kept constant by a feedback circuit. The established ECCD is not large enough to drive I_p completely, and so the loop voltage is only reduced below its ohmic value. The EC driven currents have been derived from a comparison of the residual loop voltages for co- and counter-drive discharges: $I_{ECCD} = [(V_{cntr} - V_{co}) / (V_{cntr} + V_{co})] (I_p - I_{boot})$, where V_{cntr} and V_{co} represent the loop voltages during counter- and co-drive, respectively; the bootstrap current, I_{boot}, is small and has been taken zero. The experimental results are summarised in Fig. 2.

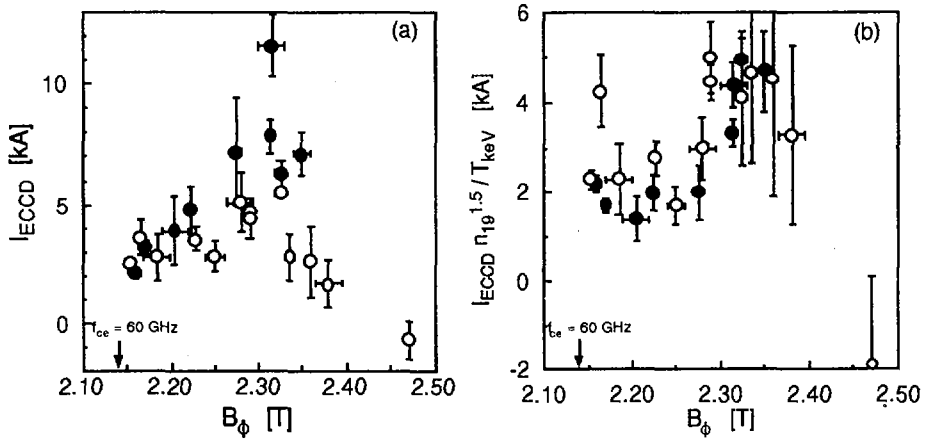

Fig. 2. Experimental I_{ECCD} as a function of B_ϕ for 30° off-perpendicular injection. Open and full circles: One and two gyrotrons respectively; (a) I_{ECCD}; (b) I_{ECCD} normalised with a scaling factor $n^{1.5}/T$.

Linear theory predicts for the scaling with temperature and density $I_{ECCD} \sim T_e/n_e$; the Fokker-Planck simulations suggest for the RTP regime an even stronger influence of the density: $I_{ECCD} \sim T_e/n_e^{1.5}$, where the temperature scaling may be complicated further by a dependence on the magnetic field on axis. The temperature effect is clearly demonstrated in Fig. 2a. The maximum driven current (11 kA) was obtained at $B_\phi = 2.33$ T for $T_e \approx 3$ keV and $\langle n_e \rangle \approx 1.0 \times 10^{19}$ m^{-3}. This is consistent with the largest possible resonance downshift at the plasma centre while still retaining efficient central heating. For one gyrotron the maximum temperature reached is lower ($T_e \approx 1.5$ keV) and the I_{ECCD} shows a maximum (≈ 6 kA) at $B_\phi \approx 2.30$ T. For higher values of the magnetic field (2.46 T) the off-axis heating leads to a decreased central temperature during ECH — this resembles 2X-mode off-axis heating results with the 110 GHz gyrotron [4] — and, apparently, to a small negative current. The dependence on B_ϕ is in qualitative agreement with predictions (see Fig. 3a).

Current drive results at the non-standard injection angles ±23° and ±11° indicate a decrease in efficiency as theory predicts, but error bars are too large for a quantitative comparison with the numerical predictions given in Fig. 3a. Results at the different plasma currents of 40 and 80 kA are, so far, not distinguishable from 60 kA results.

Fokker-Planck calculations, without inclusion of radial transport, predict the local generation of high-energetic electron populations. In many cases, these non-thermal electrons may locally even account for an equal or even much higher energy density than the thermal plasma. This is shown in Fig. 3b for a case with both LFS O-mode heating and HFS X-mode ECCD. The large population of energetic electrons is reflected by a strong increase of $T_e = (2/3\ \varepsilon/n_e)$, where ε is the energy density. When radial transport is included in the calculations with a relatively large anomalous diffusion coefficient $D = (1 + 3\ (r/a)^2)$ m^{2}s^{-1}, the

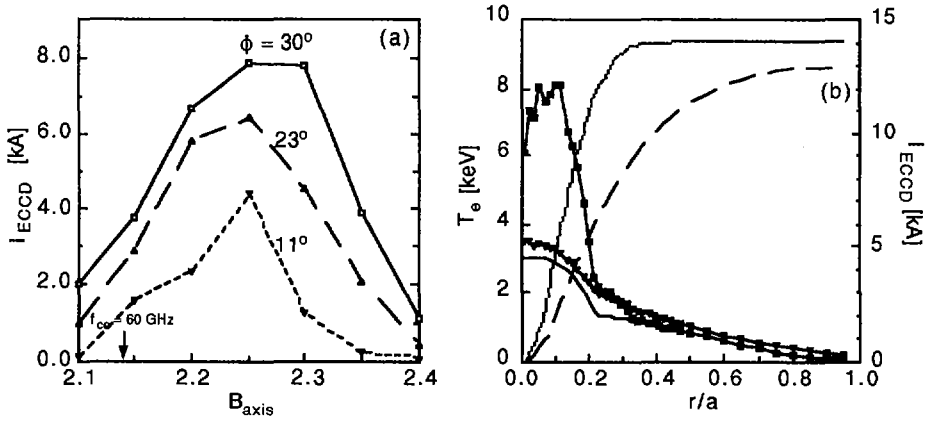

Fig. 3. (a) Simulated I_{ECCD} as function of B_ϕ for 11°, 23°, and 30° off-perpendicular injection. Plasma parameters: $T_e(0) = 1.5$ keV, $n_e(0) = 1.7 \times 10^{19}$ m^{-3}, EC power: 135 kW X-mode. (b) Simulated profiles of "temperature" (i.e. 2/3 of energy density divided by the particle density) and integrated EC driven current profile without (squares, dotted curve) and with (triangles, long-dashed curve) the inclusion of anomalous radial diffusion. The same density and ECH X-mode power were used as in (a), but additionally 120 kW of ECH O-mode power (LFS) was included. The full curve without symbols gives the input T_e-profile.

highly localised non-thermal electrons are redistributed such that globally the contribution of non-thermal electrons is almost the same and the total EC driven current decreases only slightly (by at most 20%). In these calculations the anomalous inward pinch was chosen such that the density profile was not affected. As mentioned in Sect. 1 these types of Fokker-Planck calculation lead also to accurate predictions of ECE-spectra measured both from LFS and HFS side.

3. SLIDE-AWAY DISCHARGES

A comprehensive study of slide-away (SA) discharges was carried out [5], with emphasis on the diagnosis of the non-thermal electron population using ECE (both X and O-mode, and including HFS measurements). Also the influence of ECH on a slide-away discharge was investigated (see Fig. 4). It was shown that at $n_e(0) < n_{c1} = 1 \times 10^{19}$ m^{-3} the discharge is always in SA, whereas it never is at $n_e(0) > n_{c2} = 2 \times 10^{19}$ m^{-3}. At the intermediate densities, application of a short ECH pulse always brings the discharge in SA. The intensity of the emission at the Lower Hybrid frequency was measured and shown to be linearly proportional to the run-away birth rate over four orders of magnitude. The high intensity of the measured ECE spectra requires a large ($\approx$ 5%) population of trapped electrons, with energies up to 30 keV, as compared to 1 keV for the bulk plasma.

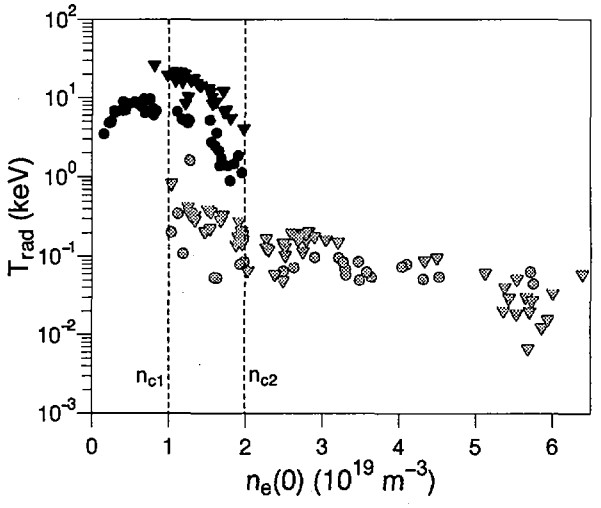

Fig. 4. The LFS (circles) and HFS (triangles) ECE X-mode radiation temperatures at 105.5 GHz indicate the slide-away (black) and the normal ohmic (grey) regimes.

4. HOLLOW TEMPERATURE PROFILES

Steady-state hollow T_e-profiles are reproducibly produced by strong off-axis ECH (110 GHz) in high-density ($n_e(0) > 4.0 \times 10^{19}$ m^{-3}), low current ($I_p \leq 80$ kA) discharges (see Fig. 5a). The steady-state hollow T_e-profile leads to a hollow current density profile and reversed shear in the region inside the resonance

position r_{res}. A new equilibrium is reached typically after 50 ms. Local power balance analysis showed that the net electron heat flux is very small inside r_{res} and may even be directed outwards, i.e. up the gradient of T_e [4]. This points to the existence of an electron heat flux not driven by ∇T, which is confirmed by the propagation of heat pulses induced by modulated ECH [9].

The transition from ohmic to reversed shear profiles has been investigated in more detail. A bifurcation into two levels of confinement appears (see Fig. 5b). The subtlety of the bifurcation is exemplified by one discharge which hesitates and then crosses over from the low to the high confinement branch. The pressure profile for the high confinement branch exhibits a steep gradient near the deposition radius, which is an indication for a region of improved confinement.

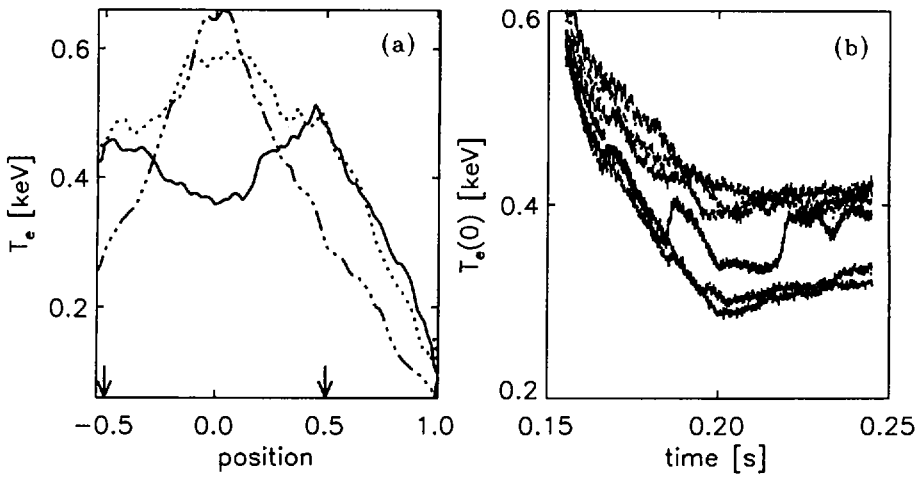

Fig. 5. (a) Evolution of $T_e(r)$ as measured with Thomson scattering in a series of identical discharges. Shown are profiles measured at -1 ms (dotted line), 5 ms (dash-dotted line) and 40 ms (solid line) with respect to the time ECH is switched on. The deposition radius is indicated by arrows. (b) Evolution of $T_e(0)$ as measured by ECE in six near identical discharges after switch on of ECH at t = 150 ms, showing the bifurcation in the confinement.

In all other parts of the plasma the gradients in the pressure profiles for the two branches are rather similar.

In many discharges in the high confinement branch vigorous MHD activity occurs. A fast sawtooth-like relaxation of T_e occurs in a small region around the heat deposition region (rise phase 1 ms, crash phase 200 μs). Moreover, a slower reconnection process takes place throughout the central part of the plasma (rise phase typically 10 ms, crash phase 500 μs). An explanation is sought in terms of double tearing modes. The q-profile derived from $T_e(r)$ after 50 ms, when a new equilibrium is reached, shows a pronounced minimum near the ECH deposition radius with q just below 3. The central value of q is just above 4. The fast modulations are attributed to a double-tearing mode involving the two q=3 surfaces near the deposition radius, whereas the slower process is interpreted as a reconnection process involving both q= 3 surfaces and the central q=4 surface.

5. SAWTOOTH ANALYSIS

Measurements on sawtoothing RTP plasmas with the five-camera 80-channel soft x-ray tomography system were interpreted with a new analysis method that makes use of special functions of the emissivity that are conserved under ideal MHD action [7]. The aim of the study was to find out whether sawteeth in RTP follow the ideal MHD behaviour or whether they show features of reconnection. In particular the influence of the plasma resistivity on the development of the sawtooth instability was investigated. For this purpose a series of discharges in which the magnetic Reynolds number, S, was systematically varied between $(0.8 - 3.5)\times 10^5$ has been analysed. With increasing values of S, the m = 1 precursor instability of the sawtooth crash changes from a clear magnetic reconnection behaviour towards a combination of ideal and resistive MHD behaviour. The transition does not seem to be influenced by the absolute pressure value.

6. DISRUPTIONS

A systematic study of the evolution of the T_e, n_e and j-profiles during the thermal and current quench phases of disruptions has been started. The preliminary results seem to confirm earlier observations reported by the DIII-D team [8], that the j-profile only changes at the end of the energy quench. The disruptions were initiated by a rather fast current rise followed by a density ramp-up. Under apparently the same external conditions most of the discharges show strong MHD activity and disrupt at a low density, while in the other discharges the density can be ramped up almost twice as high without major MHD activity. Subtle differences in current penetration must be the cause of this branching. In Fig. 6a

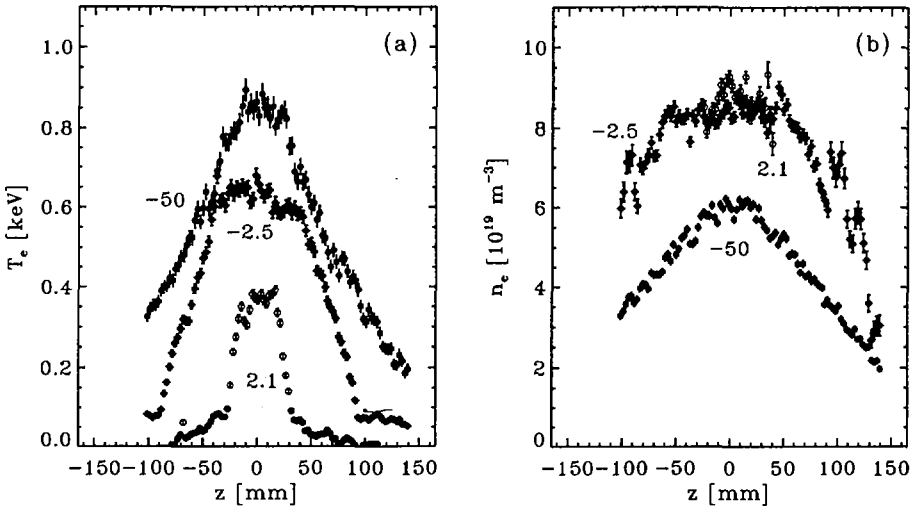

Fig. 6. (a) T_e -profiles 50 and 2.5 ms before the quench of a major disruption of an Ohmic $q_a = 4.2$ discharge and one taken 2.1 ms after the quench during an inward movement of the plasma. (b) The corresponding n_e-profiles.

profiles of T_e are shown at -50, -2.5 and +2.1ms (the start of the current quench is at t =0). The huge m=2 island enforces a cold area between 0.6 < r/a < 1.0, whilst simultaneously an m=1 structure flattens the T_e-profile for r/a < 0.3. Figure 6b shows the corresponding n_e profiles. Due to a vigorous inward movement with 7.5 cm the radius of the plasma column is reduced to 10 cm and the (vertical) Thomson scattering observation chord traverses only the outer part. It should be noticed that the electrons in the centre still have a temperature of at least 400 eV in contrast to ECE measurements which indicate a complete collapse.

ACKNOWLEDGEMENTS

This work was performed under the Euratom-FOM Association agreement with financial support from NWO and Euratom.

REFERENCES

[1] GELDER, J.F.M. van, et al., in Electron Cyclotron Emission and Electron Cyclotron Heating (Proc. 9th Joint Workshop Borrego Spring, 1995), World Scientific, Singapore (1995) 239.
[2] ROMMERS, J.H., HOWARD, J., Plasma Phys. Control. Fusion (in press).
[3] WESTERHOF, E., et al., in Controlled Fusion and Plasma Physics (Proc. 22nd Eur. Conf. Bournemouth, 1995), Vol. 19C, Part I, European Physical Society, Geneva (1995) 385.
[4] HOGEWEIJ, G.M.D., et al., Phys. Rev. Lett. **76** (1996) 632.
[5] SCHOKKER, B.C., PhD thesis, Eindhoven Technical University (1996).
[6] De BAAR, M.R., in Controlled Fusion and Plasma Physics (Proc. 23rd Eur. Conf. Kiev, 1996), Vol. 20C, European Physical Society, Geneva (1996).
[7] TANZI, C.P., et al., Rev. Sci. Instrum. **66** (1995) 537.
[8] TAYLOR, P.L., et al., in Controlled Fusion and Plasma Physics (Proc. 22nd Eur. Conf. Bournemouth, 1995), Vol. 19C, Part IV, European Physical Society, Geneva (1995) 49.
[9] HOGEWEIJ, G.M.D., et al., IAEA-CN-64/AP1-9, these Proceedings, Vol. 1, p. 655.

LOCAL CURRENT PROFILE MODIFICATION IN TOKAMAK REACTORS IN VARIOUS RADIOFREQUENCY RANGES

O. DUMBRAJS[1], J.A. HEIKKINEN[2], S.J. KARTTUNEN[2], T. KIVINIEMI[1], T. KURKI-SUONIO[1], M. MANTSINEN[1], T.J.H. PÄTTIKANGAS[2], K.M. RANTAMÄKI[1], R.R.E. SALOMAA[1], S.K. SIPILÄ[1]
TEKES–Euratom Fusion Association

[1] Department of Technical Physics, Helsinki University of Technology

[2] VTT Energy

Espoo, Finland

Abstract

LOCAL CURRENT PROFILE MODIFICATION IN TOKAMAK REACTORS IN VARIOUS RADIOFREQUENCY RANGES.

The authors have evaluated the magnitude of localized current modification for intense off-axis RF heating in nearly burning reactor plasmas. The modification consists of the bootstrap current perturbation and of the current driven by RF momentum transfer and asymmetric heating. The results are used in a transport code to study the dynamics of current generation and its response to source frequency tuning.

1. INTRODUCTION

The current density can be modified with localized RF power deposition, *e.g.*, by ion or electron cyclotron heating. Current modification is beneficial for stabilizing MHD modes, and may even enhance confinement by reverse shear generation. The fast frequency tuning of RF sources can also provide a novel way to control the power deposition profile in the plasma. To investigate the limits of such frequency tuning for moving the current generation region, the current rise and decay times have to be evaluated and compared with the tuning rate. At the same time, for strong wave absorption the characteristics of the current and possible problems related to power launching have to be assessed. Since the RF heating can be well localized, the resulting perturbation in the bootstrap current may become large. This is because the radial gradient of the local perturbation in the plasma stress is steep, even though the perturbation is much smaller than the background pressure.

2. CURRENT DRIVE MODEL

Models for the RF-induced bootstrap current have been recently developed for ICRF heated minority ions [1], ECRF-heated electrons [2], and for LH-heated alpha particles [3]. In order to obtain the total driven current, the bootstrap current perturbation due to the heated particles is added to the current driven by momentum transfer and asymmetric heating. For ECCD and LHCD, there exist analytical expressions for the driven current in terms of power absorption[4], but for the minority-ion current drive a full kinetic simulation is needed because of the finite-ion-orbit effects [5].

ICRF model. To calculate the ICRF power absorption and the driven current, toroidal Monte Carlo guiding-center code ASCOT [6] is used. The calculations include the self-consistent effects of a minority ion distribution in velocity and configuration space, finite orbit effects, radial neoclassical diffusion, and current generation in a tokamak. In the simulations, the ICRF operators

$$\Delta v_\perp = \frac{Z_i}{2M}\tau e^{-z/L_{IC}} e^{i\delta}\left[E_{IC+}J_{n-1}\left(\frac{k_{I\perp}v_\perp}{\Omega}\right) + E_{IC-}J_{n+1}\left(\frac{k_{I\perp}v_\perp}{\Omega}\right)\right] \quad (1)$$

$$\Delta p_\phi = \frac{k_\phi}{\omega}\Delta W \quad (2)$$

for the change in the ion (charge Z_i, mass M) perpendicular velocity and toroidal momentum, respectively, are applied. Here, ΔW is the change in the particle energy, k_ϕ is the toroidal wave number, Ω is the minority ion cyclotron frequency, z is the vertical coordinate from the equatorial plane, and the phase angle δ is a random number between 0 and 2π. The change in $v_\perp$ is calculated only when the ion passes through the ion cyclotron resonance. This incremental change is proportional to the resonance duration time τ calculated in Ref. [7] for different orbit topologies. The left-hand and right-hand components $E_{IC\pm}$ of the wave field are evaluated either from a 1-D FEM full wave code, or modelled analytically.

ECRF model. For ECRH, the quasilinear diffusion coefficient D for the electron-microwave interaction is evaluated from a model [2,8], where the finite width of a microwave beam is accounted for. Here, ordinary wave mode propagation and a fundamental cyclotron resonance with electrons are assumed. The diffusion coefficient is limited by the relativistic heating out, giving the maximum $D = (c^2\Delta k_{||}v_{||}/L\omega v_\perp)^2/(2\tau_1)$, where $\Delta k_{||}$ is the spread in the parallel wavenumber spectrum, $\tau_1 = \tau 2\pi Rq/L$, R is the major radius, q is the safety factor, and L is the microwave beam width. In the present model the wave power absorption density is given by $p_{RF} = \int_0^c 4\pi m[\partial(v^3\hat{D})/\partial v]fdv$, with distribution function $f(r,v)$ obtained from the isotropic Fokker–Planck equation $\partial f/\partial t = (1/v^2)(\partial/\partial v)[v^2\hat{D}(\partial f/\partial v)] + (\partial f/\partial t)_{coll}$, where $(\partial f/\partial t)_{coll}$ denotes the electron-electron collision operator, v is the total electron velocity, and $\hat{D} = (1/2)\int_{-1}^{1}(1-\mu^2)Dd\mu$ is the pitch averaged diffusion coefficient with $\mu = v_{||}/v$.

Transport model. The transport code ASTRA[9] is used to follow the temporal evolution of plasma temperature, inductive electric field, and the thermal bootstrap current. The power input to the code is the absorbed power density given by the RF models, and the current input consists of the currents driven by the asymmetric wave heating and momentum transfer also given by the RF models. Because the transport model operates in the fluid limit, the bootstrap current due to the ICRF heated fast ion tail given by the ASCOT simulations is also included in the current input. In the cases considered, no significant fast electron tail formation is found for ECRF heating. Because of the localized heating of thermal electrons, however, a bidirectional perturbation in the bootstrap current,similar to that in the ICRF minority heating, can arise. For thermal diffusion, a combination of anomalous thermal conductivities for the Alcator and η_i modes [10] has been applied.

3. RESULTS

Minority ion current drive. In the Monte Carlo simulations, reactor-scale parameters are used: $R = 7.75$ m, $a = 2.8$ m, $B = 6.2$ T, $I = 15$ MA, $T_{e,i} = 20$ keV, and $n_e = 0.84 \times 10^{20}$ m^{-3}. Equal deuterium and tritium concentrations are assumed. A hydrogen minority concentration $n_H = 2 \times 10^{18}$ m^{-3} is also included. Here, B is the toroidal magnetic field on the axis, I is the total plasma current, and T_i is the ion temperature for each ion species. The density and temperature profiles are given by $n, T = n_0, T_0 \times (1 - r^2/a^2)^{\alpha_n, \alpha_T}$ with $\alpha_n = \alpha_T = 0.5$; the current density profile is parabolic. The wave parameters for the reference case are $E_{IC+} = 3000$ V/m, $|E_{IC-}/E_{IC+}| = 0$, $k_\perp = 30$ m^{-1}, $k_{||} = 0$, and $L_{IC} = 1$ m. The cyclotron resonance layer, $\omega = \Omega$, intersects the equatorial plane at $r_{IC} = 0.8$ m either inboard or outboard. The $k_{||} = 0$ -case is considered to eliminate current sources other than the diamagnetic one.

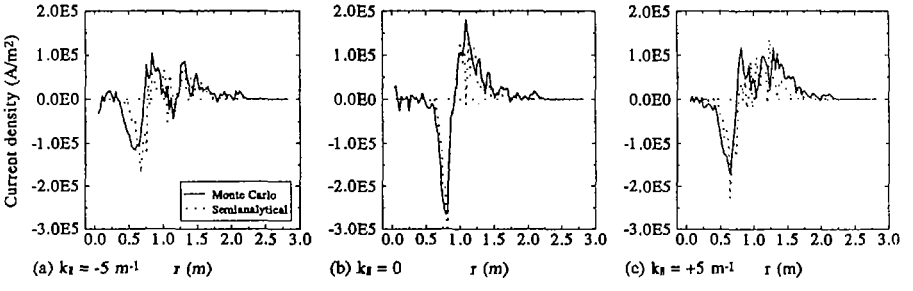

FIG. 1. Minority ion current density profile obtained from the Monte Carlo simulation for $k_\parallel = 0$ and for $k_\parallel = \pm 5$ m^{-1} versus outboard resonance position. The analytical result is shown for comparison.

Figure 1 shows the current density of the hydrogen ions obtained from the Monte Carlo simulation for various values of $k_{||}$. The total integrated current increases for increasing $k_{||}$. However, only small changes in the maxima or minima of the current density around the cyclotron resonance are seen in this parameter range, thus indicating that the diamagnetic bidirectional current density seen for $k_{||} = 0$ dominates the shape and magnitude of the current profile also for $k_{||} \neq 0$. An analytical estimate for the current profile, calculated from the trapped fast ion contribution to the bootstrap current given by Eq. (2) in Ref. [11], is also shown. A satisfactory agreement in both magnitude and profile shape is found. The pronounced diamagnetic effect in the present example is due to the strong fast ion tail generation typical for minority heating. There is also evidence that the diamagnetic effect has played a dominant role in recent minority current drive experiments in JET [5].

Dynamics of current generation. Figure 2 shows the results from an ASTRA simulation of ECRF heating for a reactor-scale tokamak. Here, a fixed density profile has been assumed. The electron cyclotron resonance (in the low velocity limit) is taken to be at $r = 0.8$ m, and the beam radius is $L = 0.1$ m. Fifty 2 MW beams with oblique propagation ($k_{||} = 1000$ m^{-1} with $\delta k_{||} = 60$ m^{-1}) are assumed. The power absorption is localized near $r = 0.9$ m. The plasma profiles are shown for $t = 10$, 100, 200 ms, and 400 ms, as well as 10 ms after a rapid frequency change from 156 GHz to 149 GHz at $t = 200$ ms. The electron (and ion) temperature grows locally near the absorption regime and leads to the formation of a bidirectional bootstrap current on the time scale of tens of milliseconds characteristic to the heating rate. The bootstrap current

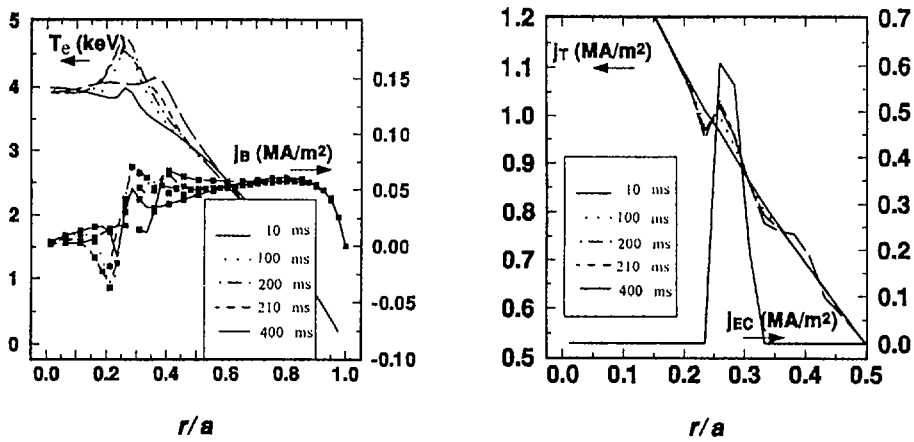

FIG. 2. Evolution of plasma temperature and current density profiles obtained from the ASTRA transport simulation for ECCD.

density j_B is found to be a significant fraction of the total driven current j_T. The time scale for the corresponding local changes in the total current is $50-100$ ms, restrained by induction. Similarly, the total current density profile doesn't seem to respond to the fast frequency change until about 200 ms after the change. This is partially due to the slow decay of the temperature perturbation, and partially due to the inductive delay. At the lower frequency, the current density profile is found to be strongly deformed at $r = 1.3$ m corresponding to the electron cyclotron resonance layer at that frequency.

For ICRF heating the evolution of the profiles is found to be similar. Here, absorption of 100 MW of ICRF power at $k_{||} = 5$ m^{-1} is assumed. The other parameters are the same as in Fig. 1. Fifty percent of the fast ion tail energy is assumed to be deposited on electrons. Only the minority absorption is considered. A frequency change of $\Delta f = 4$ MHz at $t = 200$ ms corresponds to an abrupt change in the resonance position from $r = 0.8$ m to $r = 1.2$ m. Here, the fast ion bootstrap current is included in the driven RF current j_{CD}, while the bootstrap current j_B includes only that of the background plasma. The latter current evolves as in Fig. 2. For both the minority current drive and ECCD, a current drive efficiency of about 0.005 A/W is found, and thus the total current response and response to the resonance position change are similar for both cases.

Figure 3 presents the evolution of the ECCD case without a frequency jump but including additional LH heating of 100 MW. The LH launching parameters have been optimized for electron current drive. Interestingly, the local ECRH heating tends to attract the LH power deposition to the EC resonance region.

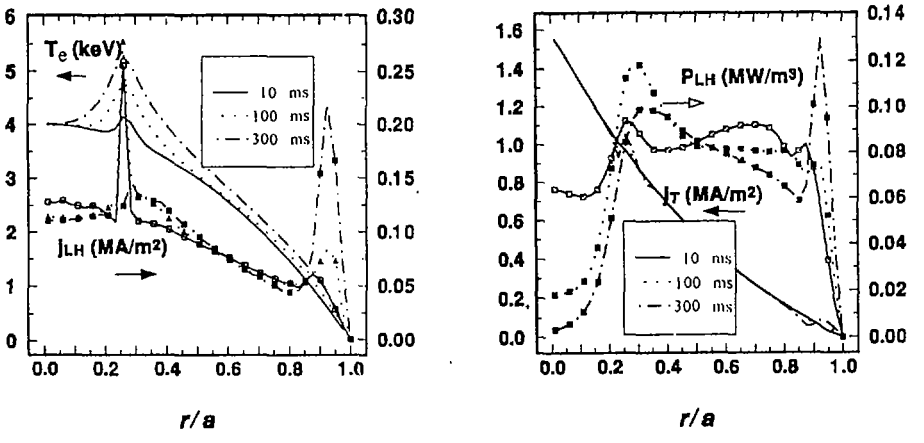

FIG. 3. Evolution of plasma temperature and current density profiles obtained from the ASTRA transport simulation for synergic ECCD and LHCD.

The increase in the local temperature by ECRH at $r = 0.9$ m, although relatively small, appears to increase the local LH-wave absorption and, consequently, localize the LH-driven current there. This mechanism might be useful for applying LHCD in synergy with either ICRH minority or mode conversion current drive, or with ECCD. The observed synergy appears to be lost when the electron temperature grows too much and, consequently, the LH absorption regime moves suddenly to the peripheral region.

Generation of Fast Electrons near the LH Grill. The absorption of LH waves and the generation of fast particles near the wave guide mouths have been investigated with particle-in-cell (PIC) simulations[12]. For this purpose, a model of an LH grill was included in the two-dimensional electrostatic PIC code XPDP2. The generation of hot electrons has been investigated in the near field of the grill where the spectrum contains high mode numbers, $n_{||} \simeq 20$.

Near the grill mouth the spectrum contains extra peaks at $n_{||} \simeq 9.6$ and $n_{||} \simeq 17$ in addition to the peak at $n_{||} \simeq 1.9$. The spectrum changes rapidly

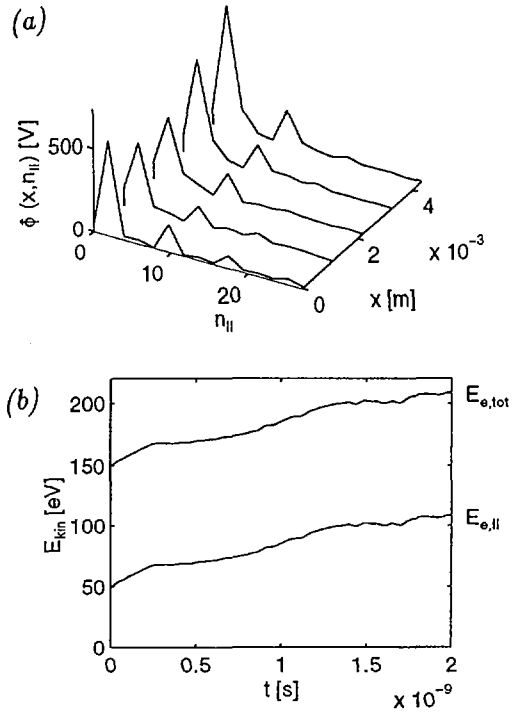

FIG. 4. (a) Absorption of the LH field near the grill mouth. (b) Increase in total ($E_{e,tot}$) and parallel ($E_{e,\parallel}$) kinetic energy of electrons near the grill mouth.

as the wave penetrates into the plasma because of the strong absorption of the $n_{||} \simeq 17$ -mode in the region $x < 2$ mm. For $T_e = 100$ eV, the parallel phase velocity of this mode is only $v_{ph||} \simeq 2.9 v_e$, where v_e is the thermal velocity. The absorption of the field near the grill mouth is illustrated in Fig. 4(a).

The modes at $n_{||} \simeq 17$ accelerate bulk electrons which are further accelerated by the peak at $n_{||} \simeq 9.6$ having a parallel phase velocity of $v_{ph||} \simeq 5.2 v_e$. The main peak at $n_{||} \simeq 1.9$ has such a high phase velocity ($v_{ph||} \simeq 26 v_e$) that it does not interact with the electrons. The time evolution of the average electron energy in the region $0 < x < 1.5$ mm is illustrated in Fig. 4(b). In a short time of only 2 ns, the average parallel energy increases by 100 %. At this time, part of the electrons have kinetic energies of 7 keV.

The fast electrons accelerated by the near field of the LH grill may cause high heat fluxes on connected components[13,14].

4. SUMMARY

For intense, local off-axis RF current drive, the local heating of the plasma may create a bidirectional local perturbation in the bootstrap current profile. For the ICRF minority current drive, the generation of a fast ion tail around the ion cyclotron resonance creates a diamagnetic source of current which can dominate the conventional minority current drive for high heating powers and small minority concentrations. Analytical expressions are found to give a satisfactory agreement with the current density profiles obtained from a fully toroidal Monte Carlo simulation of ion heating by RF waves. According to the transport analysis presented here, the achieved local perturbations in the plasma stress can be sufficiently large to produce a significant bootstrap current perturbation – provided that such modifications remain MHD stable. A stability analysis is therefore needed in the future.

Considering fast tuning of the power deposition, a strict time constraint of about 100 ms is observed for the response in the total current modification. The frequency tuning of high-power microwave sources can be accomplished in several ways. For example, in the case of a gyrotron it has been shown theoretically [15] that the frequency of a high-power gyrotron could be changed very fast (in microseconds), in steps of a few GHz, by changing the accelerating and modulation voltages. This requires a very sofisticated power supply. In Ref. [16] this method has been demonstrated experimentally, although for a low-power gyrotron. Another way of tuning the gyrotron frequency is to change the magnetic field. In the experiment of Ref. [17] it was demonstrated that this way it was possible to step-tune a high-power coaxial gyrotron between 116 GHz and 164 GHz. Also, output powers of around 1 MW have been achieved. Unfortunately, due to the large inertia of the magnetic field, this process may take several minutes. Much faster tuning should be possible in a smaller frequency range of a few GHz by keeping the main magnetic field constant and varying only an additional magnetic field produced by an extra small solenoid.

It is much easier to tune the frequency of a free electron laser where only the accelarating voltage needs to be changed. For example, the high-power (1 MW) free electron laser developed for fusion purposes [18] offers a fast continuous tuning in the entire frequency range from 130 GHz to 260 GHz.

REFERENCES

[1] HEIKKINEN, J.A., et al., Plasma Phys. Control. Fusion **38** (1996) 2063.
[2] HEIKKINEN, J.A., et al., in Controlled Fusion and Plasma Physics (Proc. 23rd Eur. Conf. Kiev, 1996), Vol. 20C, European Physical Society, Geneva (1996) paper E051.
[3] HEIKKINEN, J.A., SIPILÄ, S.K., Nucl. Fusion **37** (1997) 835.
[4] FISCH, N.J., Rev. Mod. Phys. **59** (1987) 175.
[5] HELLSTEN, T., et al., Phys. Rev. Lett. **74** (1995) 3612.
[6] HEIKKINEN, J.A., et al., Comput. Phys. Commun. **76** (1993) 215;
HEIKKINEN, J.A., SIPILÄ, S.K., Phys. Plasmas **2** (1995) 3724.
[7] O'BRIEN, M.R., et al., Nucl. Fusion **26** (1986) 1625.
[8] KOVANEN, M., CORE, W.G.F., J. Comput. Phys. **105** (1993) 14.
[9] PEREVERZEV, G.V., et al., Rep. IPP-5/42, Max-Planck-Inst. für Plasmaphysik, Garching (1991).
[10] ROMANELLI, F., et al., Nucl. Fusion **26** (1986) 1515.
[11] HEIKKINEN, J.A., SIPILÄ, S.K., in Controlled Fusion and Plasma Physics (Proc. 23rd Eur. Conf. Kiev, 1996), Vol. 20C, European Physical Society, Geneva (1996) paper E031.
[12] RANTAMÄKI, K.M., et al., ibid.
[13] GONICHE, M., et al., ibid.
[14] HARRIS, J.H., et al., Europhys. Conf. Abstr. **19C**, Part IV (1995) 397.
[15] DUMBRAJS, O., NUSINOVICH, G.S., IEEE Trans. Plasma Sci. **20** (1992) 452.
[16] IDEHARA, T., et al., Phys. Plasmas **1** (1994) 1774.
[17] PIOSCZYK, B., in Proc. 21st Int. Conf. on Infrared and Millimetre Waves, Berlin, 1996, p. AM2.
[18] VERHOVEN, A.G.A., et al., in Proc. 3rd Int. Workshop on Strong Microwaves in Plasmas, Nizhnij Novgorod, 1996, p. S9.

REACTOR STUDIES

(Session G1)

Chairperson

V. GOLANT
Russian Federation

ASSESSMENT OF TOKAMAK PLASMA OPERATION MODES AS FUSION POWER PLANTS: THE STARLITE STUDY

F. NAJMABADI, ARIES TEAM
Department of Electrical and Computer Engineering
and
Fusion Energy Research Program,
University of California,
San Diego, La Jolla, California,
United States of America

Abstract

ASSESSMENT OF TOKAMAK PLASMA OPERATION MODES AS FUSION POWER PLANTS: THE STARLITE STUDY.

During the past several years, the ARIES/Starlite Team has investigated the feasibility and potential features of tokamak fusion power plants. The research also has aimed at identifying both the trade-offs that lead to the optimal regime of operation for a tokamak power plant and the critical plasma physics and technology issues. During the initial phase of the Starlite study, an assessment of various tokamak plasma operation modes as candidates for fusion power plants was made. Five different regimes of operation were considered: (1) steady state operation in the first stability regime, e.g. ARIES-I; (2) pulsed plasma tokamak operation, e.g. Pulsar; (3) steady state operation in the second stability regime, e.g. ARIES-II and ARIES-IV; (4) steady state operation with reversed shear profile; and (5) low aspect ratio tokamaks (spherical tokamaks). The extent of the plasma physics database as well as the performance as a power plant were considered. On the basis of the above analysis, the Starlite project has chosen reversed shear operation for its reference design. The paper summarizes the results of this assessment.

1. INTRODUCTION

The demand for substantial increases in electric power supplies has been forecast for decades. Fusion offers the promise of an abundant energy source that is not tied to national resources and will only minimally affect the environment. However, fusion will be a new technology in the energy marketplace; hence, it must demonstrate clear advantages over other technologies in use at the time in order to offset the inherent technical risk of a new technology, or it will never be widely endorsed. During the past several years, the ARIES Team has investigated the feasibility and potential features of tokamak fusion power plants [1–4]. On the basis of this research, the Starlite project was initiated to develop the goals and requirements of fusion demonstration and commercial power plants and to assess the potential of tokamaks to meet these goals and objectives. In addition, the research has aimed at identifying both the trade-offs that lead to the optimal regime of operation for a tokamak power plant and the critical plasma physics and technology issues.

TABLE I. TOP LEVEL REQUIREMENTS AND GOALS FOR COMMERCIAL AND DEMONSTRATION FUSION POWER PLANTS

Element	Demo	Commercial
Must use technologies to be employed in commercial power plant	Yes	Yes
Net electric output must be greater than	75% commercial	N/A
Cost of electricity (COE) must be competitive (in 1995 mill/kW·h)	80 (goal) 90 (required)	65 (goal) 80 (required)
No evacuation plan required for any credible accident: Total dose at site boundary	<1 rem	<1 rem
Must not generate radioactive waste greater than	Class C	Class C
Must demonstrate that public day to day activity is not disturbed	Yes	Yes
Must not expose workers to a higher risk than other power plants	Yes	Yes
Must demonstrate robotic maintenance of power core	Yes	Yes
Must demonstrate routine operation with less than (x) unscheduled shutdowns per year including disruptions	1	1/10
Must demonstrate a closed tritium fuel cycle	Yes	Yes
Must demonstrate operation at partial load conditions at	50%	50%

On the basis of interaction and advice from the US electric utilities and industry, a set of criteria for fusion power is derived [5–7]. A similar set of criteria has been developed by the Electric Power Research Institute (EPRI) fusion working group [8]. These criteria and associated top level requirements and goals (Table I) can be divided into three general categories: (1) cost; (2) safety and environmental features; and (3) reliability, maintainability and availability.

Top level requirements and goals for cost of electricity (COE) were adopted for the Starlite project on the basis of the estimated cost of competitive sources of electricity at the time of introduction of fusion in the marketplace [9]. These requirements and goals for COE also are in line with projections of future power plant costs based on energy forecasting models [10]. Safety and environmental requirements are included to circumvent the difficulties experienced by fission and, to some degree, faced by fossil fuels in the future. Fusion should be easy to license by the national and local regulating agencies and should be able to gain public acceptance. Fusion power plants should only generate low level waste (i.e. with a waste storage time less than a few hundred years). Realization of the full safety and environmental potential of fusion will also help fusion to achieve a cost advantage over other sources of electricity. Fusion power plants can be designed to achieve these criteria only through the use of low activation material and care in design. However, these requirements result in stringent constraints on the subsystem choices and the design. Lastly, it should be demonstrated that Demo and commercial power plants can achieve the

necessary degree of reliability. The conceptual design studies can partially address this issue (e.g. by including maintenance considerations in the design). To a large degree, this criterion should be addressed in the development path of fusion power. Today's experiments are not intended to provide detailed engineering data to support the design, construction and operation of a power plant.

During the initial phase of the Starlite study, an assessment of various tokamak plasma operation modes as candidates for fusion power plants was made. Five different regimes of operation were considered: (1) steady state operation in the first stability regime, e.g. ARIES-I [1]; (2) pulsed plasma tokamak operation, e.g. Pulsar [4]; (3) steady state operation in the second stability regime, e.g. ARIES-II and ARIES-IV [3]; (4) steady state operation with reversed shear profile; and (5) low aspect ratio tokamaks (spherical tokamaks). The extent of the plasma physics database as well as the performance as a power plant were considered. In parallel, several options for engineering design (e.g. choice of structural material, coolant, breeder for first wall and blanket) have been developed and assessed. In each area, this assessment was aimed at investigating (1) the potential to satisfy the requirements and goals, and (2) the feasibility, e.g. critical issues and credibility (i.e. the degree of extrapolation required from the present database).

In the next section, a brief summary of each physics regime of operation will be given (Sections 2 to 6). In order to provide a common basis for comparing the costs of power plants, a similar blanket and shield concept has been used, which is described in Section 7. This assessment has led to the choice of the reversed shear as the tokamak plasma operation regime and a self-cooled lithium design with vanadium alloy blanket and in-vessel structures for detailed design (ARIES-RS study). Detailed accounts of this research can be found in the Interim Starlite [6] and the ARIES-RS reports [7] and in Refs [5, 11–17].

2. FIRST STABILITY STEADY STATE REGIME

In the late 1980s, operation at a high bootstrap current fraction as the approach to steady state operation was proposed by ARIES [1] and SSTR [18] studies simultaneously and independently. In order to reduce the current drive power, the plasma current is reduced while the bootstrap fraction is maximized. In the first stability regime, this can be accomplished by operating with a moderately high plasma aspect ratio ($A \equiv 1/\epsilon \sim 4.5$) and low plasma current ($I_p \sim 10$ MA) at a relatively high poloidal beta ($\epsilon\beta_p \sim 0.6$). Detailed MHD and current drive analyses have shown that the maximum bootstrap fraction in this class is about $\sim 70\%$, with most of the driven current located near the magnetic axis, leading to current drive powers of about 100 MW delivered to the plasma.

This mode of operation, however, leads to a low value of plasma beta, i.e. $\beta \cong 2\%$, because the important parameter $\epsilon\beta_p$ (which determines the bootstrap fraction) is related to the achievable plasma β by

$$(\epsilon\beta_p)(\beta/\epsilon) \leq (\beta_N/20)^2 S \quad (1)$$

where $S = (1 + \kappa^2)/2$ is the plasma shape factor, κ is the plasma elongation, and β_N is defined by $\beta \leq \beta_N(I_p/B_T a_p)$. For a conventional first stability configuration, optimally shaped current and pressure distributions and sufficient triangularity in the cross-sectional shape, this equation must be satisfied with a Troyon coefficient of $\beta_N \simeq 3.5$. If a high bootstrap fraction (f_{BS}) is desired for steady state operation (such as ARIES-I), one can reduce the current or raise q_*, resulting in a lower β. In order to optimize the equilibrium and bootstrap current profile, these discharges operate with moderately elevated central q_0. For values of $q_0 \simeq 1.3$, the discharges are stable to kink modes without conducting wall. High plasma β values can be obtained by further increasing q_0, but these discharges would require a conducting wall nearby and plasma rotation to stabilize the kink modes.

There is an ample experimental database for this regime; however, operation in discharges with durations longer than the current diffusion time is needed.

3. FIRST STABILITY PULSED PLASMA REGIME

Since the recirculating power for inductive current drive is small, it is argued that pulsed tokamak power plants avoid the problem of non-inductive current drive: the constraint on β_p is removed, and the plasma β can be higher. However, inductive current drive also imposes certain constraints on the plasma operating regime. First, because large and expensive poloidal field coils are needed to supply inductive flux, these devices also tend to be optimized at moderately high aspect ratio, low current and a moderately high bootstrap current fraction. Second, because the loop voltage is constant across the plasma, the current density (induced and bootstrap) and pressure profiles are set for a given pair of density and temperature profiles. In principle, because the current density profiles cannot be tailored, both the normalized β value and the bootstrap fraction are limited ($\beta_N \sim 30$, $f_{BS} \lesssim 40\%$). As a result, the plasma β for optimum pulsed plasma operation is only marginally ($\sim 25\%$) larger than that of a steady state plasma.

In addition, many critical engineering problems have to be resolved. For example, cyclic fatigue and eddy currents induced in the structural support of the toroidal field (TF) coils become major issues limiting the maximum toroidal field (e.g. the superconducting coil technology that yields a maximum field of 16 T in a steady state power plant leads to a maximum field of about 13 T in a pulsed plasma system). This decrease in the toroidal field strength more than offsets the gains in plasma β values for a pulsed device, i.e. even though the plasma β is higher in a pulsed device, the fusion power density is lower. Another key issue is the energy storage as the heat transport system cannot tolerate rapid changes in the thermal power of the power plant during recharge of the OH transformer. Conventional designs for energy storage lead to large and expensive systems. An innovative,

sensible heat storage system in the outer shield was developed for the Pulsar design [4], which has removed the cost of energy storage as a barrier to a pulsed tokamak power plant.

As a whole, even on the assumption of identical reliability and unit cost for the components, pulsed power plants are substantially more costly than steady state plants. On the other hand, this regime of operation is supported by the main body of tokamak experimental data.

4. SECOND STABILITY STEADY STATE REGIME

As is seen from Eq. (1), the only way to increase the plasma β and still have a large bootstrap current fraction is to increase the value of β_N. It may be possible to violate the Troyon limit if certain conditions are met such as those provided by an elevated central safety factor ($q_0 \geq 2$) [19] as in the ARIES-II/IV designs, reversed magnetic shear [20, 21] or very low aspect ratios [22]. In addition to these requirements, stabilization of the external kink mode in these regimes requires a close fitting conducting wall and sufficient plasma rotation [23].

Second stability operation (i.e. operation at elevated values of the central safety factor) allows a higher bootstrap current fraction than first stability operation. While the bootstrap current can become as large as the total plasma current (or larger), the bootstrap current density profile is different from that needed for equilibrium and stability. As a result, current should be driven both on the axis and at the plasma edge while cancellation of part of the bootstrap current in the middle of the plasma is required. Essentially, the optimum configuration has a bootstrap current fraction of $\sim 90\%$. Compared to the steady state, first stability optimum regime, the current drive power is somewhat smaller and the plasma β is about twice as large (a conducting wall for stabilization of kink modes is required). The critical physics issues for this regime of operation include startup and access to the second stable operating point, as well as the complexity of the current drive system. In addition, there is very little experimental evidence for this mode of operation.

5. REVERSED SHEAR STEADY STATE REGIME

Reversed shear plasma operation combines the best features of steady state, first and second stability modes. There is a much better match between the bootstrap current density profile and that needed for equilibrium and stability, and therefore higher values of plasma β can be achieved with moderate current drive power and a less complicated current drive system. The primary characteristics of a reversed shear plasma are a hollow density profile, a non-monotonic safety factor (q) profile and relatively peaked pressure profiles. The hollow current density profile gives rise to a safety factor profile which initially decreases from its value at the plasma centre

to a minimum value and then rises to its value at the plasma edge. It is the initial decrease in the q value away from the magnetic axis that provides the negative magnetic shear, which is responsible for stability to $n \rightarrow \infty$ ballooning modes. It also appears that, in this regime, the plasma transport is suppressed and a more peaked pressure profile consistent with the high β and high bootstrap current fraction can be sustained. There is ample theoretical research on this regime, and some experimental database is available. An extensive experimental exploration of this regime of operation is currently under way.

Analyses have shown that, to zeroth order, the cost of the device is independent of the plasma aspect ratio in the range of $A \sim 3$–4 (lower plasma β at the higher A is compensated for by higher toroidal field strength on-axis as well as lower current drive power). In the Starlite study, an aspect ratio of $A = 4$ was chosen as a result of engineering considerations. At this aspect ratio and with a plasma current of ~ 11 MA, the maximum theoretical plasma β is $\sim 5.5\%$, and the bootstrap current fraction is $\sim 90\%$. Non-inductive current drive is required to supplement the bootstrap current on-axis (e.g. a fast wave), at the plasma edge (e.g. a lower hybrid wave) and in mid-plasma. While several candidate current drive options exist for driving the current in mid-plasma (e.g. a high frequency fast wave, or mode conversion), the database for these current drive schemes is very small.

6. LOW ASPECT RATIO (SPHERICAL) TOKAMAK

Operation at a low plasma aspect ratio (low aspect ratio or spherical tokamaks) is another approach to achieving high plasma β and a high bootstrap current fraction. Unfortunately, the low aspect ratio of plasma rules out the use of superconducting toroidal field coils as there is not enough space for a shield in the inboard. Therefore, a low aspect ratio tokamak requires equilibria with very high plasma β (in order to minimize the Joule losses in the normally conducting centrepost). In addition, since the plasma current is very large (~ 30 to 40 MA) in a low aspect ratio tokamak, a very high bootstrap current, which is also well aligned to the equilibrium current profile, is essential (to minimize the current drive power). Precise alignment of the bootstrap current density with the equilibrium current density is essential. Detailed current drive analysis has shown that, even for a bootstrap current fraction of 95%, the current drive power can easily exceed several hundreds of MW, because the mismatch is usually at the plasma edge and mid-plasma, where the current drive systems are inefficient.

Since the power requirements associated with the edge current drive have turned out to be so high, we have concentrated on a series of equilibria that require only central current drive. We impose the constraint that the surface averaged parallel current density should be a linear function of the poloidal flux ψ, interior to the point where the linear profile is tangent to the bootstrap current profile and equal to the bootstrap current outside this point (Fig. 1). This constraint completely specifies the

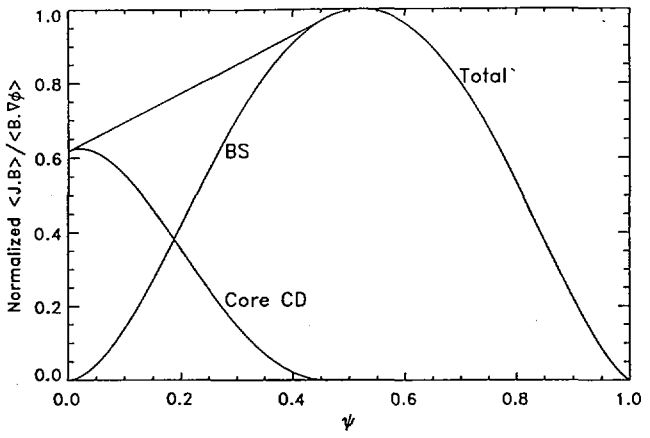

FIG. 1. Parallel currents as functions of the poloidal flux, ψ, for a high bootstrap fraction spherical tokamak equilibrium which does not require edge current drive.

profiles and ensures that the first derivatives of the equilibrium quantities are continuous everywhere. An extensive scan of MHD equilibria led to an equilibrium with A = 1.25, $\beta \simeq 40\%$ and over 99% of the plasma current is self-driven (the current drive power is ≤ 10 MW). This equilibrium has an elongation of 3.0, which will certainly necessitate a vertical position control system. We note that these cases would require a conducting wall to stabilize the external kink mode.

In the case noted above, preliminary system studies and engineering analyses were conducted. A major conclusion of the system studies was that, even for cases with low current drive power requirements, there was still significant recirculating power (i.e. a recirculating power fraction of ~ 0.6) associated with the resistive losses in the copper centrepost and return legs of the toroidal field coils. Because of the high recirculating power fraction, the low aspect ratio tokamak is quite sensitive to the choice of plasma β, the design of the centrepost and a detailed analysis of the current drive requirements. Other studies suggest lower values of the recirculating power fraction in low aspect ratio power plants.

The spherical tokamak offers unique features and is currently vigorously pursued in the physics community. However, the level of analysis has not reached the stage needed to permit a sound assessment of this concept. Many critical issues have to be resolved such as the sensitivity of the current drive power requirements to variations in plasma profiles, the centrepost design, the startup, the design of in-vessel components subject to high heat and particle loads, etc. The true potential of a low aspect ratio tokamak power plant can only be assessed after a comprehensive design study.

7. ASSESSMENT

A system assessment of the above five tokamak plasma regimes has been performed [6, 12]. In order to provide a common basis for comparing the costs of power plants, a similar blanket and shield concept has been used which uses vanadium alloy as structural material of first wall, blanket and divertor, and liquid lithium as the breeder, which is a modification of the ARIES-II fusion core design. It should be noted that it is not clear whether such a design can be utilized in a spherical tokamak (i.e. most probably, the performance of the thermal power system would be lower because of the higher wall loading and the presence of water as

TABLE II. PARAMETERS FOR THE FIVE STARLITE POWER PLANT CANDIDATES

	FS	PU	RS	SS[a]	LAR
Plasma aspect ratio, $A = R/a_p$	4.0	4.0	4.0	4.0	1.25
Major radius, R (m)	7.96	8.68	5.04	6.40	5.00
Plasma minor radius, a_p (m)	1.99	2.17	1.26	1.60	4.00
Plasma elongation, κ_X	1.81	1.80	1.99	2.03	3.40
Plasma triangularity, δ_X	0.71	0.50	0.69	0.67	0.55
Cylindrical safety factor, q_*	3.77	2.40	2.37	4.60	3.54
Central safety factor, q_0	1.3	0.7	2.8	2.0	2.9
Stability parameter, $\epsilon\beta_p$	0.54	0.32	0.56	1.22	1.14
Normalized beta, β_N (%)	2.88	2.70	4.76	5.28	6.42
Beta parameter, β/ϵ (%)	8.12	10.00	21.24	12.17	45.36
Confinement ratio, τ^*_{He}/τ_E	10.0	10.0	10.0	10.0	10.0
Ignition parameter, $\beta\tau_E/a_p^2$ (%·s/m^2)	0.78	2.18	4.17	1.35	11.05
ITER-89 scaling multiplier, H	1.71	2.38	2.40	2.47	3.02
Normalized confinement multiplier, H/q_*	0.45	0.99	1.01	0.54	0.85
Plasma current, I_p (MA)	12.6	15.0	10.3	7.72	40.1
Bootstrap current fraction, f_{BS}	0.57	0.34	0.89	>1	0.997[b]
Current drive efficiency, γ_B (10^{20} A·W^{-1}·m^{-2})	0.56	NA	2.02	0.49	34.2
Current drive power to plasma, P_{CD} (MW)	236.6	0	64.7	199.1	7.3
On-axis toroidal field, B_T (T)	8.99	7.46	7.35	8.37	1.77
Peak field at TF coil, B_{TF} (T)	16.0	13.1	15.7	15.9	14.8
Normalized heat flux, P_{HEAT}/R (MW/m)	71.2	29.5	71.3	89.0	124.2
Recirculating power fraction, $(1/Q_E)$	0.29	0.06	0.13	0.33	0.63
COE (mill·kW^{-1}·h^{-1})	99.7	130.2	69.7	92.6	116.0

[a] This design is not optimized to the lowest COE.

[b] Includes diamagnetic current.

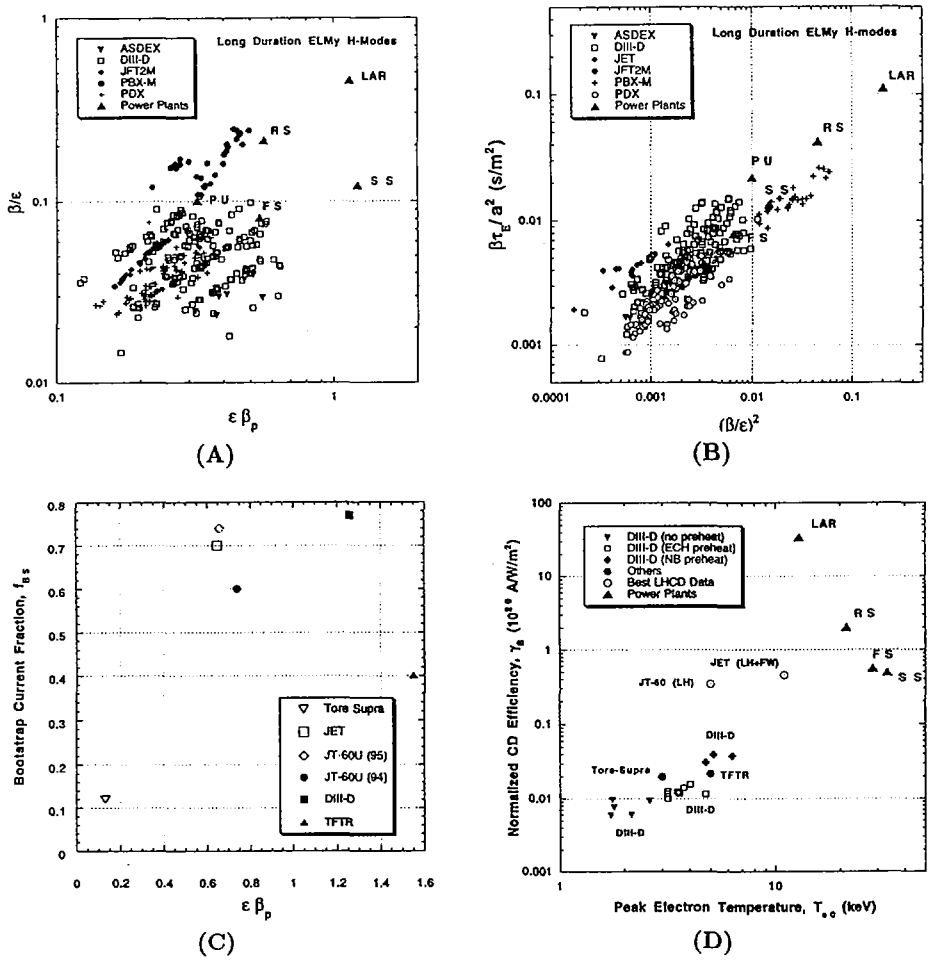

FIG. 2. (A) MHD figures of merit for long pulse ELMy, H mode discharges in several existing devices. (B) Energy confinement figures of merit for a number of existing tokamaks and the Starlite fusion power plants (data provided by Stan Kaye, PPPL). (C) Large tokamak experiments displaying substantial bootstrap fraction at high poloidal beta. Note that the poloidal beta definitions vary; plasma conditions (collisionality, density gradient, impurity content, etc.) also vary. (D) Fast wave current drive experimental database on DIII-D [25], Tore Supra [26] and TFTR [27]; best data point for lower hybrid current drive on JT-60 [28] and for lower hybrid and FWCD synergy on JET [29]. The five Starlite fusion power plant options (FS, PU, RS, SS and LAR) are also shown.

centrepost coolant). In addition, we have utilized a maintenance scheme for radial removal sectors (similar to those of the ARIES-IV design [3]). This integrated sector arrangement eliminates in-vessel maintenance operations and provides a very sturdy continuous structure able to withstand large loads. The penalty is the increased size of the TF coils needed to allow adequate space for sector removal. Lastly, in order to minimize unscheduled interruptions of plant operation, all designs operate at 90% of the maximum theoretical β in order to avoid plasma disruption. The major parameters of the five Starlite candidates are shown in Table II.

In addition to economic performance, an assessment of the maturity of each concept was made. To do so, several figures of merit were identified [6, 24]. The MHD figures of merit are β/ϵ and $\epsilon\beta_p$, as they indicate progress towards high β discharges with a high bootstrap current fraction. The current drive figure of merit is defined as $\gamma_B = (\bar{n}_e/10^{20})\, I_p R/P_{CD}$, which is the conventional measure of the current drive efficiency, but with the total plasma current appearing to account for bootstrap effects. The energy confinement figures of merit are chosen to be $\beta\tau_E/a^2$ as a function of $(\beta/\epsilon)^2$ to indicate progress towards discharges with high energy confinement time and high plasma β. Figure 2 (see Refs [25–29]) shows the existing tokamak database in two dimensional parameter spaces of these figures of merit. The five Starlite candidates are also shown.

An assessment of the five tokamak physics regimes of operation was made on the basis of economic performance as summarized in Table II and of the maturity of the database as summarized in Fig. 2. The first stability pulsed plasma and steady state regimes are closest to the present database. Of course, these regimes should be demonstrated at long pulse discharges with burning plasmas. On the other hand, the economic performance of pulsed plasma operation is poor. First stability steady state did not achieve the economic requirements for the Starlite project. High field TF coils can improve the attractiveness of this regime of operation. The second stability regime has a better economic performance but the experimental database for this regime is very small. The database for the spherical tokamaks is not mature, and, in addition, many critical issues remain. Detailed design studies are needed before the true potential of a spherical tokamak power plant can be assessed. The reversed shear of operation offers the best economic performance. The database for this regime, while small, is growing rapidly. As a result of the superior economic performance and the growing experimental and theoretical database, the Starlite project has chosen the reversed shear as the reference plasma operation regime for the ARIES-RS design [7].

ACKNOWLEDGEMENTS

Institutions involved in the Starlite study, in addition to the University of California at San Diego, are Argonne National Laboratory, General Atomics, Idaho National Engineering Laboratory, Los Alamos National Laboratory, Massachusetts

Institute of Technology, McDonnell Douglas Aerospace Co., Princeton Plasma Physics Laboratory, Raytheon Engineers and Constructors, Rensselaer Polytechnic Institute and the University of Wisconsin-Madison.

REFERENCES

[1] NAJMABADI, F., et al., The ARIES-I Tokamak Fusion Reactor Study — The Final Report, Rep. UCLA/PPG-1323, California Univ., Los Angeles, CA (1991); also CONN, R.W., in Plasma Physics and Controlled Nuclear Fusion Research 1990 (Proc. 13th Int. Conf. Washington, DC, 1990), Vol. 3, IAEA, Vienna (1991) 659.

[2] NAJMABADI, F., et al., The ARIES-III D-^{3}He Tokamak Reactor Study — The Final Report, Rep. UCLA/PPG-1323, California Univ., Los Angeles, CA (to be published); also NAJMABADI, F., et al., in Fusion Engineering (Proc. IEEE 14th Symp. San Diego, 1991), IEEE No. 91CH3035-3, IEEE, Piscataway, NJ (1992) 213.

[3] NAJMABADI, F., et al., The ARIES-II and -IV Second-Stability Tokamak Fusion Power Plant Study — The Final Report, Rep. UCLA/PPG-1461, California Univ., Los Angeles, CA (to be published); also NAJMABADI, F., et al., in Plasma Physics and Controlled Nuclear Fusion Research 1992 (Proc. 14th Int. Conf. Würzburg, 1992), Vol. 3, IAEA, Vienna (1993) 295.

[4] NAJMABADI, F., et al., The PULSAR Study — A Pulsed-Tokamak Fusion Power Plant, Rep. UCSD-ENG-003, California Univ., San Diego, CA (1996).

[5] NAJMABADI, F., ARIES TEAM, in Technology Fusion Energy (Proc. ANS 12th Top. Mtg Reno, NV, 1996); Fusion Technol. (in press).

[6] NAJMABADI, F., et al., The Starlite Project — Assessment Phase Report, Rep. UCSD-ENG-005, California Univ., Los Angeles, CA (1996).

[7] NAJMABADI, F., et al., The ARIES-RS Reversed-Shear Tokamak Fusion Power Plant Study, Rep. UCSD-ENG-005, California Univ., Los Angeles, CA (1997).

[8] KASLOW, J., et al., Criteria for Practical Fusion Power Systems — Report from the EPRI Fusion Panel, Rep. EPRI-BR-104469, Electric Power Research Institute, Palo Alto, CA (1994).

[9] MILLER, R., et al., in Fusion Engineering (Proc. IEEE 16th Symp. Champaign, 1995), IEEE No. 95CH35852, IEEE, Piscataway, NJ (1995).

[10] CLARKE, J., ibid.

[11] MILLER, R.L., in Technology of Fusion Energy (Proc. ANS 12th Top Mtg Reno, NV, 1996); Fusion Technol. (in press).

[12] BATHKE, C.G., et al., ibid.

[13] TILLACK, M.S., et al., ibid.

[14] SZE, D.-K., et al., ibid.

[15] BROMBERG, L., et al., ibid.

[16] EL-GUEBALY, L.A., BATHKE, C.G., et al., ibid.

[17] EL-GUEBALY, L.A., KHATER, H.Y., et al., ibid.

[18] SEKI, Y., et al., Concept Study of the Steady-State Tokamal Reactor (SSTR), Rep. JAERI-M-91-081, Japan Atomic Energy Research Inst., Tokyo (1991); also SEKI, Y., in Fusion Engineering (Proc. IEEE 13th Symp. Knoxville, TN, 1989), IEEE No. 89CH2820-9, IEEE, Piscataway, NJ (1990).

[19] RAMOS, J.J., Phys. Fluids B **3** (1991) 2247.

[20] OZEKI, T., et al., in Plasma Physics and Controlled Nuclear Fusion Research 1992 (Proc. 14th Int. Conf. Würzburg, 1992), Vol. 2, IAEA, Vienna (1993) 187.

[21] KESSEL, C.E., et al., Phys. Rev. Lett. **72** (1994) 1212.

[22] MENARD, J., et al., Bull. Am. Phys. Soc. **40** (1995) 1655.

[23] BONDESON, A., WARD, D.J., Phys. Rev. Lett. **72** (1994) 2709.
[24] MAU, T.K., in Fusion Engineering (Proc. IEEE 16th Symp. Champaign, 1995), IEEE No. 95CH35852, IEEE, Piscataway, NJ (1995).
[25] DeGRASSIE, J.S., et al., in Radio Frequency Power in Plasmas (Proc. 11th Top. Conf. Palm Springs, CA, 1995) 173. The data point at T_{e0} = 6.3 keV is unpublished and was provided by C.C. PETTY.
[26] EQUIPE TORE SUPRA (presented by X. LITAUDON), in Radio Frequency Power in Plasmas (Proc. 11th Top. Conf. Palm Springs, CA, 1995). Data point from R.J. GOLDSTON.
[27] ROGERS, J.H., PPPL, personal communication (1995).
[28] IMAI, T., et al., in Plasma Physics and Controlled Nuclear Fusion Research 1990 (Proc. 13th Int. Conf. Washington, DC, 1990), Vol. 1, IAEA, Vienna (1991) 645.
[29] JET TEAM (presented by C. GORMEZANO), in Plasma Physics and Controlled Nuclear Fusion Research 1992 (Proc. 14th Int. Conf. Würzburg, 1992), Vol. 1, IAEA, Vienna (1993) 587.

THE SPHERICAL TORUS APPROACH TO MAGNETIC FUSION DEVELOPMENT*

R.D. STAMBAUGH, V.S. CHAN, R.L. MILLER,
P.M. ANDERSON, C.B. BAXI, R.W. CALLIS, H.K. CHIU,
S.C. CHIU, C.B. FOREST, R. HONG, T.H. JENSEN,
L.L. LAO, J.A. LEUER, Y.R. LIN-LIU, M.A. MAHDAVI,
A. NEREM, P.A. POLITZER, R. PRATER, M.J. SCHAFFER,
D.L. SEVIER, T.S. TAYLOR, A.D. TURNBULL, C.P.C. WONG
General Atomics,
San Diego, California,
United States of America

Abstract

THE SPHERICAL TORUS APPROACH TO MAGNETIC FUSION DEVELOPMENT.

The low aspect ratio tokamak or spherical torus (ST) approach offers two key elements needed for an attractive magnetic fusion development path: a low cost, low power, small size market entry vehicle and a strong economy of scale in larger devices. In their studies of the ST approach, the authors found a very small device (A = 1.4, major radius about 1 m, a similar size to the DIII-D tokamak) that would produce ~800 MW thermal power and 160 MW net electric power, and would have a gain, defined as Q_{PLANT} = gross electric power over recirculating power, of ~1.7. Such a device would have all the operating systems and features of a power plant and would therefore be acceptable as a pilot plant. At about double the linear dimension of the pilot plant, the authors find 4 GW thermal power plants with an economically viable Q_{PLANT} = 4–5 but which remain a factor of 3 smaller than superconducting tokamak power plants. Large ST power plants might be able to burn the advanced fuel D-He^3 if the copper toroidal field coil can be replaced with a superconducting toroidal field coil and suitable shield.

1. INTRODUCTION

The advantages of the spherical tokamak approach have been discussed for many years [1,2]. In recent years, interest in the ST approach has grown rapidly, spawning a number of workshops [3] and a number of new experimental machine proposals [4–6]. Reference [7] is a valuable review of the field. Some studies projecting the ST approach to burning plasma devices have appeared [8,9].

The ST approach minimizes the size of a tokamak power core by discarding components from the inner side of the plasma: no inboard blanket or shield, no inboard poloidal coil (PF) systems, no Ohmic heating (OH) solenoid, resulting in low aspect ratio tokamaks, with aspect ratio A generally less than 1.5. The only customary tokamak component that remains is a single turn copper toroidal field (TF) coil centerpost. Consequently, the ST shrinks to the absolute minimum size and cost fusion system that is still a tokamak.

* Work partially supported by US Department of Energy grant DE-FG03-95ER54309 and GA internal R&D funding.

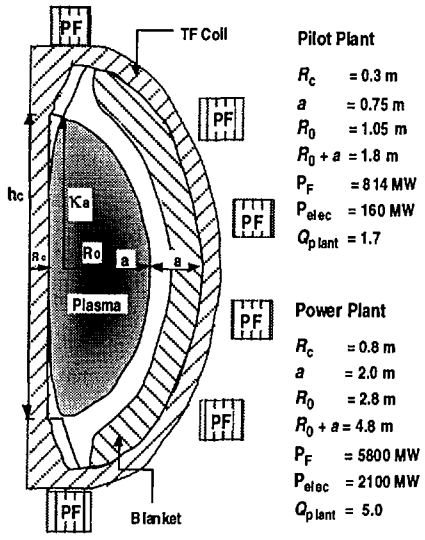

FIG. 1. An ST power plant is 2–3 times the linear dimension of an ST pilot plant. Both cases are for A = 1.4, neutron wall loading at the blanket 8 MW/m², β_T = 62%, β_p = 1.48, f_{bs} = 0.9, κ = 3.0.

The key to the ST approach is that the beta values made possible by the combination of high elongation and low aspect ratio are sufficiently high that limits on the neutron wall loading of the blankets determine the machine size. The fusion power produced far exceeds the Ohmic losses in the copper TF coil. With no OH transformer, the ST devices are of necessity steady-state with full non-inductive current drive. High beta equilibria with self-driven current fractions up to 100% have been calculated. The current drive power and the TF coil Ohmic power remain small enough to project systems with reasonable levels of plant recirculating power. E×B shear stabilization of turbulence will be maximized in the ST. The copper TF coil can be jointed and allows simple full dissassembly for replacement of all components, including the centerpost. Estimates of the increase in resistivity of the centerpost from neutron induced transmutation indicate a multi-year lifetime before replacement. The single turn centerpost requires unusual power supplies (few volts, MA currents) which appear possible. The high power density is a challenge to the divertor.

We find a pilot plant (Fig. 1) the size of the present DIII–D tokamak would still produce some net electric power. At 2–3 times the size of the pilot plant, full 1–2 GW net electric power plants have acceptable economics [10].

2. FUSION POWER AND BETA

A large excess of fusion power P_F must be produced relative to the resistive power in the TF centerpost P_c. We calculated a "centerpost gain" (P_F/P_c) and looked at optimizations. The centerpost is a straight cylinder of radius R_c and height h_c. No other inboard space allowance is taken. We took as independent variables R_c, aspect

ratio A, and elongation κ, since the centerpost power consumption is the main issue and we are interested in optimization of performance versus A. The plasma major radius R_0 and minor radius a are then derived. The centerpost current density J_c defines the problem. The fraction of the centerpost area that is copper is λ.

Using standard forms for the D-T fusion reactivity [11], the optimum D-T mix, $n_D = n_T = 1/2 n_e$, and parabolic profiles with exponents $S_n = 0.25$ and $S_T = 0.25$ to conform to the pressure profile in stability calculations, we can express the fusion power P_F in terms of the volume average plasma toroidal β_T and the vacuum toroidal field B_T to keep contact with the β-limit scaling for higher aspect ratio tokamaks [12] $\beta_N \equiv \beta_T / \left(I_p / aB_T\right)$ (%,MA,m,T).

$$P_F = 0.88\left(\beta_T B_T^2\right)^2 V(\mathrm{MW,T,m^3}) \quad . \tag{1}$$

A relation for the β-limit as a function of aspect ratio is needed. Using poloidal circumference $= 2\pi a\,[(1 + \kappa^2)/2]^{1/2}$, one obtains

$$\beta_T \beta_p = 25\left(\frac{1+\kappa^2}{2}\right)\left(\frac{\beta_N}{100}\right)^2 \quad . \tag{2}$$

Equation (2) squarely puts the major conflict in advanced tokamak design at any aspect ratio. One wants high β_T for fusion power and high β_p for high bootstrap fraction. But β_T and β_p trade-off against each other, given conventional β-limit scaling $\beta_N =$ constant. The way to increase β_T and β_p *simultaneously* is to increase κ and β_N.

3. STABILITY STUDIES

To determine β_N (A), we have explored a range of equilibria at low A varying the pressure profile, the current profile, the plasma shape, and aspect ratio [13]. Equilibria with complete bootstrap alignment were made by constraining the pressure and current profile using the TOQ fixed boundary equilibrium code [14]. Examples of fully aligned bootstrap current with bootstrap fraction f_{bs} 90%–100% at aspect ratio of 1.4 have been obtained.

Stability to ideal kink modes and ballooning modes was evaluated. Kink modes with n = 1, 2, and 3 are stable (GATO [15]) for β_N of 8 or larger with wall stabilization for a moderately placed wall. Higher triangularity δ is more favorable for wall stabilization of low mode number kink modes. Wall stabilization is also required for n = 0 axisymmetric modes. Regarding stability to ballooning modes, two paths were pursued to optimize ballooning stability with fully driven bootstrap current. One used a finite pressure gradient at the plasma edge p'_{edge} as is usual in DIII–D H–mode. A stable equilibrium with β_N = 10 and finite p'_{edge} (77% of the maximum p′) has been found and confirmed by several different codes [13]. A second path optimized β_N with p'_{edge} = 0 through an iterative calculation of marginal stability with variation of the pressure profile while maintaining full bootstrap alignment. Our results show a clear dependence of the β limit on δ and κ. Scanning δ at fixed κ (=2.5), both β_N – and β_T–limits show a maximum at δ = 0.4 owing to the competition between the stabilizing effect of a deeper magnetic well at higher δ and higher edge bootstrap current at lower δ. At fixed δ, both β_N- and β_T- limits increase with κ (Fig. 2). At κ = 3, equilibria with

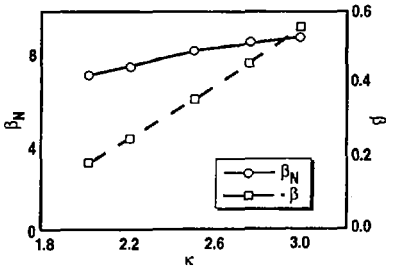

FIG. 2. β and β_N as functions of elongation, κ, δ = 0.4 and A = 1.4.

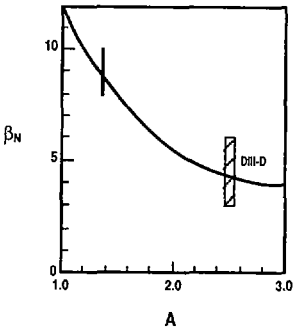

FIG. 3. The relation β_N = 12/A. Values achieved in DIII-D experiments are shown at A = 2.5. A range of theoretical calculations from Ref. [13] are shown at A = 1.4.

β_N exceeding 8 and β_T exceeding 50% with full bootstrap alignment are stable to n = infinity ballooning modes.

Our stability calculations [13] support a *specific advantage* of low aspect ratio in plasma stability. The function $\beta_N = 12/A$ passes through our theory results at A = 1.4 (Fig. 3) and the center of the range of data from DIII–D [16]; $\beta_N = 6$, more optimistic than our assumed function, has been achieved transiently and is expected to be stable in steady-state in second stable core VH–mode (SSC-VH [17], negative central shear mode [18]).

4. POWER GAIN

In our scoping studies, we used the relation β_N = 12/A in Eq. (2) to allow a tradeoff of β_T and β_p with a basis point at the $\kappa = 3$, $\beta_N = 8.6$, $\beta_T = 56\%$,$f_{bs} = 100\%$ case in Fig. 2. From a study of the dependence of f_{bs} on density and temperature scale lengths we adopted profiles for which $L_n = L_T$ and for which the pressure profile was as broad as in the stability results. In this case $f_{bs} = 0.72\ \beta_p/\sqrt{A}$. Using β_N = 12/A in Eq. (2) to eliminate β_T in Eq. (1),

$$\frac{P_F}{P_c} = \frac{(0.88)(0.2)^4 \pi^5 \lambda}{\eta_c} \left(\frac{0.36[(1+\kappa^2)/2]}{\beta_p} \right)^2 \times J_c^2 R_c^4 \frac{(A-1)^2}{A^7} \quad . \tag{3}$$

This relation implies an optimum aspect ratio of 1.4. The relation [Eq. (3)] shows a very strong economy of scale in the low aspect ratio approach since $P_F/P_c \propto R_c^4$. Shortfalls in plasma parameters which lower P_F/P_c can easily be made up by making the machine only slightly larger.

Since $P_F/P_c \propto J_c^2$, we need to ask what limits J_c? Centerpost cooling is an obvious candidate but turns out to not be restrictive. For a water temperature rise of

100°C, a flow velocity of 10 m/s, and λ = 1/2, we can express $J_c^2(\mathrm{MA/m^2}) = 6.2\times10^4/h_c$ [19], which leads to very small machines $(R_c = 0.2\,\mathrm{m})$ with enormous power outputs (11 GW!) and high toroidal field (10 T) devices because the centerpost cooling limit supports J_c as high as 200 MA/m^2. Such machines are unrealistically small; the neutron wall loading would be far beyond what blankets could handle.

5. NEUTRON WALL LOADING LIMITS

A neutron wall loading constraint will be the limiting factor in performance. We take 8 MW/m^2 to be at the high end of possibility. We assumed the neutrons are emitted uniformly onto a sphere of radius $R_0 + 2a$, *i.e.*, the blanket is spaced one minor radius from the edge of the plasma.

The family of machines with constant wall loading is defined by $J_c^4 R_c^5 =$ constant. With this constraint, the centerpost gain P_F/P_c will have the size scaling $R_c^{3/2}$, much weaker than the R_c^4 scaling considering only operation at the β-limit with a fixed J_c. At the neutron wall loading limit of 8 MW/m^2, we found an interesting family of machines, all of small size, but with high gain and fusion power output.

We found that increasing κ from 2 to 3 is able to effect a factor 2 reduction in plasma and machine volume, providing strong motivation to increase the elongation.

Our choice κ = 3 lies above the passive stability limit [7] but below the feedback stability limit [20].

6. INTEGRATED DESIGNS

We constructed a complete plant model in a spreadsheet. The current density J_c is adjusted to give the specified wall loading power. Some allowance for the elevated operating temperature of the centerpost is made by taking $\eta_c = 2.0\times10^{-2}$ $\mu\Omega$m and we took λ = 0.8. A water flow velocity V_w = 10 m/s always gives a small temperature rise. The twelve outer legs of the TF coil are sized to obtain a resistive dissipation equal to 0.5 of the centerpost power and the resulting cross-sections are modest (0.2 to 0.6 m on a side). The total voltage drop on the TF coil, V_{TF}, ranges from 10 to 7 V. With semiconductor power supplies for the TF with an internal voltage drop of about 1 V, we take the electrical efficiency of the TF power source to be 0.9 $\left(1-1\mathrm{V}/\mathrm{V}_{TF}\right)$.

We specify $f_{bs} = 0.9$ and compute $\beta_p = f_{bs}\sqrt{A}/0.72$. The β_T is calculated from Eq. (2) with β_N = 12/A. Then $I_p/aB_T = 100\,\beta_T/\beta_N$ and $I_p(\mathrm{MA}) = aB_T\left(I_p/aB_T\right)$. The safety factor q is always unrestrictive (~6). The product of central density n_0 and temperature T_0 is computed from β_T. We assume T_0 = 30 keV and calculate n_0, which ranges from 3 to 2×10^{20} m^{-3}. These densities range from 0.3 to 0.6 times the Greenwald limit $n_{GR} = I_p(\mathrm{MA})/\pi a^2$.

We compute the power required P_{CD} to drive the remainder of the current $I_{CD} = I_p(1-f_{bs})$ [21]. We compute $P_{CD} = nR_0 I_{CD}/\gamma$, where γ is the usual current drive figure of merit for the various current drive schemes evaluated at the volume average temperature and density [19]. The values P_{CD} were similar for the various rf and NBCD schemes; in our power balance, we used the NBCD result which ranged from 7 to 24 MW.

The electrical efficiency of the current drive system is taken as $\eta_{CD} = 0.4$. All other plant systems are assumed to require 7% of the gross electric power generated.

So the power recirculating in the plant is $P_{RECIRC} = P_{CD}/\eta_{CD} + P_{TF}/\eta_{TF} + 0.07P_{GROSS,E}$. A blanket multiplier $M = 1.25$ was taken. None of the power collected as heat $\left(P_\alpha + P_{CD,E} + P_{TF,E}\right)$ was taken into the thermal cycle. The efficiency of the thermal cycle was taken as 46%. The gross electric power is $P_{GROSS,E} = \left[M\left(P_F - P_\alpha\right)\right]/0.46$. $Q_{PLANT} = P_{GROSS,E}/P_{RECIRC}$.

We found the low aspect ratio path does contain a small pilot plant type device and an attractive economy of scale to power plants. All of the designs considered have in common $A = 1.4$, $\beta_T = 62\%$, $\beta_p = 1.48$, $f_{bs} = 0.90$, $\kappa = 3.0$, neutron power at blanket $= 8$ MW/m^2.

Figure 4 shows P_F/P_c and Q_{PLANT} versus machine size as gauged by R_c. At the low end, $R_c \sim 0.2$ to 0.3 m, we find pilot plants with $P_F/P_c = 5$ to 10 and $Q_{PLANT} = 1.0$ to 1.7. At larger $R_c = 0.6$ to 0.8 m, we find a suitable range for a power plant with $P_F/P_c = 25$ to 40 and $Q_{PLANT} = 3.8$ to 5.4. The pilot plant makes a fusion power in the range 360 to 800 MW and a net electric power in the range 0 to 160 MW. The power plants make fusion power 3000 to 6000 MW and net electric power in the 1000 to 2000 MW range. These are all small devices. The pilot plant has $R_0 = 0.7$ to 1.0 m and $a = 0.5$ to 0.8 m. The power plants have $R_0 = 2.1$ to 2.8 m and $a = 1.5$ to 2.0 m.

The wall loading constraint forces J_c to decrease as R_c increases as shown in Fig. 5. The pilot plants have $J_c = 90$ to 50 MA/m^2 and toroidal fields 3.2 to 2.9 T. The power plants have $B_0 = 2.4$ to 2.2 T and $J_c \sim 22 - 16$ MA/m^2, a technically unchallenging value. The centerpost power ranges from 90 MW in the pilot plant to 140 MW in the power plant. The plasma current ranges from 15 MA to 30 MA. The neutral beam current drive power range is from 7 to 24 MW.

Taking account of bremsstrahlung and assuming $P_{RAD} = 25\%$ of the sum of $P_\alpha + P_{CD}$, we calculate the index of divertor power handling P/R_0 and find values ranging from 80 to 300 MW/m; P/R_0 in ITER is ~40 MW/m. It appears these devices will need to use a radiating mantle to deliver the power to the large area outer wall instead of trying to handle a majority of the power in the small divertor volume.

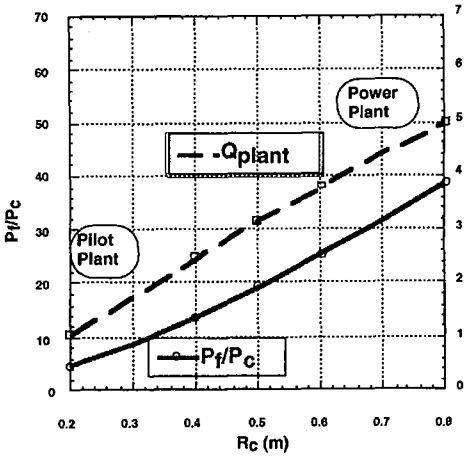

FIG. 4. The ST approach includes a small pilot plant with plant Q = 1–2 and a strong economy of scale to power plants with plant Q = 4–5.

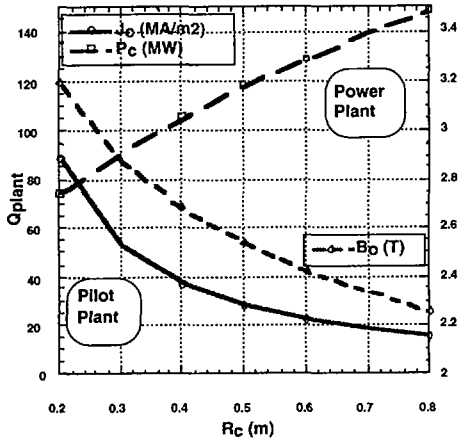

FIG. 5. Allowable neutron wall loading (8 MW/m^2) forces J_c and B_0 to decrease with increasing R_c, β_T = 62%, β_p = 1.48, f_{bs} = 0.9.

7. CONFINEMENT AND E×B SHEAR

We have examined operation at the β-limit. The total heating power $P_\alpha + P_{CD}$ has also been calculated, so we can calculate the energy confinement time required to provide a steady-state at the β-limit. Those confinement times are then compared to the ITER89–P L–mode scaling [22] to define $H = \tau_E/\tau_{89P}$. The absolute energy confinement times are reasonable, ranging from 0.6 to 1.0 s. An H factor of 5 in the pilot plant range and 3 in the power plant range is required. We note that the H–mode scaling predicts a τ_E about half of L–mode at $A = 1.4$, which makes no sense.

Prospects for obtaining this required confinement quality are excellent. The transport barriers formed in H–mode, VH–mode, and negative central shear (NCS) mode all derive from stabilization of turbulence by sheared E×B flow [23]. Turbulence suppression is strong when the shearing rate [24] exceeds the growth rate of the modes. Assuming isotropy for the turbulence correlation lengths in the plane perpendicular to $\vec{B}$ [24,25] and flat density profiles, the shearing rate is approximately

$$\omega_E = \frac{(RB_\theta)^2}{B}\left|\frac{\partial}{\partial\psi}\left(\frac{E_r}{RB_\theta}\right)\right| \cong \frac{(RB_\theta)^2}{Z_i n_i e B}\frac{\partial^2 P}{\partial\psi^2} \quad (\nabla P \text{ term only}) \quad . \qquad (4)$$

An experimental calibration point is available in that when $\omega_E \gtrsim 100$ kHz, turbulence suppression has been essentially complete, leaving only residual neoclassical transport.

We have evaluated Eq. (4) for ω_E exactly in our highest β equilibrium. Figure 6 shows that ω_E reaches enormous values of 30 MHz in the high pressure gradient region near the outer midplane. Such values are 300 times the 100 kHz values in present experiments that achieve neoclassical transport levels. ω_E is greater than 100 kHz over the outer 20% of the minor radius on the outboard side so a transport

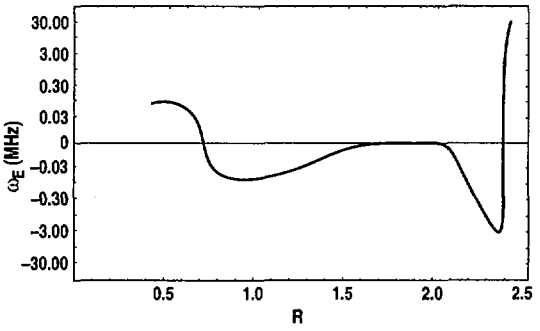

FIG. 6. Turbulence shearing rate versus major radius at the midplane for $n_i = 10^{20}$ m^{-3}.

barrier with only residual neoclassical transport should form there to support the high pressure gradient this equilibrium requires. Estimates of the confinement times resulting from neoclassical ion heat transport alone exceed our required confinement times by a very large factor.

8. HELICITY INJECTION CURRENT DRIVE

Besides estimating the current drive power from the standard RFCD and NBCD schemes, we also looked at helicity injection current drive derived from an electrode as in the HIT experiment [18]. We estimate the HICD power as ten times the Ohmic dissipation in the plasma assuming a flat current profile in the presence of a temperature profile given by

$$T_e(r) = T_0\left[1-\left(1-T_b/T_0\right)(r/a)^2\right]^{S_T} \quad , \tag{5}$$

$$P_{\mathrm{HICD}}(\mathrm{MW}) = \frac{0.56\pi R_0 I_{\mathrm{CD}}^2(\mathrm{MA})}{\pi a^2 \kappa} \frac{1}{T_0^{3/2}(\mathrm{keV})} \left[\frac{1-\left(T_b/T_0\right)^{1-(3/2)S_T}}{\left(1-\frac{3}{2}S_T\right)\left(1-T_b/T_0\right)}\right] \quad . \tag{6}$$

We have taken $Z_{\mathrm{eff}} = 1$. The values P_{HICD} that result for our broad profiles $S_T = 0.25$ with $T_0 = 30$ keV and $T_b = 0.2$ keV are very small, of order 10 kW. In previous studies [10,26] using a peaked profile $S_T = 2$, PHICD ranged from 60 to 100 MW, twice the RFCD and NBCD values. The possible extreme efficiency of HICD for broad T_e profiles warrants further investigation.

9. TECHNOLOGY ISSUES

We calculated the lifetime of the centerpost in the power plant ($R_c = 0.6$ m case) against the nuclear transmutation induced increase in resistance, using 2-D distributions of dpa calculated in an $R_c = 0.14$ m centerpost [27] adapted to our larger center-

post. One MW-yr/m^2 produces 10 dpa in the copper surface at the midplane. The change in resistivity per dpa is 2.8×10^{-10} Ω-m/dpa. With an 8 MW/m^2 neutron flux on the centerpost, we find a 10% increase in resistance in one year, 50% increase in 7 years, and a 100% increase in 22 years. The centerpost changeout time for economic reasons (too high P_c) would be ~7 years.

We also looked at the unusual low voltage, high current semiconductor power supplies needed for the one turn in each return leg TF coil. To keep reasonable the transmission line power losses, the power supplies must closely ring the device (5 m transmission line lengths) with a floor space requirement of 0.3 m^2/MVA and a 6 m height. The cost for a 12 return leg system for the power plant is about $70M–$110M.

10. PROSPECTS FOR ADVANCED FUEL BURNING

Because of the strong scaling of gain P_F/P_c with size (α R_c^4), the question naturally arises as to whether there is enough excess capacity in the ST at large size to burn advanced fuels like D-He^3 despite their lower reactivity. A D-He^3 system can produce as low as 1% of the neutrons from a D-T system, effectively removing centerpost radiation damage as a design issue. We developed the formula for fusion power from D-He^3 [26] in terms of β and obtained $P_F = 0.016 \left(\beta_T B_T^2\right)^2 V$ (MW, T, m^3).

The basic difficulty with realizing an effective D-He^3 system is a surprising one; for systems with high gain, the absolute value of the fusion power produced is too

Table I
Devices at an 8 MW/m^2 Neutron Wall Load

	D-He^3		D-T
Parameter	Copper	Superconducting	Superconducting
R_c (m)	3	1.5	1.5
R_0 (m)	10.5	5.25	5.25
a (m)	7.5	3.75	3.75
J_c (MA/m^2)	6	$\gtrsim 60^*$	$\gtrsim 60^*$
Fusion power (MW)	23,000	1,400	10,000
Q_{PLANT}	3.4	4.3	12
Net electric power (MW)	7,600	500	4,200
Current drive power (MW)	105	42	30
I_P (MA)	175	73	44
B_0 (T)	3.2	2.7	1.6
τ_E (s)	5.7	8.1	2.1
H	2.1	4.5	2.4
P_F/A_{wall} (MW/m^2)	5.7	1.4	4.0†
T_0 (keV)	100	60	30
n_0 (10^{20} m^{-3})	1.4	1.7	1.0

*Assuming one meter thick neutron shield.
†Neutron power at the blanket.

large. The D-He^3 fusion power output is 55 times less than the D-T output at the same β_T. To get the same gain P_F/P_c we must increase the size of the machine like $R_c \alpha (55)^{1/4}$. But P_F scales like R_c^7. Hence the ratio of P_F in our larger D-He^3 device to P_F in our smaller D-T power plant will be

$$\frac{P_{D-He^3}}{P_{D-T}} = \frac{1}{55}\left[(55)^{1/4}\right]^7 = (55)^{3/4} = 20 \quad . \tag{7}$$

We get 20 times more fusion power out at the same gain P_F/P_c!

We have not been able to find a sensible set of parameters for a copper TF coil ST burning D-He^3. One is led to large devices with a very large centerpost $R_c \sim 3$ m and extremely low $J_c \sim 6$ MA/m^2. Within the space envelope afforded by $R_c = 3$ m one could replace the copper TF coil with a superconducting TF coil and include a cryostat and neutron shield. This step eliminates the ohmic dissipation in the TF from the power balance and allows a plant Q = 4.3. Parameters of copper and superconducting D-He^3 systems are given in Table I.

We also looked at D-T systems in the large sizes required to shield a superconducting centerpost (Table I). The endpoint of a copper TF ST development path starting at small $R_c = 0.3$ m pilot plants could be superconducting STs with $R_c >$ 1.5 m.

11. SUMMARY AND CONCLUSIONS

We examined the ultimate performance of the ST at its beta limit and the neutron wall loading limit at the blanket. Full stability calculations at A = 1.4 found $\beta_N = 8$ to 10 with 100% fully aligned bootstrap current.

We demanded a 90% bootstrap fraction. We calculated the current drive power requirements for the various standard schemes to drive the remaining 10% of the current. We performed basic physics studies of FWCD in the low A regime. We also evaluated helicity injection current drive.

We evaluated the energy confinement required to reach the β_T limit. We found that owing to the high βB_T product in the ST the stabilization of turbulence by sheared E×B flow should be one to two orders of magnitude greater than in existing devices which are seeing only residual neoclassical transport in their transport barriers.

We found systems with the centerpost gain P_F/P_c greater than 20 and a strong size dependence $\left(R_c^4\right)$ of the gain. The cooling of the centerpost imposes no meaningful restriction on the design of ST machines. The high beta potential of the ST is so great that the neutron flux into the fusion blankets was found to limit the size of the device. An aggressive assumption of 8 MW/m^2 at the blanket then led to the small pilot plant and power plant possibilities that we have found.

We found an acceptable centerpost lifetime against transmutation induced resistance increase and an acceptable technical path to the low voltage, high current TF power supplies.

We found the possibility of D-He^3 burning devices at large size $R_c > 1.5$ m with a superconducting TF centerpost and suitable shield.

The pilot plant is the key to the ST fusion development path. It appears possible to design a pilot plant that would only be the size of the present DIII–D tokamak and yet still produce 0–160 MW net electric. The plant Q, defined as the ratio of gross electric power to internal recirculating power is only 1–2. The low plant Q will be acceptable

in a pilot plant if the concept has a strong economy of scale. The ST size scaling is very strong; the ratio of fusion power to the Ohmic dissipation in the copper TF coil magnet scales as the fourth power of the linear dimension. Consequently, we easily found small power plants with economically acceptable recirculating power (plant Q ~ 4–6, net electric power 1–2 GW) just by doubling the linear dimensions of the device with no changes in technology. The ST is a simplified tokamak with no hard to service inboard blankets, shields, PF or OH coils. Because the TF coil is copper, it can be jointed and so afford easy complete dissassembly of the machine for service. The ST concept offers high elongation and a natural divertor without a divertor coil. Finally, because the ST pilot plant is a full net electric and tritium producer, it will provide a full exercise of the siting and licensing process, but again at a low cost, low financial risk scale. The fact that a viable concept for a pilot plant exists is the principal attraction of the ST approach to fusion development.

REFERENCES

[1] PENG, Y.-K.M., STRICKLER, D.J., Nucl. Fusion **26** (1986) 769.

[2] PENG, Y.-K.M., HICKS, J.B., "Engineering feasibility of tight aspect ratio tokamak (spherical torus) reactors", Proc. 16th Symp. on Fusion Technology, London, 1990.

[3] PENG, Y.-K.M., et al., Fusion Technol. **29** (1995) 210.

[4] DARKE, A.C., et al., "The Mega Amp Spherical Tokamak", Proc. 16th IEEE/NPSS Symp. on Fusion Engineering, Champaign, IL, 1995, IEEE Service Center, Piscataway, NJ (1995) 1456.

[5] CHRZANOWSKI, J.H., et al., "Engineering overview of the National Spherical Tokamak Experiment", ibid., p. 1430.

[6] FRC STAFF, USTX — The University Spherical Tokamak Experiment, Rep. DOE/ER/542-41-159, US Dept. of Energy, Washington, DC (1996).

[7] SYKES, A., Plasma Phys. Control. Fusion **36** (1994) B93.

[8] PENG, Y.-K.M., et al., in Plasma Physics and Controlled Nuclear Fusion Research 1994 (Proc. 15th Int. Conf. Seville, 1994), Vol. 2, IAEA, Vienna (1995) 643.

[9] BUTTERY, R., et al., ibid., p. 633.

[10] STAMBAUGH, R.D., et al., The Spherical Tokamak Path to Fusion Power, Rep. GA-A22226, General Atomics, San Diego, CA (1996) and Fusion Technol. **30** (1996) 1380.

[11] NRL Plasma Formulary, NRL/PU/6790-94-265 (HUBA, J.D., Ed.), Naval Research Lab., Washington, DC (1994).

[12] CALLEN, J.D., et al., Phys. Today **45** (1992) 34.

[13] MILLER, R.L., et al., Stability for Bootstrap-Current Driven Low Aspect Ratio Tokamaks, Rep. GA-A22321, General Atomics, San Diego, CA (1996).

[14] MILLER, R.L., VAN DAM, J.W., Nucl. Fusion **27** (1987) 2101.

[15] BERNARD, L.C., et al., Comput. Phys. Commun. **24** (1981) 377.

[16] FERRON, J.R., et al., Phys. Fluids B **5** (1993) 2532.

[17] DIII-D TEAM, in Plasma Physics and Controlled Nuclear Fusion Research 1994 (Proc. 15th Int. Conf. Seville, 1994), Vol. 1, IAEA, Vienna (1995) 83.

[18] LAZARUS, E.A., et al., Higher Fusion Power Gain With Pressure Profile Control in Strongly Shaped DIII-D Tokamak Plasmas, Rep. GA-A22292, General Atomics, San Diego, CA (1996) and Phys. Rev. Lett. **77** (1996) 2714.

[19] MONTGOMERY, D.B., Solenoid Magnet Design, Wiley-Interscience, New York (1972).

[20] STAMBAUGH, R.D., et al., Nucl. Fusion **32** (1992) 1642.

[21] TONON, G., "Current drive efficiency requirements for an attractive steady-state reactor", Proc. Workshop on Tokamak Concept Improvement, Varenna, Italy, 1994, p. 233.
[22] YUSHMANOV, P.N., et al., Nucl. Fusion **30** (1990) 1999.
[23] DOYLE, E.J., et al., these Proceedings, Vol. 1, p. 547.
[24] HAHM, T.S., BURRELL, K.H., Phys. Plasmas **2** (1995) 1648.
[25] HAHM, T.S., BURRELL, K.H., personal communication.
[26] MILEY, G.H., TOWNER, H., IVICH, N., Fusion Cross Sections and Reactivities, Rep. COO-2218-17, Univ. of Illinois, Urbana (1994).
[27] CHENG, E.T., et al., Study of a Spherical Tokamak Based Volumetric Neutron Source, Rep. TSIR-45, TSI Research Inc., Solana Beach, CA (1996).

DISCUSSION

D.D. RYUTOV: An important feature of the existing spherical tokamak experiments is the absence of major disruptions. Still, the degree of extrapolation from current experiments to a spherical tokamak reactor is considerable. Have you analysed what the consequences could be of even one major disruption in a spherical tokamak reactor?

R.D. STAMBAUGH: No. I note the absence of hard current terminations in START.

H. TOYAMA: You have calculated the case of 10% HICD. How critical is the HICD in your power plant?

R.D. STAMBAUGH: We did not use our estimates of HICD power in our power plant power balance calculations because the calculated HICD power was so very low. HICD is the only effective means of driving current at the plasma edge, if lack of full bootstrap alignment requires it.

R.J. TAYLOR: In present experiments the electron χ_e seems to be a limiting element in achieving sufficient confinement. How limiting is the electron physics for you at low aspect ratio?

R.D. STAMBAUGH: There appears to be an abundance of $\mathbf{E}\times\mathbf{B}$ shear available in the spherical tokamak concept to lower χ_i to neoclassical levels within internal transport barriers. However, in experiments χ_e only drops by a factor of 2. We need to do 1-D transport calculations, but the expected result is that electron channel transport will be limiting.

K.I. THOMASSEN: What schemes do you imagine, or have you analysed, for startup of these devices?

R.D. STAMBAUGH: Three schemes are at present being explored in experiments: (1) inductive startup using outer multipole coils, as has been successful on START; (2) helicity injection derived from an electrode, as in HIT (200 kA); (3) pressure driven currents as on CDX.

THE HELIAS REACTOR

C.D. BEIDLER, G. GRIEGER, E. HARMEYER,
F. HERRNEGGER, J. KISSLINGER, J. NÜHRENBERG,
F. RAU, J. SAPPER, H. WOBIG, A.V. ZOLOTUKHIN
Max-Planck-Institut für Plasmaphysik,
Euratom–IPP Association,
Garching, Germany

N. KARULIN
Russian Research Center,
Kurchatov Institute,
Moscow, Russian Federation

W. MAURER
Kernforschungszentrum Karlsruhe,
Karlsruhe, Germany

Abstract

THE HELIAS REACTOR.

The Helias reactor (HSR) is an extrapolation of the Wendelstein 7-X configuration to reactor dimensions. The major radius is 22 m and the average plasma radius 1.8 m. The magnetic field on the axis is 5 T and the maximum field on the coils 10.6 T, allowing the use of super-conducting coils based on NbTi technology. The coil system, consisting of 50 modular coils, has been optimised using a finite-element stress analysis. The stresses can be kept below present technical limits. The divertor concept makes use of the magnetic islands in the boundary region; a system of target plates is proposed to collect the plasma outflow. Various physics studies — alpha-particle confinement and ignition scenarios — are described. Recent empirical scaling laws of confinement in stellarators have been taken into account. The thermal output of the Helias reactor is about 3500 MW.

1. Introduction

The Helias configuration [1,2] is one of the favorite candidates for a steady-state fusion reactor. Helias (Helical Advanced Stellarator) configurations have been developed at the IPP Garching in a long phase of analytical and numerical studies to improve the reactor prospects of a classical stellarator. Experimentally the Wendelstein 7-AS device was the first step along the line of advanced stellarators; the Wendelstein 7-X device (W 7-X) is designed to explore the reactor potential of this line. The basic physical features of a Helias configuration are:

- its capability to confine an MHD-stable plasma up to $<\beta>=5\%$,
- the low neoclassical losses, which are not prohibitive to ignition,
- the good confinement properties of highly energetic alpha-particles.

These novel properties have eliminated the objections against former stellarator reactor studies, where good performance of the plasma was assumed and attention

was focussed on technical implications. The stellarator as a fusion power plant offers several advantages compared to tokamak reactors among which are

- the inherent potential of steady-state operation,
- the modular arrangement of only one coil system with its implications on maintenance and repair,
- the absence of current disruptions in stellarator experiments,
- no need to drive a toroidal current.

These properties are the justification for intensive stellarator reactor studies based on the Helias concept [3,4]. So far these studies have been focussed on specific issues characteristic for this type of stellarator and attention has been paid mainly to the coil system and the magnetic field. Physics issues such as power balance and the confinement of α-particles have also been considered. The guidelines used to specify the dimensions of a Helias reactor include:

- the desire to keep the magnetic field as low as possible so that NbTi-technology can be applied,
- the need to provide sufficient space for blanket and shield,

The dominating criterion is the necessity to provide sufficient space for blanket and shield in the order of 1.2 to 1.3 m. The fusion output is in the range 2.5 - 3.8 GW. The extrapolation of W 7-X towards a reactor following the criteria listed above leads to a minimum size of the reactor with a major radius of R_0 = 20 - 22 m. The dimensions of these reference reactors are listed in Table I.

Table I: Parameter list of Helias reactors

Average major radius	20	22	m
Average plasma radius	1.6	1.8	m
Magnetic field on axis	5.0	5.0	T
Maximum field on coils	10.9	10.6	T
Rotational transform on axis	0.84	0.84	
Rotational transform on boundary	0.98	0.98	
Plasma volume	1000	1400	m^3
Number of coils	50	50	
Number of field periods	5	5	
Stored magnetic energy	82	110	GJ
Magnetic well (vacuum field)	-0.01	-0.01	
Magnetic mirror on axis	10 %	10 %	
Effective helical ripple	2%	2%	
Ratio $\langle \lvert j_{par} / j_{dia} \rvert \rangle$	0.7	0.7	

2. The magnetic field

The magnetic field of the Helias reactor is very similar to the field of the Wendelstein 7-X device. The field is generated by 50 modular coils arranged toroidally in five field periods. As in Wendelstein 7-X, there are 10 coils per period which exhibit a symmetry such that there are only 5 different coil types. No further coils are required since a variation of the magnetic field --- which is useful in experimental devices --- is not required. In contrast to Wendelstein 7-X, the magnetic mirror on the magnetic axis is increased to 10%, which is necessary to confine highly energetic α–particles for more than one slowing-down time.

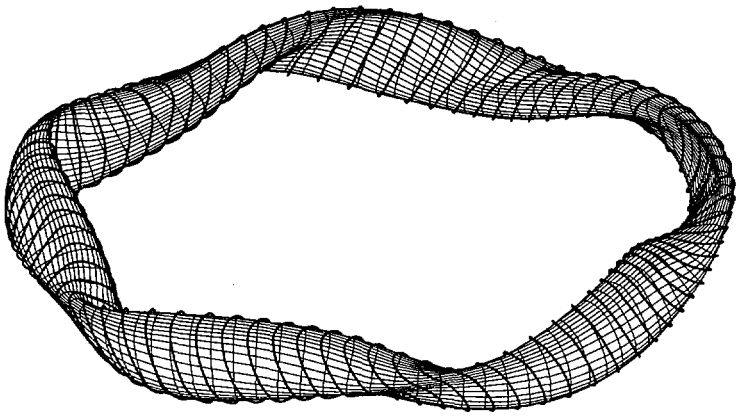

FIG. 1. Last magnetic surface of the Helias reactor. Thick solid lines indicate the plasma current.

One of the basic properties of a Helias configuration is the reduction of the Pfirsch-Schlüter currents (see Fig. 1) which has its consequences for plasma equilibrium and transport. The resulting small Shafranov shift prevents the hot plasma center being shifted radially towards the outer boundary. This avoids peaking of the neutron wall load on the outboard side.

Qualitatively the neoclassical transport properties of the Helias reactor may be illustrated by a simple model field containing the three largest harmonics in the B spectrum

$$B/B_0 = 1 + b_{10}\cos\theta + b_{01}\cos(5\varphi) + b_{11}\cos(\theta - 5\varphi).$$

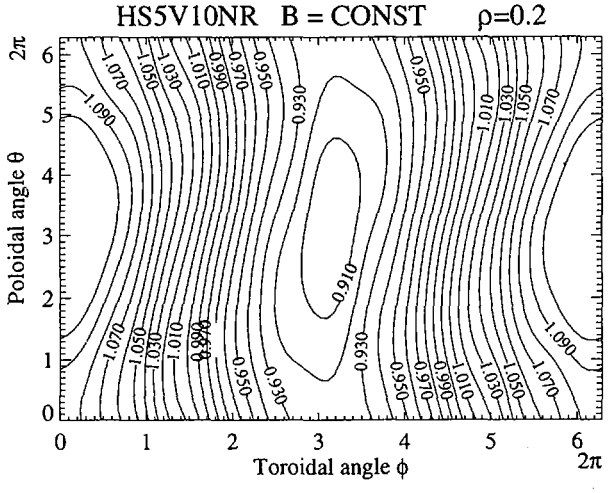

FIG. 2. |B| = const on magnetic surface. Average radius r/a = 0.2, one field period.

The coefficient b_{10} characterises the toroidal curvature effect. For standard stellarators and circular tokamaks the term is equal to r/R (the inverse aspect ratio) but in the Helias reactor it is less than half this large. A large toroidal mirror term, b_{01}, is the most striking characteristic of B near the magnetic axis (see Fig. 2). The majority of trapped particles are localised within a single field period and their orbits precess poloidally around the magnetic axis; this effect is critical for the confinement of fast α-particles. The combination of toroidal mirror and principal helical harmonic, b_{11}, also provides reduced bulk transport by means of the so-called "drift optimisation" effect. Various analytic and numeric methods have confirmed that the Helias reactor has an effective helical ripple of less than 2.5%, implying that neoclassical losses are low to allow ignition even for the "ion root" solution of the ambipolarity constraint. Finally, the B spectrum also determines the bootstrap effect; a small bootstrap current is obtained for $b_{10}/b_{11} = 0.5$.

3. The coil system

The main technical component of the Helias reactor is the coil system which consists of 50 coils with only five different coil types. So far attention has been focussed on employing NbTi superconductor in these coils and to profit from the current development of NbTi-cable for Wendelstein 7-X. To allow a peak magnetic field of 10.6 T at the coils cooling must be done at 1.8 K (4.2 K in W 7-X). The 3D-geometry of the coil system leads to a complex distribution of electromagnetic forces, however extrapolating the support system developed for W 7-X to a Helias reactor shows that stresses and strains are within technical limits. The task which remains is to optimise the intercoil support system, taking into account the requirements of maintenance and access for heating and pumping systems.

The magnetic field in the reference reactor HSR is 5 T on axis. The impact of higher magnetic fields has been studied in a short survey. A magnetic field higher than 5 T certainly improves confinement and the parameter space in beta; it allows operation at values of beta lower than 4.5% and increases the safety margin in the MHD-stability limit. Or, keeping the beta value at its limit, the size of the reactor may be reduced until the new limit is set by the space needed for blanket and shield.

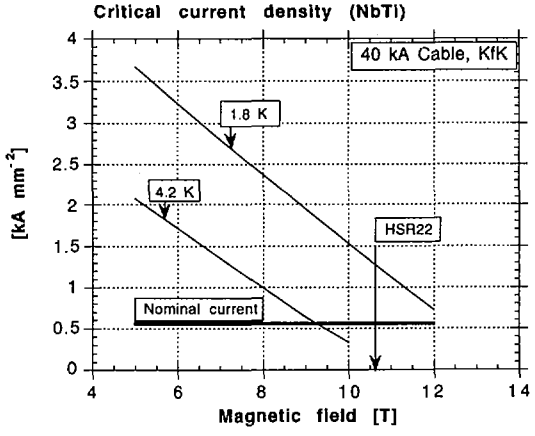

FIG. 3. Critical current density of NbTi filaments at 4.2 K and 1.8 K as a function of the magnetic field. The horizontal line indicates the operational current density of 552.6 A/mm^2.

A lower magnetic field would alleviate the issue of forces and stresses, however confinement is reduced and ignition becomes more difficult. The L-mode confinement envisaged so far in the ignition studies does not allow the reduction of the magnetic field by more than 5%; H-mode confinement or improved confinement as a result of the special Helias geometry would provide a new and more favourable basis for selecting the dimensions of HSR.

The winding pack of the superconducting modular coils for HSR is similar to that of the Wendelstein 7-X experiment, although some modifications are forseen. A 'cable-in-conduit' conductor is proposed by KfK, using NbTi at 1.8 K with forced-flow cooling of superfluid helium. The operational current will be 40 kA. The

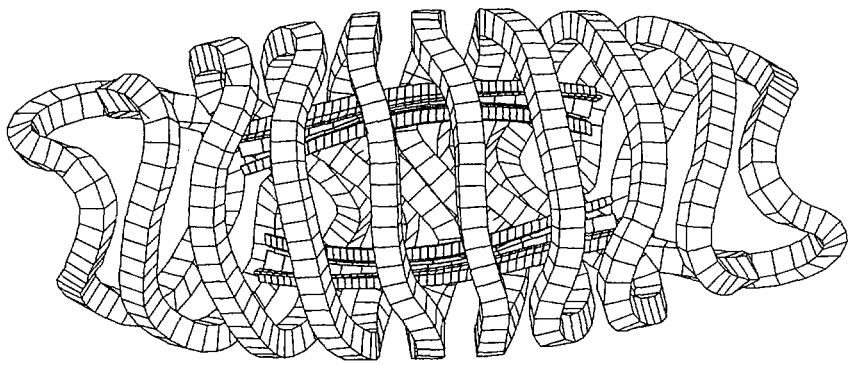

FIG. 4. One period of the coil system and the divertor components.

Table II: Coil system of Helias reactors

Helias Reactors		HSR18	HSR20	HSR22	HSR24
Average major radius	[m]	18	20	22	24
Average coil radius	[m]	4.1	4.6	5.0	5.5
Radial height	[m]	0.5	0.55	0.6	0.65
Width	[m]	0.56	0.63	0.7	0.77
Volume	[m^3]	7.8	10.8	14.4	18.7
Number of coils		50	50	50	50
Specific weight	[t/m^3]	6.4	6.4	6.4	6.4
Total volume	[m^3]	391	540	720	936
Total mass of wdg. pack	[t]	2513	3455	4607	5989
Current density	[MA/m^2]	33.3	29.9	27.1	24.8
Total current	[MA-turns]	9.3	10.3	11.4	12.4
Mass of structure	[t]	8100	11000	14400	17700
Tot. mass of coil system	[t]	**10613**	**14455**	**19007**	**23689**
Field on axis	[T]	5	5	5	5
Max. field on coils	[T]		10.9	10.6	
Magnetic energy	[GJ]		**82**	**110**	**143**
Virial stress	[MPa]		151.9	152.8	152.8

dimensions of the cross-section without insulation are 32x32 mm, and the bore for the SC-cable and the He is 22 mm. For the proposed 40 kA conductor, 192 strands of pure copper and NbTi-filaments are cabled together in order to keep AC losses sufficiently low. The operational current density is a factor of about 2 and 2.5 for HSR20 and HSR22, respectively (see Fig. 3). So far, the studies have shown that the coil system of the Helias reactor is technically feasible on the basis of NbTi-technology. The construction of the coil system for Wendelstein 7-X will provide further results on this important issue. Fig. 4 shows one period of the coil system, the data of the coil system with various major radii are summarized in Table II.

The SAP V(2) finite-element code is used to compute the stresses and strains of the system. One period of the coil system with 10 coils is modelled by 6384 elements and 9600 nodes. Each individual coil is represented by 576 elements, 96 per winding pack and 480 per housing; the remaining elements model the support structure. Since gap elements cannot be treated by SAP V(2) the winding pack is rigidly connected to the coil housing. The results of the linear finite-element calculations show that the coils tend to become more circular and planar under the magnetic load. This causes bending stresses and related shear stresses in the coils. The maximum displacement value occurs in coil 5 at the outer side, and amounts to about 50 mm. The maximum stresses for the compound of the coil winding pack of HSR in these calculations are found to be $\sigma_T \approx 65$ MPa and $\sigma_{ST} \approx 20$ MPa, using the elastic data of the conductor winding pack introduced above.

In order to obtain the stress values in the aluminium alloy jacket of this conductor its percentage ($\approx 50\%$) must be considered. Furthermore, the increase of tensile stress at the surface must be taken into account. For these reasons, a local enhancement factor of 2.5 is assumed. Using this enhancement factor, maximum stresses for the aluminium alloy of $\sigma_T \approx 160$ MPa are estimated which is far below the expected yield stress of $\sigma_{0.2} \approx 350$ MPa for this material. The maximum shear stress is $\sigma_{ST} \approx 30$ MPa and the maximum compression stress is $\sigma_T \approx 60$ MPa, acting mainly on the winding insulation. The maximum equivalent stress for the coil housing is found for coil 5 and amounts to about $\sigma_{vM} = 600$ MPa. All stress values are considered to be within the safety margins of the respective materials. These stress maxima are rather localized, and it is expected that a further reduction is possible by optimizing the support system.

For initial conditions in the above calculations the coil system is considered to be cold, free of gaps and free of stresses. The stresses described above arise from magnetic forces only; those caused by cooling-down and manufacturing processes are not considered here. Further studies investigating these issues and other non-linear effects are in progress [5].

4. The divertor concept

The divertor concept in HSR follows the concept developed for Wendelstein 7-X [6]. Since the magnetic field configuration is fixed and needs no variation as in the experiment, the divertor geometry in HSR can be adjusted to the islands in the boundary region. The key element of the island divertor is the X-point where the plasma flows along the separatrix onto the target plates. Except for the 3-D geometry there is a strong similarity to the divertor concept of tokamaks.

The target plates and baffle plates are arranged at the top and bottom of the magnetic surfaces following the islands toroidally (Fig. 5). About 50% of the circumference is covered by these divertor plates; there are no divertor plates in the plane of triangular plasma cross section. The angle of inclination between field lines and target plates is about 1° and nearly constant around the torus. The target plates are arranged in such a way that the "shadow" effect avoids the leading edge problem.

An important issue is the thermal load onto the target plates. Monte-Carlo calculations have assumed a diffusion coefficient of 1 m^2/s in the scrape-off layer which led to a wetted area of about 40 m^2; therefore the average thermal load at a total power of 300 MW on the targets is below 10 MW/m^2, however the peak value may reach 20 MW/m^2, which is too high for steady-state operation. A radiative boundary layer and ergodisation of the magnetic field will alleviate this situation. Because of the large aspect ratio and the large connection length the volume of the SOL in a Helias reactor is significantly larger than in a tokamak reactor.

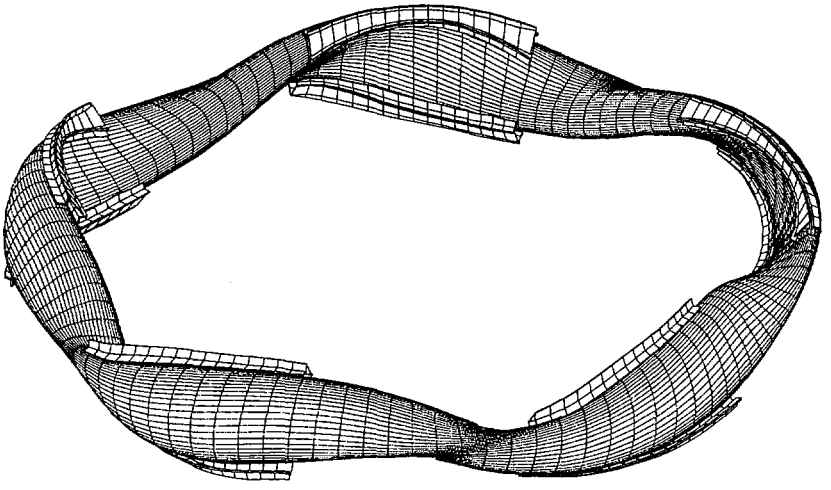

FIG. 5. Toroidal arrangement of divertor elements in HSR.

5. Blanket and shield

One of the constraints in designing the Helias reactor is to provide sufficient space for blanket and shield; this has been achieved in HSR22 and larger devices. Extrapolation of one-dimensional neutron calculations made for the US stellarator reactor study SPPS and for SEAFP show that a breeding ratio higher than one and sufficient shielding of the coils can be reached in this approximation. However, some details remain to be clarified since the 3-D geometry with its strong inhomogeneity of neutron emission and the specific limits of superconducting coils at 1.8 K have not yet been taken into account. Furthermore, the large area of the first wall ($\approx$ 3000 m^2) which must be covered by a blanket requires a careful design in order to minimise the costs. The critical region exists on the inboard side in the plane $\varphi = 0°$. As in tokamaks, the narrowest distance between plasma and coils is found here (see Fig.6).

In this plane the distance between last closed flux surface and the center of the coils is 177 cm; at the outboard side this distance is 200 cm or more. Taking into account the 7 cm distance between plasma and first wall and the 30 cm of half the winding pack leaves 140 cm between first wall and winding pack. This region is available for the coil casing, thermal insulation, neutron shield and breeding blanket. The coil casing in this region need only be 10 cm thick as stress analysis has shown. About 5 cm are needed for thermal insulation which provides finally a clearance of 125 cm for shield, breeding blanket and first wall.

Neutron wall load due to the 14 MeV neutrons originating in the plasma has been computed by a Monte-Carlo method taking the toroidal geometry into account only approximately. However, this approximation is sufficient to give results on the poloidal asymmetry of the neutron emission and the peaking factor. The average fast neutron wall load is rather small since the first wall area in HSR22 is about 3000 m^2 which yields roughly 0.9 MW/m^2 at a fusion power of 3500 MW.

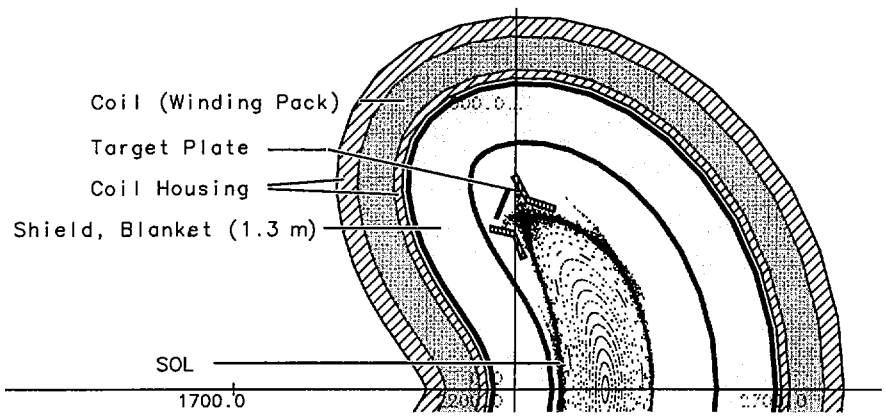

FIG. 6. Poincaré plot of magnetic surfaces in the plane $\varphi = 0°$. The width of blanket and shield is 1.3 m. The SOL is modelled by Monte Carlo calculations of particle orbits.

6. Physics Studies

From the large palette of physics issues in a Helias reactor, some stellarator specific topics, α-particle losses and the ignition conditions, have been considered so far. As demonstrated by numerical calculations the prompt losses of fast α-particles are avoided in a Helias reactor by the particular structure of the magnetic field at finite beta. Although there is no absolute confinement of trapped particles in a configuration without symmetry, improved confinement of these particles in a Helias reactor can be achieved by localizing the trapped particles in one field period and by utilizing the poloidal magnetic drift to avoid the formation of superbanana orbits. That this method is indeed effective has been demonstrated numerically by Lotz et al.[7] (see Fig. 7). The strike points of lost α-particles on the first wall have been computed [8].

The result is that nearly all highly energetic α-particles are confined for one slowing down time if the plasma beta is sufficiently large. The poloidal magnetic drift already becomes effective at $\langle\beta\rangle = 2\%$. In view of this result, prompt losses of α-particles have been neglected in the power balance. In this context the role of Alfvén waves excited by alpha particle needs to be clarified. Less is known about the confinement of thermal α-particles; it is expected that the lifetime of thermal α-particles and thus the dilution effect through ash accumulation is limited by neoclassical losses and anomalous particle transport.

Ignition in the Helias reactor has been investigated on the basis of various empirical scaling laws: LHD-scaling, Gyro-Bohm-scaling, Lackner-Gottardi scaling, ITER-L-mode scaling. Among the various empirical laws of energy confinement the Lackner-Gottardi scaling law, which also fits well to the Wendelstein 7-AS data, provides ignition without an improvement factor or isotope factor. As an example the result of a POPCON analysis using the LG-scaling is shown in the Fig. 8.

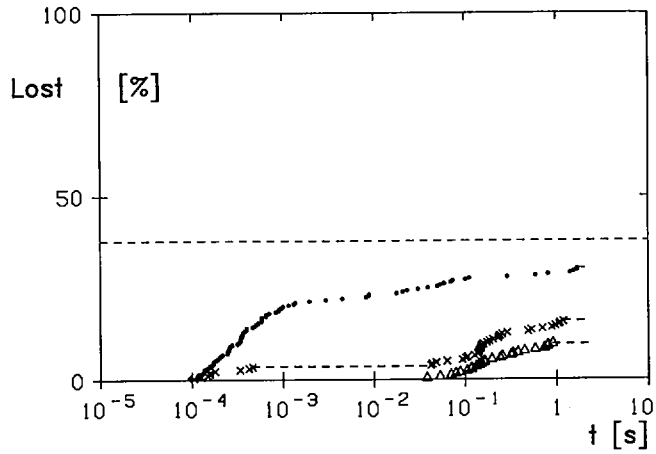

FIG. 7. α-particle losses as a function of collisionless time of flight. Fraction of reflected particles which are lost. Dots: ⟨β⟩ = 0%; crosses: ⟨β⟩ = 2.4%; triangles: ⟨β⟩ = 4.9%.

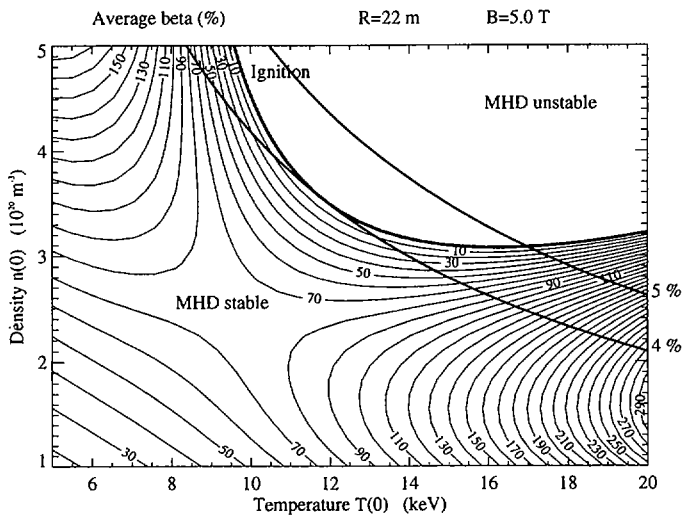

FIG. 8. POPCON plot of HSR22 standard case.

Contours of constant plasma pressure are also shown in this graph (<β> = 4% and 5%). Ignition is possible at <β> = 4%, while the maximum beta is expected around 5% where the plasma becomes MHD-unstable. The region between the ignition contour with $P_{ex} = 0$ and the <β> = 5% contour is the operational regime of the burning plasma. The α-particle heating power in this regime is between 500 and 900 MW. The minimum heating power is given by the parameters at the "Cordey pass" and in the reference case of HSR this minimum heating power is 80 MW. The density is 2.5×10^{20} m^{-3} and the temperature T(0) = 10 keV. The minimum heating power and the point of ignition strongly depend on the parameters of the fusion device: size, magnetic field, impurity content etc. Extensive studies have been made to explore the impact of parameter variations on the ignition conditions.

Table III: Plasma parameters in HSR22

Major radius	22	m	Temperature T(0)	14	keV
Av. plasma radius	1.8	m	Temperature T(a)	1	keV
Plasma volume	1407	m^3	Density n(0)	3.5×10^{20}	m^{-3}
Field on axis	5	T	Density n(a)	0.5×10^{20}	m^{-3}
Rot. transform	0.95		Av. temperature	6.6	keV
Equivalent current	3.50	MA	Av. density	2.15×10^{20}	m^{-3}
Alpha-fraction	0.050		Max. beta	0.153	
Oxygen	0.001		Av. beta	0.045	
Carbon	0.001		P_{alpha}	718	MW
Z_{eff}	1.186		P_{brems}	147	MW
f_{D+T}	0.886		P_{fusion}	3592	MW
Eff. mass	1		τ_E	1.65	s

A consistent set of parameters of a burning plasma with given plasma profiles are shown in Table III.

Neoclassical transport taking into account the self-consistent radial electric field is small and provides no barrier to ignition. The calculation using empirical scaling laws has been confirmed by start-up calculations using the ASTRA-code which provides radial profiles as a function of time (see Fig. 9). In the first calculations emphasis has been placed on the energy balance; the particle balance is modelled by neoclassical and anomalous transport and refuelling by pellet injection. The anomalous particle transport is assumed to be a factor of five smaller than the energy transport. The minimum heating power of the start-up phase is found to be about 50 MW. Global data such as energy confinement time and plasma energy obtained from ASTRA coincide well with the results of empirical scaling laws.

To date, all studies on ignition have been based on L-mode-like confinement, but any improvement of confinement by the specific properties of the Helias configuration may increase the ignition margin appreciably, however, the improvement factor is not yet known. Several specific effects may lead to an improved confinement: 1) Reduction of banana orbit widths and the anomalous radial transport of trapped particles, 2) Reduction of free energy to drive instabilities, 3) Reduction of magnetic pumping and the excitation of poloidal rotation in context with H-mode confinement.

Assuming improved confinement, ignition conditions can be relaxed and less heating power is needed for start-up. Another consequence could be to reduce the magnetic field of the reactor and thus simplify the technical issues. These options underline the necessity to test this concept of an optimised stellarator in the Wendelstein 7-X experiment.

7. Conclusions

The present status of Helias reactor studies is characterised by the identification and investigation of specific issues which result from the particular properties of this type of stellarator. On the technical side these are issues related to the coil system, while physics studies have concentrated on confinement, alpha-particle behaviour and ignition conditions. The usual assumptions have been made in those fields which are common to all toroidal fusion reactors: blanket and shield, refuelling and exhaust,

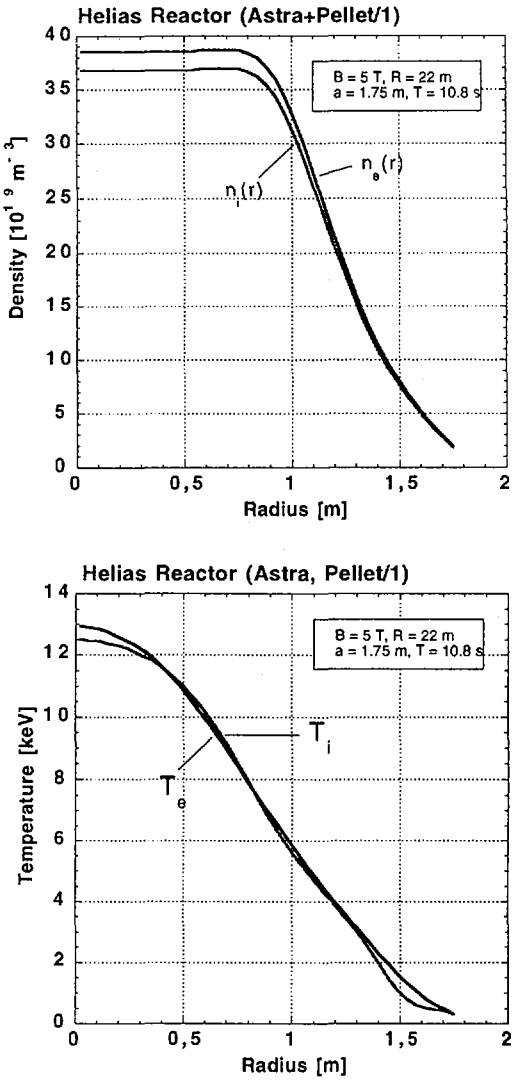

FIG. 9. Self-consistent density and temperature profiles obtained with ASTRA.

safety and economic aspects. For blanket and shield sufficient space has been provided, a detailed concept will be developed in future. To date more emphasis has been placed on scoping and parameter studies as opposed to fixing a specific set of parameters and providing a detailed point study.

One result of the Helias reactor studies is that physical dimensions are on the same order as those of tokamak reactors. However, it should be noticed that this comparison is difficult in view of the large spectrum of tokamak reactors ranging from a small reactor like Aries, to a large device such as SEAFP. The notion that the

large aspect ratio of 10 or more in Helias configurations also leads to large reactors is misleading, since the large major radius of 22 m is compensated by the average plasma radius of 1.8 m and the average coil radius of 5 m. The plasma volume of 1400 m^3 is about the same as in the ITER reactor and the magnetic energy of the coil system is about the same or even slightly smaller than envisaged in ITER.

The main technical component of the Helias reactor is the coil system which consists of 50 coils with only five different coil types. It has been found possible to employ a NbTi superconductor in these coils and to profit from the current development of NbTi-cable for Wendelstein 7-X. In order to sustain the magnetic field at 10.6 T at the coils, cooling must be done at 1.8 K (4.2 K in Wendelstein 7-X). The 3D-geometry of the coil system leads to a complex distribution of electromagnetic forces, however extrapolating the support system developed for W 7-X to a Helias reactor shows that stresses and strains are within technical limits.

One of the constraints in designing the Helias reactor was to provide sufficient space for blanket and shield; this has been achieved in HSR22 and larger devices. Extrapolation of one-dimensional neutron calculations made for the US stellarator reactor study SPPS and for SEAFP show that a breeding ratio higher than one and sufficient shielding of the coils can be reached in this approximation. However, certain details remain to be clarified since the 3-D geometry with its strong inhomogeneity of neutron emission and the specific limits of superconducting coils at 1.8 K have not been taken into account. Furthermore, the large area of the first wall ($F \approx 3000\ m^2$) which must be covered by a blanket requires a careful design in order to minimise the costs.

Although these Helias reactor studies are far from being complete it can be said that major insurmountable issues are not in sight; solutions of the main problems can be found, at least in principle. In order to judge the economic feasibility of a Helias reactor, however, safety aspects, availability of the reactor and, last but not least, costing need to be investigated in more detail.

REFERENCES

[1] NÜHRENBERG, J., ZILLE, R., Phys. Lett. A **114** (1986) 129.

[2] NÜHRENBERG, J., ZILLE, R., Phys. Lett. A **129** (1988) 1139.

[3] BEIDLER, C.D., et al., in Plasma Physics and Controlled Nuclear Fusion Research 1992 (Proc. 14th Int. Conf. Würzburg, 1992), Vol. 3, IAEA, Vienna (1993) 227.

[4] GRIEGER, G., NÜHRENBERG, J., RENNER, H., SAPPER, J., WOBIG, H., Fusion Eng. Des. **25** (1994) 73.

[5] HARMEYER, E., JAKSIC, N., SIMON-WEIDNER, J., in Proc. 19th Symp. on Fusion Technology, Lisbon, 1996.

[6] KISSLINGER, J., et al., in Controlled Fusion and Plasma Physics (Proc. 21st Eur. Conf. Montpellier, 1994), Vol. 18B, Part I, European Physical Society, Geneva (1994) 386.

[7] LOTZ, W., MERKEL, P., NÜHRENBERG, J., STRUMBERGER, E., Plasma Phys. Control. Fusion **34** (1991) 1037.

[8] ZOLOTUKHIN, A.V., et al., in Controlled Fusion and Plasma Physics (Proc. 23rd Eur. Conf. Kiev, 1996), Vol. 20C, European Physical Society, Geneva (1996).

DISCUSSION

B. COPPI: Could you be specific on the values of T and n. Are they local or average?

G. GRIEGER: Both are average values. The peak density is 3.5×10^{20} m^{-3} with $\langle n \rangle \approx 2.5 \times 10^{20}$ m^{-3}, and the peak temperature is 13 keV with $\langle T \rangle \approx 10$ keV.

A. GIBSON: The Helias reactor concept as you describe it has many attractions. It may be, however, in view of long approval and construction times, that W7-X is rather small when viewed as a stepping stone to a reactor. In the meanwhile, the reactor size device which may be built is ITER. Can you indicate key areas where experience with ITER may enable the development time for a Helias reactor to be shortened?

G. GRIEGER: Yes. There are several fields which are also of direct relevance to Helias reactors. These include DT operation in contrast to DT simulation in W7-X, all fields of technology development, to some extent plasma edge physics, etc. In my view, these items together with the results from W7-X may allow direct transition to a Helias reactor. However, shortening the approval times would also be of great help.

DESIGN ASSESSMENT OF HELIOTRON REACTOR

K. YAMAZAKI, A. SAGARA, O. MOTOJIMA, M. FUJIWARA,
T. AMANO, H. CHIKARAISHI, S. IMAGAWA, T. MUROGA,
N. NODA, N. OHYABU, T. SATOW, J.F. WANG,
K.Y. WATANABE, J. YAMAMOTO, H. YAMANISHI
National Institute for Fusion Science,
Nagoya, Japan

A. KOHYAMA
Kyoto University,
Uji, Japan

H. MATSUI
Institute for Materials Research,
Tohoku University,
Sendai, Japan

O. MITARAI
Kyushu Tokai University,
Kumamoto, Japan

T. NODA
National Research Institute for Metals,
Tsukuba, Japan

A.A. SHISHKIN
NSC Kharkov Physics and Technology Institute,
Kharkov, Ukraine

S. TANAKA, T. TERAI
University of Tokyo,
Tokyo, Japan

Abstract

DESIGN ASSESSMENT OF HELIOTRON REACTOR.

Helical reactor designs are studied on the basis of the physics and engineering concept of the Large Helical Device (LHD), which is characterized by two advantages: an efficient, closed helical divertor and a simplified continuous coil system. First, optimization studies of $\ell \approx 2$ conventional LHD type reactors (LHD-R) have been carried out. One point plasma modelling, in addition to 3-D equilibrium/1-D transport analysis, has clarified the D-T ignition condition. An accessible design window for reactor parameters is found by using physics and engineering constraints. A cost estimate suggests the importance of the compact design in reducing the cost of electricity. Second, a new reactor

design candidate, the modular heliotron reactor (MHR), is proposed; it is focused on the advantage of an efficient helical divertor that is compatible with the modular helical coil system. A special coil winding system permits an appropriate coil gap for reactor module maintenance, and makes good plasma confinement and an efficient helical divertor configuration compatible with each other. Two MHR design options are selected on the basis of the LHD-R system analysis. Third, by making use of the advantage of the simplified continuous coil design, a high field force free helical reactor (FFHR) is proposed in order to reduce the electromagnetic force by adopting an $\ell = 3$ force free like continuous coil system. The molten salt FLiBe, $LiF-BeF_2$, is selected in FFHR as a self-cooling tritium breeder, from the viewpoint of safety and compatibility with the high magnetic field design.

1. INTRODUCTION

In helical reactor design, plasma and helical coil systems are strongly coupled to each other; detailed optimal plasma–coil design studies are required. At present, two large optimized experimental helical machines, the Large Helical Device (LHD) and the Wendelstein 7-X (W7-X), are being designed and constructed [1]. The LHD concept, different from that of W7-X, is characterized by two advantages: (1) an efficient, closed helical divertor and (2) a simplified superconducting (SC) continuous coil system.

The present LHD SC machine was optimized on the basis of physics criteria [2] and engineering system analysis [3]. Here, we apply the same system analysis to LHD-type continuous coil helical reactors (LHD-R) and demonstrate the existence of an accessible design window. From this LHD-R system analysis, the modular heliotron reactor (MHR) design is proposed, with a new modular coil system, which retains the useful features of the helical divertor configurations of conventional continuous coil design. In addition, the $\ell = 3$ helical reactor is studied in order to reduce the electromagnetic force on the continuous helical coils as the force free helical reactor (FFHR).

These coil designs are shown schematically in Fig. 1.

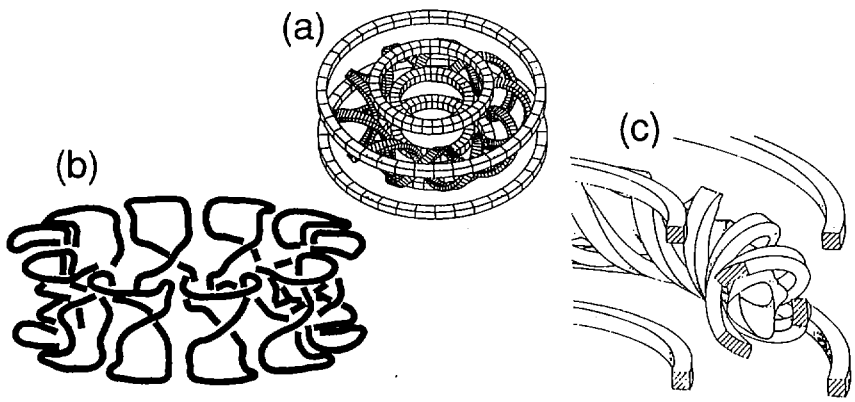

FIG. 1. Schematic coil configurations of (a) LHD, (b) MHR and (c) FFHR.

2. OPTIMIZATION OF LHD TYPE HELICAL REACTORS (LHD-R)

System assessment of the heliotron reactors was started from an LHD type $\ell = 2$, m = 10 coil system and the magnetic configurations. Physics optimization was carried out by equilibrium/stability beta limit analysis and a transport model projecting the D–T ignition condition. An engineering analysis has also been performed, taking into account maximum permissible magnetic field, coil stress, wall neutron loading, etc. Finally, a cost estimate was carried out for optimizing the reactor system. The design flow chart is shown in Fig. 2.

First, we will concentrate on the $\ell = 2$ continuous coil reactor design. The physics properties of the LHD configuration have been broadly studied, and beta achievement ($\sim 5\%$) and plasma transport projections are already clear [2].

The ignition conditions of D–T burning plasmas in LHD-R are studied by using zero dimensional power balance equations with profile corrections based on several empirical confinement scalings (LHD, gyroreduced Bohm (GRB), Lackner–Gottardi (LG) or international stellarator (IS) scaling) and a one point neoclassical ripple loss model (a combined model of the $1/\nu$, $\nu^{1/2}$ and ν regimes). A typical POPCON plot is shown in Fig. 3, which is bounded by anomalous plasma loss, neoclassical ripple loss, density limit and beta limits. A confinement improvement factor, f_H (H factor), of 2 is assumed for anomalous transport, and a 1.5 times larger density limit is required. The ripple transport loss is dominant in the high temperature regime, and the effective helical magnetic ripple should be smaller than $\sim 5\%$.

The effect of H factor and helical magnetic ripple on the reactor size is shown in Fig. 4. Without improvement of anomalous transport (LHD scaling in the left hand diagram), a 20 metre major radius machine is required in the case of 6 T. The effects of other confinement scaling laws without neoclassical ripple loss are shown in the right hand diagram. LG scaling yields the most optimistic results, while LHD scaling suggests a rather high field (high density) compact machine. The same dependence is obtained for IS and GRB scalings.

A detailed transport analysis using a three dimensional equilibrium/one dimensional transport code [3] has been performed; achievement of D–T ignition has been confirmed. The time evolution and typical radial profiles of the LHD-R plasma are shown in Fig. 5. Plasma density and external heating power, P_{ex} (initially 200 MW), are feedback controlled to produce and sustain 500 MW of alpha power, P_{alpha}. Direct alpha loss power, P_{direct}, and helium ash accumulation effects are also included in this simulation. Ripple ion transport is dominant in the central region, and the self-consistent negative radial electric field, E_r, reduces the ion heat loss in the outer region (see lower right diagram of Fig. 5).

The magnetic configuration and the coil–divertor clearance are evaluated by using simplified systematic scalings [4]. The system studies, including engineering design criteria for Nb_3Sn SC helical coils, are carried out to establish the plasma ignition conditions. The reference magnetic configuration adopted here is an m = 10, $\gamma_c = 1.2$ system with a closed helical divertor. A maximum magnetic

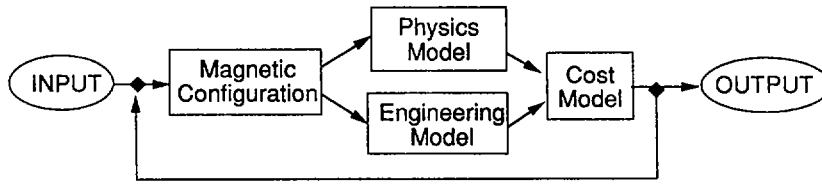

FIG. 2. Flow chart of helical system optimization.

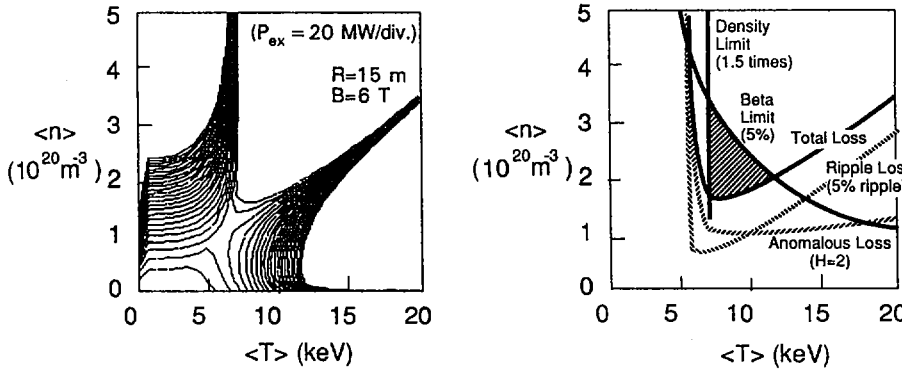

FIG. 3. POPCON plot for LHD-R.

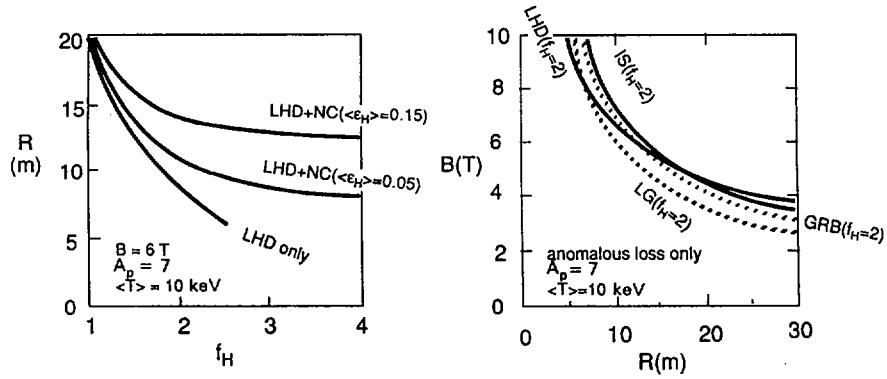

FIG. 4. Effect of ripple transport and H factor (left) and several confinement scalings (right) on the ignition machine size parameters.

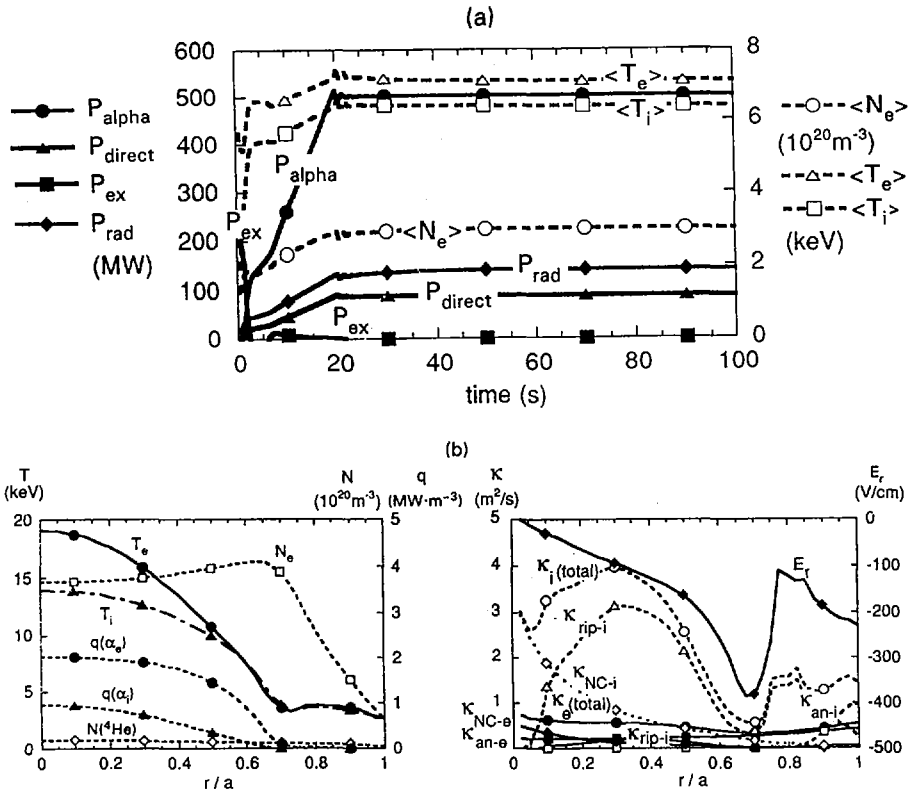

FIG. 5. Example of 3-D equilibrium/1-D transport simulation of LHD-R ignition. (a) Time evolution of plasma parameters for R = 12.5 m, B = 6.5 T reactor; (b) radial profiles of temperature T, electron and helium density N, alpha heating power density q(α), thermal conductivity κ and radial electric field E_r at t = 100 s.

field $B_{max} < 16$ T with a coil current density of ~30 A/mm^2 is allowed for Nb_3Sn superconducting coil systems. A neutron wall loading of $L_n < 3$ MW/m^2, a coil–divertor clearance of $\Delta_{cd} > 1$ m for standard blanket space and $\Delta_{cd} > 0.4$ m for compact design, and a coil stress limit of $\sigma_{coil} < 250$ MPa are required. The conditions of total fusion thermal power, $P_{fusion} > 1$ GW and a coil magnetic energy of $W_{mag} < 500$ GJ should be included in the criteria for a cost effective system. A confinement enhancement factor f_H of 2 and a density limit factor of 2 (during the startup phase only) are assumed in LHD scaling. To reduce neoclassical ripple loss, the average effective helical ripple should be less than 5%, which is attainable in LHD-R by means of an inward shift of the plasma column and/or coil pitch modulation to the so-called transport optimized heliotron. Among these criteria, we found a design window for LHD-R as shown in Fig. 6. This analysis is also applicable to the modular heliotron reactor (MHR) to be discussed later.

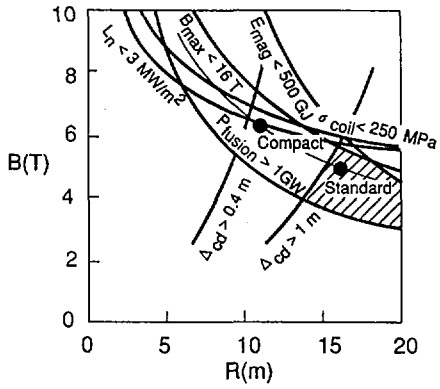

FIG. 6. Design window of LHD-R.

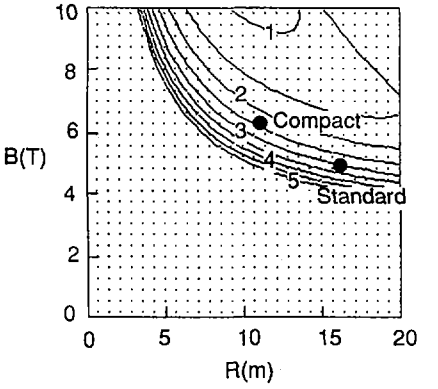

FIG. 7. Cost estimate of LHD-R (contours of normalized cost of electricity).

For D–T reactors, the standard design with a major radius of 16.5 m and a magnetic field strength of 5 T is obtained. The compact system, with a major radius of 10.5 m and a magnetic field strength of 6.5 T, is evaluated by sacrificing the divertor clearance. A D–^{3}He reactor analysis is also carried out, and the scale requirements for these reactors are clarified: a confinement enhancement factor of ~ 3 and a helical ripple configuration of $< 2\%$.

The cost estimate was carried out by using a model similar to that used in Ref. [5]; it is now clear that the compact model is more cost effective than the standard design (Fig. 7).

3. MODULAR HELIOTRON REACTOR (MHR) BASED ON LHD-R

In helical systems with continuous helical coils it is usually difficult to achieve a modular structure for easy reactor maintenance. On the other hand, a conventional modular stellarator is mainly designed to optimize core magnetic confinement, and it is not easy to reserve sufficient divertor space for heat load reduction and helium ash exhaust. It is hence important to look for a new divertor configuration that is compatible with a modular coil system. Using the LHD physics concept we proposed a modular heliotron [6, 7]. The coil system of the reference modular heliotron without one turn poloidal field coils was constructed on the basis of the conventional heliotron by combining sectored helical field coils with sectored returning poloidal field coils. The connection current feeders were arranged so as to avoid destruction of the divertor layer and to keep a large space for the divertor chamber. Figure 8 shows the one coil module and the magnetic divertor structure.

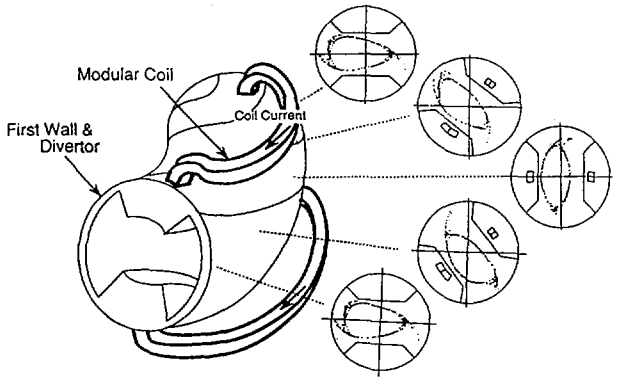

FIG. 8. Magnetic divertor configuration of MHR.

The LHD design study was carried out on the basis of the physics concept with respect to equilibrium/stability beta limit, particle orbit confinement, divertor layer clearance, energy transport, etc. [2, 3]. In a similar way, physics optimization for the MHR system was performed with three main criteria: the gap angle between adjacent modular coils (coil modularity index), the branching-off of the divertor separatrix layers (closed divertor index) and the magnetic properties such as plasma radius, rotational transform, beta limit, particle confinement, etc. (good plasma confinement index). The standpoint of our proposal is that the closed helical divertor configuration with tolerable neoclassical ripple transport loss might be important in reactor design to improve the edge confinement, leading to H mode transition in addition to helium ash exhaust.

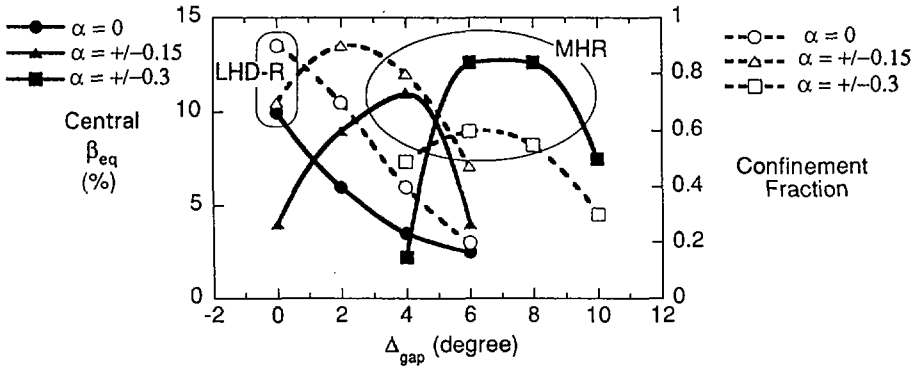

FIG. 9. Physics optimization for MHR as a function of the coil gap.

TABLE I. LHD AND THREE REACTOR DESIGN PARAMETERS

	LHD	MHR-C	MHR-S	FFHR-1
Plasma parameters				
Number of poles, ℓ	2	2	2	3
Toroidal pitch number, m	10	10	10	18
Major radius, R (m)	3.9	10.5	16.5	20
Average plasma radius, $\langle a_p \rangle$ (m)	<0.65	1.5	2.36	2
Fusion power, P_f (GW)	—	2.8	3.8	3
External heating power, P_{ex} (MW)	<20	55	80	100
Toroidal field on axis, B_0 (T)	4	6.5	5	12
Average beta, $\langle \beta \rangle$ (%)	>5	5	5	0.7
Enhancement factor of τ_{LHD}	—	2	2	1.5
Plasma density, $n_e(0)$ (m^{-3})	1×10^{20}	7.8×10^{20}	4×10^{20}	2×10^{20}
Plasma temperature, $T_e(0)$ (keV)	>10	15.6	15.6	22
Engineering parameters				
Average helical coil radius, $\langle a_c \rangle$ (m)	0.975	2.52	3.56	3.33
Pitch parameter, $\gamma_c = m\langle a_c \rangle/(\ell R)$	1.25	1.2	1.2	1
Coil to plasma clearance, Δ (m)	0.03	0.43	1.14	1.1
Coil current, I_H (MA/coil)	7.8	34.1	41.25	66.6
Coil current density, J (A/mm^2)	(53)	30	30	27
Maximum field on coils, B_{max} (T)	(9.2)	14.7	14.9	16
Stored energy with poloidal coils (GJ)	1.64	210	221	1290
Neutron wall loading, P_n (MW/m^2)	—	3.4	1.9	1.5
SC material	NbTi	Nb_3Sn	Nb_3Sn	Nb_3Al or $(NbTi)_3Sn$

Good magnetic configurations are found to be produced by adopting optimum coil winding modulation (using the outside plus/inside minus pitch modulation parameter α [3]) as a function of the coil gap, Δ_{gap}, even in the case of a large increase in the gap angle. Figure 9 shows the equilibrium beta limit and confinement fraction defined by minimum B contours for LHD-R ($\alpha = 0$ and $\Delta_{gap} = 0°$ (continuous coil)) and MHR ($\alpha = +/-0.15$–0.3 at $\Delta_{gap} = 4$–$8°$). Mercier mode analysis also suggests that the stability properties of the MHR are comparable with LHD-R. More optimized configurations are being searched by adjusting the coil shaping parameters.

MHR system evaluation was carried out by using the above mentioned continuous coil optimization results; two typical design candidates, MHR-C (compact design without high field inboard blanket) and MHR-S (standard design), are selected (Table I). For a ~ 10 m major radius, ~ 6 T magnetic field machine with a coil current density of ~ 30 A/mm^2 the required coil gap is larger than 4° (0.7 m distance). The construction and maintenance concept of this reactor design is based on the ten period good coil modularity without poloidal coils. Moreover, large ports are available to allow helical divertor plate repair by remote handling. Detailed engineering design studies on MHR are under way.

4. FORCE FREE HELICAL REACTOR (FFHR)

On the basis of the SC continuous coil system of LHD, a conceptual design of a force free helical reactor (FFHR) was carried out in order to clarify key issues of power plant engineering, including materials development, and in order to introduce innovative concepts expected to be available during the few decades to come. As the first stage of FFHR concept definition, the reference reactor FFHR-1 has been designed [8–11]. Cost estimation and design optimization are planned in the second stage of the present study of Phase I.

The main specifications of FFHR-1 are listed in Table I. The $\ell = 3$ system is adopted to obtain a force free like coil configuration compatible with sufficient space for plasma confinement as shown in Fig. 1. From the design window shown in Fig. 10, where the coil cross-section is rectangular, the ignition case A for $B_0 \sim 12$ T and $R \sim 20$ m is almost optimum as far as the following three parameters are concerned: $B_{\perp max}$ in helical coils below 15 T; a coil-to-plasma clearance of Δ over 1 m needed for blanket and shield; and the enhancement factor, f_H, for τ_{LHD} less than 2. Under these conditions, Nb_3Al or $(NbTi)_3Sn$ is chosen as a primary candidate for the SC material.

FFHR has two main features: the first feature is the reduction of the electromagnetic force between continuously winding SC helical coils by reducing the helical pitch parameter, $\gamma_c = (m/\ell)(a_c/R)$, as shown in Fig. 11, where the averaged minor radius hoop force on the helical coils, $\langle f_a \rangle$, normalized by B_0 and the coil current I_H, in FFHR-1 is reduced to 35% of the value in LHD. Since the ratio a_p/a_c

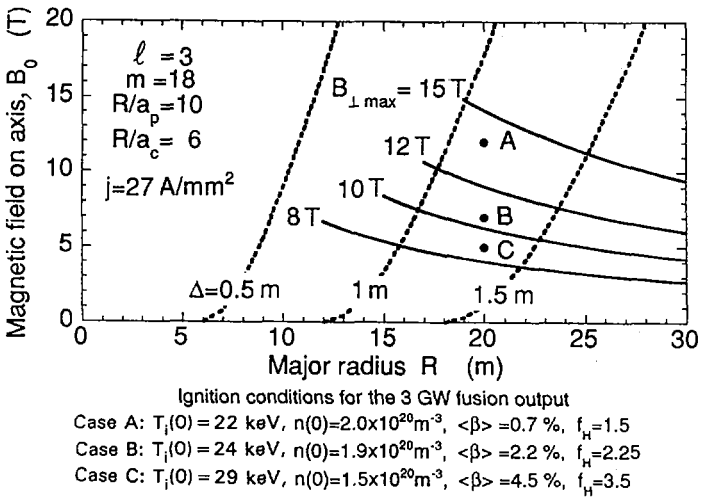

FIG. 10. Design window for B_0 and R under constraints of maximum perpendicular field in helical coils, $B_{\perp max}$, coil-to-plasma clearance Δ and ignition conditions.

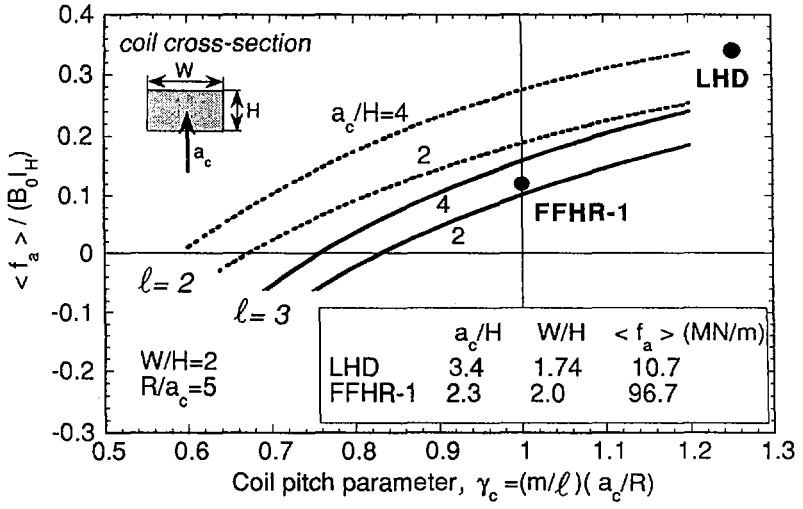

FIG. 11. Averaged minor radius hoop force on helical coils, $\langle f_a \rangle$, normalized by $B_0 I_H$ as a function of coil pitch parameter, γ_c.

decreases with γ_c, the reduction of γ_c is also needed to create a wide coil-to-plasma clearance for the blanket and shield space. In FFHR-1 the ratio a_p/a_c is about 0.6, and a coil-to-plasma clearance of about 1 m is obtained. In case of the $\ell = 2$ system, on the other hand, since no closed magnetic surface is formed ($a_p = 0$) at $\gamma_c < 0.9$, a great reduction of the hoop force at $\gamma_c < 0.9$ is of no use for plasma confinement.

An ideal force free condition on the helical coils is possible under the combination with vertical field coils reducing the toroidal hoop force, but requires a decrease in a_c or an increase in the helical coil current, I_H, to obtain a fixed value of the toroidal field B_0, because of the reduction of γ_c. In the FFHR design, however, the ideal force free condition is not adopted from the viewpoint of engineering safety or magnetoelastic stability and an excessive shrinkage of the plasma minor radius, a_p. Even with a moderate reduction of the magnetic force, there are two attractive merits: one is the simplification of the coil supporting structures, which creates a wide, open area for the maintenance of in-vessel components, and the other is the use of high magnetic fields leading to some margin in the plasma beta, $\langle\beta\rangle$, for self-ignition, with a permissible amount of He ash and requiring a less severe enhancement factor for the energy confinement time. In fact, as is shown in Fig. 10, case A with $B_0 = 12$ T requires a $\langle\beta\rangle$ value of only 0.7%, but case C with $B_0 = 5$ T requires a $\langle\beta\rangle$ of 4.5% and an f_H as high as 3.5. Therefore, in the next stage of concept optimization, there is wide flexibility to find a compromise between the two merits of simple structure and high magnetic field.

The second feature in FFHR is to select the molten salt FLiBe, $LiF\text{-}BeF_2$, as the self-cooling tritium breeder, for the main reason of safety, i.e. there are the following properties: low tritium inventory, low reactivity with air and water, low pressure operation and low MHD resistance, which is quite compatible with the high magnetic field in FFHR-1. Because of the extremely low tritium solubility, which is about eight orders lower than that of liquid Li [12], the T_2 gas separation system becomes quite simple. The total flow amount of FLiBe is about 7 m^3/s, and the operation pressure, with a Reynolds number of over 10^5, is estimated to be less than 0.5 MPa, with a total pump power of only 0.8% of the fusion output, P_f.

Owing to the large reactor size, the neutron wall loading is reduced to 1.5 MW/m^2, which allows the in-vessel components to be used for the full lifetime of 30 years, without being replaced if structural materials reliable up to 450 dpa at temperatures above 600°C are developed. Here, the low activation ferritic steel JLF-1(Fe_9Cr_2W) is selected, which should be used at a temperature of 550°C for up to 100 dpa; ODS steel and vanadium alloys are further options [11]. Figure 12 shows the blanket and shielding structure in FFHR [8]. The Mo–TiC alloy, which has high resistance against neutron irradiation, is used for the first wall. The W–TiC alloy, which is currently being developed by replacing Mo with W in view of the induced radioactivity [11], is the second option. The double walled blanket and transfer tube are covered with He gas to sweep out the permeated T_2 and to monitor drain events. The neutron multiplier Be is also used as metal scavenger ($Be + 2TF \rightarrow BeF_2 + T_2$) in order to reduce the amount of severely corrosive TF molecules. The total tritium breeding ratio TBR is over 1.1, and the first neutron flux (>0.1 MeV) is successfully reduced by more than five orders at the SC coils. The volumetric nuclear heating in FLiBe is more than 60% of the fusion output, P_f.

Blanket replacement may be required at least every ten years. The basic design for this procedure is to use blanket units which are replaced through maintenance

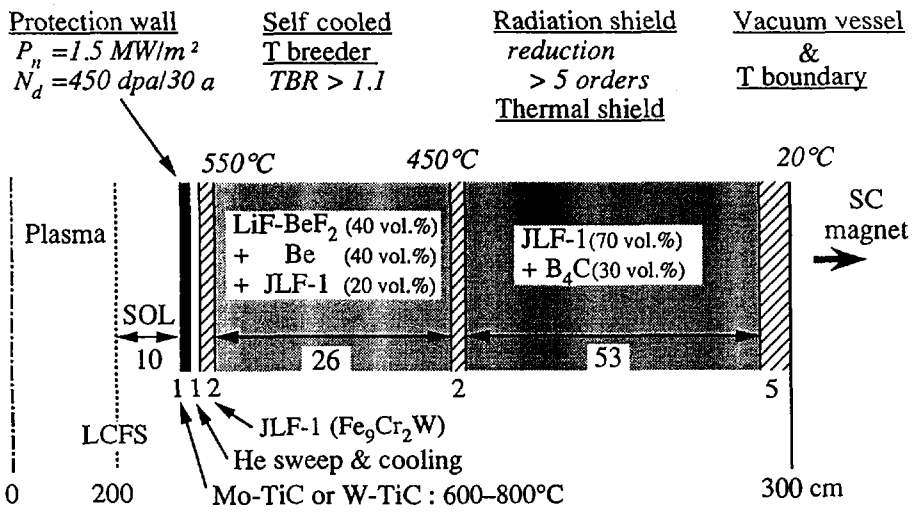

FIG. 12. Blanket and shielding structure in FFHR.

ports by sliding along the continuous helical coils. At this time, since the total mass of 400 t of FLiBe is moved to a drain tank, the weight of each blanket unit can be below 5 t. The radioactive wastes in each replacement are 800 t of JLF-1, 160 t of Mo–TiC or 300 t of W–TiC, which amounts to only 16 m^3 in volume and can hence be managed, and 350 t of Be, which is the mass to be recycled.

Important subjects in FFHR are under investigation: (1) optimization of the magnetic field configuration to improve the MHD stability; (2) design of divertor pumping systems for the He ash; (3) scenario for large scale SC helical coil manufacture; (4) control of material corrosion in the FLiBe system; (5) maintenance and repair techniques.

5. SUMMARY

In this paper, we have assessed heliotron reactors based on LHD physics and engineering design and have clarified the following points:

(1) Optimization studies of $\ell = 2$ conventional LHD type reactors (LHD-R) have been carried out by physics, engineering and cost analyses. One point plasma modelling, in addition to 3-D equilibrium/1-D transport analysis, has clarified the condition for DT ignition. A typical reactor design window was derived by using physics and engineering constraints, and two design options were selected within the limits of permissible blanket space, neutron wall loading, coil stress, etc. The cost estimate suggested the importance of compact designs in reducing the cost of electricity.

(2) The new modular heliotron reactor (MHR), compatible with a well defined and efficient closed helical divertor was studied. The physics optimization of this system has been carried out on the basis of the large helical device (LHD) physics concept by means of vacuum magnetic surface analyses and finite beta calculations. The effectiveness of this new coil system and its magnetic configuration was clarified. The engineering design of the MHR was also carried out on the basis of this physics concept, and the required machine parameters for DT ignition were clarified.

(3) The high field force free helical reactor (FFHR) was proposed for the reduction of the electromagnetic force by adopting an $\ell = 3$ force free like continuous coil system, and the engineering issues for the power plant reactor were clarified. Molten salt FLiBe, LiF-BeF_2, as self-cooling tritium breeder was selected with in-vessel structural material of low radioactive ferritic steel JLF-1 for the following reasons of safety: low tritium inventory, low reactivity with air and water, low pressure operation and low MHD resistance, which is compatible with high magnetic field design.

REFERENCES

[1] IIYOSHI, A., YAMAZAKI, K., Phys. Plasmas **2** (1995) 2349.
[2] YAMAZAKI, K., et al., in Plasma Physics and Controlled Nuclear Fusion Research 1990 (Proc. 13th Int. Conf. Washington, DC, 1990), Vol. 2, IAEA, Vienna (1991) 709.
[3] YAMAZAKI, K., AMANO, T., Nucl. Fusion **32** (1992) 633.
[4] YAMAZAKI, K., MOTOJIMA, O., ASAO, M., Fusion Technol. **21** (1992) 147.
[5] SHEFFIELD, J., et al., Fusion Technol. **9** (1986) 199.
[6] YAMAZAKI, K., Plasma Fusion Res. **70** (1993) 281 (in Japanese).
[7] YAMAZAKI, K., WATANABE, K.Y., Nucl. Fusion **35** (1995) 1289.
[8] SAGARA, A., et al., Fusion Eng. Des. **29** (1995) 51.
[9] MITARAI, O., et al., Trans. Fusion Technol. **27** (1995) 278 (in Japanese).
[10] MOTOJIMA, O., et al., Trans. Fusion Technol. **27** (1995) 264 (in Japanese).
[11] MATSUI, H., et al., in Technology of Fusion Energy (Proc. 12th Top. Mtg. ANS, Reno, NV, USA, 1996).
[12] CAORLIN, M., et al., Fusion Technol. **14** (1988) 663.

TECHNOLOGY AND NEW DEVICES

(Session G2)

Chairperson

E. SALPIETRO
European Community

CONCEPTUAL DESIGN OF THE INTERNATIONAL FUSION MATERIALS IRRADIATION FACILITY (IFMIF)

T.E. SHANNON[1], M.J. RENNICH
Oak Ridge National Laboratory,
Oak Ridge, Tennessee,
United States of America

T. KONDO[2], H. KATSUTA, H. MAEKAWA
Japanese Atomic Energy Research Institute,
Tokai-mura, Japan

R.A. JAMESON
Los Alamos National Laboratory,
Los Alamos, New Mexico,
United States of America

M. MARTONE
Euratom-ENEA Association,
Frascati, Italy

A. MÖSLANG
Forschungszentrum Karlsruhe,
Karlsruhe, Germany

V. TEPLYAKOV
Institute for High Energy Physics,
Protvino, Moscow Region,
Russian Federation

Abstract

CONCEPTUAL DESIGN OF THE INTERNATIONAL FUSION MATERIALS IRRADIATION FACILITY (IFMIF).

The International Fusion Materials Irradiation Facility (IFMIF) Conceptual Design is being carried out as an activity of the IEA Executive Committee on Fusion Materials. Initial workshops were held in 1995, in which specialists from Europe, Japan, the United States of America and the Russian Federation came together in small groups to define the concepts for the three major technical systems (Accelerator, Target and Test Cell). The overall design and cost estimate is being developed in design integration meetings in which members of the four parties work together for up to a two week period.

[1] University of Tennessee, Knoxville, Tennessee, USA.
[2] Tohoku University, Sendai, Japan.

The conceptual design activity (CDA) final report was published in December 1996. The goal of the IFMIF is to provide an irradiation facility for use by fusion material scientists in the development of low activation and damage resistant materials. An accelerator-based neutron source has been established through a number of international studies and workshops as an essential step for near-term materials development and testing. IFMIF would also provide calibration and validation of data from fission reactor and other accelerator-based irradiation testing. The IFMIF concept is derived from requirements from the materials community for test volumes and neutron fluences needed to obtain useful irradiation data in a reasonably short operating time. Studies indicate that a volume of about 0.5 L is required in a region producing a flux equivalent to 2 MW/m^2 (0.9×10^{18} $n \cdot m^{-2} \cdot s^{-1}$, uncollided flux) or greater. A fraction of this volume, about 0.1 L, would be available at a flux equivalent to 5 MW/m^2 for accelerated testing. The design concept consists of a deuteron accelerator producing particle energies in the range of 30 to 40 MeV. The deuterons interact with a flowing liquid lithium target (d-Li) producing high energy neutrons with a peaked flux around 14 MeV. The resulting high energy neutrons will interact with a test assembly to irradiate test samples of candidate materials up to full lifetime of anticipated use in future fusion energy reactors.

1. INTRODUCTION AND DESIGN CONCEPT

Neutronics calculations indicate that 35 to 40 MeV deuterons provide a sufficiently large volume of high-flux irradiation with a reasonable simulation of the fusion energy gaseous and solid transmutation rates in most metallic components. However, some of the transmutation components in ceramic materials are best simulated by lower energy deuterons; therefore, IFMIF is staged to permit changes in deuteron energy from 32 to 40 MeV during irradiation campaigns thus allowing the influence of certain transmutation products to be identified.

The IFMIF Test Cell consists of five modular assemblies containing the irradiation specimens. The different modules provide different environments (coolant and temperature). Each module is supported by a self-contained cooling/shielding arrangement that can be removed and replaced with vertical access and is thus referred to as a vertical test assembly (VTA). The VTA design is based on configurations and technologies currently used in similar fission reactor and accelerator experiments. The five VTAs including the specimen cooling system and instrumentation and controls for the test modules are supported from one end which penetrates through the Test Cell shield plug.

The lithium jet target flows across a back wall, perpendicular to the beam, with dimensions of 2.4 cm thick, 20 cm wide and 5 cm high. Neutrons are produced by the interaction of the deuterons with the lithium while the beam energy is absorbed and transferred by lithium. A critical design issue in the target assembly is the lifetime of the back wall which will be exposed to the maximum neutron flux. The back wall will be designed for easy replacement and the IFMIF facility will be started with campaigns designed to evaluate the back wall life and reliability. The loop which circulates the lithium to and from the target assembly and removes the heat deposited by the deuteron beam also contains systems for maintaining the high purity required for removal of induced radioactivity and for minimizing corrosion of the loop structure by the hot flowing lithium.

The neutron fluence and testing requirements necessitate the use of continuous wave (cw), high current accelerators. Quasi-continuous operation is mandatory because annealing times of point defects shorter than the repetition time of pulses and rate effects would introduce unacceptable uncertainties in the observed radiation effects. Thus, IFMIF will operate with two accelerators providing identical overlapping beam footprints on either one of two lithium targets. Conservative design studies show that 250 mA of deuteron beam current delivered to the target by two 125-mA, 40-MeV accelerators can be accomplished using a reasonable extrapolation of existing technology.

2. GOALS AND MISSION

The enormous progress in fusion energy research over the past decade is due in large part to international collaboration. The ITER project is well along in the engineering design of the first major fusion device to demonstrate the scientific and technological feasibility of fusion energy. Continued progress toward the development of a fusion power plant will require addressing a broader set of issues. Environmental acceptability, safety, and economic viability will ultimately be the keys to the widespread introduction of fusion power. This will entail the development of radiation - resistant and low-activation materials. These low-activation materials must also survive exposure to damage from neutrons having an energy spectrum peaked near 14 MeV with annual radiation doses in the range of 20 displacements per atom (dpa). Testing of candidate materials, therefore, requires a high-flux source of high energy neutrons. The problem is that there is currently no high-flux source of neutrons in the energy range above a few MeV. The goal is therefore to provide an irradiation facility for use by international fusion material scientists in the search for low-activation and damage-resistant materials. An accelerator-based neutron source has been established through a number of international studies and workshops [1] as an essential step for materials development and testing.

The mission of the International Fusion Materials Irradiation Facility (IFMIF) is to provide an accelerator-based, deuterium-lithium (d-Li) neutron source to produce high energy neutrons at sufficient intensity and irradiation volume to test samples of candidate materials up to about a full lifetime of anticipated use in fusion energy reactors.

IFMIF would also provide calibration and validation of data from fission reactor and other accelerator-based irradiation tests. It would generate material-specific activation and radiological properties data and support the analysis of materials for use in safety, maintenance, recycling, decommissioning and waste disposal systems.

3. CONCEPTUAL DESIGN ACTIVITY

The objective of IFMIF conceptual design activity (CDA) is to provide a reference design and a project basis, including a schedule and cost estimate, satisfying the mission and the requirements for a facility as described above. The CDA is being carried out under the direction of a subcommittee of the International Energy Agency (IEA), Executive Committee on Fusion Materials.

The design team consists of specialists in all technical areas relevant to IFMIF, working, most of the time in their home institutions in Europe, Japan, the United States and the Russian Federation. The design work is being done over a 2-year period, 1995—96, through a series of technical meetings and workshops in which tasks are defined and discussed and to be completed at the home institutions. After a joint technical preparation workshop held at FzK at Karlsruhe, Germany in September 1994 [2], specific area meetings were held during the summer of 1995 in Europe (test facilities) [3], Japan (target systems) [4], and the United States (accelerator) [5]. The initial baseline design concept was developed during a 2-week design integration workshop, October 16 - 27, 1995, at Oak Ridge National Laboratory [6]. The first draft of the interim report was also produced during that workshop. The second design integration workshop was held at the Japanese Atomic Energy Research Institute, Tokai, Japan, May 20-24, 1996 [7,8]. At this meeting, the baseline design was revised to reflect several changes discussed by the design team. The first draft of a cost estimate and schedule as well as a plan for the Engineering Validation Phase was also produced. This information along with the changes in the design will be included in the final Conceptual Design Report to be published December 31, 1996 [9]. The entire CDA effort will be accomplished with a work force of approximately 25 person years per year.

The work breakdown structure (WBS) for the project has four major elements that define the technical focus for the CDA as follows:

1. Project management/design integration,
2. Test facilities,
3. Target facilities, and
4. Accelerator facilities.

The schedule of meetings and activities for the CDA is as follows:

Form international procedural concept	June	1994
Formulate initial requirements and CDA tasks	Sept.	1994
Preliminary system design layouts		
Test facilities	July	1995
Target system	July	1995
Accelerator system	Sept.	1995
Design integration workshop		
Design layout and establish baseline design	Oct.	1995
Interim report	Dec.	1995
Preliminary project plan and cost estimate	May	1996
Final design integration workshop		
Update baseline design, plan, and cost	Oct.	1996
Conceptual design report	Dec.	1996

The CDA relies on an international electronic network system for communication among the project groups of various countries and institutions. To set up an efficient communication system, protocols and software have been specified. The basic set includes: EUDORA for electronic mail; Microsoft Word 6.0 for text format, Microsoft Excel 5.0 for spreadsheet format, Microsoft Project for Schedules and AUTOCAD 12 (.DXF) format for drawings. A computer server has been set up at ENEA Research Center of Frascati where

project documents (reports, drawings, etc.) released from project management are stored and easily accessible to all the project participants.

In addition to providing up-to-date design information, the common server could provide the design team with a data base of supporting information, such as technical reports and results of research and development programs. Large data bases such as the files from the U.S. Fusion Materials Irradiation Test (FMIT) Project, or the Japanese Energy Selective Neutron Irradiation Test Facility (ESNIT) could be transferred to this system.

4. USER REQUIREMENTS

The design concept for IFMIF is based on input from the materials community on the estimated test volume required to obtain useful irradiation data in a reasonably short operating time. Detailed design studies of the test assembly indicate that a test volume of about 0.5 L is required in a region producing a flux equivalent to 2 MW/m^2 (0.9×10^{18} n/m^2-s, uncollided flux) or greater. A fraction of this volume, about 0.1L, is available at a flux equivalent to 5 MW/m^2 for accelerated testing.

The accelerator system will provide deuterons at 32, 36, or 40 MeV. The 40 MeV deuterons provide the maximum high-flux irradiation volume and provide a reasonable simulation of the fusion energy gaseous and solid transmutation rates in most metallic components. Some of the transmutation components in ceramic materials are best simulated with 32 or 36 MeV deuterons. The flexibility of choosing deuteron energies between 32 and 40 MeV during irradiation campaigns allows experiments designed to establish the influence of certain transmutation products to be conducted.

An estimate of the test volume and the corresponding displacement rate in a test assembly with iron-based specimens per year of facility operation (including scheduled outage time) is as follows:

0.1L > 50 dpa/year
0.4L > 20 dpa/year
6.0L > 1 dpa/year

A quasi-continuous operation is mandatory. Annealing times of point defects shorter than the repetition time of pulses and rate effects in the case of low duty-cycle sources would introduce unacceptable uncertainties in the observed radiation effects. It is planned that IFMIF will operate with two accelerators providing identical overlapping beam footprints on either one of the two lithium targets. This configuration minimizes flux perturbations caused by a beam-off transient in one of the accelerators (i.e., the maximum likely temporal variation in the flux would be a factor of 2).

Because of the level of uncertainty in the amount of testing and development needed to characterize the damage effect of 14 MeV neutrons and to quantify materials for reactor lifetime service, the IFMIF facility has been designed from the outset to accommodate a possible future expansion in irradiation capacity and test volume. Two additional accelerators can be added so that two test cells could be operated simultaneously. The lithium system can be expanded so that both

target systems can operate at the same time. At full-power operation, this expansion would double the test volume for the displacement rates as shown above. If needed, this additional volume would allow much more flexibility in the range of operating conditions within the test assemblies and thereby significantly reduce the time to characterize and test new material options.

5. TEST FACILITIES

Complete design concepts are available for three Vertical Test Assemblies considered in the present design that provide four flux regimes. That is, test beds for instrumented and/or in situ experiments in metals and nonmetals can be provided meanwhile for any loading regime from >20 dpa/y to 0.01 dpa/y. Detailed test matrixes have been defined for the high and medium flux regions, showing that on the basis of small specimen test technologies, a database for an engineering design of an advanced fusion reactor can be established for a variety of structural materials and ceramic breeders. Design concepts for VTAs with instrumented capsules for post irradiation and in-situ experiments using either NaK or helium gas as coolant have been developed together with the design concepts for remote handling and Hot Cell facilities with capacity for investigating all irradiation specimens on the IFMIF site.

The Test Cell (Fig. 1) has an actively cooled steel liner and a removable shield plug with ports which allow flexible installation of two Vertical Test Assemblies (VTA-1 and VTA-2) for the high and medium flux regions, and a Vertical Irradiation Tube (VIT) system for the low and very low flux regions. The Vertical Assemblies penetrate through the test cell ceiling and include the primary coolant, instrumentation and the test modules to be irradiated. This concept maintains a high degree of flexibility with respect to any future needs. In the present reference design the high flux region consists of either NaK cooled test modules for low and medium irradiation temperatures or helium gas cooled test modules for high temperature applications. There is an option to replace the NaK cooled version after the feasibility of the helium concept has been shown experimentally. Major advantages of helium gas instead of NaK are flexibility with respect to irradiation temperatures as well as safety and maintenance considerations (NaK has more than 10 times higher decay heat than He during the first day after irradiation). Several types of in-situ tests are foreseen in the medium flux region. The VIT system in the low and very low flux region is presently planned for tests on special purpose materials like ceramic insulators, RF windows, diagnostic materials or superconducting materials.

Major engineering efforts have been undertaken to completely remote control any maintenance and assembling/disassembling activities in the Test Cell, the Access Cell and the Service Cell during normal and off-normal operation scenarios. Once the specimens are retrieved from the capsules in the Test Module Handling Cell, they will be mechanically tested in the PIE Hot cells followed by microstructural investigations like SEM or TEM in the Glove Box Laboratory (Fig. 2). Tritium containing or contaminated specimens will be analysed in detail in the Tritium Facility. Any tritium exposure to personnel or environment will be avoided by effective tritium retention systems.

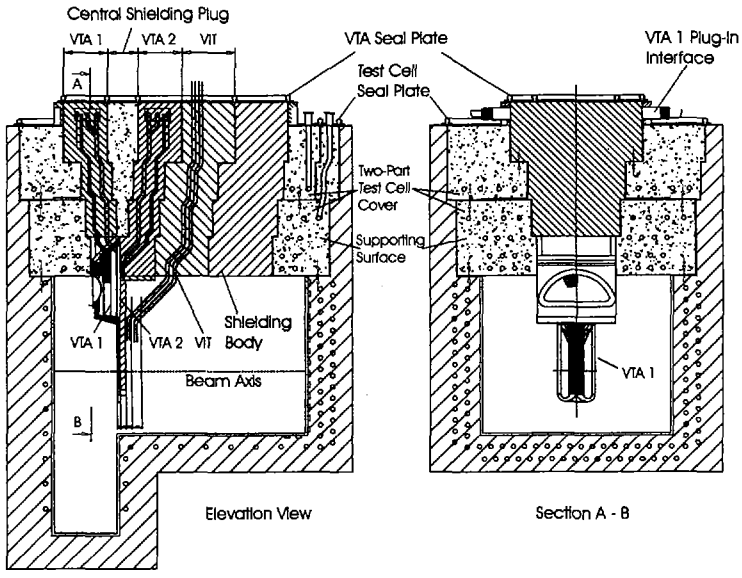

FIG. 1. Test cell arrangement.

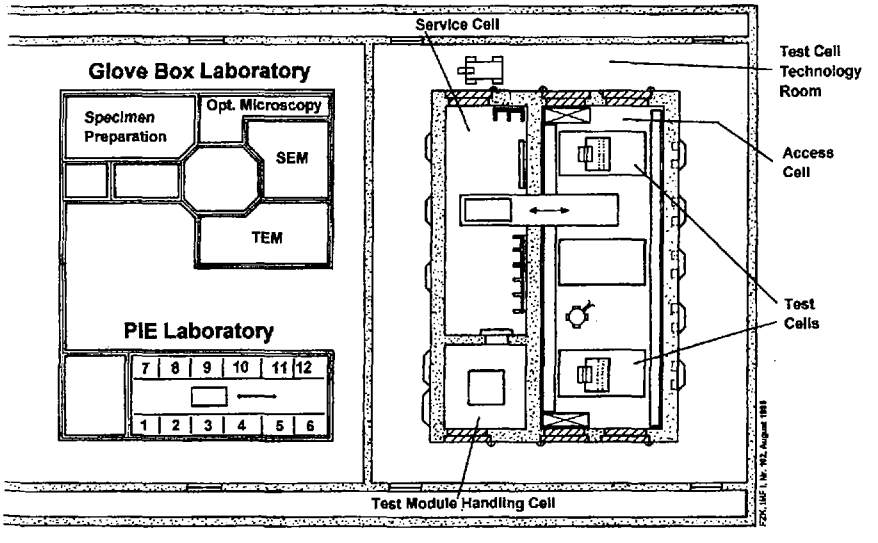

FIG. 2. Testing facilities.

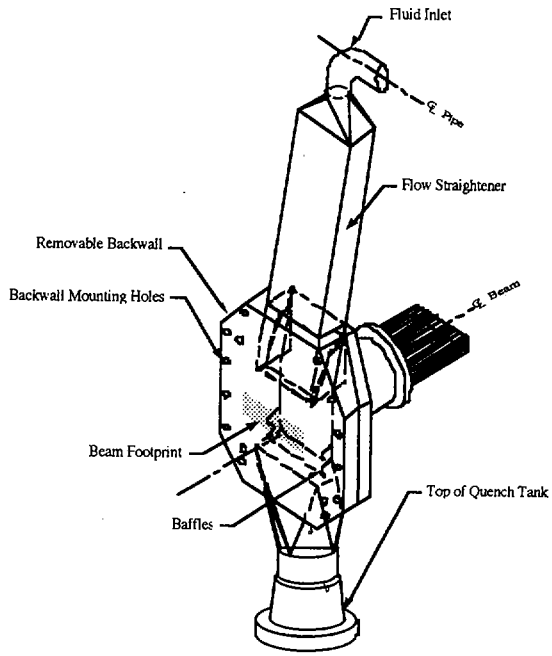

FIG. 3. Target assembly with removable backwall.

6. LITHIUM TARGET SYSTEM

The lithium target may be divided up into two basic components. The first is the target assembly itself, which must present a stable lithium jet to the beam, where the kinetic energy of the deuteron beam is deposited and where neutrons are produced. The second is the lithium loop, which circulates the lithium to and from the target assembly and removes the heat deposited by the deuteron beam. This loop also contains systems for maintaining the high purity of the lithium metal required for radiological safety and for minimizing corrosion of the loop structure by the hot flowing lithium. A single lithium loop provides flow to either of the target assemblies in the two Test Cells. A maximum 10% flow is provided to the inoperative target for decay heat removal. The target assembly and lithium loop will be briefly described.

The target assembly, shown in Fig. 3, consists of the inlet pipe, the transition component from inlet pipe to flow straightener, the flow straightener, the nozzle, the backwall, the downstream diffuser with built-in drain baffles and a vacuum port for connection to the deuteron beam tube. The total vertical distance from the highest point of the inlet pipe to the beam centerline is about 1.5 m. For a 40 MeV deuteron beam and a beam footprint of 5 x 20 cm, the nozzle lip dimensions will be 2.4 cm thick and 26 cm wide. Based upon a thorough assessment of various target designs, the modified FMIT-type target

with a replaceable backwall has been selected for the baseline design. In addition there are two alternative options: (1) a scale-up version of the original FMIT target and (2) a free jet target.

The replaceable backwall is bolted to the back and sides of the target assembly. Seals around the edges will be needed to maintain different vacuum conditions in the target chamber (10^{-3} Pa) and in the Test Cell ($\sim 10^{-1}$ Pa). Several mechanical sealing options are proposed. The target assembly, with exception of the replaceable backwall, is designed to withstand neutron damage for a potential 20-years lifetime. To minimize the effect of neutron damage, permanent structural components are at least 10 cm away from the beam footprint. Part of the assembly sidewalls will be separately cooled on the outside by routing a small lithium stream from the inlet pipe. Because there is no welding, the replaceable backwall can be made of a different material if desired. For example a combination of ferritic steel target assembly and vanadium alloy backwall could increase the target system lifetime. The final backwall material choice will be determined by actual beam-on-target testing during the initial 2-years of operation of IFMIF.

TABLE I. LITHIUM JET PARAMETERS

Jet thickness (m)	0.024–0.025
Jet width (m)	0.26
Jet velocity (m/s)	15 (range 10–20)
Inlet temperature (°C)	250
Outlet temperature (°C)	300 (for 15 m/s)
Surface temperature (°C)	290 (for 15 m/s)
Peak temperature (°C)	400 (for 15 m/s)
Beam footprint (cm)	5 × 20

The lithium loop is divided into three basic functional systems. The first is the main loop, which circulates the lithium to and from the target assembly with the parameters shown in Table I. Since two targets are assumed, the loop must be able to deliver flow to either of the Test Cells. The major components in this loop are the target quench tank, the surge or overflow tank, the lithium dump tank, the organic dump tank, the main electromagnetic pump, and the two heat exchangers. All of the piping and tanks are constructed of austenitic stainless steel (either 304 or 316). There are, in addition, a trace heating system, to maintain the temperature throughout the loop above the melting point of the lithium at all times the metal is present in the loop, thermal insulation, valves, electromagnetic flow meters, instrumentation, and connections to vacuum and argon headers. The total lithium inventory is 12 600 L.

7. ACCELERATOR SYSTEM

The IFMIF requirement for 250 mA of deuteron beam current delivered to the target will be met by two 125-mA, 40-MeV accelerator modules operating in

parallel. This technological approach is conservative with respect to the current capabilities of rf linac technology and provides operational redundancy by allowing operation to continue at 125 mA when one or the other of the two accelerators is temporarily removed from service for repair. Each 125-mA accelerator is designed with sufficient derating but not with a significant upgrade capability. Additional beam current, if desired, would be provided by adding additional 125-mA modules.

The IFMIF deuteron accelerator, shown in Fig. 4 (plan and elevation views), comprises a sequence of acceleration and beam transport stages. The ion source generates a cw 140-mA deuteron beam at 100 keV. A low-energy-beam-transport (LEBT) guides the deuteron beam from the operating source to a radio-frequency-quadrupole (RFQ). The RFQ bunches the beam and accelerates 125 mA to 8 MeV. The 8 MeV RFQ beam is injected directly into a room-temperature (RT), drift-tube-linac (DTL) of the conventional Alvarez type with post couplers, where it is accelerated to 32, 36, or 40 MeV.

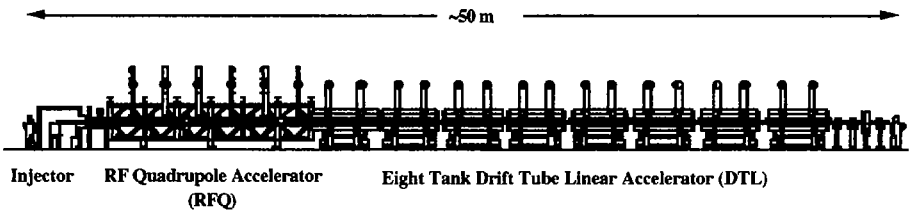

FIG. 4. Accelerator configuration.

The baseline rf power system for the IFMIF accelerator is the existing Eimac 4CM2500KG tetrode (or equivalent), operated at a power level of 1.0 MW and a frequency of 175 MHz. Operation of both the RFQ and the DTL at the same relatively low frequency is a conservative approach for delivering the high current deuteron beam with low beam loss in the accelerator. This will facilitate the achievement of "hands-on" maintainability without remote manipulators. The use of only one rf frequency also provides some operational simplification.

As shown in Fig. 5, the DTL output beam is carried to either of the targets or to the tune-up beam calibration station by a high-energy-beam-transport (HEBT) that also provides the desired target spot distribution tailoring and energy dispersion.

Extensive trade-off studies have been conducted on this baseline design, using the accelerator system model (ASM) [5]. ASM is a new code that allows consideration of physics, engineering, cost, and reliability, availability, maintainability (RAM) information in a consistent framework for the first time.

8. PROJECT COST AND SCHEDULE

The cost of manufactured items including complex one-of-a-kind machinery is driven by international competition among industrial firms. Companies in Europe, Japan and the U.S. are well aware of the market value of their goods and

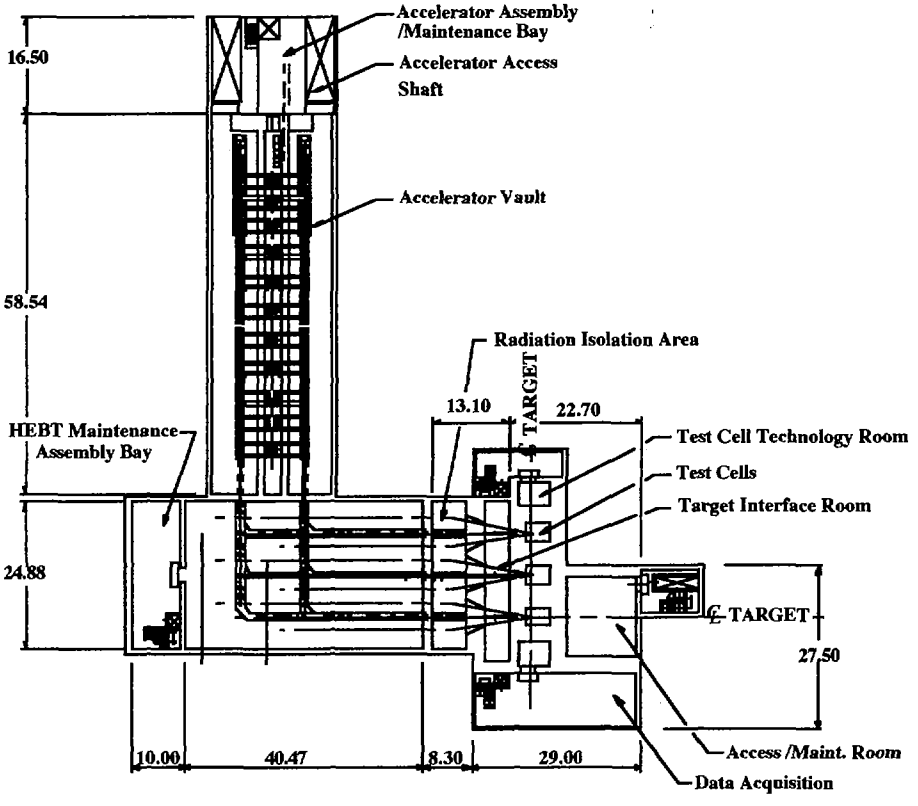

FIG. 5. Overall accelerator layout.

services and how to compete in the international market place. Therefore, the cost of procured items for the IFMIF project such as power supplies, accelerator and target components and test cell equipment can be estimated by different countries within a similar range of uncertainty.

The cost of construction and operation is a much different matter. Each country must satisfy national requirements for building codes and standards, safety and environmental considerations and rules for construction of facilities on government sites. It is clearly not possible to estimate a single project cost that would apply equally for the construction of IFMIF in Europe, Japan, Russia and the U.S.

The IFMIF design team is developing the overall cost estimate in a very open way so that each of the countries is aware of the areas where national considerations are different. Rather than selecting an average cost within the range of the difference, the final estimate for the CDA will be more representative of the cost for construction in Europe and the U.S. rather than Japan and Russia. The Japanese have more rigid standards for construction of nuclear facilities at JAERI for both environmental and safety requirements. The estimate quoted internally by Japan is expected to be somewhat higher.

The present estimate will be referred to as the baseline cost estimate. It will be published as part of the CDA report. Each country is expected to produce an internal estimate to best reflect the needs for construction within their national sites.

The proposed long range schedule for the IFMIF activity is shown in Figure 6.

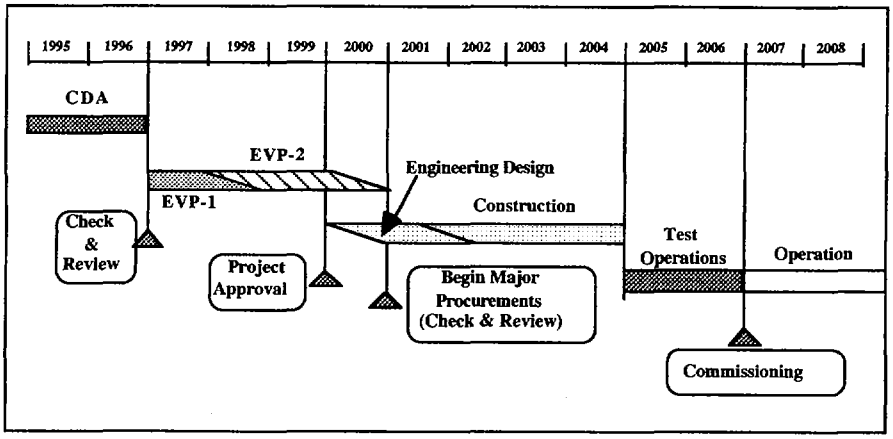

CDA: Conceptual Design Activity
EVP-I: Engineering Validation Phase-1
EVP-2: Engineering Validation Phase-2

FIG. 6. Proposed top level IFMIF schedule.

The Engineering Validation Phase (EVP) which follows the CDA will include design, research, development and other validation activities as listed in the Figure. This work is defined as that necessary to "validate" the baseline design concept prior to the start of the Engineering Design and Construction Phase. In addition to research and development activities, the EVP will sustain development work on the baseline design concept. There is additional, more conventional engineering development work that will be carried out as a normal part of the Engineering and Construction Phase. This work will be included as part of the project cost estimate [10].

REFERENCES

[1] SHANNON, T.E., et al., in Plasma Physics and Controlled Nuclear Fusion Research 1994 (Proc. 15th Int. Conf. Seville, 1994), Vol. 2, IAEA, Vienna (1995) 725.

[2] International Fusion Materials Irradiation Facility (IFMIF) (Proc. IEA-Techn. Workshop Karlsruhe, 1994); Rep. FZKA-5553, Forschungszentrum Karlsruhe, Germany (1995).

[3] Test Cell System for an International Fusion Materials Irradiation Facility (Proc. IEA-Techn. Workshop Karlsruhe, 1995); Rep. FZKA-5633, Forschungszentrum Karlsruhe, Germany (1995).

[4] IFMIF-CDA TARGET GROUP, Lithium Target System (Proc. IFMIF-CDA Techn. Workshop Naka, 1995); Rep. JAERI-Conf. 95-019 (1995).
[5] ACCELERATOR TEAM (Proc. Mtg for IFMIF CDA Santa Fe, 1995); Rep. LA-UR-95-4416, Los Alamos Scientific Lab., NM, USA (1995).
[6] RENNICH, M.J., IFMIF International Fusion Materials Irradiation Facility Conceptual Design Activity Interim Report, Rep. ORNL/M-4908, Oak Ridge National Laboratory, Oak Ridge, TN, USA (1995).
[7] IFMIF-CDA TEAM, Design Integration (Minutes 2nd IFMIF-CDA Workshop Naka, 1996); Rep. JAERI-Conf. 96-012 (1996).
[8] IFMIF-CDA TEAM, Addendum to IFMIF-CDA Interim Report, Rep. JAERI-Tech. 96-036 (1996).
[9] MARTONE, M., IFMIF CDA Final Report, Rep. RT/ERG/FUS/96/11 (1996).
[10] RENNICH, M.J., IFMIF International Fusion Materials Irradiation Facility Conceptual Design, Preliminary Cost Report, Rep. ORNL/M-5230, Oak Ridge National Laboratory, Oak Ridge, TN, USA (1996).

DESIGN PROGRESS OF JT-60SU

M. KIKUCHI, N. MIYA, K. USHIGUSA, G. KURITA,
K. NAGASHIMA, T. AOYAGI, N. TOYOSHIMA,
Y. NEYATANI, Y. TAKAHASHI, K. MATSUI,
T. HAYASHI, Y. YAMANISHI, M. KURIYAMA, T. ITOU,
T. YAMAMOTO, T. OZEKI, K. TOBITA, H. KUBO,
N. HOSOGANE, A. NAGASHIMA, K. MASAKI,
A. KAMINAGA, K. NAKAGAWA, K. MORI, T. KITAI,
S. OGURI, M. NAGAMI, H. KISHIMOTO, M. OTSUKA[1],
M. ABE[1], H. TSUKAMOTO[1], S. NAKAGAWA[2],
M. SHIBUI[2], J. OHMORI[2], K. NAKAJIMA[3],
Y. SUZUKI[3], M. HASEGAWA[3], T. SUZUKI[4],
G. IWAKI[5], Y. SAKAGAMI[6], Y. YAMADA[7]
Naka Fusion Research Establishment,
Japan Atomic Energy Research Institute,
Naka-machi, Naka-gun, Ibaraki-ken,
Japan

Abstract

DESIGN PROGRESS OF JT-60SU.

JT-60SU has been designed as an experimental device to establish an integrated scientific basis for steady state tokamak operation. Long pulse (1000 s to 1 h), fully non-inductive current drive will be investigated at a plasma current of 5–6 MA. The physics and engineering features of the JT-60SU design are given and the tritium system is investigated for small scale use of deuterium–tritium as an option.

1. INTRODUCTION

The primary objective of JT-60SU is an integrated demonstration of steady state operation in a tokamak [1–3]. In addition, the research on JT-60SU will supplement the ITER programme [4] in establishing a scientific basis for the DEMO reactor. The necessity of such a study is mentioned in the Third Phase Basic Programme of Fusion Research and Development by the Atomic Energy Commission of Japan.

---

[1] Hitachi.
[2] Toshiba.
[3] Mitsubishi.
[4] Kawasaki.
[5] Hitachi Cable.
[6] Showa.
[7] Sumitomo.

The key research elements of this objective are the achievement of a high performance core plasma with a large bootstrap current fraction and divertor heat load reduction as well as particle control consistent with the high performance core plasma.

In the following sections, the JT-60SU device, its physics design characteristics, steady state operation, technical features, radiation shield, fuel handling system, and confinement and cleanup systems will be described. A summary is given in the last section.

2. THE JT-60SU DEVICE

JT-60SU is designed as a superconducting tokamak device for integrated R&D of the steady state operation in a tokamak. Figure 1 shows cross-sectional views of JT-60U and JT-60SU. The cryostat diameter and the height of JT-60SU are 22 m and 17.5 m, respectively. The total weight of the tokamak device including the cryostat is ~11 000 t.

The toroidal field magnet consists of 18 coils for producing 6.25 T at 4.8 m. Various plasma shapes can be generated by ten poloidal field coil blocks. The magnetic energies of the toroidal field (TF) and poloidal field (PF) coils are ~24 GJ and ~2 GJ, respectively. The cold mass of the magnets is ~4000 t, which is cooled down within one month by a 36 kW cryogenic system. The vacuum vessel is made of 316SS, with low Co concentration, and the extra shield made of reduced activation ferritic (RAF) steel will be installed for possible DT option. The one turn resistance of the vacuum vessel is $\leq 25\ \mu\Omega$ to allow plasma initiation with $E_\phi \leq 0.2$ V/m. Vacuum pumping and particle exhaust are made from four divertor ports with a pumping speed of 20 m^3/s. The exhaust gas is processed in the fuel handling system. The main fractions of the neutron and gamma rays are shielded by the vacuum vessel, the TF shear panel and the cryostat.

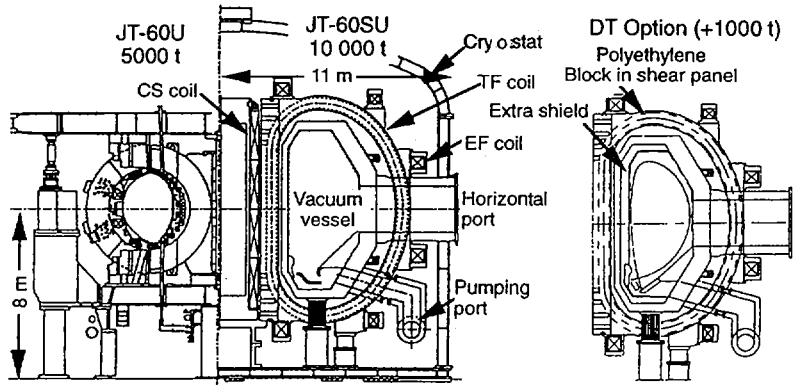

FIG. 1. Cross-sections of JT-60U and JT-60SU and DT option in JT-60SU.

TABLE I. MAIN MACHINE PARAMETERS OF JT-60SU

Plasma current, I_p	10 MA	Total CD power	P_{CD}	60 MW
Toroidal field, B_t	6.25 T	750 keV NBI	P_{NB}	~40 MW
Major radius, R_p	4.8–5.2 m	220 GHz ECH	P_{ECH}	~20 MW
Minor radius, a_p	1.3–1.5 m	Divertor peak heat load	(DD)	6 MW/m^2
Elongation, κ_{95}	1.6–1.8		(DT)	10 MW/m^2
Triangularity, δ_{95}	0.4 (SN)	Maximum neutron rate	(DD)	1×10^{18}/s
	0.8 (DN)		(DT)	1×10^{20}/s
Number of TFCs	18	Annual neutron	(DD)	4×10^{22}/a
B_t ripple	0.8%		(DT)	4×10^{23}/a
Total V·s, Φ	170 V·s	Tritium inventory	(DD)	<2 g
Flat-top (inductive)	200 s		(DT)	<100 g
(non-inductive)	<1 h	Cryogenics capacity		36 kW

The machine parameters of JT-60SU are shown in Table I. A maximum plasma current of 10 MA is chosen to study the reactor relevant plasma. A flexible shaping capability for elongation/triangularity and single/double null is adopted to explore the optimum plasma shape in a tokamak. The current drive system with a total injection power of 60 MW is a combination of N-NBI and ECH to allow a wide range of current profile control. The divertor heat flux will be reduced to a technically achievable level of 6–10 MW/m^2. To supplement the ITER programme, the machine

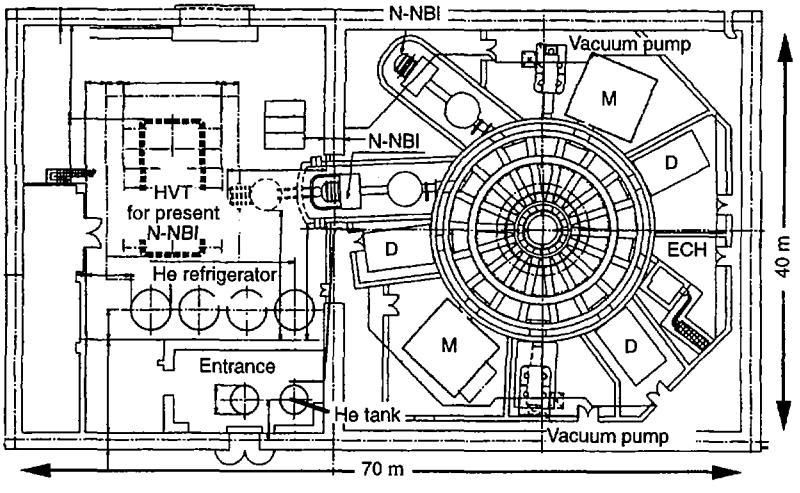

FIG. 2. Arrangement of JT-60SU device and its auxiliary systems in the experimental building. Four large EF coils will be introduced through the narrow roof slit (1.26 m × 20 m). A high voltage table for the new N-NBI will be located in the neighbouring building (M = maintenance; D = diagnostics).

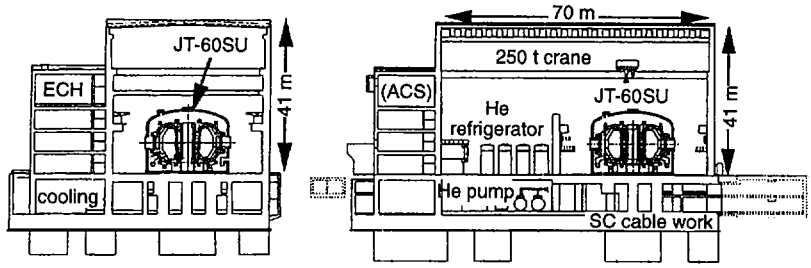

FIG. 3. Side views of experimental building.

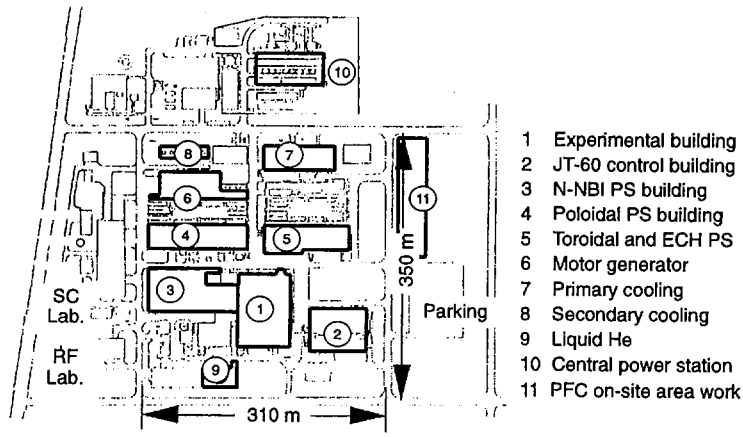

FIG. 4. Planned site arrangement for JT-60SU.

parameters in Table I are chosen so that ITER objectives are more compatible with JT-60SU research and various ideas can be studied in order to improve the economics and safety aspects of the reactor.

Figure 2 shows the plan of the building for the experiments. Around the tokamak device, two tangential NB injectors and one ECH launcher are arranged for heating and current drive. Two horizontal ports are prepared for remote maintenance. Refrigerator and tank for the helium are located in the assembly room.

Figure 3 shows two side views of this building. The primary cooling and baking systems for the vacuum vessel are located on floor B1. The ECH gyrotrons are situated on the fourth floor.

Figure 4 shows the planned site arrangement of JT-60SU. The power supply for N-NBI is located west of the experimental building. The ECH and toroidal power supplies including the quench protection circuit are located northeast of the experimental building while the poloidal power supply lies northwest of the experimental building. All systems can be arranged within the JT-60 site.

3. PHYSICS DESIGN CHARACTERISTICS

3.1. Long pulse operation

Long pulse operation is an important research topic since the maximum duration of high performance ELMy H mode discharges was limited to 1.5 s in JT-60U [5]. The divertor plasma temperature is so high (> 100 eV) that these ELMy H mode discharges are not sufficient for long pulse operation.

To guarantee success of ignition and long burn in ITER, JT-60SU will extend its operation regime in the duration–fusion triple product space as is shown in Fig. 5. By exploring the ITER relevant regime, it becomes possible to identify and solve physics and engineering problems of ITER ignition and long burn.

3.2. High density operation

A recent assessment of the database supports the Greenwald limit, $n_{GW} = I_p/(\pi a_p^2)$, as a density limit. The ITER EDA design (R_p = 8.1 m, B_t = 5.7 T) has resulted in a somewhat lower Greenwald density limit, and physics R&D undertaken to increase the density beyond the Greenwald limit becomes an important physics R&D item. Since high density steady state operation is important for the DEMO reactor, a complementary approach is adopted in JT-60SU to achieve a high Greenwald density limit by choosing $B_t/R \sim$ 1.1–1.3 T/m as compared with $B_t/R \sim$ 0.63–0.7 T/m in ITER and $B_t/R \sim$ 1.3 T/m in SSTR as is shown in Fig. 6.

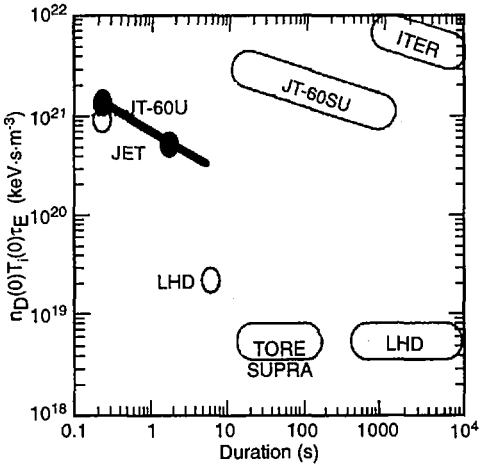

FIG. 5. Operation of various devices in (duration, fusion triple product) space.

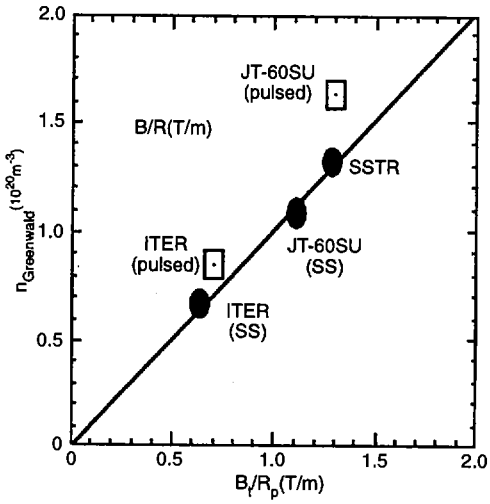

FIG. 6. Greenwald density limit as a function of B_t/R_p.

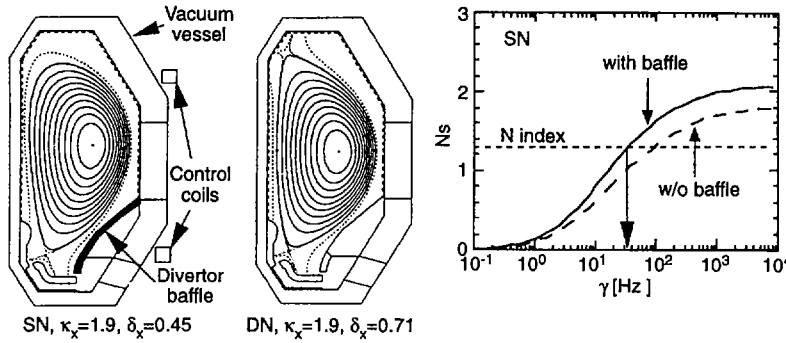

FIG. 7. Single and double null divertor configurations and the effect of divertor baffle on the Ns frequency characteristics to reduce vertical instability growth rate.

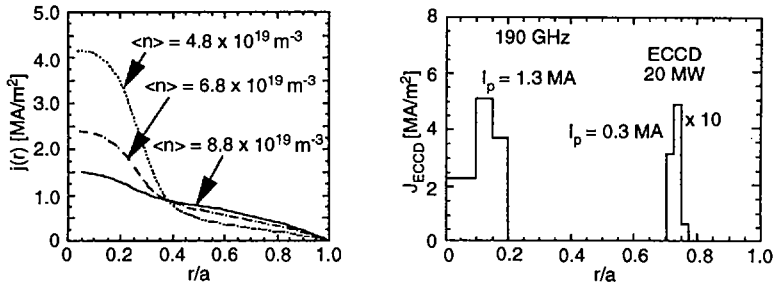

FIG. 8. NBCD and ECCD current profiles for steady state operation scenario as given in Table II.

3.3. Plasma shape control

It is an important issue in JT-60SU studies to identify the optimum plasma shape of the DEMO reactor. The maximum triangularity of a plasma (δ_{95}) is limited to ~ 0.4 for a single null configuration with $\kappa_{95} = 1$–1.8. The double null will be investigated if the highly shaped plasma is essential for improving the overall fusion performance as is shown in Fig. 7. To allow such a shape control, the passive stabilizing effect of the vacuum vessel is improved by adding a toroidally continuous divertor baffle.

3.4. Current profile control

The main heating and current driver is a 750 keV N-NBI system, because of the remote access to the plasma. However, beam penetration and current profile are simply determined by the beam energy and the operating density as is shown in Fig. 8. Therefore, a combination with the 150–220 GHz ECH system is adopted to provide a flexible current profile control.

3.5. Divertor design

Two types of divertor concept are shown in Fig. 9; they satisfy the design guidelines for particle control as given in Ref. [6]. Type 1 is a conventional divertor flexible to produce various triangularities. The particle exhaust from the outer leg is, however, not good enough. Type 2 is a W shaped divertor similar to that for JT-60U [7]; it is suitable for increasing the flux multiplication factor at the outer divertor plate.

4. STEADY STATE OPERATION

Demonstration of steady state operation at $I_p \sim 5$ MA is an important target for the JT-60SU programme. For this current, full CD is possible with the 60 MW CD power up to a high density of $\langle n_e \rangle \sim 8.8 \times 10^{19}$ m^{-3}, which is below the Greenwald limit (resulting from high values of B_t/R and aspect ratio). The ITER scaling law for the H mode power threshold gives ~ 40 MW for the parameters of JT-60SU ($B_t = 6.25$ T, $n_e = 4 \times 10^{19}$ m^{-3}). The energy confinement scalings (τ_{th}^{ELMy} or $0.85\tau_{th}^{ELM\text{-}free}$) gives $H^{ITER\text{-}89P}$ of 2.5–3 favoured by the GyroBohm characteristics of the scalings. The achievable bootstrap current fraction, f_{boot}, depends on the pressure profile; it amounts to 50–60%.

Since high β_p operation with considerable alpha heating produces a strong coupling between pressure and current profiles, DT operation is considered an important option in JT-60SU. Table II gives the major parameters of the DD and DT steady state operations. An energy gain of $Q \sim 5$ with an f_{boot} of $\sim 50\%$ becomes possible if $H^{ITER\text{-}89P} \sim 3$ and $\beta_N = 3$ are stably maintained.

TABLE II. MAIN PARAMETERS OF DD AND DT FULL CURRENT DRIVE OPERATION

	DD	DT option		DD	DT option
Plasma current, I_p	5 MA	6.2 MA	Average density, $\langle n_e \rangle$	8.8×10^{19} m^{-3}	8.4×10^{19} m^{-3}
Toroidal field, B_t	6.25 T	5.77 T	Heating power, P_{heat}	60 MW	50 MW
Major radius, R_p	4.8 m	5.2 m	Confinement time, τ_E^{global}	1.54 s	1.71 s
Minor radius, a_p	1.3 m	1.35 m	H factor, $H^{ITER-89P}$	3.1	3.1
Elongation, κ_{95}	1.8	1.8	Normalized beta, β_N	2.0	3.0
Triangularity, δ_{95}	0.4	0.4	Poloidal beta, β_p	1.73	2.0
Safety factor, q_{95}	6.2	4.5	Bootstrap fraction, f_{boot}	50%	51%

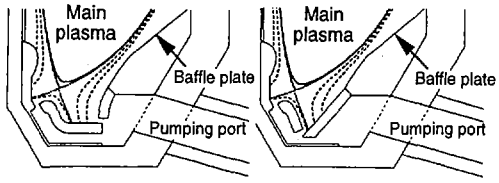

Total heating power	60 MW
Radiation loss fraction	75%
Pellet fuelled particles	2.5×10^{21}s
Divertor gas puffing	5 Pam^3/s
Pumping rate	4×10^{-3}
Backflow rate	1.1×10^{-2}
Mag. flux expansion	5
Divertor temperature	9.2 eV
Divertor density	1.4×10^{20}m^{-3}
Recycling rate	0.84

FIG. 9. Two reference divertor concepts and target divertor parameters for JT-60SU [6].

5. TECHNICAL FEATURES

5.1. Toroidal magnet

In JT-60SU, a 5-6 MA, long pulse, non-inductive CD will be used, with an advanced confinement mode of operation ($H^{ITER-89P} \sim 3$). A conservative choice for the beta limit ($\beta_N = 2$ for DD and $\beta_N = 3$ for DT) is adopted, on the basis of a stability limit without wall stabilization. This choice requires $B_t \sim 6$ T at $R_p = 5$ m. The TF coils are designed on the basis of a disc double pancake winding with Nb_3Al cable in conduit conductor covered by the coil case. The centring force is wedge supported. The number of TF coils (18) is chosen so as to allow tangential NBI at $T_{tang} = 4.8$ m and minimization of the field ripple (a TF ripple of 0.8%). Two important design characteristics are the use of an Nb_3Al conductor and significant weight reduction by the twin coil concept, as is shown in Fig. 9.

The first feature is based on the fact that the Nb_3Al conductor has better mechanical and J_c properties [8] than the $(NbTi)_3Sn$ conductor for the purpose of the DEMO reactor and satisfies most of the design requirements with recent strand R&D [9]. Table III is a summary of the strand R&D results. Case 1 is fairly close to the design requirements; the cross-section of the strand is shown in Fig. 10.

TABLE III. Nb_3Al STRAND R&D RESULTS
(Case 2 is for large scale production)

Item	Case 1	Case 2	Case 3
J_c at 12 T (A/mm^2)	805	615	655
Filament diameter (μm)	50	49	33.2
Cu ratio	2.1	1.4	2.2
Cr coating (μm)	2	2	—
RRR	132	~100	—
Strand diameter (mm)	0.805	0.805	0.813

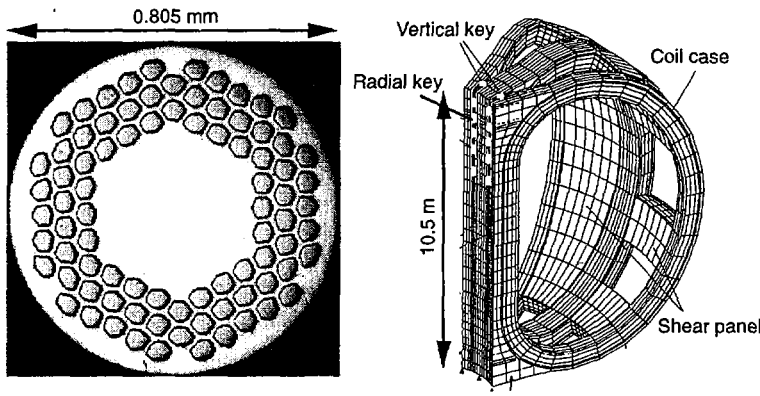

FIG. 10. Cross-section of Nb_3Al strand (Case 1 of Table III) and twin TF coil.

TABLE IV. MAJOR DESIGN PARAMETERS OF TF MAGNET

Item	Value	Item	Value
Maximum field	11.4 T	Conductor	Nb_3Al
Total A-turns	150 MAT	Conduit diameter	32 mm
Coil current	55.6 kA	I_c/I_{ope}	2.2
Total weight	3000 t	Number of strands	960
Weight/coil	130 t	Manufacture	Jelly roll
Winding disk		Void fraction	34%
pancake conduit	SS	Limiting current	61.2 kA

The second feature is chosen as an attempt to improve the reactor economics through weight reduction; a weight/magnetic energy ratio of 125 t/GJ is realized on the basis of the twin coil concept, with two TF coils whose coil cases are connected with shear panels to increase the coil rigidity against the out of plane force. This choice reduces the number of large horizontal and lower ports to nine (half the number of TF coils). A finite element modelling (FEM) analysis shows that the maximum coil displacement, case stress and insulator shear stress are 11 mm, 570 MPa and 22 MPa, respectively. A local FEM analysis of the radial disc shows that the maximum local stress is 750 MPa.

The basic design parameters of the TF magnet are shown in Table IV. A DC power supply of 55.6 kA·310 V is sufficient to charge the TF magnet within one hour. A quench protection circuit is prepared for all three coils to reduce the number of current leads.

TABLE V. BASIC DESIGN PARAMETERS OF CS AND EF COILS

Item	CS	EF	Coil block	R (m)	Z (m)	AT (MA)
Maximum field	9 T	5 T	PF1(EF)	9.5	2.2	6.72
Conductor	$(NbTi)_3Sn$	NbTi	PF2(EF)	7.45	5.21	4
Current	40 kA	40 kA	PF3(EF)	3.02	5.67	7.84
Conduit diameter	25.5 mm	29 mm	PF4(CS)	1.69	3.47	20.2
Strand diameter	0.85 mm	0.83 mm	PF5(CS)	1.69	1.16	20.2
Number of strands	540	720	PF6(CS)	1.69	−1.16	20.2
Filament diameter	10 μm	10 μm	PF7(CS)	1.69	−3.47	20.2
First conduit	Ti	SS	PF8(EF)	3.02	−5.67	8.96
			PF9(EF)	7.45	−5.21	4.8
			PF10(EF)	9.5	−2.2	7.84

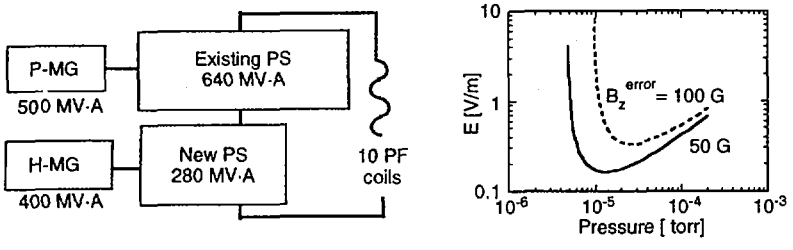

FIG. 11. Structure of JT-60SU power supply and required E field for plasma breakdown ($E = 0.1$ V/m; $V_{loop} = 3$ V for breakdown).

5.2. Poloidal magnets and power supplies

The PF coils consist of four central solenoid (CS) coils and six outer equilibrium field (EF) coils as shown in Fig. 1. The conductors for CS and EF coils are $(NbTi)_3Sn$ and NbTi, respectively. A wide variety of shape control and a flux swing of 170 V·s become possible with this ten coil system. The basic design parameters are given in Table V. Four large EF coils (diameters 14.9 and 19 m) will be manufactured on site and transferred into the experimental building through a slit in the roof of the JT-60 experimental building.

For the best use of the present JT-60 power supply (PS), the PS system is structured as shown in Fig. 11. Two motor generators that are at present used for the poloidal coils and the heating systems of JT-60U are connected to the air cooled short pulse PS (present PS for F and V coils) and the water cooled long pulse PS (new system). This choice will result in a very small investment for the PS. This PS can induce an initial breakdown voltage of ~6 V. The whole system including the quench protection circuits can be arranged in the present PS building.

5.3. Cryogenic system

The heat load from the tokamak consists of a steady load of ~6.4 kW and ~8.4 MJ for a standard 360 s pulsed operation. A shot interval of 30 min is sufficient to cool down the magnets between the shots. However, a major current disruption produces ~16 MJ of eddy current loss, and the shot interval must be increased after the disruption. The total superconducting helium (SHe) flow rate is 4800 g/s provided by three SHe circulation pumps. The system capacities for refrigeration and liquefaction are 31 kW and 1600 L/h, respectively, during the day and 19 kW and 5200 L/h during the night to minimize the system size. The total electric power for the cryogenic system is estimated to be 11 MW.

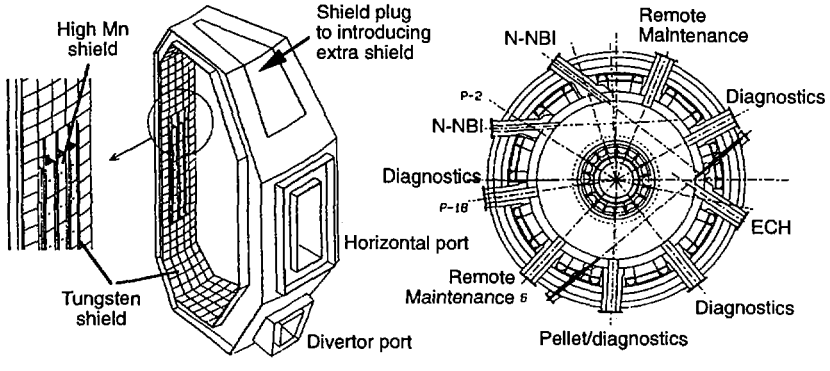

FIG. 12. Structure of vacuum vessel and horizontal view.

5.4. Vacuum vessel and primary cooling system

High Mn steel and water are filled inside the 316SS double walled vacuum vessel as is shown in Fig. 12. The total weight of the vacuum vessel is ~3000 t. For the DP option, an extra shield of ~1000 t (of reduced activation ferritic steel F82H) is required. The vessel is designed to have a good stabilizing effect (growth rate: $\gamma < 30$/s, stability margin: $m_s \sim 0.5$) to the vertical displacement with a stabilizing baffle. The primary cooling system for the vacuum vessel is designed to have a system capacity of 310 MW. This system consists of the divertor cooling system (flow rate of 2230 t/h) and the first wall cooling system (4450 t/h). The system can be arranged in two rooms on the B1 floor of the experimental building which is at present used for the heating PS (Fig. 3).

5.5. Heating and current drive system

N-NBI and ECH are considered as heating and current drive systems; beam line and launcher are shown in Fig. 13. The N-NBI system for JT-60SU is a new system designed to be more compact, with a beam line length of ~20 m. The maximum local nuclear heating rate of the TF conductor near the N-NBI port is ~1 mW/cm^3. At present, a maximum system capability of 60 MW is under investigation. The power supply including a high voltage table will be placed in the N-NBI PS building.

The ECH launching system is designed to be compact, and there are no mirrors inside the extension port for easy maintenance. A gyrotron with energy recovery will be used. At present, a maximum system capability of 40 MW is being studied.

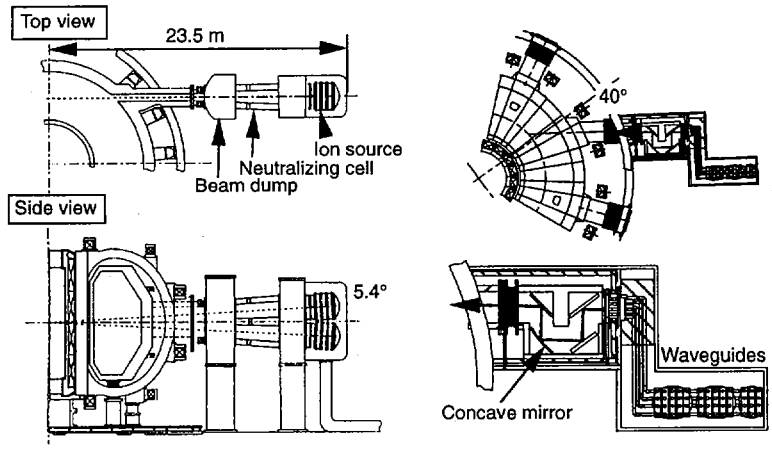

FIG. 13. N-NBI beam line and ECH launcher for JT-60SU.

6. RADIATION SHIELD [10]

The induced radioactivity inside the vacuum vessel is one of the important issues for which the flexibility of modification of the first wall or the divertor configuration after high power DD operation must be maintained. A significant reduction of the radiation dose rate inside the vacuum vessel is possible for 316SS, with a low Co concentration (0.05%), whose inner wall is covered with a 3 cm W shield. The relative γ dose rates of 316SS(0.2% Co), Ti-6Al-4V and 316SS(0.05% Co) + W are shown in Fig. 14. The radioactivity decays more quickly for high Mn steel than that for 316SS after DT operation.

The radiation shield against DD neutrons and induced γ rays consists of an 80 cm thick vacuum vessel and a 50 cm thick cryostat to reduce the radiation dose rate outside the cryostat so as to allow free access one day after the experiments. An additional shield inside the vacuum vessel and the TF magnet with polyethylene blocks filled inside the TF shear panel are sufficient to keep the radiation dose of the DT option on a level suitable for DD experiments.

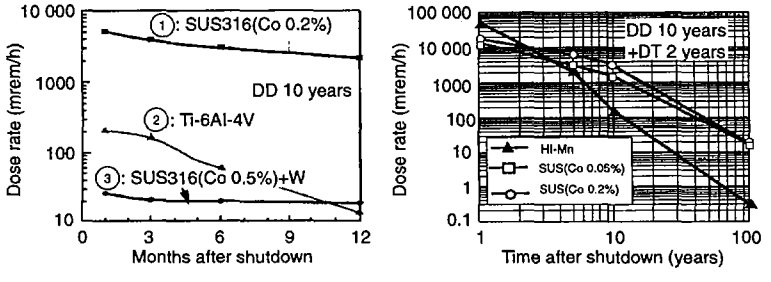

FIG. 14. Gamma ray dose rates inside the vacuum vessel for various selections of material for the vacuum vessel after ten years of DD operation and two extra years of DT operation.

7. FUEL HANDLING SYSTEM [11]

The fuel handling system for JT-60SU consists of fuel storage and injection systems (FSS & FIS), a vacuum pumping system (VPS), a fuel cleanup unit (FCU), an isotope separation system (ISS) and an effluent tritium removal system (ERS). The basic design philosophy of the system is to enable the system to be extended to the DT option. To realize this option, significant efforts are made to reduce the total tritium inventory to less than that available at present in the tritium process laboratory (TPL) at JAERI.

The Zr-Co alloy will be used for the FSS. Both gas puff and centrifugal pellet injection are planned for the FIS. The T inventory in the pellet injector becomes fairly high for the DT option and should be reduced significantly if pellet injection is needed.

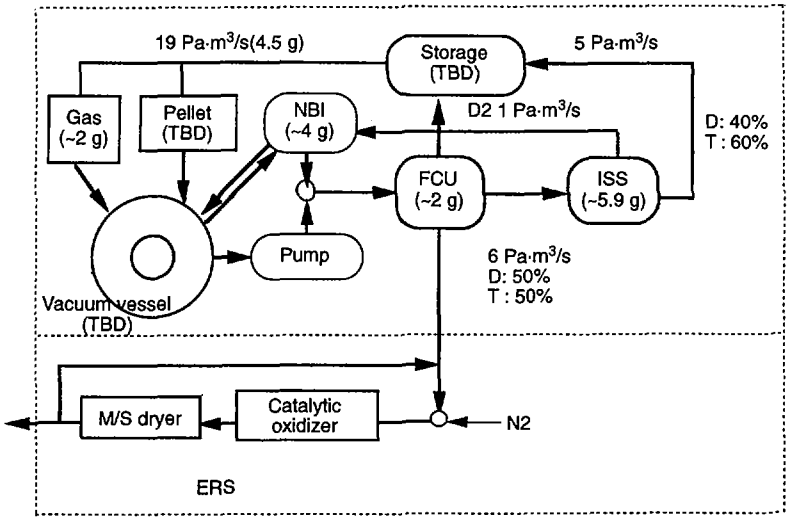

FIG. 15. Schematic flow diagram of fuel handling system for JT-60SU.

Four divertor pumping ports are connected to two manifolds each equipped with 12 oil free thermomechanical pumps (TMPs) (0.9 m^3/s at 1 Pa), whose forepump is the scroll pump. Caution is observed for the neutron and γ ray streaming along the duct.

The FCU for JT-60SU is a modification of the JFCU (Pd diffusers/electrolysis scheme) at the TPL and the tritium system test assembly (TSTA). This system consists of the purification system, the impurity treatment system and the recovery system.

The ISS is necessary only for the DT option. Gas flow rate and purity are 'sacrificed' so as to minimize the T inventory as shown in Fig. 15.

The ERS system for JT-60SU is basically the same system as that used in TPL.

8. CONFINEMENT AND CLEANUP SYSTEM [11]

The maximum tritium production rate from intense auxiliary heating of deuterium plasmas is estimated to be 2000 $Ci \cdot a^{-1}$ (7.4×10^{13} $Bq \cdot a^{-1}$). Therefore, the fuel treatment system, even in the DD experiments, should be designed to have multiple confinement barriers and to meet the defense-in-depth philosophy, similar to that in the TPL. The last confinement barrier is the experimental building in which the air volume is 112 000 m^3. An air cleanup system (ACS) is designed on the assumption of an in-leak rate of 1120 m^3/h. A gas separation membrane module

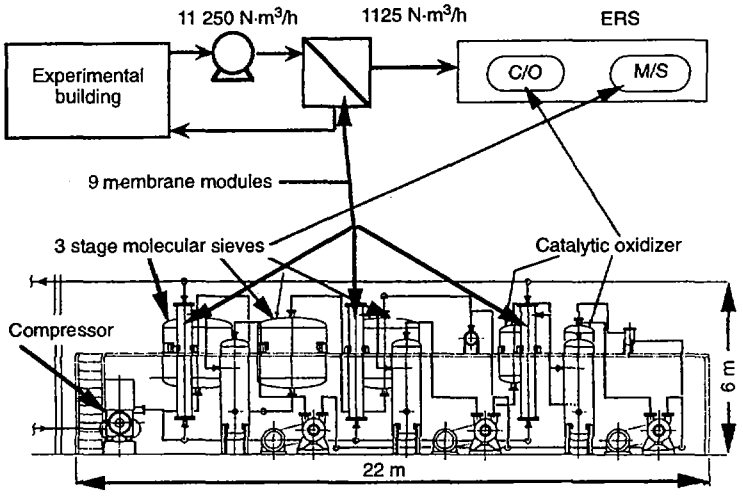

FIG. 16. ACS system with membrane modules.

made of polyimide hollow filaments is adopted, and nine modules (inlet pressure: 1 MPa) are necessary for the ACS as shown in Fig. 16. Cryostat and subsystem boxes can be constructed as another confinement barrier whose gas cleanup system is similar to the ACS.

9. SUMMARY

A continuous concept study has been made on the physics, device and safety system for JT-60SU. It is shown that a superconducting tokamak device relevant to steady state research could be designed by making best use of the existing JT-60 infrastructure, with a possible extension to small scale DT operation.

ACKNOWLEDGEMENTS

The authors would like to express their gratitude to the JT-60 team, the Tritium Process Laboratory and the Superconducting Magnet Laboratory for their support.

REFERENCES

[1] NAGAMI, M., et al., in Fusion Technology (Proc. 17th SOFT Symp. Rome, 1992), Vol. 2, North-Holland, Amsterdam (1992) 163.

[2] NINOMIYA, H., et al., in Plasma Physics and Controlled Nuclear Fusion Research 1994 (Proc. 15th Int. Conf. Seville, 1994), Vol. 2, IAEA, Vienna (1995) 613.
[3] KIKUCHI, M., et al., in Fusion Engineering (Proc. 16th Symp. Urbana-Champaign, 1995).
[4] REBUT, P.H., in Plasma Physics and Controlled Nuclear Fusion Research 1994 (Proc. 15th Int. Conf. Seville, 1994), Vol. 2, IAEA, Vienna (1995) 451.
[5] KAMADA, Y., et al., ibid., Vol. 1, p. 651.
[6] NAGASHIMA, K., et al. (in preparation).
[7] HOSOGANE, N., et al., IAEA-CN-64/GP-11, this volume.
[8] TSUJI, H., et al., in Plasma Physics and Controlled Nuclear Fusion Research 1992 (Proc. 14th Int. Conf. Würzburg, 1992), Vol. 3, IAEA, Vienna (1993) 271.
[9] TAKAHASHI, Y., et al. (in preparation).
[10] MIYA, N., et al. (in preparation).
[11] HAYASHI, T., et al. (in preparation).

SUPERCONDUCTING MAGNET DESIGN AND CONSTRUCTION OF LARGE HELICAL DEVICE

O. MOTOJIMA, N. YANAGI, S. IMAGAWA, K. TAKAHATA,
S. YAMADA, A. IWAMOTO, H. CHIKARAISHI, S. KITAGAWA,
R. MAEKAWA, S. MASUZAKI, T. MITO, T. MORISAKI,
A. NISHIMURA, S. SAKAKIBARA, S. SATOH, T. SATOW,
H. TAMURA, S. TANAHASHI, K. WATANABE, S. YAMAGUCHI,
J. YAMAMOTO, M. FUJIWARA, A. IIYOSHI
National Institute for Fusion Science,
Oroshicho, Toki,
Japan

Abstract

SUPERCONDUCTING MAGNET DESIGN AND CONSTRUCTION OF LARGE HELICAL DEVICE.

The Large Helical Device (LHD) project is now successfully executing the seventh year programme of the eight year construction period. Superconducting (SC) research and development tasks for the LHD SC coil construction have already been completed, and now more than 75% of the whole construction schedule has been accomplished. In the paper, the recent progress of SC R&D and the fabrication technology developed for a huge and reliable SC coil system are reported. These results are applicable to a future experimental reactor in the next decade with a much larger SC coil system. The LHD is called heliotron and has $\ell/m = 2/10$ SC helical coils and three sets of SC poloidal coils, whose coil currents are 7.8, 5.0, −4.5 and −4.5 MA, respectively. Major radius, minor helical coil radius, minor plasma radius and plasma volume are 3.9 m, 0.975 m, 0.5–0.65 m, and 20–30 m^3, respectively. In addition to an SC coil system, the main body of the LHD consists of huge supporting structures for the electromagnetic forces, a vacuum chamber, an outer cryostat and a machine base. The total weight is about 1500 t, of which the LHe cooled mass amounts to 850 t. The LHD has a maximum stored energy of 1.6 GJ (4 T at the plasma centre). The major goal of the LHD project is to demonstrate the high potentiality of the helical type device producing currentless steady state plasmas with a sufficiently large Lawson parameter in the absence of any danger of plasma current disruption. It provides a useful and reliable database making it possible to predict fusion reactor conditions. The realization of steady state operation requires a large extent of engineering innovation, primarily in the areas of superconducting technology, plasma facing materials, cooling systems and heating systems. It also contributes to building up the engineering scenario required for long pulse, regulated plasma operation necessary for fusion research.

1. INTRODUCTION

The LHD, a heliotron type apparatus, is a superconducting (SC) toroidal device with a major radius of 3.9 m. It has $\ell/m = 2/10$ SC helical coils and three sets of SC poloidal coils, whose coil currents are 7.8, 5.0, −4.5 and −4.5 MA, respectively. The major goal of the LHD project is to demonstrate a high potential of the

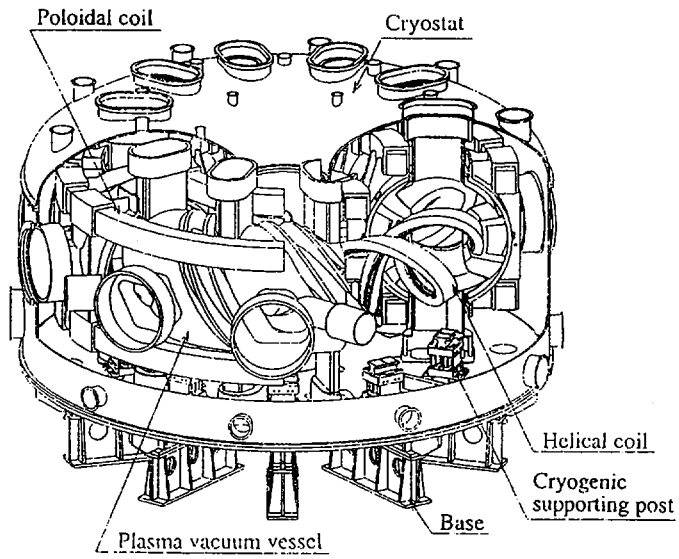

FIG. 1. Bird's eye view of LHD.

TABLE I. SPECIFICATIONS OF LHD

Major radius	3.9 m
Averaged plasma radius	0.5–0.65 m
ℓ, m	2, 10
Magnetic field	3 (4) T
Helical coil current	5.85 (7.8) MA
Coil minor radius	0.975 m
LHe temperature	4.4 (1.8) K
Poloidal coil current	
Inner vertical coil	5.0 MA
Inner shaping coil	−4.5 MA
Outer vertical coil	−4.5 MA
LHe temperature	4.5 K
Plasma volume	20–30 m^3
Heating power	40 MW
Coil energy	0.9 (1.6) GJ
Refrigeration power	9 (15) kW

TABLE II. LIST OF COIL PARAMETERS

Items	Helical coil	IV coil	IS coil	OV coil
Superconductor	NbTi/Cu	←	←	←
Conductor type	Compacted strands	CICC	←	←
Cooling method	Pool cooled	Forced flow	←	←
Conductor size (mm × mm)	12.5 × 18.0	23.0 × 27.6	23.0 × 27.6	27.5 × 31.8
Major radius (m)	3.9	1.80	2.82	5.55
Weight per coil (t)	120	16	25	50
Maximum field in coil (T)	9.2	6.5	5.4	5.0
Stored energy (GJ)	1.6	0.16	0.22	0.61
Nominal current (kA)	17.3	20.8	21.6	31.3
Coil current density ($A \cdot mm^{-2}$)	53	29.8	31.5	33.0
Magnetomotive force (MA)	7.8	5.0	−4.5	−4.5
Hoop force (MN)	356	262	116	263
Up-down force (MN)	240	−60.2	95.6	72.2
Diameter of filament (μm)	47	15	12	14
Diameter of strand (mm)	1.74	0.76	0.76	0.89
Number of strands	15	486	←	←

heliotron type device in producing currentless steady state plasmas with a sufficiently large Lawson parameter and without any danger of plasma current disruption. SC is a key technology in the LHD project. A schematic view and the specifications of the LHD are shown in Fig. 1 and in Table I. In Table II, the parameters of the LHD SC coils are listed. Both the helical and the outer vertical (OV) poloidal coils are the largest SC coils in existing fusion devices.

The main objectives and the target parameters of the LHD [1-3] are: (1) confinement studies and the demonstration of high temperature plasmas such as a density of $\langle n \rangle = 10^{20}$ m^{-3} and a temperature of $\langle T \rangle$ = 3-4 keV, or $\langle n \rangle = 2 \times 10^{19}$ m^{-3} *and* $T(0) = 10$ *keV under an input heating power of* 20 MW; (2) MHD studies and the realization of high beta plasmas with $\langle \beta \rangle \geq 5\%$; (3) studies on confinement improvement and steady state experiments by a divertor; and (4) developments in physics and technology of a fusion reactor. The realization of the steady state operation requires a large extent of engineering innovations, primarily in the areas of superconducting technology, plasma facing materials, water cooling systems and heating systems. It also contributes to building up the engineering scenario for long pulse, regulated plasma operation. In this paper, we generally review the major progress of the LHD project, i.e. the present status of construction, recent progress achieved in SC R&D, and the fabrication technique developed for the

construction of a large and reliable SC magnet system. These are the necessary goals of the LHD project; they are expected to contribute to a future experimental reactor to be built during the next decade.

The LHD project is now successfully executing the seventh year of its eight year construction programme. Engineering research and development for the LHD have almost been completed, and we have now accomplished more than 75% of the tough and long construction schedule.

2. SC MAGNET TECHNOLOGY

In this section, we shall set forth the new SC magnet technology developed in NIFS to execute the LHD construction, which consists of (1) development of helical and poloidal coil conductors; (2) coil fabrication technique; (3) test procedure and quality control; (4) mechanical design; (5) bus lines, etc.

2.1. Development of helical coil conductor and test procedure

Many types of superconductor with different internal structures were proposed and examined practically with short sample tests [4]. The final conductor size is 12.5 mm × 18.0 mm, and the nominal current is 13.0 kA (4.4 K/Phase I, 17.3 kA for 1.8 K/Phase II). The main specification of the superconductor is listed in Table II, and the cross-sectional configuration is shown in Fig. 2. Pure aluminium (5 nine) is the main stabilizer. The conductor size has been optimized not only as to the mechanical flexibility, in order to facilitate the on-site winding process, but also as to cryogenic stability due to the increment of the surface/volume ratio. Fifteen NbTi superconducting strands are twisted and formed into a Rutherford type flat cable. Instead of the conventional OFCu, Cu-2%Ni (thickness: 0.4 mm, resistivity: $\sim 2.5 \times 10^{-8}\ \Omega \cdot m$) was selected as the cladding material around the

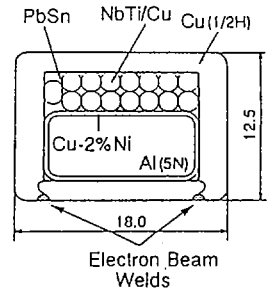

FIG. 2. Cross-sectional view of superconductor.

aluminium in order to insulate the Hall current [5] while maintaining smooth current transfer from the superconducting strands to the aluminium. Another important development with the conductor is the use of electron beam welding to the half-hard copper sheath, which has drastically enhanced the mechanical toughness of the conductor, not only against compressional stresses of up to 100 MPa during the excitation but also against plastic deformation during the three dimensional winding process. The conductor surface is oxidized to improve the heat transfer to the liquid helium.

A total length of more than 36 km has been fabricated, with a unit length of 600–1100 m, wound in 38 bobbins. Each unit produced has been carefully inspected for necessary items, such as critical current of strands, resistivity of pure aluminium, mechanical toughness and heat transfer coefficient. Short sample tests have been carried out to evaluate the basic properties of each superconductor, using test facilities with 9 T split coils, 100 kA current leads and 75 kA DC power supplies.

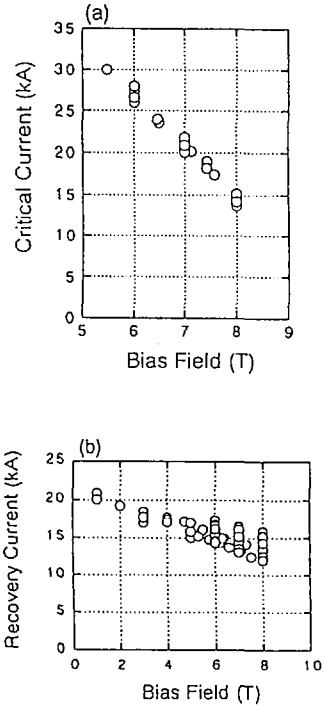

FIG. 3. (a) Critical currents and (b) recovery currents versus bias magnetic fields for all short samples.

Figure 3 shows the critical currents and the recovery currents obtained for all conductors as a function of the bias magnetic field. The critical current shows good agreement with the value predicted by integrating the critical current of each single strand, taking account of the three dimensional self-field effect. The scattering of the critical currents is in the range of 4% at 7 T. Stability tests have also been carried out by initiating a normal zone with heaters and by measuring the recovery current. It should be noted that the recovery currents exceeded the nominal current value for the 4.4 K in the operating conditions (13.0 kA at 6.9 T).

2.1.1. Mechanical requirement for helical coil

The fabrication error for the coil position is required to be below 2 mm, which corresponds to a relative accuracy of 5×10^{-4} of the major radius [6]. Furthermore, the elastic deformation of the coil by the electromagnetic force is specified to be below 1.9 mm at 3 T operation. The helical coil conductors are, therefore, designed to be packed into a thick coil can made of SUS316 stainless steel. Since the coil can is used as a bobbin for the winding, it must be fabricated with high accuracy. A torus shaped winding core was, therefore, prepared with a high accuracy of 0.2 mm. The top or bottom half-pitch of the coil can was manufactured with NC machinery in a factory. These parts were assembled and welded to each other at the Toki site. As a result of R&D for the new welding technique, the fabrication error of the coil can has been made sufficiently small for adequate helical coil winding. The movement and the stress of each conductor were calculated by using ANSYS 4.4 as shown in Fig. 4. The electromagnetic force is applied to the node that is the centre

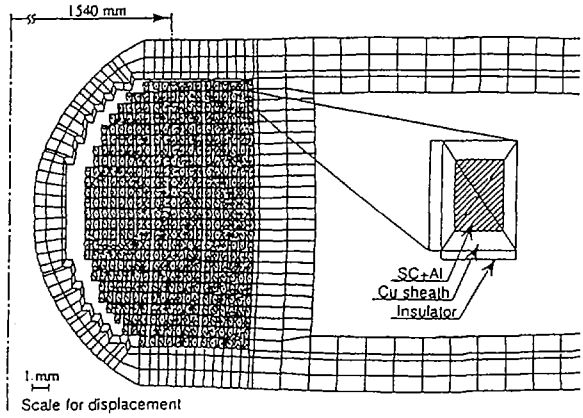

FIG. 4. Deformed shape of helical coil with rigidity of insulators and spacer factor 22 GPa and 0.5, respectively.

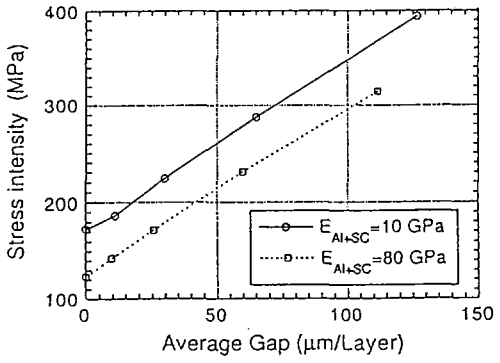

FIG. 5. Calculated maximum stress on conductors for various fabrication gaps where Young's modulus of the insulator is 22 GPa.

of each conductor. Since the insulators between the conductors are separated, compressive Young's modulus (E) is calculated by multiplying the actual value by a spacer factor. Young's modulus along the conductor is negligibly small. The inner materials of the composite conductor, which are superconducting strands, CuNi clad pure aluminium and solder, are represented by homogeneous elements.

We have developed a new GFRP insulator with high rigidity. Young's modulus is larger than 22 GPa, and the compressive strength is over 1000 MPa. Maximum stress and maximum movement of the coil occur at the bottom layer. Adopting a rigidity of 22 GPa and a spacer factor of 0.5, they are 173 MPa and 1.1 mm, respectively, i.e. values that are sufficiently below the acceptable level. These mechanical analyses depend on averaged Young's modulus (E_{Al+SC}) of the conductor, which contains the aluminium stabilizer and the SC strands. It was given as 10 GPa, which was established by mechanical tests on real size modules of the helical coil package. Since the fabrication gap between conductors and insulators was expected to collapse owing to a high electromagnetic force, the equivalent coil rigidity was reduced in accordance with this collapse. Therefore, the necessary thing was to decide the nominal design value of the fabrication gaps. It could be assumed that the total of the gaps was equal to the displacement of the bottom layer. The result of the design calculation is shown in Fig. 5. The larger the gap, the higher the stress that appears in the conductor. Since the stress on the copper in the bottom layers should be below the yield strength of 290 MPa, the averaged fabrication gap should be within the 65 μm/layer. This value was achieved in the practical coil winding process. Thus, we can avoid the coil quench caused by the plastic deformation of the conductors.

2.2. Poloidal coil development

To fabricate the poloidal coils, a forced flow cooled conductor with a high stability margin (NbTi cable-in-conduit type, Table II) has been developed to reduce

the AC loss due to the coil current shift during the plasma experiments (about 1 kA/s). Cooldown and current excitation tests on the smallest poloidal coil (inner vertical (IV) coil) was a highlight of the poloidal coil R&D [7]. Without experiencing any coil quench, we could raise the current to the nominal value of 20.8 kA.

2.2.1. *Poloidal coil configuration*

The poloidal coils consist of IV, inner shaping (IS) and OV coils. The IV and IS coils have been completed in the factory and shipped to the institute. The on-site winding of OV coils has been finished, and the lower three coils have already been installed into the lower part of the LHD supporting structure.

NbTi cable-in-conduit conductors are adopted since they have a high stability margin and low AC loss. The specifications are listed in Table II. The void fraction is 0.38, which is optimized from the viewpoint of strand movement and interstrand coupling losses. The strand surface is not coated by any resistive layer. Taking care of current distribution and heat transfer to the helium, we have confirmed that a bare strand provided a high stability margin. The critical current was chosen to be three times as high as the operating current at maximum field since the stability conditions necessary for quench protection were satisfied when the critical current was more than twice as high as the operating current.

An important issue of design and fabrication is error field reduction from the poloidal coils. The required accuracy is 1×10^{-4} at the plasma surface. To minimize the error field, the moulded pancakes kept tolerances of ± 2 mm for the inner and outer diameters and ± 1 mm for the height. The tolerances correspond to a relative accuracy of about 5×10^{-4} for the diameter. As for the electric joints between the pancakes, a solid state bonding method was applied. The NbTi filaments were joined while trying to keep their superconductive performance. The required space for the joint is only 37 mm wide, 50 mm high and 60 mm long. The joint was small enough to reduce the error field.

2.2.2. *Performance test of IV coil*

One of the IV coils was installed in a single coil testing cryostat and connected to the test facilities in NIFS. The helium refrigerator capacity is 600 W at 4.4 K or 250 L/h. The inlet gas temperature was controlled by mixing cool (~ 80 K) and hot (~ 280 K) gases from the cold box. The temperature difference between the inlet and the outlet was then kept at less than 50 K. After the initial cooling phase, steady cooling was carried out by a supercritical helium centrifugal pump. The specified mass flow rate was 50 g/s, and the inlet pressure was about 0.9 MPa. The pressure drop was continuously measured during the cooldown and steady cooling phases. An extended summary of the results of the single cooldown and excitation tests of an IV coil is as follows: (1) The total cooldown time was about 250 h. (2) The coil contracted uniformly, coinciding with the design value, by about 6 mm. (3) The

relationship between the friction factor and the Reynolds number of the He coolant in the cooldown phase agreed well with the results obtained by the R&D coils previously tested. (4) Thus, the friction factor decreased by increasing the operating current, which might be explained by the narrow gap produced by the electromagnetic force inside the conduit. (5) The coil current was successfully raised to the nominal value of 20.8 kA, without any perturbation. We could confirm that the conductor possessed a high stability margin. (6) The heat generation of a joint was 0.06 W at 20.8 kA, which was negligible for conductor stability. (7) The radial displacement and acoustic emission observed suggested that the coil was mechanically stable.

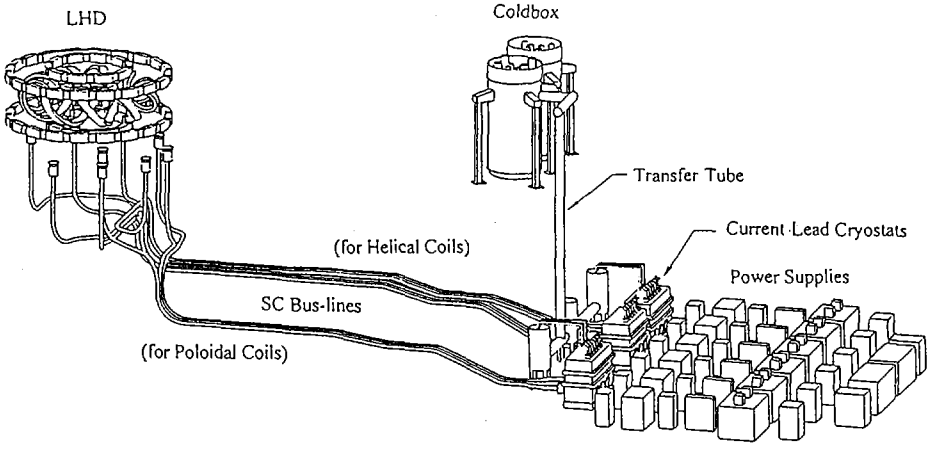

FIG. 6. Layout of superconducting bus lines.

TABLE III. SPECIFICATIONS OF SC BUS LINE

Number	6 (helical coils) 3 (poloidal coils)
Rated current (kA)	32
Rated voltage (kV)	5.7 (80 K GHe)
Length (m)	45–65
Minimum bending radius (m)	1.5
Heat load (W/m)	0.3 (80–4.2 K) 3 (300–80 K)
Type	Five corrugated tubes

2.3. SC Bus line system

A superconducting flexible bus line has been developed for a current feed system for the LHD. An aluminium stabilized NbTi/Cu compacted strand cable is used to satisfy the requirement of full stabilization at a nominal current of 32 kA. We use SC bus lines for both helical and poloidal coils. The bus line system is shown in Fig. 6.

The design concepts for an SC current feeder system for the LHD are as follows: (1) Fully stabilized SC properties should prevail for a nominal current of 31.3 kA (for OV coils). (2) The breakdown voltage should be higher than that of the SC coils. (3) The system should be able to maintain its rated current carrying capacities for 30 min, even if the coolants supplied to the current feeder system are stopped. The SC current feeder system is required to have a sufficient safety margin exceeding that of the SC coils because the stored magnetic energy of the coils must be extracted safely through the SC bus lines when the coils quench. The SC bus lines should be flexible since the routes from the coils to their power supplies have many corners and bends. The minimum bend radius is designed to be 1.5 m, because of the restrictions on height and width. The design specifications for the SC bus lines are listed in Table III.

We have manufactured the full scale model of a 20 m long SC bus line as is shown in Fig. 7 [8]. Performance tests of the full scale model were successfully carried out. A minimum propagation current, for normal transition, higher than 32.5 kA was observed when a perturbation energy of 80 J was added. We also successfully conducted an over-current operation up to 40 kA without any quench.

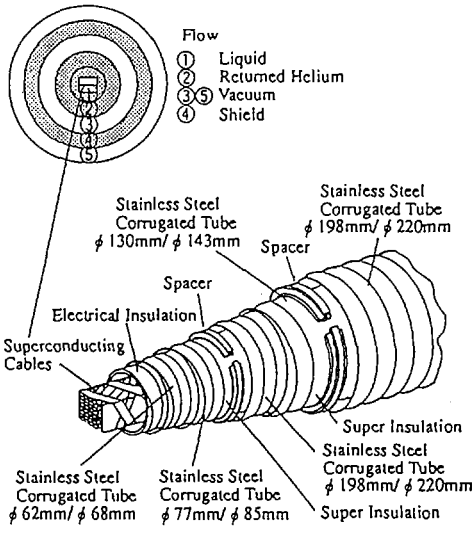

FIG. 7. Cross-section of superconducting bus line.

The current distribution among the SC strands was investigated for ramp rates from 100 to 2 kA/s, and the deviation of the distributed currents was less than 7%. The heat load onto the returned cold gas helium through the corrugated transfer tube was 4.55 W/m.

The breakdown voltage between +/− cables was measured with R&D test pieces of SC bus lines of 150 mm in length. Both ends of the test pieces were covered by electrical insulators. The tests were conducted over a wide temperature range from 4.2 to 294 K using temperature regulated helium gas. The maximum voltage of the coils induced is 1.9 kV, which corresponds to the 20 s rapid coil current rampdown assumed in the case of coil quench. The result of the breakdown tests was that it was 8.33 kV at 80 K and more than 20 kV at 4.4 K. This means that the insulation structure of the SC bus line has a sufficiently large voltage margin.

3. SUMMARY

Performing LHD R&D, engineering design and construction, we have developed a great deal of SC magnet technology that is contributing to the development of fusion technology.

In the following, we briefly add further information on major progress in SC magnet technology during LHD construction: (1) *Helical coil conductor joints:* there are 32 joints, in which we could obtain a sufficiently low value of the resistance of each joint, i.e. less than 0.7 nΩ (0.2 W at 17.3 kA). (2) *Evaluation of AC loss in the helical coil conductor:* the AC loss of the helical coil conductor is evaluated by applying a time varying magnetic field. From the magnetization of the conductor, a time constant of 4.3 s was obtained. (3) *Coil protection:* the coil protection circuit for the helical and poloidal coil systems is a pressing issue for the LHD operation. A 30 kA range DC circuit breaker using power fuse and an AC vacuum breaker has been developed for this circuit with a dump resistor. After the demonstration tests using practical circuit and dummy coils, the operation sequence and the possibility of faults less than 5×10^{-3} have been confirmed. (4) *A supercritical helium pump for forced flow cooling:* an SHe circulating pump for poloidal coils has been developed and tested during the IV coil test (50 g/s). The mechanical performance with a high pressure drop between inlet and outlet (1 atm) was confirmed.

In this year (1996), the major activity of LHD construction will move towards the finalizing phase at the Toki site. The completion of the construction schedule is end of 1997. We shall continue performing the tasks necessary for the construction and the assembly of the LHD.

REFERENCES

[1] MOTOJIMA, O., Fusion Technol. 26 (1994) 437.

[2] MOTOJIMA, O., in Fusion Engineering (Proc. 16th SOFT Symp., Urbana-Champaign, 1995), IEEE, Piscataway (invited paper).

[3] MOTOJIMA, O., et al., Fusion Technol. **27** (1995) 123.
[4] MITO, T., et al., Fusion Eng. Des. **10** (1993) 233.
[5] YANAGI, N., et al., Adv. Cryog. Eng. **40** (1994) 459.
[6] YAMAZAKI, K., Fusion Eng. Des. **10** (1993) 79.
[7] SATOW, T., et al., paper presented at ICEC16, Kitakyushu, Japan, 1995.
[8] YAMADA, S., et al., in Fusion Technology (Proc. SOFT 18th Symp. Karlsruhe, 1994), Karlsruhe (1994) D-425.

TECHNOLOGY, NEW DEVICES AND REACTOR STUDIES

(Poster Session GP)

DEVELOPMENT OF INNOVATIVE FUELLING SYSTEMS FOR FUSION ENERGY SCIENCE

M.J. GOUGE[1], D.Q. HWANG[2], L.R. BAYLOR[1], S.K. COMBS[1], P.W. FISHER[1], C.R. FOUST[1], S.L. MILORA[1], H.S. McLEAN[2], R.D. HORTON[2], R.W. EVANS[2], J.C. THOMAS[3], R. RAMAN[4], B.J. DENNY[5], R.S. WILLMS[5], A. FRATTOLILLO[6], S. MIGLIORI[6]

Abstract

DEVELOPMENT OF INNOVATIVE FUELLING SYSTEMS FOR FUSION ENERGY SCIENCE.

The development of innovative fuelling systems in support of magnetic fusion energy, in particular the International Thermonuclear Experimental Reactor (ITER), is described. The ITER fuelling system will use a combination of deuterium–tritium (D–T) gas puffing and pellet injection to achieve and maintain ignited plasmas. This combination will provide a flexible fuelling source with D–T pellets penetrating beyond the separatrix to sustain the ignited fusion plasma and with deuterium rich gas fuelling the edge region to meet divertor requirements in a process called isotopic fueling. More advanced systems with potential for deeper penetration, such as multistage pellet guns and compact toroid injection, are also described.

1. INTRODUCTION

In contemporary tokamaks, fuelling provides the required density level for a particular plasma experiment lasting, typically, from a fraction of a second to several seconds. Recently, the Oak Ridge National Laboratory (ORNL) development programme has focused on meeting the International Thermonuclear Experimental Reactor's (ITER's) complex fuelling needs. For ITER [1] and fusion power plants, the fuelling system has to provide deuterium–tritium (D–T) fuelling for much longer pulse lengths, in the range of ~1000 s to steady state. The system also must serve multiple, diverse functions including control of the plasma ion density to maintain a specified fusion power, replenishment of the fuel burned in the D–T fusion reaction,

---

[1] Oak Ridge National Laboratory, Oak Ridge, Tennessee, USA. Research performed by ORNL, managed by Lockheed Martin Energy Research Corp., for the US Department of Energy under Contract No. DE-AC05-96OR22464.

[2] Department of Applied Science, University of California Davis/Livermore, California, USA. Research performed by U.C. Davis, Livermore, for the US Department of Energy under Contract No. DE-FG03-90ER-54102.

[3] Present address: PSI Inc., San Leandro, California, USA.

[4] Affiliated with Canadian Fusion Fuel Technology Project.

[5] Los Alamos National Laboratory, Los Alamos, New Mexico, USA.

[6] Frascati Energy Research Centre, Frascati, Rome, Italy.

establishment of a flow of hydrogenic ions into the scrape-off layer and influence of plasma edge conditions on optimum divertor operation. The ITER fuelling system will use a combination of gas puffing and pellet injection [2] to achieve and maintain ignited plasmas. This combination will provide a flexible fuelling source with D–T pellets penetrating beyond the separatrix to sustain the ignited fusion plasma and with deuterium rich gas fuelling the edge region to meet divertor requirements in a process called isotopic fuelling [3]. Several advanced fuelling schemes for tokamak fusion reactors are under study. Technologies with potential for deeper penetration include multistage pellet guns and compact toroid (CT) injection.

2. PELLET FUELLING SYSTEMS

The baseline ITER pellet injector concept is the centrifuge acceleration device. A major objective of the development programme is to improve the performance and reliability of the centrifuge pellet injection system. An existing centrifuge accelerator facility provides a test bed for experimental investigations and hardware development. In the present effort, a standard ORNL extruder and an innovative pellet punch mechanism have been fitted to the existing centrifuge accelerator facility. The new, punch type pellet feed/cutter device is closely coupled to the arbor and is adjustable, including the capability to change pellet lengths remotely in 0.2 mm increments over the 1.6 to 2.8 mm range. Deuterium testing is being carried out to optimize system performance and reliability with a goal of retrofitting this feed and punch system on the Tore Supra centrifuge injector. To date, the feed system has produced over 400 cylindrical pellets (2.3 mm diameter by 1.6 mm length) at low repetition rates of 1 to 2 Hz. At higher repetition rates in the 10 to 20 Hz range, pellet sequences of several seconds length have been produced, the pulse length being limited by the ability of the centrifuged vacuum pumping system to maintain sufficient vacuum for thermal insulation of the extruder cryostats. This constraint can be removed by a separation of the cryostat guard vacuum from the centrifuge spin tank vacuum. Sequences of up to ~ 100 pellets have been accelerated to speeds of 500 m/s, with a high fraction of intact pellets hitting the pellet target plate in the pellet injection line.

For ITER application and fusion reactors, a feed system capable of providing a continuous supply of frozen isotopic hydrogen is required. A straightforward technique, in which multiple extruder units of identical design operate in tandem, is being developed for steady state operation. The extruder design was updated with a version that doubles the available hydrogenic ice volume over the design used on the Joint European Torus and the Tokamak Fusion Test Reactor (TFTR) pellet injectors. A prototype consisting of three extruder units, each with a deuterium ice volume of ~ 8 cm^3, is under assembly. Deuterium extrusions with a nozzle producing 4 mm diameter pellets were carried out recently on a single extruder assembly. The system performed as expected, providing a good ribbon of deuterium ice for multiple seconds. A transition piece that accepts the three individual feeds and releases one

single feed is the key new component to be developed for this design. The equipment described here should be adequate to demonstrate steady state feed rates as are required for pellet injector operation at frequencies of up to ~10 Hz and pellet sizes in the 2 to 8 mm range.

A pellet injection system to test the thermomechanical properties of the extruded tritium has been fabricated. This repeating, single stage pneumatic injector, called the tritium-proof-of-principle phase II (TOP-II) pellet injector [4], has a piston driven mechanical extruder and is designed to extrude and accelerate hydrogenic pellets sized for the ITER device. In initial tests with deuterium feed at ORNL, up to 13 pellets have been extruded at rates of up to 1 Hz and have been accelerated to speeds of ~1.0 km/s. The pellets, typically 7.4 mm in diameter and 7 to 11 mm in length, are the largest cryogenic pellets produced by the fusion programme to date. These pellets represent about 5 to 10% density perturbation to ITER. In a series of successful experiments at the Los Alamos National Laboratory, solid tritium was extruded and used to produce repetitive tritium and D–T pellets (Fig. 1). This is the first known extrusion of solid tritium.

ORNL, in collaboration with ENEA Frascati, has developed a repeating two stage light gas gun [5] to evaluate the technology issues of a high muzzle velocity pneumatic injector utilizing an extruder based pellet feed system. Figure 2 shows the results of many single pellet and repetitive deuterium pellet sequences; muzzle velocities of 2.5 km/s have been attained at repetition rates of 1 Hz.

The production of impurity pellets (Ne, Ar, Kr) has been demonstrated by using the DIII-D and TFTR pneumatic pellet injection systems; such pellets will be used in experiments to optimize the edge plasma/divertor conditions and to evaluate the rapid plasma shutdown capability for a mitigation of the effects of a major plasma disruption.

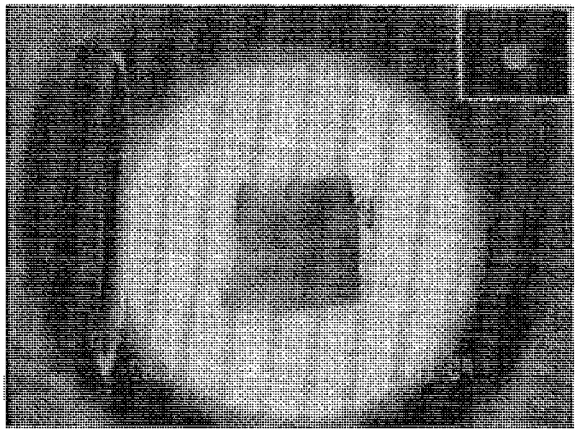

FIG. 1. Photograph of D–T pellet (7 mm diameter, ~8 mm length).

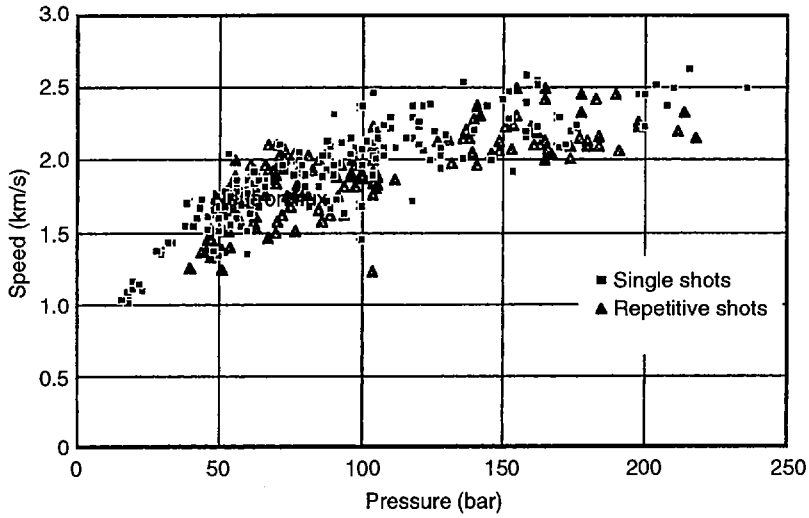

FIG. 2. Muzzle velocity as a function of breech pressure for repeating two stage pneumatic injector.

3. CT FUELLING

As tokamak parameters approach the fusion reactor regime, it becomes increasingly clear that the ability to centrally fuel a tokamak reactor is crucial to its overall efficiency. For example, a recent parametric study [6] of the ITER operating regime has shown that a centrally peaked density profile can lower the ignition parameter and the relative plasma pressure, β, required for ignition. Spheromak-like compact toroids (SCTs) are self-contained, magnetized plasma structures that have an internal toroidal and poloidal magnetic field, with associated internal poloidal and toroidal plasma currents [7]. This CT type has been demonstrated to withstand great accelerating forces using coaxial electrodes [8]. Unlike CTs formed by reverse field processes, SCTs are low β plasmas with relatively high magnetic binding energy per ion. This is expected to result in a more robust magnetized plasma with increased capability of remaining intact during the tokamak–CT interaction phase. The use of accelerated SCTs to centrally fuel tokamak plasmas has been demonstrated on experiments on the TdeV tokamak [9], during which central plasma penetration was obtained without any adverse effect to the tokamak discharge.

The first goal of the University of California at Davis experimental programme is to understand the stopping mechanism of an accelerated SCT in a vacuum magnetic field. By assuming that the SCT behaves as an incompressible, perfectly conducting rod, we obtain a simple estimate of its penetration into a magnetic field. Taking the mass density, ρ_{ct}, to be constant, the SCT kinetic energy density at velocity v is $K = \rho_{ct}v^2/2$, while the energy density required to exclude the magnetic field, B,

from the SCT volume is $P = B^2/2\mu_0$. The total energy $K + P$ is conserved, so that an SCT with initial velocity $v = v_0$ in a field free region has a final velocity of $v_f = \sqrt{v_0^2 - 2P/\rho_{ct}}$ in the presence of a vacuum magnetic field. The condition that the SCT be stopped ($v_f = 0$) at the final magnetic field, B_f, is therefore $\rho_{ct}v_0^2 = B_f^2/\mu_0$. The experimental data that are in general agreement with the equation for v_f are shown in Fig. 3. The extra SCT penetration at high fields may be caused by finite compressibility.

Using this model, SCT injection data to date can be summarized on a plot of mass density ρ versus the initial velocity v_0, with an estimate of the parameter region needed to centrally fuel an ITER class tokamak. Data for CT experiments at CTIX (U.C. Davis/Livermore), RACE (Livermore), MARAUDER (Phillips Lab.), and CFFTP (TdeV) are shown in Fig. 4. Note that the energy density required for penetration of a 5 T magnetic field has already been obtained on the MARAUDER accelerator, using argon SCTs [10].

For an SCT injector to fuel a reactor class tokamak, repetitive operation is essential because a discharge duration of ~1000 s is planned. Moreover, repetitive operation at a high repetition rate can minimize the plasma disturbance by delivering a relatively small mass of neutral density per SCT injection. We have developed the first operating repetitive SCT injector by making use of fast gas puffing and saturable core reactors, thus obtaining power switching without use of active external switching devices such as spark gaps or ignitrons. To date, this injector has produced up to 1000 consecutive shots into our small tokamak, DDT, which is pulsed in synchronism with the injector.

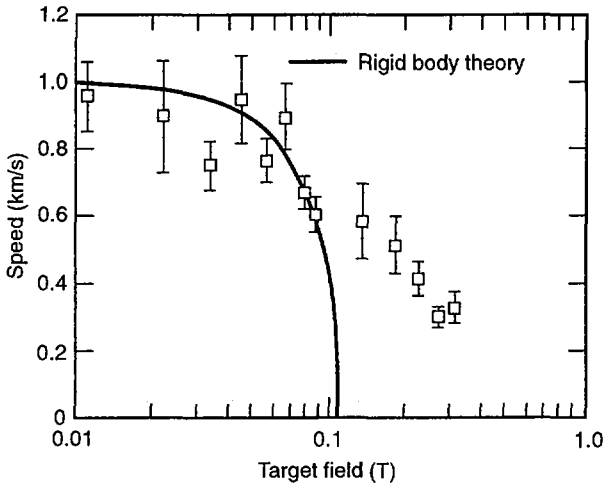

FIG. 3. Fitting of SCT vacuum field penetration to rigid body model.

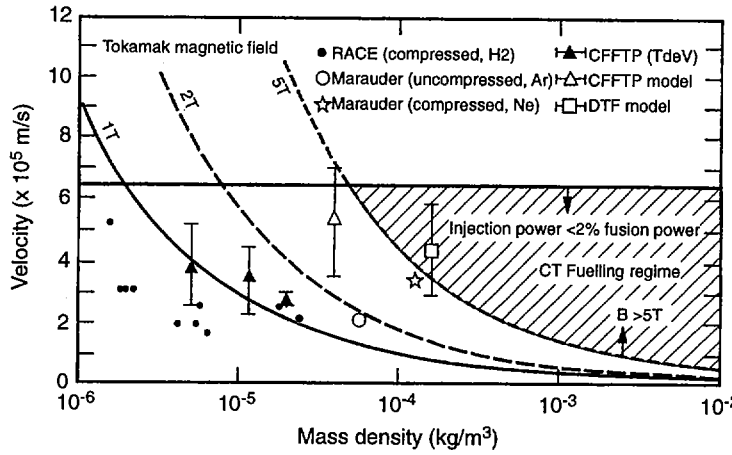

FIG. 4. Comparison of energy displacement model of SCT penetration with existing experimental data.

Another area of interest is the effect of repetitive pulse operation on the SCT impurity content. This effect is under investigation on DDT by using time resolved spectrometry. Repetitive SCT operation is expected to have the advantages of continuous electrode cleaning and maintenance of electrode surfaces at high temperatures, reducing impurity redeposition. Spectroscopic data of SCT impurities are measured with a gated visible optical multichannel analyser (OMA). A total of 100 shots at a 0.2 Hz repetition rate were recorded at a distance of 91 cm from the SCT formation region, with the OMA gated on for 10 μs, starting 5 μs after SCT formation. O_{III} is the predominant radiation in the wavelength region studied (370 to 400 nm). The 100 shots show no dramatic increase in impurity radiation, despite significant wall dissipation and heating.

Time resolved measurements with silicon X ray photodiodes (Fig. 5, bottom trace) indicate that virtually all emission occurs during the 10 μs OMA gating interval. Wall field measurements at the same location (Fig. 5, top and middle traces) indicate that most radiation is contained in the accelerating sheath, and not in the SCT itself, because visible light is seen to peak after the poloidal field has significantly decayed from its maximum value. Since the radiating impurities are not contained within the SCT, they are not expected to penetrate the closed field region of the tokamak plasma but will instead be swept away by the divertor action of the open field line region. The SCT plasma would, of course, penetrate deep into the discharge. The impurities associated with the acceleration plasma should therefore not contribute to contaminating the tokamak discharge.

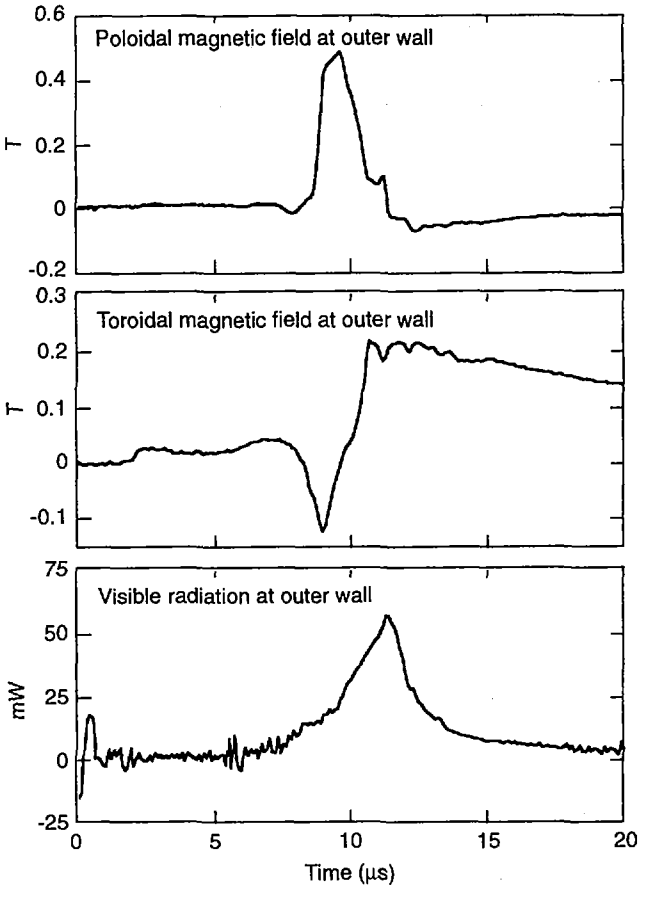

FIG. 5. SCT measurements at outer wall, 91 cm port. Top: SCT field (poloidal field), middle: accelerating field (toroidal field), bottom: radiation signal at outer wall (photodiode).

In summary, we have shown that it is possible to form and accelerate SCTs by purely passive switching, greatly reducing the complexity associated with an actively switched injector. Experiments with other SCT devices have demonstrated disruption free tokamak fuelling at directed energy densities close to that required for reactor fuelling. Together, these results suggest that the SCT is a viable candidate for tokamak reactor fuelling.

REFERENCES

[1] GOUGE, M.J., et al., Fusion Eng. Des. 19 (1992) 53.
[2] MILORA, S.L., et al., Nucl. Fusion 35 (1995) 657.

[3] GOUGE, M.J., et al., Fusion Technol. **28** (1995) 1644.
[4] FISHER, P.W., GOUGE, M.J., Fusion Technol. **28** (1995) 603.
[5] FRATTOLILLO, A., et al., Rev. Sci. Instrum. **67** (1996) 1834.
[6] INTERNATIONAL ATOMIC ENERGY AGENCY, ITER Performance Report 22, IAEA, Vienna (1991).
[7] TAYLOR, J.B., Rev. Mod. Phys. **58** (1986) 741.
[8] HAMMER, J., et al., Phys. Fluids B **3** (1991) 2236.
[9] RAMAN, R., et al., Phys. Rev. Lett. **73** (1994) 3101.
[10] DEGNAN, J.H., et al., Phys. Fluids B **5** (1993) 2938.

THE U.S. PROGRAM TO DEVELOP STRUCTURAL MATERIALS FOR NEAR- AND LONG-TERM FUSION SYSTEMS

A.F. ROWCLIFFE[1], E.E. BLOOM[1], R.H. JONES[2], D.L. SMITH[3], F.W. WIFFEN[4], W.R. JOHNSON[5]

[1] Oak Ridge National Laboratory, Oak Ridge, Tennessee

[2] Pacific Northwest Laboratory, Richland, Washington

[3] Argonne National Laboratory, Argonne, Illinois

[4] United States Department of Energy, Washington, D.C.

[5] General Atomics, San Diego, California

United States of America

Abstract

THE U.S. PROGRAM TO DEVELOP STRUCTURAL MATERIALS FOR NEAR- AND LONG-TERM FUSION SYSTEMS.

The U.S. structural materials program is pursuing a near-term effort related to the International Thermonuclear Experimental Reactor (ITER) and a long-term effort related to the development of reduced-activation materials for future power systems. The response of the principal ITER structural materials, austenitic stainless steels and copper alloys, to ITER irradiation conditions has been explored using fission reactor facilities. The primary radiation damage phenomena have been identified and the neutron dose and temperature conditions have been determined which will ensure adequate ductility during ITER operation. A new, reduced activation ferritic-martensitic steel has been shown to have exceptionally promising resistance to low temperature radiation embrittlement. A newly-developed V-Cr-Ti alloy has been successfully produced on a commercial scale and is being used to fabricate components for the DIII-D Radiative Divertor; recent experimental data on the irradiation performance of this alloy are discussed. Sources of radiation-induced property changes in SiC composite materials have been identified and strategies developed to improve mechanical performance of these materials during irradiation.

1. INTRODUCTION

The time scale for the ITER Engineering Design Activity (EDA) precludes the development of new materials with properties tailored to meet the unique demands of the ITER operating environment; the structural materials for the in-vessel components must be selected from materials for which there is existing experience in the fabrication, construction, and operation of commercial-scale systems. Consequently, the potential for controlling radioactivation is limited to minimizing certain impurity concentrations while remaining within commercial alloy specifications. On the other hand, the realization of the environmental attractiveness of fusion systems beyond ITER depends upon the development of new materials with controlled, reduced radioactivation properties. Working in collaboration with our partners in Europe, Russia, and Japan, the U.S. materials program has contributed strongly towards defining operating limits for structural materials in ITER and has achieved encouraging progress in the development of advanced materials with reduced activation characteristics. Some of these recent advances are highlighted in this paper.

2. ITER STRUCTURAL MATERIALS

The primary structural material for the first wall/blanket/shield and for the vacuum vessel is an austenitic stainless steel (316LN-IG) with a composition that is based primarily upon the extensive experience within European fast breeder reactor programs [1]. For various parts of the divertor, high strength copper alloys are utilized because of their higher conductivity and thermal stress resistance; copper alloys are also used for the heat sink material bonded to the first wall. Because ITER is a water cooled machine, the operating temperatures for stainless steel and copper alloys are relatively low (150-250°C), although transient temperatures that are 200-300°C higher can be achieved in certain components during disruptions. Under these operating conditions, the primary radiation phenomenon of concern, which has the potential to seriously affect mechanical performance, is radiation hardening. Although strengthening itself is not necessarily deleterious, it is invariably accompanied by significant changes in flow and fracture properties. Radiation hardening is temperature dependent. At ITER operating temperatures, yield strength increases rapidly with neutron dose and approaches a saturation value at a neutron dose of <1 dpa, which is well within the ITER range, 1 dpa $\equiv$ 0.1 MWa $\cdot$ m^{-2}. The yield stress (σ_y) increases more rapidly than the ultimate tensile stress (σ_u) and there is a progressive loss of strain hardening capacity as the yield stress approaches the ultimate stress and the uniform elongation drops to very low levels. On a microscopic level, this behavior is believed to be related to the annihilation of small defect clusters by the mobile dislocations released on yielding and the creation of cleared channels for subsequent dislocations; this localization of flow on the microscopic scale reduces the ability of the material to strain-harden. On a macroscopic scale, the inability to strain-harden creates a strong potential for failure through plastic instability in regions of the component where the yield stress is exceeded.

To identify the neutron dose and temperature regimes within which the loss of strain-hardening capacity could significantly impact the design of ITER components, a series of fission reactor irradiation experiments were recently completed. Type 316 stainless steel in a solution-annealed condition (316 SA) was irradiated to 7 and 18 dpa at temperatures of 60, 200, 330, and 400°C under spectrally-tailored conditions which reproduced the helium generation rate characteristic of ITER [2]. Postirradiation tensile testing showed that radiation hardening occurs at all operating temperatures and reaches a maximum at around 300-330°C (Fig. 1) before decreasing steadily at higher temperatures; the dominant microstructural features which contribute to radiation hardening are also indicated. The stress-strain behavior was analyzed and then combined with other data in the literature to develop a dose-temperature map (Fig. 2) illustrating various regimes of ductility (ε_u). Engineering design codes use ε_u to characterize steels as ductile ($\varepsilon_u \geq 5\%$), semi-brittle ($1\% \; \varepsilon_u < 5\%$), or brittle ($\varepsilon_u \leq 1\%$) [3].

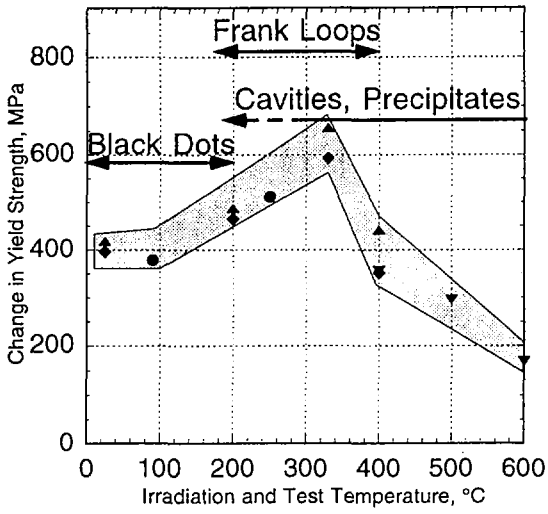

FIG. 1. Temperature dependences of radiation hardening for Type 316 stainless steel irradiated to neutron doses of 3–19 dpa.

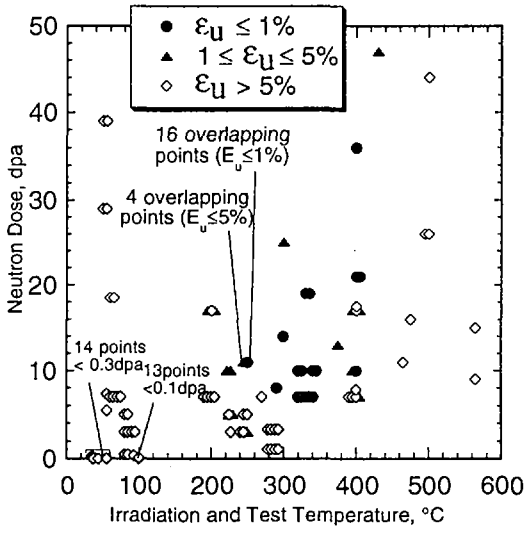

FIG. 2. Dose-temperature map for Type 316 stainless steel showing various regimes of uniform elongation (ϵ_u).

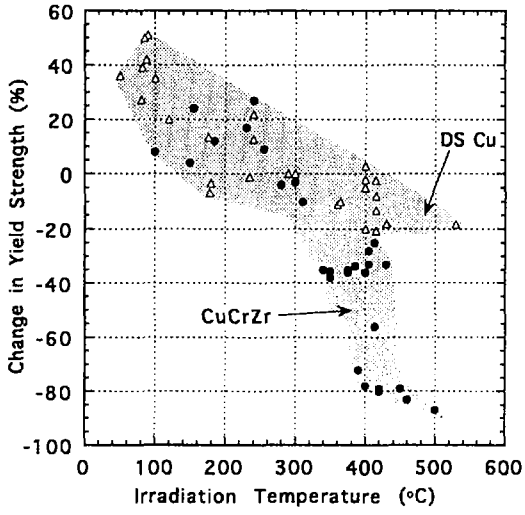

FIG. 3. Radiation hardening/softening for ODS alloys (open symbols) and Cu-Cr-Zr alloys (closed symbols) irradiated to 1-10 dpa.

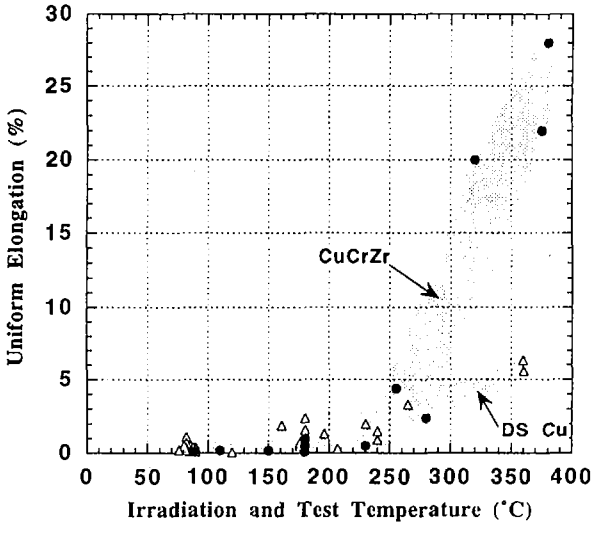

FIG. 4. Uniform elongation for ODS alloys (open symbols) and Cu-Cr-Zr alloys (closed symbols) irradiated to 1-10 dpa.

The data show that for the lifetime of the primary wall during the Basic Performance Phase (2-3 dpa) the austenitic stainless steel will remain in the ductile regime. However, for extended performance beyond 10 dpa, uniform elongation will drop to values ≤1% for operating temperatures in the range 250-400°C. Severe ductility loss in the higher dose-temperature regime has implications with regard to loss of fracture toughness and the possibility of alternative failure modes.

The high yield strengths achievable in precipitation-hardened (PH) copper alloys (e.g., Cu-Cr-Zr, Cu-Ni-Be) and oxide-dispersion-strengthened (ODS) (e.g., GlidCop Al-25) alloys, combined with their high conductivity results in thermal stress parameters that are over an order of magnitude higher than stainless steel.[4] In collaboration with our ITER partners, irradiation experiments have been carried out in the SM-2 reactor at Dimitrovgrad, Russia, to explore ITER-relevant temperatures and doses. The copper alloys derive their initial high yield strength from dense dispersions of second phase particles and in some cases, a high dislocation density, which results in a different hardening response compared to stainless steels. Radiation hardening occurs very rapidly at temperatures in the range 100-250°C; this is followed by a transition temperature regime at ~300°C, above which radiation-induced softening occurs (Fig. 3). The magnitude of the radiation-induced softening is much less pronounced for the ODS alloys compared to the PH alloys. The hardening that occurs in the 100-250°C regime is accompanied by major changes in flow properties; strain-hardening capacity is severely diminished and uniform elongation (ε_u) drops to very low values (≤1%). This phenomenon is similar to that described above for stainless steels; however, it maximizes at lower temperatures and is manifest at substantially lower doses. Figure 4 shows that irradiation to ~1 dpa at temperatures below ~100°C results in very low ductilities; however, the decreased hardening above the transition temperature range is accompanied by a rapid improvement in strain-hardening capacity and ε_u. In contrast to the stainless steels, the radiation hardening in copper alloys arises from the formation of small vacancy defect clusters (stacking fault tetrahedra and dislocation loops); at temperatures above ~150°C, the defect cluster density begins to decrease, corresponding to Stage V annealing of vacancy defects. Significant losses in ε_u actually occur for neutron doses as low as 0.01 dpa for irradiation temperatures ≤100°C, and these data have a major impact on the applications of high temperature copper alloys [5]. To maintain satisfactory ductility, ITER in-vessel components should be operated at temperatures above 150°C. If other engineering requirements dictate lower operating temperatures, then periodic annealing at 300-350°C of the radiation damage during the bake-out cycle could provide an approach to maintaining adequate ductility.

3. ADVANCED MATERIALS FOR POWER SYSTEMS

To maintain a range of options for the future development of thermally efficient breeding blankets and high heat flux components, the U.S. materials program is pursuing the development of reduced activation materials in three different materials systems, namely ferritic-martensitic steels, vanadium alloys, and SiC/SiC composites. The three systems are widely different in terms of physical and mechanical properties, fabrication methods, compatibility with chemical environments and current levels of commercialization. However, they are linked in terms of the allowable major alloying constituents and the degree to which impurities must be controlled in order to develop desirable low activation properties.

The underlying body-centered-cubic (BCC) crystal structure of the ferritic-martensitic steels confers improved physical properties compared to austenitic stainless steels; lower thermal expansion coefficients and higher thermal conductivities result in a greatly improved thermal stress resistance. The steels containing 8-12 wt % Cr and alloyed with Mo, Nb, and C are at an advanced stage of commercial maturity, being widely used in nuclear and non-nuclear power plants as steam generator materials. In addition, fission reactor irradiation programs have demonstrated good mechanical performance and swelling resistance over the range 400 to 550°C. The U.S. fusion materials program has developed reduced-activation

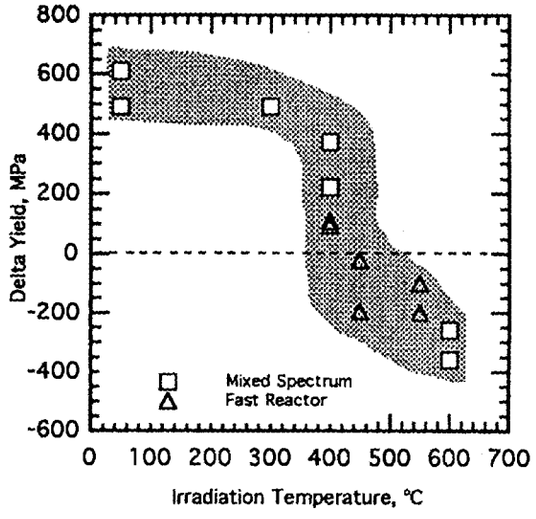

FIG. 5. Temperature dependence of yield strength for 9Cr–1MoVNb steels irradiated in fast and mixed-spectrum reactors to ~20 dpa.

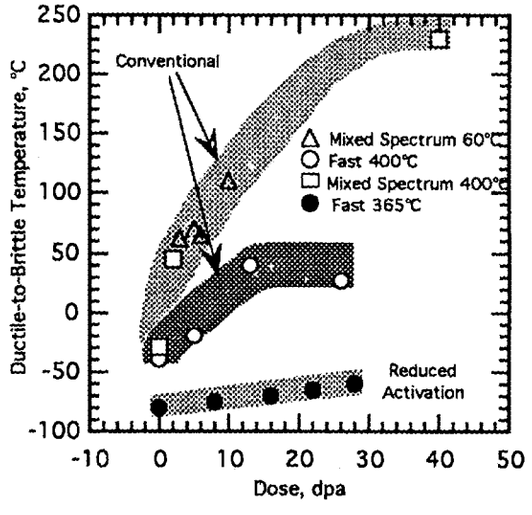

FIG. 6. Neutron dose dependence of DBTT for conventional 9Cr–1MoVNb steels and reduced activation 9Cr–1WVTa steel.

versions of these alloys which retain the performance of their conventional pre-cursors in terms of fabricability, thermal stability, corrosion resistance, mechanical behavior, and irradiation performance at 400 to 550°C [6]. However, in common with all BCC alloy systems, there exists a critical temperature below which these materials undergo a relatively sharp transition in fracture behavior from a ductile to a brittle failure mode. Neutron irradiation temperatures below 400-450°C produce an increase in this critical temperature thereby increasing the risk of brittle failure under certain combinations of flaw geometry, loading mode and rate, and section geometry. This issue is a primary focus of the U.S. program. Miniaturized Charpy v-notch (MCVN) impact specimens are being utilized to define the neutron-dose-temperature regimes within which major changes in fracture behavior may occur. It must be emphasized that the ductile-to-brittle transition temperature (DBTT) determined in this manner is not a fundamental property measurement [7]. However, MCVN testing provides a useful means of (a) indexing radiation-induced changes in fracture toughness, (b) comparing the relative behavior of different materials, and (c) assessing the influence of refinements to composition and microstructure.

Recently completed fast reactor irradiation experiments in the range 365-400°C have demonstrated significant gains in controlling the radiation-induced shift in DBTT. Figures 5 and 6 summarize some salient features of the response of 8-9% Cr ferritic martensitic steels. The temperature dependence of radiation-induced changes in yield strength is qualitatively similar to that of the high strength copper alloys. A low temperature region of radiation hardening is followed by a transition region around 400°C above which radiation softening occurs. Radiation hardening is accompanied by reductions in ε_u, but more significantly, there is also an increased propensity for brittle failure. For the conventional Fe-9Cr-1MoVNb steels, the DBTT (determined by MCVN testing) is increased by ~100°C during neutron irradiation in the 365-400°C range, the increase saturating with dose at ~10 dpa (Fig. 6). Under similar testing conditions, a new reduced activation steel (Fe-9Cr-2WVTa) undergoes very little change in impact properties and the DBTT remains below -50°C for neutron doses approaching 30 dpa [8].

Also shown in Fig. 6 are the MCVN impact data for the conventional alloy irradiated in a different neutron spectrum, both at ~60 and ~400°C, in the High Flux Isotope Reactor (HFIR) at Oak Ridge. The higher hardening rate is primarily responsible for the more rapid increase in DBTT at ~60°C. Because of the very high thermal to fast flux ratio (3:1), significant nuclear transmutation rates occur for several alloying elements. The transmutation of Ni via a two-step $^{58}Ni\ (n,\gamma)\ ^{59}Ni(n\alpha)\ ^{56}Fe$ enhances helium formation and at 40 dpa, the conventional Fe-9Cr-1MoVNb contains ~30 appm of helium. It has been proposed that the presence of helium is primarily responsible for the more rapid increase in DBTT that occurs with increasing neutron dose during HFIR irradiation at ~400°C [9]. These data highlight the importance of exploring in detail the effect of irradiation temperature to define lower operating temperature limits for the new reduced activation steels and the effects of neutron spectrum and transmutation production. A collaborative program within the framework of the IEA is in place to investigate these parameters and also to provide the data base required for the design of blanket modules to be tested in ITER.

Vanadium-based reduced activation alloys also have a BCC structure and possess physical properties that are even more attractive than those of the ferritic-martensitic steels. Coupled with their higher melting point and compatibility with liquid Li, the vanadium alloys have the potential for accommodating higher heat fluxes than the ferritic steels, and for operating at significantly higher temperatures up to ~650°C. Over the past several years the U.S. program has made strong advances in this area culminating in the identification of a new alloy containing 4 wt % Cr and 4 wt % Ti, which has an attractive combination of physical and mechanical properties, compatibility with liquid Li, and radiation damage resistance [10]. The V-4Cr-4Ti alloy, containing controlled levels of carbon, oxygen, and nitrogen, exhibits the remarkable property for a BCC alloy of maintaining a ductile failure mode in static and dynamic fracture testing at temperatures down to -150°C [11]. This alloy has recently been

successfully scaled-up with the commercial production of a 500 kg ingot and, most recently, a 1200 kg ingot, while maintaining the full range of properties exhibited by the laboratory-made alloys. A recently completed experiment demonstrated that the new composition of V-4Cr-4Ti has promising resistance to radiation-induced embrittlement and swelling during irradiation at temperatures in the range 420-600°C to neutron doses of 24-32 dpa, and with helium generation rates in the range 0.4-4.2 appm/dpa. The DBTT, measured by dynamic MCVN testing, did not increase above -100°C, and density changes did not exceed 0.5% [10].

As described above in the discussion on ferritic-martensitic steels, for all BCC alloys there is a dose-temperature regime in which the magnitude of radiation-hardening is sufficient to promote low ductility failure modes under certain conditions. To determine the extent of this regime for V-4Cr-4Ti, a series of low temperature (<425°C), low dose (≤1 dpa) experiments are in progress using the water cooled High Flux Beam Reactor (HFBR) at Brookhaven National Laboratory. Initial results show that radiation hardening increases rapidly with increasing irradiation temperature over the range 100 to 275°C and is accompanied by severe loss of work hardening capacity. Irradiation to 0.4 dpa at 275°C increased the DBTT, measured by dynamic MCVN testing, from around -150 to around +200°C [12]. These data indicate that in its present form, the V-4Cr-4Ti alloy would not be suitable for operation in a neutron environment at temperatures as low as ~275°C. Further irradiation testing is in progress to complete the mapping of the radiation-hardening regime in terms of neutron dose and temperature and to carry out relevant fracture testing to define the lower operating temperature limits for this material.

The new V-4Cr-4Ti alloy is currently being utilized in the manufacture of a portion of the Radiative Divertor in the DIII-D tokamak at General Atomics [13]. A 1200 kg ingot has been produced at Teledyne Wah Chang, extruded into rectangular billets and machined into sheet bar; further processing into sheet and rod forms is in progress. Preliminary success has been achieved in developing similar and dissimilar metal welds by resistance, inertia, portable friction, and electron beam welding methods. The eventual operation of the water-cooled divertor will provide a significant step in the development of reduced activation materials by (a) demonstrating the in-service behavior of V-4Cr-4Ti in a tokamak environment and (b) developing experience in the design, processing, and fabrication of full scale vanadium alloy components.

The attractiveness of SiC composite materials stems from their potential for high operating temperatures and the utilization of thermodynamically efficient He gas cycles, and their inherently low induced radioactivity. SiC composite materials are produced by chemical vapor infiltration (CVI) into a continuous SiC fiber cloth to produce a crystalline beta SiC matrix. There is not a great deal known about the radiation performance of these materials, but recent experiments in the U.S. program have shed some light on this topic. It is known that beta SiC exhibits good radiation stability with the linear swelling decreasing from about 0.5% at 500°C to less than 0.1% at 1000°C. Recent neutron irradiation data have shown that linear swelling of SiC/SiC composites produced by CVI matches the low swelling behavior of the monolithic beta SiC [14]. In another area, recent irradiation experiments using 0.56 MeV Si ions indicate that large volume expansions from radiation-induced amorphization are unlikely to occur at neutron irradiation temperatures above ~100°C [15].

Initial irradiation experiments on commercially available SiC/SiC composite materials have shown that a serious degradation of mechanical behavior occurs, which is related to the radiation-induced densification of the standard Nicalon^{TM} SiC-based fiber [16]. Several grades of SiC fiber have been now identified with greatly improved dimensional stability during neutron irradiation. Prominent among these is the reduced oxygen High-Nicalon^{TM}, Nicalon-Type S and the Dow Corning Stoichiometric SiC. The High Nicalon^{TM} fiber has been incorporated into composites which exhibit substantially better strength and toughness properties than the standard materials. To further improve resistance to radiation damage, new interfacial structures between fiber and matrix are being developed utilizing both porous SiC and multilayer SiC; promising initial results have been obtained from the composite materials containing these interfaces.

REFERENCES

[1] TAVASSOLI, A.A., Fusion Eng. Des. **29** (1995) 371.

[2] PAWEL, J.E., GROSSBECK, M.L., SHIBA, K., ROWCLIFFE, A.F., ALEXANDER, D.J., "Effects of low temperature neutron irradiation on deformation behavior of austenitic stainless steels", Proc. 7th Int. Conf. on Fusion Reactor Materials, Obninsk, 1995, J. Nucl. Mater. **233–237** (1996) 202.

[3] MAJUMDAR, S., Design standard issues for ITER in-vessel components, Fusion Eng. Des. **29** (1994) 158.

[4] ZINKLE, S.J., FABRITSIEV, S.A., "Copper alloys for high heat flux structural applications", Atomic and Plasma-Material Interaction Data for Fusion, Vol. 5, IAEA, Vienna (1994) 163.

[5] FABRITSIEV, S.A., POKROVSKY, A.S., ZINKLE, S.J., EDWARDS, D.J., "Low-temperature radiation embrittlement of copper alloys", Proc. 7th Int. Conf. on Fusion Reactor Materials, Obninsk, 1995, J. Nucl. Mater. **233–237** (1996) 513.

[6] KLUEH, R.L., Developing steels for service in fusion reactors, J. Metals **44** (1992) 20.

[7] EDSINGER, K., ODETTE, G.R., LUCAS, G.E., SHECKHERD, J.W., "The effect of size, crack depth and strain rate on fracture toughness-temperature curves of a low activation martensitic stainless steel", Proc. 7th Int. Conf. on Fusion Reactor Materials, Obninsk, 1995, J. Nucl. Mater. **233–237** (1996) 342.

[8] KLUEH, R.L., ALEXANDER, D.J., "Tensile and Charpy impact properties of irradiated reduced-activation ferritic steels", Proc. 18th ASTM Symp. on Effects of Radiation on Materials, Hyannis, MA, 1996, US Govt Printing Office, Washington, DC (1996).

[9] KLUEH, R.L., ALEXANDER, D.J., Impact behavior of 9Cr-1MoVNb and 12Cr-1MoVW steels irradiated in HFIR, J. Nucl. Mater. **179–181** (1991) 733.

[10] SMITH, D.L., CHUNG, H.M., LOOMIS, B.A., TSAI, H.-C., "Reference vanadium alloy V-4Cr-4Ti for fusion applications", Proc. 7th Int. Conf. on Fusion Reactor Materials, Obninsk, 1995, J. Nucl. Mater. **233–237** (1996) 356.

[11] ODETTE, G.R., LUCAS, G.E., DONAHUE, E., SHECKHERD, J.W., Fracture toughness and micromechanics in a V-4Cr-4Ti alloy, J. Nucl. Mater. **233–237** (1996) 502.

[12] ALEXANDER, D.J., et al., "Effects of irradiation at low temperature on V-4Cr-4Ti, Fusion Reactor Materials Semiannual Progress Report for Period Ending June 30, 1996, Rep. DOE/ER-0313/20, US Govt Printing Office, Washington, DC (1996) 87.

[13] SMITH, J.P., et al., "Vanadium alloys for the radiative divertor program at DIII-D", Proc. 16th IEEE/NPSS Symp. on Fusion Engineering, Champaign, IL, 1995, Vol. 2 (MILEY, G.H., ELLIOTT, C., Eds), IEEE Service Center, Piscataway, NJ (1995) 858.

[14] JONES, R.H., HENAGER, C.H., YOUNGBLOOD, G.E., HEINISCH, H.L., SiC/SiC composites for structural applications in fusion energy systems, Fusion Technol. **30** (1996) 969.

[15] ZINKLE, S.J., SNEAD, L.L., "Influence of irradiation spectrum and implanted ions on the amorphization of ceramics", Proc. 8th Int. Conf. on Radiation Effects in Insulators, Catania, Italy, 1995, Nucl. Instrum. Methods B **116** (1996) 92.

[16] SNEAD, L.L., JONES, R.H., KOHYAMA, A., FENICI, P., "Status of silicon carbide composites for fusion", Proc. 7th Int. Conf. on Fusion Reactor Materials, Obninsk, 1995, J. Nucl. Mater. **233–237** (1996) 26.

DEVELOPMENT OF LOW ACTIVATION FERRITIC AND MARTENSITIC STEELS FOR FUSION REACTORS

A. KOHYAMA
Institute of Advanced Energy,
Kyoto University,
Kyoto, Japan

A. HISHINUMA
Tokai Establishment,
JAERI,
Tokai, Japan

D.S. GELLES
Battelle Pacific Northwest National Laboratory,
Richland, Washington,
United States of America

R.L. KLUEH
Oak Ridge National Laboratory,
Oak Ridge, Tennessee,
United States of America

W. DIETZ
EC/DGXII/Fusion Program,
Brussels, Belgium

K. EHRLICH
Forschungszentrum Karlsruhe,
Karlsruhe, Germany

Abstract

DEVELOPMENT OF LOW ACTIVATION FERRITIC AND MARTENSITIC STEELS FOR FUSION REACTORS.

The development of low activation ferritic/martensitic steels is a key to the achievement of nuclear fusion as a safe, environmentally attractive and economically competitive energy source. The Japanese and the European Fusion Materials programmes put R&D on low activation ferritic and martensitic steel at the highest priority for a demonstration reactor (DEMO) and beyond. An international collaborative test programme on low activation ferritic/martensitic steels for fusion is in progress as one of the activities of the International Energy Agency (IEA) fusion materials working group. The objective of the test programme is to verify the feasibility of using ferritic/martensitic steels for fusion by an extensive test programme covering the most relevant technical issues for the qualification of a

material for nuclear application. The development of a comprehensive database on representative, industrially processed reduced activation steels of 8-9Cr-2WVTa type is under way in order to provide designers with a preliminary set of material data, within about three years, for the mechanical design of components, e.g. for DEMO relevant blanket modules to be tested in the International Thermonuclear Experimental Reactor (ITER). Knowledge of the current limitations of low activation ferritic steels for application in advanced fusion systems is reviewed and future prospects are outlined.

1. INTRODUCTION

One of the most important challenges in fusion technology R&D is the development of low activation materials. At present, low activation ferritic/martensitic steels (LAFs), vanadium alloys and SiC/SiC composite materials are considered to be promising candidates. Among them, the LAFs R&D is placed at the highest priority in the Japanese and the European programmes.

To accelerate the development of LAFs, a working group under Annex II of the International Energy Agency (IEA) implementing agreement on a programme of R&D on fusion materials has been formed in order to co-ordinate a collaborative programme between the European Union (EU), the USA and Japan [1].

This paper will describe the status and the future perspectives of the programme in some detail.

2. SELECTION OF REFERENCE LAFs AND IEA ACTIVITY

Beginning in the mid 1980s, programmes in Japan, the USA and Europe sought to develop LAFs. Alloying elements that had to be eliminated from the conventional Cr–Mo steels that were then considered candidate materials were Mo and Nb. Molybdenum was replaced by W and Nb by Ta to produce Fe-Cr-W-Ta steels. The IEA LAFs working group reviewed potential materials at its Tokyo meeting in 1992. Steels reviewed included the Japanese F82H and JLF-1, the US 9Cr-2WVTa steel, and the European steels LA12TaLC, CeTa, BATMAN and EUROFER. Each party proposed quite similar alloy compositions and fabrication methods at the Tokyo meeting, where a proposal was made by the Japanese to fabricate two large heats of steel [1]. Figure 1 shows the materials and participants of the IEA collaborative activity. The steels for the IEA test programme have been provided by the two Japanese research sectors: The Monbusho university programme and the STA JAERI programme. Two 1-tonne heats of JLF-1 steel (a 9Cr-2W steel) and two 5-tonne heats of F82H steel (an 8Cr-2W steel) were produced. Plates with thicknesses from 7 to 25 mm and plates of these thicknesses with EB or narrow gap TIG welded joints were distributed in 1995 to the participating parties, and some of the remaining materials were available by the end of 1996.

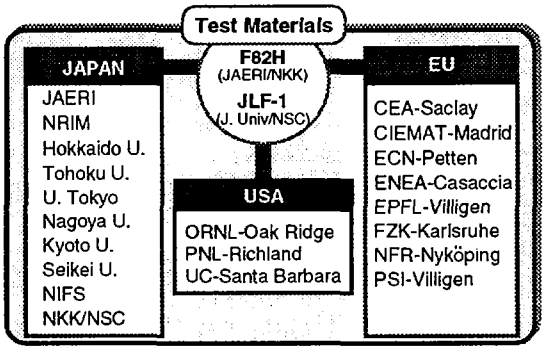

FIG. 1. IEA collaborative test programme.

TABLE I. IEA COLLABORATIVE TEST MATRIX

Unirradiated steels	Irradiated steels
(a) Metallurgical and mechanical characterization	(a) Electron and charged particle irradiation effects
(b) Thermal stabilities of steels and welds	(b) Neutron irradiation of steels and welds
(c) Composition optimization	*Tensile, Charpy and fracture toughness, creep rupture, irradiation creep, LCF, fatigue crack growth, swelling, microstructural evolution, microchemical evolution, helium effects, hydrogen effects, solid transmutant effects, dynamic and complex irradiation effects*
(d) Dynamic and static fracture toughness	(c) Modelling and theoretical studies of radiation effects
(e) Micromechanics of fracture	*Microstructure–hardening–fracture correlations*
(f) Size effects/crack geometry effects	
(g) Fatigue, crack growth and creep fatigue	
(h) Welding technologies	
(i) Environmental effects	
Compatibility with LI/H/He: Magnetomechanical property	
Aqueous corrosion and SCC: Vacuum property	
(j) Physical properties	

The IEA activities on LAFs emphasize the international collaborative test programme on the two large IEA heats. The overall objective of the combined test programme is to determine the possibility to use ferritic steels for fusion by a comprehensive qualification test programme and the development of a database on key technical issues for representative low activation steels. The most important question involves the temperature versus total wall loading window within which the steels can be used for fusion applications. It is expected that the upper temperature will be determined by either coolant compatibility (i.e. Li, Pb–Li, etc.) and/or creep and should

approach 550–600°C. The lower temperature is expected to be determined by radiation embrittlement effects that cause a decrease in toughness. At present, only a few data on a limited number of heats are available to discuss the high temperature limit, especially data including irradiation effects. Likewise, few ductile to brittle transition temperature (DBTT) and fracture toughness data are available for LAFs irradiated at temperatures lower than 365°C. Therefore, crucial tests for these steels will involve the determination of fracture toughness after irradiation at 200–350°C. Table I lists the types of tests envisaged for the large IEA heats. Tests cover both irradiated and unirradiated materials. Since welds will be important to any fusion structure, weldability tests and mechanical property tests on prototypical welds are important.

For alloy tailoring, an understanding of hardening mechanisms is needed. Combined reactor and cyclotron experiments have been started to separate helium and radiation hardening effects. Effects of heat treatment on DBTT behaviour will be tested for the understanding of fabrication process effects. For the application of toughness data from various types of tests with different specimen geometries, quantification of size effects on toughness and DBTT is needed for design considerations. This is also of concern for the application of results from the high energy neutron source (International Fusion Materials Irradiation Facility (IFMIF)), which is being planned.

3. IRRADIATION RESPONSES OF LAFs

The IEA collaborative irradiation experiments have been in progress since 1994, e.g. in the HFR in Petten, Netherlands, and in the Studsvik reactor (irradiation assisted corrosion) in the European programme, together with previously initiated experiments in the HFIR in Oak Ridge (USA) and in the JOYO in PNC (Oarai, Japan) and in the JMTR in JAERI (Oarai, Japan).

The data of Vickers hardness tests collected in laboratories in the EU and Switzerland on the IEA heat of F82H show the homogeneity in location and orientation of the 5-tonne heat. Other tests done in parallel with the hardness tests also show excellent homogeneity in mechanical properties and chemical compositions.

Several LAFs were irradiated to 0.8 dpa in HFR, which induced large DBTT shifts at 250°C with the smallest shift of 24°C for the ORNL alloy (9Cr–2WVTa) and of 64°C for F82H. At higher temperatures, the DBTT shifts are smaller than at 250°C, except for the ORNL steel above 350°C. The results also confirm a smaller shift of DBTT of the 9CrWVTa (F82, ORNL, ...) compared to the conventional 11CrMoVNb steels (MANET type, Kastencharge). These results will be confirmed by ongoing experiments in HFR up to a dose of 3 dpa and higher. Also, other irradiation experiments are planned for IEA heats of F82H and JLF-1, using HFIR target and RB* position capsules, including tensile Charpy impact and fracture toughness specimens.

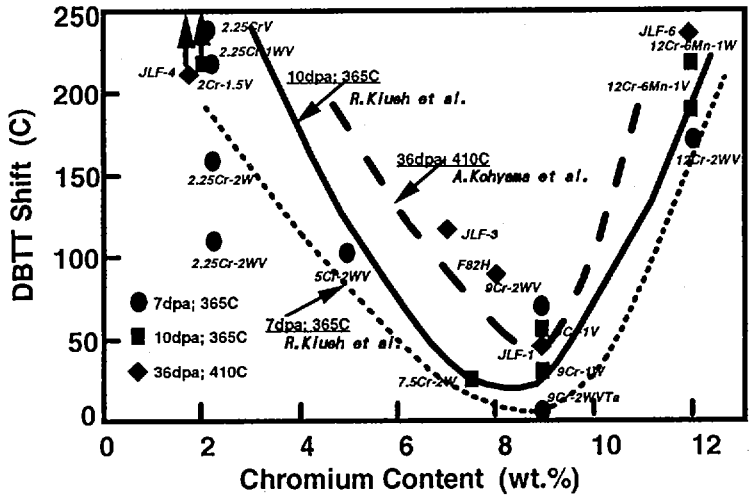

FIG. 2. Effect of chromium addition on DBTT shift in LAFs due to fast neutron irradiation.

Efforts have been concentrated on critical issues such as low temperature radiation hardening and embrittlement phenomena as measured by impact properties, such as DBTT. Irradiation creep is considered to be a phenomenon of concern for dimensional instability. Tensile properties have been obtained on neutron irradiated F82H, JLF-1 and 9Cr-2WVTa steels, along with steels containing 2.25–12% Cr, with 2% W and a small amount of V. The tensile tests of FFTF/MOTA irradiated Japanese steel specimens for displacement damage up to 62 dpa [2] have yielded the following results: the 7 to 9 Cr steels (including JLF-1 and F82H) showed less irradiation hardening at lower temperature, and the yield strength was fairly stable up to 550°C and 62 dpa. In contrast, the 2.25Cr and 12Cr steels showed high irradiation hardening in the lower temperature range. Similar behaviour was reported from the USA and EU. For considerations on the toughness of these steels, embrittlement due to irradiation is commonly measured by the shift in DBTT in a Charpy impact test. Figure 2 shows the effect of chromium addition on the DBTT shift in LAFs due to fast neutron irradiation in FFTF. The 9Cr-2WVTa steel produced a shift in DBTT of only 4° and 15°C after irradiation in FFTF at 365°C to approximately 6 and 10 dpa, respectively. A DBTT shift of 130°C was observed for HT-9 and of 50°C for modified 9Cr-1Mo irradiated in similar conditions. The results from 365°C irradiation in FFTF showed that the 7 to 10 Cr range was the most resistant to a DBTT increase due to neutron damage. At the same time, the addition of up to 2% W, V and Ta additions were shown to effectively reduce the DBTT shift due to neutron irradiation. Likewise, irradiation to 36 dpa at 410°C indicated that the 7 to 9 Cr addition also suppressed the DBTT shift over the lower and higher Cr concentrations.

Swelling and irradiation creep behaviour for JLF-1 and F82H as a function of irradiation temperature to a maximum dose of 62 dpa was investigated as a part of the Japan–US collaboration programme utilizing FFTF/MOTA. To 550°C, the irradiation creep coefficient is smaller than, or comparable to, those for the conventional high temperature Cr–Mo steels. At temperatures higher than 550°C, thermal creep overwhelms irradiation creep. Swelling enhanced creep can be identified at around 420°C and is a concern from both the creep and swelling mechanism viewpoints. An explanation for these observations should be determined with high priority, along with the issue of low temperature irradiation embrittlement. However, both the enhanced creep and the swelling response are expected to remain manageable, which needs to be confirmed by design analysis. Further irradiation creep tests are planned in the Phénix reactor and HFIR.

Most of the tests on irradiated LAFs have been on steels irradiated in fast and mixed spectrum reactors, and the effects of nuclear transmutation, such as the formation of helium, hydrogen, manganese from Fe and Re + Os from W, on irradiated properties is not understood. In order to clarify the transmutation effects, a 14 MeV neutron source (IFMIF) is urgently required.

4. LIMITATION AND FUTURE PROSPECTS FOR LAFs IN FUSION

As was described above, the present available data are insufficient to quantitatively draw a design window for fusion applications. Also, compatibility with coolant and other blanket materials is recognized to be an important issue for fusion and is considered one of the high priority tasks in the IEA collaborative programme. Figure 3 presents an example of R&D strategy for F82H to be used in ITER, DEMO and power reactors. In the figure, JFT-2M is proposed for testing of the ferromagnetic effects in a tokamak reactor. The ferromagnetic effects of JLF-1 in a helical reactor will also be studied in the NIFS university programme. A potential use for testing LAFs in the ITER are the DEMO relevant blanket test modules under consideration by the different parties for the ITER Extended Performance Phase (EPP). Testing of DEMO relevant blankets in ITER with a new low activation ferritic material may be possible if

(i) the general qualification tests are performed within the next three to four years;
(ii) on the basis of this phase 2 work, a reference material specification including weld material can be defined; and
(iii) the preliminary data and design methods can be verified in the next phase up to about the year 2005.

As is usual for development projects that are carried out in parallel with design and fabrication, there is still further work to be done for qualification and validation of data and processes.

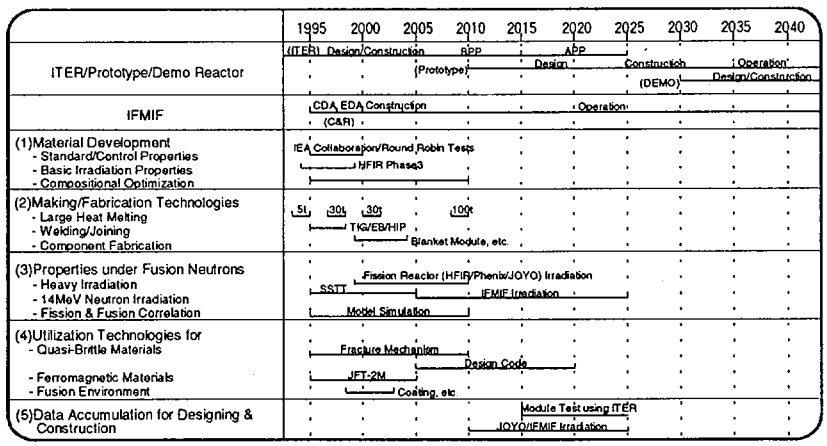

FIG. 3. R&D schedule for F82H for fusion application.

For a qualification of new materials such as LAFs for nuclear application, about ten years from now on will be needed to develop the data, assuming that adequate resources and tools are available for the test programme.

5. CONCLUSIONS

(1) On the basis of a critical review of research on ferritic/martensitic steels, the IEA low activation ferritic steel working group has initiated a collaborative programme on large heats of LAFs. The working group has been, and is, effective in planning and co-ordinating the international and domestic R&D programmes on LAFs.

(2) Preliminary data from the IEA activities on LAFs and the current individual efforts are quite promising, but further co-ordination efforts and support are required to accomplish the international programmes.

(3) To qualify and finally validate the application of 8-9CrWVTa steel, a sufficient design database must be set up, including code approval aspects. Continuous use of mixed and neutron spectra irradiation facilities (HFR, Phénix, ...) is needed, however, for final validation of alloy performance under irradiation more relevant to fusion, the high energy neutron source IFMIF should be available soon.

(4) As an important milestone in the development of a blanket test module in ITER, a preliminary set of material design data is required by about 1999. For further verification and qualification, significant efforts are needed for a next milestone in about 2005.

REFERENCES

[1] Papers presented at IEA Working Group Meetings on Ferritic/Martensitic Steels, Tokyo (1992), Oak Ridge (1993), Sun Valley (1994), Oak Ridge (1995) and Baden (1995).
[2] KOHYAMA, A., et al., J. Nucl. Mater. **212–215** (1994) 684.

DISCUSSION

W.M. NEVINS: What is the magnetization (at saturation) of the low activation ferritic steel that you are developing?

A. KOHYAMA: As the IEA working group on ferritic steels for fusion, we have two large heats for IEA collaborative research activities. These are F82H(8Cr–2W type) and JLF-1(9Cr–2W type), where there are no significant differences in the saturation magnetization value (B_s). For the case of F82H, B_s at room temperature, at 200°C and at 400°C is 1.96 T, 1.88 T and 1.74 T, respectively. The residual magnetization value for this temperature range is 0.021–0.016 T. The preliminary calculations performed by Dr. Kikuchi of JAERI and his co-authors concerning the effect of using ferromagnetic material on fusion plasma are quite positive, and JAERI and a Japanese university propose to make a small plasma machine to verify the simulation results in the near future.

PROGRESS IN RADIATION EFFECT STUDIES OF LOW ACTIVATION VANADIUM ALLOYS FOR FUSION

H. MATSUI, K. FUKUMOTO, A. KIMURA,
K. KANEDA, T. KONDO
Institute for Materials Research,
Tohoku University,
Sendai, Japan

Abstract

PROGRESS IN RADIATION EFFECT STUDIES OF LOW ACTIVATION VANADIUM ALLOYS FOR FUSION.

Vanadium alloys have a number of attractive features for fusion reactor structural applications. Their inherent low induced radioactivity, high operating temperature, high thermal stress factor and superior resistance against radiation damage are essential for the attractiveness of fusion systems. The emphasis of recent vanadium studies has been on alloy compositions centred about V-4Cr-4Ti. These alloys have a very low ductile to brittle transition temperature (DBTT) and good high temperature mechanical properties. Among a number of radiation induced effects, swelling, DBTT shift and helium embrittlement may be the most important phenomena for fusion structural materials. Data for V-4Cr-4Ti on swelling caused by neutron irradiation are available only up to about 30 dpa; swelling is less than 0.5% at this dpa level in the swelling peak temperature region around 600°C. The DBTT shift caused by neutron irradiation above about 400°C is very small for V-4Cr-4Ti alloy. A larger DBTT shift has been reported after irradiation at temperatures below about 300°C. Low dose irradiation in this low temperature range resulted in a greater radiation induced hardening for a higher irradiation temperature. This result is in accordance with the larger DBTT shift after irradiation at a higher temperature. Although the design temperature of vanadium alloys is well above these temperatures, this low temperature radiation embrittlement needs closer examination. Helium embrittlement has been studied using a variety of helium doping techniques in the past. The degree of embrittlement depends strongly on the method of helium doping. Helium preinjection by the tritium trick yielded rather severe ductility loss in all the vanadium binary alloys tested at 800°C. There was some doubt about this strong embrittlement, which was suspected to be due to the peculiar helium configuration inherent to the tritium trick technique. A new technique called the dynamic helium charging experiment has been adopted to study helium effects on the high temperature ductility. With this technique helium is generated concurrently with neutron irradiation. Vanadium binary alloys have been demonstrated to retain almost the same level of ductility as those specimens with simple neutron irradiation. Thus helium embrittlement is probably not so significant as once suspected. The paper reviews the status of vanadium alloy studies, especially of radiation effects, and also presents recent results concerning helium effects on the swelling and mechanical properties.

1. INTRODUCTION

Fusion is one of the most promising power sources for the next century. The estimated cost for plant construction and the cost of electricity, however, are rather high compared with other energy sources, e.g. advanced light water reactors and

fossil fuelled power plants. Along with economic factors, if fusion is to become a major power source in the future, public acceptance, including considerations of safety and environmental compatibility, will be equally important. These requirements are reflected in the material performance needs in a variety of aspects. A high operation temperature and long life in fusion environments are essential from the economic viewpoint. Low induced activation, both short term and long term, is important for environmental safety and public acceptance. From these viewpoints, vanadium alloys have a number of attractive features as structural materials for fusion reactors. In the present paper, the status of vanadium alloy studies, especially of radiation effects, is briefly reviewed. New experimental results concerning helium effects on the swelling and mechanical properties are also presented.

2. BASELINE PROPERTIES

For fusion structural applications, alloys with compositions close to V–4%Cr–4%Ti seem most promising. The ductile to brittle transition temperature (DBTT) of these alloys determined from 1/3 size Charpy tests is below 77 K [1]. It has been found that the fabrication details — e.g. hot forging, cross-sectional reduction in each rolling step, the final annealing temperature and the atmosphere or vacuum during each annealing [2, 3] — have profound effects on the performance of these alloys. A rather detailed procedure for achieving optimum performance has been recommended by Argonne National Laboratory. Essentially, it may be summarized that a final annealing temperature between 950 and 1000°C is optimum and that each annealing should be done in a good vacuum, i.e. better than 10^{-6} torr. The latter condition is necessary to avoid impurity pick-up, e.g. of oxygen. The maximum allowable oxygen concentration is approximately 1000 wt ppm, and ductility loss results for higher oxygen concentrations. Hydrogen concentration also must be kept below approximately 1500 appm in order to avoid hydrogen embrittlement. In previous studies it has been reported that up to 1200 appm hydrogen does not cause significant DBTT shift in similar alloys [4], while the present authors have recently found significant ductility loss with hydrogen doping up to 1600 appm. Since hydrogen can easily enter or leave vanadium alloys because of its high diffusivity and abundance in the environment, some means must be built into the blanket design to keep the hydrogen isotope concentration below the level quoted above.

3. RADIATION EMBRITTLEMENT

The resistance to radiation embrittlement of V–4Cr–4Ti alloy is very good. The DBTT shift resulting from irradiation up to 24–34 dpa in the temperature range 410–600°C is almost negligible [1]. Unfortunately, data on this alloy at still higher fluences are not available at present. Since reduction of tensile elongation saturates

for damage levels above 20 dpa, the DBTT shift is also likely to saturate until some other factor such as transmutation comes into play for fluences over 100 dpa with fusion neutrons. Irradiation at temperatures lower than the above mentioned range can result in more significant ductility loss. The DBTT of V-4Cr-4Ti alloy has been reported to shift significantly after irradiation at temperatures below approximately 300°C [5], where the DBTT shift was greater for higher irradiation temperatures. A series of microhardness tests conducted on vanadium base binary alloys after irradiation at 90 and 150°C in the Japan Materials Testing Reactor (JMTR) up to 0.02 dpa have shown an inverse irradiation temperature dependence; radiation induced hardening is greater for higher irradiation temperature [6]. This result is in accordance with the DBTT shift data mentioned above. It has been suggested that interstitial oxygen in solution promotes dislocation loop nucleation.

4. SWELLING

The swelling of vanadium alloys is generally good, a property common to most bcc metals and alloys. Although neutron irradiation data on V-4Cr-4Ti are limited to approximately 34 dpa, other V-Cr-Ti alloys with higher chromium content show a swelling level below 2% at about 100 dpa. Since the dependence of swelling on chromium content is positive in the low chromium range, the swelling of V-4Cr-4Ti alloy may be estimated to be below 1% at 100 dpa. Moreover, there is a tendency for swelling in V-1%Si, V-5%Mo and V-Cr-Ti alloys to saturate or even decrease with damage level [7, 8]. Although this phenomenon is still to be verified with well controlled irradiation experiments, it is possible that radiation induced fine precipitation changes the sink balance and leads to the saturation.

Swelling may become rather significant in vanadium binary alloys with undersized solutes such as iron or chromium [9, 10]. Although the swelling of V-Fe alloy can become quite large, it has been demonstrated that the swelling can be very effectively suppressed by titanium addition [11]. In V-Cr-Ti alloys, this swelling inherent to V-Cr binary alloys is effectively suppressed by the titanium. The suppression mechanism is still not clear, and clarifying it will be an important task if V-Cr-Ti alloys are to be adopted in fusion reactors.

Helium has been known to increase swelling. It has been well recognized that the helium injection rate relative to the displacement damage rate has a strong influence on the microstructural evolution as well as on the mechanical properties, as described in the next section. In the absence of a fusion neutron source with sufficient intensity, some technique is necessary to simulate fusion relevant helium generation and displacement damage. The dynamic helium charging experiment (DHCE) technique has been developed for this purpose [12]. Essentially, this technique is a modified version of the tritium trick. The tritium decay in this case takes place during neutron irradiation in a fast reactor. Vanadium alloy specimens are lithium bonded and encapsulated in a TZM alloy subcapsule. Along with the

specimens, a metal piece called the 'mother alloy' containing a predetermined amount of tritium is loaded into the capsule. Upon startup of the irradiation, an increase of temperature results in lithium wetting the mother alloy, and tritium transfers to the liquid lithium and further to the specimens. Tritium uniformly distributed in the specimens decays to ^{3}He with concurrent displacement damage by neutrons. The ratio of helium generation to dpa rate can be controlled by adjusting the amount of tritium, and the loss of tritium through decay can be compensated for by adjusting the $^{6}Li/^{7}Li$ ratio of the bonding lithium.

Several vanadium model alloys as well as V–4Cr–4Ti alloy were irradiated using the DHCE technique [13–15]. In the model binary alloys, helium doping generally resulted in greater swelling from helium charging by DHCE. In high swelling alloys, however, swelling was reduced by helium because of the small cavity size resulting from their very high density. In V–4Cr–4Ti group alloys, there was very little or no cavity formation even with helium doping by DHCE [15]. In V–5Cr–5Ti–AlYSi alloy, no cavity formation was observed either at 430°C with 27 dpa and 177 appm helium or at 600°C with 15 dpa and approximately 30 appm helium doped using the DHCE technique [16]. Although the damage level is limited to below 30 dpa, it can be concluded that no unexpected extraordinary swelling phenomenon is observed even under concurrent helium injection with displacement damage. Further study is, however, obviously required to cover higher damage levels.

5. HELIUM EMBRITTLEMENT

The upper temperature limit of the design window is determined by the creep rupture life of the material. This life may be further reduced by helium generated by transmutation reactions with 14 MeV neutrons. This 'high temperature helium embrittlement' has been studied using a variety of helium doping techniques in vanadium alloys. Figure 1 plots the reduction of total elongation resulting from helium doping by the tritium trick technique. It is seen from this figure that the ductility of most of the binary vanadium alloys starts to decrease above 600°C. All the alloys become very brittle at 800°C. Since these are relatively high strain rate tensile tests, the effect of helium on the ductility or rupture life may be more significant in creep tests. It should be noted that the reduction in elongation is also remarkable in some of the alloys even in tensile tests done at room temperature. This is because the grain boundaries of these specimens are covered with helium bubbles [17]. In the tritium trick technique, helium is introduced on interstitial sites, which provides a high mobility migration path. Helium atoms thus introduced migrate readily to grain boundaries either during the tritium decay period at 400°C or during the subsequent tritium degassing period at 700°C.

Embrittlement resulting from helium doping by the ^{10}B technique is much less significant than with the tritium trick technique. It is believed that vacancies produced

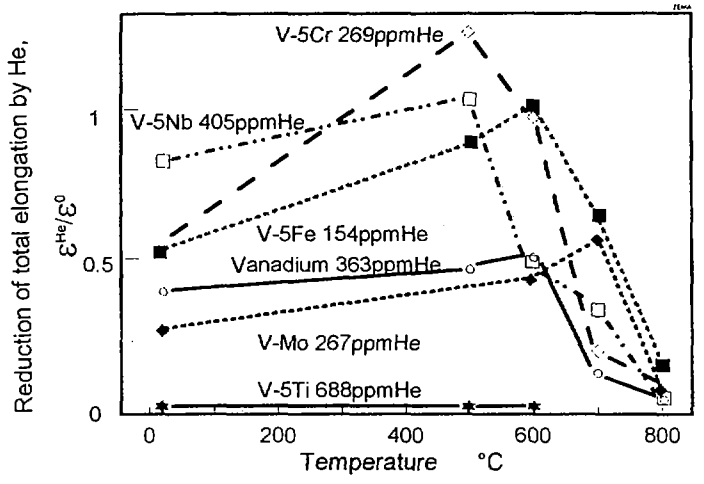

FIG. 1. Reduction of total elongation of vanadium binary alloys by helium doping using the tritium trick technique. Significant ductility reduction occurs above 700°C.

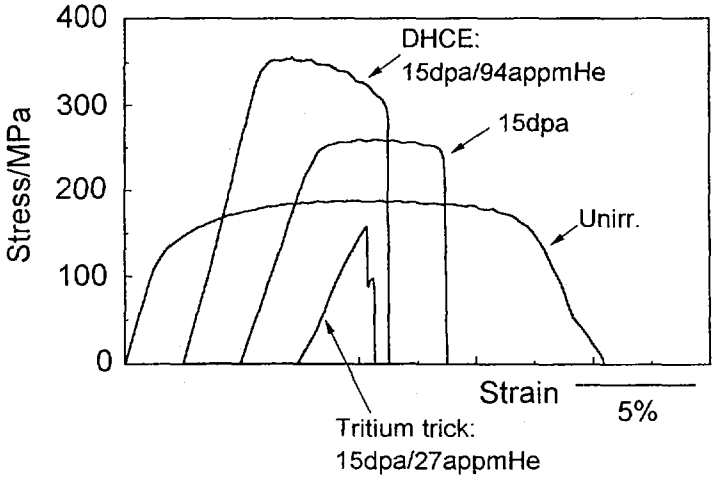

FIG. 2. Stress–strain curves of V–5%Fe alloy tested at 700°C after irradiation up to 15 dpa with and without He: simple neutron irradiation, He preinjection followed by neutron irradiation and He co-implantation using DHCE.

by neutrons trap interstitial helium atoms, resulting in substitutional helium with very limited mobility. Thus the ratio of the helium generation rate to the displacement rate is a very important factor.

Figure 2 shows the stress–strain curve of V–5%Fe alloy after irradiation at 600°C using DHCE helium doping up to 15 dpa and tested at 700°C. Results for unirradiated control specimens, for simple neutron irradiation without helium, and for helium doping by the tritium trick followed by neutron irradiation are also included in the figure. The unirradiated control specimens show good ductility at 700°C. Neutron irradiation caused significant reduction in ductility, but the total elongation is still about 10% without helium. The tritium trick specimens containing 26.5 appm helium after irradiation show almost no elongation. The DHCE specimens containing 93.6 appm helium show almost the same level of ductility as simple neutron irradiation specimens without helium. Helium gas released from the deforming specimens was measured during tensile tests. It is noted that significant helium release occurred in association with the rupture process of specimens containing helium. Scanning electron micrographs (not shown) indicate that the fracture mode of unirradiated specimens is ductile rupture and that the fracture of specimens with simple neutron irradiation without helium occurred along grain boundaries with significant deformation. The fracture mode of DHCE specimens is transgranular with some reduction in area. The failure in tritium trick specimens occurred entirely along grain boundaries.

This set of experimental data demonstrated that helium doped with concurrent neutron damage does not cause any significant reduction of ductility in this alloy. Results from a similar experiment on V–5%Ti alloy are shown in Fig. 3. The ductility of the irradiated tritium trick specimen is very poor; the total elongation of this specimen is only 5%. Although the total elongation of the DHCE specimen is significantly lower than that of the simple irradiation specimen, it is still much greater than that of the tritium trick specimen. The fracture surface (not shown) indicates a complete knife edge type for the unirradiated specimen, ductile dimple failure in the simple neutron irradiation specimen and intergranular fracture in the tritium trick specimen. In the DHCE specimen, the intergranular fracture region is visible in the middle of the fracture surface. For tritium trick specimens, intergranular failure is usually associated with helium bubble formation along grain boundaries. Observation with transmission electron microscopy (TEM) showed no bubble formation in this specimen before deformation. It is likely that helium segregation takes place during the tensile test, where helium atoms are swept by moving dislocations.

In this case, the concentration of helium in DHCE irradiation is rather low, i.e. 8.26 appm, so that it is difficult to draw a definite conclusion from this experiment. Further study using DHCE with a higher helium concentration is necessary. Since helium concentration differs from alloy to alloy, an attempt was made to normalize the effect of helium by dividing the ductility reduction by the helium concentration. Figure 4 shows the fractional decrease in total elongation of DHCE irradiated vanadium alloys relative to conventional irradiation data normalized by the helium

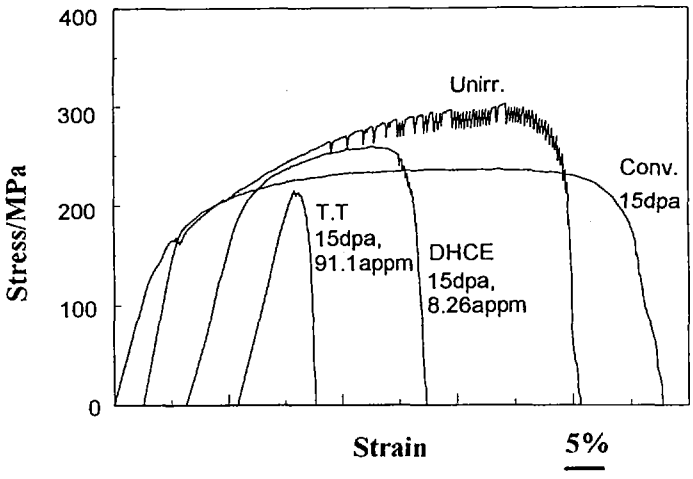

FIG. 3. Stress-strain curves of V-5%Ti alloy tested at 700°C after irradiation up to 15 dpa with and without He: simple neutron irradiation, He preinjection followed by neutron irradiation and He co-implantation using DHCE.

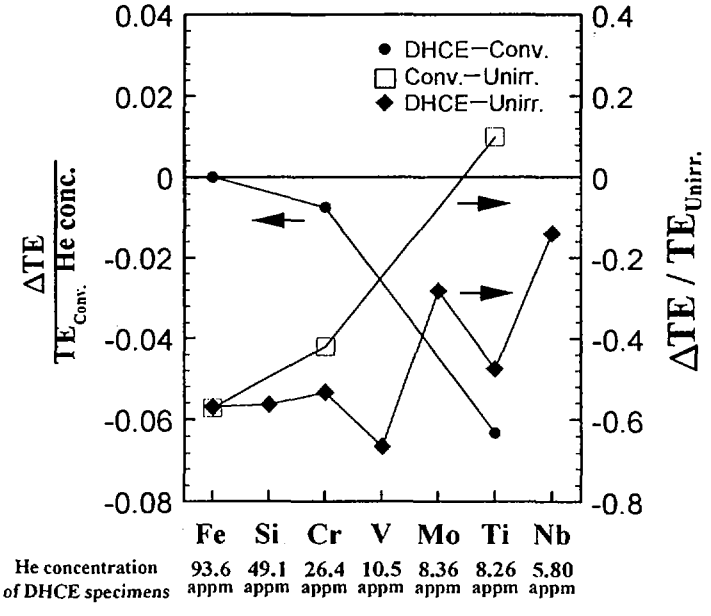

FIG. 4. Fractional decrease in total elongation of DHCE irradiated vanadium alloys relative to conventional irradiation data normalized by the helium concentration (left scale). A similar value relative to unirradiated data is plotted on the right scale.

concentration (left scale). It is seen from this figure that the ductility reduction by helium is small for V–Fe and V–Cr alloys, i.e. undersized solute alloys. A similar value relative to unirradiated data is plotted on the right scale. It can be deduced from this plot that the reduction in ductility by displacement damage alone is small for alloys with oversized solute. As observed by TEM, in alloys with undersized solute the dislocation evolution rate is much faster than for oversized solute alloys. It has been shown in our previous study that undersized solute has much larger binding energy with helium and that more helium atoms are retained within grain matrices [18]. This is in good agreement with the present observation.

6. SUMMARY AND CONCLUSION

The status of vanadium alloys for fusion applications has been summarized with emphasis on the effect of concurrently injected helium using the DHCE technique. From experimental data with limited displacement damage and helium level, it can be concluded that fusion relevant helium injection does not cause any serious deterioration of the swelling and helium embrittlement behaviours of candidate vanadium alloys. The low temperature ductility of V–4Cr–4Ti alloy has been reported [13] to be essentially retained after helium injection with DHCE irradiation. Thus the performance of selected vanadium alloys is rather good within the conditions experimentally covered so far. In view of their favourable properties, vanadium alloys could be developed as structural materials appropriate for fusion DEMO and power reactors, provided that a sufficient and timely R&D effort is made.

ACKNOWLEDGEMENTS

The authors would like to express sincere appreciation to the staff members of the Oarai Facility of the Institute for Materials Research, Tohoku University, for providing experimental support. This work is partly supported by the Japan–USA collaboration programmes, FFTF/MOTA and JUPITER. The authors would like to thank all of their colleagues who have supported this programme.

REFERENCES

[1] CHUNG, H.M., LOOMIS, B.A., SMITH, D.L., in Rep. ANL/FPP/TM-287, ITER/US/IV MAT 10, Argonne Natl Lab., IL (1995) 147.

[2] MATSUI, H., et al., in Proc. 7th Int. Conf. on Fusion Reactor Materials (ICFRM-7), Obninsk, 1995.

[3] CHUNG, H.M., NOWICKI, L., SMITH, D.L., in Rep. ANL/FPP/TM-287, ITER/US/IV MAT 10, Argonne Natl Lab., IL (1995) 17.

[4] LOOMIS, B., CHUNG, H.M., NOWICKI, L., SMITH, D.L., J. Nucl. Mater. **212–215** (1994) 799.

[5] ALEXANDER, D.J., SNEAD, L.L., in Proc. 18th Int. Symp. on Effects of Radiation on Materials, Hyannis, MA, 1996, American Society for Testing and Materials, Philadelphia.
[6] CANDRA, Y., FUKUMOTO, K., KIMURA, A., MATSUI, H., in preparation.
[7] MATSUI, H., NAKAJIMA, H., YOSHIDA, S., J. Nucl. Mater. **205** (1993) 452.
[8] CHUNG, H., LOOMIS, B.A., SMITH, D.L., J. Nucl. Mater. **212–215** (1994) 804.
[9] MATSUI, H., GELLES, D.S., KOHNO, Y., in Proc. 15th Int. Symp. on Effects of Radiation on Materials, ASTM-STP-1125 (STOLLER, R.E., et al., Eds), American Society for Testing and Materials, Philadelphia (1992) 928.
[10] NAKAJIMA, H., YOSHIDA, S., KOHNO, Y., MATSUI, H., J. Nucl. Mater. **191–194** (1992) 952.
[11] MATSUI, H., et al., in FFTF/MOTA Annual Progress Report, 1993, Natl Inst. of Fusion Science, Nagoya, p. 241.
[12] SMITH, D.L., MATSUI, H., GREENWOOD, L., LOOMIS, B.A., J. Nucl. Mater. **155–157** (1988) 1359.
[13] CHUNG, H.M., LOOMIS, B.A., TSAI, H.-C., SMITH, D.L., in Proc. 7th Int. Conf. on Fusion Reactor Materials (ICFRM-7), Obninsk, 1995.
[14] SATOU, M., et al., ibid.
[15] FUKUMOTO, K., CHUNG, H.M., GAZDA, J., SMITH, D.L., MATSUI, H., in Proc. 18th Int. Symp. on Effects of Radiation on Materials, Hyannis, MA, 1996, American Society for Testing and Materials, Philadelphia.
[16] SATOU, M., et al., Tohoku Univ., Sendai, personal communication.
[17] MATSUI, H., TANAKA, M., YAMAMOTO, A., HASEGAWA, A., ABE, K., in Proc. 16th Int. Symp. on Effects of Radiation on Materials, ASTM-STP-1175, American Society for Testing and Materials, Philadelphia, p. 1215.
[18] TANAKA, M., MATSUI, H., Mater. Trans. JIM **34** (1993) 1083.

DEUTERIUM–TRITIUM NEUTRON ACTIVATION EXPERIMENTS AT TFTR*

A. KUMAR
School of Engineering and Applied Science,
University of California,
Los Angeles, California

H.W. KUGEL, G. ASCIONE
Plasma Physics Laboratory,
Princeton University,
Princeton, New Jersey

United States of America

Abstract

DEUTERIUM–TRITIUM NEUTRON ACTIVATION EXPERIMENTS AT TFTR.

Measurements of short-lived and long-lived radioactivity of direct relevance to ITER and DEMO reactors have been carried out at TFTR by taking advantage of the D–T neutron flux available during the last three years. These measurements permit benchmarking of three dimensional calculations of neutron and gamma ray transport for application to the design and regulatory licensing of large complex fusion reactors, such as ITER. A large number of samples of materials have been irradiated at various locations close to, and around, the TFTR vacuum vessel. Results from ongoing measurements are presented. The role of the measurements in validation of calculational methods, nuclear data, and future licensing requirements is discussed.

1. INTRODUCTION

The licensing of high power fusion reactors will require certification of calculations of induced radioactivity. It is quite difficult to perform reliable calculational predictions of the cross-sections, for long half-life producing reactions, due to large uncertainties on fitted nuclear model parameters. These radioactive products could pose serious problems for maintenance and near-surface burial of the first wall materials, particularly if they emit high-energy gamma-rays [1,2]. Little is known experimentally on most of the long-lived products. A data base of measured radioactivity in environments with prototypical neutron spectra is crucial for this purpose. Neutron production from D-T fusion reactions at TFTR allows unique experiments to measure activation in materials of direct use in ITER and DEMO reactors. The availability of numerous spatial locations close to, and around, the TFTR

* Work sponsored by US Department of Energy contracts DE-AC02-76CH03073 and DE-FG03-86ER52124.

vacuum vessel has allowed the irradiation of a large number of elemental materials and alloys [3-5]. These locations provide neutron energy spectra similar to a future tokamak driven fusion reactor. The elemental materials include aluminum, silicon, titanium, vanadium, chromium, iron, cobalt, nickel, copper, zinc, zirconium, niobium, molybdenum, silver, indium, tin, europium, terbium, dysprosium, holmium, hafnium, tungsten, rhenium, iridium, gold, lead, and bismuth. Some of these materials would either be initially present in ITER/DEMO, or would be generated by neutron induced transmutations of other materials. The alloys include V-Cr-Ti, stainless steel 316, inconel 625 and 718, and manganese-copper.

The initial experiments focused on shorter half-life products, and have demonstrated the prototypicality of these TFTR measurements in relation to ITER [3,4]. The TFTR reentrant irradiation location that is closest to the plasma, for example, exhibits large contributions to radioactivity from both threshold and capture type activation reactions. Similar situations are expected near the ITER first wall [3]. We have measured radioactivity of isotopic products of half-lives ranging from 2.24 minutes (^{28}Al) to 5.3 years (^{60}Co). These measurements are valuable for characterizing the activation properties of these materials, and in addition, they provide an invaluable resource for realistic bench marking of ITER calculational models.

Currently, irradiation of materials for measuring long lived activity - half-life ranging from a few years to millions of years - is still in progress as neutron fluences in the range of 10^{13} n/cm^2 and above are needed to obtain the required activations [5]. Subsequently, the irradiated samples will be allowed to cool for long times, to permit gamma-ray spectroscopic measurements under low background conditions. Some of the reactions of interest are as follows: ^{27}Al(n,2n)^{26}Al (half-life=0.72My), ^{182}W(n,n'α)^{178m2}Hf (half-life=31y), ^{94}Mo(n,p)^{94}Nb (half-life=20.3ky) etc.

These TFTR neutron activation measurements will help in identification and quantification of the troublesome isotopic components of the irradiated materials, and are providing an experimentally validated database to accelerate the development of the low activation materials for ITER and DEMO [5].

2. ACTIVATION EXPERIMENTS

Calculations were performed for assessing the feasibility of D-T activation measurements of various materials from titanium to bismuth. The neutron flux was adopted from a 2-D poloidal model of TFTR to simulate neutron and photon transport [6]. REAC3 was employed for radioactivity calculations [7]. We assumed TFTR D-T operation over a 200-day period for a total D-T neutron yield of 2 x 10^{21}. The results indicated that the available neutron flux did not permit practical measurements involving the radioactivity of minute amounts of impurities, for example, in the range of one tenth per cent of the weight or less, but would allow significant bench marking measurements of the radioactivity from long half-life products from many materials.

A number of options pertaining to sample types, sample weights, and their locations near the plasma and at farther locations were explored. It was found most convenient to utilize two complementary approaches that were based on deploying plastic capsules of sample foils. Each plastic capsule had ID of ~20 mm and height of ~50 mm and could house up to about 20 samples. The first approach involved positioning one capsule in each of three available irradiation stations referred to as "Irradiation Ends" (IE) of the TFTR pneumatic transport system. The second approach involved manually placing similar capsules at more than twelve geographic locations inside the TFTR Test Cell, at distances ranging from ~0.5 m to ~22 m from the edge plasma. Fig. 1 shows a partial schematic of the foil irradiation locations inside the TFTR Test Cell. The Irradiation End (IE) locations are shown as IE#1 (Bay B, top), and IE#4 (Bay F, mid-plane). The manual locations are IE#3 (Bay B, mid-plane), BB (blue box, detector enclosure), IL (intermediate location), TCW#1 (Test Cell wall, east), TCW#2 (north wall), TCW#4 (north-end of NW labyrinth), TCW#5 (entrance of NW labyrinth), and TCW#7 (west wall). A total of 3 capsules have been irradiated at IE#3 (Bay F, mid-plane) and BB. In addition, 2 capsules were irradiated at the NW Bay S location (not shown in Fig.1). The sample (foil) compositions of various capsules are not the same.

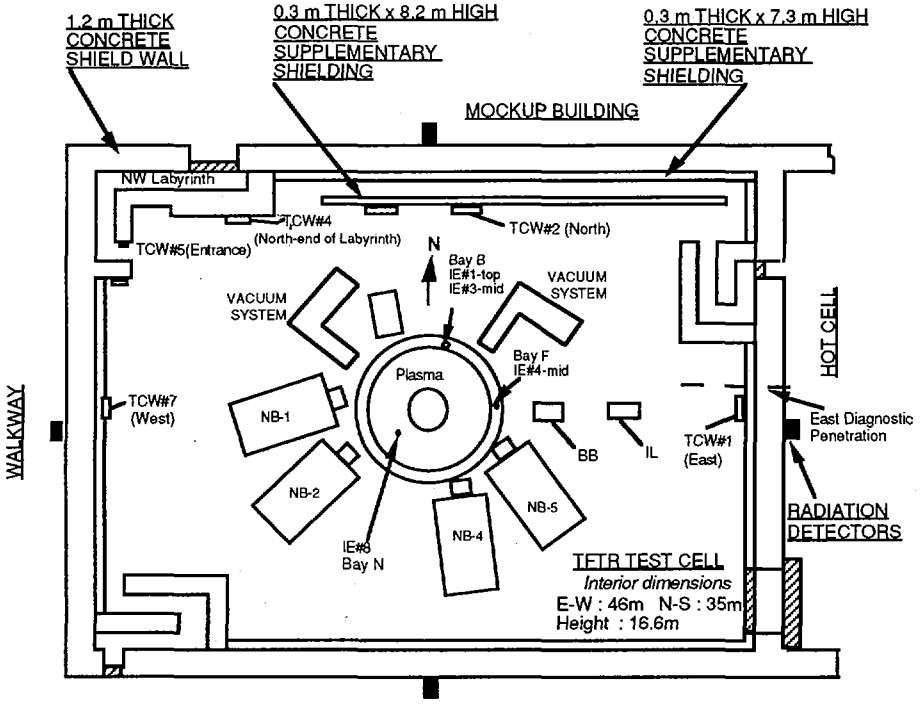

FIG. 1. Partial schematic showing the foil irradiation locations in the TFTR Test Cell.

Table 1 Saturation activities for production of D-T induced radioactivity in materials irradiated in Irradiation End 4 (IE#4) of TFTR.

Material (foil)	Product	Half life	Saturation activity[a]	Material (foil)	Product	Half life	Saturation activity[a]
Ti	^{47}Sc	3.34 day	4.99×10^{-33}	Mo	^{99}Mo	66 hour	1.35×10^{-31}
	^{46}Sc	83.8 day	4.35×10^{-33}		^{92m}Nb	10.2 day	2.37×10^{-33}
					^{95}Nb	35 day	1.23×10^{-33}
Mn	^{54}Mn	312.2 day	1.64×10^{-31}				
				Eu	^{154}Eu	8.8 year	3.33×10^{-31}
Fe	^{51}Cr	27.7 day	8.27×10^{-34}		^{152}Eu	13.33 year	4.44×10^{-31}
	^{59}Fe	44.6 day	5.07×10^{-34}				
	^{54}Mn	312.2 day	6.75×10^{-33}	Tb	^{160}Tb	72.3 day	1.22×10^{-30}
Co	^{59}Fe	44.6 day	1.02×10^{-32}	Hf	^{181}Hf	42.4 day	4.46×10^{-31}
	^{58}Co	70.8 day	1.26×10^{-31}		^{175}Hf	70 day	1.20×10^{-32}
	^{60}Co	5.3 year	4.66×10^{-30}				
				W	^{181}Hf	42.4 day	2.60×10^{-35}
Ni	^{58}Co	70.8 day	8.75×10^{-32}		^{182}Ta	115 day	1.49×10^{-34}
	^{57}Co	271 day	6.96×10^{-32}				
	^{60}Co	5.3 year	1.08×10^{-32}	Re	^{186}Re	3.8 day	6.01×10^{-30}
					^{184}Re	38 day	9.98×10^{-32}
Cu	^{60}Co	5.3 year	6.21×10^{-33}		^{184m}Re	165 day	1.70×10^{-32}
Zn	^{65}Zn	244.1 day	9.38×10^{-32}				
				Au	^{198}Au	2.7 day	2.92×10^{-29}
Nb	^{92m}Nb	10.2 day	8.44×10^{-32}		^{196}Au	6.2 day	3.54×10^{-31}

[a] *Each activity represents number of radioactive nuclides produced per contributing source neutron per material atom at saturation. One standard deviation of mean experimental error is ~10% on all saturation activities.*

3. CHARACTERISTICS OF MEASURED DATA

Capsules were placed at various times during the previous experimental campaign that began in January 1996. Some of the capsules were removed for intermediate counting during days of maintenance, and subsequently, were replaced for further irradiation. The capsule at IE#4 was positioned in early 1996, and was exposed for 60 days during the D-D and D-T neutron fluxes resulting from the experiments in progress at that time. The capsule was left to cool for 18 days to let the shorter half-life isotopes decay as much as possible. It was then opened and the foils were separated for individual counting. The foils were counted on high purity germanium detectors at PPPL Health Physics Radiological Environmental Measurements Laboratory. The radioactivities were then determined from the measured counts [3-5]. Prior to counting campaigns, the intrinsic germanium detectors were calibrated extensively with standard

sources in the sample-detector geometry to be used later for the counting. The saturation activities for the observed products of various materials are shown in Table 1. Note that each saturation (equilibrium) activity in the table stands for reaction rate per contributing source neutron per atom of the sample. For isotopic products generated by only high threshold reactions, only D-T neutrons are considered for normalization, whereas, for all other products, both D-T and D-D neutrons are included. Data for titanium, manganese, iron, cobalt, nickel, copper, zinc, niobium, molybdenum, europium, terbium, hafnium, tungsten, rhenium, and gold is shown. We also observed products of impurities in a number of materials, even though all these samples were of high purity. Note that both long half-life products in europium were observed, namely, ^{154}Eu (half-life = 8.8 years), and ^{152}Eu (half-life = 13.33 years). The largest saturation activity, 2.92 x 10^{-29}, is from ^{198}Au in gold, whereas the lowest saturation activity, 2.60 x 10^{-35}, is contributed by ^{181}Hf in tungsten.

The measurements at the locations spread over the TFTR Test Cell indicate that saturation activity of a high threshold reaction product undergoes a relatively sharp fall as a function of distance from the plasma, relative to that of the capture (exothermic) reaction product. As a typical example, Fig. 2 shows the spatial dependence profile of a threshold reaction, ^{59}Co(n,2n)^{58}Co, as well as a capture reaction, ^{59}Co(n,γ)^{60}Co, in cobalt samples at various locations inside the TFTR Test Cell. The spectral locations are IE#8, IE#3, BB, and TCW#1 - being at respective major radii of 2.6 m, 4.1m, 7.9m, and 24.2m. Note that, whereas the (n,2n) reaction undergoes four orders of magnitude fall in going from the plasma to the east wall of the TFTR Test Cell, the (n,γ)

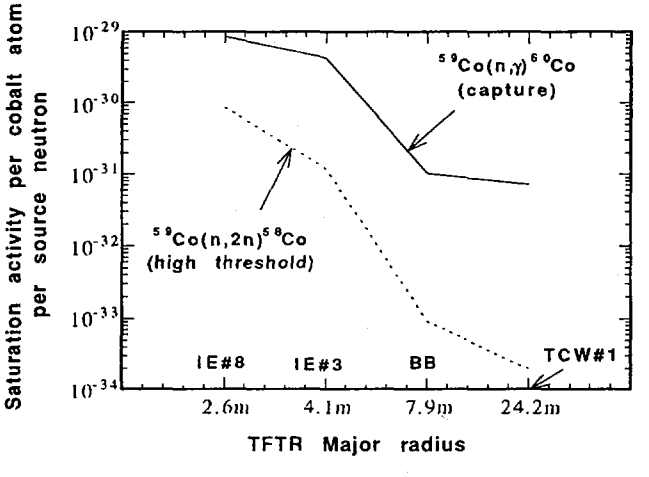

FIG. 2. Spatial dependence of saturation activities of high threshold and capture reactions in irradiated samples of cobalt inside the TFTR Test Cell.

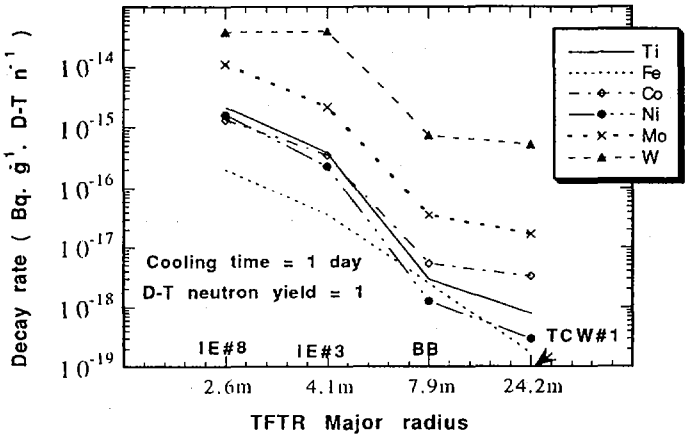

FIG. 3. Dependence of decay rate ($Bq \cdot g^{-1} \cdot D\text{-}T\ n^{-1}$) of irradiated samples on spatial location inside the TFTR Test Cell. Cooling time is 1 day.

reaction suffers only two orders of magnitude drop. To place the relative activation potential of various materials and spatial locations into perspective, Fig. 3 shows decay rate as a function of the location after a cooling time of one day. Two to four orders of magnitude change in decay rate occurs from one location to another.

4. ROLE OF MEASUREMENTS IN METHODS, DATA VALIDATION AND LICENSING

The measurements have demonstrated the prototypicality of the TFTR measurements in relation to ITER in various ways. For example, the TFTR reentrant irradiation location that is closest to the plasma exhibits large contributions to radioactivity from both threshold and capture type activation reactions. Similar situations are expected near the ITER first wall [3]. Fig. 4 shows a spectral comparison for Irradiation End No. 8 (IE#8) of TFTR, an ITER first wall ("ITER FW", *for a self-cooled Li-V option of an ITER blanket optimization study*), and first wall of an accelerator based D-T neutron driven USDOE-JAERI experimental assembly ("US/J-FW"). The spectrum for TFTR IE#8 was obtained by unfolding of the measured saturation activities [3,8]. One can observe differences in the three spectra. The TFTR spectrum lies between the other two spectra from 1 to 7 MeV, and below the other two from 8 to 13 MeV. The observed differences in the spectra are expected due to wide differences in the source conditions, and the geometrical and material composition of the three systems being compared. However, TFTR IE#8 follows well the large dynamic range of saturation activities, that goes from $\sim 10^{-26}$ to $\sim 10^{-23}$, and is sensitive to the entire neutron energy spectrum. Also, from the complexity standpoint, TFTR geometry comes closest to ITER's, and hence provides a natural choice for simulation of ITER-like conditions.

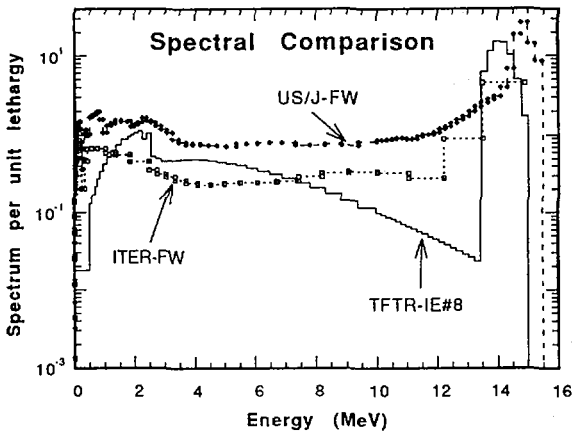

FIG. 4. Comparison of normalized spectrum per unit lethargy (lethargy = log(E_m/E), E_m being the largest value of neutron energy E) for the first wall of ITER (ITER-FW), the first wall of a United States Department of Energy-Japan Atomic Energy Research Institute (US/J-FW) experimental assembly and TFTR Irradiation End No. 8 (TFTR-IE#8).

An example of the use of measured saturation activities as normalization while dealing with elaborate calculations inside a part of the complex TFTR Test Cell is best brought out by our measured and the calculated $^{93}Nb(n,2n)^{92m}Nb$ saturation activities at the mouth of the NW personnel labyrinth entrance to the Test Cell. This provided a large improvement between the calculations and the measurements [9]. Another application of dosimetry foil measurements has been in resolving helium-3 detector efficiency and tritium breeding issues [10]. Tritium retention issues are reported elsewhere [11].

Calculations show relatively significant deviations from the measurements of induced radioactivity and related quantity of nuclear heating, even for relatively simple systems driven by well-defined accelerator D-T neutron sources [12-14]. The concept of safety factor was introduced to measure the degree of reliability of the calculations to assure that the calculations did not under predict the measurements [12-14]. Safety factors as high as three are needed to ensure more than 95% reliability. Large safety factors lead to conservatism in nuclear design and an attendant economic penalty. One practical way to confidently reduce these safety factors is to accumulate experimental data on similar or related components in the realistic tokamak environment of TFTR, and to compare the results with proposed improvements in calculational models. Regulatory licensing requirements for qualifying ITER are expected to be based on the experimental data base and validated calculational methods.

5. SUMMARY AND FUTURE PLANS

The ongoing program on radioactivity measurements at TFTR has been described. New results from Irradiation End 4 have been reported. Future efforts will maximize the activation data that can be obtained during the remaining TFTR Experimental Program in order to confidently reduce ITER safety factors and provide improved economics in future reactor designs.

ACKNOWLEDGMENTS

We thank D. Meade (PPPL), R. Hawryluk, (PPPL), G. Lemunyan (PPPL), and C. Tilson (PPPL) for encouraging and supporting this collaborative effort. We thank D. Smith and H. Tsai of ANL for supplying us with V-9Cr-5Ti and V-10Cr-5Ti samples for irradiation. This work was supported by USDOE Contracts DE-AC02-76CH03073 and DE-FG03-86ER52124.

REFERENCES

[1] CHENG, E.T., SAJI, G., J. Nucl. Mater. **212-215** (1994) 621.
[2] ZUCCHETTI, M., Fusion Technol. **19** (1991) 294.
[3] KUMAR, A., ABDOU, M.A., BARNES, C.W., KUGEL, H.W., LOUGHLIN, M.J., Fusion Eng. Des. **28** (1995) 415.
[4] KUMAR, A., ABDOU, M.A., KUGEL, H.W., Fusion Eng. Des. **28** (1995) 492.
[5] KUMAR, A., KUGEL, H.W., ASCIONE, G., "Activation experiments at TFTR for development of low activation materials for ITER and DEMO", Proc. 12th ANS Topical Mtg on Technology of Fusion Energy, Reno, NV, 1996, Fusion Technol. **30** (1996) 1113.
[6] KU, L.P., Nuclear Radiation Analysis for TFTR, Rep. PPPL-1711, Plasma Physics Lab., Princeton Univ., NJ (1980).
[7] MANN, F.M., REAC*2: Users Manual and Code Description, Rep. WHC-EP-0282, Westinghouse Hanford Co., Richland, WA (1989).
[8] PEREY, F.G., STAY'SL: Least Squares Dosimetry Unfolding Code System, RSIC Computer Code Collection PSR-113, Radiation Shielding Information Center, Oak Ridge, TN (1984).
[9] KUMAR, A., et al., "Measurement and calculation of doses in and around north-west labyrinth in TFTR Test Cell shielding for D-T operation", Proc. 16th IEEE/NPSS Symp. on Fusion Engineering, Champaign, IL, 1995, Vol. 1, IEEE Service Center, Piscataway, NJ (1995) 630.
[10] JASSBY, D.L., et al., Rev. Sci. Instrum. **68** (1997) 540.
[11] SKINNER, C.H., et al., J. Vac. Sci. Technol. **A14** (1996) 3267.
[12] KUMAR, A., et al., Fusion Technol. **28** (1995) 99.
[13] KUMAR, A., et al., Fusion Technol. **28** (1995) 173.
[14] KUMAR, A., IKEDA, Y., "On disagreement between measurements and calculations of D-T neutron driven induced radioactivity and nuclear heating", Proc. Int. Conf. on Nuclear Data for Science and Technology, Gatlinburg, TN, 1994, Vol. 2, American Nuclear Society, La Grange Park, IL (1994) 883.

REDUCTION OF EROSION YIELD OF GRAPHITE MATERIALS UNDER HIGH FLUX BEAM IRRADIATION

Y. UEDA, Y. OHTSUKA, M. ISOBE, M. NISHIKAWA
Graduate School of Engineering,
Osaka University,
Suita, Osaka,
Japan

Abstract

REDUCTION OF EROSION YIELD OF GRAPHITE MATERIALS UNDER HIGH FLUX BEAM IRRADIATION.

Erosion yield of various graphite materials at elevated temperatures due to high flux beam irradiation was studied. The irradiation was performed by a 5 keV argon beam with a maximum flux of about 10^{21} Ar·m^{-2}·s^{-1}, about two orders of magnitude higher than that of previous beam experiments. It was found that the total erosion yield of graphite materials at elevated temperatures (1780–1980 K) in high flux regions shows a significant reduction with flux, which was not observed in the previous low flux experiments. The flux dependence of the radiation enhanced sublimation (RES) yield, which is the total yield minus the physical sputtering yield, is consistent with the model based on C self-interstitial diffusion with stable defects as sinks of interstitials in both high and low flux regions. According to the experimental data and this model, much less erosion of graphite materials under actual deuterium edge plasma conditions with a high heat flux to the plasma facing components (PFCs) can be expected.

1. INTRODUCTION

Graphite materials are planned for use in the plasma facing components (PFCs) in ITER. Radiation enhanced sublimation (RES) of graphite at elevated temperatures has been believed to be a key process in determining the lifetime of graphite for PFCs. In our study, the erosion yield of RES under high flux conditions (almost equivalent to the edge plasma conditions) was measured with a high flux argon beam with a flux of 10^{21} m^{-2}·s^{-1} (5 keV). This flux is about two orders of magnitude higher than that in previous low flux beam experiments.

According to the present understanding, RES is a physical process whose yield scales with the energy transferred to the carbon atom by nuclear collisions [1]. The range of the 5 keV Ar ion in graphite is nearly the same as that of 0.5 keV D beam, and the damage rate of the Ar ion is about 50 times higher than that of the D ion calculated by TRIM92. Therefore, the 5 keV Ar beam in this experiments could simulate RES of graphite by a 0.5 keV D beam with a flux that is about 50 times higher than that of the Ar beam, which can be very close to the edge plasma conditions.

In this paper, a new high flux irradiation system, the evidence of the reduction of RES yield in the high flux region, a possible mechanism of the reduction and erosion of graphite in PFCs are described.

2. HIGH FLUX BEAM IRRADIATION SYSTEM

A high flux beam irradiation system [2] consists of a conventional bucket type ion source equipped with a spherical multiaperture extractor and an irradiation chamber with a movable sample stage (Fig. 1). The effective diameter and the radius of curvature of the extractor are 14 cm and 50 cm, respectively. The electrode geometrically focuses the broad beam on the focal point, at which the flux of the beam increases by a factor of about 20, compared with the flux at the extractor. This system operates in a pulsed mode with a typical pulse length of 1 s (duty cycle of about 2 min), owing to the accumulation of discharge gas in the irradiation chamber. The impurity content in the Ar beam is less than 6%, and its effect on the yield estimate is very small (less than 3%). The irradiation samples were directly heated by passing a current through them, and during the irradiation the current was reduced in order to compensate for the increase in heating power from the beam. The erosion yield (eroded flux divided by beam fluence) is measured by a weight loss method.

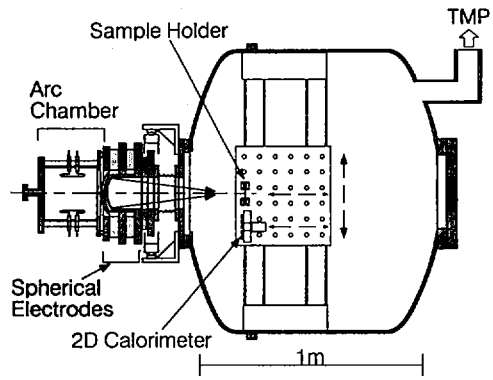

FIG. 1. Schematic of high flux irradiation apparatus (TMP: turbomolecular pump).

3. REDUCTION OF EROSION YIELD IN THE HIGH FLUX REGION

High flux irradiation experiments were carried out with three types of carbon based material: isotropic graphite (ISO-630, Toyo Tanso Co.), pyrolytic graphite (Union Carbide) and RG-Ti (NIIGrafit). The isotropic graphite ISO-630 is polycrystalline, with a density of 1.82 g/cm^3, while pyrolytic graphite is highly crystallized with a density of about 2.2 g/cm^3. RG-Ti is recrystallized graphite with 1.7 at% Ti, which appears in the microstructures in the form of crystalline TiC grains with a mean size of 2 μm. Most of the microstructures of RG-Ti are formed by graphite layers containing very little Ti.

The total erosion yield of these materials as a function of the 5 keV Ar flux is shown in Fig. 2. The samples were heated up to 1980 K, except for RG–Ti (1780 K), in which thermal sublimation is not negligible at 1980 K. It is clearly seen that the total erosion yield is reduced with the Ar flux in all specimens. The flux dependence of the total yield of ISO-630 over a flux of 10^{20} Ar·m^{-2}·s^{-1} is about $\phi^{-0.23}$ (ϕ being the flux). In the previous low flux experiments [3, 4], the dependence is much weaker, with an exponent of about -0.1. The reduction of the graphite yield in high flux is also proved by surface observations of RG–Ti after irradiation. Since the erosion of TiC is independent of the flux, the graphite layers are eroded faster than the TiC grains in the lower flux, which was observed by a SEM micrograph.

The total erosion yield can be the sum of RES yield and the physical sputtering yield. The RES yield is strongly temperature dependent over 1400 K, with an effective activation energy of about 0.8 eV, while the physical sputtering yield is independent of temperature and incident flux. The RES yield of ISO-630 is plotted in Fig. 3, with the low flux irradiation data taken from Philipps et al. [3]. The difference of the flux dependence between the high (our data) and the low (reference) regions suggests that some RES mechanism changes with flux.

Our results affect both theory and technology of the PFCs. From a theoretical point of view, our results provide a new key to clarifying the RES mechanism of graphite. This point will be discussed in the next section. From a technological viewpoint, the lifetime of the graphite tiles as PFCs, at elevated temperatures, can be longer than that given by a previous evaluation using low flux irradiation data. This point will be discussed in Section 5.

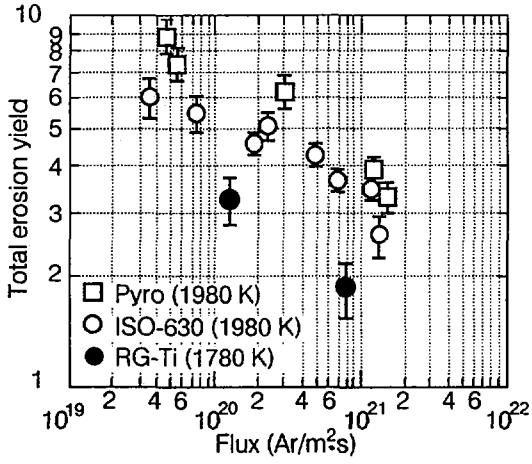

FIG. 2. Total erosion yield of various graphite materials as a function of irradiation flux of a 5 keV Ar beam.

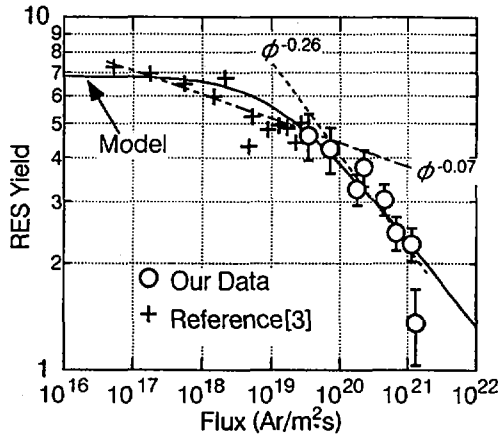

FIG. 3. RES yield (total erosion yield minus physical sputtering yield) as a function of irradiation flux of 5 keV Ar beam. The reference data [3] were taken with pyrolytic graphite at 1820 K. The reference data were given by arbitrary units and are normalized so that their absolute values are almost the same as those of our data at a flux of $3 \times 10^{19}\ m^{-2} \cdot s^{-1}$. *The absolute value of the model calculation is determined by least squares fitting to our experimental data.*

4. MECHANISM OF RES IN THE HIGH FLUX REGION

The basic RES processes have been thought to be generation and diffusion of C self-interstitials produced by nuclear collisions between incident ions and lattice C atoms [5]. The interstitials produced in the bulk diffuse to the surface and easily sublime owing to the low binding energy with the lattice atoms. In the course of diffusion, some of the interstitials recombine with vacancies and some stable defects; then are annihilated. This recombination process reduces the number of interstitials reaching the surface. If the sinks of the interstitials are the vacancies only, the RES yield is proportional to $\phi^{-0.25}$, according to a simple analytical model to be shown below. The exponent of ϕ does not change much, even with complicated assumptions (-0.2 to -0.3) [6]. Our results (RES yield: $\sim\phi^{-0.26}$) seem to agree with this case. Conversely, if the stable defects dominate the recombination of the interstitials, the RES yield is independent of the flux. The reference data in Fig. 3 seem to be consistent with this picture.

The basic equation for the diffusion of interstitials and vacancies can be written as follows:

$$\frac{\partial c_{i,v}}{\partial t} = D_{i,v} \frac{\partial^2 c_{i,v}}{\partial x^2} + P(x) - K_{iv} c_i c_v - K_{si,v} c_{i,v} s_{i,v} \tag{1}$$

Here, $c_{i,v}$ denotes the density of the interstitials and the vacancies normalized to the carbon density, n_c. The subscripts i, v denote the interstitials and the vacancies. The values of $s_{i,v}$ denote the effective density of stable defects for the sinks of interstitials and vacancies normalized to n_c. The function P(x) denotes the distribution of the generation rate of interstitials and vacancies, which are assumed to be the same. The coefficients K_{iv} and $K_{si,v}$ are the recombination rates for interstitials and vacancies, and for interstitials and vacancies at stable defects, respectively. The details of this model are described elsewhere [7].

The RES yield calculated from the time independent solution of Eq. (1) is shown in Fig. 3. The production rate of interstitials, P(x) is assumed to be constant, P_0; it is defined as the total generation rate divided by the averaged depth of the distribution by TRIM92. It is found that the RES yield calculated by the analytical model including stable sinks for the interstitials shows a flux dependence similar to that of the experimental data of the RES yield in both high and low flux regions. Before our experimental results were shown, only data with weak flux dependence were present, and the correlation between the experiment and the model, in terms of flux dependence, was not satisfactory. However, our data gave rise to more consistent understanding of the RES mechanism.

5. EROSION OF GRAPHITE IN PLASMA FACING COMPONENTS

The depth profile of the irradiation damage in graphite due to 5 keV Ar is similar to that due to 0.5 keV D, which was already stated in Section 1. The flux dependence of the RES yield of 0.5 keV D is also calculated in the same manner at 1980 K

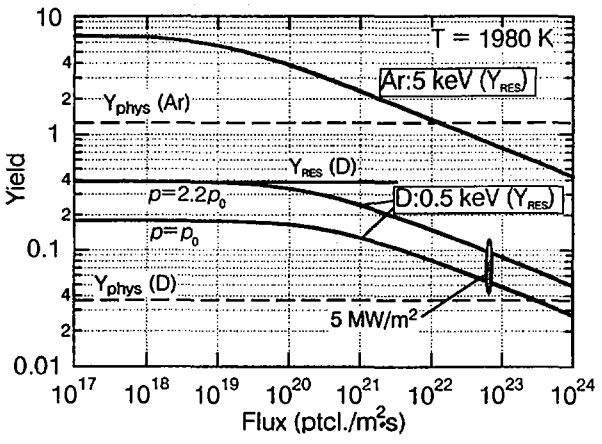

FIG. 4. Model calculation of RES yield of 5 keV Ar and 0.5 keV D. p is the production rate of interstitial per unit volume, and p_0 is defined as the number of interstitials produced by one incident ion divided by the averaged depth of the interstitial distribution multiplied by the incident flux.

(Fig. 4). If the production rate of the interstitials, p, is assumed to be p_0 for D, the calculation shows an RES yield that is about a factor of two lower than the experimental yield, $Y_{RES}(D)$, obtained by low flux beam experiments [1]. If production rate, p, is set as $2.2p_0$, the calculated value in the low flux region agrees with the experimental RES yield. The other parameter affecting the RES yield is the density of stable sinks, s_i. However, by reducing this parameter the RES yield increases only in the low flux region, and the yield does not change in the flux region over 10^{21} $m^{-2} \cdot s^{-1}$. For constructing a more reliable model, a more experimental database such as irradiation with different ions and different energies in the high flux region would be needed.

Although some uncertainty remains in estimating the RES yield in 0.5 keV D by this model, we can claim that the RES yield shows a significant reduction in the actual edge plasma conditions (an ion heat flux of 5–10 MW/m^2). In Fig. 4, at an ion heat flux of 5 MW/m^2, the RES yield could be reduced by at least a factor of about 4. At this heat flux, the RES yield becomes only two to three times larger than the physical sputtering yield while the RES yield is about ten times larger in the low flux region. This means that the lifetime of graphite (inversely proportional to the erosion speed) under high heat flux conditions (ion heat flux: 5 MW/m^2, D ion energy; 0.5 keV) could at least be about three times longer than that evaluated on the basis of low flux irradiation data.

REFERENCES

[1] PHILIPPS, V., VIETZKE, E., TRINKAUS, H., J. Nucl. Mater. **179–189** (1991) 25.
[2] NISHIKAWA, M., UEDA, M., GOTO, S., Fusion Eng. Des. **16** (1991) 351.
[3] PHILIPPS, V., VIETZKE, E., SCHORN, R.P., TRINKAUS, H., J. Nucl. Mater. **155–157** (1988) 319.
[4] HAASZ, A.A., DAVIS, J.W., J. Nucl. Mater. **151** (1987) 77.
[5] ROTH, J., MÖLLER, W., Nucl. Instrum. Methods **B7/8** (1985) 788.
[6] DAVIS, J.W., HAASZ, A.A., 12th Conf. in Plasma-Surface Interactions (Proc. 12th Int. Conf. St. Raphaël, May 1996).
[7] UEDA, Y., NAKANO, K., OHTSUKA, Y., ISOBE, M., GOTO, S., NISHIKAWA, M., J. Nucl. Mater. **227** (1996) 251.

STUDY ON THE APPLICATION OF HIGH Tc SUPERCONDUCTORS TO IMPROVE THE POSITIONAL STABILITY OF TOKAMAK PLASMAS

T. UCHIMOTO, Y. FUKUZAKI, N. IKATSU, K. MIYA
Nuclear Engineering Research Laboratory,
University of Tokyo,
Tokai-mura, Ibaraki-ken,
Japan

Abstract

STUDY ON THE APPLICATION OF HIGH Tc SUPERCONDUCTORS TO IMPROVE THE POSITIONAL STABILITY OF TOKAMAK PLASMAS.

High Tc superconductors can improve the positional stability of tokamak plasmas if they are arranged at the plasma periphery. In the paper, the magnetic interaction between high Tc superconductors and tokamak plasmas is experimentally examined; a precise estimate of the stabilizing effect of high Tc superconductors on the plasma position is desired. For this purpose, experimental and numerical analyses were carried out, in which a change of the magnetic field comparable to that in reactors was applied to high Tc superconductors. Through these analyses, the shielding current model was confirmed, and the critical parameter of high Tc superconductors in this model was successfully specified.

1. INTRODUCTION

Improvement of the vertical stability is one of the critical issues in the design of fusion reactors because the vertical instability may subject a plasma to vertical disruptions known as vertical displacement events (VDEs), which may induce severe forces on the vacuum vessel and its components.

The authors have proposed a new method of improving the plasma positional stability with the use of high Tc superconductors (HTSCs). HTSCs possess a relatively strong 'pinning' property so that the magnetic flux can be trapped in them effectively. Therefore, if HTSCs are arranged at the plasma periphery, they are expected to trap the flux generated by the plasma, leading to an improvement of the positional stability. This stabilizing system has some advantages over the conventional systems:

(1) unlike feedback control systems, the system does not require any power supply;
(2) its stabilizing effect on plasmas is free of decay, which would be inevitable if eddy currents were induced in the structures.

In order to verify the feasibility of the proposed method, we have carried out numerical simulations in which an HTSC shielding current analysis and an MHD equilibrium analysis of the tokamak plasma are coupled. The numerical results showed that the millisecond order of magnitude of the plasma duration was extended to a minute order of magnitude if HTSCs were arranged around a tokamak plasma [1]. In this computation, the shielding current in the HTSC was estimated on the basis of a critical state model valid for a primary approximation. However, the interaction between plasmas and HTSCs must be elucidated for a more precise estimation of the stabilizing effect to be carried out.

In this paper, the magnetic interaction between HTSCs and tokamak plasmas is experimentally examined. For this purpose, an experiment using an HTSC sample was performed by simulating the plasma current by a circular coil. In addition, the electromagnetic force due to the HTSC in the configuration of the experiment was estimated numerically. Through a comparison between experimental and numerical results, the superconducting shielding current model in the vicinity of the tokamak plasma was confirmed, and the parameters dominating the fast changing shielding currents in the HTSC were examined.

2. EXPERIMENT AND COMPUTATION

2.1. Description of experiment

In order to simulate the change of the magnetic field applied to the HTSCs during the plasma instability, the experimental apparatus was set up as shown in Fig. 1. It consisted of an exciting coil and an HTSC sample attached to a cantilever

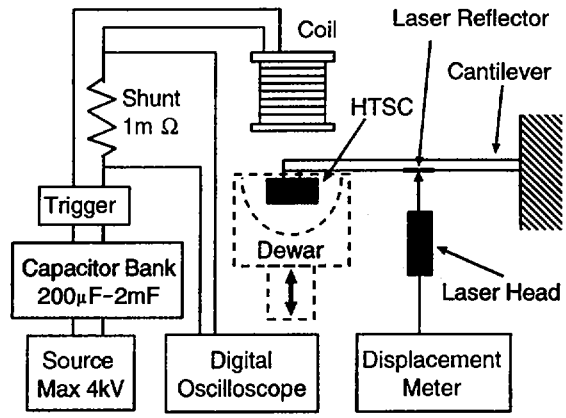

FIG. 1. Schematic drawing of experimental set-up.

beam and cooled at 77 K in an LN_2 dewar. The superconductor sample was melt-powder melt-growth (MPMG) processed YBaCuO [2] and of cylindrical shape, 17 mm in diameter and 18 mm high. The coil current was supplied by a condenser bank with a capacity of 2 mF maximum. The exciting coil could supply a maximum magnetic field of 0.5 T in the superconductor region. The electromagnetic force due to the HTSC was estimated by measuring the displacement of the cantilever beam with a laser displacement meter.

2.2. Numerical formulation

To estimate the electromagnetic force due to the HTSC, the shielding current in the HTSC is computed by applying the current vector potential method (T method). The critical current density in Y based HTSCs is anisotropic because of its grain structure, and the shielding current can be assumed to flow only in the a–b plane of the grain structure. Therefore, the thin plate approximation can be applied [3]. The governing equation for the normal component of the current vector potential ($\mathbf{J} = \nabla \times \mathbf{T}$) is introduced as follows:

$$\nabla \cdot \frac{1}{\sigma} \nabla T - \mu_0 \frac{\partial T}{\partial t} - \frac{\mu_0}{4\pi} \mathbf{n} \cdot \int_S \frac{\partial T}{\partial t} \nabla \frac{1}{R} dS = \frac{\partial B_0}{\partial t} \tag{1}$$

where σ is the electrical conductivity, B_0 the applied flux density, μ_0 the permeability in the vacuum and R the distance between the source and the field points.

As to the model of shielding current in the HTSC, the flux flow and the creep model were adopted here, and the constitutive equations between J and E based on the model are [4]:

$$\begin{aligned} E &= 2\rho_c J_c \sinh\left(\frac{U_0}{k\theta}\frac{J}{J_c}\right) \exp\left(-\frac{U_0}{k\theta}\right) && 0 \le J \le J_c \\ E &= E_c + \rho_f J_c (J/J_c - 1) && J_c \le J \end{aligned} \tag{2}$$

where E_c is the critical electric field, ρ_c the creep resistivity, θ the temperature, U_0 the pinning potential, k the Boltzmann constant, ρ_f the flow resistivity and J_c the critical current density.

The magnetic force, **f**, is computed as follows:

$$\mathbf{f} = \int_{sc} (\mathbf{J} \times \mathbf{B})\, dV \tag{3}$$

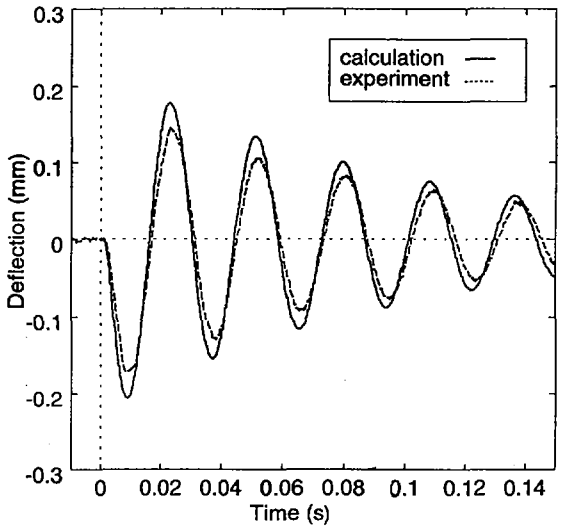

FIG. 2. Wave forms of cantilever beam deflection (pulse length 4.8 ms, maximum field 0.21 T).

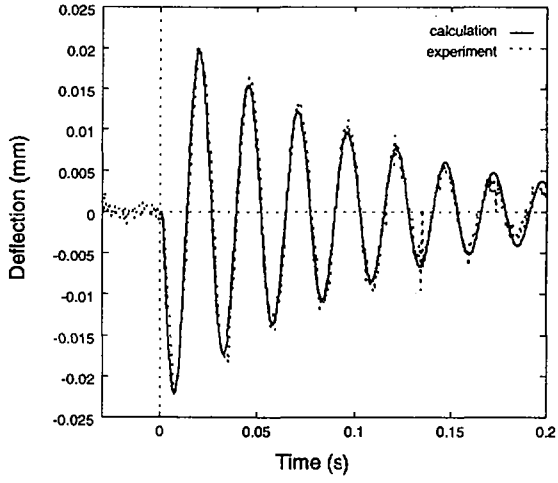

FIG. 3. Wave forms of cantilever beam deflection (pulse length 1.0 ms, maximum field 0.14 T).

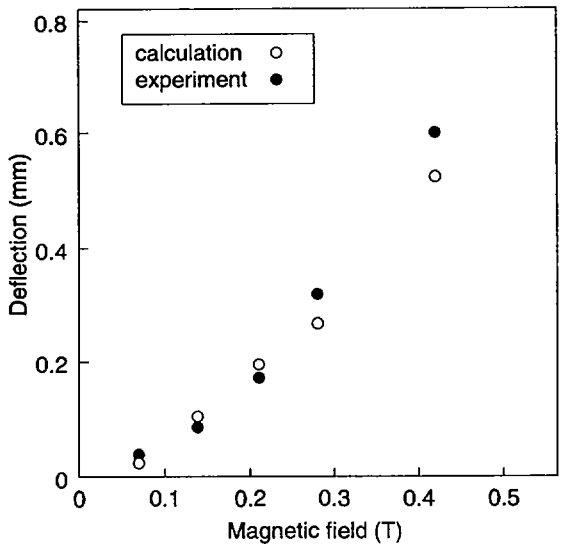

FIG. 4. Relationship between applied magnetic flux density and maximum deflection of cantilever beam.

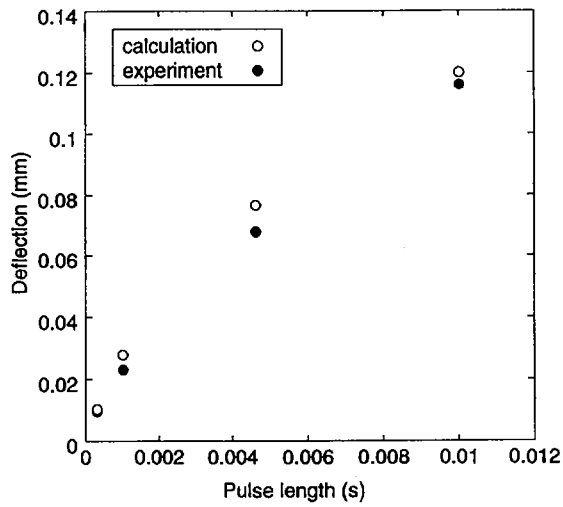

FIG. 5. Relationship between pulse lengths of coil currents and maximum deflection of cantilever beam.

2.3. Results

Figures 2 and 3 show the experimental and numerical results of the wave forms of the cantilever beam deflection. In the former case, the pulse length of the coil current was 4.8 ms and the maximum magnetic flux density applied in the HTSC sample was 0.21 T; in the latter case, these values were 1.0 ms and 0.14 T, respectively. In the computation, we assume $U_0 = 0.1$ eV, $E_c = 10^{-4}$ V/m. The critical parameters which determine the electromagnetic forces due to HTSC are J_c and ρ_f, because the electric field induced in the HTSC sample is so high that the flux flow phenomenon is dominant in the HTSC. The former parameter, J_c, can be specified by measuring the static electromagnetic force [5]; that of the sample in the experiment was 2.0×10^6 A/m^2. Here, the value of ρ_f can be determined so that the computed wave forms of the deflection coincide with the experimental ones. Here, a value of 8.0×10^{-6} $\Omega \cdot$m was chosen, and good agreement was obtained in the both cases as is shown in Figs 2 and 3.

Next, the relationship between the applied magnetic flux density and the maximum deflection of the cantilever beam was investigated by fixing the pulse lengths of coil currents at 4.8 ms. In the computations, the parameters were not changed from the above values. The experimental and numerical results are shown in Fig. 4; they agree well. In the same way, the relationship between the pulse lengths of the coil currents and the maximum deflection of the cantilever was examined, and the maximum magnetic flux density was fixed at 0.14 T. The results are shown in Fig. 5, and the numerical and experimental results also agree well, which supports the application of the flux flow creep model and the specification of the critical parameter, ρ_f.

3. CONCLUSIONS

In this paper, the magnetic response of HTSCs to plasmas is experimentally investigated with the aim of applying HTSCs to an improvement of the positional stability of the tokamak plasma. From the experiment it follows that the shielding current in the HTSC can be described on the basis of the flux flow and creep model when the applied field changes as fast as that due to unstable plasmas. Furthermore, the flow resistivity of HTSC, which is one of the critical parameters, is experimentally specified. From now on a more precise estimation of the stabilizing effect of the HTSC will be possible as a result of the knowledge obtained here in order to optimize the arrangement of the HTSC and to estimate the electromagnetic force on the HTSC.

ACKNOWLEDGEMENT

This work was partially supported by a grant in aid for scientific research from the Japanese Ministry of Education, Science, Sports and Culture.

REFERENCES

[1] UCHIMOTO, T., IKATSU, N., MIYA, K., Stud. Appl. Electromagn. Mech. (1996) (in press).
[2] MURAKAMI, M., et al., Jpn. J. Appl. Phys. **29** (1990) 1991.
[3] UESAKA, M., YOSHIDA, Y., TAKEDA, N., MIYA, K., Int. J. Appl. Electromagn. Mater. **4** (1993) 13.
[4] YOSHIDA, Y., UESAKA, M., MIYA, K., IEEE Trans. Magn. **30** (1994) 3503.
[5] TAKEDA, N., UESAKA, M., MIYA, K., Cryogenics **34** (1994) 745.

DEVELOPMENT OF NEGATIVE ION BASED NEUTRAL BEAM INJECTOR FOR THE LARGE HELICAL DEVICE

O. KANEKO, Y. TAKEIRI, K. TSUMORI,
Y. OKA, M. OSAKABE, R. AKIYAMA,
T. KAWAMOTO, E. ASANO, T. KURODA
National Institute for Fusion Science,
Oroshi, Toki,
Japan

Abstract

DEVELOPMENT OF NEGATIVE ION BASED NEUTRAL BEAM INJECTOR FOR THE LARGE HELICAL DEVICE.

A high power neutral injection heating system based on negative ion beam technology is under construction for the Large Helical Device (LHD). An injection power of 15 MW is expected for 10 s, with 180 keV for the hydrogen beam. High energy is required to inject the beam tangentially into the LHD so that the use of negative ions is inevitable. The system consists of two beam lines with four negative ion sources. A large negative ion beam (160 A) is required, with a high current density (>35 mA/cm^2). The design of the ion source is carried out on the basis of the authors' R&D during the past seven years, where highly efficient negative ions and a high quality beam could be produced. The other components of the beam line and the power supplies are designed on the basis of conventional neutral beam technology. Although an NBI system is designed in pulse operation, its duty cycle is rather high (10 s every 5 min) because the magnetic field of the LHD is generated in a steady state. This is a difficult situation for heat removal systems such as beam dumps.

1. INTRODUCTION

The Large Helical Device (LHD) is the world's largest superconducting heliotron/torsatron device under construction [1]; the first plasma is expected early in 1998. High power (15 MW) neutral beam injection is planned as the main plasma heating tool. In the LHD, the beam should be injected tangentially to avoid being trapped in the helical ripples of the magnetic field [2]. Although the average plasma minor radius is not very long (0.6 m), the beam path in the plasma is long, because of the high aspect ratio (6.2). Then the required beam energy becomes as high as 180 keV for hydrogen. With this high energy, the conventional positive ion system is useless, and negative ion based technology must be introduced.

The production of the high power negative ion beam is one of the key technologies in heating and current drive of the next large tokamak fusion devices such as ITER; R&D in this field has been carried out in many laboratories [3]. There are two methods of producing high power beams: increasing the energy and/or increasing the current. For the LHD, the latter method is more important because our beam energy

is moderate, a situation that differs from that of ITER. Therefore, we have started our own R&D programme to develop a high current negative hydrogen ion source in 1990.

Our R&D was successful. We extracted 1.2 A of H^- with a current density of 54 mA/cm^2 through a small area of the large ion source [4], and then extracted 16 A with 45 mA/cm^2 through the whole extraction area [5]. We tried to operate the ion source at low gas pressure and obtained 16.2 A of H^- at 0.5 Pa [6]. The design of our neutral beam injection system is based on our latest R&D results; it will be described in the following sections.

2. DESIGN OF THE NEUTRAL BEAM INJECTION SYSTEM

2.1. Physics requirements for NBI in the LHD

NBI heating in the LHD has to satisfy the following conditions: (1) the absorbed beams must be passing particles; (2) the deposition profile of the beam is to be peaked at the plasma centre; and (3) no net current should be induced. The first condition is to avoid helical ripple loss of fast ions, which is essential in the helical system. The second condition comes from the experimental result that the helical plasma has no profile consistency and the central heating is hence important. The third condition is linked to our experimental purpose, i.e. studying net current free plasma in the LHD.

From the first and the third conditions, the neutral beam lines are designed so as to provide tangential, balanced injection. The beam energy is determined from the second condition, for a high density plasma of 10^{20} m^{-3} in average, because from empirical scaling high performance is expected for high density plasmas in the LHD [7]. For the hydrogen beams, the energy was chosen to be 180 keV, where the beam shinethrough at low density operation is also taken into account. A total 'port through' power of 15 MW by two beam lines is planned at the beginning of the experiment. So far, NBI heating is only planned in pulsed operation, up to 10 s, although the duty factor is rather high (1/30).

2.2. Design of a negative ion based NBI

2.2.1. Arrangement of beam lines

In order to realize the required NBI system, it is necessary to use negative ions. The design of the system depends on the structure and the performance of the negative ion source we use. Here, we have adopted a caesiated multicusp ion source with external magnetic filter; we had studied it in our R&D programme. Two ion sources are installed in each beam line. The ion source has a beam extracting area 0.25 m wide and 1.2 m high. An H^- current of 40 A is expected from this ion source, i.e.

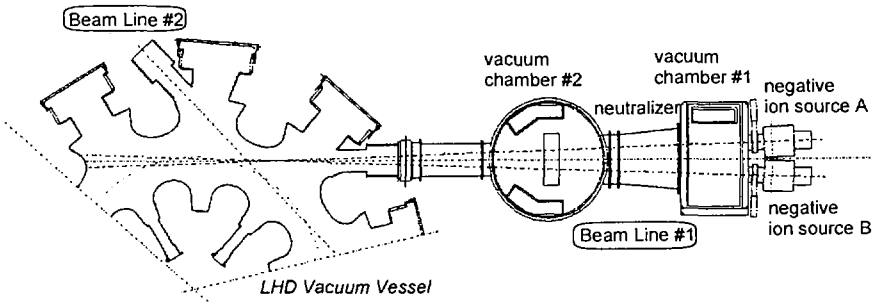

FIG. 1. Sectional plan of LHD vacuum vessel and NBI beam line.

TABLE I. SPECIFICATION OF LHD-NBI AND R&D RESULTS FOR NEGATIVE ION SOURCE

	LHD-NBI	R&D
Beam species	H/D	H
Beam energy (keV)	180/360	125
Beam extraction area (cm)	25 × 120	25 × 50
Beam current (A)	40/20	16
Current density (mA/cm^2)	35/18	45
Beam divergence (mrad)	10	9 (multiholes) 5 (single hole)
Operating pressure (Pa)	0.4	0.4
Pulse length (s)	10	10
Electron content in the beam (%)	10	17
Accelerator	Electrostatic (single stage)	Electrostatic (single/two stage)
Focusing	Geometrical and beam steering	Beam steering

a current density of over 35 mA/cm^2 must be realized. The design of the ion source will be described in detail later on.

Figure 1 shows an equatorial plan view of the LHD vacuum vessel and the NBI beam line. Two ion sources are installed side by side on the beam line. It should be noted that the plasma cross-section is a twisted ellipsoid in the LHD; its minimum radius is only 0.4 m, which is comparable to the beam size. Since the shape of the vacuum vessel follows that of the plasma, the injection angle is almost uniquely determined by the necessity to keep the beam away from the wall of the LHD vacuum vessel. Fortunately, this angle satisfies the condition that all injected beams become passing particles. The specification of the NBI system is summarized in Table I, with our R&D results that are the design basis for the system.

2.2.2. *Negative ion based beam line*

The beam line consists of two vacuum chambers and a long gas neutralizer cell between them. The ion sources are installed on the first chamber, which has a cryopump with a capacity of 360 m^3/s and works as an expansion chamber. It is very important to reduce the gas pressure in the accelerator of the ion source in order to avoid stripping loss of accelerated negative ions, while the vacuum pressure in this chamber must be so high as to maintain the line density for the purpose of neutralization. We want to reduce the length of the beam line; hence, the designed pressure is 0.05 Pa, and the neutralizer cell is 3.5 m long. The second chamber consists of a bending magnet, beam pumps and calorimeters. It also has a 1000 m^3/s cryopump in order to prevent reionization loss of the beam higher than 5%.

We have adopted the gas line density for neutralization so that the residual numbers of positive and negative ions become equal, in order to reduce the maximum heat flux on the beam dumps. This condition should be met, independently of the operating conditions of the ion source, although the gas from the ion source is utilized for neutralization. Therefore, we normally feed hydrogen gas into the first chamber to control the gas line density between the ion source and the second chamber.

We use an ion bending magnet to separate the ions from the neutrals. We have chosen this active magnetic separation because our beam is so thick — to achieve high current — that electrostatic separation is difficult. The idea of using a magnetic leakage field from the LHD cannot be used for separation because the strength of the field varies among the operating modes and in some of them is very weak. The beam dumps are formed by the swirl tube array; the maximum heat flux on them is 16 MW/m^2. This value is tolerable for a single shot, but life after many heat cycles is unknown. Since the LHD magnetic field operates in steady state, the repetition of the experimental shot depends on the pulsed heating system; the minimum interval is 5 min. Then the number of shots may exceed 10 000 per year. An estimate based on data from the American Association of Mechanical Engineers (ASME) shows that the lifetime is over 10 000 cycles, but the critical conditions are not clear. The best approach is to reduce the heat load so that we have adopted a reflecting magnet in order to diverge the ion beam on the beam dumps.

TABLE II. SPECIFICATION OF POWER SUPPLIES

	Voltage (V)	Current (kA)	Pulse width (s)	Features
Filament	14	6	30	12 individual outputs
Arc	100	5	20	Fast switching circuit
Bias	10	1	20	
Extraction	−15 000	75	10	Includes electron current
Acceleration	−170 000	90	10	Common to two sources

A newly developed large cryosorption pump [8] is adopted as the main vacuum pump. The advantage of this pump is that its operating range of temperature is wide (up to 20 K) and the cryopanel is directly connected to a refrigerator. Therefore, it is stable against the pulsed heat load, and no (power consuming) long cryogenic transfer tube is needed. The pump is composed of several modules (a set of panel and refrigerator). We have used a 300 m^3/s cryosorption pump using small modules for the NBI of the JIPP T-IIU tokamak; the result is satisfactory.

2.2.3. Power supplies

The power supplies are similar to those of a positive ion system: a filament, an arc and acceleration DC power supplies. The power supplies for the negative ion system that are different from those of the positive ion system are the bias power supply and the extraction power supply. The former is needed to reduce the electrons that are accompanied by negative ions from the ion source, and the latter is needed to prevent the electrons from flowing into the accelerating region. The specifications of the power supplies are shown in Table II.

The acceleration power supply is common to the two ion sources of a beam line because they are installed so closely that the high voltage between them cannot be restrained. This cannot be helped since the two beams must merge at the injection port so as to pass through it and they should not be separated widely in the plasma at a distance from the port (Fig. 1).

One of the crucial components of the acceleration power supply is the fast switch for breakdowns in the accelerator. We have adopted a conventional gate turn-off (GTO) thyristor switch in the DC circuit [9], because our beam energy is not very high. Then we can switch the output in less than 1 ms. This fast switching is convenient for the beam modulation that we are planning for the experiments. We also use this GTO switch for the arc power supply. Since its capacity is very large (100 V, 5 kA), it is very important to detect abnormal discharges and to switch off the current as soon as possible in order to protect the plasma source from damage.

2.3. Negative hydrogen ion source

2.3.1. High performance negative hydrogen ion source

The ion source design is based on our latest R&D results. It is a caesiated multicusp ion source with a strong external magnetic filter. This ion source does not have a plasma loss region in front of the plasma grid and hence can be operated at low gas pressure [10]. There are several performance aspects that are important in designing the ion source: (1) high H^- production efficiency; (2) low operating gas pressure; (3) small electron content in the beam; (4) low beam divergence; (5) good uniformity; and (6) stable operation.

For high efficient H^- production at low gas operating pressure, we have already demonstrated 16.2 A of H^-, with a current density of 31 mA/cm^2 at 0.5 Pa. At this pressure, the stripping loss of H^- in the accelerator is below 10%. So far, the obtained negative ion current has been proportional to the arc power into the ion source, i.e. the plasma density. This fact is encouraging for the production of high current negative ions; what we have to do is to increase the discharge power density in the ion source. One problem comes from the low gas pressure operation. In order to do this, we have to improve the plasma confinement in the ion source. Usually, this can be achieved by increasing the confining magnetic field strength, which corresponds to a decrease of the anode area in the arc discharge. In the magnetic multicusp ion source, there is a threshold of the ratio of anode to cathode areas for a good discharge [11], which means that the cathode area (i.e. the number of filaments) must be reduced when the anode area decreased. This condition is opposed to that for high power discharge. We have designed the maximum arc current so as not to exceed the current that flows in the directly heated cathode filaments as shown in Table II.

The other important, but not yet well established, technology aimed at improving the H^- production is the caesium adjunct discharge. Caesium enhances the H^- producing efficiency drastically, but the optimization of the amount of caesium in the discharge has so far been only empirical. Recently, we have found that a long pre-arc discharge of 10 s improves the production efficiency by 1.5; so we think that a favourable equilibrium has been achieved between the caesium in the plasma and on the plasma grid. Actually, in the long pre-arc discharge, the H^- production efficiency does not depend strongly on the temperature of the plasma grid, at least not in the range of 180–300°C, which is different from the result of a strong temperature dependence in short pulse operation. This is a favourable result because a temperature increase of the grid during the discharge cannot be avoided.

2.3.2. High quality beam formation

It is well known that the divergence of the H^-/D^- beam is small. We have also shown in the single hole experiment that a minimum divergence of 5 mrad was obtained, even at a low energy of 80 keV and with a high current density of 28 mA/cm^2 [12]. This is a good result, but for the multihole system several problems arise:

One is the magnetic field in the accelerator, which is due to the magnetic filter and the extraction grid. For the latter, we install magnets between the rows of extraction holes in order to repel the electrons that are extracted, accompanied by H^-. The magnetization of these magnet rows is opposite side by side and is not perfectly cancelled along the ion orbit. Then, the ions are deflected and separated. We have succeeded in compensating this deviation by beam steering, using the grid hole displacement technique [13]. However, these two effects have a different dependence on the beam energy and cannot be compensated for in all conditions.

Another problem is the inhomogeneity of the ion production over the grid area. Two causes are possible: non-uniform discharge and a non-uniform caesium cover on the grid. As to the discharge, we have found that the arc current is not distributed uniformly over the filaments. When the arc current heats up the filaments, a greater emission current can be extracted. This positive feedback enhances the non-uniform discharge and can be suppressed by adding a variable resistor to the circuit. This stabilization is also necessary for long pulse operation, which may improve the caesium conditions qualitatively and spatially, as we have shown in the previous section.

3. CONSTRUCTION SCHEDULE

Commissioning of the first beam line will start in 1997. The ion sources will be conditioned and tested in the neutral beam test stand where the R&D has been carried out. The first NBI experiment is scheduled for mid-1998.

ACKNOWLEDGEMENTS

The authors would like to express their gratitude to Drs T. Watari and A. Iiyoshi for their support and encouragement.

REFERENCES

[1] IIYOSHI, A., YAMAZAKI, K., Phys. Plasmas **2** (1995) 2349.
[2] KANEKO, O., et al., Fusion Eng. Des. **26** (1995) 455.
[3] INOUE, T., et al., in Plasma Physics and Controlled Nuclear Fusion Research 1994 (Proc. 15th Int. Conf. Seville, 1994), Vol. 2, IAEA, Vienna (1995) 687; PAMELA, A.J., et al., ibid., p. 695.
[4] TSUMORI, K., et al., Fusion Eng. Des. **26** (1995) 473.
[5] ANDO, A., et al., Phys. Plasmas **1** (1995) 2813.
[6] TAKEIRI, Y., et al., Rev. Sci. Instrum. **66** (1995) 2541.
[7] SUDO, S., et al., Nucl. Fusion **30** (1990) 11.
[8] OKA, Y., et al., Fusion Eng. Des. **31** (1996) 89.
[9] WATANABE, Y., et al., in Power Electronics (Proc. Int. Conf. Tokyo, 1983), Vol. 1, Tokyo (1983) 808.
[10] TAKEIRI, Y., et al., J. Plasma Fusion Res. **71** (1995) 605 (in Japanese).
[11] GOEBEL, D.M., Phys. Fluids **25** (1982) 1093.
[12] ANDO, A., et al., Rev. Sci. Instrum. **66** (1995) 5412.
[13] TAKEIRI, Y., et al., Rev. Sci. Instrum. **66** (1995) 5236.

PRODUCTION OF MULTI MW DEUTERIUM NEGATIVE ION BEAMS FOR NEUTRAL BEAM INJECTORS

K. MIYAMOTO, N. AKINO, T. AOYAGI, N. EBISAWA,
Y. FUJIWARA, A. HONDA, T. INOUE, T. ITOH,
M. KAWAI, M. KAZAWA, J. KOIZUMI, M. KURIYAMA,
N. MIYAMOTO, K. MOGAKI, Y. OHARA, T. OHGA,
K. OHSHIMA, Y. OKUMURA, H. OOHARA, F. SATOH,
K. USUI, K. WATANABE, M. YAMAMOTO, T. YAMAZAKI
Japan Atomic Energy Research Institute,
Naka-machi, Naka-gun, Ibaraki-ken,
Japan

Abstract

PRODUCTION OF MULTI MW DEUTERIUM NEGATIVE ION BEAMS FOR NEUTRAL BEAM INJECTORS.

The construction of the 500 keV, 10 MW negative ion based neutral beam injector (N-NBI) for JT-60U has been completed, followed by the first neutral beam injection experiment in March 1996. Up to now, a 350 keV, 1.9 MW deuterium neutral beam has been injected into the tokamak plasma. It was confirmed that the neutralization efficiency in the energy range of 250 to 370 keV was approximately 60%, which was in good agreement with the theoretical value predicted by the cross-section data. High current negative ion acceleration towards 1 MeV has been carried out as one of the major R&Ds for the ITER NBI, where a 1 MeV, 40 A D^- ion source/accelerator is required. Up to now, a hydrogen negative ion beam of 805 keV, 150 mA (power supply drain current) has been successfully obtained for a pulse duration of 1 s.

1. INTRODUCTION

A negative ion based high energy neutral beam injector (N-NBI), which can deliver multi MW deuterium neutral beams, is one of the promising candidates not only for plasma heating, but also for current drive and plasma control in future fusion devices such as ITER. In the ITER NBI system, 1 MeV, 50 MW neutral beams are to be injected into the tokamak for more than 1000 s by using three injector modules [1].

The key issues for the development of the ITER N-NBI system are high current deuterium neutral beam production and high energy acceleration of ampere class negative ion beams of up to 1 MeV range. Two major R&D activities are carried out at JAERI: (1) the JT-60U N-NBI system for high current deuterium neutral beam production, and (2) the ITER prototype accelerator for high energy acceleration.

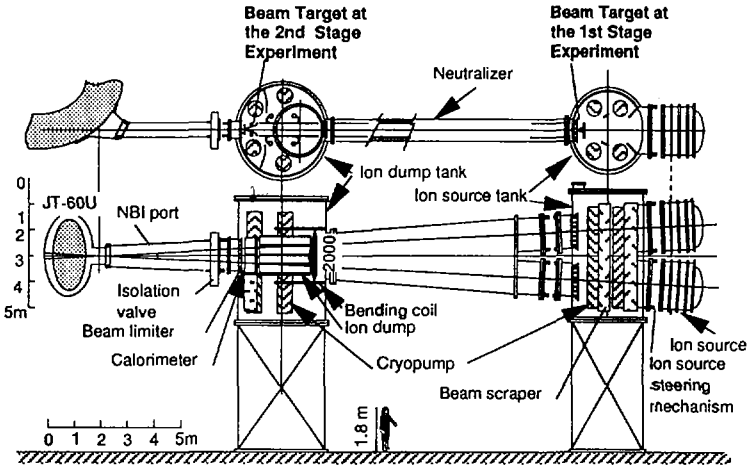

FIG. 1. JT-60U N-NBI system.

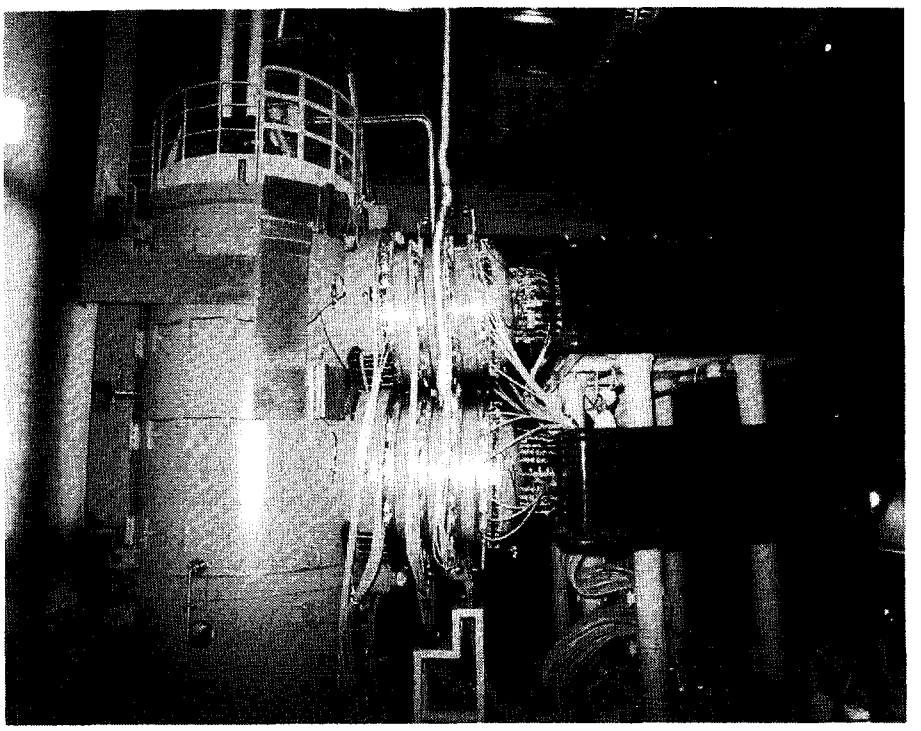

FIG. 2. Two ion sources mounted on JT-60U N-NBI beamline.

The JT-60U N-NBI system, which is designed to deliver a 500 keV, 10 MW neutral beam into the plasma in order to demonstrate core plasma heating, current drive and plasma control [2], has been constructed. This is the first neutral beam injector in the world using negative ions as the primary ions. The ion source is designed to produce 22 A, 13 mA/cm^2 D^- ion beams [3], whose current and current density are relevant to ITER specifications. After confirming ion source, beamline and power supply performances [4], we have started the neutral beam injection experiment in March 1996.

To establish the technology for stable acceleration of high current negative ions up to 1 MeV, a prototype accelerator, which is designed to produce a 1 MeV, 1 A H^- ion beam, has been tested at the MeV Test Facility [5].

In this paper, recent experimental achievements on these R&D activities are described.

2. DEVELOPMENT OF THE JT-60U N-NBI SYSTEM

2.1. System design

The JT-60U N-NBI system is designed to deliver 500 keV, 10 MW deuterium neutral beams. It is composed of two ion sources, a beamline system, a power supply system, a control system and auxiliary subsystems [2]. An illustration of the N-NBI system is shown in Fig. 1. Deuterium negative ions are produced in a caesium seeded multicusp plasma generator via both volume and surface processes [6], then extracted by a multiaperture extractor and accelerated in a three stage electrostatic accelerator. Two ion sources are mounted on the beamline system as shown in Fig. 2. The produced D^- ion beam is neutralized through the gas neutralizer cell. The line density is attained by the gas feed into the neutralizer in order to obtain the designed neutralization efficiency of 60% for 500 keV beam energy. The neutral beam is injected into the plasma through the injection port.

Taking the beam geometrical efficiency, the neutralization efficiency, the reionization loss due to the collision of neutral beams with the residual gas and the power supply loss into account, the total system efficiency is estimated to be 40%.

2.2. D^- ion beam production

A negative ion beam production test was conducted by using one ion source to test the ion source performance. The accelerated D^- ion beam current was measured calorimetrically at a target located 3.5 m downstream of the source. Figure 3 shows the D^- ion beam current and the extracted electron current as a function of the arc power in the ion source. The D^- ion beam current increased as the arc power increased, and reached 13.5 A at an arc power of 125 kW. This current and the beam power (400 keV $\times$ 13.5 A = 5.4 MW) are world records for D^- ion beams.

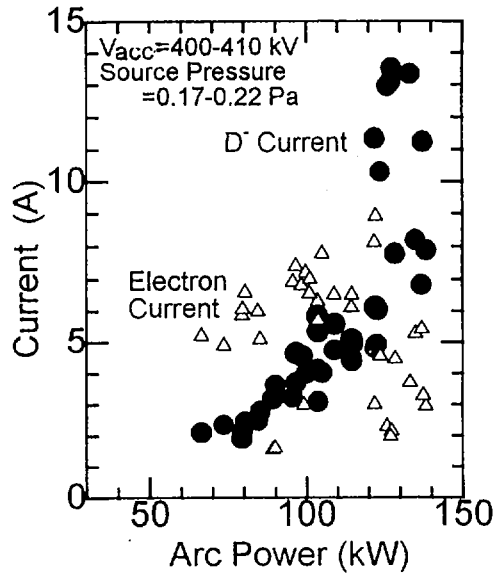

FIG. 3. D^- ion beam current and extracted electron current versus arc power.

TABLE I. COMPARISON OF NEGATIVE ION SOURCES FOR JT-60U AND ITER

	ITER	JT-60U	
	Design	Design	Achieved
Beam energy	1 MeV	500 keV	400 keV
Beam current	40 A, D^-	22 A, D^-	13.5 A, D^-
Current density	20 mA/cm^2	13 mA/cm^2	8 mA/cm^2
Source pressure	<0.3 Pa	0.3 Pa	0.22 Pa
Electron current, I_e/I_{D^-}	<1	1	~0.4

In the high current D^- ion beam production, the suppression of electrons is important because the acceleration of the electrons not only causes low acceleration efficiency but also high heat loads in the extractor and accelerator grids. The ratio of the extracted electron current to the D^- ion beam current is less than unity ($I_e/D^- < 1$) in the higher arc power operation, where the negative ion production efficiency is improved by caesium seeding. The operating gas pressure is as low as 0.22 Pa. The extracted electron current and the operating source pressure are low enough to satisfy the ITER requirements as shown in Table I.

2.3. Neutralization and injection

The advantage of N-NBI systems is a high neutralization efficiency in the high energy range of more than a few hundred keV. To confirm the neutralization efficiency in the high energy range, a neutralization experiment has been carried out in the JT-60U N-NBI.

After passing the neutralizer, the beams consist of three components: neutral beams (D^0), unneutralized negative ion beams (D^-) and reionized positive ion beams (D^+). The neutralization efficiency is given by the fraction of D^0 power to the total power of all species (D^0, D^+ and D^-). The power of the neutral beams was measured by a calorimeter placed just in front of the injection port. The powers of both the D^+ and D^- ion beams were measured calorimetrically by the ion dump. Figure 4 shows the neutralization efficiency as a function of the deuterium beam energy [7]. The calculated neutralization efficiency of approximately 60% was obtained up to 370 keV at optimum gas line density. The measured neutralization efficiency is in good agreement with the calculation.

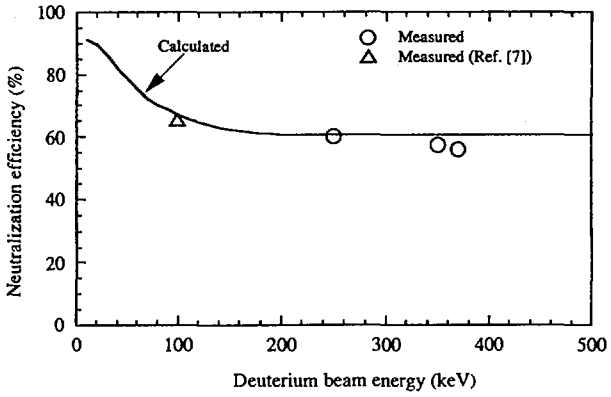

FIG. 4. Neutralization efficiency versus beam energy for D^-.

The neutral beam injection into JT-60U was started by using two ion sources. The injection power was increased gradually with the conditioning time. Up to now, a 1.9 MW, 350 keV neutral beam was injected into the plasma. We have observed a considerable increase in the neutron yield from the plasma. So far, the NBI system has been working without any serious problems in the tokamak environment. The conditioning of the ion sources is to be continued until full power injection of 500 keV, 10 MW is achieved.

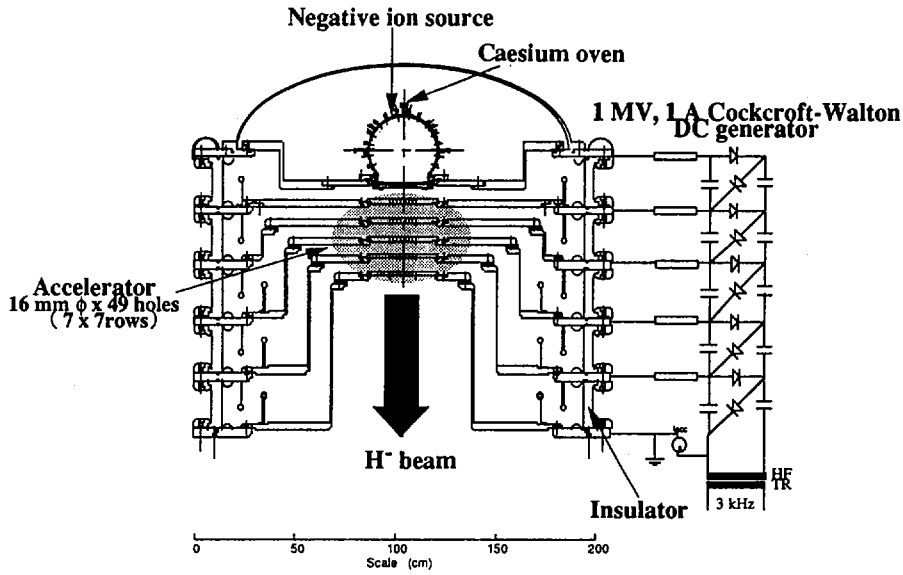

FIG. 5. Cross-section of ITER prototype accelerator.

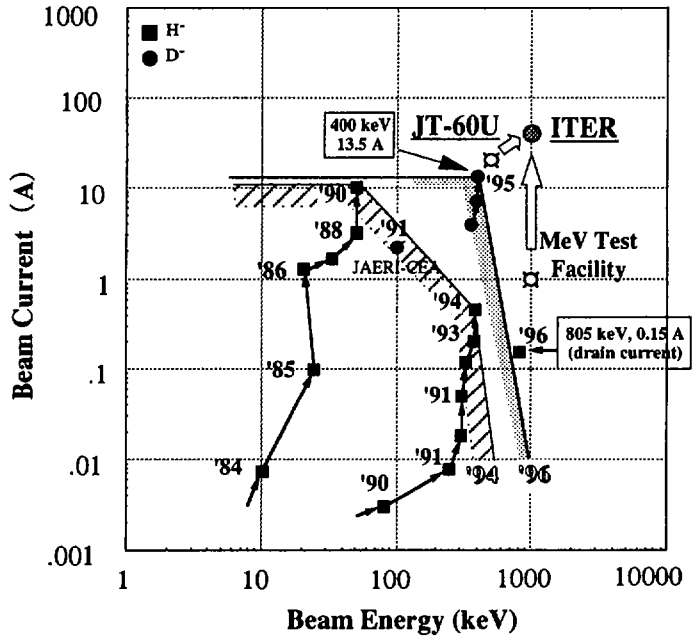

FIG. 6. Present state of negative ion beam development at JAERI and future plan for ITER.

3. DEVELOPMENT OF AN MeV CLASS ACCELERATOR FOR ITER

The key component in the ITER-NBI system is the high current negative ion accelerator with a capability of accelerating 40 A D^- ion beams up to an energy of 1 MeV. In order to establish the 1 MeV acceleration technology, the ITER prototype accelerator has been developed. The accelerator has a multiaperture, multistage system. Figure 5 shows a cross-sectional view of the accelerator. The advantage of the acceleration system is that the high current negative ion beams can be focused at each stage by the electrostatic lens, which is formed by increasing the electric field in the downstream stages. This acceleration system is also adopted as the reference design of the ITER accelerator [8].

The H^- acceleration started after conditioning the accelerator up to a voltage of 820 kV. Up to now, a 805 keV, 150 mA (power supply drain current) H^- ion beam has been successfully accelerated for a pulse duration of 1 s. At present, to enhance the negative ion current, caesium has been seeded into the ion source. It has turned out that, once the accelerator is conditioned, the voltage holding capability is not affected by the presence of negative ion beams or the caesium seeding. These results for the H^- beam acceleration and the voltage holding capability encourage the development of the ITER accelerator. The conditioning of the accelerator and the optimization of the beam optics are being continued in order to achieve 1 MeV acceleration of 1 A H^- ion beams.

4. SUMMARY

The construction of the JT-60U N-NBI system is complete, and neutral beam injection has started. Considerable progress has been achieved in high current D^- ion beam production (13.5 A, 400 keV, 5.4 MW) and high energy negative ion acceleration (>800 keV). The results obtained in the present R&D phase are becoming close to the values required for ITER as is shown in Fig. 6.

ACKNOWLEDGEMENTS

The authors would like to thank the members of the NBI Heating Laboratory and the NBI Facility Division for valuable discussions. They are also grateful to M. Ohta, A. Funahashi, H. Kishimoto and S. Shimamoto for continuous encouragement and support, as well as to R.S. Hemsworth and P.L. Mondino of JCT-Naka for their co-operation in the ITER R&D.

REFERENCES

[1] HEMSWORTH, R.S., et al., Rev. Sci. Instrum. 67 (1996) 1120.

[2] KURIYAMA, M., et al., in Fusion Engineering (Proc. SOFE 16th Symp. Urbana-Champaign, IL), IEEE, Piscataway (1996) 491.

[3] OKUMURA, Y., et al., Rev. Sci. Instrum. 67 (1996) 1018.
[4] WATANABE, K., et al., "Beam acceleration test in negative-ion based NBI system for JT-60U", Production and Neutralization of Negative Ion Beams (Proc. 7th Int. Symp. Upton, 1995).
[5] INOUE, T., et al., "High energy acceleration of H^- ion beam at MeV test facility", ibid.
[6] OKUMURA, Y., et al., "Cesium mixing in the multi-ampere volume H^- ion source", AIP Conf. Proc. No. 210 (1990) 169.
[7] PAMELA, J., et al., Nucl. Instrum. Methods Phys. Res. B73 (1993) 289.
[8] HEMSWORTH, R., et al., IAEA-CN-64/FP-18, these Proceedings, Vol. 2, p. 927.

A COMPACT W-SHAPED PUMPED DIVERTOR CONCEPT FOR JT-60U

N. HOSOGANE, S. SAKURAI, K. SHIMIZU,
S. TSUJI-IIO[1], M. SHIMADA, K. KODAMA,
K. MASAKI, N. ASAKURA, K. ITAMI, T. TAKIZUKA
Naka Fusion Research Establishment,
Japan Atomic Energy Research Institute,
Naka-machi, Naka-gun, Ibaraki-ken,
Japan

Abstract

A COMPACT W-SHAPED PUMPED DIVERTOR CONCEPT FOR JT-60U.

In JT-60U, the open divertor was modified to the pumped W-shaped divertor in February to May, 1997. The new divertor consists of inclined divertor plates and a dome in the private flux region. The performance of this divertor was assessed by numerical simulations. A sufficient reduction in the back-flow of neutral particles is found by the baffling effect of the inclined divertor plates. The dome is expected to increase the pumping efficiency from the private region; this is to be used for controlling the pumping speed and to reduce the influx of methane gas to the X point region. However, the particle flux ionized around the X point region will increase, because of the shallow divertor.

1. INTRODUCTION

The radiative divertor, which is effective in power exhaust, is considered to be a promising divertor concept in the design of ITER [1]. However, in radiative divertor experiments [2, 3], as the radiation loss increases up to a certain level, the strongly radiating region always develops to the X point MARFE or spreads to the main plasma surface. The energy confinement time of the H mode degrades, and the impurity level in the main plasma rises in these states. Thus, a radiative divertor with good main plasma performance has not yet been achieved. To maintain a good H mode in a radiative divertor, a reduction in particle recycling around the main plasma by optimizing the divertor geometry is considered necessary. The development of control techniques such as pumping or gas puffing is essential not only to reduce the impurity levels, but also to control highly radiative plasmas. Therefore, divertor modifications are in progress in the major tokamaks [4, 5]. In JT-60U, the open divertor was modified to a W-shaped divertor in February to May, 1997, aiming at the development of a new compact radiative divertor compatible with the main plasma performance.

---

[1] Tokyo Institute of Technology, Tokyo, Japan.

This paper presents the design concept and the expected performance of the new W-shaped divertor. In Section 2, the modification concept of the W-shaped divertor and the related systems is described. In Section 3, the performance of the new divertor as assessed by numerical simulation codes is presented. A summary is given in Section 4.

2. MODIFICATION CONCEPT OF THE JT-60U DIVERTOR AND RELATED SYSTEMS

Figure 1 shows a cross-sectional view of the W-shaped divertor designed for the modification. The new divertor consists of inclined divertor plates and a dome arranged in a W-shaped configuration, as well as inner and outer baffles for the pumping duct. The inclined target type divertor with a dome was adopted because of its effectiveness in achieving dense and cold divertor plasmas [6] and baffling the backflow of neutral particles. The dome is also expected to increase the pumping efficiency from the private flux region by increasing the deuterium molecule density through compression and, at the same time, to function as a baffle for reducing the neutral particle flux to the X point region. The angle of inclination of the divertor plate to the separatrix is about 60°, and the divertor depth from the X point to the divertor plate is about 0.2 m. The divertor shape and size were determined so as to allow various configurations with high triangularity, inward shifted plasma for the high β_p experiment, etc., and to attain 3 MA discharges within the limitation of the divertor coil current.

Highly radiative long pulse operation (<10 s) with 70% radiation loss of net heating power and low radiative short pulse operation (<4 s) with 30% radiation loss were considered for a net heating power of 30 MW. CFC tiles are used for divertor

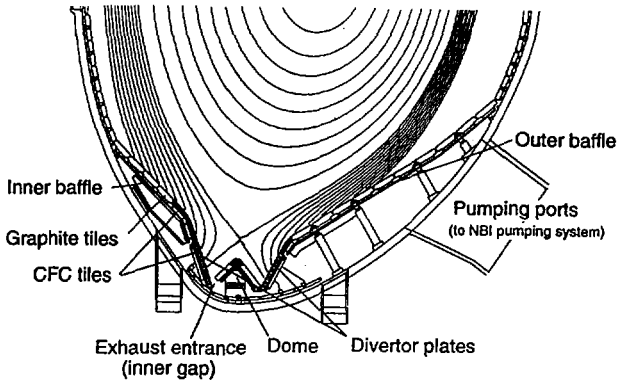

FIG. 1. Cross-sectional view of W-shaped divertor.

plates, top tiles of the dome and baffle tiles at the divertor throat, where a heat flux of 5 MW/m^2 × 10 s to 10 MW/m^2 × 4 s is expected in these operations. These tiles are inertially cooled on the basis of thermal analysis, which shows that operation with an interval of 20 min is possible without water cooling. For other parts, graphite tiles are used.

Three NBI cryopumps, with a pumping speed of 1000 m^3/s each, will be modified for the divertor pumping system, equipped with argon frost for helium exhaust. The neutral particles will be exhausted through the gaps between the divertor plates and the dome in the private flux region. For the experimental campaign of the first year, the outer gap is sealed and only the inner gap is used for pumping in order to study the effects of pumping location. The net pumping speed at the exhaust entrance is expected to be in the range of 35–70 m^3/s at 0.1–1 Pa with a Knudsen flow effect at a vessel temperature of 300°C. The throughput in the radiative divertor, where the neutral pressure is expected to be higher than 0.2 Pa, corresponds to a particle fuelling by NBI of 30 MW, 90 keV. For active control of the particle exhaust, fast shutter valves, with an aperture that can be changed during the shot, will be installed at the three pumping ports.

The leakage of neutral gas from the gaps between the segmented structures of divertor (125 segments) and baffles (72 segments) should be lowered from the viewpoint of particle exhaust and plasma performance. These gaps are carefully sealed by stainless steel plates insulated by a ceramic plasma spray. The total leak conductance is reduced to less than 7 m^3/s; i.e. we have 10% of the pumping speed at the exhaust ports.

The gas puffing system will be rearranged into three systems: fuelling at the top of the vacuum vessel (three ports), on the wall side of the main plasma (one port) and in the divertor region (two ports), for experiments such as impurity gas injection to enhance the radiation loss, SOL flow, etc., and to study the effects of the location of gas injection on the plasma performance. Moreover, the present pneumatic pellet injector will be modified to a centrifuge pellet injector to avoid edge cooling by gas puffing and to achieve densities above the Greenwald limit.

A detailed design of the W-shaped divertor is presented elsewhere [7].

3. ASSESSMENT OF PERFORMANCE OF THE JT-60U W-SHAPED DIVERTOR

3.1. Accessibility to dense and cold divertor

In H mode plasmas with good particle confinement time, the particle flux from the main plasma to the divertor is reduced. To realize a radiative divertor and good H mode confinement simultaneously, it is necessary to develop a divertor concept which can form dense and cold divertor plasmas with a relatively low incoming particle flux.

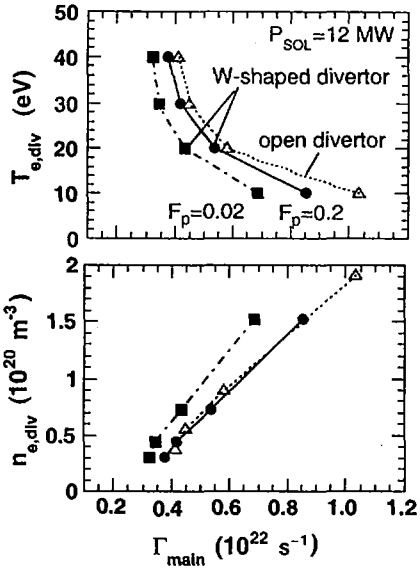

FIG. 2. Characteristics of divertor electron temperature and density in open and W-shaped divertors.

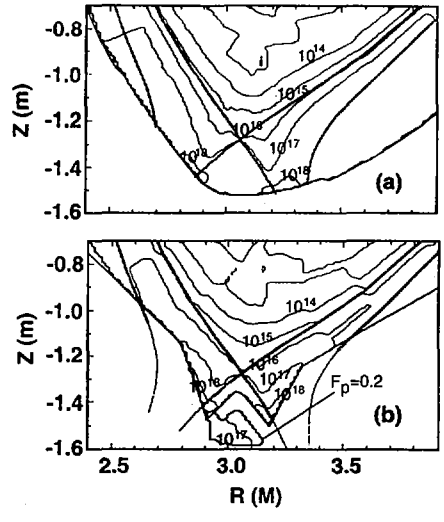

FIG. 3. Contour maps of neutral particle density in (a) the open and (b) the W-shaped divertor.

Figure 2 shows the characteristics of divertor electron temperature, $T_{e,div}$, and density, $n_{e,div}$, plotted as functions of the particle flux from the main plasma, Γ_{main}, in the open divertor and the W-shaped divertor calculated by a two dimensional neutral transport code, NEUT2D. Here, electron temperature profiles with peak values of 10, 20, 30 and 40 eV and a power flow to the SOL of 12 MW (corresponding to an absorbed power of 16 MW, assuming 25% of main radiation loss) are given as boundary conditions, and $n_{e,div}$ and Γ_{main} are calculated. Γ_{main} is defined as $\Gamma_{main} = S_{main} + \Gamma_{pump} + \Gamma_{wall}$, where S_{main} is the particle flux ionized in the main plasma (particle source), Γ_{pump} is the throughput from the divertor and Γ_{wall} is the particle flux pumped by the wall (albedo of 0.02). $F_p = 0.2$ and $F_p = 0.02$ stand for fractions of pumped particles through the narrowest gap in the dome (Fig. 3), corresponding to albedo values of 0.8 and 0.98, respectively. As is shown in this figure, in the W-shaped divertor with small pumping ($F_p = 0.02$), an electron temperature of 10 eV is obtained with 65% of Γ_{main} for the open divertor. Even with a strong pumping of $F_p = 0.2$, a low divertor electron temperature is expected to be obtained with a particle flux that is smaller than in the case of the open divertor. This demonstrates the effectiveness of the W-shaped divertor in achieving a dense and cold divertor plasma. In the W-shaped divertor, by adjusting the pumping speed, it is possible to access a high density plasma (relatively speaking) while keeping the divertor electron temperature in a suitable range.

3.2. Suppression of backflow of neutral particles

Suppression of the backflow of neutral particles from the divertor to the main plasma is one of the important requirements the divertor design should meet in order to maintain good H mode confinement in the radiative divertor.

Figure 3 shows contour maps of the neutral particle density in the open and W-shaped divertors, with $F_p = 0.2$, calculated by NEUT2D for $T_{e,div} = 10$ eV and $P_{SOL} = 12$ MW. In the W-shaped divertor, the neutral particle density at the main

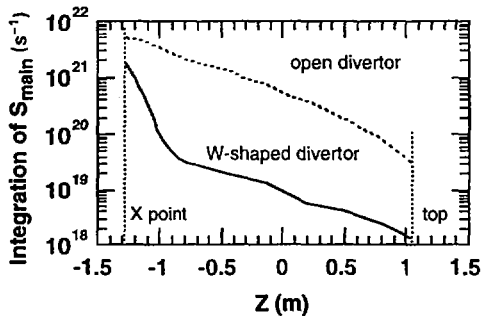

FIG. 4. Total ionized particle source integrated from the plasma top.

plasma periphery is remarkably reduced (more than 1/50) compared with the open divertor. In the W-shaped divertor, the neutral particles are released with a cosine distribution towards the vicinity of the X point. Accordingly, the fraction of neutral particles spreading outside is small, and the narrow throat formed by the inclined divertor plates baffles the backflow of these neutral particles. However, this mechanism increases the neutral particle density near the X point. This is due to the shallow divertor. In view of the influence of the backflow on H mode confinement, the fraction of neutral particles ionized in the main plasma is considered to be important. Figure 4 shows the total ionized particle sources integrated from the plasma top to height Z as a function of Z. The total ionized particle source in the W-shaped divertor is reduced to about one half of the open divertor case. Most of the ionized particle source is limited in the X point vicinity of $Z < -1.0$ m, and the rest is very small (about 1/50), in contrast to the open divertor in which the ionized particle source in the main plasma is larger than that around the X point. The influence of the distribution of ionized particle source on the H mode confinement is not clear and will have to be investigated experimentally.

3.3. Particle exhaust performance

The dome is expected to increase the neutral pressure by compression in the pumping region for effective particle exhaust and, at the same time, to function as a baffle to reduce the neutral particle flux to the X point region. Also, by shifting the separatrix position towards or away from the dome, the net pumping speed is expected to be changeable during a shot as was done in DIII-D [5].

Table I shows a list of parameters: the deuterium molecule density N_{D2}; the throughput, Γ_{pump}; the particle flux ionized in the main plasma, S_{main}; and the

TABLE I. GEOMETRICAL EFFECT OF DOME ON THROUGHPUT AND BAFFLING

	W-shaped δ_s = 5 cm	W-shaped δ_s = 3 cm	Without dome
Deuterium molecule density, N_{D2} (m^{-3})	2.3×10^{19}	3.3×10^{19}	—
Throughput, Γ_{pump} (s^{-1})	2.0×10^{21}	2.8×10^{21}	1.4×10^{21}
Particle flux ionized in main plasma, S_{main} (s^{-1})	3.6×10^{21}	3.0×10^{21}	3.9×10^{21}
Particle flux from main plasma, Γ_{main} (s^{-1})	8.5×10^{21}	8.7×10^{21}	7.5×10^{21}

particle flux from the main plasma, Γ_{main}, calculated by NEUT2D for the W-shaped divertor with plasma configurations with separatrix distances δ_s of 5 cm and 3 cm from the dome and an inclined target divertor without dome. The calculation was done for $T_{e,div}$ = 10 eV and P_{SOL} = 12 MW. By shifting the separatrix towards the dome from 5 to 3 cm, N_{D2} and Γ_{pump} increase by about 45%, and S_{main} decreases by about 17%. By removing the dome, Γ_{pump} decreases by 27% and S_{main} increases by 8%. The dome increases the throughput as expected, but the reduction in S_{main} is not large. This is because the angle of inclination of the divertor plate is not optimized owing to the limitation of space and the limitation of the divertor coil current.

The neutral pressure in the dome is 0.18–0.26 Pa at a vessel temperature of 300°C. The expected throughput by the designed pumping system is (2–3.1) $\times 10^{21}$ s^{-1} for this pressure range, which is sufficient for exhausting the particles supplied by NBI of 16 MW, 90 keV as is discussed here.

3.4. Reduction of methane gas influx

As the electron temperature decreases to 10 eV, carbon impurities generated by chemical sputtering become predominant over the total source of carbon. According to an impurity transport analysis of JT-60U experiments [8], the reduction in influx of methane gas generated in the private flux region is considered to be a key factor in suppressing the growth of the X point MARFE. In this respect, simulations with the two dimensional impurity transport Monte Carlo code (IMPMC) show that the dome in the W-shaped divertor works so as to reduce the influx of methane gas as a geometrical effect.

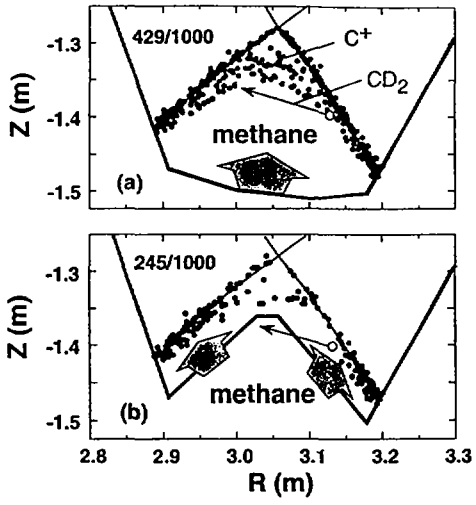

FIG. 5. Comparison of generation distributions of C^+ dissociated from methane gas between the inclined target divertor without dome and the W-shaped divertor with dome.

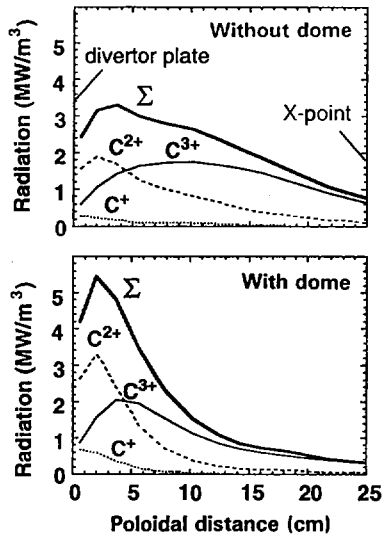

FIG. 6. Comparison of carbon radiation loss profiles along the poloidal distance from the divertor plate to the X point between the inclined target divertor without dome and the W-shaped divertor with dome.

Figure 5 shows the spatial distributions of the C^+ carbon impurity dissociated from the methane gas generated in the private flux region in the W-shaped divertor and the divertor without a dome. In this calculation, the source distribution of methane gas is given in proportion to the flux of charge exchange neutrals to the wall of the private flux region. In the divertor without a dome, the neutral hydrocarbons CD_3 and CD_2 in the dissociation process can spread in the private flux region; 43% of methane gas is ionized to C^+. However, in the W-shaped divertor, the motion of these neutral hydrocarbons is intercepted by the dome, which prevents the methane gas from being ionized to C^+ around the X point. Most of the hydrocarbons return to the wall, and the methane gas ionized to C^+ reduces to 25% of the generated methane gas. Accordingly, as is shown in Fig. 6, the radiation loss in the W-shaped divertor becomes large near the divertor plates, in contrast to the radiation loss spreading upstream, which is considered as one of the causes of the X point MARFE, in the divertor without a dome. Thus, the W-shaped divertor is expected to prevent the strong radiating region from moving towards the X point.

4. SUMMARY

The modification to the W-shaped divertor with inclined divertor plates and a dome in JT-60U aims at developing a new compact radiative divertor which realizes

radiative divertor and good H mode confinement at the same time. The performance of this divertor was assessed by the NEUT2D and IMPMC codes. The reduction in the backflow of neutral particles, which is one of the requirements for maintaining a good H mode, is fulfilled by the baffling effect of the inclined divertor plates. The dome will increase the pumping efficiency from the private flux region and will be used to control the pumping speed and to reduce the influx of methane gas to the X point region. These factors are considered to improve the radiative divertor. However, the particle flux ionized around the X point region is expected to increase because of the shallow divertor. This influence has not become clear so far and will be investigated experimentally. Understanding the physics of the influence of such neutral particles on H mode confinement and understanding control techniques developed in this divertor will contribute to establishing divertor operation scenarios for ITER. Moreover, this will lead to the development of compact divertors for future tokamaks.

ACKNOWLEDGEMENTS

The authors would like to thank the members of the Japan Atomic Energy Research Institute who have contributed to the JT-60 project.

REFERENCES

[1] INTERNATIONAL ATOMIC ENERGY AGENCY, Technical Basis for the ITER Interim Design Report, Cost Review and Safety Analysis, ITER EDA Documentation Series No. 7, Ch. V, IAEA, Vienna (1996).

[2] HOSOGANE, N., et al., J. Nucl. Mater. **220–222** (1995) 420.

[3] REICHLE, R., et al., in Controlled Fusion and Plasma Physics (Proc. 22nd Eur. Conf. Bournemouth, 1995), Vol. 19C, Part III, European Physical Society, Geneva (1995) 85.

[4] JET TEAM, in Plasma Physics and Controlled Nuclear Fusion Research 1994 (Proc. 15th Int. Conf. Seville, 1994), Vol. 1, IAEA, Vienna (1995) 51.

[5] MAHDAVI, M.A., et al., J. Nucl. Mater. **220–222** (1995) 13.

[6] TSUJI, S., et al., J. Nucl. Mater. **220–222** (1995) 400.

[7] SAKURAI, S., et al., in Fusion Technology (Proc. 19th Symp. SOFT, Lisbon, 1996).

[8] SHIMIZU, K., et al., in Plasma Physics and Controlled Nuclear Fusion Research 1994 (Proc. 15th Int. Conf. Seville, 1994), Vol. 1, IAEA, Vienna (1995) 431.

HIGH HEAT FLUX EXPERIMENTS ON A SADDLE SHAPED DIVERTOR MOCK-UP

S. SUZUKI, M. ARAKI, K. SATO,
K. NAKAMURA, M. AKIBA
Japan Atomic Energy Research Institute,
Naka-machi, Naka-gun, Ibaraki-ken,
Japan

Abstract

HIGH HEAT FLUX EXPERIMENTS ON A SADDLE SHAPED DIVERTOR MOCK-UP.

In development activity related to an actively cooled divertor structure, a saddle shaped divertor mock-up with parallel cooling channels has recently been developed and tested at Japan Atomic Energy Research Institute (JAERI). High heat flux experiments were performed to evaluate the durability of the divertor bonded structure under cyclic thermal loads and to demonstrate thermal performance under simulated thermal loading conditions of the ITER divertor plates. These experiments were carried out under two different loading conditions which simulated operation scenarios of ITER. For the simulation of the normal operation condition of ITER, a heat flux of 5 MW/m^2, 15 s was cyclically loaded for a repetition of 10 000 cycles; for the simulation of the transient period condition, a heat flux of 15 MW/m^2, 15 s was loaded for 1000 cycles. On the basis of the critical heat flux experiments, a coolant flow velocity of 4 m/s, which was proposed for the ITER design by JAERI, was chosen for both experiments. In these experiments no degradation of the thermal response of the mock-up was found during the normal operation condition; no excursion of the surface temperature due to thermal fatigue damage was observed during the transient period condition. The mock-up has shown excellent durability and successfully sustained its thermal performance. The saddle shaped divertor structure with parallel cooling channels was found to be one of the most promising divertor structures for ITER application from the thermomechanical point of view.

1. INTRODUCTION

In the next generation tokamak fusion devices, such as ITER, plasma facing components (PFCs) will be subjected to severe thermal and particle loadings. Therefore it is essential for ITER to develop PFCs with high thermal performance. In particular, the development of divertor plates is a critical issue for ITER because of its longer burn time and higher heat load to the divertor plates compared with the present tokamak devices, such as JT-60U. For instance, in ITER the divertor plates are required to withstand a cyclic thermal load of 5 MW/m^2 for 1000 s at a repetition of 1000 discharges and to sustain thermal performance under a transient heat load (15–30 MW/m^2, 10 s) with no major damage to the divertor structure. In off-normal events, such as plasma disruptions, extremely high heat fluxes of more than 1 GW/m^2 for up to several milliseconds are loaded onto the divertor plates in ITER. Therefore, to realize ITER, the cooling structure and the refractory surface materials for the divertor plates should be urgently developed.

The development of the divertor plates has been under way in many laboratories around the world [1–3]. Japan Atomic Energy Research Institute (JAERI) has energetically developed divertor mock-ups [4–6] and divertor surface materials [7–9] for fusion application. In developing the actively cooled divertor structure for ITER, JAERI has developed a 1 m long divertor mock-up with a single cooling channel which could survive a steady state heat flux of 25 MW/m^2 for over 1000 thermal cycles [4]. In the present study, a saddle shaped divertor mock-up with parallel cooling channels has been developed and has been tested in the JAERI Electron Beam Irradiation System (JEBIS) [10]. High heat flux experiments on this mock-up were performed to evaluate the durability of the divertor structure under cyclic thermal loads that simulated the normal operation condition of ITER and to demonstrate the thermal performance under the simulated transient period condition. In this paper, the results of the high heat flux experiments on the saddle shaped divertor mock-up are presented.

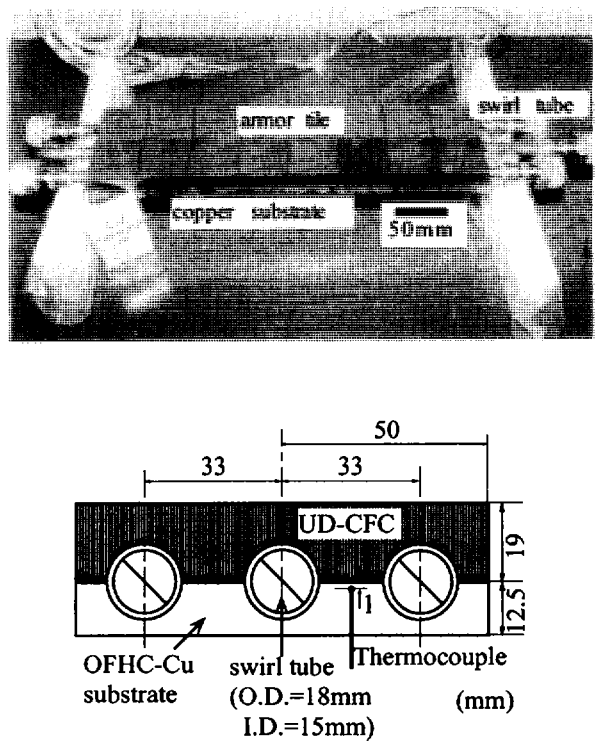

FIG. 1. Photo and schematic cross-section of the saddle shaped divertor mock-up with parallel cooling channels.

2. SADDLE SHAPED DIVERTOR MOCK-UP

Figure 1 shows a photo and a schematic cross-section of the divertor mock-up. The major dimensions of the mock-up are 400 mm length and 100 mm width. The mock-up has three parallel cooling channels with an outer diameter of 18 mm and an inner diameter of 15 mm. The cooling channels are made of oxygen free high conductivity copper (OFHC-Cu) pipe with stainless steel twisted tape inserts to enhance the heat transfer; this is known as a swirl tube. Large (50 mm × 50 mm) armour tiles were selected to simplify the fabrication of the mock-up. These armour tiles were made of unidirectional carbon fibre reinforced carbon composite (UD-CFC) material. The thermal conductivity of this UD-CFC material is over 600 $W \cdot m^{-1} \cdot K^{-1}$ along the carbon fibre direction and 25 $W \cdot m^{-1} \cdot K^{-1}$ perpendicular to it at room temperature. The saddle shaped armour tiles and the cooling channels were brazed on the heat sink substrate with a silver braze material at the same time. The heat sink substrate consisted of a single OFHC-Cu plate to avoid misalignment of adjacent armour tiles. As shown in Fig. 1, thermocouples (type K, 0.5 mm dia., sheathed) were also brazed in the OFHC-Cu substrate between the cooling channels at a depth of 11.5 mm from the rear side of the substrate. The brazing process was performed at about 850°C. The brazing process and the thickness of the braze filler material were optimized to minimize residual stress and to reduce braze defects at the braze interface. This saddle shaped divertor structure with UD-CFC armour tiles was originally developed at JAERI to achieve high heat transfer performance on the basis of data on and experience with [11] an externally finned tube invented for use in JT-60 as a neutral beam dump. From the thermal hydraulic point of view, the saddle shaped cross-section with UD-CFC materials has an advantage under a one sided heating condition, because the heat flux distribution along the inner circumference of the cooling tube can be more uniform than in the case of other geometries, such as a flat plate or a monoblock geometry. However, in such a bonded structure with larger armour tiles, higher residual and thermal stresses are expected at the braze interface. In particular, the thermal fatigue behaviour of such a divertor structure should be evaluated because the cyclic thermal stress imposed by the repetitive operation would cause the degradation or detachment of the braze interface.

3. HIGH HEAT FLUX EXPERIMENTS

Thermal cycling experiments were performed in JEBIS to evaluate the thermal fatigue behaviour of the mock-up. The experimental conditions and the ITER divertor requirements are summarized in Table I. A surface heat flux of 5 MW/m^2 with a heated area of 50 mm × 100 mm, which corresponded to the area of two armour tiles, was loaded. Since the thermal time constant of the mock-up was estimated to be less than 15 s, the heating duration of 15 s was selected so that the mock-up reached a thermal steady state. On the basis of the results of the critical heat flux

TABLE I. EXPERIMENTAL CONDITIONS AND ITER DIVERTOR REQUIREMENTS

	Experiment (simulation of normal operation)	ITER normal operation	Experiment (simulation of transient period)	ITER transient period
Surface heat flux (MW/m^2)	5	5	15	15 [12]
Pulse duration (s)	15	Steady state	15	Up to 10
Coolant pressure (MPa)	2	4	2	4
Coolant flow velocity (m/s)	4	10	4	10
Coolant temperature (°C)	25	150	25	150

experiments [11], an axial flow velocity of 4 m/s, which was proposed for the ITER divertor design by JAERI, was selected. Though it is lower than the ITER requirement, this flow velocity has the advantages of reducing both the pumping power and the corrosion by water.

The surface temperature and the heat sink temperature were monitored with an infrared camera and with a thermocouple brazed in the heat sink substrate, respectively. Figure 2 shows the temperature evolution of the heat sink obtained from the thermocouple for the simulated normal operation condition of ITER. The mock-up reached a thermal steady state within 15 s. The difference between the steady state temperature obtained at the first cycle and at the 10 000th cycle is attributable to the deviation of the heat flux loaded onto the mock-up; the deviation is estimated to be within $\pm 10\%$ of the nominal heat flux. A comparison of the thermal response of the first cycle with that of the 10 000th shows no major evidence of degradation of thermal performance. It is expected that the soundness of the braze interface could successfully be sustained against the cyclic thermal loading. During the experiment no surface cracking of the UD-CFC armour tiles due to thermal stress was observed. In addition, the temperature evolution shows good agreement with the numerical result from 2-D finite element analyses, as shown in Fig. 2. On this basis, it is shown that the thermal performance of the mock-up can be stably sustained through 10 000 cycles. The saddle shaped divertor structure has successfully been demonstrated to have sufficient fatigue strength for the design lifetime (1000 discharges) of the ITER divertor plates from the thermomechanical point of view.

To demonstrate the thermal performance of the mock-up under the simulated transient period condition of ITER, a thermal cycling experiment at a heat flux of 15 MW/m^2 for a repetition of 1000 cycles was conducted using other armour tiles.

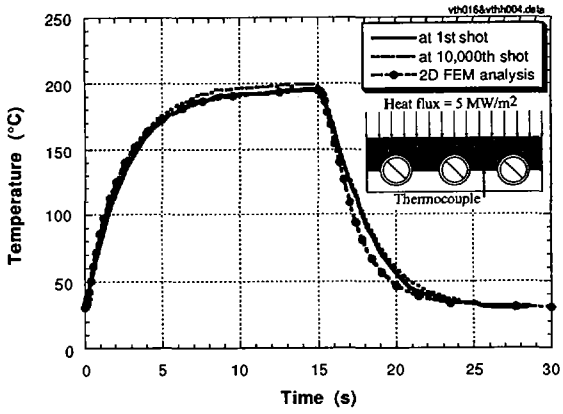

FIG. 2. Temperature evolution obtained from the thermocouple at the first and the 10 000th thermal cycle, compared with the analytical result from 2-D finite element analyses.

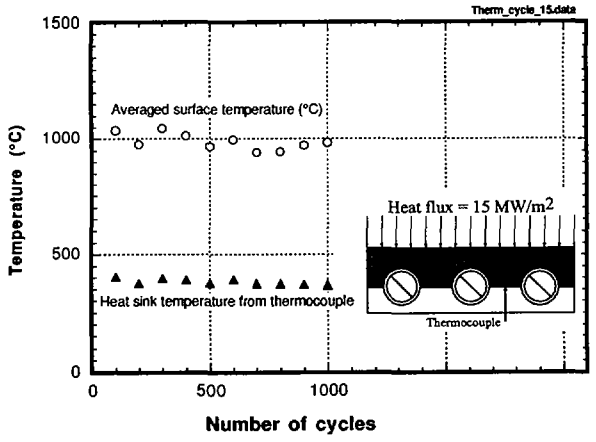

FIG. 3. Transition of averaged surface temperature and heat sink temperature through 1000 thermal cycles.

The heating duration of 15 s was again selected to obtain the thermal steady state of the mock-up. The heated area and the cooling conditions were the same as described above. Figure 3 shows the averaged surface temperature and the heat sink temperature at the end of the heating period for every 100 cycles. The surface temperature and the heat sink temperature were consistently around 1000°C and 400°C, respectively, through 1000 cycles. It is significant that these temperatures did not change in each cycle. The thermal performance of the mock-up was successfully demonstrated even at a low axial flow velocity of 4 m/s. The mock-up could withstand the heat flux of 15 MW/m^2 without any change of the thermal performance through 1000 cycles.

4. CONCLUSIONS

At a flow velocity of 4 m/s, which is lower than the ITER design (10 m/s), the saddle shaped divertor mock-up successfully proved its durability under cyclic thermal loads and demonstrated its thermal performance under the simulated ITER divertor thermal conditions. The results imply that the saddle shaped divertor structure could be one of the most promising divertor structures for the ITER divertor plates from the thermal hydraulic and thermal fatigue lifetime point of view.

On the basis of these successful experimental results, a full scale saddle shaped divertor mock-up, 1.5 m in length, with parallel cooling channels, will be developed for the integrity tests of the ITER divertor plates, which will be carried out in the United States of America in early 1998.

ACKNOWLEDGEMENTS

The authors would like to thank Y. Ohara and other staff of the JAERI NBI heating laboratory for valuable discussions and comments. They also express their gratitude to M. Ohta, S. Matsuda and S. Shimamoto for their support and encouragement.

REFERENCES

[1] CARDELLA, A., et al., "Design, manufacturing and thermo-mechanical testing of a relevant size monoblock divertor prototype", Fusion Technology 1994 (Proc. 18th Eur. Symp. Karlsruhe, 1994), Vol. 1, Elsevier, Amsterdam (1995) 283.

[2] YOUCHISON, D.L., et al., "Thermal fatigue testing of a diffusion-bonded beryllium divertor mock-up under ITER relevant conditions", ibid., p. 287.

[3] BARABASH, V.R., "Beryllium mock-ups development and ultrasonic testing for ITER divertor conditions", ibid., p. 307.

[4] SUZUKI, S., et al., in Proc. 12th Topical Mtg on the Technology of Fusion Energy, Reno, NV, 1996.

[5] SUZUKI, S., et al., "Development of the divertor plate at JAERI", Fusion Technology 1994 (Proc. 18th Eur. Symp. Karlsruhe, 1994), Vol. 1, Elsevier, Amsterdam (1995) 311.

[6] AKIBA, M., et al., "Thermal cycling experiments of monoblock divertor mock-ups for International Thermonuclear Experimental Reactor", High Heat Flux Engineering (KHOUNSARY, A.M., Ed.), SPIE, Bellingham, WA (1992) 300.

[7] NAKAMURA, K., et al., J. Nucl. Mater. **220–222** (1995) 890.

[8] LINKE, J., et al., "Evaluation of cooling concepts and specimen geometries for high heat flux tests on neutron irradiated divertor elements", Fusion Engineering and Design (Proc. 3rd Int. Symp. on Fusion Nuclear Technology, Los Angeles, 1994), Fusion Eng. Des. **28** (1994) 72.

[9] ARAKI, M., et al., Fusion Eng. Des. **19** (1992) 101.

[10] TANAKA, S., Rev. Sci. Instrum. **62** (1991) 3.

[11] ARAKI, M., et al., "Development and testing of divertor mock-ups for ITER/FER at JAERI", Fusion Technology 1992 (Proc. 17th Symp. Rome, 1992), Vol. 1, Elsevier, Amsterdam (1993) 166.

[12] Technical Basis for the ITER Interim Design Report, Cost Review and Safety Analysis, ITER EDA Documentation Series No. 7, IAEA, Vienna (1996).

SINGAP ACCELERATION OF HIGH ENERGY NEGATIVE ION BEAMS

P. MASSMANN, J. BUCALOSSI, D. CIRIC[1], C. DESGRANGES,
M. FUMELLI, J. PAMÉLA, A. SIMONIN
Association Euratom–CEA sur la Fusion,
Centre d'études de Cadarache,
Saint-Paul-lez-Durance, France

Abstract

SINGAP ACCELERATION OF HIGH ENERGY NEGATIVE ION BEAMS.

The objective of the Cadarache SINGAP experiment is to demonstrate the acceleration of a substantial D^- current (> 100 mA) in a simplified accelerator concept as an attractive alternative to the established ITER injector reference design. For the time being, most of the measurements have been done in hydrogen and without caesium in the ion source. Steady progress is being made which has led to H^- beams of up to 910 kV, 40 mA, 1.5 s. A special infrared diagnostic is applied for the first time to high energy negative ion beams, making use of the high thermal anisotropy of a uni-directional carbon fibre composite graphite target. Infrared imaging of the rear face of the target allows high resolution beam power density profiles to be derived by a simple temperature integration of the specific heat. On the basis of the positive results, application of the SINGAP scheme to the ITER injectors is proposed. Initial calculations show that encouraging beam qualities can be obtained. The main advantages expected are less negative ion stripping in the accelerator, cheaper power supplies and a simpler transmission line.

1. INTRODUCTION

For next step fusion devices neutral beam injection using the neutralisation of positive hydrogen ions does not make sense because of the steep decrease of the charge exchange cross sections with energy. Future neutral beam injectors will therefore be based on negative ions for which neutralisation rates up to 60% can be achieved with little sensitivity to energy by interaction with a gas target.

Compared to positive ions, the acceleration of negative ions is more complex as it requires special measures to suppress electrons, either co-extracted from the ion source or created by collisions with background gas (stripping) in the accelerator. Electron stripping has to be minimised as it can lead to excessive losses and high power loadings on the extraction and aceleration electrodes. To achieve this, a low pressure source and a good vacuum in the electrode gaps are essential. The SINGAP concept tries to minimise stripping in a system which is largely simplified compared to the multi-grid reference design of the ITER injectors.

The Cadarache 1 MV experiment was set up to validate the SINGAP scheme [1]. Operational experience and latest experimental results are reported elsewhere [2]. In this paper we concentrate on the properties of the SINGAP beams. In determining

[1] JET Joint Undertaking, Abingdon, Oxfordshire, UK.

these properties both the infrared calorimetry technique and the VF SCALA 3d computer code [3] are playing vital parts. Finally, we present first results regarding the integration of this concept into the ITER injector design.

2. EXPERIMENT

2.1. Apparatus

A detailed description of the apparatus is given in [4] and only a summary is given here. The negative ion beam is produced in an UHV tank of about 30 m^3. Different to many other injectors, the source is at earth potential and the SINGAP post-accelerator tube suspended from the centre conductor of an external insulator / bushing at nominally +1 MV.

Consistent with the 120 mA current capability of the high voltage power supply the plasma electrode of the ion source is masked down, leaving 12 circular apertures of 1 cm^2 for extraction in a quasi-circular array of 65 mm diameter. The 12 beamlets are extracted and pre-accelerated by a multi-aperture 3 electrode system with magnetic electron suppression. They are then post-accelerated across a gap of 630 mm whereby they are focused into a single circular SINGAP aperture of 80 mm diameter at the entrance of the post-accel tube. The focusing is an essential feature of SINGAP optics. It is achieved by modifying the pre-accel electrode originally designed to produce a ribbon shaped beam. To provide a near symmetric positive focusing lens a cylinder has been attached at the exit of the pre-accel electrode. The SINGAP "hyper" beamlet is finally dumped onto an inertial uni-directional graphite target closing the exit of the field free post-accel tube at 2630 mm from the exit of the pre-accel electrode.

2.2 Infrared Calorimetry

The technique applied is a variant of a diagnostic developed at JET [5]. To increase the diagnostic area the uni-directional carbon fibre composite (CFC) target used here is made of 2 plates, both of Mitsubishi MFC-1A [6] material. The plates are 90 mm wide, 190 mm high and 19 mm thick, mounted side by side with the superior thermal conductivity in the depth (beam direction). Because of the restricted transverse conductivity (about 20 times lower) errors due to sideways heat conduction are negligible up to a few seconds after a beam pulse.

Beam temperature footprints are measured with an Agema 782 SW infrared system [7] yielding a thermal image of 140 x 140 pixels. In our case the infrared camera views the rear face of the target at 2 m distance through a sapphire window. The temperature calibration is obtained by an identical component setup outside the vacuum tank where the target is heated with a welding torch. The infrared temperatures are calibrated against values from a thermocouple which can be inserted in the bulk of the target. The thermal MFC-1A properties have been measured for JET [8]. The specific heat values can be fitted with good accuracy by a double exponential.

A profile measurement requires two images for each shot, one just before (index 1) and a second one after the pulse (index 2) when the temperature wave form has come into equilibrium. The power density P [W/m^2] as a function of temperature

T [K] at the location of each pixel can then be obtained from a temperature integration of the specific heat c_p[J/kg/K]:

$$P = \frac{\rho d}{\tau}\int c_p dT = \frac{\rho d}{\tau}\{A_0(T_2 - T_1) + \frac{A_1}{B_1}[\exp(B_1 T_2) - \exp(B_1 T_1)] + \frac{A_2}{B_2}[\exp(B_2 T_2) - \exp(B_2 T_1)]\} \quad (1)$$

where ρ[kg/m^3] is the density, d[m] the target thickness, τ[s] the pulse length and A_0, A_1, B_1, B_2 are constants. Beam profiles are calculated by a computer code using equ. (1) for each pixel and stored in a file which can be plotted by commercial software. The total power intercepted by the target is obtained by spatial integration of the profile. The error in the power density measurement is estimated at ±10%.

3. RESULTS

A 3d representation of beam profiles for 2 different beam energies is given in Fig. 1. Unfortunately, an electrical measurement of the drain current can only give a rough estimate of the accelerated H^- current because the drain current also contains the dark current, i.e. electrons emitted from surrounding surfaces at earth potential. The dark current depends on the accel voltage, the background pressure and the state of conditioning. This dependence is only known without beam present, e.g. at typical operating pressures of 10^{-5} mbar dropping to zero below 300 kV.

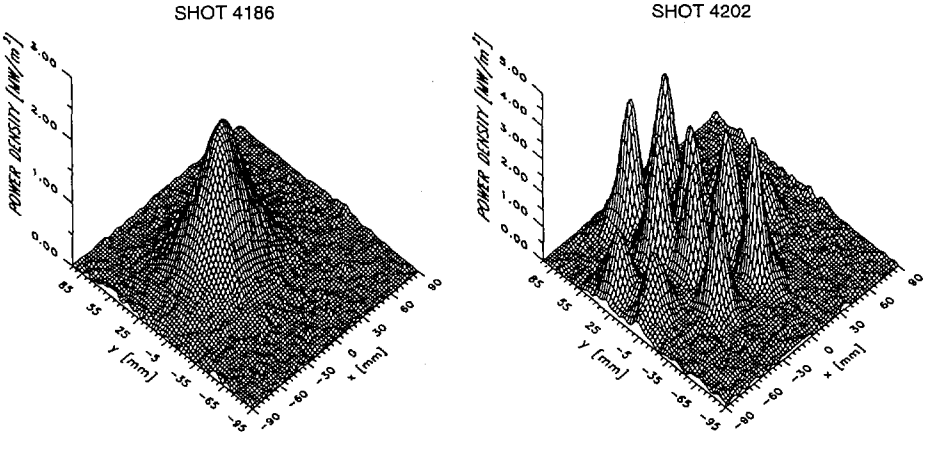

FIG. 1. Power density profiles of H^- beams. Shot 4186: energy 418 keV, intercepted current 21 mA, pulse length 1.10 s, integrated power 8.9 kW; shot 4202: energy 728 keV, intercepted current 27 mA, pulse length 1.09 s, integrated power 20.0 kW.

However, from Fig. 1 it can be seen that the beam is entirely intercepted by the target and the beam current should be close to the intercepted current derived from the integrated target power. By applying a vertical magnetic field of a few Gauss along the beam path it has been shown that the electron content is indeed negligible. Additionally, the post-accel voltage has been applied using a helium discharge in the source (thus no negative ions) yielding an accelerated electron fraction below 0.5% .

The Gauss fits through the midplanes of the 4186 beam profile show a slight misalignment by about 4 mrad to the right (viewed with the beam) and by 6 mrad upward. Comparing the profile width with the initial beam cross section at the pre-accelerator exit it follows that the beam footprint at 2.63 m has nearly the same size as the initial quasi-circle of 65 mm diameter. The slight expansion in horizontal and compression in vertical direction is due to an imperfection in the cylinder symmetry of the pre-accel lens system (Fig. 2).

If the accel voltage is gradually increased, keeping the other parameters constant, the near Gaussian profile of pulse 4186 gets larger, develops discrete structures and finally splits up into individual beamlets as in shot 4202. Such a behaviour has been predicted by 3d trajectory calculations and has been verified experimentally which is shown in Fig. 3. This effect is caused by 2 effects, the decreasing influence of space charge and a growing strength of the positive lens with increasing energy. The consequence is, for energies high enough, that the lens transforms the pre-accel object plane into an inverse geometric image of about twice the size. The horizontal displacement of the beamlets found in the measurement is due to the electron suppression magnets of the extraction electrode. These have not been included in the simulation.

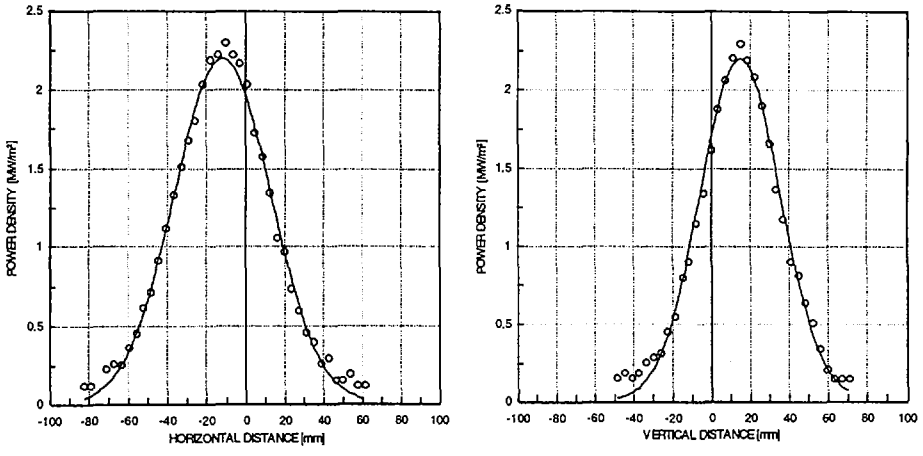

FIG. 2. Gauss fits through the midplanes of the shot 4186 beam profile. Horizontal: centre −12 mm, 1/e half-width 35 mm; vertical: centre 15 mm, 1/e half-width 29 mm.

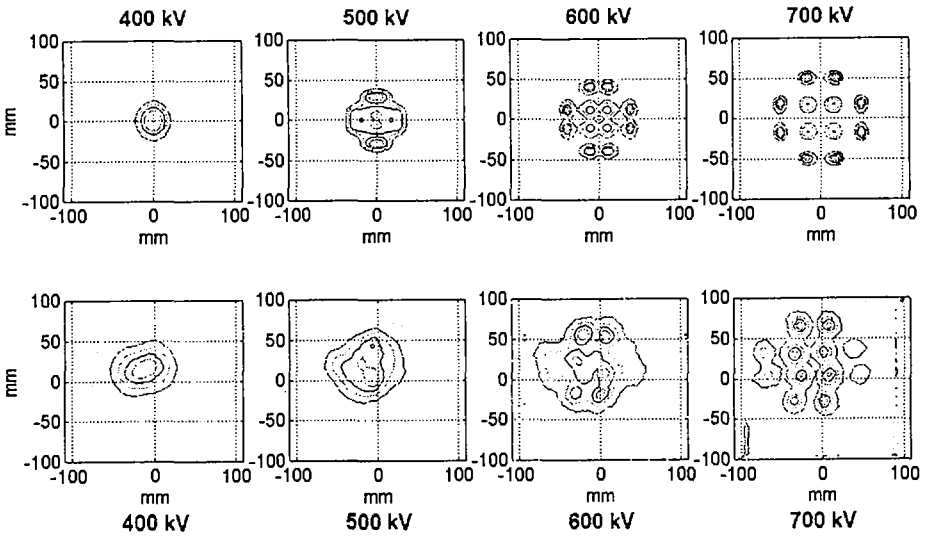

FIG. 3. Predicted and measured H^- beam contours for varied energy. The beam current is kept constant at 30 mA.

Until now beams up to 60 mA accelerated current have been generated which still were entirely intercepted by the target, resulting in peak power densities of about 10 MW/m^2. For a 1 MV, 120 mA D^- beam of optimum quality it follows from the 3d simulations (evaluating the space charge and lens effect) that the post-accel gap needs to be increased to about 900 mm. The predicted peak power density is about 60 MW/m^2.

4. INTEGRATION OF "SINGAP" INTO THE "ITER" INJECTORS

The reference design of the ITER N-NBI modules [9] uses multi-aperture, multi-gap electrostatic extraction and acceleration. Negative ions are extracted from the plasma source (at -1 MV potential) at energies up to 10 keV by a 2 electrode system with electron suppression. Subsequent acceleration is achieved in steps of 200 kV by 5 multi-aperture electrodes. The electrodes are composed of an array of 5 x 5 rectangular grid sections each with 52 circular apertures. As pumping of the gaps is limited by the conductance through the apertures the pressure profile in the elctrode stack gets more unfavourable the more electrodes are employed [10]. An additional limitation of the conductance is given by the 1 MV cylindrical insulator which surrounds the whole of the electrode system.

Implanting the proposed concept into the ITER injector configuration 25 SINGAP rectangular apertures are chosen rather than one, thus merging the 4 x 13 pre-accelerated beamlets of each grid section into one "hyper" beamlet. Adequate spacing between the SINGAP apertures could provide the amount of beam steering required. Finally, to

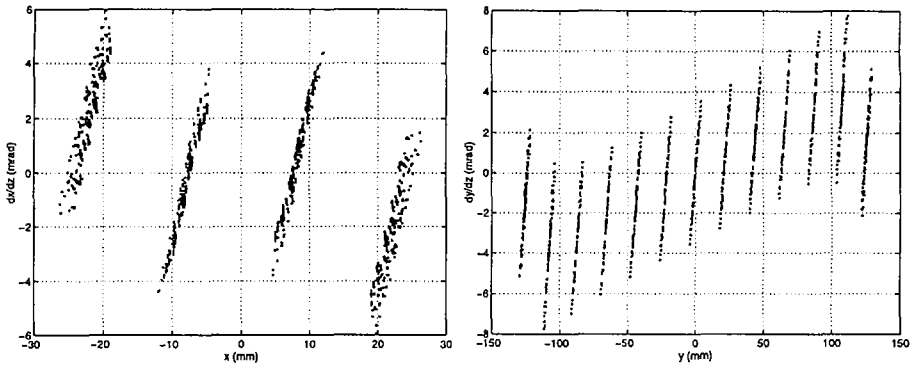

FIG. 4. Emittance of an ITER SINGAP "hyper" beamlet. Left: horizontal, divergence 3 mrad (rms); right: vertical, divergence 4 mrad (rms). Pre-accel conditions: 50 kV, 20 mA/cm^2 D$^-$, divergence 8 mrad (rms), post-accel gap 350 mm.

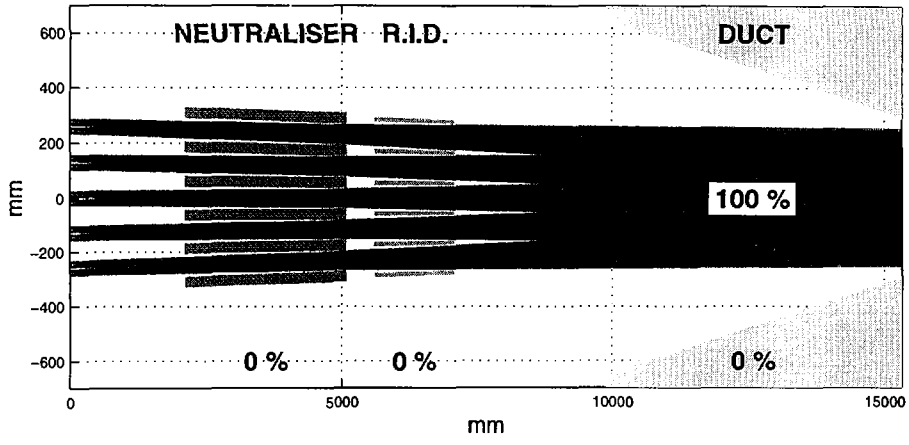

FIG. 5. Plan view of calculated trajectories along the ITER beam line. Steering: 8 mrad for the outer "hyper" beamlets and 4 mrad for the next inner ones.

take full advantage of an improved gas conductance, it is proposed to replace the internal insulator of the reference design by an external 1 MV insulator / bushing from which the ion source / pre-accel system could be suspended [11].

Trajectory simulations of an ITER SINGAP injector have been started recently with the SCALA 3d code. A first and not yet optimised example of the achievable beam quality is given in Fig. 4. Shown are the horizontal and vertical emittances of a 1 MV "hyper" beamlet emerging from the SINGAP centre aperture. With a post-accel gap of 350 mm the SINGAP electrode is about at the same location as the ground electrode of the reference design. The positive lens effect is created by a kerb along the edge of the pre-accel grid section.

A plan view of trajectories along the ITER beamline is shown in Fig. 5. The conditions are the same as for Fig.4, except that the "hyper" beamlets have been steered by displacement of the SINGAP apertures, i.e. ±9 mm for the outer beamlets and ±4.5 mm for the next inner ones. The mutual influence between the beamlets due to space charge has been taken into account. The calculated beam transmission is 100% with no direct losses on the neutraliser, residual ion dump (RID) or duct.

5. CONCLUSION

It has been shown experimentally and by simulation that the SINGAP concept can produce negative ion beams of remarkable quality. The beam transmission measured at still comparatively low current densities around 5 mA/cm^2 is close to 100%.

Thanks to the high spatial resolution of the novel infrared calorimetry technique the predicted lens and space charge effect on beams of varying energy could be verified, yielding quite satisfactory agreement between experiment and simulation.

Using the obtained results we have started to implant the SINGAP scheme into the ITER injector configuration. First results of simulations are promising and suggest that an excellent beam transmission can also be obtained under ITER conditions.

It should be noted that the "SINGAP" concept, despite its simplicity, is quite flexible and not limited to a single aperture - single gap. A second post-accel electrode (double gap) and merging less multi-beamlets into one or more SINGAP apertures is conceivable, e.g. for beams of higher current densities or at lower energies.

ACKNOWLEDGEMENTS

The invaluable contribution of G. Delogu, S. Dutheil, P. Heister, P. Vancoillie and R. Yattou to the experiment is greatly acknowledged.

REFERENCES

[1] FUMELLI, M. et al., 6th Int. Symp. Prod. and Neut. of Negative Ions, Brookhaven, NY, 1992
[2] BUCALOSSI, J. et al., 19th SOFT, Lisbon, Portugal, 16 - 20 Sept. 1996
[3] SIMKIN, J., Vector Fields Ltd, 24 Bankside, Kidlington OX5-1JE, U.K.
[4] MASSMANN, P., 16th SOFE, Champaign, Il., USA, 1995
[5] CIRIC, D. et al. 18th SOFT, Karlsruhe, Germany, Sept. 1994
[6] MITSUBISHI - KASEI Corporation, Tokyo, Japan
[7] AGEMA Infrared Systems, Danderyd, Sweden
[8] CIRIC, D., JET, Abingdon OX14-3EA, U.K., private communication
[9] DI PIETRO, E. et al., F1-CN-64/FP-18, this conference, 1996
[10] SIMONIN, A. et al., 19th SOFT, Lisbon, Portugal, 16 - 20 Sept. 1996
[11] MASSMANN, P., ITER NBI R&D and Design Review Meeting, Cadarache, France, 1996

THE IGNITOR EXPERIMENT AND ITS PERSPECTIVES*

B. COPPI[1], A. AIROLDI[2], F. BOMBARDA,
F. CARPIGNANO, G. CENACCHI, W. DAUGHTON[1],
P. DETRAGIACHE, C. FERRO, M. GASPAROTTO,
M. HAEGI, L. LANZAVECCHIA, R. MAGGIORA[3],
G.M. McCRACKEN[4], S. MIGLIUOLO[1], A. PIZZUTO,
M. RICCITELLI[3], M. ROCCELLA, J.A. SNIPES[1],
L.E. SUGIYAMA[1], G. VECCHI[3],
IGNITOR PROJECT GROUP
ENEA, Italy

Abstract

THE IGNITOR EXPERIMENT AND ITS PERSPECTIVES.

The goal of ignition is shown to be possible at present by means of high field, high density compact experiments such as Ignitor. The conclusions of studies on relevant physics issues such as plasma stability against large scale internal modes, time dependent simulations of the approach to ignition conditions, as well as transport and confinement, are reported. The results of experiments carried out by the Alcator C-Mod machine, which can operate in regimes with global parameters similar to those expected for Ignitor, are discussed. From the observations of the confinement characteristics in these experiments and theoretical considerations, a composite transport coefficient for the electron thermal energy that features a thermal energy inflow component degrading with the heating power has been identified. This reproduces the experimentally measured confinement times for both ohmic and RF heated L-mode discharges. Extrapolations to Ignitor based on these findings are quite favourable. Recent developments in the machine design include the optimization of the currents in the different coils of the Poloidal Field System, the introduction of a horizontal electromagnetic press and in depth analyses of the antenna coupling properties for the ICRF auxiliary heating system and of the relevant heating scenarios. The construction of prototypes of all the main machine components has been completed, and the present new phase of construction is described.

1. INTRODUCTION

Reaching ignition is the primary goal of fusion research at this time. The validity of the Ignitor approach is affirmed by the recognition that "the initial model (experiment) need not resemble the one that is later commercialized" [1]: achievement of ignition and exploration of burning plasma physics are the main purposes of this experiment. Ohmic heating, which is associated with the best energy

* Work supported in part by ENEA and CNR of Italy, and by the US Department of Energy.

[1] Massachusetts Institute of Technology, Cambridge, Massachusetts, USA.
[2] Istituto di Fisica del Plasma-CNR, Milan, Italy.
[3] Politecnico di Torino, Turin, Italy.
[4] Present address: JET Joint Undertaking, Abingdon, Oxfordshire, UK.

confinement properties, is exploited to the maximum extent to reach D-T burn conditions, while the ICRF heating system has the (auxiliary) functions of accelerating the ignition process and controlling the current density distribution. Ignition is expected to be reached with high densities ($n_0 \simeq 10^{21}$ m^{-3}) and relatively low temperatures ($T_{e0} \simeq T_{i0} \gtrsim 12$ keV) [2], at the end of the current ramp, when the still diffusing current density profile allows a significant ohmic heating rate at the edge of the plasma column. The burning phase is planned to last until the toroidal field is ramped down to end the discharge, some 200 times longer than the α-particle slowing down time, and to involve approximately 20 MW of α-particle heating. A good degree of confinement can be expected, given the relatively high current (limited by a minimum desirable value of $q_a \simeq 3.3$), which keeps the poloidal β_p sufficiently low for the plasma to be stable [3] against large scale internal modes.

2. THE IGNITOR-ULT DESIGN AND PRESENT STATUS

Ignitor is the natural development in the line of high magnetic field, high density experiments represented by the Alcator machines built at M.I.T., and the FT machines at Frascati. Its main characteristics are a toroidal field $B_T \lesssim 13$ T, a plasma current $I_p \lesssim 12$ MA with a high current density, tight aspect ratio, and considerable elongation and triangularity (major radius $R_0 \simeq 1.32$ m, minor radii $a \times b \simeq 0.47 \times 0.86$ m^2, triangularity $\delta \simeq 0.4$). Given the high ratio B_T/R_0, peak electron densities $n_0 \simeq 10^{21}$ m^{-3} can be supported in the ohmically heated plasma (this value has repeatedly been obtained in the Alcator C and C-Mod devices with pellet injection). The low value of the poloidal β ($\beta_P \simeq 0.25$) also implies that a significant poloidal current, $I_\theta \lesssim 9$ MA, is produced, which can contribute up to 1.4 T to the toroidal field on axis.

Supercooled, normal conducting magnets have been adopted. An initial temperature of 30 K (obtained using He gas cooling) and relatively low current densities in the magnets allow plasma lifetimes relatively long compared to the intrinsic plasma time scales. A careful optimization of the Poloidal Field Coil (PFC) system has resulted in increased average plasma current and/or flat-top duration for all the reference scenarios of operation. The flux capability of the PFC has been raised to 37 V-s to match the flux requirements, without considering the positive contributions of the bootstrap current and ICRF heating. These correspond to a

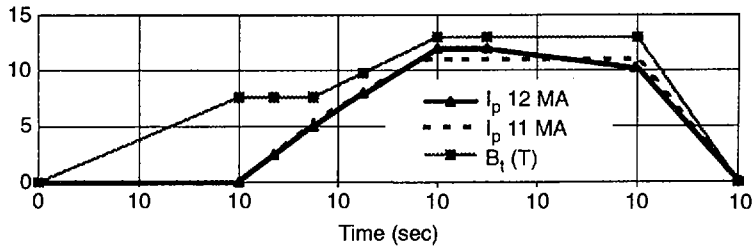

FIG. 1. Toroidal field and plasma current time evolution for the 12 and 11 MA scenarios.

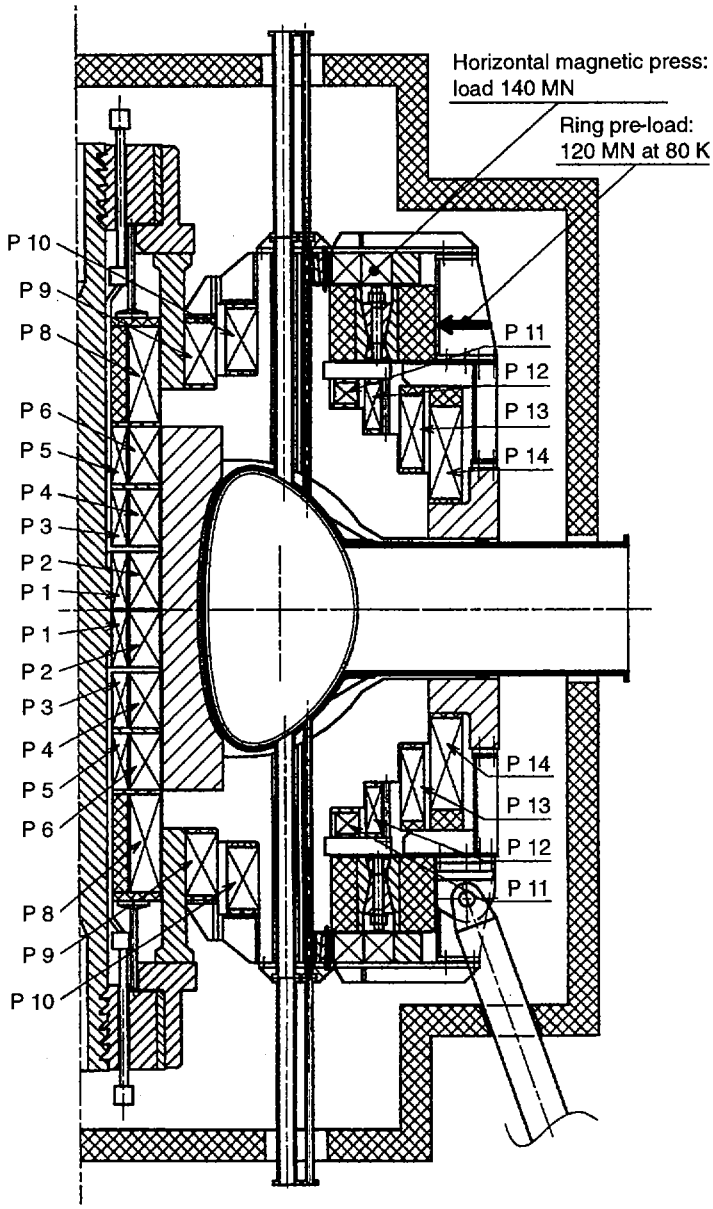

FIG. 2. Cross-section of the Ignitor machine, including the horizontal magnetic press. The poloidal field coils are labelled P1 to P6 and P8 to P14.

saving of about 2.5 and 3 V-s respectively. The time evolution of the plasma current and toroidal field are shown in Fig. 1 for two reference ignition scenarios (at 12 and 11 MA). For the highest parameter scenario, the current is decreased from 12 to 10 MA after 1 sec, for the purpose of increasing the edge q and controlling the current density profile, while the plasma remains in ignited conditions.

The structural performance of the machine relies on an optimized combination of "bucking" between the toroidal field (TF) coils, and the central solenoid and central post, and "wedging" of the magnet and the surrounding C-clamps. The TF coils are pre-stressed through the C-clamps by two bracing rings, applying a load of 120 MN, and a horizontal electromagnetic press (140 MN), as shown in Fig. 2. This press has been introduced recently, replacing the original vertical one, with several favorable consequences for the machine operation, the primary being that of simpler maintenance.

In order to extend the operating scenarios, an ICRH system capable of delivering ~18 MW at frequencies $f \leq 140$ MHz has been incorporated in the machine design. This will allow ^{3}He minority heating at full field and H minority heating at lower fields. The antennas will be housed in six of the twelve horizontal ports of the plasma chamber. It will be used to accelerate the approach to burn condition at full current, to control the evolution of the current density, to produce significant power from D-^{3}He reactions, and to access the high-β second stability region at relatively low values of B_T. Furthermore, this heating system gives the possibility to attain ignition in high-q_ψ regimes, like reversed shear, where the plasma current cannot provide adequate ohmic heating [4]. Extensive calculations of the 4-strap antenna coupling properties have been carried out by 3-D codes, originally developed at ORNL. Simulations have been performed, most recently, using codes available at PPPL (CARDS, SHOOT, METS95), taking into account the effects of collisions, to study the dependence of the absorbed power by the plasma species for all the operational scenarios.

The good impurity screening properties of high density plasmas have been verified many times, most recently, on the FTU [5] and Alcator C-Mod devices [6], for both limiter and divertor configurations. The estimated edge values of the density, n_a, and the temperature, T_a, in Ignitor, based on both empirical scaling and global particle and energy balance considerations, are $n_a \simeq 2 \times 10^{20}$ m^{-3} and $T_a \simeq 15 - 40$ eV [7,8]; the average surface power load is also expected to be relatively low (~ 0.5 MW/m^2), with peak loads estimated around 1.35 MW/m^2. These and other considerations have led to the decision to not include a divertor in the Ignitor design, thus avoiding a considerable degradation of the machine performance. The choice of the first wall material has been decided in favor of a high-Z metal, molybdenum, for which very supportive results have been produced by the Alcator C-Mod experiment.

A consortium of industrial groups, Ansaldo, FIAT and ABB, has carried out the detailed engineering design of the Ignitor machine, under the sponsorship of ENEA. The site chosen for the experiment is associated with one of the existing ENEA research centers and is located at Saluggia (Piedmont). Full size prototypes of all the main components of the machine have been constructed. These include one sector (1/12th) of the plasma chamber, including a major access port (Fig. 3a), one full module of the toroidal magnet (Fig. 3b), one C-clamp (the main structural

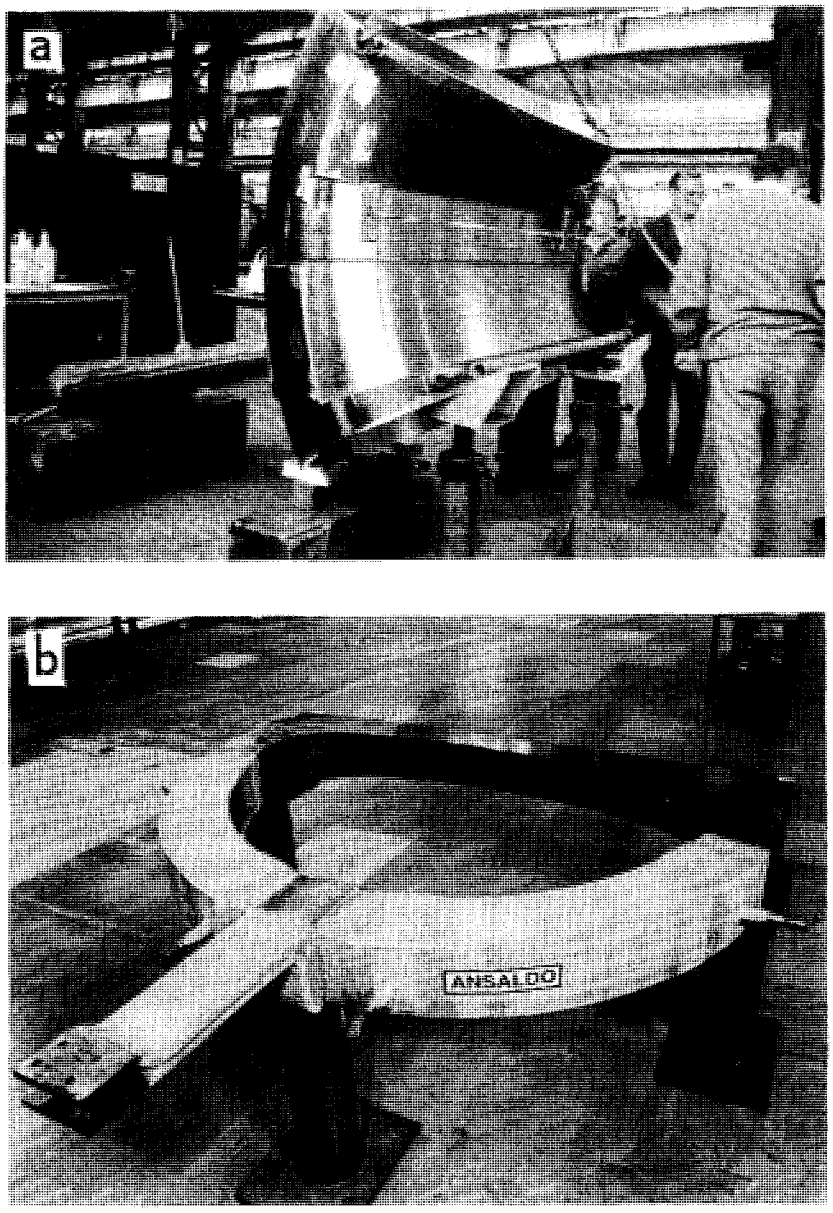

FIG. 3. (a) One sector of vacuum vessel; (b) toroidal field coil prototype.

element outside the toroidal field coil), the innermost element of the central solenoid, and a section of the machine's wedge tensioning system. The construction of the complete central solenoid system, of the central post, of an entire section ($1/12^{th}$) of the machine, including a fully tiled sector of the plasma chamber, and their assembly, have been funded.

3. RELEVANCE OF RESULTS FROM EXISTING EXPERIMENTS

Both the Alcator C-Mod machine at M.I.T. and the FTU machine at Frascati are designed to operate at $B_T \sim 8$ T and densities $n_e \leq 10^{21}$ m^{-3} (with pellet fueling). FTU is a machine with a circular plasma cross section, employing a limiter and having considerably lower current densities and poloidal fields than Alcator C-Mod, which has an elongated cross section, a smaller major radius, and a divertor. Alcator C-Mod is particularly significant for Ignitor, as some of its parameters have already achieved the design values envisaged for Ignitor, such as peak plasma current density, electron density and elongation. It is the first experiment to prove the effectiveness of ICRF heating in a high density plasma and its thermal energy confinement properties show a very encouraging positive dependence on the plasma current, for Maxwellian plasmas similar to those expected in Ignitor.

Both the analysis of experiments covering a relatively wide range of parameters carried out by the Alcator C-Mod machine and theoretical considerations have led us to identify a new composite transport coefficient for the electron thermal energy. This consists of two terms [9]: one producing outflow of thermal energy, and one, inflow. The latter term has the same form as that of the so called CMG diffusion coefficient [10] that has been found to reproduce the results of ohmic heating experiments. The present transport coefficient, D_e^{th}, applies both to ohmic and RF heating regimes and produces the degradation of the energy confinement time as a function of additional heating power as a consequence of the reduction of thermal energy inflow. In cylindrical geometry D_e^{th} can be written as

$$D_e^{th} \cong \mathcal{V}_0 I(r^2) \frac{a^2}{r^2} \frac{1}{8\pi^2 n(r) T_e(r)} \frac{1}{R_0} \mathcal{F}_D \tag{1}$$

where

$$\mathcal{F}_D = \begin{cases} 2C_1 \left(\dfrac{5\beta_{p*}}{q_E^{2/3}} \right) - 1 & \text{for} \quad \left(\dfrac{5\beta_{p*}}{q_E^{2/3}} \right) > \dfrac{1}{C_1} \\ 1 & \text{for} \quad \left(\dfrac{5\beta_{p*}}{q_E^{2/3}} \right) < \dfrac{1}{C_1} \end{cases}$$

$$\mathcal{V}_0 = \alpha_v \frac{T_e}{e} \left(\omega_{pi} \frac{c^2}{\omega_{pe}^2} \frac{\nu_e}{v_{the}^2} \right)^{2/5}$$

Here α_v and C_1 are finite numerical coefficients and $\mathcal{V}_0$ is a characteristic voltage (typically, $\mathcal{V}_0 \approx 0.25$ for Alcator C-Mod). In addition, a is the radius of the plasma column, $\beta_{p*} = 2\mu_0 p_{e*}/B_p^2$, $p_{e*} = -(r(dp_e/dr))_{r=r_*}$, $r = r_*$ being the surface where $|dp_e/dr|$ is maximum, $q_E = 2\pi a^2 B_T/(\mu_0 I_p R_0)$, $I(r)$ is the toroidal current within the surface of radius r and I_p is the total plasma current. This is consistent with the following scaling:

$$\frac{P_H}{I_p \mathcal{V}_0} \cong 15.2\left(\frac{5\beta_p}{q_E^{a\,2/3}}\right) - 4.8 \tag{2}$$

that is a good fit of the experimental results as indicated in Fig. 4. Here, $\beta_p = 2\mu_0 [p]/\langle B_p^2 \rangle$, [] represents a volume average, $\langle\rangle$ represents a surface average, and $q_E{}^a \equiv 2\pi a^2 B_T/(\mu_0 I_p R_0)$ where now a indicates the horizontal minor radius. The scaling of the relevant energy confinement time (see Appendix A) following from Eq. (2) is

$$\tau_E \propto I_p q_E^{a\,2/3}\left(1 + 4.8\frac{I_p \mathcal{V}_0}{P_H} f_1\right) f_2 \tag{3}$$

where f_1 and f_2 are functions mainly of the geometrical parameters a, R_0, and κ such that $f_1 = f_2 = 1$ for $a = 0.2$ m, $R_0 = 0.67$ m, and $\kappa = 1.6$, the typical values of the considered Alcator C-Mod plasmas. The functions f may also contain weaker

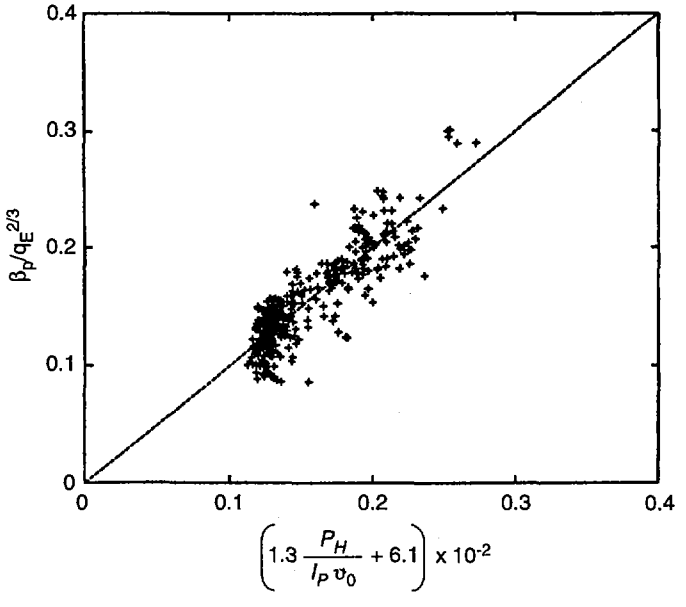

FIG. 4. Fit of Alcator C-Mod experimental data to the scaling given by Eq. (2).

dependences on other plasma parameters, like for example density and ion mass. For ohmic discharges, $\beta_p/q_E^{a\,2/3}$ is approximately constant, forcing many points in Fig. 4 to be grouped. For example, the most extreme point at 1.5 MA on the W_{MHD} diagram of Fig. 1A and 2A falls in the cluster of points around $\beta_p/q_E^{a\,2/3} \approx 0.2$ in Fig. 4.

The expression for D_e^{th} in generalized geometry is

$$D_e^{th} \cong \alpha_v \left(\omega_{pi} \frac{c^2}{\omega_{pe}^2} \frac{\nu_e}{v_{the}^2} \right)^{2/5} \frac{I(\psi)}{en(\psi)} \frac{V_a}{\langle |\nabla V|^2 \rangle} \left\langle \frac{Z_*}{A_i} \right\rangle^{1/2} \mathcal{F}_D \qquad (4)$$

where

$$\mathcal{F}_D = 2C_1 \left(\frac{5\beta_{p*}}{q_E^{a\,2/3}} \right) - 1 \quad \text{or} \quad \mathcal{F}_D = 1 \qquad (5)$$

and ψ indicates the magnetic surface, V_a is the total plasma volume, V is the volume enclosed by the surface ψ, and the dimensionless quantity $(\,)^{2/5}$ in (4) is evaluated as a function of ψ. The ratio $\langle Z_*/A_i \rangle^{1/2}$ is introduced to account for the isotopic effect and $Z_* = A_i \sum_j (n_j Z_j^2)/(n_e A_j)$ is a measure of the degree of plasma purity. The definition of β_{p*} is extended to general geometry as $\beta_{p*} = 2\mu_0\, p_{e*}\, /\langle B_p^2 \rangle$, and $p_{e*} = -((dp_e/d\psi)\langle |\nabla\psi| \rangle)_{max} r_*$, where r_* is the horizontal half-width of the surface of maximum pressure gradient. The values of α_v and C_1 evaluated from detailed numerical simulations of actual discharges are $\alpha_v \approx 0.045$, and $C_1 \approx 1.6$.

It is evident that the expected confinement in Ignitor on the basis of the derived scaling for τ_E is quite favorable. The possibility for Ignitor to access the H-mode regime is being considered in the light of the most recent analyses of the threshold power. According to these, the available power in Ignitor (including ICRH) is likely to be insufficient or marginally sufficient at full parameters. It becomes possible to access the H-mode during the density and toroidal field ramp up phase, or in lower parameter scenarios. A better understanding of the H-mode threshold hysteresis is required to estimate how close to ignition Ignitor can come while in the H-mode. An analysis of the approach to ignition with the broader density profiles that characterize the H-mode is also needed.

4. SIMULATIONS, STABILITY

The dynamic nature of the path to ignition in Ignitor requires that simulations based on complex time evolution codes to be used. The results obtained with the TSC code [2], showing that ignition could be reached for the plasma parameters mentioned above, have recently been confirmed by a new analysis of the plasma evolution during the current ramp-up and the flattop phase. An updated version of the free boundary 1 1/2 D code JETTO [11] has been employed. The nominal parameters of the 12 MA scenario of Fig. 1 have been considered in a set of simulations, starting at $t = 0.3$ sec where I_p is grown from 1 to 12 MA while B_T varies from 7.6 to 13 T. The values of the density are always much lower than the

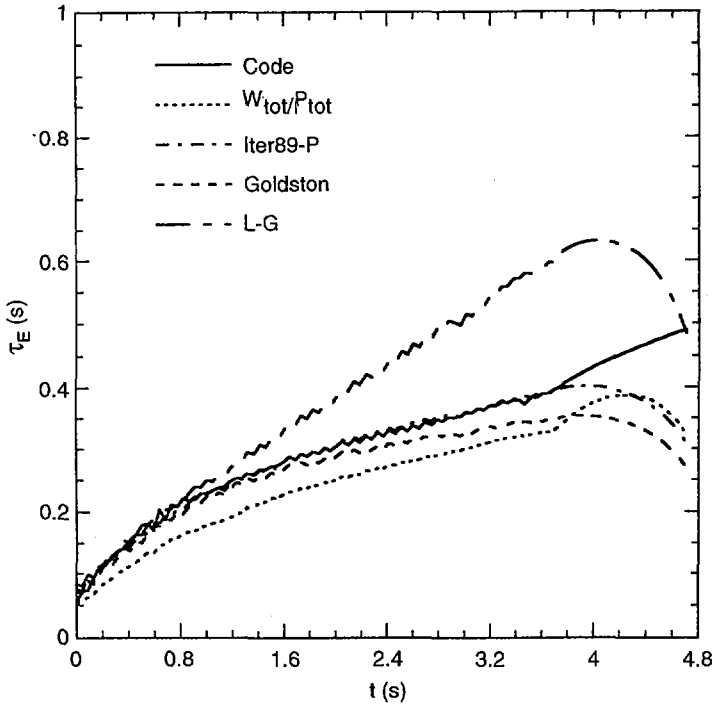

FIG. 5. Energy confinement times (in seconds) for a representative simulation. Full line: $\tau_E = W_{tot}/(P_{tot} - dW_{tot}/dt)$; dotted line: $\tau_E = W_{tot}/P_{tot}$. The other lines correspond to the ITER89-P, Goldston and Lackner-Gottardi scalings. The total power P_{tot} is the sum of ohmic and alpha powers. The simulation ends when ignition is attained.

Greenwald limit and the avoidance of the empirical disruption boundaries in the (l_i, q_ψ) diagram can be assured. The results confirm that, assuming transport coefficients close to "L-mode", ignition can be reached during the flattop when the impurity content assures a [Z_{eff}] lower than 1.5 (Fig. 5). It should be noted that Ignitor is optimized to attain ignition in the low temperature area of the relevant Lawson-type diagram [12] and that there is a relatively large region in parameter space when a central ignited core is present even when global ignition is not achieved.

Ignitor is, by design, a low-β_p device and so it has a high degree of immunity against pressure-driven internal modes, such as the macroscopic $n = m = 1$ internal mode and the high nq ballooning modes. We have carried out a study of the linear stability of Ignitor equilibrium configurations, under the approximation of ideal-MHD. Specifically, we have considered situations with $\beta \leq 1.7$ % (where $\beta \equiv 8\pi\langle p\rangle / B^2$ involves the volume average of the plasma pressure and 1.7 % corresponds to the design value at ignition), where the pressure and q profiles are of the same form as

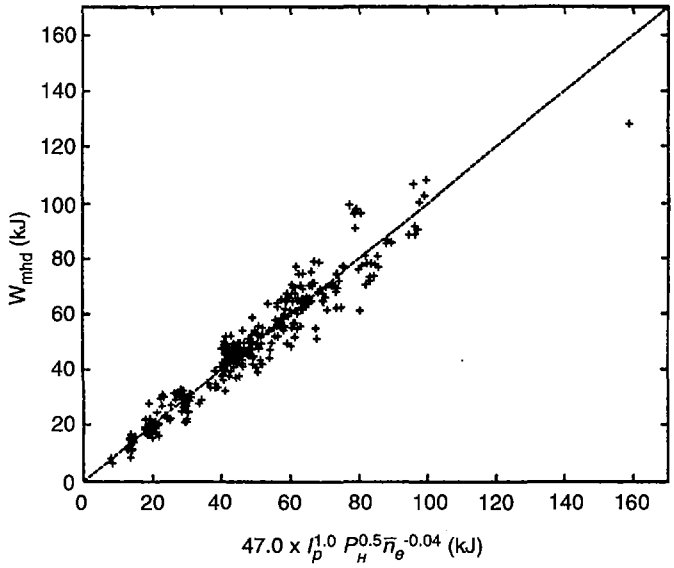

FIG. 6. Power law scaling of Alcator C-Mod discharge, where I_p is the plasma current in MA, P_H the total heating power in MW, and $\bar{n}_e \times 10^{20}$ the line average electron density in m^{-3}.

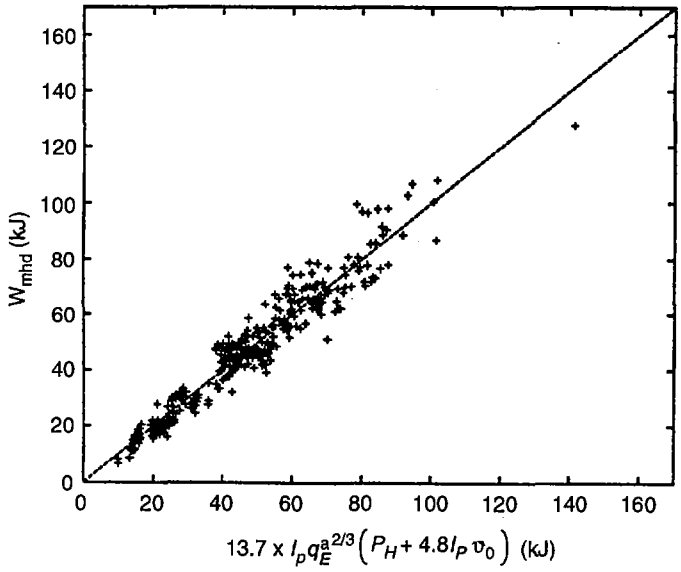

FIG. 7. Scaling consistent with Eq. (2). Units are the same as in Fig. 6.

those adopted to analyze corresponding discharges produced by Alcator C-Mod. In particular we take $q_\psi \simeq 3.6$, corresponding to $I_P \simeq 11$ MA in Ignitor, and q_0 varying between 0.85 to 1. The numerical stability analysis that has been carried out by the PEST-1 [13] and DCON [14] codes clearly indicates that $n= 1$ and short wavelength ballooning modes are not unstable for these low values of β. The issue of modes involving magnetic reconnection is a subject of current investigation based on the results of the Alcator C-Mod experiments [3].

Appendix A

It is considered more meaningful to find a scaling relating relevant dimensionless quantities as in the case of Eq. (2) rather than a scaling for a dimensional quantity such as the plasma stored energy. Such dimensional scalings can be quite different and still appear to be consistent with the data. Figures 6 and 7 show a comparison of two scalings for the stored energy of Alcator C-Mod L-mode discharges. The first was obtained from a power law regression while the second is the result of Eq. (2).

ACKNOWLEDGEMENTS

This work is supported primarily by the ENEA of Italy, and in part by the CNR of Italy and the US Department of Energy. The sponsorship of ASP of Piedmont and of the Politecnico di Torino is also acknowledged. Special thanks are due to our experimental colleagues for providing the data of Alcator C-Mod.

REFERENCES

[1] PCAST Report of the Fusion Review Panel, Publ. O.S.T.P., White House (1995).
[2] COPPI, B., NASSI, M., SUGIYAMA, L.E., Phys. Scr. **45** (1992) 112.
[3] COPPI, B., et al., IAEA-CN-64/D2-1, these Proceedings, Vol. 2, p. 397.
[4] SUGIYAMA, L.E., Reversed Shear Ignition in High Toroidal Field Experiments, Rep. PTP-95/3, MIT Research Laboratory of Electronics, Cambridge, MA, USA (1995).
[5] BARTIROMO, R., et al., J. Nucl. Mater. **220–222** (1995) 571.
[6] McCRACKEN, G.M., et al., in Plasma-Surface Interactions in Controlled Fusion Devices (Proc. 12th Int. Conf. St. Raphaël, France, 1996), J. Nucl. Mater. (in press).
[7] FERRO, C., ZANINO, R., J. Nucl. Mater. **176–177** (1990) 543.
[8] McCRACKEN, G.M., Plasma Physics Laboratory, Princeton University, personal communication, 1996.
[9] COPPI, B., PEGORARO, F., Phys. Fluids **B** (1991) 2583.
[10] COPPI, B., MAZZUCATO, E., Phys. Lett., Sect. A **71** (1979) 337.
[11] AIROLDI, A., CENACCHI, G., Fusion Technol. **25** (1994) 276.
[12] LAWSON, J.D., Proc. Phys. Soc., Sect. B **70** (1957) 6.
[13] GRIMM, R.C., DEWAR, R.L., MANICKAM, J., J. Comput. Phys. **4** (1983) 94.
[14] GLASSER, A.H., Phys. Plasmas (in press).

BASIC PROPERTIES OF THE GLOBUS-M SPHERICAL TOKAMAK PROJECT

V.E. GOLANT, V.K. GUSEV, V.V. D'YACHENKO,
M.A. IRZAK, V.B. MINAEV, A.N. NOVOKHATSKIJ,
K.A. PODUSHNIKOVA, A.Yu. POPOV, N.V. SAKHAROV,
O.N. SCHERBININ, K.G. SHAKHOVETS, V.S. UZLOV
A.F. Ioffe Institute,
St. Petersburg

V.A. BELYAKOV, A.A. KAVIN, V.A. KOROTKOV,
Yu.A. KOSTSOV, E.G. KUZMIN, I.A. MIRONOV, V.F. SOIKIN
D.V. Efremov Institute, Metallostroy,
St. Petersburg

E.A. AZIZOV, E.A. KUZNETSOV, V.A. YAGNOV
TRINITI,
Troitsk

N.Ya. DVORKIN, G.P. GARDYMOV, V.V. MIKOV
Northern Plant,
St. Petersburg

A.R. POLEVOJ, S.V. TSAUN
Russian Research Center, Kurchatov Institute,
Moscow

Russian Federation

Abstract

BASIC PROPERTIES OF THE GLOBUS-M SPHERICAL TOKAMAK PROJECT.

Physical background, expected plasma parameters and design principles, together with the current status of the GLOBUS-M tokamak project, are presented. GLOBUS-M is a spherical tokamak now under construction at the A.F. Ioffe Institute. The experimental programme is briefly outlined. The expected plasma parameters are estimated by using the ASTRA transport code. A novel approach to plasma auxiliary heating, with a high harmonics fast wave within the frequency range of 30 to 50 MHz and RF current drive, is described. The methods of plasma positioning and automatic feedback shape control are described. The machine design is outlined.

1. INTRODUCTION

The principal factor determining the high performance of spherical tokamak plasmas is, inherently, the current for the given toroidal field, which is higher than that of conventional aspect ratio tokamaks. The GLOBUS-M tokamak aims at creating and investigating highly elongated, high current, low aspect ratio plasma columns in quasi-stationary discharge conditions [1, 2]. The main machine parameters are: plasma major radius — 0.36 m; plasma minor radius — 0.24 m; aspect ratio — 1.5, axial toroidal magnetic field — 0.5 T, nominal plasma current — 0.3 MA; plasma pulse duration — 0.2 s; auxiliary heating power — 1 MW. A general view of the tokamak is shown in Fig. 1.

The GLOBUS-M tokamak is designed to fit supplies of 125 MW total power existing at the A.F. Ioffe Institute. It is a rather compact ($\sim$2 m $\times$ 2 m) device which creates a relatively large, strongly shaped plasma column with a vertical axis of 1 m and a horizontal axis of 0.5 m length. A high plasma current at a relatively low magnetic field, together with RF auxiliary heating, is the basis for achieving high beta regimes. It is shown that about 1 MW of auxiliary heating power is enough to reach a toroidal beta value of at least 10%. High performance, low collisionality regimes, which are expected during auxiliary plasma heating, allow reactor relevant issues such as a non-inductively generated plasma current to be studied. The density limit scaling could be investigated as the current density in the GLOBUS-M tokamak is high enough for a high Murakami limit to be achieved. The small major radius circumference in GLOBUS-M permits studying RF current drive methods at relatively high plasma densities (3–5) $\times$ 10^{19} m^{-3}.

Together with operating spherical tokamaks (START (UK); CDX-U (USA); etc.) and tokamaks which are under construction (MAST (UK)) or being designed (NSTX (USA)), the GLOBUS-M programme will be focused on establishing an experimental database as is necessary to understand new fundamental plasma physics properties and to solve engineering problems of spherical tokamaks.

2. OPERATIONAL REGIMES AND EXPECTED PARAMETERS

GLOBUS-M is capable of maintaining and controlling limiter and single and double X point magnetic configurations with plasma vertical elongations of up to 2.2. An example of equilibrium magnetic configurations for a plasma column with $\beta_l = 0.3$ and $\ell_i = 0.7$ is shown in Fig. 2.

The expected plasma parameters were simulated by using the 1.5-D ASTRA code [3]. Heat and particle transport was estimated by using the Merezhkin–Mukhovatov scaling for electrons and neoclassical transport for ions [4]. The auxiliary heating power of 0.5–1 MW was absorbed inside the central plasma kernel of 5–10 cm width. The temporal evolution of plasma current, electron and ion temperatures, toroidal beta and the bootstrap fraction is shown in Fig. 3.

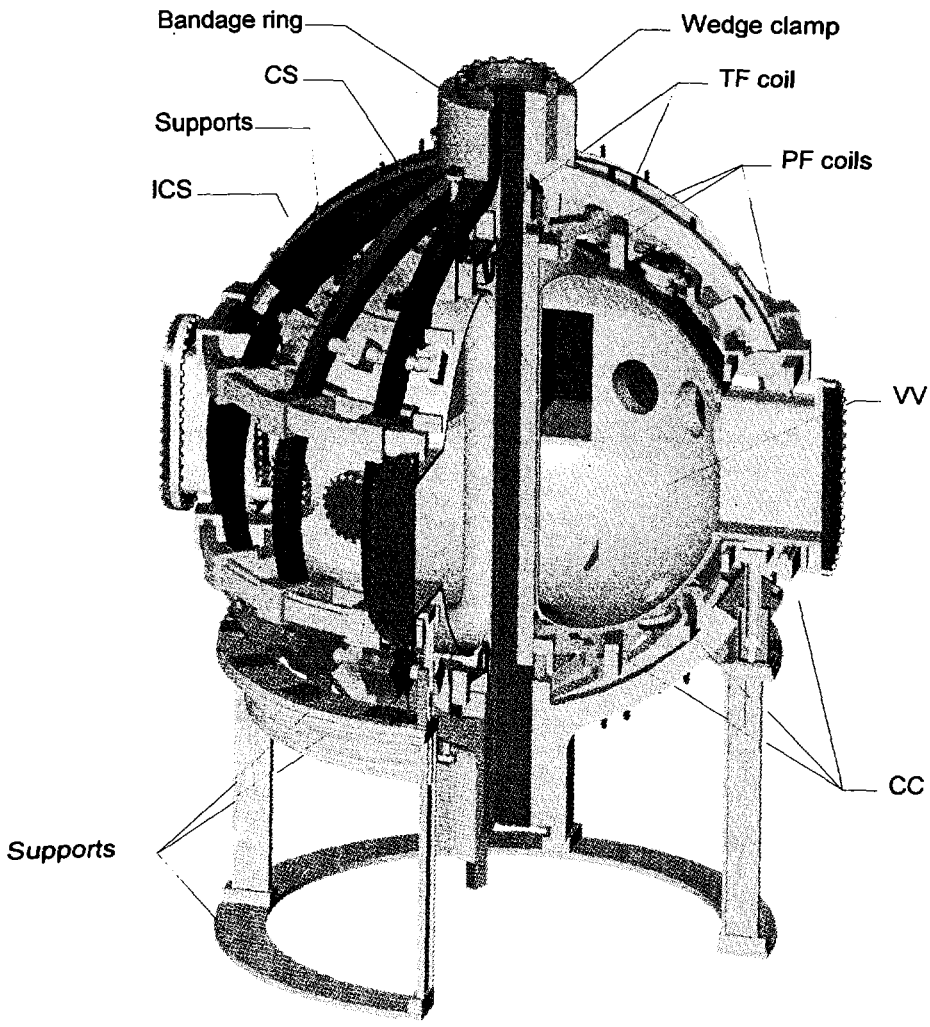

FIG. 1. General view of GLOBUS-M tokamak (CS: central solenoid; ICS: intercoil structure; TF: toroidal field; PF: poloidal field; VV: vacuum vessel; CC: compensation coil).

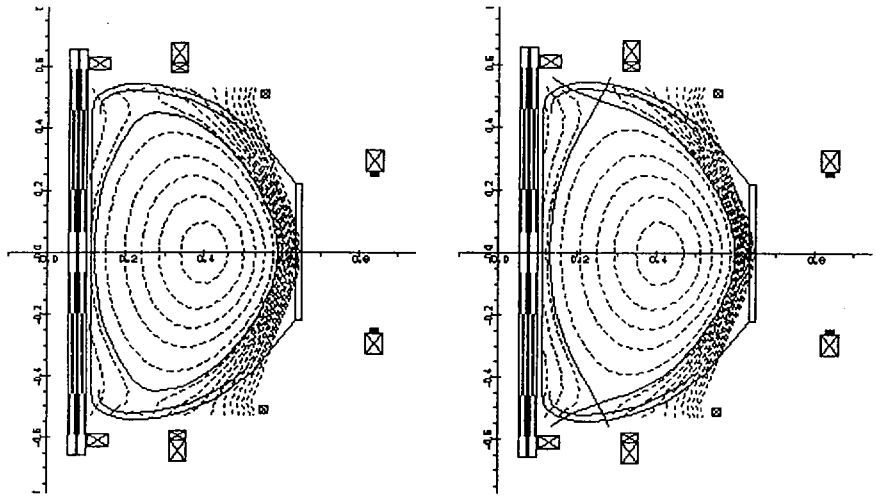

FIG. 2. Magnetic configurations: limiter with $k = 2.2$, double X point with $k = 2$.

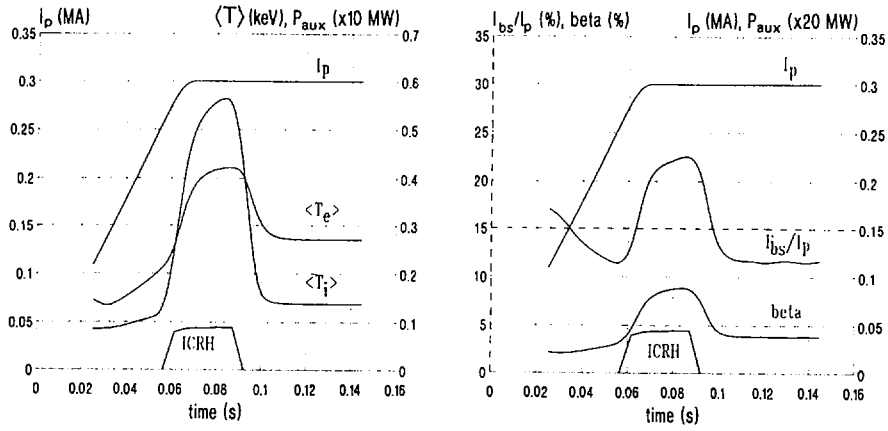

FIG. 3. Simulation of temporal evolution of plasma parameters in an 0.9 MW discharge with auxiliary heating (I_p: plasma current; I_{bs}: bootstrap current).

3. AUXILIARY HEATING AND CURRENT DRIVE

Two methods are now being considered for auxiliary plasma heating in GLOBUS-M. The first method is ion cyclotron heating on the fundamental cyclotron harmonic of the hydrogen minority. The second is high harmonic fast wave heating in the range of 4–13 harmonics of the deuterium cyclotron frequency. Since $\omega_{pe}/\omega_{ce} \gg 1$ in spherical tokamaks, the use of electron cyclotron and lower hybrid frequency ranges is virtually impossible. On the other hand, the conditions are favourable for accessibility, propagation and absorption of waves in the frequency range mentioned above.

Both heating methods were numerically modelled by a 1-D code [5] for the estimated operating GLOBUS-M parameters: $B_{t0} = 0.5$ T, $n_{e0} = 5 \times 10^{13}$ cm^{-3}, $T_{e0} = 500$ eV, $T_{i0} = 200$ eV, f = 15–50 MHz, deuterium. For both scenarios the efficiency of the single pass absorption was in the range of 30–60%, depending on the electron temperature and the parallel refractive index. In the first scenario (at f = 8 MHz), about half of the RF power was absorbed by the hydrogen ions but a considerable part of the power was absorbed at the Alfvén resonance from the high field side of the torus, which could cause some unfavourable effects. In the second scenario (at f = 15–50 MHz), wave damping with two different $k_{\parallel}$ of 15 and 10 m^{-1} was simulated for central electron temperatures of 500–1000 eV. Strong single pass absorption up to 67% was obtained for 40 MHz and 1000 eV. The absorption coefficients increased with rising toroidal beta as was predicted by Ono [6]. Wave absorption takes place in a rather broad hot plasma kernel.

Severe accessibility problems are predicted for conventional LH frequency range waves in spherical tokamaks. An attractive alternative for current drive and profile control at the edge are slow waves in the frequency range of $\omega \gg \omega_{LH}$.

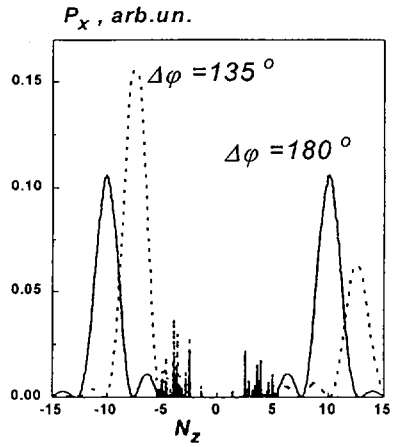

FIG. 4. Power spectrum excited by the grill.

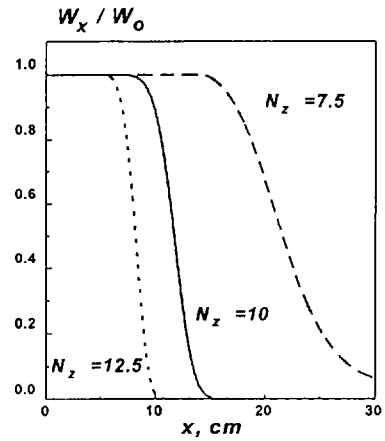

FIG. 5. Energy fluxes for different N_z.

Numerical modelling of an eight waveguide lower hybrid antenna with independently fed waveguides was carried out. The wave spectra excited in the plasma by such a grill were computed for different waveguide phasings, using the GRILL3D code [7] for the following operating parameters: $n_{e0} = 3 \times 10^{13}$ cm^{-3}, $T_{e0} = 500$ eV, $Z_{eff} = 1.5$, f = 2.45 GHz. The excited wave spectra for 180° and 135° phasing are presented in Fig. 4. In the first case, a spectrum with a parallel refractive index N_z of about 10 is formed; in the second case, 70% of the RF power resides in the waves around $N_z \approx -7.5$ and 30% around $N_z \approx 12.5$. The damping of the waves along the minor radius (due to the Landau mechanism) is seen in Fig. 5. The energy flux in arbitrary units for different N_z is shown versus the distance from the antenna. The RF energy is, in fact, absorbed in a narrow region, and its localization depends on the waveguide phasing. Further analysis by the ray tracing code is necessary but even the preliminary results are quite attractive. Other RF methods of heating and current drive, e.g. 'poloidal resonance' heating at frequencies of 2–8 GHz are also considered [8].

4. PLASMA CONTROL SYSTEMS

Basic feedback systems are used for the control of plasma current, toroidal magnetic field, vertical and horizontal positions of plasma column and plasma shaping. Plasma current and toroidal magnetic field control is performed through phasing of thyristor rectifiers capable of 70 kA maximum current at a voltage of 480 V.

The highly elongated plasma is unstable with respect to vertical displacement, with a high instability growth rate. In GLOBUS-M, the characteristic vertical displacement time for elongation of up to 2.2 and an internal inductance of $\ell = 0.7$, calculated by taking into account the stabilizing effect from the vacuum vessel, lies in the range of 0.5–2 ms, depending on the plasma–vessel spacing. To provide vertical plasma stability, high frequency thyristor convertors ($f \leq 3$ kHz) with 500 A and 500 V are being developed. A similar convertor will be used to control the horizontal position of the plasma column.

For the case of an equilibrium double X point magnetic configuration with an aspect ratio of A = 1.5 as shown in Fig. 2, plasma shape control simulations were performed. In this model, an instantaneous 15% drop of the β_p and ℓ_i parameters resulted in a 10 mm displacement of the plasma centre, Z_c; shape perturbation was introduced. The control parameters are the innermost point of the separatrix, R_i; the outermost point of the separatrix, R_0; and the radial and vertical displacements of the X point, R_x and Z_x, respectively. The result of the plasma shape control simulations is shown in Fig. 6. We see that the control parameters of the plasma shape are relaxing at a time-scale of about 10 ms.

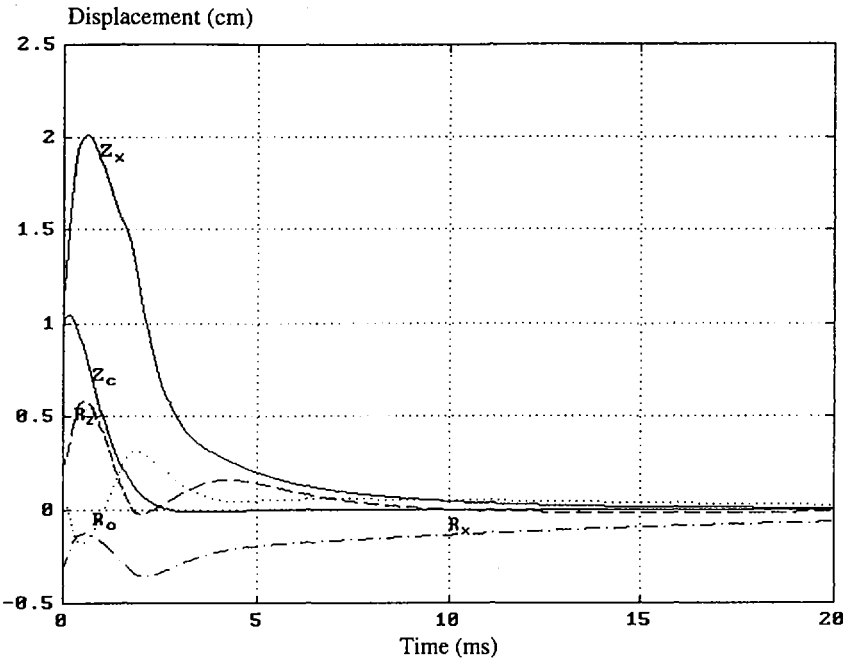

FIG. 6. Relaxation of plasma shape control parameters.

5. DESIGN DETAILS

GLOBUS-M is designed by using a disposition of machine parts that is traditional for most tokamaks, i.e. the vacuum vessel is the innermost element of design, and the poloidal and toroidal field coils are placed outside the vacuum vessel. The basic design features are outlined in Refs [1, 2].

There are 16 single turn toroidal field coils connected in series through crossovers located at the machine bottom. The total central rod current of 875 kA creates a toroidal magnetic field of about 0.5 T at a radius of 0.36 m. The TF coils are used to support the poloidal field coils. The TF coil construction, reinforced by a closed hoop intercoil structure, is stiff enough to withstand acting in-plane and out-of-plane loads.

The most critical component of the GLOBUS-M electromagnetic system is the central core. The central core consists of the central solenoid and the bundle of TF coil straight inner legs [2] of wedge-like cross-section and about 2.3 m length, inserted into the inner bore of the central solenoid. The central solenoid [9] is a two layer coil wound with a conductor of 20 mm $\times$ 20 mm cross-section. The number of turns per layer is 62. The overall length is 1313 mm. The outer coil diameter is 200 mm. The maximum coil current of ± 70 kA creates an axial magnetic field of 8.3 T and a magnetic flux swing of 0.31 Wb. For the solenoid winding, a special high strength conductor is used with an overall length of 66 m and a central hole of 6 mm diameter for the water cooling [2]. The central core development requires modelling of its components. The testing of the upper contact toroidal field coil joint was already performed, and the test of the central solenoid prototype full scale in radius and one sixth in height is in progress.

The vacuum vessel (Fig. 1) is an all welded stainless steel unit with a 'near-pure compression' shape to increase the vessel stability against the atmospheric pressure [2]. It is supported by a 14 mm thick equatorial plane ring, supplied with ports and manholes for plasma observation, heating and in-vessel component maintenance. The vacuum vessel bakeout temperature is 200°C. The vessel volume is 1.1 m^3, and the surface area is 5.7 m^2. The details of the design are published in Ref. [1].

6. PROJECT STATUS AND SCHEDULE

Among the project activities three basic groups can be outlined. The first group is the experimental machine hall construction, which is nearly finished. The second group is the detailed design and construction of the basic device (the tokamak proper) and of additional systems that are necessary for tokamak tests and shakedown, i.e. vacuum pumping, cooling and backing systems. The basic device construction is on the schedule (all main parts of the vacuum vessel have been constructed now, and the construction of the electromagnet system has started). The vacuum pumping system is already built and tested. The third group of project activities is related to

the modification of the power supplies and the design and construction of the power feeders. For this part of the task, some site reconstruction was also performed. The construction of the electrical high current feeders will start soon. The basic device, the plasma control systems, the additional systems and part of the power supplies will be completed in 1998.

ACKNOWLEDGEMENTS

This work is funded by the International Science and Technology Center, Russian Ministry of Science and Technical Policy, and the Russian Academy of Sciences. The conductor for the central solenoid was developed with the help of Finnish collaborators [9].

REFERENCES

[1] GOLANT, V.E., et al., in Fusion Engineering (Proc. 16th Symp. Urbana-Champaign, Illinois, 1995), IEEE, Piscataway, Vol. 2 (1995) 1464.

[2] GOLANT, V.E., et al., in Controlled Fusion and Plasma Physics (Proc. 23rd Eur. Conf. Kiev, 1996), Vol. 20C, European Physical Society, Geneva (1996).

[3] PEREVERZEV, G.P., et al., Rep. IPP5/42, Garching, Germany (1991); Rep. IAE-5358/5, Moscow (1992).

[4] MEREZHKIN, V.G., et al., Fiz. Plazmy **14** (1988) 131.

[5] IRZAK, M.A., et al., in Controlled Fusion and Plasma Physics (Proc. 19th Eur. Conf. Innsbruck, 1992), Vol. 16C, Part II, European Physical Society, Geneva (1992) 1025.

[6] ONO, M., Phys. Plasmas **2** (1995) 4075.

[7] IRZAK, M.A., SHCHERBININ, O.N., Nucl. Fusion **35** (1995) 1341.

[8] ESTERKIN, A.R., et al., in Controlled Fusion and Plasma Physics (Proc. 22nd Eur. Conf. Bournemouth, 1995), Vol. 19C, Part IV, European Physical Society, Geneva (1995) 389.

[9] GUSEV, V.K., et al., in Fusion Engineering (Proc. 16th Symp. Urbana-Champaign, Illinois, 1995), IEEE, Piscataway, Vol. 2 (1995) 1460.

INERTIAL FUSION ENERGY DEVELOPMENT APPROACHES FOR DIRECT AND INDIRECT DRIVE*

B.G. LOGAN, J.D. LINDL, W.R. MEIER
Lawrence Livermore National Laboratory,
Livermore, California,
United States of America

Abstract

INERTIAL FUSION ENERGY DEVELOPMENT APPROACHES FOR DIRECT AND INDIRECT DRIVE.

Consideration of different driver and target requirements for inertial fusion energy (IFE) power plants together with the potential energy gains of direct and indirect-drive targets leads to different optimal combinations of driver and target options for each type of target. In addition, different fusion chamber concepts are likely to be most compatible with these different driver and target combinations. For example, heavy-ion drivers appear to be well matched to indirect-drive targets with all-liquid-protected-wall chambers requiring two-sided illuminations, while diode-pumped, solid-state laser drivers are better matched to direct-drive targets with chambers using solid walls or flow-guiding structures to allow spherically symmetric illuminations. R&D on the critical issues of drivers, targets and chambers for both direct and indirect-drive options should be pursued until the ultimate gain of each type of target for IFE is better understood.

1. INTRODUCTION

Initiation of the US National Ignition Facility (NIF) construction brings the possibility of achieving inertial fusion ignition and energy gain in the laboratory by about the year 2005. [1] The NIF will ultimately allow testing of both direct and indirect-drive targets, providing data needed to predict the requirements for each type of target to achieve the high gains necessary for inertial fusion energy (IFE). Beyond NIF, IFE will need a development facility (which will be referred to here as a Post-NIF Facility (PNF)) with an efficient driver capable of demonstrating high gain at high pulse rates. The feasibility of candidates for such a driver must also be demonstrated along with ignition and gain by 2005 to proceed with a PNF. The choice between direct and indirect-drive for a PNF must take into account the most appropriate driver for each type of target, and the projected lifetime of fusion chambers that are compatible with each target's illumination requirement. Figure 1 shows a conceptual indirect-drive target driven by ion beams from two sides (Fig. 1a) and a conceptual direct drive target driven by lasers from all directions (Fig. 1b). For adequate symmetry, the ion indirect-drive case typically requires a minimum of 6 to 12 beams per side, while the laser driven direct-drive case typically requires of order 60 beams with spherically-distributed illuminations of the target. IFE power plant economics will depend strongly on both the driver energy requirement and cost (which depends on the driver efficiency and target gain), as well as on the reliability and lifetime of the fusion chamber with many penetrations for beam illuminations of the target.

* Prepared by Lawrence Livermore National Laboratory for the US Department of Energy under contract W-7405-ENG-48.

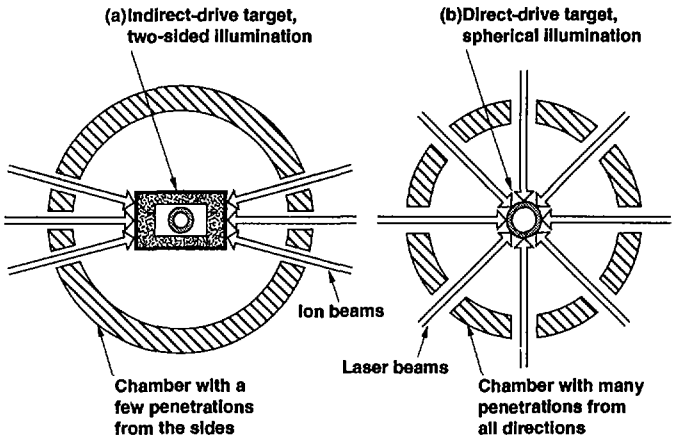

FIG. 1. Conceptual target designs for (a) indirect drive with ion beams and (b) direct drive with laser beams, showing representative beam illumination geometry and penetrations through chamber walls for each case.

2. DRIVER AND TARGET COMBINATIONS FOR IFE

There have been many design concepts of IFE power plants with different drivers [2], including studies for indirect drive based on heavy-ion accelerator (HIA) drivers [3] and on light-ion accelerator drivers [4], and for direct drive based on KrF gas laser drivers [5] and on diode-pumped solid-state laser (DPSSL) drivers [6]. All of these drivers could conceivably lead to an IFE driver. To contrast IFE development requirements for combinations of drivers, targets, and chambers based on direct and indirect-drive targets, this paper considers two cases: case 1- indirect-drive with HIA drivers and all-liquid-wall chambers (chambers such as described in [3]), and case 2- direct-drive with DPSSL drivers and dry-wall or guided-flow chambers (chambers such as described in [6]). In principle, both HIA and DPSSL drivers could be used for either direct or indirect drive. However, the choices of case 1 for indirect-drive IFE and case 2 for direct-drive IFE are based on several considerations to optimize each combination of driver and target:

(a) Product of projected driver efficiencies and target gains;
(b) Beam transport and chamber geometry for target illumination; and
(c) Shared technology development costs with other (non-IFE) applications.

2.1 Product of projected driver efficiencies and target gains

IFE power plant studies [2] find optimal designs require a minimum product of driver efficiency and gain ($\eta_d \cdot G$) > 7 to 10 to keep the recirculating power for the drivers to less than 35% to 25%, respectively, of the gross electric output of steam-turbine generators, where η_d is defined as the ratio of beam energy delivered to the target over the electrical energy input to the driver. With projected driver efficiencies of < 10% for DPSSL drivers and < 35% for HIA drivers, the above condition on ($\eta_d \cdot G$) leads to requirements for gains G greater than 70-100 for DPSSL drivers, and greater than 20 - 30 for HIA drivers. Given uncertainties in the ultimate target performance of mass-produced, injectable targets in a power plant environment, it is desirable to seek target designs capable of gains higher than what may

ultimately be needed for each driver, e.g., G > 140 for DPSSL drivers, and G > 40 for HIA drivers would give a safety margin of ~two. Target designs for laser-driven indirect drive fall far short of this gain goal with a safety margin, but calculations by the University of Rochester Laboratory for Laser Energetics [7] suggest that such gains are energetically achievable for direct drive, if hydrodynamic and laser-plasma constraints are favorably resolved. For HIA drivers, ongoing work in 2-D indirect-drive target designs [8] suggests that gains over 40 should be achievable with two-sided illuminations.

2.2 Beam transport and chamber geometry for target illumination

A recent study of DPSSL drivers for indirect-drive [9] considered use of more than 340 laser beams, more than enough to meet direct drive symmetry requirements if applied to direct drive. The direct cost of all of the optics, including the laser optics, beam transport, and final optics, was estimated to be $116 M, less than 10% of the direct driver cost, so adapting this system to direct drive (work in progress) should not significantly change the driver cost. An all-liquid wall protection scheme such as the HYLIFE-II concept [3] is compatible with indirect drive with two-sided illumination as shown in Fig. 1a, but such a wall-protection scheme is incompatible with direct drive because it does not allow beam access from the top and bottom of the chamber. The large number of beam penetrations from all directions required for direct-drive may require a dry-wall chamber such as described in the SOMBRERO study [10], and which was incorporated in the DPSSL study [9]. Previous design studies for heavy-ion drivers [11, 12] have estimated a direct cost of beam transport (for beam bending and pulse drift-compression) plus final focusing of ~ $5M per beam. For HIA indirect-drive designs with 12 to 24 beams, these costs are less than 10 to 20% of the cost of the accelerator. However, for direct drive with more than 60 beams, heavy-ion beam transport costs would become much higher, especially if the beams had to be routed out of the ground plane of a single accelerator to provide spherically-distributed beam illuminations of the target with > 50 m beam ion bending radii.

2.3 Shared technology development costs with other applications

Minimizing development costs is also important in this era of tight research budgets. The DPSSL driver design in [9] incorporates many of the laser system features now being developed for the NIF, including a multi-pass amplifier architecture with large aperture Pockels cell optical switches, gas-cooling of the amplifier slabs (moderate cooling to reduce time between shots for the NIF) , high damage-fluence mirrors, spatial filters, and frequency-conversion crystals. HIA drivers using induction technology can utilize high-pulse rate solid state switching also being developed for application to advanced multi-pulse flash radiography machines [13]. Also, development of high-average power induction cores and pulsers, ion beam transport with gas neutralization, and many features of ion target physics are common to both light and heavy ion drivers, and these areas are being shared in a tri-lab cooperation between LLNL, LBNL and SNL [14].

3. CRITICAL DEVELOPMENT ISSUES FOR IFE

Figure 2 summarizes the top level development issues for IFE in the left column showing four development areas in target physics, driver technologies, target systems, and chamber technologies. Successful resolution of these individual issues over the next decade would allow the initiation of integrated systems development and testing in a Post-NIF Facility, followed by a Pilot Plant and finally a Demo, as shown in Fig. 2. The most important development need to qualify both the HIA and DPSSL driver options for a PNF is to test prototypes of each at the kJ beam energy level or higher, with beam quality sufficient for target interaction experiments. In the DPSSL case, it is important that the prototype tests be done at high pulse rates because of the influence of thermal gradients on wave-front

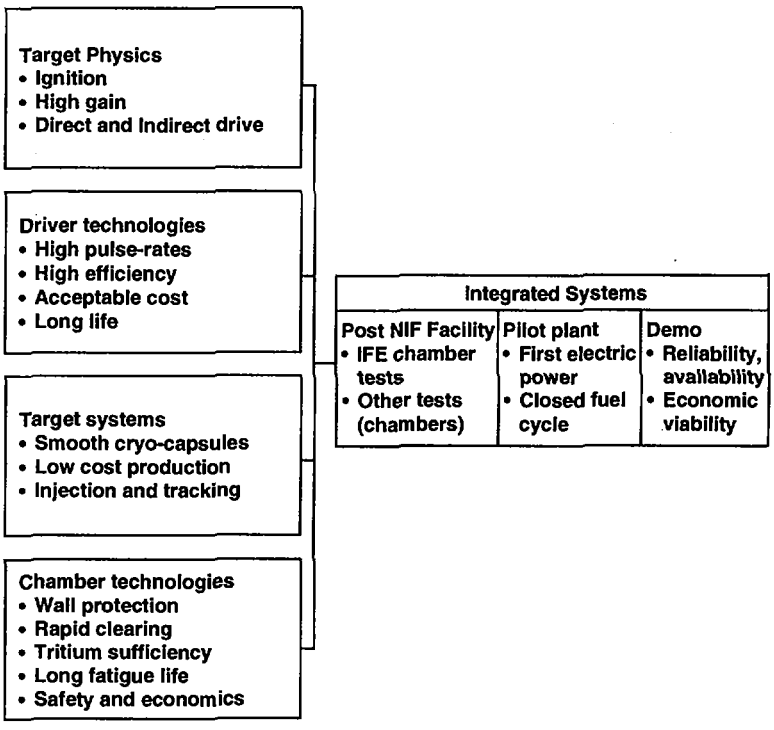

FIG. 2. Research and development to resolve critical development issues precede integrated systems tests for IFE development.

distortions. Cost reduction R&D is important for the HIA components (cores, pulsers, quadrupole magnets and insulators), and for pump diode arrays for the DPSSL, to reduce the cost of these prototypes as well as to reduce the projected IFE driver costs.

Eventual 3-D target designs are needed to refine the driver requirements for both direct and indirect-drive approaches. Qualified high gain target designs, together with the development of adequately smooth DT cryolayers are also needed to guide later R&D on methods to mass manufacture such targets at low cost, with adequate precision, and with sufficient robustness to survive acceleration and injection into hot fusion chambers. More work is also needed on beam transport to targets in the chamber, particularly, on final focusing with partial beam neutralization in the case of heavy-ions, and on beam transport through gas-filled chambers and beam tubes for mitigation of damage to the final optics from soft x-rays and target debris in the case of lasers. Selection of chamber concepts for direct and indirect-drive cases will depend critically on evaluation of wall-protection schemes that are compatible with the beam-illumination geometry required for each type of target. More international cooperation in all of these critical developments would be important for IFE success.

REFERENCES

[1] PAISNER, J.A., CAMPBELL, E.M., HOGAN, W.J., National Ignition Facility Project, Fusion Technol. **26** (1994) 755.

[2] Energy from Inertial Fusion, IAEA, Vienna (1995) 457 pp.

[3] MOIR, R.W., The High-Yield Lithium-Injection Fusion-Energy (HYLIFE)-II inertial fusion energy (IFE) power plant concept and implications for IFE, Phys. Plasmas **2** (1995) 2447.

[4] KULCINSKI, G.L., et al., LIBRA-LITE: A 1000 MWe reactor, J. Fusion Energy **10** (1991) 339.

[5] WAGANER, L.M., et al., Inertial Fusion Energy Reactor Design Studies: Prometheus-L and Prometheus-H, Rep. DOE/ER/54101; MDC-92E0008, US Govt Printing Office, Washington, DC (1992).

[6] MIMA, K., et al., "Design of inertial confinement fusion reactor driven by laser diode pumped solid state laser", Plasma Physics and Controlled Nuclear Fusion Research 1992 (Proc. 14th Int. Conf. Würzburg, 1992), Vol. 3, IAEA, Vienna (1993) 381.

[7] LINDL, J.D., Physics of indirect drive inertial fusion, Phys. Plasmas **2** (1995) 3133–4024 (see Fig. 44 for direct drive gain with parameter $\alpha = 3$, based on the work of C. Verdon of the Lab. for Laser Energetics, Univ. of Rochester).

[8] HO, D.D.-M., HARTE, J.A., TABAK, M., in Plasma Physics and Controlled Nuclear Fusion Research 1994 (Proc. 15th Int. Conf. Seville, 1994), Vol. 3, IAEA, Vienna (1996) 167.

[9] ORTH, C.D., PAYNE, S.A., KRUPKE, W.F., A diode pumped solid-state laser driver for inertial fusion energy, Nucl. Fusion **36** (1996) 75.

[10] MEIER, W.R., et al., Osiris and SOMBRERO Inertial Fusion Power Plant Designs, Rep. WJSA-92-01, 2 vols, W.J. Schafer Associates, Wakefield, MA (1992).

[11] LEE, E.P., Heavy Ion Driven LMF Design Concept, Rep. LBL-31248 Rev., UC-421, HIFAN-721, Lawrence Berkeley Natl Lab., CA (1995).

[12] BARNARD, J.J., et al., Study of Recirculating Induction Accelerators as Drivers for Heavy Ion Fusion, Rep. UCRL-LR-108095, Lawrence Livermore Natl Lab., CA (1991).

[13] KIRBIE, H.C., et al., "Development of solid-state induction modulators for high PRF accelerators", Proc. 10th IEEE Pulsed Power Conf. Albuquerque, NM, 1995.

[14] OLSON, C.L., QUINTENZ, J.P., BANGERTER, R.O., LOGAN, B.G., LINDL, J.D., Drivers for Inertial Confinement Fusion (Proc. IAEA Tech. Comm. Mtg Paris, 1994), Commissariat à l'énergie atomique, Saclay (1995).

DEVELOPMENT OF LASER FUSION POWER PLANT KOYO — SYSTEM OPTIMIZATION AND DEVELOPMENT OF KEY TECHNOLOGIES

S. NAKAI, K. MIMA, Y. KITAGAWA, S. SAKABE,
Y. IZAWA, M. NAKATSUKA, M. YAMANAKA, H. FUJITA,
T. JITSUNO, T. KANABE, N. MIYANAGA, H. TAKABE,
T. NORIMATSU, Y. KOSAKI, T. YAMANAKA, C. YAMANAKA
Institute of Laser Engineering,
Osaka University,
Suita, Osaka,
Japan

T. SASAKI, Y. MORI, K. MIYAZAKI,
M. NISHIKAWA, T. IIDA, H. HORIIKE
Faculty of Engineering,
Osaka University,
Suita, Osaka,
Japan

H. KAN, T. HIRUMA
Hamamatsu Photonics,
Hamakita, Shizuoka,
Japan

Y. SOMAN
Mitsubishi Heavy Industries,
Hyogoku, Kobe,
Japan

H. ITO
Kawasaki Heavy Industries,
Kotoku, Tokyo,
Japan

MEMBERS OF LASER FUSION REACTOR COMMITTEE
OF THE LASER SOCIETY OF JAPAN

J.M. PERLADO, E. ALONSO, E. MUÑOZ, J. SANZ
Instituto de Fusión Nuclear,
Universidad Politécnica de Madrid,
Madrid,
Spain

Abstract

DEVELOPMENT OF LASER FUSION POWER PLANT KOYO — SYSTEM OPTIMIZATION AND DEVELOPMENT OF KEY TECHNOLOGIES.

The design study for the laser fusion power plant KOYO has been conducted as a joint programme of universities, national laboratories and industries in Japan and also with international collaboration. In the design of KOYO, gain scaling of direct drive implosion with 0.35 mm wavelength laser light is used. A driver of diode pumped solid state laser (DPSSL) generates 4 MJ per pulse with 12 Hz, and the output pulses are switched so as to deliver the laser energy successively to four chambers, which operate with 3 Hz. The chamber wall is protected by thick liquid metal which flows down in a SiC woven tube. Following the conceptual design study, the critical key issues which may affect the technical and economic feasibility of the commercial power plant KOYO have been examined. Research and development of some key technologies have been performed. As a result of the KOYO studies, it is concluded that the technical and economic feasibility of laser fusion reactor is well within the authors' scope.

1. INTRODUCTION

The design concept of KOYO is based on: (i) the use of gain scaling of direct drive implosion taking into account the tolerable non-uniformity of fuel pellet and irradiation intensity; (ii) the use of high efficiency diode pumped solid state laser (DPSSL) as a fusion driver; (iii) the protection of the structural walls from micro-explosions by liquid metal flowing down in a woven SiC tube; and (iv) a modular power plant, where multireaction chambers are driven by one driver laser.

The major parameters of KOYO are shown in Table I. The driver of KOYO is the DPSSL, whose efficiency and repetition rate are 12% and 12 Hz; it drives four reaction chambers with 3 Hz. The laser energy is 4 MJ per pulse at a wavelength of 0.35 mm. The number of beams is 32 in order to achieve the required uniformity of irradiation. The moderate modular output of 1980 MW(th) and 850 MW(e) and the conservative pulse rate of 3 Hz are chosen in order to enable reactor chamber restoration.

Economic modelling and parametric system studies have been carried out to assess the sensitivity of the above design points to key physics and engineering parameters and uncertainties in the assumptions, and to find the most attractive design point [1].

In the present paper, investigations on critical issues such as laser driver, dynamic response of the reaction chamber to microexplosions, and activation of the chamber materials are reported.

TABLE I. MAJOR PARAMETERS OF THE LASER FUSION MODULAR POWER PLANT KOYO

Plant power balance	
Fusion power, P_f (MW(th))	7200
Thermal power, P_t (MW(th))	7920
Gross electric power, P_e (MW(e))	3406
Net electric power, P_n (MW(e))	2840
Reactor module thermal power, P_{et} (MW(th))	1980
Reactor module number, n	4
Driver	
Laser energy, E_L (MJ)	4
Laser wavelength (μm)	0.35
Number of beams	32
Laser repetition rate, r_L (Hz)	12
Laser efficiency, η_D (%)	12
Reactor	
Microexplosion output (MJ)	600
Reactor pulse repetition rate, r_c (Hz)	3
Tritium breeding ratio	1.1
Reactor radius (at first wall) (m)	4
Reactor radius (at vessel steel) (m)	5.45

2. FUSION DRIVER

2.1. Laser diode development

A high power AlGaAs laser diode (LD), which satisfies the required specifications for pumping Nd doped solid state laser materials, has been successfully developed [2]. Spectral control of the LD to match the laser materials and to reduce the frequency chirping of the LD within the absorption line width of the materials has been achieved. A two dimensional quasi-CW LD array of high power intensity (2.5 kW/cm^2), a high electrical to optical conversion efficiency (50%), and a long lifetime ($>7 \times 10^8$ shots) have been achieved as is shown in Fig. 1.

The uniformity of the output power on the 2-D LD array is high enough for the construction of a large scale KOYO driver system as is shown in Fig. 2.

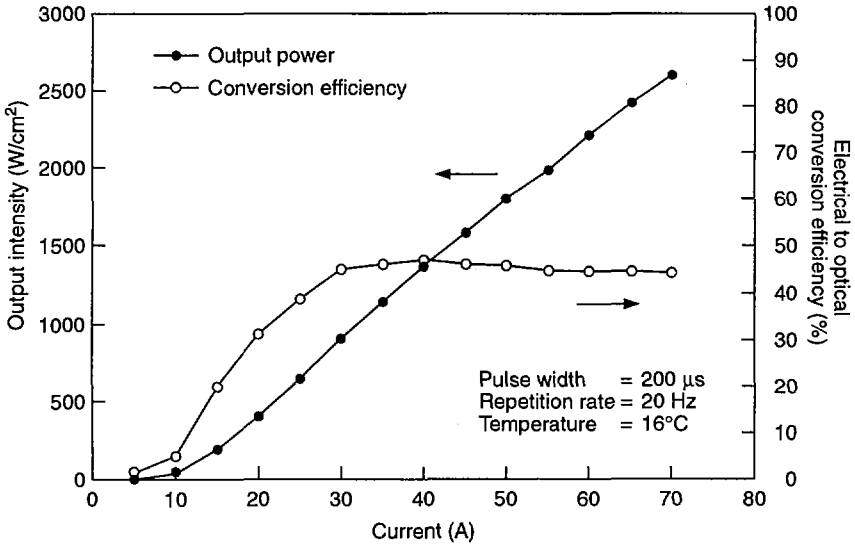

FIG. 1. Output intensity and electrical to optical conversion efficiency versus current with two dimensional 0.8 μm AlGaAs LD array.

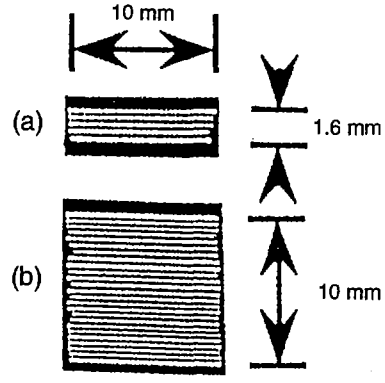

FIG. 2. 2.5 kW/cm² two dimensional LD arrays near field laser output pattern of (a) five bars with 33 laser junctions per bar; (b) 25 bars with 66 laser junctions per bar.

Since a 2.5 kW LD array has a 1 cm × 1 cm aperture, as is seen in Fig. 2(b), a 1 MW LD array can be stacked in a 10 cm × 40 cm aperture to pump the Nd:glass disc. To collimate the LD output beam, a microlens array can be directly allotted to each LD bar.

A high power 0.9 mm InGaAs quasi-CW LD array with an electrical to optical conversion efficiency as high as 60% has also been developed for pumping Yb doped laser materials such as Yb:glass and Yb:S-FAP.

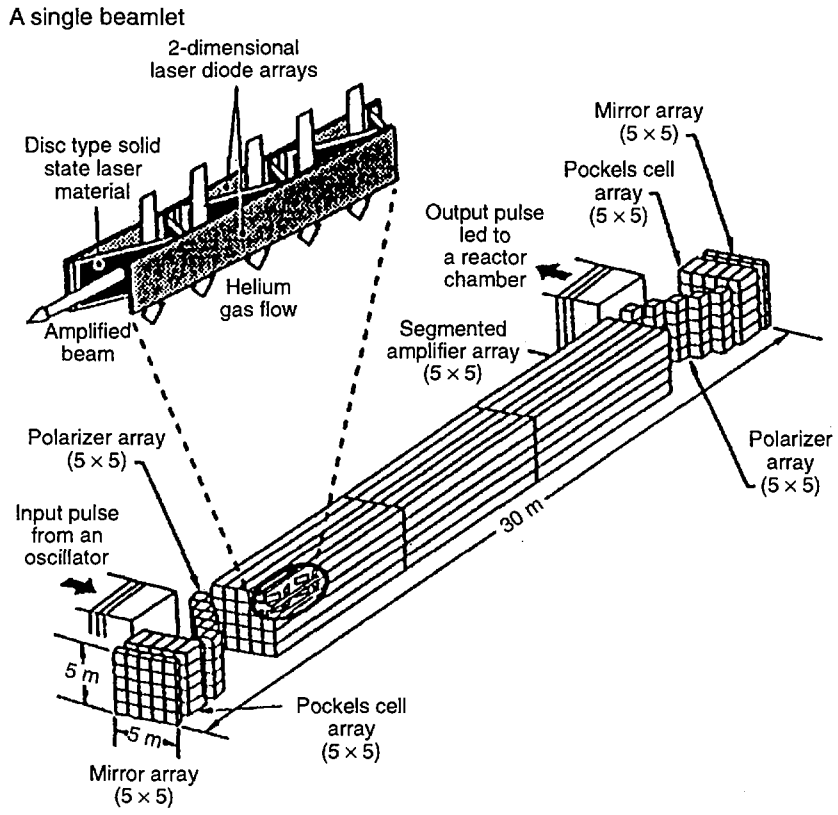

FIG. 3. Conceptual main segmented amplifier of 200 kJ output energy per pulse at 1054 nm, consisting of 25 single segmented amplifiers in a 5 × 5 array. These amplifiers are surface pumped and use AlGaAs LD arrays.

2.2. Diode pumped solid state laser system

The technical and economic feasibility of a diode pumped solid laser (DPSSL) driver for fusion reactors such as KOYO is examined. Nd doped solid state laser materials with a laser wavelength of 1 μm are selected. Using a conceptual designing technique [3], a prototype model driver with the specifications for a reactor driver of an output of 4 MJ per pulse at a wavelength of 351 nm, an overall efficiency of 12% and a repetition rate of 12 Hz is designed.

The DPSSL system for KOYO consists of 32 beams. An example for the set-up of the main amplifier in one beam line is schematically shown in Fig. 3 [3]. To achieve 12% overall efficiency at 351 nm for the system, a regenerative amplifier as pre-amplifier and a multipass saturation amplifier as main amplifier will be adopted.

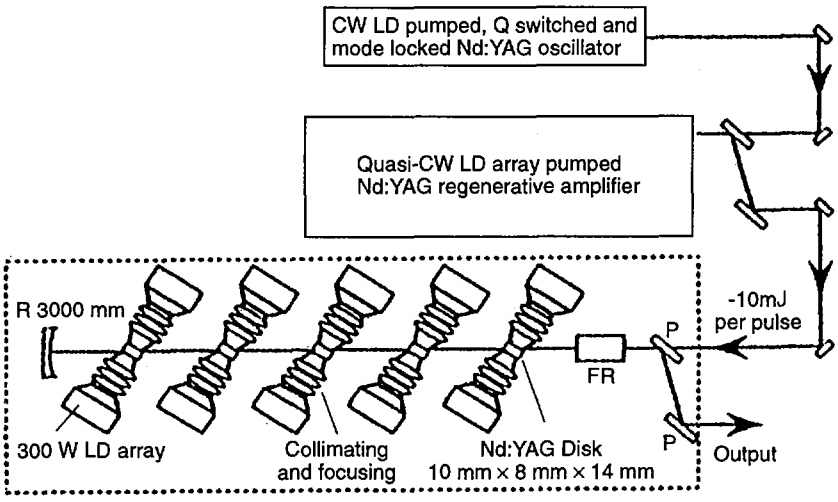

FIG. 4. Experimental set-up of LD array surface pumped Nd:YAG disc amplifier system. P: thin film polarizer; FR: Faraday rotator.

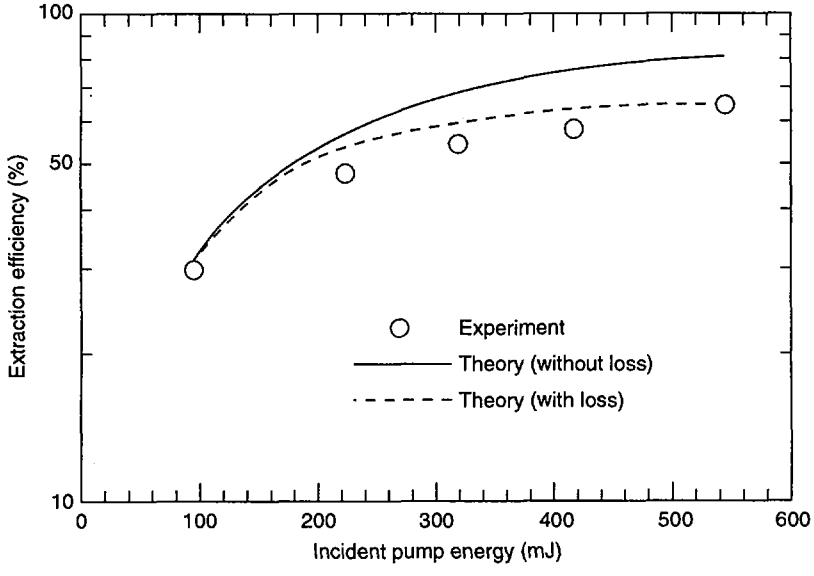

FIG. 5. Energy extraction efficiency measured as a function of incident LD pump energy. Theoretical curves without (solid line) and with (dotted line) thermal birefringence loss are shown.

The Nd:glass (HAP4) discs of 1.5 cm × 30 cm × 55 cm are pumped by 1.3 kW/cm^2 AlGaAs LD arrays and cooled by helium gas from both sides.

A small scale DPSSL system [4], which has all the elemental components for the large scale system (Fig. 4), has been constructed, with a high pumping density of 3 kW/cm^2, to investigate the technical problems of high repetition operation with good beam quality and high efficiency. They are the thermal lens and the thermally induced birefringence effects in the LD surface pumped disc, the energy extraction effciency by saturation amplification and the cooling technique of the laser discs. A net extraction efficiency of 65% was achieved by taking into account a thermally induced birefringence loss of 11%, as shown in Fig. 5. It was demonstrated in the experiment on Nd:glass (HAP4) rod laser that the thermally induced birefringence loss of about 10% has been compensated down to 1% by using a 90° quartz rotator between two identical LD pumped Nd:glass rods [5]. This compensation technique can be useful for the DPSSL driver.

The overall efficiency and that of each elementary process in the small scale DPSSL have been experimentally examined and compared with the values which are designed in the reactor driver for KOYO. It seems to be reasonable to achieve 12% of driver efficiency, even for the large system with the 4 MJ/pulse.

2.3. New non-linear optical crystal $CsLiB_6O_{10}$

For application to the laser driver with repetitive operation, much effort has been spent on developing the borate series as new non-linear optical (NLO) materials because of their higher NLO susceptibility and their lower temperature sensitivity, in phase matching (PM) conditions, compared to potassium dihydrogen phosphate (KDP). Recently, a new NLO crystal, caesium lithium borate, $CsLiB_6O_{10}$ (CLBO), has been discovered [6], which exhibits excellent NLO properties and simplicity in growth.

Table II shows angular, spectral and temperature bandwidths and walk-off angles for various frequency conversion processes in CLBO. For comparison, values of KDP and $C_{27}H_{21}NO$ (BBO) calculated from the refractive index data are shown. For second and third harmonic generation (SHG&THG), CLBO shows relatively smaller values of angular and spectral bandwidths compared to a KDP crystal with the same thickness. On the other hand, because of the ~2.5 times larger d_{eff} of CLBO with respect to KDP, the same non-linearity can be obtained with the thinner CLBO crystal. This means that increased values for angular, spectral and temperature bandwidths of CLBO compared to KDP can be obtained. For example, the temperature bandwidth of CLBO, with a thickness of 0.4 cm, becomes 108°C for SHG, which is over five times larger than that of a 1 cm thick KDP crystal (ΔT = 19.1°C), leading to higher stability of frequency conversion of the high average power laser output.

TABLE II. NLO PROPERTIES OF CLBO, KDP AND BBO

Wavelength (mm)	Crystal	PM angle (°)	Calculated d_{eff} (pm/V)	$\Delta\theta$ (mrad·cm)	$\Delta\lambda$ (nm·cm)	ΔT (°C·cm)	Walk-off angle (°)	Damage threshold (GW/cm^2)
1064 + 1064 = 532	CLBO (Type II)	42.3	0.95	1.7	5.6	43.1	1.78	26
	KDP (Type II)	59	0.38	3.4	11.5	19.1		~20
	BBO	22.8	2.06	0.92	2.1	37.1	3.20	13.5
1064 + 532 = 355	CLBO (Type II)	48.5	0.94	0.82	0.84	21.3	2.10	
	KDP (Type II)	58	0.38	1.06	0.95			
532 + 532 = 266	CLBO	61.6	0.84	0.49	0.13	8.3	1.83	
	KDP	78	0.51	1.7	0.13	1.2		
	BBO	47.5	1.32	0.17	0.07	4.5	4.80	
1064 + 266 = 213	CLBO	67.3	0.87	0.42	0.16	5.1	1.69	
	BBO	51.1	1.26	0.11	0.08	3.1	5.34	

3. NEUTRON ACTIVATION AND MATERIAL CHOICE

In connection with the material and structural design of KOYO, an estimate of the neutron activation is indispensable for studying the burial and recycling of reactor components and for a consideration of the environmental contamination. A fully coupled system of computer codes from neutron and gamma to consequent activation has been used for this estimate [7]. The system includes the codes MCNP-4A [8], ACAB [9], with the libraries EAF-3 [10] and GENII [11], for the neutron and gamma transport, induced activity and dose rate calculations, respectively.

The reactor can be modelled by a large cylindrical cavity, 20 m in height and 10 m in outer diameter, which contains the following components from the inside: (1) a 5 cm thick blanket I with SiC coolant tubes (tube packing fraction: 0.785); (2) a 95 cm thick blanket II (tube packing fraction: 0.6); (3) a 45 cm thick graphite reflector; and (4) a 5 cm thick HT-9 ferritic steel chamber wall. Moreover, the reactor chamber is covered with 3.5 m thick biological concrete shielding.

The results of the neutron transport calculation show that the maximum neutron fluxes in the blanket region and the chamber wall are about 4×10^{15} and 4×10^{13} $n \cdot cm^{-2} \cdot s^{-1}$, respectively, and that the graphite reflector effectively lowers the neutron energy and makes a sufficient contribution to the reduction of neutron damage and activation as well as to the acceptance of shallow land burial for the steel chamber wall. As to the SiC tubes located close to the target, the long half-life induced activity of ^{26}Al is a problem for waste disposal although this problem is expected to be solved by the use of woven graphite fabric tubes instead of the SiC tubes. Details of the calculated results on the neutron flux and energy spectrum in each region of the reactor, the induced activity and the surface gamma dose rate of the reactor components and their handling availability after shutdown are given in our previous paper [7].

4. DYNAMIC RESPONSE OF LIQUID METAL SURFACE AND BLANKET

4.1. Dynamic response of LiPb filled SiC tube

In the structural design of KOYO, the use of woven SiC tubes has been adopted for the protection of the structural wall from target debris, X rays and neutrons. The tube surface is covered with seepaged coolant (liquid metal: Li–Pb). To analyse the dynamic response of the SiC tube, the kinetic energy of the vaporized fluid and the impulsive pressure per unit surface area are calculated. The wall loading energy and the mass of ablated fluid are estimated to be 200 MJ and 20 kg, respectively. The maximum dislocation of the tube is estimated to be about 50 cm, and the subsequent oscillation is about 5 cm at the chamber centre for 3 Hz operation. The maximum tension in the axial direction is of the order of 10 MPa, which is well below the SiC tensile strength of 2750 MPa, and the oscillation amplitude is of the order of 1 MPa

for 3 Hz operation. It should be noted that these dislocation and tension values are calculated for a single tube against the target plasma; if neighbouring tubes surrounding the outer side are taken into account, these values should decrease significantly.

4.2. Evaporation and vacuum recovery in the chamber

The evaporation and subsequent condensation processes of LiPb are calculated so that the recovery time of the chamber vacuum can be estimated. The flow velocity of the coolant in the SiC tube is determined to be 6 m/s for a maximum surface temperature of 550°C. The surface temperature is calculated for different flow conditions as a function of the distance from the top of the tube. The evacuation time of the chamber is calculated as a function of the chamber radius. The chamber can be evacuated to 5×10^{-4} torr within 0.1 s, for a radius of 4 m. The condition for the generation of LiPb mist is also investigated, and if the gas pressure is less than 10 mtorr at a gas temperature of 1000 K, no mist will be generated. This condition is estimated to be achieved for a chamber radius of less than 5 m. Although a study of KOYO indicates that the reactor chamber can be operated up to 3 Hz, a detailed investigation of the evacuation conditions is required, including heat deposition on the tube surface due to LiPb vapour condensation and localized tube surface heating moving down during successive shots. The evacuation conditions and the mist generation are the most critical issues in realizing the ICF reactor; further studies are necessary.

5. SUMMARY

The major components of the laser fusion power plant KOYO have been examined as to technical feasibility, the present progress of technology being taken into account. It was shown that the diode pumped solid state laser (DPSSL) is promising as a reactor driver and the concept of liquid metal protection of the chamber wall is effective in reducing wall loading and chamber activation.

The understanding of the implosion physics and the reliable gain scaling of laser fusion, together with the progress in reactor related technologies, have provided us with motivation and good timing for the co-ordination of an international programme towards inertial fusion energy.

REFERENCES

[1] MIMA, K., et al., in Plasma Physics and Controlled Nuclear Fusion Research 1994 (Proc. 15th Int. Conf. Seville, 1994), Vol. 2, IAEA, Vienna (1995) 663.

[2] KAN, H., et al., Rev. Laser Eng. 23 (1995) 541.

[3] NAITO, K., et al., Jap. J. Appl. Phys. 31 (1992) 259.

[4] OHMI, M., et al., in Laser Interaction and Related Plasma Phenomena (Proc. AIP Conf. 1996), 369, Part Two, Am. Inst. Phys. (1996) 836.

[5] KIRIYAMA, H., et al., Opt. Rev. 3 (1996) 14.
[6] MORI, Y., et al., Appl. Phys. Lett. 67 (1995) 1818.
[7] PERLADO, J.M., et al., J. Nucl. Mater. (in preparation).
[8] BRIESMEISTER, J., MCNP — A General Monte Carlo Code for Neutron and Photon Transport, Version 3A, Rep. LA-7396-M, Rev. 2 (September 1986) and MCNP4 Newsletter, Los Alamos Natl Lab., Los Alamos, NM, USA (1991).
[9] SANZ, J., et al., ACAB: Activation Code for Fusion Applications User's Manual V2.0, Rep. UCRL-MA-122002, Lawrence Livermore Natl Lab., Livermore, CA, USA (1995).
[10] KOPECKY, J., et al., The European Activation File EAF-3 with Neutron Activation and Transmutation Cross Sections, Rep. ECN-C-92-058, Netherlands Energy Research Foundation (1992).
[11] NAPIER, B.A., et al., GENII The Hanford Environmental Radiation Dosimetry Software System, Rep. PNL-6584, Battelle Pacific Northwest Lab., Richland, WA, USA (1988).

DISCUSSION

D.D. RYUTOV: What assumptions did you make regarding the shot to shot reproducibility of the yield?

S. NAKAI: The shot to shot reproducibility is not so critical because of the high repetition rate of the fusion implosions. If the average yield is constant, the large thermal capacity of the blanket gives a constant output.

D.D. RYUTOV: My concern was the possibility of very rare events. You will have a few hundred million shots per year. What if in one shot the yield were, say, 1.5–2 times higher than the average yield? Would the system survive such an event?

S. NAKAI: We do not expect to see an extraordinarily large fusion yield such as 1.5–2 times higher than average, since we inject pellets of almost the same size and content of D–T fuel. The burning fraction cannot vary shot by shot so much as to give a 1.5–2 times larger yield. We do expect occasionally to obtain an extraordinarily low fusion yield due to the misfiring of several beams, or to poor pellet quality. Such events will have little effect on the chamber and also on the output power as long as their number is not large.

H.L. BERK: How much of a technological challenge is it to produce the needed repetition rates, ~ 10–50 Hz, in inertial drivers?

S. NAKAI: High repetition rate operation with good beam quality is required for inertial fusion. The cooling of the laser material is the key issue. Diode pumping gives less dispersed energy in the lasant and allows better performance in the high repetition rate mode. A repetition of ~ 10–50 Hz is much less than that of industrial lasers, which are progressing in beam quality and also output power. In the USA, Japan and Europe, many groups are working on high repetition rate operation of solid state lasers.

HIGH DENSITY, HIGH MAGNETIC FIELD CONCEPTS FOR COMPACT FUSION REACTORS*

L.J. PERKINS[1], R.P. DRAKE[1], J.L. EDDLEMAN[1],
J.H. HAMMER[1], C.W. HARTMAN[1], N.N. MATTOR[1],
B. MOOSMAN[2], A.A. NEWTON[3], P. NEY[4], H.U. RAHMAN[4],
N. ROSTOKER[2], D.D. RYUTOV[1], U. SHUMLAK[5],
Y.S. SONG[2], A. VAN DRIE[2], F.J. WESSEL[2]
Lawrence Livermore National Laboratory,
Livermore, California,
United States of America

Abstract

HIGH DENSITY, HIGH MAGNETIC FIELD CONCEPTS FOR COMPACT FUSION REACTOR.

One rather discouraging feature of conventional approaches to fusion energy is that they do not appear to lend themselves to a small reactor for developmental purposes. This is in contrast to the normal evolution of a new technology, which typically proceeds to a full scale commercial plant via a set of graduated steps. Accordingly, several concepts concerned with dense plasma fusion systems are being studied theoretically and experimentally. A common aspect is that they employ: (a) high to very high plasma densities ($\sim 10^{16}$–$\sim 10^{26}$ cm^{-3}) and (b) magnetic fields. If they could be shown to be viable at high fusion Q, they could conceivably lead to compact and inexpensive commercial reactors. At least, their compactness suggests that both proof of principle experiments and development costs will be relatively inexpensive compared with the present conventional approaches. In the paper, the following concepts are considered: (1) the staged Z pinch; (2) liner implosion of closed field line configurations; (3) magnetic 'fast' ignition of inertial fusion targets; (4) continuous flow Z pinch.

* Work performed for the US Department of Energy under Contract Nos W-7405-ENG-48 at LLNL and DEFG03-93ER54220 at University of California Irvine and Riverside. Additional (hardware) support was provided to UCI by Air Force Phillips Laboratories, Maxwell Laboratories, Inc., and Sandia National Laboratories.

[1] Lawrence Livermore National Laboratory, Livermore, California, USA.
[2] Department of Physics and Astronomy, University of California, Irvine, California, USA.
[3] Culham Laboratory, Abingdon, Oxfordshire, United Kingdom.
[4] University of California, Institute of Geophysics and Planetary Physics, Riverside, California, USA.
[5] University of Washington, Seattle, Washington, USA.

1. STAGED Z PINCH

A staged Z pinch [1-3] is projected to achieve breakeven fusion in a compact laboratory device. Initially a pulsed, electrical generator drives current through an annular plasma shell of several centimetres radius (Fig. 1). A cryogenic fibre is located on-axis [4,5]. Between the shell and the fibre there is a magnetic field. As the shell implodes, eddy currents are induced on the fibre surface via flux compression. The result is a fibre current risetime that is decreased by orders of magnitude and a fibre current that is amplified several fold relative to the shell current. The large value of compressed field confines alpha particles and provides transient shear to improve stability against MHD instabilities [6] as the target heats adiabatically.

The experiment at the University of California, Irvine (UCI) utilizes a low-voltage-capacitor-bank driver. At full charge the characteristics are: W_{stored} = 62.5 kJ, V_{charge} = 50 kV, I_{max} ~ 2 MA, $\tau_{1/4}$ ~ 1.8 μs. Diagnostics include: current and voltage monitors, multi-channel XRD array, PIN diode spectrometer, X ray pinhole camera, X ray spectrometer, laser imaging, visible-light framing and streak imaging. Two capacitor banks, each 25 μF, 60 kV and switched by railgaps, symmetrically feed a plate-transmission line, 6.4 mm thick, 2 m wide, and 2.5 m long. The anode-cathode gap is 1.5 cm and the gas puff is 5 cm diameter; the total system inductance is 32 nH. The puff valve and annular-gas nozzle are mounted on the cathode electrode and provide access for the fibre target. The pinch gas is Ne, Ar or Kr. Cryogenic fibres of H_2, D_2, and Ne have been extruded on a separate test stand [7]. An external guiding system positions the fibre with mm accuracy.

Our analysis has considered a range of UCI parameters that will achieve break-even yield using single-step staging. In zero-D with a D-T target, our code [1] predicts: 5 MA fibre current, τ ~ 0.1 ns confinement time, 6.10^{25} cm^{-3} density, 10 keV ion temperature, $n\tau$ ~ 3.10^{14} cm^{-3}-s, and a 10-fold energy gain ($E_{neutrons}/E_{bank}$). One-dimensional calculations, using the LLNL TRAC-2 MHD code, including ideal equation of state, magnetic diffusion, radiation losses and thermal transport give similar results. Figure 2 displays the 1-D results for a krypton Z pinch and DT target. These outputs were compared with another LLNL radiation MHD code (run in 1-D "non-optimized" configuration). The outputs were comparable, confirming current transfer, amplification and fibre heating.

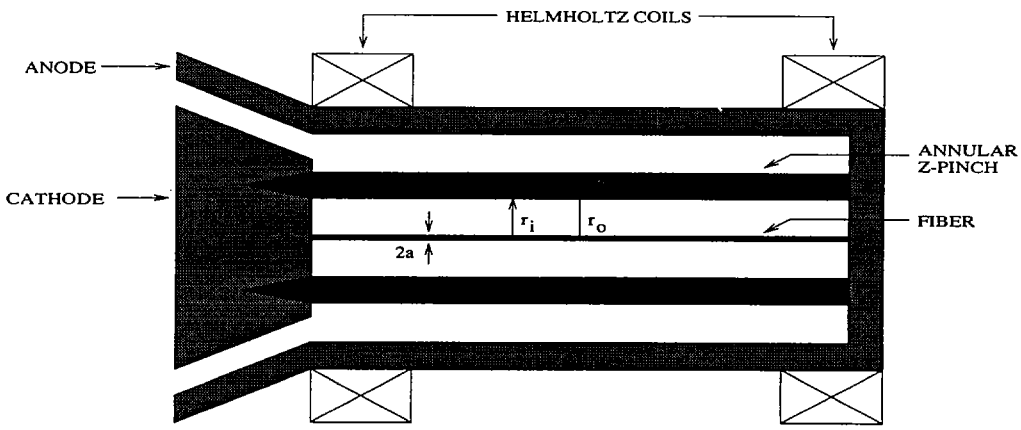

FIG. 1. Staged Z-pinch.

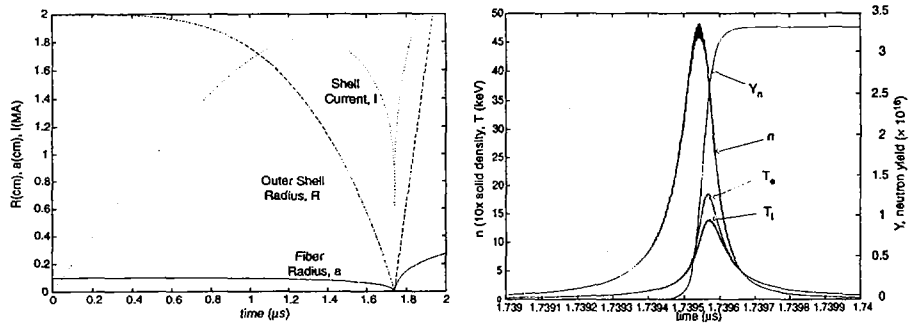

FIG. 2. TRAC2 1-D outputs for a krypton liner staged pinch onto a DT fiber; left: current and radii; right: density, temperature and neutron yield.

2. ADIABATIC COMPRESSION OF CLOSED FIELD LINE CONFIGURATIONS BY CENTIMETRE SIZE LINERS

Imploding liners have been considered for generating fusion-grade plasma since the '70s. However, in these early assessments, systems with large dimensions and, accordingly, large energy inputs (~10s–100s MJ) were considered. In the last decade, remarkable progress has been made in two relevant areas of plasma physics and technology: (i) Achievement of high convergence ratios in implosions of centimetre size liners [8]; (ii) Much better understanding of the properties of dense wall-confined plasmas (see, e.g., Ref. [9]). Accordingly, we have reconsidered the fusion prospects of the liner concept.

We consider small initial dimensions and relatively short implosion times ~ 1-2 μs. Initial liner length, radius and weight are assumed to be in the range 5-10 cm, 1-2 cm, and 5-10 g, respectively. We consider an option provided by a self-similar implosion of the liner in both r and z directions and show that this has advantages over purely radial implosion. We consider only closed field line configurations which would provide good plasma thermal insulation from the liner and the end walls; we seek conditions under which the fusion alpha particles would also be confined. We focus on the situation in which the initial plasma has a pressure comparable with or exceeding the initial magnetic pressure of the magnetic field inside the liner, so that essentially all the energy of the implosion goes to plasma heating and not on the increase of the energy of the B-field. We find that it is possible to achieve a plasma density ~10^{21}cm^{-3} and fusion break-even (Q = 1) at a plasma energy level ~0.1 MJ while values of Q as high as 5-6 are probably within the reach of the experiments with a plasma energy content ~1 MJ. We have considered the following magnetic configurations: FRC; spheromak; and Z-pinch (in the latter case, there is no confinement of alpha-particles).

A candidate system geometry is shown in Fig. 3, where the magnetic configuration is of the FRC type, with the field reversal maintained by plasma currents (not by an electron or ion beam). Initially, a magnetically confined FRC has β_0~1 as a "natural" state (see, e.g., [10]). Here, with the confinement volume restricted on all sides by conducting material walls, an FRC configuration with $\beta > 1$ is also possible. After the initial configuration is prepared, an external voltage is applied between the electrodes (Fig.3) with a pulse-length short compared to the liner skin-time. The liner is assumed to be made of some heavy material and its velocity during all phases of the implosion is assumed to be much smaller than the plasma sound velocity. Therefore, plasma compression occurs in the adiabatic manner.

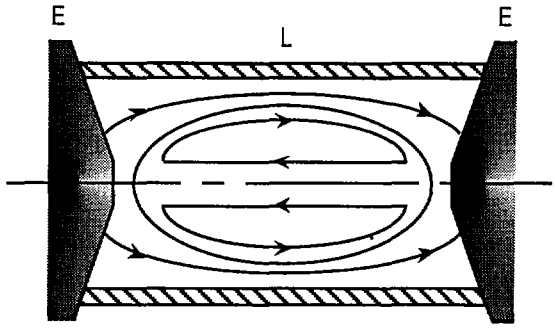

FIG. 3. Schematic of imploding liner system for our reference FRC plasma configuration. Electrodes (E) drive the current in liner (L).

We consider a self-similar compression which maintains a constant length/radius ratio of the FRC. This is achieved by properly tailoring the mass density of the liner along the axis. If the central part is heavier than the ends, its compression lags behind, maintaining an approximate constancy of the length/radius ratio of the plasma object nesting inside the liner.

Due to heat flow from the plasma and Joule dissipation in the skin layer at the inner side of the liner, this inner surface will be evaporated and ionized. As both the ion gyroradius and mean free path of these relatively cold ions will be two to three orders of magnitude smaller than the plasma radius, they will not directly penetrate the plasma. In addition, in a high beta plasma, the impurities get repelled from the hot region, under the action of the thermal force and plasma convection towards the walls.

Analysis presented in Ref. [11] has shown that even with quite pessimistic assumptions regarding thermal conductivity to the liner walls, thermal losses do not limit the quality of pellet performance. Bremsstrahlung also constitutes an insignificant energy sink (unless one deliberately seeds the plasma with heavy impurities, in order to use the system as a pulsed source of X rays).

The plasma gain Q, is limited by a relatively short liner dwell time near the turning point [11]. The Q value determined by this process can be presented as:

$$Q = 0.5(\beta_0^{1/3}\rho_L/E^{2/3}T_0)^{1/2}(W_{max}B_0)^{1/3}$$

Here liner density is measured in g/cm^3, initial temperature T_0 in eV, plasma energy E in the final state in kJ and initial magnetic field in T.

We have considered a hypothetical breakeven experiment with a 5 MA pinch current and 2 μs implosion time. The initial characteristics of the FRC are: diameter 2 cm, length 5 cm, plasma density 10^{24} m^{-3}, plasma temperature 100 eV, magnetic field 10 T, linear convergence of the liner = 10 (volume convergence = 1000).

3. MAGNETIC FAST IGNITION

This is a scheme to ignite fuel compressed to ICF densities (~few x 10^2 g/cm^3), where the compression is achieved by laser or x-ray driven implosion but the ignition hot spot is generated from the JxB collapse of a magnetic "bubble" within the imploded capsule. The ignition is "fast" ignition in the sense of the fast ignitor concept [12] and offers advantages of improved gain and a reduction in the required convergence ratio. The magnetic bubble must be established within an electrically conducting region in the capsule before the implosion.

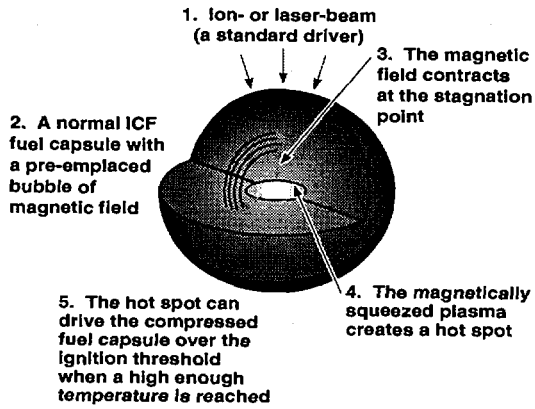

FIG. 4. Schematic of magnetic fast ignition within an ICF capsule.

In conventional, isobaric ICF burn initiates from a low density, central hot spot in near pressure equilibrium with high density cold fuel. An interesting alternative is "isochoric" ignition where the density is nearly uniform. The hot spot is then at much higher pressure than the surrounding fuel. Because of the rapid disassembly, high power "fast" ignition is required employing, for example, a short pulse laser [12]. Here we discuss the use of magnetic forces to achieve fast ignition.

Consider a compressed, nearly Fermi-degenerate cold fuel mass, with a magnetic-field-containing toroidal void (Fig. 4). The void, or magnetic bubble, will not close if it contains an azimuthal field with magnetic pressure about equal to the surrounding fuel pressure and the conductivity prevents diffusion of field. Because of the 1/r dependence of the field, the bubble cannot be in exact equilibrium and it will distort radially inward. The initial motion of the bubble is of the order of the cold fuel sound velocity. This is also of the order of the final assembly velocity in the capsule implosion as required to reach this state in a realistic implosion. As the distortion extends to smaller radius, the flows accelerate because the magnetic pressure increases as $1/r^2$. A narrow, rapidly collapsing neck forms as in sausage instabilities in a Z pinch. The plasma pressure and temperature climb in the neck until the ignition temperature is reached. Ignition occurs if there is sufficient $\rho.r$ (density x radius). This ignition method has also been suggested for a high current Z pinch [13].

2D radiation MHD simulations of the ignition process starting from the compressed state show isochoric (or density enhanced) ignition can occur. We have modeled an initially stationary sphere of DT with a radius of 105 μm, density of 320 g/cc, temperature of 220 eV and total energy of 54 kJ. The initial state has a small toroidal void centred at 52.5 μm with a mean magnetic field of 1.5×10^5 T and 5 kJ of magnetic energy. The "neck off" occurs after 60 ps, igniting a burn wave that encompasses the fuel mass by 110 ps. The yield is 122MJ, corresponding to a gain of 68 for a 1.8MJ driver and driver to capsule energy conversion efficiency of 0.03.

Achieving the desired compressed state is a challenging 2-D design problem. An azimuthal magnetic field ~ 10^2T must be established within the capsule before implosion, possibly employing laser generated fields. Fields of order 25×10^2T have been produced in CO_2 laser experiments [14]. Initial 1- and 2-D calculations show

that field diffusion into the conducting (beryllium) structure may be important in the early portion of the implosion. In the calculations, diffusion can be limited with thicker conductors, aided by plasma conductivity. This leads to good conservation of magnetic flux and compression of the magnetic field to the required conditions. Future calculations will include the 2-D implosion of conductors and D-T fuel.

4. CONTINUOUS FLOW PINCH

We are also revisiting the prospects for high power density fusion devices based on the continuous flow Z pinch [15,16]. In particular, existing experiments and new theory suggest that the instability modes of the conventional Z pinch may be fully stabilized by the addition of plasma flow. This, at least, suggests the potential for low cost, intense fusion neutron sources for various practical applications [16].

The continuous flow pinch (CFP), one of the simplest magnetic confinement fusion systems, is a Z pinch with axial plasma flow formed by injection of magnetized plasma from a coaxial plasma gun. The CFP was extensively studied in the former Soviet Union and successfully developed as a high purity source of accelerated plasma. In 1967, a Marshall plasma gun [17] operating regime was discovered which resulted in the formation of a continuous-flow Z pinch (CFP). The pinch column was ~50cm long, <1cm dia, with $n \sim 10^{24} m^{-3}$, and $T \sim 0.15$ keV [4]. It demonstrated a fusion product of $n\tau \sim 5 \times 10^{17} m^{-3} s$, about the same as the "break-through" value achieved by the low density, closed confinement in the T3 tokamak of that time which exhibited an $n\tau$ of $\sim 4 \times 10^{17} m^{-3} s$ [18]. Most remarkably, this CFP appeared to be stable for many hundreds of Alfvén times against the conventional sausage and kink instabilities that have continued to plague conventional, static Z pinches.

We now believe we may understand the reason for this stability and predict that it can be exploited to realize a stable, high gain fusion plasma based on the Z pinch, provided a radial velocity shear is induced in the axial plasma flow stream [19,20]. In the 1967 experiment, a sheared flow was probably induced by the method of formation as suggested by our recent 2-D modeling studies. In a high power fusion neutron source based on this principle, we would propose actively tailoring the shear profile though electrode control [16]. Note, however, that a recent parallel study has suggested that the required flow velocities may be high [20]. If so, this would require pulsed operation to realize acceptable fusion gain, Q.

We have also performed a conceptual design of a high power D-T neutron source based on the CFP applied to the transmutation of long lived radioactive waste from fission reactors [16]. The design is configured in a reflex configuration to ensure electrode survivability. The injectors, typical Marshall guns with tailored electrodes, introduce plasma which flows radially inward and divides at a null point into oppositely directed flow pinches. The core of each pinch column enters an end burial chamber where rapid expansion takes place and the exhaust power is dissipated over a large surface. The capital and development costs are projected to be low for a neutron source based on this principle

REFERENCES

[1] RAHMAN, H.U., et al., Phys. Rev. Lett. **74** (1995) 714.
[2] RAHMAN, H.U., et al., J. Plasma Phys. (in press).
[3] WESSEL, F.J., ETLICHER, B., CHOI, P., Phys. Rev. Lett. **69** (1992) 3181.
[4] SETHIAN, J.D., et al., Phys. Rev. Lett. **59** (1987) 892.
[5] HAMMEL, J.E., et al., Nucl. Instrum. Methods **207** (1983) 161.
[6] ALBARES, D.J., et al., Phys. Fluids **4** (1961) 1031.

[7] RUDEN, E., Air Force Phillips Laboratories, Albuquerque, NM (personal communication, 1995).
[8] DEGNAN, J.H., et al., Phys. Rev. Lett. **74** (1995) 98.
[9] VEKSHTEIN, G.E., in Reviews of Plasma Physics (KADOMTSEV, B.B., Ed.), Vol. 15, Consultants Bureau (1990) 1.
[10] HOFFMAN, A., Trans. Fusion Technol. **27** (1995) 91.
[11] DRAKE, R.P., et al., Fusion Technol. **30** (1996) 423.
[12] TABAK, M., et al., Phys. Plasmas **1** (1994) 50.
[13] VIKHREV, V.V., IVANOV, V.V., Sov. Phys. — Dokl. **30** (1985) 492.
[14] HAUER, A., MASON, R., Phys. Rev. Lett. **51** (1983) 459.
[15] HARTMAN, C.W., Comments Plasma Phys. Control. Fusion **17** 5 (1996).
[16] PERKINS, L.J., HARTMAN, C.W., Fusion Technol. (in press).
[17] NEWTON, A.A., MARSHAL, J., MORSE, R.L., in Controlled Fusion and Plasma Physics (Proc. 3rd Eur. Conf. Utrecht, Netherlands, 1969), European Physical Society, Geneva.
[18] ARTSIMOVICH, L., in Plasma Physics and Controlled Nuclear Fusion Research 1968 (Proc. 3rd Int. Conf. Novosibirsk, 1968), Vol. 1, IAEA, Vienna (1969) 157.
[19] SHUMLAK, U., HARTMAN, C.W., Phys. Rev. Lett. **75** (1995) 3285.
[20] ARBER, T.D., HOWELL, D.F., Phys. Plasmas **3** (1996) 554.

CONCEPTUAL DESIGN OF A 2 MJ KrF LASER FUSION FACILITY

M.W. McGEOCH
PLEX Corporation,
Brookline, Massachusetts

P.A. CORCORAN, R.G. ALTES, I.D. SMITH
Pulse Sciences,
San Leandro, California

S.E. BODNER, R.H. LEHMBERG, S.P. OBENSCHAIN,
J.D. SETHIAN
Plasma Physics Division,
Naval Research Laboratory,
Washington, D.C.,

United States of America

Abstract

CONCEPTUAL DESIGN OF A 2 MJ KrF LASER FUSION FACILITY.

A KrF amplifier model verified against Nike laser data is used to design higher energy modules with segmented pumping. A 68 kJ module is designed, incorporating a new water line geometry and a combined switch/bushing. Two 68 kJ modules are combined in a 136 kJ multiplexed beamline incorporating incoherent spatial imaging that fits within a compact beam tunnel. A total of 16 such beamlines are arranged on four floors to deliver 64 beams to a target, the net energy being 2.0 MJ. The wallplug efficiency of this laser is 4%. Detailed calculations of prepulse ASE energy are given, and the levels are designed to be low enough not to initiate a prepulse plasma. The basic geometrical uniformity of target illumination is shown to be better than 0.3% for a 64 beam illumination geometry which has a high degree of symmetry. Amplification fidelity is verified.

1. INTRODUCTION

Direct illumination of a laser fusion pellet can be achieved with relatively high coupling efficiency, 70–90% of laser energy being absorbed by the pellet, compared to 10–15% for indirect illumination using a hohlraum. The energy gains can be in the range of 100–200, using a few megajoule laser.

The krypton fluoride (KrF) laser at 249 nm has several properties that combine to make it the most attractive of currently available lasers for a direct fusion driver, which requires high uniformity to maintain good implosion symmetry:

(a) The short wavelength provides high coupling to the pellet and good collisional damping of the deleterious laser–plasma instabilities.

(b) The gaseous laser medium, with its broad 2–3 THz bandwidth, is consistent with the implementation of optical smoothing using echelon free induced spatial incoherence (ISI) [1, 2]. Experiments with the Nike laser at NRL [3, 4] using 1.3 THz (FWHM) bandwidth have demonstrated focal non-uniformities of only 1% rms, averaged over a 4 ns pulse, in accordance with theoretical modelling.
(c) The 7.5% system laser efficiency meets the requirement for a power reactor [5].
(d) The gas laser medium is compatible with moderate repetition rates (a few Hz) through recirculation and heat exchange.
(e) The cost of a 2 MJ KrF laser system is comparable to, or less than, that of a glass laser.

The subject of this short paper is a conceptual design [6] for a 2 MJ laser fusion facility that operates single pulse, designed to demonstrate high energy gains from a pellet. We do not discuss reactor design, but note that the present laser architecture is compatible with future development in the direction of moderate repetition rate and long life.

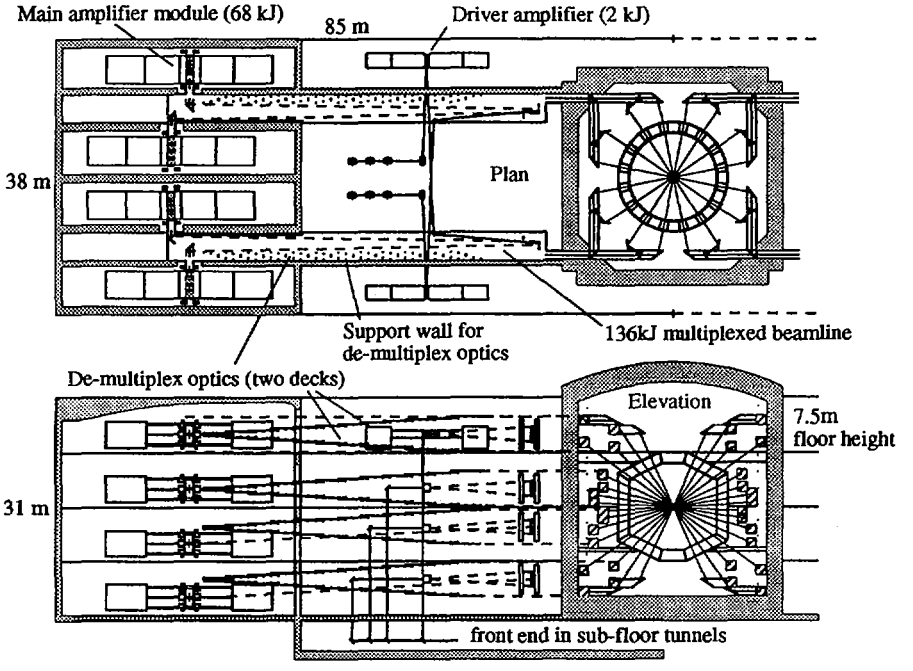

FIG. 1. Plan and elevation views of one side of 2 MJ KrF laser facility showing major structural elements.

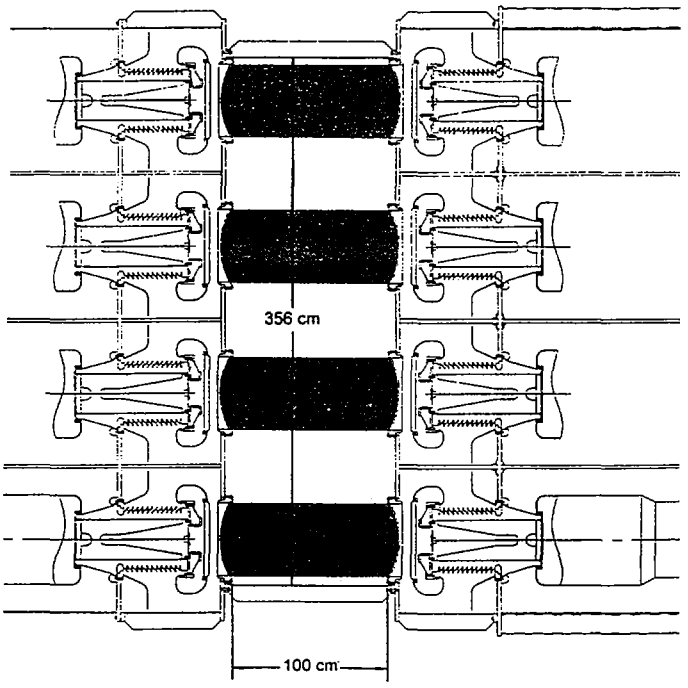

FIG. 2. Plan view of 68 kJ module showing four segments pumped by electron beams from each side.

2. LASER ARCHITECTURE

The main challenge in the design of a KrF fusion laser is that the desired laser pulse is of the order of 7 ns in duration, which is longer than the energy storage time of the KrF* upper laser level, so that this level cannot be used for energy storage and time compression. The voltage, current and geometric limitations of pulsed power are such that the required pumping energy cannot be delivered in times shorter than about 250 ns. Consequently, the technique of multiplexing has been developed [7–9], in which copies of the desired laser pulse are passed through the KrF amplifier in an angle coded sequence lasting 250 ns before being recombined on target. For a 7 ns fusion laser pulse, there are 36 beams in the sequence.

The number (sixteen) of separate multiplexed beamlines in the 2 MJ facility is determined by considering: (a) the maximum energy of the amplifier module that is technically feasible with only a modest extension of present day technology; and (b) the need for sixty or more separate directions of illumination possessing a high degree of spherical symmetry, and the related problem of distribution of the optical beams. Too high an energy for the amplifier module will make the distribution optics

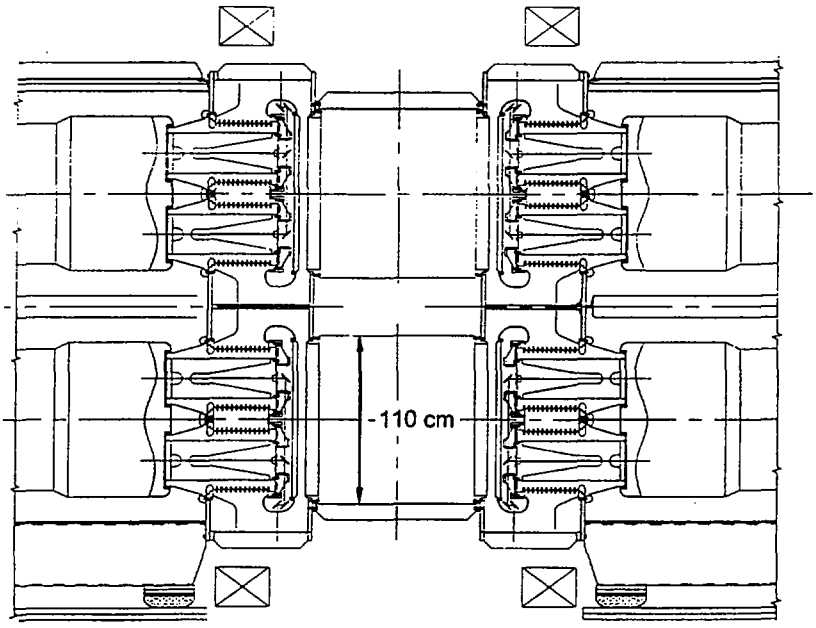

FIG. 3. Elevation view of diode region of 68 kJ module, showing two 1 m^2 apertures.

more complex. The facility floor area is found to decrease with increasing beamline energy up to the 200 kJ level, because of increased packing efficiency, but does not decrease much with additional beamline energy because of increasing distribution complexity.

One design constraint was the self imposed limit of 1 m on the area of fused silica amplifier windows. This size is currently the largest to have been manufactured with adequate optical homogeneity. From detailed KrF amplifier modelling (to be discussed below) and pulsed power simulations we found that a laser output of 34 kJ was feasible from a 1 m^2 optical aperture. Our basic amplifier module incorporates two such apertures, stacked vertically, to yield 68 kJ. The 136 kJ (crude energy) that is needed for each of the sixteen multiplexed beamlines is obtained by 'aperture sharing' of two 68 kJ modules, to generate a 2 m × 2 m effective amplifier aperture. The arrangement of the sixteen 136 kJ beamlines feeding a target chamber is shown in Fig. 1. Details of the 68 kJ amplifier module are shown in Figs 2 and 3.

3. AMPLIFIER MODULE

The size, complexity and cost of the facility can all be greatly reduced if improvements can be made in design of the final KrF amplifier module. For this

reason, it is important to have as a design tool the best possible quantitative model of the amplifier. From studies of the kinetics and gain of KrF amplifiers and other development work on kilojoule class lasers [10, 11], it has recently been possible to construct an amplifier model [12] which includes local time dependent kinetics, optical propagation and losses due to amplified spontaneous emission (ASE). This model has given an accurate description of the performance of both the 20 cm and 60 cm (aperture) electron beam pumped amplifiers of the NRL (Nike) facility. The comparison with data from the first major experimental run of the NRL 60 cm amplifier (Fig. 4) shows that the majority of shots lie within 10% of the theoretical curve up to an output energy of 5 kJ. The output during this run was sometimes affected by fluorine depletion before the shot, accounting for the occasional data below theoretical. The most solid data point, consisting of the average of five measurements, is slightly above theoretical, and the output trend was accurately predicted, without any adjustments to the model.

Calculations were then performed on a novel segmented amplifier geometry that allows the electron beam to be broken into manageable subunits, each with no more stored energy than currently used in the Nike 60 cm device. The question to be answered was whether the fluorine absorption of the unpumped regions would affect the efficiency too greatly. It was found, to the contrary, that segmented designs had smaller ASE losses, owing to the distributed geometry, and that the modelled energy output remained essentially constant during the introduction of unpumped regions. In

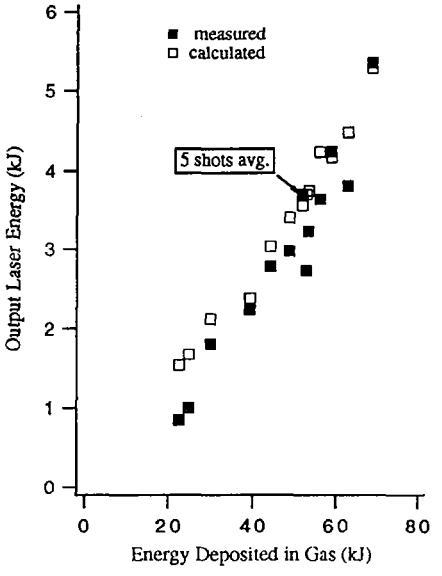

FIG. 4. Nike 60 cm experiment and theory.

each of its 1 m^2 subapertures, the 68 kJ module has four pumped regions (each 48 cm in the optical direction × 100 cm × 100 cm), separated by three gaps of 48 cm. The specific pump power is 800 $kW \cdot cm^{-3}$. The electron beams feeding each 1 m^2 subaperture are generated by eight large area cold cathode diodes. Efficient transport of the electron beams into the laser gas is achieved through the use of a 'suspension bridge' foil support structure similar to that tested at Los Alamos [13].

Each diode, with a nominal cathode dimension of 48 cm × 100 cm, is fed by a water PFL of depth 1.0 m and length 5.0 m, corresponding to a pulse duration of 300 ns with a 250 ns 'flat-top' duration [14]. Each centre plate is charged to −1.64 MV in a 1.8 μs pulse by a Marx bank before being switched through two parallel laser triggered switches to generate 800 kV in the diode load. The classical 'Z stack' bushing of the Nike 60 cm machine and its separate elaborate switch modules have been greatly simplified by their combination into an integrated switch/bushing, as is seen in Figs 2 and 3. Apart from reducing the cost this simplification leads to a lower inductance which translates into a faster diode risetime. The circuit has been simulated in detail to verify its performance into the slowly varying impedance of the diode.

4. OPTICAL SYSTEM

As in the Nike facility this amplifier system images onto the target the incoherent scattering from a diffuser located at the front end. This diffuser is illuminated by a small broadband multimode KrF laser. The optical system accepts a 25 mrad cone of incoherent light and irradiates targets up to 0.4 cm in diameter without edge losses. Throughout the optical system, uniformity and spatial incoherence are preserved through the use of large Fresnel numbers. Further constraints are:

(a) Amplifiers are located at, or near to, the Fourier transform plane of the image or target so that spatial non-uniformity of pumping does not create any appreciable fluence non-uniformity on target.
(b) Each amplifier stage is 'overfilled' by beams from the previous stage in order to suppress parasitic oscillations.
(c) The preamplifier is imaged (via the driver amplifier) onto the main amplifier in order to satisfy the Fourier transform requirement at the relatively large separation between these amplifiers. The driver amplifier is not exactly at a transform plane.
(d) The beams downstream of the main amplifier must not strike the metalwork at the edges of the recollimation, demultiplexing and final lens optical elements. Overfilling of these elements would be a source of image distortion, as well as of inefficiency.
(e) In order to control aberrations the angles of incidence onto spherical reflectors must be kept as low as possible. If necessary, the convex mirrors of the main

feed array can be replaced by planar mirrors with tilted concave lenses in front, to cancel off-axis aberrations, as in the Nike laser.

The recollimated beams from the sixteen beamlines are propagated to the target chamber enclosure in arrays of 144 beamlets, 6 wide by 24 high, each beamlet 18 cm × 18 cm in area. The 64 final lens arrays have 36 elements each and illuminate the target from 64 directions to achieve $<0.3\%$ rms non-uniformity (calculated geometrically, and not including plasma effects such as refraction).

The final lenses are of fused silica, so the fluence is limited to 4 $J \cdot cm^{-2}$ (in 7 ns) to avoid significant two photon absorption.

5. ASE PREPULSE

For the first time in a KrF design we have estimated the exact level of prepulse energy arriving on target. We have shown analytically and computationally that the exit axial ASE brightness of an electron beam pumped amplifier is given by $B = 2 \times 10^4 G_0$ ($W \cdot cm^{-2} \cdot sr^{-1}$), where G_0 is the line centre gain of the (two pass) amplifier. From each driver amplifier there are 36 optical paths that can be travelled by ASE to the target, 35 of which have it arriving before the main energy pulse. The ASE arrives in an intensity ramp of 250 ns duration. For our 2 MJ design, we are able to keep the ASE fluence down to 0.6 $J \cdot cm^{-2}$, a level which does not initiate plasma formation on the surface of metal coated targets, or in appropriately chosen plastic coated targets.

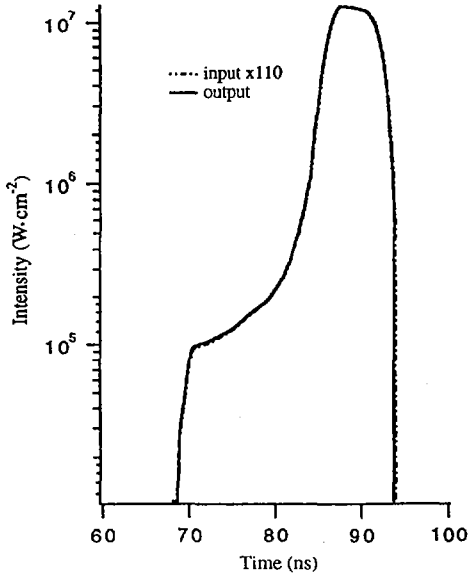

FIG. 5. Amplification fidelity, 1.8 MJ pulse.

6. AMPLIFICATION FIDELITY

Using the time dependent amplifier code we have investigated the degree to which an arbitrary low isentrope optical pulse shape is preserved in the amplification process. We considered the effect of a sequence of overlapping pulses executing double pass amplification. It was found that provided the pulse FWHM is equal to the (7 ns) spacing of the multiplexed beamlets, and certain small adjustments are made to the trailing edge of the pulse, the amplification fidelity of arbitrarily rising smooth pulses is excellent. An example is shown in Fig. 5.

7. CONCLUSIONS

We have presented a KrF laser design, traceable to data from the Nike laser at NRL, that is compact and has relatively low technical risk. Only a modest extension of performance is now required in a number of amplifier parameters. The facility design may be verified by the construction of a single 68 kJ segmented module.

ACKNOWLEDGEMENT

This work was supported by the US Department of Energy.

REFERENCES

[1] LEHMBERG, R.H., OBENSCHAIN, S.P., Opt. Commun. **46** (1983) 399.
[2] LEHMBERG, R.H., GOLDHAR, J., Fusion Technol. **11** (1987) 532.
[3] LEHECKA, T., LEHMBERG, R.H., DENIZ, A.V., GERBER, K.A., OBENSCHAIN, S.P., PAWLEY, C.J., PRONKO, M.S., SULLIVAN, C.A., Opt. Commun. **46** (1995) 485.
[4] OBENSCHAIN, S.P., et al., Phys. Plasmas **3** (1996) 2098.
[5] MEIER, W.R., Fusion Eng. Des. (Netherlands) **25** (1994) 145; also MEIER, W.R., et al., Rep. DOE/ER/54100-1,WJSA US Department of Energy, Washington (1992).
[6] The present work has been documented in much more detail in a full length paper to be submitted for publication.
[7] EWING, J.J., HAAS, R.A., SWINGLE, J.C., GEORGE, E.V., KRUPKE, W.F., IEEE J. Quant. Electron. **QE-15** (1979) 368.
[8] PARKS, J.H., Conceptual Design for an Angularly Multiplexed Rare Gas Halide Laser Fusion Driver , Rep. DOE/DP/40113-1, Department of Energy, Avco Everett Research Laboratory (1980).
[9] HARRIS, D.B., SULLIVAN, J.A., PENDERGRASS, J.H., KURNIT, N.A., ROSE, E.A., McCLEOD, J., KrF Laser-Driven Laboratory Microfusion Facility, Rep. LA-UR-91-2915, Los Alamos Laboratory, NM (1991).
[10] DIVALL, E.J., et al., J. Mod. Optics **43** (1996) 1025.

[11] OWADANO, U., et al., in Plasma Physics and Controlled Nuclear Fusion Research 1994 (Proc. 15th Int. Conf. Seville, 1994), Vol. 3, IAEA, Vienna (1996) 121.

[12] McGEOCH, M.W., "A simplified KrF kinetics model" and "Time-dependent amplifier with kinetics and ASE", KrF Laser Technology (Proc. 4th Int. Workshop Annapolis, Maryland, USA) NRL (1994).

[13] YORK, G., An advanced electron beam hibachi design and performance , ibid.

[14] SETHIAN, J.D., OBENSCHAIN, S.P., McGEOCH, M.W., SMITH, I.D., CORCORAN, P.A., ALTES, R.A., Pulsed power requirements for a high power KrF laser for a high gain inertial confinement fusion system, Power Modulators (Proc. 22nd Int. Symp. Boca Raton, 1996).

STABILIZATION OF THE RESISTIVE SHELL MODE IN FUSION REACTORS*

R. FITZPATRICK
Institute for Fusion Studies,
University of Texas at Austin,
Austin, Texas,
United States of America

Abstract

STABILIZATION OF THE RESISTIVE SHELL MODE IN FUSION REACTORS.

Stabilization of the 'resistive shell mode' is vital to the success of the 'advanced tokamak' concept. The most promising reactor relevant approach is to apply external feedback using, for example, the previously proposed 'fake rotating shell' scheme. This scheme, like other simple feedback schemes, only works if the feedback controlled conductors are located inside the 'critical radius' at which a perfectly conducting shell is just able to stabilize the ideal external kink mode. In general, this is not possible in a reactor since engineering constraints demand that any feedback controlled conductors be placed *outside* the neutron shield blanket (i.e. relatively far from the edge of the plasma). However, the fake rotating shell feedback scheme can be modified so that it works even when the feedback controlled conductors are located well beyond the critical radius. The gain, bandwidth, current and total power requirements of such a feedback system for a reactor sized plasma are estimated to be less than 100, a few Hz, a few tens of kA and a few MW, respectively. These requirements could easily be met by using existing technology. It is concluded that feedback stabilization of the resistive shell mode is feasible in a tokamak fusion reactor.

Introduction

The eventual aim of the "advanced tokamak" concept [1] is the design of an attractive fusion power plant which can operate in steady state, at high fusion power density, with low recirculating power. Acceptable beta limits are only obtained in advanced tokamak designs if the effect of a close fitting *ideal* shell is taken into account in the magnetohydrodynamical (MHD) stability calculations [2]. According to conventional theory, a close fitting *resistive* shell can convert the fast growing ideal external kink mode into the far slower growing "resistive shell mode," but it *cannot* completely stabilize the mode. Unfortunately, the growth time of the resistive shell mode is still much shorter than the expected pulse length of a reactor discharge. It follows that the full advantages of the advanced tokamak concept are only achievable if the resistive shell mode is somehow stabilized.

There are two main approaches to suppressing the resistive shell mode. The first involves spinning the plasma toroidally using unbalanced neutral beam injection (NBI). However, it is highly unlikely that the necessary levels of toroidal

* Research funded by the US Department of Energy under Contract No. DE-FG05-80ET-53088.

rotation could be maintained in a tokamak reactor by realistic levels of NBI power. The second, more reactor relevant, approach is to employ a network of feedback controlled conductors surrounding the plasma. Most simple feedback schemes (*e.g.*, the fake rotating shell scheme [3]) only work if the feedback controlled conductors are situated *inside* the "critical radius" at which a complete perfectly conducting shell causes the ideal external kink mode to become marginally stable. Unfortunately, engineering constraints require that any feedback controlled conductors must be placed *outside* the neutron shielding blanket in a reactor, which implies that under most circumstances the conductors are situated *well beyond* the critical radius. A *reactor relevant* feedback scheme must be able to operate successfully in this configuration.

The fake rotating shell feedback scheme

Consider the fake rotating shell feedback scheme, which is described in detail in Ref. 3. The plasma (which is a standard, low β, large aspect ratio, tokamak plasma) is surrounded by a uniform *network* of wires of diameter d. Let $\Delta\theta$ and $\Delta\phi$ be the angular spacing of the network cells in the poloidal and toroidal directions, respectively. Consider, for the sake of simplicity, the limit $n^2 r_w \Delta\phi \ll m^2 R_0 \Delta\theta$ in which the resistance and inductance of the poloidal legs of the network are negligible. Here, r_w is the minor radius of the network, R_0 is the major radius of the plasma, and m and n are the poloidal and toroidal mode numbers of the external kink mode, respectively. It is assumed that $m\Delta\theta \ll 1$ and $n\Delta\phi \ll 1$. The network acts like a "fake shell" whose L/R time is $\tau_w = \mu_0 \sigma_w r_w \delta_w$, where σ_w is the resistivity of the wires and $\delta_w = \pi d^2/4 r_w \Delta\theta$ is the "equivalent thickness" of a uniform shell of radius r_w containing the same amount of metal as the network. The "effective radius" of the fake shell is $r_e = r_w (1 + 2m/\Delta_c)^{1/2m}$, where $\Delta_c = 2\pi/\Delta\theta \ln(r_w \Delta\theta/\pi d)$. Thus, the network of wires acts like a uniform shell containing the same amount of metal, whose radius r_e is somewhat larger than the actual radius of the network.

Suppose that each network cell is accompanied by a high impedance sensor loop of equal area which measures the rate at which magnetic flux escapes through the loop (see Fig. 1). The voltage generated in each sensor loop is integrated, amplified by a factor $1/\tau$, and then fed into the network, as shown in Fig. 1. The feedback causes the fake shell to *rotate* poloidally with the apparent angular velocity $\Omega_w = -m\Delta\theta/\tau$. Note that Ω_w is directly proportional to the gain in the feedback circuits.

Suppose that the plasma is surrounded by a complete non-rotating shell (*i.e.*, the vacuum vessel) of radius r_v and L/R time τ_v ($\tau_v \gg \tau_w$). This, in turn, is surrounded by the feedback controlled network of conductors, which acts like a fake rotating shell of effective L/R time τ_w, effective radius r_e, and apparent angular rotation frequency Ω_w. The growth rate of the resistive shell mode is

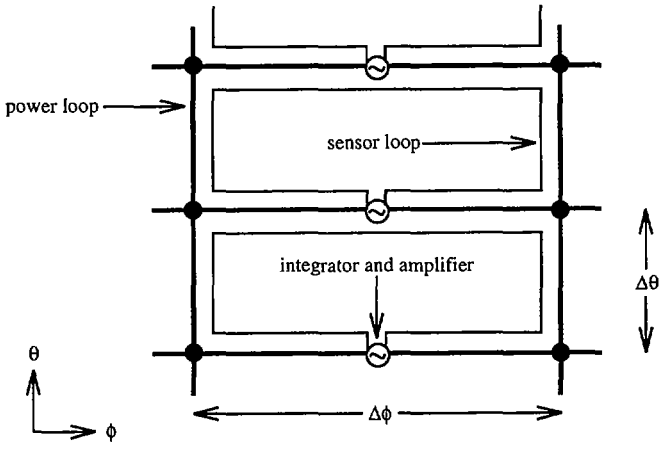

Figure 1: *Schematic diagram showing a few loops of a uniform two dimensional network of wires, surrounding the plasma, which is subject to feedback. The signals detected by the high impedance sensor loops are integrated, amplified and then fed into the power loops, as shown.*

given by

$$\gamma\tau_v \simeq \frac{2m}{(r_c/r_v)^{2m}-1}\left(\frac{1-\hat{\Omega}_w^2[(r_c/r_e)^{2m}-1]/[1-(r_v/r_e)^{2m}]}{1+\hat{\Omega}_w^2}\right) - \mathrm{i}\frac{2m}{(r_e/r_v)^{2m}-1}\frac{\hat{\Omega}_w}{1+\hat{\Omega}_w^2} \quad (1)$$

where $\hat{\Omega}_w = (\Omega_w\tilde{\tau}_w/2m)\left[1-(r_v/r_e)^{2m}\right]$. Here, r_c is the critical radius beyond which a perfectly conducting shell is unable to stabilize the external kink mode.

In the absence of feedback (*i.e.*, $\Omega_w = 0$), the resistive shell mode takes the form of a non-rotating mode growing on the L/R time of the vacuum vessel. Feedback causes the resistive shell mode to propagate in the direction of apparent rotation of the fake shell, but it also modifies the growth rate of the mode. If the effective radius of the fake shell r_e is *less than* the critical radius r_c of the m/n mode then feedback causes the growth rate to *decrease*. Above a critical value of Ω_w the resistive shell mode is stabilized. The corresponding critical "voltage gain" $G = 1/|\gamma|\tau$ in the feedback circuits (*i.e.*, the ratio of the voltage put out by an individual feedback amplifier to that which is generated by magnetic induction in the corresponding network loop) is given by

$$G_c = \frac{\tau_v}{m\Delta\theta\,\tau_w}\left(\frac{r_w}{r_v}\right)^{2m}\frac{(r_c)^{2m}-(r_v)^{2m}}{(r_c)^{2m}-(r_e)^{2m}} \quad (2)$$

The critical current which must be supplied by an individual feedback amplifier is of order

$$I_c \sim g_c \frac{r_w \Delta\theta\, b_r}{\mu_0} \tag{3}$$

where b_r is the perturbed radial magnetic field strength at radius r_w, and

$$g_c = 2\,\frac{(r_w)^{2m}}{\sqrt{(r_c)^{2m}-(r_e)^{2m}}\sqrt{(r_e)^{2m}-(r_v)^{2m}}} \tag{4}$$

The *total* power which must be supplied by the feedback amplifiers is

$$P_c \sim {g_c}^2\,\frac{2\pi^2 {r_w}^2 R_0\, {b_r}^2}{\mu_0 \tau_w} \tag{5}$$

Note that the total power expended by the feedback system whilst stabilizing the resistive shell mode is independent of the number of cells in the network.

A reactor relevant feedback scheme

The feedback system described above has many attractive features. In particular, stabilization of the resistive shell mode is achieved at comparatively modest voltage gains ($G_c \sim 20$), unlike a previously proposed feedback scheme which requires very high gains [4]. A low gain feedback scheme is far more resilient to the phase lags and time delays introduced by realistic power amplifiers that a high gain scheme. Unfortunately, the fake rotating shell scheme is *not* reactor relevant, since it actually increases the growth rate of the resistive shell mode when $r_e > r_c$, as is almost certain to be the case in a fusion reactor.

Consider a modified feedback scheme in which the network of wires (the "power network" actual radius r_w, effective L/R time τ_w) is connected to *two* arrays of sensors located at radii r_l and $r_{l'}$. Both sensor arrays have a sensor loop corresponding to each cell of the power network. The signals detected by the two sensor arrays are integrated, amplified by factors $1/\tau$ and $1/\tau'$, respectively, and then fed into the power network in an analogous manner to that shown in Fig. 1. Suppose that the inner sensor array lies between the passive shell (radius r_v, L/R time τ_v), which, for the case of a reactor, corresponds to the first wall, and the power network, but that the second array lies outside the power network. Thus, $r_v < r_l < r_w$ and $r_w < r_{l'}$. The dispersion relation for the resistive shell mode is given by

$$\gamma\tau_v \simeq \frac{2m}{(r_c/r_v)^{2m}-1}\left(\frac{1-\hat{\Omega}_w^2[(r_c/r_e)^{2m}-1]/[1-(r_v/r_e)^{2m}]}{1+\hat{\Omega}_w^2}\right) - \mathrm{i}\,\frac{2m}{(r_e/r_v)^{2m}-1}\,\frac{\hat{\Omega}_w}{1+\hat{\Omega}_w^2} \tag{6}$$

where $\hat{\Omega}_w = (\Omega_w \tau_w / 2m)\left[1 - (r_v/r_w)^{2m}\right]$. Note that Eq. (6) is analogous in form to Eq. (1), except that the effective radius of the fake shell is now given by

$$r_e = r_l \left(\frac{1 - \lambda (r_w/r_l)^{2m}}{1 - \lambda} \right)^{1/2m} \tag{7}$$

where $\lambda = -(\tau/\tau')(r_l/r_{l'})^m$. The apparent angular rotation frequency of the fake shell is

$$\Omega_w = -\frac{m\Delta\theta}{\tau} \left(\frac{r_w}{r_l} \right)^m \frac{(r_e)^{2m} - (r_v)^{2m}}{(r_w)^{2m} - (r_v)^{2m}} \frac{(r_w)^{2m} - (r_l)^{2m}}{(r_w)^{2m} - (r_e)^{2m}} \tag{8}$$

Thus, the effective radius of the fake shell is determined by the ratio of the two amplification factors $1/\tau$ and $1/\tau'$. The apparent rotation frequency depends on the magnitude of the amplification (the larger the amplification the faster the shell appears to rotate). In the absence of feedback from the outermost sensor array ($1/\tau' = 0$), the effective radius of the fake shell is the same as the radius of the inner array. However, it is possible to project the fake shell *inside* the inner sensor array by introducing an appropriate amount of feedback from the outer array into the overall feedback algorithm. As before, the feedback scheme is only capable of stabilizing the resistive shell mode if the effective radius of the fake shell r_e is less than the critical radius r_c for the m/n mode. There is an additional constraint, however, since if r_e becomes less than the radius of the passive shell r_v then the system goes into positive feedback, and intrinsically stable kink modes are destabilized. The critical voltage gain, current, and power needed to stabilize the resistive shell mode (for $r_v < r_e < r_c$) are given by Eqs (2), (3), and (5), respectively, provided that r_e is determined by Eq. (7).

The feedback scheme described above preserves all of the attractive features of the original fake rotating shell scheme (in particular, the low critical voltage gain), but is also capable of operating successfully in the reactor relevant situation in which the power network and the sensor arrays are located outside the critical radius. Stabilization of the resistive shell mode is possible whenever the fake rotating shell (radius r_e) is projected *between* the passive shell (radius r_v) and the critical surface (radius r_c).

Implications for ITER

The major radius, average minor radius and on-axis toroidal magnetic field strength of the proposed ITER [5] tokamak are $R_0 = 8.1$ m, $a = 3$ m, and $B_\phi = 5.7$ T, respectively. The first wall possesses an average minor radius of $r_v \sim 1.1\,a$ and an L/R time of $\tau_v \sim 1$ s. Consider a fake rotating shell feedback scheme which is required to stabilize the $m = 3$ resistive shell mode in ITER at perturbed magnetic field levels up to 1% of the edge poloidal magnetic field strength. Suppose that the sensor arrays and the power network are located *outside* the vacuum vessel (which is the only feasible location), so that $r_w = 1.6\,a$,

$r_l = 1.55\,a$, and $r_{l'} = 1.65\,a$. An appropriate number of network cells in the poloidal direction is 32 (this reduces troublesome inductive coupling between the sensor arrays and the power network). An appropriate number of network cells in the toroidal direction is 8. The closest to the plasma that the fake shell (radius r_e) can be projected without driving the system into positive feedback is $r_e = 1.24\,a$. Note that this is considerably closer to the plasma than either the sensor arrays or the power network. Suppose that the system is required to stabilize the $m = 3$ resistive shell mode whenever its critical radius lies beyond $1.3\,a$. This implies that the $m = 3$ kink stability boundaries of the plasma are equivalent to those calculated in the presence of a perfectly conducting shell located at radius $1.3\,a$ (this is sufficiently close to the plasma to significantly increase the β limit [6]). Assuming that the power network is constructed from 5 cm diameter copper wires, the critical voltage gain in the feedback circuits is around 50, the critical current which must flow in the power network is around 20 kA, and the critical power expended by the feedback amplifiers is around 3 MW. Note that the feedback amplifiers only have to respond to magnetic fields which are able to diffuse through the first wall. Thus, the bandwidth of the amplifiers need only be about 1 Hz.

Summary

It appears likely that a feedback system which mimics the effect of a relatively close fitting ideal shell can be installed on a tokamak reactor, despite the fact that all of the feedback controlled conductors and sensor loops are located relatively far from the plasma (*i.e.*, at least outside the blanket, and possibly outside the vacuum vessel). The gain, bandwidth, current and total power requirements of the system are extremely modest (*i.e.*, less than 100, a few Hz, a few tens of kA, and a few MW, respectively), and could easily be achieved using *existing technology*. Thus, an "advanced tokamak" reactor appears eminently feasible.

REFERENCES

[1] KESSEL, C., MANICKAM, J., REWOLDT, G., TANG, W.M., Phys. Rev. Lett. **72** (1994) 1212.

[2] MANICKAM, J., CHANCE, M.S., JARDIN, S.C., KESSEL, C., MONTICELLO, D., POMPHREY, N., REIMAN, A., WANG, C., ZAKHAROV, L.E., Phys. Plasmas **I** (1994) 1601.

[3] FITZPATRICK, R., JENSEN, T.H., Phys. Plasmas **3** (1996) 2641.

[4] BISHOP, C.M., Plasma Phys. Control. Fusion **31** (1989) 1179.

[5] REBUT, P.-H., Fusion Technol. **27** (1995) 3.

[6] STRAIT, E.J., TAYLOR, T.S., TURNBULL, A.D., FERRON, J.R., LAO, L.L., RICE, B., SAUTER, O., THOMPSON, S.J., WRÓBLEWSKI, D., Phys. Rev. Lett. **74** (1995) 2483.

IGNITION AND BURN IN ELECTRIC TOKAMAKS AT LOW MAGNETIC FIELDS

R.J. TAYLOR, P.A. PRIBYL, L.W. SCHMITZ, G.R. TYNAN
UCLA Laboratory for Energy Science,
Los Angeles, California,
United States of America

Abstract

IGNITION AND BURN IN ELECTRIC TOKAMAKS AT LOW MAGNETIC FIELDS.

It is argued that vast improvements in the physics and implementation of a tokamak reactor core are possible if one (1) operates at unity beta to exclude the magnetic field from a large fraction of the plasma volume, (2) adopts a large enough aspect ratio for equilibrium control, (3) chooses a magnetic geometry with a volumetric belt-like 'magnetic centre' instead of the more common magnetic axis, and (4) uses rapid poloidal flow to maintain a dynamic equilibrium. The flows are needed for simultaneously reducing the effects of plasma granularity (finite gyroradius effects) on confinement and stabilizing the low n number MHD modes. These elements define the 'electric' aspect of the tokamak both at the microscopic equilibrium level and the H mode type global confinement level. When combined with the omnigenous magnetic surfaces (closed mod-B surfaces) of a high beta plasma (PALUMBO, D., Nuovo Cim. **53B** (1967) 507), nearly classical confinement in a plasma with otherwise significant Larmor scale granularity is predicted. Ignition and burn in a D-T plasma would then be possible at $B_\phi \sim 2$ T and $I_p \sim 4$ MA, while a device with ITER-like parameters would be capable of burning advanced fuels.

1. INTRODUCTION

Current tokamak reactor designs call for steady state magnetics with a line-like magnetic axis. The toroidal current density close to the axis is limited by low values of local plasma elongation although reverse shear offers some improvement on the situation. The approach to unity beta operation at a convenient aspect ratio ($A \sim 4$–5) is not possible within the limits of these conventional topologies. Cowley et al. [1] have shown that it may be possible asymptotically to reach unity beta with large Shafranov shifts by using a constant $q(\psi)$ profile, but these configurations have unacceptably large pressure gradients at the plasma edge. We find that both reverse shear and large elongation, particularly at the magnetic axis, are required for practical devices.

We assume a conventional line magnetic axis at the beginning of the discharge which then evolves into a belt shaped magnetic centre, followed by a slab-like magnetic centre in the steady state. Similar shapes have been considered by Jensen et al. [2] without using electric fields. By excluding the magnetic fields and pressure gradients adiabatically, we evolve a core volume that is free of magnetic fields, as in Ref. [2]. It is in this sense of operating in a new magnetic configuration that ours

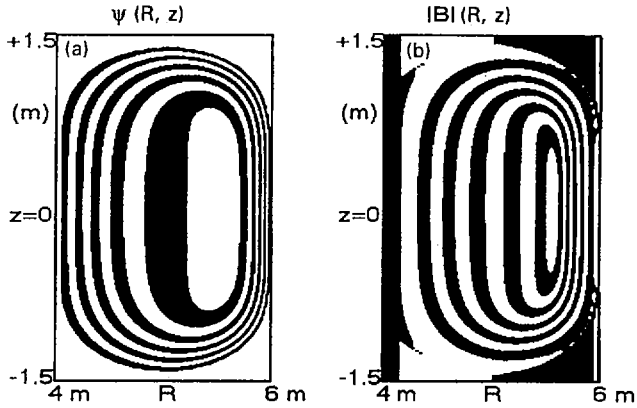

FIG. 1. (a) Flux surfaces; (b) mod-B surfaces.

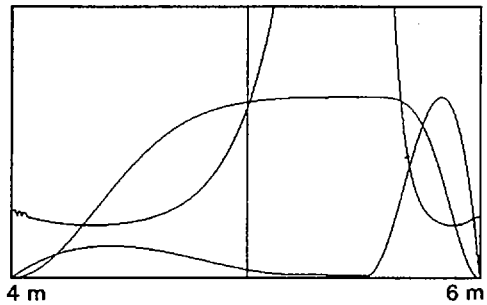

FIG. 2. Pressure, q and J_ϕ profiles.

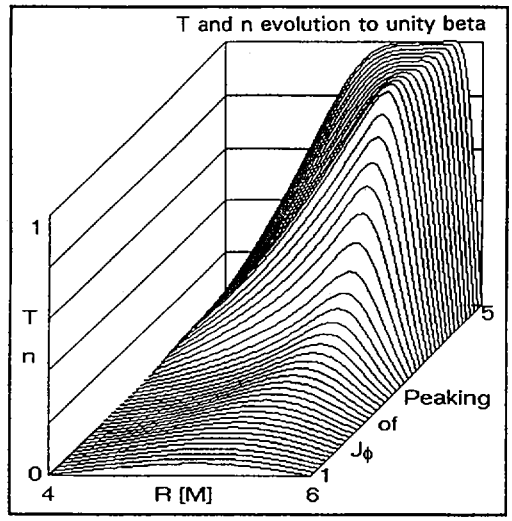

FIG. 3. Time evolutions of temperature and density.

is an alternate concept tokamak reactor. These devices may be used for advanced fuel fusion applications since low synchrotron radiation levels are achievable.

The development of our equilibrium requires poloidal rotation for two reasons: (1) to reduce anomalous ion heat transport by locking the ion drifts to the magnetic surfaces until omnigenous magnetic surfaces can develop, resulting in classical ion confinement at all betas and (2) to provide stability against MHD kink and ballooning modes.

The full solution to the Grad–Shafranov equation results in the magnetic surfaces and the mob-B surfaces shown in Fig. 1.

Figure 2 shows the pressure, the toroidal current and the q profile along the midplane. We note that the central q is very large, because of the elongation of the magnetic axis, and that the toroidal current profile is shifted relative to the magnetic surfaces. The anticipated temperature and density evolutions are shown in Fig. 3. Broad profiles are achievable for this equilibrium, and 50% volume averaged beta is possible.

The electric nature of these devices favours high aspect ratio, owing to the reduced torque requirement. A compromise with $A \sim 4$ is reasonable when the central shift of the plasma column due to high beta is also taken into account. Once the aspect ratio is chosen, the minor radius is, in turn, determined by neutral screening requirements and by the Lawson criterion.

We argue that the thermal ion dynamics can be made classical at the orbit level by poloidal rotation in the low beta portion of the profile and by the omnigenous magnetic configuration in the high beta core (once it develops). The electron dynamics may not approach their classical limit because of the lack of perfect symmetry on the magnetic surfaces. Some amount of symmetry defect is unavoidable, owing to (1) curvature effects, (2) engineering limitations and (3) control dynamics related fluctuations.

Our investigations (experimental and theoretical) so far indicate that classical ion confinement may be achieved at low magnetic fields in a large but cost efficient device. D–T plasma ignition conditions could be simulated in a hydrogen plasma at low cost in a device with $R = 5$ m, $a = 1$ m, $\kappa_{chamber} = 1.5$ and $B = 1.5$ T.

2. ION ORBIT DYNAMICS AND REDUCTION OF MAGNETIC FLUCTUATIONS

In electric tokamaks, thermal ion transport can be assumed classical provided the orbit drift away from the magnetic surfaces is smaller than the ion gyroradius. This is achievable with sufficiently rapid poloidal rotation, the condition being given by $E_r > v_{thi}B/A$, where v_{thi} is the ion thermal speed, A is the local aspect ratio R/r, B is the total magnetic field and E_r is the radial electric field. We denote this as 'ion locking' to the surfaces. For E_r above this value, thermal ion drift orbits align with magnetic surfaces to within one gyroradius; tail ions are lost at the neoclassical rate

modified by magnetic well effects. These conditions can be achievable with subsonic ($v_\theta/v_i < 1$) poloidal rotation but would require *supersonic* toroidal rotation for convenient aspect ratios. The electric field is maintained by balancing driven fast particle losses against neoclassical damping. The above condition on the radial electric field has been exceeded in the H mode layer in some tokamaks [3, 4].

In addition, omnigenous magnetic conditions, where the |B| surfaces align themselves with the magnetic surfaces, can be achieved as the central beta is raised and the plasma digs a magnetic well. This condition further results in increased confinement of both electrons and superthermal ions.

Irregularities of the magnetic surfaces remain a concern in high beta equilibrium since the instantaneous and localized force imbalance across the gyroradius can be very large. The local force imbalance across a flux tube of dimension ρ_i is related to $\rho_i \nabla^2 p$. The coefficient of proportionality is given by the ratio of the decay rate of the flux tube perturbation to the ion cyclotron frequency, $\omega_{\text{flux tube}}/\Omega_{ci}$; $\omega_{\text{flux tube}}$ is, in turn, given by the electron transit frequency. The resulting random radial velocity is then approximately given by $\delta V/v_i = (\rho_i/\tau_{\text{flux tube}})(\rho_i/a)^2/V_{E\times B}$. This type of finite gyroradius effect can be reduced by poloidal rotation as indicated by the $V_{E\times B}$ term, allowing classical confinement to be reached for relatively small devices, $L_p/\rho_i \sim 50$, where L_p is the pressure gradient scale. Because of the toroidal shift associated with high beta in general, L_p cannot be made larger than $\sim a/4$.

3. ELECTRON HEAT TRANSPORT REDUCTION DUE TO MAGNETIC OMNIGENEITY

Electrons are considerably less affected by device electric fields, owing to their small drift orbits and their large parallel velocity. Consequently, in our model, they remain turbulent at the level dictated by the parallel gradients and the associated electron relaxation dynamics. We assume that there is no additional instability involving the flux tubes; this is made plausible by the orbit locking mechanism introduced above. From the correlation dynamics point of view, the size of the flux tube is associated with the ion gyroradius and not with c/ω_{pe} in these plasmas ($\rho_i > c/\omega_{pe}$). The fluctuation driven radial heat transport is then related to the parallel current relaxation and the remaining flux tube fluctuations. We assume that the total heat transport will reduce with an increase in the toroidal field symmetry within a flux surface, as in both NeoAlcator confinement scaling and the refined IOC modes [5]. The toroidal asymmetries are obtained from the effective aspect ratio, defined as $A_{\text{eff}} = 2B/\delta B$, where δB is the variation of B on a magnetic surface. For conventional tokamaks, this reduces to $A_{\text{eff}} = A = R/r$.

The importance of poloidal symmetry is emphasized by plotting the effective inverse aspect ratio normalized to the geometrical value in Figs 4 and 5, for a near unity beta equilibrium. In applying our projections to a reactor we require omnigeneity levels and flux tube symmetry such that the resultant χ_e be less than classical χ_i.

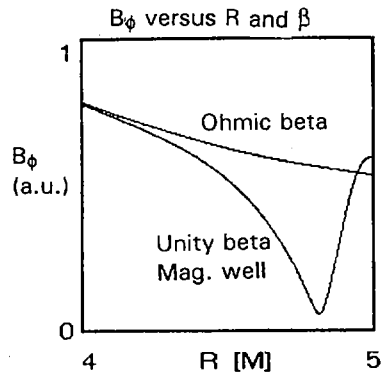

FIG. 4. Mod-B profiles.

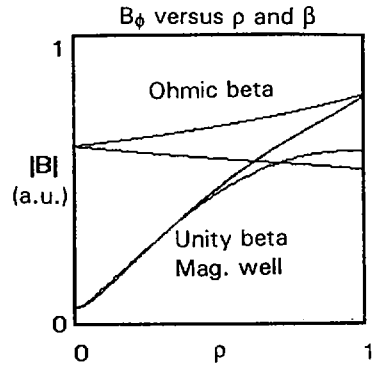

FIG. 5. Omnigeneity profiles.

4. LOCAL AND GLOBAL STABILITY CONSIDERATIONS

Rapid plasma rotation provides stabilizing properties not available in standard tokamaks through three effects: (1) ion orbits are strongly 'locked' to the flux surfaces; (2) plasma flux tubes rotate rapidly through regions of bad and good curvature, resulting in a mechanical averaging of the curvature; and (3) shear in the rotation profile contributes additively to magnetic shear. In particular, we expect that rapid poloidal averaging will contribute to the stabilization of ballooning modes (and any modes that are locked to the machine structure). Mercier stability is typically only violated near the magnetic axis for highly peaked pressure profiles associated with broad current profiles, a configuration that is not relevant to the electric tokamak. Broad profiles will similarly preclude internal kink modes from developing. We may run peaked profiles at the highest beta, but only in the presence of a significant magnetic well, a configuration which is absolutely stable to these modes.

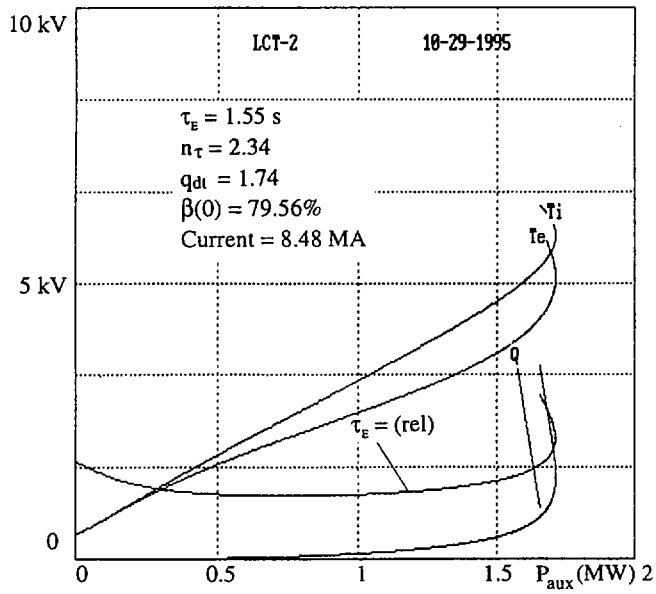

FIG. 6. Classical ignition predictions.

External kink modes limit conventional tokamak operation to below the Troyon stability limit. These can be either current or pressure driven and typically represent the most severe stability criterion in the system. In the rotating plasma configuration of an electric tokamak, this traditional 'first stability' boundary no longer applies, i.e. we are operating in the 'third stability' regime [6]. In the simplest case, this can be verified by analytic solution of the cylindrical kink stability problem including macroscopic sheared poloidal rotation. The mode is stabilized if it is sheared apart faster than its (non-rotating) growth rate. Numerical studies are under way for the toroidal pressure driven case.

5. OMNIGENOUS IGNITION PREDICTIONS AT UNITY CORE BETA

Figure 6 shows the ignition trajectory for an electric tokamak with our projection of classical ion confinement. Ignition can be achieved with a few MW of auxiliary heating. The central pressure is 5 atm and the confinement time is 5 s. Our scenario is to first bring the plasma to omnigenous conditions and then to adiabatically raise the toroidal field and the plasma current to the required values. During this phase and the subsequent burn phase, the plasma current is derived from radial transport [7] and from neoclassical bootstrap. In the burn conditions, both toroidal and poloidal rotations need to be controlled by fuelling and magnetic intervention.

6. SUMMARY AND CONCLUSIONS

An electric tokamak reactor using magnetoelectric confinement and stability has been described and its performance evaluated. Both stability and confinement are greatly improved over the standard tokamak, enabling operation at near unity beta in the plasma core at modest power levels.

Thermal ion transport in an electric tokamak can be reduced to its classical value by imposing a sufficiently large radial electric field, $E_r > v_{thi}B/a$. Non-thermal ion losses will be used to generate this electric field. Omnigenous magnetic surfaces are used in which the mod-B surfaces align with the magnetic surfaces. This alignment increases the effective aspect ratio, resulting in an improved electron confinement.

Stability is also improved by plasma rotation combined with reverse shear until a magnetic well can be formed.

If both pressure and confinement can indeed be improved simultaneously in such a low field tokamak, then ignition becomes possible at low cost with less than 5 MW of auxiliary heating.

REFERENCES

[1] COWLEY, S.C., KAW, P.K., KELLEY, R.S., KULSRUD, R.M., Phys. Fluids B 3 (1991) 2066.

[2] JENSEN, T.H., MILLER, R.L., LIN-LU, Y.R., Pressure Driven Tokamaks, Rep. GA-A22126, General Atomics, San Diego, CA (1995).

[3] TAYLOR, R.J., et al., Phys. Rev. Lett. 63 (1989) 2365.

[4] GROEBNER, R., Phys. Fluids B 5 (1993) 2343.

[5] WOLF, G.H., et al., IAEA-CN-64/O2-5, these Proceedings, Vol. 1, p. 177.

[6] ITOH, S.I., et al., "Theory of anomalous transport in the H-mode", paper presented at the 4th IAEA H-mode Workshop, Naka, Japan (November 1993).

[7] NUNAN, W.J., DAWSON, J.M., Phys. Rev. Lett. 73 (1994) 1628.

STEADY STATE LITHIUM PLASMA AND LIQUID LITHIUM DIVERTOR EXPERIMENTAL VALIDATION

N.V. ANTONOV, V.B. PETROV, A.S. PLESHAKOV,
A.S. RUPYSHEV, Y.A. SOKOLOV, B.I. KHRIPUNOV,
V.V. SHAPKIN, V.I. PISTUNOVICH
Nuclear Fusion Institute,
Russian Research Center,
Kurchatov Institute,
Moscow

A.V. VERTKOV, V.A. EVTIKHIN, I.E. LYUBLINSKIJ
State Enterprise 'Red Star',
Moscow

L.G. GOLUBCHIKOV
Ministry for Atomic Energy of the Russian Federation,
Moscow

Russian Federation

Abstract

STEADY STATE LITHIUM PLASMA AND LIQUID LITHIUM DIVERTOR EXPERIMENTAL VALIDATION.

Lithium is considered to be a possible plasma facing material in some divertor concepts of a future thermonuclear tokamak reactor. Lithium is evaporated from the divertor plate surface and ionized under reactor exhaust plasma impact, thus carrying out two main functions: preventing plate structure erosion and taking out very high thermal loads from the plate. Experiments are described in validation of the choice concerning the practical realization of a liquid lithium evaporating surface (capillary structure). First, the steady state lithium plasma parameters were investigated in the SPRUT-4 linear device, in beam–plasma discharges in crossed electric and magnetic fields. The next part of the experiments was devoted to the high power load of a lithium capillary porous target with an electron beam followed by lithium vapour and plasma generation. The results were obtained for high efficiency of heat removal from the loaded surface in the range of 1–25 MW/m^2. The measured lithium evaporation rate was established to reach 1 $kg \cdot m^{-2} \cdot s^{-1}$.

1. INTRODUCTION

Different approaches are now being investigated to find an appropriate solution to the tokamak reactor divertor problem among materials with low Z number. The gaseous divertor concept and liquid metal films and spray are also proposed for this

purpose [1, 2]. The steady state power load on the divertor plate is now evaluated at a level of 5 MW/m^2 for the ITER reactor and becomes even higher for future DEMO size reactors [2]. Hence, the problem of the divertor wall material is still a very serious one. Here, we are concerned with the recently proposed liquid metal divertor concept based on a capillary porous structure filled with liquid lithium which is used for the divertor plate surface structure [3]. Evaporation of lithium after the plasma has hit the surface ensures effective cooling of the structure. One of the advantages of the concept is self controlled lithium transport to the surface, according to the power taken up.

Since direct experimental lithium plasma studies are needed for the work on this concept, we here report experimental results of steady state lithium plasma investigations in the linear device SPRUT-4 at the Kurchatov Institute as well as the results of high power load experiments with the capillary lithium structure. The characteristics of the lithium evaporation which can be taken as a basis for further development of the concept are presented.

2. THE SPRUT-4 LINEAR DEVICE

For the last fifteen years, a series of SPRUT linear machines has been used at the Kurchatov Institute in order to carry out experimental research of lithium plasma and to develop plasma isotope separation methods. SPRUT-4 is the last device of the series and has so far been in operation in the present day modification as is shown in Fig. 1. It is designed for experimental investigation in steady state operation. An

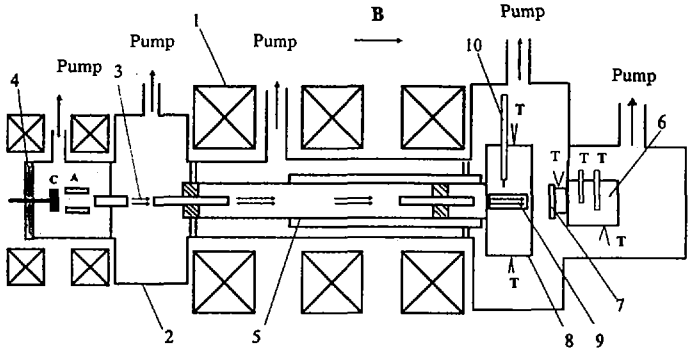

FIG. 1. Schematic of SPRUT-4 device (1 — magnetic coils; 2 — vacuum chamber; 3 — electron beam; 4 — insulator; 5 — water cooled condensator; 6 — capillary target; 7 — evaporation surface of capillary target; 8 — shield condensator; 9 — observation window; 10 — Langmuir probe; C — cathode; A —anode; T — thermocouple).

electron beam is generated on the axis of the vacuum chamber in a longitudinal magnetic field. It is received by the lithium capillary target which is at the same time the beam collector. Langmuir probe measurements, optical spectrum studies, video recording and temperature and calorimetric measurements are available as are the main electrical parameters.

3. STEADY STATE LITHIUM PLASMA EXPERIMENTS

In this section, we present some important results on lithium plasma in the SPRUT-4 device in its previous modification, which was intended for plasma isotope separation. In contrast to the design shown in Fig. 1, the former device had a hot cylindrical discharge zone (L = 1 m, D = 0.12 m) surrounding the electron beam (d = 7 mm), where the plasma column was generated (Fig. 2). The principle of plasma production was a beam–plasma discharge in a longitudinal magnetic field of 0.08–0.85 T. In addition, an electrical field was applied in radial direction in order to obtain the discharge in the crossed **E** × **B** fields. Figure 2 also shows the lithium vapour feed (F) and the extraction system outlets (P, W) needed for steady state operation of the device.

It was shown that the beam–plasma discharge in lithium had the same features and the same structure as in other substances (gases; see Ref. [4]). The characteristic properties of the lithium discharge were essentially determined by the low lithium ionization potential ($U_{ion} \sim 5.4$ eV), which led to a relatively low discharge ignition power threshold (~ 2 kW) and a low electron temperature ($\sim U_{ion}$). The lithium discharge in crossed fields proved to be even more effective than the discharge without external electric field in that it ignited with the electron beam at relatively low power and was essentially sustained by the acoustic instability effect, with a high energy input from the radial electric source [5], the radial lithium current reaching a maximum of 65 A.

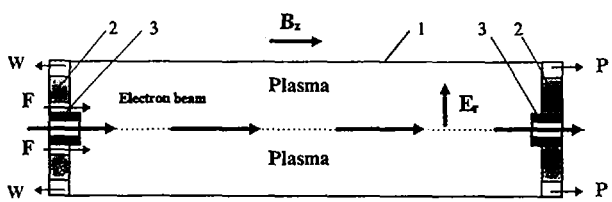

FIG. 2. Schematic of SPRUT-4 discharge zone for lithium plasma separation experiments (1 — conducting cylinder; 2 — insulator; 3 — positive electrode).

The plasma parameters were measured by stationary and movable Langmuir probes. The lithium steady state plasma density ranged in an interval of 10^{12}–10^{14} cm^{-3}; the electron temperature was 2–5 eV. An important characteristic of the device was the fact that the mass flow rate through the discharge zone varied between 10^{-4} and 1.2×10^{-2} kg/h (3.3×10^{20} atom/s), depending on the experimental conditions. The maximum separation factor for lithium isotopes was observed in longitudinal direction; it was found to be $\alpha = 2.1$ for machine operation at high density ($> 10^{13}$ cm^{-3}).

The experience gained in our work with beam–plasma lithium discharges has proven to be useful in the experiments on high power loading of the capillary divertor model with electron beams, to be described below, because here the behaviour of the lithium plasma again appeared as an accompanying effect.

4. HIGH POWER LOAD CAPILLARY STRUCTURE EXPERIMENTS

As was mentioned in Section 2, the loading of the porous capillary structures was performed with a steady state electron beam (d = 18 mm at the target) of SPRUT-4 at 1–9 keV and 0.1–2.0 A in a magnetic field of 0.1 T at the target (Fig. 1). The specific power load was 1–50 MW/m^2, and duration of the load pulse ranged from 34 to 1000 s. The porous capillary structure was made of molybdenum and filled with liquid lithium. The total lithium volume of the supply vessel was 150–350 cm^3 [6, 7].

The target response to the durable electron beam loading was investigated as were the material and energy balances. The characteristics of electron beam and target current were recorded. The temperature of the capillary target was measured at several points, including one point near the evaporating surface. The plasma was monitored by integral optical light signals and a single electric probe ion saturation current. Video recording of the process was carried out.

The data analysis resulted in the lithium evaporation rate as a function of the target power load (Fig. 3). With a load increase from 1 to 25 MW/m^{-2}, it rose from 10^{-2} to 0.82 $kg \cdot m^{-2} \cdot s^{-1}$. The target surface temperature was estimated by a balance analysis and by direct measurement with a thermocouple placed near the surface (Fig. 4, open and solid symbols, respectively). These values are found to correlate well and to rise from 650 to 950°C in the power interval covered. The corresponding neutral vapour density changes from 10^{15} to 10^{17} cm^{-3} in the same interval.

The accompanying plasma of the beam generated discharge was found not to play an important role in energy absorption and transport in our case, and the initial energy of the electron beam was transferred to two channels: lithium evaporation and target heating. The results of plasma density measurements 6 cm from the target surface and 1.5 cm from the beam axis with a single electrical probe are shown in Fig. 5. The maximum measured plasma density value was 10^{14} cm^{-3}, but it is

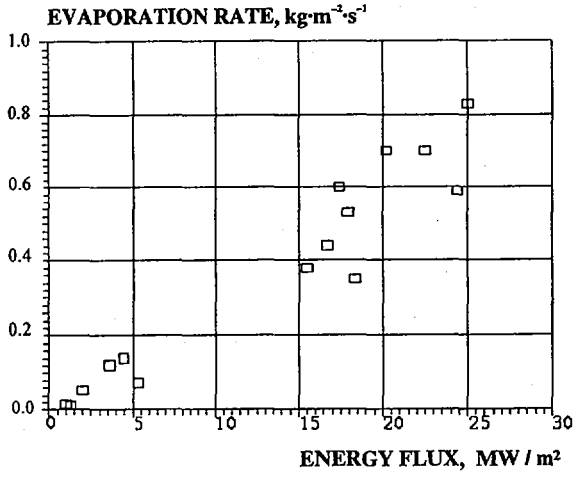

FIG. 3. Lithium evaporation rate from capillary structure under power load.

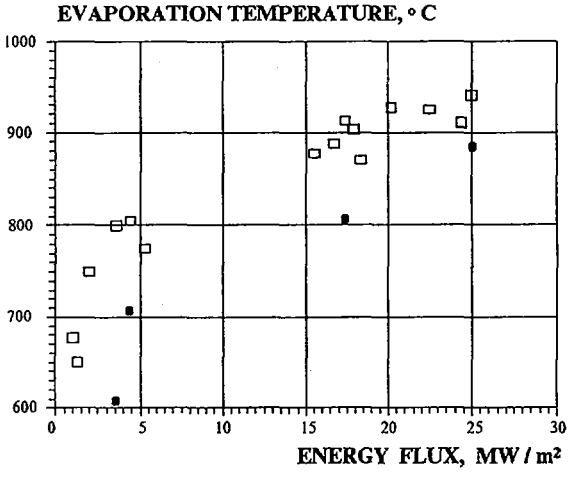

FIG. 4. Lithium capillary target surface temperature (open symbols: result of balance estimation; solid symbols: direct measurement near the surface).

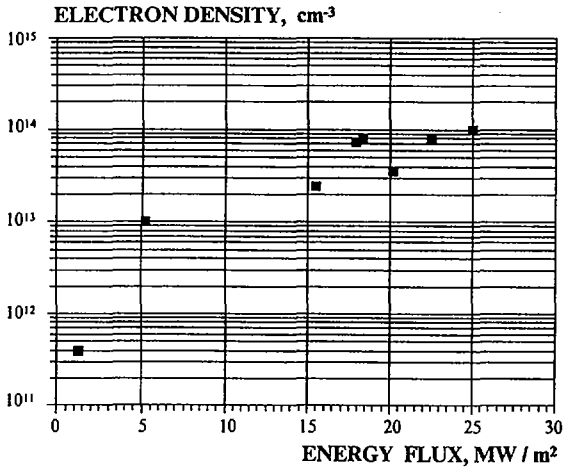

FIG. 5. Electron density in lithium plasma flame.

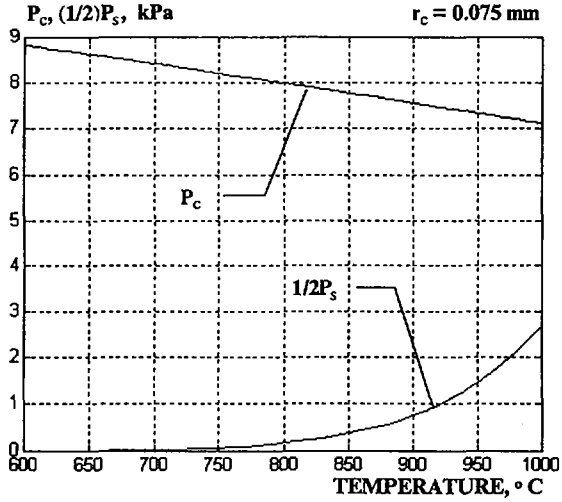

FIG. 6. Target capillary pressure and saturated vapour reaction factor.

obvious that closer to the surface it must be higher. It could not be measured by stationary probes because of the high energy concentration in this area.

We observed that sufficient lithium transport by the capillaries to the target surface must be ensured. Otherwise, the capillary structure would immediately be damaged. The condition for normal operation of the capillary structure can be written as $\Delta P = P_c - 1/2\ P_s - P_{mg} - P_h > 0$, where P_c is the capillary pressure in the system, P_s the reactive pressure of the saturation vapour, P_{mg} the magneto-hydrodynamic pressure losses, and P_h the hydrostatic losses. The results of the analysis in our case are shown in Fig. 6, where the capillary pressure and the saturated vapour reaction factor, $(1/2)\ P_s$, are compared in the corresponding temperature interval. According to this figure, our capillary system should operate with a certain pressure reserve. The hydrostatic losses were estimated to be very low ($\sim$400–500 Pa) and negligible in our targets. Unfortunately, it was difficult to evaluate the magnetohydrodynamic losses in capillaries without an appropriate model, but in our target design the reserve to overcome these losses seemed to be sufficient.

The exposition time was 1000 s for a load of 1–5 MW/m^2, 100 s for 15–20 MW/m^2 and 5 s for 45–50 MW/m^2 in these experiments and depended on the experimental task and on the behaviour of the target.

5. CONCLUSIONS

Experiments were performed in the SPRUT-4 device on continuous lithium plasma and capillary lithium structure loading with electron beams at a specific power of 1–50 MW/m^2.

The beam–plasma discharge in crossed electric and magnetic fields was characterized by densities of 10^{12}–10^{14} cm^{-3} and electron temperatures of 2–5 eV.

Stable operation of an open lithium capillary structure under high power electron beam loading with continuous lithium evaporation from the target surface was demonstrated. The maximum lithium evaporation rate was measured for a load of 25 MW/m^2 and reached 0.8 kg/m^2 at a temperature of 950°C.

The experiments performed confirm that a liquid lithium evaporating surface can be used, operating in steady state conditions at power loads that are considered of relevance in actual large tokamak thermonuclear projects, a capillary porous surface being employed as the basis of the design.

These results can be used for further development of the liquid lithium divertor concept. The SPRUT-4 linear device has proved to be very useful for the experimental validation of the concept considered. With the results of numerical calculations for lithium plasma diffusion from the divertor surface into the bulk plasma [7] and with the possibility of generating deuterium plasma in this machine, further experiments in this direction are planned in order to establish the importance of the effect of ionized lithium penetration along the magnetic field.

REFERENCES

[1] JANESCHITZ, G., et al., J. Nucl. Mater. **220–222** (1995) 73.
[2] SOKOLOV, Yu.A., Fusion Eng. Des. **29** (1995) 18.
[3] GOLUBCHIKOV, L.G., et al., "Development of the liquid metal fusion reactor divertor with capillary structure of the target", paper presented at the International Conference on Fusion Research Materials, Obninsk, 1995.
[4] GADEEV, K.K., et al., Beiträge aus der Plasmaphysik **24** (1984) 143 (in German).
[5] KHRIPUNOV, B.I., et al., "Ionization process features of beam–plasma discharge in crossed electric and magnetic fields", Physics of Ionized Gases (Proc. 21st Int. Conf. Bochum, 1993), Ruhr-Universität Bochum, Arbeitsgemeinschaft Plasmaphysik (1993) 195.
[6] PISTUNOVICH, V.I., et al., "Research of the target capillary structures effectiveness at the divertor conditions", paper No. 080047 presented at the International Conference on Fusion Reactor Materials, Obninsk, 1995.
[7] PISTUNOVICH, V.I., et al., in Plasma-Surface Interactions (Proc. 12th Conf. St. Raphaël, 1996).

THE LIQUID LITHIUM FUSION REACTOR

V.A. EVTIKHIN[1], V.I. PISTUNOVICH[2], L.G. GOLUBCHIKOV[3], V.M. KORYAVIN[3], I.E. LYUBLINSKIJ[1], A.V. VERTKOV[1], V.A. POZHAROV[2], D.Yu. PROKHOROV[2]

[1] Red Star State Enterprise

[2] Russian Research Center, Kurchatov Institute

[3] Russian Federation Ministry for Atomic Energy

Moscow, Russian Federation

Abstract

THE LIQUID LITHIUM FUSION REACTOR.

A conceptual study of a tokamak reactor with liquid lithium and with evaporative cooling and protection of the blanket and the divertor has been conducted and its advantages are discussed. Up to now, no self-consistent solution of the problem of the divertor has been found for ITER conditions, and it is not likely to be found during the ITER Engineering Design Activities (EDA). The little space left after allowing for the magnetic coil systems, auxiliary heating, diagnostics, and the blanket tritium breeding and cooling system does not permit use of an ordinary cooling system, as used in a fission reactor, at a fusion power level of over 1.5 GW. The following issues have been considered in the Liquid Lithium Fusion Reactor project: the necessity of liquid metal for the development of a tokamak based reactor to produce electricity, the advantages of lithium, possible fabrication solutions for the liquid metal blanket and divertor systems, reactor structural materials, reactor safety, and tritium and helium extraction. Along with the conceptual design studies, the paper presents results of calculations and experiments aimed at reactor validation.

1. INTRODUCTION

For decades, fusion reactor conceptual designs based on different principles have been proposed, considered and evaluated. A variety of design versions and technical approaches at different project stages were dictated by the fabrication technology for each specific case, experimental confirmation, safety priority issues, scientific and engineering situations, subjective factors, etc. However, the approach to solving scientific and engineering problems that will result in the creation of an energy source based on a fusion reactor remains elusive. It requires correct answers and optimal engineering solutions to develop a safe, ecologically sound, efficient and profitable reactor with its own fuel cycle.

ITER, which is being designed at present, will be able to demonstrate steady state thermonuclear burning. The accepted engineering decisions for reactor design aimed only at safety issues do not solve other technical problems. They include the 'cold' shielding blanket design and the development of a divertor operating at the limit of calculated conditions which has not been confirmed experimentally or technologically. That is why the fusion reactor prototype must be based on other technical principles.

The application of lithium in a fusion reactor is considered to be extremely effective because lithium, which ensures tritium breeding, possesses a unique set of suitable physical and thermophysical properties and has been confirmed technologically [1]. Lithium is considered, in various approaches, acceptable for use in the first wall shielding of inertial plasma confinement reactors [2, 3]. A filmy liquid metal shield has been proposed for a tokamak reactor first wall and divertor [4]. Liquid lithium was chosen for use in the Experimental Fusion Reactor (EFR) blanket [5]. The concept of a DEMO type reactor at present under development is also based on the application of high temperature liquid lithium [6]. The concept of a self-cooled liquid lithium blanket was proposed for simultaneous tritium breeding and heat removal [7]. Just as fast reactors with their compact, high specific energy output core could not be built without a liquid metal coolant [8], so a fusion power reactor with a high temperature coolant and extremely high specific stationary and peak thermal loads cannot be built without liquid lithium and new engineering and fabrication principles.

The application of liquid lithium has previously been considered for the solution of separate problems in fusion reactor design but these studies did not include a broad description of all the possible advantages of this material. The essential limitation was the lack of fabrication and engineering information that would have validated the use of all the attractive capabilities of liquid lithium in a fusion reactor design.

This paper presents the Liquid Lithium Fusion Reactor (LLFR) concept, which applies new technical principles. Results of calculations and experiments related to the 'liquid lithium metal divertor with capillary-pore protection system' [9] concept are given.

2. LLFR BLANKET

In the blanket, lithium will provide three main functions. First, natural lithium possesses the required high tritium breeding capability. According to calculations, the DEMO type blanket zone thickness including shielding need not exceed ~ 0.8 m for a tritium breeding ratio of ≥ 1.05.

Secondly, liquid lithium in a self-cooled blanket is found to be the most effective coolant when compared with other liquid metals. Owing to lithium's unique thermophysical properties and extremely low operating pressure (for example, in comparison with helium cooling), there is no alternative to lithium cooling at the

blanket operating temperature of ~700°C [1]. The use of V–Ti–Cr alloy with electrically insulating coatings (AlN or CaO) will provide material compatibility with liquid lithium systems and an acceptable pressure drop for lithium pumping in strong magnetic fields [10].

Because of the high blanket temperature, the energy conversion efficiency will exceed the best values of conventional thermal electric power stations. The radiation safety of the energy converter will be ensured by a three loop system. The sodium cooled fast reactor BN-350 (~800 t sodium), based on such a scheme, has operated since 1973 and has confirmed the effectiveness and the operating safety of a sodium–water steam generator. The accidental injection of 1 t of liquid sodium into water (sodium is more chemically reactive than lithium) did not result in an explosion or fire [8].

The circulating lithium outboard blanket will be purified of tritium. For example, the application of the twice non-equilibrium molecular distillation method at the lithium evaporation temperature 600–750°C will provide a tritium concentration in liquid lithium of ~1 appm.

The third lithium function will be the evaporative shielding of the components subjected to high thermal loads (limiters, baffles) and probably of the whole plasma chamber first wall surface. This function will be provided through use of the capillary–pore system; the principles of operation and characteristics of the shielding system are given in the following section.

3. LLFR DIVERTOR

Up to now, no solution to the problem of the divertor target plates, which must be operated under quasi-stationary thermal loads of 100 MW/m^2 and above, has been proposed. Such loads will be typical for a fusion reactor.

The new divertor and reactor concept is based on the use of evaporative cooling for eliminating high thermal loads. Evaporation–condensation devices with liquid metal as the working fluid are known to be the most effective means for energy transfer in high temperature facilities [11]. If the design of the target substrate is done properly, this means of eliminating high thermal loads can provide excellent performance which eliminates hundreds of megawatts per square metre [11]. To supply the evaporation surface with liquid metal, a porous construction of the target plate with a capillary–pore system is used. The characteristics of the capillary–pore system (changing porosity, permeating anisotropy, working surface geometry, etc.) are maintained in broad ranges by using appropriate manufacturing technologies. The design provides sufficient working fluid pressure in the coolant supply system without applying external pressure but by using only capillary force pressure. This system is self-sustaining and self-regulating because the pressure distribution of the liquid metal coolant in the capillary–pore structure reacts to local changes of the thermal load distribution on its surface. This phenomenon is similar to that observed

in heat pipes [11]. The use of such a technological approach satisfies all of the critical requirements that designers might have when selecting materials and divertor design and fabrication approaches.

If the divertor replacement frequency is to satisfy economic requirements (not more than once per year) for a commercial reactor, the following attractive features of the liquid metal divertor will be relevant:

- Divertor target plate surface erosion is almost entirely absent owing to the constant supply of liquid lithium.
- Temperature gradients in the capillary–pore system filled with liquid metal will not produce thermal stress; therefore cracking and fracturing of the target plates, which are typical of a solid type divertor, are not expected.
- The problem of capillary–pore system bonding with the supporting structure of the divertor does not exist.
- There is no problem with the radiation stability of the capillary–pore system material.
- Tritium accumulation in the liquid metal divertor target systems can be managed by limiting its concentration to a low level by circulating the liquid metal in the tritium recovery system.
- After having been liquefied (from the gaseous phase) in the condenser zone, the metal will enter the liquid metal recirculation system and, unlike the case of the solid divertor, it will not be accumulated in the divertor and adjacent areas of the reactor.
- Both the low speed of the liquid lithium flow and the self-healing electrically insulating coating [10] formed on the inner surfaces of the liquid metal ducts allow a significant reduction of MHD effects.

Liquid lithium is the best and indeed only choice of working fluid for a liquid metal divertor. Owing to its particular combination of nuclear, physical and chemical properties, it is uniquely suited for use in liquid metal systems of a fusion reactor [1].

The use of lithium makes the divertor concept developed in this work most effective, with a number of essentially new characteristics due to the following:

- The Z value of lithium is low, which practically eliminates its influence on plasma radiation if present in the plasma burning zone.
- The high value of the latent heat of lithium vapour formation and effective reradiation and ionization in the vapour cloud absorb a significant part of the energy from the high energy particle flux from the plasma into the divertor volume. In this case, a gas dynamic target is achieved, thus decreasing the divertor's specific power loads without creating the need for a heavy gas.
- Lithium possesses a unique complex of thermophysical properties [1, 11] and is extremely effective for the implementation of the proposed concept of divertor target plate heat load discharge by evaporation/reradiation.

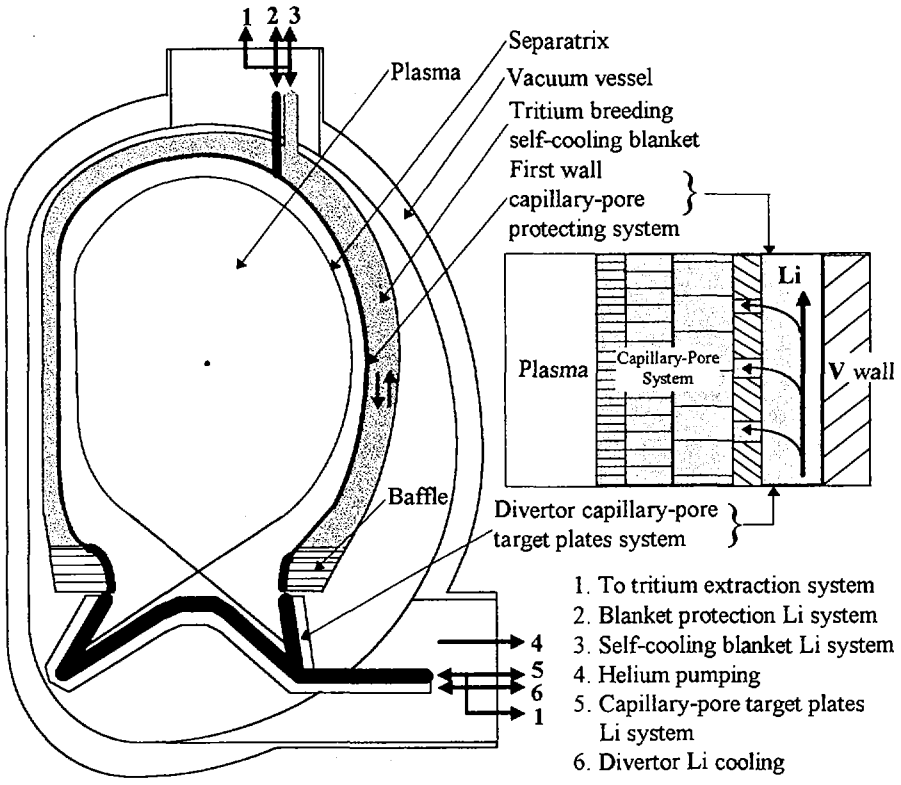

FIG. 1. Cross-section of LLFR.

Lithium actively interacts with hydrogen and its isotopes, forming solutions and hydrides [1]. Helium and other inert gases do not interact with lithium. This property and the appropriate selection of the cooler-condenser temperature modes make it possible to separate helium from hydrogen isotopes and to remove it through the pumping system (by dissolving hydrogen isotopes in lithium and then removing them into an extraction system). This can either altogether eliminate the need for cryogenic panels or reduce their area.

The capillary-pore system with liquid lithium metal has the capability of absorbing the energy from plasma disruptions without failure. If a specific energy on the order of 100 MJ/m^2 is released onto the surface of such a divertor during several milliseconds, the evaporating lithium can effectively cool and shield the capillary-pore system substrate and thus protect it.

The use of liquid lithium in the divertor fits in with the self-cooling liquid lithium blanket reactor design (Fig. 1). It makes possible the use of the same servicing systems, the same tritium extraction technology and the same construction material — low activation vanadium base alloys compatible with lithium in a wide range of temperatures up to 700°C for both the blanket and the divertor.

4. CALCULATED AND EXPERIMENTAL BASIS OF LLFR

Experimental models of the liquid lithium capillary structure have been tested at long pulse length and high heat load [12]. Power loads of up to 50 MW/m^2 were provided by an electron beam with an electron energy of ≤ 9 keV in an axial magnetic field of 0.25 T. Nine experiments were performed with different capillary targets.

The lithium capillary target has been successfully tested at a specific thermal load of up to 50 MW/m^2 during 5 s. Long duration tests have been performed at 20 MW/m^2 and 30 MW/m^2 for 60 s and 30 s, and at 5 MW/m^2 for 10 min. These tests have shown that the lithium capillary–pore structure is promising for its high heat removal capacity in a fusion reactor as well as in other devices.

The effects of disruption discharges in tokamaks have been simulated by means of magnetized hydrogen plasma flows with a pulse length of 0.2 ms and an energy flux of up to 4 MJ/m^2 [13]. The plasma flow was generated by a quasi-stationary plasma accelerator and directed at a lithium capillary structure.

These experiments have shown the capabilities of lithium capillary targets to withstand high pulse loading and to operate for a long time without destruction of the capillary–pore structure. The surface layer porosity of such targets remains unchanged after multiple pulsed tests, and the target is capable of operating continuously under stationary conditions.

The experiments show that, as a result of magnetized plasma flow, a dense plasma layer with $n \geq 5 \times 10^{16}$ cm^{-3} is formed on the target. The thickness of the layer reaches 1–2 cm. The main part of the plasma flow energy is absorbed and radiated in this layer, which plays the role of a shielding layer.

A 2-D hydrodynamic code (DDIC95) has been used to simulate the relation of the lithium target and plasma parameters in ITER [13]. This code has been specially produced to simulate the behaviour of the main plasma and of impurities, at arbitrary densities, in a real divertor geometry. The self-consistent simulation of the background plasma, neutral gas and impurities is a specific feature of this code.

The calculations show that the power which enters the divertor is radiated in the vicinity of the divertor plates by the lithium neutrals, which screen the target and reduce the power density onto the lithium target to 1.3 MW/m^2. The lithium ion (Li^+ and Li^{2+}) density is concentrated in the vicinity of the divertor plate. A noticeable fraction of the Li^{3+} ion density only reaches the X point. In the symmetry plane, the Li^{3+} ion density is about 10^{10} cm^{-3}. The maximum Z_{eff} is attained in the divertor region and Z_{eff} is considerably reduced in the space between the X point and the symmetry plane. These results are promising for the creation of a pure plasma in a tokamak reactor. The calculations show that the thermal loading on the divertor plates is substantially reduced without the addition of any heavy impurities for an electron density at the separatrix in the symmetry plane of $n_e = 6 \times 10^{13}$ cm^{-3}. The shielding of the target by lithium evaporation is accomplished.

5. CONCLUSION

The proposed concept of LLFR is based on a liquid lithium cooling blanket and divertor (without water cooling) and on the evaporation–reradiation principle of protecting high thermal load elements. The advantages of LLFR are achieved by: a new design of the blanket and divertor high thermal load elements with a capillary–pore system which operates under steady state and plasma disruption conditions; the resolution of technological problems related to the assembly, connection and filling with lithium of the complex capillary–pore structure; design with plasma facing 'non-sacrificial' plates; use of low activation materials in the design (vanadium alloys and natural lithium, which have the best properties for a fusion reactor); use of self-healing electrically insulating coatings in liquid lithium systems, which reduces MHD effects; and keeping the tritium concentration at an acceptable level in the liquid metal systems by controlling the lithium purification processes. The use of liquid lithium in the reactor as a whole makes it possible to use the same servicing systems and the same technology for tritium extraction from both the blanket and the divertor. The use of liquid lithium in the divertor will allow separation of gases and their subsequent removal without additional energy demand and design complexity.

REFERENCES

[1] GRIAZNOV, G.M., et al., Materials Science for Liquid Metal Systems of Fusion Reactors, Energoatomizdat, Moscow (1989) 240 pp.

[2] BOOTH, L.A., Central Station Power Generation by Laser-Driven Fusion, Rep. LA-4858-MS, Vol.1, Los Alamos Scientific Lab., NM (1972).

[3] KULCINSKI, G.L., J. Nucl. Mater. **85–86** (1979) 87.

[4] KARASEV, B.G., et al., Fusion Eng. Des. **8** (1989) 283.

[5] ORLOV, V.V., Development of Experimental Fusion Reactor, Issues of Atomic Science and Technics (Fusion) No. 2 (1986) 3.

[6] DEMO Design, Russian Research Center, Kurchatov Inst., Moscow (1993) 353 pp.

[7] SMITH, D.L., "Self-cooled liquid metal blankets", Tokamak Concept Innovations, IAEA-TECDOC-373, IAEA, Vienna (1986) 414.

[8] SUBBOTIN, V.I., Thinking about Atomic Energy, Russian Scientific Academy, St. Petersburg (1995) 195 pp.

[9] GOLUBCHIKOV, L.G., et al., "Development of a liquid metal fusion reactor divertor with a capillary-pore system", Proc. 7th Int. Conf. on Fusion Reactor Materials (ICFRM-7), Obninsk, 1995, J. Nucl. Mater. **233–237** (1996) 667.

[10] EVTIKHIN, V.A., LYUBLINSKI, I.E., KORJAVIN, V.M., J. Adv. Mater. **1** 6 (1994) 38.

[11] BYSTROV, P.I., KAGAN, D.N., KRECHETOVA, G.A., SHPILRAIN, E.E., Liquid Metal Heat Carriers of Heat Pipes and Power Facilities, Science, Moscow (1988) 263 pp.

[12] PISTUNOVICH, V.I., et al., "Research of the capillary structure heat removal efficiency under divertor conditions", Proc. 7th Int. Conf. on Fusion Reactor Materials (ICFRM-7), Obninsk, 1995, J. Nucl. Mater. **233–237** (1996) 650.

[13] BELAN, V.G., et al., "Experimental and calculated basis of lithium capillary system as divertor materials", Proc. 12th Int. Conf. on Plasma-Surface Interactions in Controlled Fusion Devices, St. Raphael, France, 1996.

IMPROVED VERSION OF A MIRROR BASED 14 MeV NEUTRON SOURCE

A.A. IVANOV, E.P. KRUGLYAKOV, Yu.A. TSIDULKO,
V.I. VOLOSOV, A.V. ANDRYASH[1], A.V. LUKIN[1],
K.F. GREBENKIN[1], V.G. KRASNOPEROV[2],
H. KUMPF[3], K. NOACK[3], V.V. ROBOUCH[4],
S. BILIKMEN[5], S. CAKIR[5], V.V. MIRNOV[5]
Budker Institute of Nuclear Physics,
Novosibirsk, Russian Federation

Abstract

IMPROVED VERSION OF A MIRROR BASED 14 MeV NEUTRON SOURCE.

Recently, significant progress has been achieved in the development of a 14 MeV neutron source based on the gas dynamic trap (GDT) concept. The results obtained on a new phase of the neutron source conceptual design are reported. In the neutron source version under consideration, recent advances in superconducting magnet technology are used; one conclusion is that a fully superconducting magnet system with the required magnetic field strength can be built. Calculations show that the neutron load on the main source elements can be decreased to an acceptable level. Operational regimes of the neutron source are considered in which the electron temperature is reduced to 650 eV, which is just about 2.5 times higher than what has already been achieved in mirror machines. In spite of a significant decrease of a number of neutron source parameters, in the new version a neutron flux density of 1.8 MW/m^2 can be obtained in the area of the order of 1 m^2. It is important to note that, if necessary, the total neutron flux can be increased to 5–10 MW, and the test zone area can be enlarged up to 5 m^2. Accordingly, the tritium consumption will be increased to 350–700 g·a^{-1}. It should be noted that experimentally measured parameters of the plasma and the fast sloshing ions in the GDT device are in a good agreement with a code that has been developed. However, further verification and a relevant database for plasma parameters close to those expected in the neutron source are necessary before its construction. For this purpose, the hydrogen prototype of the GDT based neutron source is now under construction in Novosibirsk.

1. INTRODUCTION

At present, it is well understood among the fusion community and materials scientists that the development of powerful 14 MeV neutron sources (NSs) is a very urgent task. Future fusion power stations cannot be constructed without a wide programme of material studies (end of life, H, He, dpa production rates, activation

---

[1] Institute of Technical Physics, Snezhinsk, Chelyabinsk District, Russian Federation.
[2] Efremov Institute, St. Petersburg, Russian Federation.
[3] Forschungszentrum Rossendorf, Dresden, Germany.
[4] ENEA, Frascati, Italy.
[5] Middle East Technical University (METU), Ankara, Turkey.

of nuclei, resistivity of metals, etc.). To realize this programme, a high power 14 MeV NS, covering a sufficiently large test zone, should be constructed within a short period of time. In addition, such a source could be used to create new materials of low activation for the first wall and breeding blanket components. The general requirements determined by the International Energy Agency specifications of such a volumetric 14 MeV NS for materials studies can be formulated as follows:

(1) The uncollided neutron flux should be above 2 MW/cm^2;
(2) The test zone volume should exceed 30 L;
(3) The flux gradient should be less than 10%/cm.

At present, a number of different approaches to a solution to the problem of high power NS creation are described (see the review given in Ref. [1]).

Among the existing proposals there are accelerator based NS projects (D–Li and spallation sources, one on the basis of muon catalysis) and a laser initiated NS with a repetition rate. There exist a lot of plasma type NS projects (tokamak based and mirror based). In each approach, in addition to physics and engineering problems, which should be solved so that a high power neutron flux can be produced, there are also economic problems. To produce a flux of 2 MW/m^2, about 140 g of tritium should be spent per year for each square metre of the test zone. Hence, a conventional tokamak, because of its large first wall area, is not the best candidate for the role of a high power NS, since here the annual tritium consumption would be comparable with the world tritium production. Besides, power consumption would also be too high. A high beta spherical tokamak with a tight aspect ratio [2] looks rather promising among the tokamak based NSs, but even in this case the first wall area should be within 10–20 m^2. Thus, the tritium consumption should be 1.4–2.8 kg·a^{-1}. At the same time the world tritium production, estimated to be 5 kg·a^{-1}, tends to decrease. In this context, the perspectives of mirror based NSs looks more optimistic. At present, the most carefully studied mirror type NS is based on the gas dynamic trap (GDT) [3], which is an axisymmetric mirror trap with a high mirror ratio. The concept of a GDT based NS was proposed by Ryutov et al. in 1984. The idea was rather clear. If fast deuterium and tritium atoms are injected obliquely into a 'warm' plasma, the density maxima of the energetic ions trapped in the plasma will be localized in the vicinity of the turning points near the mirrors. Hence, the distribution of the neutrons produced almost exclusively by collisions of fast deuterons and tritons will be strongly inhomogeneous along the trap axis. As estimates show, the maximum neutron flux will be obtained near the turning points in an area of the order of 0.5–1 m^2 for a moderate power consumption of about 60 MW.

The first version of a GDT based NS was designed by the Efremov Institute in St. Petersburg together with the Budker Institute of Nuclear Physics (INP) in Novosibirsk in 1985. The main parameters of this source are given in Ref. [4]. As to the NS parameters presented there we should mention that the operational characteristics of the source were quite moderate: the power consumption was 50–60 MW

and the tritium consumption was less than 150 $g \cdot a^{-1}$. Nevertheless, the test zone area was of the order of 0.5–1 m^2, and the 14 MeV neutron flux amounted to 2.5–3.9 MW/m^2. One of the weak points of the project was that mirror coils were used, with a magnetic field strength, in the mirrors, of up to 26 T.

Some years ago, the Budker INP started work on an improved version of the GDT based NS. In the Russian Federation, the Institute of Technical Physics (former Chelyabinsk-70) and the Efremov Institute were involved in this project. The scientific centres of Rossendorf (Germany) and Frascati (Italy) also co-operated in the project. Recently, a group from the Ankara Technical University (METU) has joined the project. New data on a modified version of the GDT based NS are presented in the following.

2. EXPERIMENTAL SIMULATIONS OF A PLASMA NEUTRON SOURCE BASED ON THE GDT CONCEPT

The major physics aspects to be considered in the plasma chamber of the neutron source are: MHD equilibrium and stability, microstability of the energetic sloshing ions, plasma startup, cold ion fuelling and electron heat conduction onto the end walls. Startup, MHD stability, equilibrium control and microstability were all demonstrated in the GDT experiment for moderate plasma parameters [5]. The transverse plasma losses were measured and proved to be small compared to the losses through the mirrors, at least for mirror ratios less than 25. Strong reduction of the longitudinal electron heat flux was also observed. Electron temperatures of about 100 eV were measured in the regimes with 3 MW, 14–16 keV neutral beam injection. The further temperature increase was limited by the available beam duration. In these regimes, the plasma energy balance was essentially determined by classical energy loss mechanisms. This was confirmed by comparing the measured sloshing ion energy content with that predicted by the numerical code.

In order to understand the observed sloshing ion behaviour in a GDT, simulations of the neutral beam trapping and subsequent energy loss and angular scattering of the sloshing ions were carried out by using a specially developed code. The treatment of the problem is based on a Monte Carlo method in order to account for ion–ion and ion–electron collisions. Charge exchange processes are also taken into account via the effective neutral gas density taken from experiments. The time evolution of the energy stored in the sloshing ions is simulated for a typical shot, on the assumption of Coulomb relaxation rates of the fast ions before a given plasma background.

As is seen from Fig. 1, the simulated behaviour of the sloshing ion energy content agrees rather well with the experimental observations. The measurements of the energy and angular distributions of the sloshing ions as compared with the simulations did not produce any evidence of anomaly, either.

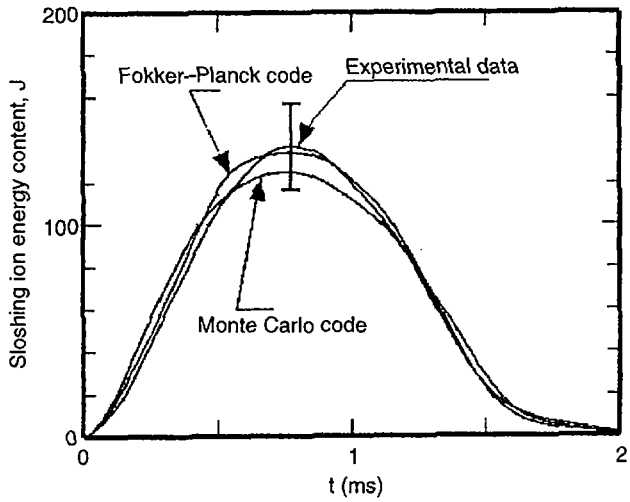

FIG. 1. Stored sloshing ion energy versus time. Experimental data and results of calculations are shown.

3. PROBLEMS OF PLASMA MHD STABILITY

An oblique injection of high energy sloshing ions creates a strongly anisotropic plasma pressure, $P_\parallel \gg P_\perp$, that drives the 'fire-hose' instability if ($\beta_\parallel = 8\pi P_\parallel/B^2 > 2$). Besides the 'fire-hose' instability, there exist also ballooning modes in the GDT. Their marginal stability and their connection with the 'fire-hose' modes have been treated on the basis of the paraxial MHD energy principle by taking into account pressure anisotropy, radial plasma profile and longitudinal magnetic field inhomogeneity.

The longitudinal pressure profile is evaluated from the kinetic equation while the radial profile is adopted in two forms: sharp distributions, $P_\parallel^{(S)}(\psi) = P_0[1 - \psi/\psi_0)^n]$, $\psi \geq \psi_0$, and an exponential profile, $P_\parallel^{(E)}(\psi) = P_0 \exp[-(\psi/\psi_0)^n]$. Two specific configurations of magnetic field lines are analysed: the linear and the optimal 'square root' r(z). The latter configuration has been accepted for the magnetic system of the BINP project 'hydrogen prototype' to be discussed later.

Comparing the limits imposed by the different surfaces yields a stability margin of $\beta_0 = 8\pi P_o/B^2_{min}$. For small n (flat radial profiles), the 'fire-hose' instability is dominant, $\beta_0^{(cr)} = 2$, and the most unstable magnetic surfaces are localized near the maximum of the pressure gradient. The resulting limits on β are found to be not severe, so that the criterion $\beta_o^{(cr)} \leq 2$ can be used for a rough estimate of the marginal stability (Fig. 2).

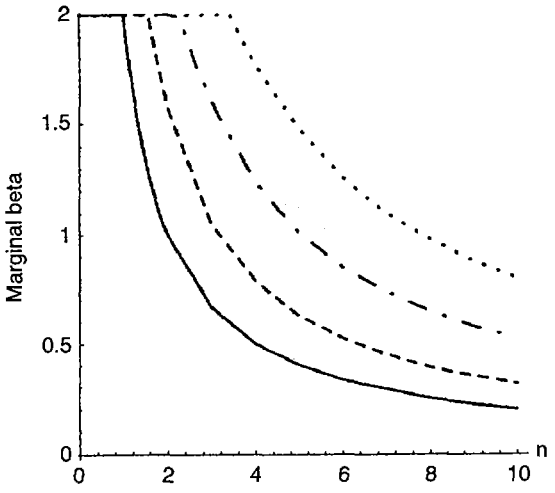

FIG. 2. Dependence of $\beta_0^{(cr)}$ on n. Full curve: sharp radial profile and linear field line geometry r(z); dashed curve: sharp radial and 'square root' r(z); dot-dashed curve: exponential radial profile and linear r(z); dotted curve: exponential radial profile and 'square root' r(z).

4. MAIN PARAMETERS OF IMPROVED NS VERSION

Recently, significant progress has been achieved in the new phase of NS conceptual design. By making use of recent advances in superconducting magnet technology, the version of a source with a fully superconducting magnet system was considered.

Achievements in neutral beam injection were also used. To optimize the plasma physics parameters of the source, numerical codes based on a Monte Carlo method for the detailed simulation of fast ion and bulk plasma behaviour were developed. As a result of a revision of the magnetic system, the estimated mean time between failures, which in the previous design was mainly determined by the lifetime of the resistive mirror solenoids (two weeks), was substantially increased.

The neutron flux in the test zone is very sensitive to the attainable plasma performance, in particular, the electron temperature and the permissible plasma beta. The capability to operate at high beta has already been demonstrated in many mirror experiments. At the same time, the maximum electron temperature in the relevant experimental conditions was limited to 260 eV, which is still significantly lower than that assumed in the first version of our neutron source (IN-1). A positive finding in mirror experiments is the rather long electron energy confinement time which approaches 0.45–0.9 ms; this is quite close to, or even higher than, what is needed ($\sim$0.5 ms in IN-1). Here, we consider operational regimes of the source in which

TABLE I. NEUTRON SOURCE PARAMETERS

Power consumption	60[a]/47.1 MW
Neutron flux density	2.5[a]/1.8 MW/m^2
D^0 beam energy	80[a]/65 keV
T^0 beam energy	94[a]/65 keV
Electron temperature	1.1[a]/0.65 keV
'Warm' plasma density	1.7×10^{14} [a]/2.0×10^{14} cm^{-3}
Mirror-to-mirror size	10[a]/11.4 m
Injection angle	30°
Mirror field	26[a]/13 T
Mirror ratio	20[a]/10

[a] Data for IN-1.

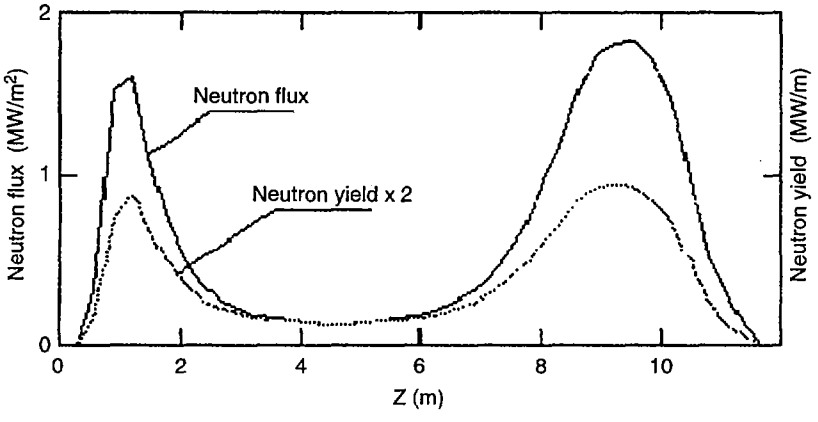

FIG. 3. Profiles of 14 MeV neutron flux and neutron yield along the axis.

the electron temperature is reduced to 650 eV, which is just about 2.5 times higher than what has already been achieved.

The parameters of two versions of the GDT based NS (IN-1 and improved NS) are presented in Table I.

In the simulations of the NS plasma, a self-consistent numerical model which incorporates fast ion–ion collisions was used. This affected the positions of the test zone, which required a readjustment of the magnetic field profile in order to keep the same z positions of the test zones as in the IN-1 design. A version of the magnet system was calculated that allowed the injection ducts to be accommodated at an angle of 30° with respect to the axis. The calculated distribution of neutron flux and neutron yield along the system axis is shown in Fig. 3.

A conceptual design for the vacuum–tritium complex of the source was developed. The concept adopted for this NS differs from that already being used in JET, TFTR and being discussed for ITER. Our concept assumes that the same DT mixture will be used for target plasma feeding and for the NB injector. It allows specialized facilities for hydrogen isotope separation to be dispensed with, thus simplifying and cheapening the complex.

5. NEUTRON SHIELDING

The problems of the neutron shield in the NS equipment were considered in Ref. [6].

Starting from a crude non-optimized overshielding (to check the feasibility of survival protection), simulations have been carried out to establish the damage on the sensitive components. The results are:

(1) The extreme local dose (Grad) on the exposed ion head insulating alumina and on the sweep magnet insulator, once a local adequate shield has been inserted, allows survival of the parts beyond the natural life of the ion source. Thus, the protection is such as to make replacement interventions determined by the natural consumption of the ion source, not by radiation damage. It is to be recalled that while the heat load (MW) is an integral volumetric value whereas an insulator dose (Grad) is a maximum *local* value and has to be treated as such.

(2) The present, unsophisticated shield lets through an extreme 'local' insulator dose (Grad) at the hot magnet that is too high and allows too short a survival time (six to twelve months) against the required two to three years. A local redesign of the shield is under way to ensure the prescribed survival time while preventing the inner coil radius from expanding.

(3) Among the SC coils the most critical ones are those that are in direct contact with the injector tubes that hinder good shielding. The central, and most critical, coil was shown to be at the limit of tolerance for the dpa, while it is safe for the other parameters. Its shield has now been redesigned, and the coil is expected to outlive the GDT based NS ten year operation period. This study is under way, and the crude shield design is being optimized.

Although the above results have been derived from the unoptimized crude shield, the simulations already show that the GDT based NS operation is viable at the level of the present design and shielding concept. Several design modifications have been suggested to improve the GDT based NS properties, and some have been evaluated. Several details of the design can be improved but compatibility between engineering solutions and neutronic demands is of paramount importance.

6. POSSIBLE APPLICATIONS OF THE NEUTRON SOURCE

Initially, the NS project was primarily developed for fusion materials tests. It has, however, a number of attractive features (compactness, moderate power and tritium consumption, intrinsically high level of safety and reliability, easy maintenance) which allow its application to a wide variety of problems.

Use of the GDT based NS for electronuclear energy production was considered. Initially, two versions of the device, single cascade and two cascade schemes, were evaluated. An assessment of feasibility of the required neutron filter characteristics in two point approximation was carried out. The total output power was estimated to be 77–154 MW and 210–750 MW for single and double cascade schemes, respectively, in the case of a 2 MW neutron flux.

The application of the GDT based NS as a transmutator of radioactive waste was considered. Minor actinide burn-out was identified as the most attractive option for the transmutator based on the GDT based NS. The concept of a low waste power plant has been proposed in which the GDT based NS transmutator burns out minor actinides produced by three to four light water fission reactors of 1000 MW(e) each. The thermal power of the transmutator was estimated to be about 500 MW.

7. CONCLUSIONS

The experimentally measured plasma parameters were found to be in reasonable agreement with the code predictions. This provides us with a quite reasonable level of confidence in the applicability of this concept to NS design. However, further verification and the generation of a relevant database for plasma parameters that are maximally close to those expected in the NS are necessary before its construction. For this purpose, the hydrogen prototype of the GDT based NS (HPNS) is now under construction in Novosibirsk. We have also developed a self-consistent numerical model which incorporates fast ion–ion collisions. This model enables us to readjust the magnetic field profile to keep the same position of the test zones. The IN-1 predesign options were chosen to meet the requirements of material and component (welds, joints, etc.) tests. Recently, testing of larger size reactor submodules (e.g. blanket elements, etc.) was identified as an important goal for the volumetric neutron source [7]. In principle, the GDT based NS is capable of providing a larger size zone for these tests although its advantages are much more evident in compact, higher flux designs. Nevertheless, an NS version with a 5–10 m^2 test area and moderate tritium and power consumption can be developed.

This work was supported in part by ISTC through Research Grant No. 050–94.

REFERENCES

[1] KRUGLYAKOV, E.P., in Plasma Physics (Proc. Int. Conf. ICPP, 1994), AIP Conference Proceedings, Woodbury, New York (1995) 247.

[2] HENDER, T.C., et al., in Controlled Fusion and Plasma Physics (Proc. 22nd Eur. Conf. Bournemouth, 1995), Vol. 19C, Part III, European Physical Society, Geneva (1995) 233.
[3] MIRNOV, V.V., RYUTOV, D.D., Sov. Tech. Phys. Lett. 5 (1979) 279.
[4] IVANOV, A.A., et al., in Fusion Technology (Proc. SOFT Symp. Rome, 1992), Vol. 2 (1992) 1394.
[5] ANIKEEV, A.V., et al., in Controlled Fusion and Plasma Physics (Proc. 22nd Eur. Conf. Bournemouth, 1995), Vol. 19C, Part IV, European Physical Society, Geneva (1995) 193.
[6] ROBOUCH, B.V., et al., in Fusion Engineering (Proc. 16th Symp. Urbana-Champaign, 1995), Vol. 2 (1995) 313.
[7] ABDOU, M.A., et al., in Plasma Physics and Controlled Nuclear Fusion Research 1994 (Proc. 15th Int. Conf. Seville, 1994), Vol. 2, IAEA, Vienna (1995) 733.

DESIGN OF A VOLUMETRIC NEUTRON SOURCE BASED ON A STEADY STATE TOKAMAK

Y. OGAWA, N. INOUE, Z. YOSHIDA, T. YAMAMOTO,
R. HIWATARI, K. TAKEMURA, K. TOKIMATSU
School of Engineering,
University of Tokyo,
Hongo, Tokyo

K. OKANO, Y. ASAOKA, T. YOSHIDA, K. TOMABECHI
Central Research Institute of Electric Power Industry,
Komae

T. AMANO, J.F. WANG
National Institute for Fusion Science,
Nagoya

Y. MURAKAMI
Toshiba Research and Development Center,
Kawasaki

Japan

Abstract

DESIGN OF A VOLUMETRIC NEUTRON SOURCE BASED ON A STEADY STATE TOKAMAK.

A volumetric neutron source for testing large scale blanket components, based on a steady state tokamak device with superconducting coils, has been designed. It is found that a neutron flux of 0.8–1.0 MW/m^2 is available in a medium size device (R = 4.5 m, a = 1.0 m, κ = 1.8, I_p = 5.6 MA) under the conditions of enhancement factor H = 1.6–2.2 and β_N = 2.8–3.5 with NBI power P_b of 50–80 MW. The controllability of the current profile required for high β plasmas up to β_N = 3 with a combination of bootstrap current and neutral beam driven current (E_b = 1.0 MeV) at a plasma density $\langle n_e \rangle = 1.0 \times 10^{20}$ m^{-3} was demonstrated. If an advanced performance scenario such as a reversed shear configuration is available, a neutron flux of 1.4 MW/m^2 is achievable. To produce a reversed shear current profile stable for MHD modes, external current drive not only in the plasma central region but also in the pitch minimum region is required. NBI power of 28 MW is employed in the plasma central region and LHW power of 6 MW in the outer region of the plasma column. A transport calculation estimates the accumulation of helium ash to be f_{He} = 4–7% with τ_p^*/τ_E = 7–10. This low helium fraction can be explained by the short particle/energy confinement time in a small device. Since tritium consumption is ~10 kg/a, the installation of a breeding blanket is indispensable. The capability for tritium breeding of Li_2O/Be and Li–Pb breeders has been evaluated and it is found that a local tritium breeding ratio of 1.4 or more is feasible for the Li–Pb case.

1. INTRODUCTION

With the aim of early realization of a fusion reactor, we have been considering a strategy of fusion energy development and have designed a low wall loading Demo reactor [1] and inductively operated long pulse commercial reactors [2, 3], which might launch fusion energy into the argument on energy strategy. In our scenario of fusion energy development, a volumetric neutron source (VNS) for testing large scale blanket components plays an important role for a Demo reactor design, in parallel with ITER, which will provide a useful but necessarily limited reference on blanket design. We believe that ITER and the VNS are complementary in respect of plasma physics and fusion technology because the VNS proposed here is suitable for studying fusion plasma physics in a large aspect ratio device and in a non-inductively driven current regime, and it has the flexibility to test various candidates for the blanket system within a short period.

Many types of VNS based on non-tokamak [4] and spherical torus [5] devices have been proposed. It seems, however, that R&D issues of plasma physics and fusion technology need to be solved for these devices. A tokamak device is a prominent candidate for a VNS, and two distinct designs have been promoted [6, 7]. One is a small device ($R < 2$ m) with a copper conductor and the other a medium size device ($R > 4$ m) with a superconductor. In the former case the tritium consumption is 1–2 kg/a, which could be supplied by an external tritium facility. The power consumption of the normal conductor is, however, estimated to be a few hundred megawatts. In the latter case a breeding blanket would need to be installed, because the annual tritium consumption is a few kilograms or more, owing to the large plasma volume. The necessity for a breeding blanket is quite similar to the case of the ITER Enhanced Performance Phase (ITER EPP) [8].

Through the design activities of the ITER CDA and EDA, the fusion community has made great strides in plasma physics and fusion technology. Here, on the basis of established concepts of plasma physics and a reasonable extension of engineering, which have mainly been developed in the ITER research and design activities, we present a design for a VNS device based on a steady state tokamak plasma with a neutron flux of ~ 1 MW/m^2, with the aim of providing information and a database for a Demo reactor with high reliability.

2. DESIGN PARAMETERS OF A VNS

In designing a VNS device, we have employed the physical and engineering guidelines of the ITER EDA design [8], where a conventional device with an aspect ratio $A > 2.5$ is considered and superconducting magnets are used with a maximum field strength of 12.5 T. The radial distance between the plasma surface and the inner edge of the toroidal field coils is chosen to be 1.4 m. Since high neutron fluence is also required for blanket testing, steady state operation with non-inductive current

TABLE I. TYPICAL PARAMETERS OF A VNS
(R = 4.5 m, a = 1.0 m, κ = 1.8, B_t = 5.8 T)

	Standard	Advanced
Neutron wall loading (MW/m^2)	1.0	1.4
Electron density $\langle n_e \rangle$ (10^{20} m^{-3})	1.0	1.2
Ion temperature $\langle T_i \rangle$ (keV)	13.9	13.3
Bootstrap current (%)	53	72
H factor	2.2	2.9
Normalized β β_N	3.0	3.8
Beam power P_b (MW)	58	28
LHW power P_{LH} (MW)	0	6
Energy gain Q	5.2	11.5

drive is preferable. Here we adopt NBI for plasma heating and current drive, expecting an enhancement of the neutron flux due to the two component torus effect and strong ion heating. Taking these parameters and constraints into account, we find that a device with an aspect ratio of 4–5 is optimum for achieving the highest possible neutron flux.

The reference parameters of our VNS are R = 4.5 m, a = 1.0 m, κ = 1.8, I_p = 5.6 MA ($q_\psi(95\%)$ = 3), f_{He} = 5% and Z_{eff} = 1.5. Typical plasma parameters are listed in Table I. A parameter study with a system code shows that a neutron wall loading P_n of 0.8–1.0 MW/m^2 is available under the conditions of enhancement factor H = 1.6–2.2 and β_N = 2.8–3.5 with NBI power P_b of 50–80 MW. We should remark that the beam pressure is not negligibly small (typically 15–18% of the total pressure). To reduce the beam pressure and to increase the neutron flux due to the two component torus effect, a moderate beam energy is preferable, while high efficiency of the NBI current drive is achievable with higher beam energy. Taking these contradictory factors into account, the optimum beam energy is evaluated to be ~1.0 MeV.

By adjusting the profile of the injection beam power, we can control the plasma current profile to be suitable for high β plasmas [9]. This flexibility of our VNS device might yield the possibility of advanced plasma performance. If an advanced scenario (e.g. with H = 3 and β_N = 4) is expected, the neutron flux can be increased to 1.4 MW/m^2.

The accumulation of helium ash is evaluated with a 1.5-D transport code, where the ratio between the effective particle confinement time τ_p^* and the energy confinement time τ_E is adjusted to be τ_p^*/τ_E = 7–10. It is found that the helium fraction of the electron density ($f_{He} = \langle n_{He} \rangle / \langle n_e \rangle$) is around 4–7% for the inward pinch parameter C_v (i.e. $V_{pinch} = -C_v(2r/a^2)D$) of 0.0–1.0. This small helium fraction

compared with that of the ITER plasma (f_{He} = 10–15%) is roughly accounted for by the short particle/energy confinement time in a small plasma, i.e. $\tau_E \approx 1$ s in the VNS, $\tau_E \approx 6$ s in ITER EDA.

The operation density $\langle n_e \rangle$ of (1.0–1.2) $\times 10^{20}$ m^{-3} is sufficiently under the Greenwald density limit ($n_{GR} = 1.8 \times 10^{20}$ m^{-3}), while the low density operation in a small device might result in severe conditions for the divertor design. A simple analysis with no momentum loss along the magnetic field line in the scrape-off layer shows a divertor heat load of 10 MW/m^2 and a divertor plasma temperature of 100 eV or more. We incorporate a large area for the divertor (typically the poloidal length of the divertor leg is ~2 m) to accommodate the momentum loss region, as for a vertical plate or gas box divertor in ITER EDA [8].

The poloidal field coils are mainly located outside the toroidal field coils, and an equilibrium calculation shows that the stored energy of the poloidal field coil system is 11.5 GJ. A feedback coil of copper conductor is mounted inside the toroidal field coils, because of the large plasma elongation and the long distance between the plasma and the main poloidal field coils.

3. MHD ANALYSIS AND CURRENT PROFILE CONTROL

To achieve and maintain high β plasmas ($\beta_N \approx 3$), the plasma current profile should be carefully controlled from the viewpoint of MHD stability. Here we show the controllability of the current profile through a combination of bootstrap current and neutral beam driven current. First a current profile which is stable for kink and ballooning modes is calculated with the ERATO code and ballooning mode analysis. Figure 1 shows the current profile with $\beta_N = 3.0$, along with the bootstrap current profile. Since about 50% of the total plasma current is sustained by the bootstrap current, the remainder should be driven by NBI. A neutral beam with $E_b = 1.0$ MeV is tangentially injected at $R_{tang} = 4.0$ m; the beam box size is 3.2 m in height and 0.25 m in width. By adjusting the beam power density within the injection beam box, we can produce a current profile stable for kink and ballooning modes, as shown in Fig. 1. The beam power required is 58 MW, and the global current drive efficiency is estimated to be γ ($= n_{20} I_{CD} R / P_{CD}$) $= 0.19$ MA·m^{-2}·MW^{-1}.

High performance operation with a reversed shear configuration is also examined with the combination of bootstrap current and neutral beam driven current. A high β plasma with $\beta_N = 3.8$ and safety factor profile $q_{min} = 2.13$ and $q(0) = 2.61$ is calculated with an MHD stability code, where a kink mode is expected to be stabilized by the wall located at b/a = 1.3. Figure 2 shows the current profile necessary for MHD stable high β plasmas. Beam injection with a beam energy of 1.0 MeV is quite effective in driving the plasma current in the central region of the plasma column. In the reversed shear case a large plasma current in the pitch minimum region (r/a ≈ 0.7) is necessary for maintaining sufficient shear, while

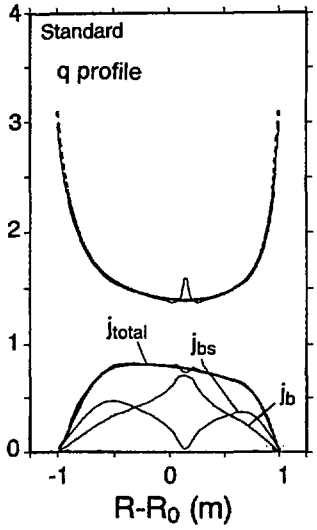

FIG. 1. Safety factor q and plasma current j_{total} profiles for β_N = 3.0; also shown are bootstrap current j_{bs} and neutral beam driven current j_b.

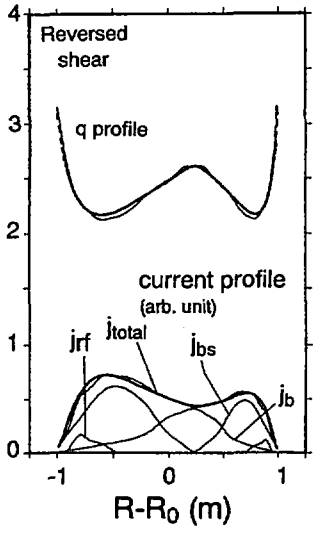

FIG. 2. Safety factor q and plasma current j_{total} profiles for β_N = 3.8 with q_{min} = 2.13 and q(0) = 2.61; also shown is current profile j_{rf} due to the LHW.

MHD stability requires a low pressure plasma, resulting in a low bootstrap current. It might be impossible to drive a sufficient current with monoenergy NBI in both regions (the plasma central region and the pitch minimum region). We would have to introduce another non-inductive current drive system such as low energy NBI or a lower hybrid wave (LHW). In Fig. 2 the LHW is introduced to drive the plasma current in the outer region of the plasma column. Consequently, NBI power of 28 MW and LHW power of 6 MW are required, and the global current drive efficiency for these non-inductive current drive systems is estimated to be $\gamma = 0.244\ \mathrm{MA \cdot m^{-2} \cdot MW^{-1}}$.

4. BLANKET AND SHIELDING DESIGN

The total fusion power is about 300 MW in this VNS device, yielding a tritium consumption of ~ 10 kg/a with 50% availability. Since it seems unrealistic that this amount of tritium could be supplied by another nuclear facility, tritium breeding should be accommodated within this VNS device itself.

Compared with ceramic breeders such as Li_2O/Li_2ZrO_3, the Li–Pb breeder has the potential for a high tritium breeding ratio (TBR). In addition, Li–Pb has better compatibility with water coolant. However, we should remark that the TBR of the Li–Pb breeder is strongly degraded by the introduction of structural materials; for example, the structural content of 20% ferritic steel causes degradation of the TBR from 1.7 to 1.0 [10]. Here we examine the tritium breeding capability of Li–Pb breeders as well as solid breeders. As a reference, the Li_2O solid breeder blanket design of ITER EDA [8] is adopted and the radial build of the blanket region is employed in the ANISN code. Figure 3 shows TBR as a function of the total thickness of the breeder and Be multiplier. In the Li–Pb breeder case, the region of the Li_2O breeder and Be multiplier is replaced with the Li–Pb breeder. We can see from this figure that the maximum value of the local TBR is less than 1.4 in the Li_2O breeder, while a local TBR of 1.4 or more is achievable in the Li–Pb breeder with a sufficient thickness of the breeding zone (>50 cm).

The inner region of the torus is, in general, very tight in a tokamak device. As the thickness of the shielding materials decreases, the plasma performance is improved dramatically. This is true especially in a small major radius device, because the toroidal field strength at the plasma centre is given by $B_t/B_{t,max} = (R - a - \Delta)/R$, where Δ denotes the radial distance between the plasma surface and the inner edge of the toroidal field coils. Here we perform a preliminary optimization of the shielding thickness in the inner region of the torus. The radial build of the ITER EDA design is again employed [8], and the shielding materials (60% stainless steel and 40% water in the ITER EDA case) are replaced with mixtures of tungsten, stainless steel and 5% boric water. The introduction of tungsten and boron is effective for suppressing neutron and γ ray fluxes, and when 40% of the shielding

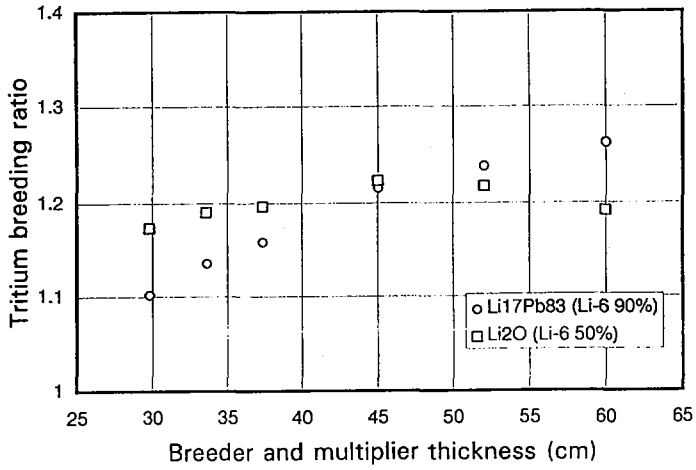

FIG. 3. Local TBRs for Li_2O/Be and Li–Pb breeders as a function of breeder/multiplier thickness.

material is replaced by tungsten, the nuclear heating at the toroidal field coils is suppressed by a factor of 7–10. This might yield a reduction of the shielding thickness by ~20 cm, giving a higher toroidal field at the plasma (B_t = 5.83 T → 6.39 T).

5. SUMMARY

In the case of a VNS design based on a steady state tokamak device with superconducting coils, a neutron flux of 0.8–1.0 MW/m^2 is available in a medium size device (R = 4.5 m, a = 1.0 m, κ = 1.8, I_p = 5.6 MA) under the conditions of H = 1.6–2.2 and β_N = 2.8–3.5 with NBI power P_b of 50–80 MW.

We have calculated a current profile stable for kink and ballooning modes for β_N = 3 plasmas, and have shown that this current profile is produced through a combination of bootstrap current and neutral beam driven current, where a beam energy of 1.0 MeV is required at a plasma density $\langle n_e \rangle = 1.0 \times 10^{20}$ m^{-3}. If an advanced scenario with a reversed shear configuration (H = 3, β_N = 4) is available, a neutron flux of 1.4 MW/m^2 is achievable with reduced beam power, because of the large fraction of bootstrap current (f_{bs} = 72%). To produce a reversed shear current profile stable for MHD modes, external current drive not only in the plasma central region but also in the pitch minimum region is required. We employ NBI power of 28 MW with a beam energy of 1.0 MeV for the current drive in the plasma central region and LHW power of 6 MW for the outer region of the plasma column.

A transport calculation estimates the accumulation of helium ash to be f_{He} = 4–7% with τ_p^*/τ_E = 7–10. This low accumulation of helium ash can be explained by the short particle/energy confinement time in a small device.

Since the tritium consumption is ~10 kg/a, the supply of tritium by another nuclear facility seems to be unrealistic. We include a breeding blanket in this VNS device and have evaluated the capability for tritium breeding of Li_2O/Be and Li–Pb breeders. Even if the structural materials employed in the ITER EDA design are adopted in our VNS device, we find that a local TBR of 1.4 or more is achievable with the Li–Pb breeder. To reduce the shielding thickness at the inboard side of the torus, the optimization of the shielding materials has been carried out, and it is found that the proper combination of tungsten, steel and boric water yields a reduction of the shielding thickness of ~20 cm.

ACKNOWLEDGEMENTS

We are grateful to H. Naitou of Yamaguchi University for his help on MHD analysis and Y. Seki at Japan Atomic Energy Research Institute for neutronics calculations.

REFERENCES

[1] OGAWA, Y., et al., in Proc. 16th IEEE Symp. on Fusion Engineering, Champaign, IL, 1995, IEEE Service Center, Piscataway, NJ (1995).

[2] INOUE, N., et al., in Plasma Physics and Controlled Nuclear Fusion Research 1992 (Proc. 14th Int. Conf. Würzburg, 1992), Vol. 3, IAEA, Vienna (1993) 347.

[3] OGAWA, Y., et al., in Plasma Physics and Controlled Nuclear Fusion Research 1994 (Proc. 15th Int. Conf. Seville, 1994), Vol. 2, IAEA, Vienna (1995) 803.

[4] MIYAHARA, A., COENSGEN, F.H., Proceedings of the Japan–U.S. Workshop P-119 on 14 MeV Neutron Source for Material R&D Based on Plasma Devices, Rep. IPPJ-T-37, Natl Inst. for Fusion Science, Nagoya (1988).

[5] PENG, Y.-K.M., et al., Fusion Technol. 21 (1992) 1729.

[6] ABDOU, M., et al., Phase I Report of the IEA Study on High Volume Plasma-Based Neutron Source (HVPNS), Rep. UCLA-FNT-94, Univ. of California, Los Angeles (1994).

[7] FILATOV, O.G., et al., Fusion Eng. Des. 31 (1996) 69.

[8] Technical Basis for the ITER Interim Design Report, Cost Review and Safety Analysis, ITER EDA Documentation Series No. 7, IAEA, Vienna (1996).

[9] OKANO, K., et al., Plasma Phys. Control. Fusion 32 (1990) 225.

[10] EL-GUEBALY, L.A., in Proc. 16th IEEE Symp. on Fusion Engineering, Champaign, IL, 1995, Vol. 2, IEEE Service Center, Piscataway, NJ (1995) 1198.

HIGH FIELD TOKAMAK REACTOR WITH FORCE BALANCED COILS AS A VOLUMETRIC NEUTRON SOURCE

S. TSUJI-IIO, H. TSUTSUI, J. KONDOH, T. OBARA, T. YANO,
M. IGASHIRA, M. SAITO, M. ARITOMI, H. SEKIMOTO,
R. TAKAGI, M. OKAMOTO, R. SHIMADA
Research Laboratory for Nuclear Reactors,
Tokyo Institute of Technology,
O-okayama, Meguro-ku, Tokyo

Y.M. MIURA
Japan Atomic Energy Research Institute,
Naka-machi, Naka-gun, Ibaraki-ken

Japan

Abstract

HIGH FIELD TOKAMAK REACTOR WITH FORCE BALANCED COILS AS A VOLUMETRIC NEUTRON SOURCE.

A DT sub-ignited tokamak reactor has been investigated that has an average neutron wall loading of 1 MW/m^2 and is based on a novel coil concept to generate a strong magnetic field. When the aspect ratio of the coil winding is about 1.7, the forces in the major direction are balanced with the winding pitch of two poloidal rotations round the torus. Thus force balanced coils can be designed which consist of twisted loops in a shape like a figure of eight. Although the coil current has a toroidal component, the poloidal component of the produced magnetic field is made to be negligible inside the winding by modulating the winding pitch. The net centring force is reduced by a factor of 10 from that exerted on toroidal magnetic coils of the same dimension. The authors designed a steady state tokamak reactor with force balanced coils. The fusion reaction of $Q_{DT} \approx 3.7$ is maintained with 58 MW of neutral beam power into a plasma with a major radius of 3.64 m, a minor radius of 0.80 m, an elongation of 1.7, a plasma current of 6.0 MA, an H factor of 2 and a toroidal field on the axis of 8.4 T.

1. INTRODUCTION

If fusion reactors are utilized as volumetric neutron sources, tokamak reactors below the ignition condition could be put into practical use for purposes such as neutron irradiation tests of materials, tritium breeding and transmutation of long lived radioactive wastes [1].

High field tokamaks with higher plasma current are attractive for raising the plasma performance with smaller device sizes. However, requirements for the coil support structures become more demanding because of the need to withstand the stronger electromagnetic forces. We have developed force balanced coils (FBCs) to

reduce the electromagnetic forces drastically [2] and have designed a steady state tokamak reactor with FBCs based on the same physics and engineering employed in the ITER design activities.

2. FORCE BALANCED WINDING

Multipole helical coils are used to balance the net radial hoop force and the net centring force due to the toroidal current component and the poloidal current component, respectively [3]. The winding pitch is modulated in such a way that the direction becomes more horizontal at the inner side of the torus, where the toroidal magnetic field is the strongest, to reduce the Lorentz force, while the direction becomes nearly vertical at the outer side of the torus. Although the winding is helical, the toroidal component of the produced magnetic field is designed to be dominant in the vacuum vessel.

In the case of coils with a circular poloidal cross-section, the net force in the major direction is balanced when the following equation is satisfied from the principle of virtual displacement:

$$\partial(LI^2/2)/\partial R|_{I=\text{const}} = 0 \tag{1}$$

The coil inductance L is expressed as the sum of the inductances due to the poloidal and the toroidal current components.

$$L_p = \mu_0 N^2 (R - \sqrt{R^2 - a^2}) \tag{2}$$

$$L_t = \mu_0 R(\ln(8R/a) - 2) \tag{3}$$

where N is the number of poloidal rotations round the torus. By inserting Eqs (2, 3) into Eq. (1), the relationship between N and the aspect ratio of the force balanced winding A = R/a is uniquely determined by

$$N = \sqrt{(\ln 8A - 1)/(A/\sqrt{A^2 - 1} - 1)} \tag{4}$$

The distribution of the toroidal current is determined so as to make the magnetic surface coincide with the coil surface, thereby minimizing the poloidal magnetic field inside the FBC winding. The aspect ratio of the FBC must be a discrete value which corresponds to an integer in Eq. (4) when the current distribution is concentrated on a finite number (pole number) of coil currents.

Superconducting FBCs were fabricated to verify that support of the coils would be practicable. The parameters of the winding are summarized in Table I. Since the aspect ratio is about 3, the number of turns along the minor circumference was chosen to be five to establish the net radial force balance. NbTi superconductor was

TABLE I. PARAMETERS OF A NbTi SUPERCONDUCTING FBC

	Designed	Achieved
Major radius (m)	0.18	
Minor radius (m)	0.061	
Coil winding	5 turns, 5 poles	
Coil current (A)	200	180
Current density (A/mm^2)	400	360
Maximum field (T)	2	1.8
Maximum stress (MPa)	100	80

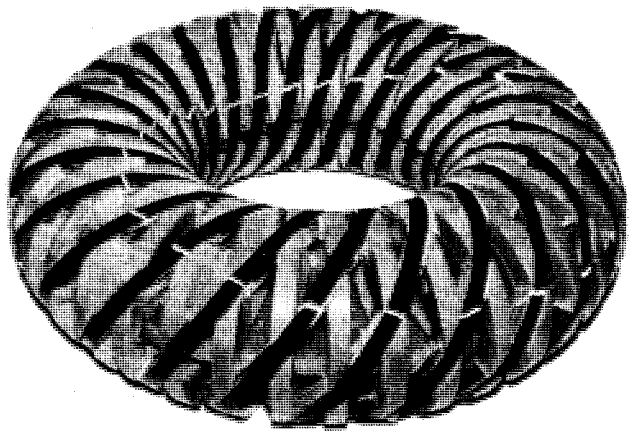

FIG. 1. FBCs made of NbTi.

wound by hand on a coil form made of glass fibre reinforced plastic (GFRP), as shown in Fig. 1. The 15 layers of 15 turn conductor and a preimpregnated glass fibre tape for layer insulation were fixed by resin impregnation. Even without coil casing, a maximum magnetic field at the winding of up to 1.8 T was produced with liquid helium pool cooling.

We have also started experiments in a small (R = 30 cm) pulsed device with normal conducting FBCs to demonstrate tokamak-like plasma confinement.

TABLE II. KEY REACTOR PARAMETERS

Plasma major radius	3.64 m
Plasma minor radius	0.80 m
Plasma elongation	1.7
Plasma triangularity	0.3
Plasma current	6.0 MA
Toroidal field on axis	8.4 T
q_ψ	3.01
Average density $\langle n_e \rangle$	1.05×10^{20} m^{-3}
Average temperature $\langle T \rangle_n$	15 keV
Poloidal β	1.02
Troyon factor	2.15
Z_{eff}	1.59
Neutral beam drive power	58 MW
Bootstrap current fraction	0.30
Q_{DT}	3.7
Neutron wall loading	1.0 MW/m^2

3. HIGH FIELD TOKAMAK REACTOR

Table II summarizes the plasma and machine parameters of a tokamak reactor with FBCs which we designed for a volumetric neutron source. To increase the neutron fluence, steady state operation is adopted with beam driven current and bootstrap current. We assumed an energy confinement enhancement a factor of 2 over the ITER89P scaling [4] and a current drive efficiency of 0.3×10^{20} A·W^{-1}·m^{-2}. The fusion reaction of $Q_{DT} \approx 3.7$ is maintained with 58 MW of neutral beam power, and thereby an average neutron wall loading of 1.0 MW/m^2 is achieved.

Figure 2 shows the radial build of the machine. The aspect ratio of the winding becomes lower with increased space for blanket and shield. When the ratio is about 1.7, the net radial forces are balanced with a winding pitch of two poloidal rotations round the torus. Figure 3 illustrates the force balanced winding composed of nine coils with a major radius of 3.8 m, a minor radius of 2.2 m, an elongation of 1.4 and a triangularity of 0.25. Two coils are plotted in the lower boxes. Each coil is a twisted loop in a shape like a figure of eight. A three dimensional view of the winding is shown in Fig. 4 together with the plasma and tangential ports. The ripple of the toroidal magnetic field at the plasma edge (R = 4.44 m, z = 0 m) is 0.6%. If we reduce the number of coils to eight to enlarge the coil gap for tangential ports, the ripple increases to 1.1%.

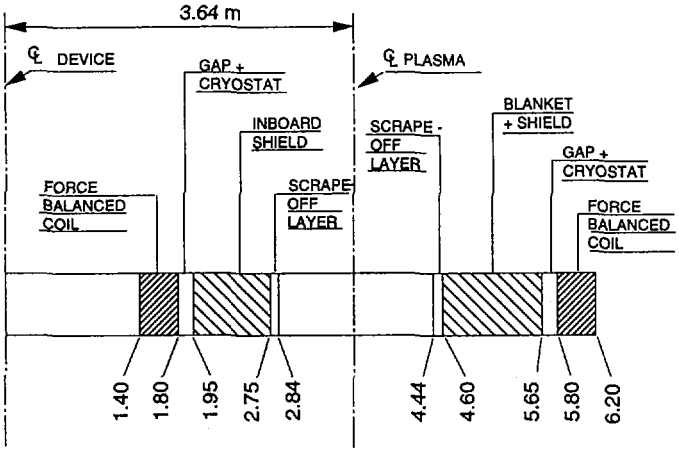

FIG. 2. Radial build of a fusion reactor configuration.

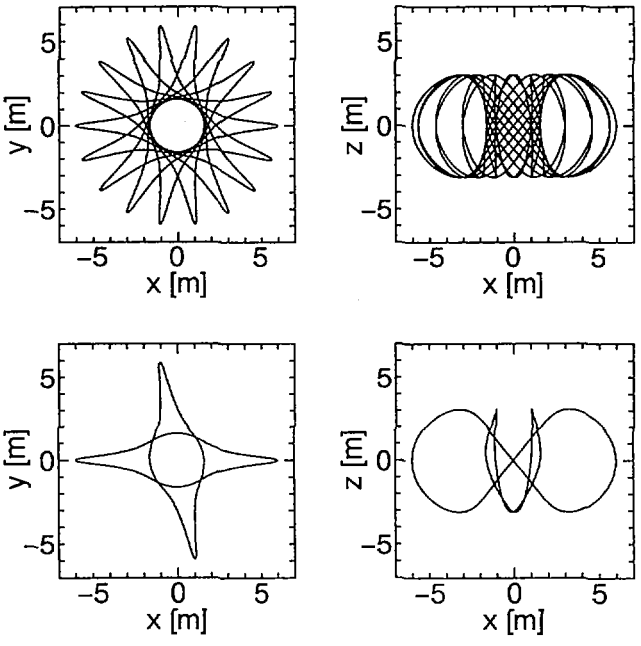

FIG. 3. Plan and elevation of the centrelines of 2 turn and 9 pole FBCs. Lower boxes show two coils.

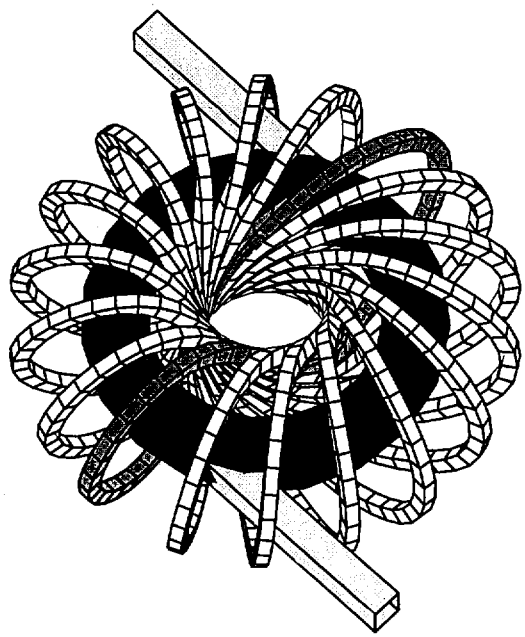

FIG. 4. Three dimensional view of the FBC winding shown in Fig. 3 and the plasma with tangential ports.

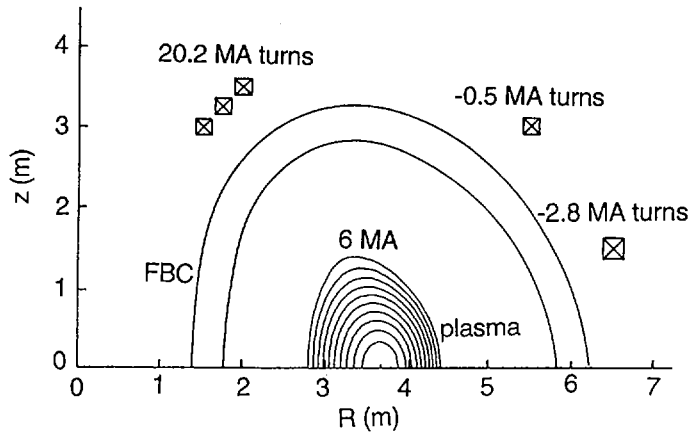

FIG. 5. Example of MHD equilibrium with poloidal coil currents.

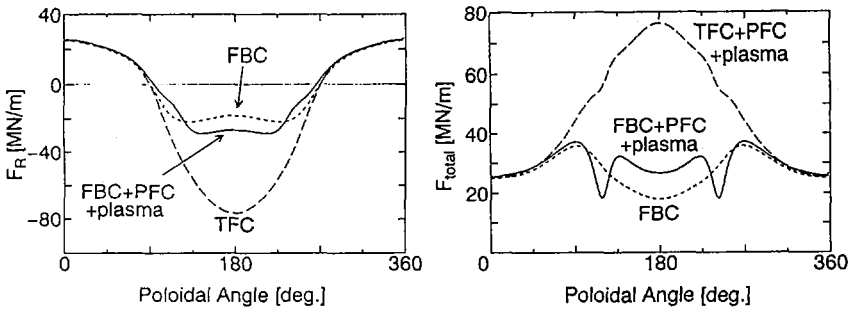

FIG. 6. Comparison of force distribution along the coil winding with the poloidal coil currents shown in Fig. 5.

No central solenoid is placed in the device. Since the force balanced winding provides poloidal magnetic flux, the plasma current can be raised in the ramp-up phase of the coil current. A null point of the poloidal magnetic field, where a discharge can initiate, appears in the vessel. It can be shifted horizontally by pre-biasing the vertical field. The plasma current is controlled with neutral beam current drive. Poloidal field coils are required to control the plasma equilibrium. Figure 5 shows an example of the plasma equilibrium with poloidal field coils. With this magnetic configuration, we confirmed that the flux surfaces are closed in the main plasma by a field line trace calculation.

Provided that the maximum field at the windings is 17 T, the net centring force is reduced to 1.5×10^7 N, compared with 2.6×10^8 N exerted on 18 toroidal field coils of the same dimension. Moreover, an appropriate pitch modulation reduces the maximum and the variance of the electromagnetic forces by a factor of more than 2, as shown in Fig. 6. Two dips in the total force appear owing to the localized out-of-plane forces generated by the inner poloidal coil currents which produce the triangularity of the plasma cross-section.

The average current density of the FBC is 6.1×10^7 A/m^2, which is about a quarter of the critical current density of Nb_3Al superconductor at 4.2 K and 17 T. Although the current density margin is not sufficient, it can be increased if we exploit the effect of the current component parallel to the magnetic field [5]. The longitudinal critical current density is typically larger by an order of magnitude than the transverse one [6].

4. CONCLUSIONS

We designed a high field tokamak reactor with an average neutron wall loading of 1 MW/m^2 utilizing the force balanced winding of twisted loops in a shape like a figure of eight. The net radial force is reduced by a factor of 10 from that exerted

on toroidal magnetic field coils of the same dimension. The maximum and the variance of the electromagnetic forces drop by a factor of more than 2 with an appropriate pitch modulation. A tokamak reactor with $Q_{DT} \approx 3.7$ with nearly the same plasma size as the existing large tokamaks could be realized provided that the force balanced magnets are fabricated with Nb_3Al superconductor.

REFERENCES

[1] PARISH, T.A., DAVIDSON, J.W., Nucl. Technol. **47** (1980) 324.
[2] MIURA, Y., KONDOH, J., SHIMADA, R., in Fusion Technology 1994 (Proc. 18th Eur. Symp. Karlsruhe, 1994), Vol. 2, Elsevier, Amsterdam (1995) 957.
[3] VAN SCIVER, S.W., et al., in Proc. 8th Symp. on Engineering Problems of Fusion Research, San Francisco, 1979, Vol. 2 (1979) 759.
[4] YUSHMANOV, P.N., TAKIZUKA, T., RIEDEL, K.S., Nucl. Fusion **30** (1990) 1999.
[5] FURTH, H.P., JARDIN, S.C., MONTGOMERY, D., IEEE Trans. Magn. **24** (1988) 1467.
[6] CODY, G.D., CULLEN, G.W., RCA Rev. **25** (1964) 466.

MAINTENANCE ORIENTED TOKAMAK REACTOR WITH LOW ACTIVATION MATERIAL AND HIGH ASPECT RATIO CONFIGURATION

S. NISHIO, S. UEDA, I. AOKI, R. KURIHARA,
T. KURODA, H. MIURA, T. KUNUGI, Y. SEKI
Naka Fusion Research Establishment,
Japan Atomic Energy Research Institute,
Naka-machi, Naka-gun, Ibaraki-ken

J. ADACHI, S. YAMAZAKI, I. KAWAGUCHI, T. HASHIMOTO
Kawasaki Heavy Industries,
Tokyo

K. SHINYA, Y. MURAKAMI, H. TAKASE, T. NAKAMURA
Toshiba Corporation,
Tokyo

Japan

Abstract

MAINTENANCE ORIENTED TOKAMAK REACTOR WITH LOW ACTIVATION MATERIAL AND HIGH ASPECT RATIO CONFIGURATION.

Some of the difficulties of maintenance of a tokamak system are due to the radioactivity of its materials and the complexity of its configuration. To mitigate these difficulties, very low activation SiC/SiC composite material and a torus configuration with a high aspect ratio of eight are introduced. The torus system is divided radially into equal sectors, each of which forms an assembling unit. All piping and feeder systems are shifted to the spacious central torus region. The new concept is called DREAM tokamak reactor, which is an acronym for DRastically EAsy Maintenance. The maximum toroidal field strength of 20 T and the plasma major and minor radii of 16 m and 2 m lead to a high fusion power of 5.5 GW, under moderate physics constraints such as an MHD safety factor of three, a Troyon factor of three for the beta limit and an energy confinement time enhancement factor of two.

1. INTRODUCTION

A tokamak reactor using D–T fuel seems to be the most promising concept for the first generation of fusion power plants. In a mature stage of tokamak power plants and as a final goal, the three major requirements of low construction cost, high availability operation and environmental safety must be met simultaneously. It is widely recognized that in an experimental reactor long pulsed or steady state burn and basic fusion technologies such as tritium handling are to be demonstrated. The final goal and the mission of the next step device are precisely given. On the basis of the present

status or a realistic extrapolation of the existing physics and technological database, it is, however, impossible to provide a reactor concept that satisfies these requirements simultaneously. Hence, certain requirement priorities are important as an intermediate step from where the final goal can be envisaged. If we consider a DEMO reactor or the early stage of the commercial reactor age, we deem it meaningful to ask which requirement should have the highest order of priority. From the viewpoint of public acceptance, high availability and environmental safety should be demonstrated preferentially. Then, construction cost will be gradually reduced through experience gained in the construction process and innovations in technology. This approach will prove to be less expensive.

Since the configuration is so complex and the materials are radioactive, it seems still to be difficult to realize high availability and environmental safety during the early stage of the commercial reactor age. For high availability operation, an easy maintenance scheme is an indispensable condition. To create an easy maintenance scheme, very low activation material and a high aspect ratio configuration are inroduced. In ARIES-I [1], also low activation material is adopted as the structural material. In our reactor concept, the torus system is divided radially into equal sectors, each of which forms an assembling unit. One advantage of the high aspect ratio configuration is that it allows all piping and feeder systems to be arranged in the torus inboard region. The new concept is called DREAM tokamak reactor (for DRastically EAsy Maintenance).

In Section 2, the design drivers are described. Plasma engineering and fusion power core engineering are treated in Sections 3 and 4, respectively. Section 5 is devoted to safety and environmental considerations. Section 6 is a summary of the paper.

2. DESIGN DRIVERS FOR THE DREAM TOKAMAK

The design drivers and major features of the DREAM tokamak are as follows:

(1) SiC/SiC composite, a very low activation material, is used for the structure. Thereby, the level of radioactivity one day after shutdown can be reduced by five orders of magnitude.

(2) Because of the electrical insulation properties of the SiC/SiC composite, electromagnetic loads on the in-vessel components can be eliminated in a plasma disruption. Thereby, the design conditions for the supporting structures of the replaceable components are remarkably alleviated.

(3) To compensate for the increased plasma position instabilities caused by the loss of conducting shell around the plasma, the vertical elongation of the plasma is reduced.

(4) The torus system is divided radially into equal sectors, each of which forms an assembling unit. Each sector of the torus system is removed horizontally in a single radial, straight motion between adjacent toroidal field coils (TFCs).

(5) The vacuum seal between adjacent sectors is eliminated, and a modular concept is adopted for the blanket structure system. The size of one module is at most 1 m. Hence, the demand on the manufacturing technology of the SiC/SiC composite is lowered substantially.

(6) A torus configuration with very high aspect ratio is chosen. All piping and feeder systems are extracted towards the spacious central torus region that is made available by the high aspect ratio configuration. Since a major part of the plasma current is a bootstrap current, the apparatus for plasma current drive becomes compact. Thus the surrounding area of the tokamak is free of components.

(7) A high temperature helium cooling system is introduced in order to achieve high thermal efficiency and enhanced safety. The SiC/SiC composite is also compatible with high temperature operation.

(8) The fusion power capacity is increased in order to gain an economic reward due to upscaling.

The component layout and the major specifications of the DREAM tokamak are shown in Fig. 1 and Table I, respectively.

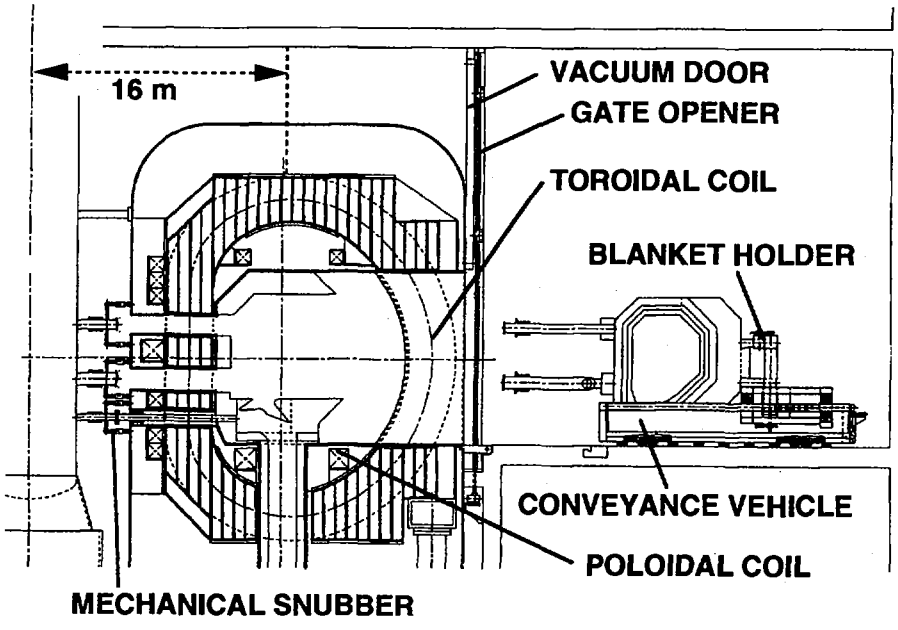

FIG. 1. Component layout of the DREAM tokamak.

TABLE I. MAJOR SPECIFICATIONS OF THE DREAM TOKAMAK

Assembling scheme	Sector cassette
Number of assembling units	16
Structural material	SiC/SiC composite
Coolant	Helium
Coolant pressure (MPa)	10
Plasma major radius, R_p (m)	16
minor radius, a_p (m)	2
elongation, κ_{95}	1.3
Burn time, T_{burn}	∞
Maximum toroidal field, $B_{t\,max}$ (T)	20
Neutron wall loading, P_n (MW/m^2)	3
Fusion power, P_{fus} (GW)	5.5
Fusion gain, q	>50
Plasma current, I_p (MA)	9.2
Bootstrap current fraction, γ_{bs}	0.87
Current driving power, P_{aux} (MW)	50
Thermal power, P_{th} (GW)	6.4
Coolant temperature, T_{in}/T_{out} (°C/°C)	600/900
Thermal efficiency (gross/net), η_{th}/η_{net} (%/%)	50/45

3. PLASMA ENGINEERING

The small elongation of 1.3 is consistent with the fact that the location of the conducting shell stabilizer for the plasma vertical instability is 2 m apart from the plasma surface. As typical design values for the physics constraints, an MHD safety factor of three, a Troyon factor of three for the beta limit and an energy confinement time enhancement factor of two are chosen. In these conditions, the achievable maximum fusion power is only determined by the maximum toroidal field and the plasma minor radius. A relatively small minor radius of 2 m is found to be able to produce 5.5 GW of fusion power when the maximum toroidal field is 20 T. In this case, the optimized major radius is 16 m and the aspect ratio is eight. A high aspect ratio device allows better use to be made of the toroidal field. The toroidal field at the plasma centre is 14.5 T. The plasma temperature is 14 keV, and the electron density is 1.7×10^{20} m^{-3}, where the point of operation is stable with respect to the thermal instability. The reflection rate of SiC for synchrotron radiation is asumed to be 50%.

The DREAM reactor is operated in a steady state mode. The large major radius degrades the current drive efficiency when neutral beam injection (NBI) is used.

Operation at a higher aspect ratio, however, maximizes the self-induced bootstrap current. The bootstrap current density is calculated by using Hirshman's model [2]. The beam line is designed in 3-D geometry, and the NBI driven current profile is calculated by using the DRIVER code [3] including a 2-D Fokker–Planck calculation for the slowing-down process. By using 2 MeV, the neutral beam can penetrate into the plasma centre and drive the peaked NBI current which is necessary for seeding the bootstrap current. The NBI current drive power necessary for steady state operation is about 50 MW.

A reliable divertor also constitutes one of the critical issues of a fusion power plant. Therefore, we adopt a conventional divertor design and aim at clarifying the technological goals for the divertor component to be developed. The plasma parameters are optimized from the point of view of divertor heat load. The divertor conditions are estimated by using a two point model, a scaling formula and a simple 2-D edge plasma code. The divertor heat load of the DREAM reactor is of the same order as that of ITER [4], even though the fusion power is more than three times higher than that of ITER. The maximum heat flux and electron temperature were evaluated to be less than 5 MW/m^2 and 100 eV, respectively.

4. FUSION POWER CORE ENGINEERING

The breeding blanket and the divertor structure were designed to use SiC/SiC composite and high temperature helium gas as structure material and coolant. A modular 'mushroom' shape was chosen for the blanket structure, and its plasma facing area of 0.5 m × 0.5 m was optimized with a view to coolant pressure, coolant velocity, thermal stress and the fabrication technology of the SiC/SiC composite. The inlet and outlet coolant temperatures of 600 and 900°C, respectively, provide a gross plant efficiency of higher than 50%, with the Brayton cycle system. The 'mushroom stem' is the co-axial cooling pipe. The maximum stress in the first wall, due to a surface heat flux of 0.5 MW/m^2 and a coolant pressure of 10 MPa, is kept lower than the 200 MPa permitted by the design. In the breeding region of the 'mushroom cap', small lithium oxide and beryllium pebbles are filled in as breeder and neutron multiplier, respectively.

The gas divertor concept was adopted to reduce the peak heat flux and the particle energy incident onto the divertor surface. The maximum heat flux and the electron temperature were evaluated to be less than 5 MW/m^2 and 100 eV, respectively. The surface is coated with a tungsten or CVD SiC layer of 2 mm in order to resist sputtering erosion. The coolant, under a pressure of 10 MPa, enters at 600°C and is heated up to 800°C in the divertor structure. Then the coolant is further heated up to 900°C in the hot shield structure. The maximum temperature and the thermal stress are evaluated to be around 1100°C and 120 MPa, respectively.

5. SAFETY AND ENVIRONMENTAL CONSIDERATIONS

The activation dose of the SiC/Li_2O blanket and the SiC/TiH_2/B_4C shields one day after shutdown, after a full power reactor operation of 20 years, has been evaluated. It was found that one day after reactor shutdown the blanket activation has decayed by five orders of magnitude, but the dose from the SiC/TiH_2/B_4C shields has decayed little so that the maximum dose in the blanket and shield is reduced by only three orders of magnitude, instead of five for the case when SiC only is used as a shield material. The use of TiH_2, which is a very good neutron shielding material, enables a reduction of the radial thickness of 157 cm by more than 50 cm. Further optimization of the shield composition or arrangement is needed to reduce the dose rate for easy maintenance and to reduce the radial thickness. In a more accurate dose map evaluation, the gamma dose from the divertor plates and the stabilizing metal shell should be considered.

The tritium produced in the blanket is directly released into the helium coolant. In order to reduce the tritium inventory in the helium coolant to less than 100 g, the tritium is recovered from the coolant by the tritium recovery system, through which 0.15% of the coolant flow is bypassed, when a recovery fraction of 0.99 is assumed.

A possible radioactive waste disposal scenario for the DREAM reactor in Japan has been investigated. It is found that radioactive waste from the irradiated SiC/SiC composite with impurities could be disposed by nearly the same method as that used for shallow land burial which is at present applied to low level waste in Japan [5].

6. SUMMARY

The three key requirements of low construction cost, high availability operation and environmental safety should be realized simultaneously in a matured tokamak power plant. The latter two requirements should at first be satisfied at an intermediate point such as the DEMO reactor or in the first generation of commercial reactors. High availability operation is made possible by an easy maintenance scheme which is provided by using a very low activation material, the SiC/SiC composite, and a high aspect ratio configuration of eight. Because of the relatively low plasma current of 9.2 MA and a high bootstrap current fraction of 87%, a fusion gain of $Q > 50$ is expected. The high toroidal field strength of 20 T leads to a high fusion power of 5.5 GW, in spite of the relatively small plasma volume (80% of the ITER plasma volume). A high temperature helium cooling system of 900°C is introduced in order to achieve a high thermal efficiency of more than 50%. In addition to high availability operation, the high fusion power and the high thermal efficiency could remarkably improve the economical aspects of the device.

ACKNOWLEDGEMENTS

The authors would like to express their gratitude to A. Kohyama, R. Yamada and S. Ishiyama for stimulating discussions on the SiC/SiC composite, and to K. Okano and Y. Ogawa for valuable comments on plasma engineering. Thanks are also due to M. Seki, T. Nagashima and M. Ohta for their continuous encouragement.

REFERENCES

[1] CONN, R.W., NAJMABADI, F., in Plasma Physics and Controlled Nuclear Fusion Research 1990 (Proc. 13th Int. Conf. Washington, DC, 1990), Vol. 3, IAEA, Vienna (1991) 659.

[2] HIRSHMAN, S.P., SIGMAR, D.J., Nucl. Fusion **21** (1981) 1079.

[3] OKANO, K., et al., Nucl. Fusion **29** (1989) 199.

[4] INTERNATIONAL ATOMIC ENERGY AGENCY, ITER EDA Documentation Series No. 7, IAEA, Vienna (1996).

[5] SEKI, Y., et al., in Technology of Fusion Energy (Proc. 12th ANS Top. Mtg Reno, NV, USA, 1996), to be published in Fusion Technol.

A COMPACT TOKAMAK TRANSMUTATION REACTOR

L.J. QIU, Z. GUO, B.J. XIAO, Y.P. CHEN,
L.L. LIU, S.J. WANG, Y.C. WU, Q. XU,
Q.Y. HUANG, M.H. KONG
Institute of Plasma Physics,
Academia Sinica,
Hefei, Anhui, China

Abstract

A COMPACT TOKAMAK TRANSMUTATION REACTOR.

The paper proposes a low aspect ratio tokamak for the driver of a transmutation reactor. The main parameters of the reactor core and a neutronic analysis of the blanket are given. The previous analysis showed that the neutron wall loading can be lowered to the order of 1 MW/m^2 for an adequate transmutation capacity and efficiency. The recent analysis confirms this conclusion. The neutron wall loading could be lowered even further to the order of 0.5 MW/m^2, which could easily be reached in the near future. It is also shown that the transmutation efficiency (fission/absorption ratio) is higher than in the previous analysis. The blanket power density is about 200 MW/m^3, which is not difficult to deal with. The key components of a low aspect ratio transmutation reactor, such as the divertor and the centre conducting post, are also analysed and compared with those of a conventional tokamak. Finally, a comparison is made with other drivers such as fast breeder reactors, pressurized water reactors and accelerators. The low aspect ratio transmutation reactor is one of the applications of fusion energy that could be realized in the near future.

1. INTRODUCTION

In accordance with the previous fusion–fission hybrid reactor design [1, 2], our new concepts are based upon a small DT fuelled tokamak device (conventional or low aspect ratio (low A) tokamak) serving as a strong neutron source, with fusion power as low as 10–100 MW, to drive a power plant for the transmutation of high level waste.

The new blanket concept relies on an intense neutron flux to achieve a blanket energy multiplication of the order of 10–100. When subcriticality k_{eff} of up to 0.95 is maintained with a neutron wall loading of about 1 MW/m^2 or even of 0.5 MW/m^2, the intense thermal neutron flux ($>5 \times 10^{15}$ n·cm^{-2}·s^{-1}) in the blanket ensures adequate neutron economy.

2. REACTOR CORE CONCEPT AND PARAMETERS

A compact tokamak reactor (Fig. 1) is proposed for application as a neutron source, for which the parameter requirements in both plasma physics and nuclear

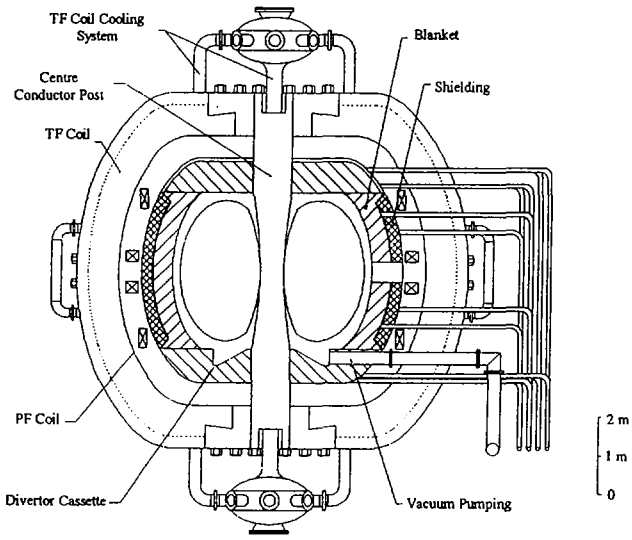

FIG. 1. Schematic view of the Hefei Low Aspect Ratio Tokamak Reactor.

technology are far less stringent than those for a tokamak fusion reactor. For several decades, high β, good confinement and steady state operation have been pursued by generations of scientists in magnetic fusion research. To accomplish these goals, a low A tokamak was proposed about a decade ago, but this proposal was not considered in detail at that time only because of the uncertainties of plasma production. However, HIT and START have successfully proven that a low A plasma can be

TABLE I. POSSIBLE CORE DESIGN PARAMETERS OF A LOW ASPECT RATIO TOKAMAK TRANSMUTATION REACTOR

Major radius R (m)	1.4	1.4
Minor radius a (m)	1	1
Plasma current I_p (MA)	12.54	8.7
Toroidal field B_t (T)	2.5	2.5
Plasma edge q	4.5	6.5
Average density $\langle n_e \rangle$ (10^{20} m^{-3})	1.6	1.1
Average ion temperature $\langle T_i \rangle$ (keV)	10	9.5
Plasma volume (m^3)	50	50
Bootstrap current fraction	0.54	0.4
Fusion power P_{fus} (MW)	100	50
Drive power P_d (MW)	40	50
Neutron wall loading P_w (MW/m^2)	1.02	0.5

reliably produced, so the low A tokamak should be given sufficient attention by the fusion community. The low A reactor core must be configured for full remote access for the critical components, which include the divertors, the first wall tiles, the transmutation blanket system and the normal conducting centre leg of the toroidal field coils. The features that can influence the low A reactor core are summarized in Table I [3].

3. NEUTRONICS OF THE TRANSMUTATION BLANKET

A blanket is designed to accomplish a dual function, namely, transmuting high level nuclear waste (Np, Am, Cm and Pu isotopes produced in a fission reactor) and breeding tritium for use in a fusion reactor core. We present here a neutronics analysis performed using the code BISON 1.5 [4], which has been revised to include the resonance self-shielding effect and a more complete burnup process through modification of the burnup calculation method and the burnup chains. The transport data library originally used in BISON 1.5 [4] has been changed to include all the relevant actinides. However, the analysis presented here does not consider the resonance self-shielding effect because it is not significant in the case of fast fission and low k_{eff}.

The one dimensional layout and the material composition of the blanket are shown in Fig. 2.

Table II gives the results for the nuclides transmuted after 500 days of burning. The goal is to maintain the NpAmCm transmutation capacity at about ten light water reactors (normalized). From the results, we have found that by raising the fuel loading density and hence raising k_{eff} and the neutron flux, we can reach the transmutation objective with a lower neutron wall loading (0.5 MW/m^2), which should be possible to achieve in the near future.

One of the main figures of merit of transmutation is the transmutation efficiency, that is, the ratio of the total fission reaction rate to the total absorption reaction rate. Table III shows the ratios with neutron wall loadings of 0.5 and

FIG. 2. Blanket configuration and material composition. 1: SS-316 70%; 2: SS-316 5% + NpAmCm 5% + Pu 1.8% + Zr 1% when neutron wall loading is 1 MW/m^2, or 2: SS-316 5% + NpAmCm 5.7% + Pu 2.1% + Zr 1% when neutron wall loading is 0.5 MW/m^2; 3: SS-316 80%; 4: Li_2O 75% (with Li^6 enrichment 80%) + SS-316 5% or 4: C 80%.

TABLE II. TRANSMUTATION OF HIGH LEVEL WASTE AFTER 500 d AT NEUTRON WALL LOADINGS OF 0.5 AND 1 MW/m^2

	Am-241	Am-243	Cm-244[a]	Np-237	Pu-238[a]	Pu-239	Pu-240	Pu-241	Pu-242[a]
Nuclides transmuted (10^{24})									
0.5 MW/m^2	2910	360	−18	2250	−1107	1470	270	273	−99
1 MW/m^2	3331	404	−31.3	2549	−1343	1532	321	301	−129
Number of light water reactors[b] (normalized to 1 GW·a)									
0.5 MW/m^2	13	9	−2	11	−18	0.6	0.3	0.8	−0.5
1 MW/m^2	14	9	−4	12	−20	0.6	0.3	0.8	−0.6
Transmuted fraction									
0.5 MW/m^2	11	7.8	−2.2	10	−358	12.9	5.1	16	−9.3
1 MW/m^2	13.3	9.12	−3.9	11.7	−444	15.3	6.22	17.5	−12

[a] Negative values indicate that the nuclide density increased.

[b] Normalizing factor: nuclides transmuted in 1 GW·a of operation of a thermal power hybrid reactor blanket/nuclides produced in 1 GW·a of operation of a thermal power light water reactor.

TABLE III. TRANSMUTATION EFFICIENCY[a] FOR NEUTRON WALL LOADINGS OF 0.5 (1) MW/m^2

	Am-241	Am-243	Cm-244	Np-237	Pu-238	Pu-239	Pu-240	Pu-241	Pu-242
0	1.0 (1.1)	1.4 (1.4)	3.3 (3.4)	1.6 (1.7)	5.3 (5.4)	14 (14)	5.0 (5.2)	12 (11)	4.6 (4.7)
500 d	1.0 (1.1)	1.4 (1.5)	3.4 (3.5)	1.6 (1.7)	5.3 (5.5)	14 (15)	5.1 (5.3)	11 (12)	4.7 (4.8)

[a] Total fission reaction rate/(n,γ) reaction rate.

TABLE IV. k_{eff}, TBR AND POWER DENSITY OF THE BLANKET FOR NEUTRON WALL LOADINGS OF 0.5 (1) MW/m^2

	Time (d)					
	0	100	200	300	400	500
k_{eff}	0.89 (0.97)	0.88 (0.95)	0.87 (0.94)	0.86 (0.93)	0.85 (0.92)	0.85 (0.92)
TBR	8.3 (29)	7.6 (18)	7.1 (14)	6.6 (13)	6.3 (12)	6.1 (11)
P (W/cm^3)	180 (348)	162 (211)	148 (170)	138 (149)	130 (135)	123 (124)

1 MW/m^2. The results show that the efficiency of this kind of blanket is so high that even if the neutron wall loading is lowered to 0.5 MW/m^2, the transmutation efficiency and the tritium breeding ratio (TBR) are still high enough. The thermal power in the blanket is 4.9 (initial)–3.4 (after 500 d) GW and 9.7–3.4 GW with neutron wall loadings of 1 and 0.5 MW/m^2, respectively. Table IV gives k_{eff}, TBR and power density. It is shown that k_{eff} decreases with time, which is beneficial for the safety of the blanket, and that the TBR is so high that tritium can be provided for several fusion reactors of the same fusion power. The heat generated in the blanket can be removed with the existing technology used in fast fission reactors.

4. NATURAL DIVERTOR

The low A tokamak configuration offers a possible mechanism to maintain a thick plasma scrape-off layer (SOL). An increasing fraction of such a thick SOL

TABLE V. MAIN EDGE PLASMA PARAMETERS FOR LOW A AND CONVENTIONAL TOKAMAKS

	Low A tokamak	Conventional tokamak
SOL thickness (cm)	15	5
Peak ion temperature (eV)	14.646	15.6
Peak electron temperature (eV)	31.1	157.7
Peak ion energy flux (MW/m^2)	10.44	8.168
Peak electron energy flux (MW/m^2)	17.93	50.1
Peak ion density (10^{22}/m^3)	1.072	0.37
Peak pressure (Pa)	5152	5446
Total energy flux (MW/m^2)	26.73	55.85
Ion flux (10^{24}/m^2)	2.796	1.61

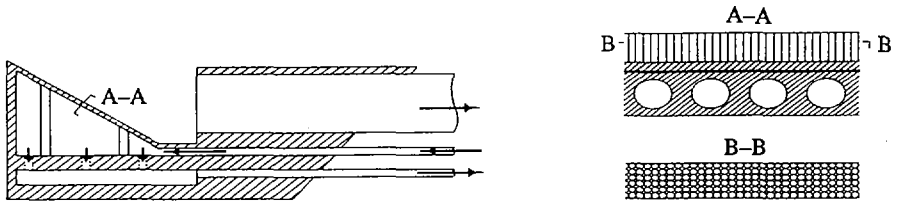

FIG. 3. Conceptual structural design of the divertor in the Hefei Low Aspect Ratio Tokamak Reactor.

becomes diverted naturally without a divertor coil in a low A tokamak for the plasma parameters shown above. Table V shows the main differences in the plasma parameters near the divertor plate for $\delta = 15$ cm (low A) and $\delta = 5$ cm (conventional). The wider SOL, which can reduce damage to the divertor target plate, is a great benefit for the low A tokamak. The conceptual structural design of this kind of divertor is shown in Fig. 3.

5. ENGINEERING FEASIBILITY OF THE CENTRE CONDUCTING POST

A compact design with very limited space requires an unshielded centre conducting post (CCP) as part of the toroidal field coil. The fully exposed CCP will be subject to neutron damage and to resistive and nuclear heating power. It is one of the key components and requires replacement at regular intervals. Tables VI–VIII show the analysis results for the CCP of a low A tokamak reactor, such as average neutron wall loading, nuclear heating and radiation damage. These results are compared with those for the first wall of a conventional tokamak with similar technical requirements.

TABLE VI. AVERAGE VALUE OF P_w (MW)

	Total plasma face of components	Outer first wall	Inner first wall
Compact tokamak	1.0	1.023	0.722[a]
Regular tokamak	1.0	1.083	0.812

[a] For the surface of the exposed CCP.

TABLE VII. AVERAGE VALUE OF H_n (W/cm^3)

	Total CCP	Outer first wall	Inner first wall
Compact tokamak	4.35	7.26	6.39[a]
Regular tokamak	—	8.28	5.72

[a] For a 1 cm thick surface layer of the CCP.

TABLE VIII. COMPARISON OF dpa OF REFERENCE REACTORS

	Compact tokamak			Regular tokamak		UWMAK-1	ITER	
	CCP	Inner first wall[a]	Outer first wall	Inner first wall	Outer first wall	First wall	First wall	
Material	Cu	Cu	Cu	Cu	Cu	SS-316	SS-316	Cu
dpa/a[b]	8.7	12.2	14.0	15.5	18.0	18	9.0	11.1

[a] For a 1 cm thick surface layer of the CCP.
[b] Normalized to an average neutron wall loading of 1 MW/m^2.

6. FUTURE PROSPECTS FOR A LOW ASPECT RATIO TRANSMUTATION REACTOR

(1) A comparison of the fusion core plasma assumptions of a low A reactor and of TFTR and JET shows that the required plasma parameters for the purpose of waste transmutation are attainable (Table IX).

(2) Comparing a spallation transmutation reactor with a low A tokamak transmutation reactor, both concepts include similar target/blanket systems, subcriticality, low nuclear heat deposition density and optimum construction for high level waste transmutation. The only difference is the driver: accelerator or tokamak. The selection of the driver depends on the development of the relevant technologies. Table X gives a comparison of several approaches for high level waste transmutation. We can see that the transmutation prospects of the hybrid reactor are very attractive and the present technology development would indicate that the requirements for transmutation hybrid reactors will be reached in the near future.

TABLE IX. TWO LOW A REACTOR DESIGNS COMPARED WITH TFTR AND JET

	TFTR	JET	Low A reactor	
Major radius R (m)	2.9	3.0	1.4	1.4
Minor radius a (m)	0.9	1.2	1	1
Plasma current I_p (MA)	2	5	12.54	8.7
Toroidal field B_t (T)	5	2.8	2.5	2.5
Average density $\langle n_e \rangle$ (10^{20} m^{-3})	0.3	0.4	1.6	1.1
Plasma volume V (m^3)	45	100	50	50
Average ion temperature T_i (keV)	20	10	10	9.5
Fusion power P_{fus} (MW)	9	15	100	50
Drive power P_d (MW)	30	15	40	50
Bootstrap current fraction	0.4	0.35	0.54	0.4
Duration of DT burn (s)	1	2	Steady state	Steady state
Average wall loading (MW/m^2)	0.2	0.2	1.02	0.5

TABLE X. COMPARISON OF DIFFERENT APPROACHES FOR HIGH LEVEL WASTE TRANSMUTATION

	Pressurized water reactor	Fast breeder reactor	Accelerator Transmutation of Waste	Hybrid reactor
Neutrons in the device	Thermal, 10^{14} $cm^{-2} \cdot s^{-1}$	Fast, 10^{14}–10^{15} $cm^{-2} \cdot s^{-1}$	Thermal, 10^{16} $cm^{-2} \cdot s^{-1}$	Thermal/fast, 10^{17} $cm^{-2} \cdot s^{-1}$
Fission products (Tc, I, Sr, Cs)	Yes	No	Yes	No
Actinides (Pu, NpAmCm)	No	Yes	Yes	Yes
Fission material inventory	Large	Large	Small	Small
Time needed	0	Short	15–20 a	15 a

7. SUMMARY

According to the above results, the low A tokamak reactor presented here is very attractive and has many advantages such as:

(1) The transmutation blanket can be designed to accomplish a dual function: transmuting high level waste and breeding tritium very efficiently even under the

condition of 0.5 MW/m^2 neutron wall loading, which will be reached in the near future. The engineering problems, such as heat removal, can be solved.

(2) Low A tokamaks offer the possibility of a compact fusion reactor requiring a relatively low toroidal field.

(3) The natural divertor has a wide SOL, which can lower the damage to the divertor target plate.

(4) The large elongation and high plasma current can be obtained with a simple poloidal field system.

The most serious engineering problem is the CCP, but from our analysis, this problem is not much more serious than in the case of the conventional tokamak reactors.

The compact tokamak might offer attractive advantages if it employs a fusion–fission hybrid blanket with large gain (M = 10–100). This kind of small reactor could be applied economically and safely for the burning of long lived actinides and fission products.

REFERENCES

[1] QIU, L.J., et al., in Plasma Physics and Controlled Nuclear Fusion Research 1994 (Proc. 15th Int. Conf. Seville, 1994), Vol. 2, IAEA, Vienna (1995) 741.

[2] QIU, L.J., et al., "Some key issues of compact tokamak reactor design for volumetric neutron source (VNS) application", paper presented at 3rd Japan–China Symp. on Materials for Advanced Energy Systems and Fission and Fusion Engineering, Chengdu, China, 1995.

[3] LIU, Lili, QIU, Lijian, WANG, Shaojie, "The physics basis of low aspect ratio tokamaks", paper presented at 4th Japan–China Symp. on Materials for Advanced Energy Systems and Fission and Fusion Engineering, Hokkaido Univ., Sapporo, Japan, 1996.

[4] CCC-464, BISON 1.5, A One Dimensional Discrete Ordinate Neutron Transport and Burnup Calculation Code System, RSIC Computer Collection, Radiation Shielding Information Center, Oak Ridge Natl Lab., TN.

MEASUREMENTS AND CALCULATIONS OF NEUTRON LEAKAGE SPECTRA FROM LEAD SLABS IRRADIATED WITH 14 MeV NEUTRONS

J. JORDANOVA, O. PENCHEV
Institute for Nuclear Research and Nuclear Energy,
Bulgarian Academy of Sciences,
Sofia, Bulgaria

Abstract

MEASUREMENTS AND CALCULATIONS OF NEUTRON LEAKAGE SPECTRA FROM LEAD SLABS IRRADIATED WITH 14 MeV NEUTRONS.

Neutron leakage spectra through lead slabs with thicknesses of 0.05, 0.075 and 0.125 m were measured by using a proton recoil technique and a differentiation unfolding procedure. The measurements were performed on an absolute basis. The results were compared with the prediction of Monte Carlo calculations by using the MCNP-4A code and pointwise cross-sections from ENDF/B-IV and ENDF/B-VI data files. The calculations employing ENDF/B-VI data show good agreement with the experimental results, with the exception of the energy region between 5 and 10 MeV, where an underestimation of up to 29% was obtained.

1. INTRODUCTION

Among the materials foreseen as neutron multipliers in some blanket concepts, lead and, in particular, $Li_{17}Pb_{83}$ eutectic are considered to be promising candidate materials. Sensitivity/uncertainty analyses [1] have shown that the tritium breeding ratio in the Li–Pb blanket is mainly sensitive to the Pb(n, 2n) cross-section. Therefore, accurate (n, 2n) and neutron emission cross-section data for lead are required. The measured (n, 2n) cross-sections as summarized in Ref. [2] show discrepancies of about 20% among each other and of 10% from the evaluated data. On the other hand, the evaluated data display considerable differences among each other in the secondary neutron angle and energy distributions. The results from neutron multiplication experiments reviewed in Ref. [3] and from neutron leakage spectra measurements [4–6] suggest the necessity of an improvement of the (n, 2n) and emission cross-section data in currently used cross-section files and their further testing in independent integral experiments.

This paper presents experimentally obtained leakage neutron spectra through lead slabs of different thicknesses (0.05, 0.075 and 0.125 cm). A proton recoil method was used to measure the spectra for neutron energies between 1 and 15 MeV. To provide a theoretical estimate for comparison, neutron transport calculations using the MCNP-4A Monte Carlo code [7] were performed.

2. EXPERIMENTS

The neutron generator D150 Sames with a Ti–T target and deuterons accelerated to an energy of 0.15 MeV was employed as a source of 14 MeV neutrons. Lead slabs with laminated dimensions of 0.40 m × 0.40 m were placed at a distance of 0.42 m from the tritium target, thus ensuring irradiation with monoenergetic neutrons. The leakage spectra were measured on the deuteron beam axis, 0.03 m from the rear wall of the slab.

A proton recoil spectrometer with a stilbene scintillator (3 cm diameter × 3 cm height) mounted on an XP2230 photomultiplier tube and an ORTEC 265 base was used to measure the neutron leakage spectra. The standard ORTEC technique based on leading edge timing was used to discriminate between gamma ray events and neutrons. The detector was irradiated from the curved side. As was pointed out in our previous paper [8], this position of the detector results in a reduced neutron energy uncertainty arising from light output anisotropy. From an expression given in Ref. [8], the energy error was estimated to be 12%. Energy calibration of the spectrometer was performed by employing a set of gamma ray sources. Two gain measurements were carried out in order to cover the energy range from 1 to 15 MeV. To account for the non-linear neutron energy dependence and the anisotropy of the light output the experimental data from Ref. [9] were used.

For an absolute monitoring of the source neutrons, a silicone surface barrier detector was employed to count the associated alpha particles and protons from the T(D, n)^{4}He and D(D, p)T reactions. The latter was used to estimate the D–D neutron contribution to the spectra. The anisotropy coefficients used to determine the neutron yield from the D–T and D–D reactions are given in Ref. [10]. The error of the absolute monitoring totals 3%. The contribution from the neutron reactions with carbon nuclei in the scintillator to the spectra of alpha particles was corrected as was described in our previous paper [8].

The neutron spectra were reduced from the measured pulse height distributions by employing the differentiation unfolding code described in detail elsewhere [11]. Its main features are a global smooth, orthonormal polynomial approximation of the experimental data in a specially built basis as well as subsequent stable differentiation [12]. Before fitting the data an appropriate functional transform was applied to make them more suitable for polynomial approximation. The light output data and the Compton electron distributions needed for the energy calibration were treated by using the same approach. The maximum of the first derivative of the Compton distribution was used to locate the position of the Compton edge. The code generates error limits of the unfolded spectrum which include the approximation and derivative errors of both pulse height distribution and light output data, the spectrometer gain error, the uncertainty in the absolute monitoring of the source neutrons and the maximum error in the neutron energy arising from anisotropy of the light output.

3. CALCULATIONAL PROCEDURE

The calculated energy distributions were obtained by means of the Monte Carlo transport code MCNP-4A and continuous energy cross-sections from the ENDF/B-IV and ENDF/B-VI data libraries. Since the energy of the source neutrons varies slightly within the solid angle subtended by the barrier to the tritium target, a point isotropic source uniformly distributed over an energy interval of 14.75–14.5 MeV was started. A point detector tally and a cone biased source were used in the calculations. The neutron spectra were scored until a maximum error of 5% was achieved in all energy bins. The calculated results were normalized to one source neutron and convoluted by a Gaussian function with a standard deviation corresponding to the detector energy resolution.

4. RESULTS AND DISCUSSION

The measured and calculated spectra for the three slab assemblies are compared in Figs 1 to 3. The error limits of the measured spectra are denoted by crosses. The measured results are displayed at the upper end of each energy bin.

The measured and calculated integrals and ratios of calculated to measured (C/E) integrals over four wide energy intervals, i.e. 1 to 2, 2 to 5, 5 to 10 and

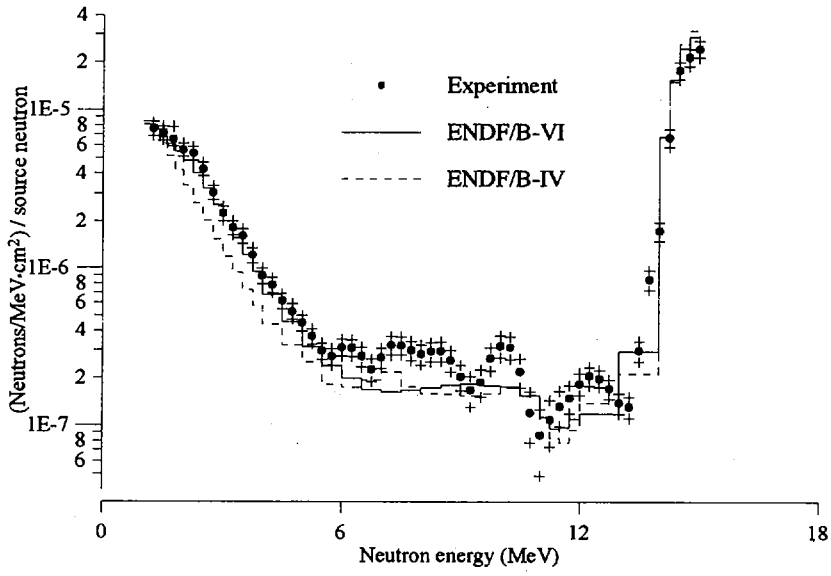

FIG. 1. Results of measurements and calculations for a 0.05 m thick slab.

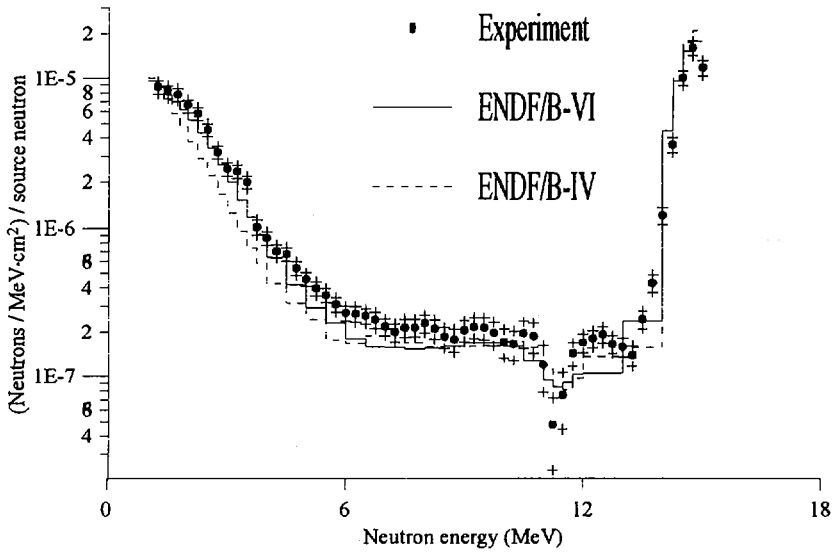

FIG. 2. Results of measurements and calculations for a 0.075 m thick slab.

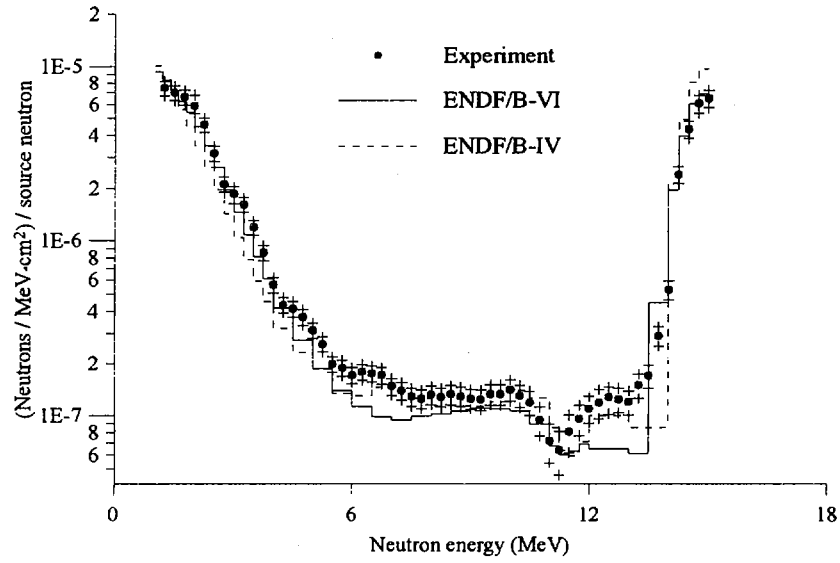

FIG. 3. Results of measurements and calculations for a 0.125 m thick slab.

TABLE I. MEASURED AND CALCULATED INTEGRALS PER SOURCE NEUTRON BEHIND A SLAB WITH A THICKNESS OF d

Energy (MeV)	Experiment	Calculation		C/E[a]	
		IV[b]	VI[c]	IV	VI
		d = 0.05 (m)			
15–10	1.864 – 5[d] (15%)	2.037 – 5	1.925 – 5	1.09	1.03
10–5	1.387 – 6 (16%)	9.103 – 6	9.810 – 6	0.66	0.71
5–2	5.697 – 6 (11%)	3.630 – 6	5.649 – 6	0.64	0.99
2–1	6.728 – 6 (11%)	6.246 – 6	6.795 – 6	0.93	1.01
		d = 0.075 (m)			
15–10	1.129 – 5 (14%)	1.380 – 5	1.227 – 5	1.22	1.09
10–5	1.183 – 6 (16%)	8.963 – 7	9.129 – 7	0.76	0.77
5–2	6.058 – 6 (11%)	3.890 – 6	5.840 – 6	0.64	0.96
2–1	7.777 – 6 (11%)	7.238 – 6	7.846 – 6	0.93	1.01
		d = 0.125 (m)			
15–10	5.395 – 6 (14%)	6.571 – 6	5.184 – 6	1.22	0.96
10–5	7.658 – 7 (13%)	6.702 – 6	5.819 – 7	0.88	0.76
5–2	4.366 – 6 (11%)	3.377 – 6	4.475 – 6	0.77	1.02
2–1	6.740 – 6 (11%)	7.101 – 6	7.274 – 6	1.05	1.08

[a] Calculated integral/measured integral.
[b] ENDF/B-IV.
[c] ENDF/B-VI.
[d] Read as 1.864×10^{-5}.

10 to 15 MeV, are listed in Table I. The intervals are chosen with respect to the reaction type contributing to the spectrum. The 15 MeV transmitted peak is composed of uncollided and elastically scattered neutrons. In the energy range higher than 5 MeV, the inelastic scattered neutrons through discrete levels and continuum excitations dominate the spectrum. Below 5 MeV, the spectrum consists of neutrons from (n, 2n) reactions and (n, n′) continuum excitations.

To interpret the comparisons between experiment and calculation, cross-sections for the ENDF/B-IV and ENDF/B-VI data libraries are presented in Table II.

The measured spectra decrease by almost two orders of magnitude in the energy range from 1 to 6 MeV and continue varying slowly in the energy range from 6 to 10 MeV. This calculational situation results in oscillations in the unfolded spectra

TABLE II. CROSS-SECTION DATA OF LEAD AT 14.8 MeV (barn)

Library	Total	Elastic	Inelastic discrete	Inelastic continuum	(n, 2n)
ENDF/B-VI	5.5139	3.0169	0.0910	0.3062	2.0931
ENDF/B-IV	5.5146	3.0102	0.1138	0.2214	1.9430

over the 6–10 MeV interval, which are, however, thought to be due to insufficient performance of the orthonormal polynomial fit in this energy interval.

As is seen from Figs 1 to 3, the spectra calculated from the ENDF/B-VI data are in good agreement with the experiment at the 15 MeV peak while the ENDF/B-IV calculations tend to become higher with increasing slab thickness. Since the values of the total and elastic cross-sections are the same in the two libraries (Table II), this could be explained with the lower (n, 2n) cross-section in the ENDF/B-IV data file compared to those of the ENDF/B-VI library. As a result, fewer neutrons are removed from the 15 MeV peak to the energy region below 5 MeV, this effect being enhanced by multiple neutron scattering. The results obtained suggest that the (n, 2n) cross-section in the ENDF/B-VI library at 14.8 MeV is more correct than that in the ENDF/B-IV data file.

The comparisons in Figs 1 to 3 and Table I show that the ENDF/B-IV calculations underestimate the measurements in the 1–5 MeV energy interval, which could be interpreted as resulting from the too soft emission spectrum of the (n, 2n) secondary neutrons [13]. The spectra calculated with ENDF/B-IV cross-sections underpredict the experiment in the 5–10 MeV interval, and the difference decreases with larger slab thickness, i.e. with increasing neutron multiple scattering. The result obtained reflects the evaluation in the 6–10 MeV interval made with isotropic neutron emission which, according to Ref. [13], does not agree with the experiment.

The spectra obtained experimentally with the use of ENDF/B-VI data show good agreement, within the experimental error, in the energy range from 1 to 5 MeV, while an underprediction of as much as 29% is observed in the energy interval from 5 to 10 MeV. The higher values assigned to the (n, 2n) and (n, n′) continuum cross-sections in the ENDF/B-VI library may contribute to bringing together the measured and calculated results below 5 MeV. The agreement indicates that the emission spectra of the (n, 2n) neutrons are correct. To confirm this fact, however, comparisons with measurements below 1 MeV are needed. The underprediction in the 5–10 MeV interval could be due to the too soft energy distribution of the secondary neutrons resulting from the level density formulas used in the compound and precompound parts of the TNG code [14].

5. CONCLUSIONS

Neutron leakage spectra through 0.05, 0.075 and 0.125 m thick lead slabs were measured in the energy range from 1 to 15 MeV. The results of the measurements were compared to the predictions by using the MCNP-4A Monte Carlo code and pointwise cross-sections from the ENDF/B-IV and ENDF/B-VI data files.

The good agreement between the measured spectra and those calculated with the ENDF/B-VI data at the 15 MeV peak and below 5 MeV, in contrast to the ENDF/B-IV calculations, implies that the (n, 2n) cross-sections and the energy distributions of neutrons from the (n, 2n) reaction in the ENDF/B-VI data library are more correct than those in the ENDF/B-IV data file. The underestimation by the ENDF/B-VI calculations in the 5–10 MeV energy region suggests that the energy spectrum of secondary neutrons from the (n, n′) pre-equilibrium continuum scattering is too soft.

REFERENCES

[1] YOUSSEF, M.Z., ABDOU, M.A., Fusion Technol. **9** (1986) 286.
[2] CHENG, E.T., "Review of the nuclear data status and requirements for fusion reactors", Nuclear Data for Science and Technology (Proc. Int. Conf. Mito, 1988), Saicon Publishing, Tokio (1988) 187.
[3] NAKAMURA, T., "Integral experiments for fusion reactors", ibid., p. 171.
[4] HANSEN, L.F., et al., Nucl. Sci. Eng. **92** (1986) 382.
[5] GOLDBERG, E., et al., Nucl. Sci. Eng. **105** (1990) 319.
[6] MAEKAWA, H., OYAMA, Y., Fusion Eng. Des. **18** (1991) 287.
[7] LOS ALAMOS NATIONAL LABORATORY, OAK RIDGE NATIONAL LABORATORY, MCNP 4A Monte Carlo N-Particle Transport Code System, CCC-200 (1994).
[8] JORDANOVA, J., et al., Progr. Nucl. Energy **28** (1994) 129.
[9] TRIKOV, L., TRIKOVA, V., Investigation of the Characteristics of Neutron Spectrometer with Stilbene Crystal, Rep. FEI-329, Institute for Energy Research, Obninsk (1972).
[10] JORDANOVA, J., J. Radioanal. Nucl. Chem. Lett. **200** (1995) 127.
[11] GADJOKOV, V., JORDANOVA, J., Nucl. Instrum. Methods A **253** (1986) 93.
[12] GADJOKOV, V., JORDANOVA, J., Comput. Phys. Commun. **31** (1984) 53.
[13] TAKAHASHI, A., et al., J. Nucl. Sci. Technol. **25** (1988) 215.
[14] FU, C.Y., Nucl. Sci. Eng. **100** (1988) 61.

CHAIRPERSONS OF SESSIONS

Session B1	C. YAMANAKA	Japan
Session B2	J.D. LINDL	United States of America
Session E	R. BOLTON	Canada
Session G1	V. GOLANT	Russian Federation
Session G2	E. SALPIETRO	European Community

SECRETARIAT OF THE CONFERENCE

T.J. DOLAN	Scientific Secretary
U. SCHNEIDER	Scientific Secretary
E. PILLER	Conference Organizer
J. WEIL	Editor
M. SPAK	Editor
I. WARDELL	Records Officer

AUTHOR INDEX

HOW TO ORDER IAEA PUBLICATIONS

No. 5, May 1997

☆ ☆ **In the United States of America and Canada**, the exclusive sales agent for IAEA publications, to whom all orders and inquiries should be addressed, is:

Bernan Associates, 4611-F Assembly Drive, Lanham,
MD 20706-4391, USA

☆ ☆ **In the following countries** IAEA publications may be purchased from the sources listed below, or from major local booksellers. Payment may be made in local currency or with UNESCO coupons.

AUSTRALIA	Hunter Publications, 58A Gipps Street, Collingwood, Victoria 3066
BELGIUM	Jean de Lannoy, 202 Avenue du Roi, B-1060 Brussels
BRUNEI	Parry's Book Center Sdn. Bhd., P.O. Box 10960, 50730 Kuala Lumpur, Malaysia
CHINA	IAEA Publications in Chinese: China Nuclear Energy Industry Corporation, Translation Section, P.O. Box 2103, Beijing
CZECH REPUBLIC	Artia Pegas Press Ltd., Palác Metro, Narodni tř. 25, P.O. Box 825, CZ-111 21 Prague 1
DENMARK	Munksgaard International Publishers Ltd., P.O. Box 2148, DK-1016 Copenhagen K
EGYPT	The Middle East Observer, 41 Sherif Street, Cairo
FRANCE	Office International de Documentation et Librairie, 48, rue Gay-Lussac, F-75240 Paris Cedex 05
GERMANY	UNO-Verlag, Vertriebs- und Verlags GmbH, Dag Hammarskjöld-Haus, Poppelsdorfer Allee 55, D-53115 Bonn
HUNGARY	Librotrade Ltd., Book Import, P.O. Box 126, H-1656 Budapest
INDIA	Viva Books Private Limited, 4325/3, Ansari Road, Darya Ganj, New Delhi-110002
ISRAEL	YOZMOT Literature Ltd., P.O. Box 56055, IL-61560 Tel Aviv
ITALY	Libreria Scientifica Dott. Lucio di Biasio "AEIOU", Via Coronelli 6, I-20146 Milan
JAPAN	Maruzen Company, Ltd., P.O. Box 5050, 100-31 Tokyo International
MALAYSIA	Parry's Book Center Sdn. Bhd., P. O. Box 10960, 50730 Kuala Lumpur
NETHERLANDS	Martinus Nijhoff International, P.O. Box 269, NL-2501 AX The Hague Swets and Zeitlinger b.v., P.O. Box 830, NL-2610 SZ Lisse
POLAND	Ars Polona, Foreign Trade Enterprise, Krakowskie Przedmieście 7, PL-00-068 Warsaw
SINGAPORE	Parry's Book Center Pte. Ltd., P.O. Box 1165, Singapore 913415
SLOVAKIA	Alfa Press Publishers, Križkova 9, SQ-811 04 Bratislava
SPAIN	Díaz de Santos, Lagasca 95, E-28006 Madrid Díaz de Santos, Balmes 417, E-08022 Barcelona
SWEDEN	Fritzes Customer Service, S-106 47 Stockholm
UNITED KINGDOM	The Stationery Office Books, Publications Centre, 51 Nine Elms Lane, London SW8 5DR

☆ ☆ Orders (except for customers in Canada and the USA) and requests for information may also be addressed directly to:

Sales and Promotion Unit
International Atomic Energy Agency
Wagramerstrasse 5, P.O. Box 100, A-1400 Vienna, Austria

Telephone: +43 1 2060 22529 (or 22530)
Facsimile: +43 1 2060 29302
Electronic mail: Sales.Publications@IAEA.Org